The calculated neutronic characteristics against reconstructed ones at (U-Pu) experiments

E.F. Mitenkova, N.V. Novikov

Nuclear Safety Institute of Russian Academy of Sciences

Presented by E.F. Mitenkova

Abstract.

The different uranium-plutonium fuel compositions are considered for next generation of sodium fast reactors. A special attention of the world nuclear professionals is drawn to the generation of benchmarks based on experiments with (U-Pu) fuel and to benchmark calculations with a detailed analysis of experimental and calculated values. The neutronic characteristics sensitivity to the extra steel allocation in the core, the presence of plutonium in the fuel rod, evaluated nuclear data files is performed for few models of BFS-62-3A. The comparative analysis of calculated values of $K_{eff,}$ spectral indices $^{U238}\sigma_f/^{U235}\sigma_f$ and $^{Pu239}\sigma_f/^{U235}\sigma_f$, and radial fission-rate distributions leads to quite different models, providing the best and the worst agreement with the experimental values. In terms of efficiency of comparative analysis between experimental and calculated values, some provisions, regarding the quality of performed neutronic calculations are considered by the example of BFS-62-3A. All calculations are carried out using MCNP5 code with the neutron history of 2×10^9.

Introduction

Experiments at critical assemblies with plutonium fuel have always been unique. In fact, during the last decade integral experiments with (U-Pu) fuel have been only maintained at BFS critical facilities at the Institute of Physics and Power Engineering (IPPE) in Obninsk (Russia). In this context, special attention of the world nuclear professionals is drawn to the generation of benchmarks based on such experiments and to benchmark calculations with a detailed analysis of experimental and calculated values. High expectations for the results of such studies initiate additional calculations in the framework of comparative analysis and justification of presented calculated neutronic characteristics. At the same time, specific layout of critical assemblies at BFS facilities (assigning as a multi-zone structure, modeling Fuel Assemblies (FA) by small fuel rods with a high axial heterogeneity, using a large number of materials of various compositions, etc.) imposes additional conditions on the computational studies with extended analysis of the dependence of key neutronic characteristics on the parameters of layout and the specificity of recording during measurements.

When comparing experimental and calculated results, the issues of benchmark model efficiency from the viewpoint of analyzed neutronic characteristics brings up. The development of an adequate calculated benchmark model requires special calculations on its adjustment and adaptation taking into account measured neutronic characteristics of the studied system. The developed benchmarks should meet several requirements that take into consideration:

- inability of full (100%) reconstruction of experimental conditions (layout geometry, temperature, peculiarities of measurements, etc.);

- sensitivity of measured characteristics to macro-features of geometric parameters of the layout and registration areas, and to changes in the composition of individual materials, etc.;
- noticeable distinctions of the sensitivity of analyzed neutronic characteristics to the same varying geometrical parameters and isotopic composition of individual materials between the experiment and the calculation.

The benchmark model, generated on the basis of calculations correlate to some extent with the peculiarities of the calculated "adjusting" code. Such conditioning increases noticeably when generating full-scale models of highly heterogeneous systems in terms of their geometric layout and the used material compositions. Any benchmark study focuses to some extent on the refinement of computational models and nuclear data. Because a comparative analysis of neutronic characteristics calculated by different codes (with different calculated models) and nuclear-data libraries (generated from various ENDF nuclear data via different procedures) is one of the main tasks of benchmark studies, both provision of calculated values to justify important specifications and indication of “adjusting” values for key neutronic characteristics used for reconstructions of experimental data are appropriate in benchmark descriptions.

By the example of BFS-62-3A [1] some provisions regarding the quality of performed neutronic calculations in terms of efficiency of comparative analysis between experimental and calculated values are considered.

Major parameters of BFS-62-3A critical assembly and calculated models

There are two configurations in BFS-2 facility to simulate the BN-600 core with a steel shield. Both configurations are composed of two layout sectors (120° and 240° degree) with different compositions. The BFS-62-3A consists of three UO_2 fuel sub-zones with the average enrichment 15, 18, 21% respectively and MOX area (between the middle and the outer sub-zones) with 17% enrichment (Fig. 1).

The BFS-62-3A core size is approximately 100 cm height, 200 cm in diameter with 50-70 cm thickness of SS reflector. BFS-62-3A assembles from tubes in diameter 50×1 mm with the step 51 mm. The BFS-62-3A critical assembly is a system without control rods in the core. The fuel assemblies (FA), safety and compensator rods, steel shield (SS) rods are simulated by the tubes, filled by pellets having various sizes, material compositions and densities in different core areas.

The analysis of neutronic characteristics is done for marked calculated areas (Fig. 1). The average coordinates of detector location and the centers coordinates of calculated cells are indicated on the left and the right scale respectively. The calculations of the effective multiplication factor K_{eff}, spectral indices and radial fission-rate distributions are performed for the pin-by-pin heterogeneous models with all features of heterogeneous structure of fuel rods [2–4] using MCNP5 [5] and libraries, generated by NJOY99 [6] (versions 161 and 304) from basic evaluated nuclear data files ENDF/B-VII.0 [7], ENDF/B-VII.1 [8], JEFF 3.1.1 [9], JENDL3.3 [10] and BROND-3 [11] at temperature T=300 K and fractional reconstruction tolerance 0.1%.

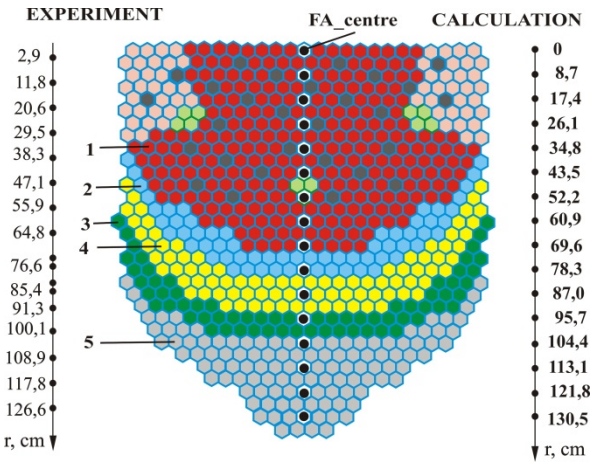

Figure 1. BFS-62-3A layout sector with calculated cells "⊙": 1 – inner (z=15%), 2 – middle (z=18%), 3 – outer (z=21%) sub-zones with UO_2 fuel, 4 – MOX area (17%), 5 – SS steel shield.

The hard spectrum and considerable discrepancies in axial and radial neutron spectra for hybrid systems compared to uranium-oxide fuel cores increase uncertainty in determinant calculated neutronic characteristics of hybrid systems. Three basic models are used in calculations to analyze the neutronic characteristics sensitivity to the local spectra features due to extra steel allocation in the core, fuel rod compositions and the ENDF/B nuclear data sources.

In *A* model the core sector (approximately 240° degree) is filled by steel tubes which is similar steel shield in the other sector. In *B* model there is the same sector structure (120° degree) as in the *A* model but the rest core area contains the UO_2 blanket instead of steel tubes. As the sticks allocation is possible in the BFS-62-3A [1] a few models with different sticks allocation in the inter-tube spaces are also considered. There are no steel sticks in *A* and *B* models. The regularly spaced steel sticks are in all core sub-zones in major *C* model (Fig. 1). The other models with different steel sticks allocation are shown in Table I.

Table I. Analyzed BFS-62-3A models with different steel sticks allocation

Sub-zone	Model				
	C	*D*	*E*	*F*	*J*
Inner	+	–	–	–	+
Middle	+	+	+	–	+
Outer	+	+	+	+	–
MOX	+	+	–	+	+

In basic models and the other models (Table I), an analysis is performed for basic neutronic characteristics (K_{eff}, $^{U238}\sigma_f/^{U235}\sigma_f$ and $^{Pu239}\sigma_f/^{U235}\sigma_f$ spectral indices, radial fission rate distributions for ^{235}U, ^{238}U, ^{239}Pu), depending on 'extra' steel (dowels) placed in inter-tube gaps of the core and ^{239}Pu replacement by ^{235}U. The impact of different evaluated nuclear data files on the calculated parameters is also considered.

Fission Rate Distribution in different calculated models

For ^{235}U, ^{238}U and ^{239}Pu the reconstructed and calculated fission rate distributions, normalized to 1.0 at r=0 are shown in Figure 2, 3 for different models.

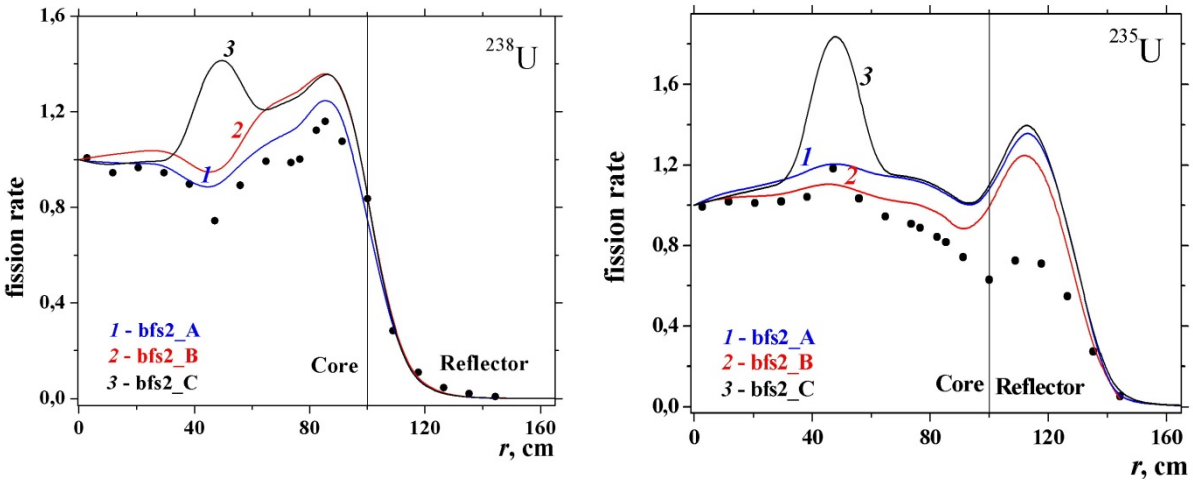

Figure 2. Calculated and experimental (•) radial ^{235}U fission rate distributions for major models

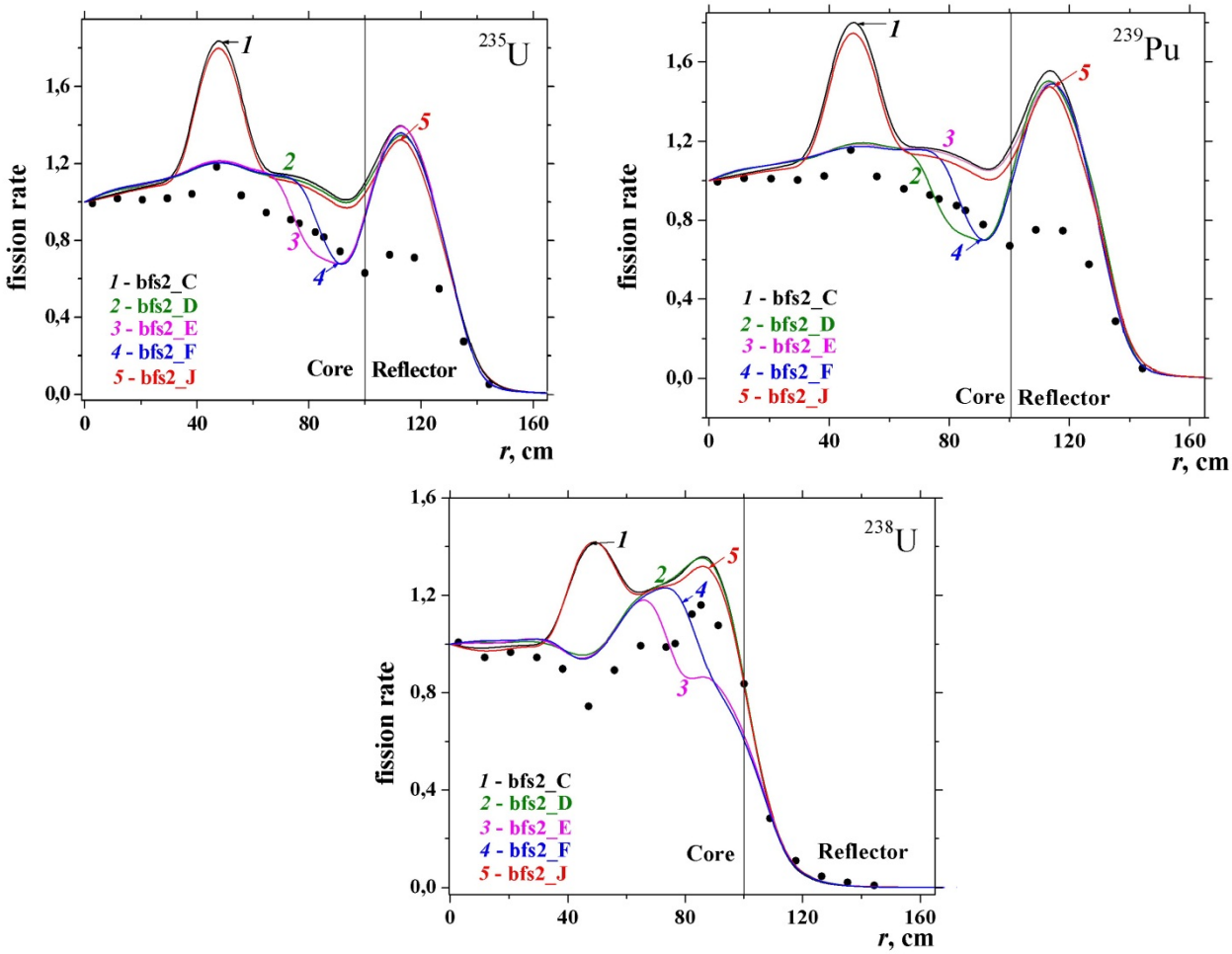

Figure 3. Calculated and experimental (•) radial fission rate distributions in the modified models

The analysis shows that for ^{235}U and ^{239}Pu the basic *A* and *B* models provide the best fission rate distribution than *C* model. Also for ^{235}U, *E* and *F* models provide a good agreement with experimental values up to $r \sim 100$ cm. *E* и *F* models provide the more compatible distributions with experiment up to $r \sim 100$ cm. For ^{239}Pu the best distributions are

observed for *D* and *F* models. For ^{238}U is rather difficult to determine the preferable model. Perhaps for the type of the distribution curve, *D* model can be considered as the best one.

Effective multiplication factor K_{eff} and spectral indices

The comparative calculations results are represented for basic models (Table II) when using nuclear data libraries, generated from ENDF/B-VII.0, ENDF/B-VII.1, JEFF-3.1.1, JENDL-3.3, BROND-3. For other models (Table I) the results are presented, using ENDF/B-VII.0 (Table III). For *B* and *C* models the discrepancies of K_{eff} and spectral indices reach 0.1 and 0.6% respectively. One more calculations are produced for *C* and *E* models with the homogenized sticks into the core gaps (C^{gom}, E^{gom}). For both *C* (C^{gom}) and *E* (E^{gom}) models the major characteristics values agree within their errors. For *A* model the detailed results of neutronic calculations are represented in [3].

Table II K_{eff} and spectral indices in FA_centre for base models of BFS-62-3A

Library	Model	K_{eff}	E_{av} (Mev)	$^{U238}\sigma_{fis}/^{U235}\sigma_{fis}$	$^{Pu239}\sigma_{fis}/^{U235}\sigma_{fis}$
ENDF/B-VII.0	*A*	1.0202 ± .0001	0.685	0.0211± .0002	0.9381 ± .0040
	B	1.0080 ± .0001	0.716	0.0216 ± .0002	0.9393 ± .0040
	C	1.0069 ± .0001	0.688	0.0204 ± .0002	0.9368 ± .0040
ENDF/B-VII.1	*C*	1.0059 ± .0001	0.688	0.0203 ± .0002	0.9358 ± .0040
JEFF-3.1.1	*A*	1.0195 ± .0001	0.685	0.0209± .0002	0.9370 ± .0040
	B	1.0076 ± .0001	0.715	0.0218 ± .0002	0.9366 ± .0040
	C	1.0068 ± .0001	0.687	0.0202 ± .0002	0.9325 ± .0040
BROND-3	*B*	*1.0053 ± .0001*	0.724	*0.0221 ± .0002*	*0.9340 ± .0040*
JENDL-3.3	*B*	0.9993 ± .0001	0.728	0.0217 ± .0002	0.9434 ± .0040
	C	0.9981 ± .0001	0.699	0.0204 ± .0002	0.9416 ± .0040
Experiment		**1.0008 ± .0005**		**0.0202 ± .0004**	**0.9370 ± .0150**

Table III. K_{eff} and spectral indices in FA_centre of BFS-62-3A

Library	Model	K_{eff}	$^{U238}\sigma_{fis}/^{U235}\sigma_{fis}$	$^{Pu239}\sigma_{fis}/^{U235}\sigma_{fis}$
ENDF/B-VII.0	*B*	1.0080 ± .0001	0.0216 ± .0002	0.9393 ± .0040
	C	1.0069 ± .0001	0.0204 ± .0002	0.9368 ± .0040
	C^{gom}	1.0068 ± .0001	0.0201 ± .0002	0.9372 ± .0040
	D	1.0080 ± .0001	0.0218 ± .0002	0.9360 ± .0040
	E	1.0083 ± .0001	0.0218 ± .0002	0.9421± .0040
	E^{gom}	1.0085 ± .0001	0.0217 ± .0002	0.9415 ± .0040
	F	1.0087 ± .0001	0.0217 ± .0002	0.9411 ± .0040
	J	1.0053 ± .0001	0.0203 ± .0002	0.9364 ± .0040
Experiment		**1.0008 ± .0005**	**0.0202 ± .0004**	**0.9370 ± .0150**

As an example the calculated neutron spectra in central FA core mid-plane, calculated for *C*, *F*, *J* models are presented in Figure 4. The discrepancies in spectra for *C*, *F*, and *J* models at intermediate energies E_n up to 10 keV cause the distinctions in fission rate distributions and spectral indices $^{U238}\sigma_{fis}/^{U235}\sigma_{fis}$ and $^{Pu239}\sigma_{fis}/^{U235}\sigma_{fis}$ up to 7,5 and 0,5% respectively (Table III).

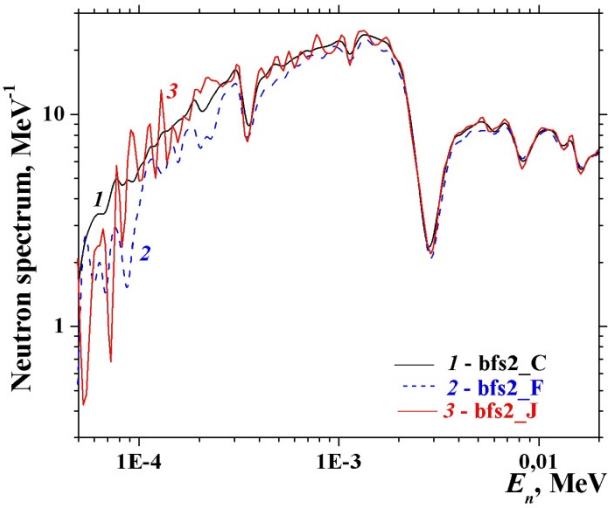

Figure 4. Comparative neutron spectra in core mid-plane for *C*, *F*, *J* models of BFS-62-3A

The Features of Fission Rate Distribution based on local axial changes

To estimate the sensitivity of fission rate distributions to local axial features the fission rate distribution at different FA planes are analyzed. On the base of *A* and *B* models, the comparative fission rate distributions are presented (Fig. 5, 6) for the core mid-plane, height *H* = 30 and 50 cm (*H* is determined from the core mid-plane). For *A* model the comparative fission rate distributions (Fig. 5) show their weak discrepancies for different axial planes. For *B* model (Fig. 6) the ^{235}U fission rate distributions have distinct discrepancies at different FA planes (the same for ^{239}Pu), the ^{238}U fission rate distributions practically have no differences.

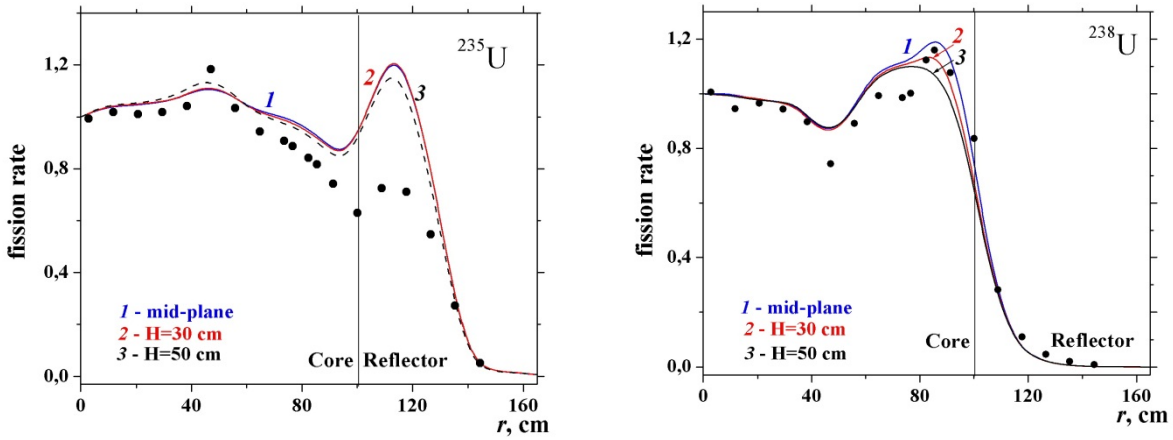

Figure 5. Comparative fission rate distributions at different FA planes in *A* model

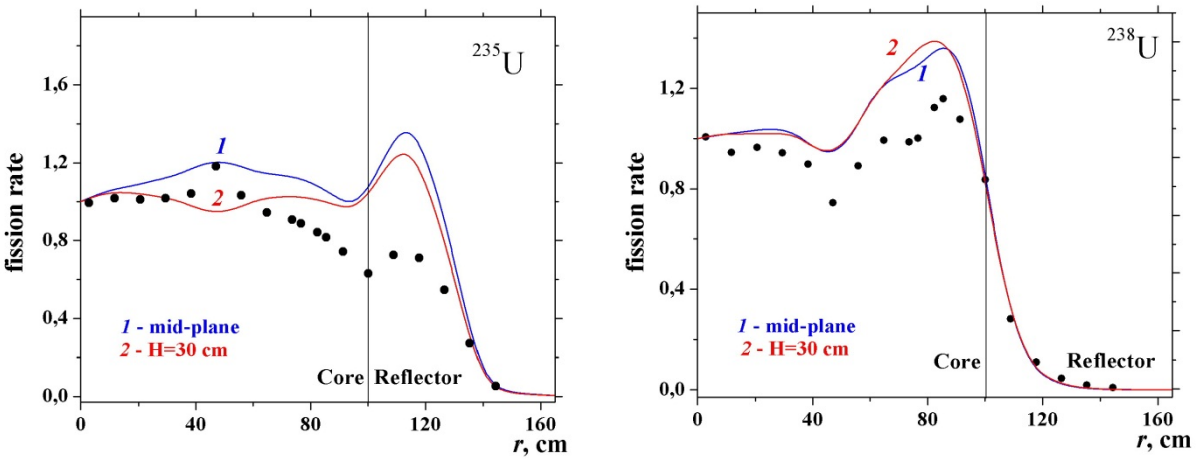

Figure 6. Comparative fission rate distributions at different FA planes in *B* model

For analyzing the fission rate sensitivity to the plutonium presence in fuel compositions, the special calculations are performed when substituting ^{239}Pu for ^{235}U. The option of replacing the plutonium in uranium enrichment 90% is done because of the presence of such uranium in fuel rods. The replacement is done in all fuel rods, containing plutonium. The rod with MOX fuel is shown in Fig. 7**.** Effect of the substituting ^{239}Pu for ^{235}U can be estimated in Fig. 8.

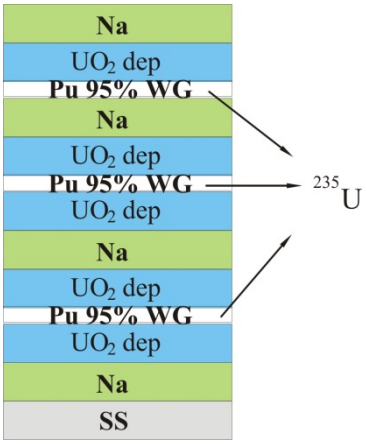

Figure 7. A rod with MOX fuel of BFS-62-3A

The Figure 8 demonstrates the radial fission rate distributions when substituting ^{239}Pu for ^{235}U and U with ^{235}U enrichment 90% in FA areas containing the plutonium [2, 3]. The fuel compositions with enrichment 90% are used in different BFS-62-3A core areas. These calculations allow estimating the sensitivity of fission rate distributions to local features of axial fuel allocation.

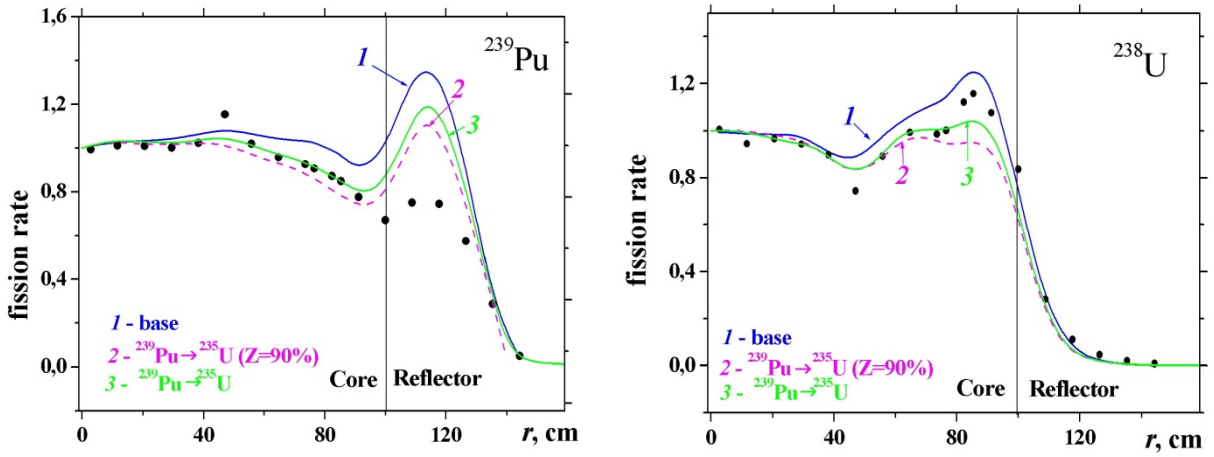

Figure 8. Calculated and experimental (•) radial fission rate distributions in *B* model

Radial fission rate distributions at different Evaluated Nuclear Data Files

In *B* model for ^{235}U, ^{238}U and ^{239}Pu the best coincidence of calculated and reconstructed values is observed for JEFF 3.1.1 (Fig.9). The peaks fall on the last row of MOX sub-zone (r ~ 85 cm) for ^{238}U and on the steel reflector (r ~ 110 cm) for ^{235}U, ^{239}Pu. The calculated fission rates overestimate up to 20% for ^{235}U and ^{239}Pu in the core. In the reflector these values are about 55 and 65% for ENDF/B-VII.0, BROND-3 and JENDL-3.3 respectively. The fission rate of ^{238}U is overestimated on about 8% for JEFF-3.1.1, ~12% for ENDF/B-VII.0 and ~15% for JENDL-3.3, BROND-3. The similar results are obtained in *A* model [4].

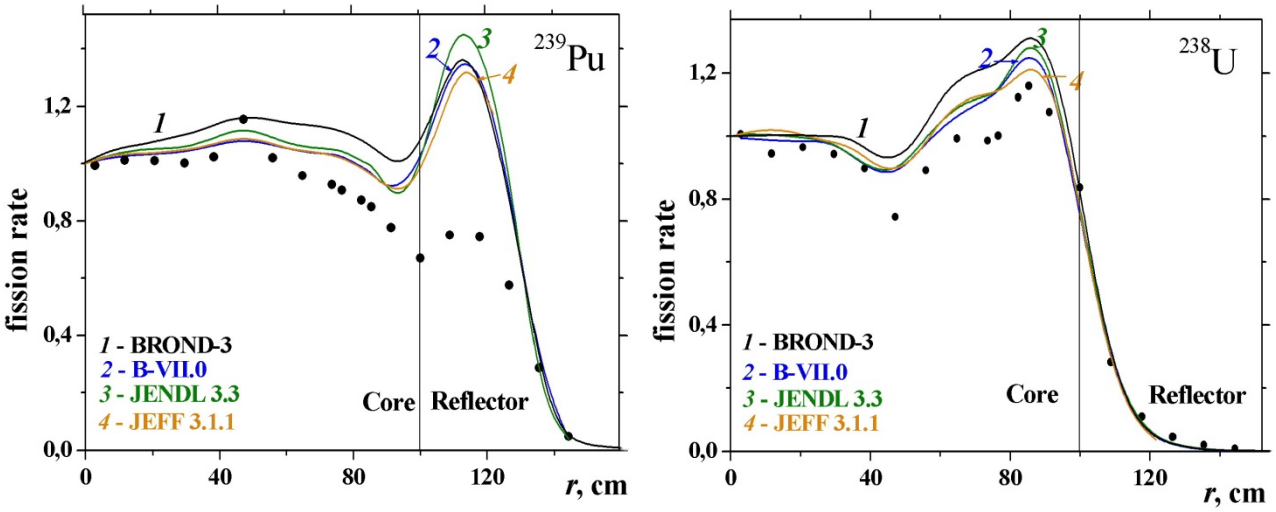

Figure 9. Calculated and experimental (•) fission rate distributions in *B* model

Summary and Conclusions

The analysis of basic neutronic characteristics has demonstrated the following:

- **Effective multiplication factor K_{eff}.** For BFS-62-3A critical assembly the MCNP5 calculations demonstrate significant sensitivity of K_{eff} to the models and ENDF libraries. In *A* model the calculated K_{eff} values overestimate from 1.1 up to 2% experimental ones. The general trend is: in *C* model the K_{eff} values are by ~ 0.1% less compared to the relevant values of *B* model. The best K_{eff} value is observed when using BROND-3 nuclear data.

- **Spectral indices.** The $^{U238}\sigma_{fis}/^{U235}\sigma_{fis}$ values are in a good agreement with the experimental data in *C* model, when using nuclear data of any standard ENDF source file, the $^{Pu239}\sigma_{fis}/^{U235}\sigma_{fis}$ values agree well with the experimental values in aforementioned models with nuclear data of any standard ENDF source.
- **Radial fission rate distributions**. For ^{235}U and ^{239}Pu the best radial distributions are achieved in *A, B, D* and *F* models. For ^{238}U is rather difficult to determine the preferable model.
- **Local features of fission rate distributions.** The knowledge of sensitivity of fission rate distributions to local features of axial fuel allocation can be taken into account when data reconstructing. The changes in height distributions of fission rate are different in considered models – they vary slightly in *A* model, the discrepancies are more noticeable for ^{235}U and ^{239}Pu in *B* and *C* models. At ^{239}Pu substitution for ^{235}U when softening neutron spectrum the calculated results are really closer to the experimental ones, and the peaks decrease by ~ 30% compared with the original distribution.

REFERENCES

[1] *BFS-62-3A Experiment: Fast Reactor Core with U and (U-Pu) Fuel of 17% Enrichment and Partial Stainless Steel Reflector*, IRPhEP Handbook, NEA/NSC/DOE (2006)1

[2] E. F. Mitenkova, N. V. Novikov. Neutronic calculation features of fast sodium cooled reactor with MOX fuel, *Atomic Energy*, Vol. 109, issue 5, pp. 253–262 (2010) (in Russian).

[3] E.F. Mitenkova, N.V. Novikov, A.I. Blokhin. The Features of neutronic calculations for fast reactors with hybrid cores on the basis of BFS-62-3A critical assembly experiments, *Proc. PHYSOR 2012*, Knoxville, Tennessee, April 15–20, 2012, ANS, (2012) (CD-ROM).

[4] E.F. Mitenkova and N.V. Novikov. Application of Nuclear Data Libraries to Fast Reactor Design with (U-Pu) fuel, *Proc. PHYTRA2*, Fez, Morocco, September 26–28, 2011, Paper 056.

[5] X-5 Monte Carlo Team, MCNP - A General Monte Carlo N - Particle Transport Code, version 5, April 2003, CCC-710.

[6] R. E. MacFarlane. NJOY99.0 - Code System for Producing Pointwise and Multigroup Neutron and Photon Cross Sections for ENDF/B Data, *PSR-480*, ORNL, USA (2000).

[7] M. B. Chadwick, P. Oblozinsky, M. Herman et al. ENDF/B-VII.0: Next Generation evaluated Nuclear Data Library for Nuclear Science and Technology, *Nucl. Data Sheets*, Vol. **102**, p. 2931 (2006).

[8] M.B. Chadwick, P. Oblozinsky, M. Herman et al. ENDF/B-VII.1 Nuclear Data for Science and Technology: Cross Sections, Covariances, Fission Product Yields and Decay Data, *Nucl. Data Sheets*, Vol. 112, p. 2887 (2011).

[9] (Ed.) A. Santamarina, D. Bernard, Y. Rugama. The JEFF-3.1.1 Nuclear Data Library, JEFF Report 22 (2009).

[10] K. Shibata, T. Kawano, T. Nakagawa et al: Japanese Evaluated Nuclear Data Library Version 3 Revision-3: JENDL-3.3, *J. Nucl. Sci. Technol.*, Vol. 39, p. 1125 (2002).

[11] A.V. Ignatyuk, B.I. Fursov. The latest BROND-3 developments, Proceedings of the International Conf. on Nucl. Data for Science and Technology, Nice, France, April 22–27, Vol. 2, p.759 (2007).

Fuel Behavior Simulation Code FEMAXI-FBR Development for SFR Core Disruptive Accident Analysis

T. Okawa[a], Y. Tsuboi[b], H. Saitou[c], I. Tatewaki[a], T. Ishizu[a], H. Endo[a]

[a] Japan Nuclear Energy Safety Organization, 4-1-28 Toranomon, Minato-ku, Tokyo 105-0001, Japan

[b] Toshiba Corporation, 8, Shinsugita-cho, Isogo-ku, Yokohama 235-8523, Japan

[c] Itochu Techno-solutions Corporation, 3-2-5, Kasumigaseki, Chiyoda-ku, Tokyo 100-6080, Japan

Presented by T. Okawa

Abstract. Japan Nuclear Energy Safety Organization (JNES) has been developing ASTERIA-FBR code system for SFR core disruptive accident analysis to contribute as a part of the regulation activity for Japanese prototype FBR, MONJU. The ASTERIA-FBR code system consists of detailed fuel behavior analysis module (FEMAXI-FBR), neutronic Monte-Carlo calculation module (GMVP), and thermal hydraulic module (CONCORD). The calculation scope of the ASTERIA-FBR covers the initiating, transitional and post disassembly expansion processes. The FEMAXI-FBR is based on LWR fuel behavior simulation code FEMAXI-6 and modified the material properties and the calculation models under steady state and transient operational condition. The FEMAXI-FBR has been verified in steady state calculations compared with those of SAS-4A code. Furthermore, the code has been validated by French CABRI slow-TOP (E12) and fast-TOP (BI2) transient calculations. Through these verification and validation, good agreement has been obtained with the FP-gas release ratio, the fuel restructuring, the gap width between pellet and cladding, and the fuel pin failure position.

1. Introduction

JNES is a special support organization for Japanese Nuclear Regulation Authority, NRA (former Nuclear and Industrial Safety Agency) to provide technical information on the safety review including incident and accident analyses of Nuclear Power Plants (NPPs). Sodium cooled Fast breeder Reactor (SFR) is capable of nuclear energy source for generating electricity and a transmutation device to reduce radioactive toxicity. In the last decades, numerous SFR designs have been studied in core performances such as Minor Actinides (MAs) burning capability, high power density and inherent core safety.

However, in terms of safety, it is desirable that SFRs should be designed to prevent Core Disruptive Accident (CDA) or to eliminate energetics induced by the super-prompt criticality during CDA, since SFR is not designed to be optimum core configuration from the view point of criticality. It is strongly required to mitigate severe re-criticality leading to the energetics during CDA. This is because the mechanical energy due to the energetics threatens the reactor vessel integrity. In order to promote a wide public acceptance for SFR construction and operation, the mechanical energy released should be evaluated against the scram failure events such as Unprotected Loss Of Flow (ULOF) which is a typical CDA initiator of SFR, since ULOF introduces positive reactivities as a result of coolant boiling and fuel-coolant interaction (FCI) which may cause super-prompt criticality within a short time **[1]**.

For the purpose of evaluating and confirming the CDA safety review, JNES has been developing ASTERIA-FBR code system **[2]** to evaluate the mechanical energy release during CDA in SFRs. The code system is composed of neutronic (Dynamic-GMVP), thermal hydraulic (CONCORD) and fuel behavior (FEMAXI-FBR) calculation modules so that the CDA phenomena could be analyzed realistically, consistently and simultaneously.

For evaluating the initial state of CDA, SAS-4A had been developed in U.S. and used extensively to analyze unprotected SFR accident sequences mechanically and it has been used in Japanese safety review for the prototype SFR, Monju. The SAS-4A evaluates fuel performance for the steady state and transient conditions, and the fuel failure condition for the initial phase. After the SAS-4A analysis, SIMMER **[3]** code calculates the fuel disruption and following sequences for the whole core accident. However, there is an inconsistency in data transfer between the SAS-4A and the SIMMER code calculation such as the fuel composition and the power. To improve the accuracy of safety analysis, fuel performance under steady state and transient conditions should be evaluated consistently.

CEDAR code developed by JAEA evaluates the performances before accident in detail, however, it cannot evaluate the fuel performance after accident conditions including fuel melting. The FEMAXI-FBR calculates from a steady state to a final CDA state. The FEMAXI-FBR evaluates up to a cladding surface. After a melting fuel flows out from the cladding surface, the fuel mass and temperature are transferred to thermal-hydraulic code CONCORD and the mass and temperature are conserved. The CONCORD calculates thermal hydraulic behavior including fuel particle formation in the outside of the cladding. Additionally, the FEMAXI-FBR continues to calculate the remaining fuel. Hence there is no inconsistency between inside fuel pin behavior and outside fuel pin behavior. The FEMAXI-FBR has been developed by adding physical models for evaluating the SFR fuel behavior based on LWR fuel analysis code FEMAXI-6 **[4]**. However, a SFR fuel is irradiated in a higher temperature and faster neutron atmosphere, and the fission gas release ratio (higher gas pressure) is higher than LWR so it is necessary to take account of these differences.

In the present work, in order to evaluate the inherent SFR phenomena, fuel restructuring and material migration models have been developed to estimate center void formation. The gas release model considers gas diffusion in a grain, growth of bubbles on a grain boundary as same as the original FEMAXI-6 code. The models have been developed for fuel melting, cavity formation and pressure caused by melting fuel expansion and gas release in cavity during the transients. For the fuel deformation and stress, a swelling model which is linked to the gas release model, and an irradiation creep model are adopted. Empirical equations on the basis of irradiation data are employed for the material properties and irradiation characteristics. For the fuel failure criteria, the failure is judged when the hoop stress of cladding exceeds the ultimate tensile strength.

This paper describes the constitution of ASTERIA-FBR code system, the calculation models in the FEMAXI-FBR and the results of fuel pin behavior analysis under steady and transient states of CABRI slow-TOP (E12) and fast-top (BI2) program in France **[5]**.

2. Development of SFR Integral core disruptive accident analysis code, ASTERIA-FBR

For the purpose of evaluating the ULOF event of SFR cores, the ASTERIA-FBR has been developed as an integrated CDA analysis code, which simulates the Initial Phase (IP), Transition Phase (TP), and Post Disassembly Expansion Phase (PDE) during the ULOF. **Figure 1** depicts the code structure of the ASTERIA-FBR that consists of three main modules, thermal-hydraulics calculation module; CONCORD, fuel behavior calculation module; the FEMAXI-FBR, and neutronic calculation module; dynamic-GMVP. These modules connect via the control module ASTERIA-CNTL, which collects the major calculation results from all modules and sends the next time step interval for each module. All calculation results are transferred as input or output data via the ASTERIA-CNTL.

3. Calculation model of FEMAXI-FBR code

3.1. General description

The FEMAXI-FBR is modified from LWR fuel analysis code, FEMAXI-6 **[6, 7]**. The original FEMAXI-6 code was developed focusing on fuel deformation during burn-up. The FEMAXI-6 has a detailed mechanistic model described for creep and plasticity of a fuel and a cladding, however additional models are needed for calculating SFR-CDA condition, that is, fuel restructuring, center-hole generation, fuel pin failure and fuel disruption. Hence JNES has introduced the models above and developed the FEMAXI-FBR. **Figure 2** shows a geometrical fuel pin model of the FEMAXI-FBR. The axial-symmetric finite element model with four joints is used for stress analysis. The physical model of the fuel pellet and the cladding is divided into maximum forty nodes in the axial direction

and ten nodes in the fuel pellet radial direction. The cladding is divided into two nodes in the radial direction. The fuel behavior model takes account of the fuel melting cavity pressure.

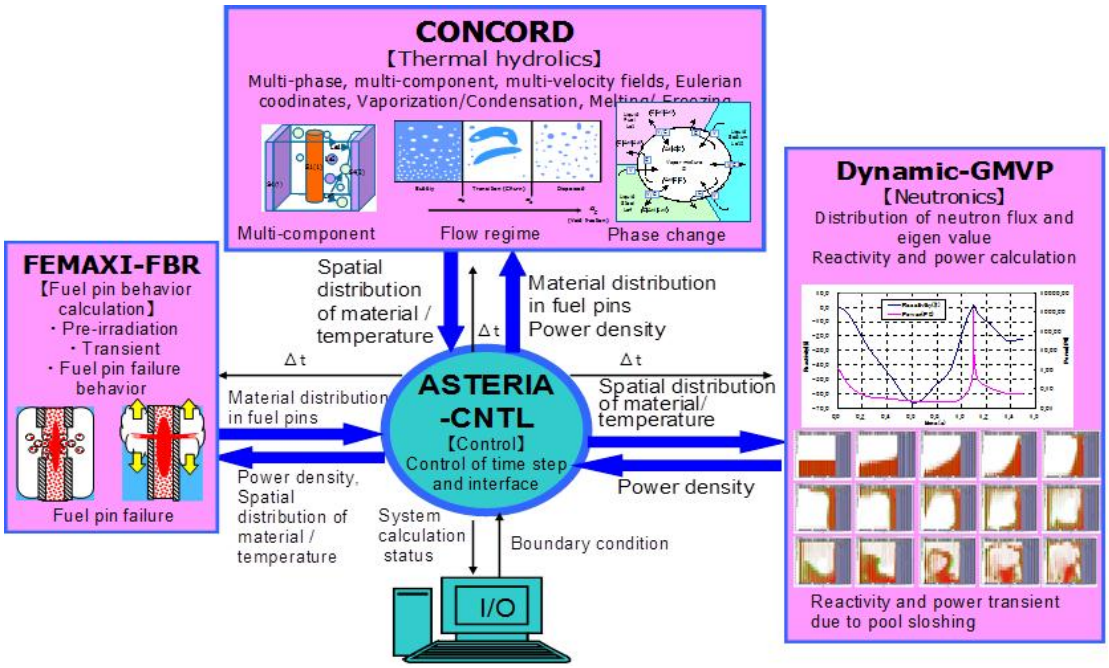

Fig. 1. ASTERIA-FBR code system.

Fuel restructuring is characterized for steady state irradiation due to the higher temperature and the higher gas release ratio than LWR fuel. The fuel restructuring phenomenon is caused by the movement of porosity to the center of a pellet, the center void formation after forming the densified region caused by sweeping out of pores and grain size growing. During transient, it is considered that a fuel failure occurs by increasing Pellet-Cladding Mechanical Interaction (PCMI) pressure as a result of increasing the pellet thermal expansion and the cavity gas pressure in the melting region. Hence the failure behavior is affected by the gas quantity, the melting radius and the melted fuel temperature which depends on the fuel condition during the steady state. In order to simulate these phenomena, the fuel restructuring model and the pore migration model with the vapor transportation are improved to analyze the center void formation and the density change. The gas release models used in the FEMAXI-6 are based on a combination of gas diffusion in a grain, growth of a grain boundary bubble and gas release from a grain boundary. The swelling and irradiation creep models are related to gas release models for stress and deformation analysis. The empirical equations of material properties and irradiation are used for analyzing cladding performance. Fuel failure is judged when the hoop stress exceeds the ultimate strength of a cladding. As the mechanical model, the FEMAXI-6 model is applied. **Figure 2** shows the analysis flow of the FEMAXI-FBR code. The fuel temperature is calculated by considering the heat generation, the thermal conductivity and the geometry of previous time step. Following the temperature calculation, the FP (Fission products) gas diffusion, the FP gas release from a pellet, the gas pressure in a fuel pin, fuel restructuring and fuel swelling are evaluated. By using these results, the contact pressure between a pellet and a cladding is analyzed. The calculation for thermal and mechanical behavior is iterated and it converges in one time step.

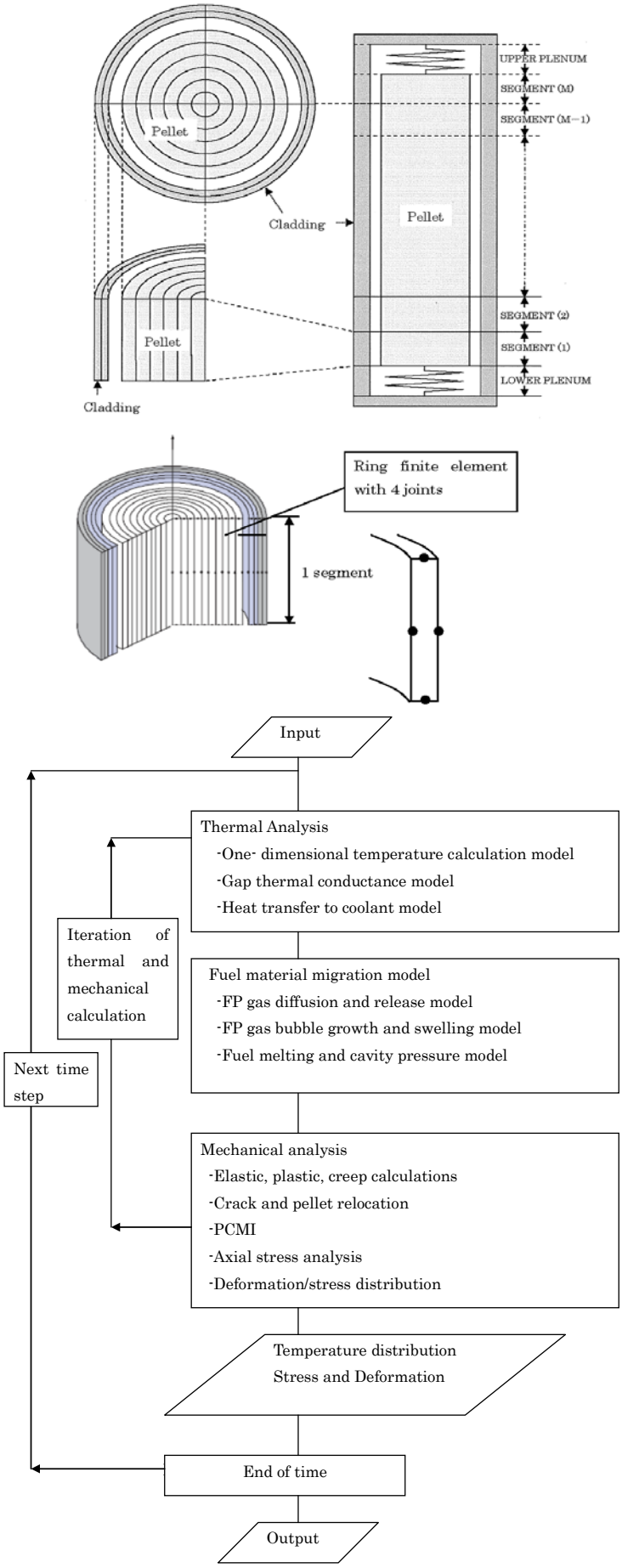

Fig. 2. FEMAXI-FBR calculation model and flow.

3.2. Thermal calculation models

The coolant temperatures of each axial node during steady and transient conditions are calculated by the power, and the coolant flow rate. One dimensional thermal conductance model in radial direction is used for the temperature calculation. Before fuel melting, the fuel thermal conductivity is the functions of a porosity and a temperature. The pellet temperature is calculated by considering the fuel restructuring and the formation of center void. The FEMAXI-FBR was modified by applying the Ross and Stoute gap conductance model in the FEMAXI-6. The detail model describes actual phenomena during operation and the model was applied to the commonly used fuel performance evaluation code CEDAR **[8]**. This model consists of three components: the gas conductance; the solid contact conduction through the cladding and the pellet surface; and the radiation between the cladding and the pellet surface. It evaluates the gap conductance under a gap width change with burnup during the steady state and with a contact force change during the transient. Hence the migration model should be included in the FEMAXI-FBR code, because the gap conductance strongly relates to fuel restructuring, depending on fuel temperature change.

3.3. Migration models

Central void formation caused by pore migration and restructuring by grain growth occurs in SFR fuel, since the temperature of SFR fuel is higher than LWR fuel.

(1) Pore migration model

A central hole is formed by pore migration and large pores are transported by vapor transportation from the central high temperature region to the peripheral cold region and by surface diffusion for small pores

(2) Fuel restructuring model

After fuel restructuring, the central void, the columnar region and the equiaxed regions are formed and densities change by pore migration. Grain growth is by movement of atoms from convex to concave side of curved grain boundary. This phenomenon is dominated by surface diffusion and grain growth.

(3) Fuel melting and cavity models

Fuel melting is judged when the fuel temperature exceeds the solidus temperature. The fuel melting radius is determined between the solidus and the liquidus radii. The melting fraction in a node depends on the solidus temperature and the liquidus temperature. Pores, cracks and bubbles in the grain boundary in the melting region combine and form a cavity. Gases in pores, cracks and bubbles collect in the cavity. The pressure is calculated by using the cavity volume and an amount of gas. **Figure 3** is the sketch of a melting cavity model.

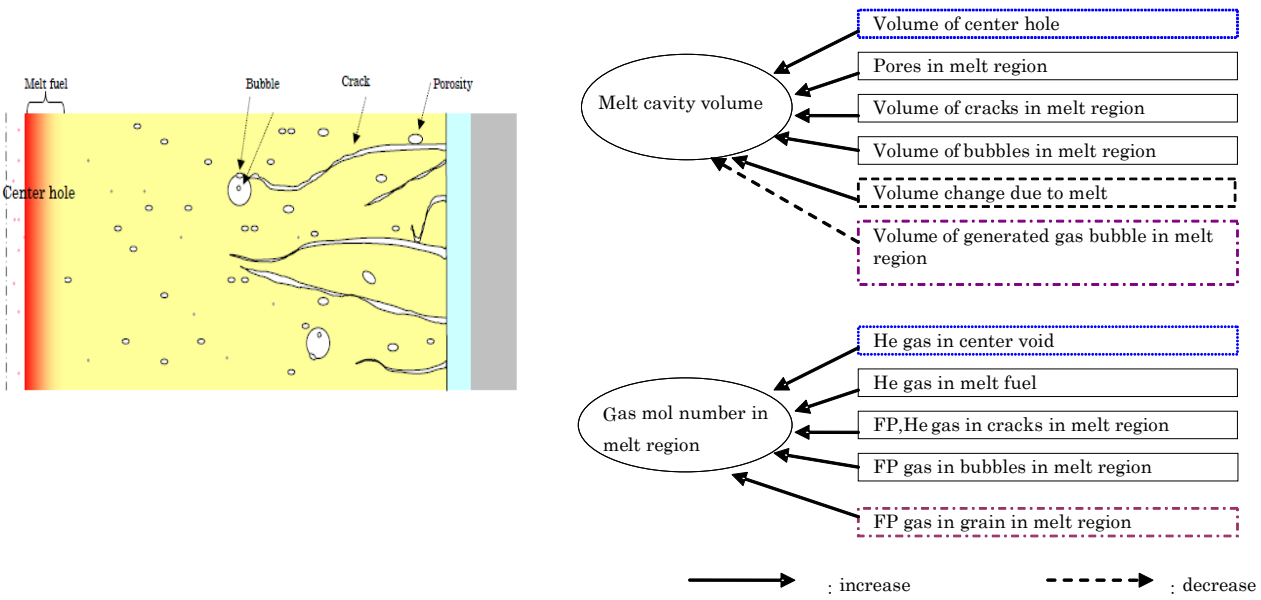

Fig. 3. Fuel migration model.

3.4. Mechanical calculation models

(1) Stress calculation model

Mechanical analysis of a pellet employs Finite Element Method (FEM) adopted in the FEMAXI-6. The ring FEM model with four joints and axial deformation in the pellet and the cladding is adopted. Due to thermal expansion difference, axial interaction between the pellet and the cladding is considered "slip model." When fuel melting occurs, radial direction meshes for the temperature calculation are not re-meshed because temperature is calculated including the melting region.

(2) Mechanical properties of cladding

Since the FEMAXI-FBR takes account of the thermal expansion, elastic deformation, irradiation creep and swelling, in general, the SFR fuels are used under high temperature and large damage dose. Material properties for swelling, and irradiation creep of cladding, etc. were made on the basis of SFR irradiation database.

(3) Criteria of failure

Fuel failure is judged to occur when the cladding hoop stress is higher than the Ultimate Tensile Strength (UTS).

4. Validation of FEMAXI-FBR for steady state

The fuel pin characteristics under the steady state condition are calculated using the FEMAXI-FBR and the SAS-4A, and the results are compared with the experimental data. **Table I** indicates the results on CABRI-I Rig-1 pin for fast-Transient OverPower (TOP) BI2 test, of which burn-up corresponds to about 1at.%. The FEMAXI-FBR estimates the fission product gas release rate precisely. **Figure 4** shows a comparison between the FEMAXI-FBR and the SAS-4A on the fuel pellet radial expansion, the fuel restructuring, and the central hole generation at the peak power node. Although the results of the FEMAXI-FBR underestimates a little the central hole radius and the outer radius of columnar region of the experimental data, the FEMAXI-FBR simulates the conditions of fuel pin at the steady state before the transient with an equivalent calculation accuracy of the well validated SAS-4A code.

Table I Comparision of Experiment and Analyses by SAS-4A and FEMAXI-FBR on MOX Fuel Characteristics at the Steady State

Item	unit	Experiment (PIE data)	SAS-4A	FEMAXI-FBR
Burn-up	at%	0.95	0.97	0.94
FP-gas release ratio	%	40	39	40
Fuel pellet outer radius	mm	3.27	3.34	3.28
Outer radius of equiaxed region	mm	2.34	2.48	2.69
Outer radius of columnar region	mm	2.06	2.00	1.82
Central hole radius	mm	0.6	0.5	0.45
Gap between fuel pellet and cladding	μ m	20	0	8

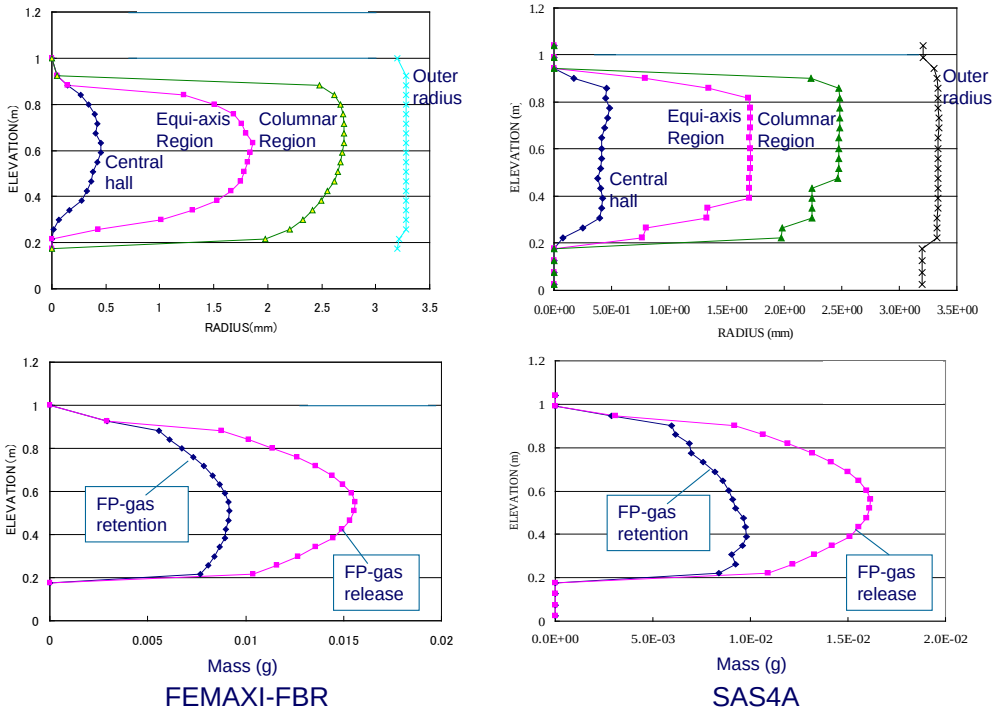

Fig. 4. Comparison between FEMAXI-FBR and SAS-4A calculation results for fuel pellet radial expansion, fuel restructuring and center hole generation.

5. Validation of FEMAXI-FBR for CABRI slow and fast-TOP transient states

5.1. Experimental condition

In-pile simulations of accidental SFR transients have been conducted at French CABRI reactor operated by CEA at Cadarache centre about thirty years ago. The fuel specifications and test conditions of slow-TOP E12 and fast-TOP BI2 are shown in **Table II.** The fuel dimensions are typical SFR values. **Figure 5** shows power insertion profiles at the transient for E12 and BI2

The E12 test fuel pin had been irradiated up to 11.5 at% in French Phenix prototype SFR. The slow-TOP E12 test was performed within the frame work CABRI-2 experiment program for clarifying the fuel failure limit under operational transients and accidents. In E12 test, the power increment is ～ 1% of nominal power per sec (**see Figure 5**).

The purpose of fast-TOP test, BI2, is to clarify the fuel failure mode, and the migration, fission gas effects and Fuel Coolant Interaction (FCI) before coolant boiling with using pre-irradiated fuel pin. It is very important to find out the phenomenon after FCI. The BI2 burn-up is 0.95 at%. The maximum BI2 power of $256P_{max}/P_0$ is input at coolant temperature 850 ^oC. The transient is a single-power burst generated by a sudden step input of the reactivity initiated at a very low power level and terminated by the negative temperature coefficient of reactivity, the resulting in a Gaussian, or a bell-shaped power curve.

5.2. Slow TOP experiment, E12 test

The fuel failure point from the bottom of the fuel column is shown in **Table III**. As transient overpower condition, the power was increased up to 81kW/m. **Figure 6** shows the comparison of melting fuel region between the experimental data and the calculation result of the FEMAXI-FBR. The FEMAXI-FBR simulates fuel pin failure behavior such as the melt fraction at the fuel pin failure time and the failure location are in good agreement with the experimental data.

Fuel failure occurs when the hoop stress caused by PCMI stress exceeds the ultimate strength. The failure will take place at the high temperature location such as near axially top region. The PCMI pressure is caused by difference between pellet expansion and cladding expansion due to temperature increase during the transient. The pellet expansion is caused by the thermal and swelling deformation before melting. The cladding expansion occurs by the thermal expansion. At fuel melting, melting

cavity pressure adds on the inner side of pellet and increase the PCMI stress. In the analysis of E12 test, the fuel did not melt at the failure node. The measured data shows that the melting cavity extends from 200 mm to 613 – 660 mm and failure position is 670 mm from the bottom of the fuel column. The analysis result is consistent with the measured value.

5.3. Fast TOP experiment, BI2 test

In the BI2 test, we tried to compare the validated SAS-4A code and the FEMAXI-FBR code. The fast-TOP experimental results are shown in **Table IV and Figure7.** The FEMAXI-FBR cladding failure position from the bottom of fuel column is good agreement with the SAS-4A results. At the fuel failure zone, the cladding UTS became lower than the cladding hoop stress by inner gas pressure increasing. The FEMAXI-FBR calculation position 42 - 52cm (an axial calculation mesh length) covers the experimental position. The fuel failure occurs in the no boiling zone, since the transient power was inserted before coolant boiling. The FEMAXI-FBR fuel melting starting times, 15.359 sec coincides with that of the SAS-4A code, and also the cladding failure initiation time of the codes coincides with that of experiment. The input power to fuel failure with the FEMAXI-FBR code is corresponding to that of the SAS-4A. There is no marked difference between the FEMAXI-FBR code results and the experimental results. The both FEMAXI-FBR and SAS-4A results are good agreement with experimental data.

Table II E12 and BI2 CABRI MOX Fuel Specifications and Test Conditions

Items	Unit	Slow TOP E12 Test	Fast TOP BI2 Test
1. Fuel pellet			
Pellet diameter	mm	5.427	6.4
Pellet height	mm	8.0	10.0
Pellet density	%TD	95.5	93.1
Grain size	μm	10.0	6.0
Pellet dimension		Flat end	Flat end
U-235 enrichment	%	0.6	0.6
Pu weight fraction	%	27.0	15.5
2. Cladding			
Outer diameter	mm	6.55	7.6
Inner diameter	mm	5.65	6.6
Material		5-15Ti CW	SUS-316
3. Fuel pin			
Pin length	mm	1050.0	1050.0
Lower blanket	mm	200.0	200.0
Fuel length	mm	750.0	750.0
Upper blanket	mm	100.0	100.0
Gas plenum length	mm	450.0	450.0
Gap	μm	223.0	200.0
Initial gas pressure	MPa	0.1	0.1
Gas contents	%	100%-He	100%-He
4. Coolant			
Pressure	MPa	0.76	0.30
Temperature	^{o}C	386	389
Velocity	kg/cm^{2}s	0.280	0.148

Table III Slow-TOP E12 Transients Analysis Results with Experimental Data

	Experiment	Analysis
Linear heat ratio at failure (kW/m)	81	81
Fuel failure point from bottom of fuel column (mm)	670 with microphone 570 - 710 with the hodoscopes	653 - 720

Table IV Fast-TOP BI2 Transient Analysis Results with Experimental Data

Items	Experimental data	FEMAXI calculation	SAS-4A calculation
Cladding failure position from bottom of fuel column (cm)	51	42 - 52	52
Input power up to fuel failure (kJ/g)	-	1.023	1.024
Fuel melting initiation time (sec) *TOP initiation time: 15.3 sec	-	15.359	15.360
Fuel cladding failure initiation time (sec)	15.38	15.383	15.380
Failure time from TOP initiation (msec)	80	83	80

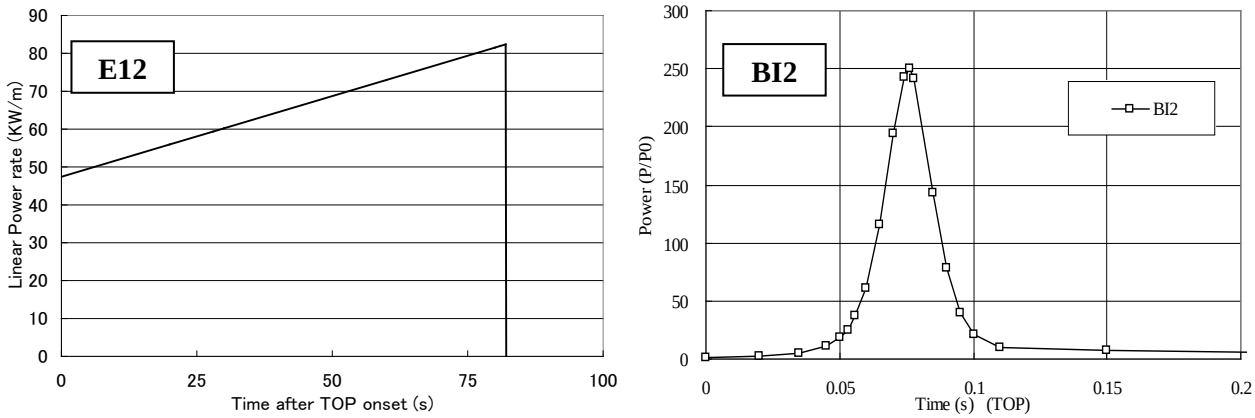

Fig. 5. Comparison of input power at the transient for E12 (left-hand side) and BI2 (right-hand side).

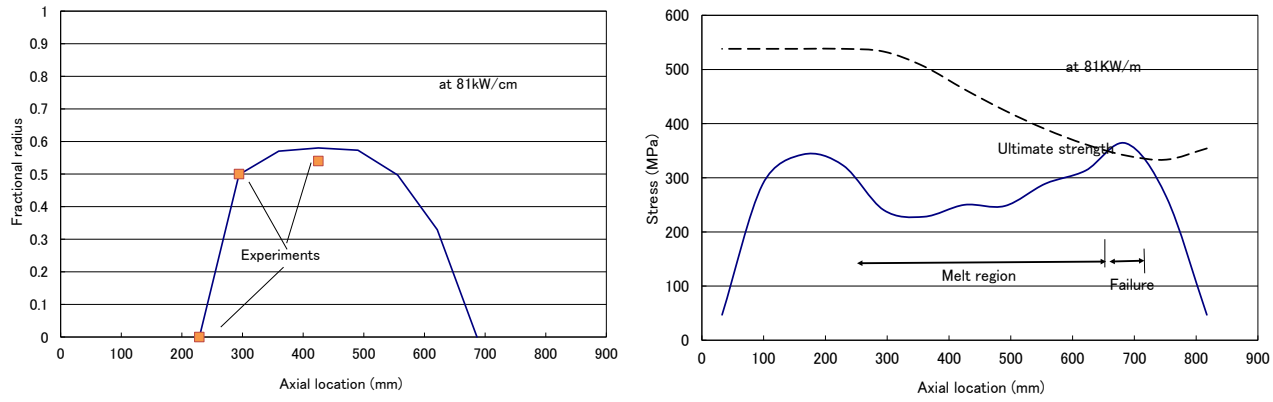

Fig. 6. Comparison of the melting radius between E12 experiment and analysis results, and hoop stress and failure position at 81kW/m.

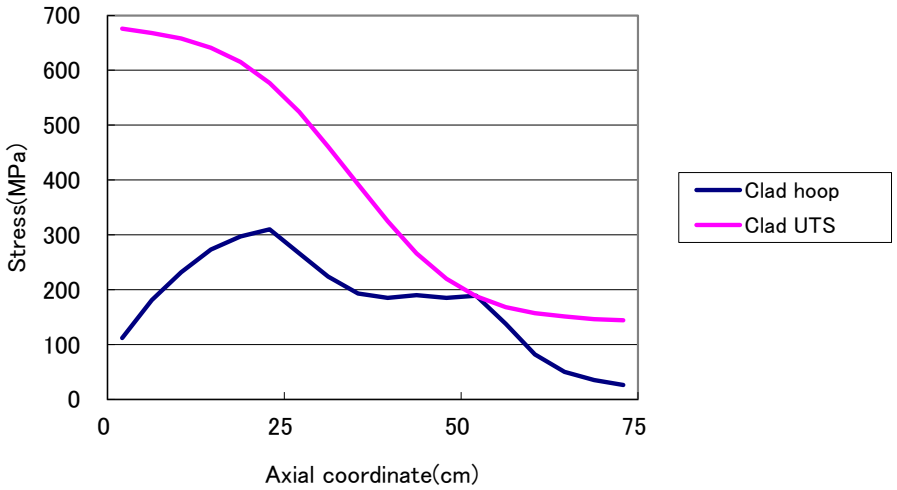

Fig. 7. Calculation result of hoop stress and UTS at the failure position.

6. Conclusions

(1) In JNES, the FEMAXI-FBR has been developed for improving the accuracy of safety analysis of SFR fuels. It can evaluate the fuel performance under steady, transient and fuel melting consistently. In order to evaluate the characteristic of SFR fuels such as central hole formation and fuel restructuring caused by high temperature, the material migration model and the grain growth model were developed. For the transient, the fuel melting model, the cavity formation and the cavity pressure model by considering melting fuel expansion and gas in the cavity are developed.
(2) In the steady state calculation, the FEMAXI-FBR simulates fuel pellet radial expansion, fuel restructuring, and center hole generation, comparing with experimental results at the peak power node.
(3) The FEMAXI-FBR evaluates the fuel failure positions for the slow-TOP E12 and fast-TOP BI2 experiments precisely. In other word, the code is possible to simulate PCMI failure for the slow-TOP and also cladding rapture phenomenon for the fast-TOP.

REFERENCES

[1] T. Ishizu, H.Endo, I. Tatewaki, T. Yamamoto, and N. Shirakawa, “Development of Integrated Core Disruptive Accident Analysis Code for FBR –ASTERIA-FBR,” Proceedings of 19th International Conference on Nuclear Engineering (ICONE19), Chiba, Japan (2011).
[2] T. Ishizu, H.Endo, I. Tatewaki, T. Yamamoto, and N. Shirakawa, “Development of Integrated Core Disruptive Accident Analysis Code for FBR – ASTERIA-FBR,” Proceedings of 2012 International Congress on Advances in Nuclear Power Plants (ICAPP12), Chicago, USA (2012).
[3] A. E. Walter and A. B. Reynolds, Fast Breeder Reactors, Pergamon Press, New York (1980).
[4] M. Suzuki, “Light Water Reactor Fuel Analysis Code FEMAXI-6 (Ver. 1) - detailed Structure and User’ Manual –,” JAEA-Data/Code 2005-003, (2005).
[5] A.M. Tentner, “Severe Accident Approach – Final Report Evaluation of Design Measures for Severe Accident Prevention and Consequence Mitigation,” ANL-GENIV-128, Nuclear Engineering Division, Argonne National Laboratory, (2010).
[6] Y. Tsuboi, H. Endo, T. Ishizu, I. Tatewaki, H. Saito and H. Ninokata, “Analysis of fuel pin behavior under slow-ramp type transient overpower condition by using the fuel performance evaluation code ‘FEMAXI-FBR’,” Journal of Nuclear Science and Technology, Volume 49, Issue 4, 2012
[7] Y. Tsuboi, H. Endo, T. Ishizu, I. Tatewaki, H. Saito and H. Ninokata, “Sensitivity analysis of fuel pin failure performance under slow-ramp type transient overpower condition by using a fuel performance analysis code FEMAXI-FBR,” Journal of Nuclear Science and Technology, Volume 49, Issue 10, (2012).
[8] Nagai, H. et a l . A development of fast breeder reactor fuel pin performance code - CEDAR. Presented at the 1983 Annual Meeting of the Atomic Energy Society of Japan, 1983, March.

Physical and numerical methods for the dynamic behavior of the Fast Reactor cores

Daniel BROC[a], ***Jérome CARDOLACCIA***[a], ***Sabine DURAND***[a], ***David GENTET***[b], ***Jean Paul MAGNAUD***[a]

[a] CEA, DEN, DM2S, F-91191 Gif-sur-Yvette, France

[b] CEA, CAD, DER, 13 108 Saint Paul lez Durance, France

Presented by Edouard HOURCADE

Abstract.

In the frame of the GEN IV Forum and of the ASTRID Project, a program is in progress in the CEA (France) for the development and the validation of numerical tools for the simulation of the dynamic mechanical behavior of the Fast Reactor cores, with both experimental and numerical parts.

The cores are constituted of Fuel Assemblies (of FA) and Neutronic Shields (or NS) immersed in the primary coolant (sodium), which circulates inside the Fluid Assemblies. The FA and the NS are slender structures, which may be considered as beams, form a mechanical point of view. The dynamic behavior of this system has to be understood, for design and safety studies. Two main movements have to be considered: global horizontal movements under a seismic excitation, and opening of the core. The dynamic behavior of the core is strongly influenced by contacts between the beams and by the sodium. The contacts between the beams limit the relative displacements. The fluid leads to complex interactions between the structures in the whole core.

The paper presents the physical and numerical methods and tools used to describe and simulate the phenomena. A key point is the Fluid Structure Interaction (or FSI): the interactions between the beams and the liquid sodium. The fluid movement is assumed to be described by the equations of a perfect fluid. Simple and efficient homogenization methods may be used to reduce the size of the problem. These methods are integrated in a general computer code, CAST3M developed at the CEA Saclay. This computer code allows to take into account the impacts between the beams. Some applications are presented.

1. Background, presentation of the dynmaic of the Fast Reactor cores

A fast reactor core is schematically constituted of Fuel Assemblies and Neutronic Shields, immersed in the primary coolant (sodium). Two main physical phenomena have a strong influence on the dynamic behavior of this system: the impacts between the beams and the interactions with the fluid. The fluid leads to “inertial effects”, with globally lower vibration frequencies, and “dissipative effects”, with higher damping. Two kinds of excitation (or movements) are considered in the studies of the dynamic behavior of the core: a seismic excitation, with a global horizontal movement for the core, and an opening of the core.

The section 2 presents a short description of the mechanical structures of the reactor, with the kinds of movements to be considered. The section 3 presents some elements on the FSI: physical phenomena and numerical methods. It has to be noticed that, for many applications, the methods to take into account the FSI phenomena have been improved from the first studies on the Fast Reactors, in the understanding of the physical phenomena, in the numerical methods, and in the capacities of the computers. The section 4 summarizes the different available numerical tools, corresponding to the different physical phenomena. The last section presents some examples of application.

2. Description of the structures

The core is constituted of different kinds of beams (fuel assemblies, neutronic shields, etc) immersed in the sodium. The FIG. 1 presents an example of Fuel Assembly and Neutronic Shields and a picture of a mock up tested during the Symphony program (references [5] and [6]), with 5 FA rows and 4 NS rows. The confinement is high (thin space between two assemblies), leading to high Fluid Structure Interaction phenomena (see section 3). Impacts may occur betwwen the beams, at the so-called "pads level" or at the top. The feet of the beams are inserted in a grid plate, with gaps which may lead to an important damping.

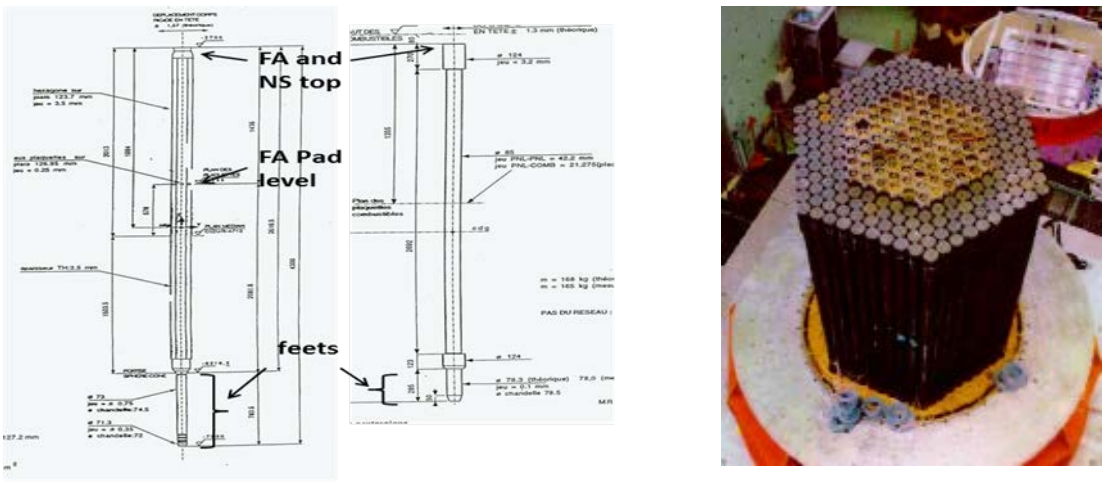

FIG. 1: Fuel Assemblies and Neutronic Shields, hexagonal Symphony mock up

The models have to be able to describe different phenomena, to consider different kinds of strucures, with different excitations. The fluid has to be taken into account, as well as the different non linear behaviors of the structures: impacts between the beams, gaps at the feet and plastification of the feet. As this model has to be used for design studies different kinds of structures may be considered, for example the adjunction of a second pads level or structures to limit the displacements of the tubes bundle (restrained configuration core). Different excitations are of interest, as seismic excitations, leading to global horizontal movements of the beams, with a risk of plastification of the feet, or excitation leading to an opening of the core, with changes of the reactivity.

3. Fluid Structure Interaction in the Fast Reactor cores

3.1. Elements on the Fluid Structure Interaction phenomena in a Fast Reactor core

If a vibrating structure is immersed in a dense fluid, the fluid leads, schematically, to "inertial" and "dissipative" effects (reference [1]). The "inertial effects", with globally lower vibration frequencies, correspond to the kinetic energy of the fluid. For a structure with various degrees of freedom, this effect, also called "added mass" depends on the movement. For example, in the case of a tubes bundle, the frequencies are lower for a flowering movement than for a globally horizontal movement. The "dissipative effects", with higher damping for the structure, correspond to head loss in the fluid movements between the assemblies. In the case of a Fast Reactor core (FIG. 2) the confinement is high. The space between two assemblies is thin and the fluid velocity may be much higher than the structure ones (a). Important FSI will take place, with inertial effects (with lower natural frequencies) and dissipative effects also (with higher damping). FSI will be higher for "opening" modes (b, decrease of 60% of the frequencies) and lower for global movements (c, decrease of 15% of the frequencies).

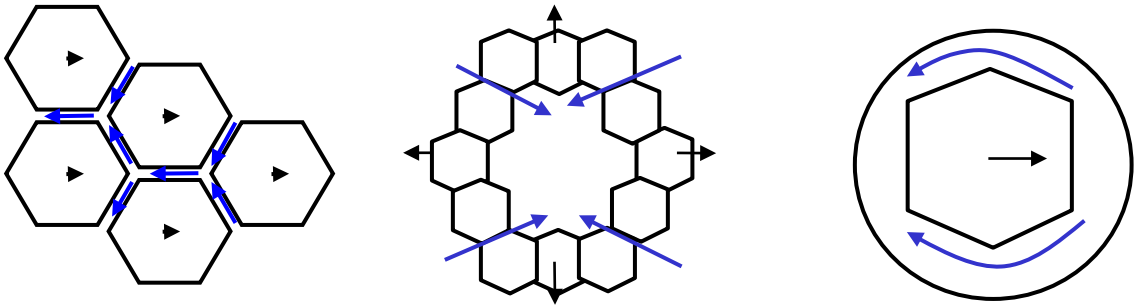

FIG. 2: Elements on FSI phenomena in a Fast Reactor core

Methods to take into account FSI

It is necessary, in a FSI problem, to solve the coupled system constituted of the structure equations and the fluid equations. In the general case, the Navier-Stokes equations are used for the fluid. In the case of little displacements, the Euler equations (more simple than the Navier Stokes) may be used. This method theoretically only considers the "inertial" effects, even if the "dissipative" ones may be roughly takes into account by using a Rayleigh damping. The use of homogenization methods for the dynamic behaviour of tubes bundles immersed in a fluid reduces the size of the problem and allow to perform simulations and analysis on a whole core.

3.2. Homogenization methods

Homogenization methods have been studied and developed for many years for tubes bundles immersed in a fluid. The homogenization method presented in this section is based on the results of Brochard and Hammami (reference [2]), and has been developed and presented by Sigrist-Broc (references [3] and [4]). The fluid motion is assumed to be described by the perfect fluid equation (Chassaing 2010). The homogenization method is based on the assumption that one elementary cell, corresponding to one tube, is a two degrees of freedom system: the acceleration of the tube and the mean acceleration of the fluid. FIG. 3 presents an elementary cell corresponding to one tube, for a bundle of circular tubes arranged in a square array. The building of the homogenization method doesn't depend on the kind of bundle, and could be made on an hexagonal array, as in the case of the Fast Reactor cores.

.

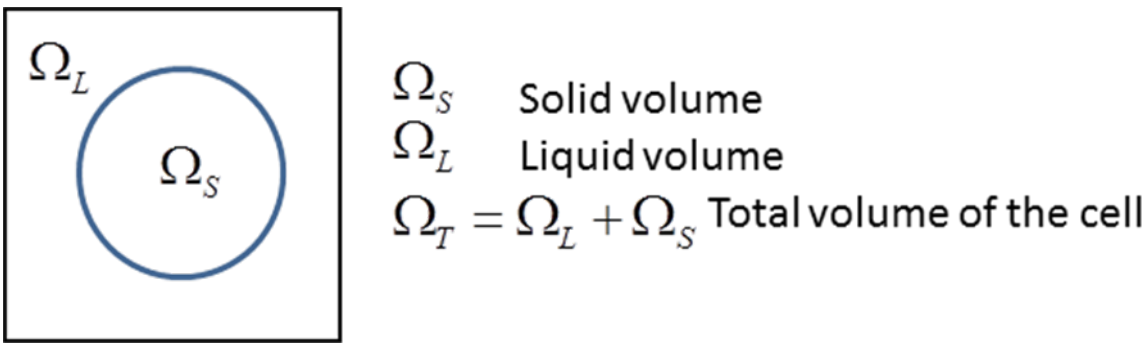

FIG. 3: Tubes bundle, elementary cell

Forces applied by the fluid on an elementary tube

The force applied by the fluid to one tube is assumed to be: $F = -m_a\ddot{\vec{X}_S} + (m_a + \rho\Omega_S)\ddot{\vec{X}_L}$, where m_a is the added mass and $\ddot{\vec{X}_L}$ the mean acceleration in the cell, defined as: $\ddot{\vec{X}_L} = \left(\frac{\Omega_L}{\Omega_T}\right)\ddot{\vec{x}_L} + \left(\frac{\Omega_S}{\Omega_T}\right)\ddot{\vec{X}_S}$. $\left(\frac{\Omega_L}{\Omega_T}\right)$ and $\left(\frac{\Omega_S}{\Omega_T}\right)$ are the ratio of fluid and solid on the total volume of the fluid cell. $\ddot{\vec{x}_L}$ is the acceleration of the fluid in the cell and $\ddot{\vec{X}_S}$ is the solid acceleration. If and $\ddot{\vec{X}_S} = \ddot{\vec{X}_L} = \gamma$, an Archimedes force $\rho\Omega_S\gamma$ is applied to the tube. FIG. 4 presents the fluid acceleration for two cases: on the left of the figure: $\ddot{\vec{X}_S} = 1 \; and \; \ddot{\vec{X}_L} = 0$, on the right of the figure: $\ddot{\vec{X}_S} = 0 \; and \; \ddot{\vec{X}_L} = 1$.

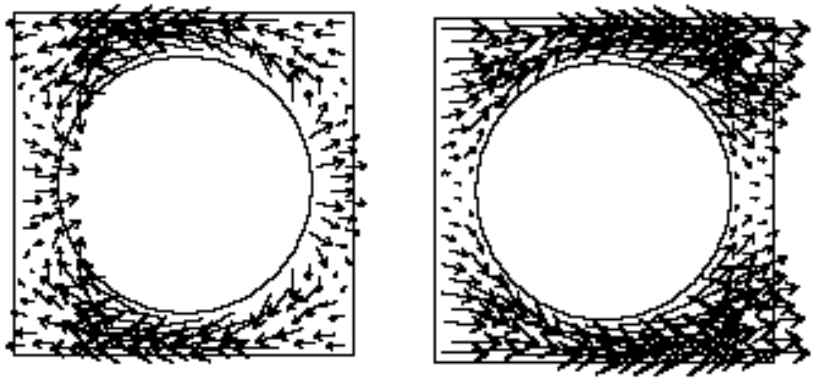

$\ddot{X}_S = 1$ and $\ddot{X}_L = 0$ $\qquad$ $\ddot{X}_S = 0$ and $\ddot{X}_L = 1$.

FIG. 4: Fluid acceleration in an elementary cell

Equations for the fluid

Equations for the fluid may be derived from the momentum equation for the fluid in the cell on the fluid volume Ω_L : $\rho\Omega_L\ddot{\vec{x}}_L = -\Omega_T\vec{\nabla}P + m_a\ddot{\vec{X}}_S = \ddot{\vec{X}}_S - (m_a + \rho\Omega_S)\ddot{\vec{X}}_L$.

By using the coefficient $J = (m_a + \rho\Omega_S)/(m_a + \rho\Omega_S + \rho\Omega_T)$ and by using the mean acceleration in the cells $\ddot{X}_L$ this momentum equation becomes: $\rho\ddot{\vec{X}}_L = -(1-J)\vec{\nabla}\overline{P} + \rho J\ddot{\vec{X}}_S$.

The mass equation for the fluid is $P = -\rho c^2(\Omega_T/\Omega_L)\nabla\cdot\vec{X}_L$.

Equations for the solid

Equations for the solid may be written by introducing the mass correction $M^* = \rho(J\Omega_T - \Omega_S)$).

It may be demonstrated that the force applied by the fluid on the tube is: $-M^*\ddot{\vec{X}}_S - J\Omega_T\vec{\nabla}P$ and the equation for the solid becomes: $(M + M^*)\ddot{\vec{X}}_S + J\Omega_T\vec{\nabla}P + K\ddot{\vec{X}}_S = 0$ (reference [3]).

Numerical equations

Numerical equations may be derived, by using the basis of the so-called $(\mathbf{u}, p, \varphi)$ formulation (structure displacement field, fluid pressure and potential displacement fields). More details may be found in the references [3] and [4]. The numerical equation obtained for the fluid is: $-\mathbf{C}\,\ddot{\mathbf{X}}_L + J\mathbf{C}'\,\ddot{\mathbf{X}}_S - \mathbf{A}\,\ddot{\mathbf{P}} - (1-J)\,\mathbf{G}\,\mathbf{P} = 0$, where the matrix $\mathbf{C}'$ corresponds to the term $\rho\,\ddot{\vec{X}}_L = \rho\, J\,\ddot{\vec{X}}_S$ in the fluid momentum equation.

The numerical equation obtained for the solid is: $(\mathbf{M}+\mathbf{M}^*)\,\ddot{\mathbf{X}}_S + \mathbf{K}\,\mathbf{X}_S - \mathbf{C}\mathbf{P} + J\mathbf{C}'\,\mathbf{P} = 0$ with the same matrix $\mathbf{C}'$ used in the fluid equation, corresponding here to the force applied by the fluid to the tube, expressed as $J\,\Omega_T \vec{\nabla} P$.

This system is modified, in order to get a symmetric formulation. The variable Φ, defined as $\ddot{\Phi} = P$, is introduced and the previous system becomes:

$$\begin{bmatrix} \mathbf{M}+\mathbf{M}^* & \mathbf{0} & -\mathbf{C}+J\mathbf{C}' \\ \mathbf{0} & \mathbf{0} & -\mathbf{A}(\Omega_L/\Omega_T) \\ -\mathbf{C}+J\mathbf{C}' & -\mathbf{A}(\Omega_L/\Omega_T) & -(1-J)\,\mathbf{G} \end{bmatrix} \begin{Bmatrix} \ddot{\mathbf{X}}_S \\ \ddot{\mathbf{P}} \\ \ddot{\mathbf{\Phi}} \end{Bmatrix} + \begin{bmatrix} K & \mathbf{0} & \mathbf{0} \\ \mathbf{0} & \mathbf{A}(\Omega_L/\Omega_T) & \mathbf{0} \\ \mathbf{0} & \mathbf{0} & \mathbf{0} \end{bmatrix} \begin{Bmatrix} \mathbf{X}_S \\ \mathbf{P} \\ \mathbf{\Phi} \end{Bmatrix} = \begin{Bmatrix} \mathbf{0} \\ \mathbf{0} \\ \mathbf{0} \end{Bmatrix}$$

4. Numerical models for the dynamic behavior of the Fast Reactor cores

Elementary model for the beams

The FA and the NS are represented by finite element beams. The gaps at the feet lead to a non linear behavior, with a natural frequency and a damping depending on the amplitude of the displacement. Linear equivalent models are used in the numerical simulations.

Fluid Structure Interaction

The so-called $\boldsymbol{U\,P\,\Phi}$ formulation (structure displacement field, fluid pressure and potential displacement fields) for the Fluid Structure Interaction is integrated in a general computer code, CAST3M, developed at the CEA Saclay (reference [7]). The homogenization method also have been integrated, which allows to reduce the size of the problem. FIG. 5 presents an example of finite elements for a tubes bundle arranged in an hexagonal array. On this finite element is built the matrix $\mathbf{C}'$ (see previous section) which links the degrees of freedom of the structure (the displacements and the rotations of the beam) with the degrees of freedom of the fluid (P and Φ).

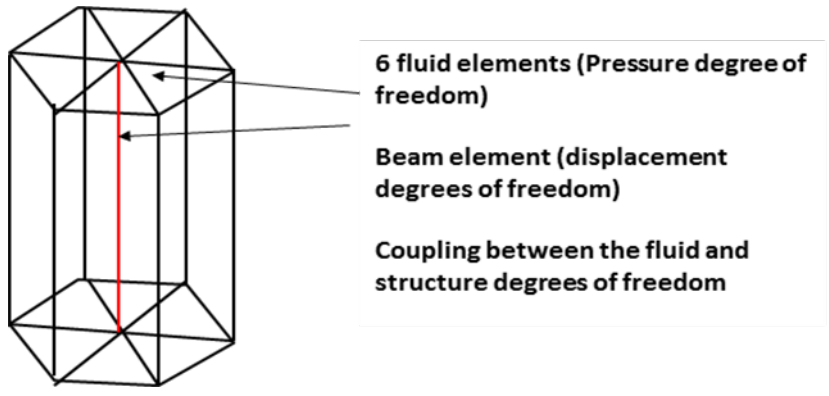

FIG. 5: Finite element for the homogenization of he FSI

Non linear behavior

Non linear behaviors have to be considered: the impacts at the pads level of the FA or at the top of the FA and the NS, the plastification of the feets. The numerical methods for these phenomena are available in CAST3M. The impacts between the beams is taken into account by using an impact stiffness.

5. Elements of validation and examples of applications

Elements of validation

The validation of the methods is based on the results of different programs, already performed or in progress. The Symphony program (references [5] and [6]) was devoted to the study of the seismic behavior od a core, with elementary tests on one FA or one NS, on row or in hexagonal configuration, with 5 FA rows and 4 NS rows (and a total of 271 beams). Tests were performed in air or in water, in order to take into account the effects of the sodium: the density of the water is close to the density of the liquid sodium. Injection tests have been performed in a little scale mock up, to study the opening of the core. Analytical tests are in progress to study in detail the influence of the fluid, particularly the dissipative effects.

Example of applications

The FIG. 6 presents the results obtained for simulations with a “direct” description of the beams, without using the homogenization method. The excitation is the injection of fluid in the center of the bundle. This excitation doesn’t correspond to a real situation but allows to test the opening on fht core. A deformation of the bundle is presented on the left of the figure. A pressure field is presented on the right.

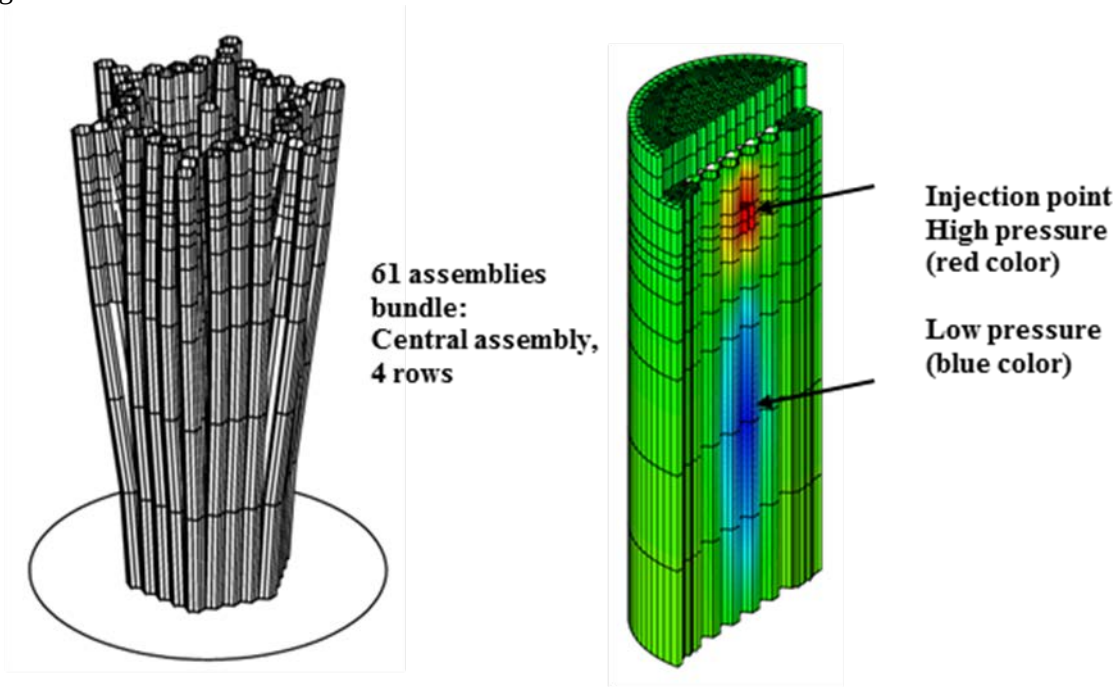

FIG. 6: Numeraical simulations with “direct” description of the beams

The FIG. 7 presents the results obtained for simulations with the homogenization method. The excitation is a seismic excitation (interpretation of the Symphony tests, references [5] and [6]). or the injection of fluid in the center of the bundle.

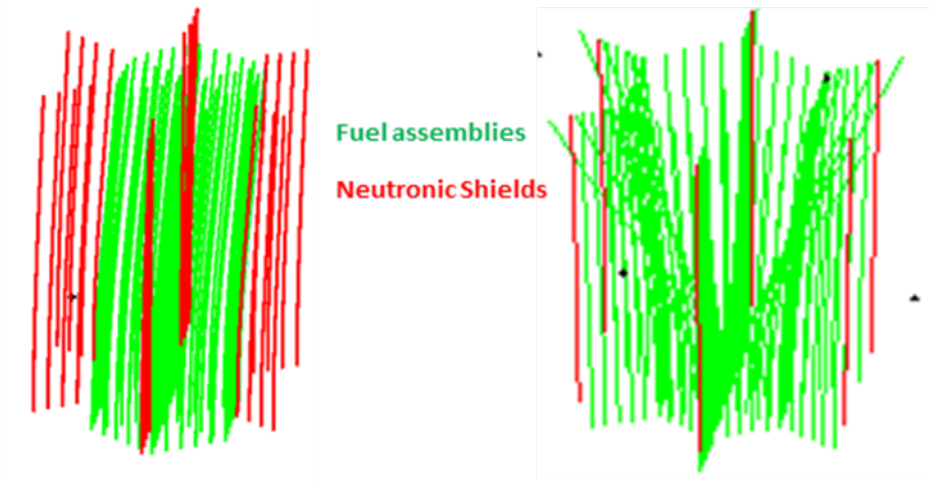

FIG. 7: Numerical simulations with homogenization techniques: deformations of the tubes bundle for a seismic excitation and for an opening of the core

The FIG. 8 presents impact forces in a core, during a seismic movement. and the pressure field in the fluid for a seismic excitation. The impacts are mainly at the pads level on the left of the figure and at the top on the center. The deformation of the free surface may be seen on the right of the figure.

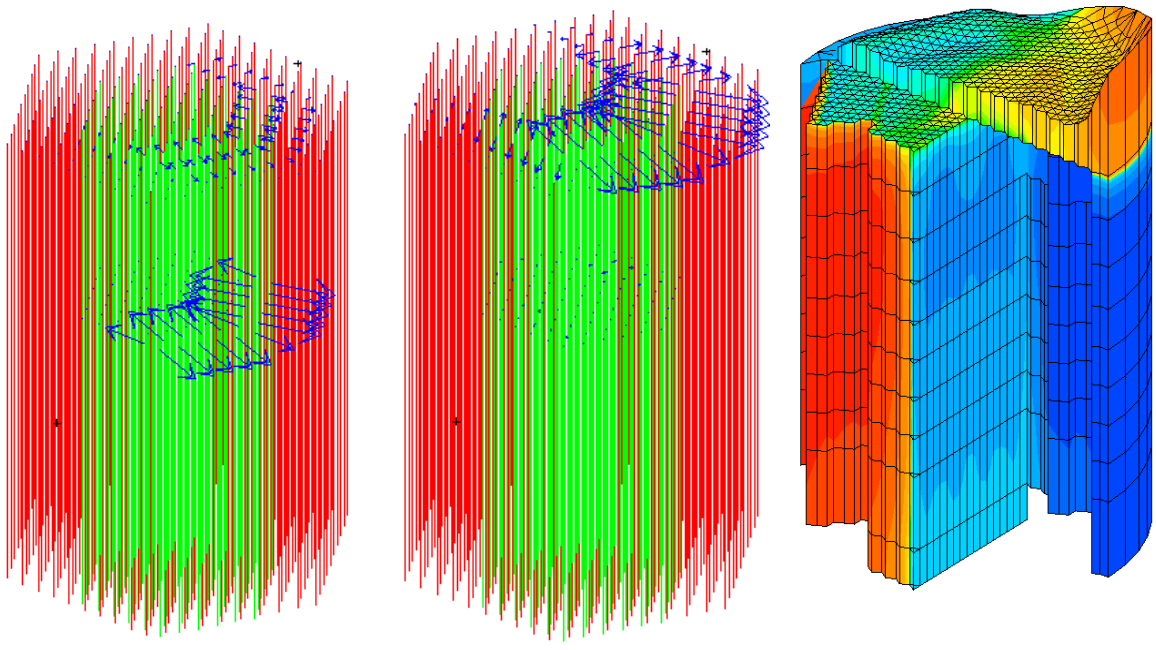

FIG. 8: Numerical simulations with homogenization techniques: impacts forces between the tubes (blue arrows on the two first figures and pressure (figure at the right)

6. Perspectives

Methods have been developed to describe the dynamic behavior of a Fast Reactor core. A key point is the description of the Fluid Structure Interaction phenomena. A method based on the Euler equations for the fluid and the use of homogneization techniques has been implemented in CAST3M, general computer code of structure mechanics and fluid mechanics. Methods to describe non linear behavior are avalaible in this computer code. Numerical simulations may be performed, taking into the different physical phenomena, with different excitations, applied to different kinds of structures.

The main perspectives of development concern the Fluid Structure Interaction. The Euler equations only describes, theoretically, the intertial effects of the fluid (with lower frequencies). Dissipative effects (leading to damping) may only globally be taken into account, by using a so-called Rayleigh damping. A program is in progress for the development of homogenization methods based on the more general Navier Stokes equation to describe the movements of the fluid.

7. Conclusion

The physical phenomena involved in the dynamic behavior of the Fast Reactor cores are identified: the interactions due to the fluid between the Fuel Assemblies and the Neutronic Shields and the impacts.

Numerical methods have been developed for the fluid structure interaction, and integrated in CAST3M, computer code developed in the CEA Saclay. Homogenization techniques are powerful engineering methods for analyzing the dynamic behavior of tube bundles, by drastically reducing the size of the numerical system, while accounting for the main physical aspects of the fluid/structure problem. Numerical simulations may be performed for a wide range of configurations and excitations, as all the functionalities of the code are available. Examples of applications have been presented, with seismic excitation and global horizontal movement, or with an opening of the core.

Further developments of the models will concern the Fluid Structure Interaction. The models actually only consider, theoretically, the “inertial” effects, even if the “dissipative” ones may be roughly taken into account by using a Rayleigh damping. A work is in progress on homogenization methods based on the Navier Stokes equations.

REFERENCES

[1] F. Axisa Modeling of Mechanical systems, Fluid Structure Interaction, Vol 3: Elsevier 2006.

[2] D. Brochard & al: Homogenization of tube bundle, application to LMFBR core analysis: SMIRT 9 Lausanne 1987,

[3] J.F. Sigrist, D. Broc: Dynamic analysis of a tube bundle with Fluid Structure Interaction modeling using a homogenization method. Computer Methods in applied mechanics and engineering 2008.

[4] D. Broc, J.F. Sigrist, Fluid Structure Interactions for tube bundles, physical meaning of a Rayleigh damping, PVP 2010.

[5] P. Buland & al: Symphony experimental Mock-up, SMIRT 13 Porto Alegre 1995.

[6] D.Broc & al: Dynamic behvior of the Fast Reactor cores, the Symphony program. FR 13 Paris 2013.

[7] CAST3M: www-cast3m.cea.fr

Review Paper

Dynamic behavior of the Fast Reactor cores: the Symphony program

Daniel BROC[a], ***Jérome CARDOLACCIA***[a], ***Sabine DURAND***[a]

[a] CEA, DEN, DM2S, F-91191 Gif-sur-Yvette, France

Presented by Edouard HOURCADE

Abstract.

A fast reactor core is schematically constituted of Fuel Assemblies and Neutronic Shields, immersed in the primary coolant (sodium) which circulates inside the assemblies. Two main physical phenomena have a strong influence on the dynamic behavior of this system: the impacts between the beams and the interactions with the fluid. The impacts between the beams limit the relative displacements. The fluid leads to "inertial effects", with globally lower vibration frequencies, and "dissipative effects", with higher damping.

Symphony is an important research program on the seismic behaviour of the fast reactor cores, developed from 1993 to 1998 at the CEA Saclay, with both experimental and theoretical parts. The experiments are at a representative scale, with Fuel Assemblies (or FA) and Neutronic Shields (or NS). Test are made "in air" (without fluid) and "in water", to study the influence of the fluid (the sodium).

A numerical model has been built for the interpretation of the tests. The interpretation of the tests is made by using a simple and efficient numerical method, based on the Euler equations for the fluid and homogenization techniques, which yields low computational costs. Impacts between the beams are taken into account also. The gaps between the feet and the grid plate lead to high damping for the beams if the gaps are important. The fluid leads to a strong coupling between the FA and the NS in the whole core, and limits the relative displacement.

1. Background, presentation of Symphony program

During a seismic excitation the core of a Fast reactor has a global horizontal movement. The displacements and the deformations of the assemblies have consequences on the drop of the control rods: it has to be checked that this drop remains possible. Differential movements, dues to different mechanical characteristics of the assemblies, lead to impacts between the assemblies, with risks of damage of the pads (pads located on the assemblies in order to limit the relative displacements), and with variations in the volume of the core, with changes of the reactivity of the reactor.

The paper presents the interpretation of the seismic tests of the Symphony program. This program has been performed in the 90's, but the numerical models available at this time where not able to describe the complex FSI phenomena.

The section 2 presents the mockup and the experimental program. The section 3 is devoted to some aspects on the Fluid Structure Interaction phenomena for the Fast Reactor cores. The section 4 presents the building of elementary models for the Fuel Assemblies and the Neutronic Shields, models based on the first test, for which the interactions between the beams are relatively limited. The section 5 presents the interpretation of the tests in the hexagonal configuration.

2. The Symphony program

Different kinds of tests are performed, in air or in water (the density of the water at 20 °C is close to the density of the liquid sodium) and on different structures (reference **[5**]).

- One single beam (FA or NS),
- One row, with only FA or with FA and NS,
- Hexagonal configuration.

The FIG. 1 presents the Fuel Assemblies and the Neutronic Shields. The mass of the beams is 170 kg for the FA and 200 kg for the NS. The total heigth 4 300 mm for the FA and 4370 for the NS. The feets of the beams are inserted in a grid plate. A scheme is presented of the small gaps which lead to a non linear dynmaic behavior: the natural frequency and the damping depend on the amplitude of the displacement. This point has been studied, with the aim to build linear equivalent models, which could be used in the interpretation of the one row and hexagonal tests.

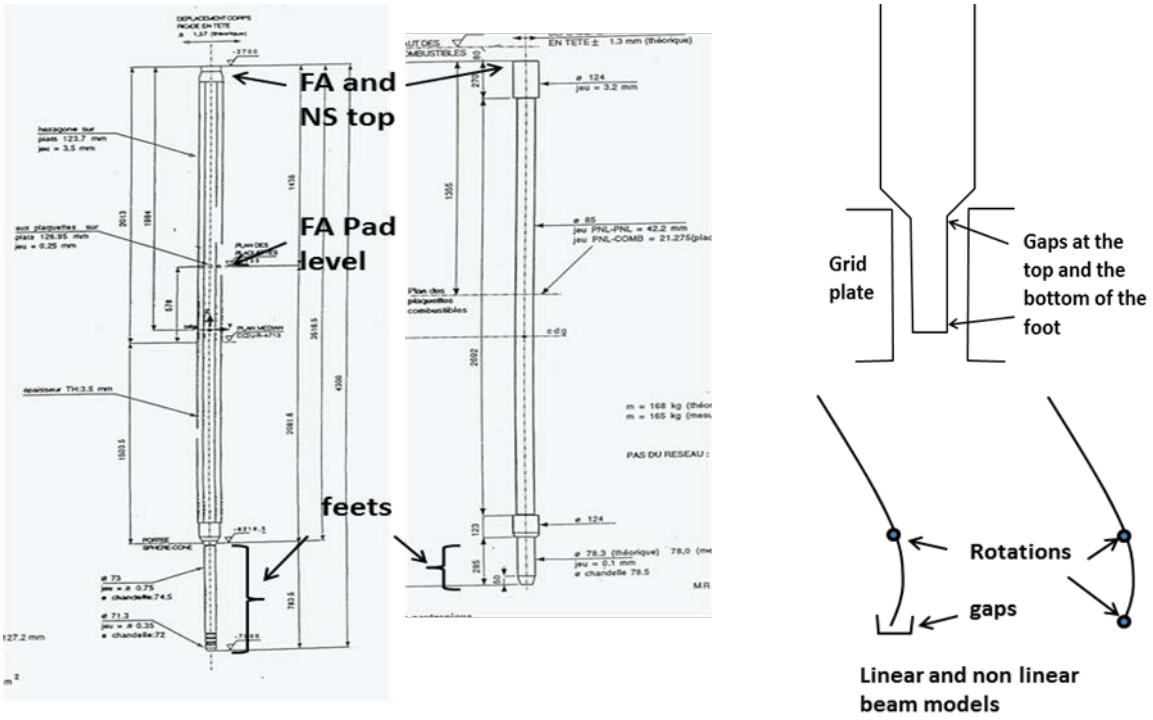

FIG. 1: Fuel Assembly (FA) Neutronic Shild (NS) and non linear behavior due to gaps ate the feet

The FIG. 2 presents a scheme of the one row test. The level of the grid plate is 30 cm higher for the NS than for the FA.The height above the foot is 3.45 m for the FA and 3.16 m for the NS. The tops of all the beams are at the same level. Impacts may occur at the top of the beams or at the pads level. “One row“ tests have been made with only FA (22 beams), or with FA and NS (12 NS the NS at the left of the row, 22 FA in the center and 12 NS at the right). FIG. 2 also presents and a picture of the mockup in the hexagonal configuration, with 5 FA rows (91 beams) and 4 NS rows (180 beams). The pitch of the array is 127 mm. The gap between two adjacent FA is 3 mm, and close to 0 at the pads level of the FA.

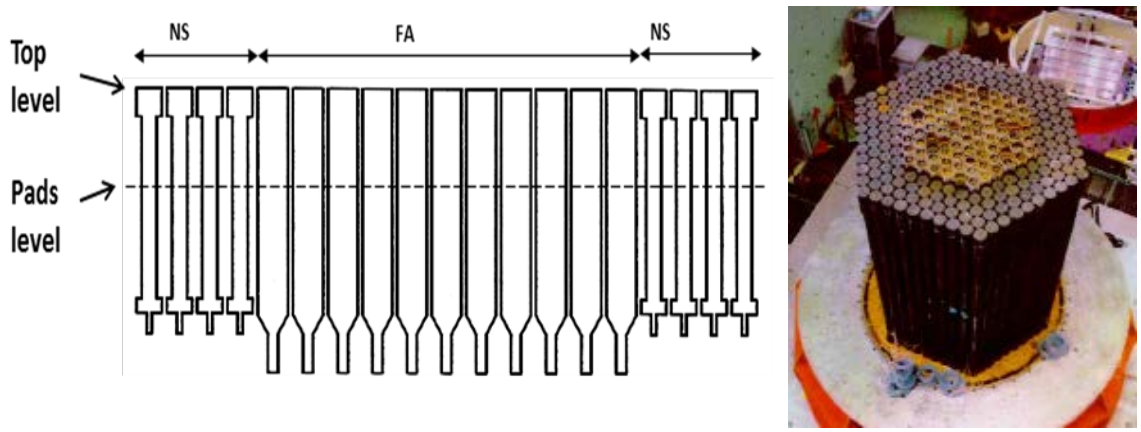

FIG. 2: Scheme of a “one row” test, with FA and NS

The tests in the hexagonal configuration in water, with both FA and NS, exhibit a particular behavior, with strong interactions by the fluid between the beams in the whole core. The other tests (one beam or one row in air or in water, and hexagonal configuration in air) exhibit a more simple behavior. The coupling between the beams is relatively limited, and due to the contacts at the pads level or at the top. These tests will be used to build elementary models for the dynamic behavior of the Fuel Assemblies and the Neutronic Shields.

3. Fluid Structure Interaction in a Fast Reactor core

Elements on FSI phenomena in a Fast Reactor core are presented in FIG. 3. The confinement is high (a). The space between two assemblies is thin and the fluid velocity may be much higher than the structure ones (a). Important FSI will take place, with inertial effects (with lower natural frequencies) and dissipative effects also (with higher damping). FSI will be higher for “opening” modes (b, decrease of 60% of the frequencies) and lower for global movements (c, decrease of 15% of the frequencies).

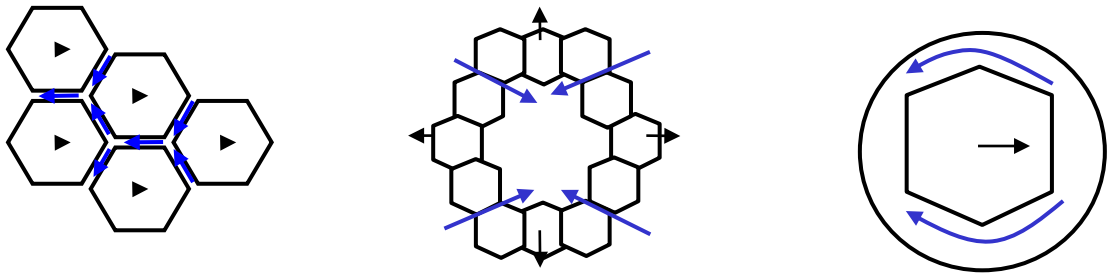

FIG. 3: Elements on FSI phenomena in a Fast Reactor core

Methods to take into account FSI

Different ways may be used to take into account the interactions between the fluid and the structure. In the general case, the Navier Stokes equations are used for the fluid. Depending on the conditions, simplifications can be made (reference **[1**]) . In some cases (for example little displacements of the structure) the Euler linear equations may be used, more simple than the Navier Stokes. The movement of the fluid is described by : $\rho \, {d\vec{V}}/{dt} = -\vec{\nabla} P$, where ρ and $\vec{V}$ are the density and the velocity of the fluid and P the pressure, with $div\,\vec{V} = 0$. The continuity at the fluid structure interface leads to: $\vec{V}\,\vec{n} = \dot{\vec{X}}\,\vec{n}$, where $\vec{n}$ is the normal vector to the interface and $\dot{\vec{X}}$ the velocity of the structure.

This method theoretically only takes into account the “inertial effects”, even if the “dissipative effects may be globally taken into account by using a Rayleigh damping. In the case of a tubes bundle the size of the mesh may be very huge. The use of homogenizations methods allows to reduce the number of elements (references [2], [3], [4] and [6]).

4. Building of elementary models for the Fuel Assemblies and the Neutronic Shields

Elementary models are build for the FA and the NS, from the results of the tests where the interactions between the beams is limited to the contacts: one beam tests, one row tests or hexagonal tests in air. Preliminary tests and analysis with only one beam show that the first natural frequency of the FA and NS is close to 3 Hz. An important damping is observed, due to gaps at the feet. This damping depends on the amplitude of the movement. It is higher for the NS than for the FA. The aim of the building of elementary models is mainly to determine this damping. The numerical simulations are made with CAST3M, computer code developed at the CEA Saclay (reference [7]).

Tests results

The FIG. 4 presents the maximum and minimum displacements obtained for a seismic excitation in a one row test, with 12 NS (23 W to 12 W), 22 FA (11 W to 11 E) and 11 NS (12 E to 23 E). The movement of the central Fuel Assemblies (like 1W and 1E) is not influenced by the NS, with maximum displacements of about 50 mm. The movement of the Neutronic Shields at the periphery (like 23 W and 23 E) is not influenced by the FA, with maximum displacements of about 20 mm. Interactions between FA and NS take place at the boundaries between FA and NS zones (near to 111 W and 11 E).

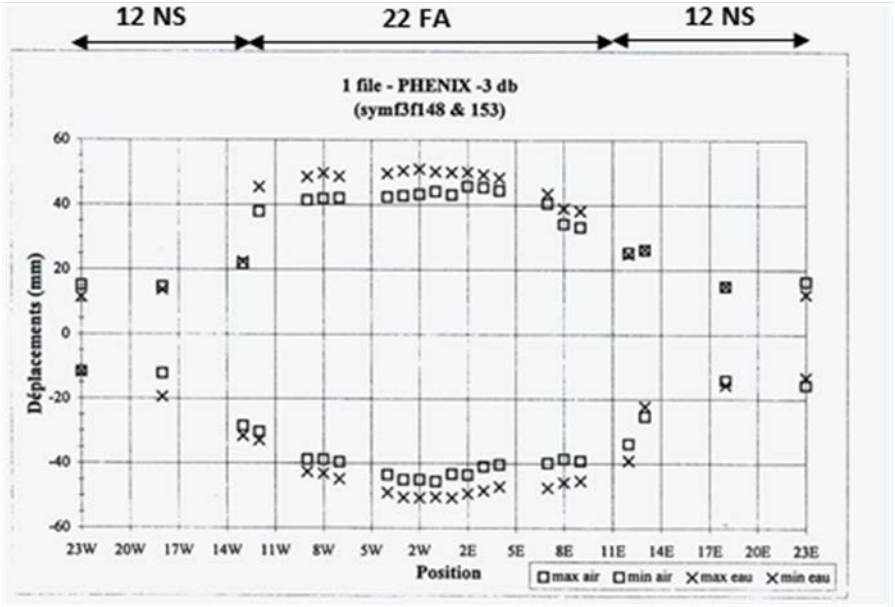

FIG. 4: One row test: maximum displacements of the NS and the FA

The FIG. 5 presents the displacements at the top of the beam in an hexagonal configuration, in air, with 91 FA and 180 NS (the positions of the top of the assemblies for a seismic excitation. As for the one row test, the interactions are low between the central FA and the NS at the periphery. The displacements are is the direction of the seismic excitation, and are higher for the FA than for the NS. An “interaction zone” is observed, with movements I in the direction orthogonal to the excitation, due to the impacts.

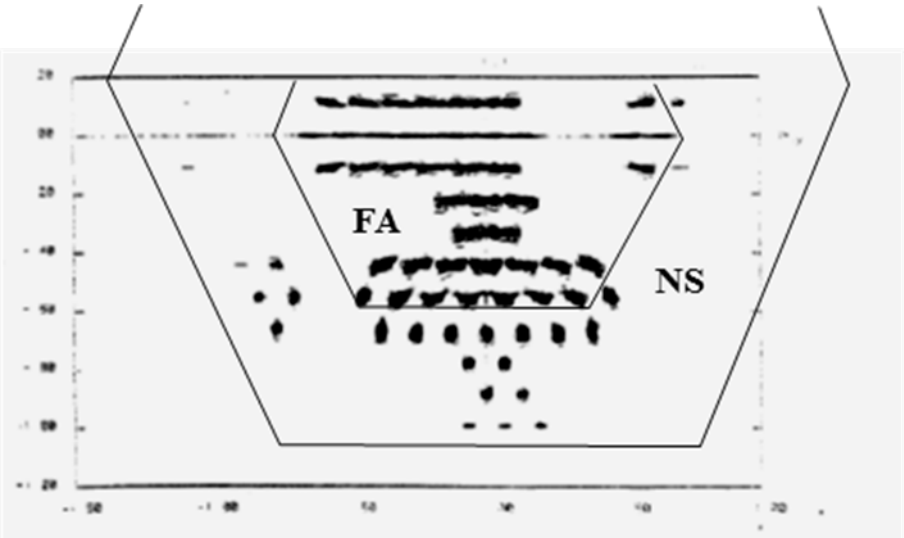

FIG. 5: Hexagonal test in air, displacement of the FA and NS

Simulations results

The FIG. 6 presents the acceleration versus time used in the One row and Hexagonal tests (FIG. 4 and FIG. 5) and which will be used in the numerical simulations.

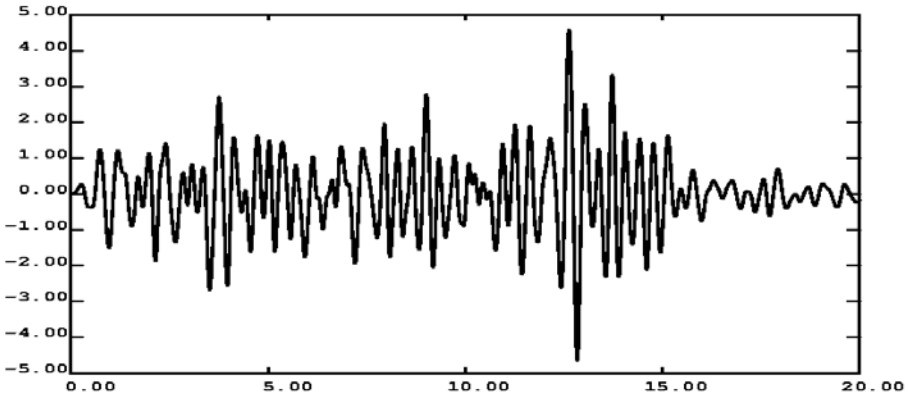

FIG. 6: Seismic excitation for the One row and Hexagonal tests

The FIG. 7 presents the displacement versus time of the top of the central Fuel Assembly for a seismic excitation in the hexagonal configuration in air, with the results of the test and of a numerical simulation. The beam is described by a linear model, with a natural frequency of 3.04 Hz and dampings of 12%, 15% and 20% (curves green, red and blue). The comparison between the results of the experiment and of the numerical simulations is relatively good, if we consider that the dynamic behavior of the Fuel Assemblies is not completely linear (see section 2 and FIG. 1).

The FIG. 8 presents the displacement versus time for a seismic excitation of the top of a Neutronic Shield in a row test (beam 23W, see FIG. 4), with test and simulations results. The NS are assumed to be 3.08 Hz beams, with dampings of 40% and 80% (curves red and blue).

From the results of the interpretation of the tests where the coupling between the FA and the NS is reltively limited, linear beam models have been built, with 3.04 Hz first frequency for the FA (and 15 % damping) and 3.08 Hz frist frequency for the N (and 80% damping)..

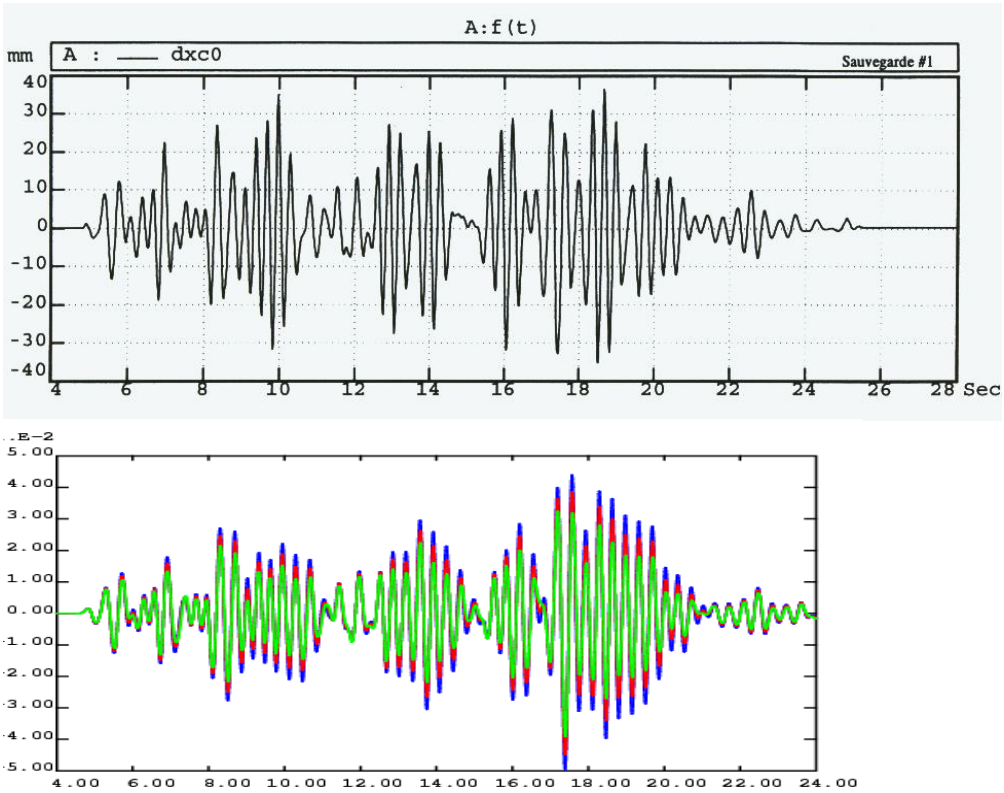

FIG. 7: Hexagonal configuration, top displacments for the central Fuel Assembly, test and simulation

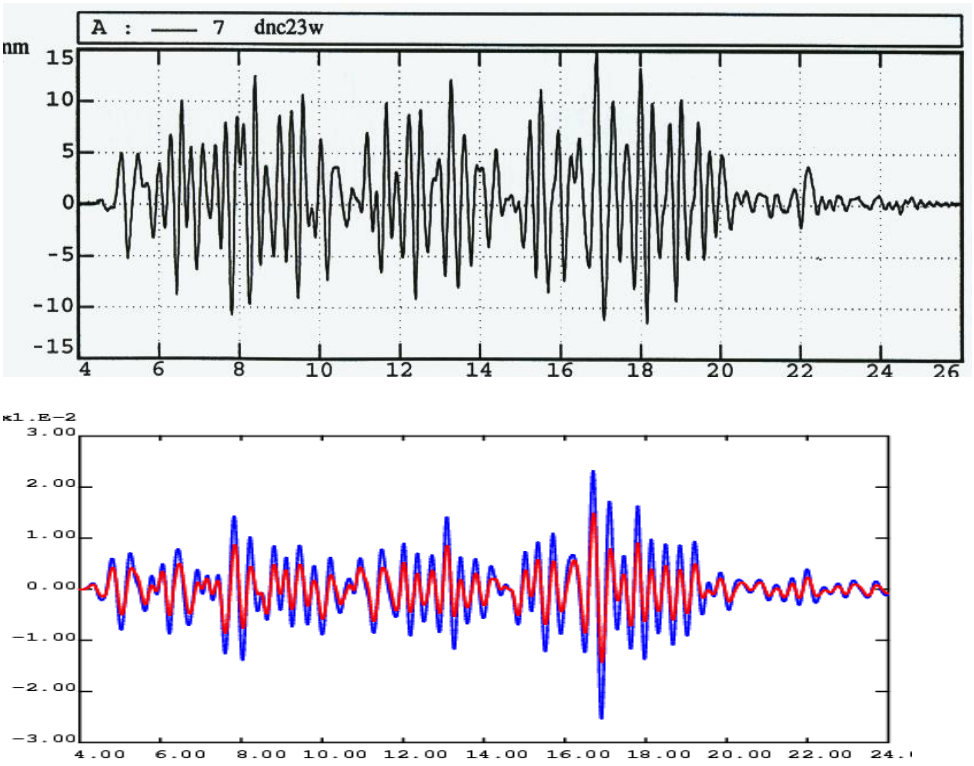

FIG. 8: One row test, top displacement for a Neutronic Shield, test and simulation

5. Interpretation of the tests in the “in water” hexagonal configuration

A strong coupling takes place betwwen the FA and the NS in the test in the hexagonal configuration, “in water”. The simulation of theses tests are made by using linear equivalent models for the beams, built in the previous section. The fluid is taken into account by using the methods presented in the section 3. Impacts are taken into account at the pads level (for the FA) and at the top (FA and NS). The FIG. 9 presents the mesh used for the numerical simulations, with:

- The beams: green for the 91 FA and red for the 180 NS,
- The fluid finite elements: green near to the FA, red near to the NS and black between the beams bundle and the vessel.
- An example of one finite element used for the homogenization of the FSI.

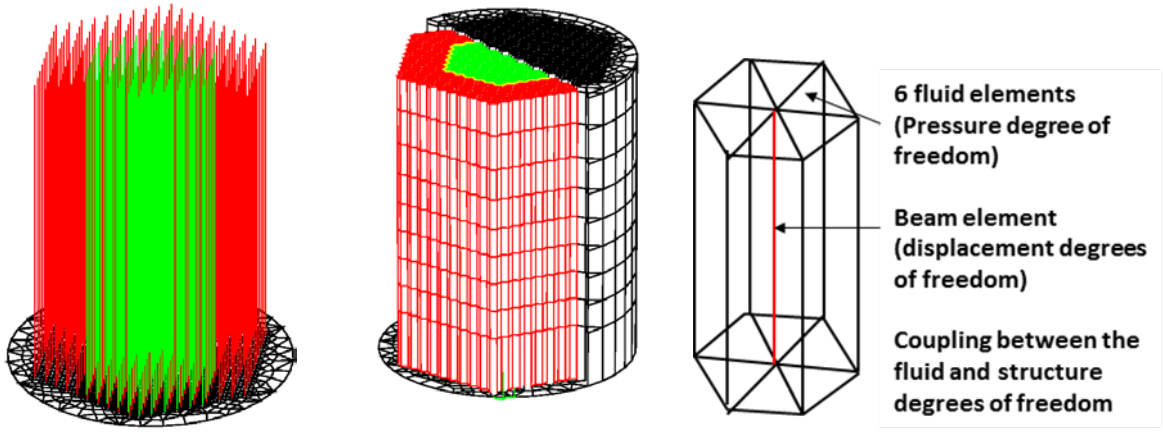

FIG. 9: Hexagonal configuration, top displcaments versus time for the central Fuel Assembly: modeling

The FIG. 10 presents examples of the deformations of the bundle and under a seismic excitation (acceleration versus time presented FIG. 6). The relative displacements between the FA and the NS are much higher for the “in air” simulations than for the “in water” ones.

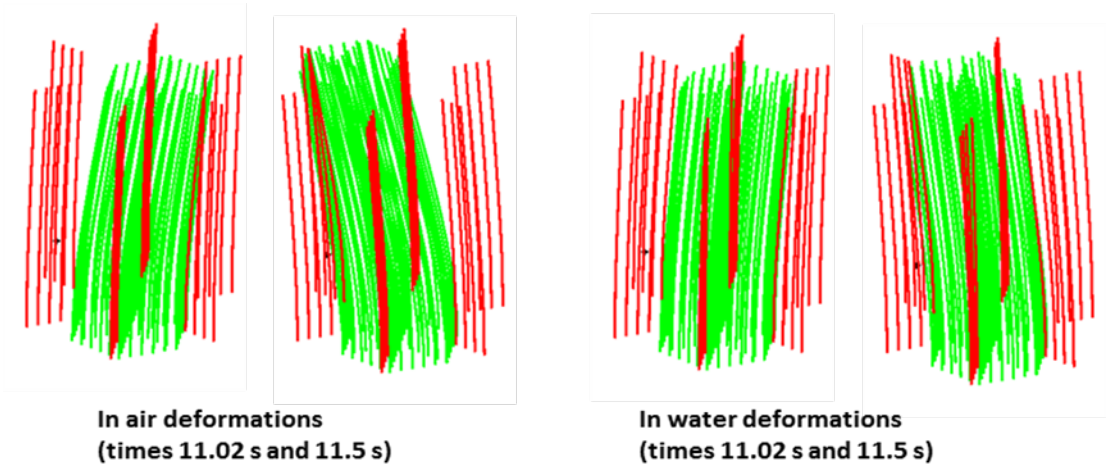

FIG. 10: deformations of the assembies during a seismic excitation

The FIG. 11 presents an example of the pressure field (with the deformations of the free surface) and impacts forces between the assemblies. The blue arrows represent the forces applied on the assemblies. The impacts are mainly at the pads level in this figure.

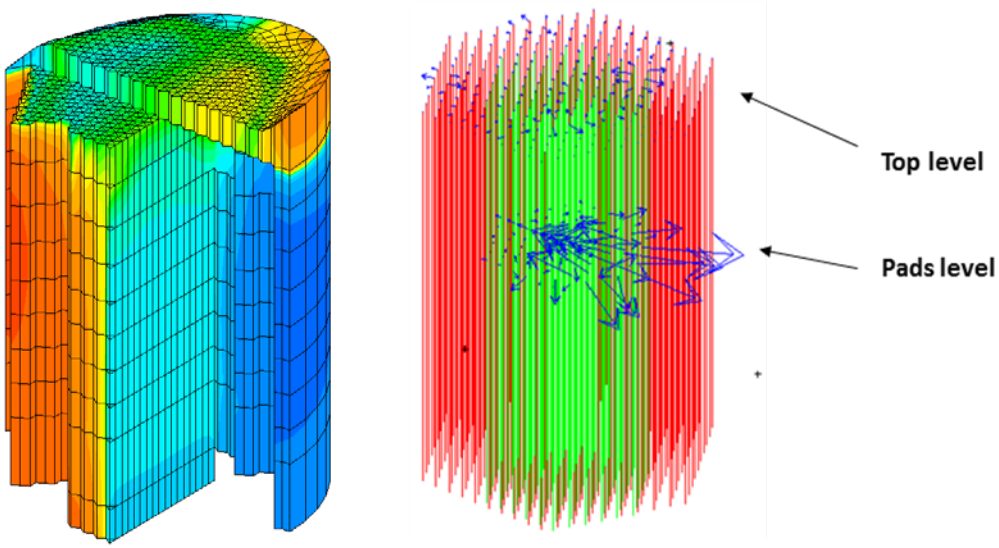

FIG. 11: deformations of the assembies during a seismic excitation

The FIG. 12 and FIG. 13 presents the displacements versus time at the top of the assemblies of the central row (11 FA and 8 NS). The displacements are presented with shifts of 3 mm between two curves, corresponding to the gaps between the beams. It is so possible to see the impacts between two adjacent assemblies, for example at about 2.8 seconds, whith the 4 red curves, corresponding to the displacement of 4 Neutronic Shields. The relative displacements between the different beams are much higher in the “in air” simulations than in the “in water”. During the impact at the time 2.8 seconds, the space between the FA and the NS is about 20 mm in the FIG. 12 and 8 mm in the FIG. 13.

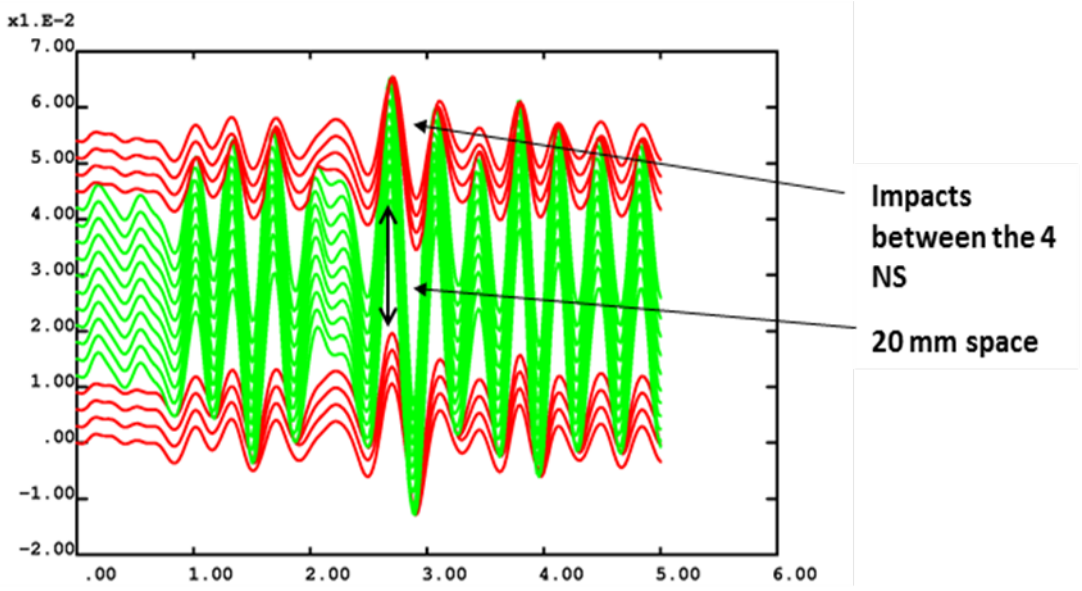

FIG. 12: seismic excitation in air, displacements sersus time of the assemblies

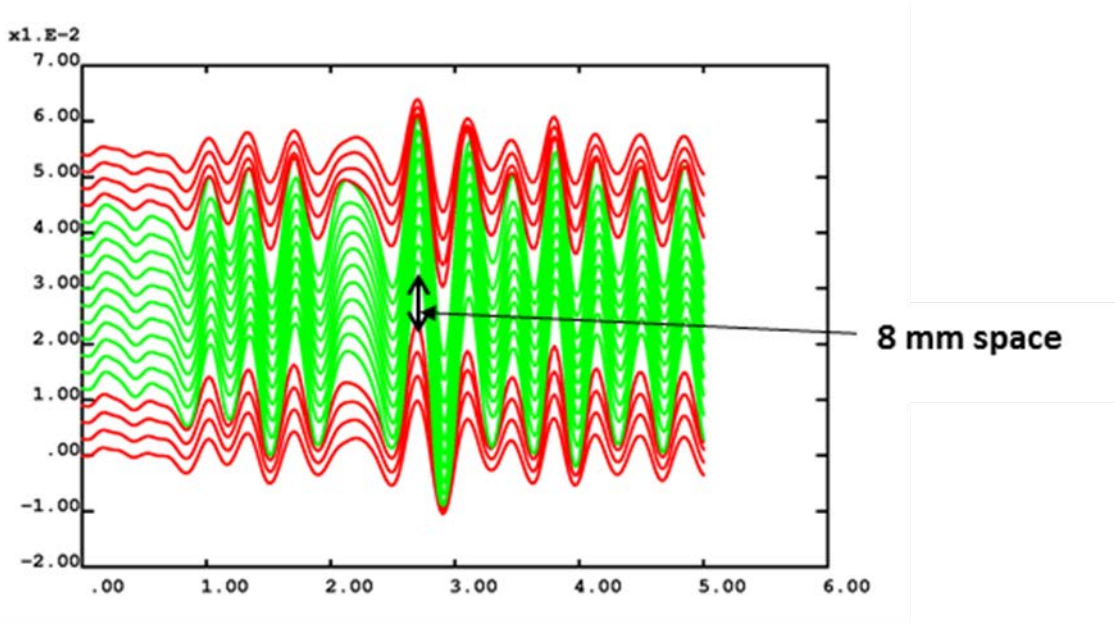

FIG. 13: seismic excitation inwater, displacements versus time of the assemblies

The FIG. 14 presents the maximum displacements obtained for the FA and the NS in the hexagonal configuration, with 5 rows of FA and 4 rows of NS, with test and simulation results for the “in air” and “in water” case. The displacements of Neutronic Shields are very close in the two cases. The displacement of the central Fuel Assembly is lower in the ”in water” case. The interactions by the fluid between all the beams in the whole core limit the relative displacements.

The evolution versus time of the volume of the core has been calculated from the numerical simulations. The maximum radius variation of the 5th row at the core level (2 meters under the top of the FA) is 0.5 mm for the “in air” and 0.15 mm for the “in water” case. This variation is lower if the fluid is taken into account and much lower than the absolute displacement of the beams (about 30 mm at the top and 10 mm at the core level.

The limitation of the relative displacements of the assemblies in the whole core by the fluid is related to the high confinement. Relative displacements of the beams lead to high velocities in the fluid, with both “inertial” and “dissipative” effects. It has to be noticed that the simulations may describe the tests by taking into account only the inertial effects. The interpretation of the experiment doesn’t give informations on the dissipative effects due to the fluid.

Seismic hexagnal tests	**FA**	**NS**
In Air Test (mm)	**35**	**19**
In Air Simulation (mm)	37	21
In Water Test (mm)	**28**	**20**
In Water Simulation (mm)	28	18

FIG. 14: Hexagonal tests in water, max displacements for the FA and the NS

6. Conclusion

The Symphony program provides an important amount of reliable experimental data on the seismic behavior of the Fast Reactor cores. The interpretation of the tests allows to get a better uderstanding of the beahvoir of the structure. This interpretation contributes also to the validation of the numerical methods for the study of the dynamic behavior of the Fast Reactor cores.

The mechanical behavior of the assemblies is sensitive to the gaps which may lead to high damping for the structures (up to 80% for the NS in the experiment). The interactions by the fluid between the FA and the NS in the whole core have a strong influence on the dynamic behaviour of the system. The tests in the hexagonal configuration in water with both Fuel Assemblies and Neutronic Shields exhibit a particular behavior, with strong interactions by the fluid between the assemblies. Under a seisimc excitation the relative displacements between the beams is much lower than the globally horizontal displacement of the bundle. These relative displacements are lower if the fluid is taken into account.

A simple and efficient numerical method is used, based on the Euler equations for the fluid, and homogenization techniques allowing reducing the size of the numerical simulations. The numerical models available in the 90's were not able to describe the complex interaction by the fluid between the Fuel Assemblies and the Neutronic Shields in the whole core.

REFERENCES

[1] F. Axisa Modeling of Mechanical systems, Fluid Structure Interaction, Vol 3: Elsevier 2006.

[2] D. Brochard & al: Homogenization of tube bundle, application to LMFBR core analysis: SMIRT 9 Lausanne 1987,

[3] J.F. Sigrist, D. Broc: Dynamic analysis of a tube bundle with Fluid Structure Interaction modeling using a homogenization method. Computer Methods in applied mechanics and engineering 2008.

[4] D. Broc, J.F. Sigrist, Fluid Structure Interactions for tube bundles, physical meaning of a Rayleigh damping, PVP 2010.

[5] P. Buland & al: Symphony experimental Mock-up, SMIRT 13 Porto Alegre 1995.

[6] D.Broc & al: Physical and numerical methods for the dynamic behavior of the fast reactor cores. FR 13 Paris 2013.

[7] CAST3M: www-cast3m.cea.fr

Evaluation on Calculation Accuracy of the Sodium Void Reactivity for Low Void Effect Fast Reactor Cores with Experimental Analyses

K. Sugino[a], **K. Numata**[b], **M. Ishikawa**[a]

[a] Japan Atomic Energy Agency

[b] NESI Inc.

Abstract. Calculation accuracy of the sodium void reactivity for safety-enhanced fast reactor core concepts was evaluated with analyses of critical experiments. In these concepts, heterogeneous core configuration and sodium plenum replacement are adopted to reduce the sodium void reactivity to around zero. In the past, a variety of critical experiments for heterogeneous cores had been carried out in the ZPPR facility, some of which are compiled in the IRPhEP handbook. Further, several experiments for core with sodium plenum had been performed in the BFS-2 facility. Calculation analyses of above mentioned critical experiments have been performed by using the Japanese current reactor physics analytical system. These analyses clarified that accuracy for homogeneous and axially-heterogeneous cores was sufficient, though accuracy for the radially-heterogeneous core and/or core with sodium plenum was not satisfactory. In order to achieve satisfactory accuracy for various types of cores, investigation on several design methods was performed.

1. Introduction

Sodium-cooled fast reactor (SFR) is one of the most promising energy sources that can support sustainable development of human civilization. However, sodium might be expelled and considerable positive reactivity would be inserted in the unlikely event of an unprotected transient. Therefore, reduction of sodium void reactivity is significantly important issue in order to enhance the safety of SFRs.

Major basic mechanisms of measures for reducing the sodium void reactivity are increase of the neutron leakage from core and/or softening of the neutron spectrum. Measures for increase of the neutron leakage are to reduce the core height[1], to deploy the heterogeneous core concept[1] and/or to set the sodium plenum[2]. Measures for softening of the neutron spectrum are to add the moderator layer[3], and/or to restrain the contents of minor actinides and/or fission products.

In recent fast reactor core designs to enhance the safety, sodium plenum and/or heterogeneous core concepts were adopted[4][5][6] to achieve negative or low sodium void effect.

In order to clarify and investigate the issues on the calculation accuracy of sodium void reactivity for such core concepts as low sodium void effect, experimental analysis results of a standard data base for FBR code design compiled by JAEA[7] were utilized.

2. Issues on experimental analyses

2.1. Calculation conditions

Now we focus on the calculation accuracy with the current standard calculation system applied in the Japanese core neutronics design, which are represented by the latest Japanese evaluated nuclear data library JENDL-4.0[8][9] and the code system for fast reactor neutronics analysis JOINT-FR[7][10][11]. In detail, effective cross-sections are produced with the one-dimensional plate-stretch heterogeneous cell model[10]. Simultaneously, anisotropic diffusion coefficients are calculated by the Benoist's theory[12] with the modification in order to correct the plate-cell-parallel leakage component of the sodium void reactivity[13]. Base core calculation is performed with the almost constant lethargy 70-group energy structure with the diffusion theory. For obtaining best estimated calculation results, ultra-fine energy group effect[11] and the transport theory effect are considered.

For an evaluation of calculation accuracy of sodium void reactivity, following critical experiments were treated: ZPPR-9 of homogeneous core[14], ZPPR-13A of radially-heterogeneous core[15], ZPPR-17A of axially-heterogeneous core[16] and BFS-66-1 of core with upper sodium plenum[17]. Experiments on ZPPR-9, 13A and 17A were performed by using the critical facility ZPPR in US, and experiments on BFS-66-1 were carried out with the critical facility BFS-2 in Russia.

Figures 1 through 4 present the schematic view of each sodium void reactivity experiment. Regions indicated by IC-#, OC-#, C-#, AB-#, IB-# and Na-# (#: numbers) show the step-wise sodium voided spaces in inner core, outer core, single core, axial blanket, internal blanket and sodium plenum, respectively. Step-wise sodium void sequences are described under each figure. Off-center sodium void spaces were not fully but partly voided in the azimuthal direction except for the C-3 void case of ZPPR-13A. In the calculation, cumulative sodium void reactivity was treated in each sodium void sequence.

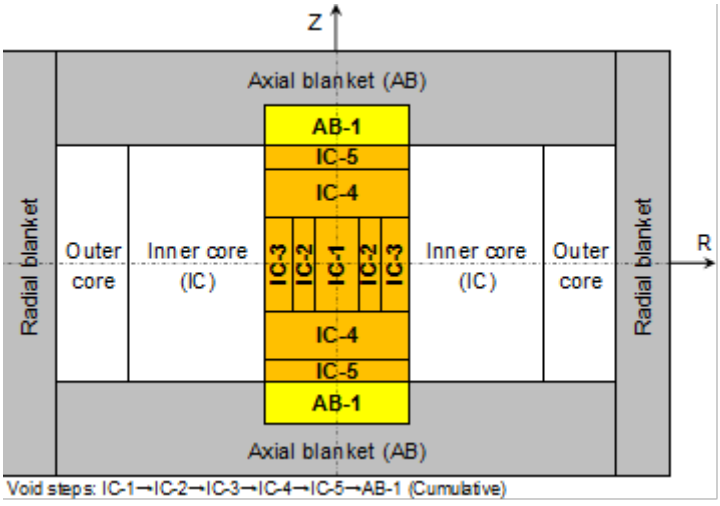

FIG. 1. Sodium void reactivity experiment in ZPPR-9 (R-Z geometry)

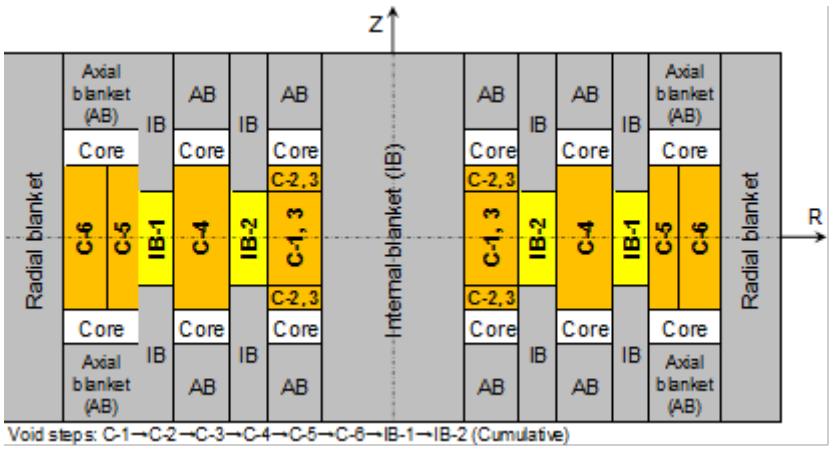

FIG. 2. Sodium void reactivity experiment in ZPPR-13A (R-Z geometry)

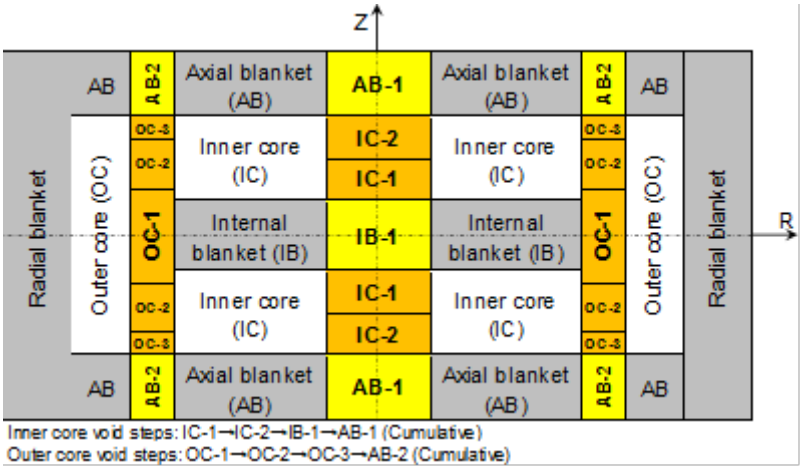

FIG. 3. Sodium void reactivity experiment in ZPPR-17A (R-Z geometry)

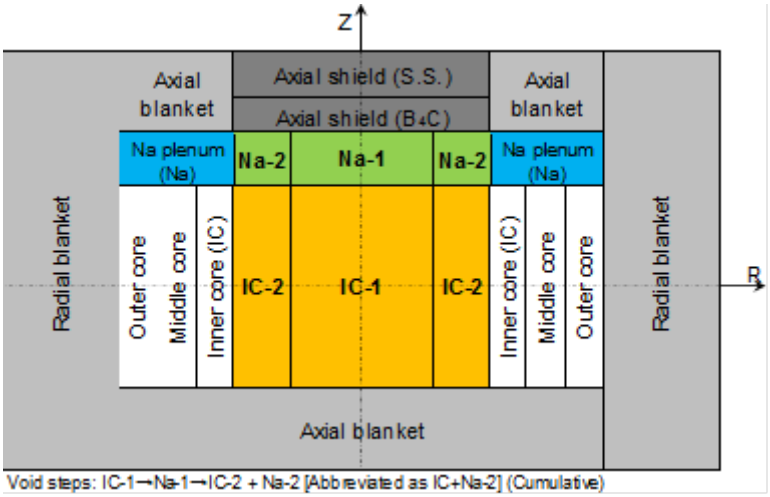

FIG. 4. Sodium void reactivity experiment in BFS-66-1 (R-Z geometry)

2.2. Calculation results

Reference calculation results were presented in Fig. 5, where results were shown in both the absolute difference between calculation (C) and experiment (E): C-E value and relative difference: C/E-1 value. From Fig. 5, followings were observed:

- ZPPR-9: Calculations agreed with experiments within 10% or 3¢.

- ZPPR-13A: Calculations systematically overestimated experiments by 10 through 20% or maximum did beyond 10¢, however, which were evaluation in the safe side.

- ZPPR-17A: Calculations agreed with experiments within 2¢ though overestimated by 10 through 50% in the outer core void cases.

- BFS-66-1: Calculations maximum overestimated experiments beyond 45% or maximum underestimated beyond 20¢, which were evaluation in the unsafe side and issued.

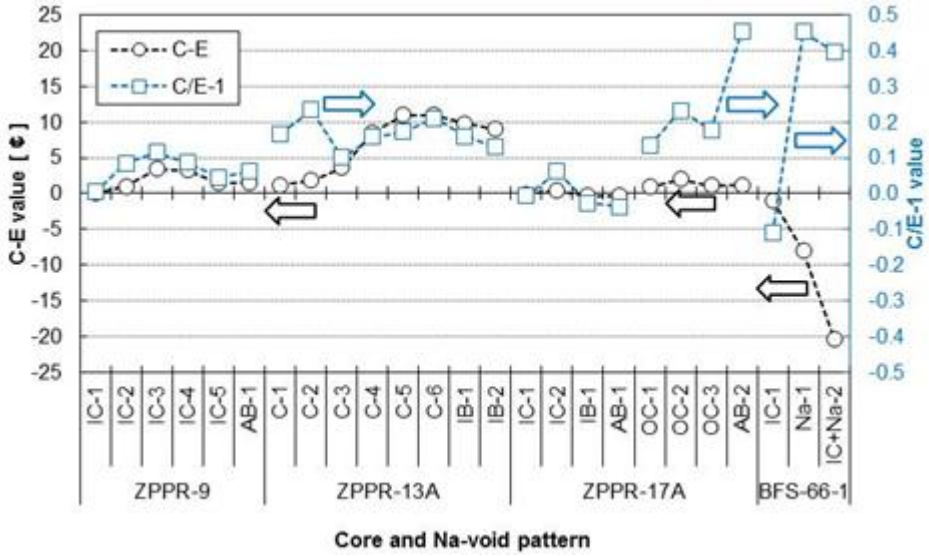

FIG. 5. Results of the reference calculations

3. Evaluation of uncertainty in experimental analyses

In order to investigate the cause of discrepancy between calculation and experiment values, prediction uncertainties were evaluated. Prediction uncertainties treated in the present study were experimental, calculation modeling and cross-section induced ones. Experimental uncertainties were referred to Refs. [14][15][16][17]. Calculation modeling uncertainties were estimated by combining the magnitudes of calculation corrections or errors[7], which were ultra-fine group correction (half of effect), transport theory correction (half of effect) and error or difference of the one-dimensional plate-stretch modeling (5%)[18]. Cross-section induced uncertainties were obtained by multiplying the covariance data of JENDL-4.0[19] with the sensitivity coefficients of sodium void reactivity to cross-sections.

Comparison in the experimental, calculation modeling and cross-section induced uncertainties was shown in Fig. 6. There was little difference in experimental uncertainties among cores and sodium-void patterns. On the contrary, calculation modeling and cross-section induced uncertainties of ZPPR-13A and BFS-66-1 were much larger than those of ZPPR-9 and ZPPR-17A. Thus, it was clarified that

the calculation accuracies of sodium void reactivity for ZPPR-13A and BFS-66-1 were worsened due to their uncertainties.

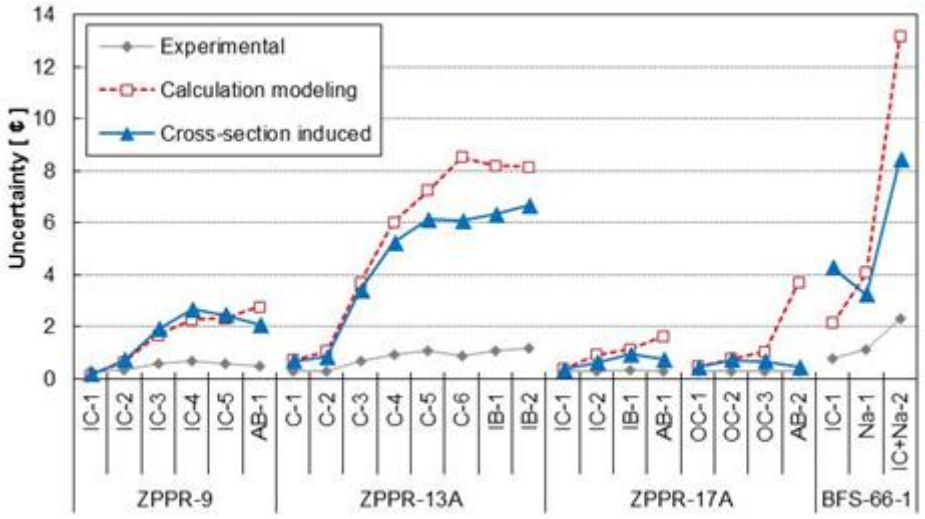

FIG. 6. Results of uncertainty evaluations

4. Investigation with the Monte Carlo method and other nuclear data adoption

Now we focus on the issue of the BFS-66-1 sodium void reactivity because of its larger uncertainties and unsafe side evaluation. In terms of investigation on the calculation modeling, the continuous energy Monte Carlo method[20] was applied. Further, evaluated nuclear data libraries ENDF/B-VII.1[21] and JEFF-3.1[22] were adopted instead of JENDL-4.0 for investigation on the nuclear data.

Figure 7 showed the comparison in results between calculation models and nuclear data. It was observed that the results with the Monte Carlo method showed same tendency as the deterministic standard calculation system. In addition, results with different nuclear data presented similar results. Thus, the issue on BFS-66-1 sodium void reactivity is considered to be placed in the nuclear data field, which would be common among the world-wide research organizations.

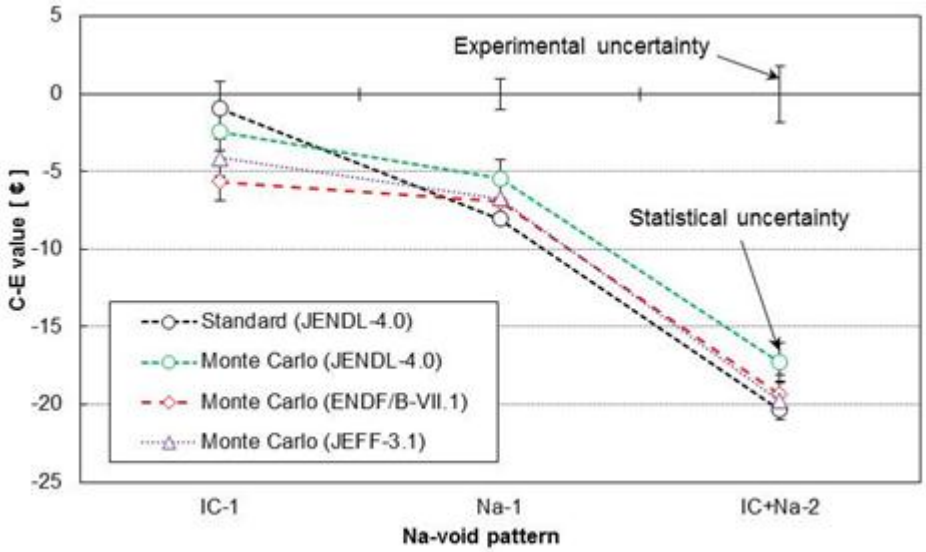

FIG. 7. Results of calculations with the Monte Carlo method

5. Investigation on the measures for an improvement

As shown in the previous chapter, an improvement on the BFS-66-1 sodium void reactivity would be achieved by such a method as applied in the core design works like a bias-factor technique which can cover nuclear data issues. In the present study, conventional two-component bias-factor method and cross-section adjustment method were applied.

In the two-component bias-factor method, bias-factors of both non-leakage and leakage components were estimated by using the least-squared fitting technique with the 81 sodium-void reactivity experimental analysis data in the standard data base[7] so as to minimize the square sum of C-E values with constant weight for each experiment.

In the cross-section adjustment method[23], 643 experimental analysis data of various core characteristics including criticality, reaction rate and control rod worth in the standard data base[7] were used, eliminating the abnormal data for an adequate cross-section adjustment[7]. Further, calculation results with the Monte Carlo method were adopted as much as possible for reduction of calculation modeling uncertainties, which were specified by the statistical uncertainties of reasonably small values.

Preliminary, the effect on the addition of the BFS-66-1 sodium-void reactivity data was checked in two-design methods. It was found that addition of the BFS-66-1 data was essential for a better prediction of the BFS-66-1 sodium void reactivity, because predicted results were worse than reference results without BFS-66-1.

In the two-component bias-factor method, representative or average bias-factors of 0.90/0.92 were obtained for non-leakage/leakage components. In addition, region-wise bias-factors can be applied instead of average ones like factors for core, blanket and sodium plenum regions. In the same manner, non-leakage/leakage components bias-factors of 0.95/1.06 for core region, 1.09/1.01 for blanket region and 0.84/0.80 for sodium-plenum region were obtained. Here, core-region sodium void cases of cores with sodium plenum, e.g. IC-1 case of BFS-66-1, were grouped into the sodium plenum region void case, because sodium plenum void cases were only two and bias-factors obtained from only two cases had little reliability.

In the cross-section adjustment method, it was clarified that abnormal behaviors of cross section adjustment was not observed and adjustments were almost equivalent to those in the production of the adjusted cross-section set ADJ2010[7], which was produced without BFS-66-1 data. Major feature of the present adjustment is alterations of Mn-55 capture and Fe-56 capture cross-sections, which were around twice as much as those in the production of ADJ2010, which was caused by addition of the sodium void reactivity data in the sodium plenum region.

Figures 8 and 9 showed the comparison in results among reference and two design methods, that is, region-wise two-component bias-factor method and cross-section adjustment method. Both design methods produced better results particularly in the sodium plenum void cases of BFS-66-1.

Thus, agreements of sodium-void reactivity were improved to range of 14% or 3¢ by the two-component bias-factor method and to range of almost 17% or 8¢ in the cross-section adjustment method though agreement of the reference calculation was in the range of 45% or 20¢.

Now, evaluation of prediction accuracy of target cores with low void effect concepts[4][5][6] is desired to be performed. In the present study, preliminary evaluation was carried out for one of the low void core concept[5]. It was found that the whole core void reactivity would be increased by 60¢ with region-wise two-component bias-factors, which was considerable.

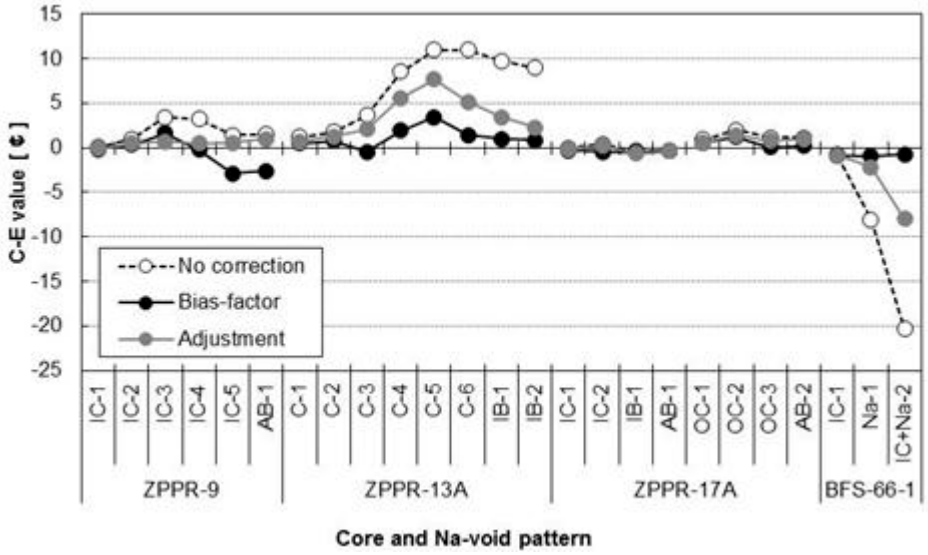

FIG. 8. Comparison in the C-E results among design methods

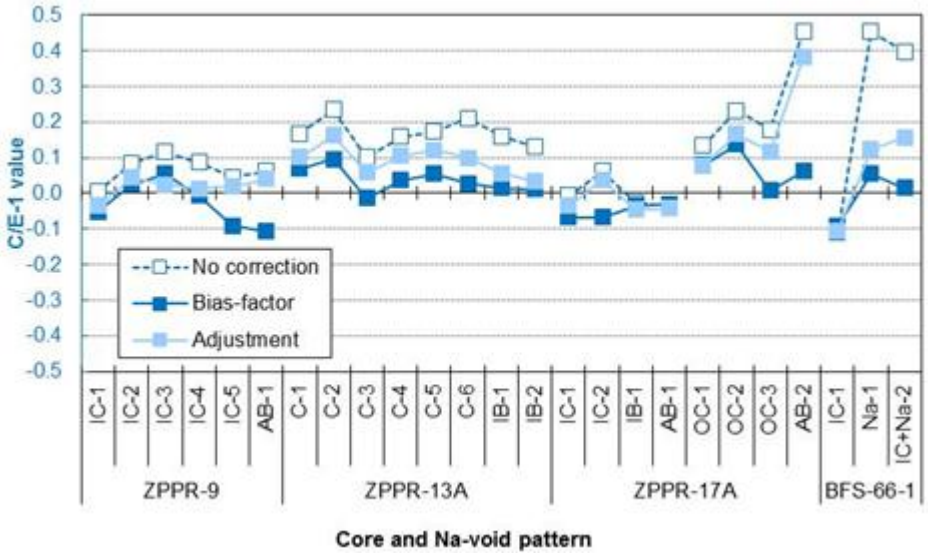

FIG. 9. Comparison in the C/E results among design methods

6. Conclusions

In the calculations of sodium-void reactivity experiments with a standard core neutronics design system, the rooms for improvements were observed for radially-heterogeneous core and core with sodium-plenum. These rooms were significantly reduced by applying such a core design method as two-component bias-factor method or cross-section adjustment method. In addition, it was found that addition of the experimental analysis data of cores with sodium-void plenum was essential for a better prediction the sodium void reactivity for cores with sodium plenum.

In the future, improvement on the reliability of the sodium-void reactivity data for cores with sodium plenum is desired, one of which is experimental analysis of the FCA XVII-1 core with sodium plenum[24] because it is an independent experiment of BFS-66-1. Further, evaluation on prediction accuracy of target cores with low void effect concepts is desired to be performed.

REFERENCES

[1] WALTER, A. E., TSVETKOV, P. V. and TODD, D. (Editos), Fast Spectrum Reactors, Springer.

[2] KIRYUSHIN, A. I., VASILIEV, B. A., et al., BN-800 - Next Generation of Russian Sodium Fast Reactors, Proc. of 10th Int. Conf. on Nucl. Eng. (ICONE10), Arlington, VA, Apr. 14-18, 2002.

[3] JEVREMOVIC, T., OKA, Y. and KOSHIZUKA, S., Effect of Zirconium-Hydride Layers on Reducing Coolant Void Reactivity of Steam Cooled Fast Breeder Reactors, J. Nucl. Sci. Technol., Vol. 30, No. 6, p. 497-504, 1993.

[4] POPLAVSKY, V. M., MATVEEV, V. I., et al., Studies on Influence of Sodium Void Reactivity Effect on the Concept of the Core and Safety of Advanced Fast Reactor, J. Nucl. Sci. Technol., Vol. 48, No. 4, p. 538-546, 2011.

[5] SCHMITT, D., MASSARA, S., et al., Design of a Sodium-cooled Fast Reactor with Innovative Annular Geometry and Very Low Sodium Void Worth, Proc. of ICAPP 2011, Nice, France, May 2-5, 2011, Paper 11073.

[6] VARAINE, F., MARSAULT, P., et al., Pre-conceptual Design Study of ASTRID Core, Proc. of ICAPP'12, Chicago, USA, Jun. 24-28, 2012, Paper 12173.

[7] SUGINO, K., ISHIKAWA, M., et al., Development of a Standard Data Base for FBR Core Design (XIV) - Analyses of Extensive FBR Core Characteristics Based on JENDL-4.0 -, JAEA-Research 2012-013, 2012 [in Japanese].

[8] SHIBATA, K., IWAMOTO, O., et al., JENDL-4.0: A New Library for Nuclear Science and Engineering, J. Nucl. Sci. Technol., Vol. 48, No. 1, p. 1-30, 2011.

[9] CHIBA, G., OKUMURA, K., et al., JENDL-4.0 Benchmarking for Fission Reactor Applications, J. Nucl. Sci. Technol., Vol. 48, No. 2, p. 172-187, 2011.

[10] ISHIKAWA, M., Consistency Evaluation of JUPITER Experiment and Analysis for Large FBR Cores, Proc. of Int. Conf. on the Physics of Reactors (PHYSOR 96), Sep. 16-20, 1996, Mito, Ibaraki, Japan, p. E-36.

[11] HAZAMA, T., CHIBA, G. and SUGINO, K., Development of a Fine and Ultra-Fine Group Cell Calculation Code SLAROM-UF for Fast Reactor Analyses, J. Nucl. Sci. Technol., Vol. 43, No. 8, p. 908-918, 2006.

[12] BENOIST, P., Streaming Effects and Collision Probabilities in Lattices, Nucl. Sci. Eng. 34, p.285-308, 1968.

[13] CHIBA, G., Overestimation in Parallel Component of Neutron Leakage Observed in Sodium Void Reactivity Worth Calculation for Fast Critical Assemblies, J. Nucl. Sci. Technol., Vol. 43, No. 8, p. 946-949, 2006.

[14] IKEGAMI, T., ZPPR-9 Experiment: A 650 MWe-class Sodium-cooled MOX-fueled FBR Core Mock-up Critical Experiment with Clean Core of Two Homogeneous Zones, International Handbook of Evaluated Reactor Physics Benchmark Experiments (IRPhE), ZPPR-LMFR-EXP-002, NEA/NSC/DOC(2006)1, OECD/NEA, 2010.

[15] SANDA, T., ZPPR-13A Experiment: A 650 MWe-class Sodium-cooled MOX-fueled FBR Radial Heterogeneous Core Mock-up Critical Experiment with Central Blanket Zone and Two Internal Blanket Rings, International Handbook of Evaluated Reactor Physics Benchmark Experiments (IRPhE), ZPPR-LMFR-EXP-007, NEA/NSC/DOC(2006)1, OECD/NEA, 2011.

[16] SANDA, T., ZPPR-17A Experiment: A 650 MWe-class Sodium-cooled MOX-fueled FBR Axial Heterogeneous Core Mock-up Critical Experiment with Central Internal Blanket Zone, International Handbook of Evaluated Reactor Physics Benchmark Experiments (IRPhE), ZPPR-LMFR-EXP-009, NEA/NSC/DOC(2006)1, OECD/NEA, 2012.

[17] HAZAMA, T., IWAI, T. and SHONO, A., BFS Critical Experiment and Analysis - Analysis of BFS-62-5 and 66-1 Cores -, JNC TN9400 2005-011, 2004 [in Japanese].

[18] TAKEDA, T., UNESAKI, H., et al., Two-Dimensional Cell Heterogeneity Effect in Analysis of Fast Critical Assemblies, Nucl. Sci. Eng., 98, p.128-138, 1988.

[19] IWAMOTO, O., NAKAGAWA, T., et al., Covariance Evaluation for Actinide Nuclear Data

in JENDL-4, Proc. the 2010 International Conference on Nuclear Data for Science and Technology (ND2010), J. Korean. Phys. Soc., 59(23), p. 1224-1229, 2011.

[20] NAGAYA, Y., OKUMURA, K., et al., MVP/GMVP II: General Purpose Monte Carlo Codes for Neutron and Photon Transport Calculations based on Continuous Energy and Multigroup Methods, JAERI 1348, 2005.

[21] CHADWICK, M. B., HERMAN, M., ENDF/B-VII.1 Nuclear Data for Science and Technology: Cross Sections, Covariances, Fission Product Yields and Decay Data, Nucl. Data Sheets, 112, p. 2887-2996, 2011.

[22] (Eds.) KONING, A., FORREST, R., et al. The JEFF-3.1 Nuclear Data Library, JEFF Report 21, 2006.

[23] DRAGT, J. B., DEKKER, J. W. M., et al., Method of Adjustment and Error Evaluation of Neutron Capture Cross Sections; Application to Fission Product Nuclides, Nucl. Sci. Eng., 62, p. 117-129, 1977.

[24] OIGAWA, H., IIJIMA, S. and ANDOH, M., Experiments and Analyses on Sodium Void Reactivity Worth in Mock-up Cores of Metallic Fueled and MOX Fueled Fast Reactors at FCA, J. Nucl. Sci. Technol., Vol. 35, No. 4, p. 264-277, 1998.

Benchmark Analyses of Sodium Natural Convection in the Upper Plenum of the MONJU Reactor Vessel

H. Ohira[a], Y. Xu[b], U. Bieder[c], K. Velusamy[d], H. Mochizuki[e], S. Choi[f], Y. Shvetsov[g], T. Sofu[h], J. Thomas[h], S. Monti[i], S. Yoshikawa[a], A. Stanculescu[i,·]

[a] Japan Atomic Energy Agency, Tsuruga, Japan

[b] China Institute of Atomic Energy, Beijing, China

[c] French Alternative Energies and Atomic Energy Commission, Saclay, France

[d] Indira Gandhi Center for Atomic Enerhy, Kalpakkam, India

[e] University of Fukui, Tsuruga, Japan

[f] Korea Atomic Energy Research Institute, Daejeon, Republic of Korea

[g] Institute of Physics and Power Engineering, Obninsk, Russian Federation

[h] Argonne National Laboratory, IL, USA

[i] International Atomic Energy Agency, Vienna, Austria

Abstract. IAEA's Coordinated Research Project on Benchmark Analyses of Sodium Natural Convection in the Upper Plenum of MONJU Reactor Vessel was carried out between 2008 and 2012, with the aim to improve the Member States' analytical capabilities in the field of fast reactor in-vessel sodium thermal hydraulics. Eight research organizations from seven countries with an active programme on Sodium-cooled Fast Reactors - namely China, France, India, Japan, Republic of Korea, Russian Federation and USA – contributed to this CRP. The experimental data for the benchmark analysis were provided by the JAEA and concerned the measurements of thermal stratification of sodium observed in the MONJU reactor vessel at a turbine trip conducted in December 1995 during the original start-up tests. In particular the CRP participants were provided with the vertical temperature distribution and outlet temperatures of fuel subassemblies measured during the turbine trip test from the 40% rated power condition. The thermal-hydraulic simulations performed in view of the subsequent comparison with the experimental data were rather challenging due to the complex geometry of the upper plenum of the MONJU reactor vessel which, in particular, includes an inner barrel with several flow holes, as well as an upper core structure composed of fingers, control rod guide tubes, and flow guide tubes. The paper presents the results of these simulations and the comparison with the experimental data. The CRP allowed validation of the different thermal-hydraulics codes used by the involved organizations, and helped identification of the key parameters that affected the thermal stratification phenomena in the upper plenum of an advanced Sodium-cooled Fast Reactor.

· Present affiliation; Idaho National Laboratory (INL), Idaho, USA

1. Introduction

The thermal hydraulic effects in the upper plenum of a sodium cooled fast reactor vessel (RV) such as thermal stratification in the post-scram transients may cause severe thermal stress problems. Mock-up tests using water and sodium as working fluid had been conducted in many organizations in order to evaluate these phenomena and validate numerical simulation codes. However in the past detailed calculations were not feasible and/or satisfactory because of the limited computational power and lack of suitable numerical algorithms. Recently, numerical analysis codes with highly advanced algorithms have been developed and the computational performances have been also improved remarkably [1]. As a consequence thermal-hydraulic analyses of large and complex regions has turned out to be practicable with reasonable computational costs, making the utilization of high performance thermal-hdraulic codes is becoming common practice for the design and the safety analysis of sodium-cooled fast reactors (SFRs). However, due to the limited availability of experimental data coming from the few SFRs in operation, these codes have not been extensively validated so far. One of the important phenomena in the field of thermal hydraulics is the thermal stratification in the upper plenum of SFR RVs. The evaluation of moving up rates is essential for assessing structure integrity. JAEA performed a turbine trip transient test from 40% rated electrical power in December 1995, as a system start-up test (SST) of the Japanese Prototype Fast Breeder Reactor MONJU and obtained detailed experimental data in the upper plenum of the RV. These measurements captured the thermal stratification phenomena. The data were considered to be useful for the validation of SFR thermal-hydraulic codes, offered to the IAEA, which decided to launch a Coordinated Research Project (CRP) effort titled “Benchmark Analyses of Sodium Natural Convection in the Upper Plenum of MONJU Reactor Vessel”.

The CRP was carried out between 2008 and 2012, with the aim to improve the Member States' analytical capabilities in the field of fast reactor in-vessel sodium thermal hydraulics. Eight research organizations from seven countries with an active programme on SFRs - namely China, France, India, Japan, Republic of Korea, Russian Federation and the USA - contributed to this CRP. The experimental data for the benchmark analysis were provided by JAEA and concerned the measurements of thermal stratification of sodium observed at the turbine trip test during the original SST. In particular the CRP participants were provided with the vertical temperature distribution and outlet temperatures of fuel subassemblies measured during the test [2]. The thermal-hydraulic simulations performed in view of the subsequent comparison with the experimental data were rather challenging due to the complex geometry of the upper plenum of the MONJU RV which, in particular, includes an inner barrel with many flow holes, as well as an upper core structure (UCS) composed of fingers, control rod guide tubes (CRGTs), and flow guide tubes (FGTs). The model development and various parameter simulation approaches of the participating organization were discussed at the last Research Coordinated Meeting (RCM) held in Tsuruga from 16 to 20 April 2012. Preliminary results were also presented at various international Conferences, namely NURETH-14 [3-9] and ICAPP’12 [10], etc. by the various organizations participating in the IAEA CRP.

This paper describes the main results of the simulations and the comparison with the experimental data. These comparisons substantiate the claim that the CRP was successful since (i) it contributed towards validating different thermal-hydraulic codes used by the participants in this efforts, and (ii) it identified the key parameters that affected the thermal stratification phenomena in the upper plenum of advanced SFRs.

2. Prototype Fast Breeder Reactor MONJU

2.1. Outline of MONJU

MONJU is a nuclear power plant with a sodium cooled fast breeder reactor. It is a prototype reactor and has been developed to confirm its function as a power-generating plant, and to allow the accumulation of operational experience that would provide the basis for judging the technical feasibility of FR power rate increases. Thus, the MONJU data obtained during power operation will be utilized for the development of future fast breeder reactors. The main cooling system of this reactor

consists of three loops; each loop has a primary and a secondary heat transport system (PHTS and SHTS, respectively) with auxiliary cooling system (ACS), as is illustrated in Fig. 1. The dotted circle area in Fig. 1 is the upper plenum, which is the calculation domain of this CRP. MONJU's high thermal efficiency allows 280MW electric output from the reactor's 714MW thermal power rating.

2.2. Upper plenum of reactor vessel and calculation region

A close-up rendition of the RV upper plenum and the calculation region in this CRP is given in Fig. 2(a). The upper instrument structure (UIS) is installed in the center of the RV through the shield plug to the upper region of the core. Thermocouples are positioned at the flow guide tubes (FGTs) outlet centers, installed at the bottom ends of fingers which are connected to the UIS. The honeycomb structure (HS) supports these FGTs and control rod guide tubes (CRGTs), and is supported by the UIS. The HS has various kinds of flow holes (FHs) in additional penetrations for these tubes. The inner barrel, which is a vertical circular cylinder with upper and lower lines of FHs, is set up on the support plate in order to mitigate the severe thermal stress to the RV wall mainly caused by the thermal stratification. The inner barrel has 24 upper FHs and 48 lower FHs both of which are equally spaced in the peripheral direction and of 92 mm inner diameter, in order to decrease the moving up rate of the thermal stratification front. Fuel Handling Machine (FHM) guide equipped with Hold Down Arms, which is also illustrated in Fig. 2(a), is installed approximately 2,470 mm off-center of the RV. TC-plug with 38 thermocouples illustrated in Fig. 2(b) is installed to measure the vertical temperature distribution in the upper plenum.

The MONJU core has 108 inner and 90 outer driver zones of fuel subassemblies. Surrounding the two driver zone, there are 172 blanket and 324 neutron shielding subassemblies. Figure 2(c) shows the top view of the MONJU core. In the upper plenum, set up on the upper support plate outside of the core, there are 10 In-Vessel Racks and an In-Vessel Transfer Machine (IVTM) Lower Guide. The detailed benchmark specifications are reported in [2].

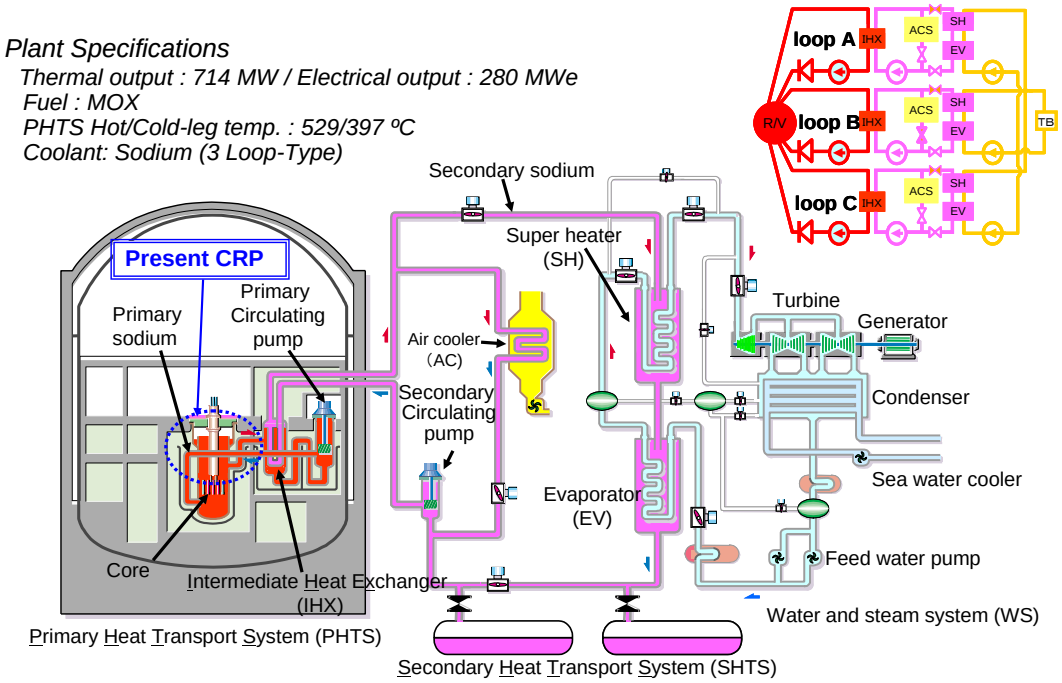

FIG. 1. Main cooling systems of MONJU

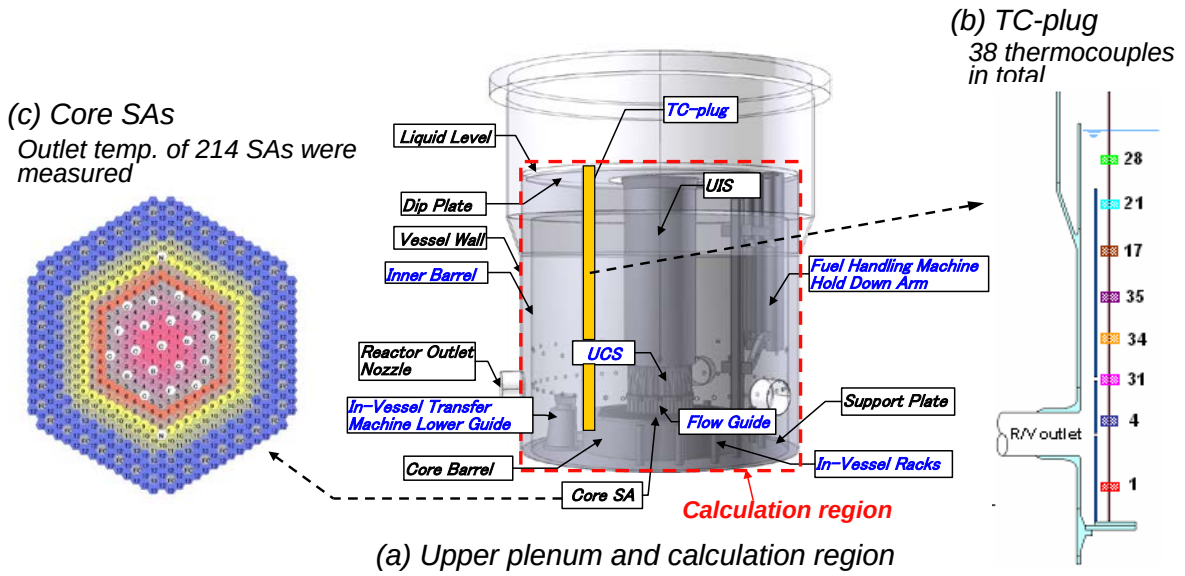

FIG. 2.Upper plenum of MONJU reactor vessel and measuring points

2.3. Plant trip test from 40% electric output condition

The purpose of this test is to confirm the plant safety feature of MONJU against turbine failure, by generating a simulated "condenser vacuum low" signal to confirm that the plant is safely shutdown as designed. Major plant responses after the control rod insertion are (i) main motors of primary pumps tripped and (ii) the pony motors start up for both PHTS and SHTS. The blowers of air coolers (ACs) in ACS are started at the same time and the steam control valves and stop valves are quickly closed. After these actions, the decay heat is removed to the atmosphere through sodium-air heat exchangers installed in parallel with the steam generators (SGs), via sodium circulation of PHTS and SHTS, which is maintained at approximately 10% and 8% of the nominal flow rates, respectively, by pony motor operation. The decay heat removal capability in case of turbine failures has been confirmed, though the PHTS sodium flow rate was so small that sodium temperature stratification formed in the RV upper plenum. Temporal changes of the temperature distribution along the TC-plug measured in this test are shown in Fig. 3.

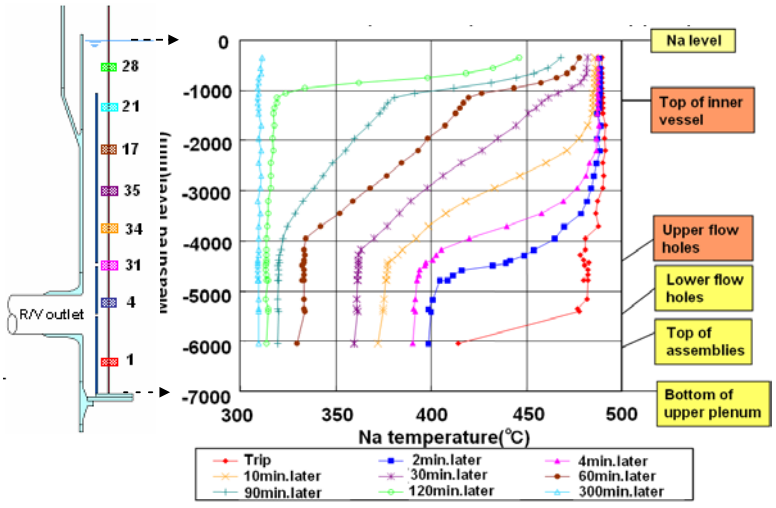

FIG. 3. After the pump trip measured temperature distribution on TC-plug

The thermal stratification front moved up just after the reactor scram and the temperature in the upper plenum became almost constant in approximately 300 minutes. These thermal stratification phenomena were clearly captured from these data.

3. Description of models

In the first stage of the CRP, a simplified model, which modelled the upper plenum in a 1/6 sector, was developed by ANL [8]. The flow holes on the inner barrel had high resolution meshes without applying pressure loss coefficients. The UCS of this sector model was modelled by a porous media with equivalent pressure loss coefficients in the vertical and horizontal directions, which was developed by CEA [6]. The honeycomb structure in the UCS was also modelled as a thin plate with an average surface porosity and a pressure loss coefficient. The schematics of this simplified model are shown in Figs. 4(a) and 4(b). This model was constructed in approximately 1 million meshes. In addition, full sector (360º) models were also developed in order to investigate asymmetric effects of the structures such as FHM guide and the boundary conditions of subassembly (SA) outlets. The FGTs and fingers in the UCS were also divided into high resolution meshes. These models were constructed in the range of 5.6 to 25 million meshes [3, 4]. An example of these meshes is shown in Fig. 5 which was developed by CIAE. Both 1/6 sector and full sector models were analyzed using the same boundary conditions but different temporal and grid resolutions by CRP participants.

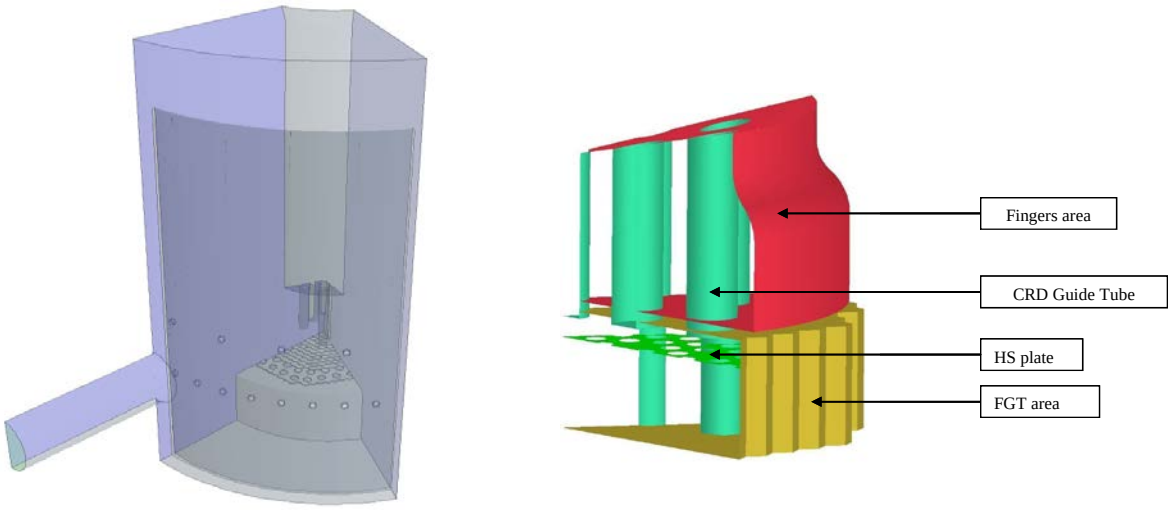

(a) 1/6 sector model of upper plenum *(b) 1/6 sector model of UCS*

FIG. 4. Simplified model of upper plenum and UCS

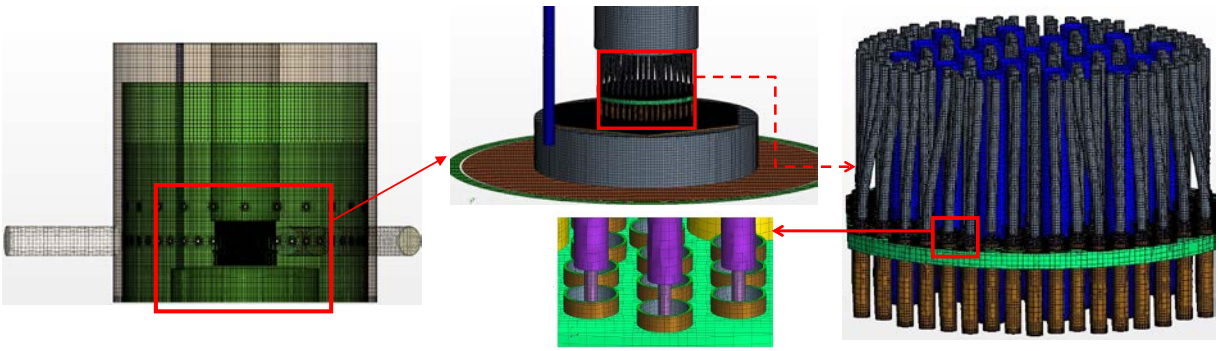

FIG. 5. Full sector model with high resolution meshes

4. Analyses conditions

In the present benchmark analyses, the sodium temperature and SA outlet flow rate distributions were given as the inlet boundary conditions of the upper plenum, while the constant flow rates or pressures were considered on the outlet surfaces of the RV outlet nozzles. The inner barrel and UIS were modelled by the equivalent thermal conductivities with the heat transfer coefficients on their surfaces in case of considering the effect of their thermal capacities. Constant temperature and/or stationary fluid were assumed in the upper plenum as initial conditions of the steady state calculations. First or second order upwind scheme were applied to the advection terms of momentum and energy equations, while 2nd order central difference was applied in the diffusion terms of these equations. The 1st or 2nd order temporal difference scheme such as Euler explicit/implicit or PISO scheme were also used by CRP participant. Turbulence models were mainly standard k-ε model for high Reynolds numbers; however RNG k-ε, Realizable k-ε and Share Stress Transport (SST) model were also applied in order to investigate the effects to the thermal stratification.

Before calculating the turbine trip transient, steady state calculations were performed by two different methods; one was a time-marching method from an initial field and another was an iterative method of time-independent equations. Using these results, the transient calculations were performed and compared with measured TC-plug temperatures.

5. Results and discussions

5.1. Steady state solutions

The time-marching approaches provided two kinds of flow patterns in the steady state solutions: one is called “buoyancy driven solution”, in which sodium flows from UCS in the upward direction along UIS surface, and another is called “momentum driven solution”, in which a sodium jet flows across the sodium pool from UCS to the inner barrel. These two typical solutions calculated by CEA are shown in Figs. 6(a) and 6(b). The buoyancy driven flow was obtained in case of using 2nd order upwind method and high resolution grids, while the momentum driven flow was obtained with the 1st order upwind method and comparatively low resolution grids. Temperature profiles along the TC-plug agreed well with measured temperature in both approaches, as shown in Fig. 7, although there are some differences of stratification front (in the region from 1.0 to 1.5 m in Fig. 7), the measured data do not allow making a determination of the flow pattern in the upper plenum at the beginning of the pump trip experiment. These buoyancy driven solutions were also calculated by KAERI and JAEA when time-marching approaches were applied to the 1/6 sector and full sector models. IPPE calculations showed the flow pattern depended on specified initial patterns.

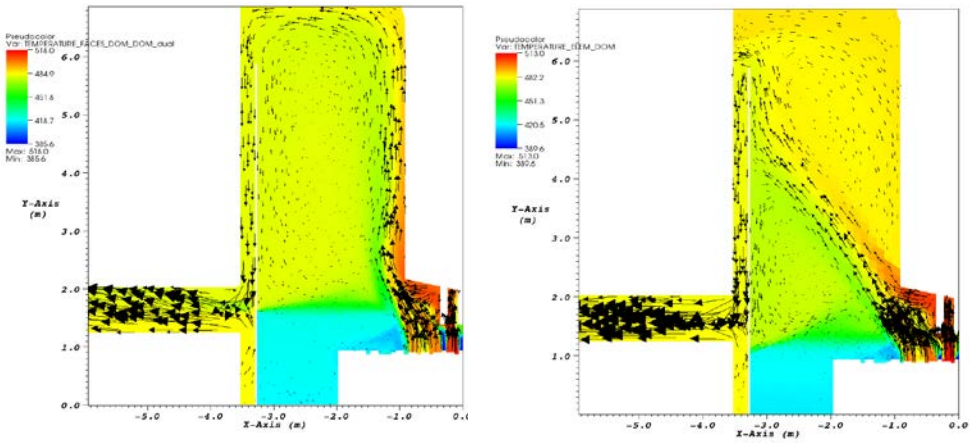

(a) Buoyancy driven solution *(b) Momentum driven solution*

FIG. 6. Two kinds of solutions and temperature distribution on TC-plug

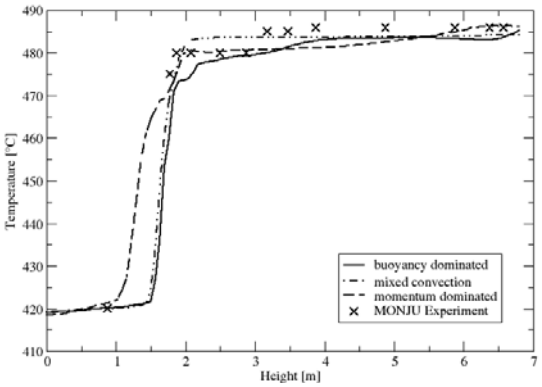

FIG. 7. Temperature distribution of two solutions on TC-plug

However, the flow pattern became a momentum driven solution in IPPE and JAEA even for a time-marching approach and 1st order upwind scheme when velocity fields were initially formed in some degrees and then simulations were continued with temperature fields. Other approaches of the iterative method, followed by ANL and University of Fukui, resulted in only momentum driven solutions. In the time-marching approaches, the buoyancy driven flows were formed by large buoyancy forces when stationary and isothermal fluid were assumed in the initial conditions, while the buoyancy driven flows were not formed when initially formed velocity fields were applied. However, the iterative method of time-independent equations reaches to one value when the governing equations converge to a unique solution. Therefore, steady state calculation results indicated that the momentum driven solutions ought to be considered as the actual flow pattern in the 40% rated power operational condition in MONJU.

5.2. Effects of asymmetric structures

Asymmetric temperature and velocity distribution in the circumferential direction of the plenum were addressed in this CRP because of the asymmetric location of structures such as FHM guide and also because of the asymmetric distribution of the SA outlet boundary conditions. Therefore, calculations were performed by JAEA [3], University of Fukui [4] and CIAE using full sector models. These models have also high resolution meshes of the flow holes on the inner barrel and modelled all CRGTs, FGTs and fingers in the UCS. A typical steady state temperature distribution on a horizontal cross section (HCS) at different steps; every 2,000 steps interval [3], are shown in Fig. 8.

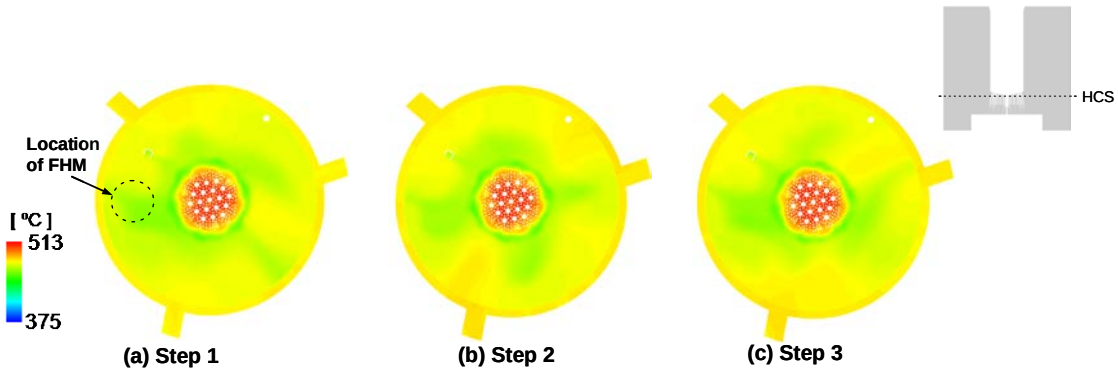

FIG. 8. Temperature distribution on HCS at different steps; every 2,000 steps interval

This HCS location is shown in the upper part of this figure. The authors are aware that the solutions of a steady state solver can only be interpreted after convergence and that intermediary solutions at different iteration numbers do not represent real physically solutions. Nevertheless, some careful conclusions can be drawn: Temperatures below the FHM guide became lower in every step; however, those of the other region changed approximately 4.0ºC in the circumferential direction. Although some fluctuations of the jet flow were calculated both on the vertical and horizontal cross sections, the

velocity distribution in the circumferential direction did not show large differences. These results also indicated the flow rates through the flow holes on the inner barrel were similar to the results obtained with the 1/6 sector simplified models both in the steady state and transient conditions. Hence, we concluded that the simplified model without asymmetric structures could predict with good accuracy the moving up rate of the thermal stratification front in the upper plenum.

5.3. Effects of turbulence model, thermal capacity and thermal conductivity

Turbulence models used in this CRP were Reynolds-averaged Navier-Stokes equation models as described in above section, although accuracy of the advection terms was different in each participant. The temperature and velocity distributions did not change much from one model to the other. Also the moving up rate of the thermal stratification front did not vary much from one turbulence model to the other. (The key factor impacting this parameter is described in section 5.4.) The CRP participants investigated also the effects of thermal capacity of UIS and inner barrel. All calculation results by CIAE, KAERI, University of Fukui and JAEA could not explain much larger moving up rate of the thermal stratification front. The effects of thermal conductivity of inner barrel were also investigated by IPPE, which showed one of the representative parameters that characterizes the moving up rate was the total duration of stage and Duration of that Stratified Stage (DSS) depended on thermal conductivity of inner barrel and was extremely sensitive to pressure loss coefficient of the FHs.

5.4. Flow holes on inner barrel

The thermal stratification front in the upper plenum is captured by the temporal changes of the temperature distribution measured by the TC-plug thermocouples. In the earlier stage of the benchmark calculations, all the CRP participants calculated faster moving up rates of the front than the measured values. Many possible explanations for these large discrepancies, such as turbulence models, grid resolutions, and thermal capacity of UIS were put forward and discussed during the Research Coordination Meetings (RCMs) of the CRP. However, all these hypotheses were rejected by the various simulation results, as already described in the above sections. As a consequence the only remaining possible explanation was the pressure losses in the flow holes of the inner barrel. All the CRP calculations were performed using flow holes with sharp edges. Usually, sharp edges yield larger pressure drops and smaller flow rates at the flow holes as compared to rounded edge; on the other hand it is well known that the edge is rounded in the usual fabrication process in factories. Hence, simulations were performed by ANL and University of Fukui using high resolution mesh models with rounded edges on both sides of the inner barrel. The curvature of the edge was unknown, but it was estimated that the effect of the curvature should not be large. Actually, the flow rate through the FHs with rounded edges became much larger than that through the FHs with the sharp edges. The calculated and measured temperature changes on the TC-plug are shown in Fig. 9, the calculations being performed by ANL and University of Fukui: both results agreed well with the measured temperatures for early stage of transient. Concerning the DSS described in 5.3, the mesh sizes was comparatively rough, however, the results shown in Fig. 10 indicated that the moving up rate agreed well with measured data during the whole transient except the temperature near the sodium surface.

These results confirm the correct simulation of the moving up rate of the thermal stratification front, in the actual conditions. In particular, based on these results, we could argue that the colder sodium flow from the SAs accumulated in the lower region of the upper plenum and mainly flowed out through the FHs. Therefore, the major impact on the moving up rate of the thermal stratification front is due to the pressure loss coefficients of the FHs.

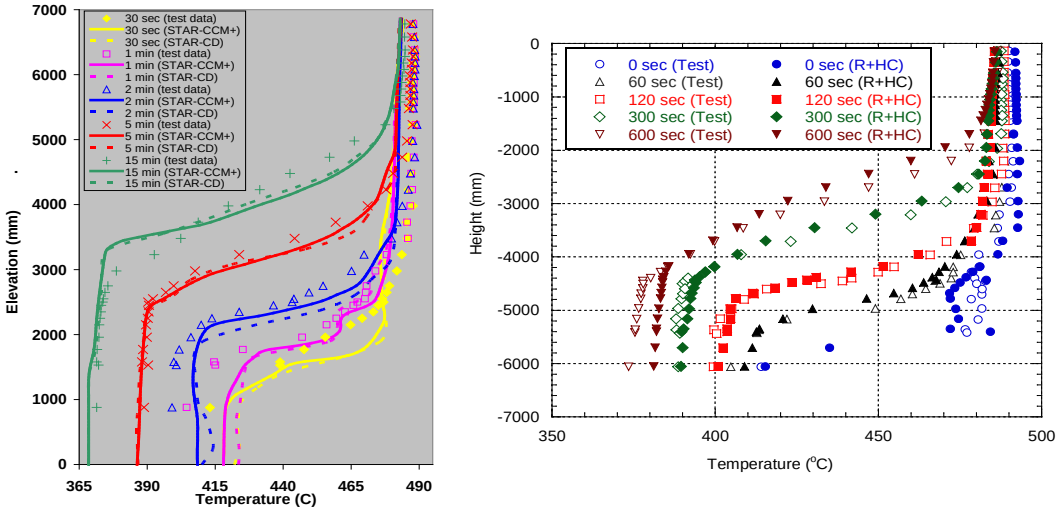

(a) Results of simplified model *(b) Results of full sector model*

FIG. 9. Calculated and measured temperature distribution on TC-plug

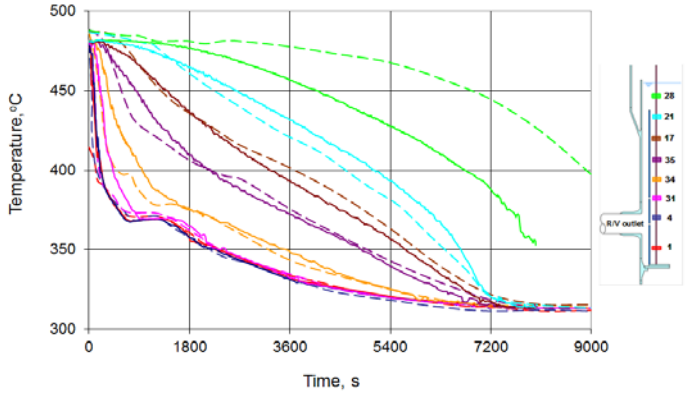

----- *Experiment* —— *GRIF calculation*

FIG. 10. Calculated and measured temperature changes on TC-plug

6. Conclusions

IAEA's CRP on "Benchmark Analyses of Sodium Natural Convection in the Upper Plenum of MONJU Reactor Vessel" has been carried out from 2008 to 2012 with eight research organizations from seven countries contributed to this CRP. The experimental data measured in the SST of MONJU were provided by the JAEA. Based on these data, each organization performed calculations with high resolution grids. The simulation results were discussed and compared in the four RCMs. The following conclusions were drawn from the benchmark analyses and the intense discussions between the CRP participants:

- Analytical capabilities of the participating organizations in the field of fast reactor in-vessel sodium thermal hydraulics, especially meshing and algorithm selection criteria, were improved by this CRP which presented challenging issues due to the complex geometry of MONJU and the involved phenomena,

- In the steady state calculations, two kinds of solutions were obtained by different calculation approaches. The momentum driven solutions were considered as the actual flow pattern in the upper plenum of MONJU RV at the 40% rated power operational condition,

- Turbulence models based on the standard k-ε model for high Reynolds number and the thermal capacity of UIS did not largely affect the moving up rate of the thermal stratification front even applying the higher order upwind method to the advection terms, and

- Since the pressure drop of the flow holes on the inner barrel strongly affected the moving up rate of the thermal stratification front, the CRP participants mainly concluded that the shape of the flow hole edge is an important factor for the prediction of this phenomena.

7. Acknowledgements

The authors would like to acknowledge Profs. A. Yamaguchi and T. Takata of Osaka University, Japan and Drs. Y. Nishi and N. Ueda of CRIEPI, Japan for giving precious advices to this CRP.

8. References

[1] M. Tsubokura, T. Kobayashi, T. Nakashima, T. Nouzawa, T. Nakamura, H. Zhang, K. Onishi, N. Oshima, "Computational visualization of unsteady flow around vehicles using high performance computing," Computers & Fluids, 38 (2009) pp. 981–990.

[2] S. Yoshikawa and M. Minami, "Data Description for Coordinated Research Project on Benchmark Analyses of Sodium Natural Convection in the Upper Plenum of the MONJU Reactor Vessel under Supervisory of Technical Working Group on Fast Reactors, International Atomic Energy Agency," JAEA-Data/Code 2008-024, Japan Atomic Energy Agency (2009).

[3] H. Ohira, K. Honda and M. Sotsu, "Numerical Simulations of Upper Plenum Thermal-Hydraulics of Monju Reactor Vessel using High Resolution Mesh Models," Proceedings of the 14th International Topical Meeting on Nuclear Reactor Thermal Hydraulics (NURETH-14), Toronto, Canada, September 25-29 (2011).

[4] H. Mochizuki and M. Takano, "Analysis of Thermal Stratification in the Upper Plenum of the "Monju" Reactor Vessel – Effect of Chamfer of Flow-Hole on Thermal Stratification," Proceedings of the 14th International Topical Meeting on Nuclear Reactor Thermal Hydraulics (NURETH-14), Toronto, Canada, September 25-29 (2011).

[5] Y. Nishi, N. Ueda, S. Yoshikawa, A. Miyakawa and M. Kato, "Benchmark Analyses of Sodium Convection in Upper Plenum of the MONJU Reactor Vessel – Comparison Between Plant System Analysis Code CERES and CFD Code," Proceedings of the 14th International Topical Meeting on Nuclear Reactor Thermal Hydraulics (NURETH-14), Toronto, Canada, September 25-29 (2011).

[6] U. Bieder, G. Fauchet and S. Yoshikawa, "Trio_U Analysis of Natural Convection in the Upper Plenum of the MONJU Reactor," Proceedings of the 14th International Topical Meeting on Nuclear Reactor Thermal Hydraulics (NURETH-14), Toronto, Canada, September 25-29 (2011).

[7] M. Shibahara, T. Takata and A. Yamaguchi, "Numerical Analysis of Thermal Stratification in the Reactor Upper Plenum of MONJU with 1/3 Sector and Full Sector Models," Proceedings of the 14th International Topical Meeting on Nuclear Reactor Thermal Hydraulics (NURETH-14), Toronto, Canada, September 25-29 (2011).

[8] T. Sofu and J. Thomas, "Analysis of Thermal Stratification in the Upper Plenum of the "Monju" Reactor Vessel," Proceedings of the 14th International Topical Meeting on Nuclear Reactor Thermal Hydraulics (NURETH-14), Toronto, Canada, September 25-29 (2011).

[9] J. Abraham, K. Velusamy and P. Chellapandi, "Computational Fluid Dynamic Investigation of Thermal Stratification in the Hot Pool of MONJU Reactor and Comparison with Measured Data," Proceedings of the 14th International Topical Meeting on Nuclear Reactor Thermal Hydraulics (NURETH-14), Toronto, Canada, September 25-29 (2011).

[10] T. Sofu, "Parametric Analysis of Thermal Stratification during the MONJU Turbine Trip Test," Proceedings of the International Congress on Advances in Nuclear Power Plants (ICAPP'12), Chicago, USA, June 24-28 (2012).

Development and Assessment of a Thermo-kinetic model on Mixed Oxide (MOX) Fuels using Dictra

E. Moore[a], C. Guéneau[a], J.P. Crocombette[b],

[a] CEA Saclay DEN-DPC-SCCME-91191 Gif-sur-Yvette Cedex-France

[b] CEA Saclay DEN-SRMP 91191 Gif-sur-Yvette Cedex-France

Abstract.

MOX fuels containing recycled plutonium are currently used in PWR throughout France. Moreover, mixed oxide fuels is the recommended fuel type for Gen IV SFR's. Thus it is of paramount importance to understand the diffusion properties within the fuel matrix. Mixed oxide fuels such as uranium-plutonium dioxide exhibits a non-stoichiometric range over a wide temperature scale. Atomic transport properties are governed by the defects in the fuel. The DICTRA-based model considers diffusion across non-stoichiometric ranges described by experimentally available data. Before considering mixed oxide fuels, the binaries $UO_{2\pm x}$ and PuO_{2-x} are assessed. A vacancy and interstitial diffusion-model for oxygen is applied to U-O and Pu-O systems as a function of defect structures, derived from CALPHAD-type thermodynamic descriptions. Oxygen and metal self-diffusion coefficients are assessed for a mobility database. Chemical diffusion coefficients are derived using the Darken relation and defect migration energies are evaluated. A diffusion model of the oxides in the C1 phase with O/M=1.85-2.15 at various temperatures is presented.

Introduction.

Mixed oxide of uranium and plutonium is commonly used as the basis for the Sodium cooled Fast Reactor (SFR). The material consists of various ratios of metal content and exists over both hypo and hyper stoichiometric ranges. Diffusion properties of the mixed oxide depend largely on the migration of the anion, which is multiple orders of magnitude larger than that of either metal. The atomic transport properties of the mixed oxide are of interest with respect to their fabrication process as well as their behaviour under irradiation.

The individual systems of $UO_{2\pm x}$ [1-15] and PuO_{2-x} [16-20] have been widely studied for their thermodynamic and diffusion properties. The oxygen self-diffusion coefficients for both systems have been investigated and extensively for $UO_{2\pm x}$. For either oxide, there is a minimum in the diffusion coefficient at the stoichiometric composition M/O=2, which corresponds to a maximum in the activation energy [12]. While defects are naturally present in the "perfect" crystalline structure, they are not as abundant as in the over or under stoichiometric compositions. Therefore, at stoichiometry, the activation energy is linked to both the formation of defects as well as their migration.

Description of Diffusion Model

Within the diffusion model, there inherently lies thermodynamic information. The Dictra code [21] is constructed within the Calphad [22] scope and therefore uses the same compound energy formalism (CEF) to describe a crystalline structure. To describe the non-stoichiometric oxides a 3-sublattice model is developed. For the uranium-oxygen system, the model is as follows:

$$(U^{+3},U^{+4},U^{+5})_1 \ (O^{-2},Va)_2 \ (O^{-2},Va)_1 \quad (1)$$

UO_2 assumes the fluorite structure, where the cations are arranged into a face centered cubic structure and the anions are located on the tetrahedral sites, creating a simple cubic sublattice within the unit cell. The first sublattice describes the uranium cations in the system with the possible charges of U^{+3}, U^{+4} and U^{+5}, the second sublattice consists of the oxygen atoms on the regular lattice sites as described above, which is capable of incorporating vacancy defects to support the hypostoichiometric compositions (UO_{2-x}). A charge balance is achieved by an increase in U^{+3} species when the oxide assumes this under-stoichiometric form. Finally, a third sublattice is added to incorporate the oxygen interstitial defects, which govern the hyperstoichiometric oxide (UO_{2+x}). The extra oxygen atoms are charge compensated by the presence of U^{+5} species.

The plutonium dioxide assumes the same fluorite structure as UO_2; we therefore consider the same three-sublattice model to describe the stoichiometric oxide. This is also useful for the addition of the two systems to achieve the ternary $(U,Pu)O_{2\pm x}$. For the non-stoichiometric composition of the plutonium dioxide, only the hypo-stoichiometric range is accessible, as a presence of the hyper-stoichiometric range has not yet been proven [1]. The PuO_{2-x} is described using a three-sublattice model, as follows:

$$(Pu^{+3}, Pu^{+4})_1 \ (O^{-2},Va)_2 \ (O^{-2},Va)_1 \quad (2)$$

In this model, the metal atoms can carry a +3 or +4 charge. In the most recent thermodynamic assessment of the Pu-O system a third sublattice was added for the oxygen interstitials for coherence with the mixed oxide model [23]. Since the PuO_{2+x} domain is not physically accesible the parameter for the thermodynamic database was set to render this state ubstable (high positive value). The defect fractions of the individual species for both the U-O and Pu-O systems are depicted in Figure 1.

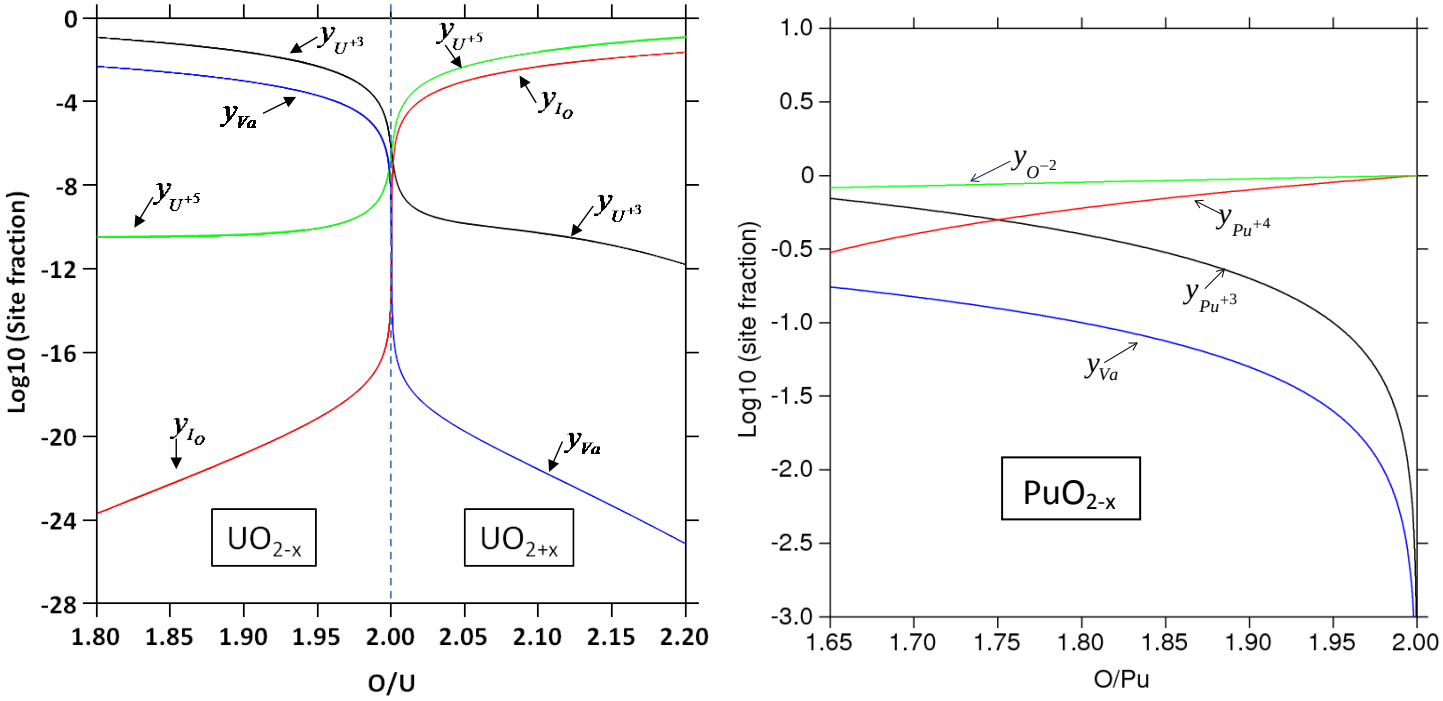

Figure 1: Defect site fractions of $UO_{2\pm x}$ (left) and PuO_{2-x} (right) as calculated by the Calphad method using [23] at 1500 K.

The site fractions correspond to those of each cationic specie (U^{+3},U^{+4},U^{+5}) for UO_2 and (Pu^{+3},Pu^{+4}) for PuO_2. The oxygen site fractions are described by the vacancy and oxygen content on the second sublattice (Va and O^{-2} respectively) and the oxygen interstitial content (I_O) on the third sublattice for UO_{2+x}.

The mobility terms which are optimized using the Parrot module [24] in Dictra are related to the self diffusion coefficient (D*) by the Nernst Einstein relation

$$D^* = M^* RT \quad (3)$$

The tracer mobility (M*) represents the overall mobility if we assume the correlation factor f=1, since it is not treatable in Dictra. The overall mobility is presented in separate terms for each sublattice. For oxygen in $UO_{2\pm x}$ and PuO_{2-x} this consists of a mobility term for vacancy and interstitial migration. The uranium sublattice is a summation, which treats the mobility of each cationic specie individually. There is no known data for plutionium diffusion, therefore we do not treat it for the binary system. The ternary system will treat the mobility terms as mentioned above. For each of the mobility parameters, interaction terms can be added to extend the fit within the composition domain. The mobility parameters for each of the species mentioned above are presented as follows:

$$M_i = y_i(1-y_i)M_i^0 \, exp\left(\frac{-Q_i + y_i(1-y_i)(A+BT)}{RT}\right) \quad (4)$$

Here, M_i is the overall mobility for the given sublattice. This term is described using an activation energy Q_i and a prefactorial term M_i^0 which includes information linked to the atomic vibrational frequency and jump distances (inter-atomic spacing). The defect site fractions are those described above. An interaction term in the general form of A+BT can be added as a Redlich Kister expansion to the activation energy term. This aids in describing the interactions between the defect species on each respective sublattice. The expressions for the mobility term for oxygen vary in terms of the parameters described above. For the oxygen vacancy mobility term in $UO_{2\pm x}$, the interaction parameter consists of (A+BT), whereas the interstitial oxygen mobility term does not include a temperature dependence.

Since the thermodynamic based model describing the metal atom species is comprised of one sublattice, only a single mobility term is needed. This mobility term, is however split into parameters for each cationic species as detailed below:

$$M_U = y_{U^{+3}} M^0_{U^{+3}} exp\left(\frac{-Q_{U^{+3}}}{RT}\right) + y_{U^{+4}} M^0_{U^{+4}} exp\left(\frac{-Q_{U^{+4}}}{RT}\right) + y_{U^{+5}} M^0_{U^{+5}} exp\left(\frac{-Q_{U^{+5}} + y_{U^{+4}} y_{U^{+5}} {}^0A}{RT}\right) \quad (5)$$

As stated above each cationic specie will have its own set of parameters such as the activation energy and prefactorial terms. A possibility of including interaction terms between the species is considered to ameliorate the fit, when necessary. All of these assessed parameters will be detailed in the results section.

Overview of Literature Data

As with all Calphad-type assessments a critical review of literature data is necessary for the developement of the thermo-kinetic database. For the thermodynamic descriptions, we use the data from Guéneau et al. [23]. A large amount of diffusion data for $UO_{2\pm x}$ has been reviewed by Matzke [12] for which we use their selected data for the oxygen self-diffusion coefficient. A more recent review by Berthenier [25] concluded that self-diffusion coefficient values higher than those of Matzkes selection were due to possible impurities and grain boundary diffusion, when measuring close to the stoichiometric region. In fact, a newer study by Garcia et al [14] found diffusion coefficients slightly lower than previously known for a quite stoichiometric single crystal oxide. The same paper confirms previous work by [15] concluding that impurities (via doping) lead to higher values for the self-diffusion coefficient. We therefore base our selection of oxygen diffusion data heavily on the data of Matzke and Garcia [12,14] for the developement of our database at the stoichiometric composition of UO_2. For the nonstoichiometric domain, we choose Kim and Olander [11] the only available data for UO_{2-x} and Contamin [9] for compositions UO_{2+x}.

The same review by [12] detailed the uranium diffusion coefficient in UO_2 and concluded that the previously measured values contain what is referred to as a literature artifacts and erroneously represent elevated values. These artifacts are most notably due to surface phenomena and lead to initial fast tracer penetration inducing a time-dependent diffusion term. Our model is fit to the selected data by [12] for uranium self-diffusion in stoichiometric UO_2 as it represents true volume diffusion and accounts for surface effects. For the hypostoichiometric composition, we follow the trend seen by Marin and Matzke [26,27].

The available literature data on diffusion in plutonium-dioxide, was mainly carried out by Bayoglu et al [19,20], who performed experiments for both the hypostoichiometric and stoichiometric oxide. Thermo-analytic methods including thermogravity and dilatometry were used to measure chemical diffusion coefficients of oxygen in PuO_2 according to Fick's law. They observed however, that the diffusion coefficient varied with stoichiometry and applied an iterative method [28] to recalculate the values of $\tilde{D}$ with varying stoichiometric deviations. This method was also used by Chereau [18]. The self-diffusion coefficients were then calculated using the Darken equation and their calculated oxygen potential [19].

Results and Discussion

The parameters for oxygen diffusion in $UO_{2\pm x}$ described in equation 4 are simultaneously fit to the available experimental data using a least squares fit in the Parrot [28] module with the Dictra software. The activation energy terms QVa and QIo for oxygen vacancy and interstitial migration are allowed to vary independently, whereas the frequency factors were given a fixed range in which they were allowed to vary, keeping the values in an acceptable physical range. Starting points for QVa and QIo were chosen to coincide with the migration energy of oxygen vacancies and interstitials respectively as detailed in [29]. Interaction parameters in the form of A-BT and A respectively, were allowed to vary independantly to be in agreement with under and overstoichiometric composition dependencies of the diffusion coefficient.

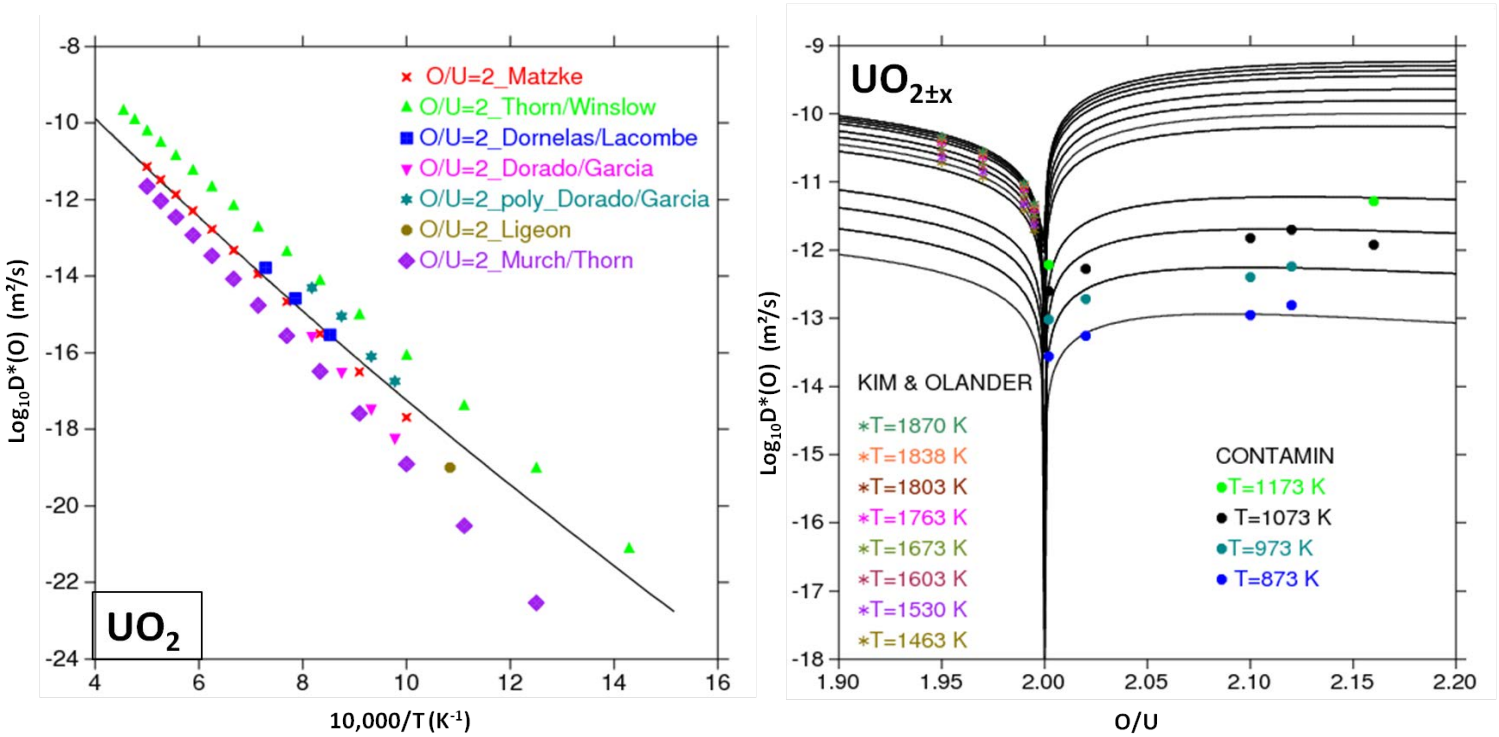

Figure 2: Assessed oxygen-self diffusion coefficients with respect temperature at UO_2 (left) and with respect to composition at various temperatures (right)

The assessed oxygen self-diffusion coefficients are simultaneously fit (Figure 2) to the temperature dependence for the UO_2 stoichiometric oxide and the composition dependence as a depature from stoichiometry $UO_{2\pm x}$ at various comparable temperatures. The data for each figure is in good agreement with experimentally and theoretically available data. [4,6,8-12]. The mobility parameters are detailed in Table 1 [29].

Table 1: Oxygen Mobility Parameters for $UO_{2\pm x}$

Assessed Oxygen Mobility Parameters			
Regular Oxygen Sublattice (M_{Va})		**Interstitial Oxygen Sublattice (M_{Io})**	
Q_{Va}	53498 (J/mol)	Q_{Io}	95411 (J/mol)
M^0_{Va}	4.38×10^{-12} (m^2/s)	M^0_{Io}	2.76×10^{-12} (m^2/s)
A+BT	2234 (J/mol) -19.91xT	A	-90548 (J/mol)

The assesed mobility terms Q_{Va} and Q_{Io} in table 1 are not exact representatives of the migration energies, since the interaction parameters play a important role in the fit. At small hyperstoichiometric deviations; $x \geq 0.005$, oxygen diffusion is heavily influenced by cluster formation. We are able to indirectly take into account defect interactions via the mixing terms, notably on the third sublattice, which describes the interactions of interstitial oxygen atoms The mixing term on the second sublattice, which describes the interaction between defects on the regular oxygen tetrahedral sites includes a temperature term, whereas a temperature dependant term for the third sublattice (oxygen interstitials) did not significantly affect the fit [29].

The assessed uranium mobility database is detailed in Figure 3 for stoichiometric UO_2 and UO_{2+x} uranium self-diffusion coefficients. Our calculated values fitted only to the values of Matzke (note that most of the values are falsely elevated) are in fair agreement with them. As with oxygen diffusion, inclusion of interaction parameters proved necessary to better describe diffusion in UO_{2+x}. Diffusion in UO_{2+x} increases rapidly between four and five orders of magnitude between UO_2 and $UO_{2.20}$ as described by [26,27] a trend which is reproduced with our model.

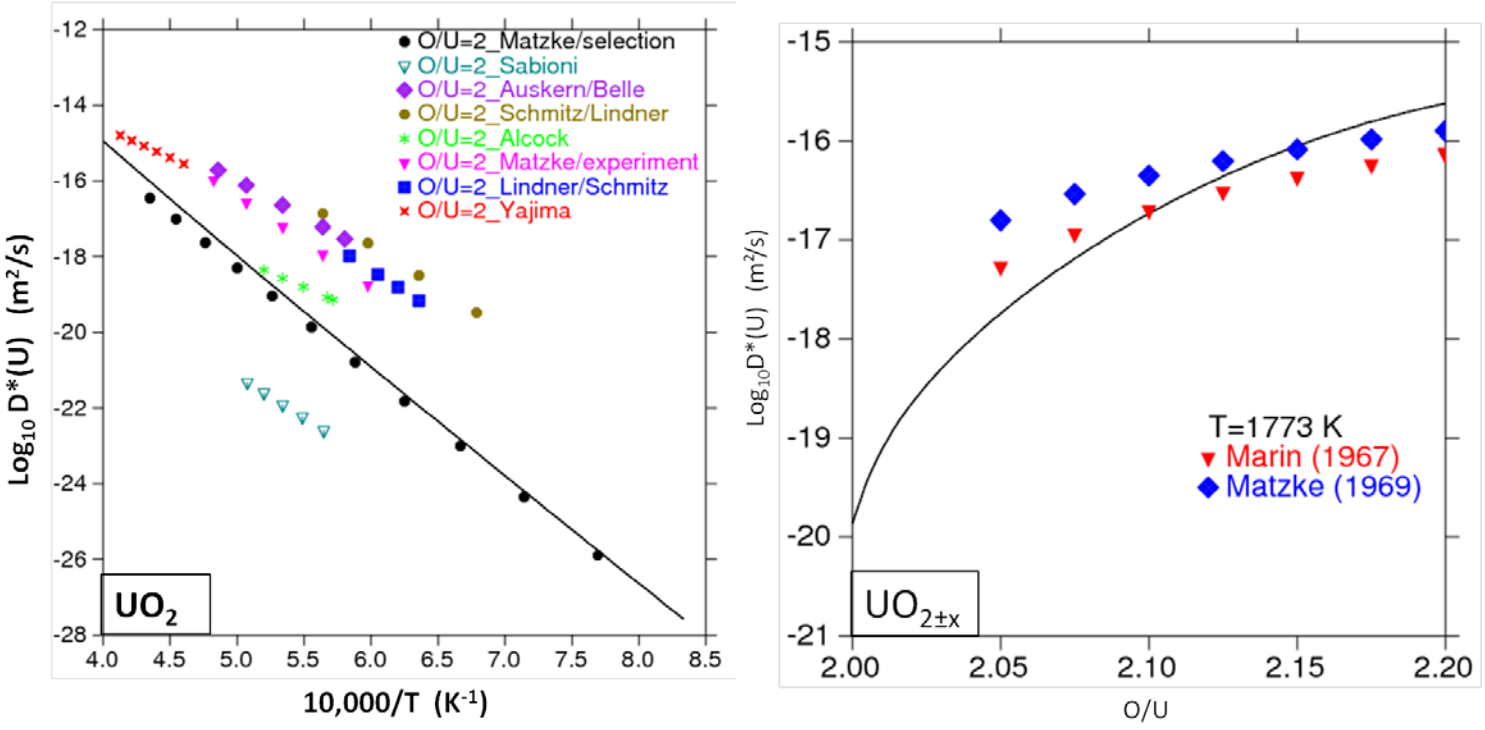

Figure 3: Uranium self-diffusion coefficient as a function of temperature at UO_2 and as a function of composition at 1773 K.

The accepted uranium migration mechanism as described by point defect models is that of uranium vacancies for the overstoichiometric oxide. The diffusion model includes interactions between the defects as seen in the mixing term as well as the defect concentrations of each of the charged states, therefore taking into account the cationic oxidation states. The terms for the assessed uranium mobility database are seen in table 2 [29]. We do not directly consider vacancies on the metal sublattice, we can only deduce the activation energy (5.3 eV at stoichiometric UO_2) for uranium diffusion, which includes the migration energy as well as the defect formation energy.

Table 2: Assessed Uranium Mobility Parameters [29]

Assessed Mobility Parameters	
U^{+3}	$Q_{U^{+3}}$ = 540,000 (J/mol)
	$M^0_{U^{+3}}$ = 1.55*10^{-8} (m^2/s)
U^{+4}	$Q_{U^{+4}}$ = 580,000 (J/mol)
	$M^0_{U^{+4}}$ = 5.5*10^{-9} (m^2/s)
U^{+5}	$Q_{U^{+5}}$ = 440,000 (J/mol)
	$M^0_{U^{+5}}$ = 1.35*10^{-9} (m^2/s)
	A = 345,000 (J/mol)

The plutonium dioxide diffusion model details the sub stoichiometric and stoichiometric compound, as the hyperstoichiometric oxide has not been observed experimentally. The phase diagram calculated by [30] includes the fluorite phase region for Pu/O values between 1.62 to 2.0. Our kinetic database does however, include an oxygen mobilty term for the third sublattice, describing oxygen interstitital migration, with a very high value for the activation barrier, as to not have any possible contribution for this term. Figure 4 shows the composition dependance of the oxygen self-diffusion coefficient at various temperatures between 853-1353 K as well as the temperature dependance of the stoichiometric oxide.

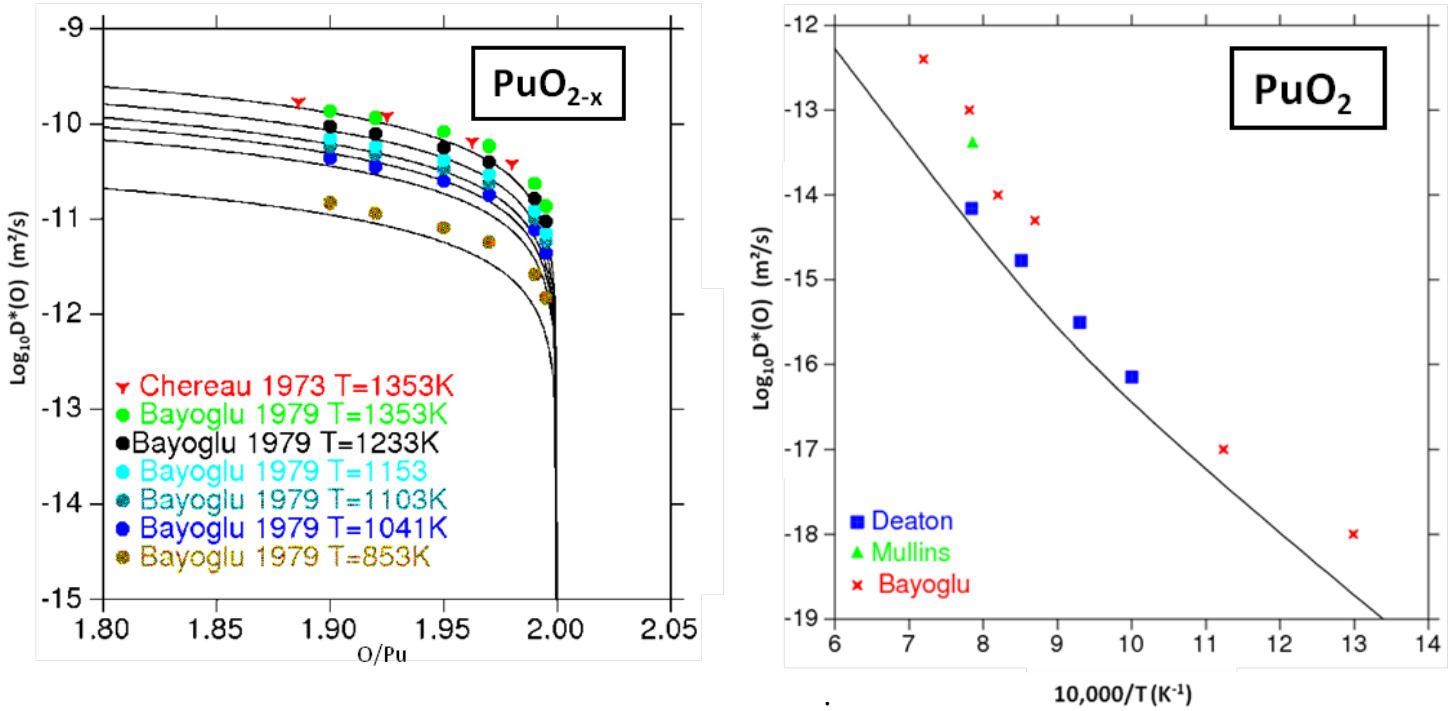

Figure 4: Oxygen self-diffusion coefficient of plutonium dioxide (PuO_{2-x}) and PuO_2 as compared with experimental data [16-20]

Our calculated values for the oxygen self-diffusion coefficients for the hypo-stoichiometric composition at various temperatures is in good agreement with Bayoglu [18] and Chereau [19], of which both sets of data were used for the fit. We slightly under calculate the value at lower temperatures. At the stoichiometric oxide, we are in best agreement with Deaton [16] for a temperature range The addition of an interaction parameter was not necessary. The optimized mobility terms are found in table 3.

Table 3: Oxygen Mobility Parameters for PuO_{2-x}

Assessed Oxygen Mobility Parameters			
Regular Oxygen Sublattice (M_{Va})		**Interstitial Oxygen Sublattice (M_{I_O})**	
Q_{Va}	38,529 (J/mol)	Q_{I_O}	$1x10^{7}$ (J/mol)
M^{0}_{Va}	$7.43x10^{-12}$ (m^2/s)		

It is interesting to note that although the interstitial oxygen mobility term does not contribute to the hypo-stoichiometric description of the self-diffusion coefficient, it is indeed necessary to include it when evaluating the mobility at O/Pu=2. This is consistent with the fact that while not dominantly present, small amounts of oxygen interstitial defects are inherent in the material. It is the combination of the mobility terms that allows the description of the stoichiometric oxide.

Conclusions:

With the Calphad method, a combination of the thermodynamic and kinetic information for both $UO_{2\pm x}$ and PuO_{2-x} systems allows for the construction of a coherent diffusion model. The self-diffusion data for oxygen is well represented for both systems. The uranium metal diffusion coefficients are also well reproduced when compared to experimental and theoretically selected values. Plutionium metal diffusion has not been measured. We have created the basis for combining the two binary systems for simulation of mixed oxide fuel conditions.

ACKNOWLEDGEMENTS

The authors would like to thank Christian Chatillon and Fiqiri Hodaj for their insights and discussions concerning the model development and their expertise in the subject area. The technical support of Bo Sundman, Lars Höglund and Qing Chen with DICTRA and Thermocalc is also greatly appreciated.

REFERENCES

[1] **Auskern, A.B. and Belle, J.** *J. Nucl. Mater.* 1961, Vol. 3, pp. 311-319
[2] **Schmitz, F. and Lindner, R.** *J. Nucl. Mater.* 1965, Vol. 17, pp. 259-269
[3] **Yajima, S. et Furuya, H. and Hirai, T.** *J. Nucl. Mater.* 1966, Vol. 20, pp. 162-170
[4] **Thorn, R.J. and Winslow, G.H.** *J. CHem. Phys.* 1966, Vol. 44, 7, pp. 2632-2643
[5] **Alcock, C.B., Hawkins, R.J. et Hills, A.W.D. and McNamara, P.** Vienna : IAEA, 1966. Vol 2
[6] **Dornelas, W. and Lacombe, P.** *C. R. Acad. Sc. Paris.* 1967, pp. C359-362
[7] **Matzke, Hj.** *J. Nucl. Mater.* 1969, Vol. 30, pp. 26-35
[8] **Ligeon, E., Fontenille, J. et Bontemps, A. and Contamin, P.** *18O (p,alpha) 15N à l'étude de l'autodiffusion de l'oxygène dans le dioxide d'uranium.* 1970. CEA-R-4095
[9] **Contamin, P. et Bacmann, J.J. and Marin, J.F.** *J. Nucl. Mater.* 1972, Vol. 42, pp. 54-64

[10] **Murch, G.E and.Thorn, R.J.** *J. Nucl. Mater.* 1978, Vol. 71, pp. 219-226
[11] **Kim, K.C. and Olander D.R.** *J. Nucl. Mater.* 1981, Vol. 102, 192-199
[12] **Matzke, Hj.** *J. Chem. Soc., Faraday Trans.* 1987, Vol. 82, pp. 2232-1142
[13]] **Sabioni, A.C.S. et Ferraz, W.B. and Millot, F.** *J. Nucl. Mater.* 1998, Vol. 257, pp. 180-184
[14] **Garcia, P. et al.** *J. Nucl. Mater.* 2010, Vol. 400, pp. 112-118
[15] **Dorado, B., et al.** *Phys. Rev. B.* 2011, Vol. 83, 035216
[16] **R.L. Deaton, C.J. Wiedenheft**, *J. Inorg. Nucl. Chem*. 1973 Vol 35 p. 649
[17] **L.J. Mullins, G.M. Matlack, J. Budernak et J.A. Leary**, LA DC, 72, 473
[18] **Chereau, P. and Wadier, J.F. .** *J. Nucl. Mater.* 1973, Vol 46 pp 1
[19] **Bayoglu, A.S. and Lorenzelli, R. .** *J. Nucl. Mater.* 1979, Vol 82 pp 403-410
[20] **Bayoglu, A.S.; Giordano, A. and Lorenzelli, R. .** *J. Nucl. Mater.* 1983, Vol 113 pp 71
[21] **Sundman, B. et Jansson, B. and Andersson, J.O.** *Calphad.* 1985, Vol. 9, p. 153
[22] **Lukas, H.L. et Fries, S.G. and Sundman, B.** *Computational Thermodynamics, The Calphad Method.* s.l. : Cambridge Univ. Press, 2007
[23] **Guéneau, C., et al.** *J. Nucl. Mater.* 2011, Vol. 419, pp. 145-167
[24] **Jansson, B.** *TRITA-MAC-0124.* Royal Institut Technology : S10044 Stockholm 70, Sweden , April, 1984
[25] **Berthinier, C., Rado, C. et Chatillon, C. and Hodaj, F.** *J. Nucl. Mater.*Vol 433 p. 265
[26] **Marin, J. F. and Contamin, P.** *J. Nucl. Mater.* 1969, Vol. 30, p. 20.
[27] **Matzke, H.j.** *J. de Physique.* Paris : s.n., 1973. Vol. 34(Coll C9, Suppl 11 and 12), pp. C9-317.
[28] **Crank, J.** *The Mathematics of Diffusion* (Oxford Press, London 1975).
[29] **Moore, E.; Guéneau, C. and Crocombette, J.P.** *J. Solid State. Chem* submitted Nov 2012.
[30] **Guéneau, C. ; Chatillon, C. and Sundman, B.** *J. Nucl. Mater.* 2008, Vol 378 pp. 257-272.

FAST CODE SYSTEM: REVIEW OF RECENT APPLICATIONS

Konstantin Mikityuk[a], Jiri Krepel[a], Sandro Pelloni[a], Gaëtan Girardin[b], Aurelia Chenu[b], Kaichao Sun[b], Mercedes Alonso[b], Alessandro Marinoni[b], Robert Adams[c], Florian Reiterer[c]

[a] Paul Scherrer Institut, Villigen, Switzerland

[b] École Polytechnique Fédérale de Lausanne, Switzerland

[c] Eidgenössische Technische Hochschule Zürich, Switzerland

Abstract. The FAST code system, consisting of coupled neutronics (ERANOS and SERPENT), thermal-hydraulic (TRACE) and fuel behaviour (FRED) modules, is currently being developed and used at Paul Scherrer Institut for static and transient analysis of different innovative fast reactors. The paper presents the review of few recent studies in which the FAST code system was used for: 1) validation of static neutronic modeling using data of PHENIX EOL control rod shift test and BFS-62-3A critical test; 2) validation of coupled neutron kinetics and system thermal hydraulics using data of PHENIX EOL natural circulation test; 3) for different fast reactor concepts: comparison of closed fuel cycles; 4) nuclear data uncertainty propagation in dynamic calculations; 5) the SFR core behaviour under unprotected loss-of-flow conditions.

1. Introduction

The paper continues a series of papers [1],[2] devoted to development and applications of the FAST code system—a tool for the numerical simulation of coupled neutronic, thermal-hydraulic, and thermal-mechanical behavior of the fast-spectrum reactor systems in static and transient conditions, being continuously developed and applied at the FAST reactors group [3] of the Paul Scherrer Institut. The code system includes well-established codes, namely: stochastic SERPENT [4] and deterministic ERANOS [5], both for static neutronics; PARCS, for reactor kinetics [6]; TRACE, for system thermal hydraulics [7]; and FRED, for thermal mechanics [8]. The stochastic SERPENT code has been recently included in the FAST code system and its application for preparation of the cross sections for PARCS is reported in [9]. The flowchart of FAST code system is presented in Fig. 1, showing the main codes used, as well as the information flow between the different codes.

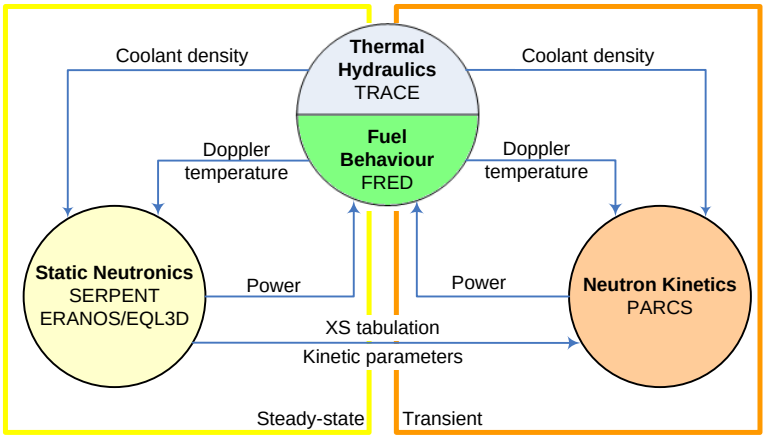

Fig. 1. FAST code system structure

Presented in the paper are selected highlights related to the FAST code system applications during the last three years. The review is mainly based on the published results.

2. Validation of static neutronic modeling

In this section the results of validation of the static neutronic codes, using measurements from the PHENIX EOL control rod shift test and BFS-62-3A zero-power critical test are briefly presented.

2.1. PHENIX EOL control rod shift test

The end-of-life (EOL) tests recently performed at the Phenix reactor present a unique opportunity to validate computational tools used for Sodium-cooled Fast Reactor (SFR) static and transient analysis. The FAST code system—including ERANOS and TRACE/PARCS—has been used to analyze test data from the control-rod-shift (CRS) experiments [10]. The test has been studied in the framework of international benchmark exercises organized by the IAEA. A static model of the Phenix core was first developed with ERANOS (see Fig. 2). This was used (i) for direct comparison with the CRS test data and (ii) to prepare the macroscopic reference cross-sections and their derivatives for use in the 3D neutron kinetics PARCS model. A coupled TRACE/PARCS static model was then developed and verified against ERANOS results. The power deformations resulting from the different control rod (CR) positions calculated with both models have been found to agree very well with the experimental data, showing that the control rods were accurately modeled (see Fig. 23). This analysis has thus provided valuable additional validation of the SFR modeling capabilities of ERANOS and TRACE/PARCS as implemented within the FAST code system.

2.2. BFS-62-3A critical test

The BFS-2 critical facility at the Institute of Physics and Power Engineering (IPPE) was designed for simulation of fast reactor core neutronics, and for the validation of codes and nuclear data. The BFS-62-3A critical benchmark experiment [13] was set-up as a mock-up of the BN-600 reactor core with $(U,Pu)O_2$ fuel of 17% Pu content and stainless-steel reflectors. It was operated to measure the effective multiplication factor, spectral indices, radial fission rate distributions, control rod worths and sodium void effects. In the present study, a 3D full-core heterogeneous model of the BFS-62-3A critical benchmark experiment was developed and validated using the Monte Carlo MCNPX-2.4.0 code [14] and the ERANOS-2.2 code (see Fig. 4). Special care was taken to run the MCNPX model to make Monte-Carlo confidence intervals comparable with uncertainties reported in the experiments; such as in material dimensions, number densities and isotopic compositions. In addition to the effective multiplication factor, sodium void effect, fission rate distributions and control rod worth were calculated (see [15] for details). To accurately reproduce highly heterogeneous structure of the BFS tubes, a special care was given in ERANOS-2.2 to the cell simulation with the ECCO cell code (see [16] for details). MCNPX simulations were carried out with four different modern nuclear data libraries; the primary aim being to estimate sensitivity of the results to the nuclear data. This task, besides being a library comparison, is also meant as a first step towards a code-to-code verification with deterministic methods, in particular used in ERANOS-2.2 (see Table 1). Results agree well with experimental values on most of the nuclear characteristics, even though a discrepancy up to more than 20% was found on the flux distribution in the stainless-steel reflector region. As an example, in Fig. 5 the calculational results are compared with the experimental values of Pu^{239} radial fission rate.

3. Validation of coupled neutron kinetics and thermal hydraulics

The results of the FAST code system validation, using experimental data from PHENIX-EOL natural circulation test, reported in detail in [17] and [18], are briefly reviewed in this Section. Another validation study, using the Superphenix start-up tests, is presented in [19].

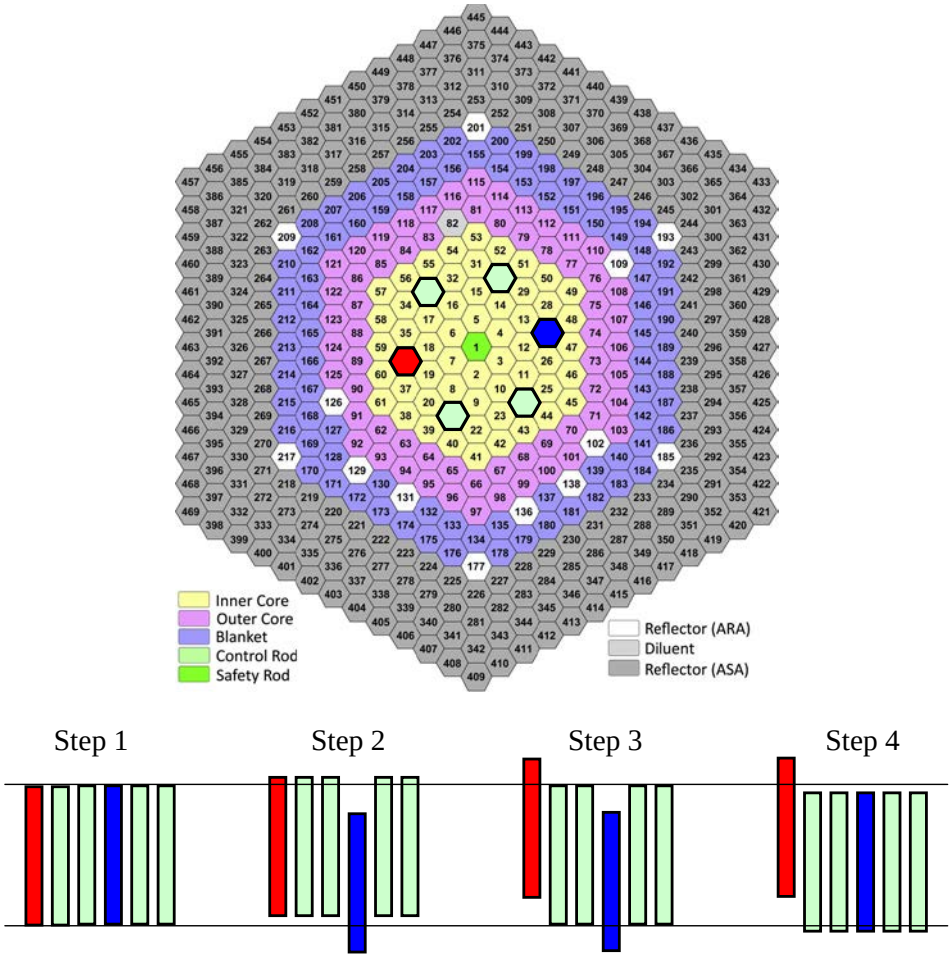

Fig. 2. Phenix core map as configured during the CRS test (adapted from [11]) and schematic of the control assembly configuration for each of the four test steps.

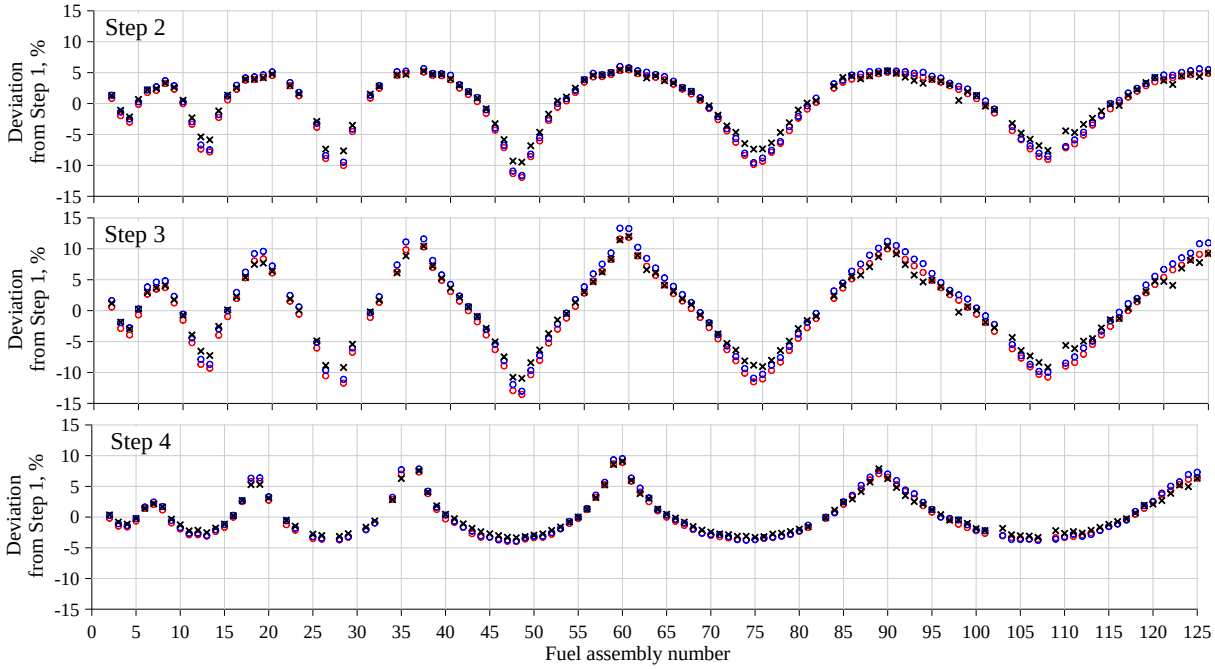

Fig. 3. Comparison of the power deformations for the different steps of the CRS test, measured (×), calculated with TRACE/PARCS (○) and with ERANOS (○).

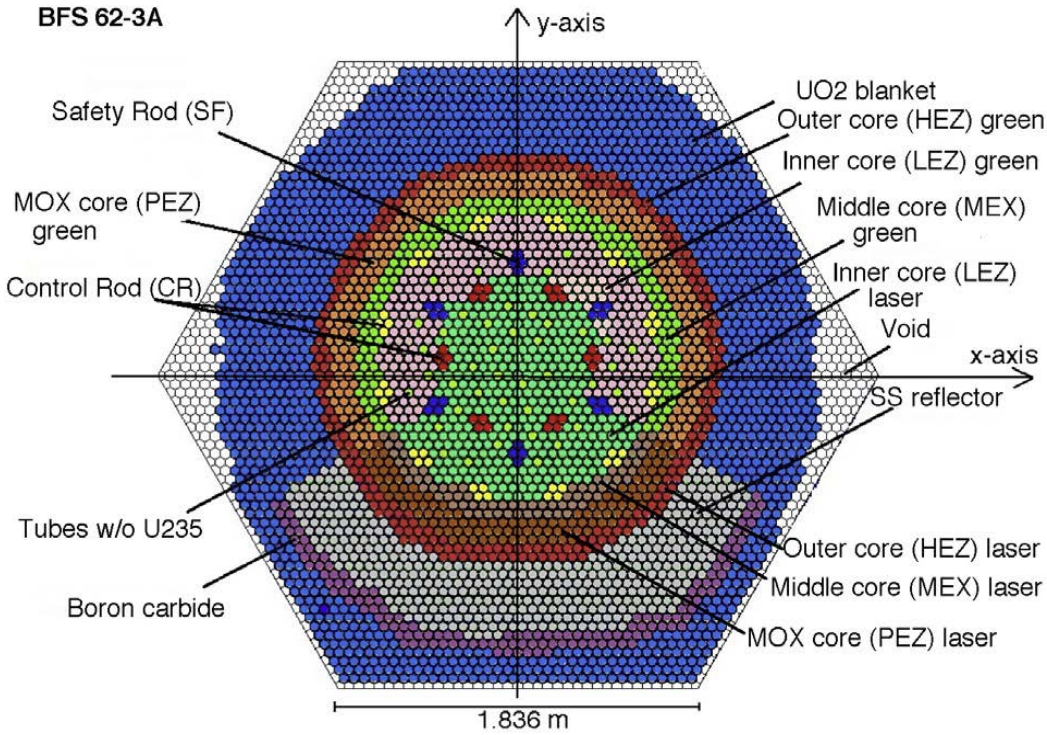

Fig. 4. Layout of the BFS-62-3A critical assembly.

Table 1. Comparison of k_{eff}, calculated by MCNPX (four different nuclear libraries) and by ERANOS.

Code/Library	k_{eff}	$1/k_{eff}^{C} - 1/k_{eff}^{E}$
Experiment	1.00080 ± 0.00300	0.00000
MCNPX/ENDF/B-VI	1.00265 ± 0.00003	0.00184
MCNPX/JEF-2.2	1.00333 ± 0.00003	0.00252
MCNPX/JEFF-3.1.1	1.00317 ± 0.00004	0.00236
MCNPX/JENDL-3.3	0.99642 ± 0.00004	–0.00439
ERANOS-2.2/JEFF-3.1	1.00031	–0.00049

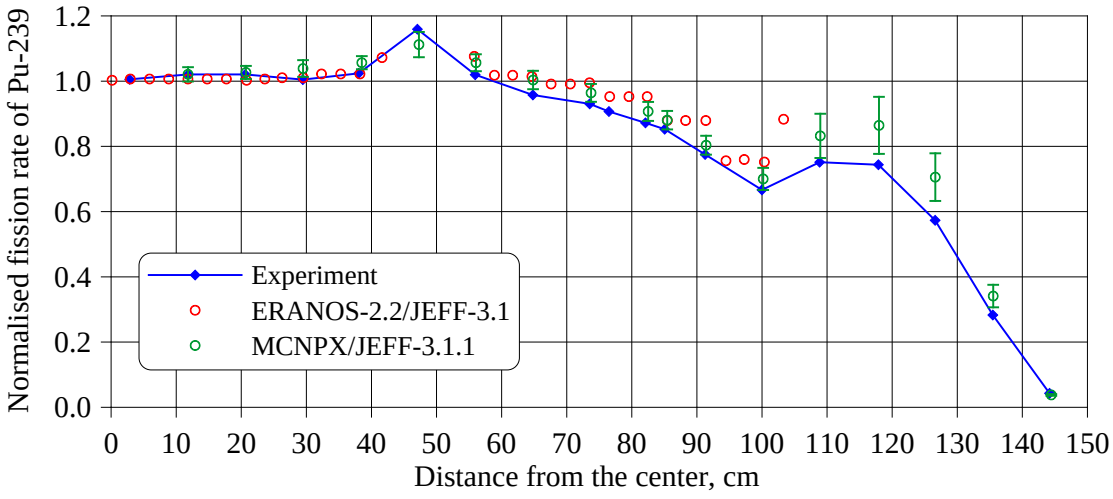

Fig. 5. Measured and calculated radial distribution of the plutonium-239 fission rate normalized to 1 at the core centre. The stainless steel reflector starts at a distance of 100 cm from the core center.

3.1. PHENIX EOL natural circulation test

In addition to PHENIX-EOL control rod shift test presented in Section 2.1, another test from this program devoted to establishment of the natural circulation in the primary system was analysed with the FAST code system in frames of the IAEA Coordinated Research Project (CRP). A simplified schematics of the PHENIX primary, intermediate and tertiary circuits is presented in Fig. 6. The PHENIX steam generator (SG) has a design in which water/steam pipings are located inside sodium tubes, which are enclosed in a large closed casing. The casing can be open from the bottom and top to establish natural convection of the atmospheric air.

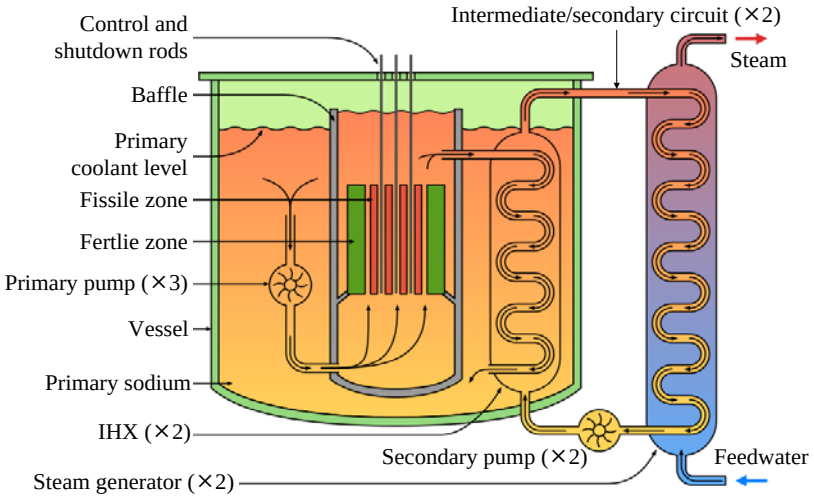

Fig. 6. A simplified representation of the PHENIX liquid-metal fast reactor cooling scheme.

Before the test the reactor was under steady-state conditions at 120 MWth with all 3 primary pumps in operation and with 2 out of 3 secondary loops operating. Sodium at core inlet was at 360ºC. At time 0, feedwater supply to 2 SGs were stopped. Phase 1 (Unprotected Loss of Heat Sink) continued ~7 min during which the secondary and primary sodium heated up and reactor power went down by 60% due to the reactivity feedbacks (diagrid radial expansion, positive Doppler followed by positive effect of the vessel axial expansion). At time 460 s, reactor was manually scrammed and in 8 s three primary pumps were manually tripped. In about 1 min the secondary pumps speed was automatically reduced to ~ 110 rpm. Phase 2 (Protected Loss of Heat Sink) lasts ~ 3 hours and characterised by establishment of natural convection under conditions of very low heat sink. In about 3 hours, the SG casing was open at the bottom and at the top in order to allow cooling of the SG tubing by natural circulation of the atmospheric air. Phase 4 (Decay Heat Removal) lasted about four hours and was characterised by stable natural convection of primary sodium. In total the test lasted about 7 hours (~25000 s).

As a first step, Phase 1 (Unprotected Loss of Heat Sink) was analysed with the FAST code system, using both point kinetics approximation and 3D neutron kinetics solver and the data for the coolant temperature evolution at the core inlet (in fact, measured was the temperature at the pump inlet) as a boundary condition [18]. As a second step, the whole test was simulated with the FAST code system (viz., TRACE) using 1D representation of the primary, secondary and tertiary systems, and the measured reactor power as a boundary condition. The results of the simulation from all participants of the CRP are reported in [17] and the FAST code system predictions are compared with selected experimental data in Fig. 7. The discrepancies between the simulated and measured data reflect the problem of simulating a complex multidimensional flow and temperature patterns in the primary pool at the phase of establishment of the natural circulation, using 1D representation of the primary system. A better agreement is obtained for the last Phase when the convection is already established. More details about the lessons learned from the test and the benchmark can be found in [17].

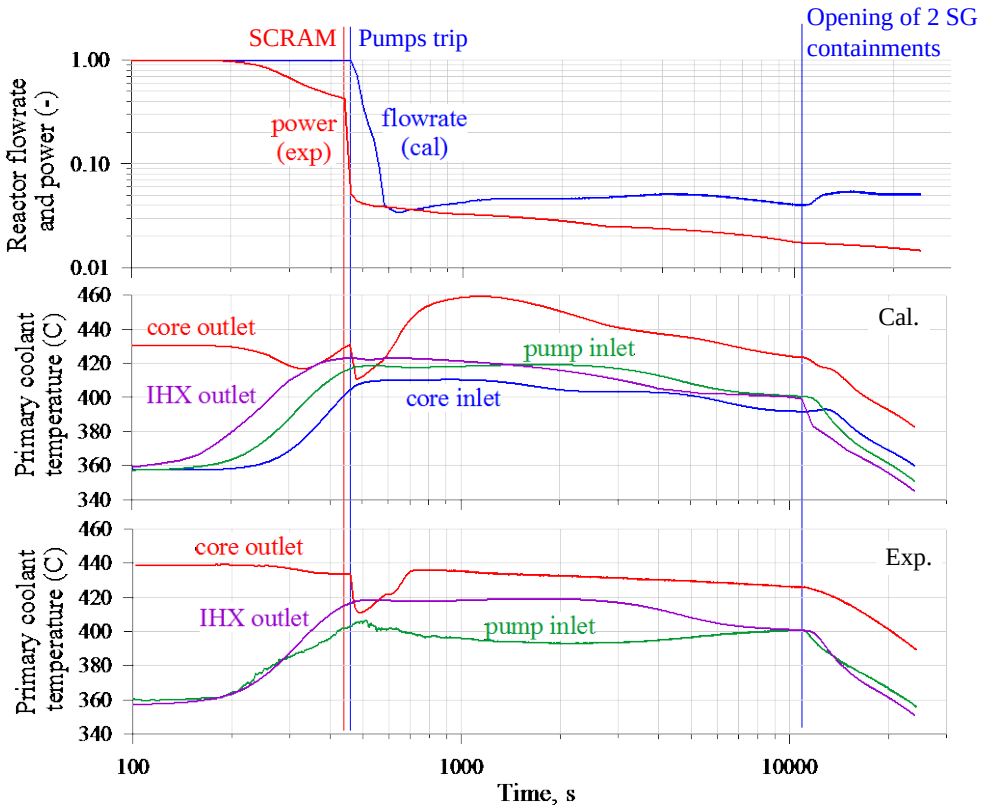

Fig. 7. Comparison of the FAST code system predictions with selected experimental data obtained in the PHENIX-EOL natural convection test.

4. Closed fuel cycle studies

The advanced fast reactors of the fourth generation should enable an indirect burning of poorly fissile U^{238} through Pu^{239} breeding and recycling of the actinides from their own spent fuel. The fuel cycle closure can reduce the amount of radioactive waste to fission products (and losses) and the U^{238} burning can multiply the sustainability of the uranium fueled reactors. Regular periodic operation with the fuel recycling converges to an equilibrium cycle. A numerical tool named equilibrium fuel cycle procedure for fast reactors (EQL3D) based on the ERANOS code was developed and applied to the Gas-, Sodium- and Lead-cooled Fast Reactors. The results of the study presented in [20] confirmed the neutronics capability of all three systems to operate in an iso-breeding regime in a closed fuel cycle (see a simplified schematics of the closed fuel cycle in Fig. 8). The problem of optimisation of the path to equilibrium is considered in [21].

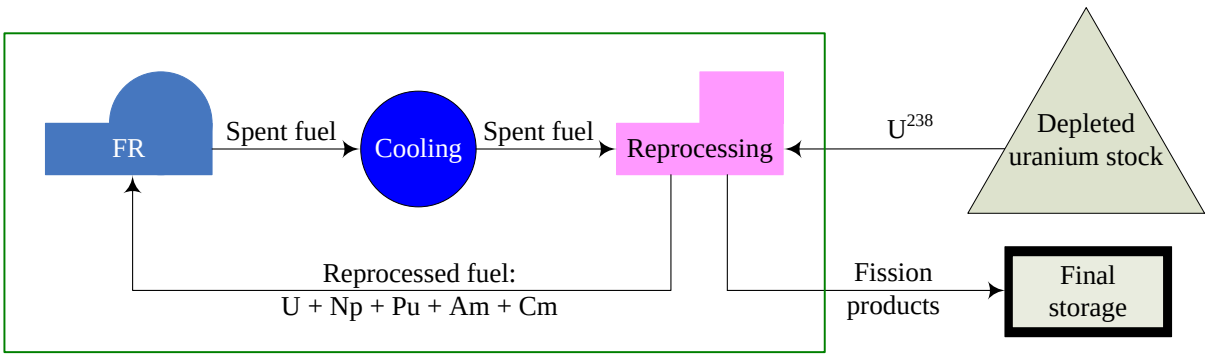

Fig. 8. Operation of iso-breeder fast reactor in a closed equilibrium fuel cycle.

5. Uncertainty analysis

The method for propagating the uncertainties proposed by McKay was implemented in the TRACE thermal-hydraulic code and successfully tested by making sample calculations of an unprotected partial loss of flow (reduction of core flowrate down to ~30% of nominal value) in the sodium-cooled fast reactor core with the use of a point kinetic model [22]. The implemented methodology was shown to be suitable for calculation of the resulting uncertainties in the output parameters and determination of their sensitivities to the perturbed input parameters. Strong assumptions on distribution of the input parameters were made to facilitate the calculatations (viz., all input parameters are normally distributed and statistically independent—covariance is zero—minimum and maximum possible value is mean plus/minus three times standard deviation). The standard deviations were selected on the basis of analysis of the available nuclear data uncertainties and engineering judgements (see Table 2). Selected results of sample calculations (100 runs) are presented in Fig. 9, while Table 3 summarises important output parameters and their uncertainties. In particular, the results of the uncertainties propagation can be used to evaluate the probability of the sodium boiling.

Table 2. Parameters and their evaluated uncertainties (1σ) selected for propagation

Input parameter	μ ± σ
Doppler constant	–1322 ± 66 pcm
Coolant density reactivity coefficient	+0.095 ± 0.010 pcm/K
Fuel expansion reactivity coefficient	–0.175 ± 0.021 pcm/K
Diagrid expansion reactivity coefficient	–0.535 ± 0.013 pcm/K
Effective fraction of delayed neutrons	265 ± 16 pcm
Power peaking factor	1.80 ± 0.04

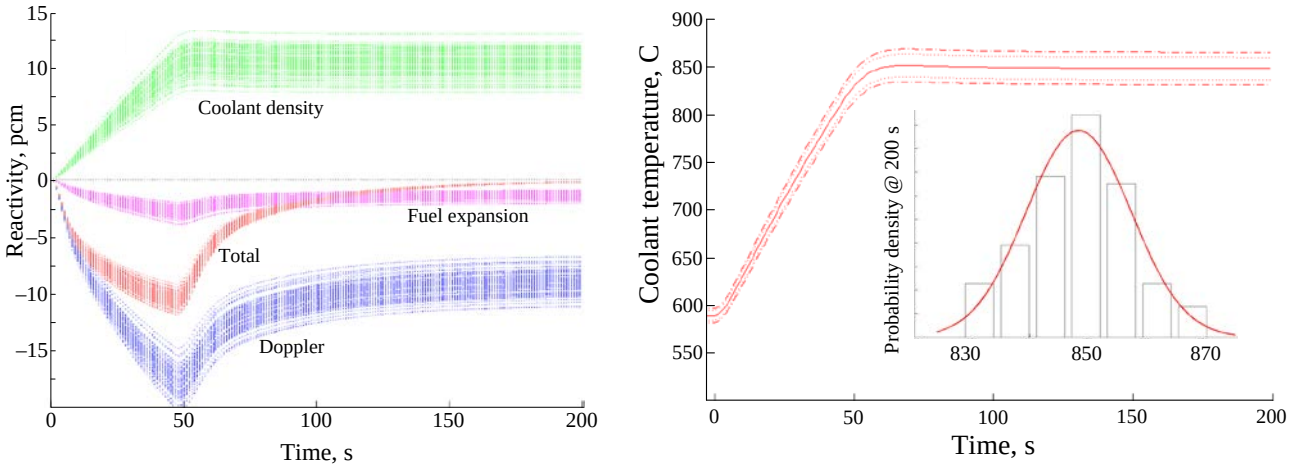

a) b)

Fig. 9. Reactivity components (a) and coolant temperature at outlet of the peak-power assembly

Table 3. Output parameters and their resulting uncertainties (1σ).

Output parameter	μ ± σ
Peak coolant temperature, ºC	849 ± 9
Peak cladding temperature, ºC	706 ± 6
Peak fuel temperature, ºC	2001 ± 30

6. Sodium-cooled fast reactor behaviour in unprotected loss of flow accident

In frame of the PhD study [23], the dynamic ESFR core behavior during a representative unprotected loss-of-flow accident scenario has been studied using the FAST code system (coupled TRACE/PARCS). An innovative wrapper design for the fuel assembly has been proposed, in order to provide bypasses for the sodium flow when sodium vapor blocks the flow area at the top of the fuel. The resulting void distribution, which covers the plenum region and the upper part of the active core, can effectively lead to negative coolant density reactivity feedback. By stabilizing the coolant flow oscillations with an innovative plenum design, a final core configuration has been achieved, which is capable to prevent the cladding and fuel from melting during the considered transient, not only for the beginning-of-life state, but also in the equilibrium fuel cycle. Selected results of the dynamic simulation of the ESFR equilibrium core behaviour in ULOF are shown in Fig. 10 and Fig. 11.

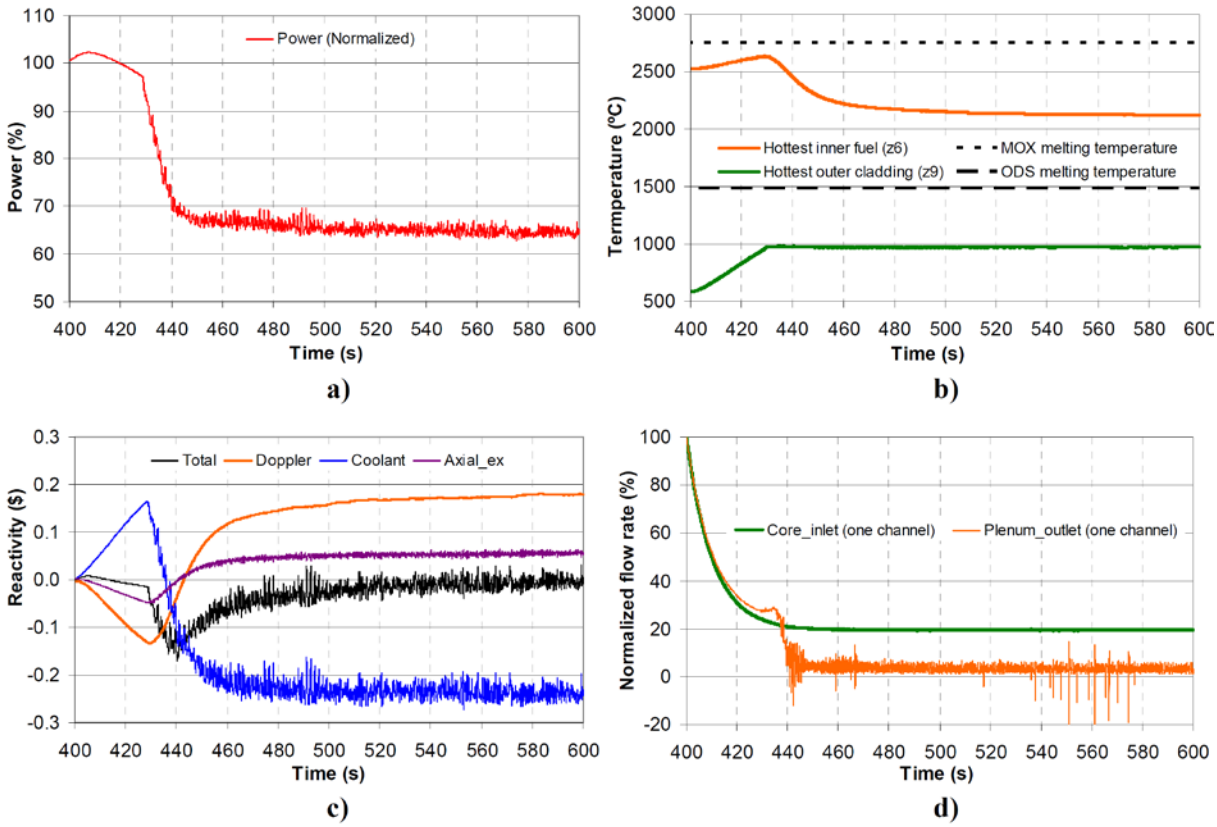

Fig. 10. ULOF for the final core configuration at Beginning of Equilibrium Cycle: evolutions of a) power, b) fuel and cladding temperatures in the hottest channel, c) total reactivity and its decomposition, d) normalized inlet and outlet flow rates in the hottest channel.

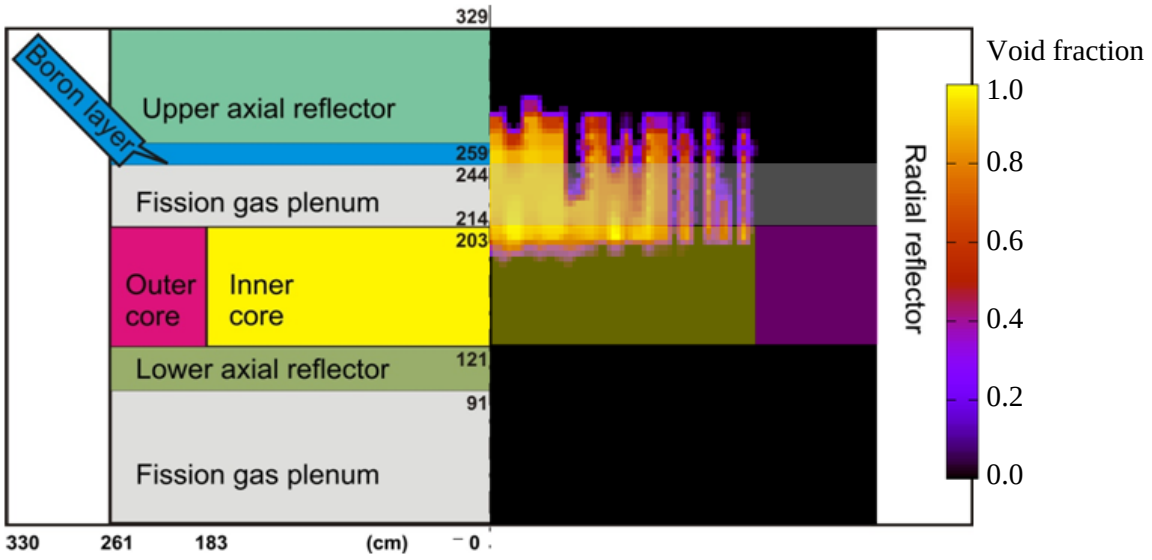

Fig. 11. A snapshot of the calculated void distribution in the optimized SFR core few minutes after the boiling onset. Due to the advanced wrapper design, the boiling is stabilised at the core outlet where the void effect is negative.

7. Conclusions

The FAST code system is a powerful calculational tool for analysis of various Generation-IV concepts (especially, sodium-cooled fast reactor), which allows coupled simulation of neutronic, thermal hydraulics and fuel behavior phenomena occuring in steady-state and transient conditions. The code system is enthusiastically developed, validated and applied. In particular, the validation database is expanding and includes now not only separate-effect tests [2], but also integral reactor experiments and tests at zero-power facilities. The code system application ranges from neutronic analysis of the closed fuel cycle to coupled simulation of sodium boiling in reactor conditions. It is also used in various EURATOM projects as a tool for transient analysis of advanced fast reactor systems.

REFERENCES

[1] K. Mikityuk, S. Pelloni, P. Coddington, E. Bubelis, and R. Chawla, 2005, “FAST: An Advanced Code System for Fast Reactor Transient Analysis,” Ann. Nucl. Energy, 32, pp. 1613–1631.

[2] K. Mikityuk, J. Krepel, S. Pelloni, A. Chenu, P. Petkevich, and R. Chawla. “FAST Code System: Review of Recent Developments and Near-Future Plans”. Journal of Engineering for Gas Turbines and Power. October 2010, Vol. 132 / 102915-1.

[3] PSI’s FAST reactor group website: http://fast.web.psi.ch.

[4] J. Leppänen, 2010. “Serpent Monte Carlo Reactor Physics Code”, In Proc. 20th AER Symposium on VVER Reactor Physics and Reactor Safety. Espoo, Finland, Sept. 20-24, 2010.

[5] G. Rimpault, D. Plisson, J. Tommasi, R. Jacqmin, J.-M. Rieunier, D. Verrier, D. Biron. “The ERANOS Code ans Data System for Fast Reactor Neutronic Analyses”, Proc. Int. Conf. PHYSOR 2002, Seoul, Korea, October 7-10, 2002.

[6] Thomas J. Downar, Douglas A. Barber, R. Matthew Miller, Chang-Ho Lee, Tomasz Kozlowski, Deokjung Lee, Yunlin Xu, Jun Gan, Han Gyu Joo, Jin Young Cho, Kibog Lee, Anthony P. Ulses. “PARCS: Purdue Advanced Reactor Core Simulator,” Proc. of the International Conference on the New Frontiers of Nuclear Technology (PHYSOR'02), Seoul, Korea, 2002.

[7] “TRACE v5.0. Field Equations, Solution Methods, and Physical Models”. US NRC

http://pbadupws.nrc.gov/docs/ML0710/ML071000097.pdf

[8] K. Mikityuk and A. Shestopalov. ” FRED fuel behaviour code: Main models and analysis of Halden IFA-503.2 tests”. Nuclear Engineering and Design 241 (2011) 2455–2461.

[9] L. Ghasabyan, K. Mikityuk, J. Krepel, S. Pelloni. “Use of Serpent Monte-Carlo code for development of 3D full-core models of Gen-IV fast spectrum reactors and preparation of safety parameters/cross-section data for transient analysis with FAST code system”. Proc of International Conference on Fast Reactors and Related Fuel Cycles: Safe Technologies and Sustainable Scenarios (FR13), Paris, March 2013.

[10] A. Chenu, R. Adams, K. Mikityuk, R. Chawla. “Analysis of selected Phenix EOL tests with the FAST code system – Part I: Control-rod-shift experiments”. Annals of Nuclear Energy. Volume 49, November 2012, Pages 182–190.

[11] F. Varaine, 2009. IAEA CRP on Phenix end of life tests: control rod withdrawal. Technical Report CEA/DEN/CAD/DER/SPRC/LEDC, to be published as IAEA CRP report.

[12] Waters, L.S. (Ed.), 2008. MCNPX User’s Manual, Version 2.6.0, LA-CP-07-1473.

[13] G. Manturov, A. Kochetkov, M. Semenov, V. Doulin, L. Lykova, Y. Rozhikhin, A. Tsiboulia, I. Matveenko, U. Wehmann. “BFS-62-3A experiment: fast reactor core with U and U-Pu fuel of 17% enrichment and partial stainless steel reflector”, NEA/NSC/DOE(2006)1, IRPHE Handbook.

[14] L.S. Waters (Ed.), 2002. MCNPX User’s Manual, Version 2.4.0, LA-CP-02-408.

[15] A. Marinoni, G. Girardin, K. Mikityuk. “Analysis of the BN-600 fast-spectrum core mock-up at BFS-2 zero-power facility using MCNPX”. Annals of Nuclear Energy 44 (2012) 26–33.

[16] M. Alonso. “Development of a full-core ERANOS Model and neutronic analysis of the BN-600 Fast Reactor Core Mock-up at the BFS-2 zero-power facility”. EPFL Master thesis. 2011.

[17] D. Tenchine, D. Pialla, T. Sofu, J. Thomas, D. Chellapandi, Y. Shvetsov, L. Maas, H-Y. Jeong, K. Mikityuk, A. Chenu, H. Mochizuki, S. Monti. “International benchmark on the natural convection test in Phenix reactor”. Submitted to Nuclear Engineering and Design.

[18] A. Chenu, K. Mikityuk, R. Chawla. “Analysis of selected Phenix EOL tests with the FAST code system – Part II: Unprotected phase of the Natural Convection Test.” Annals of Nuclear Energy. Volume 49, November 2012, Pages 191–199.

[19] K. Mikityuk, M. Schikorr. “New transient analysis of the Superphénix start-up tests”. Proc of International Conference on Fast Reactors and Related Fuel Cycles: Safe Technologies and Sustainable Scenarios (FR13), Paris, March 2013. CN-199-155.

[20] J. Krepel, S. Pelloni, K. Mikityuk. “Comparison of open and closed U–Pu equilibrium fuel cycles for Generation-IV fast reactors with the EQL3D procedure”. Nuclear Engineering and Design 250 (2012) 392– 402.

[21] J. Krepel, V. Brankov, K. Mikityuk. “Selection of Initial Fuel Composition for the THE ESFR Core Based on the Knowledge of its Equilibrium Closed Cycle Parameters”. Proc of International Conference on Fast Reactors and Related Fuel Cycles: Safe Technologies and Sustainable Scenarios (FR13), Paris, March 2013. CN-199-159.

[22] F. Reiterer. “Uncertainty Propagation in Dynamic TRACE Calculations for Gen-IV SFR”. EPFL-ETHZ Semster work report. PSI Internal Report. June 2010.

[23] K. Sun. “Analysis of Advanced Sodium-cooled Fast Reactor Core Designs with Improved Safety Characteristics.” Thèse EPFL, no 5480 (2012). http://library.epfl.ch/theses/?nr=5480

Use of Serpent Monte-Carlo code for development of 3D full-core models of Gen-IV fast spectrum reactors and preparation of safety parameters/cross-section data for transient analysis with FAST code system

Levon Ghasabyan, Konstantin Mikityuk, Jiri Krepel, Sandro Pelloni

Paul Scherrer Institut, Switzerland

Presented by K. Mikityuk

Abstract. Current work presents a new methodology which uses Serpent Monte-Carlo (MC) code [1] for generating multi-group beginning-of-life (BOL) cross section (XS) database file that is compatible with PARCS 3D reactor core simulator [2] and allows simulation of transients with the FAST code system [3,4]. The applicability of the methodology was tested on European Sodium-cooled Fast Reactor (ESFR) design with an oxide fuel proposed by CEA (France).

The k-effective, power peaking factors and safety parameters (such as Doppler constant, coolant density coefficient, fuel axial expansion coefficient, diagrid expansion coefficients and control rod worth) calculated by PARCS/TRACE were compared with the results of the Serpent MC code. The comparison indicates overall reasonable agreement between conceptually different (deterministic and stochastic) codes. The new development makes it in principle possible to use the Serpent MC code for cross section generation for the PARCS code to perform transient analyses for fast reactors. The advantages and limitations of this methodology are discussed in the paper.

1. INTRODUCTION

The FAST code system [3] is used at Paul Scherrer Institute (PSI) for static and transient analyses of the main Gen-IV fast neutron spectrum reactors, namely sodium-, gas- and lead-cooled fast reactors. The code system has been compiled from well established existing codes. Some of those codes were extended and modified for simulation of special features of fast reactors. Currently, the FAST code system uses ERANOS (v.2.2), for static neutronics and cross-section generation, PARCS (v.2.8) for reactor kinetics, TRACE (v.5.0RC2), for system thermal-hydraulics and FRED, for thermal mechanics.

The 3D neutron kinetics code PARCS, which was originally developed for light water reactors (LWR) has been revised and modified for fast spectrum analyses. PARCS solves steady state and time-dependent multi-group neutron diffusion equations. In FAST code system, PARCS is directly coupled with TRACE which provides the temperature and coolant density field information to PARCS during the transient calculation, in order to recalculate the macroscopic cross-sections of materials. TRACE solves the balance of mass, momentum and energy for the liquid and vapor phases. FRED code uses fields of coolant temperature and pressure from TRACE and power distribution from PARCS to calculate temperatures, stresses and strains in the fuel and structures (e.g., fuel pin, core diagrid, reactor vessel) and sends fuel temperature field back to PARCS to re-calculate the resulting reactivity changes. Presently FRED has been integrated into TRACE.

The basic nuclear data (macroscopic cross-sections and their derivatives) are provided to FAST code by the ERANOS code system [5] which was developed and validated by CEA with the aim of

providing a suitable basis for reliable neutronics calculations of current and advanced fast reactor cores.

To feed group constants (such as cross sections and scattering matrices) generated by ERANOS to PARCS, a special ERANOSTOPARCS wrapper code is used which converts ERANOS data to PARCS-compatible cross-section database file.

In this study the possibility of substituting ERANOS code with a recently developed Serpent Monte Carlo code is presented.

The use of Serpent MC code, which was designed specifically for reactor physics applications, has the advantage of modeling complicated 3D geometries, which is beyond the capabilities of conventional deterministic lattice transport codes. Its major advantage as a Monte-Carlo code is the capability of generating group constants (e.g. multi-group cross sections) for any geometric region of the reactor core within reasonable computational time. Furthermore, the self-shielding effects from the resonances and neutron interactions are calculated without any major approximations.

Overall Serpent has tremendous advantages and very few disadvantages compared with the conventional deterministic lattice transport codes. To use these advantages, a methodology was developed in the presented study for Serpent MC code to generate nuclear data (macroscopic cross-sections and their derivatives) necessary for the PARCS code.

To accomplish and automatize the task of nuclear data generation, a wrapper code S2P (SERPENT2PARCS) was developed which uses Serpent MC code and creates different input files with geometry, temperature and density perturbations. The final output of S2P is a cross-section database file (so called "XSEC" card) which is compatible with PARCS and contains, among many other parameters, the macroscopic cross-sections and their derivatives with respect to the fuel temperature, coolant density, diagrid pitch, fuel axial height and control rods position.

To benchmark generated cross-sections ESFR WH (Working Horse) core design was used. This design was developed by CEA in the framework of the Collaborative Project on the European Sodium-cooled Fast Reactor (CP-ESFR) realized under the aegis of the EUROATOM 7th Framework Program [6].

We made a small modification of the ESFR WH core geometry converting the core structure from 60° symmetry to 30° degree symmetry. This allowed essential simplification of the TRACE input file. The modified core geometry is given in Fig. 1. Major core design parameters are given in Table 1.

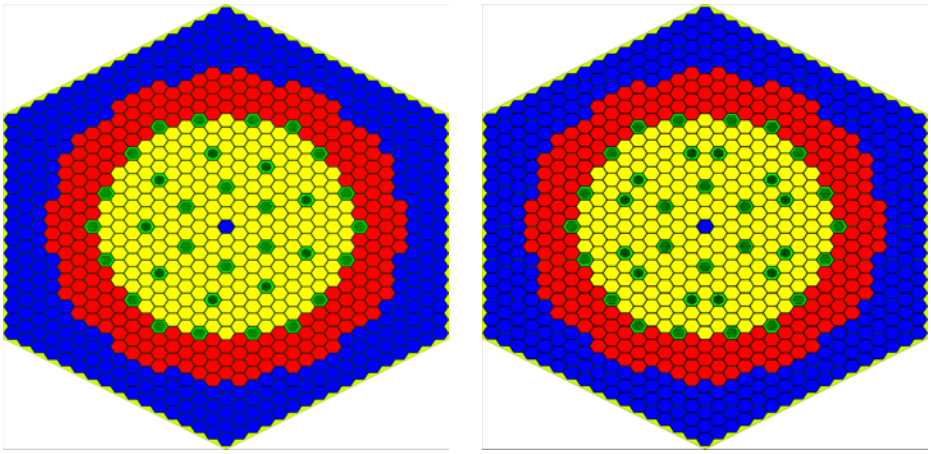

FIG. 1. ESFR WH core design (left), ESFR WH modified core, 60 degree symmetry (right). yellow – inner fuel zone, red – outer fuel zone, blue – reflector, green – control rods.

Table 1. ESFR WH major core parameters.

	Reference core	Modified core
Reactor thermal power (MWth)	3600	
Ave/Max core burnup (GWd/t)	100/145	
Power density (W/cm^3)	206	
Core radius, (cm)	300	
Core height(cm)	302	
Number of CSD / DSD[1]	24 / 9	24 / 12
Number of I/O FA[2]	225 / 228	222 / 228
PuO_2 content in I/O FA	14.05% / 16.35%	
^{10}B inside B_4C in CSD/ DSD	19.9% / 90%	
Fuel residence time (EFPD[3])	2050	

2. METHODOLOGY

Cross section parametrization

To simulate fast reactor behaviour the cross-section parametrization of PARCS code was modified to enable fast neutron spectrum system analysis [7]. The equation below represents the current procedure used by PARCS for recalculating macroscopic few-group cross-sections during transients.

$$\Sigma(T_f,\rho_C,R,H,Z)=\Sigma_0+\left[\frac{\partial\Sigma}{\partial\ln T_f}\right]_{Tf0}\left(\ln T_f-\ln T_{f0}\right)+\left[\frac{\partial\Sigma}{\partial\gamma}\right]_{\gamma c0}\left(\gamma_C-\gamma_{C0}\right)+$$
$$\left[\frac{\partial\Sigma}{\partial R}\right]_{R0}\left(R-R_0\right)+\left[\frac{\partial\Sigma}{\partial H}\right]_{H0}\left(H-H_0\right)+\left[\frac{\partial\Sigma}{\partial Z}\right]_{Z0}\left(Z-Z_0\right)$$

where Σ is the macroscopic cross-section, T_f the fuel temperature, γ the coolant density, R the average core radius, H the average fuel height and Z the control rod position. It is notable to mention that considered dependence is linear in each case, except for the Doppler effect. The partial derivatives were approximated by first order forward differencing method, which is discussed below.

$$\left.\frac{\partial\Sigma}{\partial X}\right|_{X0}\approx\frac{\Sigma_X-\Sigma_{X0}}{X-X0}$$

Cross-section generation methodology

To calculate safety coefficients, control rod worth and XS derivatives one needs to perform at least six different input simulations with Serpent MC. Each of these cases are shortly described below and correspond to different cases specified in Table 2.

(1) Case A: Reference case calculations were performed for the cold zero power ESFR core, where core geometry and material temperatures and densities correspond to 300K.

[1] CSD – Control and Shutdown Device, DSD – Diverse Shutdown Device
[2] I/O FA – Inner/Outer Fuel Assembly
[3] EFPD – Equivalent Full Power Days

(2) Case B: To calculate the Doppler constant K_D and fuel temperature derivative $\partial\Sigma/\partial \ln T_f$ $\left[\partial\Sigma/\partial lnT_f\right]_{T_{f_0}}$ we need to simulate temperature perturbation, where only perturbed parameter is the fuel temperature. Doppler constant is calculated from

$$K_{DOPPLER} = \frac{\rho_A - \rho_B}{\ln T_A - \ln T_B}$$

where ρ stands for reactivity and is calculated as $\rho = 1 - \frac{1}{k_{eff}}$.

(3) Case C: To calculate Axial Fuel Expansion coefficient α_{AFEC} α_{AFEC} and fuel expansion derivative $\partial\Sigma/\partial H$ $[\partial\Sigma/\partial \mathrm{H}]_{H_0}$ we need to run input C, where perturbed parameters are fuel height and fuel density. All other parameters have the same reference case values. The basic steps are

(a) increase fuel height
(b) decrease fuel density to conserve fuel mass

The perturbed fuel height is calculated from

$$H_C(T_C) = H_A(T_A) \times [1 - \tilde{\alpha}(T_C - T_A)]$$

where T_C is temperature of the fuel at perturbed state. Density is calculated from

$$\gamma_C(T_C) = \frac{\gamma_A(T_A)}{1 + \tilde{\alpha}(T_C - T_A)}$$

where $\tilde{\alpha}$ is the average expansion coefficient of the fuel material.

(4) Case D: To calculate Core Radial Expansion coefficient α_{CREC} and radial expansion derivative $[\partial\Sigma/\partial \mathrm{R}]_{R_0}$ $\partial\Sigma/\partial R$ we need to run input D. Input D has two perturbed parameters

(a) the width of the gap between the assemblies (Fig. 2) and
(b) lattice pitch for the whole reactor core.

The FA flat-to-flat distance stays unchanged. The pitch is perturbed as

$$p_D(T_D) = p_A(T_A) \times [1 + \tilde{\alpha}(T_D - T_A)]$$

where T_D is the inlet coolant temperature.

(5) Case E: To calculate Coolant Temperature coefficient α_{CTC} α_{CTC} and expansion derivative $\partial\Sigma/\partial\gamma$ $[\partial\Sigma/\partial\gamma]_{\gamma_0}$ we need to simulate input E. The only difference between the reference case and the perturbed case is the coolant density value.

(6) Case F: To estimate control rod worth two calculations need to be performed, one with all control rods out (input A) and one with all in (input F).

Table 2. Calculation methodology of safety coefficients and cross-section derivatives. Implicit (imaginary) parameters do not appear in the input file, but are assumed to calculate explicit parameters.

Case letter	Case Name	Governing parameters	Implicit parameter	Explicit parameter	Other Explicit parameters	Equations	Safety coefficients	$\Sigma_{A,B,C,D,E,F} = \{\Sigma_{Transport}, \Sigma_{Absorption}, \Sigma_{Production}, \Sigma_{Fission}, \Sigma_{Scattering}\}$
A	Reference	ρ_A, T_A, Σ_A	-	-	Reference	-	ρ_A	Σ_A
B	Doppler	ρ_B, T_B, Σ_B	-	T_B		-	$K_D \approx \frac{\rho_A - \rho_B}{T_A - T_B}$	$\frac{\partial \Sigma}{\partial lnT} \approx \frac{\Delta \Sigma}{\Delta \mathrm{lnT}} = \frac{\Sigma_A - \Sigma_B}{\mathrm{lnT_A} - \mathrm{lnT_B}}$
C	Axial fuel Expansion	$\rho_C, T_C, H_C, \gamma_C, \Sigma_C$	T_C	H_C		$H_C = H_A(1 + \tilde{\alpha}(T_B - T_A))$ $\gamma_C = \frac{\gamma_A}{1 + \tilde{\alpha}(T_B - T_A)}$	$\alpha_{AFE} \approx \frac{\rho_A - \rho_C}{T_A - T_c}$	$\frac{\partial \Sigma}{\partial \mathrm{H}} \approx \frac{\Delta \Sigma}{\Delta \mathrm{H}} = \frac{\Sigma_A - \Sigma_C}{H_A - H_C}$
D	Radial expansion	$\rho_D, T_D, p_D, \Sigma_D$	T_D	p_D		$p_D = p_A(1 + \tilde{\alpha}(T_D - T_A))$ $r_D = \frac{p_D}{2}$	$\alpha_{REC} \approx \frac{\rho_A - \rho_D}{T_A - T_D}$	$\frac{\partial \Sigma}{\partial \mathrm{p}} \approx \frac{\Delta \Sigma}{\Delta \mathrm{p}} = \frac{\Sigma_A - \Sigma_C}{p_A - p_C}$
E	Coolant expansion	γ_E, T_E, Σ_E	T_E	γ_E		-	$\alpha_{CTC} \approx \frac{\rho_A - \rho_E}{T_A - T_E}$	$\frac{\partial \Sigma}{\partial \gamma} \approx \frac{\Delta \Sigma}{\Delta \gamma} = \frac{\Sigma_A - \Sigma_E}{\gamma_A - \gamma_E}$
F	Control – Rods full insertion	ρ_F, Σ_F		H_F			$\Delta\rho = \rho_A - \rho_F$	$\Delta\Sigma = \Sigma_F - \Sigma_A$

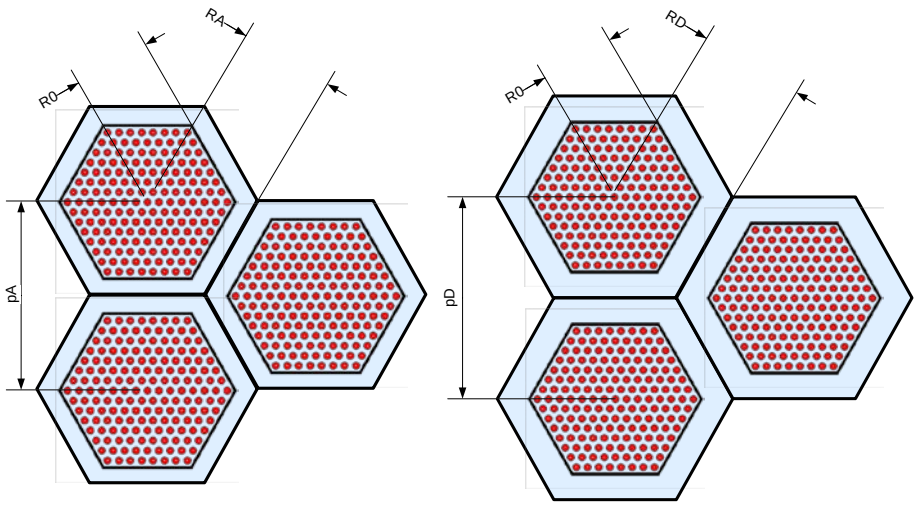

FIG. 2. Core radial expansions for input A(left) and input D(right).

S2P Wrapper

To generate reference multi-group constants and their derivates we need to perform at least one reference and five perturbed simulations (Table 2). The S2P wrapper automates the generation and simulation of those Serpent input cases and outputs XSEC formatted cross section database compatible with PARCS core simulator [2]. The structure of the wrapper code is shown in Fig. 3.

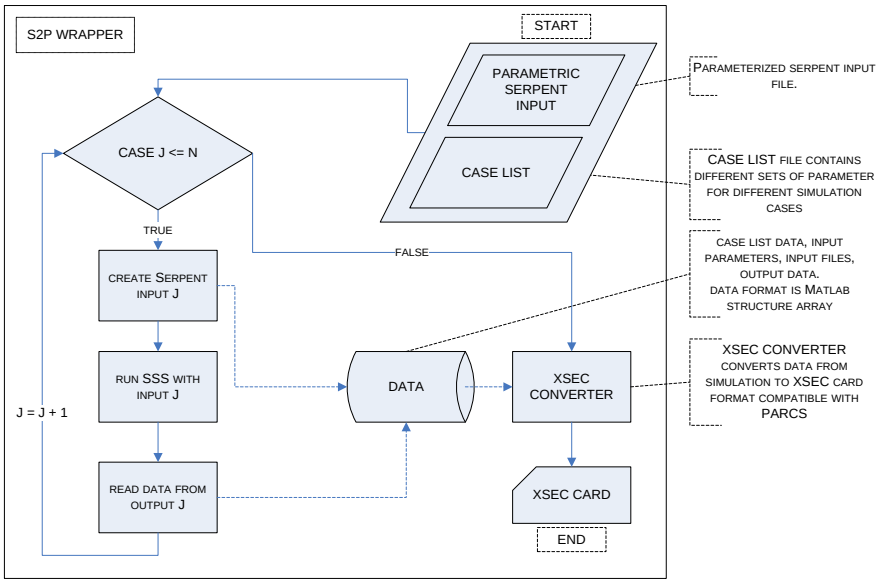

FIG. 3. Schematic flowchart of S2P wrapper code.

ESFR core model in Serpent

The Serpent MC code uses a universe-based geometry. This implies that the geometry is divided into independent simple geometric objects which are easy to model using basic and derived surface types. Then these objects are nested inside one another. Therefore, universe-based geometry allows modeling of complicated reactor geometries.

The ESFR WH Serpent input core map is shown in Fig 4, where different numbers represent different universes. Universe 1000 and 2000 (Fig 4) represent inner and outer fuel assemblies (I/O FA), which consist of upper reflector universe (102,202), upper fission gas plenum universe (101,201), fuel zone universe (100,200), lower reflector universe (99,199) and lower fission gas plenum universe (98,198). Control Assemblies (CA) on each ring are represented with universes 600, 700 and 800. Each of these CAs consists of two universes, Control Rod universe (60,70,80) and Control Rod Follower universe (61,71,81). Serpent calculates and outputs all few-group constants in each of those universes, which are crucial for PARCS input.

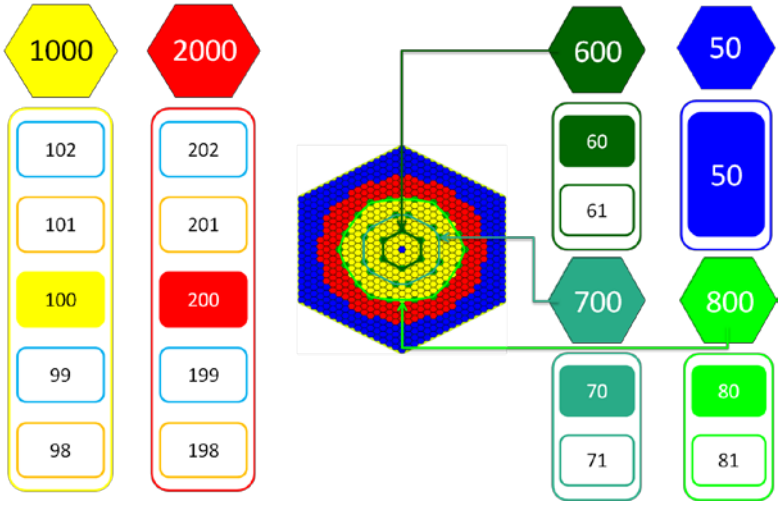

FIG. 4. Universe map of ESFR WH core. 1000 – inner FA, 2000 – outer FA, 600, 700, 800 – inner central and outer CA-s. 60, 70, 80 – inner central and outer CR-s. 61, 71, 81 – inner, central and outer CRF-s. RA – 50.

PARCS input model

Only one sixth of the ESFR core has been modeled in the PARCS input file, considering a 60° degree symmetry of the modified ESFR core (Fig. 1, right). Axially, the mesh size is about 10 cm, while radially the size of the node is equal to the core pitch. One sixth of the core contains 85 fuel assemblies, 60 reflector channels and 7 control and safety assemblies.

TRACE input model

TRACE model was constructed for 1/12th of the ESFR core (Fig. 5) for the coupled calculation with PARCS. This was possible only after modifying ESFR core design from 60° symmetry to 30° symmetry (Fig. 1). This model consists of 51 parallel channels, from which 45 are FAs and 5 are CAs. TRACE-PARCS coupled model allows simulation of radial core expansion and fuel axial expansions. Radial expansion is driven by the diagrid temperature. The corresponding thermal expansions are calculated for the diagrid material (SS316) using the inlet temperature change to provide the radial core thermal expansion. For modeling fuel axial expansion core-average fuel temperature change is used. TRACE was coupled with PARCS model by means of appropriate mapping scheme which links both the pipe component nodes and the heat-structure nodes to the corresponding neutronics nodes.

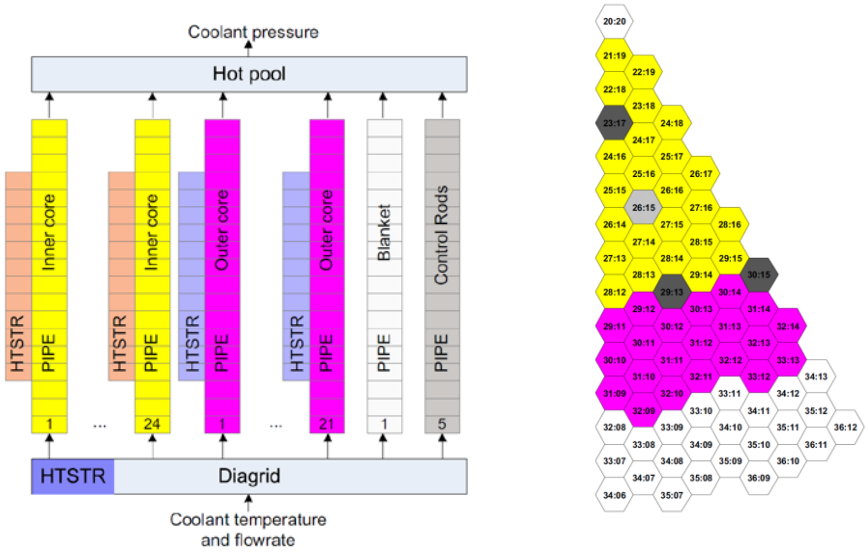

FIG. 5. TRACE model (left), 30º-symmetry sector modelled in TRACE.

3. RESULTS

Six different input calculations were performed with Serpent MC code (v. 1.1.18) to calculate safety coefficients and generate cross section database file for PARCS. First simulated case is the reference case and the other five represent perturbed cases.

(1) The reference case calculations were performed with all temperatures such as coolant temperature, fuel and material temperature set to 300°K. The geometry of the core has the dimensions corresponding to 300°K. Control rods are positioned fully out of the core.
(2) Fuel height was increased by 3.41% to simulate fuel axial expansion effect. This value corresponds to the hypothetical temperature increase of 2700°K. At the same time fuel density was decreased to keep the fuel mass constant. Linear expansion coefficient for the MOX fuel used is 1.27×10^{-5} 1/K.
(3) Fuel temperature was increased by 1500°K to simulate Doppler effect.
(4) Coolant density was decreased by 28% to simulate coolant expansion effect.
(5) Core assembly pitch was increased by 6% to simulate core radial expansion effect. The material of the diagrid was assumed to be SS316 with an expansion coefficient of 2.03×10^{-5} 1/K.

(6) Control rod fully inserted configuration was simulated to calculate control rod worth.

Abovementioned expansions can be argued to be excessive and not realistic. Nonetheless simulated reactivity feedback mechanisms are assumed linear for fast reactor cores, which makes these expansions plausible. On the other hand big geometric and material expansions are justified in Monte Carlo codes. The small reactivity effects and cross-section changes present themselves clearly within relatively short simulation time. All six simulations of 3D ESFR full core were performed with a total number of 7.5×10^7 neutron histories (batch size x number of cycles = 150000 x 500) and 500 inactive cycles.

Firsly, calculations were performed with the six different Serpent input files which provided us with all the necessary data to calculate ESFR reactivity feedback coefficients and generate XSEC cross-section library for PARCS. Secondly the XSEC card was pluged into PARCS/TRACE coupled code and the reactivity feedbacks were simulated and safety coefficients were calculated. Calculation results of k-effective for reference case are presented in Table 3. Table 4 compares the values of safety parameters calculated from Serpent and PARCS output data. A comparison of the power peaking factor for both deterministic and stochastic codes in illustrated in Fig. 6.

Table 3. k-effective of ESFR 3D core for reference case at 300°K calculated by Serpent MC and PARCS/TRACE codes.

	Serpent MC	PARCS stand alone	PARCS/TRACE
k-effective	1.03512±0.00007	1.03809	1.03809
Reactivity, pcm	3392±6	3669	3669
Core temperature, °C	27	20	20

Table 4. Safety parameters and their relative deviation calculated by Serpent MC and PARCS/TRACE for ESFR 3D core simulations.

Safety parameters	Serpent MC	PARCS/TRACE	Δ, %
Axial Fuel expansion coefficient, pcm/K	-0.158(±0.003)	-0.184	16
Core Radial expansion coefficient, pcm/K	-0.763(±0.003)	-0.656	14
Doppler constant, pcm	-1245(±5)	-1327	6
Coolant expansion coefficient, pcm/K	0.159(±0.01)	0.197	24
Control Rod Worth, pcm	5069(±10)	5167	2

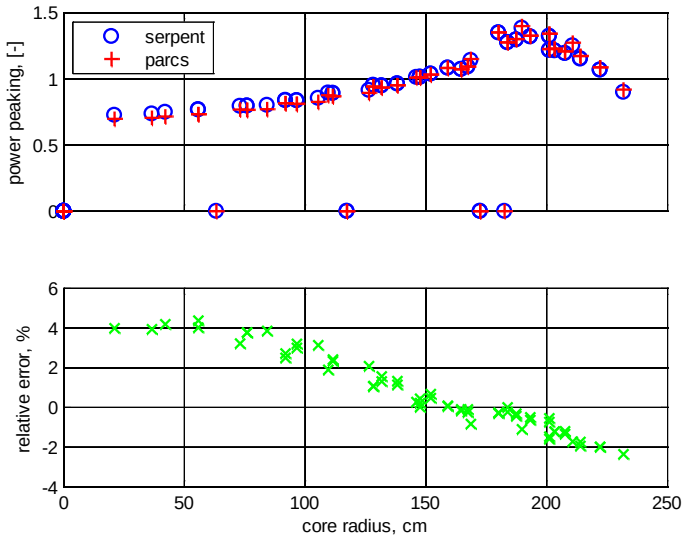

FIG. 6. Power peaking and relative error for ESFR 3D core at a reference state of 300°K.

4. CONCLUSIONS

The purpose of the study was to investigate the feasibility of using Serpent Monte Carlo code for generating multi-group BOL cross sections for all reasons of a 3D fast reactor core including control rod assemblies, control rod followers, axial and radial reflectors. The first part of a three-step procedure was to simulate six different inputs and generate cross sections and their derivatives. The second step was to convert generated homogenized cross-sections to PARCS compatible XSEC database file. The final step was to perform steady-state and zero-transient analyses with PARCS/TRACE coupled code using generated cross-section database and compare k-effective values, safety parameters and power distribution between conceptually different (stochastic and deterministic) codes.

The results show reasonable agreement between k-effective values and safety parameters. The k-effective values differ by only 277 pcm (Table 4). This is a good agreement between fundamentally different codes. The difference between estimated safety parameters can be up to 25% (Table 5). At the same time, strong agreement was observed for the control-rod worth, which differ by only 2%. The comparison of the power profile shows maximum 4% deviation between the codes (Fig. 6).

The goal of this study was not to produce the same results with stochastic and deterministic codes, but to check wether the Serpent Monte Carlo code, specifically designed for lattice physics applications can be used for 3D core simulations and at the same time provide homogenized cross sections and their derivatives for the PARCS simulator.

The positive outcome of this study is that continuous energy Serpent Monte-Carlo code may be a promising tool as a 3D reactor core design calculator and detailed homogenized group constant generator.

The downsize of the presented methodology is that only BOL cross section database can be currently generated. The burnup module of Serpent MC code has prohibitively high memory requirements for performing 3D full core burnup calculations because of unionized energy grid implementation [8]. Therefore the application of this method is presently limited to BOL calculations.

REFERENCES

[1] J. Leppänen, 2010. “Serpent Monte Carlo Reactor Physics Code”, In Proc. 20th AER Symposium on VVER Reactor Physics and Reactor Safety. Espoo, Finland, Sept. 20-24, 2010.

[2] T. Downar, “PARCS v2.7 U.S. NRC Core Neutronics Simulator USER MANUAL.” Aug-2006.

[3] K. Mikityuk, J. Krepel, S. Pelloni, A. Chenu, P. Petkevich, and R. Chawla, “FAST Code System: Review of Recent Developments and Near-Future Plans,” Journal of Engineering for Gas Turbines and Power, vol. 132, no. 10, p. 102915, 2010.

[4] K. Mikityuk, J. Krepel, S. Pelloni, G. Girardin, A. Chenu, K. Sun, M. Alonso, A. Marinoni, R. Adams, F. Reiterer. “FAST Code System: Review of Recent Applications.” Proc of International Conference on Fast Reactors and Related Fuel Cycles: Safe Technologies and Sustainable Scenarios (FR13), Paris, March 2013.CN-199-156.

[5] J.M. Ruggieri, "ERANOS 2.1: International Code System for GEN IV Fast Reactor Analysis", Proceedings of ICAPP'06, Reno, NV USA, June 4-8, 2006.

[6] G. L. Fiorini and A. Vasile, “European Commission – 7th Framework Programme: The Collaborative Project on European Sodium Fast Reactor (CP ESFR),” Nuclear Engineering and Design, vol. 241, no. 9, pp. 3461–3469, Sep. 2011.

[7] K. Mikityuk, S. Pelloni, P. Coddington, E. Bubelis, and R. Chawla, “FAST: An advanced code system for fast reactor transient analysis,” *Annals of Nuclear Energy*, vol. 32, no. 15, pp. 1613–1631, Oct. 2005.

[8] J. Leppänen, “Two practical methods for unionized energy grid construction in continuous-

energy Monte Carlo neutron transport calculation," Annals of Nuclear Energy, vol. 36, no. 7, pp. 878–885, Jul. 2009.

Reactivity Feedback Assessment of Liquid Lead Bismuth Eutectic Cooled Fast Core

A. Seubert, P. Baloche, K. Velkov

Gesellschaft für Anlagen- und Reaktorsicherheit (GRS) mbH, Forschungszentrum, D-85748 Garching, Germany

Abstract. This paper describes the application of the lattice code HELIOS to assess reactivity feedbacks of fast spectrum systems cooled by lead bismuth eutectic (LBE). The Multi-purpose hYbrid Research Reactor for High-tech Applications (MYRRHA) to be built at SCK-CEN in Belgium has been selected as model system for which evaluations of fuel Doppler coefficient, void worth, coolant temperature coefficient and radial structural expansion coefficients based on individual fuel assemblies have been carried out. The focus is on the applicability of HELIOS to LBE cooled fast spectrum systems. The validity of the different HELIOS libraries is assessed by comparing with detailed Monte Carlo calculations using MCNP with nuclear point data. It is found that the 190 energy group adjusted library compares best with the Monte Carlo results and performs even better than the 112 energy group library that is designed for fast spectrum applications. In addition, based on the study of radial expansion feedback coefficients, a simple model is given to predict reactivity changes introduced by a combination of changes in the radial fuel diameter and fuel assembly pitch.

1. Introduction

Fast spectrum liquid metal cooled reactor systems, especially Accelerator Driven subcritical Systems (ADS), currently attract renewed interest because of their capability for large-scale transmutation of nuclear waste. Lead based coolants, in particular lead bismuth eutectic (LBE), are being considered because of their favorable neutron kinetics and thermal hydraulics properties. At SCK-CEN in Belgium, the flexible fast spectrum research reactor MYRRHA is being designed as a demonstrator ADS with operation expected around 2023. Although both LBE cooled ADS and critical systems differ in, e.g., their dynamics behavior, they share common technology and, therefore, are faced with comparable safety issues, e.g. low values of negative Doppler reactivity feedback and low or even positive coolant void reactivity feedback. The assessment of reactivity feedbacks is the key to safety and requires careful validation of appropriate spectral codes and neutron data libraries used for generating few-group cross section libraries to be applied in neutron kinetics calculations.

The objective is to investigate the applicability of HELIOS [1] to LBE-cooled fast-spectrum systems. This is because the data libraries of HELIOS are primarily optimised for LWR designs. To address this topic, reactivity calculations were made with HELIOS and compared to MCNP Monte Carlo reference results to assess the HELIOS applicability. For generic MYRRHA fuel assemblies, evaluations of fuel Doppler coefficient, void worth, coolant temperature coefficient and structural expansion coefficients based on individual fuel assemblies have been carried out.

2. Generic design of MYRRHA fast core

A generic configuration of the MYRRHA core for subcritical operation [2] is depicted in Fig. 1. The three black spaces in the center are to house the spallation target. The fuel assemblies are figured in red. The white ones are supposed to house experimental devices or irradiation targets. The light blue assemblies are totally filled with coolant, and in the grey assemblies the rods are made of steel.

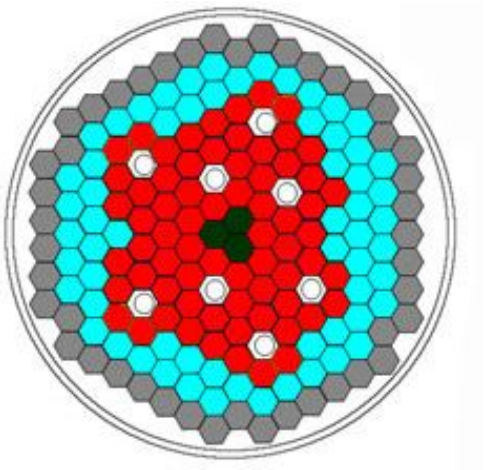

FIG. 1. Example of a geometrical configuration of the MYRRHA core for sub-critical operation.

Major design parameters of a generic MYRRHA fuel assembly have been taken from [3]. It is composed of 126 fuel rods and 1 empty cladding at the center to be used for instrumentation. The coolant between the rods is LBE, given by 44.5 wt% Pb and 55.5 wt% Bi. The temperature-dependent density [4] is shown in Fig. 2. The rods are arranged in a hexagonal lattice, and the gap between neighbouring assemblies is filled with LBE.

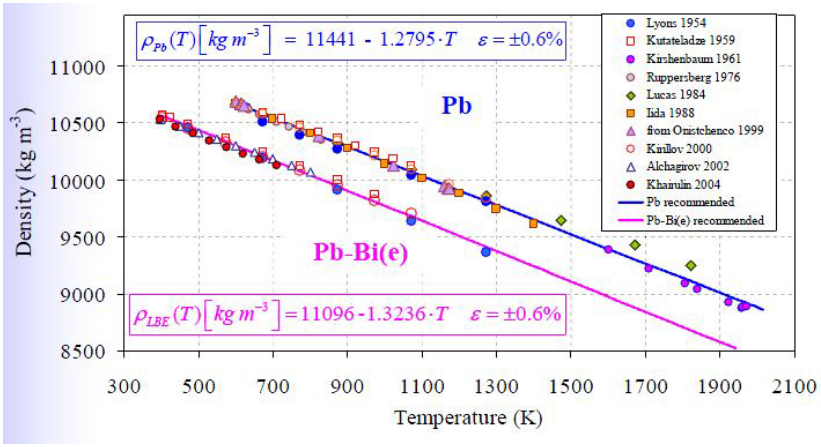

FIG. 2. Temperature-dependent density of LBE compared to Pb.

The rods are 1.4 m long with an active length of 60 cm for the fuel rods. The fuel is 30 or 35 wt% (Pu-Am) enriched MOX, with 1.65% Am in Pu-Am mix. The isotopic composition has been taken from [3] and is reproduced in Table 1.

Table 1. Fuel composition in MYRRHA sub-critical reference configuration.

Element	% in fuel	Isotopes	Individual wt%
Uranium	70	U235/U238	0.7/99.3
Plutonium	28.5	Pu238/Pu239/Pu240/Pu241/Pu242	1.27/61.88/23.5/8.95/4.40
Americium	1.5	Am241/Am243	66.67/33.33

The radial and axial fuel rod dimensions and material compositions have been taken from [3] and [5]. The rod is surrounded by a wire-wrap spacer. Since no precise material specification was available, wire-wrap spacers were not accounted for in the neutronic modeling.

3. Evaluation of the impact of different HELIOS nuclear data libraries

The nuclear data libraries used with HELIOS are largely based on the ENDF/B-VI library [1]. They are provided in 190, 112 and 47 energy groups. Except for the 112 group library, which is designed for fast spectrum reactors, they are present in both unadjusted and adjusted form. The adjustment refers to a 3.4% reduction in the resonance integral of Uranium-238 [6]. Since this adjustment is devoted to thermal spectrum systems, an important question is whether the adjusted library is more suitable than the unadjusted one to correctly capture fast spectrum systems. As the 47 group library has been developed for fast running scoping calculations, it is supposed to give less accurate results than the other libraries.

To study the impact of the individual HELIOS libraries, a single generic MYRRHA pin cell model in an infinite lattice arrangement has been prepared in HELIOS. Assessment of the HELIOS results has been done using the Monte Carlo code MCNP5 [7] and JEFF-3.1.1 nuclear point data. The temperatures of all pin cell materials were fixed to either 300, 600, 900 or 1200 K since for these temperatures nuclear point data are available for use in MCNP. The densities were set to 10.55 g/cm^3 for the MOX fuel, $2.4 \cdot 10^{-4}$ g/cm^3 for the Helium gap, 7.64 g/cm^3 for the cladding steel, and 10.33 g/cm^3 for the LBE coolant.

Fig. 3 shows the reactivity $\rho = 1 - 1/k_{eff}$ as a function of the global uniform temperature obtained with HELIOS for the different libraries and compared to MCNP results with JEFF-3.1.1 nuclear point data. Obviously, the HELIOS calculations with the adjusted 190 energy group library compares best with the MCNP results. It is found that the 47 energy group library, optimized for thermal spectrum systems, overestimates the reactivities by more than 1000 pcm and so gives entirely unacceptable results for LBE cooled fast spectrum systems.

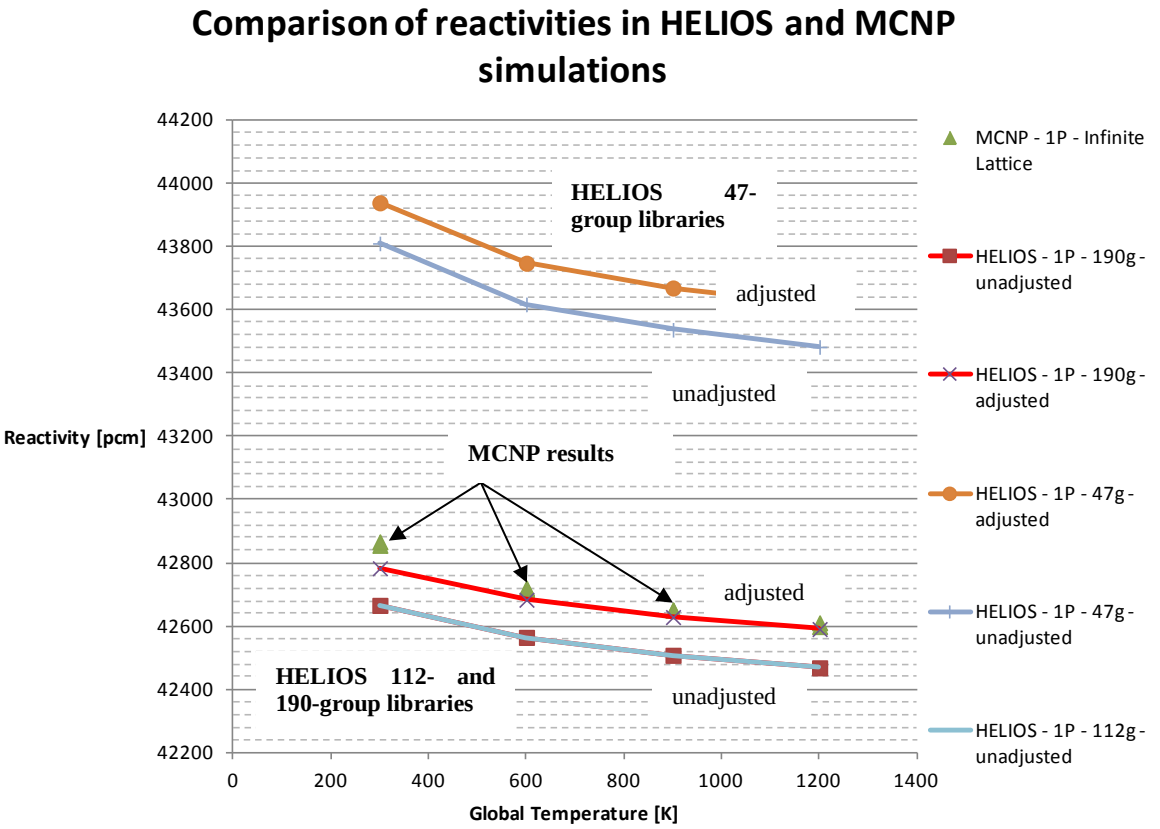

FIG. 3. Reactivities for the infinite pin cell lattice obtained with HELIOS for different data libraries and compared to MCNP results with JEFF-3.1.1 nuclear point data.

Furthermore, the adjusted 190 energy group library gives better results being more closely to the MCNP reference and should thus be preferred over the unadjusted library. In this case, where ^{238}U represents the nuclide with the largest weight fraction, the adjustment accounts for about 150 pcm. There is also a close agreement between the unadjusted 190 energy group library and the 112 energy group library that is optimized for fast spectrum systems.

4. Evaluation of reactivity feedback coefficients for generic MYRRHA fuel assemblies

4.1. HELIOS model of a generic MYRRHA fuel assembly

For the evaluation of reactivity feedback coefficients, a HELIOS model of a generic MYRRHA fuel assembly based on the specifications given in Tab. 1 and Ref. [3] and [5] has been prepared (Fig. 4).

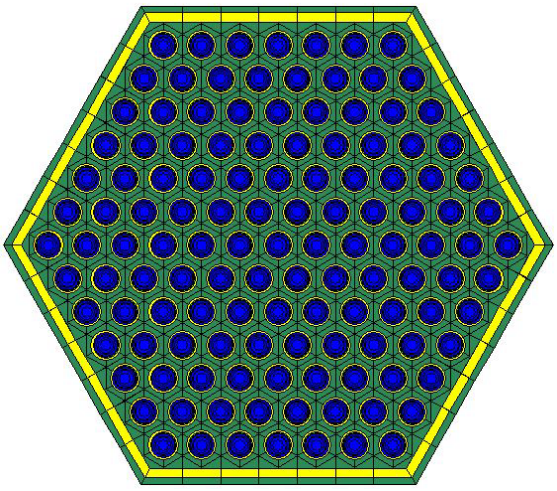

FIG. 4. HELIOS model of a generic MYRRHA fuel assembly.

To study geometric expansion effects, the geometry has been parameterized such that relative changes in both pin pitch and fuel rod diameter can easily be handled by changing only one parameter. Based on the nominal values $d_0 = 0.655$ cm for the fuel rod diameter and $p_0 = 0.84$ cm pin pitch (corresponding to a pitch-to-diameter ratio of $p/d = 1.28244$), the following parameters are used to describe geometry changes:

- relative fuel rod diameter $D = d/d_0$
- relative pin pitch $s = p/p_0$

Reflecting boundary conditions are applied to all six faces of the assembly to simulate an infinite 2-D lattice of identical fuel assemblies. According to the findings in section 3, the adjusted 190 neutron energy group library has been used for HELIOS calculations.

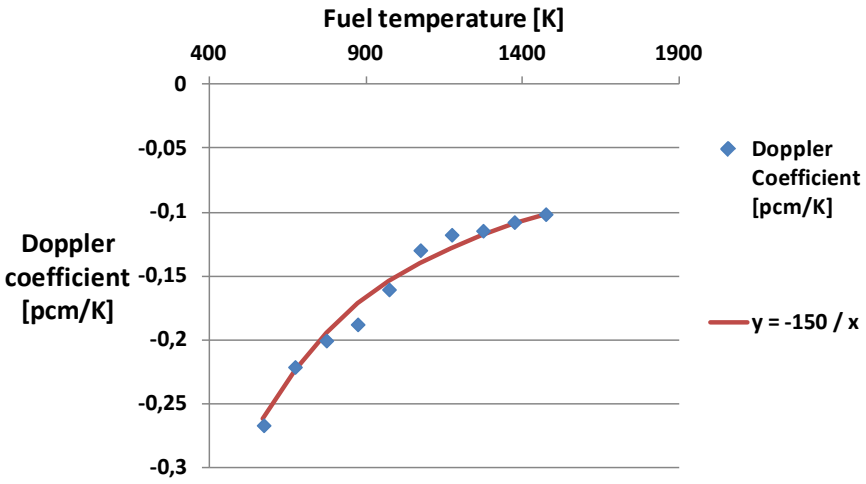

FIG. 5. Fuel Doppler coefficient for a generic MYRRHA fuel assembly in infinite lattice.

4.2. Fuel Doppler coefficient

The fuel Doppler coefficient $\frac{dk_{eff}}{dT_{fuel}}$ as a function of the fuel temperature is shown in Fig. 5. It has been evaluated for 10 different fuel temperatures by calculating the corresponding reactivity and the reactivity at elevated fuel temperature (by 200 K):

$$\mathrm{DC} = \frac{\rho(\mathrm{T_{fuel}} + 200\ \mathrm{K}) - \rho(\mathrm{T_{fuel}})}{200\ \mathrm{K}}$$

The coolant temperature is set to its nominal operating value of 573 K. The Doppler constant is obtained by fitting a 1/T function to the calculated Doppler coefficient values. The result is shown by the red curve in Fig. 5 and corresponds to a Doppler constant of

$$T_{fuel}\frac{dk_{eff}}{dT_{fuel}} = -150\ pcm.$$

The rather good agreement of the Doppler coefficient with the inverse curve derived from the Doppler constant model demonstrates the capability of HELIOS to simulate the neutronic behaviour of LBE cooled fast pectrum systems.

4.3. Void worth and coolant temperature reactivity coefficient

The void worth is calculated by the difference between the reactivities of the voided state and the state with nominal density at a given coolant temperature. The density of the voided state was taken to be 1% of the nominal density, i.e. the void worth is given by

$$\Delta\rho_V = \rho\big(0.01 \cdot q(T_{cool})\big) - \rho\big(q(T_{cool})\big),$$

where $q(T_{cool})$ is the density of the coolant at temperature T_{cool}. The coolant temperature reactivity coefficient is evaluated by the difference between the reactivities of the state with the coolant at elevated temperature (by 200 K) and the state at nominal coolant temperature:

$$CRC = \frac{\rho(T_{cool} + 200K) - \rho(T_{cool})}{200\ K}$$

In all calculations, the fuel temperature was set to its nominal value of 1473 K.

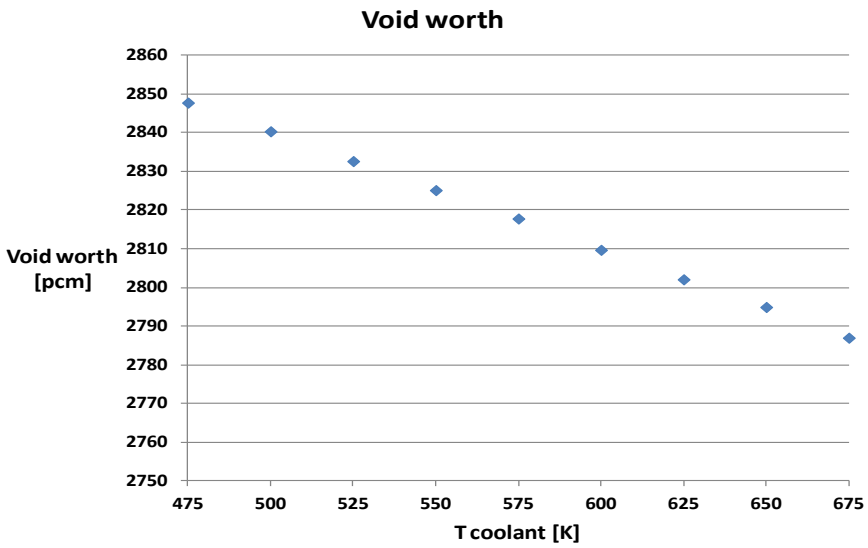

FIG. 6. Void worth as a function of LBE temperature for an infinite lattice of generic MYRRHA assemblies.

The results obtained for the void worth and the coolant temperature reactivity coefficient are shown in Fig. 6 and Fig. 7, respectively. Obviously, the void worth is lower at high coolant temperature, as the effect of the coolant is directly linked with its density. As the density varies linearly with temperature, the evolution of the void worth is also linear. This is consistent with the almost constant value of the coolant temperature reactivity coefficient (note the small ordinate scale in Fig. 7).

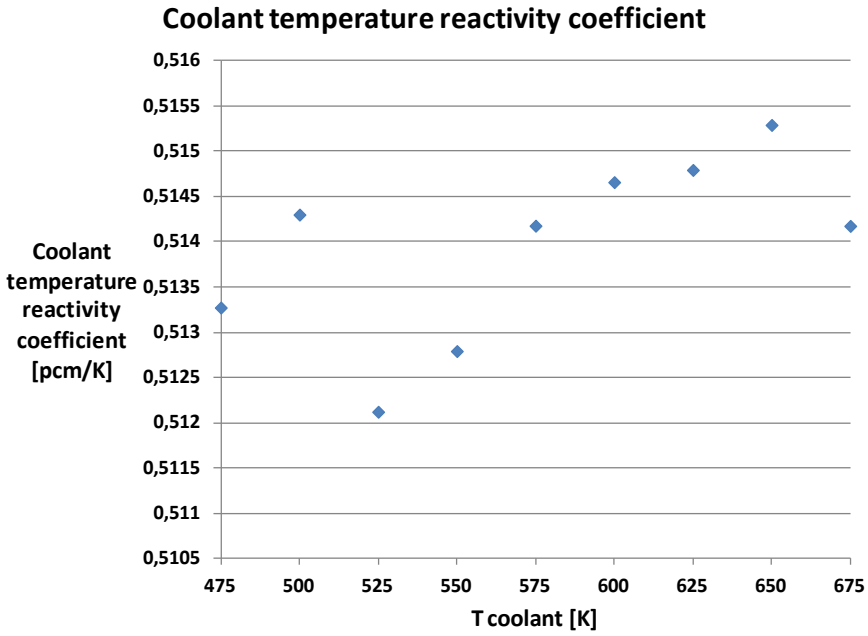

FIG. 7. Coolant temperature reactivity coefficient as a function of LBE temperature for an infinite lattice of generic MYRRHA assemblies.

From the results shown in Fig. 7, an error estimate of about 0.002 pcm/K may be derived. Using the formula for the coolant temperature reactivity coefficient, the standard error in the multiplication factor calculation by HELIOS can be estimated to about 0.2 pcm. Obviously, the convergence criteria in HELIOS are sufficiently tight enough for precise results, although this does not necessarily imply that the results are accurate.

4.4. Radial expansion reactivity coefficient and diameter expansion reactivity coefficient

Since the Doppler reactivity feedback is rather small, reactivity feedbacks from thermo-structural expansion become relevant. This has been studied for the generic MYRRHA fuel assembly in infinite lattice geometry. To this aim, the fuel assembly geometry has been expressed in HELIOS by the relative pin pitch $s = p/p_0$ and the relative fuel rod diameter $D = d/d_0$ introduced above. The reference geometry is represented by $s = 1$ and $D = 1$. Both parameters s and D are independently varied around 1.0 (with the other fixed at 1.0) to evaluate either the Pin Pitch reactivity Coefficient

$$PPC = \rho(s) - \rho(1)$$

or the Diameter Expansion reactivity Coefficient

$$DEC = \rho(D) - \rho(1)$$

where the fuel density has been assumed to be unchanged here. The results are shown in Fig. 8 for the Pin Pitch reactivity Coefficient and in Fig. 9 for the Diameter Expansion reactivity Coefficient. In the variation of s, the rod diameter was fixed at its nominal value of 0.655 cm; likewise, the pin pitch was kept at ist nominal value of 0.84 cm when D was varied. The values of D and s considered here slightly exceed the variations that can be expected in a reality. For example, the radial expansion that can be expected from coolant expansion due to a cooling from 400°C to 150°C is of around 1.5% of the nominal pitch. A linear dependency of the multiplication factor is observe in both cases. It is found that the two effects are of the same order of magnitude, although the diameter expansion coefficient is slightly higher than the radial expansion coefficient. The contrary slopes obtained for the infinite lattice model may be explained as follows: A growing pin pitch with fixed rod diameter increases the amount of coolant which has a negative effect on reactivity through neutron capture and neutron scattering. On the other hand, as the rod diameter becomes larger with fixed pin pitch and fixed fuel density, the amount of fuel material increases, which obviously has a positive effect on reactivity.

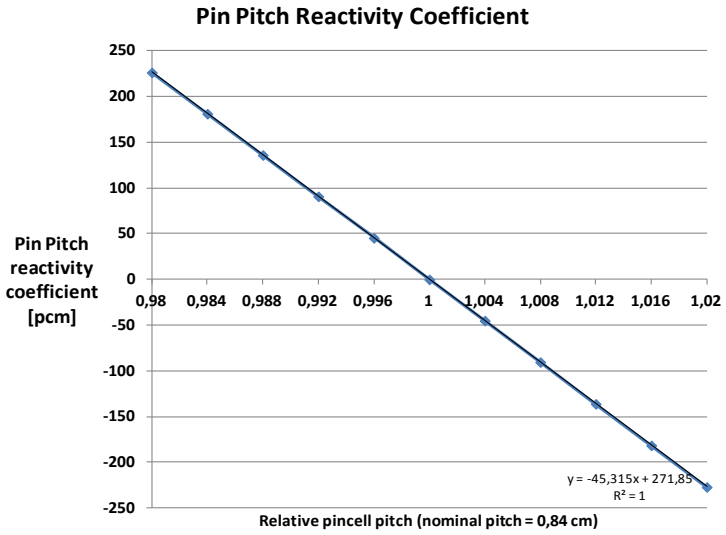

FIG. 8. Pin Pitch reactivity Coefficient for an infinite lattice of generic MYRRHA assemblies.

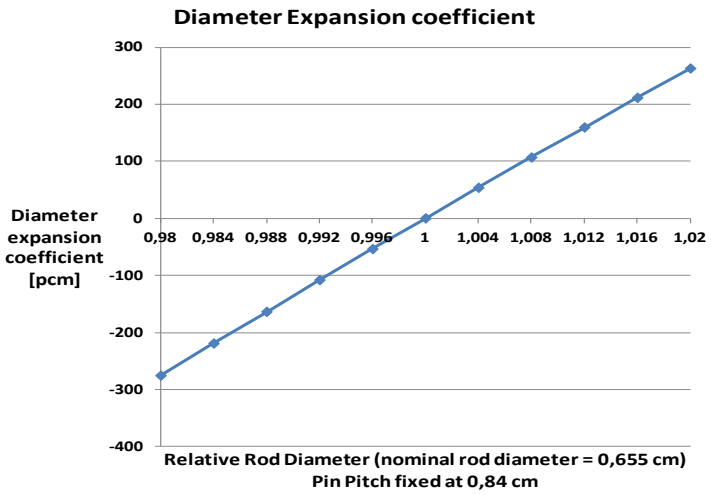

FIG. 9. Diameter Expansion reactivity Coefficient for an infinite lattice of generic MYRRHA assemblies.

Based on these findings, a model to predict the reactivity of any geometric configuration specified by the parameters *s* and *D* has been derived. It adopts the approach described in [8] according to which there can be different basic geometry changes in a given system whose effects on reactivity are assumed independent in first approximation, and which can be superimposed to obtain a reasonable estimate of the neutronic effect of a more complex geometry change. In our case, the slope of the radial expansion reactivity coefficient was estimated at c_s = –113 pcm/(%nominal pitch), and the slope of the diameter expansion reactivity coefficient was estimated at c_D = 135 pcm/(%nominal diameter). Calculations were carried out with HELIOS while varying both *s* and *D*, and the resulting reactivities were compared to the model

$$\rho_{Model} = \rho(s = 1, D = 1) + c_s \cdot (s - 1) + c_D \cdot (D - 1)$$

This model gives a reasonable approximation of the reactivity calculated with HELIOS. Table 2 gives a few statistical indicators of the error between this model and the HELIOS results. This approach may be used as a basis to model pitch or diameter expansion effects in neutronics core simulators for fast reactor transient analysis which – due to fixed spatial meshing – cannot easily account for pitch or diameter expansion by simply changing the nodalization.

Table 2. Statistical indicators of errors between the reactivity model and actual HELIOS results.

Indicator	**Value**
Average error [pcm]	2.62
Maximum error [pcm]	13.21
Error standard deviation [pcm]	2.92
Average relative error [%]	1.5
Maximum relative error [%]	34
Relative error standard deviation [%]	2.4

5. Conclusion

The lattice code HELIOS is applied to generic MYRRHA pin cells and fuel assemblies to assess reactivity feedbacks of LBE cooled fast spectrum systems. The validity of the different HELIOS libraries is assessed by comparing with detailed Monte Carlo calculations using MCNP with nuclear

point data. It is found that the 190 energy group adjusted library compares best with the Monte Carlo results with JEFF-3.1.1 nuclear point data and outperforms the 112 energy group library that is designed for fast spectrum applications. However, it is worth to make additional comparisons with MCNP using ENDF/B-VII nuclear point data. Based on generic MYRRHA fuel assemblies, evaluations of fuel Doppler coefficient, void worth, coolant temperature coefficient and structural expansion coefficients are shown. In addition, based on the study of radial expansion feedback coefficients, a simple model is given to predict reactivity changes introduced by a combination of changes in the radial fuel diameter and fuel assembly pitch.

ACKNOWLEDGEMENTS

This work was supported by the German Federal Ministry of Economics and Technology due to a resolution of the German Bundestag.

REFERENCES

[1] J. J. Casal, R. J. J. Stamm'ler, E. A. Villarino and A. A. Ferri, HELIOS: Geometric Capabilities of a New Fuel-Assembly Program, *Proc. Int. Top. Mtg. Adv. Math. Comp. Reac. Phys.*, Pittsburg, PA, USA, Vol. II, Sect. 10.2.1, 1-13 (1992).

[2] SCK-CEN, MYRRHA Technical Description (2008)

[3] Sarotto, M., MYRRHA-FASTEF FA/core design, In: Team, E. F. (Ed.), International Workshop on Innovative Nuclear Reactors cooled by HLM: Status and Perspectives. Pisa (2012).

[4] Sobolev, V., Thermophysical properties of molten Pb and Pb-Bi eutectic., SCK-CEN, Ed., Cadarache, France (2006).

[5] SCK-CEN, MYRRHA Technical Description (2008).

[6] Jatuff, F., et al., Void reactivity coefficient benchmark results for a 10×10 BWR assembly in the full 0-100% void fraction range, Annals of Nuclear Energy **36**, 853 (2009).

[7] J. F. Briesmeister ed., MCNP – A General Monte Carlo N-Particle Transport Code, Version 4C, Los Alamos National Laboratory report LA-13709-M (April 2000).

[8] Travleev, A., et al., An approach to assess reactivity changes due to core thermal expansion, Jahrestagung Kerntechnik, Berlin (2010).

Supercritical Carbon Dioxide Brayton Cycle for SFR Applications: Optimization, Transient Analysis, and Control

A. Moisseytsev, J. J. Sienicki

Argonne National Laboratory,
Argonne, IL, United States of America

Abstract. A Plant Dynamics Code (PDC) has been under development at Argonne National Laboratory for several years to investigate steady-state and transient performance and behavior of the S-CO_2 cycle as an alternative power converter for advanced SFRs. The code was specifically developed to address unique features of the S-CO_2 cycle, including operation near the critical point and the effect of properties variation on the design and transient behavior of turbomachinery and heat exchangers. A coupling approach between PDC and SAS4A/SASSYS-1 Liquid Metal Reactor Code System has been implemented to allow simultaneous investigation of transient behavior of liquid metal-cooled reactors and S-CO_2 cycle balance-of-plants. PDC has been used to optimize the S-CO_2 cycle design and to develop a control strategy. It has been demonstrated that with the proposed control systems the cycle can be effectively and stably operated over the entire range of grid loads and for decay heat removal.

1. INTRODUCTION

Liquid metal-cooled fast reactors (LMRs), such as sodium-cooled fast reactors (SFRs) and lead-cooled fast reactors (LFRs) offer significant benefits over conventional light-water reactors (LWRs). Fast reactors in general allow for better uranium resource utilization by means of internal generation of fissile isotopes. These reactors are capable of burning minor actinides significantly reducing a burden on the ultimate reactor waste storage. In addition, LMRs offer safety benefits by utilizing inherent safety features, such as natural circulation of primary and emergency decay heat removal coolants, favorable strong core reactivity feedbacks, as well as the advantages of a compact primary coolant system with a low pressure liquid metal coolant.

At the same time, there still remain challenges to fast reactor deployment. For the SFRs and LFRs, one of the most significant of those is a sometimes perceived higher capital cost than large economy-of-scale LWRs. For SFRs utilizing conventional Rankine steam cycles for energy conversion, design features to accommodate sodium-water reaction, which has a potential of producing exothermic energy release and combustible hydrogen, is a contributor to the plant cost. In particular, a system for monitoring for leaks with instrumentation capable of detecting leakage from small leaks at low thresholds is required together with a Sodium-Water Reaction Pressure Relief System (SWRPRS) for mitigating the consequences of sodium-water reactions from larger-scale leaks. Utilizing a supercritical carbon dioxide (S-CO_2) Brayton cycle for energy conversion for SFRs and LFRs has a potential of addressing these features. Moreover, the S-CO_2 Brayton cycle is matched to the SFR system in that the cycle wants to operate with a CO_2 temperature rise across the sodium-to-CO_2 heat exchanger of about 150 °C which is approximately the sodium core temperature rise of a SFR.

This paper discusses progress in the modeling of the S-CO_2 cycle in applications specific to SFRs and discusses some of the major findings about use of the cycle with SFRs that have come from analyses using the unique modeling capability for S-CO_2 cycles developed at Argonne National Laboratory.

2. S-CO_2 CYCLE FOR SFRs

The S-CO_2 cycle uses carbon dioxide in the supercritical state as a working fluid for energy conversion. The main advantages of the cycle come from the possibility to carry out the CO_2 compression immediately above the CO_2 critical point. The "convenient" CO_2 critical point at 31 °C and 7.38 MPa makes it feasible to operate the cycle with conventional water or even dry air cooling heat sinks. In the proximity of the critical point, there is a significant increase in the CO_2 density such that the compression work is much smaller than would be for an ideal gas at the same conditions. While smaller compression work leads to higher cycle efficiency, maintaining the conditions above the critical point allows operating the entire cycle within a single-phase domain, thus eliminating complications and restrictions of phase change in the cycle. Earlier analysis of the S-CO_2 cycle [1],[2],[3] have shown that the S-CO_2 cycle can provide a thermodynamic efficiency of 45% and above for turbine-inlet temperatures of 550 °C and higher. If such energy conversion efficiencies can be realized for a SFR, they would exceed those achievable with the steam cycle, thus not only increasing the power output from a reactor plant, but at the same time reducing the capital cost per unit electrical output of the entire plant. The other contributing factor to reducing the plant capital cost is a remarkably small S-CO_2 turbomachinery. The calculations have shown [1] that a turbine for a 300 MWe plant would have diameter and length of the order of 1 m, which is several times smaller in dimension than a steam turbine of the same power.

At the same time, a few challenges remain in developing the S-CO_2 cycle for SFR applications. The same properties variation near the critical point which makes it possible to achieve high cycle efficiency also proves to be challenging for design, operation, and control of the cycle. On one hand, the conditions near the compressor inlet should be selected and controlled very precisely in order to keep the compression work low and not significantly affect the compressor performance. One particular concern here is a possibility to enter the two-phase region, i.e., temperatures and pressure below the critical point, during certain off-normal events which could introduce liquid droplets inside of the compressor possibly damaging the compressor blades. Also, due to rapid properties variation, the compressor operating range is expected to be narrow (compared to an ideal gas), affecting the cycle controllability at off-design conditions.

On the other hand, strong dependence of CO_2 properties, such as specific heat, on pressure near the critical point dictated selecting of the so-called recompression cycle, where part of the CO_2 low pressure flow in the recuperator is diverted from the normal flow path through a cooler and compressor, and is instead directly compressed in a separate re-compression compressor (see Fig. 1 below). The difference in the specific heats of the high- and low-pressure flows is so significant that increasing the recuperator effectiveness and raising the cycle efficiency by means of the flow split has been proven to be more important for the S-CO_2 cycle efficiency than introducing a second, less efficient, recompressing compressor.

The importance of recuperative heat transfer for the S-CO_2 cycle efficiency presents another challenge for the cycle development. It has been shown that high cycle efficiencies can be realized only with significant recuperation of heat within the cycle, often exceeding the amount of heat added to the cycle from a reactor coolant. For heat transfer purposes, CO_2 in a supercritical state shows gas-like behavior thus requiring a large heat transfer area to achieve effective heat transfer within the cycle. Combined with relatively high cycle pressures (7 MPa on one side and 20 MPa on the other side) and relatively high temperatures (up to 550 °C), the requirement for large heat transfer area would result in very high heat exchanger costs, if conventional, e.g., shell-and-tube (S&T), heat exchangers are utilized for the S-CO_2 cycle. For these reasons, innovative heat exchanger concepts, such as compact Printed Circuit heat Exchangers (PCHE) developed by Heatric Division of Meggitt (UK) [4] or S&T heat exchanges with fins on the tube surfaces are beneficial for the S-CO_2 cycle. These concepts, however, are still costly, and development and demonstration of alternate heat exchanger technologies with an objective of reducing heat exchanger costs is an area of investigation.

Although replacing a steam cycle with S-CO_2 energy conversion eliminates the possibility of sodium-water reaction, sodium-CO_2 interaction needs to be well and technological solutions developed to

accommodate all potential physical and chemical effects (e.g., formation of solid and gaseous reaction products in sodium). The ongoing work in this area [5],[6] shows that sodium-CO_2 reaction is not as severe as sodium-water reaction; although at some conditions the reaction can be exothermic and produce carbon monoxide (CO).

A S-CO_2 cycle has never been constructed and operated on a commercial scale. A small-scale integral cycle demonstration has been assembled at Sandia National Laboratories and is commencing operation. It is planned to design and construct in the U.S. a simple recuperated S-CO_2 cycle with a 10 MWe turbine to demonstrate bearing, seal, and other technologies at a larger scale under the U.S. Department of Energy SunShot solar energy initiative [7]. In order to investigate, understand, and, overcome the initially perceived challenges and uncertainties, analytical tools specific to the S-CO_2 cycle analysis in application to SFRs had to be developed. At Argonne National Laboratory (ANL), a Plant Dynamics Code has been under development for several years for design, control, and transient analysis of the S-CO_2 cycle for fast reactor applications.

3. ANL PLANT DYNAMICS CODE

The Plant Dynamics Code (PDC) has been developed at ANL specifically for the analysis of the S-CO_2 cycle [8]. From the beginning, the focus of PDC development has been on capturing the unique features of the S-CO_2 cycle described above, such as properties variation, especially near the critical point, and the effect of the CO_2 properties on the design and performance of the cycle components and the entire system. For example, the ideal gas laws commonly used for turbomachinery and heat exchanger analysis (e.g., log-mean temperature approach) are not applicable to the CO_2 cycle and were intentionally not included into the PDC equations. Instead, the code relies on fundamental conservation laws, such as energy, mass, and momentum, and very accurate CO_2 properties calculations. In the PDC, the original Span and Wagner [9] formulations of CO_2 properties (with up to 42 polynomial terms) are used without any simplifications in both the steady-state and dynamic calculations. The PDC has two parts: steady-state and transient, intended for design and transient performance analysis, respectively.

3.1.Steady-State Design Calculations

The steady-state part of PDC was developed for predicting the cycle performance (i.e., efficiency) at design conditions. It integrates steady-state calculations of the heat exchangers, turbomachinery (turbine and compressors) and pipe pressure drops. For the steady-state heat exchanger calculations, PDC has an option of user-specified heat exchanger effectiveness and pressure drops on both sides. This option was included in the code for quick cycle calculations and also for setting the performance targets for realistic heat exchanger models. This option, however, could not be used in transient calculations, since it cannot predict heat exchanger performance at off-design conditions. For these reasons, the main heat exchanger option for both the steady-state and transient calculations in PDC has been a realistic model. In this option, the user specifies the dimensions and the internal design data for each heat exchanger and the code calculates its performance, i.e., heat transfer rate and pressure drops, for both steady-state and transient conditions. The calculations are formulated with several nodes along the heat exchanger length to account for the CO_2 properties variation inside the heat exchanger. Several design options are available in PDC for the heat exchangers, including shell-and-tube heat exchangers and PCHEs. To develop the heat transfer and pressure drop correlations for a PCHE, numerous experiments were carried out at ANL with a small-scale PCHE (17.5 kWth) under prototypic CO_2-water cooler and CO_2-CO_2 low temperature recuperator conditions [10],[11].

Similar to the heat exchangers, several options exist in PDC for turbomachinery steady-state calculations. Under a simple option, the user specifies the turbine or compressor efficiency. This option, however, is not able to predict off-design performance of the turbomachinery. Therefore, the use of this option in PDC steady-state calculations is limited to a first guess in iterations between the cycle conditions and turbomachinery performance. The main turbomachinery calculations are performed using a realistic model, where the turbine or compressor performance is calculated based on its dimensions and cycle conditions. However, unlike the heat exchanger calculations, the conditions

for the turbomachinery calculations, such as the turbine and compressor inlet temperature and inlet/outlet pressures are either specified by the user as external cycle conditions or obtained from the cycle performance calculations. Therefore, the S-CO_2 cycle turbine and compressors need to be designed to match those external conditions. For these reasons, turbomachinery design subroutines are incorporated into PDC to calculate the turbine and compressors dimensions and performance at the design conditions. These design subroutines are based on first principal analyses [12],[13] and do not use ideal gas laws. Most of the design parameters, such as blade height etc., are calculated by the code; a PDC user only provides some design choices, such as the number of stages, minimum hub diameter, blade thicknesses, etc. Since the calculated turbomachinery performance defines cycle conditions, such as outlet temperatures, which are eventually used to calculate the CO_2 flow rate, there is an inter-dependence of the cycle conditions and turbomachinery design and performance. For these reasons, the turbine and compressor design subroutines are integrated in PDC into the cycle steady-state performance calculations.

The steady-state part of PDC is organized in such a way that allows user to specify the cycle configuration in the input file. This code feature was used to investigate various cycle layouts for application to SFRs and other reactor concepts. Fig. 1 shows the steady-state S-CO_2 cycle performance, including temperatures, pressures, heat duties, and efficiencies as calculated by the steady-state part of PDC for an application to a 1000 MWth Advanced Burner Reactor (ABR-1000) SFR concept developed at ANL [14]. The conditions on the sodium side of the Reactor Heat eXchanger (RHX) are defined by the reactor design. As discussed above, the cycle uses the re-compression configuration where about 1/3 of the flow bypasses the cooler, the main compressor, and the Low-Temperature Recuperator (LTR), and is instead compressed in the re-compression compressor. This arrangement allows achieving almost 97% effectiveness of the LTR despite the differences in the specific heats between the high and low pressures flows. As observed from Fig. 1, the amount of heat recuperated in the cycle by two recuperators (about 1800 MWth) is almost twice the amount of heat input supplied by the reactor (1000 MWth).

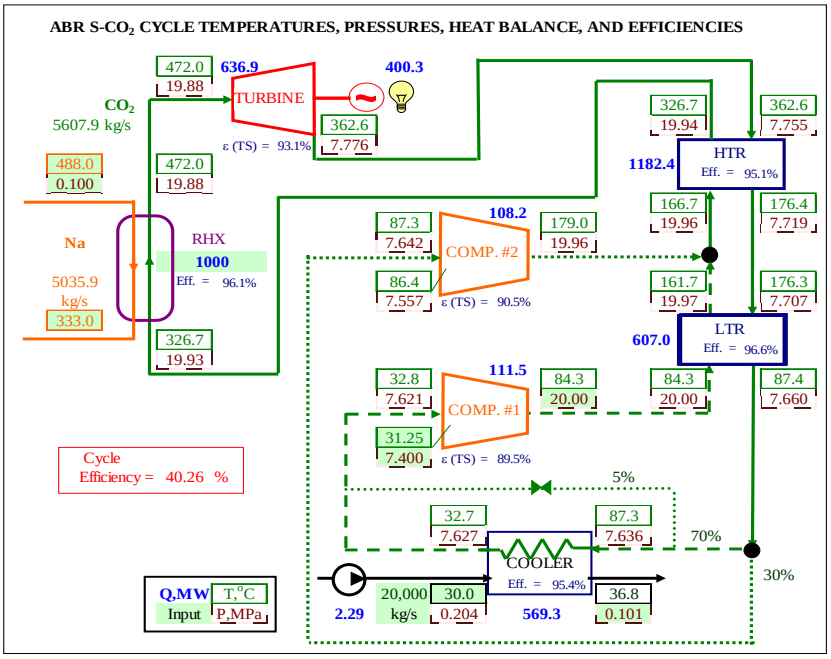

FIG. 1. S-CO_2 Cycle Steady-State Performance and Conditions for ABR-1000 SFR.

In addition to the design performance calculations of the S-CO_2 cycle, the steady-state part of PDC has been used to optimize the design of each major cycle component. A technique was developed [15] to find the optimal design of the heat exchangers and turbine which take into account the component performance in the cycle, its estimated cost, and the effect of the cycle efficiency on minimizing the cost of electricity produced at the plant.

The PDC was also used to investigate other cycle arrangements. In particular, it was found [16] that utilizing partial CO_2 condensation at the cold end of the cycle can result in noticeable efficiency increase provided that sufficiently cold heat sink is available without additional (e.g., refrigeration) systems and associated costs.

3.2. Transient Calculations

The transient calculations in PDC follow the same approach as in the steady-state part to capture the effect of the CO_2 properties variations. In particular, no ideal gas assumptions are made for either heat exchangers or turbomachinery; rather fundamental first-principle conservation laws are applied on a multi-nodal basis to track the properties variation. The time-dependent mass, momentum, and energy conservation laws are applied to each node to derive the dynamics equations for time-derivatives of density, flow rate, enthalpy ($\partial\rho/\partial t$, $\partial m/\partial t$, and $\partial h/\partial t$, respectively) solved in PDC. The form of the resulting equations depends on the component for which the fundamental conservation equations are applied. For example, in the heat exchangers, the enthalpy equation includes the heat transfer term from the heat exchanger wall. The resulting equations require knowledge of CO_2 pressures and temperatures in order to solve for the density and enthalpy. This means that all four properties need to be simultaneously solved for at each time step. Since the CO_2 properties are most efficiently calculated based on the temperature and density, the time derivatives of enthalpy and pressure are defined through the partial derivatives with respect to temperature and density in PDC as follows:

$$\frac{\partial h}{\partial t}=\left(\frac{\partial h}{\partial T}\right)_\rho \frac{\partial T}{\partial t}+\left(\frac{\partial h}{\partial \rho}\right)_T \frac{\partial \rho}{\partial t}=h_T \frac{\partial T}{\partial t}+h_\rho \frac{\partial \rho}{\partial t} \quad \text{and} \quad \frac{\partial p}{\partial t}=\left(\frac{\partial p}{\partial T}\right)_\rho \frac{\partial T}{\partial t}+\left(\frac{\partial p}{\partial \rho}\right)_T \frac{\partial \rho}{\partial t}=p_T \frac{\partial T}{\partial t}+p_\rho \frac{\partial \rho}{\partial t}$$

The partial derivatives, h_T, h_ρ, p_T, and p_ρ, are derived analytically based on the expressions for Helmholtz energy and are calculated exactly at each location at each time step in the PDC transient calculations.

Transient response of the turbomachinery is calculated based on the performance subroutines which are very similar to the design subroutines used in the steady-state calculations. These performance subroutines, however, require iterations on properties and thus are slow for dynamic calculations. To accelerate the transient calculations in PDC, turbomachinery maps are generated for the turbine and compressor designs obtained at steady-state conditions. Similar to all other calculations in PDC, the turbomachinery maps cannot rely on commonly-used scaling laws which are obtained under ideal gas assumptions. Instead, in PDC, four-dimensional maps are generated, where the turbomachinery performance (in terms of outlet temperature, flow rate, and other parameters) is calculated for all possible combinations of inlet and outlet pressures, inlet temperatures, and rotational speeds. During a transient, PDC interpolates between the map points to obtain the performance of the turbine and compressors at each time step. If, for any reasons, the map interpolation is not sufficient, a user has an option to use the actual performance subroutines instead of the maps for transient response of the turbomachinery, although this option will results in increased computational time.

3.3. S-CO_2 Cycle Control

The transient calculations of PDC incorporate the cycle control mechanisms. The control strategy for the S-CO_2 cycle has been developed using a combination of the quasi-static and dynamic analyses with PDC [17],[18],[19],[20]. The current control strategy involves a combination of the control mechanisms shown in Fig. 2 and Table 1. Prior calculations of S-CO_2 control have shown that only turbine bypass control has the ability of controlling the cycle over the entire range of power output. All other controls have limited range of applicability for various reasons, but mostly due to CO_2 properties variation and their effect on the operating range of the two parallel compressors. The turbine bypass control, however, is the least efficient control approach at partial loads, meaning that the cycle efficiency drops faster with this control at partial loads than with other controls. For this reason, the S-CO_2 cycle control strategy in Table 1 relies on a combination of various control mechanisms at partial loads. It has also been shown that the combination of cooler bypass and water flow controls is

recommended for the S-CO_2 cycle to maintain conditions close to, but above, the critical point in transients [19].

PDC transient calculations incorporate modeling of automatic control for the S-CO_2 cycle. The automatic control monitors the controllable parameter, compares it with the required set value, and applies the control action using Proportional, Integral, and Differential (PID) controllers based on the difference between the actual and set value of the controlled parameter, normalized to the steady-state value. The control action could be rate of valve opening, for example. The controlled parameter depends on the control mechanism itself and also on other inputs. For example, for turbine bypass control, the controlled parameter is the net generator output in the synchronous regime and the shaft rotational speed in asynchronous mode. The control coefficients in the above equations were optimized in PDC to obtain a favorable response of each control under various conditions.

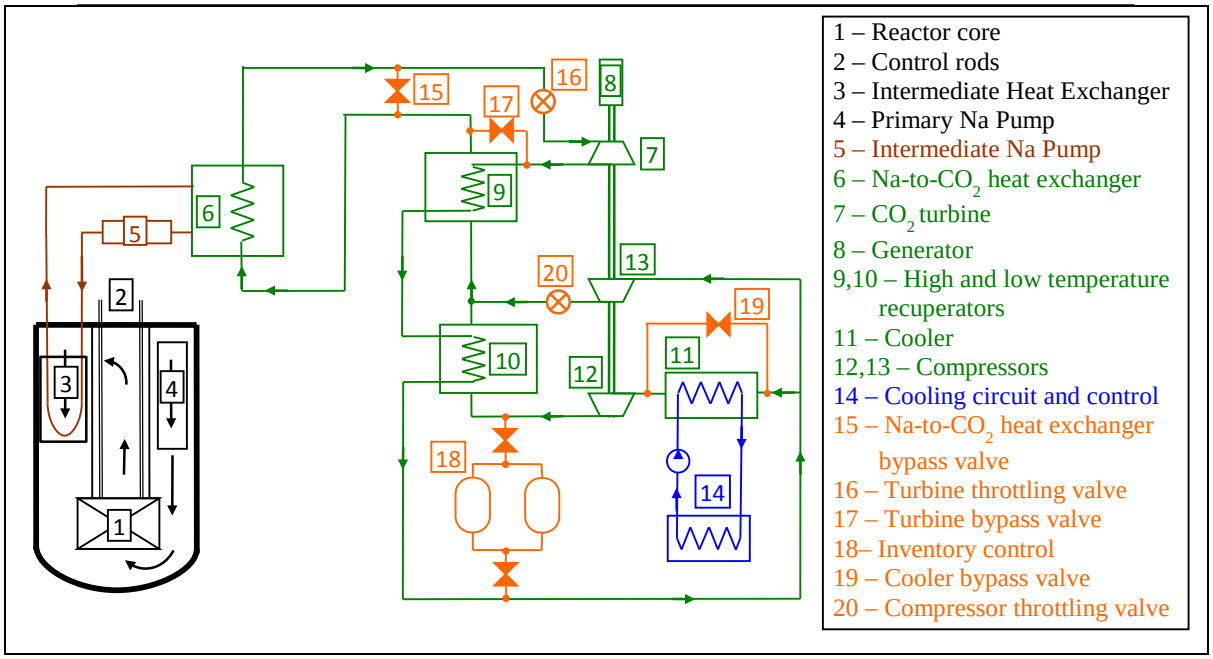

FIG. 2. S-CO_2 Cycle Control Mechanisms for SFR Applications.

Table 1. S-CO_2 Cycle Control Mechanisms and Ranges

Control Mechanism	Range,% Load
Inventory	50% - 90% and 10% - 25%
Turbine throttling	0% - 50%
Turbine bypass	90% - 100% and all other loads to assist other controls
Cooler bypass	All loads to maintain minimum temperature
Cooling water flow rate	All loads to maintain operability of the cooler bypass
Compressor surge control	When needed to avoid surge

3.4. Integration of the Reactor Dynamics

Originally, PDC was developed for the analysis of the S-CO_2 cycle coupled to the Secure Transportable Autonomous Reactor (STAR) LFR concepts developed at ANL [8]. At that stage, the code included models for the reactor thermal hydraulic and kinetics parts. Later, it was realized that in order to facilitate analysis of the S-CO_2 cycle for various reactor systems, it was necessary to separate the reactor and S-CO_2 cycle calculations. As the first step in this separation, external input tables for the reactor primary or intermediate coolant conditions at the RHX inlet were implemented in the code. This option still exists in the code.

Recently, a coupling approach was developed to integrate the calculations of PDC and the SAS4A/SASSYS-1 Liquid Metal Reactor Code System [21]. The SAS4A/SASSYS-1 code [22] is the leading capability for modeling a SFR or LFR at the system level. It incorporates detailed reactivity feedback models along with comprehensive thermal hydraulic models for the primary, intermediate, and decay heat liquid metal loops. In the coupled calculations for a SFR, the SAS4A/SASSYS-1 code calculates the conditions on the reactor side for primary and intermediate coolants, and provides the intermediate sodium conditions at the RHX inlet and its flow rate at each time step. The PDC then uses this input to calculate the transient response of the RHX, including the sodium and CO_2 sides, and the rest of the S-CO_2 cycle conditions during the time step. The RHX-outlet temperature on the sodium side is supplied back to the SAS4A/SASSYS-1 code for the calculations for the next time step.

3.5. PDC Validation

The S-CO_2 cycle is still in the early stages of the development. Until recently, virtually no experimental data on the S-CO_2 cycle components and the entire cycle performance were available. For these reasons, verification of PDC in its early development was mostly limited to benchmark calculations against similar codes being developed for the S-CO_2 cycle analysis [23].

Later, limited validation of the PDC models on an individual component basis was carried out using experimental data obtained from facilities directed at individual components. For that purpose, the components were selected to address specific features of the S-CO_2 cycle, in particular, the effect of the properties variation near the critical point. Therefore, the earlier experimental work was focused on the heat exchangers, especially the cooler and the low temperature recuperator since they operate very close to the critical point, and the CO_2 compressors designed to operate in the proximity of the critical point. An extensive validation of the heat exchanger models in PDC was carried out based on the experimental data obtained from the S-CO_2 heat exchanger testing facility at ANL [10],[11] which tested the performance of a small-scale PCHE manufactured by Heatric Division of Meggitt (UK) under both prototypical CO_2-water cooler and CO_2-CO_2 low temperature recuperator conditions. The PDC compressor performance model was validated using the data from the S-CO_2 compressor test loop constructed and operated by Barber-Nichols, Inc. (BNI) and Sandia National Laboratories (SNL) [24]. In both cases, good agreement between the model predictions and the experimental data was achieved over a wide range of the experimental conditions.

Recently, work on PDC validation against the experimental data obtained at the small-scale S-CO_2 loop operated by Sandia National Laboratories (SNL) has been started [25],[26]. The SNL S-CO_2 loop was constructed for SNL at Barber-Nichols, Inc. (BNI) in a staged fashion with the ultimate goal of demonstrating a complete recompression S-CO_2 cycle and all of its principal components, including two compressors, turbines, two recuperators, a water cooler, and heat source heat exchangers simulated by electrical heater units. The loop can currently simulate an integrated S-CO_2 cycle with two turbo-alternator-compressor (TAC) units (i.e., not the same recompression cycle described above with a single turbine and two compressors on the same shaft) and a heat input of 780 kWth. For the PDC validation work, one of the earlier configurations featuring a single TAC unit and a single recuperator was analyzed. Several challenges in modeling the loop were identified. For example, a noticeable heat loss in the turbine volute was discovered which could not be accurately measured in the experiments. Also, some information on the internal configuration of some components is not available. Therefore, some assumptions had to be made in the PDC modeling to account for this and other uncertainties in the experimental setup. However, despite all the uncertainties and assumptions, reasonably good agreement was achieved between the code predictions and the measured data for steady-state and transient conditions. This work is on-going and more comparisons of PDC prediction with the SNL S-CO_2 loop data will be carried out with the expectation to use these results to further improve the PDC modeling.

4. S-CO_2 CYCLE TRANSIENT CALCULATIONS WITH PDC

The Plant Dynamics Code has been used for the transient analysis of the S-CO_2 cycle. Earlier, the code was used to develop a control strategy and carry out accident analysis for S-CO_2 cycles coupled

to LFRs [20],[27]. Scenarios such as up and down normal load following, step changes in grid demand, loss of generator load accidents, and CO_2 pipe break accidents were analyzed.

Later the focus of the transient analysis was shifted towards SFR applications. One of the examples of PDC application was calculation of thermal transients in the sodium-CO_2 heat exchangers following postulated accidents on either the sodium or CO_2 sides. That information is input to the mechanical design of the heat exchangers.

The current focus of the PDC transient analysis of the S-CO_2 cycle for the SFR application is the development of the control strategy for the cycle. It has been demonstrated [21] that the cycle control strategy described above is efficient in allowing electrical grid load following. The calculations were carried out using the coupled Plant Dynamics Code-SAS4A/SASSYS-1 code for a linear load reduction transient for a 1000 MWth metallic-fueled SFR with autonomous reactor operation (i.e., no active reactor power control). The results of the load following calculations show a favorable response of the entire plant to the load reduction event. The S-CO_2 cycle control system is able to follow the load over its entire range – from 100% to 0%. Use of a combination of various control mechanisms allows maximizing cycle efficiency at various loads. The reactor is able to follow the response of the S-CO_2 cycle without any control action on the reactor side. The power reduction is provided by means of the internal reactivity feedbacks of the metallic-fueled sodium-cooled fast spectrum core.

In addition, PDC coupled to the SAS4A/SASSYS-1 code was used to demonstrate the transition of the plant operation from the full power down to the decay heat removal mode and the capability to operate the cycle at initial decay heat levels [28]. It has been found that this capability can be achieved by introducing a new control mechanism involving shaft speed control for the common shaft joining the turbine and two compressors following reduction of the load demand from the electrical grid to zero. Following disconnection of the generator from the electrical grid, heat is removed from the intermediate sodium circuit through the sodium-to-CO_2 heat exchanger, the turbine solely drives the two compressors, and heat is rejected from the cycle through the CO_2-to-water cooler. No deliberate motion of control rods or adjustment of sodium pump speeds is assumed to take place. It is assumed that the S-CO_2 turbomachinery shaft speed linearly decreases from 100 to 20% nominal following reduction of the grid load to zero. The reactor power is calculated to autonomously decrease down to 3% nominal providing a lengthy window in time for switchover to the normal shutdown heat removal system or for passive emergency decay heat removal to become effective.

5. SUMMARY

The supercritical carbon dioxide (S-CO_2) Brayton cycle offers benefits as an advanced alternate energy conversion approach for SFRs relative to the traditional Rankine cycle, such as potentially high cycle efficiencies, elimination of sodium-water reactions, and remarkably small turbomachinery. At the same time, there remains the need for demonstration of the cycle at larger scale.

To explore the cycle benefits and to investigate and better understand the initially perceived challenges of the S-CO_2 cycle in application to fast reactors, a Plant Dynamics Code (PDC) has been developed and operational at Argonne National Laboratory. The code was specifically developed to address the unique features of the S-CO_2 cycle, including operation near the critical point and the effect of properties variation on the design and transient behavior of turbomachinery and heat exchangers. The PDC includes both a steady-state design calculation part, as well as a transient part. The steady-state section of PDC has been used to investigate various cycle layouts and to optimize the cycle and individual components for SFR applications.

For the transient calculations, a coupling approach between PDC and the SAS4A/SASSYS-1 Liquid Metal Reactor Code System has been implemented to allow simultaneous investigation of the transient behavior of liquid metal-cooled fast reactors and S-CO_2 cycle balance-of-plants. The transient PDC calculations have been used to develop a cycle control strategy for use with LMRs and to investigate the cycle response to accident conditions. It has been demonstrated through PDC calculations that with

the proposed control systems, the cycle can be effectively and stably operated over the entire range of grid loads and for initial decay heat removal.

Overall, the calculations with the PDC for S-CO_2 cycle have shown that this cycle is a viable and promising alternative energy conversion system for SFR and other applications. *No potential show stoppers were identified for the design, operation, and controllability of the cycle for SFRs*. It was also demonstrated through the coupled PDC-SAS4A/SASSYS-1 analysis that the autonomous load following potential of LMRs can be realized with the S-CO_2 cycle.

ACKNOWLEDGEMENTS

Argonne National Laboratory's work was supported by the U. S. Department of Energy Advanced Reactor Concepts (ARC) Program under Prime Contract No. DE-AC02-06CH11357 between the U.S. Department of Energy and UChicago Argonne, LLC. The work presented here was carried out under the Energy Conversion Technology area of the ARC Program. The authors are grateful to Gary Rochau (SNL), the Technical Area Lead, Bob Hill (ANL/NE), the National Technical Director, and Brian Robinson (U.S. DOE), the Headquarters Program Manager for the Advanced Reactor Concepts (ARC) and Advanced Small Modular Reactors Programs.

REFERENCES

[1] DOSTAL, V., "A Supercritical Carbon Dioxide Cycle for Next Generation Nuclear Reactors," D.Sc. Dissertation, MIT, 2004.

[2] MOISSEYTSEV, A., "Passive Load Follow Analysis of the STAR-LM and STAR-H2 Systems", Ph.D. Dissertation, Texas A&M University, College Station, TX, 2003.

[3] MOISSEYTSEV, A., HOFFMAN, E. and GANDY, C., "Selection of Core Outlet Temperature and Impacts on Fast Reactor Economics," Nuclear Technology, Vol. 173 (2011), pp. 251-269.

[4] SOUTHALL, D., Le PIERRES, R., and DEWSON, S. J., "Design Considerations for Compact Heat Exchangers," Proceedings of ICAPP '08, Paper 8009, Anaheim, CA USA, June 8-12, 2008.

[5] GICQUEL, L., LATGÉ, C., and SIMON, N., "Supercritical CO_2 Brayton Cycle Coupled with a Sodium Fast Reactor: Na/CO_2 Interaction Experiments and Modeling," Paper 10215, 2010 International Congress on Advances in Nuclear Power Plants (ICAPP '10), San Diego, CA, USA, June 13-17, 2010.

[6] EOH, J. H., NO, H. C., YOO, Y. H., JEONG, J. Y., KIM, J. M, and KIM S. O., "Wastage and Self-Plugging by a Potential CO_2 Ingress in a Supercritical CO_2 Power Conversion System of an SFR," J. Nuclear Science and Technology, Vol. 47, No. 11, pp. 1023-1036, 2010.

[7] U.S. Department of Energy SunShort Initiative website: 10-Megawatt Supercritical Carbon Dioxide Turbine project, http://www1.eere.energy.gov/solar/sunshot/csp_sunshotrnd_nrel_turbine.html.

[8] MOISSEYTSEV, A. and SIENICKI, J. J., "Development of a Plant Dynamics Computer Code for Analysis of a Supercritical Carbon Dioxide Brayton Cycle Energy Converter Coupled to a Natural Circulation Lead-Cooled Fast Reactor," ANL-06/27, Argonne National Laboratory, July 2006.

[9] SPAN, R. and WAGNER, W., "A New Equation of State for Carbon Dioxide Covering the Fluid Region from the Triple-Point Temperature to 1100K at Pressures up to 800 MPa," J. Phys. Chem. Ref. Data, 25 (6), pp. 1509-1596, (1996).

[10] LOMPERSKI, S., CHO, D., SONG, H., and TOKUHIRO, A., "Testing of a Compact Heat Exchanger for Use as the Cooler in a Supercritical CO_2 Brayton Cycle," Paper 6075, Proceedings of 2006 International Congress on Advances in Nuclear Power Plants (ICAPP 06), Reno, NV, June 4-8, 2006.

[11] MOISSEYTSEV, A., SIENICKI, J. J., CHO, D. H., and THOMAS, M. R., "Comparison of Heat Exchanger Modeling with Data from CO_2-to-CO_2 Printed Circuit Heat Exchanger Performance Tests," Paper 10123, 2010 International Congress on Advances in Nuclear Power Plants (ICAPP 10), San Diego, CA, June 13-17, 2010.

[12] AUNGIER, R.H., Turbine Aerodynamics: Axial-Flow and Radial Inflow Turbine Design and Analysis, ASME Press, New York, 2006.

[13] AUNGIER, R.H., Centrifugal Compressors: a Strategy for Aerodynamic Design and Analysis, ASME Press, New York, 2000.

[14] KIM, T. K., YANG, W. S., GRANDY, C., and HILL, R. N., "Core Design Studies for a 1000 MWth Advanced Burner Reactor," Annals of Nuclear Energy, Vol. 36, pp. 331–336 (2009).

[15] MOISSEYTSEV, A. and SIENICKI, J. J., "Cost-Based Optimization of Supercritical Carbon Dioxide Brayton Cycle Equipment," Transactions of the American Nuclear Society, American Nuclear Society 2011 Winter Meeting, Washington, DC, October 30-November 3, 2011.

[16] MOISSEYTSEV, A. and SIENICKI, J. J., "Investigation of Alternative Layouts for the Supercritical Carbon Dioxide Brayton Cycle for a Sodium-Cooled Fast Reactor," Nuclear Engineering and Design, Vol. 239, pp. 1362-1371, (2009).

[17] MOISSEYTSEV, A. and SIENICKI, J. J., "Control of Supercritical CO_2 Brayton Cycle for LFR Autonomous Load Following," Transactions of the American Nuclear Society, Vol. 93, p. 342, American Nuclear Society 2005 Winter Meeting, Washington, DC, November 13-17, 2005.

[18] MOISSEYTSEV, A. and SIENICKI, J. J., "Automatic Control Strategy Development for the Supercritical CO_2 Brayton Cycle for LFR Autonomous Load Following", paper 6074, Proceedings of 2006 International Congress on Advances in Nuclear Power Plants, ICAPP'06, Reno, NV, June 4-8, 2006.

[19] MOISSEYTSEV, A. and SIENICKI, J. J., "Controllability of the Supercritical Carbon Dioxide Brayton Cycle Near the Critical Point," 2008 International Congress on Advances in Nuclear Power Plants (ICAPP 2008), Anaheim, CA, June 8-13, 2008, paper 8203.

[20] MOISSEYTSEV, A. and SIENICKI, J. J., "Investigation of Plant Control Strategies for a Supercritical CO_2 Brayton Cycle Coupled to a Sodium-Cooled Fast Reactor using the ANL Plant Dynamics Code," 2011 Supercritical CO_2 Power Cycle Symposium, Boulder, CO, May 24-25, 2011.

[21] MOISSEYTSEV, A. and SIENICKI, J. J., "Dynamic Analysis of S-CO_2 Cycle Control with Coupled PDC-SAS4A/SASSYS-1 Codes", Proceedings of 20th International Conference on Nuclear Engineering, ICONE-20, Anaheim, CA, July 30 – August 3, 2012.

[22] CAHALAN, J. E., TENTNER, A. M., and MORRIS, E. E., "Advanced LMR Safety Analysis Capabilities in the SASSYS-1 and SAS4A Computer Codes," Proc. of the International Topical Meeting on Advanced Reactor Safety, 1994, Vol. 2, p. 1038, American Nuclear Society, Pittsburgh, April 17-21 (1994).

[23] VILIM, R. B., and MOISSEYTSEV, A., "Comparative Analysis of Supercritical CO_2 Power Conversion System Control Schemes," Paper 8372, 2008 International Congress on Advances in Nuclear Power Plants (ICAPP 2008), Anaheim, CA, June 8-13, 2008.

[24] MOISSEYTSEV, A. and SIENICKI, J. J., "Validation of the ANL Plant Dynamics Code Compressor Model with SNL/BNI Compressor Test Data," 2011 Supercritical CO_2 Power Cycle Symposium, Boulder, CO, May 24-25, 2011.

[25] MOISSEYTSEV, A. and SIENICKI, J. J., "Modeling of the SNL S-CO_2 Loop with ANL Plant Dynamics Code", Proceedings of 20th International Conference on Nuclear Engineering, ICONE-20, Anaheim, CA, July 30 – August 3, 2012.

[26] MOISSEYTSEV, A. and SIENICKI, J. J., "Validation of the ANL Plant Dynamics Code with the SNL S-CO_2 Loop Transient Data", to be published in: Proceedings of ASME Turbo Expo 2013, GT2013, San Antonio, Texas, USA, June 3-7, 2013.

[27] MOISSEYTSEV, A. and SIENICKI, J. J., "Transient Accident Analysis of a Supercritical Carbon Dioxide Brayton Cycle Energy Converter Coupled to an Autonomous Lead-Cooled Fast Reactor," Nuclear Engineering and Design 238 (2008), pp. 2094-2105.

[28] MOISSEYTSEV, A. and SIENICKI, J. J., "Dynamic Simulation and Control of the S-CO_2 Cycle: From Full Power to Decay Heat Removal", Proceedings of 2012 Conference on Advances in Thermal Hydraulics, ATH-12, San Diego, CA, November 11-15, 2012.

MODELING SODIUM OXIDE DEPOSIT GROWTH AND SODIUM PLUGGING

J.J. SIENICKI

Nuclear Engineering Division
Argonne National Laboratory (ANL)
Argonne, Illinois, United States of America

Abstract.

A new sodium plugging model, based on first principles, has been developed and is described in this work. It integrates experiment data on the rate of formation of sodium oxide deposits, obtained from the upgraded Sodium Plugging Phenomena Loop at Argonne National Laboratory, with previous literature data referred to both small and large channels. In the Plugging Phenomena Loop, deposits are caused by the cooling-induced precipitation, upon the stainless steel walls, of sodium oxide from dissolved oxygen impurities. The novel feature of the model consists of modeling the sodium oxide deposits as highly porous, with most of the deposit volume occupied by sodium interstitial to sodium oxide, as revealed during previous investigations. The new first principles plugging model is shown to provide a fundamental understandng of the results of the first sodium plugging test conducted in the upgraded Sodium Plugging Phenomena Loop.

1. BACKGROUND

Sodium coolant in a Sodium-Cooled Fast Reactor (SFR) or test loop contains dissolved oxygen as well as other impurities. When sodium flows through a channel from which heat is removed and the sodium is cooled to temperatures below the solubility limit of oxygen in sodium (i.e., the equilibrium concentration), oxygen can precipitate out as sodium oxide (Na_2O) crystals upon surrounding colder structures as shown in Fig. 1 illustrating the solubility behavor. Typically, the sodium temperature first decreases below the temperature at which the equilibrium concentration equals the concentration of oxygen in the bulk fluid (i.e., the sodium becomes supersaturated with oxygen) before inception of nucleation of Na_2O crystals begins. The process of formation of sodium oxide deposits upon a channel wall is illustrated in Fig. 2 in which it is assumed that sodium initially containing a dissolved oxygen concentration below the solubility limit flows through a cooled channel. For sodium and alkali metals in general, it is thought that the dissolved oxygen exists in the form of O^{--} ions based upon measurements with liquid cesium [1]-[5]. Associations in the liquid involving sodium atoms and oxygen ions of the form, Na_nO^{--}, may form [4]. It is these associations that are assumed to be transferred between the bulk fluid and the surrounding structures forming deposits upon the structures. If the downstream portion of the channel and sodium is heated (Fig. 2), then the local oxygen equiliubrium concentration increases and may exceed the oxygen concentration in the bulk sodium. Deposits do not grow beyond this location. The precipitation of dissolved oxygen from sodium is utilized to purify sodium with cold trapping by deliberately passing a portion of the sodium flow through a cold trap and precipitating sodium oxide (as well as very small masses of sodium hydride and radioactive sodium tritide) on stainless steel mesh inside of the cold trap. Deposit formation and growth can be modeled with rate formulae describing the kinetics of sodium oxide crystal nucleation and growth together limitations imposed by the rate at which oxygen can be transferred from the bulk flowing fluid to the channel wall. In the present analysis, only the latter mass transfer rate limitations are modeled for initial simplification of the overall problem. Extensive research on the formation and

nature of deposits has been carried out since the early days of pioneering work on SFRs in the 1950s through at least the 1980s**.** Notable investigations relevant to the present work are documented in Refs. [6]-[10]. For several years now, there has been a renewed interest in sodium oxide depost growth and sodium plugging at Argonne National Laboratory (ANL). This interest has been driven by the development of supercritical carbon dioxide (S-CO_2) Brayton cycle power conversion at ANL for use with SFRs to improve SFR economics ($/kWe) and performance. Supercritical CO_2 cycles require compact heat exchangers for sodium-to-CO_2, CO_2-to-CO_2, and CO_2-to-water heat exchange. The use of compact diffusion-bonded heat exchangers such as those manufactured by Heatric Division of Meggitt (UK) [11] has been envisioned. There is an incentive to have small-size sodium channels to achieve compactness.

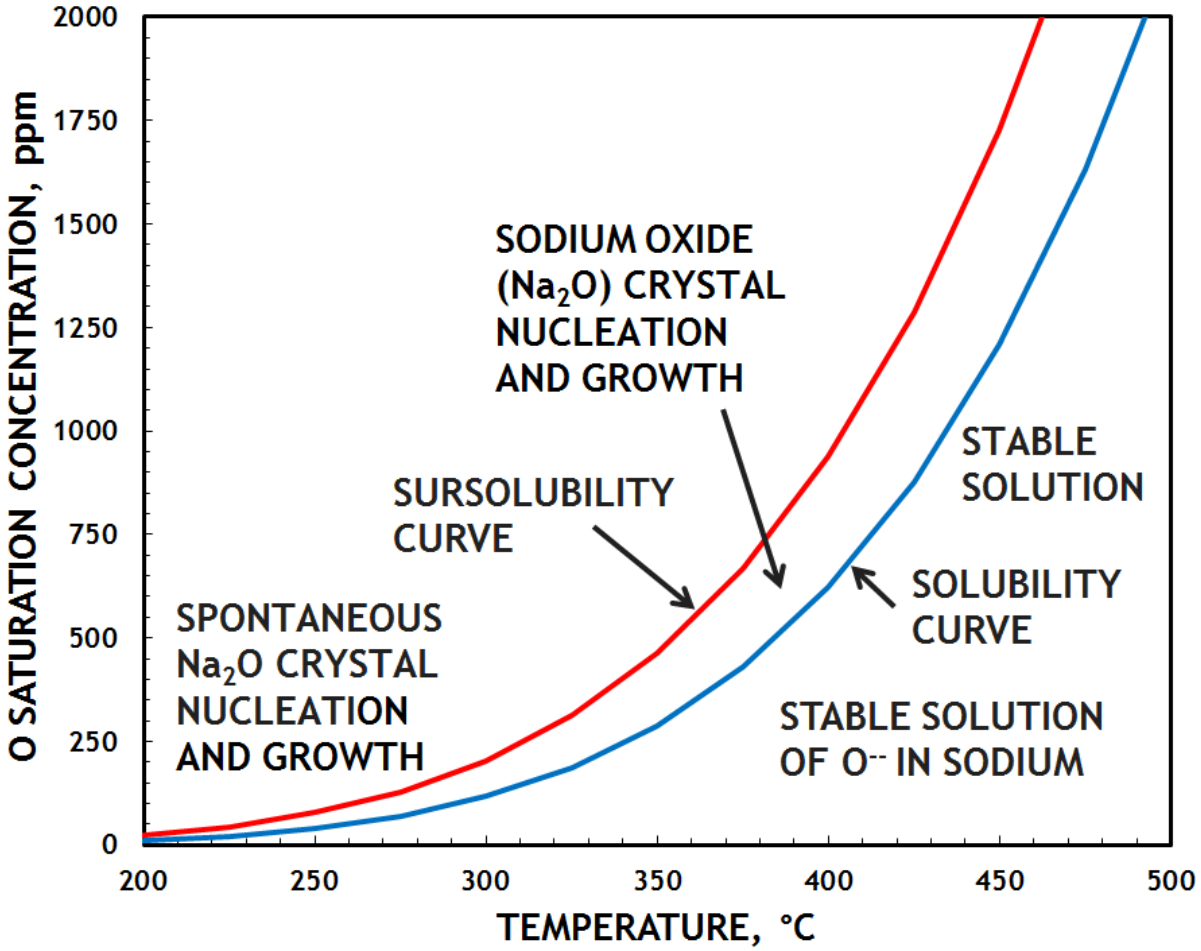

FIG. 1Assumed solubility behavior.

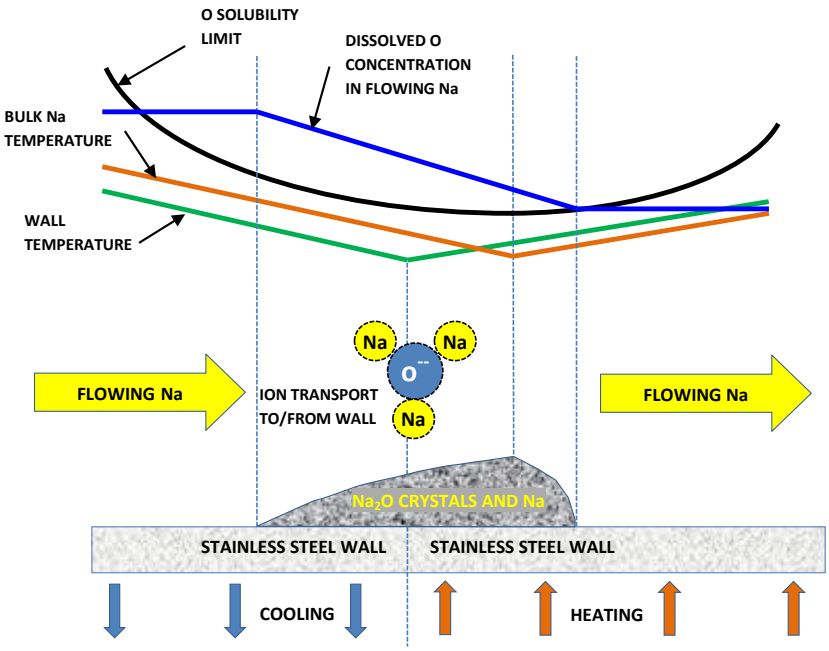

FIG. 2. Illustration of sodium oxide deposit formation phenomena.

For small-size sodium channels, there is concern about sodium plugging due to cooling-induced precipitation upon the stainless steel channel walls of sodium oxide from dissolved oxygen impurities in the flowing sodium in postulated accidents. An example of such a postulated accident is rupture of the boundary of the intermediate sodium heat transport loop resulting in ingression of air into the intermediate loop together with failure of the cold trapping circuit to remove oxygen impurities from sodium (e.g., if the cold trap circuit is out of service).

2. SODIUM PLUGGING PHENOMENA LOOP AT ANL

The Sodium Plugging Phenomena Loop at ANL has recently been upgraded to obtain fundamental data on plugging due to precipitation of oxygen impurities in sodium flowing through prototypical sodium-to-CO_2 heat exchanger channels under well-controlled experiment conditions. In particular, an objective of upgrading has been the capability to hold the temperature at the location of plug formation unvarying during the plug formation process. Fundamental data on sodium plugging is required to enable reliable design of sodium-to-CO_2 heat exchangers. In particular, it is necessary to determine how large sodium channels need to be to preclude plugging over a long enough timescale through an understanding of plugging phenomena in small sodium channels and first principles modeling of fundamental sodium plugging phenomena.

The Sodium Plugging Phenomena Loop currently utilizes a 0.78 m long stainless steel test section with three 6 mm semicircular diameter straight sodium channels side-by-side that simulate sodium channels inside of a Printed Circuit Heat Exchanger™ (PCHE™, Heatric Division of Meggitt (UK)) sodium-to-CO_2 heat exchanger. In Fig. 3, the sodium enters the test section from a single tube on the right and exits into a single tube on the left; the test section is actually installed with a slight slope to facilitate drainage of sodium. As the sodium flows from right to left, the test section and sodium are cooled by forced convection heat transfer to cooling air also flowing from right to left inside of a steel air duct. The test section length is divided into five equal-length heating zones. Ceramic band (radiant) heaters are installed in the first three zones. The ceramic band heaters can be used to shape the sodium temperture profile along the first three zones as the sodium is cooled. Platen contact heaters are installed over the last two heater zones to heat the test section and sodium to assure that the minimum in the sodium temperature and the deposit plug form inside of the test section inside of the semicircular sodium channels instead of inside of the tubing downstream of the test section. Fig. 4 shows the test section, ceramic band heaters, and platen contact heaters when the upper half of the

cooling air duct is removed. The Plugging Phenomena Loop thus provides cooling and heating of flowing sodium containing a significant concentration of dissolved oxygen as it passes through the test section as illustrated in Fig. 2.

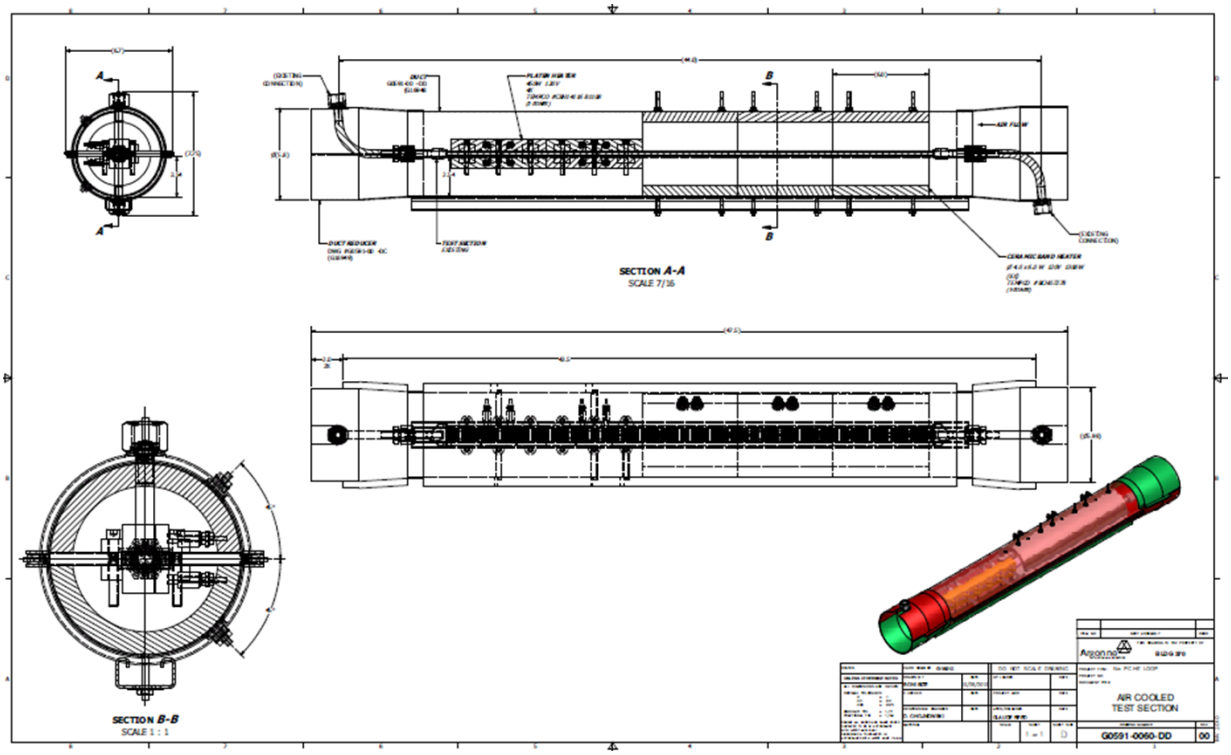

FIG. 3. Stainless steel sodium plugging test section inside of steel cooling air duct.

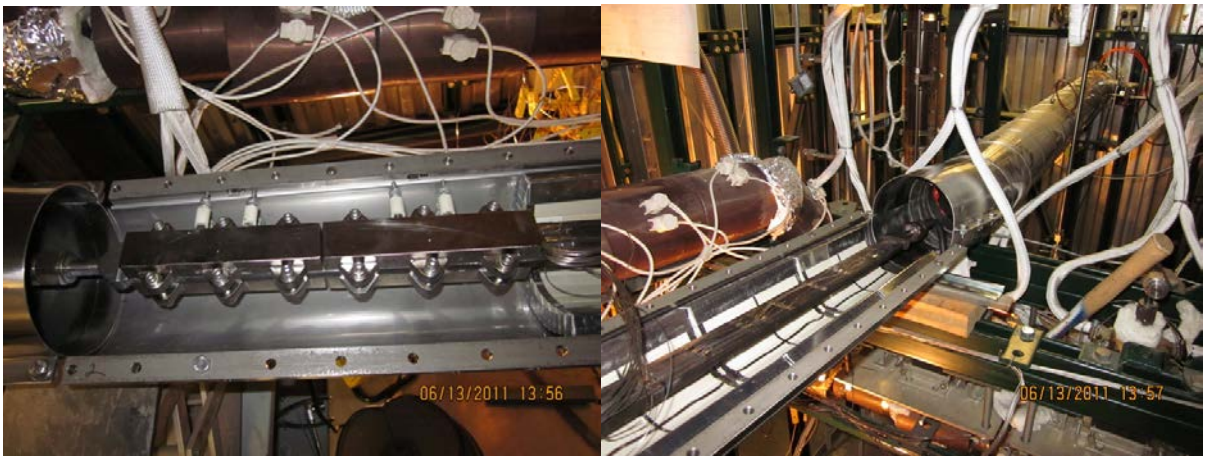

FIG. 4. Stainless steel test section and lower half of steel cooling air duct in first three heater zones with ceramic band heaters (right) and last two heater zones with platen contact heaters (left). Sodium and cooling air flow from right to left.

3. DEPOSIT FORMATION MASS TRANSFER RATE MODEL

A new first principles sodium plugging model has been developed for the analysis of sodium plugging. The novel feature of new model consists of modeling sodium oxide (Na_2O) deposits as highly porous, with most of deposit volume occupied by sodium interstitial to sodium oxide, as revealed during previous investigations. The rate of deposit growth upon the wall is assumed to be given by a product in which the first term is the difference between the bulk and equilibrium (saturation) dissolved oxygen weight concentrations and the second term is a mass transfer coefficient given in terms of a

Sherwood number dependent upon a Reynolds number and a Schmidt number (ratio of the diffusivity for momentum to the diffusivity of oxygen in sodium) [12],

$$\frac{d\delta}{dt} = \frac{(C - C_e)h_M}{\rho_{O,eff}} ,$$

where δ = deposit layer thickness, t = time, C = concentration in weight fraction of oxygen in sodium fluid, $\rho_{O,eff}$ = effective density of oxygen in the deposit,

$h_M = \frac{\rho D Sh}{d_h}$ = mass transfer coefficient,

where ρ = density of sodium with dissolved oxygen, D = diffusivity for transport of oxygen dissolved in sodium, Sh = Sherwood number, and d_h = sodium channel hydraulic diameter. In forced convection flow, the Sherwood number is a function of the Reynolds number and the Schmidt number, Sh = f (Re, Sc), where

$$Re = \frac{\rho u d_h}{\mu} , \; Sc = \frac{\mu}{\rho D} ,$$

where u = sodium velocity and μ = sodium viscosity. The Sherwood and Schmidt numbers for mass transfer are analogous to the Nusselt number, Nu, and Prandtl number, Pr, for heat transfer (ratio of the diffusivity for momentum to the thermal diffusivity), respectively, Nu = f (Re, Pr), where f is the same function,

$$h_H = \frac{k Nu}{d_h} , \; Pr = \frac{c_P \mu}{k} ,$$

where h_H = heat transfer coefficient, c_P = sodium specific heat, and k = sodium thermal conductivity.

The effective density of oxygen in the deposit accounts for the fact that the deposit consists of sodium oxide of which the transported oxygen is a fraction of the mass and that the deposit may contain porosity,

$$\rho_{O,eff} = VF_{Na_2O} \rho_{Na_2O} \frac{M_O}{M_{Na_2O}} ,$$

where VF_{Na2O} = volume fraction of Na_2O in the deposit consisting of Na_2O and sodium, ρ_{Na2O} = sodium oxide theoretical density, M_O = atomic weight of oxygen, and M_{Na2O} = molecular weight of Na_2O.

Siegel and Epstein [13] measured the diffusivity of oxygen in sodium at temperatures of 482 and 538 °C (900 and 1000 F). However, in reviewing their work, the present author found their determinations of the amounts of oxygen diffused into sodium through a porous diffusion barrier to be subject to significant uncertainties and therefore unreliable for the present application. When reliable data for the diffusivity of a species in a fluid is lacking, the diffusivity for self-diffusion of atoms or molecules in the fluid is typically used as an approximation. The diffusivity for self-diffusion in sodium was measured by Meyer and Nachtrieb [14] between 98.0 and 226.5 °C and followed by measurements by other researchers. In 1990, Qian, Weinert, Fernando, and Davenport [15] reported the results of molecular dynamics simulations of liquid sodium carried out to determine the activation energy for self-diffusion in liquid sodium. They derived a formula for the diffusivity based upon a fit to their results that were calculated over a temperature range from approximately the melting temperature to

1127 °C. Their correlation agrees well with the experiment data that they identified which encompassed the range, 98 to approximately 300 °C. The correlation is

$$D\ (m^2/s) = 8.4 \times 10^{-8} \exp\left(-\frac{E_a}{RT}\right)$$

where E_a = activation energy for self-diffusion in sodium = 9552 J/mole, R = 8.3145 J/(mole·K), and T = temperature in K.

At 150 °C, Pr = 0.0087 but Sc = 107 such that while sodium is a liquid metal for heat transfer, for oxygen mass transfer, sodium behaves as a highly viscous ordinary fluid does for heat transfer. In selecting a heat transfer correlation, Nu=f(Re,Pr), from which to derive a Sherwood number, Sh=f(Re,Sc), to use for calculating mass transfer, one must assure that the heat transfer correlation is valid in the appropriate Prandtl number range encompassing the Schmidt number.

4. REVIEW OF DATA ON SODIUM OXIDE DEPOSIT MORPHOLOGY

A set of experiments was carried out by Billuris [6] to experimentally determine the growth and features of plugs formed by impurities in sodium and their removal by cold trapping. Deposits were created by inserting a cylindrical "cold finger" having an outer diameter of approximately 2.5 cm cooled internally with flowing cooling oil to a depth of 6.4 cm beneath the surface of a sodium pool and subsequently removing the cold finger. The deposits formed on the outer surface of the cold finger. Seventeen test runs were conducted. For each test, Billuris provided among other data the weights of sodium and sodium oxide determined by chemical analysis. The present author has extended the analysis of Billuris's data to also estimate the volume fractions. In calculating the volume fractions, the density of sodium oxide is assumed to equal 2270 kg/m^3. This is the only value that could be found for the sodium oxide density and goes back to measurements by Rengade [16]. The sodium density is assumed to be the value at the cooling oil temperature in each experiment using the temperature dependent density recommended by Fink and Leibowitz [17]. Table 1 shows the calculated volume fractions for Tests Nos. 9, 10, 11, and 13 which are the most reliable. A stirrer was used on Test No. 9 but not later tests and one might speculate that this is the reason for the higher sodium oxide volume fraction obtained. The sodium oxide volume fractions for the other three tests are remarkably similar.

The deposits from the part of the cold finger submerged in the sodium were described as a silvery deposit with patches of liquid adhering to irregular, crystal-like structures. Billuris also reported on the results of experiments on purification of sodium by cold trapping [6]. For Cold Trap Test No. 4, the report presents photographs of the plug and a close up of a piece of the brittle deposit that was broken off. The deposit was described as having sharp, needle-like crystals.

Table 1. CALCULATED DEPOSIT VOLUME FRACTIONS FOR TESTS NOS. 9, 10, 12, AND 13 CONDUCTED BY BILLURIS

Test No.	Test Duration, hours	Sodium/Cooling Oil Temperature, °C	Deposit Sodium Oxide/Sodium Weight, g	Deposit Sodium Oxide/Sodium Volume Fraction
9	161	338/116	6.52/10.3	0.204/0.796
10	159	332/132	3.58/9.10	0.137/0.863
12	144	321/98.9	4.37/13.1	0.120/0.880
13	170	324/98.9	4.12/12.5	0.118/0.882

In the course of investigating the effects of oxide layer deposits upon heat removal from flowing sodium, Subbotin, Kozlov, and Ivanovskii [8] noted that the oxide layer formed near the wall is porous consisting of a mixture of sodium oxide and sodium. Porosity filled with sodium can be observed on a radiograph of a thin circular slice through the channel which also revealed that the concentration of

oxides in the deposit rises as the wall is approached. Kozlov and Antonov [9] measured the thermal conductivity of deposits created with experiments similar to those of Ref. [8] in which a 6.6 cm inner diameter tube was plugged. They presented a plot for the deposit thermal conductivity versus the weight fraction of oxide in the deposit. The weight fractions varied from as low as 0.0013 to as high as 0.59. The corresponding sodium oxide volume fractions are presently calculated to vary from 0.00053 to 0.37. Kozlov and Likharev [10] conducted experiments in which the deposit layer mean sodium oxide volume fraction as well as the mean mass transfer coefficient for mass transfer to the wall were determined. Three experiments were carried out with oxygen dissolved in the sodium. Kozlov and Likharev did not determine sodium oxide volume fractions by removing and chemically analyzing the deposits, stating that studies involving cutting and analysis of accumulated impurity are laborious. Instead, they determined local layer thicknesses and oxide volume fractions through analysis from measured temperatures and the thermal conductivity results for deposits of Kozlov and Antonov [9]. The sodium oxide volume fractions in the three experiments were determined to be 0.061, 0.076, and 0.094, respectively. It is interesting that in tests with hydrogen impurities, the sodium hydride, NaH, deposits are also calculated to be porous with sodium hydride volume fractions ranging from 0.045 to 0.351 [10].

Recently reported experiments by Nishimura, Kamide, Otake, and Sugiyama [18] on the combustion of individual sodium droplets in nitrogen-oxygen mixtures show the formation of sodium oxide dendrites. In some instances, dendrite growth was driven by precipitation of dissolved oxygen from the interior of the sodium droplet when the oxygen supply supporting combustion was stopped and the temperature of the droplet decreased. Dendrite formation is expected to result in a highly porous sodium oxide structure.

5. MODEL COMPARISON WITH THE FIRST SODIUM PLUGGING TEST IN THE UPGRADED SODIUM PLUGGING PHENOMENA LOOP

In the first sodium plugging test following upgrading [19], the air blower speed was manually controlled using a variable frequency drive to maintain the coldest test section temperature at 150 °C. The experiment was run for about 7,400 seconds during which a decrease in the sodium flowrate due to growth of a plug deposit was observed. The experiment was concluded by turning off the air blower. Figure 5 presents data from the test. The output voltage of the electromagnetic (EM) flowmeter is plotted; voltages have not been converted to volume flowrates.

The test is divided into three phases. The first phase is the interval prior to the identified “Onset of plugging” from 95 to 160 seconds. During this first phase, the sodium flowrate decreases with time as the test section temperature near the plug location decreases from the initial value to essentially the subsequently unvarying value which is held constant. This behavior is due to the increase in the sodium viscosity with decreasing sodium temperature in laminar flow. The initial Reynolds number for flow through each of the semicircular sodium channels is calculated to equal 825. The observed decrease cannot be accounted for by changes in the sodium viscosity and density, if the flow is assumed turbulent. The mechanism responsible for the continuing decrease in the flowrate during the second phase from 160 to 350 s, when the test section temperature has decreased to essentially the target unvarying temperature, is also the increase in the frictional pressure drop around the loop from the increase in viscosity with decreasing temperature. This is evident from the temperature at the outlet tube downstream of the test section that is still decreasing to about 195 °C until about 350 s. As deposits form upon the inner walls of the stainless steel test section, the sodium flowrate decreases due to the effects of the smaller remaining flow area as well as an increased pressure drop. This is the third phase which lasts until 7,400 s. The inferred onset of plug growth occurs when the test section temperature decreases to ~ 160 °C. Significant unplugging occurs when the test section is heated back up to 220 °C.

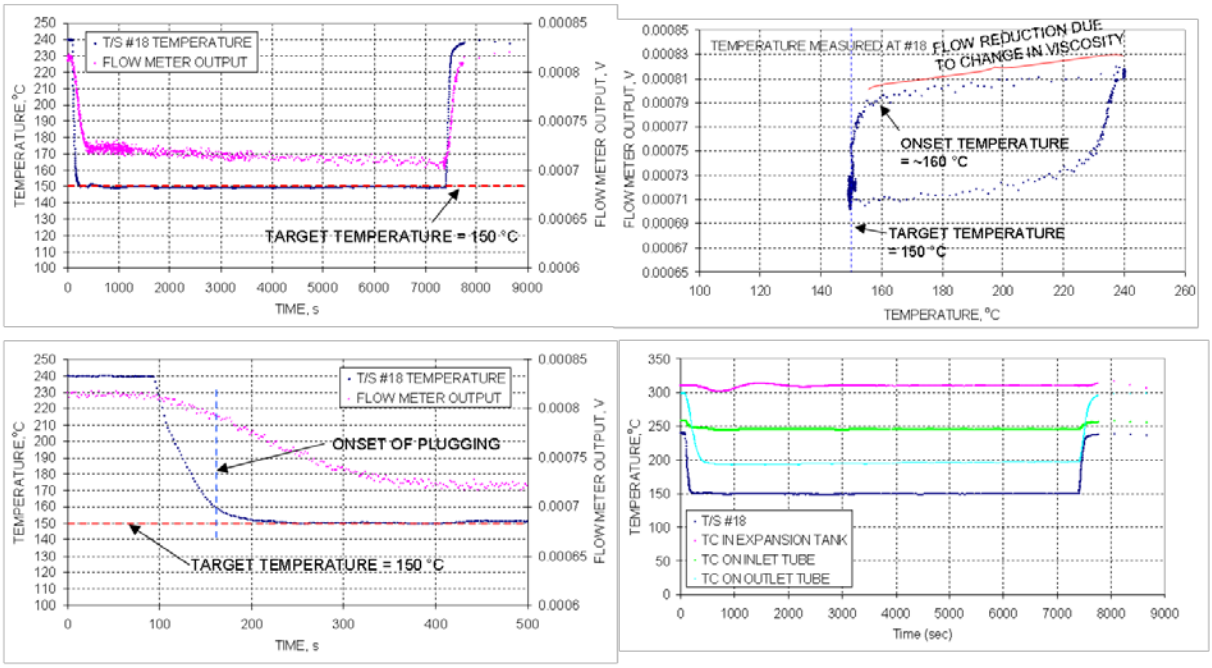

FIG. 5. Data from initial plugging test in the upgraded Sodium Plugging Phenomena Loop.

From the observed reduction in flowrate over the 7,240 second (= 7,400-160 s) deposit growth phase, the deposit thickness necessary to reduce the flowrate from the reduction in channel flow area and enhancement in laminar flow frictional pressure drop due to the reduction in hydraulic diameter is determined. The volumetric flowrate in laminar flow varies as

$$uA = \frac{\Delta P d_h^{\,2} A}{2(15.767) L \mu} \quad \text{where} \quad d_h = \frac{4A}{p}$$

where ΔP = pressure drop across the deposit, A = flow area of one sodium channel partially occluded by the deposit, p = wetted perimeter of the deposit, and L = deposit length.

The deposit is assumed to have a uniform thickness around the perimeter of the semicircular channel. As the deposit layer thickness, δ, grows with time, the radius of the circular portion decreases from the initial value, R, to R-δ while the position of the horizontal portion moves downward by δ. The resulting channel shape has a circular lower boundary that is less than a semicircle and a horizontal upper boundary. The circular arc angle of the lower boundary progressively becomes smaller and smaller until complete plugging occurs when R-δ = δ or δ = R/2. For a semicircular channel, the flow area is $A = \pi R^2/2$, the perimeter is $p = R(\pi+2)$, and the hydraulic diameter is $d_h = 4A/p = 2R/(1+2/\pi) = d/(1+2/\pi)$ where d is the semicircular diameter. Thus, for a 6 mm semicircular diameter channel, the hydraulic diameter is 6.0 mm/1.6366 = 3.666 mm. For a uniform deposit thickness, δ, the remaining flow area and remaining perimeter are

$$A = (R-\delta)^2 \left[\frac{\pi}{2} - \arcsin\left(\frac{\delta}{R-\delta}\right) - \left(\frac{\delta}{R-\delta}\right)\sqrt{1-\left(\frac{\delta}{R-\delta}\right)^2} \right]$$

$$p = 2(R-\delta)\left[\frac{\pi}{2} - \arcsin\left(\frac{\delta}{R-\delta}\right) + \sqrt{1-\left(\frac{\delta}{R-\delta}\right)^2} \right].$$

The Nusselt number for fully developed laminar heat transfer in a semicircular channel with a constant wall temperature is given by [20] Nu = 3.323. Because of the high Schmidt number, there is a long entrance length for "thermally developing flow" in the sodium channels resulting in a Sherwood

number significantly greater than the fully developed value. Nusselt numbers for a semicircular channel with hydrodynamically fully developed flow versus a Graetz number were calculated by Manglik and Bergles [21]. However, their results are presented graphically and it is difficult to extract them for use in calculations with changing Graetz number. To calculate the enhancement in the Sherwood number from the developing flow effects, the results of Lee and Garimella [22] who presented simple correlations for the laminar Nusselt number with thermally developing laminar flow in rectangular channels are used. The specific results for a rectangular channel having an aspect ratio of two-to-one are utilized since this is analogous to the case of a semicircle which has a width in one dimension equal to twice the height in the other dimension. Their correlation for the local Nusselt number is given by

$$Nu_z = \frac{1}{C_1 (z^*)^{C2} + C_3} + C_4$$

where $C_1 = -3.122 \times 10^{-3}\, e^3 + 2.435 \times 10^{-2}\, e^2 + 2.143 \times 10^{-1}\, e + 7.325$, $C_2 = 6.412 \times 10^{-1}$, $C_3 = 1.589 \times 10^{-4}\, e^2 - 2.603 \times 10^{-3}\, e + 2.444 \times 10^{-2}$, $C_4 = 7.148 - 1.328 \times 10^{1}/e + 1.515 \times 10^{1}/e^2 - 5.936/e^3$,

where e = rectangular channel height-to-width ratio = aspect ratio, $1 \le e \le 10$,

$z^* = \frac{z}{RePrd_h}$, where z = distance into channel from entrance.

The Nusselt number for fully developed flow is

$$Nu_\infty = 8.235 \left(1 - \frac{2.0421}{e} + \frac{3.0853}{e^2} - \frac{2.4765}{e^3} + \frac{1.0578}{e^4} - \frac{0.1861}{e^5}\right).$$

The local enhancement factor is obtained by taking the ratio of Nu_z and Nu_∞.

The oxygen concentration in the bulk sodium is assumed to equal the saturation value at the unplugging temperature of 220 °C or 18.7 ppm [23]. This value is assumed following the advice of Christian Latgé of CEA Cadarache who determined that the saturation concentration is given by the unplugging temperature to within ± 5 °C [24] based upon experience with SUPERPHÉNIX as well as experiments. The saturation temperature at the onset of plugging is thus approximated by the saturation temperature at the end of the test. The saturation concentration at the test section temperature at the plug location of 150 °C is 2.13 ppm. The diffusivity for self-diffusion of sodium atoms in sodium is 5.56×10^{-9} m^2/s and the Schmidt number is 107.

The ratio of the measured final and initial sodium flowrates over the duration of plug formation is 0.977 (= 0.70835 mV divided by 0.7250 mV). This is matched for a deposit thickness of only 9.85×10^{-6} m or 0.00985 mm. The flowrate reduction factor from before the start of the experiment to the onset of plug formation is 0.891 (0.7250 mV divided by 0.8133 mV). The sodium velocity at the onset of plugging is the initial velocity of 0.15 m/s multiplied by this factor providing a velocity of 0.134 m/s. The Reynolds number when the channel is occluded by half of the final deposit thickness is 823 indicative of laminar flow. The product of the Reynolds number, Schmidt number, and hydraulic diameter equals 321 m such that the non-dimensional length, z*, at the assumed plug location 0.468 m into the channel equals 0.00146. For this value, there is a strong entrance effect such that the ratio of the local Sherwood number at the plug location and the Sherwood number for fully developed flow is calculated to equal 2.61. Multiplying the Sherwood number of 3.323 for fully developed laminar flow by 2.61 provides a local Sherwood number of 8.67. The oxygen mass transfer coefficient is calculated to equal 1.32×10^{-5} m/s equivalent to 1.21×10^{-2} $kg/(m^2 \cdot s)$. Multiplying by the driving concentration difference, the oxygen mass transfer rate per unit surface area is 1.99×10^{-7} $kg/(m^2 \cdot s)$.

The deposit is assumed to have a sodium oxide volume fraction of 0.18 based upon the sodium oxide weight fractions determined from Billuris Cold Trap Test No. 4 which revealed a typical sodium oxide

weight fraction of 0.35 close to the wall. The resulting deposit thickness growth rate is 1.89×10^{-9} m/s from which the time to grow to the assumed final deposit thickness of 9.85×10^{-6} m is 5,210 s. This is in good agreement with the 7,240 s duration of deposit growth in the test before it was terminated. If the deposit were assumed to be fully dense, then the calculated deposit growth time would be more than a factor of five times 5,210 s. If the developing nature of the laminar mass transfer in the channel were not accounted for, the calculated deposit growth time would be even greater by almost a factor of three (i.e., an overall factor of about fifteen).

6. CLOSURE AND FUTURE PLANS

The new first principles sodium plugging model shows that the observed reduction in the measured flowrate during the initial sodium plugging test in the upgraded Sodium Plugging Phenomena Loop is consistent with developing laminar flow mass transfer resulting in the growth of a porous deposit that partially occludes the channel flow area and reduces the local velocity due to the reduction in the hydraulic diameter for flow. The new first principles sodium plugging model also agrees well with earlier sodium plugging data including the sodium plugging meter data of McPheeters and Biery [7] involving turbulent flow through four 1.32 mm orifices, the sodium deposit formation data of Kozlov and Likharev [10] for turbulent flow through 0.7 m long 5 cm channels, and Cold Trap Test No. 4 of Billuris [6] with natural circulation flow driven by thermal gradients inside a vertical 15.5 cm inner diameter pipe. The details of the comparisons are discussed in Ref. [25].

Following installation of a new sodium cold trap and innovative sodium plugging meter and calibration of the sodium flowmeters, it is planned to repeat the assumed conditions of the initial plugging test with regard to sodium temperatures, dissolved oxygen concentration, and the same initial sodium velocity. However, it is planned to run the test until nearly complete plugging occurs. Assuming an unvarying deposit growth rate based upon the inferred deposit thickness after 7,240 seconds of growth, complete plugging could require continuous operation of the Sodium Plugging Loop for thirteen days.

ACKNOWLEDGEMENTS

Argonne National Laboratory's work was supported by the U. S. Department of Energy Advanced Reactor Concepts (ARC) Program under Prime Contract No. DE-AC02-06CH11357 between the U.S. Department of Energy and UChicago Argonne, LLC. The work presented here was carried out under the Energy Conversion Technology area of the ARC Program. The author is grateful to Gary Rochau (SNL), the Technical Area Lead, Bob Hill (ANL/NE), the National Technical Director, and Brian Robinson (U.S. DOE), the Headquarters Program Manager for the ARC and Advanced Small Modular Reactor Programs. The author is grateful to Dave Chojnowski and Yoichi Momozaki (ANL/NE) for conducting the initial plugging test in the upgraded Sodium Plugging Loop and processing the data.

REFERENCES

[1] KENDALL, P.W., The Form of Oxygen in the Liquid Alkali Metals, Journal of Nuclear Materials 35 (1970) 41-50.
[2] HOST, I.P., SEYMOUR, E.F.W., STYLES, G.A., Nuclear Magnetic Resonance of ^{133}Cs in the Liquid Cesium-Oxygen System, Journal of Nuclear Materials, 35 (1970) 55-59.
[3] GREENWOOD, D.A, RATTI, V.K., The Stability of Negative Ions in Liquid Metals, J. Phys.: Metal Phys., 2 (1972) 289-296.
[4] BYSTROV, P.I., KAGAN, D.N., KRECHETOVA, G.A., SHPRILRAIN, E.E., Liquid-Metal Coolants for Heat Pipes and Power Plants, KIRILLIN, V.A.(Ed.), Hemisphere Publishing Corporation, New York (1990) 66.
[5] TSUCHIYA, Y., SEYMOUR, E.F.W., STYLES, G.A., An NMR Study on Liquid Caesium-Oxygen System: The State of Oxygen and Ionic Association in the Metallic Regime, J. Phys.: Condens. Matter, 6 (1994) 3389-3898.
[6] BILLURIS, G., Experimental Investigations of the Removal of Sodium Oxide from Liquid

Sodium, GEAP-3328, General Electric Atomic Power Equipment Department, San Jose, California, January 18, 1960 (1960).

[7] MCPHEETERS, C.C., BIERY, J.C., The Dynamic Characteristics of a Plugging Indicator for Sodium, Nuclear Applications, 6 (1969) 573-581.

[8] SUBBOTIN, V.I., KOZLOV, F.A., IVANOVSKII, N.N., Heat Transfer to Sodium under Conditions of Free and Forced Convection and when Oxides are Deposited on the Transfer Surface, High Temperature, 1 (1963) 368-372.

[9] KOZLOV, F.A., ANTONOV, N., Relation Between Thermal Conductivity and Oxide Concentration in Sodium, Atomic Energy, 19 No. 4 (1965) 1333-1334.

[10] KOZLOV, F.A., LIKHAREV, V.A., Study of Mass Transfer of Impurities in Sodium, Atomic Energy, 65 No. 1 (1988) 614-617.

[11] SOUTHALL, D., DEWSON, S.J., "Innovative Compact Heat Exchangers," Proceedings of ICAPP '10, San Diego, CA, USA, June 13-17, 2010 (2010) Paper 10300.

[12] ECKERT, E.R.G., DRAKE, R.M., Heat and Mass Transfer, McGraw-Hill Book Company, Inc., New York (1959).

[13] SIEGEL, S., EPSTEIN, L.F., The Diffusion of Na_2O in Sodium, in the Range 900 - 1000°F, GEAP-3357, Vellecitos Atomic Laboratory, Atomic Power Equipment Department, General Electric Company, Pleasanton, California, December 31, 1959 (1959).

[14] MEYER, R.E., NACHTRIEB, N.H., Self-Diffusion in Liquid Sodium, The Journal of Chemical Physics, 23 (1955) 1851-1854.

[15] QIAN, G-X., WEINERT, M., FERNANDO, G.W., DAVENPORT, J.W., First-Principles Calculation of the Activation Energy for Diffusion in Liquid Sodium, Physical Review Letters, 64 (1990) 1146-1149.

[16] RENGADE, E., Ann. Chim. Phys., (8) 11 (1907) 427.

[17] FINK, J.K., LEIBOWITZ, L., Thermodynamic and Transport Properties of Sodium Liquid and Vapor, ANL/RE-95/2, Argonne National Laboratory, Reactor Engineering Division, January 1995 (1995).

[18] NISHIMURA, M., KAMIDE, H., OTAKE, S., SUGIYAMA, K-I, Features of Dendritic Oxide during Sodium Combustion, Journal of Nuclear Science and Technology, 48 No. 12 (2011) 1420-1427.

[19] MOMOZAKI, Y., CHOJNOWSKI, D.B., SIENICKI, J.J., CHO, D.H., Initial Investigation of Sodium Plugging under Unvarying Temperature Conditions Using the Sodium Plugging Loop, ANL-ARC-220, Argonne National Laboratory, September 30, 2011 (2011).

[20] ROSAGUTI, N.R., FLETCHER, D.F., HAYNES, B.S., Laminar Flow and Heat Transfer in a Periodic Serpentine Channel with Semi-Circular Cross-Section, International Journal of Heat and Mass Transfer, 49 (2006) 2912-2923.

[21] MANGLIK, R.M., BERGLES, A.E., Laminar Flow Heat Transfer in a Semi-Circular Tube with Uniform Wall Temperature, International Journal of Heat and Mass Transfer, 31 (1988) 625-636.

[22] LEE, P-S., GARIMELLA, S.V., Thermally Developing Flow and Heat Transfer in Rectangular Microchannels of Different Aspect Ratios, International Journal of Heat and Mass Transfer, 49 (2006) 3060-3067.

[23] SMITH, D.L., "Monitoring and Measurement of Oxygen Concentrations in Liquid Sodium," Proceedings of the International Conference on Liquid Metal Technology in Energy Production, Champion, Pennsylvania, May 3-6, 1976, CONF-760503-P2, Vol. 2 (1976) 631-637.

[24] LATGÉ, C., Personal Communication with SIENICKI, J.J., CEA Cadarache, February 24, 2012 (2012).

[25] SIENICKI, J.J., "Unified Analysis of Sodium Oxide Deposit Growth and Sodium Plugging," Advances in Thermal Hydraulics (ATH '12) 2012 ANS Winter Meeting, San Diego, CA, USA, November 11-15, 2012 (2012) Paper 6463.

Application of statistical method for FBR plant transient computation

Norihiro Kikuchi[a], **Hiroyasu Mochizuki**[b]

[a] Graduate School of Engineering, University of Fukui,
1-2-4, Kanawa-cho, Tsuruga, 914-0055, Japan

[b] Research Institute of Nuclear Engineering, University of Fukui,
1-2-4, Kanawa-cho, Tsuruga, 914-0055, Japan

Abstract. It is obvious that design tolerances, errors included in operation, and statistical errors in empirical correlations effect on the transient behavior. The purpose of the present study is to apply above mentioned statistical errors to a plant system computation in order to evaluate the statistical distribution contained in the transient evolution. A selected computation case is the turbine trip test conducted at 40% electric power of the prototype fast reactor "Monju". All of the heat transport systems of "Monju" are modeled with the NETFLOW++ system code which has been validated using the plant transient tests of the experimental fast reactor Joyo, and "Monju". The effects of parameters on upper plenum temperature are confirmed by sensitivity analyses, and dominant parameters are chosen. The statistical errors are applied to each computation deck by using a pseudorandom number and the Monte-Carlo method. The dSFMT (Double precision SIMD-oriented Fast Mersenne Twister) that is developed version of Mersenne Twister (MT), is adopted as the pseudorandom number generator. The SFMT and MT are generally used for a computation of the Monte-Carlo method. In the present study, uniform random numbers are generated by dSFMT, and these random numbers are transformed to the normal distribution by the Box-Muller method. Ten thousands of different computations are performed at once. In every computation case, the steady calculation is performed for 12,000 seconds, and transient calculation is performed for 4,000 seconds. In the purpose of the present statistical computation, it is important that the base of distribution functions should be calculated precisely. A large number of computations are performed in order not to reduce the precision of the bases of the distributions. Through a set of computation, the effect of uncertainty on plant transient is obtained as the statistical distribution.

1. Introduction

A fast breeder reactor (FBR) can use uranium more efficiently than light water reactors (LWRs), however majority of nuclear power plants are LWRs at the present situation. In order to develop FBR as commercial reactors, it is important that a construction cost is reduced. But now, construction cost of FBR may be higher than that of LWRs. Hence, cost reduction of FBR should be considered using various countermeasures, and enhancement of safety of FBR should be taken into accout as well.

It is obvious that design tolerances, errors included in operation, and statistical errors in empirical correlations effect on the transient behavior in caluculation. A deterministic estimation method cannot compute and express effects of above mentioned errors generally. The classical design method includes large safety margins because of its uncertainty of error band. A statistical method should be used to improve this drawback. The statistical method for a boiling water reactor was investigated by Mochizuki [1]. He applied this method to the cladding temperature dryout phenomena during a blowdown test simulating a pipe break accident. Yamaguchi and Takada [2] introduced the statistical method for the fast reactor. However, it is not clear that their method can estimate properly the upper and lower boundaries of the transient. The Monte-Carlo method is usually used in order to apply the statistical method. The random number is generated in this method in order to give probability distribution for a certain parameter. The random number in the present study means pseudo-random number generated by computation.

The purpose of the present study is to apply the above mentioned statistical errors to a plant system computation in order to evaluate the statistical errors contained in the transient evolution. It is expected that a best-estimate design with an error band can be achieved by applying the new method in order to eliminate the large safety margin. The reduction of the construction costs is expected by using the best-estimate design with statistical errors.

2. Outline of the method

As the first step of the present method, effects of many parameters on the upper plenum temperature of the loop type FBR are examined by sensitivity analyses, and dominant parameters are selected. In the present study, 43 parameters are selected. As a next step, a series of the uniform pseudorandom number is generated using a uniform random number generator. Then after the pseudorandom number is converted into the statistical distribution such as the normal distribution. Then, a computation input deck is created by applying the Monte-Carlo method to the selected input parameters. The determined number of input decks should be created in order to have a sufficient density of transient . Ten thousands of different computations are performed at once. At last, a statistical procedure and a statistical characterization are performed. Through ten thousands of different computations, the effect of various errors on the plant transient is obtained as the statistical distribution.

A selected computation case is the turbine trip test conducted at 40% electric power (45% thermal power)of the prototype FBR “Monju”. "Monju" is a loop type Pu-fueled and liquid sodium cooled FBR. This case is chosen because temperatures at various locations in the plant and flow rates in the primary and the secondary heat transport systems (HTSs) were measured during the turbine trip test and computation results was compared to test result. The NETFLOW++ system code is used for plant transient computation in the present study. This code has been developed by Mochizuki [1] in order to calculate a whole plant dynamics with various kinds of HTSs that use water, heavy water or liquid metal such as sodium, lead, or lead-bismuth as coolant material, and validated for the heat transport systems with water or sodium.

3. Pseudorandom number generation

The pseudorandom numbers look like a random number sequence, but they are numbers of progression found by stochastic calculation actually. A device or a program creating pseudorandom numbers is called a pseudorandom number generator. Generally there are various pseudorandom number generators. There are several classical methods and new methods as general pseudorandom number generators. The middle-square method, linear congruential method, Linear Feedback Shift Register are included in the classical method. A new pseudorandom number generator is developed in order to improve drawbacks of the classical method. As for the new methods, the Mersenne Twister, the chaos-based random number, and other methods are proposed.

The dSFMT (Double precision SIMD-oriented Fast Mersenne Twister) [4] developed as a version of Mersenne Twister (MT) is adopted as the pseudorandom number generator in the present study. The SFMT and MT are generally used for a computation of the Monte-Carlo method. The dSFMT supports various cycles from 2^{521}-1 to 2^{216091}-1. Its cycle is long enough for the present computation. In the present study, uniform random numbers are generated by the dSFMT, and these random numbers are transformed to the normal distribution by the Box-Muller method [5]. The Box-Muller method uses two uniform random numbers of an interval, ξ_1 and ξ_2, [0,1].

$$\eta_1 = \mu + \sigma\sqrt{-2\ln\xi_1}\,\sin(2\pi\xi_2)$$
$$\eta_2 = \mu + \sigma\sqrt{-2\ln\xi_1}\,\cos(2\pi\xi_2) \qquad (1)$$

The Box-Muller method generates two independent normal random numbers, η_1, η_2, [average value = 0, variance = 1].

4. Analytical plant model

The whole heat transport systems of the "Monju" reactor is modeled with the NETFLOW++ code as illustrated in Fig. 1. All major components in the heat transport systems are modeled and linked by the network model. Some main links standing for piping are divided into sub-links where one can consider diameter change. In order to estimate pressure loss of the system, pressure loss coefficients at bends and configuration change of piping are counted, and the values are estimated based on the handbook. Friction factors are calculated based on the approximate expression of Moody's chart. Characteristics of valves with the designated throttling, i.e., Cv values, and local loss coefficients for air coolers are searched by the trial and error calculation. As for heat loss from piping, one single heat transfer coefficient is given to the code. The heat transfer coefficient from the piping to the air is calculated by the heat conduction and thickness.

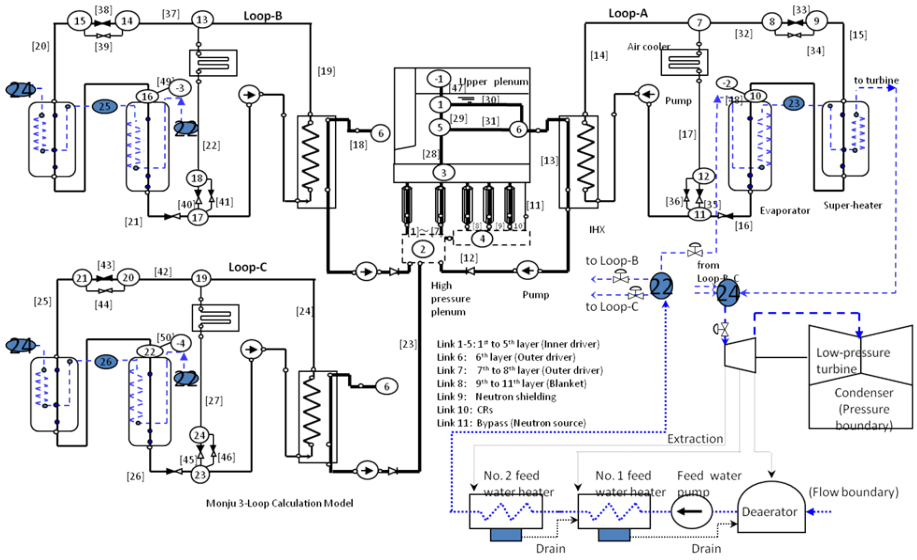

FIG. 1. A computational model using the NETFLOW++ code

The NETFLOW++ system code has been validated using the several plant transient tests of the experimental fast reactor "Joyo", and the prototype reactor "Monju". A computation result of turbine trip test conducted at 40% electric power is shown in Fig. 2. A time of 0 s is a time when the turbine trip start. And an abscissa is a time [sec], an ordinate of right side is temperature [ºC], and an ordinate of left side is flow rate [kg/s]. A solid curve shows a test result, a dashed line shows computation result. It is obvious that computation results trace test results.

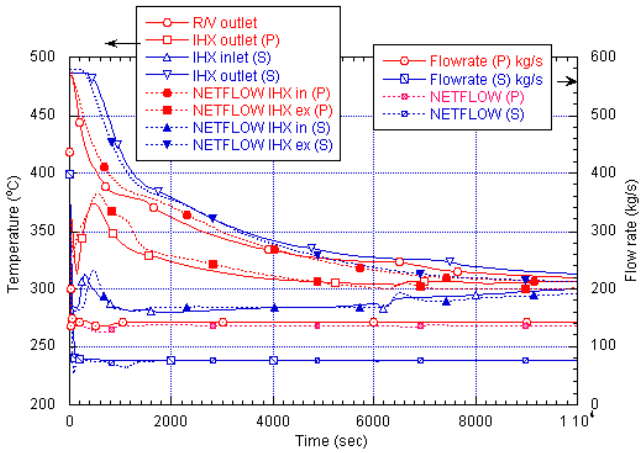

FIG. 2. Monju turbine trip test at 40% electric power

5. Sensitivity analyses

If the statistical method is applied to all parameters in the input deck, it needs a large amount of computational resources. Therefore, selection of parameters is needed. In the present study, the upper plenum temperature is focused on, because the temperature affects on the thermal stress of the reactor vessel. The thermal stress especially at the complex configuration to supper the reactor vessel is one of important factors of the plant design. A list of expected parameters that affect on upper plenum temperature are shown in Table 1. In the present study, 43 parameters are chosen such as core power, gap conductance, pressure loss, heat transfer coefficient correlation, scram timing, pump trip timing, and so on. The parameter is changed using two edges ($\mu \pm 3\sigma$), and computations are performed. Where, μ is default value and standard deviation σ is any variable, e.g., $\sigma = \mu \times 0.1, \mu \times 0.3$, etc. The steady state before the transient is calculated using time marching method for 12,000 seconds that is enough period to take the initial conditions. The transient calculation is performed for 4,000 seconds. The remainder of the greatest temperature gradient is used for the assessment of the temperature effects. The compared result is shown in Table 1. Scram timing, flow area of the core, moment of the primary pump, and the heat transfer correlation of the primary side have large effect on the temperature gradient in the upper plenum. On the other hand, the heat transfer correlation of secondary side, and factors of the intermediate reactor auxiliary cooling system (IRACS) are low effect factors. But, if these factors have large effect on different assessment cases, they should be chosen.

TABLE 1. Results of sensitivity analyses

Component	Phenomena	No	Uncertainty Contributor	delta
(A) Core	Total power	1	Power level measurment	0.072
	Total pressure loss	2	Pressure loss correlation (pin bundle)	0.008
	Pressure loss dist. in core	3	Flow area (deformation, swelling, etc.)	0.321
	Pressure loss dist. in F/A	4	Flow area (deformation, swelling, etc.)	0.001
	Inter-F/A heat transfer	5	Inter-wrapper flow effect	0.0
	Fuel pin properties	6	Gap conductance	0.154
		7	Cladding side of heat transfer coefficient correlation	0.003
		8		0.002
		9		0.005
		10		0.004
		11	Structural material side of heat transfer coefficient correlation	0.0
		12		0.0
		13		0.0
		14		0.0
	Scram	15	Scram timing	0.501
(B) Piping	Pressure loss	16	Pressure loss correlation	0.106
(C) IHX	Heat transfer	17	Heat transfer correlation (Primary)	0.055
		18		0.003
		19		0.173
		20		0.172
		21	Heat transfer correlation (Secondary)	0.008
		22		0.001
		23		0.002
		24		0.003
		25	heat transfer area	0.191
	Pressure loss	26	Pressure loss correlation (Primary)	0.003
		27	Pressure loss correlation (Secondary)	0.0

(D) Primary pump	Flow coastdown	28	Moment of inertia of pump	0.883
		29	Pressure lose correlation	0.057
		30	Pump trip Timing	0.0
		31	Flow rate of pony motor	0.396
(E) Secondary pump	Flow coastdown	32	Moment of inertia of pump	0.005
		33	Pressure loss correlation	0.12
		34	Pump trip timing	0.0
		35	Flow rate of pony motor	0.003
(F) IRACS	Heat transfer	36	Heat transfer correlation (Primary)	0.0
		37		0.0
		38		0.0
		39		0.0
		40	Heat transfer area	0.0
	Pressure loss	41	Pressure loss correlation	0.0
	Heat radiation from air cooler	42	Air inlet temperature	0.0
		43	Air flow rate	0.0

6. Monte-Carlo analyses

The distribution of parameter uncertainty is assumed as the normal distribution. Generally speaking, it is addmitted that a distribution of manufacturing error obeys the normal distribution. According to reference [1], statistical distributions of the dimensions of components of ATR (Advanced Thermal Reactor) such as the pressure tube diameters and the fuel cladding diameters obey the normal distribution. For example, the distribution of inner diameter of pressure tubes is shown in Fig. 3, and the distribution of outer diameter of claddings is shown in Fig. 4 in the form of a normal probability scale.

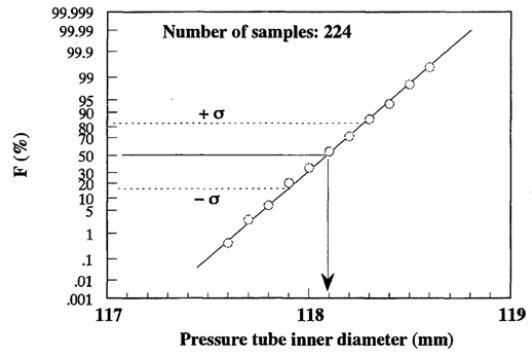

FIG. 3. Normality of pressure tube inner diameter on the normal probability scale

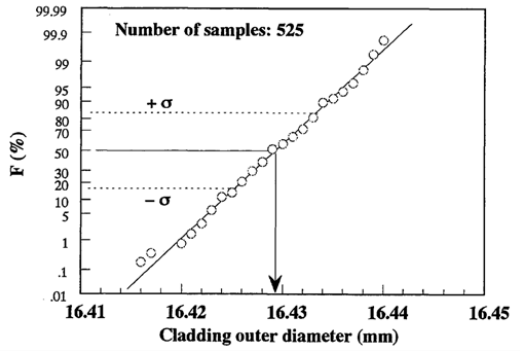

FIG. 4. Normality of cladding outer diameter on the normal probability scale

In addition, a heat transfer correlation is considered. Error of heat transfer correlation is checked by using Fig. 5 (Pe-Nu correlation [4]). Plots are picked up at around Pe = 100, 316, 1000, and 3162. Because the Pe number is in the range from 24 to 220 under the rated thermal power conditions of Monju, the number of points cover this range. Frequencies of the Nu number of experimental data are shown in Fig. 6-9. These distributions look like normal distributions, especially at Pe = 1000. Unfortunately, more precise distribution cannot be obtained because there are not much measured data. The calculated Nu number at Pe = 1000 is shown in Fig. 10 in the form of normal Quantile-Quantile Plot. The normal Q-Q Plot is used for testing whether distribution of data is same or not. If the distribution is normal distribution, the plots are close to the linear curve. When processed data

points are on a straight line, the data obey the normal distribution. Therefore, data of the Nu number at Pe = 1000 obey the normal distribution. Eq.(2) shows the heat transfer correlation proposed by Seban and Shimazaki [6].

$$Nu = 5 + 0.025 \times Pe^{0.8} \qquad (2)$$

In order to change the above correlation, constants included in the equation are reconstructed using the mean value and the standaard deviation.

$$Nu = C1 + C2 \times Pe^{R1} \qquad (3)$$

$$Coefficient(C1, C2, R1) = \mu + \mu \times Ra \times \sigma \qquad (4)$$

(μ : mean value [e.g., 5, 0.025, 0.8 for Eq. (2)], Ra : random number[-1,1], σ : arbitrary variable [e.g. 0.01])

The Nu number is calculated using Eq. (3) and random numbers with the normal distribution. A distribution of the calculated Nu number at Pe =1000 is shown in Fig. 11. The shape of the distribution in Fig. 11 is similar to that in Fig. 8 although the mean value is slightly different from the correlation. The Nu number by Eq. (2) is larger than the mean value of experimental data. Therefore, the mean value of the calculation is larger than the experimental data.

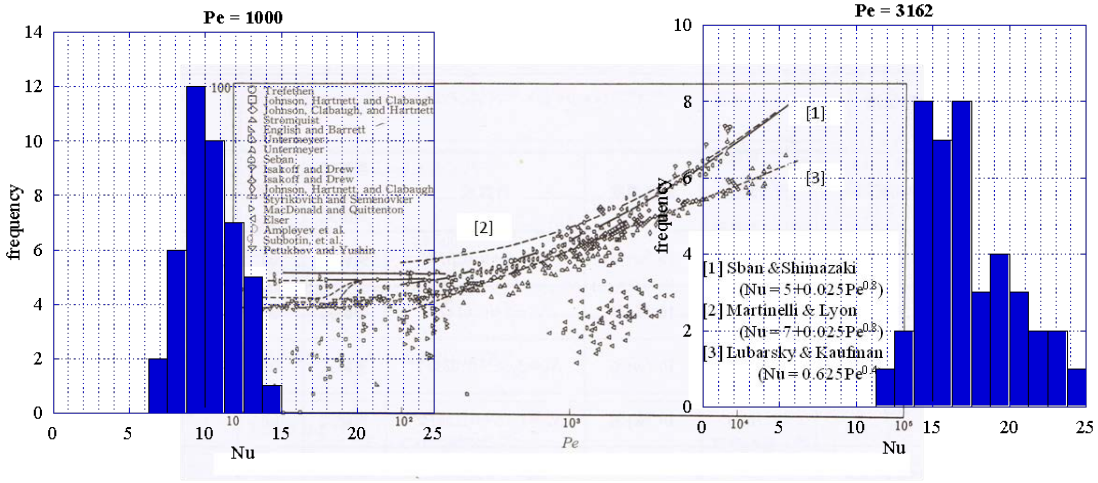

FIG. 8. Distribution of Nu number's frequency at Re = 1000

FIG. 5. Pe-Nu correlation

FIG. 9. Distribution of Nu number's frequency at Re = 3162

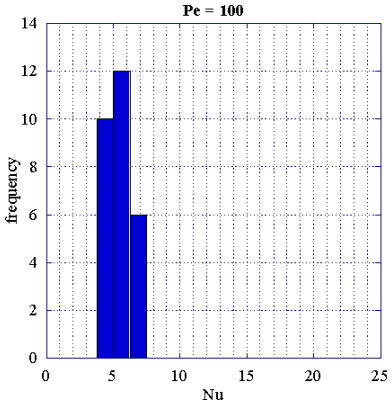

FIG. 6. Distribution of Nu number's frequency at Re = 100

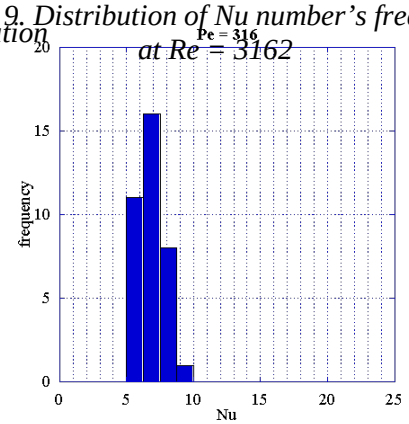

FIG. 7. Distribution of Nu number's frequency at Re = 316

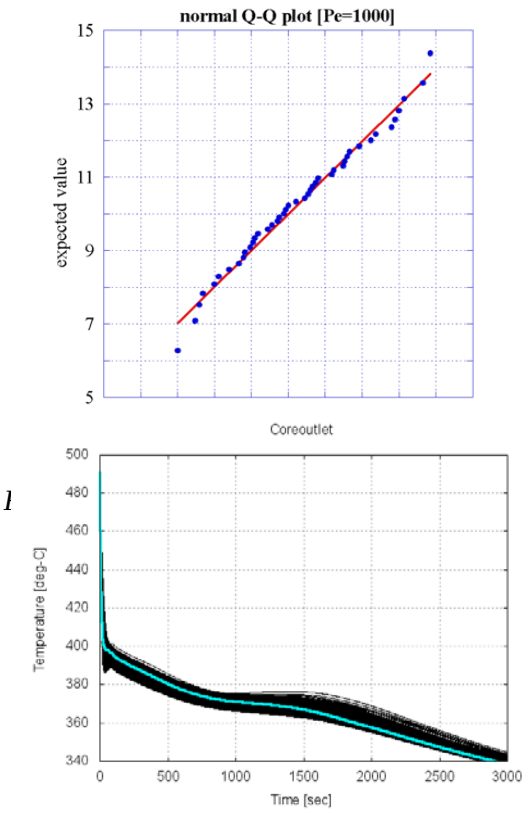

1

FIG. 12. Calculation result of upper plenum temperature (1)

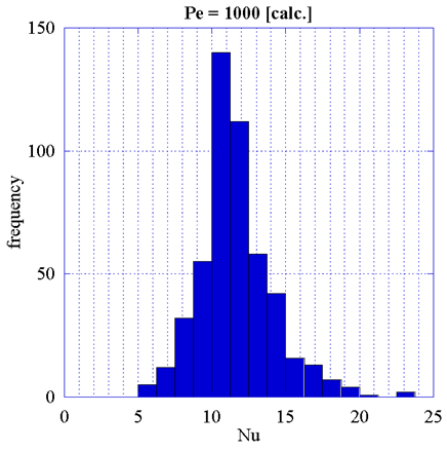

FIG. 11. Distribution of calculated Nu number's frequency at Re = 1000

Ten-thousand sets of input decks are prepared for the steady state and also the transient calculations using the MC method. Each of 43 parameters in one input deck is adopted as a new data that is edited using the pseudorandom numbers and the Box-Muller method. Ten thousands of different computations are performed one by one. In every computation case, the steady state calculation is performed for 12,000 seconds, and the transient calculation is performed for 4,000 seconds as in the case of the sensitivity analysis. In the present statistical computation, it is important that the base regions of the distribution functions should be expressed precisely. A large number of computations should be performed in order not to reduce the precision of the base regions of the distributions for the interested parameters. Through a set of computation, the effect of many kinds of errors on the plant transient is obtained as the statistical distribution.

The calculated transient curves of the upper plenum temperature during the turbine trip event are shown in Fig. 12 together with the measured curve. The time 0 sec is a time when the turbine trip event starts. The short range temperature is shown in Fig. 13. The abscissa is in the range from 0 sec to 200 sec. It is obvious that transient curves have a certain width, and the second temperature peak and the third peak are recognized in the figure. Unfortunately, the first peak is not visible in Fig. 13 because this peak appears around 1 or 2 seconds. However, it is clear that the measured temperature is in the group of the statistical computation curve. The steepest temperature gradient is shown in Fig. 14. The abscissa means the temperature gradient of upper plenum [ºC/sec], and the ordinate is frequency. The average value is -7.983 [ºC/sec] and the standard deviation is 0.543 [ºC/sec]. The distribution seem to be the normal distribution or logarithmic-normal distribution. However, but the distribution is not perfect normal distribution, because these data do not completely the curve of normal Q-Q plot. These data is shown in Fig. 15 as a form of normal Q-Q plot. The temperature of the second peak at the upper plenum is shown in Fig. 16. The abscissa is a temperature [ºC] and the ordinate is frequency. The average temperature is 392.97 [ºC] and standard deviation is 2.131 [ºC]. The distribution of the second peak temperature is not the exact normal distribution either.

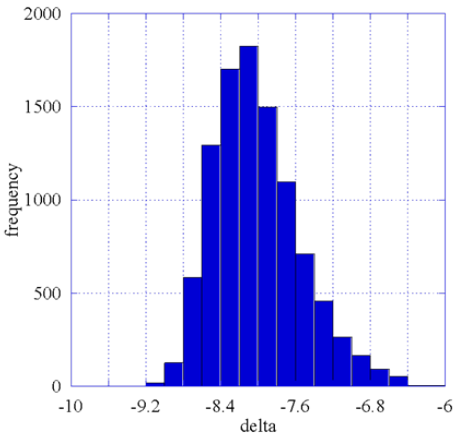

FIG.14. Distribution of the greatest temperature gradient

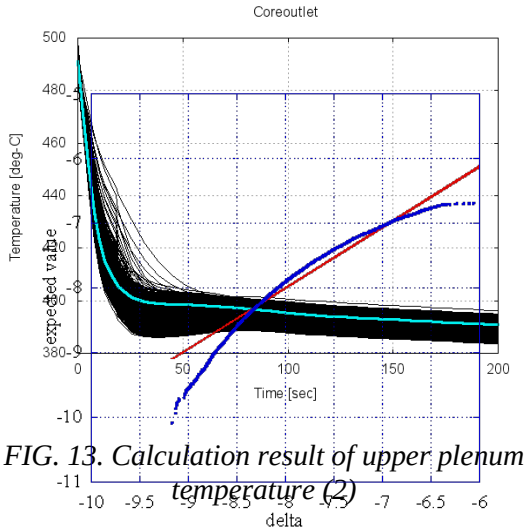

FIG. 13. Calculation result of upper plenum temperature (2)

FIG. 15. Normality of temperature gradient on normal Q-Q plot

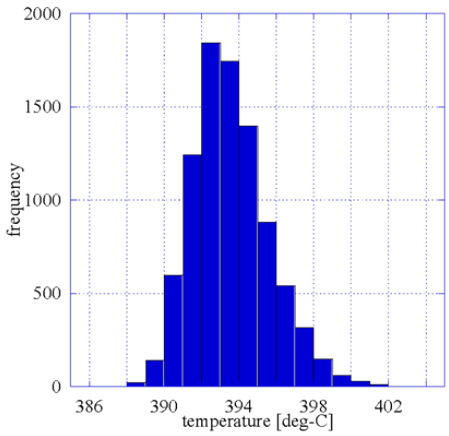

FIG. 16. Distribution of second peak temperature

7. Discussion

In the present study, all input parameters are assumed to obey the normal distribution, and the variances are defined as arbitrary variable values. Therefore, the computed result is not an exact result for the plant design. The precise variance and the distribution function of each parameter should be prepared in order to obtain the final computation result. If the final result is obtained by the statistical computation, the result is very useful for the appropriate design. On the other hand, there is a problem of computational resource when the trial number is large. Fortunately, the NETFLOW++ code can calculate a plant transient with very fast computation speed. Since the NETFLOW++ code needs low

computational resource, it can calculate ten thousands cases without any problem. However, general plant system code needs a large computational resource such as a high grade work-station, a long computational time, and so on. Hence, the tryal number of computation needs to be reduced as low as possible. When the trial number is reduced, a most probable value could be obtained, but the base region of the distribution may not be precise. Therefore, a new method is required to reduce the trial number and obtaining precise bases of the distributions. A target is to reduce the trial numbers from 10,000 to 1,000 with keeping the precision at the base regions of the selected distributions.

8. Conclusion

In the present study, the design tolerances, errors included in the plant operation, and statistical errors in the empirical correlations are taken into account in the plant transient computation using the Monte-Carlo method in order to evaluate the effect of the statistical variance contained in the transient evolution on the plant transient. A selected transient is the turbine trip test conducted at 40% electric power at the prototype fast reactor "Monju". Ten thousands of different computations are performed. Consequently, the effect of different kinds of errors on plant transient is evaluated as the statistical variance.

REFERENCES

[1] H. Mochizuki, A Validation of ATR LOCA Thermal-hydraulic Code with a Statistical Approach, Journal of Nuclear Science and Technology, **37**, 8 (2000), pp.697-709.
[2] A. Yamaguchi, et al., Stochastic Safety Analysis of Natural Circulation Decay Heat Removal in Liquid Metal Reactor, Proceeding of ICAPP 2007, Paper 7486, Nice, France (2007).
[3] H. Mochizuki, Development of the plant dynamics analysis code NETFLOW++, Nuclear Engineering and Design, 240, (2010), pp. 577-587.
[4] M. Saito, M. Matsumoto, SIMD-oriented Fast Mersenne Twister: a 128-bit Pseudorandom Number Generator, MC and QMCM 2006, (2008), pp. 607-622.
[5] G. E. P. Box and M. E. Muller, *Ann. Math. Stat.* 29(1985), 610.
[6] R.A.Seban, Shimazaki, Heat Transfer to a Fluid Flowing Turbulently in a Smooth Pipe With Walls at Constant Temperature, Transactions of the ASME, August, 1951, pp.803-809

Status and Future Challenges of CFD for Liquid Metal Cooled Reactors

F. Roelofs[a], V.R. Gopala[a], K. Van Tichelen[b], X. Cheng[c], E. Merzari[d], D.W. Pointer[e]

[a] NRG, Petten, Netherlands

[b] SCK-CEN, Mol, Belgium

[c] KIT, Karlsruhe, Germany

[d] ANL, Argonne, IL, USA

[e] ORNL, Oak Ridge National Lab, TN, USA

Abstract. Liquid metal cooled reactors are envisaged to play an important role in the future of nuclear energy production because of their possibility to use natural resources efficiently and to reduce the volume and lifetime of nuclear waste. Typically, sodium and lead(-alloys) are envisaged as coolants for such reactors. Obviously, in the development of these reactors, thermal-hydraulics is recognized as a key (safety) challenge. A relatively new technique to deal with thermal-hydraulics issues is Computational Fluid Dynamics (CFD). This technique is used increasingly nowadays for design and safety evaluation purposes.

This paper will discuss the development status of CFD application to liquid metal cooled reactors. In addition, the main challenges for future developments will be indicated. Firstly, the technological challenges will be discussed which ask for CFD application. Afterwards, the needs for CFD development and/or validation will be discussed. The discussion will also include the need for accompanying experiments.

1. Introduction

The civil utilization of nuclear energy of more than five decades shows significant advantages of nuclear power in respect of environment protection, economic competitiveness and power supply security. Nowadays, nuclear power plays an important role in power generation and produces about 16% of the total electricity worldwide. The rapidly growing energy demand suggests an important role for nuclear power in the future energy supply, as for example denoted in the projections of the World Energy Outlook 2011 [1]. On a global scale, the accident at the Fukushima Daiichi nuclear power plant in Japan in March 2011 did have a minor effect on the future demand for nuclear power. Therefore, nuclear energy is on the agenda worldwide. Apart from the widely used light water reactors, a significant role is attributed to the deployment of fast reactors [2]. In most countries, the preferred option is the sodium cooled fast reactor with the lead cooled fast reactor and the gas cooled fast reactor as back-up systems from the systems selected by the Generation IV International Forum (GIF) [3].

Over the years, more than 20 liquid metal cooled reactors have been operated around the world [2]. Currently, a few liquid metal cooled reactors are operational. The BN-600 sodium cooled power reactor is successfully operated in Russia. Additionally, Russia, China and India operate the BOR-60, CEFR and the FBTR sodium cooled research reactors. Additionally, new liquid metal cooled reactors are under construction or are being planned. India is close to finishing the construction of the sodium cooled PFBR power reactor, whereas Russia is close to finishing construction of the sodium cooled BN-800 power reactor. For an elaborate overview of the status of fast reactor development the reader is referred to the technical report about the status of fast reactors made by the IAEA [2].

Thermal-hydraulics is recognized as one of the key scientific subjects in the design and construction of liquid metal cooled reactors. To solve thermal-hydraulic issues, nuclear engineers apply analytical and empirical correlations, system thermal hydraulics (STH) codes, or subchannel codes. Additionally, Computational Fluid Dynamics (CFD) techniques are becoming more and more integrated in the daily practice of the thermal-hydraulics researchers and designers.

This paper will discuss the development status of liquid metal cooled reactor thermal-hydraulics specifically with respect to the application of CFD techniques. The main challenges for future developments will be indicated. Firstly, the technological challenges will be discussed. In many cases these technological challenges require the application of CFD. This paper will explain the status of CFD developments and the future challenges. The next section will describe the main technological challenges which thermal hydraulics engineers are facing for fast reactor development. Sections 3 will deal with the CFD challenges which are derived from the technological challenges, i.e. liquid metal turbulence, core thermal hydraulics, multi-phase flow, pool thermal hydraulics, and system dynamics. Finally, section 4 will present a summary of the status and future challenges of liquid metal cooled reactor thermal hydraulics.

2. Thermal Hydraulics Challenges in Design and Safety

The technological thermal hydraulics challenges for liquid metal cooled fast reactors will be classified and described according to the reactor subsystems to which they relate. The description starts with the challenges related to the nuclear core (1), elaborating to the ones related to reactor vessel or pool (2), extending to challenges in the heat transfer systems (3), e.g. heat exchangers and steam generators, eventually leading to the primary, secondary and intermediate heat transport systems' challenges (4).

2.1. Core

In the core of a nuclear reactor, the nuclear fission reaction takes place. In this process, heat is produced mainly in the nuclear fuel and transported to a coolant. Liquid metal cooled reactor cores generally consist of many fuel assemblies and a limited number of control rods. The fuel assemblies themselves consist of a large number of fuel rods. The technological challenges in the core relate mostly to the pressure drops and heat transport efficiency under nominal, transient and incidental conditions. The main safety issue is the limitation on the clad temperature. Furthermore, dynamic forces generated by the flow of coolant in the core could cause fuel rods to vibrate and result in gradual fretting wear and fatigue at contact surfaces. A thorough analysis of these flow induced vibrations is needed. For control and safety rods, an additional challenge is the limitation of the insertion time.

Typically, thermal hydraulic evaluations are completed in three steps. Firstly, thermal hydraulic and hydrodynamic evaluations are required at the level of the complete core. The second level of core evaluations is the (hottest) fuel assembly, and the third level of evaluations deals with a sub-channel to detect local hot spots. Numerically, these different levels require different levels of detail.

(1) Evaluations of the behaviour of the total core are traditionally performed using STH or subchannel codes. However, uncertainties rise when three dimensional effects start playing a role which cannot be captured in such codes. Such three dimensional effects may originate

from the core inlet structure designs, fuel assembly designs, spacer designs, control rod designs, but also from consideration of inter-sub assembly flows.

(2) In order to calculate the pressure drop and heat transport at fuel assembly level in a liquid metal cooled reactor core with sufficient accuracy, STH and sub-channel codes are generally used which require liquid metal specific correlations for pressure drop and heat transfer as reported in [4] and [5]. These correlations contain uncertainties and their domain of validity is limited. Therefore, experiments may be needed if the new design is out of the validity domain. For pressure drop characteristics, water (or air) tests can be used with a Reynolds similarity condition. For heat transfer and temperature field analysis, in most cases liquid metal tests are required to account for the influence of the very low Prandtl number. As experimental data in liquid metal are hard to obtain and very costly, CFD is increasingly used to reduce the size of the experimental matrix. However, CFD approaches first need to be validated against refined experimental data. The advantage of a CFD approach lies in the fact that the models used in CFD are often less case specific in comparison to correlations. Many CFD approaches are more generic and their range of validity is larger. One series of experiments can validate a specific CFD approach which can be used in a large range of thermal hydraulic cases. The primary drawback is the increased computational cost.

(3) At fuel pin level, an important challenge is to prevent or mitigate vibrations, often flow induced. Such issues are identified for LWRs e.g. during power upgrades. However, due to the high mass of the liquid metals involved in cooling lead or lead-bismuth fast reactors, prevention of fuel pin vibrations is an important prerequisite for the design. Apart from experimental investigation which needs sophisticated measurement techniques to allow proper measurement in the small space available within a fuel assembly (which is a challenge even in water experiments) and in a high temperature, highly corrosive and erosive liquid metal environment if required, also numerical tools need development to couple detailed flow field analyses to structural mechanics analyses. Most of the examples found in literature focus solely on the flow field analyses up to now, see e.g. [6], or use analytical models for slender cylinders mainly based on motion-induced inviscid forces with the effect of the viscous hydrodynamic forces is added afterwards with empirical coefficients [7].

When in an unlikely accident, the core is molten, the behaviour and interaction of the molten core with the coolant and the pool structures require special consideration. Experimental investigations to this respect are limited as it is difficult to use real irradiated spent fuel material in such studies. However, some attempts are reported. Simulations on the other hand are also quite complicated, as the simulation has to treat a liquid metal flow for which heat transport modeling is a challenge as described above, but the simulation also has to treat mixtures of multiple components (materials) and usually has to include chemical reactions. For this reason, mostly the dedicated CFD based SIMMER code [8] is used. However, within the European 7th framework project SEARCH also a CFD based approach will be developed for fuel dispersion in a lead-bismuth environment.

2.2. Reactor Vessel / Pool

Pool thermal hydraulics may be subdivided in upper plenum and lower plenum thermal hydraulics. According to [9], upper plenum thermal hydraulics is often considered as one of the noblest parts of fast reactor thermal hydraulics activities as many challenges are concentrated in the upper plenum of a fast reactor. A complete article is dedicated by [10] to the challenges which are met in the thermal hydraulic design of the PFBR pool. The following challenges are identified by [9][10]:

- Heat transfer to and from the coolant
- Core outlet temperature measurements
- Thermal fatigue due to thermal fluctuations near the core outlet
- Flow induced vibration of the above core structure
- Coolant level fluctuations leading to fluctuating thermal and/or mechanical loads
- Gas entrainment
- Thermal stratification leading to fluctuating thermal loads

- Transport of fission products in the upper plenum which support detection possibilities during cladding failure accidents
- Flow changes during transients possibly leading to stratification
- Natural circulation during decay heat removal situations
- Thermal fatigue due to thermal fluctuations near the pump/heat exchanger outlet in the lower plenum
- Heat transport and the effects on the flow in upper and lower plenum of the internal wall separating both plena
- Flow patterns in non-symmetric situations (e.g. when one or more secondary circuits are not operating)
- Cover gas thermal hydraulics

Many of the identified challenges inherit complex three dimensional flow behaviour and include heat transport. To this list, sloshing in case of seismic events should be added. The challenges with respect to heat transport in liquid metals were already mentioned in the previous subsection. The challenges with respect to the highly three dimensional behaviour of the coolant flow in the reactor vessel can only be solved by (scaled down) experimental set-ups in which these flows are simulated, or by involving CFD techniques which become more and more integrated in the daily practise of designers with the increasing computer power. However, even when such techniques are used, one should not forget that validation to well instrumented experiments is essential and that creation of computational meshes, setting up simulations, and taking into account various models for e.g. turbulent heat transport, multi-phase behaviour, fluctuating free surface levels raises serious challenges.

2.3. Heat Transfer System

Heat exchangers are used in an LMFR to transfer the heat between the primary circuit and the secondary circuit, or between the primary circuit and the decay heat removal circuit. Primary coolant is flowing around the tubes, as secondary coolant is flowing inside tubes or shells. The flow field and the temperature field in the bundle play an important role in the efficiency of the heat exchanger. Moreover, the thermal stresses induced by the possible differential dilatation between the inner and outer parts of the bundle must be evaluated as the whole bundle is connected to the two thick plates. As the flow pattern is complicated with transverse flows at the inlet and outlet of the bundle, it is important to use adapted pressure drop and heat transfer correlations. As various flow situations may occur, including low flow rate condition with buoyancy influence, the correlations must also cover these situations. In addition to past studies, in which water and liquid metal tests were performed, numerical simulation techniques were developed to simulate the bundle with sub-channel modelling. Refined CFD computations are needed to study the secondary inlet and the outlet collectors.

In the event of a pipe break or leak in a sodium-water heat exchanger, a chemical reaction between water and sodium will occur. Currently, a CFD modelling approach is under development in Japan [11].

2.4. Heat Transport System

Evaluations of the total heat transport system of a reactor are typically the domain of the integral experiments and STH codes. However, most STH codes do not allow to incorporate three-dimensional effects. With the increasing computer power and new numerical techniques, three dimensional modeling of (parts of) the heat transport system comes within reach but the new methodologies still have to be developed and validated, see e.g. [12].

3. Status of CFD and Future Challenges

3.1. Liquid Metal Turbulence

Modelling heat transport in a liquid metal is one of the fundamental challenges when application of CFD is considered for design or safety analysis of an LMFR. Current engineering tools apply statistical turbulence closures and adopt the concept of the turbulent Prandtl number based on the Reynolds analogy. Essentially, the turbulent Prandtl number concept can be considered as a structural coupling of velocity- and temperature fields, valid only for forced convective flows with Prandtl number of order of unity. In the particular case of liquid metal, the turbulent Prandtl number concept is not applicable and robust engineering turbulence models are needed [13][14][12][15]. This challenge and possible solution routes were excellently described by [16]. Figure 1 demonstrates the different heat transport behaviour of a liquid metal compared to a fluid like air or water. Direct numerical simulations of a rectangular channel flow in which turbulence behaviour is calculated using the laws of physics in stead of approximated by turbulence models clearly show a different behaviour of liquid metals. The typical high thermal conductivity of liquid metals leads to a large thermal boundary layer compared to the boundary layer which is typically of the same size as the momentum boundary layer for fluids like air and water.

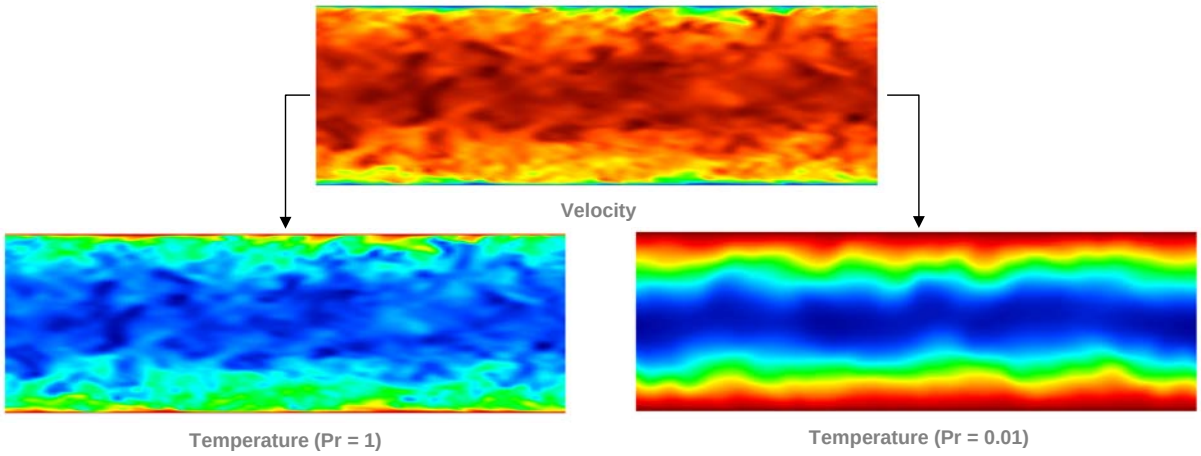

FIG. 1. Velocity and temperature field of rectangular channel heated from top and bottom by NRG applying a fluid like air and water (Pr ~1) and a typical liquid metal (Pr<<1)

Most of the identified solutions (e.g. [16]) are today only available in academic codes or are computationally too costly or unstable to be used in engineering situations and codes. Additionally, it should be mentioned that it is well known that the deviations are largest in natural and mixed convection regimes. Therefore, most solutions focus only on these regimes. However, for a stable and robust engineering tool, a model is required which can deal with all flow regimes simultaneously. Some promising routes for improvement are today subject of the European 7th framework project THINS (Thermal Hydraulics for Innovative Nuclear Systems).

Within this project, a carefully selected, existing advanced Reynolds Averaged Navier-Stokes (RANS) turbulence model based on [17] was implemented in the widely spread engineering CFD tool STAR-CCM+. This algebraic heat flux model (AHFM) adopts an expression for the turbulent heat flux which is derived from the full differential transport model on the base of a local equilibrium assumption. It retains the fundamental production terms representing the physical mechanisms which generate the turbulent heat flux, therefore permitting to accurately model natural- and mixed-convection flows. Preliminary tests using default model constants as indicated by [17] indicate stable behavior in all flow regimes ranging from natural convection to mixed and forced convection. However, it has also revealed that a robust parametric study is required to derive an appropriate set of model constants in every flow regime. Once that would be available, one could start thinking of implementing the model in such a way that it automatically switches between the different sets of model constants. In addition

to this development, various non-linear RANS turbulence models can be used in combination with an AHFM based on [18] in the TRANSAT code. The validation campaign is currently ongoing. Another approach under evaluation is to use turbulent Prandtl number distributions depending on the Reynolds number and the non-dimensional distance to the wall derived from DNS simulations by means of a look-up table. First results using this approach are promising.

With increasing computer power, Large Eddy Simulations (LES) become more and more important in predicting complex physical phenomena in complex geometries. In the well-known distribution of the turbulent kinetic energy, most energy is found at large scales and the energy is dissipated at smallest scales. The temperature spectrum has a similar distribution as the velocity spectrum. With decreasing Prandtl number also the amplitudes of the fluctuations decrease due to the higher thermal diffusivity. Analogously, the dissipation scale of the temperature fluctuations is moved to larger scales. Thus, in LES calculations the energy equation is often better resolved than the momentum equation and the turbulent Prandtl number concept leads to correct results. This is for example used in approaches which solve the momentum equations using LES while solving the temperature equations using a DNS approach [19]. However, the isotropic flux modeling with turbulent Prandtl numbers fails either when the turbulence is strongly non-isotropic or when buoyancy forces become dominant as explained by [16]. In the United States, the SHARP project is evaluating the applicability of DNS, LES, and RANS methods, as well as integrated hybrid methods, to SFR analyses as part of the development of an integrated virtual reactor toolset.

To design for the risk of thermal fatigue, which for LMFR is considered higher than for light water reactors, approaches developed for LWRs, as e.g. described in [20] and [21], should be transferred and adapted to LMFRs. As the applied approaches essentially use CFD to determine the thermal fluctuations, basically, the heat transport models need to be updated and validated. To check whether the fluctuations are correctly predicted by the numerical codes, fundamental experiments are needed e.g. to study the behaviour of jets [22]. Experiments ranging from single to multiple jets either impacting or not impacting a solid wall can be envisaged. Preferably such experiments should be performed both in water, air or another transparent fluid and in liquid metal. The latter experiments are typically missing, although some examples can be found in literature, see e.g. [23].

Flow induced vibrations are typically induced by turbulent fluctuations in the flow within e.g. a fuel assembly, a pipe bend, or by jets impinging on a structure. Well defined experiments will be needed to provide more insight and more validation data for numerical methodologies which need to be developed. Although some steps are being taken as indicated e.g. by [6][7], the important part of coupling the fluid motions to structural deplacements is certainly not proven technology.

3.2. Core Thermal Hydraulics

Within the core different levels can be identified at which evaluations are necessary. Beginning at the level of a single subchannel to a single fuel assembly, an important aspect is the correct evaluation of heat transfer and pressure drop when like in most liquid metal cooled reactor designs, wire wraps are used to separate individual pins. Many experiments have been performed in the past (a summary can be found in [22]) for different kinds of configurations. These experiments mostly aimed at derivation of empirical correlations for pressure drop and heat transfer to be employed in STH and subchannel codes. However, as currently RANS CFD techniques are increasingly used for the assessment of wire wrapped fuel assemblies, there is a need for experimental validation at the detailed level required by CFD. As these data are momentarily not available, [24] have created numerical reference data by employing LES for different sizes of wire wrapped fuel assemblies, ultimately ranging to 217 pins as shown in figure 2. Such LES data may be used to increase the confidence level of the RANS CFD approaches.

Thermal hydraulic accident analysis at fuel assembly level concentrates on blockage scenarios. Using modern CFD techniques, such blockage accidents can be analysed in three dimensions. However, most often the computational grid refinement needed for accurate predictions cannot be achieved when a complete fuel assembly including inlet and outlet header needs to be modeled. To reduce the amount

of computational effort but to maintain a reasonable accuracy, new approaches are under development at various institutes and companies. Typically, these approaches apply CFD using low resolution or underresolved meshes [25][26]. In the approaches reported in [25][26] the authors try to simplify the geometrical representation of the rod bundle, e.g. by modelling a wire wrap by either a spiral fin or a momentum source. These approaches are still inmature and need experimental validation for which proper data is lacking.

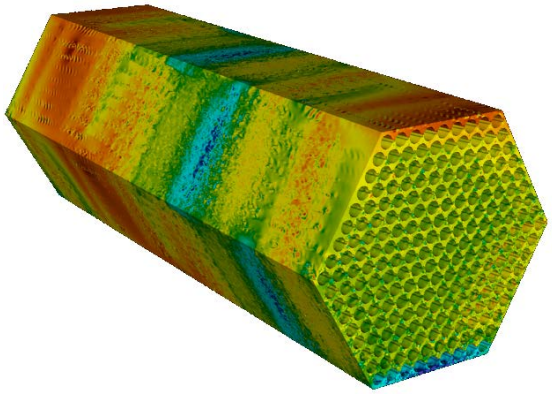

FIG. 2. LES simulation by ANL of a 217-pin wire wrapped fuel assembly [24]

Simulations at complete core level are traditionally performed using STH or subchannel codes. When the current light water reactor technology was developed, the only possibility to compute the flow inside a fuel bundle was to use one-dimensional sub-channel analysis. The sub-channel scale could not be resolved. For simulations of the whole reactor core either system codes or homogenization was employed. In system codes, resolution of individual assemblies was the state of the art. It is explained in [26] that the coarse grid CFD approach (CGCFD) combines ideas of sub-channel analysis and CFD to develop a CFD based method which takes advantage of the fast development of commercial CFD software and the efficiency of subchannel analysis. The subchannel codes use empiric correlations and case-specific model constants that have to be adjusted or adapted for each new case or geometry. The goal of the CGCFD is to provide an approach that is as efficient as subchannel codes and becomes independent from experimental or empirical data. The method should close the gap between subchannel codes and RANS simulation.

3.3. Pool Thermal Hydraulics

As mentioned by [9] pool (upper and lower plenum) thermal hydraulics is often considered one of the noblest parts of fast reactor thermal hydraulics. Within this paper, only some important challenges will be described.

In the past decades, many pool experiments have been performed in order to verify correct operation of a fast reactor design. Many of these experiments have been mentioned in [9][10][22]. With renewed interest in liquid metal fast reactors during the most recent years, and with the increased modeling capabilities of modern day computers and numerical algorithms, the traditional simulation techniques can potentially be largely improved. The inherent three dimensional flow patterns in a fast reactor pool can be accurately and efficiently modeled nowadays by CFD. However, validation data providing sufficient details for validation of CFD simulations is lacking. This will not only require new experimental set-ups, but also state-of-the-art or new measurement techniques. Once that is done, CFD modeling should be validated with respect to different aspects, like e.g. convection patterns, stratification prediction, stability analysis, or even the behaviour of and in complex internals like e.g. the above core structure or an heat exchanger. Today, in order to understand the thermal-hydraulic phenomena occuring in the MYRRHA accelerator driven system reactor pool, the E-Scape lead-bismuth and the Democritos water facilities are being erected as thermal-hydraulic scale models of the MYRRHA reactor using lead-bismuth as coolant [27].

Such large scale validation experiments to study mixing behaviour in a complete reactor pool are preceded with separate effect experiments and simulations. Such experiments typically employ one or multiple jets mixing in a small plenum. At the end of the 20th century, results of a triple parallel water jet in which a central cold jet was surrounded by two hot jets were published [28]. They measured velocity components and temperatures. They concluded that the interaction of the jets enhances the mixing largely compared to a single jet experiment. Later, [23][29] reported similar experiments using sodium. Currently, the large scale MAX facility, shown in figure 3, is under development at ANL in the USA to obtain accurate measurement data enabling validation of CFD codes. Design supporting LES simulations [30] have been performed to optimally design the experiment which is being taken in operation currently.

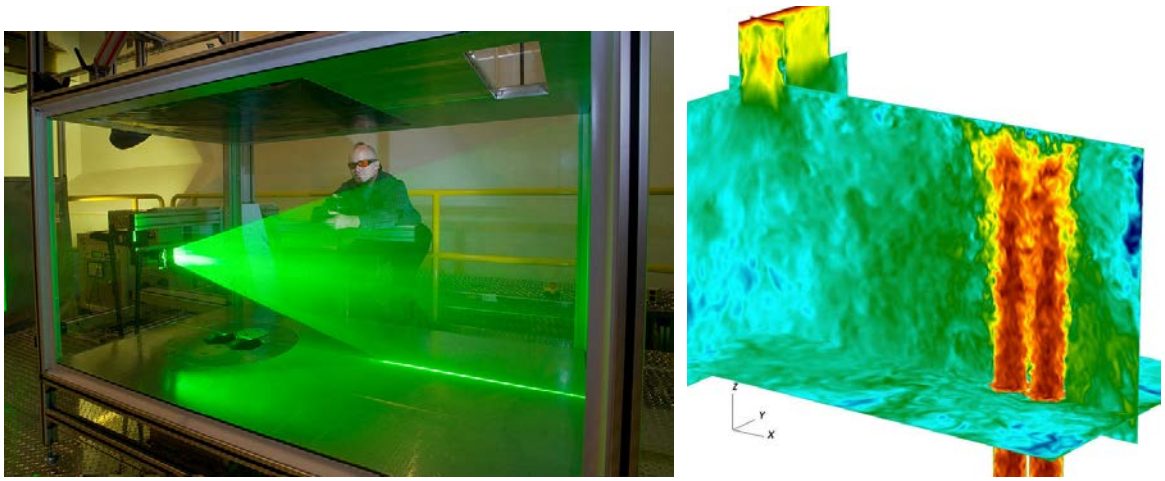

FIG. 3. The MAX facility at ANL and a design supporting LES simulation showing axial velocity on different planes[30]

Concerning gas entrainment studies, many articles have been published providing an overview of existing experience with a distinction between types of gas entrainment. A recent article nicely summarizing the existing experience was published by [31]. A distinction can be made between different types of gas entrainment. All of them are important for a real reactor application and all of them need both experimental and numerical studies to prevent and/or mitigate the risks. Experiments typically cover a range of scales. From fundamental experiments focusing on existence and occurrence of one specific type of gas entrainment (as e.g. reported in [32]), to experiments including obstacles in order to simulate to complex structure in a liquid metal reactor pool, finally to experiments simulating the complete upper plenum of a certain liquid metal reactor pool design [33]. Numerically, most effort is put in derivation of criteria to derive the risk for gas entrainment from single phase CFD simulations. However, with increasing computational power, also application of dedicated numerical free surface models like the widely used VOF approach become feasible. An example of a numerical result at reactor scale employing such a free surface model is shown in [9]. Recently, [34] showed that the influence of fluid properties is one of the significant issues in the evaluation of gas entrainment at a free surface. They performed experiments to compare the onset conditions between water and sodium as many of the gas entrainment experiment are being performed using water as a coolant simulant.

Seismic qualification of liquid metal cooled reactors is an issue because of the high density and possible sloshing effects of the coolant. To study the risks of liquid metal sloshing, experiments should be performed at reasonable scale size, with sufficient geometrical detail and employing preferably a liquid metal to avoid uncertainties occurring when a scaling fluid is used. Such expensive experiments may be partly replaced by CFD using a free surface model. An attempt in this direction is described in [22] using URANS simulations and volume of fluid (VOF) modelling. Although they performed validation analyses [35] comparing sloshing in a two dimensional tank to an analytical solution, full scale validation is lacking.

3.4. System Dynamics

In order to study the impact of the three dimensional modeling of e.g. a pool structure or other large components on the rest of the heat transport system, new approaches are under development where STH codes are coupled to CFD codes and each code does what it can do best. Such developments will require large scale integral experiments providing sufficient measurement details to serve both the STH and the CFD codes. As mentioned before, this may require development of new measurement techniques. On the numerical side, coupling different codes empoying different solver routines and operating at different spatial and temporal scales remains a challenge. Some work in this direction is reported by e.g. [36][37][38][39] coupling e.g. the ATHLET STH code to CFX, the SPECTRA STH code to OpenFOAM, the CATHARE STH code to TRIO_U, and the SAS4A/SASSYS-1 STH code to STAR-CD. Figure 4 shows an example of the ongoing development of coupling ATHLET to OpenFOAM. As a test case, one of the Phénix reactor end-of-life tests is selected. The simulation domains for the STH and CFD simulations have been set-up. In this case, the complete primary system is modelled in STH, while the three dimensional flow in the Phénix upper plenum is modelled in CFD. Today, an automated coupling between ATHLET and OpenFOAM is under development. While the ATHLET code simulates the complete primary system, it waits from time to time on OpenFOAM to receive updates about the three dimensional behaviour in the upper plenum, while it provides to OpenFOAM updated boundary conditions. To support this, an interpolation algorithm is developed which together with so-called ‘watchdog’ software which enables numerical stability and convergence.

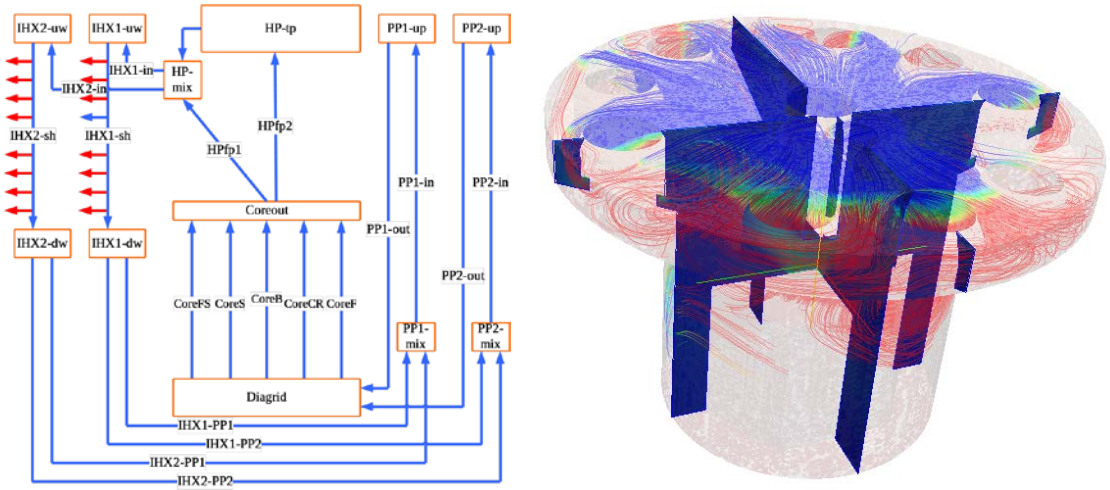

FIG. 4. ATHLET STH code coupled to the OpenFOAM CFD code by KIT
ATHLET nodalization Phénix primary system (left), upper plenum in OpenFOAM (right)

4. Summary

Liquid metal cooled reactors will probably play an important role in our future nuclear energy production. Thermal hydraulics is recognized as a key design and safety factor in the realization of such reactors. The technological thermal hydraulics challenges for liquid metal cooled fast reactors have been classified and described according to the reactor subsystems to which they relate, i.e. the nuclear core, the reactor vessel or pool, the heat transfer systems, and the heat transport systems. This is followed by a description of the status of CFD developments and their future challenges as summarized below:

(1) Liquid metal turbulence
  (a) Heat transport modelling for RANS and LES
  (b) Thermal fluctuation prediction for thermal fatigue evaluation
  (c) Flow induced vibrations of e.g. a fuel pin
(2) Core thermal hydraulics

(a) Wire wrap fuel assembly simulation and validation
(b) Low resolution CFD modelling of a fuel assembly to assess blockage scenarios
(c) Coarse Grid CFD development to allow modelling a complete core

(3) Pool thermal hydraulics
(a) Pool modelling validation using prototypical scaled down facilities
(b) Fundamental validation using separate effect facilities, e.g. multiple jets
(c) Gas entrainment modelling and validation
(d) Seismic evaluations including liquid metal sloshing

(4) System dynamics.
(a) Coupling of STH and CFD

In general, the descriptions show the simultaneous need for developments with respect to experiments including measurement techniques and numerical simulations

ACKNOWLEDGEMENTS

The work and summary described in this paper was inspired and partly funded by the FP7 EC Collaborative Project THINS No. 249337. The authors explicitely wish to acknowledge the valuable contributions of CEA colleague Denis Tenchine to this article.

REFERENCES

[1] OECD/IEA, 2011. World Energy Outlook 2011: Presentation to the Press. London, UK.
[2] IAEA, 2012. Status of Fast Reactor Research and Technology Development. Technical Report 474, ISBN 978-92-0-130610-4, Vienna, Austria
[3] GIF, 2002. A Technology Roadmap for Generation IV Nuclear Energy Systems. Generation IV International Forum, GIF-002-00.
[4] Rehme K., 1973. Pressure Drop Correlation for Fuel Element Spacers. Nuclear Technology, vol 17.
[5] Bubelis E., Schikorr M., 2008. Review and proposal for best fit of wire-wrapped fuel bundle friction factor and pressure drop predictions using various existing correlations, Nuclear Engineering and Design, 238, pp. 3299-3320.
[6] Benhamadouche S., Le-Maitre C., 2009. Large Eddy Simulation of the Flow along Four Sub-channels Downstream a Mixing Grid in a PWR. NURETH13, Kanazawa, Japan.
[7] De Ridder J., Degroote J., Van Tichelen K., Vierendeels J., 2012. Partitioned Simulation of Long and Slender Cylinders Corresponding to Nuclear Fuel Rods Vibrating in Axial Flow. Eccomas 2012, Vienna, Austria.
[8] Tobita Y., Kondo SA., Yamano H., Morita K., Maschek W., Coste P., Cadiou T., 2006. The Development of SIMMER-III, an Advanced Computer Program for LMFR Safety Analysis, and its Application to Sodium Experiments. Nuclear Tecnology, volume 153, number 3, p.p. 245-255
[9] Tenchine D., 2010. Some Thermal Hydraulic Challenges in Sodium Cooled Fast Reactors. Nuclear Engineering & Design, vol. 240, p.p. 1195-1217.
[10] Velusamy K., Chellapandi P., Chetal S., Raj B., 2010. Overview of Pool Hydraulic Design of Indian Prototype Fast Breeder Reactor. Sadhana, vol. 35, p.p. 97-128.
[11] Uchibori A., et al., 2011. Numerical Analysis of Supersonic Gas Jets into Liquid Pools with or without Chemical Reaction Using the SERAPHIM Program, Nuclear Engineering and Design 249, 35-40
[12] Arien B. Et al., 2004. Assessment of Computational Fluid Dynamic codes for Heavy Liquid Metals – ASCHLIM. EC-Con. FIKW-CT-2001-80121-Final Rep
[13] OECD/NEA, 2007. Handbook on Lead-bismuth Eutectic Alloy and Lead Properties, Materials Compatibility, Thermal-hydraulics and Technologies. OECD NEA No. 6195, ISBN 978-92-64-99002-9
[14] Grötzbach G.,2007. Anisotropy and Buoyancy in Nuclear Turbulent Heat Transfer – Critical

Assessment and Needs for Modelling. FZKA 7363, Karlsruhe, Germany
[15] Grötzbach G., 2003. Turbulence Modelling Issues in ADS Thermal and Hydraulic Analyses. IAEA Technical Meeting on Theoretical and Experimental Studies of Heavy Liquid Metal Thermal Hydraulics, Karlsruhe, Germany
[16] Grötzbach G., 2011. Challenges in Simulation and Modeling of Heat Transfer in Low-Prandtl Number Fluids. NURETH14, Toronto, Canada.
[17] Kenjeres S., Gunarjo S.B., Hanjalic K., 2005. Contribution to elliptic relaxation modelling of turbulent natural and mixed convection. Int. J. of Heat and Fluid Flow, vol 26, p.p. 569-586.
[18] Kenjeres S., Hanjalic K., 2000. Convective Rolls and Heat Transfer in Finite-length Rayleigh-Bernard Convection: A Two-dimensional Numerical Study. Physical Review E, Vol 62., N. 6.
[19] Bricteux L., Duponcheel M., Winckelmans G., Tiselj I., Bartosiewicz Y., 2012. Direct and Large Eddy Simulation of Turbulent Heat Transfer at Very Low Prandtl number: Application to Lead-bismuth Flows. Nuclear Engineering & Design, vol. 246, p.p. 91-97.
[20] Hannink M., Kuczaj A., Blom F., Church J., Komen E., 2008. A Coupled CFD-FEM Strategy to Predict Thermal Fatigue in Mixing Tees of Nuclear Reactors. Eurosafe, Paris, France.
[21] Dahlberg M., et al., 2007. Development of a European Procedure for Assessment of High Cycle Thermal Fatigue in Light Water Reactors: Final Report of the NESC-Thermal Fatigue Project. European Commission Institute for Energy, EUR 22763 EN, Petten, Netherlands.
[22] Roelofs F., Gopala V.R., Jayaraju S., Shams A., Komen E., 2013. Review of Fuel Assembly and Pool Thermal Hydraulics for Fast Reactors. Submitted to Nuclear Engineering & Design.
[23] Kimura, N., Miyakoshi, H. and Kamide, H., 2007. Experimental Investigation on Transfer Characteristics of Temperature Fluctuation from Liquid Sodium to Wall in Parallel Triple-jet, Int. J. Heat and Mass Transfer, 50, pp.2024-2036
[24] Pointer W., Fischer P., Smith J., Obabko A., Siegel A., 2009. Simulation of Turbulent Diffusion in Wire-Wrapped Sodium Fast Reactor Fuel Assemblies. FR-09, Kyoto, Japan
[25] Hu R., Fanning T., 2010. Intermediate-Resolution Method for Thermal-Hydraulics Modeling of a Wire-Wrapped Pin Bundle. Transactions of the American Nuclear Society, vol. 103, pp. 1003-1005.
[26] Roelofs F., Gopala V.R., Chandra L., Viellieber M., Class A., 2012. Simulating Fuel Assemblies with Low Resolution CFD Approaches. Nuclear Engineering & Design, vol. 250, p.p. 548-559.
[27] Van Tichelen K., Mirelli F., Greco M., 2012. The European Heavy Liquid Metal Scaled Pool Facility E-SCAPE. SEARCH HLM Workshop 2012, Pisa, Italy.
[28] Tokuhiro A., Kimura N., 1999. An Experimental Investigation on Thermal Striping Mixing Phenomena of a Vertical Non-buoyant Jet with Two Adjacent Buoyant Jets as Measured by Ultrasonic Doppler Velocimetry. Nuclear Engineering & Design, vol. 188, p.p. 49-73
[29] Kimura N., Miyakoshi H., Ogawa H., Kamide H., Miyake Y., Nagasawa K., 2005. Study on Convective Mixing Phenomena in Parallel Triple-jet Along Wall – Comparison of Temperature Fluctuation Characteristics between Sodium and Water. NURETH11, Avignon, France.
[30] Merzari E., Pointer D.W., Obabko A., Fischer P., 2010. On the numerical simulation of thermal striping in the upper plenum of a fast reactor. ICAPP 2010, San Diego, USA.
[31] Patwardan A., Mali R., Jadhao S., Bhor K., Padmakumar G., Vaidyanathan G., 2010. Argon Entrainment into Liquid Sodium in Fast Breeder Reactor. NUTHOS-8, Shanghai, China
[32] Monji H., Akimoto T., Miwa D., Kamide H., 2004. Unsteady behavior of gas entraining vortex on free surface in cylindrical vessel, NTHAS4: Sapporo, Japan
[33] Kimura N., Ezure T., Tobita A., Kamide H., 2006. Experimental study on Gas Entrainment at free surface in reactor vessel for a compact sodium cooled fast rector – evaluation of dominant factors and mechanism for gas entrainment in large scale partial model. NTHAS5: Jeju, Korea
[34] Kimura N., et al., 2010. Experimental Study on Gas Entrainment Due to Non-stationary

Vortex in a Sodium Cooled Fast Reactor—Comparison of Onset Conditions Between Sodium and Water, Journal of Engineering for Gas Turbines and Power 132, 10, 102908.

[35] Gopala V.R., Roelofs F., 2009. Numerical Simulation of Liquid Lead Sloshing in the ELSY Reactor Vessel. 5th International workshop on materials for HLM-cooled reactors and related technologies (HeLiMeRT), Mol, Belgium

[36] Papukchiev A., Lerchl G., "Extension and Application of The Coupled 1D-3D Thermal-Hydraulic Code Athlet-Ansys CFX for the Simulation of Liquid Metal Coolant Flows in Advanced Reactor Concepts", Proceedings of the 14th International Conference on Nuclear Engineering, ICONE-20, July 30 - August 3, 2012

[37] Stempniewicz M., 2012. STH/CFD Code Coupling: Methods and Techniques Applicable for SPECTRA/OpenFOAM Coupling. NRG note 23067/12.114220, Arnhem, Netherlands

[38] Baviere R., Tauveron, N., Garré, E, 2013. System-CFD coupled simulation of the Phénix Reactor Natural Circulation Test. Submitted to NURETH13, Pisa, Italy.

[39] Fanning T.H., Thomas J.W., 2010. Advances in Coupled Safety Modeling Using Systems Analysis and High-Fidelity Methods. No. ANL-GENIV-134. Argonne National Laboratory (ANL), Argonne, USA.

Calculation and Analysis of Neutron Time-spatial Kinetics in uncontrolled withdrawal accident of regulating rod in CEFR

Xu Li, Yu Hong, Hu Yun, Huo Xingkai

China Institute of Atomic Energy

Abstract

In the accident analysis of China Experimental Fast Reactor (CEFR), uncontrolled withdrawal of regulating rod without scram is a severe accident. When it happens, a large positive reactivity will be introduced and the relative space distribution of neutron flux will change significantly. Thus the analytical result of the accident by point kinetics in the safety analysis of CEFR is inaccurate. In this paper, focused on neutronics behavior, the accident is re-evaluated with NAS-K code. The NAS-K code is a CEFR-self-developed three-dimensional space-time-dependent neutron kinetics code for sodium cooled fast reactors, including thermal feedback and various kinds of reactivity feedback effects. The calculation results indicate that the maximum temperatures of fuel and cladding do not exceed the limits specified by acceptance criteria corresponding to design basis accident for CEFR, which means the accident will not cause damage to CEFR core.

1. Introduction

China Experiment Fast Reactor (CEFR), with a nuclear heat power of 65 megawatts and a power-generating capacity of 20 megawatts, is the first fast reactor researched and developed independently by China Institute of Atomic Energy. CEFR achieved criticality for the first time on July 21st 2010, and successfully integrated into the grid for the first time on July 21st 2010.

In the accident analysis of China Experimental Fast Reactor (CEFR), uncontrolled withdrawal of regulating rod without scram is a severe accident. When it happens, a large positive reactivity will be introduced. In the previous analysis, the point-reactor model was used. After developing for several years, three-dimensional space-time-dependent neutron kinetics code for sodium cooled fast reactor is developed, with which the accident is re-evaluated.

The core is composed of 79 fuel subassemblies, 3 safety rods, 2 regulating rods and 3 shim rods. The equivalent diameter of the core is 60 cm and the height is 45 cm.

2. Calculation model

This chapter introduces the three-dimensional time-spatial kinetics code for fast reactors（NAS-K）. The code solves the transient, three-dimensional, multigroup diffusion or transport equations by factorizing the total flux into a time-dependent amplitude function and a space-energy-time-dependent shape function (improved quasistatic method). In this way, the transient equations can be decomposed into two parts: the shape function calculation, which can be solved by the steady-state reactor core calculation code (NAS), and the amplitude function calculation, which can be solved with third-order Hermite polynomials method.

NAS (Neutronics Analysis System for Fast reactor) was developed by China Institute of Atomic Energy. It consists of several groups of functions: the diffusion calculations, the transport calculations, the burn-up calculations, the perturbation calculations, the dynamic parameters calculations, the in-core fuel management. NAS uses three dimensional nodal method, which has computing efficiency.

Compared with the thermal reactors, the core size is smaller and the mean free path is longer in the fast reactors. Therefore, the nodal method can reach high accuracy.

2.1. Improved Quasistatic Method

The time-dependent multigroup neutron-diffusion and delayed-neutron precursor equations in energy group *g* without external source of neutrons in the system are:

$$\frac{1}{v_g}\frac{\partial \Phi_g(r,t)}{\partial t} = D_g \nabla^2 \Phi_g(r,t) - \Sigma_{r,g}\Phi_g(r,t) + \sum_{g'}^{g-1} \Sigma_{g'\to g}\Phi_{g'}(r,t) + (1-\beta)\chi_{p,g}\sum_{g'=1}^{G}(\nu\Sigma_f)_{g'}\Phi_{g'}(r,t) + \chi_{d,g}\sum_{k=1}^{N}\lambda_k C_k(r,t) \tag{1}$$

$$\frac{\partial C_k(r,t)}{\partial t} = \beta_k \sum_{g'=1}^{G}(\nu\Sigma_f)_{g'}\Phi_{g'}(r,t) - \lambda_k C_k(r,t) \tag{2}$$

where: $D_g = 1/\Sigma_{tr,g}$ --the diffusion coefficient;

$\beta = \sum_{k=1}^{N}\beta_k$ --total delayed-neutron fraction;

G--number of energy groups;

N--number of precursor groups;

v_g --neutron velocity in energy group *g*;

$\Phi_g(r,t)$ --neutron flux in energy group *g*;

$C_k(r,t)$ --delayed-neutron precursor concentration in group *k*;

The conceptual basis of this method is the factorization of the multigroup flux into an amplitude function and a time-dependent shape function:

$$\Phi_g(r,t) = p(t)\psi_g(r,t) \tag{3}$$

where, $p(t)$ is the amplitude function, and $\psi_g(r,t)$ is the shape function.

To make sure that N(t) contains the main time dependence of the total flux, the normalization constraint of the shape function is:

$$\sum_{g=1}^{G}\int_V \frac{\Phi_g^*(r)\psi_g(r,t)}{v_g}dV = 1 \tag{4}$$

where, $\Phi_g^*(r)$ is the normalized static adjoint flux of group *g*. The shape-function equation and The spatial precursor equations are obtained by substituting Eq. (3) into Eq. (1) and Eq. (2):

$$\frac{1}{v_g}\frac{\partial \psi_g(r,t)}{\partial t} = D_g\nabla^2\psi_g(r,t) - \Sigma_{r,g}\psi_g(r,t) + \sum_{g'}^{g-1}\Sigma_{g'\to g}\psi_{g'}(r,t) + \frac{1}{p(t)}\chi_{d,g}\sum_{k=1}^{N}\lambda_k C_k(r,t) + (1-\beta)\chi_{p,g}\sum_{g'=1}^{G}(\nu\Sigma_f)_{g'}\psi_{g'}(r,t) - \frac{\psi_g(r,t)}{v_g}\frac{\dot{p}(t)}{p(t)} \tag{5}$$

$$\frac{\partial C_k(r,t)}{\partial t} = \beta_k p(t)\sum_{g'=1}^{G}(\nu\Sigma_f)_{g'}\psi_{g'}(r,t) - \lambda_k C_k(r,t) \tag{6}$$

The point kinetics equations are derived by weighting Eq. (5) and Eq. (6) with $\Phi_g^*(r)$ and integrating over volume, summing over energy and taking into account Eq. (4):

$$\begin{aligned}\Lambda(t)\,\dot{p}(t) &= [\rho(t)-\beta(t)]p(t) + s_d(t)\\ \dot{c_k}(t) &= -\lambda_k c_k(t) + \frac{1}{\Lambda(t)}\beta_k(t)\,p(t)\end{aligned} \tag{7}$$

where,

$$\Lambda(t) = \frac{K_0}{F(t)} \tag{8}$$

$$\rho(t) = 1 + \frac{1}{F(t)}\sum_{g=1}^{G}\int_V \Phi_g^*[D_g\nabla^2\psi_g - \Sigma_{r,g}\psi_g(r,t) + \sum_{g'}^{g-1}\Sigma_{g'\to g}\psi_{g'}(r,t)]dV \tag{9}$$

$$\beta_k(t) = \frac{1}{F(t)}\sum_{g=1}^{G}\chi_{d,g}\int_V \Phi_g^*\beta_k\sum_{g'=1}^{G}(\nu\Sigma_f)_{g'}\psi_{g'}dV \tag{10}$$

$$\beta(t) = \sum_{k=1}^{N}\beta_k(t) \tag{11}$$

$$c_k(t) = \frac{1}{K_0}\sum_{g=1}^{G}\chi_{d,g}\int_V \Phi_g^*\beta_k C_k(r,t)dV \tag{12}$$

$$s_d(t) = \frac{1}{F(t)}\sum_{k=1}^{N}\lambda_k\sum_{g=1}^{G}\chi_{d,g}\int_V \Phi_g^*\beta_k C_k(r,t)dV = \Lambda(t)\sum_{k=1}^{N}\lambda_k c_k(t) \tag{13}$$

$$K_0 = \frac{1}{v_g}\int_V \Phi_g^*\psi_g dV \tag{14}$$

$$F(t)=\sum_{g=1}^{G}[\chi_{d,g}\int_V \Phi_g^* \beta_k \sum_{g'=1}^{G}(\nu\Sigma_f)_{g'}\psi_{g'}dV+\chi_{p,g}\int_V \Phi_g^*(1-\beta)\sum_{g'=1}^{G}(\nu\Sigma_f)_{g'}\psi_{g'}dV] \tag{15}$$

large integration time steps ($[t_{s-1}^s, t_s^s]$) can be used for the calculation of the shape function $\psi_g(r,t)$. the largest time interval is $\Delta t_s^s = t_s^s - t_{s-1}^s$. A simple backward difference in time is used to approximate Eq. (5), from which we obtain:

$$\begin{aligned} &D_g\nabla^2\psi_g(r,t_s^s)-\Sigma_{r,g}\psi_g(r,t_s^s)+\sum_{g'}^{g-1}\Sigma_{g'\to g}\psi_{g'}(r,t_s^s)+(1-\beta)\chi_{p,g}\sum_{g'=1}^{G}(\nu\Sigma_f)_{g'}\psi_{g'}(r,t_s^s)\\ &-\frac{\psi_g(r,t_s^s)}{v_g}\frac{\dot{p}(t_s^s)}{p(t_s^s)}-\frac{\psi_g(r,t_s^s)}{v_g\Delta t_s^s}=-\frac{1}{p(t_s^s)}\chi_{d,g}\sum_{k=1}^{N}\lambda_k C_k(r,t_s^s)-\frac{\psi_g(r,t_{s-1}^s)}{v_g\Delta t_s^s} \end{aligned} \tag{16}$$

In solving Eq. (16), $p(t_s^s)$, $\dot{p}(t_s^s)$, $C_k(r,t_s^s)$ and $\psi_g(r,t_{s-1}^s)$ are all known conditions. Therefore, to solve Eq. (16) is equal to solve the steady-state diffusion equations with external source, which can be easily solved by NAS system.

Eq. (7) is point kinetics equations, of which small time steps is used for the calculation.

From Eq. (4) we obtain:

$$c_k(r,t_2)=c_k(r,t_1)\exp(-\lambda_k(t_2-t_1))+\int_{t_1}^{t_2}\exp[-\lambda_k(t_2-t)]\sum_{g=1}^{G}\beta_k(\nu\Sigma_f)_g\,p(t)\psi_g(r,t)dt \tag{17}$$

In solving Eq. (6), $p(t)$ (which is a third-order polynomial in this paper) is obtained by solving point kinetics equations. The shape function $\psi_g(r,t)$ is assumed to vary linearly over the largest time interval Δt_s^s.

2.2. point kinetics

Eq. (8) is point-reactor kinetics equation group, for which third-order Hermite polynomials[1] are used in this paper. This method is characterized by the small computational workload and time efficiency. It can not only ensure the continuity of the amplitude function, but also give the rate of the amplitude change in the node, which is a necessary parameter to calculate the shape function.

The accuracy of the method depends on whether the third-order Hermite polynomials can get desirable accuracy approaching the desired amplitude function. Variable step algorithm is used in order to ensure the required accuracy.

2.3. Inner process by NAS-K

2.3.1. Calculation method of shape function

In solving the Eq. (17), the NAS system is used, which uses the nodal expansion method with high calculation speed. It can well describe the three-dimensional layout of the components and the control rod.

2.3.2. Calculation method of macroscopic cross section and dynamic parameters

In the reactor, the control rods moving or temperature change result in local material composition changes over time. In this case, the real time group collapsing calculation and the method of flux volume weighting homogenization are used. Then the dynamic parameters can be calculated according to Eq. (8) to Eq. (15).

2.3.3. Calculation method of temperature field

In this paper, the temperature field is calculated using the single-channel model, which is developed referring on RTEMP[2] code. Fuel temperature distribution is calculated using Kirchhoff transformation, and the radial conductivity is obtained by weight residue method. Cladding transient radial heat transfer equation is dealt with lumped parameter method. Second-order upwind difference[3] is selected in discrete form of a coolant convection term, and in the calculation of the radial heat, coolant temperature and the heat transfer coefficient of the surface are also calculated using lumped parameter method.

3. Uncontrolled withdrawal of regulating rod without scram

In this chapter, the uncontrolled withdrawal of regulating rod without scram in CEFR is re-evaluated with NAS-K code, and the results are compared with the results calculated with NKF code.

The NKF code is a point-reactor neutron kinetics code for fast reactor. It is tested with a number of published benchmark problems. A good agreement on results is achieved and the program is validated.

3.1. Numerical results

With NKF code, the uncontrolled withdrawal of regulating rod without scram is simulated by introducing 0.0015Δk/k reactivity in 15s:

$$\rho_e(t) = \begin{cases} 0.0001\,t & t < 15.0\ s \\ 0.0015 & t \geq 15.0\ s \end{cases} \tag{18}$$

With NAS-K code, this accident is simulated by the withdrawal of one regulating rod from the bottom to the top in 15 s.

Table 1 lists P (t) / P (0) changes over time calculated by NAS-K and NKF. Table 1 also indicates that the results in first 10 s between two codes have larger difference than at other time, which is mainly due to that the reactivity introduced in NKF code is linear, but in NAS-K code, it is the withdrawal of the regulating rod that is linear. Thus the reactive introduced is smaller at the initial stage, and then gradually increases, and is finally equal with NKF code.

Table 1. P(t)/P(0) varying with time during transient of regulating rod uncontrolled elevation.

Time / s	NKF	NAS-K	Rel. Diff / %*
0.0	1.0	1.0	0.000
5.0	1.0575	1.0305	-2.553
10.0	1.1074	1.0923	-1.364
15.0	1.1605	1.1608	0.026
20.0	1.1596	1.1546	-0.431
50.0	1.1735	1.1649	-0.733
100.0	1.1795	1.1695	-0.848
150.0	1.1812	1.1707	-0.889
200.0	1.1817	1.1712	-0.889

*: Relative Difference = (NAS-K - NKF) / NKF×100%

Figure 1 and Figure 2 are comparisons of the relative power and reactivities calculated by NKF and NAS-K. Figure 1 and Figure 2 also show that the changes with time of the relative power with two codes coincide rather well, and the changes with time of the reactivity are also approximately the same except the one in the initial stage.

Table 2 lists the outlet temperature changes of the sodium with two codes, and shows that the final temperature rise is approximately the same.

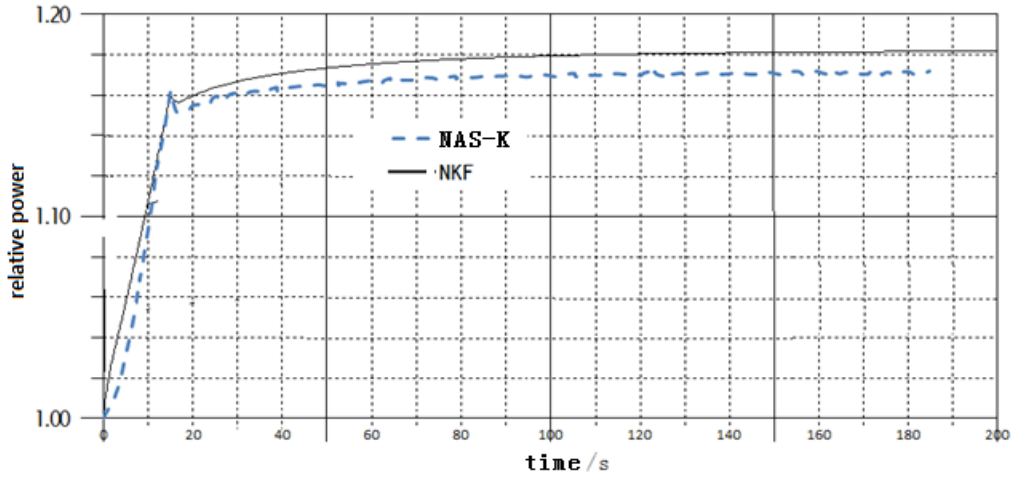

FIG. 1. Comparison of computation results of relative power.

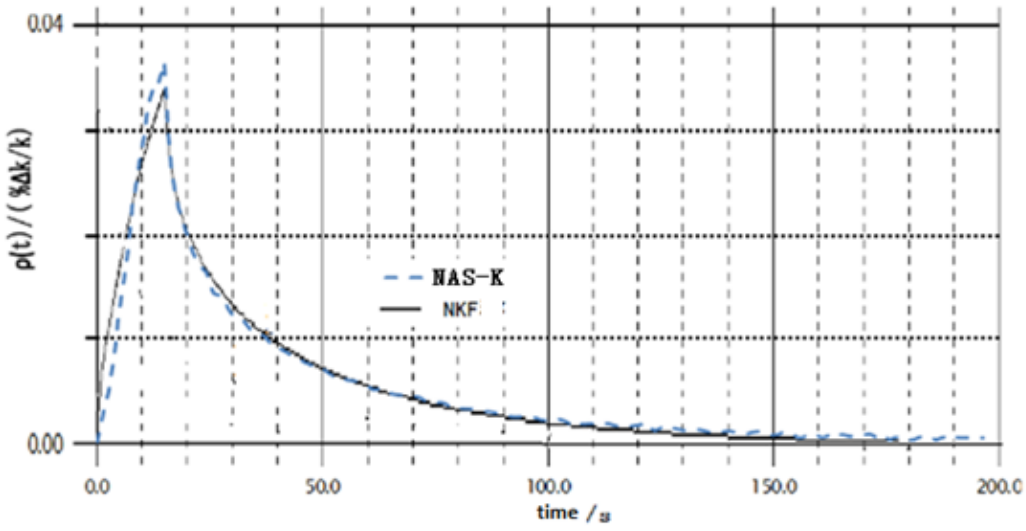

FIG. 2. Comparison of computation results of reactivity.

Table 2. Changes of coolant temperature.

Average outlet temperature /℃	NKF	NAS-K
beginning	530	555
end	561	586
Difference	31	31

3.2. Analysis of Result

Figure 1, Figure 2 and Table 1 show that the calculated results of relative power between two codes are not big differences, there are certain deviations. The reasons causing the deviation may be as following:

1) different feedback calculation model:

In NKF code, the value of the reactivity is obtained by the calculation formula of the reactivity, in which the fuel temperature and the coolant temperature and some other parameters are averages over the whole core, without considering the differences in the various components, and the temperature feedback coefficients are given in advance, and does not change with temperature.

In NAS-K code, the feedback effects are directly reflected in the cross section, considering the changes of spatial distribution and the relationship between the rate of various reactivities and the current temperature. Thus, the feedback model of the NAS-K is more accurate.

2) Spatial effect:

Figure 3 shows the spatial distribution of the relative power of each assembly at initial time. The assembly whose value is 0 is the control rod assembly or the neutron source assembly in the center. Figure 3 also shows that the power distribution is high in the middle, and low in the surrounding.

Figure 4 shows the relative deviation between the relative power at the final time and the initial time of each fuel assembly. Figure 4 also shows that the relative powers of the fuel assembly near the moved regulating rod have a greater increase, Nevertheless, in other regions although the relative power is decreased, the decreased amount is much smaller.

Figure 5 shows the relative power versus time.

Since the local power changes are relatively large, the feedback effects in the regions are more obvious. The spatial effect is not considered in the NKF, as a result a smaller feedback effect is obtained, which makes the final power larger.

The above analysis shows that compared with point reactor model NAS-K in the calculation of the transient process is greatly improved.

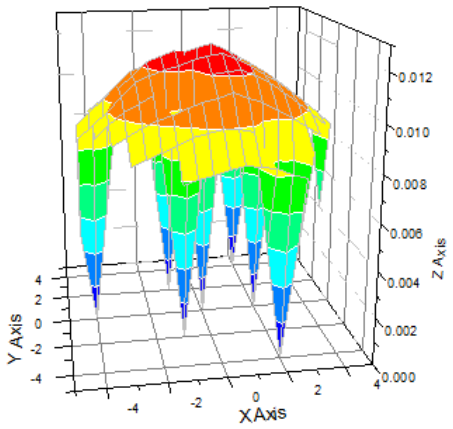

FIG. 3. Relative power distribution at initial time.

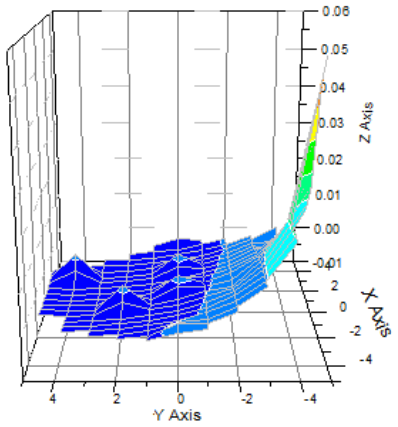

FIG. 4. Relative deviation of relative power at end time and initial time.

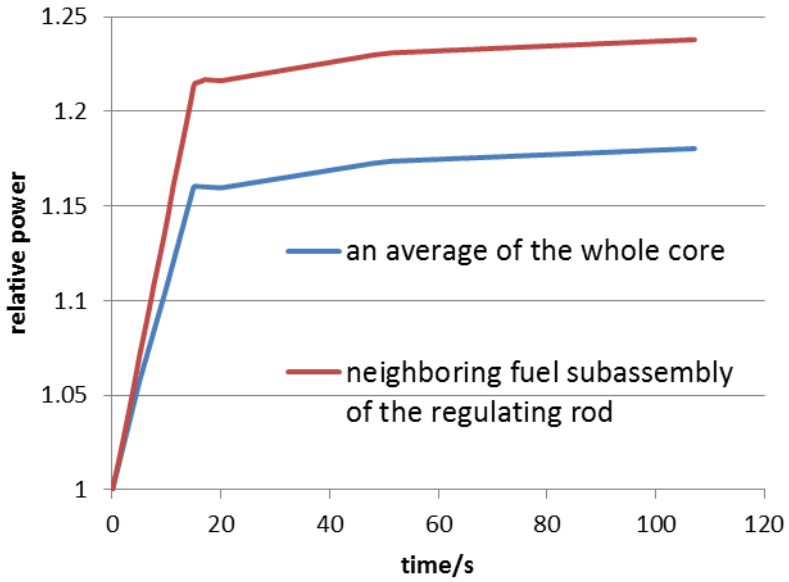

FIG. 5. Relative power distribution versus time

4. Conclusions

This paper briefly introduces the fast neutron space-time kinetics model. The uncontrolled withdrawal of regulating rod without scram in CEFR is analyzed with NAS-K code. Compared with the point reactor model, this model gives better results.

ACKNOWLEDGEMENTS

The report describes research sponsored by Chinese Ministry of Science and Technology (PROJECT No. 2011AA050301)

REFERENCES

[1] Tian Hechun. Interpolation polynomial Approach to Reactor Kinetics Equations[J]. Nuclear Power Engineering. 1989, 10(6):39-46.

[2] Jia Baoshan, Peng Muzhang, Zhao Zhaoyi, et al. RTEMP—A Computer Program for the Transient Thermal Transfer Analysis in Nuclear Fuel Elements by Using the Method of Weighted Residuals. 1983, 4(6):73-80.

[3] Wang Wujun, Shan Jianqiang, Zhu Jizhou. Method of Fully Implicit Second-order

Upwind Difference in Fast Reactor Simulation. Chinese Journal of Nuclear Science and Engineerin. 1999, 19(4):309-314.

APOLLO3® Roadmap for a new generation of simulation tools devoted to the neutronic core calculation of the ASTRID integrated technology demonstrator

B. Roque[a], P. Archier[a], P. Bourdot[a], C. De-Saint-Jean[a], F. Gabriel[b], J.-M. Palau[a], V. Pascal[a], D. Schneider[b], G. Rimpault[a], J.-F. Vidal[a]

[a] DEN/DER/SPRC/French Alternative Energies and Atomic Energy Commission, Cadarache Center, France

[b] DEN/DM2S/SERMA/French Alternative Energies and Atomic Energy Commission, Saclay Center, France

Abstract. Designing future Sodium Fast Reactors (SFR) requires enhancing their operational performance and reducing the probability to go into core disruption. As a consequence of these constraints, these novel reactors exhibit rather unusual features compared to past designs. The studies related to the development of a 4th generation fast neutron reactor called ASTRID (Advanced Sodium Technological Reactor for Industrial Demonstration) require improved tools with accuracies meeting the design team requirements. Concurrently, CEA and its industrial partners have launched a large program for developing a new generation of simulation tools facing the challenges of multiphysics coupling and high-performance computing on massively parallel computers. In this context, the new APOLLO3® code, under development at CEA, will take over, after a commissioning period, the ERANOS2 code, currently used for ASTRID conceptual design. The APOLLO3® code will take advantage of new numerical developments for neutronic core reactor calculations. The transition is defined so as to meet the ASTRID development plans and will require the achievement of five main tasks that will be described in this paper. A planning for the different actions to be conducted to achieve the uncertainty quantification of the APOLLO3® computational schemes, in time for calculating the detailed design phase of ASTRID project, is being set up.

INTRODUCTION

Sodium Fast Reactors (SFR) have acquired years of experience with the design, construction and operation of several reactors: in France, the experimental Rapsodie reactor (initially 25 MWth, later upgraded to 40 MWth), the prototype Phénix (250 MWe) and the large-size Superphénix (1240 MWe) reactors.

Designing future SFR reactors requires however to enhance their operational performance and reduce the probability to go into core disruption. These novel reactors have a rather large core with a flat shape, in particular to reduce significantly the Sodium Void Effect (SVE)[1]. This unusual shape has various design consequences on their core characteristics over the fuel cycle and for some transients.

Sodium Void Effect (SVE) is the difference between the reference configuration reactivity and the one of the void state. This effect was positive in past designs of significant sizes like Phénix and Super-Phénix and hence, although the plant is not pressurized and the margin to sodium boiling is very large, the appearance of a sodium void in some core zones (by boiling, draining or uncontrolled passage of a bubble of gas) could not be ruled out entirely. Since the future Sodium Fast reactors must have a high safety level, the reduction of the positive SVE

was looked for large reactor cores, the only ones likely to achieve a positive breeding gain and hence to use the entire Uranium ore.

The core of the ASTRID Advanced sodium technological reactor for industrial demonstration[2] has features which reduce the SVE to low values. It is called the CFV concept (Low Void Core)[3]. To reduce the sodium void worth, the first choice was to choose a rather fat pin together with a reduction of the space wire which enables to reduce the sodium volume fraction and hence the SVE. Since this was not sufficient, a sodium plenum zone at the top and an internal blanket at the mid-plane were introduced in the core. The use of an internal blanket in a core with reduced core height increases the gradient of the neutron flux level at the upper surface and even more in case of sodium voiding. The use of an absorbing zone in upper shielding prevents neutrons to return to the core during voiding.

The core lay-out of this CFV is shown in Figure 1.

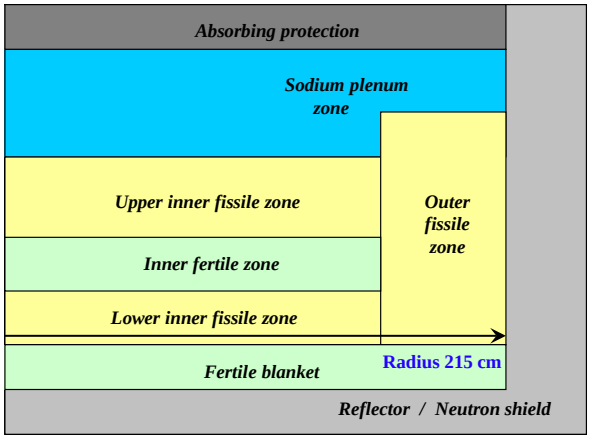

FIG. 1. section of the ASTRID core (1500 MWth)

This picture combines many geometric features (fertile, plenum sodium, absorbing plate, reduced core height configuration) that lead to negative global void reactivity changes (-$0.5 at the end of the Fuel Cycle) without degrading performance. This is obtained for a breakeven core with total breeding gain close to zero, with a rather small reactivity swing over the cycle (4.3 pcm/efpd). In the core development process, new materials are likely to be retained in order to improve the core performance. The envisaged absorbent materials are: B4C, Hf (to improve the residence time) or for reflector: steel, SiC, $^{11}B_4C$, $MgAl_2O_4$ (to improve the power map at the core edge). To increase the capability of these cores to recycle the minor actinides without degrading their intrinsic safety characteristics, fertile blankets loaded with Americium can be placed in dedicated sub-assemblies surrounding the core[4].

New computational schemes, currently being developed, are aiming at solving these new problems arising from the innovative ASTRID features:

- Fertile plate: impact of the fuel composition with burn up on the axial power distribution and on the sodium void
- Sodium Plenum
  - significant neutron leakage effects with and without sodium
  - influence of the absorbers beyond the plenum
  - control rods have a large part of their absorption in this zone
- Interaction plate/plenum (axial distribution, effect on sodium void)
- Diabolo effect with an inner core height smaller than the outer core height
- Steel reflectors or innovative materials

- Radial blankets loaded with Minor Actinides
- Compact neutron shielding.

These neutron features require more precise nuclear data, new solvers with dedicated verification and validation process, new computational schemes and experiments in support. Therefore, it is quite important to plan a set of verifications, validations and uncertainty quantifications of the computational tools to meet the designer needs and reactor safety requirements.

In this paper, we will present the different actions to be conducted over the next years to achieve the uncertainty quantification of the APOLLO3® computational schemes in time for calculating the detailed design phase of ASTRID project.

1. Overview of APOLLO3® and description of a SFR data model

1.1. Objective of the APOLLO3® platform

Improved numerical codes simulating core physics are required to assess operating margins and uncertainties in current reactor generation or to design new reactors. To meet these design objectives, the development of a new neutronic platform has been initiated by the CEA. The envisioned new platform provides a complete and coherent nuclear system from nuclear data treatment tools to cycle calculations through reactor physics codes. The APOLLO3® code[5], as a 3D deterministic multi-purpose code for any kind of reactor concepts, is a part of this neutronic platform. Its development is supported by AREVA and EDF.

Developments and calculations carried out with APOLLO2[6], CRONOS2[7] and ERANOS2[8] codes provide resourceful experiences that have been used to improve models and numerical methods (flux solvers and self-shielding methods with new acceleration or effective parallelization methods) in APOLLO3®. The main technical guidelines also leading the developments are:

- Extended application domain: criticality, shielding for all kind of reactors (PWR, BWR, GFR, SFR, SCWR…);
- Coupling through SALOME platform for multi-physics calculations (thermo-mechanics, thermal-hydraulics);
- Uncertainties assessment with perturbation methods (internal library) and non-intrusive methods (URANIE platform);
- Ability to perform high performance computing.

Another important objective is to perform reference as well as design or industrial calculation routes with a user friendly interface allowing easy implementations of new methods and models for both lattice and core flexible calculation routes.

Parallelization is also one of the major stakes for APOLLO3®. In deterministic simulation, three main levels of parallelism can be considered[9][10] :

- The first level concerns multi-parameterized calculations. It is implemented using a distributed computing approach, since each calculation is independent of the others. A classical example is the multi-parameters assemblies calculation, when one has to compute different kinds of reactor assembly for core code calculation.

- The second level corresponds to multi-domain calculations. It is implemented using a coarse grain parallelism approach. It concerns all the treatment dealing cross sections, depletion process, thermal-hydraulic feedback, etc. At this level, we usually consider that the spatial dependency of the data is very tight and a massively parallel approach is well suited. When the spatial dependency of the data is strong, domain decomposition techniques are often used.
- The third level concerns the fine grain parallelization of solvers by exploiting intrinsic parallelism of the involved numerical methods.

These levels are currently under investigation.

1.2. Development of a specific SFR data model

A specific data model will be developped, within the APOLLO3® framework, in order to meet the particular needs of SFR studies. This data model consists of a set of several abstract C++ classes allowing the implementation of generic data containers. These containers can be used to store physical quantities such as cross sections, flux or volumic power.

The SFR data model is based on the concept of “meshfield”, which can be defined as follow : “a meshfield is a “quantity” defined on a whole mesh with a set of mathematical functions attached to mesh elements”. These objects do not depend on numerical solvers but only on the problem geometry. This solver-independant approach is particularly useful for the development of calculation schemes combining several numerical solvers.

Within this approach, physical quantities can be defined and evaluated in any point of the mesh. For instance (FIG 2.), the core volumic power can be spatially defined as follow :

$$P^K(x,y,z) = \sum_{i=0}^{N} a_i * f_i^K(x,y,z), \qquad \text{where}$$

f_i^K represents a base of mathematical functions attached to the cell K.
Of course, as abstract meshes are generic objects, they can be defined in 1D, 2D or 3D and represent spatial, angular or energetic meshes.

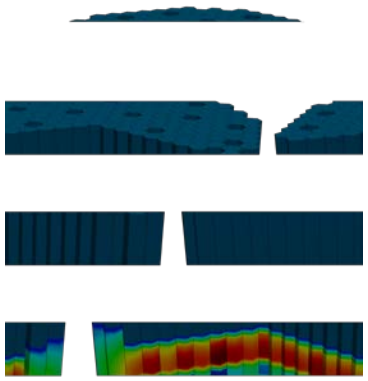

FIG. 2. Example of discrete evaluation on a 3D spatial mesh (power density)

A large set of functionalities has been defined to manipulate these objects (addition, substraction, multiplication, cross product, cell integration, mesh projection, …).

The representation of quantities, depending on several variables attached to different meshes, is based on the concept of field overlapping. This approach is detailed in the Figure 3 for the case of a multi-group angular flux based on the finite elements method for the spatial treatment. The first-level meshfield associates a one-dimensional energetic mesh to a set of second-level meshfields representing mono-energetic angular fluxes. The second-level meshfields associates an angular mesh to a set of third-level meshfields representing mono-energetic and one-way fluxes. The third-level meshfields associates a three-dimensionnal spatial mesh to a set of discontinueous finite elements bases.

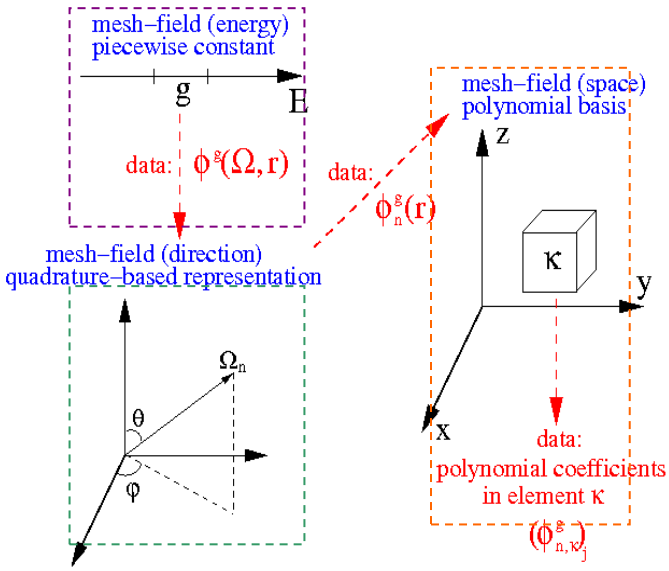

FIG. 3. Representation of a multigroup angular flux with the overlap of 3 meshfields

The implementation of this SFR data model should be done within the framework of APOLLO3®. This model will use the APOLLO3® functionnalities in terms of Application Programming Interface to ensure the quality of the final product. Some interfaces do not exist at this time and have to be developped.

A simple two-dimensionnal benchmark has been defined to test and prepare the implementation of the SFR data model. The geometry contains 100 cells for 3 mediums (MOX fuel, control rod with enriched boron carbide, radial neutronic protection), as detailed in the FIG4-a). Self-shielded effective cross sections were processed with the cell code ECCO in 33 energetic groups. The FIG4–b) presents the evaluated flux calculated with the first functionalities of the SFR data model.

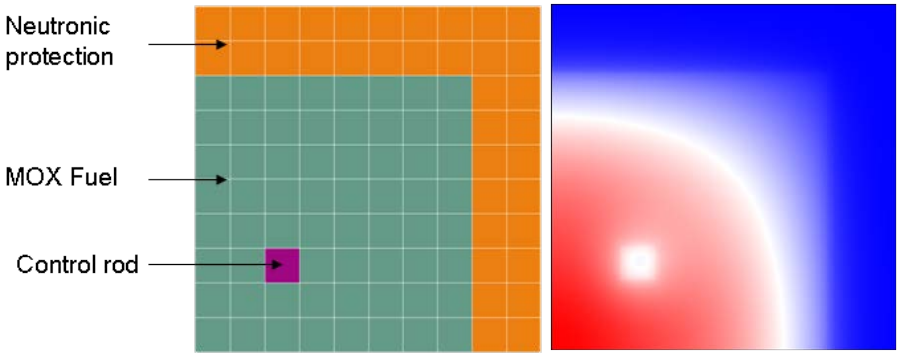

FIG. 4.(a) Simple benchmark geometry - (b) Scalar flux evaluated in any point of the grid

2. The APOLLO3® VVUQ process devoted to ASTRID

2.1. VVUQ general strategy

In order to supply a reliable code product to designers and users performing neutronic ASTRID core calculations, a rigorous method, called VVUQ is being used. VVUQ stands for Verification, Validation and Uncertainty Quantification.

a) The first step of the VVUQ process verifies that the numerical resolutions of neutronics solvers and the programming of each solver are correct. This step is important in order to avoid any possible drawback in a latter stage of the VVUQ process. A Test Machine incapsulating all the tests already approved will be available to verify the non-regressive aspect of the code.

b) The second step corresponds to the Validation, which evaluates the accuracy of the neutronics models and functionalities (Pij, resonance self-shielding, fine flux, depletion, accurate SPH homogenization, Sn, MOC) as well as calculation schemes used in APOLLO3®. This Validation is based on comparisons with continuous-energy Monte Carlo TRIPOLI4[11]. Theses comparisons are first performed on numerical benchmarks, representative of SFR geometries to identify the biases of APOLLO3® solvers. Then, choices of calculation routes will be made by comparing different cost to performance ratios for Reference Computational Scheme and the Design Computational Scheme. The final objective of this step is to calculate the associated bias of each design parameter on “true” ASTRID core configurations.

c) The Uncertainty Quantification (UQ) is finally carried out by comparing results of the global package APOLLO3®/SCHEME/JEFF3.1.1 against measurements from dedicated experimental programmes and transpose the experimental uncertainties to design neutronic parameters.

2.2. The evaluation and processing of SFR dedicated nuclear data

In the [eV;MeV] energy range, modeling of the neutron induced reactions are based on nuclear reaction models having parameters. Some of them, which are not predicted by the theory and cannot be directly measured, can be evaluated by fitting experimental data sets. Therefore, different types of experiences are analysed :

- microscopic experiences,
- analytical integral experiences that target the influence of a given isotope,
- irradiation in reactors: irradiated fuel or dedicated target,
- integral experiments involving several isotopes.

This process is illustrated on the figure 5 below :

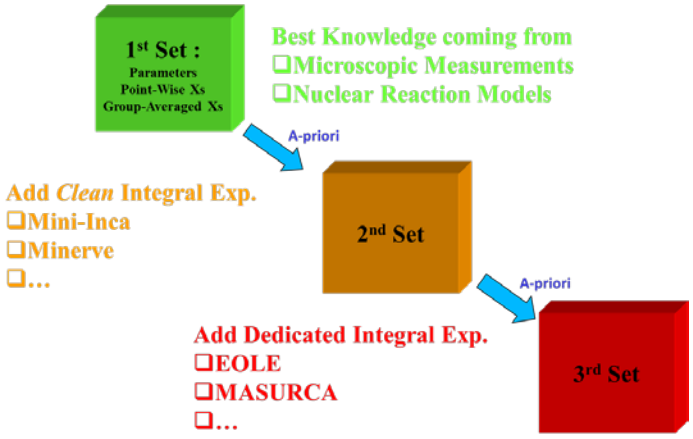

FIG. 5. Nuclear Data Improvement through Experiment Assimilation

This data assimilation procedure (Figure 5) is made with the CONRAD code[12] which proposes a mathematical framework to add integral experiments information during the evaluation process. For the first two sets of covariances, a direct contribution by isotope is considered. Nuclear data considered are then of multipurposes (PWR, BWR, FR, HTR,…). The last set, devoted to multigroup cross sections covariances, is diretly related to SFR studies and will be done in the framework of the VVUQ process.
A general nuclear data evaluation program is underway, focusing on actinides and fission products of interest for SFR as well as relevant structural or moderator materials. For exemple, a new Sodium nuclear data file was proposed to the JEFF community.

To be able to take into account integral experiments, neutronic tools must have the ability to model accurately the experiments and perform perturbation methods (Simple Perturbation Theory and Generalised Perturbation Theory) in 3D transport theory and with time dependance (burn up and kinetics). Thus, in APOLLO3®, dedicated perturbations procedures will be developped based on solvers capabilities to allow adjoint calculations.

2.3. The specific V&V APOLLO3® process for SFR

2.3.1. Validation Steps in the course of the code development

The verification and validation of the solvers are important steps in the VVUQ process of the APOLLO3® tools. In order to minimise the magnitude of this work, an incremental program has been set up. This first step will be dedicated to reproducing results achieved by the solvers of the previous computational scheme ERANOS2.2, in conditions for which it has been validated.

Of course, that stage of code development will not meet the specific requirements associated to the novel features of the ASTRID core but already some solvers will be eliminated in that process since fast reactor cores have their own specific requirements compared to PWRs.

2.3.2. V&V in progress

The verification and validation of the core solvers at the elementary stage is in progress. The objective of the current work is to test all the core solvers available in ERANOS, PARIS, CRONOS2 and APOLLO3® for specific SFR needs and especially ASTRID.

The tests are carried out on simple benchmarks of TAKEDA type[13] (anticipating needs on the SFR control and safety rods) further extended for models with a sodium plenum (anticipating needs of treatment of empty media). More complex benchmarks on large cores able to reproduce power map aspects of SUPER-PHÉNIX and to reproduce the effects of the CFV core of ASTRID, will follow.

Existing spatial solvers will be used ; they can be classified according to their mode of resolution: discrete ordinates (Sn), transport nodal finite element with spherical harmonics (Pn, and SPn, which is a simplified Pn method where the angular flow is discretized), Monte Carlo. The list of solvers is the following:

- VARIANT (Pn) and H3D (finite difference; diffusion theory) (ERANOS solvers)[14]
- SNATCH (Sn) (PARIS solver)[15]
- MINOS (SPn) (APOLLO3® solver)[16]
- MINARET (Sn) (APOLLO3® solver)[17]
- Reference: TRIPOLI4 (Monte Carlo)

First results have been obtained for the Takeda model 4 (Figure 6) which includes 3 configurations depending on the control rod position (withdrawn, half-inserted or fully inserted). These results are in good agreement with the TRIPOLI4 Monte-Carlo reference results as well as values given in the benchmark, particularly for the Sn and Pn calculations.

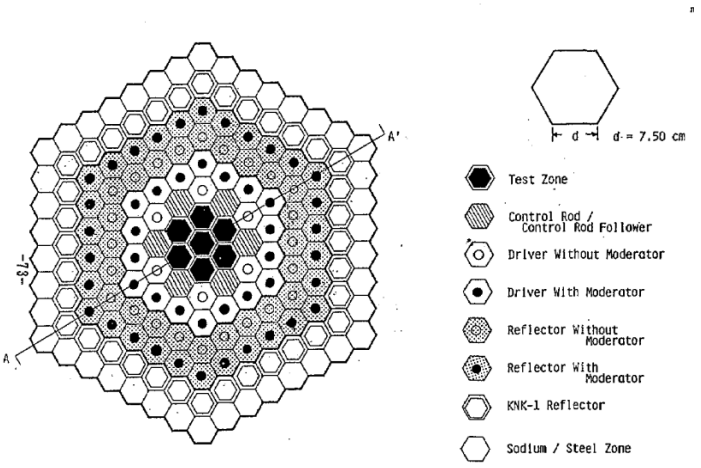

FIG. 6. Hexagonal geometry of the Takeda benchmark 4

2.4. Sodium fast reactor protocols

The V&V work is a huge work that has already began but involves the full set of solvers able to reproduce previous ERANOS2.2 computational scheme. A significant number of solvers is available at the beginning of 2013. In order to anticipate the possibility of performing relevant computational schemes for ASTRID and prior to the full V&V process, several simulations have been carried out to check the implementation of the numerical developments for static and depletion analysis, kinetics and multi-physics coupling and high performance computing applied to sodium fast reactors.

Within that purpose, a sodium fast reactor concept typical of a Generation IV fast breeder concept has been simulated. This reactor core has a 3600 MWth power and uses MOX fuel ($(U,Pu)O_2$). The studied core (see Figure 7) consists of 17 rings of assemblies. The inner and outer fuel regions have different Pu mass content. There are 225 inner fuel sub-assemblies and 228 outer fuel sub-assemblies. The control rod system is composed of 9 DSD (Diverse Shutdown Device) and 24 CSD (Control and Shutdown Device). The CSD rod absorber contains natural boron carbide (~19.9% of ^{10}B) whereas the DSD rod absorber contains enriched boron carbide (90% of ^{10}B).

B). Outside the core, the reflectors consist of three rings of assemblies.

Cross-sections in 33 or 299 energy groups have been provided by ECCO, the cell code of ERANOS2. The control rod cross sections have been processed without the reactivity equivalence procedure.

MINOS and MINARET solvers were used with various energy meshes (33 and 299 groups cross-sections libraries), with several order of angular discretization (SP1 to SP5 and S2 to S8) and several spatial mesh refinements. Effective multiplication factor, breeding gain, spectrum hardness factor, Doppler and void effects and control rod worth have been calculated in both situations and have shown the consistency of the implemented numerical

methods. A depletion analyze has also been performed with both MINOS and MINARET on a geometry composed of 18 axial plans.

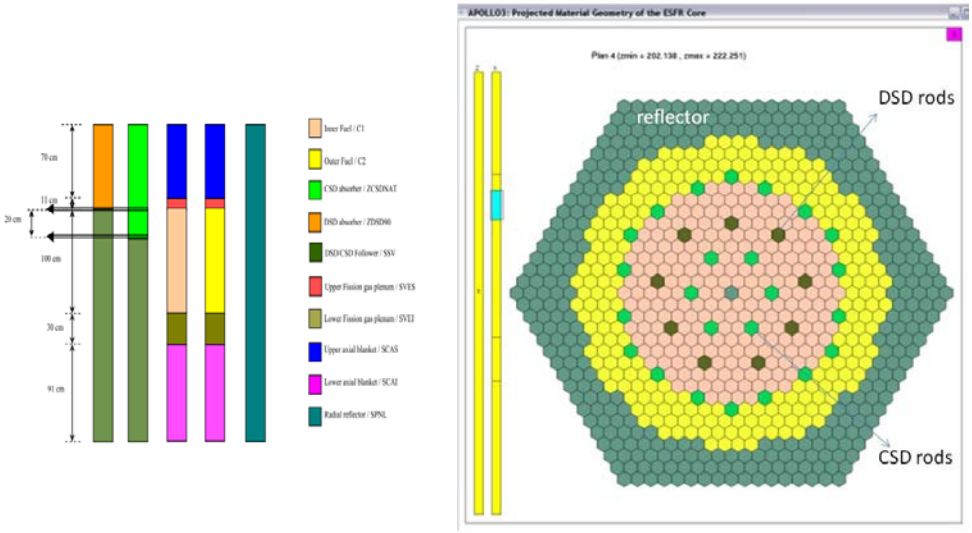

FIG. 7. ***sodium fast reactor axial and radial geometry***

Among the numerous development required to enhance the computational schemes, the ones devoted to sub-critical regions are the most difficult ones. For instance, the control rod cross sections can be processed with the reactivity equivalence procedure[18] while the steel reflector can use a condensation technique using angular fluxes and requiring many groups[19]. These developments will be introduced within APOLLO3® in a rather short time scale and new ones are still required for some other sub-critical assemblies in particular those dedicated to Minor Actinide transmutation.

2.5. Kinetics and coupling functionalities

This work has been launched to assess APOLLO3® currently developed functionalities for kinetics and coupling through the SALOME platform for multi-physics calculations. Theses functionalities have been tested on the previously presented sodium fast reactor, for Best-Estimate core performance assessment related to a rod withdrawal[20]. This simulation is based on GERMINAL best-estimate fuel physics code, the kinetics MINOS solver and thermal feedback upgraded functionalities of APOLLO3® through the SALOME platform. First results seem to show that even if the thermal feedback has a strong impact on the power evolution, neutron physics and fuel physics are not sufficient to properly assess 3D coupled analysis for this transient. Finer core thermal-hydraulics should be considered.

2.6. High performance computing functionalities

The scalability performances of the parallelization functionalities of the MINARET solver have also been assessed with flux simulation on the same sodium fast reactor[16]. All obtained results were computed using 2 massively parallel machines: *Titane* and *Tera-100* available at the CEA supercomputing center (http://www-ccrt.cea.fr/). Different simulations from S2 to S256 have been run using from 2 to more than 33.000 cores. Simulations on *Tera-100* using 16.000 and 33.000 cores for S128 and S256 approximations have also been run. These numerical experimentations showed the robustness of the MINARET solver (good keff convergence) allowing very high fidelity transport neutron simulations using very large number of cores at a petascale level. In addition, the resolution time breaks down from half a

year to less than 3.5 hours for very high fidelity neutron transport simulations (S256) and the parallel efficiency is still good (>60%) until around 5 angular directions per process.

3. Roadmap for the APOLLO3® computational scheme

The first version of the code is available since the end of 2012. The main features of this version are:

- self-shielding treatment based on the Livolant-Jeanpierre and subgroups methods,
- direct and adjoint neutron flux solvers solving the Boltzmann transport equation discretized by the classical long and short characteristic methods, a multicell collision probability method, a SPN spatially structured finite elements method and a SN spatially unstructured finite elements method,
- a solver computing isotopes depletion and production used as a common module for all the transport solvers,
- solvers for feedback effect solving simplified thermomechanical and thermal-hydraulical,
- a kinetics solver for transient calculation based on the SPN static solver.

The conceptual design of ASTRID uses a large set of “design” functionalities included in actual calculation softwares (ERANOS-2.2/PARIS). APOLLO3® final users for ASTRID will have access to a such set of functionalities dedicated to SFR core design. For exemple, users will be able to describe easily the problem geometry (core geometry, assembly geometry) and the associated compositions but also calculations schemes and options. Users will be able to realise complex calculations from unitary schemes.

The transition between ERANOS-2.2 and APOLLO3® will be effective in 2015. This deadline is required in order to prepare the safety report of the ASTRID detailed design . An inventory of all the useful calculation schemes is actually on going in order to prepare this transition. In parallel a reflexion is carried out on the definition of a design data model, integrating feedbacks of former design tools and new possibilities offered by modern CAD tools like SALOME®[21].

CONCLUSION

This paper has presented the general program devoted to ensure the transition between the ERANOS2 code, currently used for ASTRID conceptual design and a new one code, APOLLO3®, developed at CEA. This transition will enable us to take advantage of new numerical developments for neutronic core reactor calculations.
The program is defined so as to meet the ASTRID development plans and will require the achievement of many tasks involved in the VVUQ process used to supply a reliable code for designers and users performing neutronic ASTRID core calculations.
The transition between ERANOS-2.2 and APOLLO3® will be effective in 2015. This deadline is required in order to prepare the safety report of the ASTRID detailed design .

REFERENCES

[1] F. Varaine et al., “Pre-conceptual design study of ASTRID core”, Proceedings of ICAPP. ’12, Paper 12173, Chicago, USA, June 24-28, 2012
[2] P. Le Coz, J.-F. Sauvage, J.-P. Serpantie , “Sodium-cooled Fast Reactors : the ASTRID plant project”, Proceedings of ICAPP 2011, Paper 11249, Nice, France, May 2-5, 2011

[3] P. Sciora et al., “Low void effect core design applied on 2400 MWth SFR reactor”, Proceedings of ICAPP 2011, Paper 11249, Nice, France, May 2-5, 2011
[4] B. Fontaine et al., “Sodium-Cooled Fast Reactors: the ASTRID Plant Project”, Paper 432757, Proceedings of GLOBAL 2011, Makuhari, Japan, Dec. 11-16-5, 2011
[5] H. Golfier et al., “APOLLO3: a common project of CEA, AREVA and EDF for the development of a new deterministic multi-purpose code for core physics analysis”, Int. conf. on Mathematics, Computational Methods and Reactor Physics, Saratoga Springs, New York, 2009
[6] R. Sanchez et al., APOLLO2 year 2010, Nuclear Engineering and Technology, vol.42 n°.5 October 2010
[7] J.J. Lautard et al., CRONOS2 a modular computational system for neutronic core calculations, IAEA specialist meeting on Advanced Calculational Methods for Power Reactors, September 1990, Cadarache, France
[8] G. Rimpault et al., "The ERANOS Data and Code System for Fast Reactor Neutronic Analyses", Int. Conf. On the New Frontier of Nuclear Technology: Reactor Physics, Safety and High-Performance Computing, PHYSOR, 2002, Seoul, Korea
[9] C. Calvin. “HPC Challenges for Deterministic Neutronics Simulations Using APOLLO3 Code,” Joint International Conference of the 7th Supercomputing in Nuclear Application and the 3rd Monte Carlo (SNA + MC2010), Tokyo, Japan, Oct. 17 -21, 2010
[10] E. Jamelot et al. “Parallelization of 3D transport solvers within APOLLO3 code”, Proceeding of M&C 2011, Rio de Janeiro, May 08-12
[11] JC Trama et al, Overview of TRIPOLI-4 version 7 Continuous Energy Monte Carlo Code ICAPP 2011, Nice, France
[12] C. De Saint Jean, P. Archier et al, “Uncertainty Evaluation of Nuclear Reaction Model Parameters Using Integral and Microscopic Measurements with the CONRAD Code”, Journal of the Korean Physical Society, 59 (2011) 1276-1279
[13] T Takeda, H. Ikeda (1991). 3-D Neutron Transport Benchmarks, OECD/NEA Committee on Reactor Physics, NEACRP-L-330
[14] G. Palmiotti, C.B. Carrico And E.E. Lewis, “Variational Nodal Methods with Anisotropic Scattering”, Nuclear Science and Engineering, 115, 233-243, 11/93
[15] L. Gastaldo et al., “High-Order Discrete Ordinate Transport in Non-Conforming 2D Cartesian Meshes”, SNATCH, International Conference on Mathematics, Computational Methods & Reactor Physics (M&C 2009), Saratoga Springs, New York, May 3-7, 2009
[16] A.M. Baudron and J.J. Lautard “Simplified PN Transport Core Calculations in the APOLLO3 System”, Proceeding of M&C 2011, Rio de Janeiro, May 08-12
[17] J.-Y. Möller and J.-J. Lautard, ”MINARET, a deterministic neutron transport solver for nuclear core calculations, Proceeding of M&C 2011, Rio de Janeiro, May 08-12
[18] J.L. Rowlands - C.R. Eaton, “The spatial averaging of cross sections for use in transport theory reactor calculations, with an application to control rod fine homogeneization”, Specialists Meeting on Homogenization Methods in Reactor Physics, Lugano, Switzerland, 13-15/11/1978
[19] F. Vidal et al., “An improved energy-collapsing method for core-reflector modelization in RNR core calculations using the PARIS platform,” submitted tor Proc. of Int. Conf. for Advances in Reactor Physics – Linking Research, Industry, and Education PHYSOR 2012, Knoxville, USA, 2012
[20] E. Hourcade, D. Schneider, A. Bergeron, K. Ammar and C. Patricot “SFR rod withdrawal transient: presentation of a coupled neutronics/fuel thermal-mechanics calculation scheme”, proceeding of NUTHOS-9, Kaohsiung, Taïwan, September, 9-13, 2012
[21] Salomé : The Open Source Integration Platform for Numerical Simulation. http://www.salome-platform.org

Analysis of the previous and preparation of new experiments on fast multiplying assemblies for obtaining benchmark data on criticality

S. Sikorin, S. Polazau, S. Mandzik, Y. Damarad, J. Palahina, T. Hryharovich

State Scientific Institution "Joint Institute for Power and Nuclear Research – Sosny" of the National Academy of Sciences of Belarus, Minsk, Republic of Belarus

Abstract. The JIPNR-Sosny of the NAS of Belarus created and explored a number of uranium-containing critical assemblies of the BTS series in designing fast BRIG-300 reactor with $N_2O_4 \leftrightarrow 2NO_2 \leftrightarrow 2NO + O_2$ coolant and the PVER fast-resonance neutron spectrum reactor with a steam-water coolant. Research in the physics of these reactors was performed on fast-thermal critical assemblies at the critical facility "Roza". Structurally, these critical assemblies consisted of fast and thermal reactor cores and the buffer zones located between them, intended for leakage spectrum neutron conversion from a thermal zone to a spectrum of neutrons of the modelled fast reactor. Fast zones are a non-uniform hexagonal lattice of cylindrical fuel rods with fuel composition based on metal U (90% U-235), UO_2 (36% U-235), depleted U (0.4% U-235), rods with SiO_2; a buffer zone is a non-uniform hexagonal lattice of cylindrical fuel rods based on UO_2 (36% U-235), natural U and depleted U (0.4% U-235), rods with B_4C and made from stainless steel; a thermal zone is a uniform rectangular uranium-polyethylene lattice of cylindrical fuel rods based on the fuel composition UO_2+Mg (10% U-235). For obtaining benchmark data on the criticality, computational models have been developed and the analysis of experiments has been carried out to estimate the experimental results as criticality benchmark data. The JIPNR-Sosny of the NAS of Belarus also prepared experiments on the criticality of multiplying systems simulating some physical features of the core of fast low power small-size gas-cooled reactors with UZrCN nuclear fuel. For these purposes, the critical assemblies P-20 were developed at the critical facility "Giacint". These assemblies represent a uniform hexagonal lattice of fuel cassette: the central area is based on cylindrical fuel rods with UZrCN (19.75% U-235), the peripheral area is based on the cylindrical fuel rods with metallic U (90% U-235), UO_2 (36% U-235) and natural U; and the reflector on the Be (internal layer) and stainless steel (external layer). This paper describes the design and the composition of the critical assemblies BTS-4, BTS-5 and P-20, the results of calculation of k_{eff} in a criticality, and the program of work on the critical assemblies P-20.

1. Introduction

The JIPNR-Sosny (former Institute of Nuclear Power) of the NAS of Belarus has performed large-scale research experiments on fast and fast-thermal neutron multiplying systems. Currently, the analysis of the previous experiments was made in order to build analytical models of relevant multiplying systems and the possibility of including the experimental data into the international criticality benchmark [1].

The paper describes the criticality experiments on fast-thermal critical assembly BTS-4, simulating the core fast BRIG-300 reactor with $N_2O_4 \leftrightarrow 2NO_2 \leftrightarrow 2NO + O_2$ coolant and on two fast-thermal critical assemblies BTS-5-1 and BTS-5-2, simulating two states of the PVER reactors active zone, cooled by a steam-and-water mixture. The critical assembly BTS-5-1 simulated the state of an emptied reactor, i.e., the active zone did not include water coolant

and the neutron spectrum in the active zone was fast. The critical assembly BTS-5-2 simulated a fully water-filled core in the reactor, where the neutron spectrum shifted to the thermal area compared to the BTS-5-1 neutron spectrum. Two factors are essential for selection and analysis of experimental data for these critical assemblies. Firstly, fast-thermal critical assemblies of the BTS series represent complex multi-zone systems, using nuclear fuel of different enrichments and a complicated material composition in the central fast zone, the buffer zone and the thermal feeding zone. Therefore, all complex relevant factors on the geometry and the material composition of the multiplying systems active zone had to be taken into account in order to build analytical models. Secondly, the critical assemblies BTS-5-1 and BTS-5-2 had identical structure, except that first one did not have water in the central zone; however, the neutron spectrum in the central zone varied from fast for BTS-5-1 to thermal for BTS-5-2. Therefore, a comparison between the calculated and experimental data on the criticality of the investigated multiplying systems is interesting both in terms of correctness of the analytical models obtained and correctness of the constant support of the nuclear data libraries used for computerizations of fast and fast-thermal multiplying systems.

In addition to the experiments and calculations of the fast-thermal critical assemblies BTS, this paper presents the result of calculation studies for the preparation of experiments on the criticality multiplying system at the critical facility “Giacint”, simulating some physical features of cores of fast small-size gas-cooled reactors, e.g. low-power reactor with He-Xe coolant.

2. Critical assemblies BTS-5

The critical assemblies of the BTS-5 series were assembled at the critical facility “Roza”. The critical assembly casing was made of 50 mm borated polyethylene plates (3% weight of natural boron) and represented a regular dodecahedron 1060 mm high. The casing was put on the frame, including lower spacer grids for fuel rods and other elements of the critical assemblies. The control and protection system (CPS) included three emergency protection (EP) actuating elements (AEs), two manual regulations (MR) AEs, and two reactivity compensation AEs. All CPS AEs were placed in the thermal zone channels, made from aluminium tubes, ∅10x0.5 mm. The absorbing element in the CPS rods was the powdered boron B_4C, the fill density 1.3 g/cm^3 for the MR rods (500 mm fill height) and compensation AEs (750 mm fill height), and the fill density 1.35 g/cm^3 for the EP rods (735 mm fill height).

2.1. The critical assembly active zone

The active zone of each critical assembly included a fast zone, a boron filter zone, a filter zone from natural metal uranium and steel, a converter, and a thermal zone. Figures 1, 3 show the cross sections of the critical assembly BTS-4. Figures 2, 4 show the cross sections of the critical assembly BTS-5-1 (or 2). The physical use of each of these zones is as follows: the central part of the fast zone generated the spectrum of the simulated fast nuclear reactor; the boron filter zone was permeable for fast neutrons and restricted the penetration of thermal neutrons to the fast zone; the filter zone from natural metal uranium and steel provided, basically, for the fission of ^{238}U by fast neutrons and the required feed the fast zone by fast neutrons; the converter was used for effective conversion of the thermal zone neutron to the fast spectrum; the thermal zone provided most of the fissions and included critical assembly regulation and emergency protection rods.

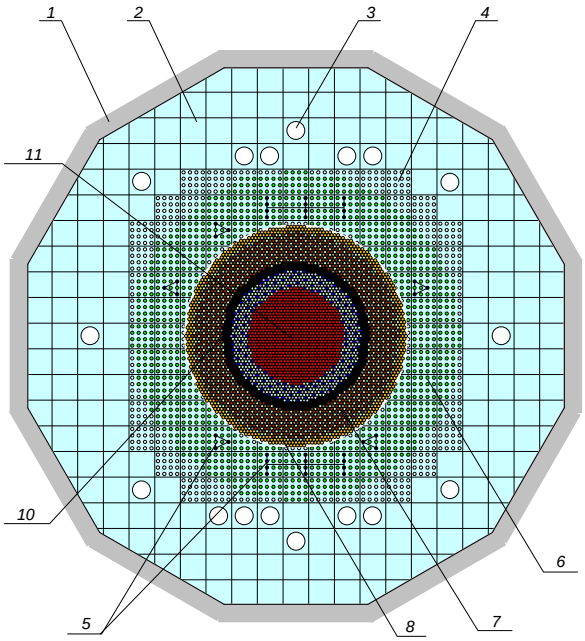

FIG. 1. Radial cross section of the BTS-4 critical assembly

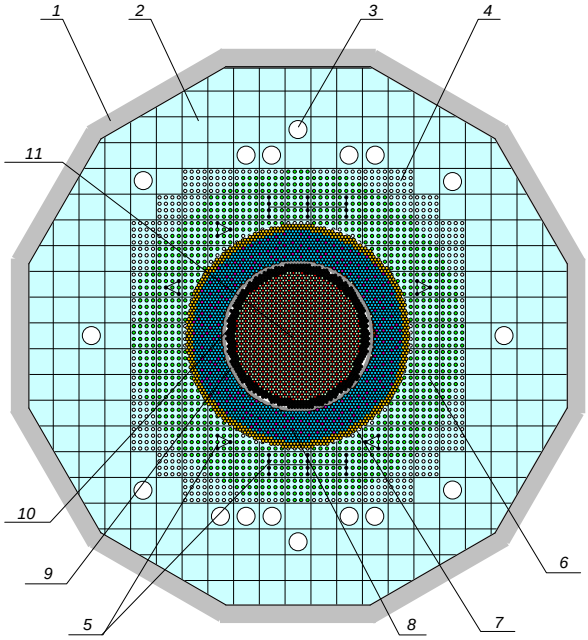

FIG. 2. Radial cross section of the BTS-5 critical assembly

Legend: 1 - critical assembly casing; 2 - polyethylene plates reflector; 3 - holes for the neutron detectors; 4 - polyethylene plates with fuel rods holes; 5 - CPS actuating elements; 6 - thermal zone; 7 - filter zone from natural metal uranium and steel; 8 - converter; 9 - stainless steel tank; 10 - boron filter zone; 11 - fast zone

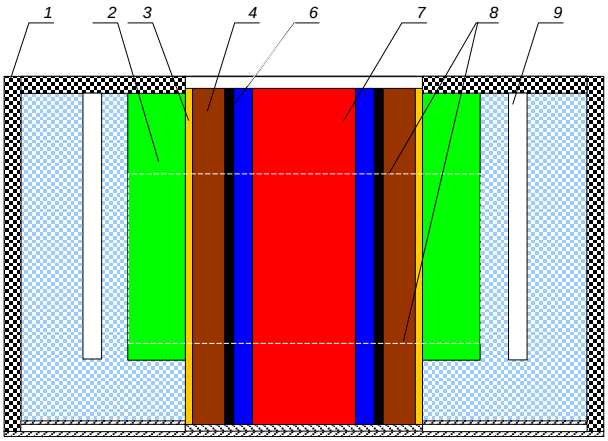

FIG. 3. Axial cross section of the BTS-4 critical assembly

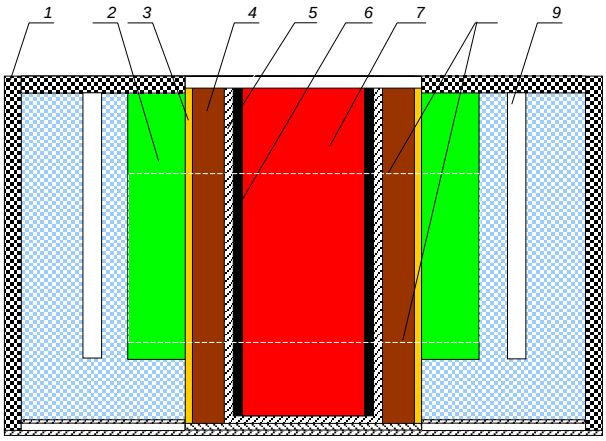

FIG. 4. Axial cross section of the BTS-5 critical assembly

Legend: 1 - critical assembly casing; 2 - thermal zone; 3 - converter; 4 - filter zone from natural metal uranium and steel; 5 - stainless steel tank; 6 - boron filter zone; 7 - fast zone; 8 - active zone boundary; 9 - holes for the neutron detectors

2.1.1. The fast zone and boron filter elements

The fast zone represented a cylindrical assembly from stainless steel tubes, ∅9x0.7 mm. The tightly filled tubes, welded at end joints, acted as the lower and upper spacer grids with a 9 mm pitch. The lower and upper spacer grids used to place three types of fuel rods: 1) with metal U(90%) fuel, 90% enrichment by uranium-235; 2) with U(36%)O_2 fuel, 36% enrichment by uranium-235; and 3) with U(0.4%)O_2 fuel, a mixture depleted to 0.4% by uranium-235. All types of fuel rods were identical in their structure, incorporating a fuel core, a cladding and end parts. The fuel rod cladding was stainless steel with the 7 mm outer diameter and 0.2 mm walls. The fuel core incorporated tablets, 6.4 mm in diameter and 4-7 mm in height, made from: metal uranium with 18.9 g/cm^3 density for 90% fuel rods; uranium dioxide UO_2 with 9.8 g/cm^3 density for 36% fuel rods and 9.7 g/cm^3 for depleted rods. The total fuel core height was 500 mm. The total length of the fuel rods was 620 mm. The mean mass of uranium-235 in the fuel rods was about 49.1 g (36%) and 260 g (90%). Rods with SiO_2 powder (the height - 500 mm, density - 0.9 g/cm^3) were used also in fast zone of facility BTS-4.

Structurally, the ring boron filter was the continuation of the fast zone; it was assembled from 567 stainless steel tubes, ∅7x0.2 mm and 620 mm long, filled up to 500 mm with the powdered boron carbide B_4C with natural boron-10 enrichment and the fill density 1.35 g/cm^3. The total fill height was 500 mm. The total length of the boron filter was 620 mm.

The fast zone and the boron filter were placed in the stainless steel tank, with the 462 mm inner diameter and 2.5 mm thick walls. The tank bottom was 10 mm. The tank was filled with distilled water when the critical assembly BTS-5-2 was used instead the critical assembly BTS-5-1.

2.1.2. The natural uranium and converter zone

The natural metal uranium and steel filter and the converter were assembled from stainless steel tubes, 10 mm in diameter and 1 mm walls, welded to the cassettes at the ends. The cassettes were regular hexagons. They included 19 tubes, 980 mm long each. The tubes were assembled in the cassette with a 10 mm pitch in a triangular grid (densely packed). The shanks of the cassettes were inserted into holes in the 20 mm stainless steel spacer plate. The spacer plate was 860 mm in diameter and attached to the 16 mm bearing plate. The holes for cassettes were spaced with the 44.7 mm pitch in the triangular grid. This pitch of the grid and the bandage assured the required dense packing of the cassettes.

Natural metal uranium fuel rods and stainless steel rods were inserted into the filter cassettes. The fuel rod from U(nat. met.) is a natural metal uranium rods, ∅6.4 mm and 622 mm long. The stainless steel rod is a ∅7.5 mm carbon steel rod, 970 mm long.

Fuel rods containing UO_2 with the mean 36.32% enrichment were placed into the converter cassettes. The fuel rod is stainless steel tube, ∅7x0.35 mm and 600 mm long, filled for 500 mm with uranium dioxide and tightly plugs from the ends by 60 mm long steel plugs. The mean content of uranium dioxide of the fuel rod core was about 82 g. The total length of the fuel rod was 620 mm.

2.1.3. The thermal zone

The thermal zone of the critical assembly was a cylindrical ring, containing the polyethylene $(–CH_2–)_n$ (0.927 g/cm^3) moderator and fuel rods with the metal ceramic core from 10% uranium dioxide and magnesium (EK-10 fuel rods), arranged in a rectangular 20 mm pitch which is close optimum for this type of fuel rods.

The thermal zone was assembled from tightly packed cassettes without hoods, each of which was formed by connecting nine polyethylene blocks, 63x80x80 mm. Each such cassette had sixteen ∅11 mm holes to insert fuel rods with U(10%)O_2+Mg (EK-10), arranged with a 20 mm pitch. The thermal zone interface was formed by shaped polyethylene cassettes tightly adjacent to the converter.

The fuel rods with U(10%)O_2+Mg (EK-10) represented a metal ceramic rod core, ∅7 mm and 500 mm long, made from uranium dioxide, 10% enrichment by uranium-235, and magnesium, tightly sealed in the aluminium casing with the aluminium shanks. The outer diameter of the fuel rod cladding was 10 mm; the total length of the fuel rod was 588 mm.

2.1.4. The critical assembly reflectors

The side reflector of the critical assemblies is represented by polyethylene blocks, with a density of 0.927 g/cm^3 (the mean polyethylene reflector thickness is ~ 300 mm) and the critical assembly casing from borated polyethylene plates, 50 mm thick and a density of 0.97 g/cm^3. The side reflectors of the thermal zone have 16 round ∅55 mm holes for the neutron detectors.

The lower end reflector of the critical assembly thermal zone is made from the lower plugs of the fuel rods, polyethylene blocks with a total thickness of 235 mm, the thermal zone support plate 3 mm thick, and the critical assembly support plate 16 mm thick.

The upper end reflector of the critical assembly thermal zone is made from the upper plugs of the EK-10 fuel rods, polyethylene blocks with the total thickness of 235 mm, and the borated polyethylene blocks 50 mm thick.

The lower end reflector of the fast insertion (the fast zone, the boron filter zone, the natural uranium and steel filter zone and the converter) is made of respective fuel rods, lower steel insertions of the fast zone tubes and the boron filter 165 mm long, the lower steel insertions of the filter cassettes and the converter 170 mm long, the fast zone tank bottom, the steel plugs of the fast insertion cassettes 10 mm long, the fast insertion spacer plate 20 mm thick, and the critical assembly support plate 16 mm thick.

The upper end reflector of the critical assembly fast insertion includes upper plugs of respective fuel rods, and upper steel cassette insertions and fast zone tubes 180 mm long.

3. Critical loads. Comparison of experimental and calculation results

Table 1 shows the critical load of the critical assemblies BTS-4, BTS-5-1 and BTS-5-2.

TABLE 1. THE CRITICAL LOAD OF THE CRITICAL ASSEMBLIES BTS-4, BTS-5-1 AND BTS-5-2

Assembly	Fast zone			Boron filter	Metal uranium and steel filter			Converter	Thermal zone
	Fuel rods U(90%) pcs	Fuel rods U(36%) pcs	Fuel rods U(0.4%) pcs	Rods B_4C pcs	Fuel rods U(nat.) pcs	Fuel rods U(0.4%) pcs	Rods steel pcs	Fuel rods U(36%) pcs	Fuel rods U(10%) pcs
BTS-4*	130	797	412	408	972	665	221	436	1044
BTS-5-1	-	583	1153	477	1586	-	202	465	1134
BTS-5-2									1162

* - 149 rods with SiO_2 were also in fast zone of BTS-4

Filling of the fast zone and the boron filter zone of the critical assembly BTS-5-2 changes substantially the neutron spectrum in these zones. The neutron spectrum is much thermal for the filled condition than for the empties condition, which is indicated by the experimental measured threshold values of the spectrum index $^{28}\boldsymbol{\sigma}_f$ /$^{25}\boldsymbol{\sigma}_f$. The respective measured (using solid-state track registration detectors) values are 0.0092+/-4% for BTS-5-2 and 0.0266+/-3% for BTS-5-1. The thermal neutron spectrum in the critical assembly BTS-5-2 not only increases the effectiveness of fuel rods in the fast zone, but also increases the neutron absorption in the boron filter. The resultant effects of these factors increases the critical load of the thermal zone in the critical assembly BTS-5-2 by 28 fuel rods U(10%)O_2+Mg with 10% uranium-235.

The MCNP4C [2] and MCUFREE [3] codes were selected for simulating and calculating critical experiments on fast-thermal neutron multiplying systems. The calculations were made using nuclear data libraries ENDF-B/VI, ENDL-85 for MCNP4C and MDBFREE50 for MCUFREE, respectively. The calculated models took into account all substantial components of the critical assemblies, including fuel rod parts, elements of the structural materials, moderator, reflector, basic metal structures of the facility and spacer grids. The neutron sensors include materials with high absorption cross section values. They were also included into calculation models. The calculation model contained the absorbing materials of the CPS rods.

The experimental and collated values of the effective multiplying factor of the critical assemblies BTS-4, BTS-5-1 and BTS-5-2, produced using MCU and MCNP codes, are given in Table 2.

TABLE 2. CALCULATIONS OF THE EFFECTIVE MULTIPLYING FACTOR OF THE CRITICAL ASSEMBLIES BTS-4, BTS-5-1 AND BTS-5-2

Assembly	Experimental k_{eff}	Calculated k_{eff}	
		MCNP	MCUFREE
BTS-4	1.00125 ± 0.00004	1.0144 ± 0.0009	-
BTS-5-1	1.00234 ± 0.00004	1.00694 ± 0.0010	1.00638 ± 0.0010
BTS-5-2	1.00000 ± 0.00004	0.99959 ± 0.0009	-

Uncertainties of geometry, material data and components temperature and its effect on k_{eff} were estimated when analyzing experimental results obtained at the critical assemblies of the

BTS series. Combined k_{eff} uncertainty caused by the above mentioned sources of uncertainty is ± 0.003. This uncertainty is defined mainly by the uncertainties of composition and dimensions of fuel rods EK-10 as well as the variation of lattice pitch in polyethylene moderator.

Comparing the calculated and experimental results, we can conclude the following: the difference between the calculated effective multiplying factor and the experiment lies in the acceptable accuracy range, given the experimental and calculation errors.

4. The planned criticality benchmark experiments at the critical facility "Giacint"

It is planned to use the critical facility "Giacint" for a set of benchmark experiments on the criticality of fast critical assemblies without moderator and with beryllium and steel reflectors. The nuclear fuel for these experiments will be mixed nuclear fuel in the form of cassettes based on: 1) fuel rods with 90% metal uranium U(90%), 2) fuel rods with U(36%)O_2, 3) fuel rods based on natural metal uranium U(nat. met.), and 4) fuel rods based on the new uranium-zirconium carbon nitride $U_{0.9}Zr_{0.1}C_xN_{1-x}$ with 19.75% enrichment by uranium-235. The fuel rods based on U(90%), U(36%)O_2 and U(nat. met.) are described above.

The fuel rods based on the new uranium-zirconium carbon nitride $U_{0.9}Zr_{0.1}C_xN_{1-x}$ fuel with 19.75% enrichment by uranium-235 comprises a fuel core, a cladding and end parts. The fuel core is made of $U_{0.9}Zr_{0.1}C_xN_{1-x}$ tablets with the 10.7 mm diameter, the fuel density of, at least, 12 g/cm^3, the uranium density over 10.5 g/cm^3 and the porosity of 12% maximum. The length of the fuel core of rod is 500 mm. The cladding material of fuel rods is stainless steel or niobium alloy. The diameter of the fuel rod is 12 mm, and the total length of the fuel rod is 620 mm.

Figures 5-7 show the cartograms of the planned critical loads for three fast critical assemblies without moderator, with beryllium and steel reflectors, rated by MCNP code.

The estimated critical mass of the assemblies by uranium-235 are 72.1 kg (for the critical assembly P-20-2), 90.7 kg (for P-20-5) and 111.2 kg (for P-20-6), respectively.

The results of benchmark experiments on the forenamed critical assemblies will be made to validate codes with nuclear data libraries. These codes will be also used for the development of perspective cores with LEU nuclear fuel for gas- and water-cooled power and research nuclear reactors.

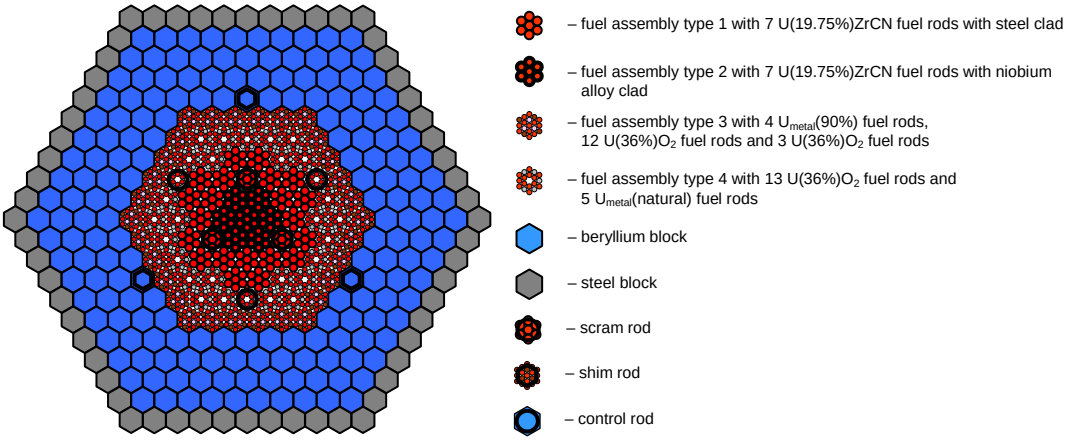

FIG. 5. The cartogram for the critical assembly P-20-2 (31 fuel assemblies with (19.75%)ZrCN fuel rods and 36 fuel assemblies with U_{metal}(90%) and U(36%)O_2 fuel rods) without moderator and with beryllium-steel reflector

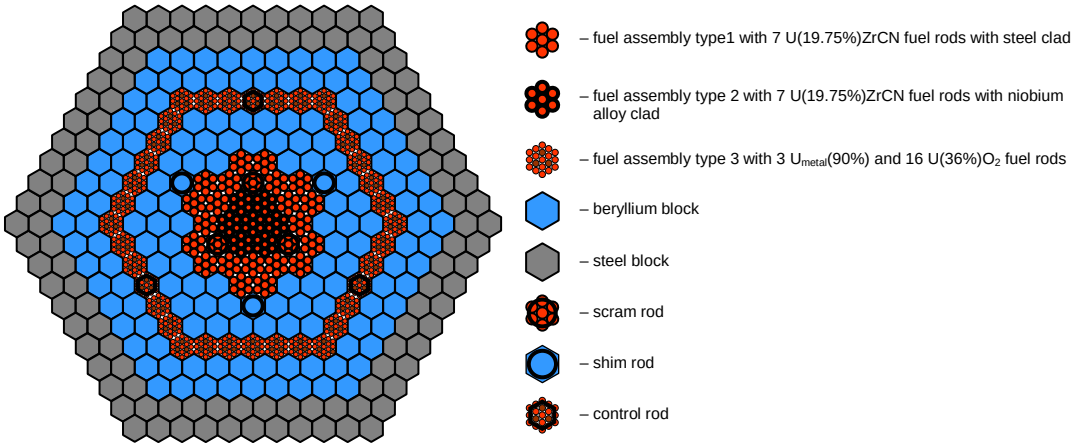

FIG. 6. The cartogram for the critical assembly P-20-5 (31 fuel assemblies with (19.75%)ZrCN fuel rods, 30 fuel assemblies with U(36%)O_2 and U_{metal}(natural) fuel rods and 30 fuel assemblies with U_{metal}(90%) and U(36%)O_2 fuel rods) without moderator and with beryllium-steel reflector

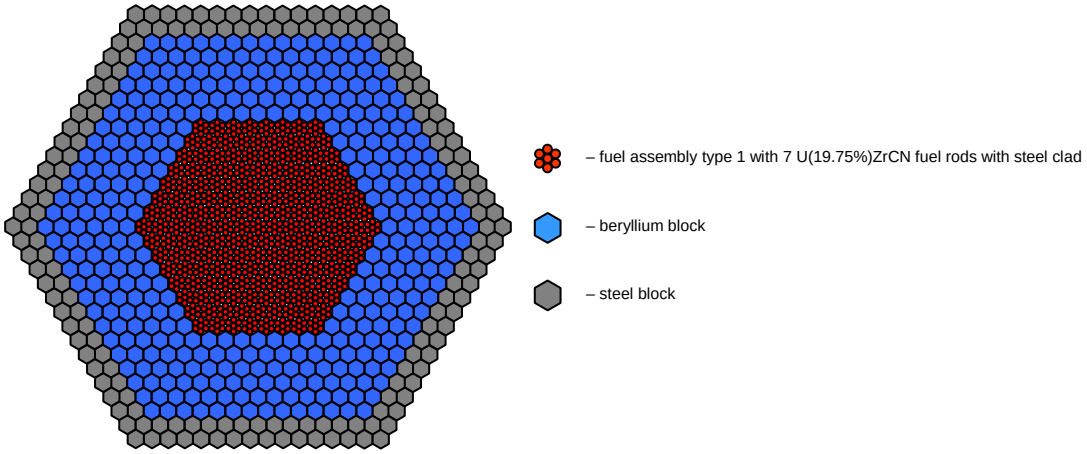

FIG. 7. The cartogram for the critical assembly P-20-6 (169 fuel assemblies with (19.75%)ZrCN fuel rods), without moderator and with beryllium-steel reflector

5. Conclusions

Analysis of the criticality experiments made on fast-thermal neutron multiplying systems BTS-4, BTS-5-1 and BTS-5-2 on the critical facility “Roza”, using the program codes MCUFREE and MCNP4C, proved the correspondence between the experiment and the calculated multiplying factor value with the acceptable accuracy, given the experimental and calculation errors. The calculation of criticality rated by MCNP code was made for the fast multiplying systems without moderator and with beryllium/steel reflector. The critical facility “Giacint” will be used to make benchmark experiments on fast multiplying systems without moderator and with beryllium and steel reflectors.

REFERENCES

[1] International Handbook of Evaluated Criticality Safety Benchmark Experiments. NEA/NSC/DOC(95)03. September 2010 Edition. http://icsbep.inl.gov/configurations.shtml.

[2] J. F. Briesmeister, ”MCNP – A General Monte Carlo N-Particle Transport Code, Version 4C,” LA-13709-M, 2000.

[3] Application and User Manual for the MCU-5 Modules Programs. Ed. by D. A. Skarovsky. Moscow, 2009, 146 p. (http://mcuproject.ru/museum/lvmvant/lvmvant07.pdf)

Yalina-Booster Assembly: from HEU to LEU.

S. Sadovich[†], H. Kiyavitskaya, V. Bournos, Yu. Fokov, Ch. Routkovskaia

Joint Institute for Power and Nuclear Research – Sosny,
National Academy of Sciences of Belarus

Abstract.

The YALINA facility is a unique facility which was designed as a zero power model of real ADS (Accelerator Driven System). It is intended to study ADS neutronics and kinetics of the subcritical reactors driven by external neutron sources. Accelerator-driven systems may play an important role in future nuclear fuel cycles to reduce the long-term radiotoxicity and volume of spent nuclear fuel.
Successful operation of this facility is a scientific contribution from the Republic of Belarus, as well as the international community. The experimental data are used to benchmark and validate methods and computer codes for designing and licensing ADS.
In this paper the investigation of spatial kinetics of the sub-critical systems with external neutron sources, validation of the experimental techniques for sub-criticality monitoring and estimation of probability of minor actinides and fission products transmutation is made for different configurations of Yalina-Booster during conversion from HEU to LEU:
- 1st configuration – with HEU fuel in the fast zone (metallic uranium of 90% enrichment by ^{235}U and UO_2 of 36% enrichment by ^{235}U) and uranium dioxide of 10% enrichment by ^{235}U in thermal zone;
- 2nd one – with 36% UO_2 in fast zone and 10% in thermal zone;
- 3rd one – with 21% UO_2 in fast zone and 10% in thermal zone;
- 4th one – with 21% UO_2 in fast zone and 10% in thermal zone, differing from the 3rd configuration by rounded shape of fast zone and annular shape of the absorber zone with permanent number of the absorbing rods.

INTRODUCTION

Accelerator Driven Systems (ADS) are considered as promising systems to decrease the volumes of long-lived radioactive fission products (^{137}Cs, ^{90}Sr, ^{129}I, ^{126}Sn, and other) and minor actinides (Np, Pu, Cm, and other). Transmutation technology is the conversion of long-lived nuclides into short-lived and stable in subcritical reactors. It is called Accelerator Driven Transmutation Technology (ADTT).

The main advantages of the Accelerator Driven Systems (ADS) are their operation in stable subcritical mode (high level of nuclear safety) and a possibility to get the flux densities of fast and thermal neutrons about 10^{15} n/(cm^2 s) and higher which are necessary for new radiation technologies.

ADS are being studied at different research institutes around the world [1][2][3]. In order to study phenomena related to problems of ADS and ADTT (Accelerator Driven Transmutation Technology) a few small-scale subcritical facilities have been constructed such as MASURCA (France) [4][5][6] and YALINA (Belarus) [7][8]. Many countries (USA [9], Italy [10], Japan [11], Ukraine [12], China [13] et al.) are interested in construction and studying ADS facilities. Main issues for Accelerator Driven Systems development in the framework of partitioning and transmutation for nuclear waste volume and radiotoxicity reduction were investigated in frame of the IP-EUROTRANS project [14].

[†] sadovichs@gmail.com

Research works in the field of ADS physics started in 1990s at JIPNR-Sosny of the National Academy of Sciences proved the possibility to use low energy ion accelerators (neutron generators, cyclotrons) to study main ADS neutronics and kinetics and transmutation technologies [15][16][17][18]. Experiments performed at the YALINA facility give information about performance representative for full-scale ADS.

One of the important problems of the physics of the subcritical systems driven by external neutron sources is development of the experimental methods to monitor neutron flux and determine a subcriticality level without reaching criticality. Additionally, it is extremely important to define the margins of validity of the experimental methods used for neutronics measurement in critical systems to use them in subcritical systems driven by external neutron sources. One of the items is studying the transmutation reaction rates in different neutron spectra.

This paper demonstrates the results of subcriticality measurements in the YALINA-Booster configurations with different uranium fuel enrichment in fast zone.

THE RESEARCH FACILITY YALINA

The research facility YALINA consists of two zero power subcritical assemblies YALINA-Thermal and YALINA-Booster, neutron generator NG-12-1 and measuring equipment. The vital support, control and physical protection systems are common for both assemblies. The layout of the facility is presented in Figure 1.

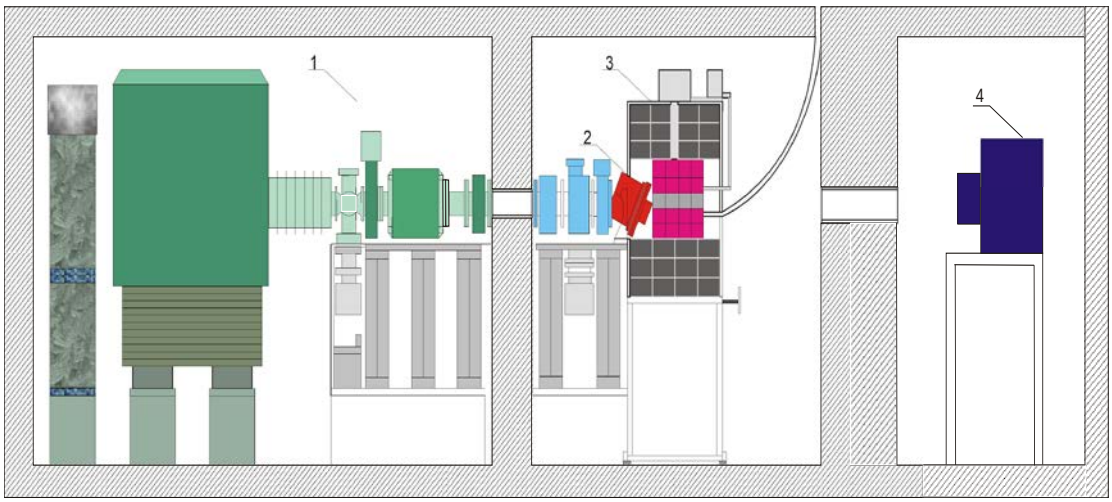

FIG. 1. Layout of subcritical facility YALINA: 1 –neutron generator, 2 – TiT (TiD) target system, 3 - subcritical assembly, 4 – measuring unit

Neutron generator NG-12-1

Neutron generator NG-12-1 is a linear deuteron accelerator with electromagnetic separation of accelerated up to 250 keV deuterium ions (D^+). Accelerator voltage is 250 kV, load current – 30 mA. Deuteron beam is aligned horizontally. It interacts with TiT or TiD targets and generates neutrons through $d(T,n)^4He$ or $d(D,n)^3He$ fusion reactions. The energies of generated neutrons are 14.1 MeV or 2.45 MeV, respectively. The generator can operate in continuous mode, producing constant current of deuterons, or in a pulse mode sending short deuteron pulses with a constant frequency.

Subcritical assembly YALINA-Booster

The YALINA-Booster is a fast-thermal subcritical assembly. The assembly core consists of two-region fast zone, thermal zone with polyethylene moderator and intermediate (absorber) zone separating fast and thermal zones. It is radially surrounded by graphite reflector and axially by borated polyethylene shielding.

The design of the subcritical assembly YALINA-Booster provides an opportunity to change the geometry and composition of the core and reflector to allow the configurations with different levels of subcriticality provided that maximum value $k_{eff} \leq 0{,}975$. There are 6 measuring and 11 experimental channels to monitor subcriticality level, to measure spatial distribution of neutron flux density, to place the samples for reaction rates measurements by method of neutron activation analysis. The design of the assembly is presented in detail in [19]. Figure 2 shows a longitudinal section of the assembly.

YALINA-Booster facility was put into operation in 2005. During 5 years a lot of experiments have been performed on core configurations differing by nuclear fuel composition and enrichment in fast zone and by number of fuel pins in thermal zone.

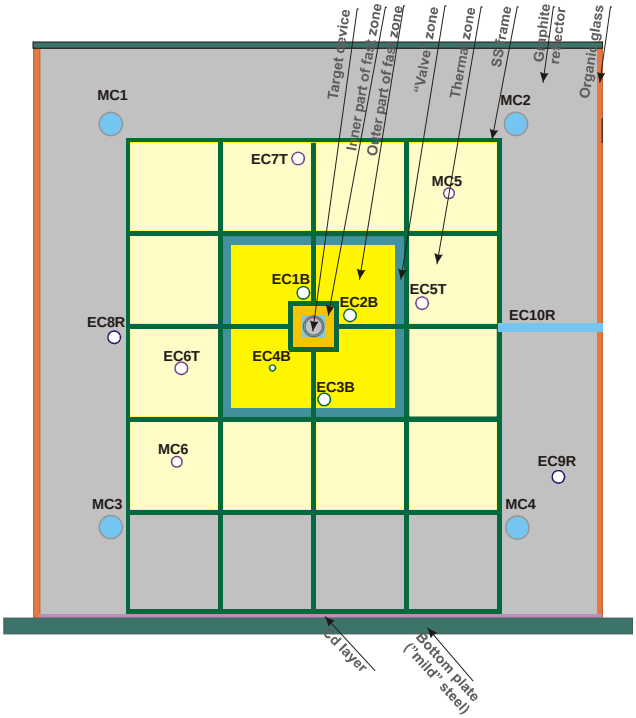

FIG. 2. Cross sectional view of YALINA-Booster assembly, EC1B-EC4B – experimental channels in fast zone; EC5T-EC7T – experimental channels in thermal zone; EC8R-EC10R – experimental channels in reflector, MC5, MC6 – measuring channels in thermal zone, MC1-MC4 – measuring channels in reflector

As it was mentioned above, the design of the subcritical assembly YALINA-Booster provides the opportunity to change the geometry and composition of the core. During participation in the international non-proliferation activity several configurations with different enrichment of the fuel were investigated:

1st configuration - HEU fuel YALINA-Booster – with HEU fuel in the fast zone (90% and 36% enrichment by ^{235}U) and fuel of 10% enrichment by ^{235}U (EK-10) in thermal zone. The 2nd configuration - YALINA-Booster - with fuel rods of 36% enrichment by ^{235}U in fast zone and fuel rods with 10% enrichment by ^{235}U in thermal zone;

The map of nuclear fuel loading for the first configuration is shown on the figure 3. The second configuration differs from the first by changing fuel rods with uranium metallic to the fuel rods with UO_2(36% enrichment ^{235}U).

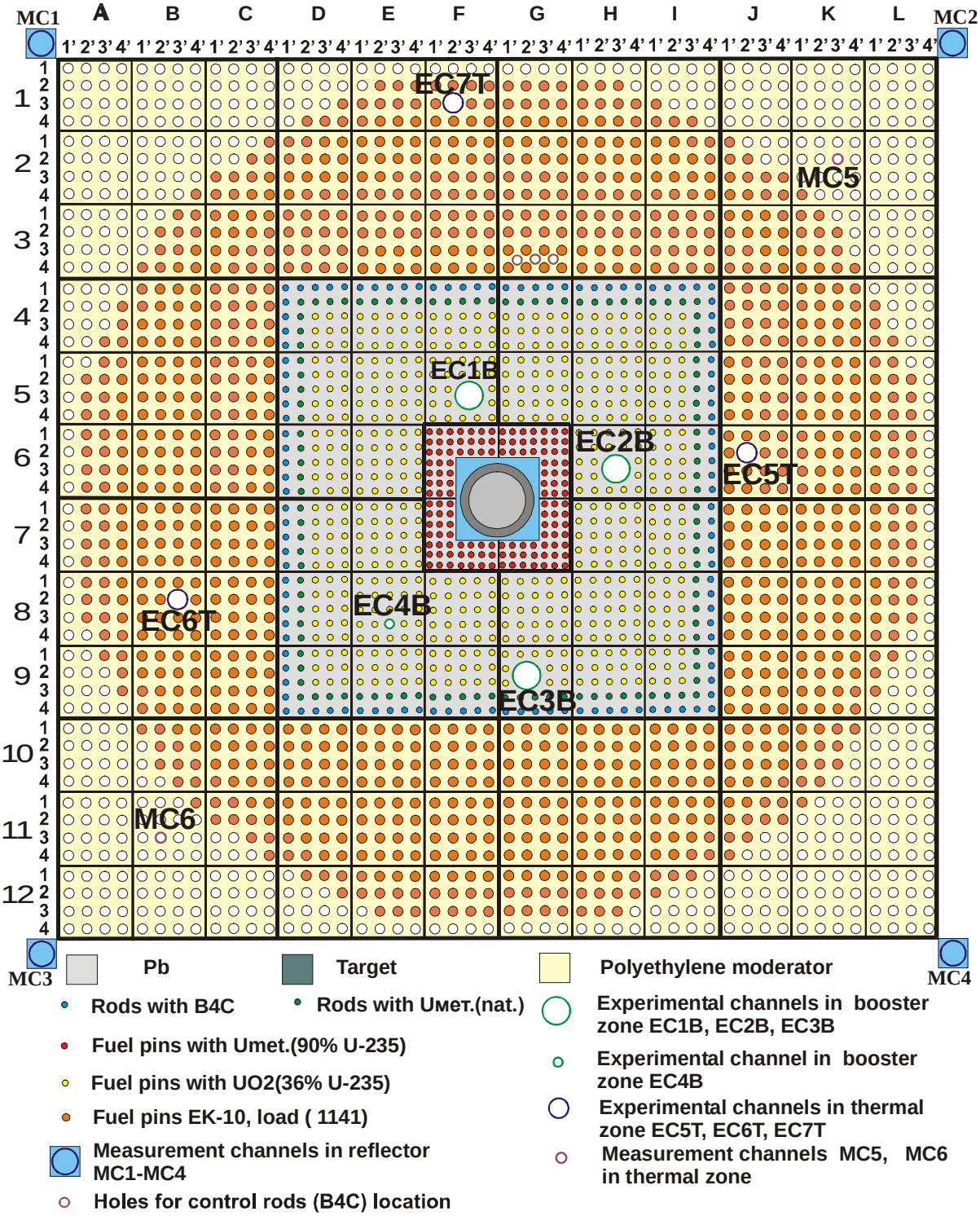

FIG. 3. Map of nuclear fuel loading of YALINA-Booster (1141 EK-10 fuel pins).

In the 3rd and 4th configurations fuel rods of 21% enrichment by ^{235}U in the fast zone were used. The difference is in the shape of the fuel position in the fast zone (rectangular and cylindrical).

The map of nuclear fuel loading for the 3rd configuration is shown on the figure 4. The maps of the fast zone for the 3rd and the 4th configurations are shown on the figure 5.

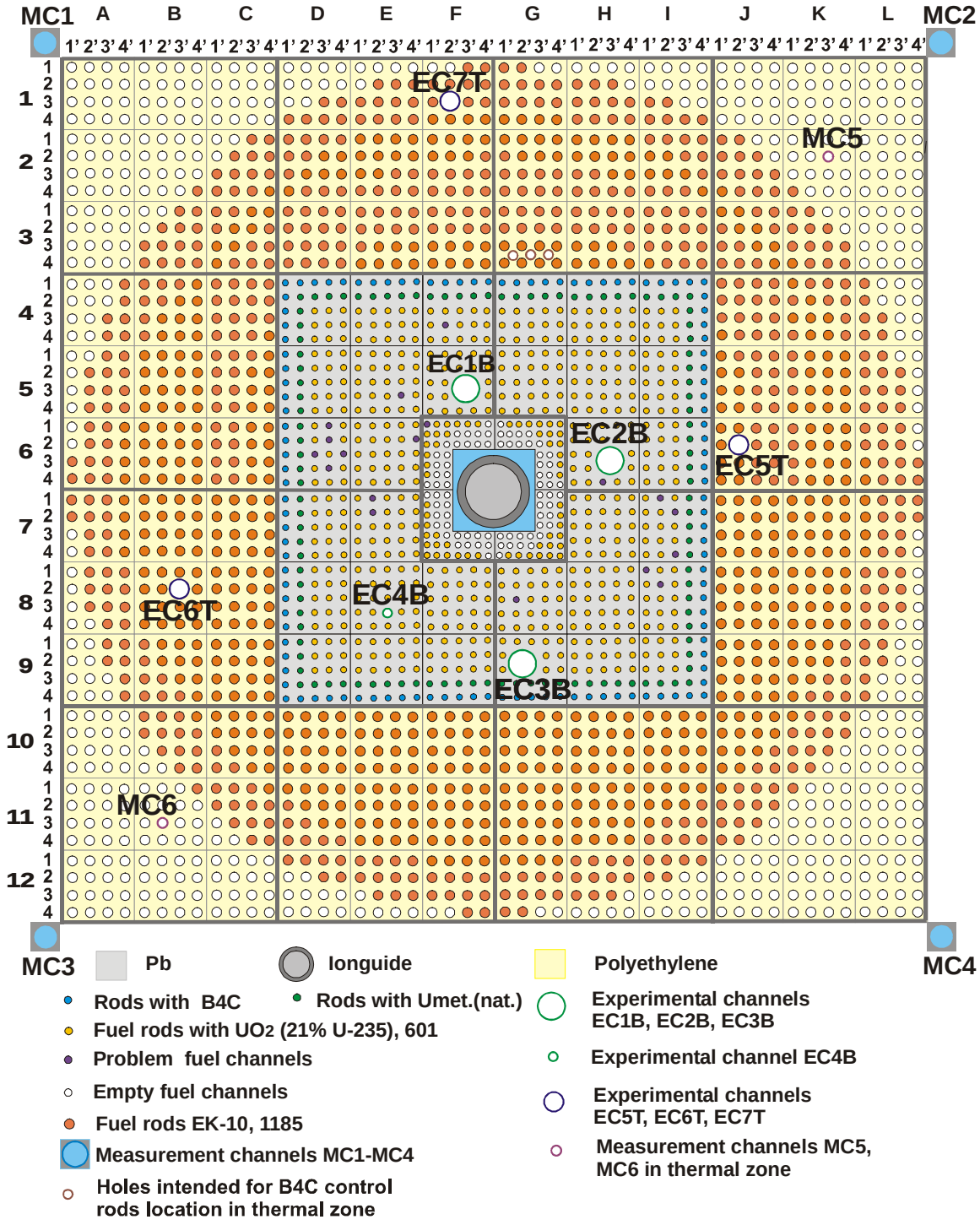

FIG. 4. Map of nuclear fuel loading of YALINA-Booster (601 fuel pins 21% in fast zone and 1185 EK-10 fuel pins in thermal zone).

Measurement channel was formed with ^{3}He detector (with 10 mm and 25 mm active length) or fission chamber (with ^{232}Th, ^{235}U, ^{235}U, ^{nat}U) with time analyzer TURBO MCS or PXI/PCI-6602 counters-timers from National Instruments.

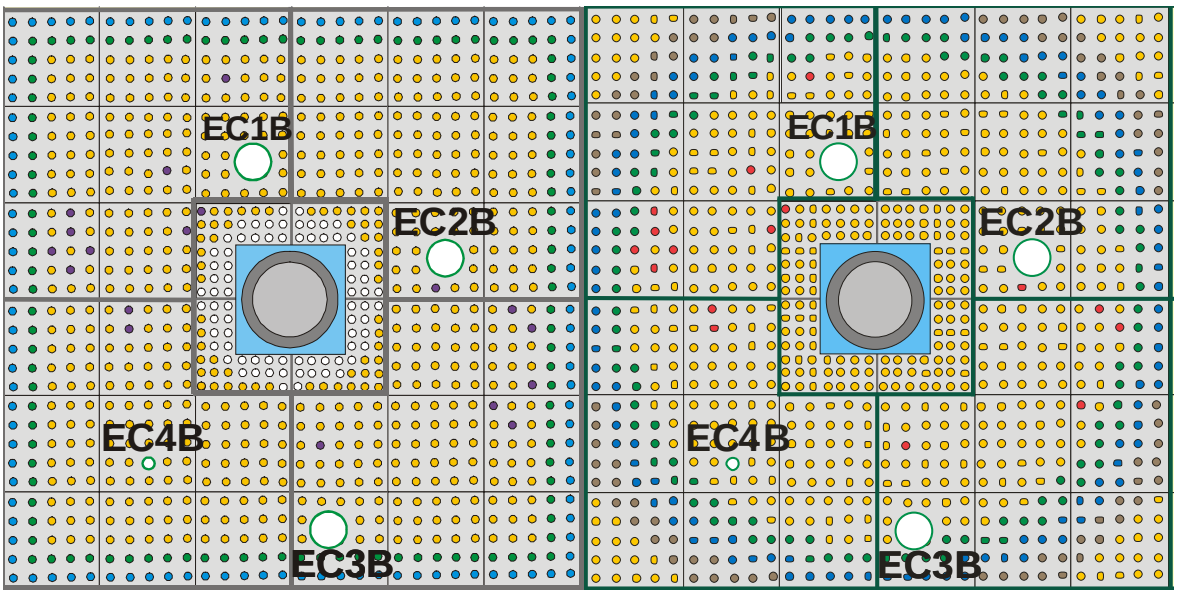

FIG. 5. Maps of the fast zones for the 3rd and 4th configurations of the Yalina-Booster.

RESULTS OF SUBCRITICALITY LEVEL MEASUREMENT WITH DIFFERENT METHODS AND TECHNIQUES AT THE YALINA-BOOSTER ASSEMBLY

For reactivity determination several methods were used, among them are statistical alpha-Rossi and alpha-Feynman, reciprocal counting method, pulsed neutron source and its modification. For every step theoretical calculations using MCNP4c [20] were performed. These methods are described in [21][22][23][24][25][26][27].

Below some results of comparing of neutron kinetic parameters for different configurations are provided.

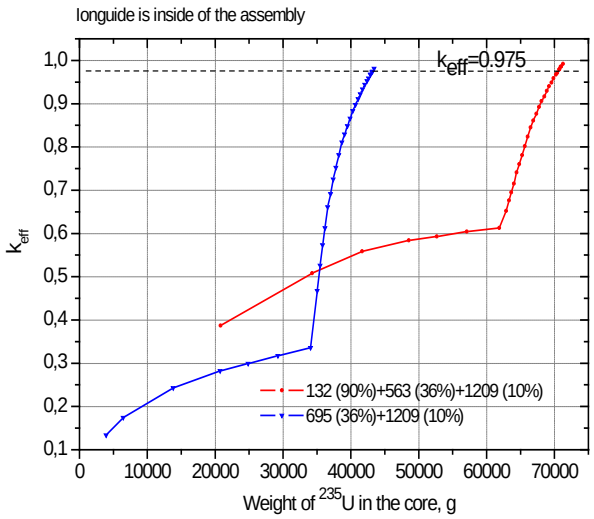

FIG. 6. Dependence of keff upon the number of EK-10 fuel rods loaded into thermal zone of the 1st and the 2nd configurations of YALINA-Booster core (calculation) – Ion guide is inserted

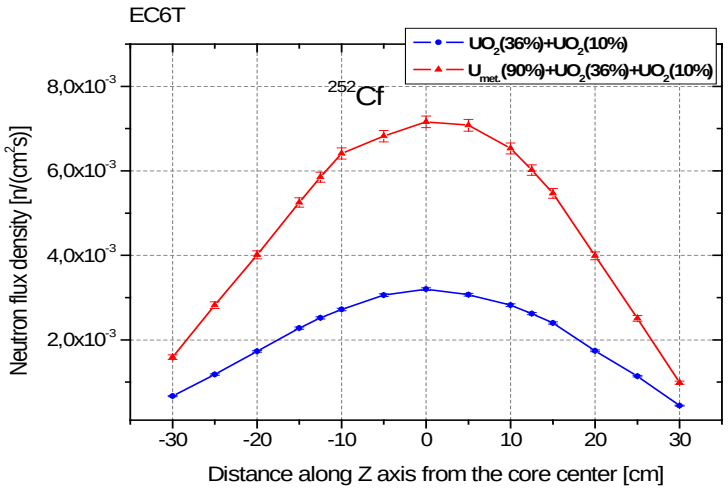

FIG. 7. Axial distribution of neutron flux density in the experimental channel EC6T by ^{252}Cf neutron source (1st and 2nd core configurations, calculation)

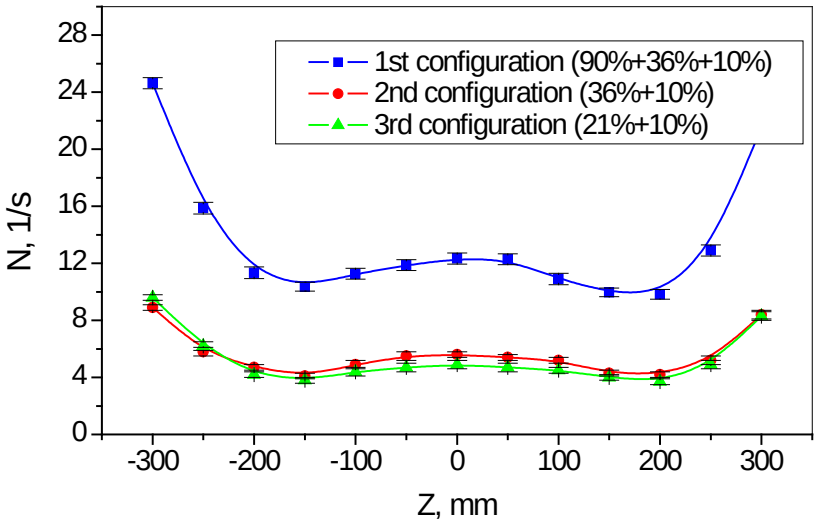

FIG. 8. Axial distribution of small size 3He detector counting rate in the experimental channel ECB1 of fast zone by ^{252}Cf neutron source

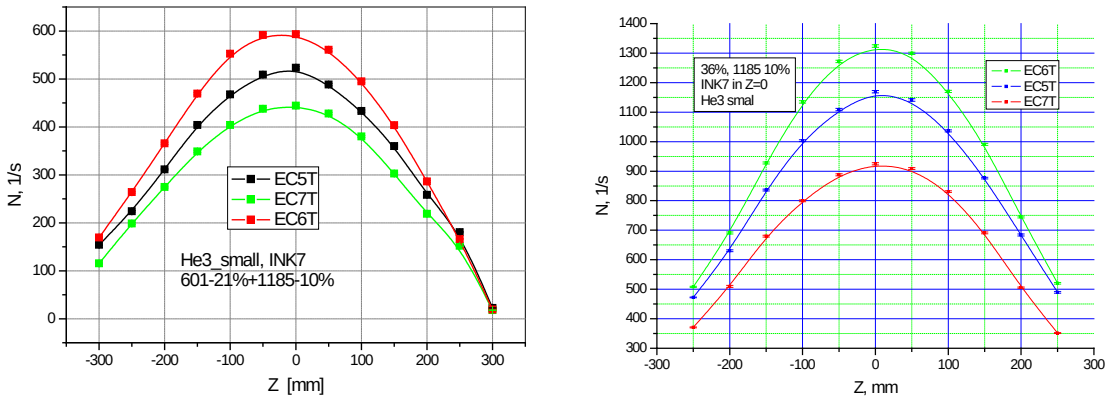

FIG. 9. Distribution of small size ^{3}He detector counting rate along the experimental channels of the 3rd (left) and the 2nd (right) configurations by ^{252}Cf neutron source situated in the axial channel inside the target hole at Z=0

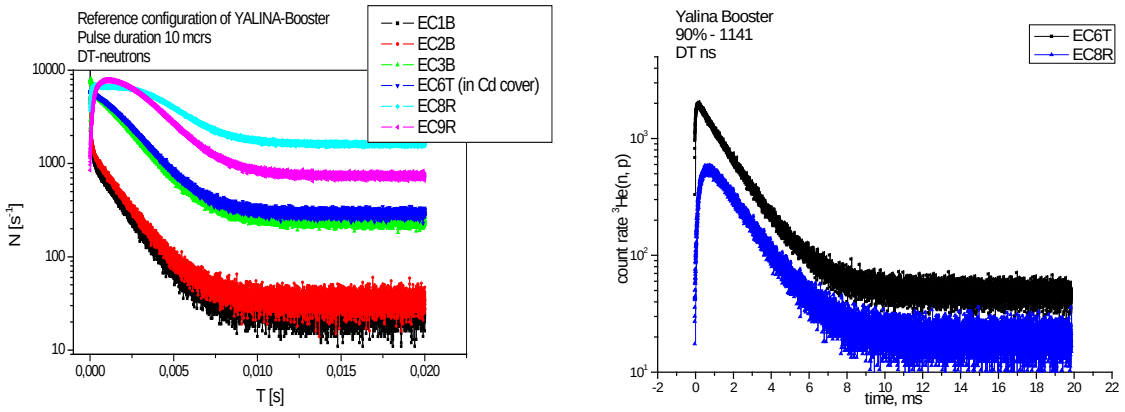

FIG. 10. Time dependence of ^{3}He detector counting rate measured in experimental channels of the core and reflector with D,T neutron source situated at Z=0, by pulse duration 10 μs for 3rd and 1st configurations.

CONCLUSIONS

Successful operation of this facility is a scientific contribution to the ADS and ADTT investigations from the Republic of Belarus, and international teams from the EU and the USA.

The experimental and theoretical studying of the main neutronics parameters of subcritical assembly YALINA-Booster with highly and lowly enriched nuclear fuel in fast zone has shown that:

The profiles of reciprocal counting numbers gained by experimental data from different measuring channels agree well enough thus demonstrating an appropriateness of the fuel load procedure chosen to reach the defined level of subcriticality;

The PNS technique has an advantage that both the reactivity and the prompt decay constant are obtained from the same set of experimental data.

It was shown that the area ratio method (Sjöstrand method) allows to measure the reactivity with high accuracy in terms of statistical uncertainty. However the method is sensitive to spatial effects caused by core heterogeneity and the detector's vicinity to the external neutron source.

Reliability of the subcriticality level estimation by PNS method goes up with rise of the assembly's effective multiplication factor. A discrepancy between the calculated and measured by PNS method k_{eff} values in the considered configuration of the assembly is less than 1%.

Main contribution to the reactivity of the assembly makes the thermal zone. It was shown that the kinetic parameters of YALINA-Booster are characteristic for thermal system, so the assembly's kinetics is defined by the thermal zone.

As far as reducing enrichment of uranium fuel is concerned, it was shown that after replacement of 90% enriched metallic uranium by 36% UO_2 in the inner region of fast zone, additional amount of 10% UO_2 fuel rods should be added into thermal zone in order to save k_{eff} on the same level In this case the main YALINA-Booster neutronics suffered not so remarkably, except for neutron spectrum softening in the inner region of the fast zone. The 2nd step of conversion to LEU fuel (21% UO_2 in fast zone) resulted in significant reduction of the effective multiplication factor for the same amount of fuel rods in thermal zone.

ACKNOWLEDGEMENTS

This work was supported by ANL(USA) in the frame of the ISTC Projects B#1341 and B#1732. The authors would like to express their gratitude to the ANL research team, especially to Dr. Yousry Gohar for the help in interpretation and analyses of the YALINA neutronics, comparison of the experimental and analytical results, explanation and elimination of any discrepancy.

REFERENCES

[1] Accelerator driven systems: energy generation and transmutation of nuclear waste, IAEA-TECDOC-985, Vienna (1997).
[2] OECD/NEA, Accelerator-Driven Systems (ADS) and Fast Reactors (FR) in Advanced Nuclear Fuel Cycles – a comparative study (2002).
[3] Salvatores, M., et al., "Global Physics Approach to Transmutation of Radioactive Nuclei", Nucl. Science&Technology, 116 (1994) 215-227.
[4] Soule, R., et al., "Validation of neutronic methods applied to the analysis of fast subcritical systems: The MUSE-2 experiments" (Proc. Int. Conf. GLOBAL'97, Yokohama, 1997).
[5] Soule, R., et. al., Neutronic Studies in Support to ADS: The MUSE experiments in the MASURCA Facility, Nucl. Sci. Eng., 148 2004 124-152.
[6] Destouches, C., The GENEPI accelerator operation feedback at the MASURCA reactor facility, Nuclear Instruments and Methods in Physics Research, A 562 (2006) 601-609.
[7] Serafimovitch, I., et al., "A small-scale set-up for research of some aspects of accelerator driven transmutation technologies", (Proc. 3rd International Conference on Accelerator Driven Transmutation Technologies and Applications, ADTTA'99, Prague, 1999).
[8] Chigrinov, S., et. al., Booster Subcritical Assembly Driven by a Neutron Generator, Preprint JIPNR-Sosny, 14, Minsk (2004), 31p. (in Russian).
[9] Beller, D., et. al. "Initial Results from the Reactor-Accelerator Coupling Experiments (RACE) Project" (Proc. 8th Information Exchange Meeting on Actinides and Fission, Products Partitioning&Transmutation, OECD/NEA Paris, 2005, 495-504.
[10] Salvatores, M., et. al., TRADE (TRIGA Accelerator Driven Experiment): A Full Experimental Validation of the ADS Concept in European Perspective (Proc. Int. Conf. ACCAPP'03, San Diego, 2004)
[11] Sasa, T., Oigawa, H., Current Plan of J-PARC Transmutation Experimental Facility (Proc. of Int. Conf. AccApp'07, Pocatello, Idaho, 2007).
[12] Gohar, Y., et. al., "Accelerator Driven Subcritical Facility Design Concept" (Proc. of 8th Int. Topical meeting on Nuclear Applications and Utilization of Accelerators, AccApp'07, Pocatello, Idaho, USA, 2007).
[13] Xia Haihong, "The Progress of Researches on ADS in China" (Proc. Int. Topical Meeting on Nuclear Research Applications and Utilization of Accelerators, AccApp'09, Vienna, 2009), IAEA-I3-CN-173. ADS/INT-01.
[14] Billebaud, A., Cahier des charges de la source de neutrons GENEPI-3C en mode continu, Technical report IN2P3_LPSC_GPR, GUI-SPE-1.1-0001-LPSC, Rev. 1, 23/07/2007.

[15] Chigrinov, S., et. al., “The Research of Transmutation of Long- Lived Fission Products and Minor – Actinides in a Sub-critical Assembly Driven by the Neutron Generator” (Proc. of 2-nd Int. Conference on Accelerator Driven Transmutation Technologies&Applications (ADTTA), Kalmar, 1996. V 2. 737-741).

[16] Chigrinov, S., et. al., “Experimental research of transmutation of long-lived fission products and minor actinides in a subcritical assembly driven by neutron generator” (Transactions of the Workshop Problems of Nuclear Energy Utilization dedicated to 85th anniversary of Academician A. Krasin, Minsk, 1996) 60-65 (in Russian).

[17] Kiyavitskaya, H., et. al., Transmutation of fission products and minor actinides in a subcritical assembly driven by a neutron generator, (NATO Advanced Research Workshop “Nuclear Science&Safety in Europe”, Yalta, Springer, Netherlands, 2005), Series B: Physics and Biophysics, 265-274.

[18] Kiyavitskaya, H., et. al., Transmutation of minor actinides in a system Proton Accelerator – Lead Neutron Producing Target – Graphite Neutron Moderator, Nonlinear phenomena in Complex systems, V.9, No. 1. 2006 87-91.

[19] Kiyavitskaya, H. (coordinator), YALINA-Booster Benchmark Specifications for the IAEA Coordinated Research Projects on Analytical and Experimental Benchmark Analysis on Accelerator Driven Systems and Low Enriched Uranium Fuel Utilization in Accelerator Driven SubCritical Assembly Systems, IAEA. (2007).

[20] Briesmeister, J.F., MCNP – A general purpose N-particle transport code, version 4B: Report LA-12625-M/ Los Alamos National Laboratory (1997).

[21] Simmons, B.E. & King, J.S., A Pulsed Technique for Reactivity Determination, Nucl. Sci. Eng. 3 1958 595-608.

[22] Keepin, G.R., Physics of Nuclear Kinetics, Addison Wesley Publishing Company Inc., USA, (1965).

[23] Bell, G.J., Glasstone, S., Nuclear Reactor Theory (1970).

[24] Sjöstrand, N.G., Measurement on a subcritical reactor using a pulsed neutron source, Arkiv för fysik 11, 13 (1956).

[25] Gozani, T., A modified procedure for the evaluation of pulsedsource experiments in subcritical reactors, Nukleonik 4 (1962).

[26] Garelis, E. & Russell, J.L., Theory of Pulsed Neutron Source Measurements, Nucl. Sci. Eng. 16 1963 263-270.

[27] Masters, C. F. & Cady, K.B., A procedure for evaluating modified pulsed-neutron source experiments in subcritical nuclear reactors, Nucl. Sci. Eng. 29 1967.

On applicability of the 3D nodal code DYN3D for the analysis of SFR cores

E. Fridman, R. Rachamin

Helmholtz-Zentrum Dresden-Rossendorf, Dresden, Germany

Presented by E. Fridman

Abstract. DYN3D is an advanced multi-group nodal diffusion code originally developed for the 3D steady-state and transient analysis of the Light Water Reactor (LWR) systems with square and hexagonal fuel assembly geometries. The main objective of this work is to demonstrate the feasibility of using DYN3D for the modeling of Sodium cooled Fast Reactors (SFRs). In this study a prototypic European Sodium Fast Reactor (ESFR) core is simulated by DYN3D using homogenized multi-group cross sections produced with Monte Carlo (MC) reactor physics code Serpent. The results of the full core DYN3D calculations are in a very good agreement with the reference full core Serpent MC solution.

1. Introduction

DYN3D [1] is an advanced multi-group nodal diffusion code originally developed for 3D steady-state, burnup, and transient analysis of Light Water Reactor (LWR) systems. Currently, the DYN3D code is being extended to the modeling of Sodium cooled Fast Reactor (SFR) cores. The purpose of this study is to demonstrate the feasibility of using DYN3D for steady-state analysis of SFR cores. In this work the burnup analysis of a reference SFR core was carried out using the DYN3D code. Homogenized few-group cross sections required by DYN3D were generated using continuous energy Monte Carlo (MC) code Serpent [2] which provides significant modeling flexibility compared with traditional deterministic lattice transport codes and tolerable execution time. The results of the DYN3D calculations were verified against full core Serpent MC solution.

2. Reference SFR core description

A simplified 2D model of the “working horse” European Sodium Fast Reactor (ESFR) core [3] was considered as a reference core in the current study. The core is loaded with 225 inner and 228 outer MOX fuel sub-assemblies with Pu content of 14.5 wt% and 17.0 wt% respectively. The core is surrounded by 3 rings of reflector assemblies. In the simplified model, the control system consists of 33 Control and Shutdown Devices (CSDs) located in the inner core region. The radial layout of the reference core is depicted in Fig. 1.

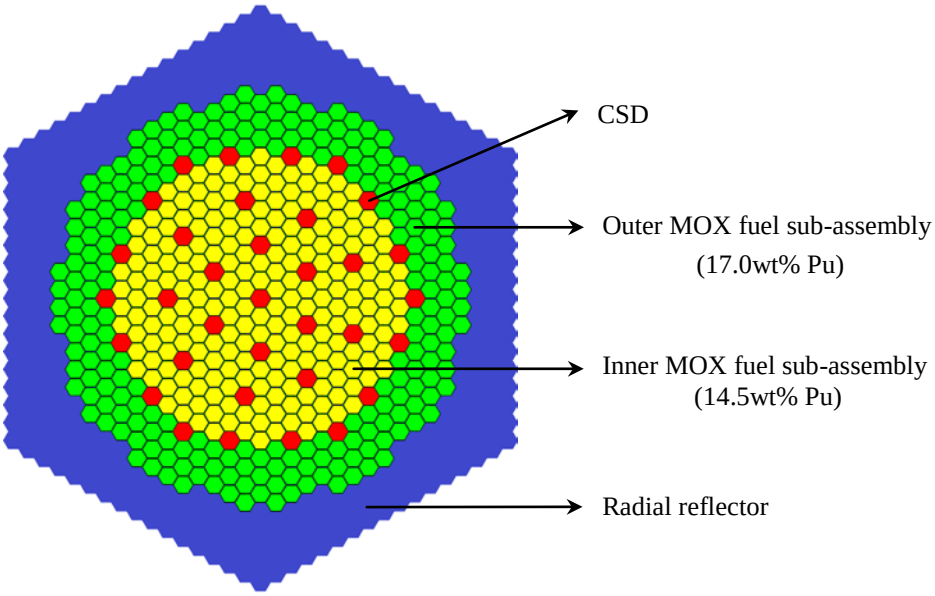

FIG. 1. Reference SFR core layout.

3. Few-group cross section generation methodology

In this work the few-group cross section sets for the fuel and non-multiplying core regions were produced by the Serpent code employing ENDF/B-VII based continuous energy library. The considered few-group energy structure is a 24-group subset of the 33-group energy structure of the ERANOS code [4] developed and validated for neutronic analyses of fast reactor cores. The 24-group structure was obtained by collapsing 10 thermal energy groups (from 33 to 24) into a single thermal group. This modification was done because Serpent calculations show large statistical uncertainties in neutron flux in thermal energy groups as demonstrated in Fig. 2.

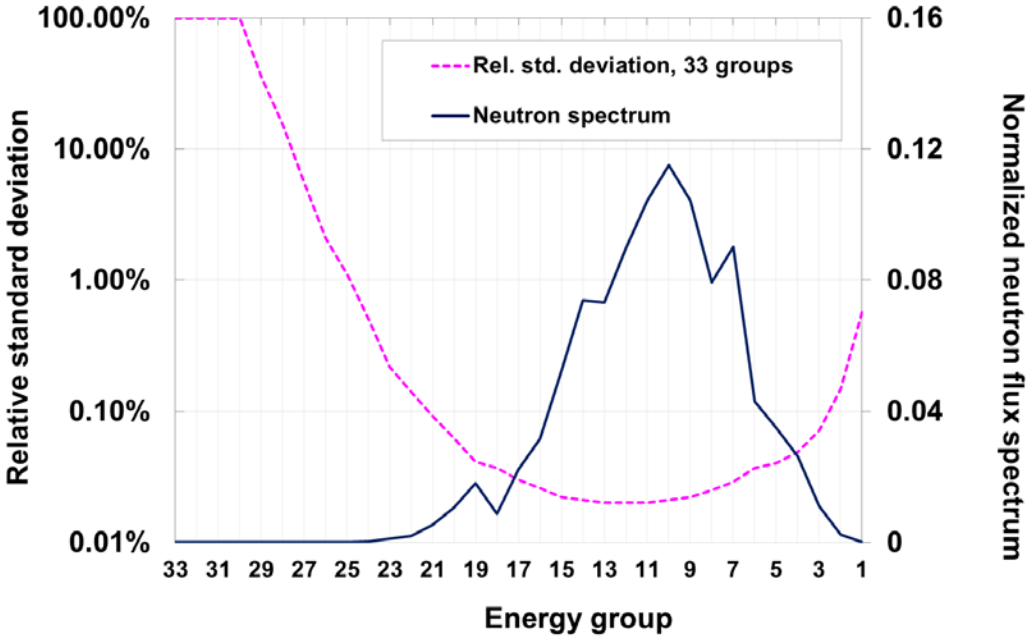

FIG. 2. Statistical uncertainty in 33-group neutron spectrum calculated by Serpent.

Burnup dependent 24-group cross sections for fuel assemblies not facing the radial reflector were generated in an infinite assembly lattice calculation (Fig. 3). The 24-group data sets for the outermost

fuel sub-assemblies facing the radial reflector and radial reflector itself were generated using 2D fuel-reflector model depicted in Fig. 4. The configuration presented in Fig. 5 was used to generate 24-group cross sections for CSD sub-assembly and burnup dependent 24-group cross sections for surrounding fuel sub-assemblies. All non-multiplying regions were modeled as homogeneous mixtures of structural materials and sodium.

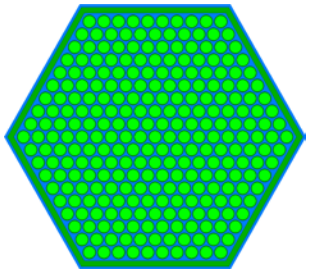

FIG. 3. ESFR fuel sub-assembly model.

FIG. 4. ESFR fuel-reflector model.

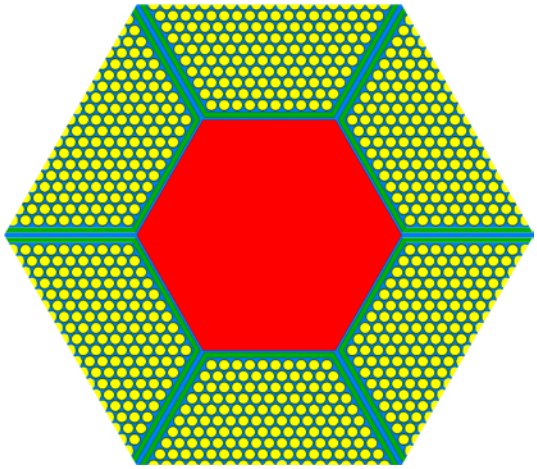

FIG. 5. ESFR fuel-SCD model.

4. Full core analysis results

In this section the full core results obtained by the Serpent and DYN3D codes are presented and compared. The operating parameters of interest include burnup dependent k-eff, beginning of life (BOL) and end of life (EOL) radial power distribution, coolant void reactivity (CVR) coefficient, and Doppler constant (k_D) as well as BOL total worth of CSDs. The Serpent radial power distribution was obtained by averaging the results of 15 independent full core runs executed with different random number seeds. Doppler Constant, k_D, was calculated as:

$$k_D = \frac{\rho_2 - \rho_1}{\ln \frac{T_2}{T_1}}$$

where T_1 and T_2 are the fuel temperatures and ρ_1 and ρ_2 are the corresponding reactivity values. In the current analysis T_1 and T_2 were assumed to be 900K and 1200K, respectively.

The k-eff as a function of burnup estimated by Serpent and DYN3D is compared in Fig. 6. An excellent agreement in k-eff values between the codes can be observed while the maximum difference does not exceed 40 pcm. The evaluated core integral parameters are compared in Table 1. The DYN3D results are very close to those of the Serpent full core MC calculations at both BOL and EOL. The difference in CVR and k_D is lower than 30 pcm and 10 pcm respectively. The CSD worth estimated by the codes at BOL agrees within less than 50 pcm.

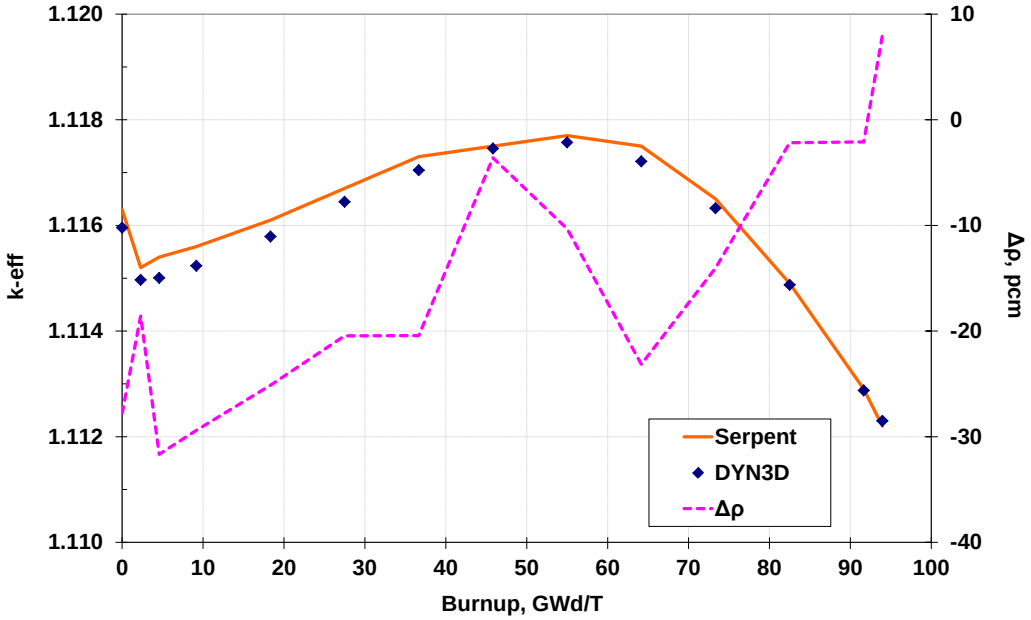

FIG. 6. K-eff as a function of burnup, Serpent vs. DYN3D.

Table 1. Comparison of safety related parameters

Parameter	Stage	Serpent	DYN3D	Difference, pcm Serpent vs. DYN3D
kD, pcm	BOL	-1062	-1072	-10
	EOL	-723	-723	0
CVR, pcm	BOL	2821	2850	29
	EOL	3654	3702	47
Total CSD worth, pcm	BOL	-4678	-4629	49

The radial power distribution for the unrodded core state calculated by Serpent and DYN3D at BOL and EOL is compared in Fig. 7 and Fig. 8 respectively. The BOL radial power distribution predicted by DYN3D agrees reasonably well with the reference MC solution while the maximum and average relative differences are about 2.1% and 0.6% (Fig. 7). At the EOL the maximum deviation between the reference Serpent solution and the DYN3D results is about 5.3% and was observed in some low power sub-assemblies located in the proximity of CSDs (Fig 8). However, the average difference is still below 1.5%.

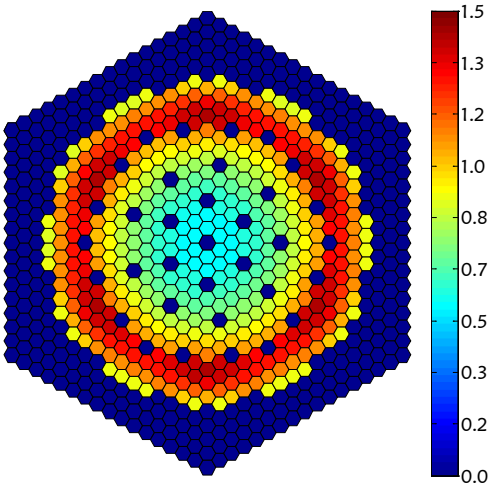

a. Relative radial power profile, Serpent

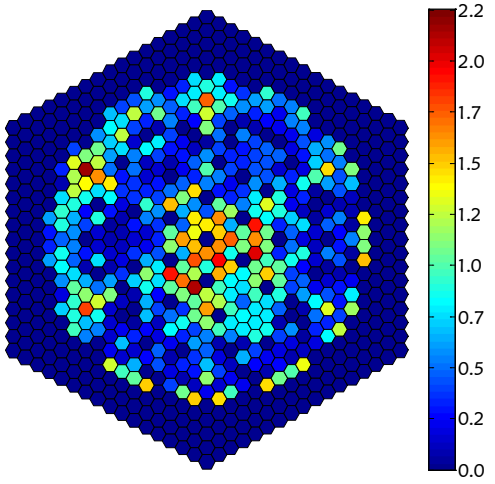

b. Relative difference in radial power profile, % Serpent vs. DYN3D

FIG. 7. Comparison of radial power distribution at BOL.

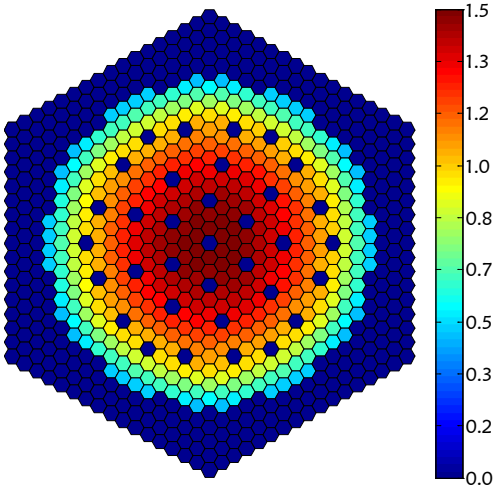

a. Relative radial power profile, Serpent

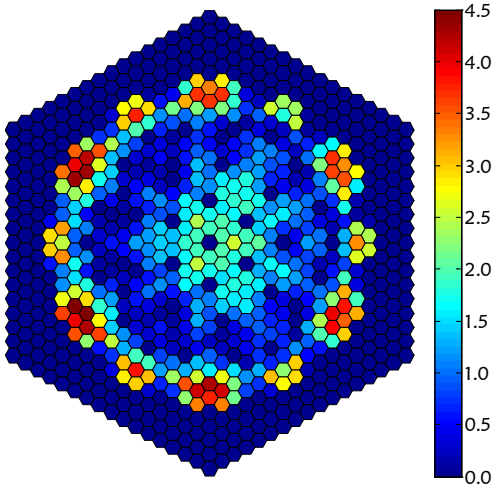

b. Relative difference in radial power profile, % Serpent vs. DYN3D

FIG. 8. Comparison of radial power distribution at EOL.

5. Summary

The objective of this study was to investigate the feasibility of modeling fast spectrum reactors with DYN3D nodal diffusion code. In this study, we used Monte Carlo code Serpent which was specifically developed for the cross sections homogenization problems and provides a great deal of additional flexibility as compared with deterministic lattice transport codes with tolerable CPU time penalty.

To demonstrate modeling capabilities of the Serpent-DYN3D code sequence, we performed a series of analyses for representative ESFR core. The results of the calculations performed with Serpent-DYN3D sequence were compared with the full core Monte Carlo solution calculated with Serpent code. Very good agreement was obtained between the codes in all calculated integral parameters such as burnup dependent core reactivity, CVR, kD, and CSD worth demonstrating the potential of the Serpent-DYN3D code sequence for modeling SFR cores.

REFERENCES

[1] RUGGERI J.-M. et al., ERANOS 2.1: The International Code System for GEN-IV Fast Reactor Analysis, Proc. ICAPP 2006, Reno, Nevada, USA, (2006).
[2] GRUNDMANN U., ROHDE U., MITTAG S., DYN3D – three-dimensional core model for steady-state and transient analysis of thermal reactors, Proc. PHYSOR 2000, Pittsburgh, Pennsylvania, USA, (2000).
[3] LEPPÄNEN J., Development of a new Monte Carlo reactor physics code. D.Sc. Thesis, Helsinki University of Technology, (2007).
[4] FIORINI G.L., VASILE A., European Commission – 7th Framework Programme: The Collaborative Project on European Sodium Fast Reactor (CP ESFR), Nuclear Engineering and Design, 241, (2011).

CEFR Irradiaton Test and Application

Chen Xiaoliang, Yu Hong, Huang Chen, Xu Baoyu, Yu Tuanjie, Xu Xi'an

China Institute of Atomic Energy, Beijing, China

Abstract. China Experimental Fast Reactor (CEFR) has completed physics start-up tests in 2010 and connected the grid on 40%FP in 2011. During start-up tests, the special irradiation test subassembly has been developed for measurement of distribution of reaction rate, spectrum index and neutron spectrum by using activation method in lower power. Characteristic of neutron field for irradiation in CEFR has been researched by calculation and experiments. In future, CEFR will been operated as an irradiation test facility for fuel, material and other application, and some irradiation projects, such as irradiation of cladding material, MOX fuel and (U, Np)O_2 pellet have been planned. Now some irradiation rigs have been developed.

1. Introduction

China Experimental Fast Reactor (CEFR) is the first fast reactor in China with thermal power of 65MW and electrical power of 20MW. CEFR is a pool type sodium cooled fast reactor which has a three circuit of sodium-sodium-water thermal transfer system consisting of two independent loops in parallel. The CEFR first fuel loading is UO_2 with 64.4% enriched ^{235}U [1] .

CEFR achieved its first criticality on 21 July in 2010. And then physics startup tests have been done in low power for a few months. CEFR physics startup consists of 4 types of tests, such as fuel loading and criticality tests, measurement of control rods value, measurement of reactivity coefficient and low power irradiation tests. After these physics tests, the accuracy of CEFR core physics calculation was verified and some key parameters about CEFR neutron field were obtained which were essential for carrying out other irradiation tests in CEFR core in future.

After a series of power up tests, CEFR connected the grid on 40%FP in July 2011, and will be operated in full power in 2013. In future the major role of CEFR is as an irradiation facility for FBRs' fuel and material development and other application. Now some programs have been conducted for transmutation, fuel and material irradiation tests in CEFR core.

This paper describes the low power irradiation test in CEFR physics startup stage. Some experimental results, such as fission ration rate distribution and neutron spectrum in CEFR core are given. Additionally, some programs about transmutation, MOX fuel and cladding material irradiation tests in CEFR are introduced in detail.

2. Low power irradiation test in CEFR

The power distribution, neutron spectrum and spectrum index etc. are some important parameters for CEFR neutron field. In order to measure these parameters some low power irradiation tests using foil activation method have been done in CEFR core[2]. In these tests, a set of foils would be irradiated in CEFR core in low power and then the activities of the foils were measured to obtain the information about CEFR neutron field.

2.1.Irradiation test subassembly

Since there is no irradiation channel in CEFR, a special irradiation test subassembly was designed and fabricated to complete the tests. There were two kinds of irradiation test subassemblies, one is using in core, another is in reflector area.

The irradiation test subassembly was the same with CEFR fuel subassembly in dimensions. It is 2592mm in length and 59mm in hexagonal distance. For fuel test subassembly, 7 central fuel pins were drawn out and an irradiation tube which is 1617mm in length and14mm in diameter is thrown into. The foil detectors were sealed in the tube with argon gas. Fig.1 shows the structure of the fuel test subassembly. This design could minimize the impact on the neutron field of irradiation position. The structure of reflector test subassembly is showed in Fig.2, same as fuel test subassembly in external dimensions, but the diameter of inner irradiation tube is 16mm. The fuel test subassembly is used in core and reflector test subassembly is in radial reflector area. One fuel test subassembly, five reflector test subassemblies and several irradiation tubes were fabricated for the low power irradiation test. Some other equipment such as shifting device of irradiation tube and platform for irradiation tube disassembly was also fabricated.

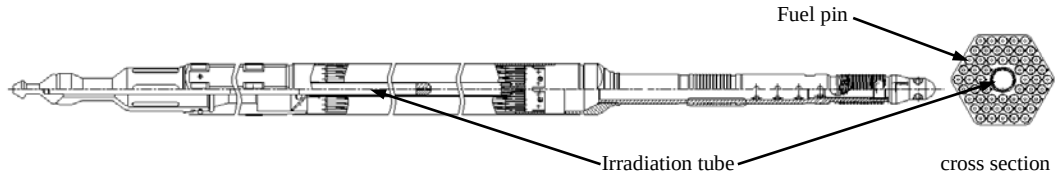

FIG. 1. Fuel test subassembly.

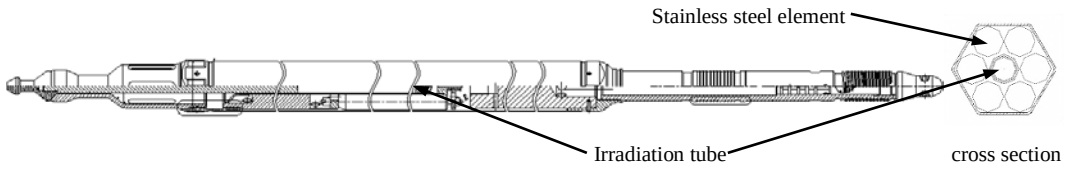

FIG. 2. Reflector test subassembly.

2.2.Low power irradiation in CEFR core

Using the shifting device the irradiation tube with foil detectors was put into the test subassembly which was located in the storage drum. After preheated by argon gas for 24 hours, the irradiation test subassembly with the irradiation tube was shifted to CEFR core by the in pile refueling system.

In order to reduce the dose of the irradiation tube, the irradiation power was set for about 0.1‰ to 1.0‰ full power, and the irradiation time was about 2 hours. The whole irradiation process was monitored by the digital reactor monitor system. After irradiation the irradiation tube was shifted from CEFR core and then was disassembled. Then the foil detectors were taken out and the activity of the foils were measured by high purity Germanium spectrometer in lab.

2.3.Fission reaction rate distribution

Fission reaction rate is a key parameter and is related to the power distribution directly. ^{235}U and ^{238}U radial and axial fission reaction rate were measured using high purity uranium foils. 8 radial positions from inner core to reflector area were set for radial distribution measurement, showed in Fig.3.

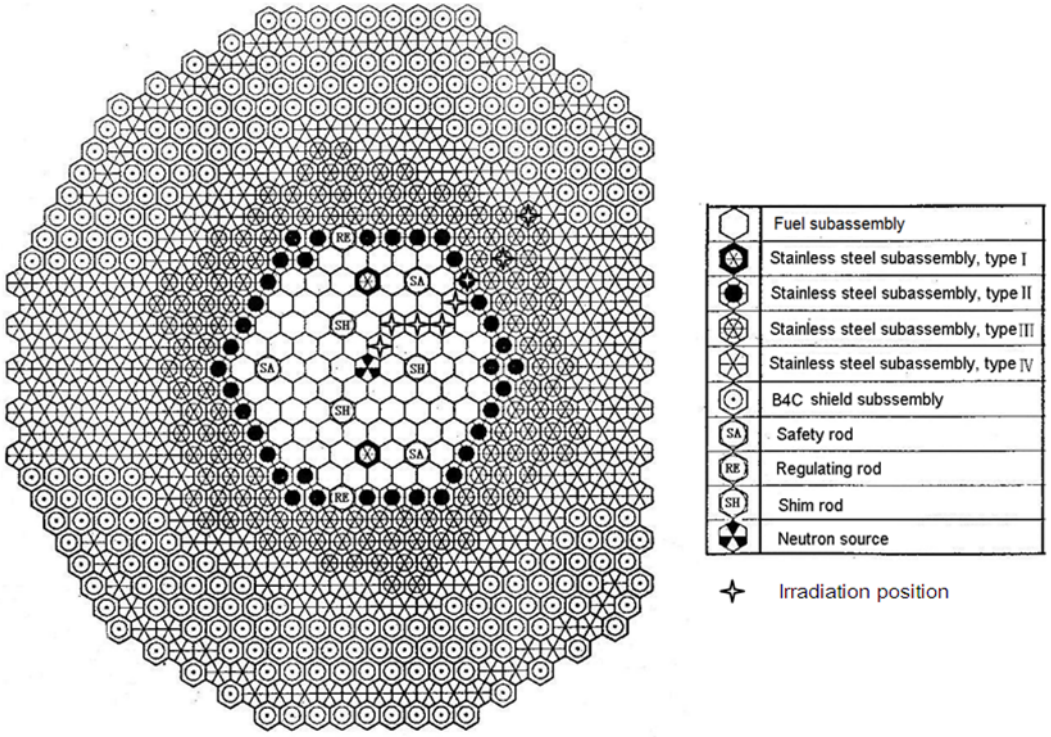

FIG. 3. Irradiation positions for fission reaction rate in CEFR core.

Fig.4 shows the result of radial distribution of 235U and 238U. Black line is the calculated value and dot is the experimental value. They are according with each other.

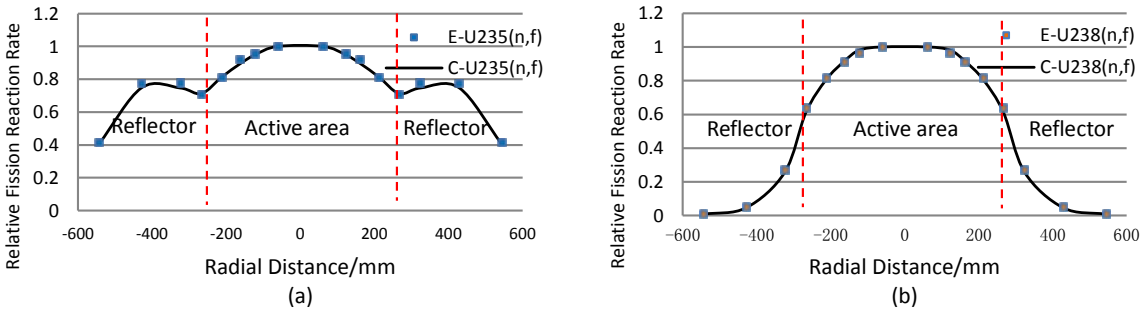

FIG. 4. *Radial Distribution of U-235 (a) and U-238 (b) Fission Reaction Rate.*

2.4.Neutron spectrum

Neutron spectrum is another important parameter in CEFR core. Neutron spectrum in position (2-2) and (7-5) were determined by means of multifoil activation method[3]. These two positions are some representative place in CEFR core for future application. In this kind of tests a dozen of foils were irradiated in same time, then the activity of every foil were measured by high purity Germanium gamma-ray spectrometer. A neutron spectrum adjusting code was compiled to determine the neutron spectrum.

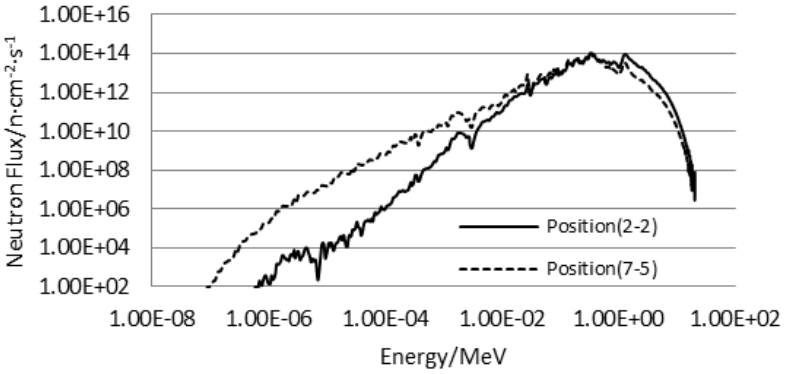

FIG. 5. Neutron Flux in Position (2-2) and (7-5).

Fig.5 shows the adjusted neutron spectrum in position (2-2) and (7-5). The neutron fluence of fast energy (E>0.1MeV) is about 2.63×10^{15} $n\cdot cm^{-2}\cdot s^{-1}$ in position (2-2), and $1.93\times10^{15} n\cdot cm^{-2}\cdot s^{-1}$ in position (7-5).

3. Other application in CEFR

CEFR will be a good irradiation bed for the fuels and materials for future FBRs and transmutation research. In order to develop the CEFR MOX fuel and cladding material for FBRs and obtain the essential experimental data about transmutation in fast reactor, some application programs have been conducted in CEFR.

3.1.CEFR transmutation test

In order to access the technology of $(U,Np)O_2$ pellets fabrication and obtain the basic data of transmutation in fast reactor, a program of transmutation test in CEFR is in progress. In this program the $(U,Np)O_2$ pellet (contained 5% Np) and fuel pin will be developed and the fuel pin will be irradiated in CEFR core using the special irradiation rig.

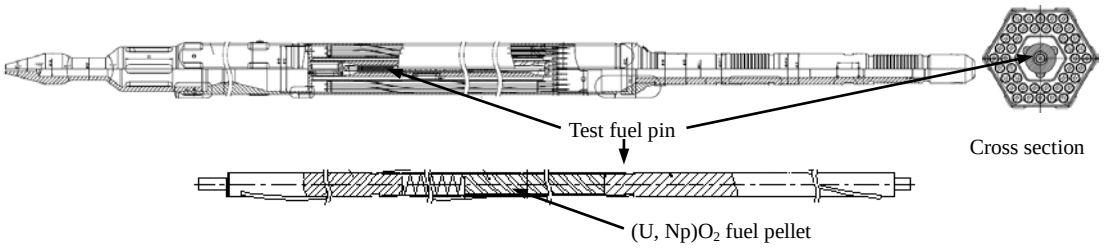

FIG. 6. Irradiation rig and fuel pin of transmutation test.

Fig.6 shows the structure of the irradiation rig. The irradiation rig is the same with fuel subassembly in dimension. The fuel pin which contains 12 $(U,Np)O_2$ pellets is set in central position of the irradiation rig. The pellet is 5mm in diameter and 6mm in length. Around the fuel pin there are 42 stainless steel tubes in irradiation rig. Now the irradiation rig is under fabricating.

3.2.CEFR MOX fuel irradiation test

MOX fuel is an inevitable choice for China fast reactor technology recently and next period of time. China MOX fuel technology is lagging behind, and there is little experience on MOX fuel fabrication for the fuel plant. So CEFR driver fuel is UO_2 with about 64.4% enriched ^{235}U. Now a program of MOX fuel development for FBRs is conducted. In this program one of important item is to develop the MOX fuel pin and bundle and to conduct steady-state irradiation in CEFR core. MOX fuel

pin is 1065mm in length and the active core is 450mm, upper blanket is 25mm and lower blanket is 50mm. The plenum is set in lower, 450mm in length. The cladding is fabricated by 316(Ti) stainless steel, and 0.4mm in thickness. For irradiation test, one irradiation test subassembly for MOX fuel pin and two test assemblies for fuel bundle were designed for the irradiation test.

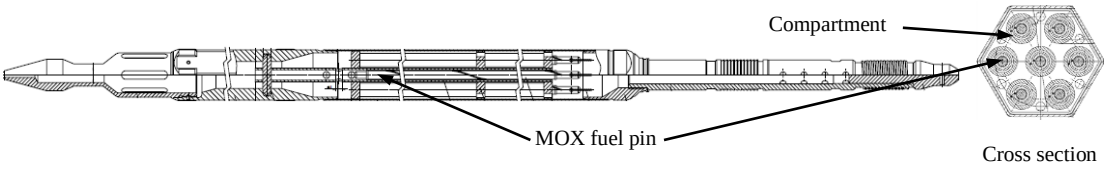

FIG. 7. Test subassembly for MOX fuel pin.

Fig.7 shows the structure of test subassembly for fuel pin. There is six fuel pins in the test subassembly. Every fuel pin is contained by a stainless steel capsule.

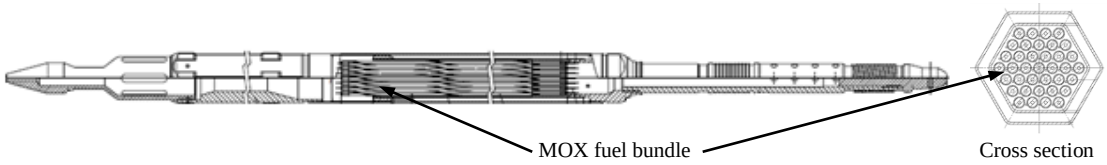

FIG. 8. Test subassembly for MOX fuel bundle.

The structure of test subassembly for fuel bundle is shown in Fig.8. There are 37 fuel pins in the test subassembly and less one circle vs. CEFR UO_2 Fuel subassembly. The whole 37 fuel pins are contained by a hexagonal capsule. The fuel pins are orientated by the spacer wire.

The target burn-up for MOX fuel pin is more than 6.0at % in irradiation test. For this purpose, the fuel pin test subassembly and fuel bundle test subassembly are will located in the second ring in CEFR core for about 300 full power days. The irradiation position is showed in Fig.9.

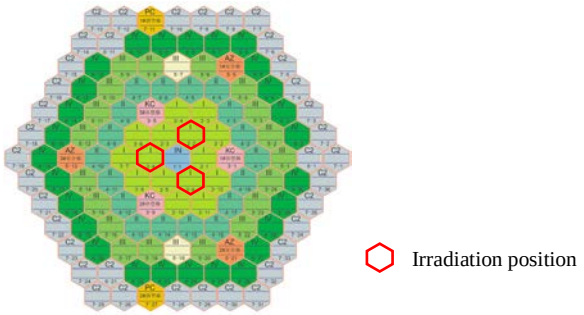

FIG. 9. Irradiation positions of MOX fuel pin and bundle

3.3.CEFR structure material irradiation test

As we known, 316(Ti) stainless steel is performance as FBR's fuel cladding material. Because of less irradiation test data of 316(Ti)SS developed by China, the Chinese 316(Ti)SS was not used in CEFR UO_2 fuel. But Chinese 316(Ti)SS is planning for commercial application as China CDFR fuel cladding material. A program has been conducted for Chinese 316(Ti)SS stainless steel irradiation in CEFR core. An irradiation facility has been designed for all kinds of material test samples' irradiation, such as for cladding tube tensile test, tensile, creep test, double axis creep test, swelling test etc. Fig.10 shows the structure of the irradiation facility. It is the same with other test subassembly in dimension.

But there are three carriages in vertical direction. The temperature in carriage is different in irradiation by setting different gas gaps. From the lower to upper carriage, the irradiation temperature is 550℃, 600℃ and 500℃. The target of the radiation damage of the 316(Ti)SS test samples is about 30 dpa(displacement per atom). For the purpose, the irradiation facility is planning for test in CEFR central position for about 300 full power days.

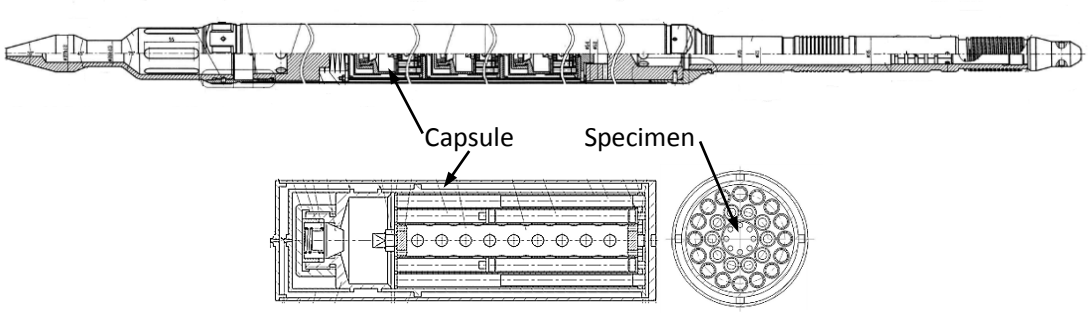

FIG. 10. Irradiation facility and carriage for structure material.

4. Conclusion

In order to measure some key parameters of CEFR core, some special irradiation test assemblies were designed and fabricated. Fission reaction rate and neutron spectrum were measured by foil activation method.

CEFR will become a well irradiation test platform for research in transmutation, fuel and material irradiation of FBRs. The $(U,Np)O_2$ pellet and fuel pin are developing and the irradiation subassembly is designed for CEFR transmutation test. In order to development the MOX fuel for FBR, the MOX fuel pin has been designed and the fuel pin and bundle will be irradiation in CEFR core using special irradiation subassembly. For cladding material, 316(Ti)SS is a good choice for China fast reactor development. In order to obtain the irradiation test data, the irradiation facility has been designed which contained three carriages. And the irradiation facility will be located in CEFR central position for more dpa.

ACKNOWLEDGEMENTS

This work was been carried out under the projects of China National high-tech R&D Program “Research in Transmutation of Long-lived Nuclide in Fast Reactor” and “Research in MOX fuel Irradiation ”.

REFERENCES

[1] Tian, H., 2002. The design description of China Experimental Fast Reactor (CEFR). Technical Report of China Experimental Fast Reactor, CEFR01Z19LWS01-SM, 2002 (in Chinese).

[2] Chen, X., 2009. Test Procedure of Foil Activation method in CEFR Core, Technical Report of China Experimental Fast Reactor.

[3] S.A.Jonah, K.Ibikunle, Neutron spectral distribution from a sealed-tube neutron generator by multiple-foil activation unfolding method, Nucl. Instr. and Meth.,2003, A501: 514-516.

Synthesis of the first experimental results obtained on the PROFIL-R and M experiments performed in the Phenix fast neutron reactor

H. ISNARD[a], P. BOURDOT[b], S. EYMARD[c], G. FERLAY[d], P. LEVEQUE[c], O. VIGNEAU[e], M. PHELIP[f]

[a] CEA, DEN/DANS/DPC/SEARS/LANIE

[b] CEA, DEN/DER/SPRC/LECy

[c] CEA, DEN/DSN/SEEC/LECD

[d] CEA, DEN/DRCP/SERA/LED

[e] CEA, DEN/DEC/SA3C/LARC

[f] CEA, DEN/DEC/CP

Abstract. The PROFIL-R (fast spectrum) and PROFIL-M (moderated spectrum) experiments were performed between 2003 and 2008 in the French fast neutron reactor Phénix. These experiments consisted of the irradiation of pure isotope samples in a well-characterized neutrons flux in order to collect accurate information on the total capture integral cross sections of the principal heavy isotopes and some important fission products in the spectral range of fast reactor. This method can be used for all isotopes transformed by neutron capture into a stable or long-lived nuclide and is based on the measurement of the composition change induced by irradiation. Therefore, accurate and reproducible measurements of isotopic compositions and concentrations of the elements (actinides and fission products) before and after irradiation are required. The major difficulty for the analyses of these actinides and fission products is the low quantity of the initial powder enclosed in steel container (3 to 5 mg) and the very low quantities of products formed (several μg) after irradiation. We present the developments performed during the last few years by laboratories of the French Commission on Atomic Energy and Alternative Energies (CEA) in order to acquire very accurate and precise isotopic and elemental data on selected irradiated powders. Among the necessary developments are the conceptions of systems set in shielded hot-cells to open the steel containers and collect the full amount of powders, and the set-up of specific analytical methods for mass spectrometry measurements in order to obtain isotopic and elemental ratios at uncertainty of few per mil level. A synthesis of the results obtained and first preliminary interpretations will also be presented.

1. Introduction

The PROFIL-R and M experiments were performed in the French fast neutron reactor Phénix and took place after previous experiments named PROFIL and PROFIL-2 [1]. PROFIL-R was performed in a standard fast spectrum and PROFIL-M in a spectrum softened by a thick $^{11}B_4C$ sheath around the

experimental pins. The experiments consisted of the irradiation of pure isotope on powder form. Each enriched powder was enclosed in steel container inserted in individual pins of identical geometry for the two experiments. The elements present in powder form are representative of actinides and fission products present in irradiated Uox and Mox fuel samples and cover all the applications for which accurate capture integral cross section are necessary. The major difficulty for the analyses of these actinides and fissions products is linked to the low quantity of the initial powder enclosed in steel container (3 to 5 mg) and the very low quantities of activation products formed (several μg or ng) after irradiation. Furthermore the presence of the activated steel container, where the powder was enclosed, increases the analytical challenges for several reasons. First if the steel container is dissolved simultaneously with the powder the activity of the solution will be higher than the maximum activity that can be handled in glove box. Secondly the presence of a steel matrice (Fe, Cr, Ni) extends the chemical separation for subsequent isotopic analysis [2] and finally the presence of Mo impurities hampers the accurate isotopic measurements of, for example, the three Mo targets (^{95}Mo, ^{97}Mo and ^{100}Mo) after irradiation. The conception of a system implanted in shielded hot-cell to open steel containers and collect all the powders after irradiation was necessary from the beginning of the project. After powder recuperation, different procedures of dissolution were necessary to dissolve all the elements present after irradiation. For several powders, like metallic ruthenium, metallic silver or metallic rhodium, this step was an analytical challenge due to the very high resistance of these metals to acid solutions and some research and development have been performed. Finally accurate and precise isotopic analyses were performed by mass spectrometry. It requires preliminary chemical separation to eliminate the elements which could prevent ionization and/or generate isobaric interferences in the mass spectrum of the analytes during measurements, thus leading to non-accurate isotopic analysis [3][4][5]. After separation several developments were performed by Thermal Ionisation Mass Spectrometry (TIMS) or Multi-Collector Inductively Coupled Plasma Mass Spectrometry (MC-ICPMS) to be able to obtain very robust elementary and isotopic data.

This paper presents the developments performed during the last few years by laboratories of the French Commission on Atomic Energy and Alternative Energies (CEA) in order to acquire very accurate and precise isotopic and elemental data on selected irradiated pure isotopes.

2. PROFIL-R and M pins

The PROFIL-R experiment involved two experimental pins (labelled A and B) containing 55 separate samples each and loaded in the 4th fissile ring of the Phenix reactor core occupying a neutronically clean zone without control rods. Axially distributed ^{235}U containers were used as fluence monitors for each pin. A standard fuel pin in the central assembly position was characterized to measure the fluence data.

The PROFIL-M experiment used six experimental pins (labelled 1 to 6) containing 21 (pin 6), 22 or 23

(pin 1) separate samples each. Axially distributed ^{235}U containers were also used as fluence monitors for each pin

The Table 1 give the number of different samples loaded in each experimental pin.

Table 1. Number of experimental sample by type in the PROFIL-R and PROFIL-M pins. For PROFIL-M the pin number is indicated ().

	PROFIL R	PROFIL-M		PROFIL R	PROFIL-M		PROFIL R	PROFIL-M
^{232}Th	2+1	3(2)	B	1+1	1(5)+1(6)	^{109}Ag	1+1	1(4)+1(5)
^{233}U	1+1	1(2)+1(4)+1(6)	^{87}Rb	1+2	3(3)	^{129}I	1+2	1(2)+1(5)
^{234}U	1+1	1(1)+1(3)+1(5)	^{91}Zr	1+2	3(2)	^{133}Cs	1+1	1(1)+1(3)+
^{235}U	5+4	4(1)+1(2)+1(3)	^{92}Zr	1+2	3(3)			1(6)
		2(4)+2(5)+2(6)	^{95}Mo	1+1	1(5)+1(6)	^{140}Ce	1+2	3(2)
^{238}U	2+1	2(3)+1(6)+1(2)	^{97}Mo	1+1	1(1)+1(2)	^{141}Pr	1+1	1(1)+1(2)
		1(5)	^{100}Mo	1+2	1(1)+2(6)	^{143}Nd	1+1	1(1)+1(6)
^{237}Np	2+2	2(4)	^{99}Tc	1+2	1(2)+1(6)	^{145}Nd	1+1	1(4)+1(6)
^{238}Pu	2+1	1(1)+1(4)	^{101}Ru	1+1	1(3)+1(5)	^{146}Nd	1+1	3(4)
^{239}Pu	1+1	2(1)+1(3)+1(5)	^{102}Ru	1+1	3(5)	^{147}Sm	1+1	1(1)+1(4)
^{240}Pu	2+1	1(4)+1(6)	^{104}Ru	1+1	1(3)+1(4)+	^{149}Sm	1+1	1(5)+1(6)
^{242}Pu	2+1				1(5)	^{150}Sm	1+1	1(1)+1(3)
$^{242}Pu^{*}$		1(2)+1(3)+1(5)	^{103}Rh	1+1	1(1)+1(4)	^{152}Sm	1+1	1(1)+1(2)
		1(6)	^{104}Pd	1+1	1(1)+1(6)	^{153}Eu	1+1	1(4)+1(6)
$^{241\text{-}243}Am$	2+1	1(2)+1(3)	^{105}Pd	1+1	1(4)+1(5)	^{154}Gd	1+1	1(3)+1(4)
^{241}Am		2(4)+1(5)+2(6)	^{106}Pd	1+1	1(1)+1(2)	^{155}Gd	1+1	1(2)+1(3)
^{243}Am		1(1)+1(2)+1(3)	^{107}Ag	1+1	1(5)+1(6)	^{156}Gd	1+1	1(4)+1(5)
		1(4)+1(6)				^{157}Gd	1+1	1(1)+1(3)
^{244}Cm		2(1)+1(3)+2(5)						
		1(6)						

* The enrichment of the powder in ^{242}Pu was different between PROFIL-R and M.

3. The opening of the steel container

The steel containers were opened in two nuclear installations of the French Nuclear Agency: the CHICADE hot cell facility located in Cadarache and the ATALANTE facility located in Marcoule. All the operations of opening and recuperation were realized by teleoperation in shielded cell. Several steps were performed to recover the totality of the powder and to avoid pollution by any radioelements or natural element that could be present in the hot cell. The main difficulty arises from the size of the telemanipulated container and the very small quantity of the powder recovered.

A specific tool dedicated to identify the container, open and recuperate the powder was concepted and

implanted in the shielded cell and was able to accomplish each of the elementary and successive operations necessary to collect the very small quantities of powders. The identification of the container (with a video camera), the decontamination of the container, the opening and removal of its lid, the collection and weight of the active powder were realized first in the CHICADE facility and after in the ATALANTE facility since 2008. The first solution chosen for the opening of the container was a technique of Electro Chemical Discharge Machining [6]. For few samples and particularly for actinides we observed the introduction of the solution of electroerosion in the container during the opening and so the preferential solubilisation of some elements (like Cs or Nd) in this solution. So in 2011 this difficulty was solved through the use of another technique with the implementation of a milling to perform the opening of the container by mechanical abrasion. Figure 1 present the principle of opening of the container using abrasion technique.

This new development simplified the phase of collection of the powder. This successful separation of the sample powder from the steel of the container simplified the isotopic and elemental analyses performed in the LANIE laboratory and permitted the recuperation of the powders without contamination of elements present in the steel (for example for Mo target).

Figure 1. Principle of the opening of the steel by mechanical abrasion

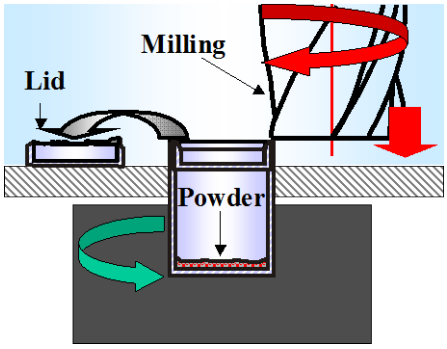

4. Dissolution of the powders

The powders enclosed in containers are enriched powders in different chemical form (oxides, metal, carbonates, sulfates). The different chemical forms for all elements of PROFIL experiments are presented in Table 2. For each powder a protocol of dissolution was developed by the Laboratoire d'Etude de Dissolution (LED) for actinides elements and by the Laboratoire d'Analyse Chimique et RadioChimique (LARC) for non-actinides elements. Protocols and conditions of dissolution were validated by previous tests performed on the non-irradiated powders. In relation to the very low quantity of powder and to avoid pollution, powders were dissolved in Teflon vials and with ultrapure acid qualified for their very low impurities contents.

The wet digestion methods involve the use of a single acid (HNO_3,...) or some combination of oxidising acids (such as HNO_3) and non-oxidising acids (such as HF, HCl...). For those wet

digestions, a variety of technique is employed from ambient-pressure wet digestion in a beaker on a hot plate to high pressure microwave heating. The digestion media used must avoided:

- the introduction of pollutants,
- the loss of some elements by volatilisation (such as Ru in nitric acid).

The media of dissolution must take into account the stability of the elements present after irradiation. For example in the case of the ^{109}Ag target activation products formed after irradiation were Cd and Pd. So these three elements must be stable in the media chosen for the dissolution. Results obtained for the ^{109}Ag target were presented in a recent publication [7].

Table 2. Chemical form of the powder present in the PROFIL-R and M container.

Group	Element	Chemical form	Group	Element	Chemical form
Alkali metals	Rb	Rubidium carbonate	Lanthanides	Ce	Cerium oxyde
	Cs	Cesium sulfate		Pr	Praseodymium oxyde
Transition metals	Zr	Zirconium oxyde		Nd	Neodymium oxyde
	Mo	Metal powder and molybdenum oxyde		Sm	Samarium oxyde
	Tc	Technetium oxyde		Eu	Europium oxyde
	Ru	Metal powder		Gd	Metal powder and Gadolinium oxyde
	Rh	Metal powder	Actinides	U	Uranium oxyde Uranium metal
	Pd	Metal powder		Pu	Plutonium oxyde
	Ag	Metal powder		Am	Americium oxide Americium metal
Nonmetals	B	Metal powder		Cm	Curium oxide
	I	Sodium iodide		Np	Neptunium oxyde
				Th	Thorium oxyde

Among the transition metals, metals of the platinum group are chemically resistants. Indeed, the wet digestion of Rh, Ru, and Pd is not trivial and needs some specific developments. As example, rhodium metal is only attack by boiling sulfuric acid. However, this mineral acid is not suitable for mass spectrometry measurement. So, a wet digestion process based on hydrochloric acid under high pressure in a microwave was developed.

5. Analytical developments for mass spectrometric measurements

The elementary and isotopic analyses were performed in the Laboratory of Analytical development for Nuclear Elementary and Isotopic Analyses (Department of Physical-Chemistry) by mass spectrometry

(TIMS, MC-ICPMS and Quadrupole-ICPMS) set up in glove boxes for the analyse of radioactive samples. To be able to determine elementary ratio (Nd/U for example in the case of ^{235}U target) at a precision better than 1% the technique of the isotopic dilution was developed. In fact, isotope dilution is the method that can provide the most accurate quantification coupled to mass spectrometric techniques. This method is based on the addition to the sample of a known quantity of the same element but with a different isotopic composition [8]. In addition, the sources of uncertainties of the isotope dilution method are well understood and controlled and this technique has been also used for different nuclear applications [9][10].

The precise and accurate determination of isotopic and elemental ratios requires preliminary chemical separation steps to prevent isobaric interferences. The LANIE perform analytical developments for the separation and measurements of isotopic composition of PROFIL targets. Innovative method of separation like the hyphenation of liquid chromatography with ICPMS or the use of collision reaction cell present in recent generation of ICPMS, have been developed.

5.1. Chromatographic separation and hyphenated techniques

Chromatographic separation to resolve isobaric interferences and matrix effect was performed in the major case for analysis of irradiated fuel samples by ion exchange resin or by high performance liquid chromatography (HPLC). These techniques developed in the LANIE for separation of elements in irradiated fuel (U-Pu, lanthanides separation (Eu-Gd-Sm-Nd), Am-Cm…) require a lot of time and are developed for quantities of μg level [9][11]. In the case of PROFIL experiments the quantity of activation products formed after irradiation are very low (several ng in some cases). So a high performance liquid chromatography (HPLC) couples on line with a mass spectrometer detector was chosen to reduce the time analysis, the quantity of sample and the time explosion of the analyst to the radiation.

For two targets (^{109}Ag and ^{153}Eu) we have developed chromatographic separation of Ag-Pd-Cd and Eu-Gd-Sm by HPLC which was directly coupled to Q-ICPMS. The choice of the chromatographic column, choice of eluents and protocol of separation had to be perfectly defined. In a second time, on-line data acquisition to be able to obtain precise and accurate isotopic ratio represented an important part of the development. All the results obtained on isotopic ratios after hyphenation between HPLC and Q-ICPMS are presented in two papers [5][7].

5.2. Direct separation using collision reaction cell

Chemical purification has the major disadvantage for trace and ultra-trace elemental analysis to introduce natural contamination and lose part of the elements during the chemical separation. In the

case of irradiated targets some isotopes are present in very low quantities, so in this context several analytical developments were conducted on the collision reaction cell implanted on Multiple Collector Inductively Coupled Plasma Mass Spectrometer (MC-ICPMS) to perform these separations directly within the cell by using a reaction gas. When the analyte and the interfering ions enter inside the cell, the gas reacts selectively with one of the species to reduce or suppress the interference [12]. If the ion-molecule reactions between the interfering ions and the reaction gas are thermodynamically and kinetically allowed, they will react quickly and specifically [13].

For three targets (^{153}Eu, ^{235}U and ^{95}Mo) analytical methods were defined to perform direct separation in the collision reaction cell of a MC ICPMS. The interference resolutions for these targets were respectively Eu/Gd-Sm, U-Pu and Mo-Zr. Developments were based on the choice of a reaction gas using thermodynamic and kinetic data collected in the literature [14] and on specific experiments performed in collision-reaction cell. The three gases selected for the interference resolution were O_2 for Eu/Gd-Sm, CO_2 for U-Pu and N_2O for Mo-Zr. All the results obtained on isotopic ratios after in situ separation in the collision reaction cell are presented in three papers [15][16][17].

5.3. Development of analytical methods for TIMS and MC-ICPMS measurements

After separation all the isotopic ratios are determined by TIMS or MC-ICPMS. The LANIE has developed analytical procedures to be able to analyse all the target of the PROFIL experiments. In the case of target where very low quantities of element was present, analytical development was performed by TIMS using the technique of Total Evaporation (TE) [18]. Several analytical developments performed by TIMS or MC-ICPMS have been recently published [10][19][20][21].

5.4. Analytical results and uncertainty

For each target, isotopic compositions and elemental ratios are required with a low level of uncertainty. In the major case uncertainties on isotopic ratio are less than 0,5% and uncertainties on elemental ratio are less than 1% (for the technique of isotopic dilution) or less than 5% (for other techniques).

6. First results and preliminary interpretations

The PROFIL and PROFIL-2 irradiation experiments performed in the early years of operation of Phenix Na cooled fast reactor about three decades ago, have been fully interpreted in the past, using different code systems and nuclear data libraries.

Results obtained with these first experiments, for heavy nuclides and some fission products, played a key role in the qualification calculation System ERANOS associated to JEFF-3.1 nuclear data library

dedicated to fast reactors and helped to precise capture, fission and (n,2n) cross-sections , as well as branching ratios in the ^{241}Am radiative capture decay chain.

PROFIL-R and PROFIL-M will definitely complete the data obtained with PROFIL and PROFIL-2 experiments. Their examinations, which are today under progress, will extend the experimental feedback to a large range of fission product nuclides representing roughly two-thirds of the loss of reactivity in fast reactor during operation. The high accuracy of measurements will also provide relevant information about the integral capture cross section of some daughter nuclides present in the fission product samples.

Preliminary calculations have been performed with the evolution code system DARWIN using JEF3.1 cross section of a standard fuel assembly. Looking at Table 3, which represents the Calculation/Experiment ratio obtained on several PROFIL-R targets, we can observe the rather good agreement between predicted values and isotopic and elemental ratios. The reproducibility of the results confirms the good quality of the isotopic analyses and the availability of the experimental techniques used.

In the future, more accurate calculations will be done using ERANOS and JEFF-3.1 nuclear data library.

Table 3. Calculation/Experimental (C/E) ratios obtained on several PROFIL-R targets obtained with the evolution code system DARWIN using JEF3.1 cross section of a standard fuel assembly.

Isotope ratio	(C/E – 1) in %
^{157}Gd/^{156}Gd	1.9
^{156}Gd/^{155}Gd	20
^{154}Eu/^{153}Eu	11.1
^{153}Eu/^{152}Sm	9.9
(^{147}Sm+^{147}Pm)/^{146}Nd	5.6
^{146}Nd/^{145}Nd	3.4
^{144}Nd/^{143}Nd	0.9
^{142}Nd/^{141}Pr	12.4
^{110}Cd/^{109}Ag	1.5

7. Conclusions

PROFIL-R and M experiments irradiated in the French fast neutron reactor Phénix will allow the

collection of accurate information on the total capture integral cross sections of the principal heavy isotopes and some important fission products. The steel containers of isotopes loaded in the pins can be now opened inside a nuclear shielded cell and the powder recuperated and dissolved under well-defined conditions. Several solutions were analyzed by mass spectrometric techniques after separation in order to eliminate the elements which could prevent ionization and/or generate isobaric interferences. This program required a lot of developments, which were implemented in several laboratories of the French Commission on Atomic Energy and Alternative Energies (CEA) during the last few years. At this stage of the project 14 targets of PROFIL-R experiment and 6 targets of PROFIL-M experiment, have been completely analysed.

REFERENCES

[1] TOMMASI, J., NOGURERE, G., Analysis of the PROFIL and PROFIL-2 sample irradiation experiments in Phenix for JEFF-3.1 nuclear data validation, Nucl. Sci. Eng. 160 (2008) 232.

[2] QUIDELLEUR, S., et al., One step U-Pu-Cs-Ln-steel separation using TRU preconditioned extraction resins from Eichrom for application on transmutation targets, J. Radioanal. Nucl. Chem. 280 (2009) 507.

[3] BETTI, M., Use of ion chromatography for the determination of fission products and actinides in nuclear applications, J. Chromatogr. A 789 (1997) 369.

[4] GUNTHER-LEOPOLD, I., et al., Characterization of nuclear fuels by ICP mass-spectrometric techniques, Analyt. Bioanal. Chem. 390 (2008) 503.

[5] BOURGEOIS, M., et al., Sm isotope composition and Sm/Eu ratio determination in an irradiated ^{153}Eu sample by ion exchange chromatography-quandrupole inductively coupled plasma mass spectrometry combined with double isotope dilution technique, J. Anal. At. Spectrom, 26 (2011) 1549.

[6] FERLAY, G., et al., From the Phenix irradiation end to the analytical results : PROFIL-R target destructive characterisation. IOP Conf. Ser. (2010): Mater. Sci. Eng. 9 012021.

[7] GAUTIER C., et al., Development of cadmium/silver/palladium separation by ion chromatography with quadrupole inductively coupled plasma mass spectrometry detection for off-line cadmium isotopic measurements, J. Chromatogr. A 1218 (2011) 5241.

[8] HEUMANN K.G., Isotope dilution mass spectrometry (IDMS) of the elements, Mass Spectrom. Rev. 11 (1992) 41.

[9] CHARTIER, F., et al., Determination of Am and Cm in spent nuclear fuels by isotope dilution inductively coupled plasma mass spectrometry and isotope dilution thermal ionization mass spectrometry after separation by high-performance liquid chromatography, Fresenius J. Anal. Chem. 364 (1999) 320.

[10] CHARTIER F., et al., Application of the isotope dilution technique for Zr-93 determination in an irradiated cladding material by multiple collector-inductively coupled plasma mass spectrometry, Int. J. Mass Spectrom. 270 (2008) 127.

[11] ISNARD, H., et al., Investigations for determination of Gd and Sm isotopic compositions in spent nuclear fuels samples by MC ICPMS, Int. J. Mass Spectrom. 246 (2005) 66.

[12] TANNER, S.D., et al., Reaction cells and collision cells for ICP-MS: a tutorial review, Spectroc. Acta Pt. B 57 (2002) 1361.

[13] BANDURA, D.R., et al., Gas-phase ion-molecule reactions for resolution of atomic isobars: AMS and ICP-MS perspectives, Int. J. Mass Spectrom. 255-256 (2006) 312.

[14] ARMENTROUT, P.B., Fundamentals of ion-molecule chemistry., J. Analyt. Atom. Spectrom., 19 (2004) 571.

[15] GUEGUEN, F., et al., Eu isotopic measurements with in situ Eu/Gd/Sm separation using O_2 as a reactant gas in collision/reaction cell based MC-ICP-MS, J. Anal. At. Spectrom. 25 (2010) 201.

[16] GOURGIOTIS, A., et al., Simultaneous uranium/plutonium separation and direct isotope ratio measurements by using CO2 as the gas in a collision/reaction cell based MC-ICPMS, J. Analyt. Atom. Spectrom. 25 (2010) 1939-1945.

[17] MOUREAU J., et al., High accuracy measurements of Mo isotopes by MC-ICPMS with in situ Mo/Zr separation using N_2O in a collision reaction cell, J. Analyt. Atom. Spectrom. 23 (2008) 1538-1544.

[18] MIALLE, S., Développements analytiques en spectrométrie de masse à thermo-ionisation pour l'analyse isotopique de faibles quantités, (2011) Thesis University of Toulouse

[19] MIALLE, S., et al., The use of total evaporation method using Channeltron electron multipliers by thermal ionization mass spectrometry for europium isotope ratio measurements on picogram sample amounts, Int. J. Mass Spectrom. 309 (2012) 141.

[20] GOURGIOTIS, A., et al., Accurate determination of Curium and Californium isotopic ratios by inductively coupled plasma quadrupole mass spectrometry (ICP-QMS) in ^{248}Cm samples for transmutation studies, Int. J. Mass Spectrom. 291 (2010) 101.

[21] ISNARD, H., et al., Comparison of thermal ionization mass spectrometry and Multiple Collector Inductively Coupled Plasma Mass Spectrometry for cesium isotope ratio measurements. Spectrochimica Acta Part B 64 (2009) 1280.

OSCAR-Na V1.3: a new code for simulating corrosion product contamination in SFR reactors

J.-B. Génin, L. Brissonneau, T. Gilardi, G. Bénier

CEA, DEN, Cadarache, Saint-Paul-Lez-Durance, France

Abstract. A new code named OSCAR-Na has been developed, in order to calculate mass transfer of corrosion products and related contamination in the primary circuits of sodium fast reactors. A solution/precipitation model has been implemented in the OSCAR code, a modular mass transfer code up to now dedicated to Pressurized Water Reactors. The key parameters of the model are 1) diffusion in the steel, considered to be enhanced under irradiation 2) diffusion through the sodium laminar boundary layer 3) equilibrium concentration of each element in the sodium and 4) velocity of the interface moving, due to bulk corrosion in hot parts (in relation with oxygen enhanced iron dissolution) and deposition in cold parts of the reactor. Thanks to a numerical method for solving the diffusion equation in the steel and to a complete mass balance involving all the elements in the sodium, the interfacial velocity due to corrosion or deposition is calculated by the OSCAR-Na code for each surface of the primary system. It is mainly determined by the iron equilibrium concentration in the sodium and its oxygen enhanced dissolution rate. These parameters concerning iron as well as the other parameters of the model have been assessed from a literature review. Even with a simplified primary system description, simulation of the French SFR reactor PHENIX with the first version V1.3 of OSCAR-Na was able to assess the correct amount of contamination and the correct contamination profiles on heat exchanger surfaces for ^{54}Mn, ^{58}Co and ^{60}Co radionuclides, compared with measurements. The analysis of the solution/precipitation model allows predicting the impact of the key parameters on the contamination of a PHENIX like reactor.

1. INTRODUCTION

In Sodium Fast Reactors (SFR), contamination of the primary circuit is due to the release of radioactive nuclides produced in the reactor core by neutron reactions on the constituent elements of the stainless steel fuel cladding and subassembly wrappers. Due to both bulk corrosion (i.e. surface loss) of the activated cladding and preferential release of highly soluble elements, a small fraction of the radionuclides is released into the flowing sodium and deposits throughout the primary circuit. This leads to contamination of the piping and components such as primary pumps or intermediate heat exchangers (IHX). The main radioactive contaminants are ^{54}Mn and ^{60}Co.

The assessment of the radioactive contamination of reactor primary circuits is necessary to address important challenges while operating or designing a nuclear power plant, such as decreasing personnel exposure to radiation during maintenance or dismantling operations on macro-components, as well as limiting the activity of wastes and effluents produced during these operations.

Therefore the computer code OSCAR-Na has been developed for SFR contamination assessment. It is based on the OSCAR code [1], a mass transfer code up to now dedicated to Pressurized Water Rectors (PWR). The OSCAR code is a modular code which can easily integrate new models.

The selected model for mass transfer in SFR primary circuit assumes that transfer between steel and sodium is primarily by solution and precipitation (rather than, for example, by particle detachment and particle deposition) and thus, it can be deduced from mass transfer theory. This model has been described in detail by Polley and Skyrme [2].

This paper describes how this model is implemented in the OSCAR-Na code, taking into account a complete mass balance around the circuit for each nuclide. After a description of the solution/precipitation model and a reminder of the analysis made by Polley and Skyrme (section 2), the implementation of the model in OSCAR-Na is detailed (section 3) and the values chosen for the key parameters are defined (section 4). Finally, first results are discussed in section 5.

2. THE SOLUTION / PRECIPITATION MODEL

2.1. Theory

As described by Polley and Skyrme [2], mass transfer of each element of interest between sodium and steel may be characterized by an expression derived by equating three relationships for the mass flux 1) across the liquid laminar boundary layer, 2) for absorption and desorption at the steel/sodium interface and 3) for diffusion in the steel. These are respectively:

$$\Phi = k \cdot (C_i' - C') \tag{1}$$

$$\Phi = k_d \cdot C_i - k_a \cdot C_i' \tag{2}$$

$$\Phi = D \cdot \left(\frac{\partial C}{\partial x} \right)_{x=0} + u \cdot C_i \tag{3}$$

Where C and C' are the nuclide concentration in the steel and bulk sodium, respectively (the subscript i indicating interfacial values at $x = 0$), k is the mass transfer coefficient for diffusion through the laminar boundary layer, k_a and k_d the "absorption" and "desorption" mass transfer coefficients, respectively (rates of transfer from the sodium to the interface and vice versa), D the diffusion coefficient in the steel, x the depth from the surface into the steel, and u the velocity of the moving sodium/steel interface ($u > 0$ in case of bulk corrosion, $u < 0$ in case of bulk deposition). The mass flux Φ is positive in case of release into the sodium, and negative in case of deposition.

In eqs. (1) and (2), first order rate theory is assumed, i.e. mass fluxes are supposed to be linearly proportional to concentrations.

Eliminating C_i' from eqs. (1) and (2) yields:

$$\Phi = K \cdot \left(\frac{C_i}{\beta} - C' \right) \tag{4}$$

Where $K = \frac{k \cdot k_a}{k + k_a}$ is the effective mass transfer coefficient and $\beta = \frac{k_a}{k_d}$ the dimensionless chemical partition coefficient.

The physical significance of β may be understood using eq. (2). At chemical equilibrium, Φ is zero and hence $\beta = \frac{C_i}{C'_{éq}}$, where $C'_{éq}$ is the concentration in the sodium in equilibrium with a solid presenting the concentration C_i at the surface. Thus, β is small or large for elements which are highly soluble or insoluble in sodium, respectively.

So the model is defined by four main parameters: K, D, β (for each element), and u. Knowing the concentration C' in the sodium, the concentration profile in the steel (and hence C_i) can be calculated by solving the relevant diffusion equation:

$$\frac{\partial C}{\partial t} = D \cdot \left(\frac{\partial^2 C}{\partial x^2} \right) + u \cdot \frac{\partial C}{\partial x} - \lambda \cdot C + R \quad (5)$$

Where λ is the decay constant due to radioactive decay and neutron capture, and R is the rate of production by neutron activation (if appropriate for the element and the surface considered).

The steel is assumed to be of infinite thickness and the boundary condition at the interface is derived from equating (3) and (4):

$$D \cdot \left(\frac{\partial C}{\partial x} \right)_{x=0} + u \cdot C_i = K \cdot \left(\frac{C_i}{\beta} - C' \right) \quad (6)$$

The mass flux between steel and sodium is then obtained by substituting for C_i in equation (4).

2.2. Analysis

Some conclusions of the analysis proposed by Polley and Skyrme [2] are reminded in this section.

2.2.1. Release from surfaces submitted to bulk corrosion (u > 0)

The release of a nuclide is said to be stoichiometric when its concentration in the steel is uniform. Hence $\Phi = C \cdot u$ from eq. (3). Let's introduce the dimensionless variable $A = \frac{K}{\beta \cdot u}$. Note that, from the definitions of A and β, A is proportional to the solubility of the element in sodium, so that it may be regarded as a solubility parameter. Then assuming the concentration of the nuclide in the sodium to be zero, Polley and Skyrme showed that release is super-stoichiometric if $A > 1$ and sub-stoichiometric if $A < 1$, in both cases becoming stoichiometric at long periods of time ($\frac{u^2 \cdot t}{4 \cdot D} >> 1$) and if the radioactive period of the radionuclide is sufficiently long ($\frac{u^2}{4 \cdot \lambda \cdot D} >> 1$). Thus stoichiometric release is favoured when diffusion is slow compared with bulk corrosion. Moreover, Polley and Skyrme showed that it is achieved more rapidly when the element is selectively leached (A > 1).

Since $D \cdot \left(\frac{\partial C}{\partial x} \right)_{x=0} \approx \left(\frac{K}{\beta} - u \right) \cdot C_i$ [cf. eq. (6)], super-stoichiometric release is associated to a depletion of the element in the steel near the surface (positive concentration gradient). This behavior is observed in sodium loop experiments for highly soluble elements like nickel, chromium and manganese. On the contrary, sub-stoichiometric release is observed for less soluble elements like cobalt, and corresponds to an enrichment of this element at the steel surface.

2.2.2. Deposition of radioactive nuclides on out-of-flux surfaces

Assuming the concentration in the bulk sodium C' to be finite and constant, Polley and Skyrme showed that deposition of radioactive nuclides on out-of-flux surfaces may be reduced to a set of simple expressions for limiting values of the relevant dimensionless parameters, for both bulk corrosion and bulk deposition cases. These asymptotic expressions depend on the parameters of the model: K, D, β, u, λ. Deposition is always proportional to C'.

For values of the main parameters representative of the conditions in sodium loop experiments, long term ^{54}Mn surface contamination (Bq/m^2) can be expressed as $I = \beta \cdot \frac{D}{u} \cdot C'$ on the surfaces undergoing bulk corrosion and $I = \beta \cdot \frac{u_d}{\lambda} \cdot C'$ on the surfaces undergoing bulk deposition (where $u_d = -u$ is the deposition velocity).

Since β and u_d increase when temperature decreases, ^{54}Mn surface contamination rises rapidly with reducing temperature on the cold surfaces. On hot surfaces undergoing corrosion, little can be said about temperature dependence without detailed knowledge of the parameters β, D and u.

Regarding cobalt, surface contamination can be expressed as $I = K \cdot t \cdot C'$ on all surfaces (or $I = \frac{K}{\lambda} \cdot C'$ at longer times : $\lambda \cdot t > 1$). Thus cobalt contamination is expected to depend on sodium velocity (if $k << k_a$) but little on temperature.

Observed differences between ^{54}Mn and ^{60}Co or ^{58}Co deposition behaviour are primarily due to differences between manganese and cobalt solubility parameters A.

3. IMPLEMENTATION OF THE MODEL

3.1. The OSCAR code package

The OSCAR code package [1] is a tool for simulating PWR contamination and has been developed for more than 30 years. The current version is fully object-oriented and its modular structure allows the implementation of new models. User friendly interfaces for input data as well as for processing and visualization of results are associated to the code package.

In the OSCAR modeling, fluid systems are discretized into as many volumes or regions as necessary. These regions are defined by geometric, thermo hydraulic, neutron flux, material property, and operating characteristics. Several media are defined, as for example “fluid” and “deposit”, and mechanisms are considered, which generate mass transfers between these media. Besides, the OSCAR code considers the convection, which transports species throughout the primary circuit, and the purification, which removes species from the circuit with a given efficiency when they go through the filters of the purification circuit. Moreover, the nuclides are described within filiation chains, taking into account radioactive decay constant and capture cross section if necessary.

Finally, for each medium, for each control volume and for each isotope considered, a mass balance is calculated.

Thus the OSCAR code is able to integrate the solution/precipitation model described in section 2, generating the new code OSCAR-Na, which allows the calculation of SFR contamination. The needed media in OSCAR-Na are “steel” and “sodium”.

3.2. The OSCAR-Na code

The mass transfer between steel and sodium is given by eq. (4): $\Phi = K \cdot \left(\frac{C_i}{\beta} - C' \right)$. The surface concentration C_i in the steel and the bulk sodium concentration C' need to be determined for each region and for each nuclide. This is done through two steps in the OSCAR-Na code:

- Given C', C_i is calculated by solving the general diffusion equation (5) with the boundary condition at the interface (6). The retained method for solving the diffusion equation is numerical. For this purpose, the metal is discretized in several layers covering the diffusion depth, which mainly depends on the interfacial velocity u and the diffusion coefficient in the steel D. Thus the metal discretization may be different for each region and for each element. Thanks to the numerical method, the concentration profile in the steel can be calculated, even if the sodium concentration or the model parameters are time dependent. Moreover nuclide concentration profiles are taken into account for calculating the production rate of their descendant by neutron activation.
- Given C_i in each region, C' is calculated through a complete mass balance around the circuit involving all the elements, and taking into account convection, purification, radioactive decay, neutron activation and mass transfer (4) due to the solution/precipitation model.

Then iterations between both steps (numerical method for solving the diffusion equation for each region and complete mass balance around the circuit) are implemented for each time step, until convergence is reached for C_i and C', for each nuclide and each region. The mass transfer between metal and sodium, as well as concentration in the sodium and concentration profile in the steel, are then calculated at all positions in the circuit as a function of time.

The OSCAR-Na code can be compared with the PSYCHE code (Iizawa et al. [3]), a Japanese mass transfer code for corrosion product behavior in primary circuits of SFR reactors, implementing the same solution/precipitation model. In PSYCHE, the diffusion equation is analytically solved for each region and a simple mass balance in the sodium is calculated, using the mass conservation law along the circuit and taking into account release or deposition in each region in the system. This mass balance concerns only the radioactive contaminants ^{54}Mn and ^{60}Co in PSYCHE when the main elements of interest (and not only radio isotopes) are considered in OSCAR-Na.

4. DETERMINATION OF THE MODEL PARAMETERS

In this section, the key parameters (u, K, D and β) of the solution/precipitation model are evaluated in order to calculate the contamination of the French SFR reactor PHENIX (see section 5). The parameters retained for OSCAR-Na are compared with the parameters used in the PSYCHE code [3].

4.1. Interfacial velocity

The interfacial velocity is the moving rate of the sodium/steel interface, due to corrosion and deposition. It may be defined as the difference between corrosion rate and deposition rate: $u = u_c - u_d$.

4.1.1. Corrosion rate

The corrosion rate u_c is the surface recession rate due to the corrosion of the steel. It can be related to the behavior of iron, as it is the major constituent of steel. In OSCAR-Na, the assumption is made that iron does not diffuse in steel. Consequently the iron profile in the steel is uniform and the iron release is stoichiometric: $\Phi_{Fe}^{rel} = C_{Fe} \cdot u_c$ [see eq. (3)].

Following eq. (4): $\Phi_{Fe} = K_{Fe} \cdot \left(C'^{éq}_{Fe} - C'_{Fe}\right)$, where $C'^{éq}_{Fe} = \dfrac{C_{Fe}}{\beta_{Fe}}$ is the iron equilibrium concentration in sodium.

We obtain the following expression for the corrosion rate:

$$u_c = \frac{K_{Fe}}{\beta_{Fe}} \cdot \left(1 - \frac{C'_{Fe}}{C'^{éq}_{Fe}}\right) \text{ when } C'_{Fe} < C'^{éq}_{Fe} \text{ and } u_c = 0 \text{ when } C'_{Fe} > C'^{éq}_{Fe} \quad (7)$$

This is in agreement with the fact that steel corrosion is governed by iron solution [4], i.e. is limited by the iron concentration in sodium.

K_{Fe} can be deduced from experimental results. Indeed, from sodium loop experiment results obtained for temperatures representative of SFR primary circuit and for oxygen concentration between 0.5 and 2.5 ppm, Brissonneau [5] proposes a mass loss equation that separates the contributions of general corrosion and preferential leaching. The general corrosion term corresponds to the following expression for the experimental corrosion rate:

$$u_{cor} = A_{cor} \cdot [O] \cdot e^{\frac{-E_{cor}}{\Re \cdot T}} \quad (8)$$

Where $[O]$ is the oxygen concentration in ppm, A_{cor} is a pre-exponential factor expressing a velocity, and E_{cor} is the activation energy. This is consistent with the fact that corrosion of steels is controlled by a surface reaction involving oxygen, which acts as a catalyst [4, 5].

In sodium loop experiments investigated in [5], iron concentration in sodium was considered to be far from equilibrium concentration, so that from eqs. (7) and (8) : $K_{Fe} = \beta_{Fe} \cdot u_{cor}$.

Moreover, corrosion of steels in sodium is known to increase with sodium velocity only up to a critical velocity, above which the corrosion can be considered as independent of velocity [4]. Above critical sodium velocity, the surface reaction limits the corrosion process. Since the surface reaction rate is very low for the considered oxygen concentration, it is likely that it effectively limits the iron release in the experiments considered in [5]. Then in these conditions: $K_{Fe} = k_a^{Fe} = \beta_{Fe} \cdot u_{cor}$.

This allows us to establish, from eq. (7) and the definition of K, the general expression for u_c used in OSCAR-Na:

$$u_c = u_{cor} \cdot \frac{k_{Fe}}{k_{Fe} + \beta_{Fe} \cdot u_{cor}} \cdot \left(1 - \frac{C'_{Fe}}{C'^{éq}_{Fe}}\right) \text{ when } C'_{Fe} < C'^{éq}_{Fe} \tag{9}$$

Brissonneau [5] gives the following values for the u_{cor} parameters (8) which will be used in the OSCAR-Na code: A_{cor} = 1.43 10^{-8} m/s, E_{cor} = 92500 J/mol. These values hold for oxygen content in the sodium lower than 5 ppm.

Unlike in PSYCHE, no downstream factor [3, 4] is taken into account in this first version of OSCAR-Na, considering that isothermal sections are short.

4.1.2. Deposition rate

The deposition rate u_d is the surface procession rate due to the deposition of stable and active corrosion products. It is defined in OSCAR-Na from the deposition flux for the different nuclides:

$$u_d = -\sum_k \frac{\Phi_k}{\rho_{steel}} \text{ (if } \Phi_k < 0) \tag{10}$$

Where ρ_{steel} is the steel density.

This definition needs all the major elements present in the steel to be calculated.

With eqs. (9) and (10) as definitions of u_c and u_d, the interfacial velocity $u = u_c - u_d$ is calculated by the OSCAR-Na code, thanks to the numerical method for solving the diffusion equation and to the complete mass balance in the sodium. It is closely related to the iron behavior, i.e. its equilibrium concentration, characterized by the β_{Fe} coefficient (see section 4.4) and its surface reaction rate, assessed through sodium loop experimental results [see eq. (8)].

In the PSYCHE code, u_c and u_d are input data, obtained from the analysis of sodium loop experiment results. Each region has to be preselected as bulk corrosion type or bulk deposition type.

4.2. Effective mass transfer coefficient

The determination of the effective mass transfer coefficient $K = \frac{k \cdot k_a}{k + k_a}$ needs to assess k and k_a.

In the OSCAR-Na code, the mass transfer coefficient k through the boundary layer in the flowing sodium is calculated from the following equation [6]:

$$k = 0{,}023 \cdot \mathrm{Re}^{0,8} \cdot Sc^{1/3} \cdot \frac{D^{Na}}{d_h} \tag{11}$$

Where Re and Sc represent the Reynolds and Schmidt numbers, respectively, D^{Na} is the diffusivity of the element in liquid sodium and d_h the equivalent hydrodynamic diameter of the flow path. D^{Na} is obtained for the different elements from the Sutherland-Einstein relation [7]:

$$D^{Na} = \frac{k_B \cdot T}{4 \cdot \pi \cdot \mu_{Na} \cdot r}$$

Where k_B is the Boltzmann constant, T the Kelvin temperature, μ_{Na} the dynamic viscosity of sodium at temperature T, and r the atomic radius of the element.

Regarding the surface reaction rate k_a, it is deduced for iron from corrosion measurements: $k_a^{Fe} = \beta_{Fe} \cdot u_{cor}$ (see section 4.1.1). For other elements than iron, it is considered in OSCAR-Na that the surface reaction rate is much greater than the diffusion rate through the sodium boundary layer, and then has no effect on the mass flux: $K = k$ (local equilibrium is obtained at the interface for these elements).

In PSYCHE, the same eq. (11) is used for k, but D_{Na} is obtained from experimental results. The same D_{Na} values are used for all the elements of interest. These values are compared in fig. 1 with OSCAR-Na values.

Moreover, an experimental value of the surface reaction rate k_a is taken into account for manganese in PSYCHE. It is obtained from ^{54}Mn deposition measurements in sodium loop experiments.

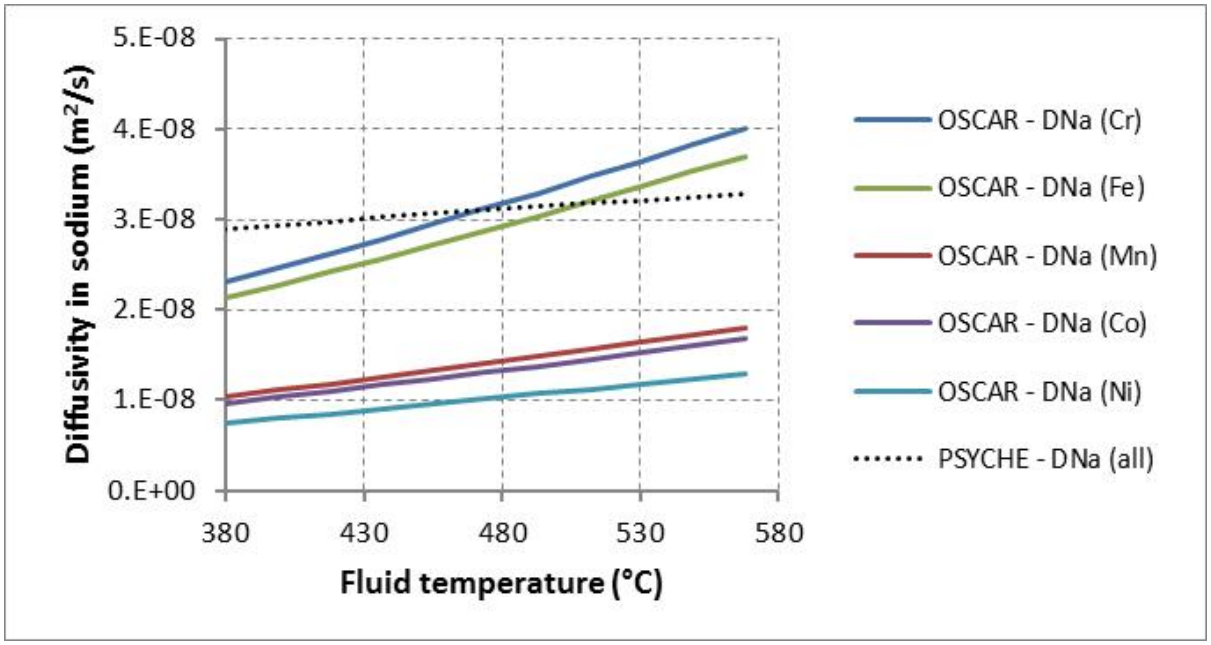

FIG. 1. Diffusivity in sodium used in OSCAR-Na and PSYCHE codes.

4.3. Steel diffusion coefficient

In this first version of OSCAR-Na, diffusion in the steel is characterized by a single diffusion coefficient D independent of depth, even if the diffusion may be enhanced in the ferrite layer which forms near the steel surface due to the nickel and chromium depletion [4]. This effective diffusion coefficient should incorporate lattice and grain boundary diffusion.

Moreover, as investigated by Brissonneau [5], diffusion enhancement due to the defects in the lattice produced by irradiation must be taken into account. Then the following equation is used for the determination of D:

$$D = D_{NP}^{irr} \cdot \sqrt{P_{loc}} + D^{eq} \tag{12}$$

Where D_{NP}^{irr} is the diffusion coefficient under irradiation at the nominal power of the reactor, P_{loc} is the local power fraction, and D^{eq} is the diffusion coefficient at equilibrium (out of neutron flux). In OSCAR-Na, the same values of D_{NP}^{irr} are considered for all elements, and correspond to the diffusion under irradiation of iron in stainless steel, given in [5]. A literature review provides the D^{eq} values for the different elements handled in the code: Mn [8], Cr [9], Ni [10], Co [11]. Note that the values retained in this first version of OSCAR-Na correspond to the lattice diffusion and do not include the grain boundary diffusion.

The retained values for OSCAR-Na (under irradiation and at equilibrium) as well as those used in the PSYCHE code are shown in fig. 2. The impact of irradiation is not taken into account in the PSYCHE code. It can be observed that PSYCHE values are close to OSCAR-Na values under irradiation, and much greater than OSCAR-Na values out of neutron flux.

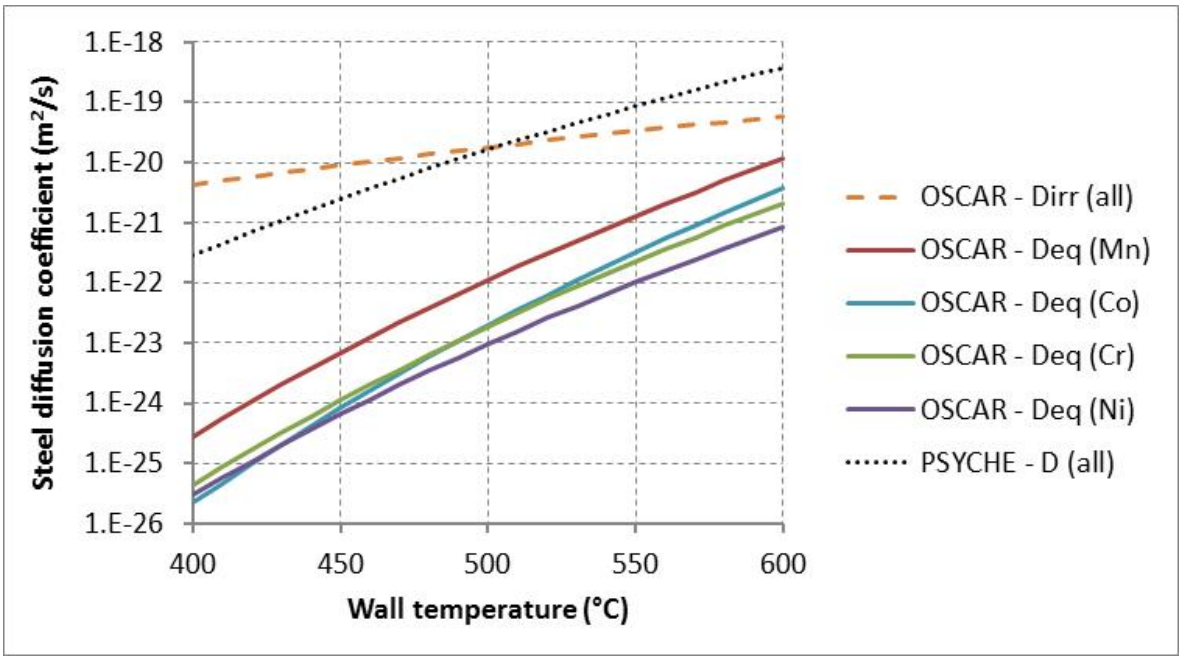

FIG. 2. Diffusivity in steel used in OSCAR-Na and PSYCHE codes.

4.4. Chemical partition coefficient

The chemical partition coefficient β is probably the model parameter which is the most difficult to assess. Unfortunately, even if solubility of each pure metal in sodium has been measured, the equilibrium concentration in sodium of the alloy constituents cannot be deduced because of the influence of interactions with other constituents in the chemical system of the primary circuit.

From analysis of sodium loop data at 604 °C, Polley and Skyrme [2] evaluate the following values: $\beta < 10^9$ for manganese and $\beta \sim 10^{11}$ for cobalt. Iizawa et al. [3] also obtained an assessment of β for manganese and cobalt by fitting the solution/precipitation model calculation to the activity profiles along a non-isothermal loop system, all the other model parameters having been assessed separately from experimental results. These values, used in the PSYCHE code, are shown in fig. 3. Note that oxygen concentration is considered to have an effect on β for cobalt in the PSYCHE code. The plotted values of β_{Co} on fig. 3 are for 1 ppm oxygen concentration.

In the OSCAR-Na code, values close to those cited above are chosen (see fig. 3). But as the driving force for mass transfer is the difference of solubility of the steel constituents in sodium in the hot and the cold parts of the reactor [5], a greater temperature dependence than in PSYCHE is retained and is based on the temperature dependence of pure iron solubility in sodium. Indeed, a too low temperature dependence of β does not allow the iron precipitation in the cold parts of the system. In this first version of OSCAR-Na, same values of β are retained for Fe, Mn, Cr and Ni. β value for Co is roughly a factor 100 higher, accounting for the less soluble trend of cobalt.

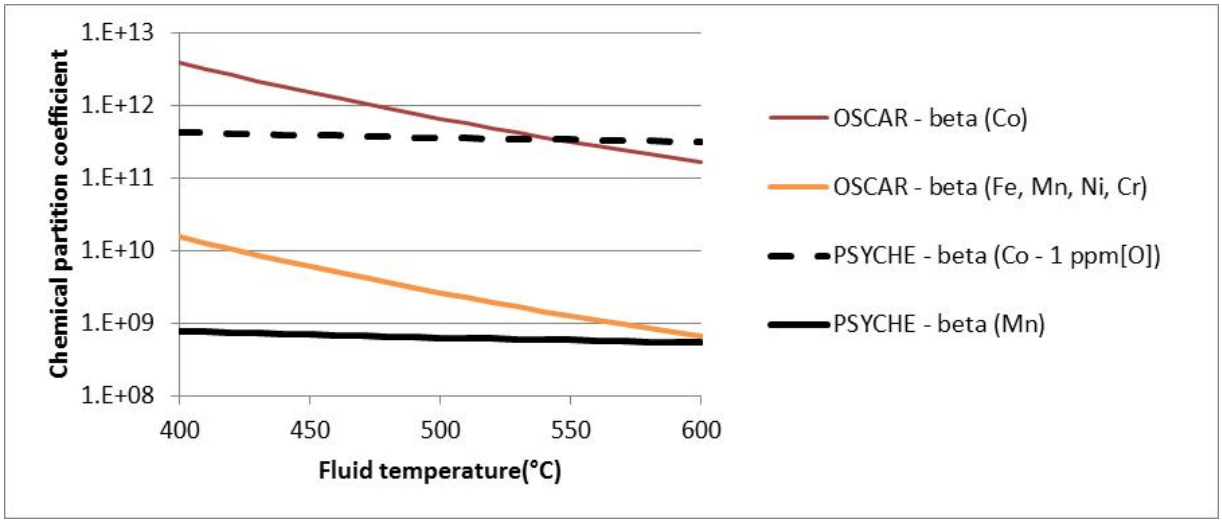

FIG. 3. Chemical partition coefficient in OSCAR-Na and PSYCHE codes.

5. Results obtained with the OSCAR-Na code

The French SFR reactor PHENIX has been simulated with this first version (V1.3) of the OSCAR-Na code, including parameters described above. For this calculation, a simple discretization of the primary system has been used. The temperature variation along the primary system is supposed to be correctly represented with 10 regions for IHX and 15 regions for the core. Core region temperatures correspond to those of an average assembly.

Other characteristics used for this calculation are as follows. Stainless steel is the material used for the cladding and the IHX. Five elements are taken into account: Fe, Mn, Ni, Cr and Co, including the filiation chains. The oxygen concentration is 1 ppm. The purification rate on cold traps corresponds to 0.14% of the primary flow rate. The simulation covers 1750 days at nominal power. In these conditions, the corresponding calculation time is roughly half-an-hour.

The calculated IHX surface contamination (i.e. surface activity) is shown in fig. 4 for ^{54}Mn, ^{60}Co and ^{58}Co. The global amount of contamination as well as the contamination profiles and their relative position for the 3 radionuclides are consistent with the measurements performed on PHENIX IHX. Moreover, the profiles are in agreement with those expected from the analysis of Polley and Skyrme model (see section 2.2.2). The surface activity (Bq/m^2) is close to the following asymptotic expressions:

— $I \approx \beta \cdot \frac{D}{u} \cdot C'$ for ^{54}Mn on surfaces undergoing bulk corrosion (dependence on temperature is undefined).

— $I \approx \beta \cdot \frac{u_d}{\lambda} \cdot C'$ for ^{54}Mn on surfaces undergoing bulk deposition (contamination rises rapidly with reducing temperature).

— $I \approx \frac{K}{\lambda} \cdot C'$ for ^{58}Co and ^{60}Co on all surfaces (little dependence on temperature).

In particular, from the ^{54}Mn profile, the transition temperature between the bulk corrosion zone and the bulk deposition zone can be assessed at around 480 °C.

The release calculation is also consistent with the known preferential leaching of manganese and retention of cobalt, associated with reduced or increased concentration at the steel surface, respectively (see section 2.2.1). This difference in calculated results for manganese and cobalt is induced by the β coefficient retained in OSCAR-Na for both elements.

The calculated interfacial velocity u is shown in fig. 5 (blue line), as well as the experimental corrosion rate u_{cor} obtained from loop experiments with low iron concentration in sodium (see section 4.1.1). The difference between u and u_{cor} is related to the calculated iron concentration in the sodium. Moreover, this graph shows the transition temperature of 480 °C calculated with OSCAR-Na. This means that bulk corrosion takes place from the upper middle part of the core to the upper middle part of the IHX and that deposition occurs in the lower parts of the core and the IHX.

The corrosion rate u_c and deposition rate u_d used in the PSYCHE code [3] are also presented in fig. 5. This shows that interfacial velocity calculated with OSCAR-Na is consistent with values used in PSYCHE.

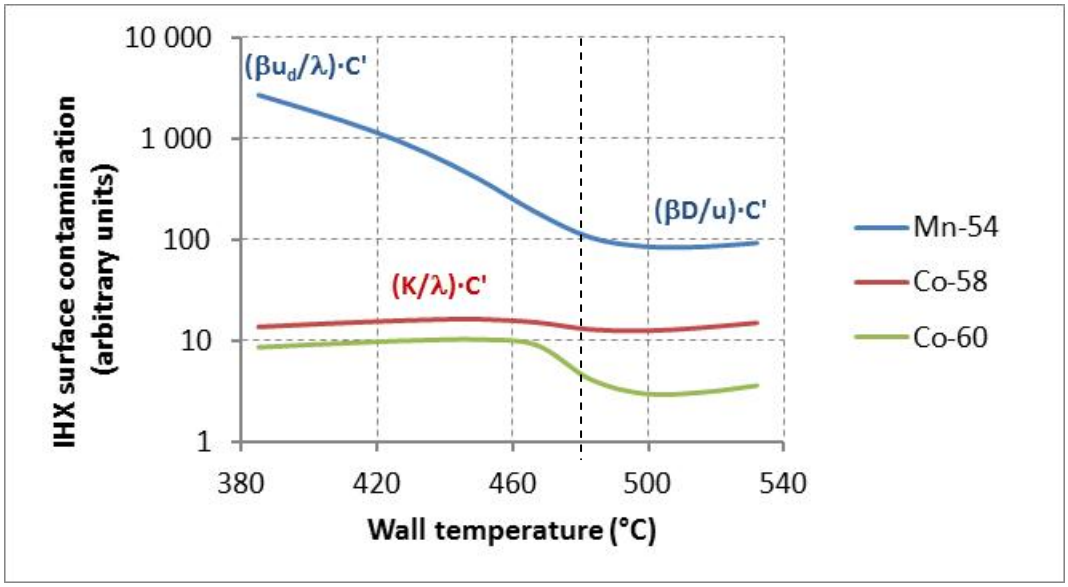

FIG. 4. IHX contamination calculated by OSCAR-Na for PHENIX reactor.

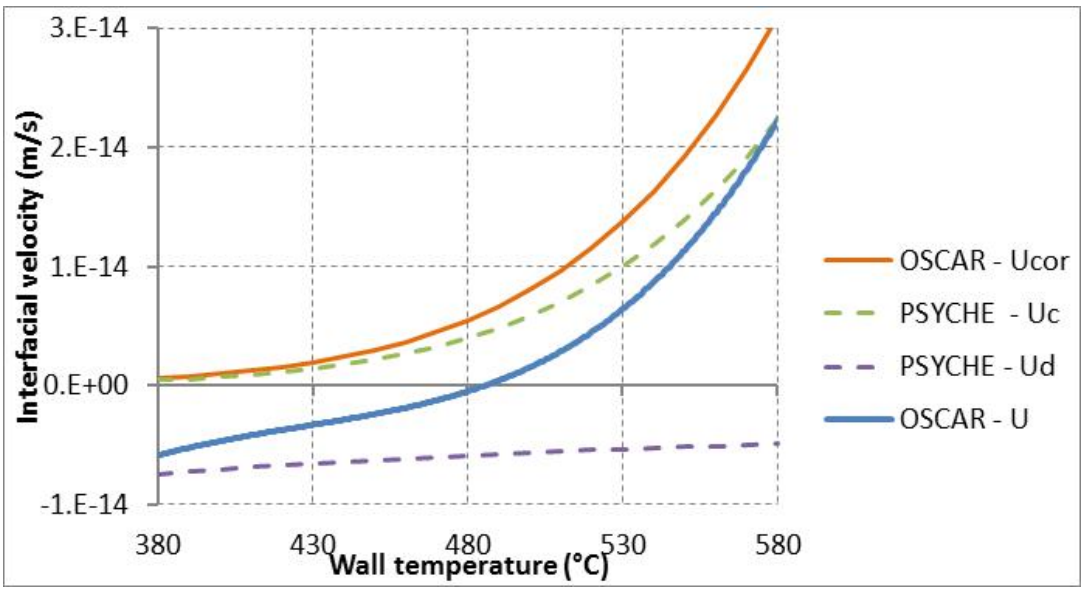

FIG. 5. Interfacial velocity in OSCAR-Na and PSYCHE.

The following additional information can be deduced from this simulation for a PHENIX like reactor:

- Calculated iron mass transfer coefficient k^{Fe} through the sodium boundary layer is much greater than the iron surface reaction rate k_a^{Fe}, so that corrosion rate can be expressed as $u_c \approx u_{cor} \cdot \left(1 - \frac{C'_{Fe}}{C'^{éq}_{Fe}}\right)$ when $C'_{Fe} < C'^{éq}_{Fe}$ [see eq. (9)].
- IHX undergoes bulk corrosion at its hotter part and a non-negligible amount of the deposition occurs in the lower part of the core.
- IHX ^{54}Mn contamination is expected to increase in cold regions (undergoing bulk deposition) and decrease in hot regions (undergoing bulk corrosion) if the corrosion rate increases (due to an increase of oxygen concentration for example). It is also expected to increase in hot regions with diffusion coefficient D^{eq}, but not in cold regions.
- IHX cobalt contamination is expected to increase with the sodium velocity.
- Super-stoichiometric trend for ^{54}Mn release and sub-stoichiometric trend for ^{58}Co and ^{60}Co release are enhanced by the diffusion coefficient under irradiation D_{NP}^{irr}.

6. CONCLUSION

A solution/precipitation model has been implemented in the OSCAR-Na code to simulate mass transfer of corrosion products and related contamination in the primary system of SFR reactors. Thanks to a numerical method used for solving the diffusion equation in steel and to a complete mass balance in the sodium, the interfacial velocity due to corrosion or deposition is calculated by the OSCAR-Na code for each surface of the primary system and is mainly determined by the iron equilibrium concentration in the sodium and its oxygen enhanced solution rate. These parameters concerning iron as well as the other parameters of the model have been assessed from a literature review. In particular, enhancement of solid state diffusion due to irradiation is taken into account.

Even with a simplified primary system description, simulation of the French SFR reactor PHENIX with the first version V1.3 of OSCAR-Na was able to assess the correct amount of contamination and the correct contamination profiles on IHX surfaces for ^{54}Mn, ^{58}Co and ^{60}Co radionuclides, compared with measurements. The analysis of the solution/precipitation model allows predicting the impact of the key parameters on the contamination of a PHENIX like reactor.

Further calculations will be performed with a more complete discretization of the primary system and taking into account as much as possible the real operating conditions, aiming at full qualification of the OSCAR-Na code by comparison with the PHENIX contamination measurements. This might lead to a better assessment of some of the not well-known parameters and further improvements of the models.

REFERENCES

[1] J.-B. Génin et al., "The OSCAR code package : a unique tool for simulating PWR contamination", Proceeding of the International Conference on Water Chemistry of Nuclear Reactors Systems, NPC, October 2010, Quebec (Canada), 2010.

[2] M.V. Polley and G. Skyrme, "An analysis of radioactive corrosion product transfer in sodium loop systems", Journal of Nuclear Materials 75 (1978) 226-237

[3] K. Iizawa et al., "Calculational model and code for corrosion product behaviour in primary circuits of LMFBRs", Proc. International Working Group on Fast Reactors (IWGFR/64), May 5-8 (1987) pp. 191-225

[4] J.R. Weeks and H.S. Issacs, "Corrosion and deposition of steels and nickel-base alloys in liquid sodium", Advances in Corrosion Science and Technology (1973) 3; 1-66

[5] L. Brissonneau, "New considerations on the kinetics of mass transfer in sodium fast reactors: an attempt to consider irradiation effects and low temperature corrosion", Journal of Nuclear Materials 423 (2012) 67-78

[6] R.E. Treybal, Mass Transfer Operations, McGraw-Hill, New York, 1965

[7] H. Borgstedt, Material behaviour and physical chemistry in liquid metal systems, Liquid Metal systems (1995) vol. 2, New York

[8] A.F. Smith et al., Diffusion of manganese in type 316 austenitic stainless steel. Metal Science, 1975. 9: p. 181-184

[9] R.A. Perkins et al., Tracer Diffusion of Fe-59 and Cr-51 in Fe-17 Wt Pct Cr-12 Wt Pct Ni Austenitic Alloy. Metallurgical Transactions, 1973. 4(11): p. 2535-2540

[10] R.A. Perkins, Tracer Diffusion of Ni-63 in Fe-17 Wt Pct Cr-12 Wt Pct Ni. Metallurgical Transactions, 1973. 4(7): p. 1665-1669

[11] R.V. Patil et al., Diffusion of ^{99}Mo, ^{95}Zr, and ^{60}Co in 316 stainless steel. Metal Science, 1980. 14(11): p. 525-528

Plutonium Usage and Management in PWR and Computing and Physical Methods to Calculate Pu

Ashraf elsayed Mohamed Mohamed

Research professor at brno univ. of technology

Tel: 002 0181027937, Email: ashraf.mohamed@saudieng.org

Main limitations due to the enhancement of the plutonium content are related to the coolant void effect as the spectrum becomes faster, the neutron flux in the thermal region tends towards zero and is concentrated in the region from 10 keV to 1 MeV. Thus, all captures by Pu240 and Pu242 in the thermal and epithermal resonance disappear and the Pu240 and Pu242 contributions to the void effect become positive. The higher the Pu content and the poorer the Pu quality, the larger the void effect.

-The core control in nominal or transient conditions.
Pu enrichment leads to a decrease in βeff. and the efficiency of soluble boron and control rods. Also, the Doppler effect tends to decrease when Pu replaces U, so, that in case of transients the core could diverge again if the control is not effective enough.

-As for the voiding effect, the plutonium degradation and the Pu240 and Pu242 accumulation after multiple recycling lead to spectrum hardening and to a decrease in control.

-One solution would be to use enriched boron in soluble boron and shutdown rods.

-In this paper I discuss and show the advanced computing and physical methods to calculate Pu inside the nuclear reactors and glovebox and the different solutions to be used to overcome the difficulties that affect on safety parameters and on reactor performance, and analysis the consequences of plutonium management on the whole fuel cycle like Raw materials savings, fraction of nuclear electric power involved in the Pu management. All through two types of scenario, one involving a low fraction of the nuclear park dedicated to plutonium management, the other involving a dilution of the plutonium in all the nuclear park.

Keywords: physical methods, PuO2, Plutonium degradation, Doppler effect, Void effect.

1. Introduction

All fissile materials must be accounted for, following any operation that causes plutonium debris, such as separation Pu from minor actinides, cutting or machining, the waste crumbs are brushed into a tray and weighed. The weight for all materials-both usable and residue-must be within a gram of the total weight prior to cutting. This system of weights and records, maintained by a dedicated computer network, verifies that all the laboratory's plutonium can be accounted for at any time -day or night-. As plutonium is dangerous, the world's most dangerous substance .Plutonium occurs naturally in trace quantities in uranium ore, but most plutonium is produced from irradiation of uranium in nuclear reactors. There are 18 different isotopes of plutonium all of which are unstable and decay into other elements by emitting various types of radiation. Because of radioactivity, a piece of plutonium is warm to the touch and the danger from swallowing plutonium is not much greater than from other heavy metals such as lead or mercury.

-Inside the laboratories' plutonium, plutonium 239 is an essential fuel for nuclear weapons and is the form of plutonium most often used in them. So, all handling of plutonium is done in a glovebox to protect workers from any airborne particles. The air pressure in the glovebox is slightly lower than the pressure in the room, which is lower than in the hall, and so on. This pressure control assures that the flow of air is always directed inward to contain and capture any plutonium that might escape from the glovebox in an accident A complex air handling system is needed that includes electrical power fans and a complete backup systems. A filtration system prevents leakage of any potentially dangerous materials into the atmosphere

-But inside the nuclear power reactors, we deal with plutonium by accounting it through analysis methods and equations with application of these equations according to the kinds of the reactors, reactors core, fissile materials, mass and other factors.

In this paper (first part of three parts that deal with accounting plutonium inside the nuclear reactors (first and second parts) and the last part will deal with plutonium inside the laboratories's plutonium by accounting plutonium critical mass, methods that use in the glovebox that deal with plutonium, equations use in the glovebox and laboratories' plutonium and the second and third parts will be published later), we will discuss the methods and experiments use in some kinds of nuclear reactors.

2. Physical Accounting methods for adjusting fissile enrichment.

It is well accepted that reactivity should be controlled by uranium enrichment (U235/U) in nuclear reactors that only uranium is used for nuclear materials based on the assumption that only U235 contributes to reactivity and U238 does not contribute to it. If uranium and plutonium mixed (MOX) fuel is used in Light Water Reactors, reactivity can be controlled by uranium enrichment, plutonium content as (x=Pu/(U+Pu)) and fissile plutonium fraction (Pu*/Pu) based on the assumption that U235 and fissile plutonium (Pu239 and Pu241) equally contribute to reactivity and U238, Pu238, Pu240 and Pu242 do not contribute to it. In this case fissile enrichment is given as :

$$(U235+Pu^*)/(U+Pu) = U/(U+Pu)\ U235/U + Pu/(U+Pu)\ Pu^*/Pu = (1-x)\ U235/U + x\ Pu^*/Pu$$

This previous equation is used for reactivity control when using MOX fuel in LWR.

-A multiplication factor 'K' can be accounted by

$$K = \nu \Sigma f / (\Sigma a + L)$$

- ν is the number of neutrons released per fission event.
- Σf is the macroscopic fission cross section of the fuel atoms in a unit volume.
- Σa is the macroscopic absorption cross section of all atoms in a unit volume.
- L is the neutron lost by leakage from a unit volume.

*For the assembly to be critical, we get the following:

$$L + \Sigma a.p = \nu \Sigma f - \Sigma a.fuel = Nh (P\ A1\ Y1 + (1 - P)\ B2\ Y2)) ,$$

where

- Nh is the total number of heavy atoms per unit volume
- P is the plutonium content.

- A1 and B2 are the isotopes compositions of plutonium and uranium, and Y1 and Y2 correspond to ($\nu \sigma f - \sigma a$) of plutonium and uranium, respectively.

σf and σa are microscope cross section for fission and absorption of an atom.

$$\Sigma a = \Sigma a.fuel + \Sigma a.p \quad \text{'non fuel materials'}$$

Here, Fi is defined by Yi/Y239 and Y239 approximately corresponds to reactivity worth of Pu239. Thus, if Fi is equivalence factor by which each uranium and plutonium isotopes must be adjusted to be an 'equivalent Pu' which generally corresponds to Pu239, then the following equation can be obtained:

$$P \Sigma i (Ai Fi) + (1 - P) \Sigma j (Bj Fj) = (L + \Sigma a.p) / Nh Y239 .$$

The right side of the equation is calculated by L and Nh which are inherently determined when reactor core design is fixed, and $\Sigma a.p$ and Y239 which have been evaluated in literatures of nuclear data. Therefore, the value of the right side of the equation is considered to be constant. So, given the critical size of a fast reactor with fuel of a certain isotopic composition, the fissile enrichment of alternative composition can be determined by using the left side of previous eq. So, the right side of the equation is defined as equivalent fissile content (E239):

$$P \Sigma i (Ai Fi) + (1 - P) \Sigma j (Bj Fj) = E239$$

Then, plutonium content 'P' can be finally given by the following relation:

$$P = (E239 - \Sigma j (Bj Fj)) / (\Sigma i (Ai Fi) - \Sigma j (Bj Fj))$$

If (U235+Pu*)/(U+Pu) is put into E239 and F for U235, Pu239 and Pu241 is set to be 1.0 and that for U238, Pu238, Pu240 and Pu242 to 0.0, then the above equation is written by:

$$P = ((U235 + Pu^*) / (U+Pu) - (U235/U)) / ((Pu239/Pu) + (Pu241/Pu) - (U235/U))$$

$$= ((U235 + Pu^* / U+Pu) - (U235/U)) / ((Pu^*/Pu) - (U235/U)).$$

3. PuO2

Plutonium-based materials have for many years been studied in connection to their usage in nuclear energy applications. Due to the restrictions in handling plutonium for fewer experiments have been done on PuO2 the magnetic susceptibility of PuO2 has been found to take a small and constant value of 5.4×10^{-4} emu/moL.

For all temperature up to 1000 K, so that the crystal electric field (CEF) ground state has been suggested to be a G1 single. On the other hand, recent neutron inelastic experiments have suggested a separation of 123 meV between the G1 ground state and the first excited G4 triple state. This value is however, in complete disagreement with that derived from the susceptibility measurements In a simple model, a separation of 123 meV corresponds to a susceptibility of -10×10^{-4} emu/moL, and requires a deviation from T constant behaviour above T= 400 K. In order to investigate the magnetic ground state of PuO2, we have performed O17 NMR measurements, for the first time, on this system. The powder sample used in our O17 NMR was prepared by oxidizing Pu metal powder in O2 gas containing O17. X -ray diffraction patterns confirmed a cubic fluorite PuO2 structure for our sample. The O17

NMR spectra were measured using a superconducting magnet and a phase coherent pulsed spectrometer at several temperatures between 6 and 70 K with the following notices:

1-The O17 NMR spectrum at (T=6.2 K). We have obtained a narrow spectrum with half-width of ~ 8 KHz. The narrow spectrum is very similar to those in the paramagnetic state of NpO2 and UO2, suggesting that there is no quadrupole splitting and no appreciable amisotropic NMR shift at the O sites. In PuO2, however, we have observed neither spectrum broadening nor splitting through the temperature region studied. This confirms the absence of magnetic ordering or structural distortions. At least, down to 6K. The knight shift values are estimated to be {K~ 0.01%}, and are nearly temperature independent. This agrees with the temperature independent magnetic susceptibility in PuO2.

2-We also plot the temperature dependence of 1/T in PuO2 where "the temperature dependence of 1/T measured at H=9.6 T for PuO2. The 1/T value was measured by the saturation-recovery method using standard spin-echo techniques. Recovery of the nuclear magnetization from a saturation pulse was found to follow in all cases a single-exponential functional form. The 1/T value in PuO2 is 2-3 orders of magnitude smaller that those in the paramagnetic state of other actinide dioxides. This small 1/T is attributed to the non-magnetic CEF ground state of PuO2. The 1/T gradually decreases with decreasing temperature bellow 50 K. For the relaxation process in PuO2, we may expect contributions from Pu-5* spins in the first-excited G4 triplet state. These contributions, however, should be more important at high temperatures, since the G1 to G4 splitting is suggested to be more than 100 meV in PuO2. At low temperatures, we can also expect relaxation processes caused by phonons and/or by a small quantity of magnetic impurities, to the extent that they exist. To completely derive the 1/T mechanisms in PuO2, further experimental effort in a wider temperature range is certainly required.

4. Plutonium properties

We evaluate the plutonium parameters DE (energy difference), DS (entropy difference), DV (volume difference) and U for the A-P model. This occurs in two stages. DV and DE come from consideration of the S-a' transformation, assuming that DS is known. DS and U come from fitting the measured temperature dependence of the lattice constant, assuming DV and DE are known. Some iteration is required, as the two stages are weakly coupled through the value of DS. For Pu-Ga alloys, we know that DV at room temperature is linear with atomic Ga concentration X from data for the a'-phase tabulated where:

$$\Delta V = (3.05 - 0.197 X) \ cm^3 /moL.$$

We assume that DE is linear with X and use the known transformation temperature at zero pressure of 1.4 and 1.9% at Ga alloys given of 223 and 163 K. We find DE=(646-172X) cal/moL.
As a check, we calculate the transformation pressure at 300 K for Pu-2 at % Ga and find 5.1 kbal. Report an onset pressure of 4 kbal for Pu-2 at %.

We next assume that DS and U are independent of X and fit the Pu242-Ga lattice constant measured using neutron diffraction to find

$$\Delta S=1.96 \ cal/moLK \quad and \quad U=3280 \ cal/moL \ .$$

In this stage of the fitting process, the low temperature data also determine the phonon gruneisen constant Y=0.49, which is needed to correct the measured lattice constants for ordinary vibrational thermal expansion. The fits are somewhat poorer than those obtained with an earlier but they are satisfactory considering the much broader scope of the A-P model.

The value of U is fair agreement with the energy difference of 2780 cal/mol found by the invar model. It is unnecessary to assume anomalous properties liquid plutonium to explain its melting behaviour. The calculated compressibility is similar to that of cerium, consistent with the observed minimum in the plutonium-melting curve. The fitted parameters are collected in both molar and atomic units. The critical point for plutonium happens to fall in the liquid state and can not be observed directly. Lattice constants calculated with the A-P model are plotted versus Ga concentration in the panel. In agreement with experiment, Ga suppresses the first order transition between the d- and a- phase by driving the zero-pressure transformation temperature to negative, via the linear Ga dependence of DE. The lower panel shows the d-a transition temperature (to) versus.

5. Pu241/Pu239 atom ratio in pressurized heavy water reactors

Data on the isotopic composition of Pu produced in power reactors are required for knowing the fissile content of Pu when used as a fuel in fast reactors. This information is useful to determine the α-specific activity of Pu, which is required to calculate the weight percentage of Am241 in any Pu sample as well as for the determination of Pu concentration by radiometric methods. The atom ratios of different Pu isotopes in a Pu sample are obtained by thermal ionization mass spectrometry (TIMS), which requires a detailed chemical separation procedure. This increases the amount of analytical effort. There are many instances where such data, for the determination of atom ratios of Pu isotopes, using the data obtained by alpha spectrometry and by thermal ionization mass spectrometry. With these correlations, the atom ratios of different Pu isotopes except for the one involving Pu241, could be obtained with reasonable accuracy (2-5%).The uncertainty on the correlation involving Pu241 was large due to its relatively short half-life (14.32 yr) which necessitates the availability of Pu samples with known irradiation and cooling history. Thus an attempt was made to develop a simple and independent method for determining Pu241/Pu239 atom ratio. This method is based on the determination of total α and total β activity of Pu isotopes using a suitable liquid scintillation counter. Pu241 being a soft β-emitter (β=20 keV) with a half-life of about 14.32 yr. It was considered worthwhile to measure the b activity of Pu241 in any Pu solution using liquid scintillation counting (LSC). To circumvent the problem of knowing the exact amount of Pu taken in the LSC vial for counting, ratio of the β due to Pu241 with respect to total α activity, also measured by LSC, due to other Pu isotopes was used.

The ratio of the β activity to total α activity was correlated with the amount of Pu241 with respect to the other Pu isotope in the sample as given bellow:

$$(A\beta(Pu\ 241)) \ / \ (A\alpha(Pu\ 238) + A\alpha(Pu239) + A\alpha(Pu240) + A\alpha(Pu241))$$
$$= (N(Pu241)\ \lambda 241) \ / \ ((N(Pu238)\ \lambda 238)+(N(Pu239)\ \lambda 239)+(N(Pu240)\ \lambda 240)+(N(Pu242)\ \lambda 242)),$$

where

-N denotes the number of atoms,

-A denotes the activity.

Denoting α and β count rates by Tα and Tβ; the atom ratio of two isotopes as R, the previous equation may be written as:

$$(T\beta / T\alpha) = (R1/9\ \lambda 1) / ((R8/9\ \lambda 8) + \lambda 9 + (R0/9\ \lambda 0) + (R2/9\ \lambda 2)) ,$$

where the subscripts 8, 9, 0, 1 and 2 stand for Pu238, Pu239, Pu240, Pu241 and Pu242, respectively;

$$R1/9 = (T\beta / T\alpha) ((R8/9\ \lambda 8) + \lambda 9 + (R0/9\ \lambda 0)+ (R2/9\ \lambda 2)) \ / \ \lambda 1 .$$

Considering the efficiency values of α and β counting by LSC as hα and hβ, respectively and the observed α and β count rates by Tα and Tβ, respectively; the above equation can be re-written as:

$$R1/9 = (T\beta\eta\alpha / T\alpha\eta\beta) ((R8/9\ \lambda8) + \lambda9 + (R0/9\ \lambda0) + (R2/9\ \lambda2)) / \lambda1$$

$$R1/9 = (\eta\alpha / \eta\beta) (T\beta / T\alpha) ((R8/9\ \lambda8) + \lambda9 + (R0/9\ \lambda0) + (R2/9\ \lambda2)) / \lambda1$$

$$R1/9 = ((\eta\alpha / \eta\beta)) \text{ X-VALUE } .$$

$$R1/9 \sim \text{X-VALUE} .$$

Thus, a correlation between R1/9 obtained by thermal ionization mass spectrometry and X-value calculated from (Tβ/Tα) determined by LSC and using the atom ratios of other Pu isotopes was established for determining Pu241/Pu239 atom ratio. It may be mentioned that atom ratios of other Pu isotopes can be obtained from the previously developed correlations. It is essential to confirm that the efficiency values of α as well as β counting by LSC have not changed after established the correlation. Otherwise, suitable correlation must be incorporated into the LSC data by using a Pu standard sample of known isotopic composition.

6-Pu ions diluted in a metallic matrix.

A comparison of actinide (U,Np,Pu) atoms diluted in Pd was provided by Russian scientists. U diluted in Pd is non-magnetic. A simple rigid –band model works surprisingly well assuming that the U 5f states contribute to the filling of the Pd 4d band for low concentrations. Once the 4d band is filled up (which happens at 8% U) U moments start to develop, which is manifest by, the kondo effect in electrical resistivity. The 4d- band filling is reflected also by the fast decrease of g (also clearly evidenced in the Th-Pd system) when the 5f states start to be occupied in UPd, g starts to rise again. The complete deplete of the 5f states does not happen in the Np-Pd system, apparently due to the higher 5f count in Np compared to U.

The Np doping leads to the fast suppression of the spin-fluctuation maximum in the susceptibility of Pd, but still contributes to U .The Np doping leads to the fast suppression of the spin –fluctuation maximum in the susceptibility of Pd, but still contributes by a curie term of 2.0 mb/Np leading to an upturn at low T. Effective moments m eff exceeding 1.1 mb/Pu were indicated also in the Pu-Pd system (doping up to 2 % Pu). Although for higher concentrations the m eff values decrease, magnetic Pu ions clearly exist. The fast decrease of the susceptibility of the Pd matrix (much faster than in the Np-Pd system) has to be again interpreted as due to the 4d band filling.

These facts support the idea that a certain reduction of the 5f count comparing to the Pu metal favours the Pu magnetic moment formation. Pu in intermetallic compounds By analogy to U ,the importance of a minimum actinide spacing has been recognized as prominent precondition for the formation of magnetic moments. Similar to U and Np, it is expected that for Pu systems also an additional hybridization with the valence states plays a role in the suppression of magnetism, when the large inter-plutonium spacing, dPu –Pu ,and the small direct 5f-5f overlap would allow for magnetism. Besides the 5f-5f overlap and the 5f –ligand hybridization, so, we can compare magnetic properties of U, Np and Pu compounds, especially of the isostructural ones, with similar inter-actinide spacing and type of coordination.

Generally, Np compounds exhibit (with few rare exceptions) a similar or stronger tendency to magnetism than their U counterparts. The reasons can be seen in a higher number of 5f electrons (about 4 comparing to 3 or little less in typical U intermetallic) which makes the

correlations in the f states more important and induces a certain contraction of the 5f orbitals, reducing the 5f-5f overlap for the same inter-actinide spacing. Continuing further to Pu, the tendency to magnetic order becomes much weaker and ,excluding actinide lases phases AnFe2,which are driven by the 3d-3d coupling (PuFe2 is ferromagnet with (Tc= 564 k), the ordering temperatures of Pu compounds typically do not reach those of U or Np counterparts. As to other Pu laves phases with transition metals, most of then are weakly magnetic (PuMn2,PuCo2,PuNi2,PuRu2,PuIr2). Particulary striking is the contrast of PuNi2 with ferromagnetic UNi2 and NpNi2 .Only PuPt2 is ferromagnet (Tc= 6 k , ordered magnetic moment m=0.2 mb/ f.u.) somewhat higher ordering temperatures were found for equiatomic bibaries PuSi (Tc =72 k , m eff in the paramagnetic state 0.72 mb, compared to Tc= 120 k in USi and PuPt (Tn= 44 k , compared to Tc= 27 k in UPt and Tn= 27 in NPPt. Important few magnetic cases also include PuPt 3 (Tn= 40 k , m eff =1.3 mb/ f.u.) , PuPd3 (Tn= 24 k , m eff =1.0 mb), and Pu Ga3 (Tc= 20 k, m=0.2 mb/f.u. or Tn= 24 k, depending on structure modification, both having m eff =0.78 mb , the only exception being the antiferromagnetic PuRh3 while URh3 and NpRh3 are non-magnetic spin fluctuators.

Easier comparison between U, Np, and Pu is possible for ternary compounds as those (unlike binaries) form large isostructural groups but , unfortunately , for many compounds only the structure is known. Exceptions are PuNiGa and PuCoGa which crystallize in the ZrNiAI structure type and are non-magnetic , whereas UNiGa ,UCo Ga and NpNiGa order magnetically. Remarkably , the discovery of superconductivity in PuCo Ga 5 and PuRhGa5 has initiated a broader study of the actinide ‘115’ compounds . In the UtGa5 group , magnetic order appears only for T=Ni ,Pd , and Pt . The particular cases of T=Co,Rh,Ir , which are very weak pauli paramagnets is clearly due to the 5f –d hybridization which is usually weak for the very late transition metals but gets stronger when moving to the left within each series. The respective Np compounds exhibit different types of antiferromagnetic order (e.g. ,NpCoGa5 has Tn = 47 k). PuCoGa5 ,PuRhGa5 , as well as PuNiGa5 are non-magnetic , the first two have a superconducting ground state.

We can conclude that also in the ‘115’ series the Pu compounds exhibit weaker magnetic properties than their Np and even U isotype. Am interesting systematics can be drawn also from binaries of the rocksalt type ,namely actinide monopnictides and monochalcogenides, the properties of which are well known. U and Np chalcogenides (AnSi,AnSe,AnTe) are magnetic metals whereas Pu chalcogenides ,despite their quite larger atomic volume, remain weakly paramagnetic semi-metals. This is different from Pu pnictides (as PuSb) that are magnetic metals similar to U and Np pnictides. PuSb in particular is a very well documented case of magnetic Pu compound with extended set of microscopic information. Photoelectron spectroscopy deduced the 5f states out of the Fermi level and concluded their localization , while neutron diffraction identified a 5f5 ground state with ordered magnetic moments 0.75 mb /Pu. To test whether a reduced 5f count would be obtained by the LDA+U calculations in such case, leading eventually to Pu magnetic moments, we performed the LDA+U calculations also on PuSb(both around meanfield ,AMF ,and fully localized limit , FLL ,LSDA+U). In case of AMF-LSDA+U, the hybridization with Sb electronic states leads to a lower 5f occupancy (n5f=5.2) than in, e.g., in d/Pu and the total magnetic moment 0.76 mb /Pu in good agreement with experiment. In case of FLL-LSDA +U , yielding the magnetic moment of 0.87 mb /Pu and 5f occupancy n5f=5.0 . My AMF-LSDA+U calculation for Pu chalcogenides (PuTe), which have one more conduction electron and less charge transfer from Pu towards the anion, gave the proper non-magnetic ground state. The FLL-LSDA+U calculations produce a magnetic solution in this case.

Phase transition in d plutonium alloy-Studies present experimental data on transformation of four plutonium –gallium alloys with 1 , 1.7 , 2.5 and 3.5 % Ga under isostatic pressure at 25 c in the Bridgman dilatometer. Large-volume d phase expectedly collapses at quite low pressures and it transforms directly from d to a’ phase with possible traces of g -phase . All the observation indicate that d----a’ transformation occurs through the martensitemechanism in cooling . The data show that the change in the specific volume of the d-phase alloy under

the positive pressure is accompanied by the work which is expended for the d---a' transformation. This means that the energy level of the alloyed d-phase is lower than that of the a' phase. On the other hand , it is well known that the unalloyed a phase is more favourable energetically than the unalloyed d-phase and that a------d phase transition at the room temperature occurs when a tensile stress of 0.35 Gpa is applied curves presented allow for the explicit determination of the d-a transformation energy as a function of gallium concentration in the alloy through the calculation of GpdV integral at the inelastic segment of the compression curve .

Energy per gallium mole in alloy is almost independent of the gallium content. This shows on the existence of a stable gallium complex in d plutonium that exists in alloys with the Ga content ranging from 1 % to 3.5 % the energy of such complex can be expressed as

DE = 67 – 100 x KJ/mole Ga.

Where X is the molar fraction od Ga in Pu-Ga alloy . In this case , the enthalpy of intermetallic compound Pu3Ga is 42 kJ/mole that is close to the value of Pu3Ga enthalpy .The pattern of the transition of gallium alloyed d -plutonium under the high pressure to the a' –phase state can be seen from the plot of the Helmholtz free energy as a function of the specific volume .Internal energy of different phases of plutonium is given by the following equation:

Es = 9 Bm / 2 De . (s1/3 - 1) 2 + C

Where ; Bm and De are the bulk models and equilibrium density for phase at ' P=0' and ' T=0' respectivity , and Ce are constants determining the minimum energy for each phase. All found curves have been calculated using bulk modules B1=30 GPa for the d phase ,B2=50 GPa d or the a' phase , the slope of the common tangent to curves FV for the two phases determines the pressure of the phase transformation at the thermodynamically equilibrium state . And other curves show that the transition occurs with changing pressure .This is concrete evidence of the absence of the thermodynamic equilibrium, the presence of hysteresis ,also indicates the absence of thermodynamic equilibrium .It is well known that at temperatures of 130-150 oC the remaining d phase gets enriched in gallium during the d---a' transformation. This kinetic process may be responsible for the formation of the thermodynamically nonequilibrium state .The tension of the P= - 0.35 GPa applied to a – plutonium corresponds , the a- d transformation in unalloyed plutonium at standard temperature with phase energy difference of 1.2 kJ/mole .This value is much less than TDS in the a---d transformation (3.6 kJ/mole at 300 k and DS= 12 J/mole). Lack of the information about the a---d transformation in tension do not allow a direct comparison of the transition energies in pure and alloyed plutonium as the fraction of d phase that therewith results is unknown . The transition from the a' phase to the pure a phase may be accompanied with the energy release of 3.6-10 kJ/mole , depending on the gallium concentration . This energy is likely the energy of pure a'- phase lattic deformation in a'-phase formation due to the capture of gallium and plutonium are bonded forming in Pu3Ga and this bond in the a' phase disappears ,we can determine from the d---a' transformation under pressure at constant temperature the Helmholtz free energy difference. This difference appears to be close to the plutonium –gallium alloy formation enthalpy .Other curves show the d plutonium alloy enthalpy calculated using expression ,divided by mole of the sum of nuclei of plutonium and complexes Pu3Ga as a function of the molar fraction of gallium in Pu-Ga alloy. Two experimental points obtained with the method of drop calorimetry fall on this calculated curve. This means that results of the calorimetric measurements and experiments on the d---a' transformation under pressure are in agreement . The studies suggest that the formation of d-phase plutonium alloy can be represented into the crystalline lattice of metallic plutonium based on this model , we can determine the dependence of the alloy density on the gallium content as the density of the metallic plutonium and Pu3Ga mixture . Alloy densities versus

Ga concentration calculated using the above mentioned model. The straight lines ‘ obey’ the vegard rule. Kinetics of phase transformations in Pu-Ga ALLOYS.
-We can form the kinetics of phase transformation in Pu-Ga alloys by the following kinds:
1- Kinetics of formation of Pu3 Ga from a d matrix in Pu-Ga alloys.
2-Kinetics of eutectoid phase decomposition in Pu-Ga alloys.
3-Kinetics of martensitic transformation in Pu-Ga alloys.

- Kinetics of formation of Pu3Ga from a d matrix in Pu-Ga alloys : this kinetics – model calculations were performed to study the formation of Pu3Ga from a d matrix of Pu-Ga as a formation of alloy composition , obviously , as already anticipated the higher the temperature is , and therefore the higher the thermodynamic force is , the shorter the time for Pu3Ga formation is , as can be concluded from the temperature –time –transformation (TTT) curves were shown .The higher the Ga composition is , the shorter the time for transformation is, because of the evolution of the thermodynamic driving force with alloy composition .This study also shows that at low temperatures the kinetics of phase formation is rather slow, and therefore from an experimental standpoint ,we can understand why the determination of the two-phase region as inaccurate . The time for formation found with this model and its kinetics database is compatible with those found experimentally.

-Kinetics of eutectoid phase decomposition in Pu-Ga alloys :this kinetics modelling was applied to the study of diffusion d---a’ +Pu3Ga with the diffusion controlled TR Ansformation (DICTRA) .The TTT curve associated with a 5% rate of transformation for the two separate reactions .Close to the temperature of the eutectoid decomposition ,the time for transformation is about 1.5 . 10 6 years , which means that Pu has long time decayed before equilibrium could be reached . This matter was confirmed by modelling the true eutectoid reaction. Although some versions of the phase diagram describes meta stable equilibrium eutectoid transformation is definitely inhibited by diffusion alone. - Kinetics of martensitic transformation in Pu-Ga alloys: to study the early stage of the d---a’ isothermal martensitic transformation . The model of martensite nucleation proposed by scientists , and successfully applied to Fe-Ni alloys , was adopted. In this model , the main idea is that a heterogeneity must pre-exists beyond a critical size , and rapidly transforms in a martensite , this embryo must go through a number of growth steps that are thermally activated . In the present case , since detailed experimental information is lacking, a rate control reaction at the higher Ga contents (i.e., between 1.0 and 2.0 % Ga) that involves the d to g (round -130 C) and d to a’ (around – 160 oC and - 90 oC at 1.9 and 0.7 % Ga, respectively)transformations , as suggested by scientists , was proposed to explain the transition from double to singe C- shape of the TTT curves with a decrease in Ga content. Despite the constraints imposed on the model parameters , the results shown that account fairly well for the change in temperature and time scale of the early stage of martesite nucleation with alloy composition , and for the transition from double to single C- curve with a decrease in Ga composition , in agreement with those from reference. As a final note , the scenario proposed here only illustrates the feasibility of explaining the transition from double to single C- curve (sorry , I will not include this curves in this studies, but in the next papers for summery) , and more in site work on time-resolved structural information as a function of temperature is required to bring a definite answer.

7. Conclusion

The 441 reactors around the world produce about 100 tonnes of plutonium and about 10 tonnes of minor actinides annually, in spent fuel, some of which is separated through reprocessing. While the recycling of plutonium as MOX fuel derives additional energy from this resource, it does little to address the issue of growing plutonium inventories.

In this first part paper, we review and discuss some methods and experiments to control and manage Pu and Pu isotopes inside some nuclear reactors.

REFERENCES

1-S.Kern, et al ., Phys. Rev. B59 (1999) 104 .
2-M.Colarieti-Tosti, et al., Phys. Rev. B65 (2002) 195102.
3-G. Rophael, R.Lallement, Solid State Commun. 6 (1968) 383 .
4-Y.Tokunaga, NMR Studies of Actinide Dioxides, Pu Confernc. 2006.
5-D.Alamelu. dete.ef Pu. dec. 2006.
6-S.K.Aggarwal, D.Alamelu, P.M. Shah. Radiochim. Acta 81 (1998) 129.

Modeling and Simulation of Operator Training Simulator for Prototype Fast Breeder Reactor

T. Jayanthi, K.K.Kuriakose, P. Selvaraj, S.A.V. Satya Murty

Indira Gandhi Centre for Atomic Research, Kalpakkam, India

Abstract. Often the challenge faced by the Nuclear Power Industry is the availability of well trained human resource for efficient power plant monitoring and control. Safety of the plant purely depends upon the plant knowledge acquired, understanding of plant dynamics and the skills possessed by the operators through systematic training. Generally the operators are given class room and field training before deploying them in the operation crew. But, for handling emergency and abnormal conditions, the formal class room training and field training have proved to be inadequate according to the expert estimates. The state- of- art computer based operator training simulators covering the full spectrum of the plant have become an essential element in bridging the gap between the inadequacy and efficiency. Gradually the training simulators are getting embedded in the operator training programme and started playing a crucial role in enhancing the ability of the operators.This paper discusses about the operator training simulator called KALBR- SIM i.e. Kalpakkam Breeder Simulator that has been built at IGCAR for training the Prototype Fast Breeder Reactor (PFBR) operators. It is a Full Scope Replica Operator Training Simulator built to replicate PFBR. The scope of the paper covers the basic modules necessary for building each process model of the simulator, design and development of the reactor sub systems like Neutronics, Primary Sodium, Secondary Sodium, Decay Heat Removal, Steam Water, Electrical systems and the associated logics and controls. It is followed by a detailed discussion on replication aspects of Simulator Control Room and its advantages, the Hardware Architecture, Instruction Station facility and loading of scenarios. It further elaborates on Steady State and Bench Mark Transients tests conducted on the Operator Training Simulator like One primary sodium pump trip, one primary pump seizure, Primary pipe rupture, one boiler feed pump trip and Station Black Out.

1. Introduction

Operator Training Simulators have become more popular with the increasing demand for highly skilled operators in the process industries and power plants. As on today, the concept of training the plant operators has undergone a major change. There is a pressing requirement for the development of highly skilled human resource i.e. operators who are familiar with all possible plant (normal and incident) conditions along with various plant scenarios. The phenomenal growth in the field of Computer Science & Technology also has added an unlimited advantage in building and realizing the Full Scope Replica Simulator for Operator Training purpose. Thus, the Operator Training Simulators have started playing an important role in the operator training program all over the world.

It has been proved through statistics that the Human Error is the main cause for most of the accidents that are taking place in the industries and nuclear reactors. The Three Mile Island accident which occurred in 1979 is one such example. Hence, the main theme of building training simulators is to provide an effective platform for transferring the plant related knowledge and improving the performance of the plant operators. Such training and qualification will instill high level of confidence in the operators with increased reflexes. As on today, one could confidently state that the plant operators around the world are receiving training through full-scope plant specific simulators. Various types of simulators are also being increasingly used to cover the entire range of training based on the requirement. It includes Part task Simulators for system specific training and Basic Principle Simulator for class room training.

2. The Need for Simulators

Simulator based training has gained more importance as it provides a platform for conducting a comprehensive training for the plant personnel thereby enhancing the skill set of the operators. To

ensure safe operation of the plant, having qualified operators possessing adequate plant knowledge is highly essential. As per the Atomic Energy Regulatory Board (AERB) guidelines, it is mandatory to have the Training Simulator Installed & Commissioned and operator training imparted in advance compared to the actual commissioning of the plant. This arrangement facilitates preparing the operators suitable for the plant operation and make them well qualified for the environment. Adequate training on various plant conditions i.e. Steady State and Plant Transient conditions with associated plant dynamics is made possible using this Knowledge Transfer Medium.

3. Brief Description of Prototype Fast Breeder Reactor (PFBR)

Prototype fast Breeder Reactor (PFBR) is a 500 MWe capacity, pool type reactor utilizing sodium as the main coolant and heat transport medium. The reactor core is a compact core containing fuel sub assemblies made up of (Uranium, Plutonium) Mixed Oxide. The heat transport system consists of primary sodium circuit, secondary sodium circuit and steam water system. The schematic diagram of PFBR is shown in FIG.1.

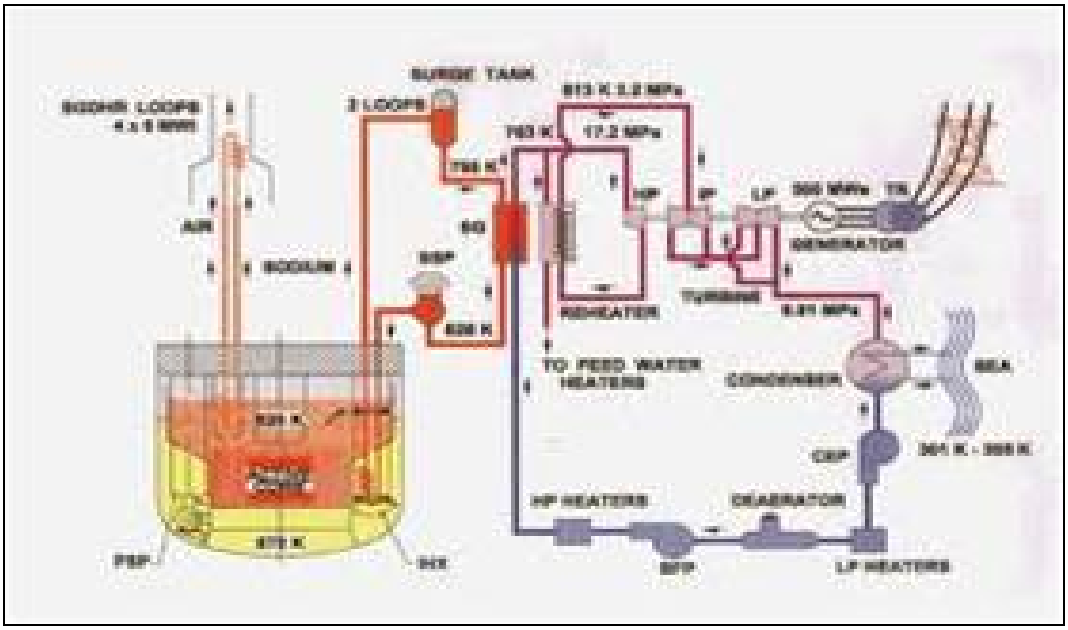

FIG. 1. Schematic Diagram of PFBR

The heat generated in the core is removed by the primary and secondary heat transport system which is in turn used to produce steam in once through type steam generators. The steam water system produces superheated steam to drive the Turbo Generator to generate 500 MW electric power. The steam water system adopts a reheat and regenerative cycle using live steam for reheating. A Turbine bypass of 60% capacity is provided to facilitate the startup, shutdown and reloading of the turbine. The decay heat system is provided to remove the decay heat generated in the core subsequent to any reactor trip.

4. Brief Description of PFBR Operator Training Simulator (KALBR-SIM)

The PFBR Operator Training Simulator is a Full Scope Replica Type Simulator and it has been built in-house with the technical expertise with in the centre. The training simulator is named as KALBR-SIM (Kalpakkam Breeder Simulator) and is designed to replicate the steady state and dynamic response of the plant to operator actions. The simulator control room layout is designed in tune with the reference plant layout comprising of Simulator Control Room, Instructor room, Backup Control room, Handling Control Room, Engineers Room, Local Control Centre Room etc as shown in *FIG.2.*

The scope of modeling and simulation includes all the reactor subsystems starting from Neutronics to Electrical systems and associated system transients. Basically, it consists of mathematical models representing various system components and processes that are executed in real time. KALBR-SIM incorporates features that are mandatory for imparting full fledged training for the plant operator on normal and abnormal plant conditions.

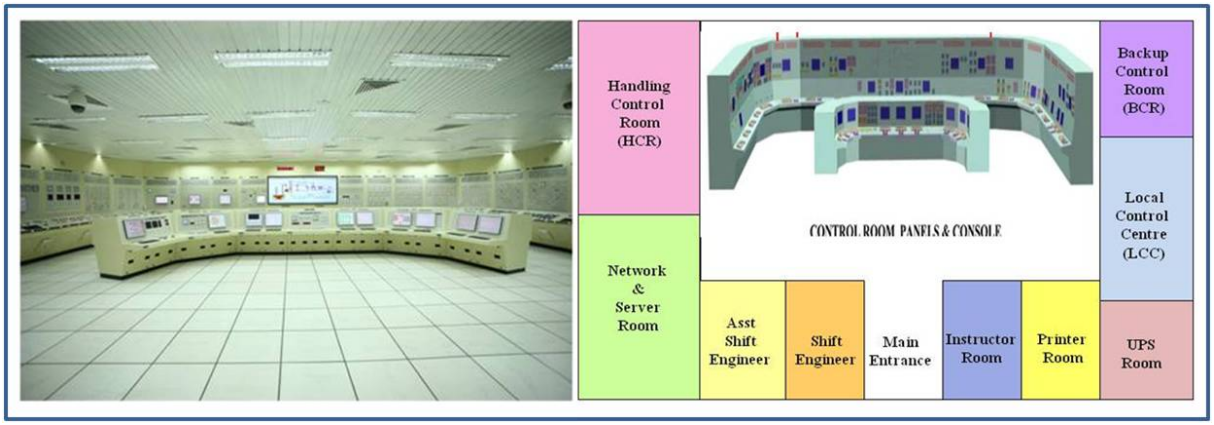

FIG. 2. PFBR Simulator and Plant Layout

4.1. Hardware Architecture of KALBR-SIM

The simulator Control Room is replicated with respect to reference Control Room in terms of selection and installation of Control Panels and Operator Console including Panel colour, display and alarm indications, layout, lighting arrangement, seating arrangement, the ambience etc.

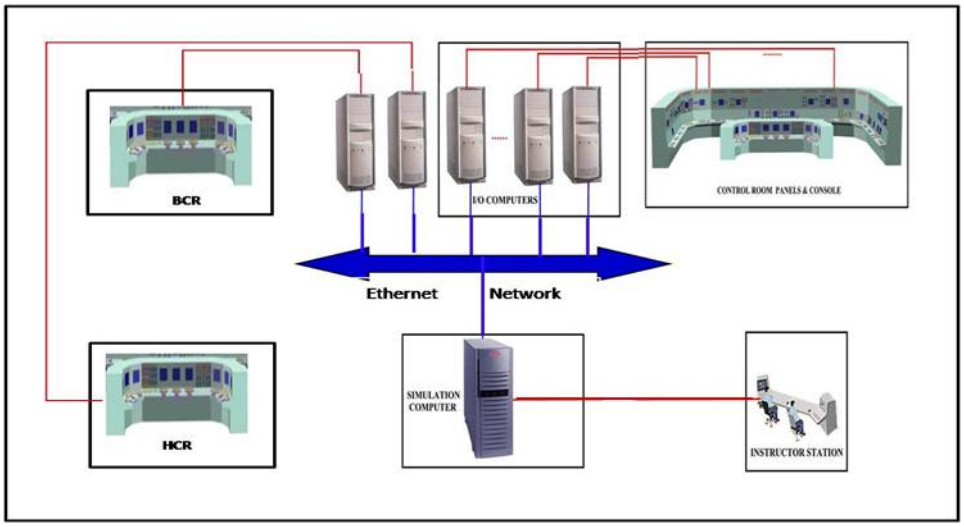

FIG. 3. Hardware Architecture of PFBR Simulator

The simulator Hardware Architecture consists of Simulation Computers, Input/ Output systems, Control Panels, Operator Information Consoles, Instructor station, Simulation Network, Power Supply and Distribution system, Backup Control Panel, Handling Control Panel as shown in the FIG. 3.The Simulation Computer/Server facilitates computation and execution of various mathematical models of the reactor components in real time. The server is interfaced with the hardware panels through I/O systems and the signal communication is established using Local Area Simulator Network. The Operator Console handles overall monitoring of the most important and frequently used control signals. The Instructor Station facilitates control and monitoring of Simulator Operations / Operator actions and conducting training sessions. All plant scenarios are loaded from here for carrying out training programme for the operators. A backup control panel is a part of the training simulator and

serves to handle emergency situations like inaccessibility of main control room in case of fire. Similarly handling control panel forms a part of hardware architecture and facilitates initial fuel loading and subsequent fuel handling operations.

4.2. Simulated Reactor Sub Systems and Related Plant Conditions

Based on the training requirements, all the important reactor sub systems are included in the development of Operator Training Simulator. Modeling and Simulation of KALBR-SIM includes systems like Neutronics, Primary & Secondary Sodium, Decay Heat Removal, Steam & Water, Electrical, Fuel Handling and PFBR Instrumentation & Control system.

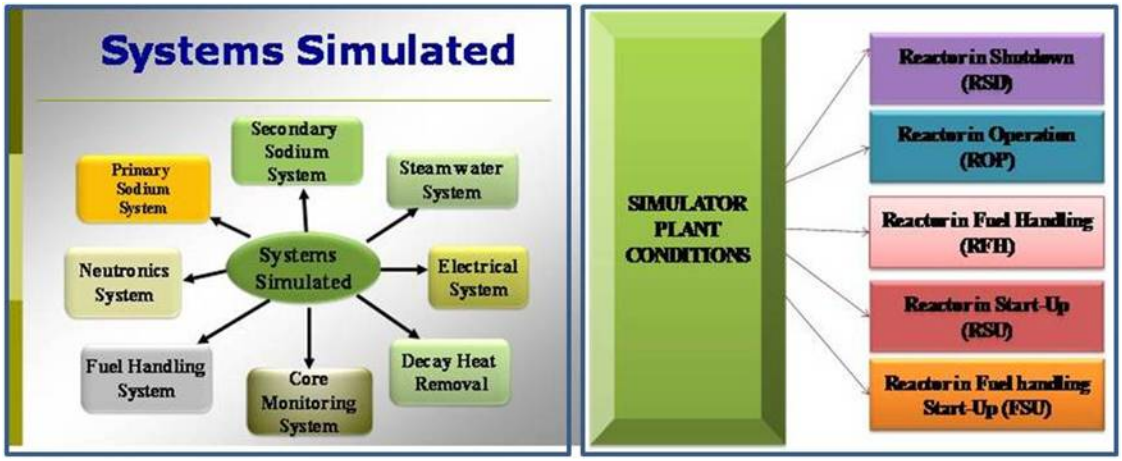

FIG. 4. Systems Simulated and Plant Conditions

The various plant operating conditions that are envisioned for modeling of KALBR-SIM Operator Training Simulator include, Shut down of Reactor, Preparation for Start Up, Reactor Start up Operation, Reactor Criticality (Hot, Cold and first Criticality), Power Rise Operation, Full / Partial Power Operation, Preparation for Fuel Handling Operation, Fuel Handling Operation, Reactor Trip under various conditions, Reactor Setback and Reactor Trip and subsequent start up (Refer Fig.4. for details).

4.3. Standards Followed

The reference standards followed for the development of PFBR Training Simulator include **ANSI / ANS – 3.5 – 1998, IAEA – TECDOC – 995 and IAEA – TECDOC – 1411.** These standards establish criteria for the degree of simulation, the functional capability, the performance requirement and the instrumentation and controls of the simulated control room.

5. Design and Development of Training Simulator

The main responsibility of Modeling & Development of Operator training simulator was entrusted to Computer Division of IGCAR and the simulator development work was carried out in collaboration with Reactor Design Group of IGCAR. In principle, the design and development of process models involve model development using simulation tools and models that need to be built in-house with special attention with respect to uniqueness of the Nuclear Power Plant. In general, the commercially available simulation tools satisfy the requirement of conventional system modeling only i.e. process model development pertaining to steam water system and electrical systems. Nuclear core being unique to each power plant depends upon the type of reactor i.e. thermal reactor or fast reactor. The core configuration and the cooling systems are quite different for the type and choice of nuclear reactor. The available simulation tools do not have the capability to build such models and they have to be developed in-house with the technical expertise available at the centre.

5.1. Classification of Simulator Models

For the above said reasons, the Simulator Models are classified into two main categories i.e. InternalModels and ExternalModels. Internal Models refer to the models that are developed using tools like Steam Water System, Electrical system, Fuel Handling System etc. ExternalModels refer to models that are developed indigenously using FORTRAN / C code. The External Models include Neutronic system, Primary & Secondary heat transport system, alarm generation system, core temperature monitoring system, safety grade decay heat removal system etc. (Refer *FIG.5.* for details).

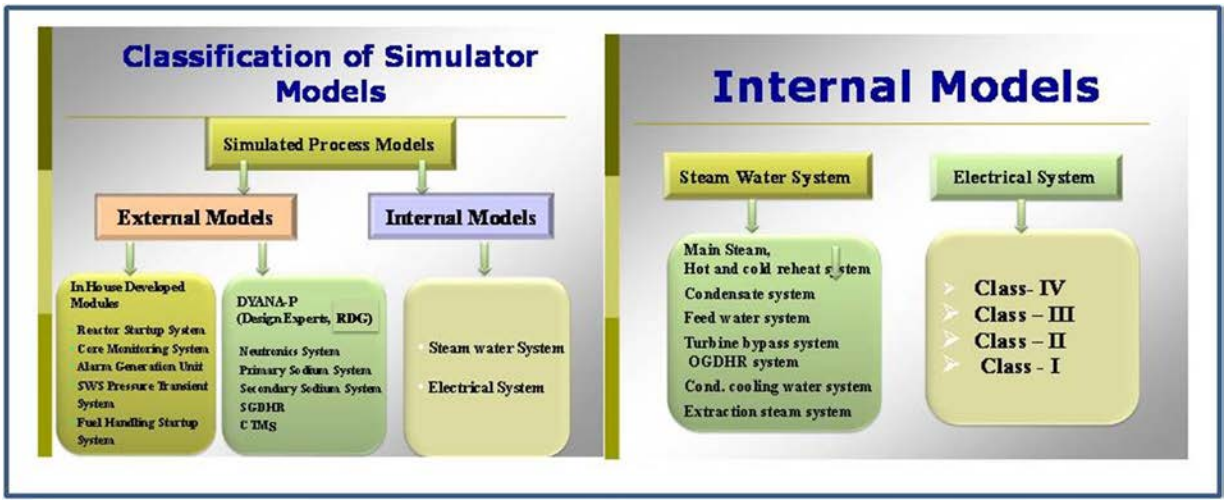

FIG. 5. KALBR-SIM External and Internal models

5.2. Development of Process Simulator

Simulation of Neutronics System, Primary & Secondary Sodium Systems and Safety Grade Decay Heat Removal System are carried out using designer's code named DYANA-P. The **DYANA-P(DYnamic ANAlysis of PFBR)** code is a validated code developed by design experts of the centre. All the plant dynamics related to above main subsystems have been analyzed using DYANA-P code and it is the base for Preliminary Safety Analysis Report preparation also. The systems are modeled by adopting the DYANA-P code and incorporating necessary changes for grouping the process variables for enabling easy migration into simulator environment. The models are integrated with the internal models using a common database by subscribing /publishing the process variables. The main components that are modeled in DYANA-P using mathematical expressions include Neutronic Core, Primary Sodium Pumps, Intermediate Heat Exchangers, Cold Pool, Hot Pool, Surge Tank, Steam Generators and Sodium Piping related kinetics and thermal hydraulic calculations based on various plant conditions. The simulated plant parameters are dynamically displayed on the mimic flow sheet (Refer *FIG.6.* for details).

The other important models which are developed in-house are the Core Temperature Monitoring System (CTMS) and Reactor Startup System. The Core Temperature Monitoring System is modeled using flow zoning concept in consultation with design experts. 2D CTMS graphic display is also modeled and integrated to display the temperature distribution. Provisions for initiating flow blockage at 10%, 20, 30 ….90% are modeled by calculating individual SA outlet temperature. The Reactor Startup System is simulated using external code written in C language by deriving the main input signals from various process models. Basically this model checks the healthiness of various processes and the poised state of all the systems which in turn permits the CSR and DSR Raise /Lower operations to start the reactor. (Refer FIG. 7. for details).

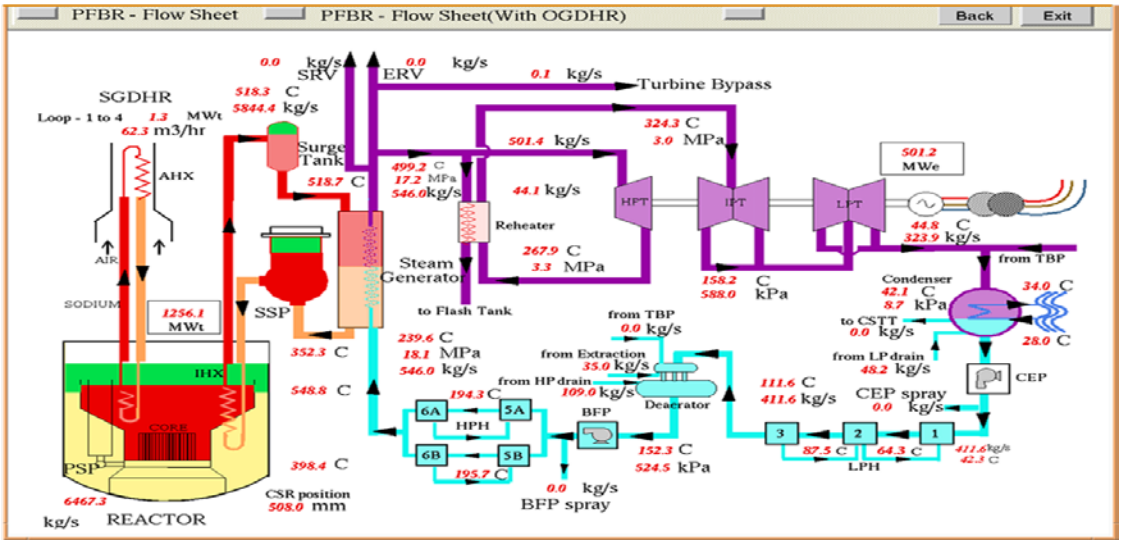

FIG. 6. Simulator Flow Sheet

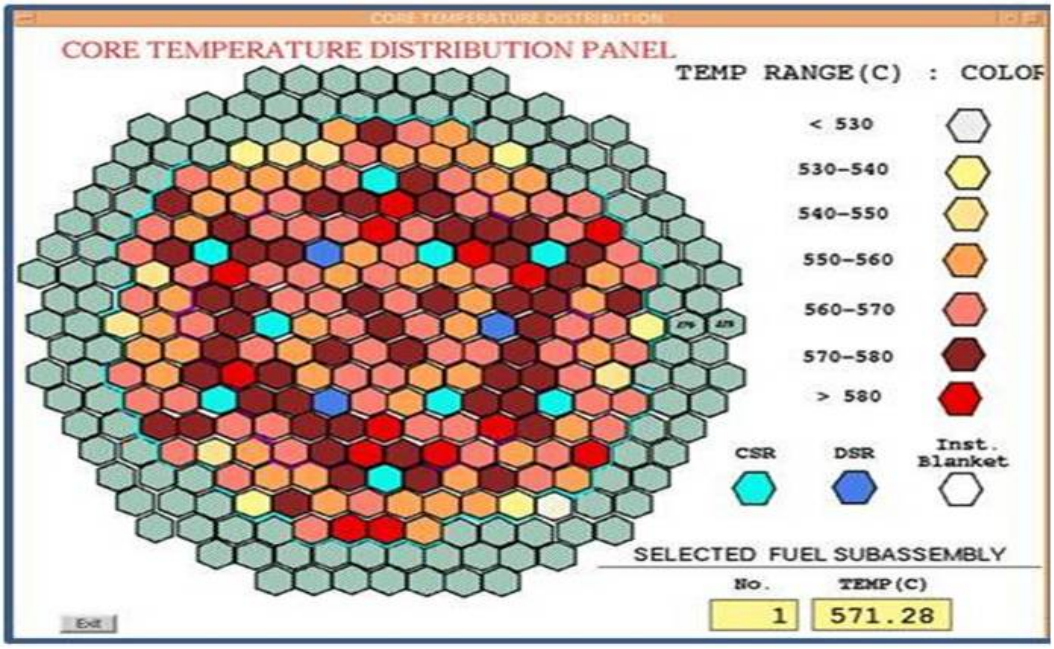

FIG. 7. Simulated Neutronics Core

The models that are necessary for the successful operation of the training simulator also are taken into account while modeling using external code. It includes alarm generation system, log message generation system, logics and controls for coolant pumps, governor models, steam generator pressure control system etc. All the models are integrated and tested for its satisfactory performance.

The Steam Water System & Electrical System is modeled using simulation tool. The modeling of Steam Water System includes Main Steam System, Condensate Extraction System, Feed Water system, Bleed Steam Extraction System, Drain and Vent System, Cold & Hot Reheat System and Condensate Cooling water System and Turbine Bypass System.The modeling of Electrical System includes Class IV, Class III, Class II, Class I power supply systems. Refer *FIG. 8.* for details.

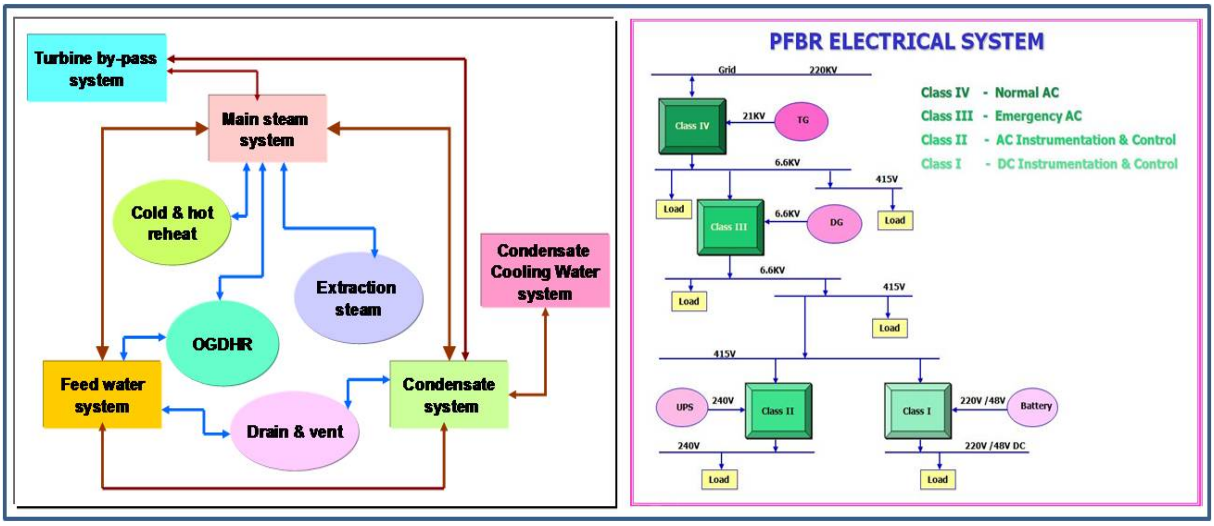

FIG. 8. Steam Water and Electrical System

6. Bench Mark Transients

As per the Preliminary Safety Analysis Report, the Design Basis Events are grouped into four categories viz. Cat-1, Cat-2, Cat -3 and Cat-4 starting from more frequently occurring incidents to less frequently occurring incidents. The list of important transients is identified based on the Training Requirement and Preliminary Safety Analysis Report. It is highly essential that all the selected plant operators are trained on bench mark transients and are familiar with the associated plant dynamics.

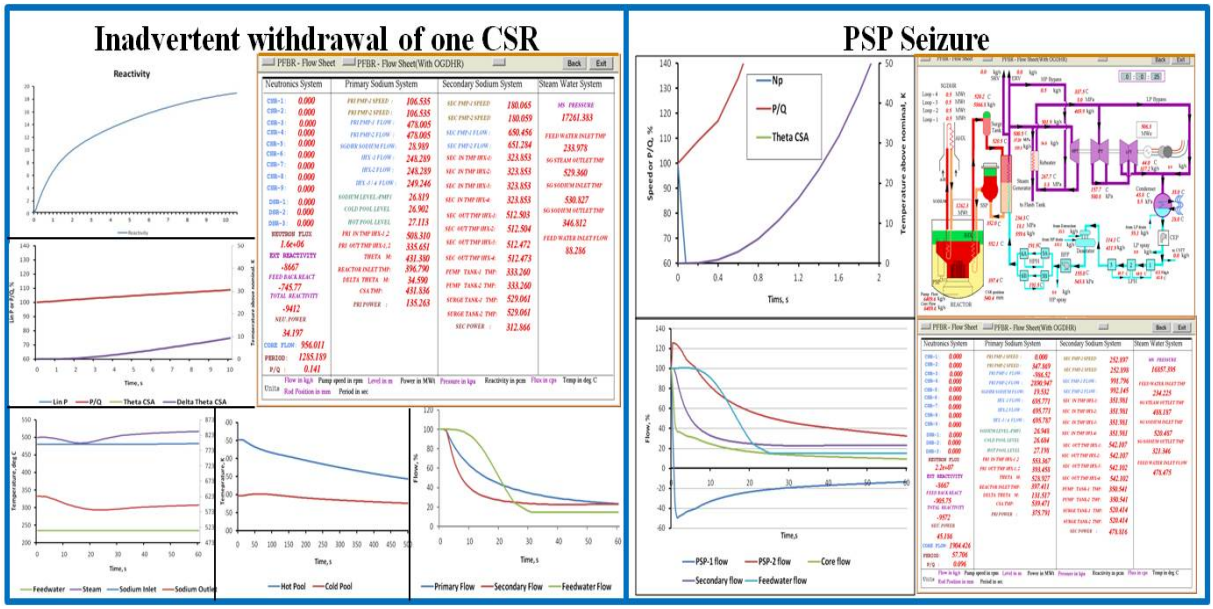

FIG. 9. Benchmark Transients

The bench mark transients that are modeled and simulated include Uncontrolled Withdrawal of Control Rod (at Low Power, Medium power, Full Power), One primary pump trip, One primary pump Seizure, , IHX sleeve valve closure, Plugging of a fuel sub-assembly, Primary pipe rupture, One secondary pump trip, One secondary pump seizure w.r.t Neutronics and heat transport systems. The events and malfunctions w.r.t steam water and electrical system include one/both boiler pump trip, one/both condensate extraction pump trip, one/both condenser cooling pump trip, turbine trip,

condenser vacuum collapse, loss of heating in HP heaters, Turbo generator operating at full power, feeding the grid and station loads, Turbo generator feeding the station loads alone, feeding station loads from the grid, Diesel Generator feeding emergency loads, Emergency Transfer System switching on of DG when class IV grid fails etc. (Refer *FIG. 9.*for details).

Relevant process parameters are captured and the profiles are plotted for further checking and analysis. The results are compared with the Preliminary Safety Analysis Report for ensuring that the model behaviour is in line with the any deviation. It is checked that the deviations are within the stipulated limits specified by the standard.

7. Integration and Testing of Process Models

On completion of the process models, all the process models are integrated and tested. Integration and performance testing is the most crucial phase in the process model development and implementation cycle. The main aspect of Integration and Testing is to ensure and verify the correct functioning of all the process models, the associated logics and controls. The other important points that are checked include the communication between various processes, cycle time of each process, logical conditions of various components, display of associated alarms and system parameters.

7.1. Performance Testing

Simulator performance testing is conducted in a fully integrated mode to check the correct functioning of the process model under steady-state and transient conditions of the plant. It checks the degree of completeness and accuracy of the models built. As per the standards, Steady State performance testing needs to be carried out at three different power levels ie 100%, 50%, 25% of the operating range. At each level, the process simulator is made to run in the integrated mode for few hours before going into further analysis. The **Transient Simulation** is carried out to ensure that the dynamic behavior of the plant under various abnormal conditions is always towards safe operation of the plant. The scenarios are loaded from the instructor station as shown in Fig-10. The Event Analysis Report forms the basis for evaluating the process simulator for transient testing.

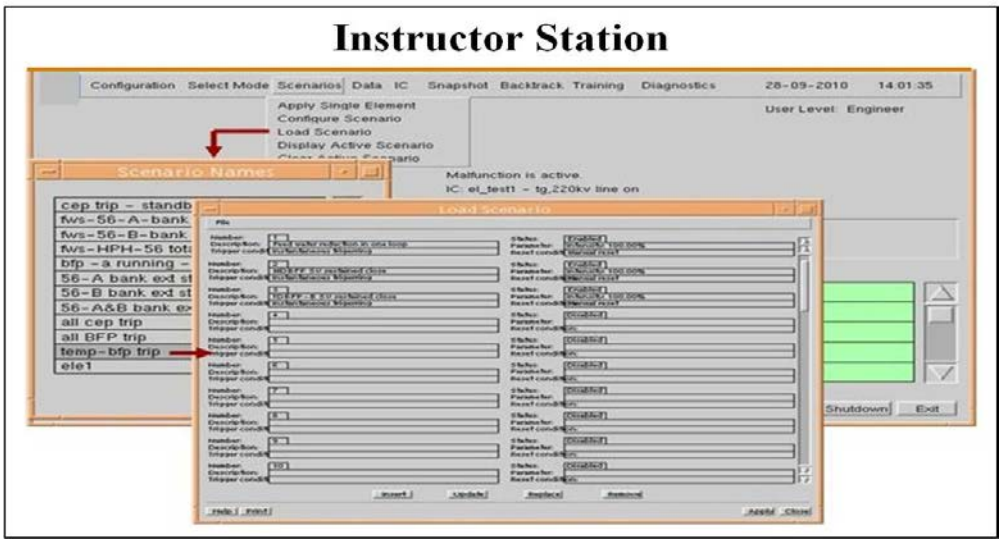

FIG. 10. Instructor Station

8. Fuel Handling

Fuel handling system modeling has been carried out in-house using C++ language. The fuel handling operations like, in-vessel and ex-vessel subassembly handling are modeled and simulated. The In-vessel core handling involves 3D modeling of components like Transfer Arm (TA), Large Rotatable Plug and Small Rotatable Plug Operations and the Ex-vessel fuel handling involves 3D modeling of

components like, Inclined Fuel Transfer Machine (IFTM), Rotatable Shield Leg, Gate valves etc. The fuel handling operations are carried out from Handling Control Room (HCR) which is exclusively set up for core related activities. The models are integrated and tested successfully by checking the operations from the HCR virtual panels. (Refer Fig-11 for details).

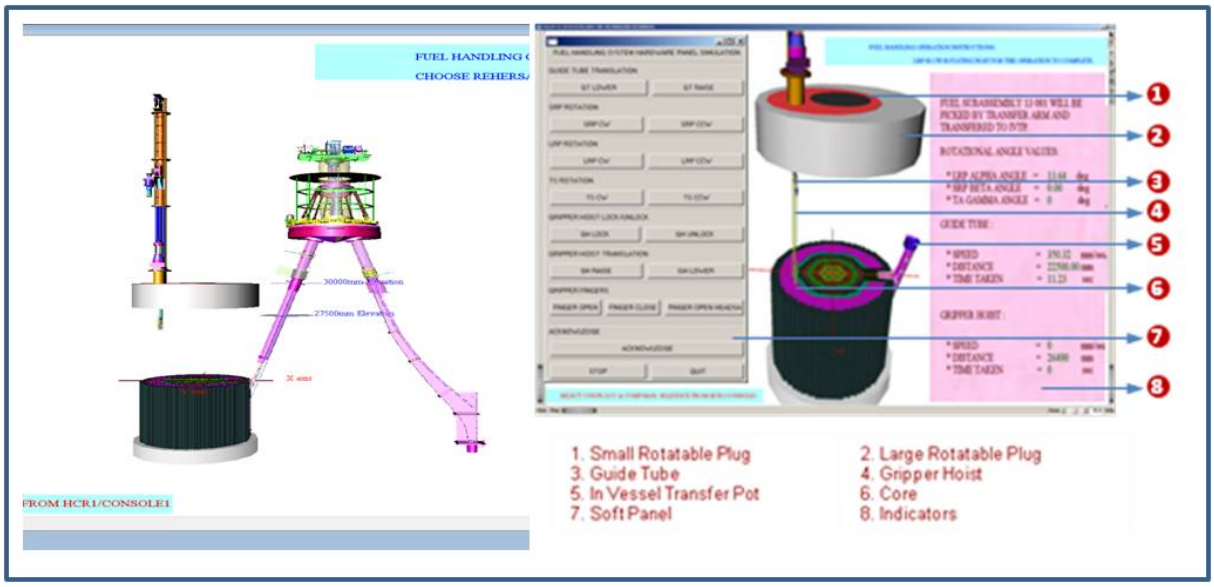

FIG. 11. 3D modelling of Fuel Handling process

9. Validation of Process Models by Local Validation Team

A Local Validation Team consisting of number of domain experts specialized in process design and instrumentation & control design is entrusted with the responsibility of verification and validation of the process models. All the models are subjected to scrutiny by the concerned system expert for qualifying the model. Where ever deviations are noticed beyond the limits specified by the standard, modification and model tuning is carried out. Thus, the first level of approval is obtained from the local validation committee.

10. Validation of Process Models by External Validation Team

As a second level of qualification, the process models are subjected to verification and validation by the External Validation Team. The team consists of experts from various units, NPCIL, BARC and IGCAR with specialization in design analysis and similar field experience. The simulated process models are demonstrated in detail to the team of experts of V&V Committee. The comments if any are recorded and discussed with the design experts for appropriate incorporation in the model. The V&V Reports are made ready (for the accepted systems) and submitted for further approval by the committee.

11. Conclusion

The PFBR Operator Training Simulator is developed successfully in-house covering all the sub systems, bench mark transients, malfunctions etc and installed at BHAVINI Training Centre for providing training to the operator's of PFBR.

ACKNOWLEDGEMENTS

The authors gratefully acknowledge the support and guidance provided by the colleagues from Reactor Design Group. The authors are greatly indebted to the constant guidance & motivation provided by Shri. S.C. Chetal, Director, IGCAR.

REFERENCES

[1] T.Jayanthi, S.A.V.Satyamurty,K.K.Kuriakose,S.Srinivasan,M.L.Jayalal, Scope Document on PFBR Operator Training Simulator - PFBR/ 08610 / DN / 1000 /Rev A, (2003).

[2] T.Jayanthi,S.Rajeswari,Training Requirements of PFBR Simulator - PFBR/08610/DN/1008/Rev-A - Released in 2008

[3] Preliminary Safety Analysis Report, Chapter 14 - PFBR Events Analysis Report

[4] Preliminary Safety Analysis Report, Chapter 8 - Instrumentation & Control System

[5] Jehadeesan,M.L.Jayalal,S.A.V.Satyamurty, Hardware Architecture of PFBR Simulator, PFBR/08610/DN/1001/Rev A, (2005)

[6] T.R.Ellapan,Athinarayanan, Design Document on PFBR Simulator - PFBR/ 08610 / DN / 1000 /Rev A, (2003)

[7] A.K.Santra,A.Takur, Design Notes on Feed Water System - PFBR/43000/DN/2050

[8] T.Jayanthi,S.Rajeswari,K.R.S.Narayanan,H.Seetha, S.Anathanarayanan,S. Athinarayanan, P. Swaminatha, Process Simulation of Nuclear Power Plant Using Latest Techniques.

[9] T.Jayanthi,S.Rajeswarai, K.R.S.Narayanan, S.Athinarayana, P.Swaminathan, Modelling of Steam Water System Simulator, PFBR/08610/DN/1007/REV-A

[10] S.Srinivasan, M.L.Jayalal. R.Jehadeesan, S.Athinarayanan, P.Swaminathan, Modelling of Core, Primary and Secondary Sodium Circuits – Adapting the plant dynamics analysis code, PFBR/08610/DN/1004/REV-A

Recent analyses of PHENIX End of Life Tests and perspectives

B. FONTAINE[a], L. MARTIN[a], G. PRULHIERE[a], R. ESCHBACH[a], J.-L. PORTIER[c], P. MASONI[b], N. TAUVERON[d], R. BAVIERE[d], D. VERWAERDE[e], J-M. HAMY[f]

[a] CEA, DEN, DER, Cadarache, F-13108 Saint Paul Lez Durance, France

[b] CEA, DEN, DEC, Cadarache, F-13108 Saint Paul Lez Durance, France

[c] CEA, DEN, DTN, Cadarache, F-13108 Saint Paul Lez Durance, France

[d] CEA, DEN, DM2S, STMF, F-38054 Grenoble, France

[e] EDF R&D1, Avenue du Général de Gaulle, F-92141 Clamart, France

[f] AREVA-NP, 10 rue J. Récamier, F-69456 Lyon cedex 09, France

Presented by B. FONTAINE

Abstract. This paper presents the recent analyses of Phénix End of Life tests performed with the most advanced modelling developments, and a global assessment of the campaign. The following items are specifically touched upon: core decay heat removal measurement and associated uncertainties, natural convection in reactor vessel using coupled system and CFD models, and neutronic/mechanical behaviour of the core during flowering test.

Finally, it appears that the Phénix decay heat measurement test can be added to the validation basis of DARWIN code associated to JEFF3.1.1. The discrepancies with experimental data are weak (under +/- 8%) and globally covered by uncertainties. Concerning the primary natural convection test, the use of a CFD/system coupled calculation allows to model very accurately the sodium temperatures during the transient. The behaviour of the core during static flowering test can be well estimated by using HARMONIE code for mechanical aspects and TRIPOLI for neutronics. A new test is scheduled in Phénix to assess the core mechanics code in case of dynamic load.

INTRODUCTION

A campaign of "End-of-Life" tests was jointly performed by CEA, EDF and AREVA in 2009 at the PHENIX French sodium fast reactor prototype, before final shut-down of the plant. The tests covered a wide range of domains: core physics, thermal-hydraulics, mechanics, fuel and some investigations related to the negative reactivity transient events that occurred in 1989 and 1990 and are not yet fully explained.

A first set of interpretation work was carried out in the past years and was published [1]. This paper will present some deeper analyses performed recently associated to further modelling developments, and a global assessment of the campaign. Some international cooperation studies have been going on regarding some tests.

The following items will be more specifically touched upon: core decay heat removal measurement and associated uncertainties, neutron physics test interpretations and feedback on codes, the primary system thermal-hydraulics, using coupled system and CFD models and the mechanical behaviour of the core.

A further test, planned in 2013, before the core unloading, will be finally described. The test will aim at assessing the mechanical dynamic behaviour of the core.

DECAY HEAT MEASUREMENT TEST

Decay Heat (DH) is an important concern to the nuclear industry. If not extracted, the heat produced by the decay of non stable fission products and heavy nuclides can lead to the meltdown of the fuel. Consequently, as decay heat has a deep impact on the design of the emergency cooling system, the cooling time necessary before maintenance in a reactor, the design of waste transport casks and storage facilities, a specific test has been performed in Phénix reactor in 2008 to measure it. This measurement will be usefull to validate the codes used to design the future sodium fast reactors.

Test description

A complete description of the test is available in [2]. Few days before the test, the reactor was operated under nominal conditions. Then, a fast shutdown was carried out. One and a half hour after the shutdown, the reactor was considered to be in isothermal conditions and behaved as a calorimeter. The decay heat is derived from sodium temperature evolution thanks to an energy balance equation :

$$DH = I\frac{d\theta}{dt} - P_{sources} + P_{losses}$$

Where DH is the estimated decay heat, I the reactor vessel inertia, θ the measured temperature of the sodium, $P_{sources}$ and P_{losses} the sources and the losses of power in the reactor block.

Decay heat calculations

In Phénix, the decay heat is generated by several sources : fuel and radial blanket assemblies of the core, spent fuel located in the internal vessel storage, neutron shielding, sodium and vessel structures. Actually, 80% of decay heat is produced by the core. To evaluate the contribution of each source to the uncertainties, a deterministic code, namely CYRUS, has been developed to propagate nuclear data uncertainties on nuclide inventory and decay heat calculations, and applied to Phénix experiment.
It appears that the uncertainty on total decay heat calculated with DARWIN and JEFF-3.1.1 ranges between 2% and 4.5% (see figure 1), depending on the integration or not of the contributions of shielding and structures. This result shows the necessity to calculate accurately neutron flux in those peripheral areas and to have reliable nuclear data for activation reactions (for example $^{59}Co(n,\gamma)^{60}Co$ and $^{62}Ni(n,\gamma)^{63}Ni$).
Taking into account these aspects, the experimental data and decay heat calculations are finally well consistent since both uncertainty domains are overlapping (see figure 2).

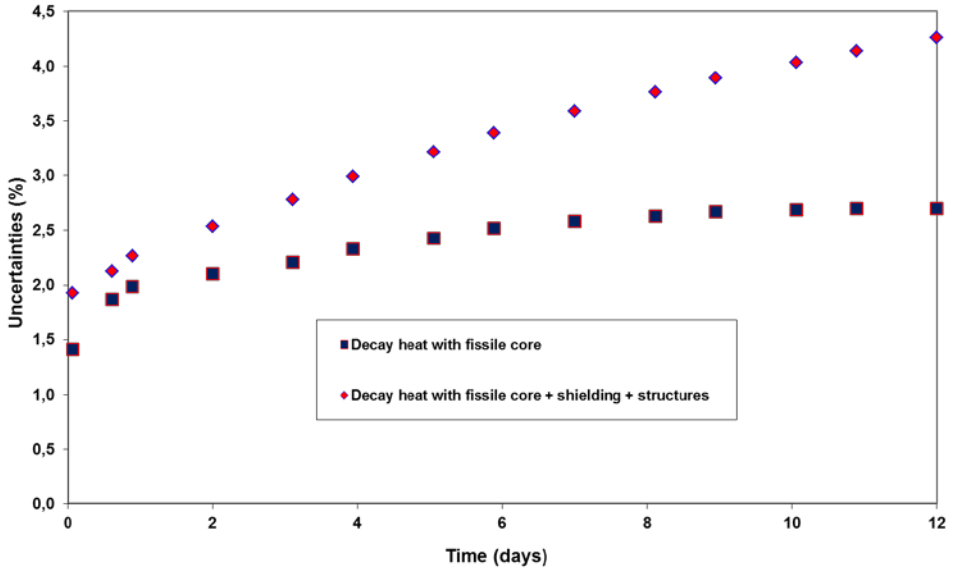

Figure 1 - Decay heat uncertainties calculated with Cyrus

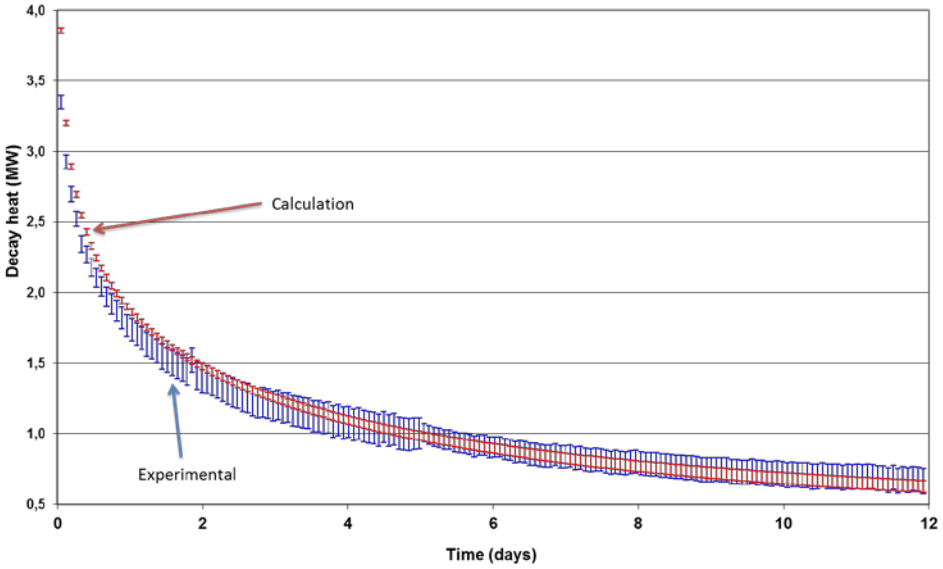

Figure 2 - Comparison of calculated and measured decay heat

As a conclusion, the Phénix decay heat measurement test can be added to the validation basis of DARWIN code associated to JEFF-3.1.1, as a global validation test for SFR applications. The discrepancies with experimental data are weak (under ±8%) and globally covered by uncertainties. Nevertheless the experimental uncertainty remains high, a more precise experiment in a controlled neutronic environment (such as experimental reactor) would be necessary to reduce this uncertainty.

NATURAL CONVECTION TEST

One of the main goal of the Phénix natural convection test (NCT) is to validate thermalhydraulics codes with respect to the establishment of natural circulation in the primary system of a pool type SFR. The present section presents the calculation of the NCT by coupling the 3D computational fluid dynamics (CFD) code TRIO_U with the best estimate thermal hydraulic system code CATHARE. It is also mentioned that Phénix NCT model has also been simulated at the system scale by CATHARE alone [3][4].

Methodology

Many SFR transients involve both the system scale, with flows and temperatures varying in different components and circuits, and local 3D effects where fluid behavior can not be modeled by 1D approach. Local simulations accuracy is usually limited by boundary conditions, but it is impossible to model the whole reactor in CFD. On the other hand, system codes do not provide capabilities to account for local extrema or fluctuations. Therefore, it appears necessary to couple a system code with a CFD code.

Because of its high computational cost, CFD-models must be used only where essential. The first phase of the Phénix NCT, a steam generator drying operation, is characterized by a hot-shock occurring at the intermediate heat exchanger (IHX) primary outlet window. During this unprotected phase of the transient, the temperature at the pump inlet is a key physical parameter for the determination of the core inlet temperature and consequently on the core neutronics. Physically, this parameter is determined by the complex 3D flow paths of the cold pool, which are likely to evolve during the transient due to buoyancy forces. After the reactor scram, the second phase begins and natural circulation rapidly takes place in the primary sodium system. It has been shown that the IHX primary inlet temperature is of greatest importance for the determination of the natural circulation mass flow-rate. This is particularly true in situation where the primary/secondary heat transfer-rate is low. The beginning of the second phase of the Phénix NCT is an example of such a physical situation.

Physically, the IHX primary inlet temperature is again determined by 3D complex thermalhydraulic effects occurring in the hot pool. It seems therefore reasonable to prescribe the use of a CFD model for both cold and hot pool. Another argument in favor of CFD-modeling for the hot and cold pool is related to the instrumentation that produces the experimental data used for the validation: some important bias effects, originating from 3D thermal hydraulics phenomena (e.g. thermal stratification, mixing with surrounding sodium ...), can be feared in the natural convection regime. Consequently, for validation purpose, these sensors have to be integrated to CFD-based models able to deal with the above-mentioned local phenomena.
The coupling methodology used is of the domain-overlapping type associated to a defect correction approach. The coupling scheme has been verified by cross-comparing the numerical predictions of a CATHARE reference calculation to a CATHARE/CATHARE coupled calculation. The coupling software architecture relies on a common application programming interface (API) named ICoCo developed by CEA for coupling activities. The methodological aspects related of this work are detailed in [5]. Figure 3 presents the initial state at the beginning of the NCT obtained by the 1D/3D coupled model.

Results

Numerical vs. experimental comparison has been performed against measured quantities consisting of inlet/outlet primary and secondary IHX temperatures, primary pump inlet temperature, core outlet temperature, primary sodium mass flow-rate as well as level measurements in the hot pool, the cold pool and in the main vessel cooling system. For the sake of briefness it is not possible to present all the available results here. Nonetheless, an interested reader can refer to [5] to have a better insight into the predictions of the 1D/3D coupled calculation. It was chosen here to present the evolution of the primary IHX outlet temperature, which illustrates the interest of thermalhydraulic multi-scale coupling for addressing SFR transient analysis.
Obtaining the 120 MWth steady state requires several thousand seconds CFD/system coupled calculation in order to correctly evaluate the cold pool thermal stratification. Stratification originates from both the heating by the hot pool and the cooling by the main vessel cooling system. It occurs at elevations where sodium is poorly mixed by the primary flow, i.e. above the top of the IHX outlet windows. Thermal stratification of the cold pool was found to significantly alter the sodium temperature at pump inlet during phase 1 of the NCT.
During the initial steady state, the primary mass flow-rate, as well as the temperature at the inlet/outlet of the main components provided by the CFD/system coupled calculation where found to be very similar to that of the system stand-alone calculation.

Primary IHX outlet temperature

The transient evolution of the primary IHX outlet temperature, as measured by a sensor located at the bottom of the IHX outlet window is shown in Fig. 4. This sensor is immersed in the sodium stream exiting the IHX in the forced convection regime. The 60 K increase, resulting from the steam generator dry out during phase 1 and during the beginning of phase 2, is very well reproduced by the CFD/system coupled calculation. A 15 K temperature drop is then observed (at t = 5490 s), 24 s after the primary pump trip. Visualization of 3D temperature and velocity fields have revealed that this temperature drop originates from the transition between the forced convection to the natural circulation regime. Indeed, when buoyancy forces become predominant, the sodium stream exits the IHX at the top of the outlet window and the measurements of the sensor experiences a sudden shift from the average outlet temperature of the IHX to the local temperature of the cold pool which happens to be 15 K lower than the former one at this stage. The predictions of the CFD/system coupled calculation are also in very good agreement with the measured values during phases 2 and 3.
To illustrate the effectiveness of coupling CFD and system codes in addressing SFR transient analysis, the predictions of the system code alone were also shown in Fig. 4. Three liquid temperatures corresponding to the 0D elements located at the elevation of the sensor are presented (the system code model of the cold pool is azimuthally sectorized into three equal parts).

More generally, the spatially averaged quantities calculated by the system code present smoother evolutions than the experimental values obtained from local measurements. If correct, the temperature field obtained from the CFD/system coupled calculation may eventually be used to define the spatially averaged quantities that could be directly compared to the results of a system code. This could lead to a more accurate validation procedure for the use of system codes to simulate SFR.

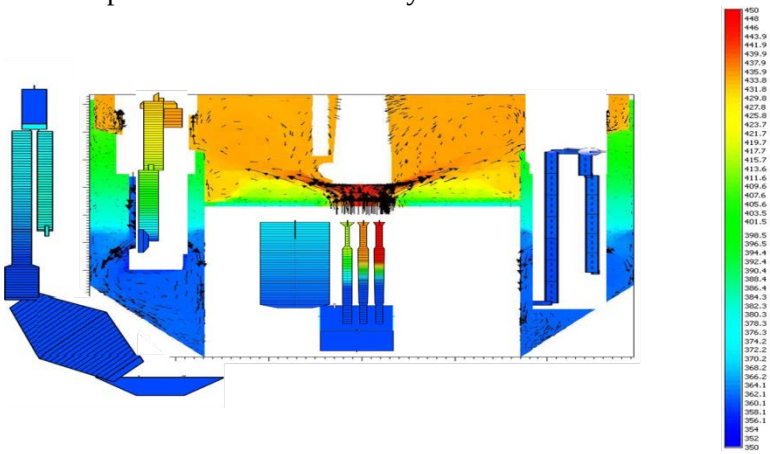

Figure 3 - Initial temperature and velocity fields in the primary circuit

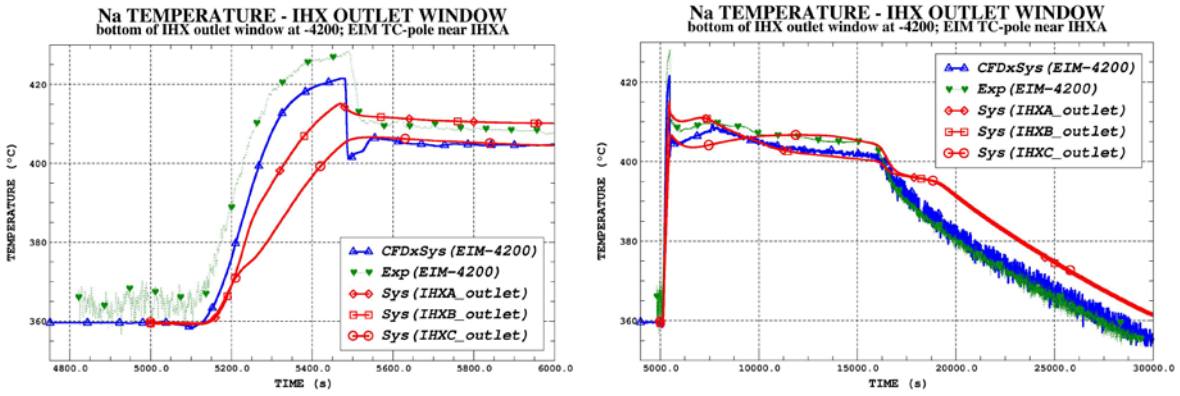

Figure 4 - Short- (left) and long- (right) term evolutions of the IHX primary outlet temperature (transient starts at to = 5000 s).

CORE MECHANICAL FLOWERING TEST

A core flowering test was carried out by introducing a mechanical pushing device inserted in the code sub-assembly lattice at two different positions: at the center and at a the periphery (figure 5). The effect of core flowering was measured at different temperatures in the range of 180 °C to 350 °C.
The purpose of this test was to measure the reactivity effect of such core deformation at subcritical and at critical zero power conditions, and to measure the core mechanical behaviour under an imposed quasi-static flowering.

During the test, the measurements relative to core mechanics were :

- pushing forces necessary to make the core flower,
- radial displacement at the top level of four assemblies located at 3rd and 7th ring (see fig. 5) The devices used for the measurement were ultrasonic transducers (SONAR system).

A detailed description of the test and instrumentation is available in [6].

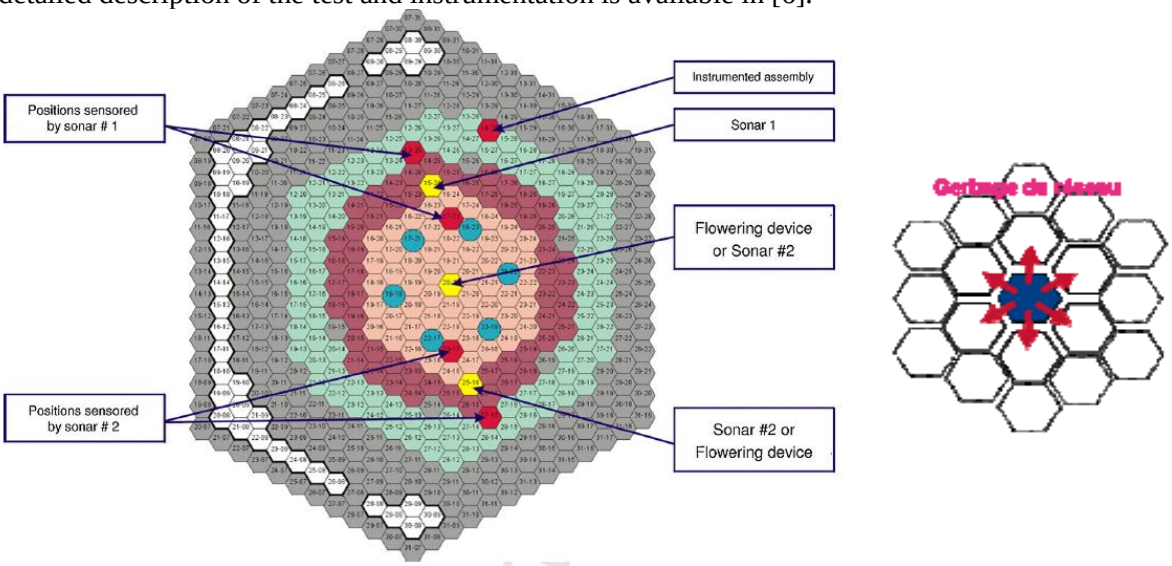

Figure 5 - Phénix core description and principle of core flowering device

Mechanical aspects

The maximal displacements of the assemblies and the interaction forces between assemblies were estimated for all experimental configurations when the flowering device was partially and completely infolded. These estimations were performed using the static mechanics code, HARMONIE, which is dedicated to the calculations of SFR core deformations.

For this analysis, the mean gaps between assemblies were calculated, taking into account the differential thermal expansion between assembly wrapper tubes and the core support plate. As the material of wrapper tube is EM10 ferritic-martensitic steel with good properties under irradiation, no irradiation swelling and creep was first considered.

The results of these calculations show that HARMONIE was able to estimate the good order of magnitude of the core stiffness. The prediction of individual assembly displacements was more difficult to achieve, due to the local distribution of gaps between assemblies which are very sensitive to manufacturing allowances and small deformations.

To complete the validation of HARMONIE, another specific test was performed in PHENIX after flowering test. It consists in measuring the vertical forces necessary to lift subassemblies during fuel-handling operation. The calculated forces issued from HARMONIE were very similar to those measured.

As the flowering test performed in 2009 was quasi-static, it would be now interesting to investigate experimentally the core behaviour under dynamic load. Indeed, when core is submitted to dynamic movement, hydrodynamic forces due to sodium acceleration occur and may strongly affect the assembly displacements. In order to observe such behaviour in fast reactor cores, a new test is scheduled in PHENIX in 2013. The aim of this test is to make the core flowering dynamically in order to observe assembly displacements of about 10 mm. This test will be performed at shutdown state, as the reactor is now in final shutdown conditions,.

The test will provide a better knowledge of core dynamic behaviour and experimental data for validation of the core mechanical modeling (French CAST3M code).

A specific device for dynamic flowering actuation is being designed on a “pushing apart/release” principle. The displacement of the sub-assemblies will be measured with the ultrasonic system already used for the static test and with a new device based on deformation gauges.

Neutronic aspects

During PHENIX flowering test, the core reactivity was monitored at zero power state and compared afterwards to calculation results.
Each assembly displacement calculated previously with the HARMONIE code at midcore level was transferred to the neutronic TRIPOLI code based on Monte-Carlo method.
In the TRIPOLI model, the distorted position of each subassembly was considered for every flowering states, taking into account two assumptions concerning the axial deflection : pure translation or beam bending. Some examples of core deformations simulated with TRIPOLI and considering the bending assumption are presented in figures 6 and 7. In the translation assumption, the bending of the assemblies is not considered and displacements calculated by the HARMONIE code at midcore level were applied all along the assemblies. This assumption seemed reasonable considering that the maximum bending deflection is lower than 0.16°.
In figure 7 are compared experimental and calculated reactivities for different flowering states with spreading device located at core center and two isothermal temperatures (180°C and 357°C). One may observe from these results that flowering always leads to negative effects. A small flowering generates an internal arrangement of fuel assemblies in a fissile core but does not still affect fissile core limit. The evolution of reactivity remains slight because the fuel displacements occur in a zone where the adjoint flux is almost uniform. With a larger flowering, the external row of fuel elements begins to move changing the fissile core size. The effect on the reactivity is greater and we can now observe an increase in the curve slopes. The discrepancies between calculations and experimental data remain relatively small, in the range of statistical errors of the TRIPOLI results (σ = 10 pcm).
The next step of the analysis will be the use of deterministic code, namely ERANOS/PARIS, to calculate reactivities in order to assess this type of codes for the evaluation of neutronic impacts of SFR core deformations.

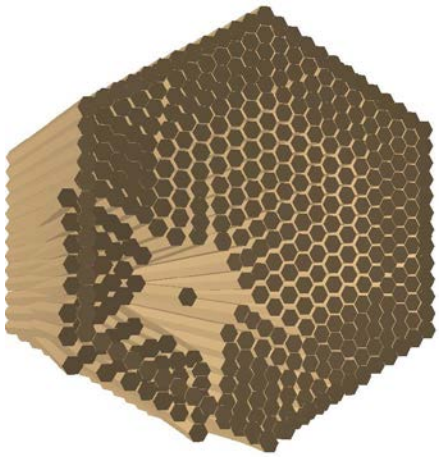

Figure 6 - Example of TRIPOLI core model with non-centred flowering device

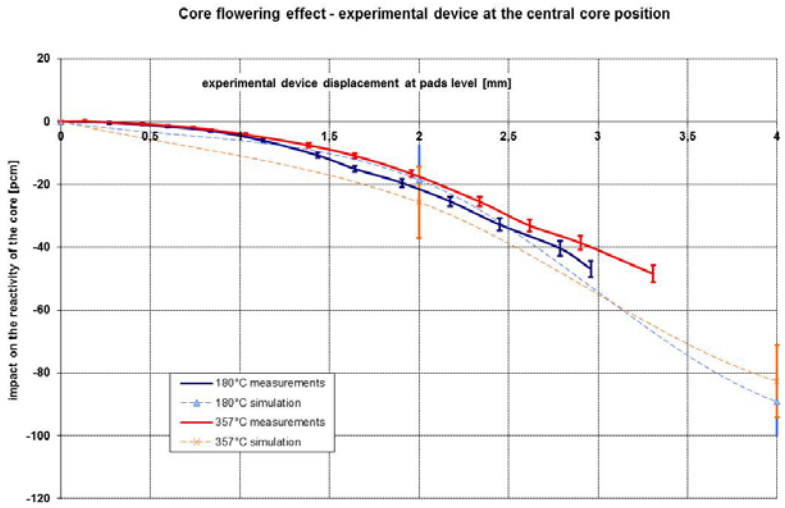

Figure 7 - Calculated and measured reactivities vs. core flowering at 180°C and 357°C

REFERENCES

[1] Vasile et al., “The final Phénix Tests”, Proceedings of the ICAPP 2011 Conference, Nice, France, May 2-5 (2011)

[2] J.C. Benoit et al. ”Decay Heat of Sodium Fast Reactor : Comparison of Experimental Measurements on the PHENIX reactor with Calculations performed with the French Darwin package”, PHYSOR 2012 Conference, Knoxville, Tennessee, USA (2012).

[3] D. Pialla, D. Tenchine, P. Gauthé, A. Vasile, “Natural Convection Test in the Phénix Reactor and Associated CATHARE Calculation”, NURETH-14 Toronto Ontario Canada, Nureth14-099 (2011)

[4] P. Gauthé et al., “The Phénix ultimate natural convection test”, Proceedings of ICAPP’12 Conference, Chicago, USA, June 24-24 (2012)

[5] R. Bavière, N. Tauveron, F. Perdu, E. Garré, “System-CFD coupled simulation of the Phénix Reactor Natural Circulation Test”, NURETH-15 Pisa Italia, Nureth15-288 (2013)

[6] B. Fontaine et al., “Description and preliminary results of PHENIX core flowering test”, Nuclear Engineering and Design 241 pp. 4143– 4151 (2011)

Recent modelling improvements in fuel performance code GERMINAL for SFR oxide fuel pins

M.LAINET, V.BOUINEAU, T.HELFER, M.PELLETIER

French Alternative Energies and Atomic Energy Commission (CEA)
CEA Cadarache DEN/DEC/SESC 13108 Saint Paul lez Durance, France

Abstract.

To support the design studies of ASTRID, the future technological Sodium Fast Reactor demonstrator in France, the modelling of mixed oxide fuel pins has been improved by developing a new version of GERMINAL fuel performance code within PLEIADES simulation framework. GERMINAL V2 is using a standard « 1D½ » representation of the fuel pin. Thermal analysis and mechanics are now based on finite elements computations. The fuel pellet is considered as a continuum, with a mechanical behaviour model managing element elimination during the central hole formation. The expansion due to cracking during heat-up, and later the free volumes closure between the fragments, are described by two imposed strain terms. By solving the fuel / cladding system equilibrium, we intend to evaluate the mechanical interaction, which can become significant, and the stresses induced by swelling gradients in the cladding thickness. Off-normal conditions are simulated by a strong coupling of thermal-hydraulics in the coolant with the thermal analysis of the fuel pin. A new neutronics scheme has also been developed, integrating progressively the evolutions of volatile fission products. Their release at high burn-up causes the "Joint Oxyde-Gaine" formation between pellet and cladding. With a refined prediction of the JOG composition, we intend to improve the evaluation of heat exchange inside gap at high burn-up, and also the description of cladding corrosion. Helium production has already been completed, to simulate fuel pins loaded with minor actinides. All these evolutions implemented in GERMINAL V2 are being validated by simulating fuel elements irradiated in PHENIX or in CABRI reactor. We are considering objects from different geometries, with various cladding materials, burn-ups and irradiation histories. The comparisons of the calculation results with the experimental data show the current abilities and limits of the code, and consequently the working perspectives we have.

1. Introduction

The modelling of uranium-plutonium oxide fuel pins has been recently improved by developing a new version of GERMINAL fuel performance code. A first version of GERMINAL [1][2][3] was developed from 1980 to 2000, gathering progressively the modelling of the behaviour of PHENIX and SUPERPHENIX fuel elements. This first version of the code represents the starting point of our work, in addition to the experience feedback collected in BREF Data Base, to be used for validation.

The developement of GERMINAL V2 takes place in PLEIADES [4] simulation platform. PLEIADES is a unified framework for fuel simulation, co-developed by CEA, Électricité de France and Areva. It includes common resources – solvers, material laws – to be shared between different applications, each one being dedicated to a precise fuel concept.

GERMINAL V2 uses classicaly a 1D½ axisymmetrical representation of the the fuel pin geometry. The fuel pin is decomposed into axial slices, which thermal evolutions are coupled by the energy transport by the coolant. Practically, the axial slicing currently in use includes from 10 to 20 slices. This has to be correlated to the axial sampling of experimental data, and also to the description of the variation of linear power and cladding damage along the fuel pin. The resolution of the physical processes in each slice uses a radial meshing of the slice. GERMINAL V2 implements finite elements computations for thermal analysis and mechanics, involving new mechanical behaviour's laws to

improve the resolution of the system equilibrium. The radial meshing of the fuel pellet is more refined near the centre, in order to describe with an acceptable precision the central hole formation. The adjusted meshing topology for the validation objects represent a compromise between reasonable calculation times and correct agreement with measures. It includes 25 radial meshes, which size is growing in geometric progression from 50 µm near the centre to 200 µm at the periphery. For the cladding, a regular meshing is used, with 10 elements in the thickness.

The applicability of the code can be summarized by the main following characteristics of oxide fuel:

As fabricated O/M: [1.90 to 1.999]	Fuel pellet external diameter: [4.2 to 12.1 mm]
Pu content (Pu/M): [0 to 45%]	Cladding external diameter: [5.1 to 13.4 mm]
Fuel relative density:[85 to 97%]	Peak linear rating: up to 550 W/cm (steady state)
Solid or annular pellets	Maximum cladding temperature: up to 650°C (steady state)

The next paragraph gives a rapid overview of GERMINAL V2: physical couplings and calculation sequence. Then the main modelling evolutions brought by GERMINAL V2 are detailed, reviewing mechanics, thermal analysis, fuel physics and chemistry. Finally, comparisons of the calculation results with the experimental data illustrate the current abilities of the code.

2. Overview of GERMINAL V2

The diagram of the physical couplings – FIG. 1 below – gives a synthetic view of the inter-dependance of all physical processes arising during the mixed oxide fuel pin irradiation. Thermal analysis is at the centre of all couplings, having direct interactions with mechanics and fuel physics, and relaying the effects of mechanics on fuel physics.

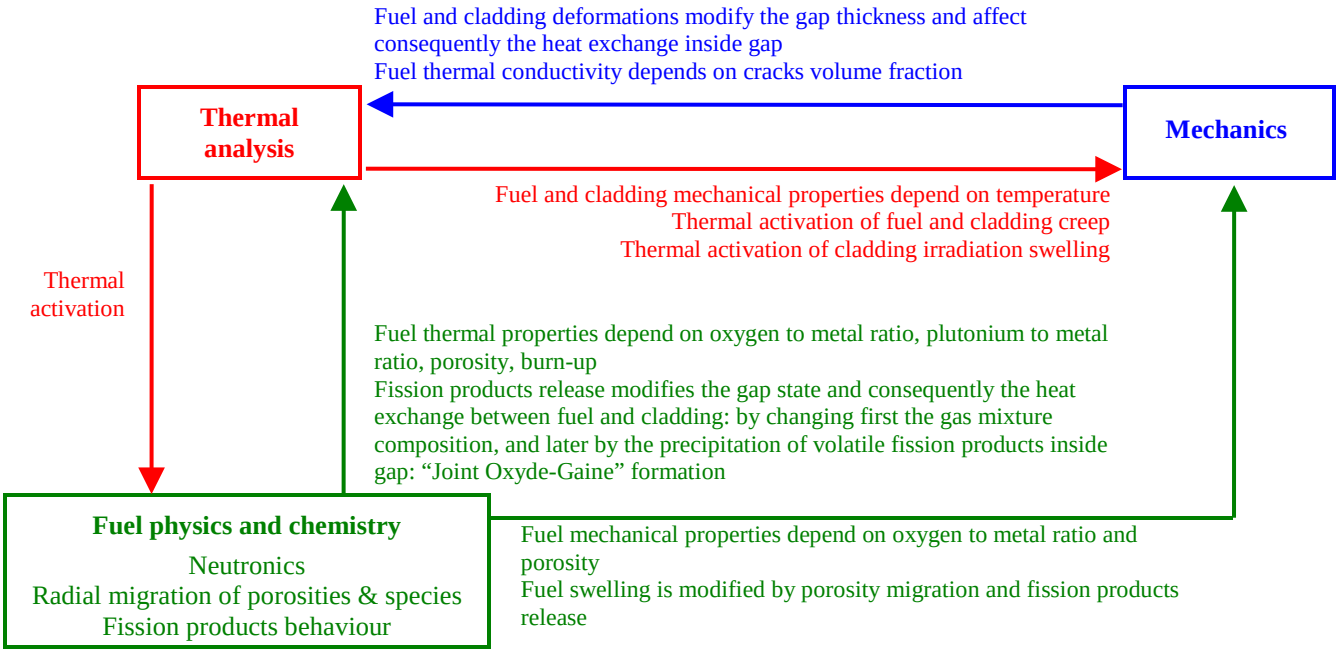

FIG. 1. Diagram of the physical couplings

The evolution of the fuel pin all along its irradiation is determined step by step by GERMINAL V2. The resolution of one time step is executed according to the sequence defined by the following FIG. 2. In this description, global resolutions refer to physical processes affecting the fuel pin in its whole height ; whereas local resolutions refer to processes evaluated in one considered axial slice.

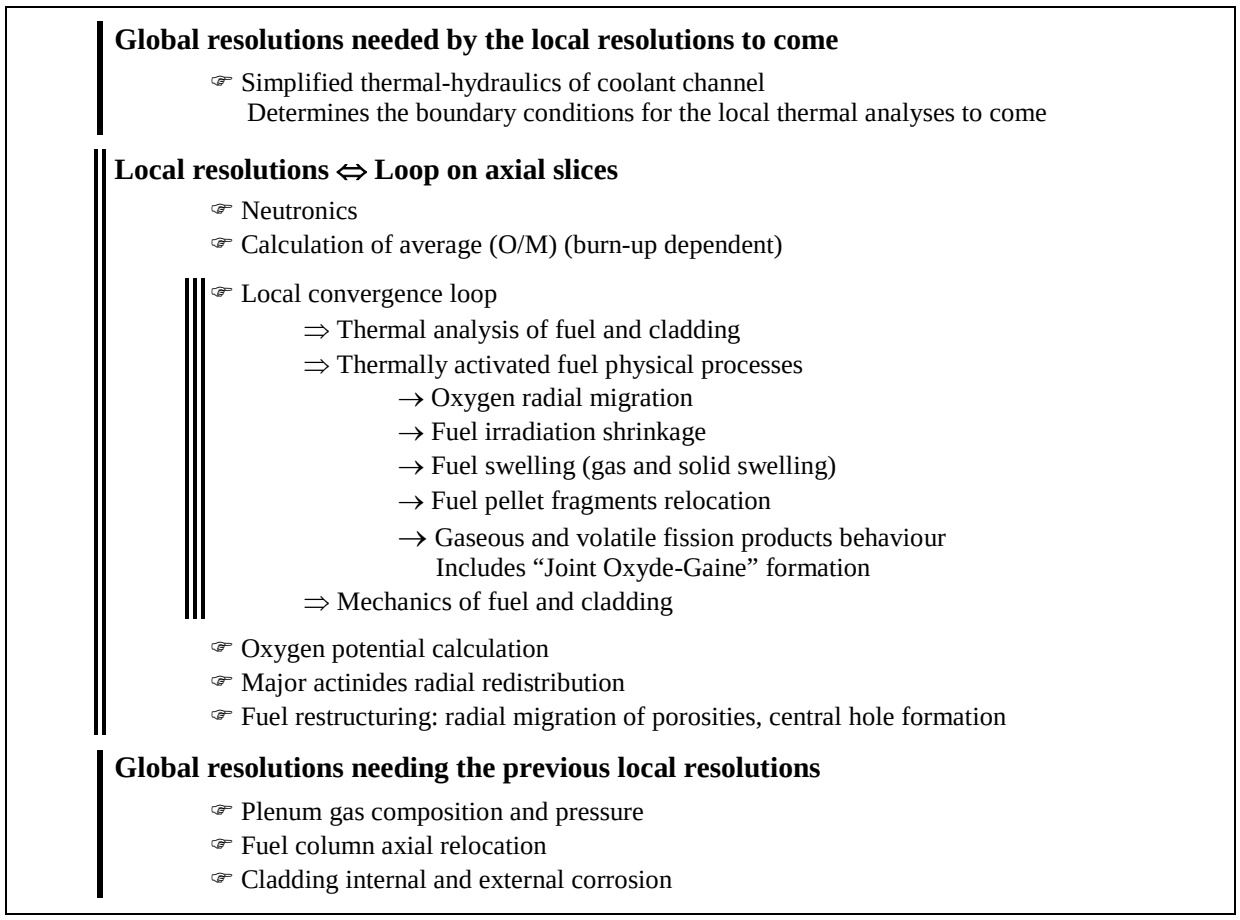

FIG. 2. One time step resolution by GERMINAL V2

3. Modelling evolutions brought by GERMINAL V2

3.1. Mechanics

3.1.1. Fuel mechanical behaviour

Mechanics are now based on finite elements computations, using CAST3M [5] solver. The description of the fuel mechanical behaviour represents a main evolution realised for GERMINAL V2 [6][7].

First of all, the behaviour law has to be compatible with the central hole formation, mainly resulting from the thermal-induced porosities expelling at the centre of the pellet. The goal is to simulate the pellet behaviour with a varying calculation domain, modified by the radial redistribution of material. The process adopted by GERMINAL V2 is based on three main principles. The central hole formation is determined by a dedicated model, solving pore transport and diffusion, determining the central hole radius as main result (see §3.3). The loadings and the boundary condition for the FE model are consequently adapted: the symmetry condition is replaced by a force applied on the internal node of the first material element, corresponding to the pressure inside the fuel pin. The element elimination is then managed by the behaviour's law. The stresses are set to zero while emptying the element, and further kept to zero ; an internal variable indicates that the integration point is already immaterial. This process is less expensive than re-defining the FE model at each iteration. It has been first validated with an elastic behaviour, by comparing the results to those of an elastic model defined on annular geometry at current time ; then it has been extended successfully to the fuel's behaviour.

To describe the fuel behaviour, we began by adapting a law combining creep with cracking. This law was previously written for uranium dioxide of PWR [8]. Its re-using in SFR operating conditions appears not satisfying. Practically, the fuel pellet cracks in many fragments very early during the

reactor heat-up: cracking begins with a linear power arround 30 W/cm, according to PHENIX operation feedback. The using of a cracking model is not adapted beyond the complete rupture of the material. The stiffness matrix of the system becomes singular when all the elements are broken, and it is not possible with an axisymmetrical representation of the geometry to handle a discontinuity in the azimuth. This is why we chose another description, by a law combining creep with perfect plasticity. The behaviour's description with perfect plasticity leads to bound stresses with the yield stress of the material. This is physically representative either for compression state or at high temperature, when the material becomes ductile. The representativeness in compression state allows to evaluate fuel/cladding mechanical interaction after the complete closure of the pellet cracks. Thus, it is necessary to associate with the fuel behaviour law another model describing the evolution of the free volumes opened by cracking: this is the goal of the fuel fragments relocation model. Afterwards, these free volumes are progressively closed when the pellet continues to grow in situation of maintained contact with cladding. This reversibility allows to account the accommodating capacity brought by the free volumes, avoiding strong mechanical interaction until their complete closure.

The earliest description we found about fuel fragments relocation was this given by D.R. Olander [9]. Later, many interesting details were brought by the documentation of IAMBUS code [10]. More recently, FEAST-OXIDE code [11] authors have mentioned the using of a relocation model, calibrated with JOYO reactor operation feedback [12]. Practically, the fuel fragments relocation model implemented in GERMINAL V2 determines an homogeneous additional stress free strain imposed to the fuel pellet. This model is fully empirical, its calibration is in progress with the code validation. The model evaluates the relocation strain rate at current time by considering the geometry of the gap:

$$\dot{\varepsilon}_{reloc}(t) = \frac{u_r^{\max}(t) - u_r(t)}{R_{pellet}^{ext}(0)} \Big/ \tilde{t}_0$$

where $u_r^{\max}(t)$ is the radial displacement upper bound (m)

$u_r(t) = R_{pellet}^{ext}(t) - R_{pellet}^{ext}(0)$ is the radial displacement of fuel pellet external bound (m)

$R_{pellet}^{ext}(0)$ and $R_{pellet}^{ext}(t)$ are the fuel pellet external radius at initial and current time (m)

$\tilde{t}_0$ is a time constant (s)

The radial displacement upper bound is calculated as this leading to contact, weighted by a power density factor that allows to close gap preferentially near the maximum power plan, for a better agreement with experience feedback.

$$u_r^{\max}(t) = Min\left(1\ ,\ \frac{P_{vol}(z,t)}{P_{vol}^{ref}}\right) \times \left(R_{clad}^{\text{int}}(t) - e_{JOG}(t) - R_{pellet}^{ext}(0)\right)$$

where $P_{vol}(z,t)$ is the local power density (W / m^3)

P_{vol}^{ref} is a reference power density (W / m^3) **1st model parameter**

$R_{clad}^{\text{int}}(t)$ and $e_{JOG}(t)$ are the cladding internal radius and the JOG thickness (m)

The relocation strain rate tends to zero when the radial displacement tends to its upper bound ; this avoids strong mechanical interaction when reaching contact. The time constant is adjusted by taking into account power density rate at current time. The principle is to increase relocation rate when power is increasing quickly.

$$\tilde{t}_0 = t_0 \times Max\left(10^{-3},\ Min\left(1\ ,\ \frac{\dot{P}_{vol}^{ref}}{\dot{P}_{vol}(z,t)}\right)\right)$$

where t_0 is a constant (s) **2nd model parameter**

$\dot{P}_{vol}^{ref}$ is a reference power density rate (W / m^3 / s) **3rd model parameter**

$\dot{P}_{vol}(z,t)$ is the local power density rate (W / m^3 / s)

When the fuel pellet continues to grow, the free volumes created by relocation are progressively closed as long as contact is maintained with cladding. To do this, an accommodating strain increment is imposed at each time step, balancing the other positive strain increments during the time step. The lower bound for accommodating is defined by the opposite of relocation. At current time, the cracks volume fraction in the fuel pellet is defined by the first invariant of the sum of the two strain tensors: relocation plus accommodating.

3.1.2. Cladding mechanical behaviour

The formulation used by GERMINAL V2 has been previously developed to describe the behaviour of cladding materials for fuel rods of Pressurized Wator Reactors. This formulation has been adopted by introducing the appropriate laws for creep, plasticity and swelling relative to cladding materials of SFR fuel pins. The cladding mechanical behaviour's law takes into account swelling as a stress free strain. Plasticity with isotropic hardening is characterised by the yield function below:

$$f = \sigma_{eq} - K\, R_{p0,2} \left(\varepsilon_{eq}^{p}\right)^{n} = 0$$

σ_{eq} and $R_{p0,2}$ are respectively the Von Mises equivalent stress and the yield stress of the material ; ε_{eq}^{p} is the equivalent plastic strain ; K, n are dimensionless constants of the plasticity law.

Creep and plasticity are supposed to be isochoric. Thus, the corresponding strain rates tensors are expressed as follows, proportional to the dimensionless stress deviator tensor, which trace is null:

$$\overline{\overline{\dot{\varepsilon}^{p}}} = \dot{\varepsilon}_{eq}^{p}\, \frac{3\,\overline{\overline{S}}}{2\,\sigma_{eq}} \qquad \overline{\overline{\dot{\varepsilon}^{creep}}} = \dot{\varepsilon}_{eq}^{creep}\, \frac{3\,\overline{\overline{S}}}{2\,\sigma_{eq}}$$

The creep equivalent strain rate is evaluated first – with the current stresses, temperature, etc. ; then the time derivative of the yield function leads to a scalar equation determining the plasticity strain rate.

$$\dot{f} = 0 \Rightarrow \left(\frac{\partial \sigma_{eq}}{\partial \overline{\overline{\sigma}}} : \overline{\overline{\dot{\sigma}}} \right) - n\, K\, R_{p0,2} \left(\varepsilon_{eq}^{p}\right)^{n-1} \dot{\varepsilon}_{eq}^{p} = 0$$

The stress rate tensor is determined by the contracted product of the Hooke tensor – elasticity tensor – applied to the total strain rate tensor, decreased by the swelling and inelastic strain rates tensors:

$$\overline{\overline{\dot{\sigma}}} = \overline{\overline{\overline{\overline{H}}}} : \left(\overline{\overline{\dot{\varepsilon}^{tot}}} - \left(\overline{\overline{\dot{\varepsilon}^{swelling}}} + \overline{\overline{\dot{\varepsilon}^{p}}} + \overline{\overline{\dot{\varepsilon}^{creep}}} \right) \right)$$

By introducing the definitions of Von Mises equivalent stress and its derivative, the scalar equation determining the plasticity equivalent strain rate can finally be re-written as follows:

$$\dot{\varepsilon}_{eq}^{p} \times \left(\left(\frac{3\,\overline{\overline{S}}}{2\,\sigma_{eq}} : \overline{\overline{\overline{\overline{H}}}} : \frac{3\,\overline{\overline{S}}}{2\,\sigma_{eq}} \right) + n\, K\, R_{p0,2} \left(\varepsilon_{eq}^{p}\right)^{n-1} \right) = \frac{3\,\overline{\overline{S}}}{2\,\sigma_{eq}} : \overline{\overline{\overline{\overline{H}}}} : \left(\overline{\overline{\dot{\varepsilon}^{tot}}} - \overline{\overline{\dot{\varepsilon}^{swelling}}} - \dot{\varepsilon}_{eq}^{creep} \frac{3\,\overline{\overline{S}}}{2\,\sigma_{eq}} \right)$$

Using this formulation with an appropriate discretization in the thickness allows to improve the prediction of the cladding geometry changes. In particular, it becomes possible to determine the stresses induced by the swelling gradients, after incubation.

3.2. Thermal analysis

Thermal analysis of the fuel pin is now based on finite elements computations. In stationary conditions, the energy produced by fuel is entirely carried out by the coolant and thermal-hydraulics of the coolant channel can be solved preliminary to all local thermal analyses in the fuel pin slices, involving only fuel and cladding. In off-normal conditions, the energy released by fission is not

instantaneously carried out by the coolant. The resolution has to be adapted consequently by extending the couplings: local themal analysis involves fuel, cladding and also coolant axial slices. The finite elements model in one slice is completed by adding a convection condition on cladding external bound, to be updated at each iteration of the thermal resolution. This allows local convergence in fuel pellet, cladding and coolant. This modelling evolution has been realised to simulate power ramps operated in CABRI reactor. Two variants of thermal-hydraulics models have been implemented. The first one describes the fuel pin in the reactor environment. The lateral surface of the coolant channel is supposed to be adiabatic: repetitiveness condition inside the fuel assembly. Whereas the second variant describes more precisely the CABRI configuration: one fuel pin, surrounded by an insulation system, which first barrier is a niobium pipe. This model takes into account the capacity of the niobium pipe. The working of both of the models has been verified with one particular experiment (see §4.2). The validation with more objects represents the next step.

3.3. Fuel physics and chemistry

Some of the models already used by the previous version of GERMINAL have been kept, despite that they are mainly based on empirical correlations. But they have been revisited for the new version. This is the case for fuel restructuring due to pore migration, described by an evaporation/condensation model [13], and for fission products behaviour: solid and gaseous swelling, gas release, volatile fission products release and precipitation inside gap – "Joint Oxyde Gaine" formation. The main modelling evolutions realised for GERMINAL V2 concern neutronics and thermochemistry.

3.3.1. Neutronics

The main purpose of neutronics is to compute the evolution of local power, burn-up and nuclides concentrations during irradiation. We use a simplified neutronics model which solves the so-called Bateman equation to describe the nuclides concentrations changes under neutron flux. Neutron reactions such as scattering, fission, capture or (n,2n) and radioactive processes are taken into account. The resolution uses nuclear data from JEFF 3.1 project library with one energy group averaged cross sections, for calculation speed up. Some species of interest have been added to the neutronics scheme: fission gases such as Xenon, Krypton ; Helium, which production mainly results from (n,α) reactions, fission and radioactive α decay ; Caesium, to predict JOG formation with a complementary description of the volatile fission products release. To validate the neutronics module, we perform a comparison with an Eranos [14] calculation. It uses the neutron flux and the typical fuel composition of PHENIX internal core (with U, Pu and slight quantity of Am). For a better agreement between GERMINAL V2 and this calculation (cf. FIG. 3), the neutronics model uses extended burn-up chains with U, Pu, Np, Am and Cm isotopes ; this allows to simulate fuel loaded with minor actinides.

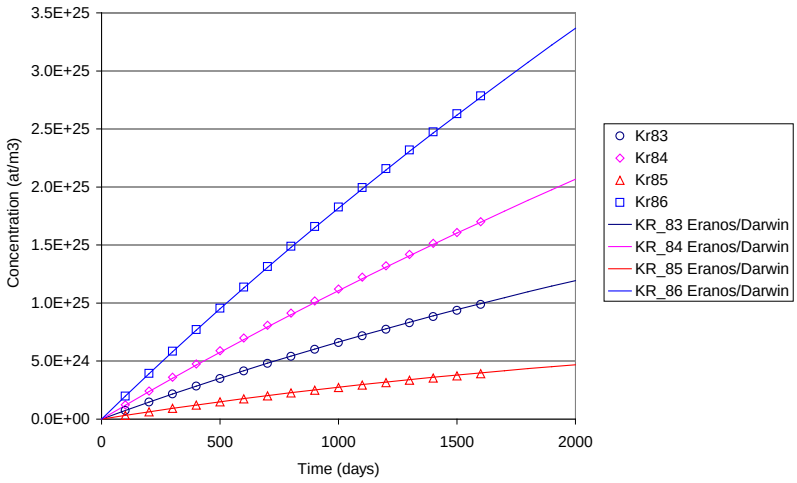

FIG. 3. Eranos and GERMINAL V2 comparison of Kr isotopes production

3.3.2. Fuel thermochemistry

In Fast Reactor oxide fuel, the radial redistributions of constituents are systematically observed, because of high temperatures and very large temperature gradients. These redistributions are possible by vapour transport thanks to radial cracks and interconnected porosity. The migration of components also occurs in solid phase by thermal diffusion. The driving forces for radial migration obey the laws of irreversible thermodynamics.

Oxygen potential is an important quantity in the thermodynamics of oxide, measuring the oxide ability to exchange oxygen atoms with its environment. It is defined as:

$$\Delta\overline{G_{O_2}} = RT\ln\left(p_{O_2} / p^0_{O_2}\right)$$

where p_{O_2} is the di-oxygen partial pressure and $p^0_{O_2}$ is a reference pressure, usually taken as 1 atm.

To evaluate the oxygen potential, we chose the model from Besmann and Lindemer [15], which is validated on a large experimental database of mixed oxide fuel and turns out to be very efficient to predict various thermodynamics quantities, such as oxygen potential or phase diagram. This approach treats the oxide as a solid solution of [$Pu_{4/3}O_2$], [PuO_2], [UO_2] and [$U_2O_{4.5}$], to describe deviation to stoichiometry. The computation of the total Gibbs energy requires a solid solution model. For a better agreement with experimental data, a general Redlich Kister parameterization was chosen:

$$\Delta G/n = \sum_i \left(x_i \Delta G_i^0 + RTx_i \ln x_i + \sum_{j>i} E_{ijk} x_i x_j \sum_k \left(x_i - x_j\right)^k \right)$$

where $x_i = n_i / \sum_i n_i$ is the molar fraction of chemical species i

$\Delta G_i^0 = \Delta H_i^0 - T\Delta S_i^0$ is the molar Gibbs energy of formation of species i at temperature T

E_{ijk} are the interaction coefficients of order k between chemical species i et j

these coefficients reflect the deviation from an ideal mixture

The computation of oxygen potential is done by minimizing ΔG.

The oxygen to metal ratio (O/M) evolves continuously with the fissions. As oxidation degree of fission product is less than this of fissioned atoms, this ratio rises with the burn-up. One of the fastest chemical mechanisms is the thermal-induced oxygen migration. Oxygen to metal ratio (O/M) measurements indicates that oxygen atoms are transported towards the cold region of the pin. The overall effect is to favour heat transfer in the periphery of the pin and decrease the centre line temperature. The redistribution of oxygen is described with Aitken model [16] which gives the deviation to stoichiometry x as a function of temperature:

$$\ln x = Q^*/RT + K$$

The constant K is determined with the known average stoichiometry $\bar{x}$. Q^*, the characteristic heat of transport, is determined empirically (the physical meaning is described by [17]). A radial normalization is used considering evolution of the oxygen to metal ratio with burn-up.

Because of the high temperatures encountered in fuel pins, oxide molecules with uranium and plutonium atoms may evaporate into several gaseous species mainly UO, UO_2, UO_3, PuO, and PuO_2. Partial pressure computation is based on gas-solid equilibrium and requires a thermodynamic model for both phases. For instance, with the Lindemer-Besmann model chosen to describe $U_{1-y}Pu_yO_{2-x}$ and an ideal model for the Gibbs free energy in the gas phase:

$$\Delta G/n = \sum_i x_i \left(\Delta G_i^0 + RT\ln\left(p_i / p^0\right)\right) \qquad i = \text{UO},\text{UO}_2,\text{UO}_3,\ \text{PuO},\ \text{PuO}_2$$

Partial pressures p_i of chemical species i are obtained by minimizing the total Gibbs energy (solid+gas). The actinide redistribution considers two competitive processes: the thermo diffusion in solid phase and the transport in vapor phase. We keep the same model than this of GERMINAL previous version.

3.3.3. Cladding internal and external corrosion

An important mechanism that can appear at low burn-up but have a more serious effect at high burn-up is the chemical interaction of fission products in the gap with the cladding compounds (Cs, Te with Fe, Cr and Ni). This FCCI Fuel Cladding Chemical interaction or internal corrosion affects the upper part of the fissile column. An empirical model already used by GERMINAL previous version describes this FCCI. External corrosion of the cladding by the sodium could occur above 550°C. A new empirical model has been implemented in GERMINAL V2, based on measurements on pins irradiated in PHENIX reactor. These two corrosion models are used to design the fuel pin with criteria calculations to ensure cladding integrity [18]. The criteria calculations take into account the safe thickness reduction on both internal and external bounds.

4. Examples of GERMINAL V2 calculation results

The validation of GERMINAL V2 is actually in progress, by simulating fuel elements irradiations in PHENIX or in CABRI reactor. The following examples illustrate the current abilities of the code.

4.1. Cladding deformation

To simulate as well as possible the physics of the fuel pin, the correct prediction of the geometry changes is absolutely necessary. All the processes are thermally activated, and thermal and geometry evolutions are closely linked. The irradiation-induced swelling of cladding can contribute very significantly to the geometry changes, when the damage inside the material exceeds a starting threshold for swelling – "incubation" period. Thus, the calibration of cladding swelling laws is a part of the code validation. Some of the objects to be considered for validation have the same cladding material, but are irradiated at various burn-ups. In this case, calibration concerns incubation threshold as well as swelling rate, after activation. This can be illustrated by the FIG. 4 below.

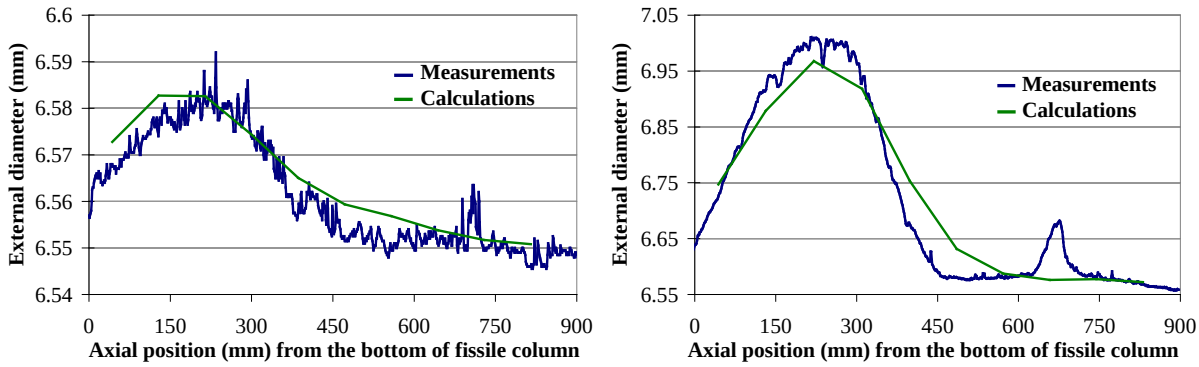

FIG. 4. Evolution of cladding diameter along the fissile column at the end of irradiation

The first considered fuel pin has a final burn-up at 7 at%. For the cladding material, the swelling starting threshold has just been exceeded. The maximum deformation is up to 0,6%. The second fuel pin has a final burn-up at 13 at%. An important swelling increase has caused a maximum deformation higher than 6%. The calibration of the cladding behaviour's law allows satisfactory predictions of geometry changes for both of these objects, at very different stages of swelling evolution.

4.2. Transient thermal analysis

The working of GERMINAL V2 transient thermal analysis has been verified by simulating E5 power ramp operated in CABRI reactor. This experiment reproduces off-normal conditions of a reactivity insertion accident, with a power peak about 40 times greater than normal operating level. FIG. 5 below shows the predicted melting front progression during the energy insertion and later, in the maximum power plan. The evolution by steps is correlated to the radial discretization of the FE model. The ratio of molten radius to external radius takes a maximum value at 0,89 ; to be compared to the ratio of restructured zone radius to external radius, measured at 0,83. This agreement confirms the working of the code. However, the inertial effects are not yet satisfactory represented, when considering the measured coolant outlet temperature. As the axial displacement of molten material is not yet modelled, the enlargement of central hole in maximum power plan is not predicted, whereas it is observed. Further improvements are thus needed, by going into in-depth interpretation of the experiment.

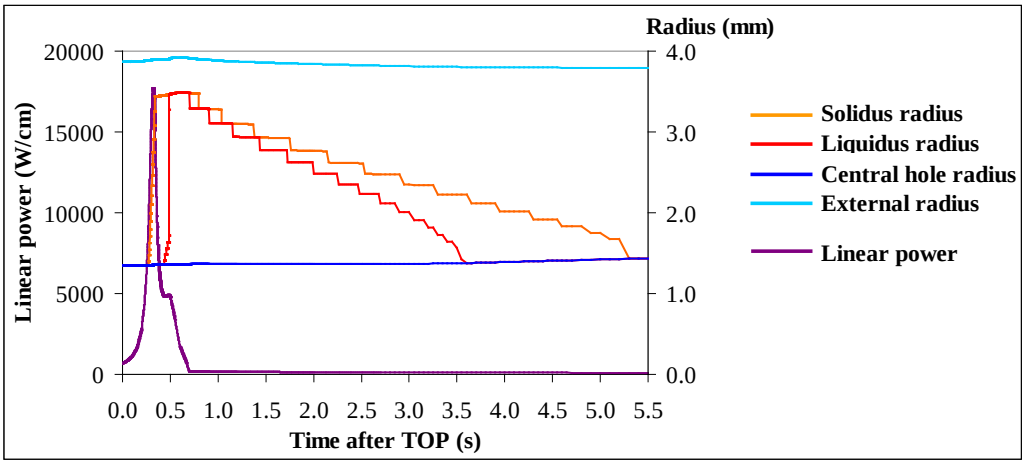

FIG. 5. E5 power ramp simulated by GERMINAL V2: melting front progression at MPP

4.3. Actinides radial migration

The following FIG. 6 shows the final radial plutonium distribution at maximum power plan observed in a standard PHENIX fuel pin irradiated up to 3,4 at%. The blue points represent the post-irradiation measurements and the green line the plutonium fraction as calculated by GERMINAL V2. It shows an internal zone with a Pu enrichment near the central hole, due to the actinide redistribution by solid diffusion and transport in vapor phase. A depletion zone appears in the mid part of the fuel, due to fuel restructuring and actinide redistribution. Nonetheless, the experimental values are a little too much scattered in this part to have a conclusive agreement. In the external zone, the Pu content stays at the initial value because the temperature was too low to engage actinide redistribution or pore migration.

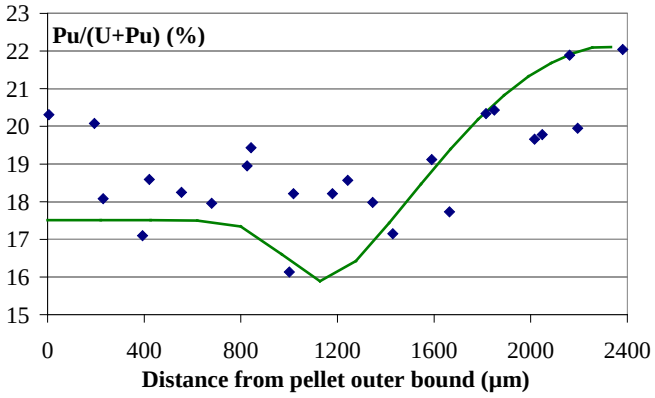

FIG. 6. Final plutonium radial distribution at MPP in one standard PHENIX fuel pin

5. Conclusion – Working perspectives

The development of GERMINAL V2 in PLEIADES simulation platform began in 2009. Most of the development tasks are now realised. The code validation is actually in progress. GERMINAL V2 has passed in 2011 a first validation step, for low burn-up irradiations of oxide fuel pins. The next steps are first the extension of the validation range to high burn-ups irradiations, then to heterogeneous fuel pins including alternatively fertile and fissile material, and later to off-normal conditions. Further works are closely linked to ASTRID project needs. The simulation of new materials, such as fuel loaded with minor actinides, will require new developments and complementary validation, especially as the operating conditions are different. The integration of GERMINAL in a wider software chain is also planned: to simulate the fuel assembly behaviour, or to determine the fuel pin state before simulating a severe accident sequence.

ACKNOWLEDGEMENTS

The authors want to thank Électricité de France and Areva for their support to the development of GERMINAL V2 within PLEIADES platform. We also thank T. Schacher for his help as well as all the users of GERMINAL at CEA, Électricité de France and Areva for their usefull feedback on the code.

REFERENCES

[1] J.C. Melis, L. Roche, J.P. Piron, J. Truffert, “GERMINAL – A computer code for predicting fuel pin behaviour”, Journal of Nuclear Materials, Volume 188, Pages 303-307, 1992

[2] J.-C. Melis, J.-P. Piron, L. Roche, “Fuel modeling at high burn-up: recent development of the GERMINAL code”, Journal of Nuclear Materials, Volume 204, Pages 188-193, 1993

[3] L. Roche, M. Pelletier, “Modelling of the thermomechanical and physical processes in FR fuel pins using the GERMINAL code”, IAEA-SM-358/25, 1999

[4] D. Plancq and al., "A unified environment for multi-dimensional fuel performance modelling", Proc. of the International Meeting on LWR Fuel Performance, Orlando, USA, 2004

[5] P. Verpeaux, T. Charras and A. Millard, “CASTEM 2000: une approche moderne du calcul des structures”, Calcul des structures et intelligence artificielle, Editions Pluralis, France, 1988

[6] M. Lainet, V. Bouineau, T. Helfer, M. Pelletier, “Recent improvements of mechanical modelling in fuel performance code GERMINAL”, MMSNF, September 2011, Aix-en-Provence, France

[7] V. Bouineau, M. Lainet, A. Courcelle, M. Pelletier, “Toward an improved GERMINAL V2 code to model oxide fuel for SFR”, SMiRT 21, November 2011, New Delhi, India

[8] B. Michel, J. Sercombe, G. Thouvenin, R. Chatelet, “3D fuel cracking modelling in pellet cladding mechanical interaction”, Engineering Fracture Mechanics, Volume 75, Pages 3581-3598, 2008

[9] D.R. Olander, “Fundamental Aspects of Nuclear Reactor Fuel Elements”, US DOE, 1976

[10] H. Többe, “IAMBUS: A Computer Code for the Design and Performance Prediction of Fast Breeder Fuel Rods”, Technical Report, Ident-No. 54.08000.1, Bergish Gladbach, 1990

[11] A. Karahan, J. Buongiorno, “Modeling of thermo-mechanical and irradiation behavior of mixed oxide fuel for sodium fast reactors”, Journal of Nuclear Materials, Volume 396, Pages 272-282, 2010

[12] M. Inoue, K. Yamamoto, T. Sekine, M. Osaka, N. Kushida, T. Asaga, “Power-to-melts of uranium-plutonium oxide fuel pins at beginning-of-life condition in the experimental fast reactor JOYO”, Journal of Nuclear Materials, Volume 323, Pages 108-122, 2003

[13] C. F. Clement, M. W. Finnis, “Plutonium Redistribution in Mixed Oxide (U,Pu)O2 Nuclear Fuel Elements”, Journal of Nuclear Materials, Volume 75, Pages 193–200, 1978

[14] G. Rimpault, “The ERANOS code and data system for fast reactor neutronic analyses”, Proceedings of the PHYSOR2002 International Conference on the New Frontiers of Nuclear Technology: Reactor Physics, Safety and High Performance Computing, October 7–10, Seoul, Korea (2002)

[15] T. M. Besmann, T. B. Lindemer, “Chemical thermodynamic representations of PuO2−x and U1−zPuzO2−x”, Journal of Nuclear Materials, Volume 130, Pages 489–504, 1985

[16] E. A. Aitken, “Thermal Diffusion in Closed Oxide Fuel Systems”, Journal of Nuclear Materials, Volume 30, Pages 62–73, 1969

[17] C. Sari, G. Schumacher, “Oxygen redistribution in fast reactor oxide fuels”, Journal of Nuclear Materials, Volume 61, Pages 192-202, 1976

[18] "Règles d'analyse mécanique des structures irradiées", Gif-sur-Yvette (France), Ed. CEA, 1992, Rapport CEA, ISSN 0429-3460 ; 5618

Code strategy for simulating Severe Accident Scenario

C. SUTEAU, F. SERRE, J.-M. RUGGIERI, F. BERTRAND

Commissariat à l'énergie atomique et aux énergies alternatives,
Saint -Paul-Lez-Durance, France

Abstract. Severe accident scenarios of Sodium-cooled fast reactors involves various phenomena: core degradation, melt progression towards the core catcher, corium behaviour on the core catcher, energetic corium/sodium interactions, structure mechanical behaviour during expansion phase, containment behaviour, and fission production release and transport. In order to simulate the complete accident scenarios, CEA strategy relies on two sets of calculation codes: a reference set of codes and a set of simplified coupled models dedicated to Probabilistic Risk Assessment analyses. Concerning the reference set, that includes SAS-SFR, SIMMER, CONTAIN, EUROPLEXUS, and TOLBIAC, CEA started, with JAEA and KIT, a validation process based on existing experimental results such as CABRI and SCARABEE programs, and recently against the EAGLE1&2 program results, in the frame of a specific contract with JAEA. Furthermore, CEA is preparing additional experimental programs including in-pile experiments in IGR (NNC reactor), and out-of-pile experiments in the future experimental FOURNAISE facility to be built in CEA Cadarache (France).

1. Introduction

Severe Accidents for Sodium cooled Fast neutron Reactors (SFR) are major safety concerns. Their study is based on hypothetical initiating events that lead to an accident with different sequences described as a scenario. Initiating events are local faults or generalized faults[1]. Loss of coolant flow due to blockage of a subassembly and withdrawal of one control rods are examples of local faults frequently considered. Unprotected loss of flow (ULOF) due to primary loop pump stop, unprotected loss of service station power (ULOSSP) and unprotected loss of heat sink (ULOHS) are examples of generalized fault.

Whatever the initiating events, the scenarios start with core degradation that is commonly described as a three phase sequence: primary phase, transition phase and secondary phase. During the primary phase, bundles of pins are disrupted and create corium pools inside the subassembly hexagonal cans. During the transition phase, corium pools produce hexagonal can failures and grow radially. During the secondary phase, a large corium pool that fills a significant part of the core can produce an important power increase and a sudden gas expansion.

In order to avoid recriticality, power peak and release of large mechanical energy that can damage the containment, some mitigation devices based on controlled material relocation [2] are introduced in core and reactor designs. Some devices such as specifically designed control rod guide tube (CRGT) can remove out of the core a significant part of the fuel and make easier corium progression towards a core catcher. Core catcher designs may include a layer of sacrificial materials that protects the core catcher from the corium jet impacts and levelling devices that spread the corium jet or debris over the core catcher. The sacrificial material layer is thermally and chemically ablated by the corium jets. After cooling, the corium forms a debris bed on the core catcher and the scenario enters a post-accident heat removal phase.

In some scenarios, contacts between corium and sodium may occur during the core degradation phase and the progression of corium towards the core catcher. The contact produces a Fuel Coolant Interaction (FCI) with various consequences. Some of them are listed below:

- During the primary phase of the core degradation, FCI ejects sodium from the bundle of pins and enhance molten fuel dispersion.
- In some the mitigation devices (for example : FAIDUS [3]), FCI occurs with in a subassembly inner duct and discharge axially upwards the corium.
- During the secondary phase of core degradation, corium pool is inside a cavity. In case of failure of the cavity walls, sodium suddenly enters in contact with the corium pool and releases an important mechanical energy [4].

When the cladding fails and fuel melts, fission products (FPs) trapped in the pin and in the fuel are released and move towards the cover gas region. The mechanical energy released during the expansion phase has an impact on the structures, the vessel and the reactor head that may be damaged resulting in leaks and failures. The source term characterizes the radioactive FPs released in the containment: flow rate, isotopes, chemical forms. It may vary a lot from one scenario to the other. It depends on the process of release and the transport of FPs towards the containment. Due to mechanical loading of the structure, sodium may leak in the containment. Chemical reactions of sodium with air and concrete are exoergic. They increase heat and pressure of the containment and produce aerosols that can be host of radioactive FPs.

The previous short overview of severe accident scenarios shows that numerous and various physical and chemical phenomena are involved sequentially or simultaneously. Moreover simulation of those phenomena needs different modelization scales. That's the reason why, it is difficult to have a single calculation code to do best estimate calculations. CEA strategy is based on the development and the validation a reference set of calculation codes that is able to deal with all the phenomena. The reference set of codes includes existing codes such as SIMMER-III [5], SIMMER-IV[6], ERANOS-2.1[7] or CONTAIN-LMR[8] and new codes that are under development at CEA. Some codes are dedicated to a single phenomenon and others are more versatile. In complement to the best estimate calculation approach, CEA wants to do Probabilistic Risk Analysis (PRA). PRA needs to perform thousands of calculation within a few minutes. Such a speed of calculation cannot be obtained with the reference set of codes. So the CEA will develop a PRA code based on simplified models that will be validated by comparison to the reference set of codes.

2. Reference set of codes

To define the needs in calculation codes for simulation of severe accident scenarios, we synthetically classify the complex sequences of severe accident into seven phenomena : core degradation, melt progression towards the core catcher, corium behaviour on the core catcher, energetic corium/sodium interactions, structure mechanical behaviour during expansion phase, containment behaviour, and fission production release and transport. For each phenomenon, CEA established a strategy to build the reference set of codes.

2.1. *Phenomena and associated codes*

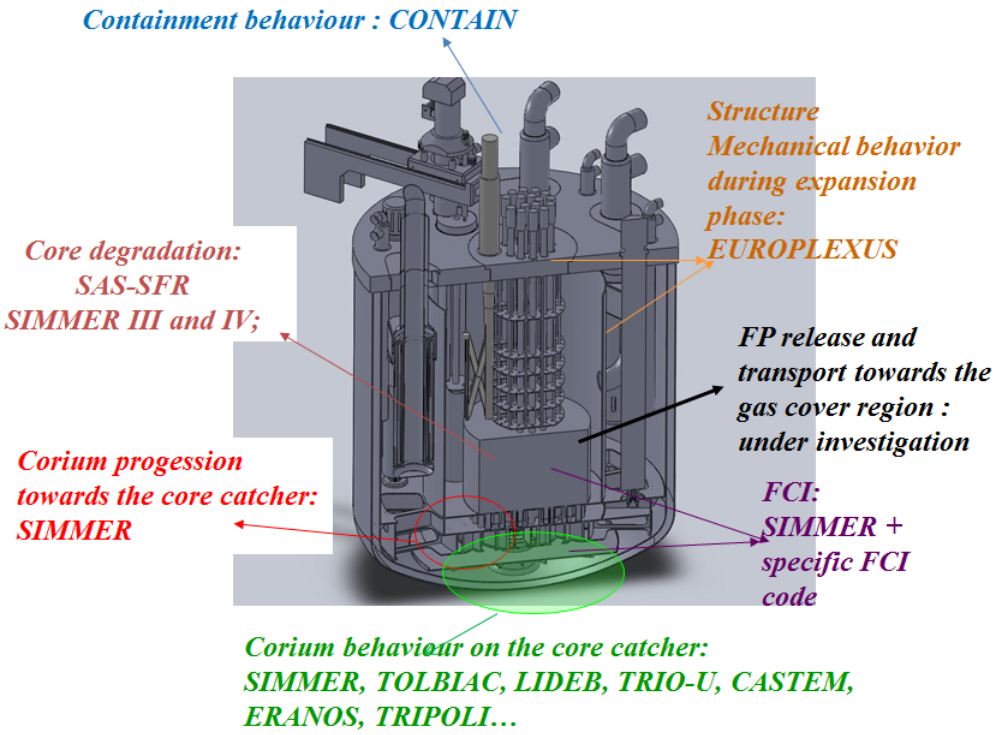

FIG. 1. Codes of the reference set and their applications

Figure 1 gives an overview of the codes used to simulate the different phenomena of severe accident scenarios.

2.1.1. Core degradation

For simulation of the core degradation, CEA has choosen to use SAS-SFR, SIMMER-III and SIMMER-IV codes. CEA uses SAS-SFR to perform analysis of the primary phase of Transient Over Power (TOP), ULOF, ULOSSP and ULOHS. SAS-SFR is an evolution of SAS4A[27]. It contains improved models for oxide fuel: improvement of the thermomechanical model used before pin failure, improved in-pin fuel motion during transient... SAS-SFR represents subassemblies or groups of subassemblies as independent channels. Each channel models an average pin and its associated coolant and hexagonal can. SAS-SFR simulates coolant heating and boiling, clad heating, failure and melting, fuel heating and melting, and relocation of the different materials. Heat transfer inside each pin is computed with a two-dimensional (r-z) heat conduction equation. Single and two-phase coolant flows are modeled with a one dimension multiple-bubble boiling model. Also included is a module that calculates the pin characterization in response to both irradiation phase and transient conditions . In SAS-SFR post pin failure phenomena such as fuel relocation and migration of all moving components in the channel are computed with the aid of a multi-component, multiphase non-equilibrium hydrodynamic model. The channels are connected at their inlet (resp. outlet) to the lower(resp. upper) sodium plenum where a uniform pressure is prescribed. The power reactor evolution is calculated by a point kinetics module that determine the power level (power distribution is constant) depending on reactivity evolution. The reactivity is calculated thanks to feedback coefficients from fuel heating (axial expansion and Doppler), coolant heating and boiling, and fuel and cladding relocation. The feedback coefficients are provided to the code for each channel.

When hexagonal can failure occurs, molten materials can go from one channel to the other. So the independent channel hypothesis is no longer acceptable. The simulation of the core degradation with SAS-SFR is stopped and is continued using SIMMER-III or SIMMER-IV.

SIMMER-IV (resp. SIMMER-III) is a three dimensions (resp. two dimensions), multi-velocity-field, multiphase, multicomponent, Eulerian fluid dynamics model coupled with a structure (pin and hexagonal can) model and a three dimension (resp. two dimension) space and energy-dependent neutron kinetics model. Its geometry is cartesien XYZ (resp. XY) or axisymetric R-θ-Z (resp. R-Z). To represent hexagonal lattice of SFRs, SIMMER-IV implements staggered meshes. The fluid-dynamics model is based on a time-factorization approach, in which intra-cell interfacial area source terms, heat and mass transfers, and the momentum exchange functions are determined separately from inter-cell fluid convection. The structure model represents the configuration and the time-dependent disintegration of fuel pins and subassembly hexagonal can. The neutronic model uses the improved quasi-static method [9] with THREEDANT [10] (resp. TWODANT) as stationary Boltzmann equation solver. With SIMMER codes, CEA perform analysis of transition phase and secondary phase of TOP, ULOF, ULOSSP and ULOHS. CEA also study degradation due to the total instantaneous blockage (TIB). In this case, the simulation is limited to the blocked subassembly and its neighbors and neutronic power is kept constant.

2.1.2. Melt progression towards the core catcher

Core disruptive accidents may produce a corium pool in the core. The corium can leave the core by melting supporting structures or by passing through mitigation devices such as CRGT with specific design. In both cases, it is a multiphase flow problem coupled with melting, freezing and vaporization. When corium reaches the cold collector, it flows down through cold sodium towards the core catcher. SIMMER-III and SIMMER-IV are sufficiently versatile to describe the geometry of the CRGT, the core supporting structure and the cold collector. That's why, CEA choose them to simulate the corium progression.

2.1.3. Energetic corium/sodium interactions

During the progression of the corium in the cold collector, FCI may occur. In that case, accurate and versatile simulations of the interaction need the use of a jet fragmentation model. SIMMER codes do not contain such a model. So the CEA plans to develop models of FCI dedicated to sodium and to implement them in a calculation code that contains a jet fragmentation model such as MC3D[1] code or TEXAS code [2]. The developed models will be extended to the simulation of sodium pouring on corium [4] for example when a corium pool is inside a cavity surrounded by sodium and the cavity walls break. Hence the FCI code improved for sodium coolant will be able to simulate all the configurations where FCI is coupled with fluid dynamics but not coupled with degradation.

When FCI and core degradation are simultaneous, for example during primary or transition phases, they are tightly coupled. The simulation of both phenomena needs a single calculation code with strong coupling solvers. To do so, CEA plan to use SIMMER code and to implement in it some simple models of FCI. The simple models of FCI do not need to be as versatile as the FCI code models, but their implementation must run fast enough in order to be compatible with SIMMER simulation time. The simple models of FCI could be simplified physic models derived from the FCI code models or back box models such as response surfaces or neural networks fitted on the FCI code results. In both cases, the simple models benefit from the validation of the FCI code.

2.1.4. Corium behaviour on the core catcher

When corium arrives on the core catcher, it forms one or many coherent jets, solid debris or a mix of jets and debris. Whatever is the form of the corium, SIMMER has the capabilities to simulate the spreading of corium on the core catcher.

To avoid corium jet impacts damaging the core catcher and to avoid re-criticality of the corium on the core catcher, specific designs based on sacrificial material layers[12] are under development. The behaviour of molten corium in contact of sacrificial layer shares some characteristics with the behaviour of molten corium interaction with concrete. CEA uses TOLBIAC –ICB[13] to simulate concrete corium interaction for pressurized water reactor (PWR). In TOLBIAC-ICB, corium contains

three phases: liquid oxide phase, liquid metallic phase and the gaseous phase. The corium pool simulation is based on the phase segregation model where the solid phase is located at the corium pool boundaries as a solid crust composed of refractory oxides and the corium pool contains no solid. In PWR, gas flow through the corium pool is important and homogenizes the corium pool. So, the corium pool is described by a zero dimension model. The interfacial temperature between the crust and the pool is the liquidus temperature calculated with the composition of the pool. The interaction between thermal hydraulics (mass and energy balances) and physico-chemistry (liquidus temperature, crust composition, chemical reaction) is modeled through a coupling between TOLBIAC-ICB and the GEMINI2[14] code for the determination of the physico-chemistry variables.

The CEA is starting the adaptation of TOLBIAC-ICB to the SFRs core catcher. SFRs core catchers have various and complex geometries (annular design with chimney, rod of sacrificial materials...) and various location (in vessel, between the primary vessel and the safety vessel, in the reactor pit). The geometry capabilities of TOLBIAC-ICB will be increased in order to make it more versatile. The second adaptation is the adding of sacrificial material physical characteristics (density, thermal conductivity…) in TOLBIAC-ICB and phase diagram in the GEMINI2 database. For SFRs core catchers, the corium pool is not boiling and contains no gaseous phase. Pool natural convection creates an axial temperature distribution. So, the 0D discretization of the pool must be replaced by an axial 1D discretization. Finally, the heat exchange between the pool and the crust must be adapted to non-boiling pool and the core catcher geometries.

In some cases, the solid corium fragments on the core catcher form a debris bed in contact with sodium. The coolability of the debris bed depends on the fragment size, porosity and the layer thickness. In the past, CEA simulated debris bed cooling with LIDEB code that is no longer maintained. CEA will make a review about debris bed cooling in order to choose a simulation strategy.

The designing of the core catcher needs the thermo mechanical calculation, criticality calculation and CFD simulation of the sodium cooling the core catcher. For criticality, TRIPOLI[15] and ERANOS codes are used. Thermo mechanical studies are performed with CASTEM[16] and CFD simulation with TRIO_U[17].

2.1.5. Structure mechanical behaviour during expansion phase

The mechanical energy release is a quick expansion of a gas bubble that interacts with the structures and the vessel. At CEA, it is simulated with EUROPLEXUS[18] that is a fluid-structure interaction code. EUROPLEXUS analyses 1-D, 2-D or 3-D domains composed of solids (continua, shells or beams) and fluids. It is adapted to fast transient dynamics such as the expansion phase because it uses an explicit algorithm (central-difference) for the discretization in time. Moreover, geometric non linearity (large displacements, large rotations, large strains), and the non-linearity of materials (plasticity, viscoplasticity, etc) are fully taken into account. The code provides arbitrary Lagrangian Eulerian description that is well adapted for fluid structure interaction simulation.

2.1.6. Fission production releases and transport

When the cladding fails and fuel melts, fission products (FPs) trapped in the pin and in the fuel are released and move towards the cover gas region. The release of gas absorbed in oxide grains or between oxide grains is a very complex phenomenon that is difficult to simulate. During the progression from the core to the cover gas region, the FPs are in contact with sodium. FPs have various chemical forms and many chemical reactions between the chemical species and the sodium occur. CEA will make a review to establish the needs in simulating of all those phenomena that have a strong influence on the source term.

2.1.7. Containment behaviour

CEA simulates the containment behaviour with CONTAIN-LMR that is an adaptation of CONTAIN-V1.1[19] to SFRs issues. Both versions predict the physical, chemical and radiological conditions in

the containment. The modeling is based on control volume method. Each control volume is simulated by a punctual model (zero dimension model). Control volumes are connected to each other by gas and liquid flow. The software architecture of the code contains three modules that are weakly coupled: thermal hydraulic module, aerosols module, and FPs modules. The thermal hydraulic module simulates:

- condensation/vaporization of water on floor, pool and aerosol
- boiling of water pools,
- bubbling of gas through water,
- hydrogen fire,
- injection of steam and incondensable gases,
- heat transfer through walls.

The aerosol module simulates:

- injection of aerosols characterized by their size classes ,
- brownian, gravitational and turbulent agglomeration,
- settling on pools, walls and floors due to diffusion, thermophoresis and diffusionphoresis,
- spray deposition due to impaction, interception, diffusion, thermophoresis and diffusionphoresis,
- fan and ice condenser deposition.

Up to 8 aerosol families are taken into account.

The FPs module simulates:

- FPs injection, transport by gas flow, deposition in water films on walls, transport by water film drain down to pool,
- FPs decay, FPs atmospheric decay heating and decay heating of structures following deposition,
- iodine removal by sprays.

For SFRs adaptation, the following features have been added :

- sodium condensation/vaporization and sodium pool boiling,
- sodium chemical reaction with water and oxygen,
- sodium spray and pool fire models,
- sodium concrete interaction model,
- debris bed cooling by sodium model.

2.2. Reference set of codes assessment

2.2.1. Core degradation and mitigation

The assessment is a major issue for safety demonstration credibility and simulation accuracy. By now, the assessment of the reference set of codes is mainly focused on the core degradation and the corium progression towards the core catcher.

The four experimental in-pile programs (CABRI1, CABRI2, CABRI FAST and CABRI RAST) [20] [21] [22] dedicated to SFRs performed in CABRI facility provide a large experimental database on pin degradation that is useful for SAS-SFR validation. CABRI experimental matrix includes various transients (slow power transients, energetically benign transients and fast/energetic transients…), various cooling conditions (nominal, Deteriorated cooling conditions up to boiling onset and beyond,

deteriorated cooling conditions up to and beyond clad relocation onset), various fuel burnup and various pin geometries (annular pellets, solid pellets…).

In-pile experimental programs performed in SCARABEE [23] reactor study the melt down of small bundles of pins (up to 37 pins) in slow power transients or resulting from loss of cooling. The seven types of test have been performed with fresh fuel. Each type is dedicated to the study of a phenomenon:

- bundle degradation during a total instantaneous blockage after a steady state corresponding to nominal reactor conditions,
- corium propagation in interassembly gap,
- corium propagation into the neighboring subassembly by melt-through of a neighboring hexagonal can,
- radial heat transfer from molten and boiling, heat generating, fuel and steel pools,
- bundle degradation during a total instantaneous blockage before startup of the reactor,
- bundle degradation in an undercooled subassembly resulting from a slow pump coast down.

The SCARABEE results are extensively used for validation of degradation models of SIMMER code.

In complement, CEA started recently, in the frame of a specific contract with JAEA, a validation process of SIMMER with experimental results from EAGLE 1&2[24] (Experimental Acquisition of Generalized Logic to Eliminate re-criticalities) programs. EAGLE is an experimental program launched by JAEA in order to evaluate the processes of fuel relocation during a Core Disruptive Accident in SFRs and demonstrate the possibility to eliminate re-criticality occurrence during core degradation, until a coolable debris bed forms. The experiments are conducted at Institute of Atomic Energy Nuclear National Center Republic of Kazakhstan (IAE NNC RK) at the Impulse Graphite Reactor (IGR) for in-pile tests and at EAGLE stand, in which a specific installation was built around an electromagnetic induction furnace, for out-of-pile tests.

EAGLE 1 out-of-pile program contains 4 integral experiments of discharge of simulant material (Al2O3) through a duct filled with sodium and 20 preliminary experiments. The EAGLE in-pile program contains 2 integral experiments of discharge of prototypic corium through a duct filled with sodium and four preliminary experiments. EAGLE 2 out-of-pile program contains 4 tests investigating steel duct failure, 4 tests to study upward discharge, 5 tests of jet fragmentation. EAGLE 2 in-pile program contains a test investigating progression of molten corium by failure of subassembly wrapper tube and the Control Rod Guide Tube, a test to obtain data to a sequence of upward discharge phenomena, 2 integral tests to obtain data to evaluate the heat transfer from the core-remaining materials (mixture of solid fuel and liquid steel) to the Control Rod Guide Tube (CRGT). CEA is using all those experimental data to validate SIMMER in mitigation configuration.

CEA also targets to increase the validation of SAS-SFR and SIMMER for pins and bundle degradation. To do so, CEA is defining the in-pile experiment program SAIGA (Severe Accident In-Pile experiments for Generation IV reactor and Astrid project). The goal is to increase the knowledge about the degradation of axially heterogeneous pins that contain two fissile zones separated by a fertile zone. The first part of the program (SAIGA) will include three tests: a loss of flow at nominal power, a fast TOP and a medium TOP.

2.2.2. Other phenomena

For FCI, jet of corium fragmentation, behaviour of corium on a core catcher; a review of existing experimental data for SFRs application shows that out-of-pile experiments with larger mass of corium and sodium are needed. To perform such experiments, CEA plans to build the versatile facility FOURNAISE (Furnace for Oxides of Uranium aimed at simulating Nuclear severe Accidents In large Scale Experiments**),** for both light water reactor and SFRs applications. FOURNAISE will permit

experiments with mass of prototypic corium up to 500kg. Three programs for SFRs will be performed: sodium FCI program, core catcher program and mitigation device program.

The sodium FCI will complement the existing experimental results such as FARO-THERMOS[25], CORECT II[4], MFTF-B05 and MFTF-B06[26]. The program will enhance the validation of the future FCI code. The core catcher program will obtain experimental data on the ablation of sacrificial materials by corium pool and the behaviour of debris beds. It will participate to the validation of the adaptation of TOLBIAC-ICB. The mitigation device program will complement the EAGLE out-of-pile experiments by obtaining data with prototypic corium at a large scale.

3. Code for Probabilistic Risk Assessment analyses

PRA analyses rely on a large (if possible exhaustive) scenario analysis for all the considered initiator events. The scenario analysis determines the sequences that occur and all their possible alternative branches. It also determines criteria for the conditional statements that connect the branches.

A PRA code must simulate the coupled phenomena of the sequences thanks to simple coupled models in order to consume little CPU time. The models can be simplified physic models derived from the models of the reference set of codes or black box models fitted on the results produced by the reference set of codes. In both cases, the models benefit from the validation of the reference set of codes.

In the context of such codes, special cares must be taken regarding the software architecture in terms of the models coupling and the associated time-marching scheme. On one hand, the models to be implemented can be very heterogeneous (steady-state balance equations, transient ordinary differential equation systems, response surfaces, …) and often are lumped-parameter models associated to a time-dependent control volume that depends on other models. Their associated time constants can be significantly different so that a two-level time scheme (intra-model and inter-model) management turns out mandatory. On the other hand, the perimeter of the code in terms of the modeled phenomena is not fixed and, driven by the scenario analysis and sensitivity studies to the existing code parameters, new or upgraded models should be easily implemented in the PRA code thanks to a well-suited Application Programming Interface (API). In this context, the object-oriented programming paradigm seems highly preferable.

For the PRA analyses, some parameters of the PRA code are sampled and simulations are run with the sampled values. The sampled parameters can be model parameters (for example: a heat exchange coefficient) scenario parameter (for example: core burn up) or reactor design parameter (for example: pump halving time). They are sampled according to distribution laws (normal, lognormal…). Hence, the code can provide results with their associated uncertainties. It is also possible to make sensitivity decomposition analyses and to determine the most sensible parameters. The PRA code is complementary to the reference set of codes.

4. Conclusion

Due to the diversity of the phenomena that occur in severe accident scenarios, CEA simulation strategy is based on the development of a reference set of codes. The codes must be chained to simulate a comprehensive scenario. They can be used as standalone application to study a sequence of a scenario and for experiment interpretation.

The reference set of codes aggregates codes dedicated to SFRs severe accident and adaptation of PWR severe accident codes. For some phenomena (debris beds, FPs release and transport), the needs in simulation are not yet investigated. So the reference set is still under construction and its advance is not equivalent for all phenomena. Its assessment is focused on core degradation and mitigation devices.

The assessment process will progressively be extended to all the phenomena. EAGLE 1&2 programs provide a large experimental database about mitigation devices. The future FOURNAISE facility will perform out-of-pile experiments to obtain data on the corium progression and its behaviour on the core catcher.

Hence, CEA plans to have the capability to perform best estimate calculations with sufficient accuracy to contribute to robust safety demonstration. In complement to the best estimate approach, CEA wants to do Probabilistic Risk Analysis with a PRA code that it will develop. The PRA code models must benefit from the reference set of codes assessment and they will be integrated in a specific software architecture that is under construction.

ACKNOWLEDGEMENTS

The authors wish to thank R. Le Tellier and L. Saas for their introduction to PRA code architecture.
.

REFERENCES

[1] PAPIN, J.,"Behavior of Fast Reactor Fuel During Transient and Accident Conditions", Comprehensive Nuclear Materials, 2012, 609-634

[2] MASCHEK, W., et al., "Prevention and mitigation of severe accident developments and recriticalities in advanced fast reactor systems", Progress in Nuclear Energy, 2011, 1-7

[3] TOBITA, Y., et al.,"Analytical study on elimination of severe recriticalities in large scale LMFBRS with enhancement of fuel discharge", Nuclear Engineering and Design, Volume 238, Issue 1, January 2008, 57-65

[4] BERTHOUD, G., et al., "A description of fuel –coolant thermal interaction model with application in the interpretation of experimental results", Nuclear Engineering and Design, Volume 82, Issues 2-3, 2 October 1984, 381-391

[5] KONDO, S., et al., "SIMMER-III: An Advanced Computer Program for LMFBR Severe Accident", ANP'92, Tokyo, Japan (1992) Oct. 25-29, No 40-5

[6] YAMANO, H., et al., "Development of a three-dimensional CDA analysis code: SIMMER-IV and its first application to reactor case", Nuclear Engineering and Design, Volume 238, Issue 1,1 January 2008, page 66-13

[7] RUGGIERI,J.-M., et al, "ERANOS 2.1 : The international code system for GEN-IV fast reactor analysis", International Conference ICAPP'06, Reno, Nevada, USA, June 04-08, 2006

[8] MURATA, K. K. , et al., "CONTAIN LMR/1B Mod. 1: A Computer Code for Containment Analysis of Accidents in Liquid-Metal Cooled Nuclear Reactors", (SAND91-1490), January 1993, Sandia National Laboratories, Albuquerque, NM

[9] OTT, K.O., NEUHOLD, R.J. Nuclear Reactor Dynamics, ANS, La Grange Park, USA (1985)

[10] LANL, 1997. DANTSYS 3.0: One-, Two-, and Three-Dimensional, Multigroup, Discrete Ordinates Transport Code System, RSICC Code Package CCC-547, Los Alamos National Laboratory.

[11] CORRADINI, M. L., et al. « Fuel fragmentation model advance using TEXAS-V » OECD/CSNI Specialist Meeting on Fuel-Coolant Interactions, JAERI, Japan, May 19-21 (1997)

[12] JOURNEAU, C., et al., "Sacrificial materials for SFR severe accident mitigation", Int. Conf. Advances Nucl. Power Plants, ICAPP 2010, San Diego, CA, 2010.

[13] SPINDLER, B., et al., "Simulation of MCCI with the TOLBIAC-ICB code based on the phase segregation model » Nuclear Engineering and Design, Volume 236, Issues 19–21, October 2006, p. 2264-2270

[14] CHEYNET, B., et al., « Thermosuite », Calphad, 26 (2) (2002), p. 167

[15] LEE, Y. K., et al. "TRIPOLI-4: verification and validation", J. Trans. Am. Nucl. Soc., 97 (2007), p. 523

[16] VERPEAUX, P., et al., « CASTEM 2000: Une approche moderne du calcul des structures » J.M. Fouet, P. Ladevèze, R. Ohayon (Eds.), Calcul des structures et intelligence artificielle,

Pluralis (1988), pp. 261–271

[17] TENCHINE, D., “Status of TRIO_U code for sodium cooled fast reactors“, Nuclear Engineering and Design, Volume 242, January 2012, Pages 307-315

[18] GALON, P., et al., “ Modelling complex fluid–structure interaction problems with EUROPLEXUS fast dynamic software”, Eighth World Congress on Computational Mechanics (WCCM8), Venice, Italy, 30 June to 5 July 2008

[19] MURATA, K. K. , et al., “User’s Manual for CONTAIN 1.1 : A Computer Code for Severe Nuclear Reactor”, (SAND87-2309), November 1989, Sandia National Laboratories, Albuquerque, NM

[20] STRUWE, D, et al.,“Fuel pin destruction modes-experimental results and theoretical interpretation of the CABRI-1 Program”, In Proceedings of the BNES Meeting on Fast Reactor Core and Fuel Structural Behaviour, Inverness, UK, June 4–6, 1990; p 127.

[21] PAPIN, J., et al., “Fuel pin behaviour under conditions of control rod withdrawal accident in CABRI-2 experiments”, In Proceedings of International Topical Meeting on Sodium Cooled Fast ReactorSafety, Obninsk, Russia,Oct 3–7, 1994; Vol. 2, p 134.

[22] FUKANO et al., “Fuel pin behaviour under slow ramp-type transient-overpower conditions in the CABRI-FAST experiments”, In 13th International Topical Meeting on Nuclear Reactor Thermal-Hydraulics (NURETH-13), Kanazawa City, Ishikawa Prefecture, Japan, Sept 27–Oct 2, 2009.

[23] KAYSER, G., at al., “Summary of the SACRABEE-N Subassembly Melting and Propagation Tests with Application to a Hypothetical Total Instantaneous Blockage in a Reactor”, Nuclear Science and Engineering, Vol. 128, (1998), pp. 144-185

[24] KONISHI, K., et al, ” Overview of the EAGLE experimental program aiming at resolution of the recriticality issue for the fast reactors”, International Conference "Nuclear Power of Republic Kazakhstan", Kurchatov, Kazakhstan, September 3-5, 2007.

[25] MAGALLON, D., et al., "Pouring of 100-kg-scale molten UO2 into sodium", Nucl. Techn., 98, 1992

[26] LE RIGOLEUR, C., et al., “Review of European out-of-pile tests and analyses of molten material movement and relocation and molten material-sodium interaction", Proceedings of the IAEA/IWGFR technical Committee Meeting on Material-Coolant interactions and material Movement and relocation in LMFR, O-arai (Japan), 1994

[27] Weber, D.P., et al., “The SAS4A LMFBR Accident Analysis Code System”, ANL/RAS, 1988, pp. 83-38.

Evaluation of Sodium-cooled Fast Reactor Neutronic Benchmarks

N.E. Stauff[a], T.K. Kim[a], T. Taiwo[a], L. Buiron[b], F. Varaine[b], J. Gulliford[c]

[a] Argonne National Laboratory, Nuclear Engineering Division, USA

[b] CEA, DEN, DER, Cadarache, F-13108 Saint Paul lez Durance, France

[c] OECD/NEA

Presented by N.E. Stauff

Abstract. *In the frame of the Working Party on Reactor and System (WPRS), an international mandate was proposed to work towards a shared neutronic analysis of several Generation-IV Sodium-cooled Fast Reactor (SFR) concepts. This paper summarizes the results obtained at ANL and at CEA while using different calculation methods and systems to estimate the core reactivity and isotopic composition evolution, neutronic feedbacks and power distribution. For the different core concepts analyzed, a satisfactory agreement between participants was obtained despite the different calculation schemes used. A good agreement is generally obtained when comparing the burnup composition evolution, the delayed neutron fraction, the Doppler coefficient, and the sodium void worth. However, some noticeable discrepancies between the k-effective values were observed and are explained in this paper. These are mostly due to the different nuclear data libraries (JEFF3.1 or ENDF/B-VII.0) employed for the calculations. Plutonium isotope fission cross sections are responsible for a large part of the difference, together with the sodium inelastic cross section.*

1 Introduction

One of the foremost Generation-IV International Forum (GIF) objectives is to design nuclear reactor cores that can passively avoid damage of the reactor when control rods fail to scram in response to postulated accident initiators (e.g., inadvertent reactivity insertion or loss of coolant flow). The analysis of such unprotected transients depends primarily on the physical properties of the fuel and the reactivity feedback coefficients of the core. In the frame of the Working Party on Reactor and System (WPRS) of the Nuclear Energy Agency of the OECD, the Sodium-cooled Fast Reactor (SFR) Task Force was proposed [1] to evaluate core performance characteristics and reactivity feedback coefficients of the large and medium SFR core concepts. These are 3600 MWth SFRs with mixed-oxide fuel (MOX-3600) and carbide fuel (CAR-3600) designed at CEA [2][3][4] and 1000 MWth SFRs with metallic alloy fuel (MET-1000) and mixed-oxide fuel (MOX-1000) based on the Advanced Burner Reactor (ABR) designed at ANL [4][5].

During the earlier stages of the SFR Task Force activities, a good agreement was generally obtained when comparing the kinetics parameters, and several reactivity feedback coefficients calculated by the participants. However, noticeable differences in the core multiplication factor (k-effective) calculated by ANL and CEA were also observed. In order to identify the discrepancy in the k-effective, additional neutronics calculations and sensitivity analysis were performed in this study and it was found that the discrepancy was mainly due to the cross sections from the different evaluated nuclear data files.

This paper summarizes the impact of the different cross sections on the core performance characteristics, reactor kinetics parameters, and reactivity feedback coefficients. The SFR core concepts and calculations tools are described in the Sections 2 and 3, respectively. The benchmark

results obtained from the various code systems used at CEA and ANL with different evaluated nuclear data files are provided in Section 4. The sensitivity analysis to evaluate the impact of the different isotopic cross sections is provided in Section 5, and the conclusions of the study are in Section 6.

2 SFR Cores Description

Four SFR benchmark core concepts were proposed in the WPRS SFR Task Force: two large size cores by CEA and two medium size cores by ANL. The detailed descriptions of the cores are available online [1][4] and the primary design parameters of the four cores concepts are compared in Table 1.

Table 1. Comparison of the cores main characteristics (hot dimensions)

	MET-1000	MOX-1000	CAR-3600	MOX-3600
Thermal Power (MW)	1000	1000	3600	3600
Type of fuel used	U-Pu-10Zr	$(U,Pu)O_2$	(U,Pu)C	$(U,Pu)O_2$
Cladding / Duct material	HT-9	HT-9	ODS / EM10	ODS / EM10
Number of fuel assemblies (inner / middle / outer fuels)	78 / 0 / 102	30 / 90 / 60	286 / 0 / 201	225 / 0 / 228
Number of control rods (primary / secondary systems)	15 / 4	15 / 4	12 / 9	18 / 9
Inlet/outlet sodium temp. (°C)	355 / 510	355 / 510	395 / 545	395 / 545
Avg. Fuel temperature (°C)	534	1027	987	1227
Height of fissile zone (cm)	85.82	114.94	100.56	100.56
Lattice pitch (cm)	16.25	16.25	20.99	21.22
Fuel cycle duration (efpd)	328.5	328.5	500	410
Mass of uranium (BOEC, HMT)	10.3	11.0	66.5	58.9
Mass of TRU (BOEC, HMT)	2.90	3.74	12.3	12.2

Core descriptions have been provided by CEA for two 3600 MW(th) large-core concepts. Both have medium power densities that result in low reactivity swing during the equilibrium burn cycle. Oxide Strengthened Steel (ODS) cladding with helium bond is used for the fuel pins. The oxide core is based on the “fat pin with small wire” concept that enables to reach self-sustainability without fertile blanket. The resulting core exhibits an average burnup around 100 GWd/tHM for a corresponding cycle length of 410 equivalent full power days (efpd) with one-fifth batch reloading scheme. The carbide core was designed to have a very low linear power rate to give an enhanced margin to fuel melting. The core exhibits an average burnup close to 70 GWd/t determined by the fuel cladding mechanical interaction limit. Both cores have the fissile breeding ratio slightly higher than one, and a low reactivity swing, they share the same basic design (pin definition) for primary and secondary control systems.

The medium core concepts were proposed from the reference 1000 MW(th) ABR metallic and oxide core concepts [5], which were developed for the study of future fast reactor design options in the United States under the Global Nuclear Energy Partnership (GNEP) program. Compact core concepts with a transuranics (TRU) conversion ratio of ~0.7 were developed for a one-year cycle length with 90% capacity factor. Conventional or reasonably proven materials were utilized in the ABR core concepts so that the core stays within current fast reactor technology knowledge base. In this work, the beginning of equilibrium cycle (BOEC) state core compositions were provided in the benchmark definition. The fuel sub-assembly is divided into five axial zones and the core is divided into inner, middle (only for MOX-1000), and outer cores with different fuel compositions. For simplification, a representative isotope, Molybdenum, replaced all fission products.

3 Calculation Tools and Methodologies

The code systems used by ANL and CEA in the SFR Task Force study are summarized in Table 2. ANL used the MC^2-3/TWODANT [6] code system to generate region-dependent, multi-group cross-sections and the REBUS-3/DIF3D [7] code system for flux and burnup calculations. The 2082-group

master isotopic neutron library for the MC^2-3 code was generated using the ENDF/B-VII.0 file [8]. A three-step procedure was adopted in this study to generate the region-dependent, multi-group cross-sections. In the first step, the MC^2-3 code was used to generate the 2082-group cross sections based on the narrow resonance approximation with the mixture composition. This was followed by fine-group flux calculations using the TWODANT code for a simplified RZ core geometry. In the final step, the MC^2-3 code condensed the cross sections into 33 neutron groups using the fine group fluxes, and the angular scattering cross sections were expanded to 5th order. The flux calculation was performed using the DIF3D code with the variational nodal transport solver (VARIANT) by employing 3rd order approximation for the angular flux and 1st order scattering approximation. The REBUS-3 code [7] was used for depletion calculations. The Doppler and sodium void worth neutronic feedback coefficients were estimated using the transport perturbation theory code PERSENT [9].

Table 2. Description of the deterministic code systems used for this comparison

	ANL System (MC^2-3/REBUS-3)	CEA System (ERANOS2.2)
Multi-group cross-section generation		
Code system	MC^2-3/TWODANT	ECCO
Evaluated nuclear data file	ENDF/B-VII.0	JEFF-3.1 & ENDF/B-VII.0
Groups in master library	2082	1968
Order of angular scattering cross section	5	1
Neutron flux solver		
Code system	DIF3D(VARIANT)	AVNM
Solving equation	Nodal transport	Nodal transport
Number of energy groups	33	33
Angular flux & scattering approximation	P3 & P1	P3 & P1
Perturbations		
Code system	PERSENT - transport perturbation solver	Direct comparison of transport

At CEA, the fast reactor neutronic calculation tool, ERANOS, was used, applying the methodology summarized in Table 2. The ERANOS2.2 code system [10] contains the ECCO code for cells calculation and the ERANOS code for flux and burnup calculations. The ECCO cell/lattice code is based on a subgroup method that treats resonance self-shielding effects within 1968 energy groups for the 37 most important nuclei of the fuel and blanket zones (33 energy groups are used for other regions and other nuclei). ECCO condenses the calculated cross sections into 33 energy groups to be used by ERANOS. Both the JEFF3.1 [11] and the ENDF/B-VII.0 nuclear data library were used for the comparisons in this work. The AVNM nodal transport solver was applied in a 3D core model. The transport approximation used for the flux angular expansion is 3rd order, with 1st order scattering approximation. The simplified spherical harmonics is used to accelerate the transport calculation, taking into account 90% of the transport effect at reduced cost. Perturbation theory calculations are performed in transport theory formulation with direct calculations. The ERANOS set of data developed at CEA were employed at ANL to run calculations using a methodology more consistent with the REBUS-3 calculations. An iterative process between the scientists in CEA and ANL provided the ERANOS results gathered in this paper.

4 Benchmark Results

The main results from ANL and CEA are compared in Table 3. Initially, the results calculated by REBUS-3 with the cross sections from the ENDF/B-VII.0 were compared with the results calculated by ERANOS with the cross sections from the JEFF3.1. It was observed that the k-effective values from the REBUS-3 calculations are consistently smaller than the values from the ERANOS calculations. In particular, about 720 pcm underestimation is observed for the beginning of cycle (BOC) of the 1000 MWth metallic core, while the differences in the large core are negligible.

Table 3. Comparison for the 4 core models

Code system	REBUS-3	ERANOS		MCNP		
Nuclear library	ENDF/B-VII.0	JEFF3.1	ENDF/B-VII.0	JEFF3.1	ENDF/B-VII.0	± *sd*
MET-1000						
BOC K_{eff}	1.0237	1.0335	1.0224	1.0373	1.0242	*6.E-5*
β_{eff}[pcm]	332	334	337	332	330	*8*
$\Delta\rho_{Na\ void}$[pcm]	2267	2356	2358	2273	2238	*8*
K_D[pcm]	-349	-397	-420			
CR worth[pcm]	21367	22120	22384	22092	21803	*8*
EOC K_{eff}	1.0042	1.0111	1.0063			
β_{eff}[pcm]	330	333	334			
$\Delta\rho_{Na\ void}$[pcm]	2348	2471	2409			
K_D[pcm]	-358	-415	-435			
$\Delta\rho$(Cycle) [pcm]	-1891	-2148	-1561			
MOX-1000						
BOC K_{eff}	1.0218	1.0265	1.0197	1.0303	1.0223	*6.E-5*
β_{eff}[pcm]	323	326	327	335	326	*9*
$\Delta\rho_{Na\ void}$[pcm]	2100	2159	2130	2050	2002	*9*
K_D[pcm]	-716	-850	-858			
CR worth[pcm]	23304	24217	24497	23428	23106	*9*
EOC K_{eff}	1.01136	1.0138	1.0139			
β_{eff}[pcm]	321	323	324			
$\Delta\rho_{Na\ void}$[pcm]	2126	2206	2122			
K_D[pcm]	-720	-866	-868			
$\Delta\rho$(Cycle) [pcm]	-1009	-1225	-565			
MOX-3600						
BOC K_{eff}	1.0077	1.0104	1.0050	1.0137	1.0075	*6.E-5*
β_{eff}[pcm]	360	362	365	354	360	*8*
$\Delta\rho_{Na\ void}$[pcm]	2044	2152	2122	2078	2033	*8*
K_D[pcm]	-915	-975	-988			
CR worth[pcm]	7020	7039	7087	7045	6952	*8*
EOC K_{eff}	1.0144	1.0152	1.0143			
β_{eff}[pcm]	351	354	356			
$\Delta\rho_{Na\ void}$[pcm]	2082	2190	2129			
K_D[pcm]	-866	-937	-943			
$\Delta\rho$(Cycle) [pcm]	661	462	913			
CAR - 3600						
BOC K_{eff}	0.9991	1.0043	0.9965	1.0085	0.9997	*6.E-5*
β_{eff}[pcm]	369	372	375	378	365	*7*
$\Delta\rho_{Na\ void}$[pcm]	2298	2378	2365	2312	2289	*7*
K_D[pcm]	-990	-1056	-1079			
CR worth[pcm]	4834	4853	4875	4781	4741	*7*
EOC K_{eff}	1.0145	1.0172	1.0144			
β_{eff}[pcm]	359	362	364			
$\Delta\rho_{Na\ void}$[pcm]	2361	2475	2419			
K_D[pcm]	-928	-1005	-1019			
$\Delta\rho$(Cycle) [pcm]	1519	1270	1766			

As shown in Table 2, the neutron flux solvers of both code systems are very similar. Thus, the discrepancies on the k-effective values were suspected due to the cross sections from the different evaluated nuclear data files, and as a result, additional ERANOS calculations were conducted employing the cross sections generated using ENDF/B-VII.0 data. For comparison purposes, MCNP calculations were also performed using cross sections from both evaluated nuclear data files. The results are summarized in Table 3, including the effective delayed neutron fraction (β_{eff}), sodium void worth ($\Delta\rho_{Na\ void}$), and Doppler constant (K_D) at beginning and end of cycle (EOC).

Results in Table 3 indicate that the cross sections obtained from the different evaluated nuclear data files (JEFF3.1 versus ENDF/B-VII.0 data) are responsible for the differences in the k-effective values. For the results of the ERANOS calculations, the k-effective values obtained using JEFF3.1 data are consistently higher compared to the ones obtained with ENDF/B-VII.0 data. These results are

consistently observed in the MCNP calculations. In order to evaluate the isotopic contributions to the discrepancy, sensitivity analyses were performed and the results are discussed in the next section of this paper. One can also observe that the different nuclear data libraries do not result in significant changes in the sodium void worth, the delayed neutron fraction, or the Doppler coefficient. It should also be noted that the reactivity change over a cycle (burnup reactivity swing) is consistently higher using JEFF3.1 cross sections by 400 to 650 pcm compared to ENDF/B-VII.0.

The REBUS-3 and ERANOS calculation results using the cross sections from the same evaluated nuclear data file (ENDF/B-VII.0) were compared. A satisfactory agreement is obtained for the calculation of the k-effective and reactivity coefficients such as the Doppler coefficient and the sodium void worth. It can be observed that ERANOS calculations tend to consistently predict higher absolute values of these coefficients compared with REBUS-3 system. A very satisfactory agreement is reached between REBUS-3/PERSENT and MCNP when predicting the sodium void worth. The control rods worth were calculated and a satisfactory agreement was observed where results are within 5% of the MCNP homogeneous estimations. Very satisfactory agreement between MCNP, ERANOS and REBUS-3 calculations of delayed neutron fraction (β_{eff}) is obtained if consistent values of isotopic delayed neutron fraction (ν_D) are used by the participants.

5 Analysis of the discrepancies observed using the ENDF/B-VII.0 and JEFF3.1 libraries

It was previously observed that the k-effective values obtained using JEFF3.1 data [11] were consistently higher compared to the ones obtained with ENDF/B-VII.0 data [8]. It is noted that the discrepancies were not due to the version of the ENDF/B-VII because the reactivity obtained from the MCNP calculations using ENDF/B-VII.0 is close to the ones obtained using ENDF/B-VII.1 data. In addition, the discrepancy was not due to the multi-group cross sections used in the REBUS-3 and ERANOS calculations because the results from the continuous energy group MCNP calculations are consistent to the results from ERANOS as evident in Table 4.

Table 4. Difference in reactivity at the BOC when using different libraries [pcm]

Code	MCNP	MCNP	ERANOS
Libraries compared	*ENDF/B-VII.0 - ENDF/B-VII.1*	*ENDF/B-VII.0 - JEFF3.1*	*ENDF/B-VII.0 - JEFF3.1*
MET-1000	+146 ± *7*	-1232 ± *9*	-1068
MOX-1000		-757 ± *9*	-655
MOX-3600	-99 ± *6*	-610 ± *9*	-547
CAR-3600		-869 ± *9*	-779

The following sensitivity analysis focuses only on the comparison of the multi-group cross section generated from the JEFF3.1 and ENDF/B-VII.0 data files, for which perturbation analyses are available with ERANOS. The first objective of this study is to investigate the observed discrepancies in the reactivity values displayed in Table 3 and Table 4, and to identify the relevant energy range of the isotope cross-sections that are the major contributors (in a 33-group energy structure). The second objective is to understand why the discrepancy is smaller for the MOX-3600 core than for the MET-1000 core.

A perturbation analysis is performed with ERANOS to evaluate the impact of the different isotopes over the observed discrepancy in the k-effective values using the multi-group cross section from JEFF3.1 and ENDF/B-VII.0. Exact perturbation calculations are performed in Hex-Z geometry in diffusion theory. The sensitivity of the reactivity changes ($\partial\rho_i$) to a specific cross section type of i was computed based on standard perturbation theory:

$$\partial\rho = \frac{1}{K} - \frac{1}{K'} = \sum_i \partial\rho_i = \frac{\sum_i \left[- < \phi *, \partial A_i . \phi' > + \frac{1}{K'} < \phi *, \partial F_i . \phi' > \right]}{< \phi *, F' . \phi' >}$$

Where :

- ϕ' is the perturbed flux obtained using the ENDF/B-VII.0 cross sections, ϕ^* is the reference adjoint flux obtained using JEFF3.1 cross sections, both are calculated in diffusion theory
- **K** and **K'** are the associated reference and perturbed multiplication factors
- **F** and **F'** are the production (by fission) operator in the Boltzmann equation and ∂F_i their difference with respect to isotope **i**
- **A** and **A'** are the remaining operators (transport, collision, in-scattering) and ∂A_i their difference with respect to isotope **i**

Results of the perturbation analyses are summarized in Table 5, which shows the reactivity change per cross section change of major isotopes. The discrepancy values are displayed as ENDF/B-VII.0 minus JEFF3.1 results: i.e. a "positive reactivity difference" should be understood as a larger calculated reactivity using the ENDF/B-VII.0 compared to the JEFF3.1 library.

Table 5. Main isotope contribution to the reactivity discrepancy (ENDF/B-VII.0 minus JEFF3.1)

[pcm]	MET-1000	MOX-1000	CAR-3600	MOX-3600
U-238	-58.6	4.3	29.2	4.1
Pu-238	-196.5	-308.1	-269.1	-258.1
Pu-239	126.2	312.4	284.5	326.6
Pu-240	-259.7	-221.2	-199.3	-177.4
Pu-241	-78.6	-66.2	-86.5	-80.1
Pu-242	-43.7	-21.1	-29.8	-22.5
Am-241	-34.4	-40.5	-13.51	-12.4
Am-243	48.4	50.4	9.95	14.3
Cm-242	-38.6	-40.6	-6.85	-18.4
Cm-244	31.1	46.5	0.90	2.81
Fe-56	-72.6	-120.0	-121.8	-103.4
Na-23	-395.5	-278.2	-260.0	-237.3
O-16	0	101.6	0.3	120.1
Sum of discrepancies	-1035	-605	-734	-502
Sum of ABS(discrepancies)	1558	1694	1452	1514

It is noted that the main contributors to the reactivity discrepancy are plutonium and sodium. The plutonium fission cross-sections have the largest absolute impact with negative contributions from Pu-238 and Pu-240 (the use of JEFF3.1 leads to larger k-eff values than ENDF/B-VII.0) and a positive contribution from Pu-239. The sodium Na-23 cross-section appears to have significant effects too. Some other isotopes such as U-238, Fe-56, Cr-52, O-16 also have potentially significant impacts.

The overall reactivity changes presented in Table 4 are comparable to the sum of the isotope contributions indicated in Table 5. However, it is noted that some discrepancies due to different isotopes strongly compensate each other (i.e., error cancelation). For instance Pu-239 has a strong positive effect that partially compensates the overall negative effect. As an indication, the sum of the absolute isotope contributions in Table 5 is intended to estimate the sum of the discrepancies without compensation among the different isotopes. It is interesting to note that the sum of the absolute isotope contributions has the same order of magnitude for each core (~1500 pcm). Thus, the difference in reactivity between the cross sections from JEFF3.1 and ENDF/B-VII.0 is comparable, but it is smaller for MOX-3600 with respect to MET-1000 because of error compensations rather than to a better

agreement. In the following, an energy breakdown will be presented for the main isotope contributors observed in Table 5.

i. Pu-238

The Pu-238 isotope is responsible for -196 pcm of reactivity discrepancy for the MET-1000 core and -258 pcm for the MOX-3600 core, despite the relatively small amount of Pu-238 in the fuel (0.5wt% of heavy material). The observed discrepancies are mainly explained by the smaller fission cross-section from ENDF/B-VII.0 compared to JEFF3.1, as illustrated in Fig 1. The relevant energy range is from 300eV to 183 keV. Some very large differences in the cross-section values are observed at low energy but they have negligible reactivity effects due to the lower neutron flux in this range. The capture cross-sections in the 25 keV to 2 MeV energy range also leads to a negative reactivity impact due to the ENDF/B-VII.0 larger capture cross-section.

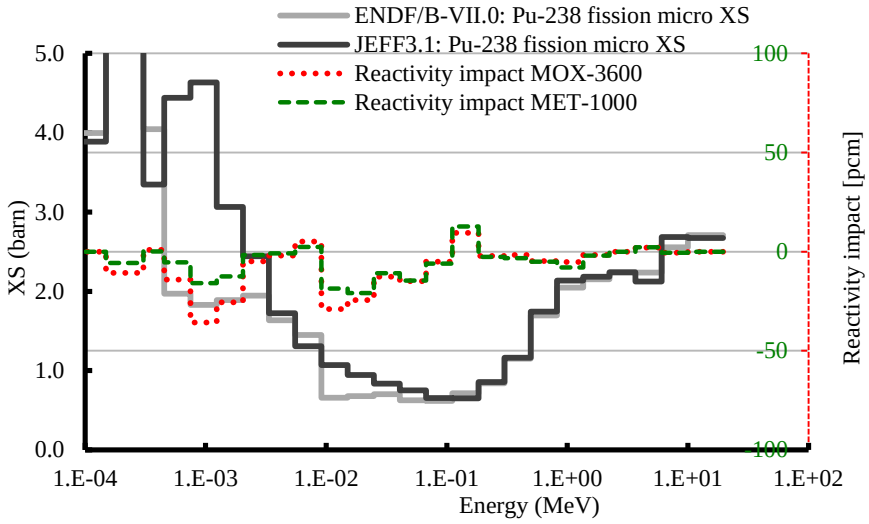

FIG 1. Comparison of JEFF3.1 and ENDF/B-VII.0 microscopic fission cross-section for Pu-238 in infinite dilution with ERANOS/ECCO. Impact estimated of this discrepancy over the reactivity of MOX-3600 and MET-1000 cores using ERANOS perturbation theory.

ii. Pu-239

The Pu-239 isotope has a positive reactivity impact of +126 pcm for the MET-1000 core and of +327 pcm for the MOX-3600 core. These significant discrepancies are due to the large fraction of Pu-239 in the investigated cores rather than to the variation in the cross-section values, which are less relevant. These reactivity effects mainly come from the fission cross-section, but also partly from the capture and the inelastic cross-sections in the energy range from 67 keV to 3.7 MeV.

The difference in the fission cross-section is presented in Fig 2. It is noted that there are 6 energy groups that have the most significant reactivity impact. Among them, two groups at high energy (0.5-1.3 Mev) have a negative impact and one at low energy (1-2 keV) has a positive impact. On one hand, this low energy group has a strong impact on the MOX-3600 softer spectrum, leading to a large positive reactivity effect. On the other hand, the high-energy groups generate a negative compensation for the MET-1000 core, leading to a smaller positive reactivity effect of Pu-239 fission. Thus, the spectrum hardness is responsible for the difference in the reactivity impact of the Pu-239 cross-section between the MET-1000 and the MOX-3600 cores. The energy-induced discrepancy compensation is very large in this example. The sum of the energy-dependent absolute reactivity values for the Pu-239 is ~900 pcm. This means that ~590 pcm discrepancy is compensated in the MOX-3600 core and that ~770 pcm of discrepancy is compensated in the MET-1000 core.

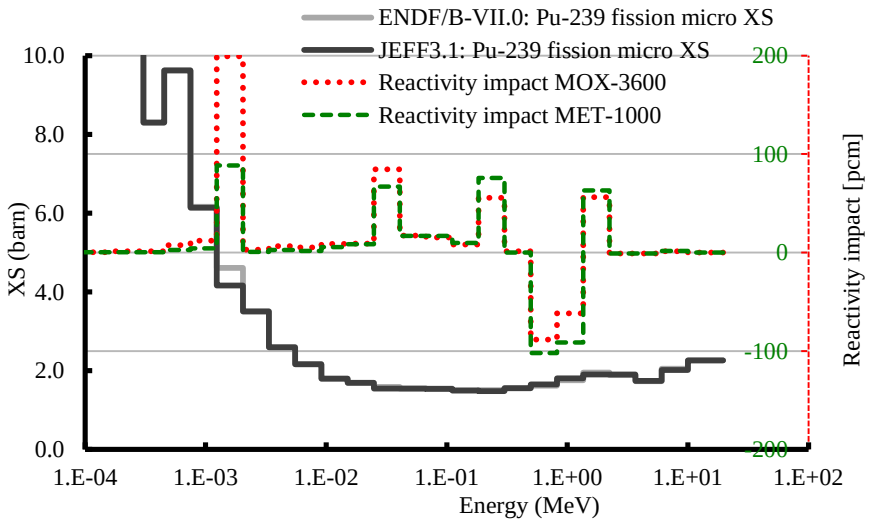

FIG 2. Comparison of JEFF3.1 and ENDF/B-VII.0 microscopic fission cross-section for Pu-239 in infinite dilution with ERANOS/ECCO. Impact estimated of this discrepancy over the reactivity of MOX-3600 and MET-1000 cores using ERANOS perturbation theory.

iii. Pu-240

The Pu-240 isotope has a negative reactivity impact of -114 pcm for the MOX-3600 core and of -223 pcm for the MET-1000 core. This is mainly due to the fission cross-section of Pu-240 that, in ENDF/B-VII.0, is smaller in the 100 keV to 500 keV energy-range and larger in the 500 keV to 1.3 MeV energy-range. The overall reactivity effect is negative and not relevant but there are very strong compensations (similar to the Pu-239 fission) as shown in Fig 3: if it was not for the cancellation of effects, the reactivity impact due to the change of data libraries with Pu-240 would be up to 985 pcm for the MET-1000 case. The capture cross-section of the Pu-240 has also a strong compensation of effects that can potentially lead to large reactivity impacts.

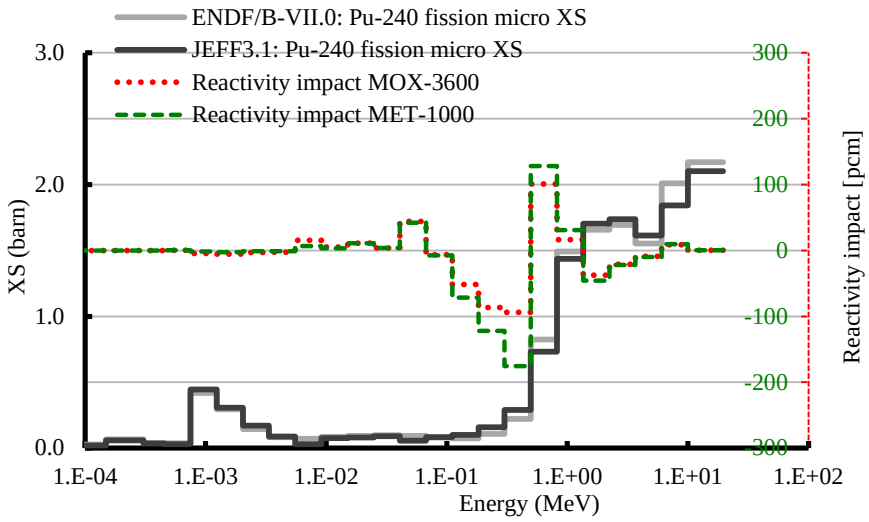

FIG 3. Comparison of JEFF3.1 and ENDF/B-VII.0 microscopic fission cross-section for Pu-240 in infinite dilution with ERANOS/ECCO. Impact estimated of this discrepancy over the reactivity of MOX-3600 and MET-1000 cores using ERANOS perturbation theory.

iv. U-238

In this case the reactivity impact of U238 is very small: from 5 to -50 pcm when using the JEFF3.1 library compared to the ENDF/B-VII.0 library. However, a strong discrepancy is observed especially for fission in the energy range from 0.8 MeV to 6 MeV, as displayed in Fig 4. The overall absolute

impact is up to 1400 pcm for both cores. Thus, the U-238 isotope provides the potentially largest impact of energy-induced discrepancies cancellation.

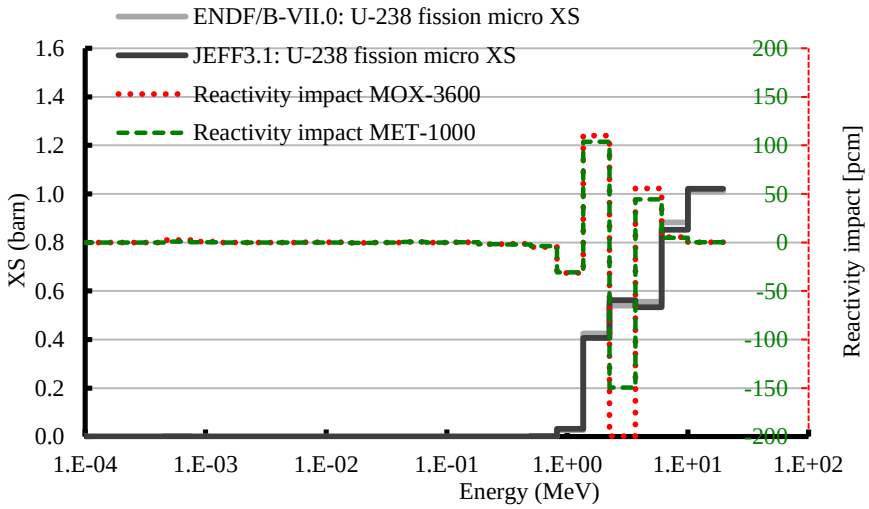

FIG 4. Comparison of JEFF3.1 and ENDF/B-VII.0 microscopic fission cross-section for U-238 in infinite dilution with ERANOS/ECCO. Impact estimated of this discrepancy over the reactivity of MOX-3600 and MET-1000 cores using ERANOS perturbation theory.

v. Fe-56 and Na-23

The Fe-56 isotope leads to a negative reactivity impact of -103 pcm for the MOX-3600 core and of -73 pcm for the MET-1000 core. In this specific case, no significant energy-compensation is observed but there is a strong compensation between the positive leakage component and the negative inelastic reaction component.

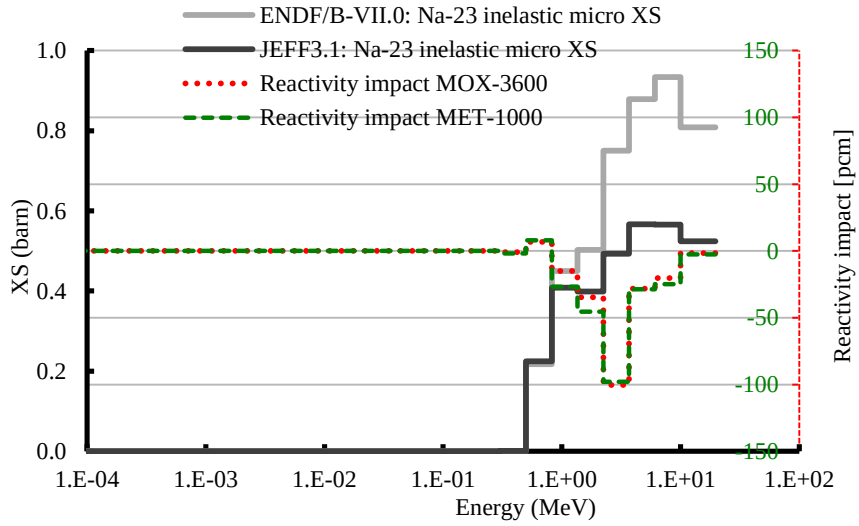

FIG 5. Comparison of JEFF3.1 and ENDF/B-VII.0 microscopic inelastic cross-section for Na-23 in infinite dilution with ERANOS/ECCO. Impact estimated of this discrepancy over the reactivity of MOX-3600 and MET-1000 cores using ERANOS perturbation theory.

Similar considerations can explain the large effect observed for Na-23 where the reactivity impact of switching from ENDF/B-VII.0 to JEFF3.1 varies by -237 pcm for the MOX-3600 core and by -395 pcm for the MET-1000 core. The main contributor is the inelastic cross-section at high energy, which is much larger with ENDF/B-VII.0 with respect to JEFF3.1, as displayed in Fig 5. The elastic cross-sections and the leakage component also have large reactivity impacts.

6 Conclusions

This paper summarizes the results obtained at ANL and at CEA from using different calculation methods and systems to analyze the SFR cores proposed within the Sodium-cooled Fast Reactor (SFR) Task Force of the Working Party on Reactor and System (WPRS) of the OECD Nuclear Energy Agency. ANL used the MC^2-3/DIF3D/REBUS-3 and PERSENT code systems for multi-group cross-section generation, neutron flux solver, and core depletion, and perturbation theory calculations, respectively, while the CEA used the ERANOS code system. The Monte-Carlo code MCNP was also used for comparison purposes. The multi-group cross sections were calculated from the JEFF3.1 and ENDF/B-VII evaluated nuclear data files. A good agreement is generally obtained when comparing the burnup composition evolution, the delayed neutron fraction, the Doppler coefficient, and the sodium void worth. However, some noticeable discrepancies between the k-effective values were observed and are mostly explained by the cross sections from the different nuclear data files of JEFF3.1 and ENDF/B-VII.0.

In this study, the reactivity impact due to the utilization of the cross sections generated using different evaluated nuclear data files was also analyzed for each isotope. It was found that plutonium and sodium are the two main contributors to the observed reactivity change. The plutonium isotopes fission cross-sections give significant impacts. Pu-238 and Pu-240 have a negative reactivity impact while Pu-239 has a positive impact. An error cancelation of the reactivity effect was observed among the different isotopes, which partly explains the smaller reactivity change observed for the MOX-3600 and the MET-1000 cores. In addition to those isotopes, compensations were also observed among energy groups and reaction types. These compensation effects were investigated and it was found that some other isotopes such as U-238, Fe-56, Cr-52, O-16 might have a significant impact depending on the flux energy spectrum. The major conclusion of this study is that the smaller reactivity change between JEFF3.1 and ENDF/B-VII.0, for MOX-3600 with respect to MET-1000, appears to be due to the error cancelation and not to a better agreement between the two libraries.

ACKNOWLEDGEMENTS

The authors acknowledge the other participants of the OECD/NEA WPRS SFR Task Force: E. Ivanov (IRSN, France), A. Kereszturi (KFKI, Hungary), Y. Lee (CEA-Saclay, France), N. Messaoudi (SCK/CEN, Belgium), A. Ponomarev (KIT, Germany), F. Michel-Sendis (OECD/NEA) and A. Yamaji (OECD/NEA). Comments and reviews from G. Aliberti on the cross section comparison study are very much appreciated. L. Mynsberge provided valuable help with the MCNP calculations.

REFERENCES

[1] AEN - WPRS website: http://www.oecd-nea.org/science/wprs/sfr-taskforce/ .
[2] P. SCIORA et al, “A break even oxide fuel core for an innovative French Sodium-cooled Fast Reactor: neutronic studies results,” *Proceedings of Global*, 9528, Paris, France (2009).
[3] F. VARAINE et al, “Comparative review on different fuels for GEN IV Sodium Fast Reactors: merits and drawbacks,” *proceedings of FR’09*, Kyoto-Japan (2009).
[4] AEN - WPRS, *Sodium Fast Reactor Core Definition*, Version 1.2 (available online).
[5] T. K. KIM, W. S. YANG, C. GRANDY and R. N. HILL, “Core Design Studies for a 1000 MWth Advanced Burner Reactor,” *Annals of Nuclear Energy*, **Vol. 36** (2009).
[6] C. H. LEE, W. S. YANG, “Verification and Validation of Multigroup Cross Section Generation Code MC2-3 for Fast Reactor System,” ANS Annual Meeting, Chicago, IL (2012).
[7] B. J. TOPPEL, “A user’s guide for the REBUS-3 fuel cycle analysis capability,” ANL-83-2 (1983).
[8] M. B. CHADWICK et al., “ENDF/B-VII.0: Next Generation Evaluated Nuclear Data Library for Nuclear Science and Technology,” Nuclear Data Sheets 107, 2931 (2006).
[9] M. A. SMITH, W. S. YANG, A. MOHAMED, E. E. LEWIS, “Perturbation and Sensitivity Tool Based on the VARIANT Option of DIF3D,” American Nuclear Society Transactions 107, San Diego, CA, Nov. 11-15 (2012).

[10] G. RIMPAULT et al, *Proceedings of Physor*, Seoul Korea, October (2002).
[11] A. KONING et al, "The JEFF3.1 Nuclear Data Library," Nuclear Energy Agency Data Bank, OECD, *JEFF Report 21*, **NEA N° 6190**, (2006).
[12] Monte Carlo Code Group, LANL, MCNP5 online documentation.
[13] M. B. CHADWICK et al., "ENDF/B-VII.1 Nuclear Data for Science and Technology: Cross Sections, Covariances, Fission Product Yields and Decay data," Nuclear Data Sheets 112, 2887-2996 (2011).

Scientific program of the Karlsruhe Sodium Laboratory (KASOLA)

Wolfgang Hering, Robert Stieglitz, Angela Jianu, Martin Lux, Alexandru Onea, Sarah Scherrer, Christoph Homann

Karlsruhe Institute of Technology (KIT), Hermann-von-Helmholtz-Platz 1
D-76344 Eggenstein-Leopoldshafen, Germany

Synopsis

At the Institute of Neutron Physics and Reactor Technology of the Karlsruhe Institute of Technology (KIT), the experimental sodium loop KASOLA (KArlsruhe SOdium LAboratory) is currently being erected, commissioning tests are scheduled in 2013. A key feature of the facility is its flexibility with respect to a wide spectrum of thermal hydraulic experiments. The facility hosts a sodium inventory of 7 m^3 and it can operate up to 550 °C. A magneto-hydrodynamic (MHD) pump can deliver a flow rate of up to 150 m^3/h at a pressure head of 0.4 MPa. Due to the specific features of this type of pump, such as flow direction reversal, the investigation of numerous potentially occurring technical scenarios can be performed.

The KASOLA facility contains in its base loop two test ports, a versatile test section and a pool test section. The versatile test section has a maximum effective height of up to 6 m to be used for component validation tests at almost typical axial heights, as well as generic thermal-hydraulic benchmark experiments. In the pool section, which has the dimensions 4x4x0.4 m^3, a core simulator, an intermediate heat exchanger, and decay heat removal coolers can be hosted to simulate the flow in a sodium pool nuclear plant. The flow patterns in the sodium pool of a nuclear plant will be studied in detail on the basis of a Hele-Shaw approximation, for the transition between forced, mixed, and natural convection. Furthermore, in the facility, measurement techniques can be qualified and in-service inspection and repair (ISI&R) measures can be tested. An additional auxiliary port will be used for smaller experiments. Due to the flexibility of the KASOLA facility, aside from nuclear applications, aspects of thermo-electric energy conversion, such as the study of Alkali Metal Thermal Energy Converter (AMTEC), as well as thermal storage using liquid metals can also be covered.

The experiments will be complemented by numerical analyses, both with CFD and with system codes such as TRACE and SIM-ADS, to tackle existing deficits in heat transfer modelling of low Prandtl number fluids. Additionally, as part of the European Framework Programme JASMIN, the new French-German nuclear system code ASTEC-Na is foreseen to be applied and qualified based on code-to-code and code-to-data comparison. As a first step, investigations are foreseen about the transition from forced to natural convection, plume formation in a backward facing step, and thermal energy storage technologies at high temperatures.

1. Introduction

Liquid metal technology is considered to be the next step for a more efficient future energy technology. This does not only concern the conversion side (fast reactor systems or concentrating solar power-CSP), but also the storage side allowing for high temperature heat storage at almost ambient pressure. Especially sodium offers a wide range of applications compared to other high temperature fluids due to its low density, high thermal conductivity, specific heat capacity and at most its high compatibility with other metallic structure materials. Due to its opaqueness and high chemical

reactivity, however, all applications require innovative sensor technologies for monitoring and control purposes.

Liquid metals are also considered as excellent coolant fluids for innovative systems to transmute long living nuclear waste. One of the technically feasible options is a sodium cooled fast transmuter. In order to maintain the technical competence with respect to the essential topics safety and operational aspects, the erection of a medium sized thermal-hydraulic test facility is mandatory to enable model validations for a future licensing process.

The loop is aimed to perform studies about specific heat transfer studies in dedicated geometries and component interaction and to qualify predictive system analysis and CFD tools at high confidence level. Both aspects are of crucial nature for the design and development of all energy conversion systems but especially of transmutation systems. Nevertheless, a validation of the physical models, used in the current computational tools (either heat transfer or system analysis) for sodium flows, is indispensable even for many steady state conditions. Moreover, it is known that in many cases the model assumptions are not adequate and new models have to be developed, especially for anisotropic turbulent flows and mixed convective flows.

Hence, establishing a centre of competence for liquid metal technology for innovative energy systems in Karlsruhe is of vital importance for the future. Furthermore, in industrial process engineering (e.g. Tantalum reduction) and particle accelerator research, targets are considered to be composed either of lithium or of sodium due to their neutronics properties and the heat removal capacity. The various aspects of fission safety research and cross-cutting issue to other fields of nuclear and non-nuclear energy science demand an experimental program, complementary to the currently on-going numerical studies.

2. The Karlsruhe Sodium Laboratory KASOLA

Based on the experience gained during the erection and operation of KALLA [1], [2], a versatile facility for sodium is currently erected to conduct research on heat storage, fission safety, fusion technology, accelerator target development and material sciences. The scientific program is focused on qualification of innovative CFD codes, safety investigations for transmutation systems, and development of high temperature concentrating solar power systems.

The KASOLA facility contributes to the Helmholtz alliance on liquid metal technology (LIMTECH [3]). With respect to the needs of innovative energy systems, which will face much higher temperatures to enhance efficiency, the Helmholtz Energy Materials Characterization Platform (HEMCP), was founded, allowing Helmholtz centres to establish a sophisticated material investigation platform. HEMCP will also boost the developments and qualification of instrumentation and materials used for liquid metal technology. The roadmap of KASOLA including LIMTECH and HEMCP is given in Fig. 2.

KASOLA is erected in the cylindrical THINA building (see Fig. 1) of the Institute of Neutron Physics and Reactor Technology at the Karlsruhe Institute of Technology. In the seventies of the last century sodium experiments were performed in the THINA facility to investigate high energetic phenomena, occurring during core disruption accidents in sodium cooled fast reactors. Therefore, the KASOLA facility takes credit from the design and construction, which was optimized to minimize the risks of sodium leakages and fires. In KASOLA various experiments can be performed focused on:

- Investigation of transition in convective flow patterns between forced, mixed and free convection modes.
- Qualification of CFD and system codes to simulate adequately the transition from the channel flow to large plenum (collector tank)
- Development of free surface liquid metal targets for accelerator applications

- Development of models to describe free surface liquid metal flow
- Validation and improvement of turbulent liquid metal heat transfer models in CFD tools on limited geometric scale

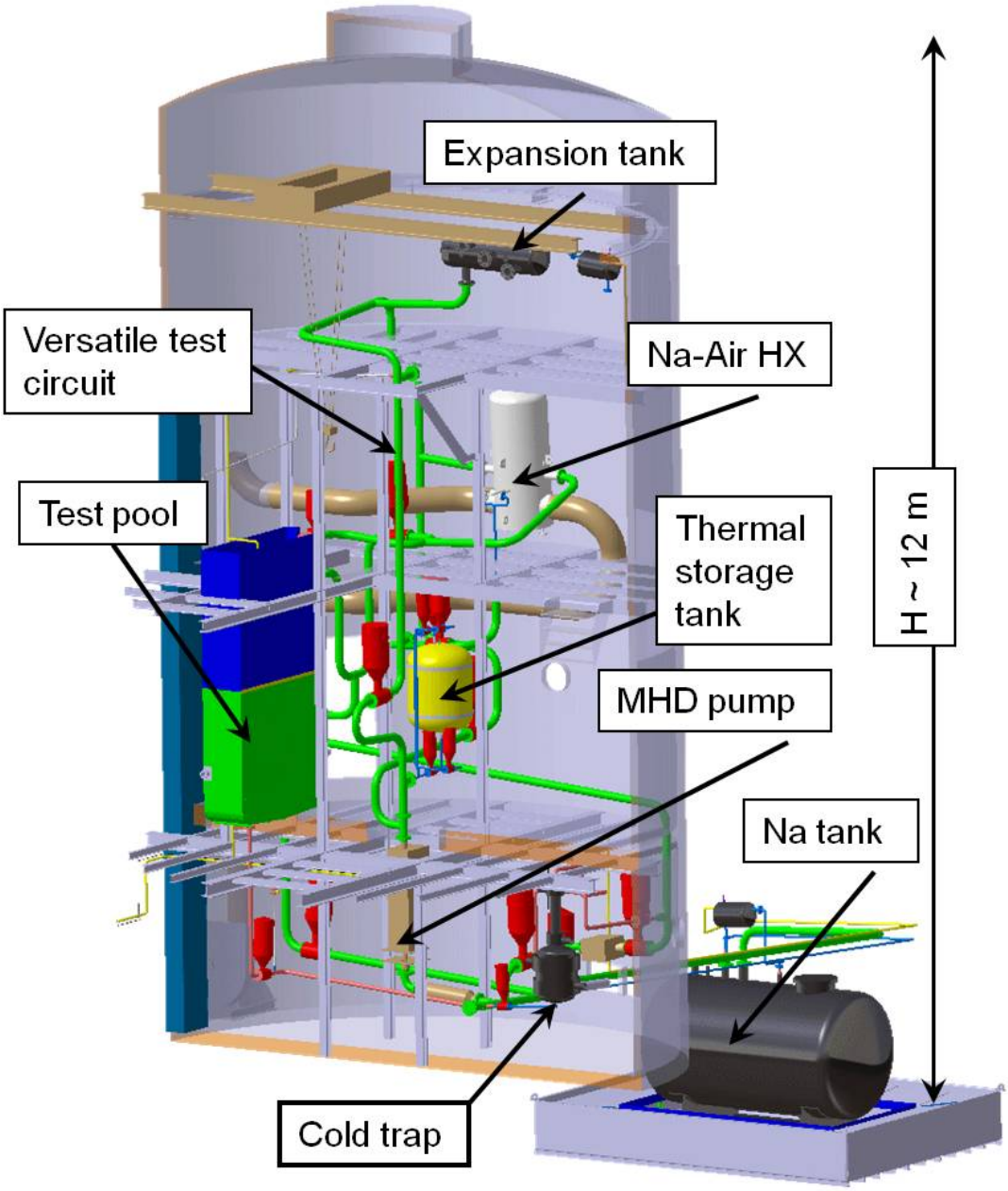

Fig. 1 Schematics of the KASOLA facility

Additionally, the following research topics could be investigated in KASOLA:

- Thermal hydraulic investigations of flow patterns in fuel bundles or pool configurations at prototypical or scaled heights
- In-Service Inspection & Repair monitors for liquid metal systems

The KASOLA facility is located in a cylindrical steel tank (see Fig. 1) with an inner diameter of 7.7 m and a usable height of 12.5 m. The tank is composed of a 6 mm thick steel hull made of 10 ring segments and supported by an external grid. The orbital crane rail is at an elevation of 11.25 m resulting in a usable height above the first floor level of app. 8 m. The floor of the first level is a massive supporting structure designed for heavy loads. This structure carries the scaffolds and the

whole loop. Two modular scaffold levels are necessary to grant access to all components. Along the axis of the hall, three steel girders support the different heavy components, such as the thermal storage or the slab pool simulator. The tank contains relief valves to avoid the pressure increase that can hinder the human access for maintenance. The sodium aerosols that can be released in case of a sodium leak are foreseen to be retained in the filter of the ventilating installation of the tank. The facility is operated outside the containment so that it can be kept closed for safety reasons during pump operation.

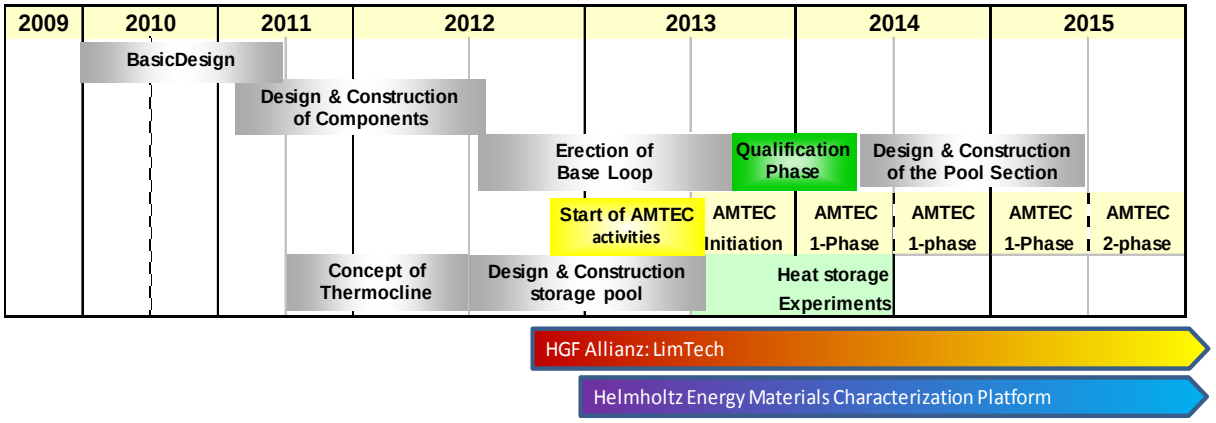

Fig. 2 KASOLA Roadmap including LIMTECH and HEMCP

2.1. Base Loop

The main part of the KASOLA facility, the base loop, is shown as 3D-schematics in Fig. 3. The base loop consists of piping, valves, MHD pump (ALIP type), air-Na-heat exchanger, expansion tank, sodium trap, the cleaning and calibration section, experimental ports, instrumentation and control. The MHD pump renders a wider range of possible transient experimental conditions than other pump types. The storage tank, also part of the base loop, is located outside the containment in a separate compartment. Below the storage tank, a safety collection tank is foreseen, which can hold the total amount of used sodium.

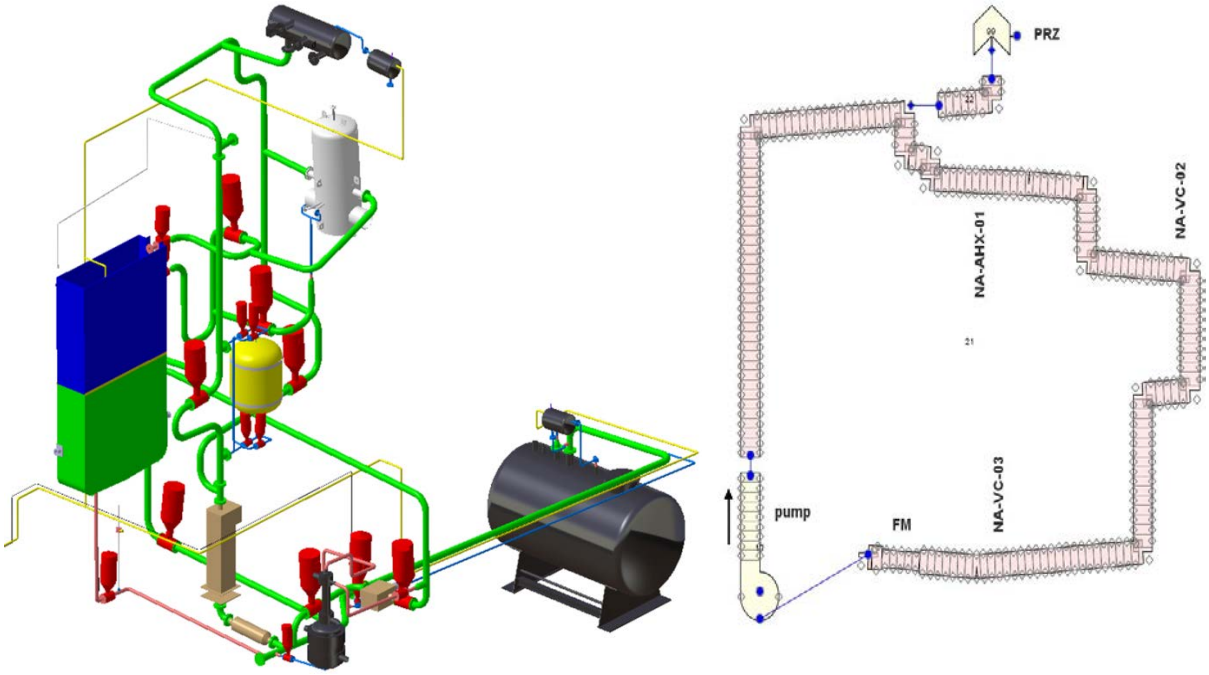

Fig. 3 3D-schematics of the KASOLA piping and component arrangements (left) and 2D simulation model using TRACE (right)

Three experimental ports are foreseen to serve all needs of liquid metal experimental investigations. The versatile test section has a height of nearly 6 m above the MHD pump and can be used for development and investigation of targets, component tests, and/or experiments, which require high mass flow rates. As an example, for the versatile test section, a high temperature thermal storage device based on thermoclines is shown in Fig. 5. For higher mass flow rates, a second MHD pump (FLIP type) can be installed in series with the first one.

The pool section is foreseen to hold a slab pool simulator, at a maximum power of 400 kW. Due to its geometry, it can be described by the Hele-Shaw approximation.

The simultaneous operation of the above described test ports is not considered, but the parallel configuration allows an easy switching between them and reduces the maintenance time.

A third port, namely a low temperature port, is foreseen to connect separate experimental loops or devices, which can use the calibration and cleaning units of KASOLA.

On the right side of Fig. 3 the representative mesh used to optimize the pressure drop with TRACE is shown. Based on simulation results and analytical calculations, the base loop pressure drop amounts to app. 0.15 MPa [7]; therefore sufficient pressure head is available for experimental devices at the test ports. The model will be updated when the final pipework geometry is fixed.

2.2. Experimental capabilities of KASOLA

Depending on the needs of an experiment, one of the three ports can be used as described in the following sections.

2.2.1. Versatile test section

The versatile test section allows various experiments to take credit from the 6 m height between pump exit and expansion tank level. Different stages are envisaged so far:

1. In a first experimental stage the versatile test section, located just above the MHD pump in the base loop (see Fig. 3 left), is realized by a straight pipe, to simulate a heater section at different elevations. Together with the sodium-air heat exchanger, natural convection can be investigated. Also detachment of flow in a backward facing step will be investigated here.

2. Sodium as a heat transport fluid and storage fluid is another research topic, dealing with storage challenges in innovative concentrating solar power systems or in the pulsed DEMO facility for nuclear fusion. Fast store and retrieve options are necessary to protect the power conversion system (PCS) and to achieve a stable operation, which is prerequisite for highly efficient energy conversion.

3. Modern accelerators achieve very high beam densities, exceeding solid material sustainable limits. Therefore, many concepts utilize liquid metals, acting simultaneously as coolant and target, since their large heat conductivity results in an effective heat transfer and a low degradation (see Fig. 4). High heat flux up to 2 MW/m² can be simulated using an electron beam heating device.

Moreover, in the versatile test section a full height subassembly (S/A) of a fast system for transmutation could be installed. Due to the capacity of the pumps (ALIP and FLIP) and the available power supply, a 19 pin bundle with nominal power can be simulated. The cooling capacity of the air-sodium heat exchanger is fixed to 400 kW, but extension using innovative heat transfer devices is possible.

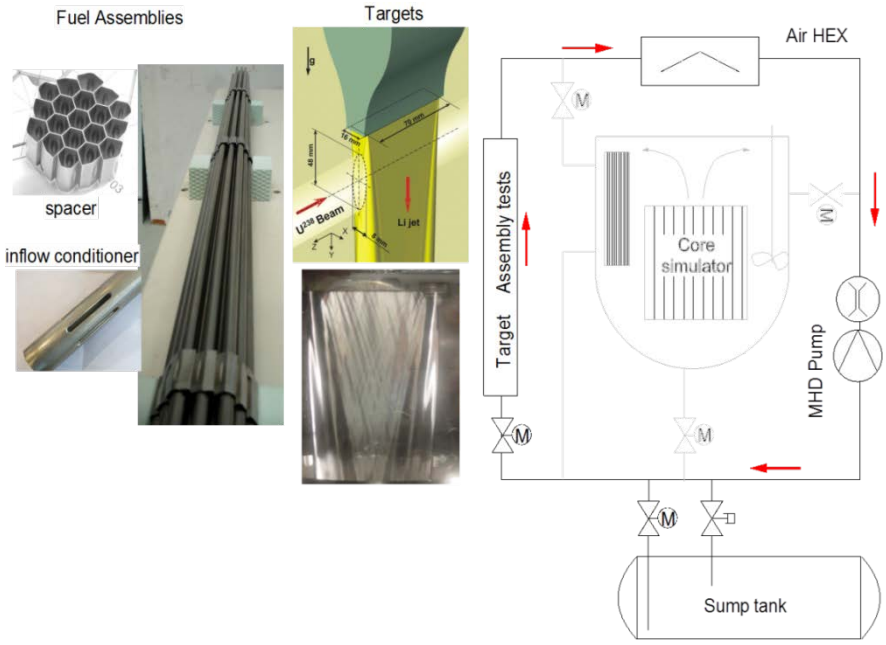

Fig. 4 Liquid metal target assembly test in the versatile test section

2.2.2. Pool test section

The pool test section port is located downstream of the heat exchanger on the second floor level providing “cold” sodium as a heat sink for experiments. It can be equipped with a 2-D pool simulator to investigate with innovative instrumentation flow patterns in complex geometries, as well as changing patterns due to change in operation modes.

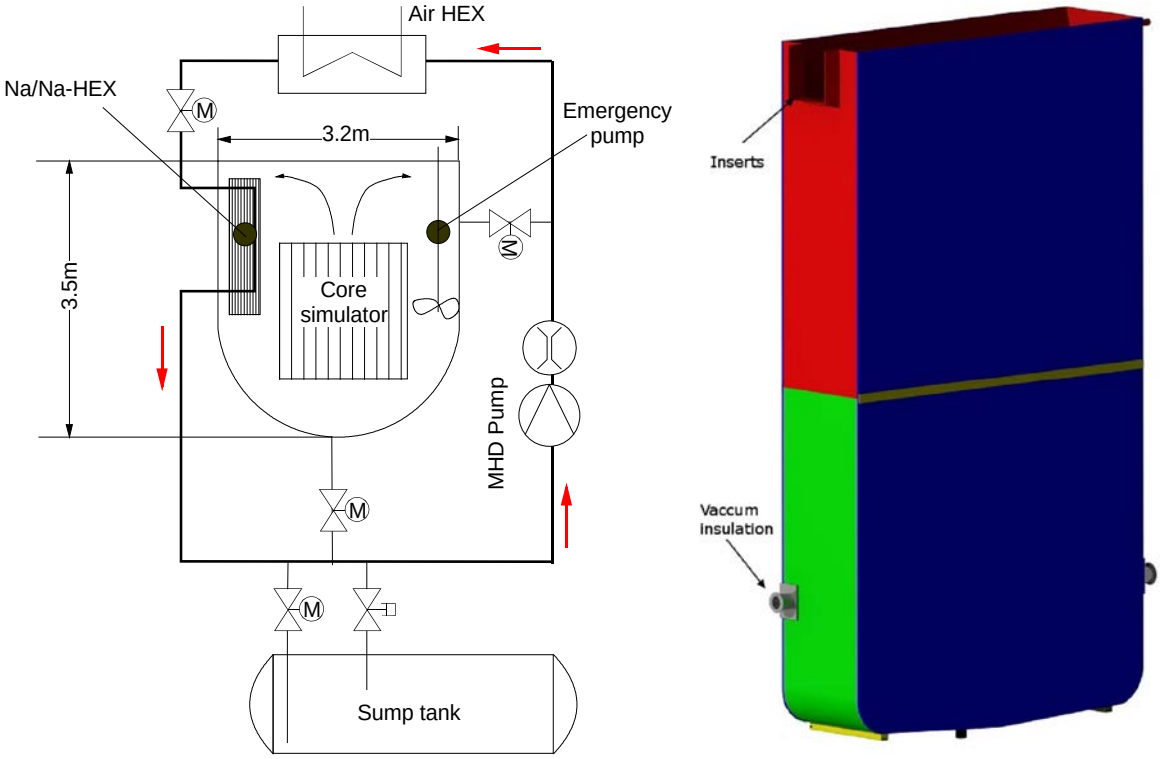

Fig. 5 2-D scenario for investigation of transition from forced to natural convection in a slab geometry (left) and actual design of the tank (right)

Typical internals are heaters, intermediate submerged heat exchanger (IHX), mechanical pump, decay heat removal (DHR) systems, etc. The sodium loop serves as heat sink for IHX or DHR system simulating the secondary loop. The pool simulator has a volume of app. 5 m³ and allows scaling in height in the range of 1:4 – 1:5. The Hele-Shaw approximation requires adiabatic boundary conditions at both cut faces.

2.2.3. Auxiliary port

For small sodium experiments, an auxiliary port is available where small test loops can be attached. However, they will operate separately at high temperature. The KASOLA facility can be used with all its auxiliary and service devices, including its sodium cleaning capabilities instead of erecting additional service components.

3. Scientific program

The present experimental program is focused to use liquid metals in energy systems as a heat transfer or cooling fluid. Experiments concerning the developments of alkali metal direct thermal energy conversion systems (AMTEC) are also in preparation.

3.1. Transition between free, mixed and forced convection

Any design optimization requires a smooth transition from forced convection to natural convection to guarantee a safe reactor state in case of a loss of off-site power or loss of flow. This is one of the most important subjects of the evaluation of different reactor designs. As a general request a stagnation of the liquid must be avoided in any active operation situation. To assess such situations and to supply CFD codes with data for qualification, model experiments with an adequate instrumentation density, providing not only steady state but also temporal data, are required.

The base loop of KASOLA offers different options to simulate such situations. First, it is intended to neglect the lateral temperature gradient, so that only the level difference between the heater and the IHX is varied between 1 and 6 m. In a second step, the straight pipe in the versatile test section is replaced by a test section, so that a noticeable lateral temperature gradient exists as outlined in Fig. 6.

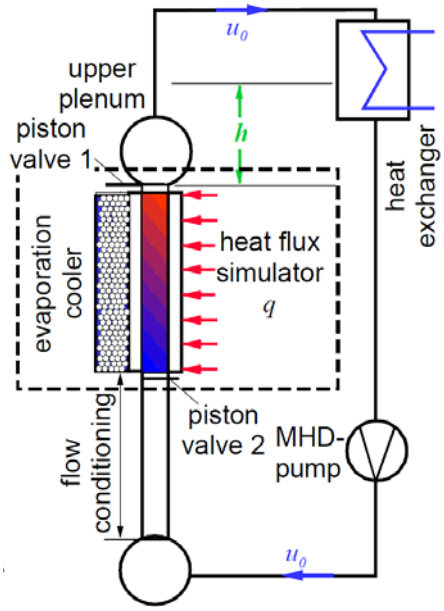

Fig. 6 Sketch of the projected experimental setup to study the transition between free, mixed and forced convection

3.2. Backward facing step

In a further step, the influence of a backward facing step on flow and fluid temperature distribution will be investigated. In this project, the transition from the heat collecting pipes or subassemblies to a collector or upper plenum is investigated. First, a general experiment is planned in KASOLA, which will be supported by experiments in the air-cooled L-STAR facility, also constructed in our institute, to define the parameter range and the geometrical scaling. The L-STAR facility has the advantage that the flow and the temperature patterns are visualised using the experimental techniques Laser Doppler Anemometry (LDA), Particle Image Velocimetry (PIV), and Planar Laser-Induced Fluorescence (PLIF).

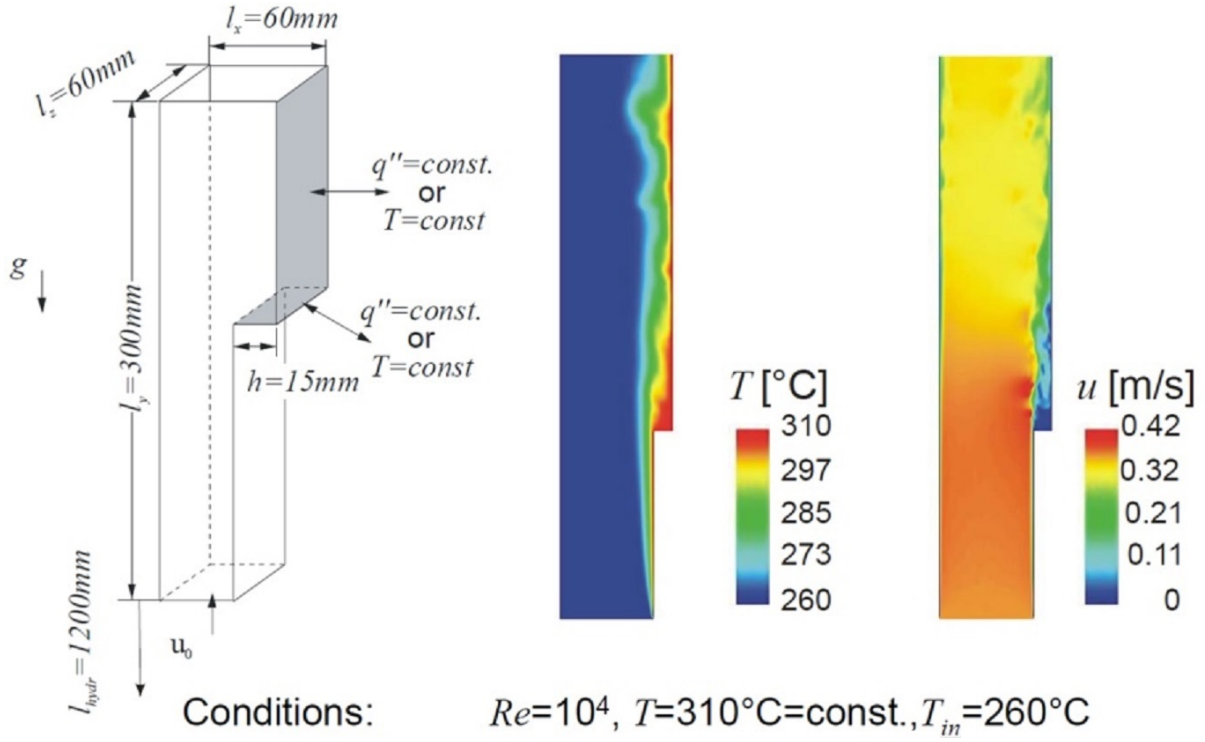

Fig. 7 Sketch of an experiment to investigate the liquid metal flow detachment in a backward facing step (left) and numerical simulation using commercial tool CFX.

3.3. Generic research

Within HEMCP, a cooperation with material research institutes is initiated to identify optimized materials for high temperature applications in liquid metals systems. In this context metal, ceramics and metal/ceramic compounds are investigated. In a first step, separate effect tests investigate material behaviour under stationary or cycling conditions. Finally, such materials are foreseen to be tested in KASOLA facility. Two applications may be considered as a first step.

For energy systems, a fast and robust monitoring of temperatures, mass flow rates at entrance and exit of components (heaters, solar heat receivers, core, etc.) and fluid density (void) is essential for a safe operation. To avoid overheating situations, the fluid state monitoring is important to identify instabilities and/or phase changes due to local overheating.

The behaviour of innovative heat exchangers under various conditions is important to assess the safety features, especially their ability to safely separate sodium in order to avoid its exposure to water or steam. Such a device can be integrated into the versatile test section of the base loop.

The alkali metal thermal energy converter represents a direct heat to electricity converter that typically operates in a temperature range of 700 to 1000 °C and at ambient pressures. The studies will be performed in the frame of the LIMTECH and HEMCP projects and will be focused on issues like material improvement and development, metal ceramic interfaces, stability improvement for long term operation, extension of the operational life time, as well as increase of the efficiency. AMTEC is based on the capability of a specific ceramic that allows the transport of sodium ions, but acts as an isolator against electrons, which are redirected and used for electricity generation. Our studies will benefit from an in-house experimental experience of about 10 years, when several AMTEC prototypes were tested in our institute.

4. Concluding remarks

Sodium has remarkable advantages to transport or to store energy; it is therefore extensively used in large-scale technical applications. Though much research concerning sodium thermal-hydraulic characteristics has been performed in the past, open questions remain for existing and for future systems. To contribute to the solution of such problems, the medium scale experimental facility KASOLA is being erected at KIT, offering three very different test ports for very different applications, such as nuclear power and concentrating solar power, and for very different scientific and technical domains. These research fields range from real size single rod experiments for the detailed investigation of heat transfer between rod surface and the surrounding cooling or heating fluid to studies of flow patterns during the transition from forced to natural convection in the 1:5 model of the upper plenum of a nuclear reactor, but it also includes basic research and the development of instrumentation. The KASOLA facility is presently under construction, and the first commissioning tests are planned for 2013.

8. ACRONYMS

ADS	*Accelerator Driven (subcritical) System*
ADRIANA	*ADvanced Reactor Initiative And Network Arrangement*
ALIP	*Annular Linear Induction Pump*
AMTEC	*Alkali Metal Thermal Energy Convertor*
CFD	*Computational Fluid Dynamics*
CSP	*Concentrating Solar Power*
DHR	*Decay Heat Removal*
FLIP	*Flat Linear Induction Pump*
HEMCP	*Helmholtz Energy Materials Characterization Platform*
HGF	*Helmholtz Society of German Research Centers*
HZDR	*Helmholtz Zentrum Dresden-Rossendorf*
I&C	*Instrumentation and Control*
IHX	*Intermediate Heat Exchanger*
INR	*Institute for Neutron Physics and Reactor Technology*
ISI&R	*In-Service Inspection and Repair*
KALLA	*Karlsruhe Liquid Metal Laboratory*
KASOLA	*Karlsruhe Sodium Laboratory*
KIT	*Karlsruhe Institute of Technology*
LDA	*Laser Doppler Anemometry*
LFR	*Lead Fast Reactor*
LIMTECH	*HGF Alliance on LIquid Metal TECHnology*
MHD	*Magneto-Hydro-Dynamics*
P&I	*Pipe and Instrumentation plan*
PIV	*Particle Image Velocimetra*
PLIF	*Planar Laser-Induced Fluorescence*
SFR	*Sodium Fast Reactor*
TC	*ThermoCouple*

ACKNOWLEDGEMENTS

The work is sponsored by the HGF, especially the HGF-Alliance LIMTECH, the HGF-Platform HEMCP (Helmholtz Energy Materials Characterization Platform), and Programme NUKLEAR at Karlsruhe Institute of Technology (KIT).

REFERENCES

[1] Hillenbrand M. P., (2008) Qualifizierung einer Messtechnik zur Erfassung freier Grenzflächen bei Flüssigmetallen, Forschungszentrum Karlsruhe (FZK) Scientific report, FZKA-7437.

[2] Lefhalm, (2005) Qualifizierung von Meßtechniken zur Erfassung von Strömungsgrößen in flüssigen Schwermetallen, Wissenschaftliche Berichte, FZKA-7111.

[3] HGF-Alliance LIMTECH (http://www.hzdr.de/db/Cms?pOid=36929&pNid=2920).

[4] W. Hering et al., Report on the present situation of instrumentation, diagnostics, experimental devices for experiments and SFR, LFR, and GFR, Deliverable D5.1, Interner Bericht INR 04/11–Nuklear 3430, EU-Programme ADRIANA, Projekt Nukleare Sicherheitsforschung, 18.05.2011.

[5] W. Hering et al., Report on infrastructure road map and future needs for innovative systems development focused on instrumentation, diagnostics and experimental devices, Deliverable D5.2, Interner Bericht INR 05/11–Nuklear 3431, EU-Programme ADRIANA, Projekt Nukleare Sicherheitsforschung, 30.06.2011.

[6] M. Humberstone, B. Wood, J. Henkel, And J. W. Hines, (2011) An Adaptive Model For Expanded Process Monitoring, Nuclear Technology Vol. 173 Jan. 2011.

[7] A. Onea, W. Hering, C. Homann, A. Jianu, M. Lux, S. Scherrer, R. Stieglitz, (2013), Optimization of the KASOLA high temperature liquid metal loop, Paper-ID 545, accepted at the 15th Int. Topical Meeting Nucl. Reactor Thermal-Hydraulics, NURETH 15, Pisa, Italy, May 12–17, 2013.

Preliminary Simulation Results of the Constituent Distribution Model Implemented into the BISON Framework for the Performance Analysis of Metallic Fuels

C. Unal[a], **N.N. Carlson**[b], **J. Galloway**[a]

[a] Nuclear Engineering and Proliferation Division
Los Alamos National Laboratory, Los Alamos, New Mexico, USA

[b] Computer, Computational, and Statistical Sciences Division
Los Alamos National Laboratory, Los Alamos, New Mexico, USA

Abstract. This paper presents the progress of the fuel performance analysis suing BISON fuel performance tool. Within the BISON framework a new Zirconium diffusion kernel was implemented that substantially improved the reliability and stability for solving Zirconium migration problems in metallic nuclear fuels. Several benchmark problems were created, including a simple 1-D rod and several 2-D segments of a fuel rod that covered several temperature regimes. The simulations were then compared to results from the code Pedernal, which is a "high-performance solver for coupled, nonlinear heat conduction and multi-component species diffusion". Comparison between the BISON based solver and Pedernal showed a good agreement for all benchmark cases. Very small differences appeared at longer time frames (2,000 days) for the hotter fuel simulations; however this is believed to be due, primarily, to the different time-stepping algorithms used in the two codes. Overall the domain of the benchmark covered all components of the U-Pu-Zr phase diagram (alpha, delta, beta and gamma phases) and showed a good agreement when compared to Pedernal based results.

1. Introduction

The prediction of fuel behavior under irradiation involves very complex material behavior. The understanding of fundamental mechanisms driving damage production and evolution is not at a desirable level of maturity and, in some cases, does not exist. To make advances toward to the development of predictive tools, it is clear that we need high-performance modeling and simulation (MS) techniques. The recent advances in computer hardware and simulation algorithms enable us now to simulate the atomistic and mesoscale behavior of materials, including radiation-induced damage at submicron scales, with the desired level of accuracy and computational efficiency.

It is also important to recognize that the fuel-clad interactions are primarily 3D in nature. The 1D capability of current models is not very useful for transients and local thermo-chemical interactions. Most material properties are affected by the microstructure characteristics of the materials. Predictions of transient behavior and fuel compressibility and fragmentation (especially for oxide fuels) will require microstructural-based swelling modeling approaches to account for the microchemical evolutions.

Current capabilities are focused on fuel pellets, although it is known that the limiting phenomenon could be associated with the behavior of the fuel assembly (assembly bowing, etc.). It is possible to design a fuel pellet for 40% burn-up, although this design may result in failures at much lower burn-ups because of 3D assembly distortions when it is placed in an assembly for many reasons. In addition, despite the fact that multiple computer codes are developed by many researchers, a robust

predictive capability for quantifying fuel behavior and its uncertainty is still lacking. Large uncertainties and scatters still exist in the predictions, mainly because

- fuel rods are 3D structures, and large deformations may occur;
- fuel assemblies are 3D structures and can behave differently from a single fuel pellet;
- the constitutive materials laws are nonlinear as a result of creep, plasticity, and other material data;
- material behavior is anisotropic and time-dependent;
- material behavior is not fully understood;
- irradiation effects on materials is not a mature science and is not well understood;
- the fundamental data to verify materials modeling is lacking (in some cases, data cannot be taken directly, only indirectly);
- the physical process involved makes it difficult to define separate effects testing by controlling the boundary conditions to validate materials models;
- processes under irradiation conditions occur in a wide variety of time and length scales, each requiring different modeling techniques; and
- integrated multiscale, multiphysics modeling that covers all scales is lacking.

The most desirable approach in fuel modeling is to develop predictive tools with 3D capabilities because the location of fuel-cladding contact becomes critical for fuel-cladding chemical interactions. Some recent attempts have been made to create 3D codes with varying degrees of sophistication.

The primary objective of this work is to develop an initial capability using available models and the 3-D simulation code BISON [1] to analyze various experiments performed by Advanced Fuels Campaign (AFC). BISON is 3-D fuel performance analysis code being developed using the MOOSE [1] framework, a general purpose framework for the solution of differential equation. We developed a constituent distribution model and implemented into BISON framework. We discussed our preliminary results.

2. Constituent redistribution model

In this section we present a model [2] of constituent migration in a binary system that is based on the model developed in [3] for U-Zr nuclear fuel and later used in [4] and [7] in a pseudo-binary study of U-Pu-Zr fuel. A similar model is considered in [5]. These models adapt the original work of Shewmon [6] in the approach to 2-phase regions.

Consider a binary system consisting of components A and B. For simplicity we suppose that within some temperature range the system has a B-poor α phase and a B-rich β phase separated by a 2-phase α+β region . Letting c denote the concentration of B (B atoms per unit volume), we have the conservation law for B:

$$\frac{\partial c}{\partial t} + \nabla \cdot \mathbf{J} = 0, \tag{0.1}$$

where $\mathbf{J}$ is the flux of B atoms. A similar equation for the concentration of A atoms holds but with the opposite flux since we will assume that the net concentration of atoms remains uniform and constant. In a single-phase region we have

$$\mathbf{J} = -D_\pi \left(\nabla c + c \frac{Q_\pi^*}{RT^2} \nabla T \right), \qquad \pi = \alpha \text{ or } \beta, \tag{0.2}$$

where T is the temperature, D_π is the diffusivity of B in phase π, Q_π^* is the heat of transport of B in phase π, and R is the gas constant. The last term involving ∇T is the so-called Soret effect or

thermal diffusion. The coefficient $Q_\pi^{\text{å}}$ may be either positive or negative. This term contributes an advective component to the B flux directed down the temperature gradient toward lower temperatures when positive, and up the temperature gradient toward higher temperatures when negative.

Next consider the 2-phase region very near the solubility limit of B in α. In this case the α phase predominates and we regard it as the connected matrix phase and the remaining B-rich β phase as the precipitant phase, which provides a reservoir of B atoms. The assumption now is that local equilibrium between α and β is maintained at each point in a temperature gradient through instantaneous adjustment of the phase fractions via rapid local diffusion processes. This means that c is constrained to lie on the solubility curve, which we will denote by $c_\alpha(T)$, and as a consequence

$$\nabla c = c'_\alpha(T)\nabla T. \tag{0.3}$$

Shewmon [6] employs a specific differential description of the curve, $c'_\alpha(T) = (\Delta H / RT^2)\, c_\alpha$, where ΔH is a certain enthalpy of solution. Note that this uniquely determines the solubility curve up to an additive constant. The models developed in [4] and [5] adopt this approach, but the expressions they use for ΔH are inconsistent with their phase diagrams, and even have the wrong sign in several cases. Thus for the sake of consistency, our model will adopt the approach where the solubility curves are given explicitly and (0.3) is used directly. If we further assume that the flux of B atoms occurs entirely through the matrix α phase, then we arrive at an expression for the flux $\mathbf{J}$ in the 2-phase region near the α solubility limit,

$$\mathbf{J} = -D_\alpha \left(c'_\alpha(T) + c_\alpha(T) \frac{Q_\alpha^{\text{å}}}{RT^2} \right) \nabla T. \tag{0.4}$$

The analogous argument can be made for the flux in the 2-phase region near the solubility limit of A in β. There the flux is

$$\mathbf{J} = -D_\beta \left(c'_\beta(T) + c_\beta(T) \frac{Q_\beta^{\text{å}}}{RT^2} \right) \nabla T, \tag{0.5}$$

Where $c_\beta(T)$ is the corresponding solubility curve. The general flux in the 2-phase region is then arbitrarily defined to be the phase fraction weighted linear combination of (0.4) and (0.5):

$$\mathbf{J} = -\left[f_\alpha D_\alpha \left(c'_\alpha(T) + c_\alpha(T) \frac{Q_\alpha^{\text{å}}}{RT^2} \right) + f_\beta D_\beta \left(c'_\beta(T) + c_\beta(T) \frac{Q_\beta^{\text{å}}}{RT^2} \right) \right] \nabla T, \tag{0.6}$$

where $f_\alpha + f_\beta = 1$ and $f_\alpha(T, c)$ is the phase fraction of α at temperature T and average composition c and is defined by the lever rule.

2.1. BISON implemention of the model

The preceding model was implemented into the BISON [1] framework. It is very similar to the model of Kim et al. [4] (also [7]). One significant difference alluded to earlier is that it corrects an inconsistency between the enthalpies of solution and the solubility limit curves of the phase diagram. In addition, the implemented form of the model, described below, adds an artificial diffusion term when in the 2-phase regime that stabilizes the standard Galerkin FE method used by BISON.

The zirconium mass conservation equation takes the form

$$\frac{\partial c}{\partial t} = \nabla \cdot \mathsf{D} \nabla c + \nabla \cdot \mathsf{S} \nabla T \tag{0.7}$$

where $c(x,t)$ is the zirconium mole fraction, and $\mathsf{D}(c,T)$ and $\mathsf{S}(c,T)$ are coefficients that depend on the temperature $T(x,t)$ and the zirconium mole fraction.

In a single-phase region of the phase diagram (here α denotes the arbitrary phase) we have the standard diffusion equation with

$$\mathsf{D}(c,T) = D_\alpha(c,T), \qquad \mathsf{S}(c,T) = D_\alpha(c,T)\, c \frac{Q_\alpha^*}{RT^2}, \tag{0.8}$$

where D_α is the diffusivity and Q_α^* the heat of transport of zirconium in the α phase.

In a 2-phase, α+β, region $c_\alpha(T) < c < c_\beta(T)$ bounded by the solubility limit curves c_α and c_β, the Soret term coefficient is

$$\mathsf{S}(c,T) = f_\alpha \mathsf{D}_\alpha(c_\alpha(T),T)\left[\frac{dc_\alpha}{dT} + c_\alpha(T)\frac{Q_\alpha^*}{RT^2}\right] + f_\beta \mathsf{D}_\beta(c_\beta(T),T)\left[\frac{dc_\beta}{dT} + c_\beta(T)\frac{Q_\beta^*}{RT^2}\right], \tag{0.9}$$

where

$$f_\alpha(c,T) = \frac{c_\beta(T) - c}{c_\beta(T) - c_\alpha(T)} \quad \text{and} \quad f_\beta = 1 - f_\alpha \tag{0.10}$$

are the phase fractions of α and β according to the lever rule. In a 2-phase region one ought to take $\mathsf{D}(c,T) = 0$, however this would result in (0.7) becoming purely hyperbolic, and it is well-known that standard centered finite difference or Galerkin finite element schemes are unstable on such equations. Thus to stabilize the scheme used by BISON, we add a bit of artificial diffusion and instead take

$$\mathsf{D}(c,T) = f_\alpha D_\alpha(c_\alpha(T),T)\, d_\alpha + (1 - f_\alpha) D_\beta(c_\beta(T),T)\, d_\beta, \tag{0.11}$$

Where d_α and d_β are dimensionless numerical parameters taken as small as possible while maintaining stability. These parameters can be taken ever smaller with increasing mesh resolution.

2.1.1. Smoothing D *and* S

As defined above, D and S do not vary smoothly (or even continuously) with (c,T) when crossing the phase diagram curves, and consequently the discretized system will be much more difficult to solve than it would otherwise be. We have ameliorated this effect by smoothing these coefficients in a small δ-neighborhood of the phase diagram curves.

First consider a time slab $T_a < T < T_b$ of the phase diagram containing a 2-phase, α+β, region. In the strip $[c_\alpha(T), c_\alpha(T) + \delta]$ bordering the solubility curve c_α we take

$$\mathsf{D}(c,T) = g(s)\, \mathsf{D}_{\alpha+\beta}(c,T) + (1 - g(s))\, \mathsf{D}_\alpha(c,T), \quad \text{with } s \equiv (c - c_\alpha(T))/\delta, \tag{0.12}$$

Where D_α and $\mathsf{D}_{\alpha+\beta}$ denote the original diffusivities in the single and 2-phase regions defined in the

previous section, and g is the smooth function $g(s) = s^2(3-2s)$, for $s \in [0,1]$. Similarly, in the strip $[c_\beta(T) - \delta_1, c_\beta(T)]$ bordering the solubility curve c_β we take

$$D(c,T) = g(s)\, D_{\alpha+\beta}(c,T) + (1-g(s))\, D_\beta(c,T), \quad \text{with } s \equiv (c_\beta(T) - c)/\delta_1. \tag{0.13}$$

Otherwise we do not modify D. The Soret term coefficient S is smoothed in exactly the same way.

Next, when $|T - T_a| < \delta_2$ where the line $T = T_a$ separates two time slabs of the phase diagram (e.g., α–δ and β–γ) we take

$$D(c,T) = (1-h(s))\, D_1(c,T) + h(s)\, D_2(c,T), \quad \text{with } s \equiv (T - T_a)/\delta_2, \tag{0.14}$$

Where D_1 and D_2 denote the *smoothed* diffusion coefficients computed in the time slab below and above $T = T_a$ as just described, and h is the smooth function $h(s) = \frac{1}{4}(s+1)^2(2-s)$, for $s \in [-1,1]$. Otherwise we do not modify the smoothed diffusion coefficient of a time slab. Again, S is smoothed in exactly the same way.

2.2. Application to U-Pu-Zr Nuclear Fuel

We apply the model described above to U-Zr and U-Pu-Zr nuclear fuel. In [4] it is argued that a pseudo-binary treatment of U-Pu-Zr, in which the Pu fraction is held fixed and uniform, is justified both theoretically and on the basis of experimental data which show that the Pu is largely immobile. We consider a fuel with a constant Pu content, and use the simple pseudo-binary phase diagram given in [7], which is based on that from [4]. There are two different sets of 2-phase regions depending on the temperature range: α+δ and β+γ. The evolving Zr mole fraction distribution, $c(x,t)$, is governed by the conservation law (0.7) with coefficients D and S computed as described in Section 2.1.1 using diffusivities, heats of transport, and solubility limit curves corresponding to the local phases involved. In addition we solve for an evolving temperature field using the standard heat equation

$$\rho c_p \frac{\partial T}{\partial t} = \nabla \cdot k \nabla T + q(c,t) \tag{0.15}$$

with a variable heat source q that will depend on the local Zr fraction (actually the local fraction of actinides, which is the complement of the Zr fraction). This is a departure from the model studied in [4] which employed an adjusted fixed temperature profile. In this preliminary work, however, we used a constant, uniform internal heat generation, which will be modified in future work. In this work we compare our results with the Pedernal code, which also used a constant, uniform heat generation source for consistency. The phase properties used in this study are given in Table 1 and are those from [4]. For the remaining material properties that appear in the heat equation we use generic values for U-Zr found on the web: ρ = 19.05 g/cm^3, c_p = 0.3 J/g-K, k = 25.0 W/m-K.

Table 1. Diffusion coefficients, $D = D_0 \exp(-Q/RT)$, and heats of transport for U-Pu-Zr phases.

Phase	α	δ	β	γ
D_0 (m^2/s)	3.0×10^{-6}	3.0×10^{-6}	1.14×10^{-5}	$10^{-5.1-8.05c+9.13c^2}$
Q (kJ/mol)	170	150	180	$128-107c+174c^2$
$Q^{å}$ (kJ/mol)	200	160	450	–200

3. Results

Results generated using Bison are compared to identical problem definitions using the diffusion code Pedernal described in [2]. Several comparison problems were created and will be described. These comparison problems include a simple one-dimensional problem, and three two-dimensional problems pertaining to a quarter disk of a fuel rod where the three problems pertain to the bottom, middle and top of a representative rod with associated temperature distributions.

Once acceptable agreement was achieved for the simple 1-D verification problem (not presented in this paper due to the page limit), with the problem domain encompassing the alpha and delta phases only, a more complex 2-D problem was used as a comparison case. As described in reference [1], this problem is based on the 4S Design 1 test problem studied in reference [4]. One of the U-Pu-Zr fuel designs studied in [4] was proposed for the conceptual 4S reactor. In design 1, the one we will consider here, the Zr content of the fuel is 22 at%, the fuel rod radius is 4.83 mm, and the fuel rod is subjected to a linear power of 19:7 kJ/m. In [4] several 1-D radial simulations were performed with different temperatures at the surface of the rod, reflecting the varying surface temperature along the length of the rod. For our 3-D test problem we will consider a rod of length 500 mm with an imposed surface temperature that varies linearly from 535 ^{o}C at the bottom (z = 0) to 605 ^{o}C at the top (z = 500 mm); these temperatures match the range of surface temperatures considered in [4]. The actual design length of the rod is 2.5 m, but even at 0.5 m the problem is essentially 1-D radial with no appreciable axial transport of heat or Zr. Using a shorter fuel rod allows the use of a somewhat smaller computational mesh with cells having a decent aspect ratio. At the ends of the rod we impose no heat flux, and impose no Zr flux on the entire outer surface of the rod. In this work we used a constant heat generation. Initially the Zr mole fraction is uniformly 0.22 and the temperature is at its quasi-steady state profile. In this study we used $q(c) = \text{constant}$ in both the Bison and Pedernal simulations.

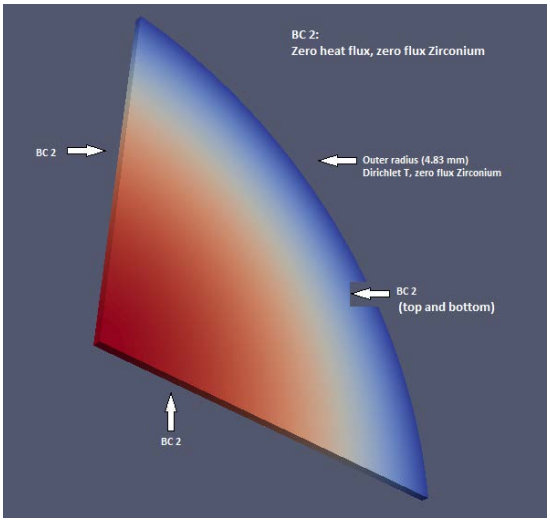

FIG. 1. 2-D rod geometry and BCs.

In reference [2] three radial disks, ¼ symmetry of a rod, were simulated at three different axial heights which span all the four phases of the U-Pu-Zr phase diagram. Figure 1 shows the geometry layout along with the boundary conditions on all sides of the 2-D disk. The outer radius of the rod containing a dirichlet boundary in temperature and a zero flux Zirconium boundary condition, then all other boundaries (top, bottom, x=0, y=0) having zero heat flux, and zero flux Zirconium boundary conditions. A constant, uniform volumetric heat source was simulated, correlated with the stated linear heat generation rate. Running this same problem geometry with Bison and Pedernal, results of Zirconium mole fraction versus rod radial distance were plotted as a function of time for both codes. The results for the rod bottom, rod middle and rod top are shown in Figures 2-4, respectively. In all

three of these cases the agreement is excellent. At most times the results overlay so closely that delineation between the Bison line and the Pedernal line is hard to discern. Particularly, this is the case for all three results for the rod bottom simulation, where the only differences show up at the very rod outer edge, in the last mesh block. For Figure 3, rod middle, this trend still holds true up until the 2000 day simulation, whereupon a very small difference can be noticed near 0.031 meters, where the slop starts to ramp back up, this is the first central where line differentials are even noticed and the results are still in excellent agreement. Finally, the simulation for rod top, Figure 4, as in all cases shows excellent agreement; however a very small difference can be seen in the 2000 day simulation. It is believed the primary reason these small differences start to appear at longer simulation times is that the time step size used in Bison was not identical to that used in Pedernal. In fact, Pedernal has an automatic time stepping algorithm that adjusts the time step size on the fly according to convergence criteria, which will be discussed further in depth later.

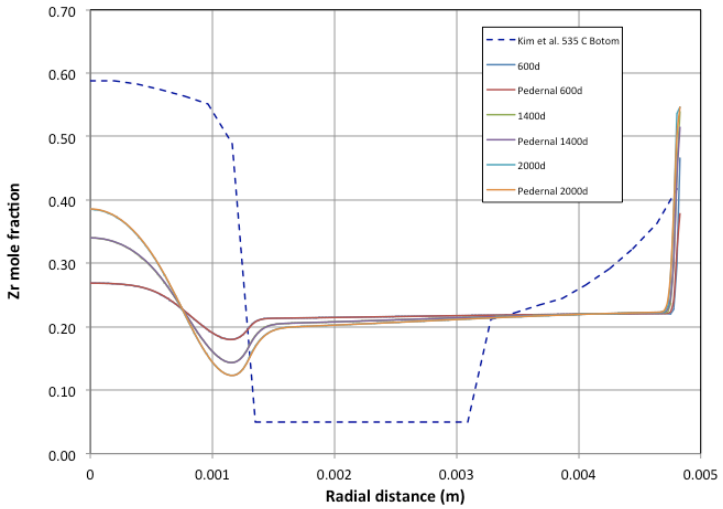

FIG. 2. 2-D rod bottom, Bison-Pedernal comparison.

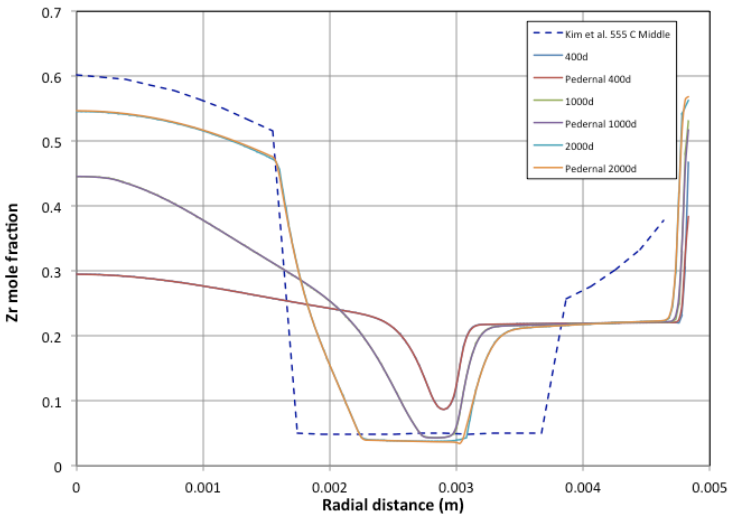

FIG. 3. 2-D rod middle, Bison-Pedernal comparison.

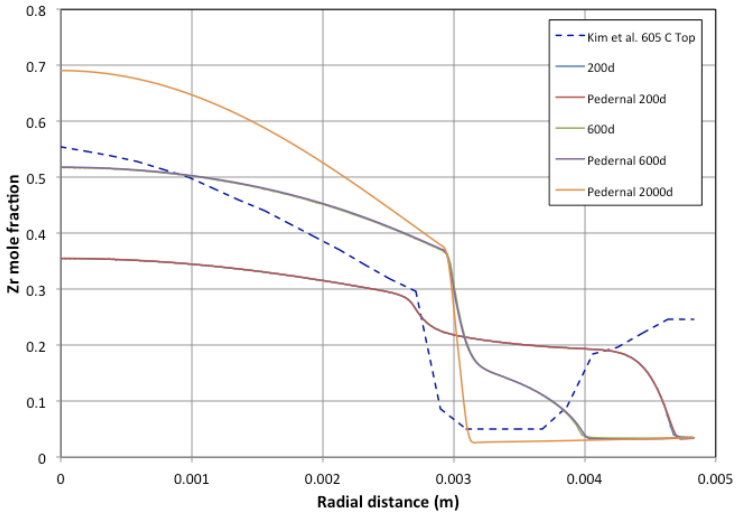

FIG. 4. 2-D rod top, Bison-Pedernal comparison.

Figures 2-4 also show the results of Kim et al. (dashed blue lines). It is clear that there are some differences in the predicted zirconium profiles by BISON [1] using the constituent distribution model presented in this paper and Kim et al. [4]. These differences are primarily due to the temperature boundary conditions that are different in this study. We used a constant heat generation in the pellet and calculate the radial temperature profile that is quite different than the temperature profile used by Kim et al. The radial temperature profile used by Kim et al. was an adjusted temperature profile. In other words the adjusted radial temperature profile is used as a boundary conditions in their diffusion calculation. We plan to use a thermal conductivity model that depends upon temperature as well as zirconium concentration, and zirconium concentration dependent heat generation feature in the future work to account temperature-concentration-power-diffusion coupling correctly.

4. Conclusions

A computer model was developed to calculate constituent redistribution in U-Pu-Zr metallic fuel under irradiation within the MOOSE/BISON framework. This model showed excellent agreement when compared to validation cases executed using the Pedernal code. The modeling and simulation of constituent redistribution is an essential component of the simulation of fuel performance because the change in local composition affects the mechanical and thermal properties of the fuel as well as the radial power distribution. The creation and validation of a robust constituent redistribution model in BISON allows for continued development and refinement of additional pieces for furthering constituent redistribution work. Particularly this can allow for the coupling of thermal conductivity solutions with Zirconium dependencies, as well as heat generation predictions based upon Zirconium concentrations. Further work based upon constituent dependent heat generation calculations may be aided by coupling the BISON constituent redistribution solver to neutronic codes for accurate heat generation calculations in an iterative process based upon the species distribution.

ACKNOWLEDGEMENTS

We would like to thank Jason Hales, Richard Williamson, Pavel Medvedev, Derek Gaston, Steve Hayes, Jon Carmack and Richard Martineau for their help and support. We are very grateful to Kemal Pasamehmetoglu and DOE program manager Frank Goldner for their vision on the science based advanced fuel development program and the support they provided to develop the current analysis capability.

REFERENCES

[1] Williamson RL, Hales JD, Novascone SR, Tonks MR, Gaston DR, Permann CJ, et al. Multidimensional multiphysics simulation of nuclear fuel behavior. Journal of Nuclear

Materials. 2012 April; 423(1-3): p. 149-63.
[2] N.N. Carlson, “Final Report for Work Package LA0915090116: Fuel Performance Simulations,” LA-UR-09-07340, (2009).
[3] G. L. Hofman et al., “Temperature Gradient Driven Constituent Redistribution in U-Zr Alloys,” Journal of Nuclear Materials, Vol. 227, pp. 277-286, (1996).
[4] Y. S. Kim et al., “Modeling of Constituent Redistribution in U-Pu-Zr metallic Fuel,” Journal of Nuclear Materials, Vol. 359, pp. 17-28, (2006).
[5] M. Ishida, T. Ogata, M. Kinoshita, Constituent Migration Model for U-Pu-Zr metallic fast reactor fuel, Nucl. Technol. 104 (1993).
[6] P.C. Shewmon, “The redistribution of a second phase during annealing in a temperature gradient”, Trans. TMS-AIME 212 (1958).
[7] A. Karahan, J. Buongiorno, Modeling of thermo-mechanical and irradiation behavior of metallic and oxide fuels for sodium fast reactors, MIT Center for Advanced Nuclear Energy Systems report MIT-NFC-TR-110 (2009).

DRESDYN - A new platform for liquid metal thermohydraulic studies and measurement technique developments

G. Gerbeth, S. Eckert, F. Stefani, Th. Gundrum

Helmholtz-Zentrum Dresden-Rossendorf, Bautzner Landstr. 400, D-01328 Dresden, Germany

Abstract. The save operation of liquid metal systems in innovative reactor concepts requires appropriate measuring systems and instrumentation, both for the liquid metal single-phase flow as well as for gas bubble liquid metal two-phase flows. At HZDR the large-scale liquid sodium facility DRESDYN (DREsden Sodium facility for DYNamo and thermohydraulic studies) is under construction that will comprise experiments with geo- and astrophysical background as well as experiments for thermohydraulic studies of sodium flows. The development of flow measurement techniques has a long tradition at HZDR. It covers contactless flow-rate sensors, local velocity measurements such as the Ultrasound Doppler Velocimetry (UDV), the Contactless Inductive Flow Tomography (CIFT), as well as X-ray visualizations of liquid metal two-phase flows, which all will be exploited and further developed at an In-Service-Inspection experiment in the framework of DRESDYN.

1. Introduction

Sodium-cooled Fast Reactors (SFR) are well known to exploit available fissile and fertile materials considerably more efficiently than light water reactors. They could also play a key role in closing the fuel cycle by managing high-level wastes, in particular plutonium and other actinides. Interestingly, SFR's have quite a number of intrinsic safety characteristics, including a large margin to the boiling point of sodium, a long thermal response time, a primary system that operates near atmospheric pressure, and an intermediate sodium system between the radioactive sodium in the primary system and the power conversion system. Supported by the Generation IV International FORUM (GIF), there is presently a remarkable renaissance of SFR's. A number of SFR projects are under deployment ore development, including the ASTRID prototype in France [1], the PFBR in India [2], CEFR in China [3], JSFR in Japan [4], BN-800 [5] in Russia, KALIMER-600 in South Korea [6], and a Travelling Wave Reactor in the US [7].

In spite of the undisputable advantages of SFR's, there are two main challenges which both are connected with the use of liquid sodium. The first one is the well-known positive void reactivity, which can possibly be mitigated, though, by the use of moderating layers of either zirconium boride or zirconium hydride [8]. The second one is the high chemical reactivity which requires special precautions to prevent and suppress sodium fires. With view on these two challenges, there is a growing need for small and medium sized liquid sodium experiments to study various thermohydraulic and safety aspects of SFR's, comprising sodium boiling, argon entrainment, bubble detection, sodium flow metering, etc. [9].

An interesting, although less discussed aspect of SFR's is the theoretical possibility of magnetic-field self-excitation (dynamo effect) in helical sodium flows which would be dangereous for a stable reactor performance. Actually, Bevir [10] and Pierson [11] had considered quite early the conditions for self-excitation in the pumps as well as in the core. A first attempt to investigate self-excitation in a liquid sodium flow was undertaken at a test facility for fast breeder pumps in the Leningrad Scientific Research Institute of Electrophysical Apparatus in 1987 [12]. In 1999, the Riga dynamo experiment led to first experimental realization of the homogeneous dynamo effect [13]. Nearly at the same time, the Karlsruhe dynamo experiment showed self-excitation in an assembly of 52 spin-generators [14], a

structure that is already very similar to the flow structure in the core of an SFR. Later then, in 2006, self-excitation was also observed in the so-called von-Kármán-dynamo experiment in Cadarache (France), though only in the presence of soft-iron impellers [15]. This latter constraint was recently explained by the key role of paramagnetic pumping at the interface between materials of different magnetic permeabilities [16][17]. This mechanism is most remarkable with view on the recent activities devoted to the replacement of austenitic steel of the claddings of SFR's by ferritic/martensitic or ODS materials [18]. Given the grave consequences of magnetic self-exsciation in such a modified core, it is certainly worthwhile to continue the investigations of Plunian et al. [19] on the possible influence of magnetic materials on the dynamo conditions in the core of an SFR.

With the planned DRESDYN project (DREsden Sodium facility for DYNamo and thermo-hydraulic studies) at Helmholtz-Zentrum Dresden-Rossendorf (HZDR) we plan to establish a European platform for investigations of various aspects of liquid sodium flows. DRESDYN will comprise experiments with geo- and astrophysical background, including the dynamo effect and the magneto-rotational instability, as well as studies of the thermo-hydraulic and safety behavior of SFR's [20]. In this paper, we will delineate the experiments planned within the DRESDYN project. Prior to this, we will give a summary of our previous achievements with possible relevance to the SFR.

2. Previous achievments

2.1. Measurement techniques for flow velocities

There are various places in an SFR where the reliable and accurate measurement of global or local flow data is of high interest. The flow rate produced by the primary pumps is certainly an important point here. Spatially resolved velocity determination above the core could help to quickly detect any sort of blockage in the subassemblies. An ambitious, though not unrealistic, project is related to the contactless determination of the complete velocity field structure within the reactor vessel.

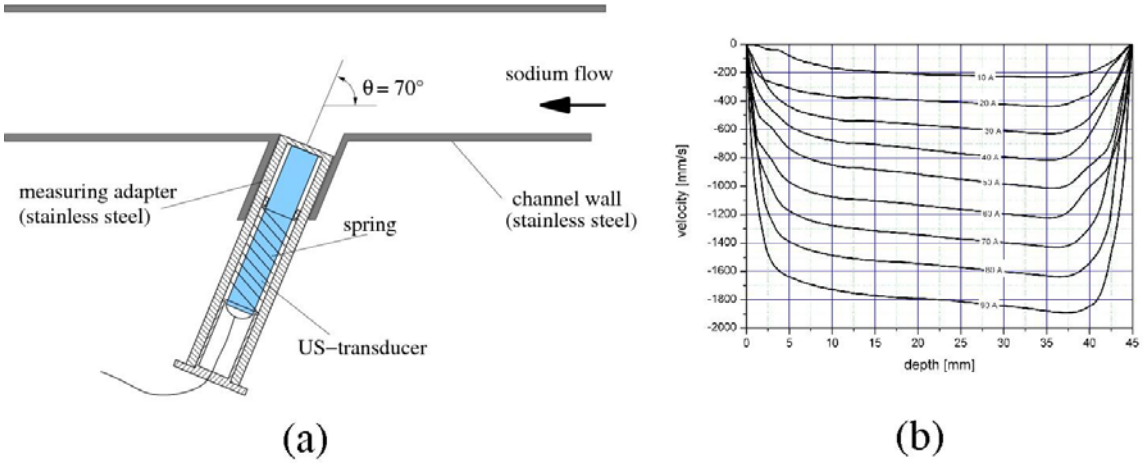

FIG. 1. Application of the Ultrasonic Doppler Velocimetry to a sodium flow in a channel. (a) Schematic view of the installation. (b) Time averaged velocity profile of the sodium flow measured by UDV for variations of the pump current between 10 and 90 A.

The Ultrasonic Doppler Velocimetry (UDV) has become a powerful technique for flow velocity measurements in opaque fluids. Figure 1 illustrates the application of the UDV technique for the determination of a sodium flow in a quadratic duct (for more details, see [21][22]). The facility operates with a sodium flow in the temperature range between 120°C and 350°C. The flow with maximum velocities of about 1.7 m/s is produced by an electromagnetic pump. As shown in Figure 1a the US transducer was installed inside a cylindrical measuring adapter with an angle of 70° with respect to the mean flow. Doppler measurements require the presence of scattering particles inside the

fluid. Artificial or natural particles, like gas bubbles, oxide particles or other solid impurities can serve for this purpose. Within our study we found that the sodium contains a sufficient amount of oxide particles which act as suitable reflecting tracers. The velocity measurement were carried out by the DOP2000 (Signal Processing Lausanne) with a 4 MHz probe of a high temperature series (TR40405). The mean velocity profiles were calculated averaging 256 single profiles corresponding to a measuring time of about 5.6 s. The spatial resolution was 1.25 mm in liquid sodium. A velocity resolution of 9 mm/s was achieved in these experiments. Figure 1b presents the time-averaged velocity profiles measured for various values of the current in the electromagnetic pump. The turbulent profiles exhibit an asymmetrical shape that may arise from the cavity in the channel wall in front of the measuring adapter which has a braking effect on the flow field in its vicinity.

Another probe developed at HZDR is a modified version of the well-known Vives probe [23], see Figure 2. In order to withstand the high velocities in the Riga dynamo experiment, is has been designed in a very robust form with the electrodes positioned at the rim of the cylinder instead of at the tip. The calibration of the probe has been carried out at the sodium loop at HZDR. Figure 2b shows a typical result of this probe from one of the recent campaigns at the Riga dynamo experiment. The red curve shows the time dependence of the propeller rotation rate, the blue and green curves show the measured axial and azimuthal velocity components. At each instant, the data are averaged over 10 seconds in order to average out the effect of the oscillating magnetic eigenfield which adds to the field of the permanent magnet. In this particular campaign the dynamo was not working properly because of the sub-optimal ratio of azimuthal to axial velocity, a fact that is clearly visible in Figure 2b.

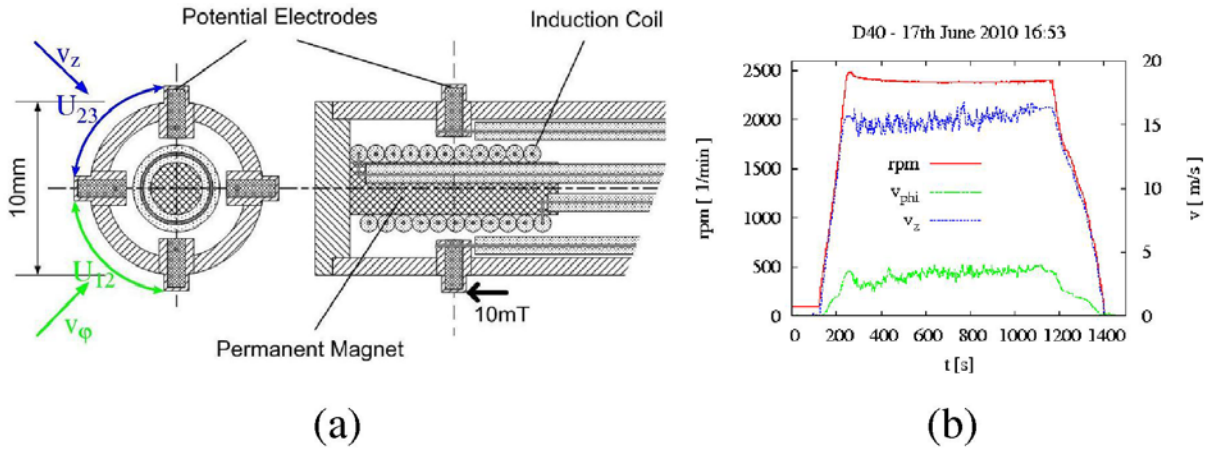

FIG. 2. Measurement of sodium flow velocities up to 20 m/s in the Riga dynamo experiment. (a) A modified Vives probe produced at HZDR. The azimuthal velocity is proportional to U_{12}, the axial velocity is proportional to U_{23}. (b) Measured axial and azimuthal velocity components in the Riga dynamo experiment, together with the rotation rate of the flow driving propeller.

Figure 3a shows a new type of a contactless flowmeter that was also developed at HZDR. This phase-shift sensor works with an alternating magnetic field produced by the emitter coil on one side of the flow channel. Two receiver coils are situated on the opposite side. This set-up is working like an intersected transformer with two secondary coils. We distinguish between the symmetric adjustment and the asymmetric adjustment with some deliberate displacement between the emitter and the receiver coils. The flow in the duct causes a change of the alternating magnetic field. In principle, the amplitude change as well as the phase change can be used for flow rate measurements. In the present realization, the phase difference between two measuring points is used as measuring quantity. More details, in particular a theoretical description of the measuring principle, can be found in [24].

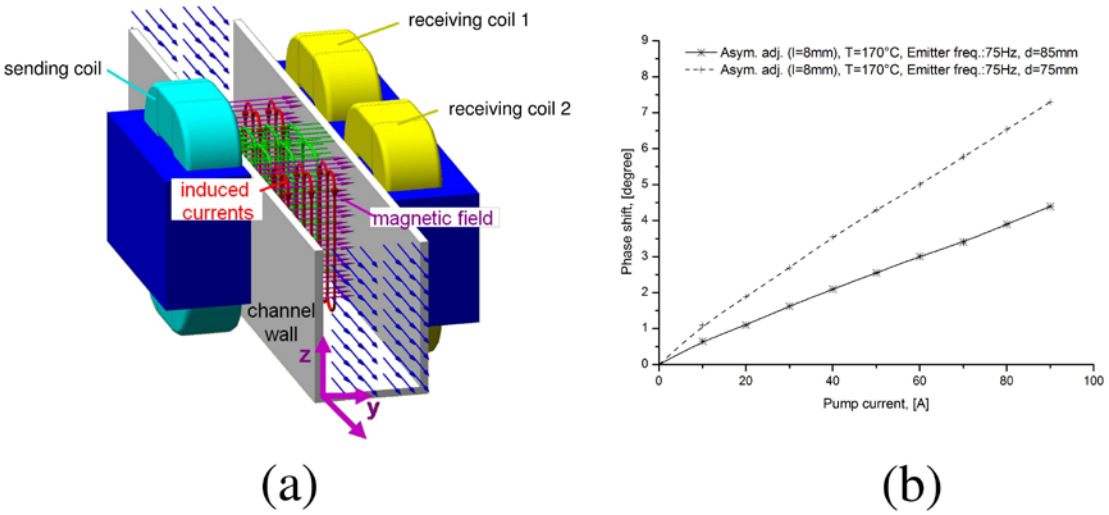

FIG. 3. Application of the contactless phase –shift flowrate sensor. (a) Principle of the sensor: the phase shift between the signals at the two receiving coils is used as a measure for the flow rate. (b) Linear dependence of the measured phase-shift in an asymmetric configuration, with a displacement length of 8 mm and two measurement widths of 75 mm and 85 mm.

Our sensor is equipped with an emitter coil of 500 turns placed at one side of the channel, whereas two receiving coils with 1000 turns are located on the opposite side. The emitter coil is fed by an alternating current up to 3 Amperes. For concentrating and conducting the magnetic flux both the emitter and the receiver coils are furnished with transformer iron of a high permeability (flux-iron). The specific arrangement has been realized for applications at higher temperatures. Both the emitter and receiver coils are protected from the hot channel or pipe by plates made of the ceramic material MARCOR which can resist temperatures up to 800°C. The measurements considered here were conducted with an asymmetric adjustment of the operating coils with a shift of 8 mm. The sensitivity of the sensor is determined by the resolution of the lock-in amplifier. For the measurements in sodium as considered here one obtains a velocity resolution of about 5 mm/s. Figure 3b presents measurements of the phase shift response in an asymmetric adjustment of the phase-shift sensor for an input current of 500 mA. The asymmetric sensor adjustment is preferred because of an increase of the sensitivity with respect to the symmetric adjustment. The measurements were performed at the same sodium channel as shown in Figure 1. Figure 3b displays the linear dependency between the flow-induced phase shift and the performance of the electromagnetic linear pump.

We have also developed a global method that aims at reconstructing whole three-dimensional velocity fields. This Contactless Inductive Flow Tomography (CIFT) relies on the fact that externally applied magnetic fields are disturbed by the flow of a conducting medium, with the magnetic Reynolds number being a measure of the ratio of disturbed to applied magnetic fields. By applying the external field subsequently in different directions it is possible to reconstruct the whole three-dimensional velocity field. For more details on the mathematical foundation of this method and its first application in the metallurgical context, see [25][26][27]. Figure 4a shows the schematic sketch of a liquid metal experiment in which the feasibility of CIFT was proved for the first time. The propeller driven flow of liquid GaInSn in a 17.2 cm diameter/18 cm height cylinder is determined by subsequently applying a magnetic field of around 4 mT in vertical and in horizontal direction. The time-resolution for the measurement of the mean velocity was 6s in those experiments. For the case of an upward pumping of the propeller, Figure 4b shows the induced magnetic fields for vertically applied field, Figure 4c the corresponding field for horizontally applied field. The mean three-dimensional velocity field that is then reconstructed from these two sets of information is shown in Figure 4d.

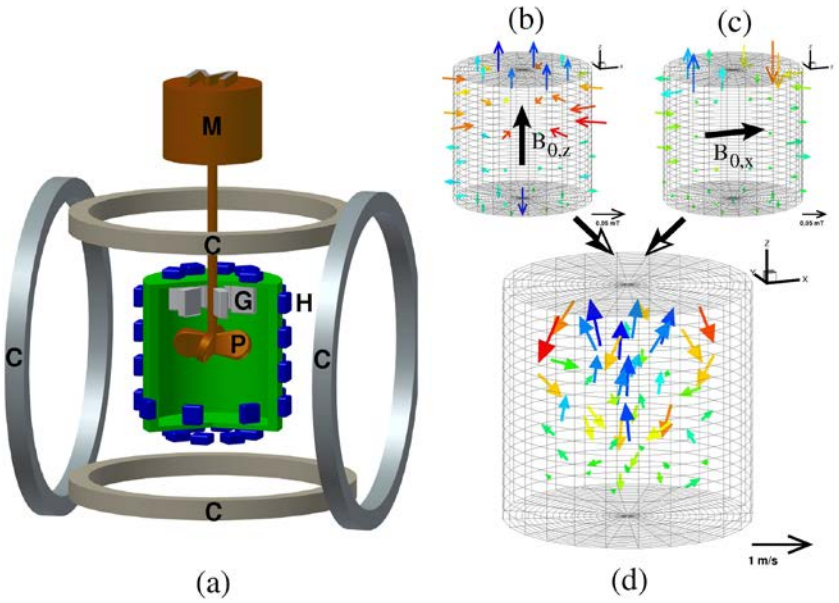

FIG. 4. Contactless Inductive Flow Tomography. (a) Schematic sketch of the CIFT experiment. Two Helmholtz like pairs of coils (c) produce subsequently a vertical and a horizontal magnetic field. The flow produced by the motor (M) driven propeller (P) induces magnetic fields that are measured at the Halls sensors (H). (b) Induced field for vertical applied field. (c) Induced fields for horizontally applied field. (d) Reconstructed velocity field.

2.2. Two-phase flows

In many SFR related problems it is important to detect and characterize two-phase flow pheneomena. This applies in particular to the possibility of argon entrainment and downward transport to the core region, to sodium boiling in the core, and to the appearance of hydrogen bubbles in the proximity of leaks in the steam-generator.

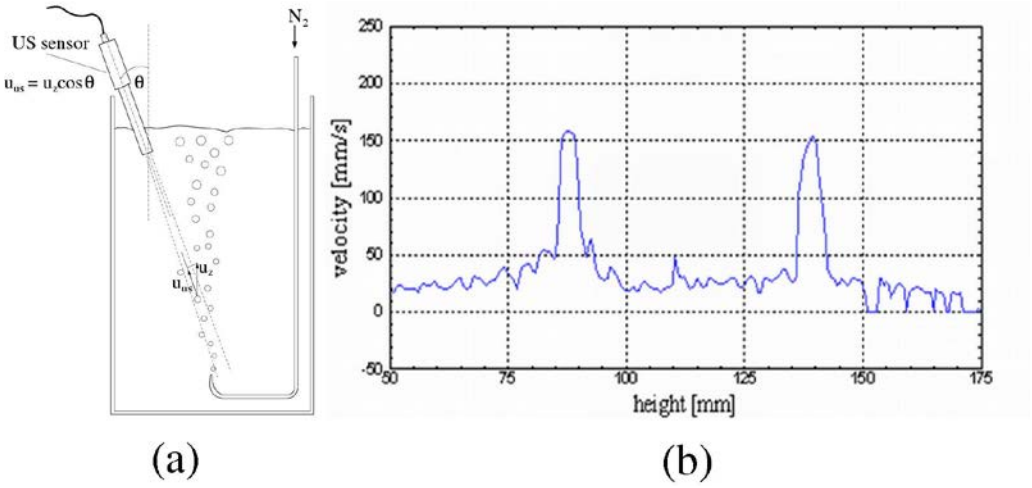

FIG. 5. UDV measurements of a bubble flow in PbBi. (a) Schematic sketch. (b) Typical height dependence of the raw velocity data, containing two bubble signals

We have developed and tested various methods for the measurement of two-phase flows. The first of them relies again on the UDV technique. It has been tested in a two-phase experiment as shown in Figure 5. Nitrogen bubbles were injected into the eutectic alloy PbBi at a temperature of 270°C by means of a single orifice with diameter 0.5 mm. A cylindrical container made of stainless steel with a diameter of 125 mm and a height of 250 mm contains a stagnant pool of about 2.5 l liquid metal. The ultrasonic probe with a special acoustic wave guide [28] was positioned through the free surface at the top with a vertical distance of 150 mm from the orifice position. The measurements were restricted to a single bubbly flow regime at small gas flow rates. Figure 5b shows a typical velocity profile obtained from the bubbly flow. The lower velocity at the small measuring depths corresponds to the liquid metal flow which is driven by the rising bubbles. Two bubble signals were detected showing a higher velocity as the surrounding liquid. In the region of low gas flow rates it was possible to clearly distinguish between the bubble and the liquid velocities.

Another method to investigate two phase flows has been developed by the group of A. Peyton at the University of Manchester. It relies on the dependence of the mutual inductance between two neighboring coils on the material properties in their vicinity. The method has been successfully applied for the determination of the two-phase flow structure in the submerged entry nozzle of a physical model of continuous steel casting at HZDR [29].

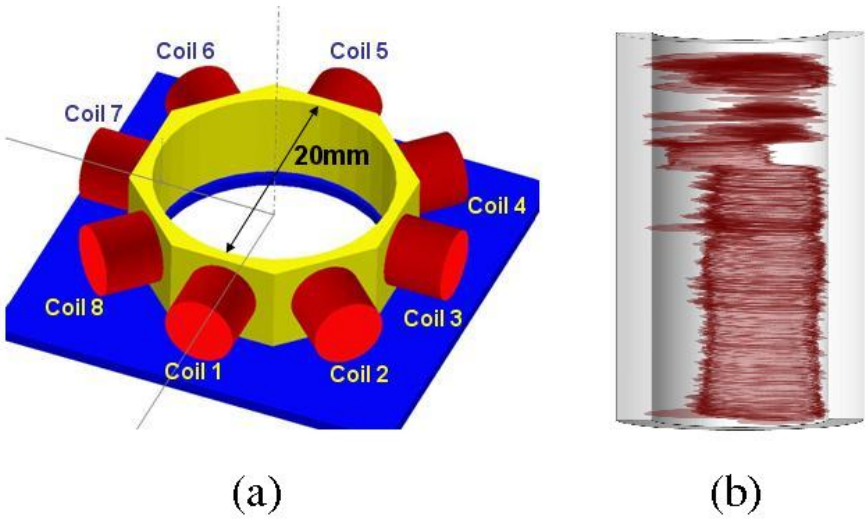

FIG. 6. Application of the Mutual Inductance Tomography (MIT). (a) Coil configuration for determining the conductivity distribution of a two-phase flow in the nozzle of a continuous casting model (figure courtesy N. Terzija). (b) Reconstruction of the surface between GaInSn and Argon in dependence on time (vertical axis).

Figure 6a shows the assembly of 8 coils surrounding the submerged entry nozzle. Using subsequently each of the coils as emitter and the remaining coils as receivers, the method allows the tomographic reconstruction of the distribution of the liquid metal (here GaInSn) and argon. Figure 6b shows an example of the reconstructed time dependence of the liquid metal boundary in the submerged entry nozzle with interesting shape changes.

2.3. Smart heat exchanger

It is well known that one of the most critical places of an SFR is the heat exchanger where large amounts of sodium are in close proximity to large amounts of water and steam. This proximity makes the system prone to energetic reactions. In principle, any sodium-water reactions due to leaks in the steam generator tubes could be avoided by using an intermediate heat transport medium.

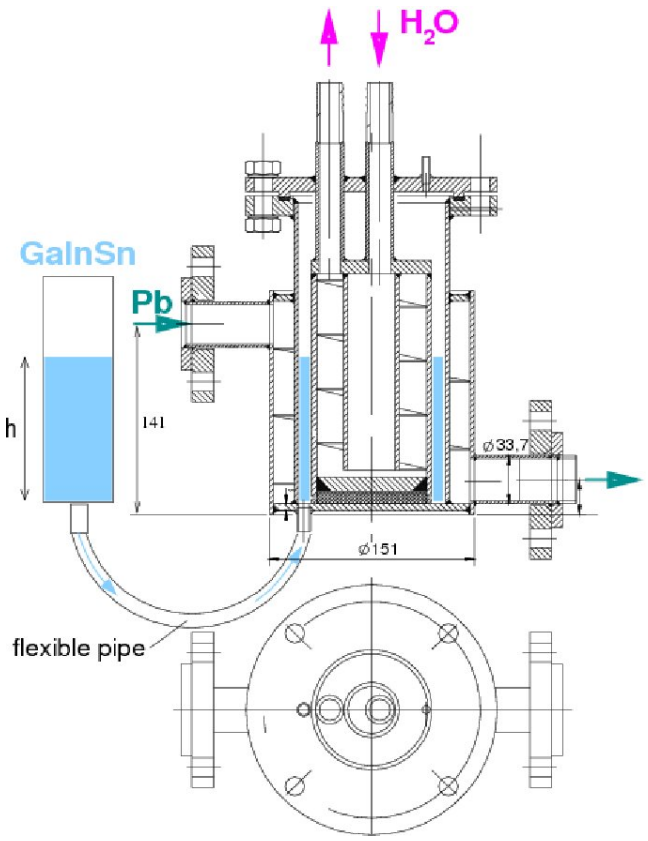

FIG. 7. Smart heat exchanger with GaInSn as an intermediate heat transport medium between hot lead and water.

Although for a quite different purpose, such a heat exchanger between a hot liquid metal and water has been constructed for use in the photo-neutron source nELBE working with a liquid lead target at HZDR [30]. Its main intention was to exclude the possibility of lead-water reactions in the case of leaks by using GaInSn as an intermediate heat transport medium. The configuration shown in Figure 7 has also the interesting advantage that the thermal expansion of GaInSn provides an ideal means for passive regulation of the heat transfer.

2.4. Magnetic field self-excitation and related instabilities

In November 1999, magnetic-field self-excitation had been observed in the Riga dynamo experiment [13] which consists basically of a strong helical flow of liquid sodium complemented by a straight back-flow. One month later, the Karlsruhe dynamo experiment became operative [14]. This experiment consisted of 52 spin generators, a configuration that is already very similar to the conditions in the core of SFR with its wire-wrapped fuel bundles [31][25]. HZDR has contributed significantly to the simulation, optimization, and data analysis of the Riga dynamo experiment [32]. Concerning the Karlsruhe experiment, we have found that a slight geometric modification would have led to a transition from a non-axisymmetric to an axi-symmetric eigenfield [33].

In 2006, a third liquid sodium experiment has shown self-excitation [34]. This so-called *von-Kármán sodium* experiment (VKS) consists if a compact cylindrical vessel wherein two counter-rotating impellers produce a flow with two poloidal and two toroidal vortices. Surprisingly, the observed magnetic eigenfield turned out to be more or less axisymmetric. This was in contrast to all numerical simulations, as was the rather low critical magnetic Reynolds number. Recently, we have explained both facts by the dominant role that is played by the soft-iron impellers [16][17], without which no self-excitation was observed up to present in the VKS experiment.

3. DRESDYN

For the liquid sodium installations in the framework of DRESDYN a new experimental hall with an area of approximately 500 m^2 will be erected between 2013 and 2014. Figure 8 shows a picture of the interiour of the planned experimental hall, with a separate containment for the precession driven dynamo, and sufficient space for a large Taylor-Couette experiment, a liquid metal battery test stand [35], an In-Service-Inspection (ISI) experiment, and a sodium loop. The total inventory of sodium will be 12 m^3.

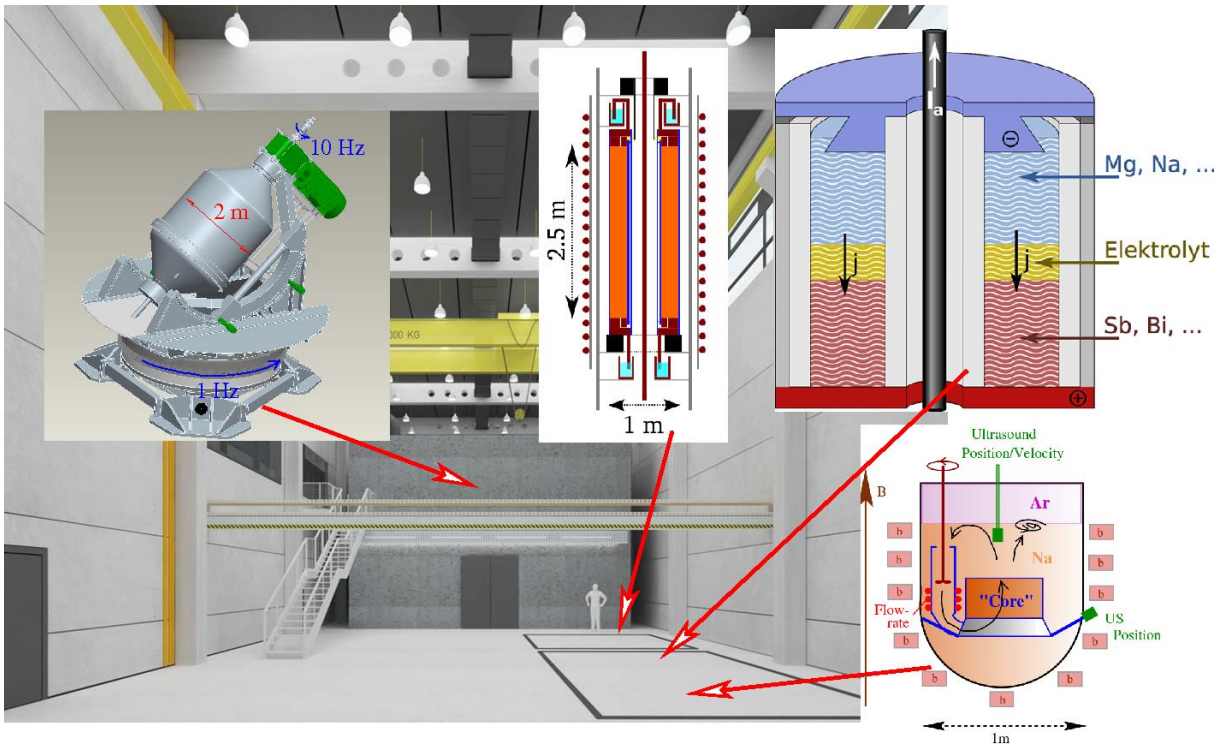

FIG. 8. DRESDYN: View of the interior of the planned experimental hall, with the precession driven dynamo experiment, a Taylor-Couette experiment, a liquid metal battery stand, and an In-Service-Inspection (ISI) experiment.

The most ambitious project in the framework of DRESDYN is a large scale precession dynamo experiment. This experiment is intended to be a truly homogeneous dynamo in the form of a cylindrical vessel of 2 m diameter and height, rotating with up to 10 Hz around its axis, and with up to 1 Hz around a perpendicular axis. The mechanical and safety demands for such a large scale sodium experiment are tremendous, in particular due to the huge gyroscopic torque which requires a massive and solid basement. The second experiment with geo- and astrophysical background is basically a large Taylor-Couette-Experiment with a diameter of 1 m and a height of 2.5 m, embedded into a large coil that produces a strong vertical magnetic field, and the possibility to guide independent electrical currents along the center and through the liquid sodium in the Tayler-Couette cell. This installation will be used to carry out experiments on the magneto-rotational instability and the Tayler instability. Related to that we plan also experiments on large-scale liquid metal batteries using liquid sodium.

A significant portion of the SFR-related experiments will be conducted at an In-Service-Inspection (ISI) experiment which is also illustrated in Figure 8. Basically, it will consist of a heated stainless steel vessel with a diameter of approximately 1 m filled with liquid sodium covered by argon. The internal components will comprise a simple mock-up of a reactor core and a primary pump. The main goal of this facility is to test a variety of measurement techniques for the position of internal components, for flow velocities and argon bubble detection. The latter will include experiments on Argon entrainment on the free surface. DRESDYN will also comprise a liquid sodium loop, which in the long term will replace the presently existing one. This loop will contain various test sections,

among them one section for the test of smart heat exchangers with intermediate heat transfer media. Another suit of experiments will be devoted to the important problem of sodium boiling [36]. Starting with very small experiments at a flat wall, we will go over later to boiling experiments at rods or rod bundles. For the visualization of the boiling we plan to use the above mentioned Mutual Inductance Tomography, as well as X-ray radiography [37] and, in collaboration with another group at HZDR, the ultrafast X-ray tomography [38].

Depending on the results of presently ongoing computer simulations concerning the effect of ferritic/martensitic materials on the self-excitation condition in the core, we also consider to do experiments on this topic.

4. Conclusions

After having summarized our previous work on measurement techniques and on the dynamo effect in liquid metals, we have sketched the liquid sodium activities that are planned first in the framework of the DRESDYN project. Yet, DRESDYN should be considered as an open platform for further projects to study various aspects of sodium flows, and corresponding proposals are highly welcome.

ACKNOWLEDGMENTS

This work was supported by Deutsche Forschungsgemeinschaft in frame of the collaborative research programme SFB 609, and by the European Commission in frame of the Project CP-ESFR under grant agreement No. 232658. We thank A. Peyton from the University of Manchester for the collaboration on the Mutual Inductance Tomography for two-phase flow.

REFERENCES

[1] BEILS, S. et al, Safety approach and R&D program for future French sodium-cooled fast reactors, J. Nucl. Sci. Techn. 48 (2011) 510.
[2] CHETAL, S.C. et al., The design of the prototype fast breeder reactor, Nucl. Eng. Des. 236 (2006) 852.
[3] MI, X., Fast reactor technology R&D activities in China, Nucl. Eng. Techn. 39 (2007) 187.
[4] KOTAKE, S. et al., Development of advanced loop-type fast reactor in Japan, Nucl. Tech. 170 (2010) 133.
[5] SAREEV, O.M. et al., BN-800 design validation and construction status, Atomic Energy 108 (2010) 248.
[6] HAHN, D. et al., Conceptual Design of the Sodium-cooled Fast Reactor KALIMER-600, Nucl. Eng. Techn. 39 (2007) 193.
[7] AHLFELD, C. et al., "Conceptual design of a 500 MWe travelling wave demonstration reactor plant", ICAPP 2011, Nice (2011), CD-ROM file 11199
[8] MERK, B. et al., Use of Zirconium-Based Moderators to Enhance Feedback Coefficients in a MOX-Fueled Sodium-Cooled Fast Reactor, Nucl. Sci. Eng. 171 (2012) 136.
[9] TENCHINE, D., Some thermal hydraulic challenges in sodium cooled fast reactors, Nucl. Eng. Des. 240 (2010) 1195.
[10] BEVIR, M.K., Possibility of electromagnetic self-excitation in liquid-metal flows in fast reactors, J. Br. Nucl. Energy Soc. 12 (1973) 455.
[11] PIERSON, E.S., Electromagnetic self-excitation in liquid-metal fast breeder reactors, Nucl. Sci. Eng. 57 (1975) 155.
[12] GAILITIS, A. et al., Experiment with a liquid-metal model of an MHD dynamo, Magnetohydrodynamics 23 (1987) 349.
[13] GAILITIS, A. et al., Detection of a flow induced magnetic field eigenmode in the Riga dynamo facility, Phys. Rev. Lett. 84 (2000) 4365.

[14] STIEGLITZ, R., MÜLLER, U., Experimental demonstration of an homogeneous two-scale dynamo, Phys. Fluids 13 (2001) 561.
[15] BERHANU, M. et al., Dynamo regimes and transitions in the VKS experiment, Eur. Phys. J. B 77 (2010) 459.
[16] GIESECKE, A., STEFANI, F., GERBETH, G., Role of soft-iron impellers on the mode selection in the von Kármán-sodium dynamo experiment, Phys. Rev. Lett. 104 (2010) 044503.
[17] GIESECKE, A. et al., Influence of high permeability disks in an axisymmetric model of the Cadarache dynamo experiment, New J. Phys. 14 (2012) 053005.
[18] DUBUISSON, P. et al., ODS Ferritic/martensitic alloys for sodium fast reactor fuel pin cladding, J. Nucl. Mater. 428 (2012) 6.
[19] PLUNIAN, F., ALEMANY, A., MARTY, P., Influence of magnetohydrodynamic parameters on electromagnetic self-excitation in the core of a fast breeder reactor, Magnetohydrodynamics 31 (1995) 382.
[20] STEFANI, F. et al., DRESDYN – A new facility for MHD experiments with liquid sodium, Magnetohydrodynamics 48 (2012) 103.
[21] ECKERT, S., GERBETH, G., Velocity measurements in liquid sodium by means of ultrasound Doppler velocimetry, Exp. Fluids 32 (2002) 542.
[22] ECKERT, S. et al., Some recent developments in the field of measurements techniques for liquid metal flows, J. Nucl. Sci. Techn. 48 (2011) 490.
[23] RICOU, R., VIVES, C., Local velocity and mass transfer measurements in molten metals using an incorporated magnet probe, Int. J. Heat Mass Trans. 25 (1982) 1579.
[24] PRIEDE, J., BUCHENAU, D., GERBETH, G., A contactless electromagnetic flowrate sensor based on phase-shift measurements, Meas. Sci. Techn. 22 (2011) 055402.
[25] STEFANI, F., GERBETH, G., A contactless method for velocity reconstruction in electrically conducting fluids, Meas. Sci. Techn. 11 (2000) 758-765.
[26] STEFANI, F., GUNDRUM, T., GERBETH, G., Contactless inductive flow tomography, Phys. Rev. E 70 (2004) 056306.
[27] WONDRAK, T. et al., Contactless inductive flow tomography for a model of continuous steel casting, Meas. Sci. Techn. 21 (2010) 045402.
[28] ECKERT, S., GERBETH, G., MELNIKOV, V.I., Velocity measurements at high temperatures by ultrasound Doppler velocimetry using an acoustic wave guide, Exp. Fluids 35 (2003) 381.
[29] TERZIJA, N. et al., Electromagnetic inspection of a two-phase flow of GaInSn and argon, Flow Meas. Instr. 22 (2011) 10.
[30] ALTSTADT, E. et al., A photo-neutron source for time-of-flight measurements at the radiation source ELBE, Ann. Nucl. Ener. 35 (2007) 36.
[31] BUBELIS, E., SCHIKORR, M., Review and proposal for the best fit of wire-wrapped fuel bundle fraction factor and pressure drop predictions using various existing correlations, Nucl. Eng. Des. 238 (2008) 3299.
[32] STEFANI, F., GAILITIS, A., GERBETH, G., Magnetohydrodynamic experiments on cosmic magnetic fields, ZAMM 88 (2008) 930.
[33] AVALOS-ZUNIGA, R. et al., Cylindrical anisotropic α^2-dynamos, Geophys. Astrophys. Fluid Dyn. 101 (2007) 389.
[34] MONCHAUX, R. et al., Generation of a magnetic field by dynamo action in a turbulent flow of liquid sodium, Phys. Rev. Lett. 98 (2007) 044502.
[35] STEFANI, F. et al., How to circumvent the size limitation of liquid metal batteries due to the Tayler instability, Energy Conversion and Management 52 (2011) 2982.
[36] KOTTOWSKI, H.M., SAVATTERI, C., Fundamentals of liquid metal boiling thermohydraulics, Nucl. Eng. Des. 82 (1984) 281.
[37] BODEN, S., ECKERT, S., GERBETH, G., Visualization of freckle formation induced by forced melt convection in solidifying GaIn alloys, Materials Letters 64 (2010) 1340.
[38] FISCHER, F., HAMPEL, U., Ultra-fast electron beam X-ray computed tomography for two-phase flow measurements, Nucl. Eng. Des. 240 (2010) 2254.

Experimental demonstration of gas entrainment into liquid metals

S. Eckert, T. Vogt, S. Boden, N. Shevchenko, G. Gerbeth

Helmholtz-Zentrum Dresden-Rossendorf (HZDR), Institute of Fluid Dynamics, 01314 Dresden, Germany

Abstract. Entrainment of cover gas into the liquid metal coolant is one of the essential safety issues in the design of innovative liquid metal-cooled fast reactors. We present experimental studies of this phenomenon in low-melting metals. Ultrasonic and X-ray were considered as diagnostic tools for a visualization of gas entrainment at the free surface of the melt. Laboratory experiments were conducted using the eutectic alloy GaInSn which is liquid at room temperature. The vortex activated entrainment of air at the free surface of a rotating flow was disclosed by means of ultrasonic techniques. The X-ray radioscopy was used to visualize the behaviour of Argon bubbles inside a slit geometry. The measurements reveal distinct differences between water and GaInSn especially with respect to the process of bubble formation, the coalescence and the breakup of bubbles. Our results emphasize the importance of liquid metal experiments which are able to provide a suitable data base for numerical code validation.

1. Introduction

The control of gas entrainment at the free surface of the liquid pool belongs to the thermohydraulic challenges for operating liquid metal cooled fast reactors [1]. The entrainment of a significant amount of cover gas by the liquid metal flow carries the risk that burst of gas bubbles may run through the reactor core causing a change in reactivity. Moreover, the occurrence of bubbles at the fuel rods impairs the heat removal, or the gas can cause other operational problems, for instance, fluctuations in the pump discharge. Several mechanism for bubble entrainment are considered to be possible in liquid metal cooled reactors [1][2][3]: vortex activated entrainment, entrainment due to surface waves, liquid fall entrainment. The main source for entrapping gas is the presence of either van-Karman vortices behind immersed structures or so-called “bathtub” vortices developing in rotating flows. A great deal of work has been conducted so far by many research groups in order to study the mechanisms of gas entrainment and to identify efficient measures for mitigation of oh this phenomenon (see for instance [2-7]). The majority of publications deal with numerical simulations and experimental studies using water models. The shortage of suitable measuring techniques can be considered as a main reason why the number of experimental studies providing data from liquid metal flows is readily comprehensible. However, the development of new innovative diagnostic tools based on ultrasonic, inductive and radiation techniques saw a boost during the last decade.

Within this paper we want to demonstrate the capabilities of ultrasonic techniques and X-ray radioscopy to detect gas entrainment at the free surface of liquid metal flows. We present two experiments here. The first example considers a rotating flow in a liquid metal column, which is driven by a combined action of a rotating and a traveling magnetic field. The gas entrainment is induced by tornado-like flow structures forming a kind of bathtub vortex. An ultrasonic method was used to track the position of the free surface and to detect gas bubbles

being entrapped inside the bulk liquid. Another experiment employs the X-ray radioscopy to visualize rising gas bubbles in a rectangular box. The bubbles drive an intensive jet-like flow which generates perturbations and waves at the free surface. The X-ray images show the entrainment of individual bubbles at outlying positions with respect to the bubble jet.

2. Rotating Flow

When rotation is added to a converging flow, an intense vortex results in many spectacular flows ranging from bathtub vortex to tropical cyclones. The spin-up of a concentrated, tornado-like vortex in a liquid metal cylinder and was realized experimentally on laboratory scale by using two independent magnetic body forces, a rotating magnetic field (RMF) and a vertically travelling magnetic field (TMF). The surface deformation and the gas entrainment into the liquid metal were observed by means of the ultrasound Doppler method.

2.1. Experimental setup

Figure 1 shows a schematic drawing of the experimental setup. The experiments were carried out in a cylindrical vessel which is made of Perspex. The cylinder has an internal diameter of $D_0 = 2*R_0 = 170$ mm and was filled up to a height of $H_0 = 170$ mm with the eutectic alloy GaInSn, which is liquid at room temperature. Material properties of the GaInSn alloy can be found in [8]. The free surface of the liquid metal was covered with a thin hydrochloric acid layer in order to avoid undesired oxidation effects of the GaInSn alloy. The measuring cylinder was placed in the middle of the 200 mm bore hole of the magnetic induction system PERM at Helmholtz-Zentrum Dresden-Rossendorf. The PERM stirrer is designed to create an RMF with field strengths up to 17 mT and a TMF up to 15 mT. The spatial homogeneity of the magnetic fields was verified using a 3-axis Gauss meter (Lakeshore model 560, sensor type MMZ2560-UH). The deviation of the field strength within the measuring volume was found to be less than 5%.

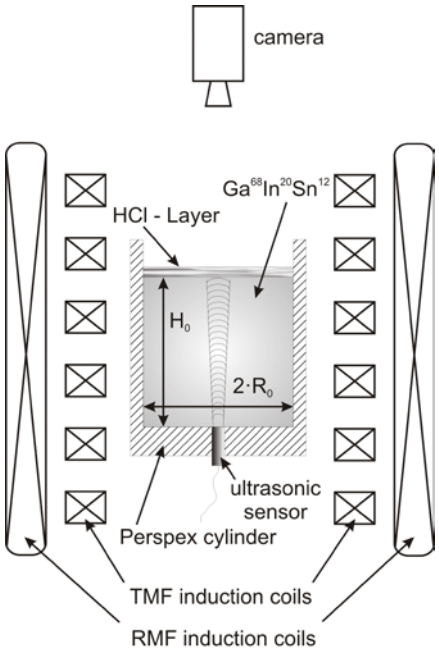

Fig 1. Schematic drawing of the experimental setup

The surface deformation and the detection of the entrained gas was realised using a modified ultrasound Doppler velocimetry (UDV). This method is based on an impulse echo technique and is suitable to deliver instantaneous velocity profiles in opaque fluids. It was adopted by Takeda [9] for experimental fluid dynamics since about 20 years. These days, the ultrasound Doppler velocimetry has become an accepted measuring technique for flow investigations in various liquid metals such as mercury [10], sodium [11] or alloys up to temperatures of about 700°C [12]. In the present study we have utilised the DOP2000 velocimeter (model 2125, Signal Processing SA, Lausanne) equipped with a 4 MHz transducer that was placed at the bottom wall of the vessel in a way that the ultrasonic beam coincides with the rotational axis of the cylindrical vessel. Instead of recording fluid velocities, we have used the UDV-device for the detection of the free surface of the liquid metal by recording the ultrasound echo of the free surface and the echo from the entrained gas bubbles.

2.2. Detection of the gas-liquid interface

In the following we will present some preliminary results that will show the ability of the measuring system to detect gas entrainment into a swirling liquid metal flow. Actually, the aim of these experiments was the funnel depth detection of a tornado which occurs when a TMF is suddenly imposed on an already slowly a rotating liquid metal driven by a weak RMF in this experiment. At the beginning of each measurement, the liquid metal was in a quasi-stationary swirling motion driven by the RMF. At the time t = 0 s, the rotating fluid is exposed to a strong, upwards directed TMF. The following transient flow pattern is accompanied by a tornado like flow pattern at the rotational axis of the liquid metal. The tornado can be observed only during the first couple of seconds where the flow field is still axisymmetric. After a few seconds, the flow is becoming highly turbulent and the liquid metal tornado breaks down into turbulent spots. The depth of the tornado mainly depends on the field strength ratio of the TMF to the RMF [13]. This ratio can be expressed in terms of non-dimensional parameters (F and Ta) as follows:

$$\frac{F}{Ta} = \frac{\omega_{TMF}}{\omega_{RMF}} * \frac{B_{TMF}^2}{B_{RMF}^2} * \frac{\kappa R_0}{2}$$

In this equation, ω_{TMF} and B_{TMF} stand for the frequency and amplitude of the TMF. Accordingly, ω_{RMF} and B_{RMF} denote the frequency and amplitude of the RMF. $\kappa = 21.8\ m^{-1}$ is the wave number of the TMF.

The higher the F/Ta ratio, the deeper the tornados funnel. But also, the deeper the tornados funnel, the narrow it becomes. Fig. 2 shows the result of the funnel depth detection using the ultrasound echo at the free surface of the liquid metal. Fig. 2(a) depicts a measurement that was recorded at a rather low F/Ta ratio. The vertical axis in these contour plots represents the height of the vessel whereas the abscissa is determined by the running time of the TMF that was switched on at the time t = 0 s. The color scale represents the echo intensity following ultrasound bursts emitted from the ultrasound transducer that was placed at the bottom of the vessel. In this particular example a very weak tornado can be observed which has its maximum depth of approximately 20 mm at t = 0.7 s. The corresponding visual monitoring of the free surface by a video camera revealed a collapse of the tornado at about 1.2 s. The following surface deformations are caused by turbulence.

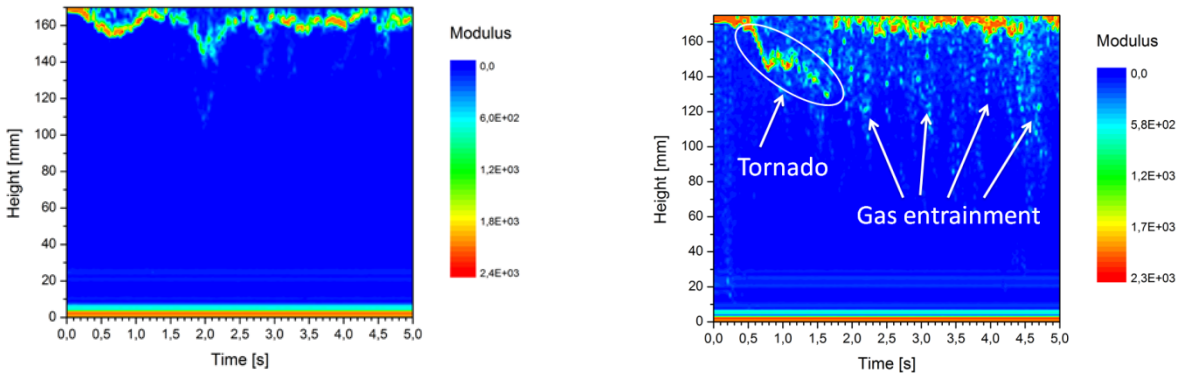

(a) (b)

Figure 2: Free surface detection by ultrasonic methods during a TMF spin-up in a rotating liquid metal: (a) F/Ta = 100, B_{RMF} = 2.71 mT; B_{TMF} = 14.1 mT; (b) F/Ta = 400, B_{RMF} = 1.36 mT; B_{TMF} = 14.1 mT.

Fig. 2(b) shows a measurement where the F/Ta ratio is significantly higher. The tornado funnel is formed at t = 0.5 s and collapses approximately at t = 1.7 s. The maximum funnel depth is about 30 mm. A snapshot of the free surface during the lifetime of the tornado is shown in Fig. 3(a). After the collapse of the tornado funnel a lot of ultrasonic echoes become visible below the free surface of the liquid metal at H_0 = 170 mm (Fig. 2(b)). These echoes are reflected at gas bubbles which are entrapped into the liquid metal. Our experiments have shown two different stages of the gas entrainment. During the first stage, air is sucked into the liquid metal at the bottom of the tornado funnel. This stage occurs in the case of very high F/Ta ratios where the tornado funnel is very deep and thin. Fig. 4 shows a measurement at F/Ta = 700 where this gas entrainment at the bottom of the tornado can be observed. The second stage of the gas entrainment occurs abruptly at the moment where the tornado collapses. The gas which is entrained during the two stages of gas entrainment remains in the liquid metal as long as the TMF is turned on. Immediately after shut down the TMF, a large amount of gas bubbles can be observed at the free surface (Fig. 3(b).

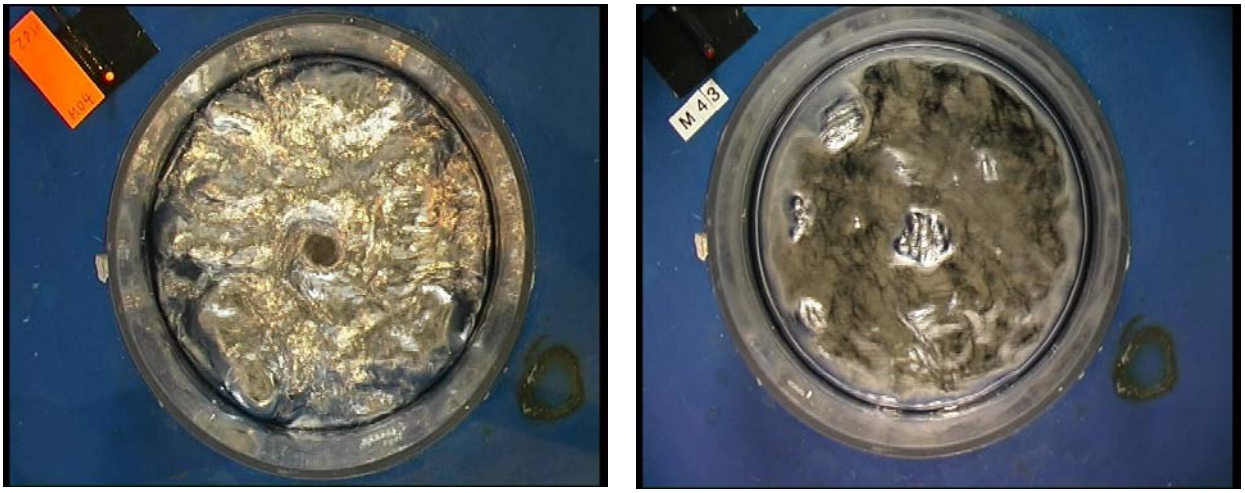

(a) (b)

Figure 3: Snapshots of the free surface of the melt: (a) Forming of a liquid metal funnel during the tornado; (b) Emergence of gas bubbles at the free surface after the TMF shut-down. F/Ta = 400.

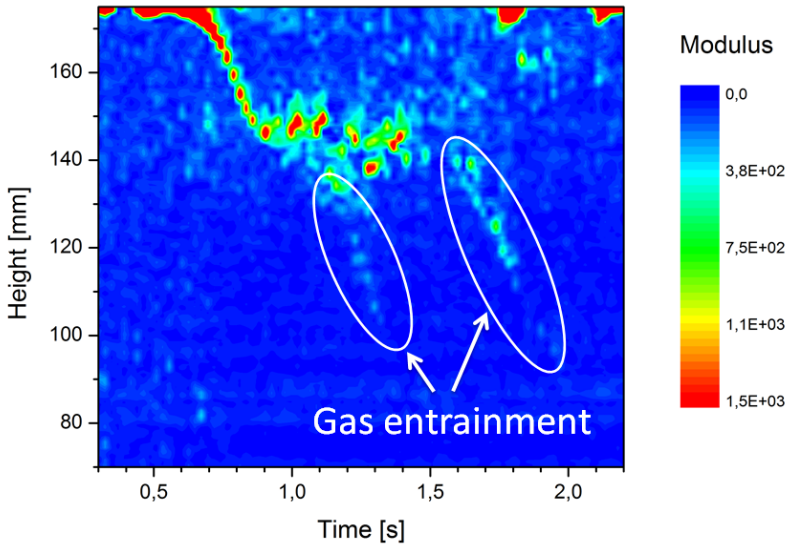

Figure 4: Detection of gas entrainment at the bottom of the tornado funnel, F/Ta = 700, B_r = 1 mT; B_t = 14.1 mT.

3. X-ray visualization of gas bubbles in liquid metals

X-ray attenuation techniques can be used to visualize multiphase flows in opaque materials, in particular liquid metals. An X-ray radioscopic visualisation method was used in the present study to investigate the behaviour of a gas-liquid metal two-phase bubbly flow arising from a horizontal gas injection into a narrow liquid metal bubble column with rectangular cross-section. Dedicated software tools provide information with respect to characteristic bubble quantities such as position, trajectory, size and velocity.

3.1. Experimental setup

A typical experimental setup used at HZDR is shown in Fig. 5(a). A parallelepidepic container of acryl glass with an rectangular inner cross section of 200 × 12 mm^2 was filled with GaInSn up to a height of 300 mm. Argon gas is injected through two opposing cylindrical nozzles made from stainless steel 30 mm above the container bottom. The inner and outer diameters of the nozzles were 0.5 mm and 4.0 mm, respectively. Argon gas flow rates through the nozzles were set independently by two mass flow controllers. The gas flow rate at the particular nozzle was varied between 100 and 3500 sccm (cm^3/min at norm conditions). The X-ray radioscopy setup used for visualisation experiments is schematically depicted in figure 5(b). An X-ray tube produces a continuous X-ray beam penetrating the liquid metal along the narrow extension of the container. The outgoing beam comes upon a scintillation screen where its intensity is converted into visible light which is deflected by a mirror and projected by a lens system onto a CCD camera. The distances between the X-ray source and the bubble column as well as between the scintillation screen and the optical system of the camera were varied to adjust different field of views (FOV). A shorter distance increases the signal to noise ratio, but reduces the FOV. FOV's of 75 × 170 mm^2 and 200 × 150 mm^2 were used for visualisations of the free surface of the liquid metal, the bubble plume and the entrainment of gas bubbles beneath the free surface.

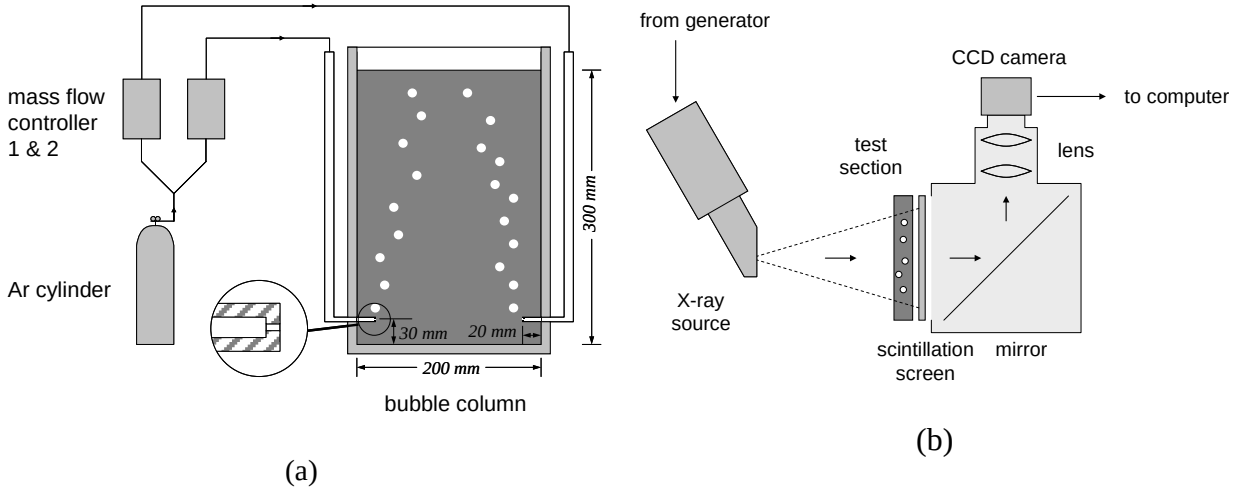

Figure 5: Experimental setup: (a) Sketch of the two-phase flow experiment (the narrow side of 12 mm was along the X-ray beam); (b) Schematic view of the X-ray radioscopy setup.

3.2. Visualization of bubbly flows and gas entrainment at a strongly perturbed surface

The presentation of the experimental results will be started with a comparison between an air-water and an argon-GaInSn flow. First experiments consider the effect of a simultaneous gas injection at gas flow rates of 1000 sccm through both nozzles at the opposite sides of the fluid vessel (see Fig. 6). The two-sided gas injection creates a double-roll convection with an ascending flow in the bubble region near the side walls and a descending flow around the centre of the container. The comparison between the water and the liquid metal flow in Fig. 6 discloses distinct differences concerning the internal structure the bubbly flow. The considerably higher surface tension of GaInSn ($\sigma_S \sim 0.53$ N/m [8]) provokes the formation of larger gas bubbles as observed in the corresponding situation for water. The liquid metal flow shows a higher tendency of bubble collision and following coalescence. The rising bubbles in GaInSn ascend closer to the container side walls having a perceptible consequence on the global flow in the cell (respective flow measurements are not shown here).

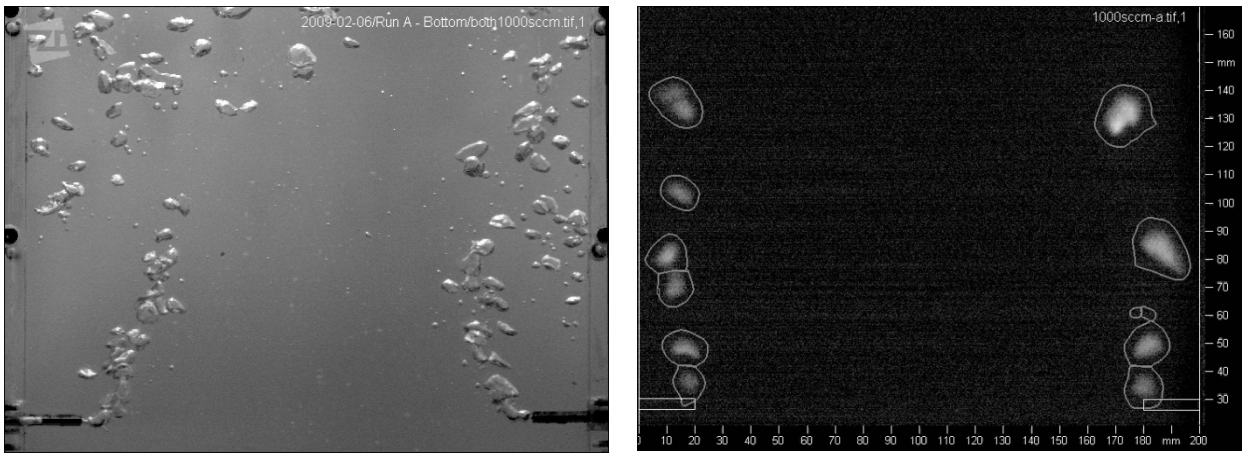

(a) (b)

Figure 6: Snapshots showing the bubbly flow resulting from a simultaneous gas injection through both nozzles (Qg = 1000 sccm): (a) air-water; (b) argon-GaInSn.

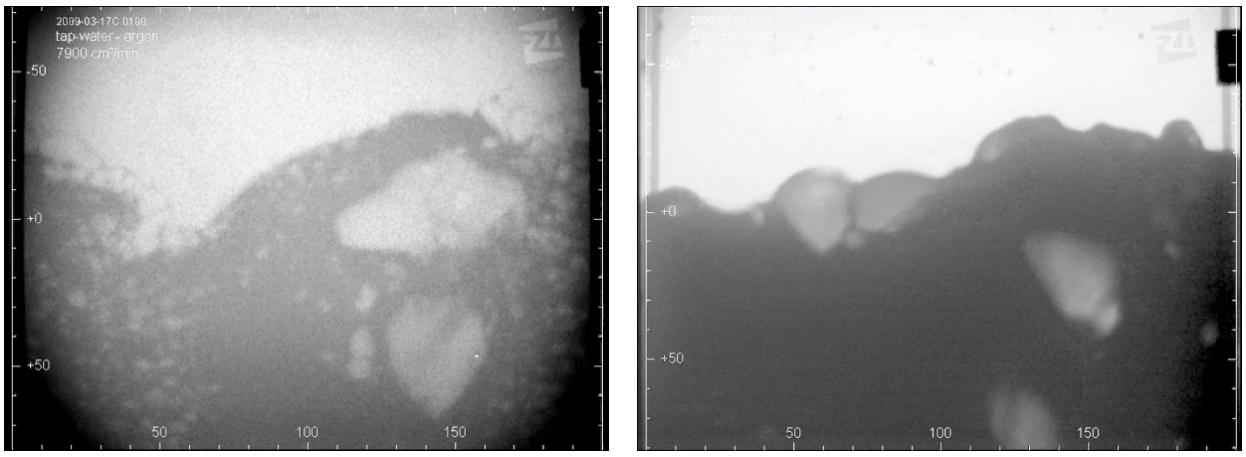

(a) (b)

Figure 7: Snapshots showing the free surface of the melt perturbed by the ascending bubbles (Qg = 1500 sccm): (a) air-water; (b) argon-GaInSn.

Fig. 7 displays the region at the free surface which is heavily disturbed by the ascending gas bubbles. A multitude of small bubbles can be detected in water (see Fig. 7(a)). The typical bubble size varies between 1 mm or less for the small bubbles beneath the free surface and about 10 mm for the rising gas bubbles. The application at high gas flow rates promotes a breakup of bubbles caused by high shearing forces and provokes a tendency to foam formation just below the surface. In contrast, the shape of the liquid metal surface is smoother at the same gas flow rate (see Fig. 7(b)). Obviously, very few smaller gas bubbles can be detected here. These observations suggest a considerable less pronounced probability for bubble entrainment in liquid metal as compared to the water case.

Further experiments were focused on the detection of bubble entrainment at the liquid metal surface. Fig. 8 contains a sequence of four X-ray images showing the occurrence of gas entrainment triggered by a bubble-induced violation of the free surface. The density distribution inside the fluid container is represented by a false color image here, whereas regions covered by the liquid metal appear as blue areas and the void zones argon bubbles are depicted in red and yellow, respectively. The ascending gas bubbles reach the free surface close to the side walls in the right part of the images. High gas flow rates generate a strong ascending flow turning round near the free surface which is associated with large deflections of the surface (fig. 8(a)). In this way a strong circulating flow is generated below the surface as shown in Fig. 8(b). A formation of bubbles can be observed at positions where indentations of the free surface occur (see the white circle in Fig. 8(c)). A sufficiently high shear stress leads to a suction of small bubbles from the free surface into the bulk and a breakup of larger bubbles just below the free surface. The bubbles are transported downwards by the circulating fluid flow. Our observations revealed that these gas bubbles keep entrapped in the vortex region for a rather long time period (Fig. 8(d), the trapped argon bubbles are marked by white circles). Residence times of such bubbles within the field of view were in the order of tens of seconds, which is much longer as the rising bubbles arriving from the nozzle. An increase of the injected gas flow rate results in higher surface velocities and an increase of the frequency of bubble entrainment. A larger number of bubbles trapped within the recirculating vortex below the free surface enhance the probability of bubble coalescence. The coalescing bubbles show a reduced residence time inside the liquid metal.

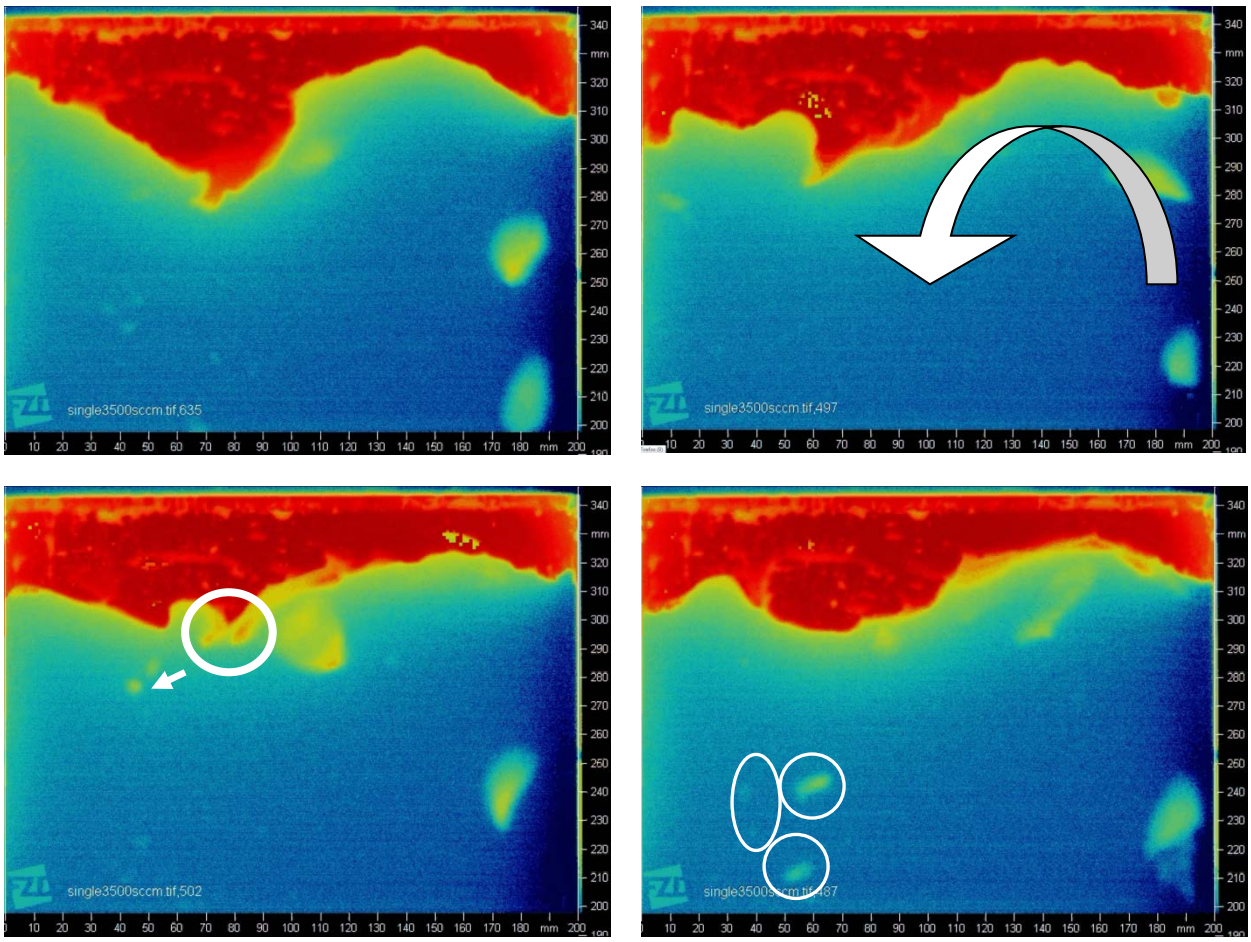

Figure 8: Sequence of X-ray images showing the process of bubble entrainment at the strongly perturbed free surface of the liquid metal.

4. Summary

The present paper demonstrates the phenomenon of gas bubble entrainment at the free surface of a liquid metal in small-scale experiments using the low-melting alloy GaInSn as model fluid. Ultrasonic and X-ray attenuation techniques have been used to study the mechanisms of bubble entrainment. A comparison between a bubbly flow in water and GaInSn disclosed substantial differences with respect to the mechanisms of bubble formation, motion, coalescence, breakup, etc. Such findings confirm the importance of suitable liquid metal model experiments as an indispensible tool for gaining an improved knowledge about liquid metal two-phase flows and gas entrainment processes.

A first series of experiments consider the transient, tornado-like flow structure arising from a TMF spin-up in a rotating liquid metal. The aim of the measurements was a monitoring of the free surface deformation and the determination of the funnel depth of the tornado. For this reason, an ultrasonic echo technique has been used with modified settings in order to achieve a proper detection of the surface position. Furthermore, this measuring approach revealed the ability for the observation of gas entrainment into the liquid metal. This gas entrainment was found to occur in two ways: frequently at the bottom of the tornado funnel and at that moment when the tornado collapses abruptly.

X-ray visualisation applied within this study gives a clear and impressive picture of the gas-liquid metal two-phase flow in a flat rectangular container. Several image processing techniques provide essential characteristics of the bubbly flow such as bubble position, velocities and size. Gas entrainment was observed resulting from strong perturbations of the liquid metal surface. Further measurements are planned for liquid sodium in frame of the upcoming DRESDYN project at HZDR [14]. The lower density of liquid sodium allows for performing these experiments in larger experimental volumes. Furthermore, we consider an application of the ultrafast X-ray tomography [15] in liquid sodium. This technique offers a very attractive possibility for a three-dimensional reconstruction of the gas-liquid interfacial structure of bubbly flows in liquid metals.

ACKNOWLEDGMENTS

The authors would like to thank Deutsche Forschungsgemeinschaft (DFG) for the granted support in the frame of the collaborative research centre SFB609 “Electromagnetic Flow Control in Metallurgy, Crystal Growth and Electrochemistry”.

REFERENCES

[1] TENCHINE D., Some thermal hydraulic challenges in sodium cooled fast reactors, Nucl. Eng. Design 240 (2010) 1195.
[2] MADARAME H., CHIBA T., Gas entrainment inception at the border of a flow-swollen liquid surface, Nucl. Eng. Design 120 (1990) 193.
[3] BANERJEE I., PADMAKUMAR G., Mitigation of gas entrainment for prototype fast breeder reactor, IGCAR Engineering (2009).
[4] EGUCHI Y. et al., Gas entrainment in the IHX vessel of top-entry loop-type LMFBR, Nucl. Eng. Design 146 (1994) 373.
[5] SATPATHY K. et al., Computational Fluid Dynamic Studies on Gas Entrainment in Fast Breeder Reactors, Energy Procedia 7 (2011) 333.
[6] Yamaguchi A. et al., Gas entrainment allowance level at free surface and gas dynamic behavior of sodium-cooled fast reactor, Nucl. Eng. Design 241 (2011) 1627.
[7] PATWARDHAN A.W. et al., Argon entrainment into liquid sodium in fast breeder reactor, Nucl. Eng. Design 249 (2012) 204.
[8] MORLEY N.B. et al., GaInSn usage in the research laboratory, Rev. Sci. Instrum. 79 (2008) 056107.
[9] TAKEDA Y., Development of an ultrasound velocity profile monitor, Nucl. Eng. Design 126 (1991) 277.
[10] TAKEDA Y., KIKURA H., BAUER G., Flow measurement in a SINQ mockup target using mercury, Proc. of ASME FED summer meeting (1998) ASME Washington DC.
[11] ECKERT S., GERBETH G., Velocity measurements in liquid sodium by means of ultrasound Doppler velocimetry, Exp. Fluids 32 (2002) 542.
[12] ECKERT S., GERBETH G., MELNIKOV V.I., Velocity measurements at high temperatures by ultrasound velocimetry using an acoustic wave guide, Exp. Fluids 35 (2003) 381.
[13] GRANTS I. et al., Experimental observation of swirl accumulation in a magnatically driven flow, J. Fluid Mech. 616 (2008) 135.
[14] STEFANI F. et al., DRESDYN - a new facility for MHD experiments with liquid sodium, Magnetohydrodynamics 48 (2012) 103.
[15] HAMPEL U. et al., Ultrafast X-ray Computed Tomography with a Linearly Scanned Electron Beam Source, Flow Meas. Instrum. 16 (2005) 65.

High Temperature of Finned-tube Sodium-to-Air Heat Exchanger in the SELFA Test Loop

Hyeog-Yeon LEE, Jae-Hyuk EOH, Yong-Bum LEE

Korea Atomic Energy Research Institute

Daedeok-daero 989-111, Yuseong-gu, Daejeon, Rep. of Korea

E-mail address of main author:**Error! Unknown document property name.** hylee@kaeri.re.kr

Abstract

A medium-scale sodium test loop named as the 'SELFA'(Sodium Thermal-hydraulic Experiment Loop for Finned-tube Sodium-to-Air heat exchanger) for simulating thermal hydraulic behavior of the FHX (Finned-tube Sodium-to-Air heat Exchanger) in Korean prototype sodium-cooled fast reactor is planned to be constructed at KAERI (Korea Atomic Energy Research Institute). In this study, elevated temperature design for the FHX and creep-fatigue damage evaluation have been conducted according to the design codes of ASME section III subsection NH and RCC-MRx based on full 3D finite element analyses. Design optimization for the finned-tubes and tube arrangements in the scaled-down FHX mock-up has been performed. The materials of the FHX and piping systems are austenitic stainless steel 316, the design temperature and of the SELFA test loop is 600°C and design pressure is 1MPa. The damage evaluation results have shown that no creep-fatigue damage occurrs in the present design of the FHX under the intended test conditions.

1. Introduction

Since safe and reliable decay heat removal after a reactor shutdown is so crucial in a generation IV (Gen IV) sodium-cooled fast reactor (SFR) design, the decay heat removal system (DHRS) is classified as safety-grade system. There are two types of the DHRSs in a Korean demonstration fast reactor [1,2] based on the design concept of diversity and redundancy. For diversity of design, one type is an active decay heat removal system (ADHRS) and the other type is a passive decay heat removal system (PDHRS) which works on the principle of natural circulation. For redundancy of design, two sets of the systems are installed.

The two heat exchangers to be installed in the ADHRS are FHX, a finned-tube air-to-air heat exchanger, and DHX, a sodium-to-sodium heat exchanger while two heat exchangers to be installed in the PDHRS are AHX, an air-to-sodium heat exchanger, and DHX. The materials of FHX and AHX are austenitic stainless steel type 316.

A large-scale sodium thermal-hydraulic test program called STELLA (Sodium Test Loop for Safety Simulation and Assessment) is being constructed by KAERI (Korea Atomic Energy Research Institute). As the first step, the construction of the sodium component test loop called STELLA-1 has been completed, which is to be used for thermal-hydraulic performance test of major components such as AHX, DHX and mechanical sodium pump, and verification & validation (V&V) of their design codes [3-5]. The integrity evaluation of the DHX and AHX in a sodium test facility has been conducted in a previous study [6,7].

Another sodium test facility of medium-scale on the finned tube heat exchanger (FHX), SELFA is planned to be constructed at KAERI which is for the performance test of the FHX in the ADHRS and V&V of the design code, FAHXSA for thermal sizing of FHX. While STELLA-1 is composed of heat exchangers of PDHRS, SELFA is composed of a heat exchangers of ADHRS.

In the present study, a high temperature design for the FHX in the SELFA test loop were conducted based on full 3D FE analyses and evaluation of creep-fatigue damage according to the

elevated temperature design codes of the ASME section III subsection NH[8] and RCC-MRx[9] were conducted.

In general, simplified 2D FE analyses have been conducted for the design evaluation of heat exchangers such as AHX, DHX and IHX(Intermediate Heat Exchanger [10-12], whose results have shown that the simplified 2D analysis and shell elements along with 2 node pipe elements[13] results showed overly conservative estimation especially at the tube-to-tubesheet and tubesheet-to-shell junctions.

2. Design features of decay heat removal system and finned-tube heat exchanger

2.1 Decay heat removal system in Prototype SFR

The reference design of the SELFA sodium test loop is the prototype SFR(150MWe capacity) under development at KAERI[1].

The importance of the decay heat removal system (DHRS) has been recently increased. The DHRS is used to remove the decay heat of the reactor core after the reactor shutdown when the normal heat transport path is not available. It is a safety-grade system and is designed to have sufficient capacity to remove the decay heat in all design basis events by incorporating the principles of redundancy and independency.

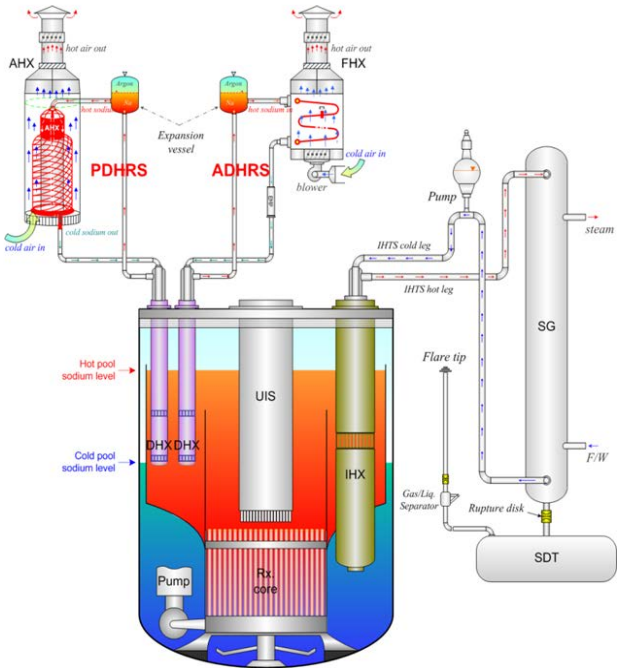

FIG. 1. Decay heat removal system in prototype SFR

The DHRS is composed of two PDHRS(Passive Decay Heat Removal System) and two ADHRS(Active Decay Heat Removal System) as shown in Fig. 1. Each ADHRS consists of a DHX, a FHX (Finned-tube sodium-to-air Heat Exchanger), an electromagnetic pump and an FHX blower. The electromagnetic pump and FHX blower derive the sodium circulation in the loop and the air flow in the shell side of FHX, respectively. Since the AHDRS can also be operated in a natural

TABLE 1. Design parameters of the FHX (prototype)

Parameters	Design values
Thermal duty (MWt)	5.0
No. of tubes	84
Tube arrangement	4-pass serpertine
Tube material	STS316
Bare tube OD/ID (mm)	34.0 /30.7
Thickness (mm)	1.65
Finned tube length (total, m)	8.978
Fin height (mm)	15.0
Fin thickness (width, mm)	1.5
Tube inclined angle (degree)	8.7
No. of fin (per unit length, m)	152
Spacing between Fins (mm)	5.08
Total heat transfer area (mm^2)	644.51
Surface area of single bare tube (mm^2)	7.67

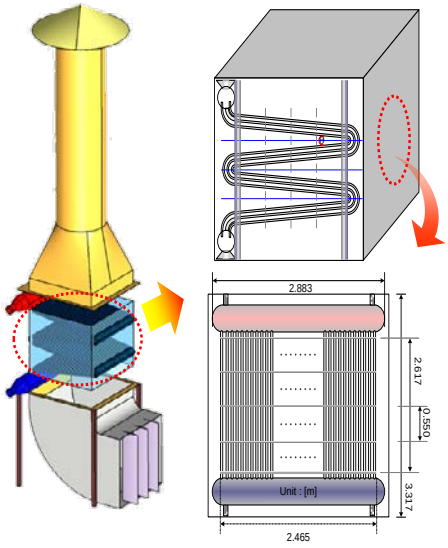

FIG.2. Schematic of a prototype FHX

convection mode against a loss of power supply, the heat transferred to DHRS can be finally dissipated to the atmosphere through AHXs and FHXs by natural convection of sodium and air only. The schematic of the prototype finned-tube heat exchanger is shown in Fig. 2. The tube arrangement of the FHX is 4-pass serpertine tubes. There are 18 rows of finned-tubes and each row of tues is composed of three tubes so that totally 84 finned-tubes are to be installed inside the FHX. The design parameters of the FHX of the Korean prototype SFR is given in Table 1. The outer diameter and thickness of the tube are 34.0mm and 1.65mm thick, respectively.

Each PDHRS is comprised of a Decay Heat eXchanger (DHX) immersed in the reactor hot pool and a natural-draft sodium-to-Air Heat eXchanger (AHX) located in the upper part of reactor building. It is operated by the natural circulation induced by the density and the elevation difference between the DHX and AHX.

TABLE 2. Comparison of FHX design parameters (prototype SFR vs test mock-up)

Design parameters		Prototype	SELFA	Scale
Thermal duty (MWt)		5.0	0.5	1/10
No. of tube rows		28	3	1/9.33
No. of tubes		84	9	1/9.33
Tube arrangement (4-pass serpertine)		P_L=2.05, P_T=2.5	P_L=2.05, P_T=2.5	preserved
Tube material		STS316	STS316	preserved
Bare tube OD/ID (mm)		34.0 /30.7	34.0 /30.7	preserved
Thickness (mm)		1.65	1.65	preserved
Finned tube length (total, m)		8.978	8.978	1/1
Fin height (mm)		15.0	15.0	preserved
Fin thickness (width, mm)		1.5	1.5	preserved
Tube inclined angle (degree)		8.7	8.7	1/1
No. of fin (per unit length, m)		152	152	preserved
Spacing between Fins (mm)		5.08	5.08	preserved
Total heat transfer area (mm^2)		644.51	69.05	1/9.33
Surface area of single bare tube		7.67	7.67	1/1
Ratio of Finned surface(A_{fin}/A_{tot})		0.877	0.877	preserved
Tube-side (sodium)	Flowrate (kg/s)	24.25	2.565	1/9.45
	Inlet/outlet T(°C)	506.1/344.9	506.1/353.6	preserved
	Re. No.	5.080×10^4	5.016×10^4	1/1.01
	Pressure drop (Pa)	1,385	1,154	1/1.2
Shell-side (air)	Flowrate (kg/s)	18.73	2.16	1/8.67
	Inlet/outlet T(°C)	40/310.6	40/276.81	preserved
	Re. No.	4.566×10^4	3.913×10^4	1/1.17
	Pressure drop (Pa)	951	68	1/14

2.2 The SEFLA test loop

A medium scale sodium test facility of the 'SELFA'(Sodium Thermal-hydraulic Experiment Loop for Finned-tube Sodium-to-Air heat exchanger) is planned to be constructed for conducting of the perfomance test of the FHX component and V&V(verification and validation) of the FAHXSA design code developed for thermal sizing of FHX.

As seen in Table 2, many design parameters including finned-tube dimensions (length, OD, thickness) and fluid temperatures of the SELFA test loop have been preserved to the prototype SFR so that thermohydraulic behaviours of the prototype can be obtained in the SELFA test loop. Scaling of the themral duty, number of tubes, flowrates and pressure drops have been done as shown in Table 2.The thermal capacity of the present FHX is 500KW which is 1/10 of the prototype SFR and total number of tubes in the SELFA test loop is 9.

The image of the SELFA test loop is shown in Fig. 3. The components in SELFA main test section are FHX, loop heater, eletctromagnetic pump, blower, expansion tank, buffer tank, sodium storage tank, sodium valves and flowmeters etc., and in auxiliary system, there are sodium supply and purification system, gas supply system, power supply system, fire protection system, sodium treatment system and thermal loss compensation system etc. The main piping in the SELFA test facility is 4 inches piping

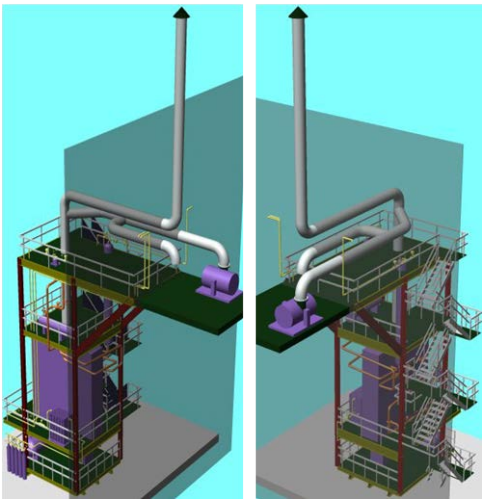

FIG.3. Images of the SELFA test loop

system. The total electricity of the SELFA test loop is within 1.0 MW. The flowrate of sodium is 1~10 kg/s while that of air is 1~20kg/s. The design temperature of sodium was set to be between 300~600°C and design pressure is 1MPa.

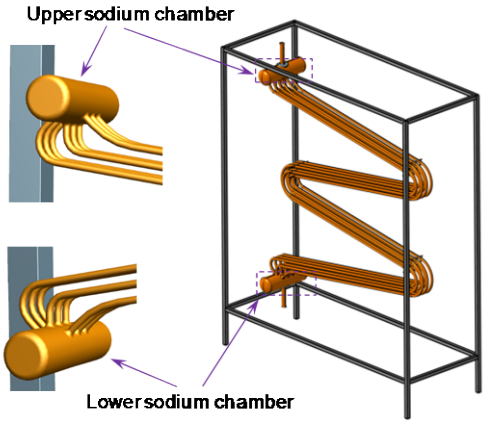

FIG.4. Schematic of the FHX mock-up

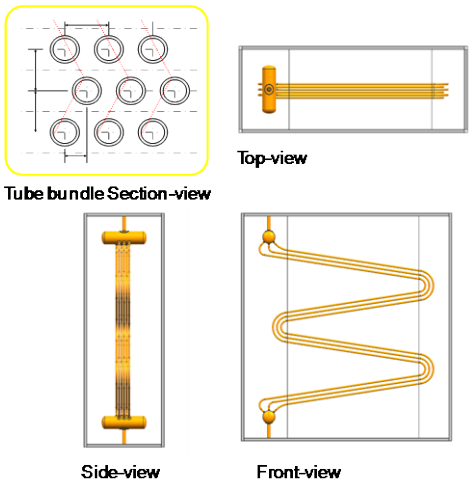

FIG.5. Section view of the FHX

2.3 Design features of the finned-tube sodium-to-air heat exchanger, FHX mock-up

The design parameters of the FHX in the SELFA test loop is shown in Table 2. The material of the shell- and tube-side of the FHX unit is austenitic stainless steel type 316. The images of the FHX to be installed in the SELFA loop are shown in Figure 4 and 5. In the FHX mock-up, 3 rows of tubes (each row consists of 3 tubes) are installed. So FHX is composed of totally 9 tubes as shown in Fig. 6. Fins are welded by high frequency resistance welding over the straight sections of the serpentine tubes. The overall size of the FHX mock-up (width×length×height) is 3.9m×3.7m×1.4m.

TABLE 3. Design parameters of the test HXs

Parameters	Design values	
	FHX	AHX
Tube arrangement	Serpertine	Helical
No. of tubes(tube row)	9 (3)	36 (3)
Tube O.D / I.D (mm)	34.0 / 30.7	34.0 / 30.7
Tube thickness (mm)	1.65	1.65
Active tube length (m)	8.978	23.76
Tube material	STS316	STS316

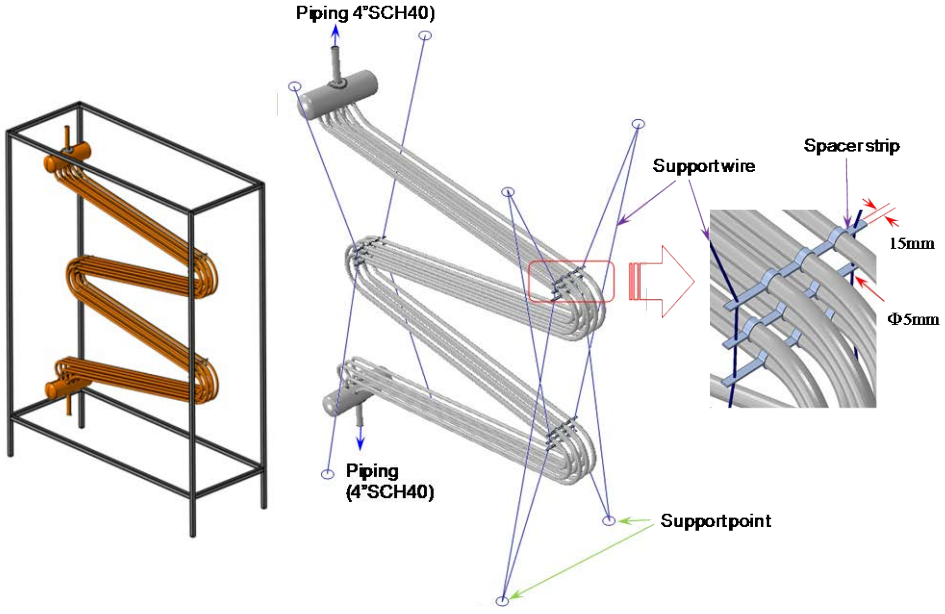

FIG.6. Configuration and supporting concept of the FHX

The FHX mock-up in the SELFA test loop is comparable with AHX in the STELLA-1 test loop as shown in Table 3. In two sodium-to-air heat exchanger of FHX (active unit) and AHX (passive unit), convection heat resistance is higher than 97% of the total heat transfer resistance in the decay heat removal system, which means convection is a dominant heat transfer mode. The tube dimensions of outer diameter and tube thickness, and tube materials of the two units are the same, and tube arrangement and active tube length are different as shown in Table 3.

The supporting of the FHX mock-up is done with spacer strip and support wire as shown in Fig. 6. This concept of support is very effective in the present finned-tube heat exchanger subjected to fluid structure interaction(FIV) under rapid forced convection in the tube bundles. Previous study reports that FIV should be taken into account in design checking for the present type of sodium-to-air heat exchanger.

3. Evaluation of creep-fatigue damage for FHX

3.1 Finite element analysis modeling

A three-dimensional finite element model has been generated based on the 3D computer-aided design model of the FHX. Since the maximum coolant temperature in the FHX is 550°C, the stress and strain states of the AHX component are greatly influenced by the boundary conditions. Since the piping design has not been finished yet, the system load has not been considered in present analysis. In stead, the top and bottom surfaces of the connecting pipes attached to the upper sodium chamber and lower sodium chamber, respectively were fixed for simple and conservative evaluation of thermal stresses. The FHX component is supported by spacer strips and support wires as shown in Fig. 6.

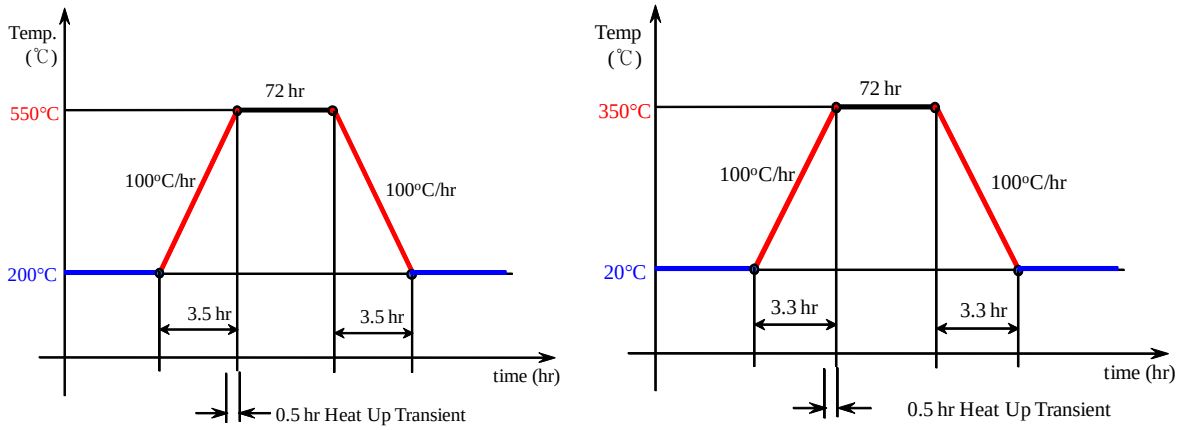

(a) Primary side of FHX (b) Secondary side of AHX

FIG. 7. Thermal loading conditions

Hot sodium flows down from upper sodium chamber to the lower sodium chamber via finned-tubes paths of sodium and air are shown in Fig. 4. In FHX of the SELFA test loop, the temperature range of the sodium side is 550°C to 200°C and that of the air side is 350°C to 20°C as shown in Fig. 7. The transients of the sodium side are composed of (1) steady state at 200°C, (2) heat-up to 550°C with rate of 100°C/hr, (3) steady state at 550°C, (4) cool-down to 500°C and (5) finally reaching 200°C as shown in Fig. 6.

The transients of the air side are composed of a (1) steady state at 20°C steady state at 350°C, (2) cool-down to 20°C with a cool-down rate of 100°C/hr, (3) steady state at 20°C, (4) heat-up to 350°C, and (5) finally reaching 350°C as shown in Fig. 7. The heat transfer coefficient of the finned-tube area on air side was assumed to be uniformly 36.4W/m^{2}K. The heat transfer coefficients of sodium side in top header, bottom header and their connecting pipes were assumed to be 10kW/m^{2}K while the coefficient of serpentine tubes was assumed to be 12.3/m^{2}K.

The design life of the FHX is 25 years, and the number of heat-up and cool-down was set as 20 times per year.

3.2 Anlaysis of heat transfer and thermal stress

Heat transfer and thermal stress analyses were conducted using ABAQUS [14] for the evaluation of creep-fatigue damage. Transient heat transfer analysis for the 3D FE model was conducted with the loading conditions Fig. 7. For simplified heat transfer analysis, it was assumed that the top header area and tubesheet area were of uniform temperatures, while there were temperature gradients at the area in between the header and bottom tubesheet, as shown in right hand side model of Fig. 5.

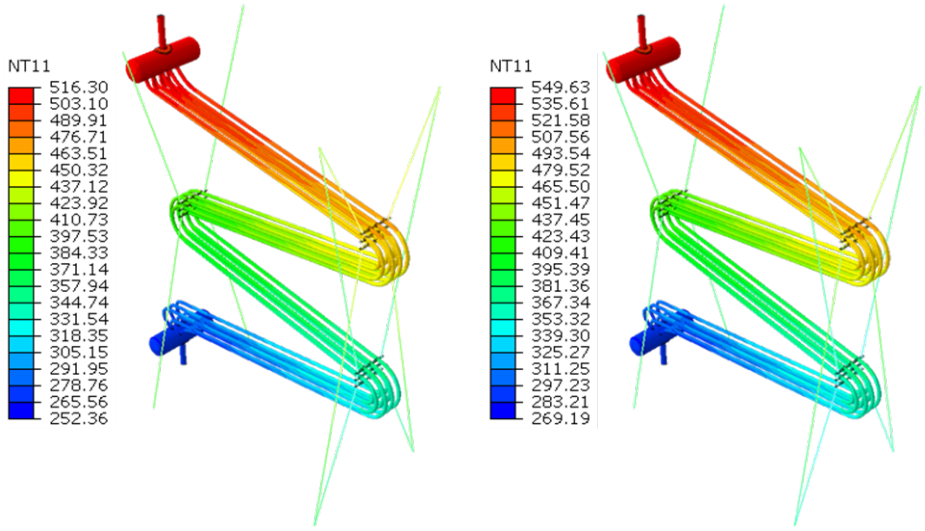

(a) after 3 hour 10 min (b) after 3 hour 30 min

FIG. 8. Temperature distributions

The temperature distributions of FHX at the end of the heat-up (after 3 hour 30 min) and at 20 minutes before end of heat-up (after 3 hour 10 min) are shown in Fig. 8, which shows a gradual change in temperature distributions along the axial direction of the serpentine tubes. The maximum temperature has been changed from 516.3°C to 549.63°C as shown in Fig. 8. Those temperature distributions were used for thermal stress analyses.

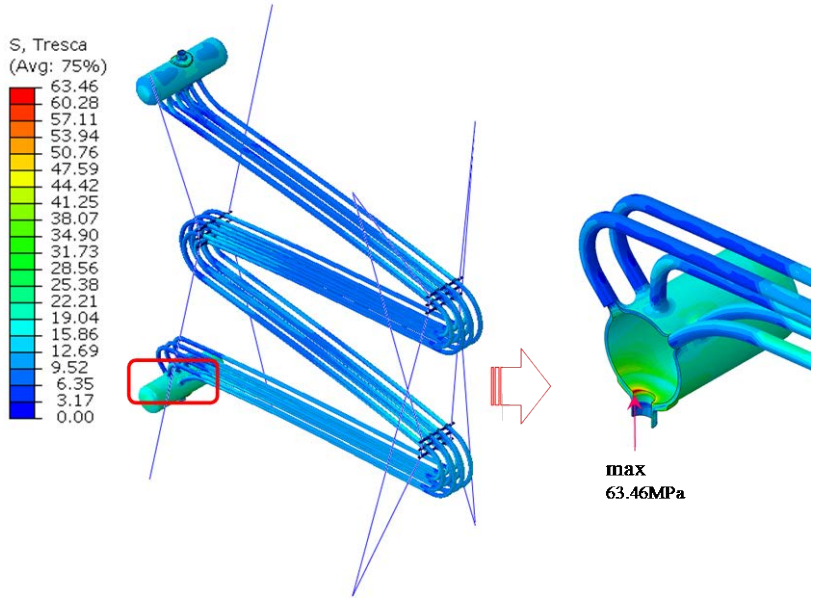

FIG. 9. Stress intensity at the end of heat-up under secondary loads

The 3D stress analyses under mechanical load only, and under thermal load only and under combined mechanical were conducted for a high temperature design evaluation according to the ASME Section III Subsection NH and French RCC-MR Code, respectively.

The stress intensity (S.I) of the whole FHX unit at the end of heat-up under the secondary load is shown in Fig. 9, which shows relatively low level of the maximum Tresca stress, 63.46MPa. The more detailed stress intensities at the top sodium chamber, bottom sodium chamber, spacer strip and support

wire are shown in Fig. 10. It was shown that the stress levels at the spacer strips and support wires were quite low due to adoption of the flexible supporting concept of the tube bundle. Those stress analysis results were used for the evaluation of creep-fatigue damage.

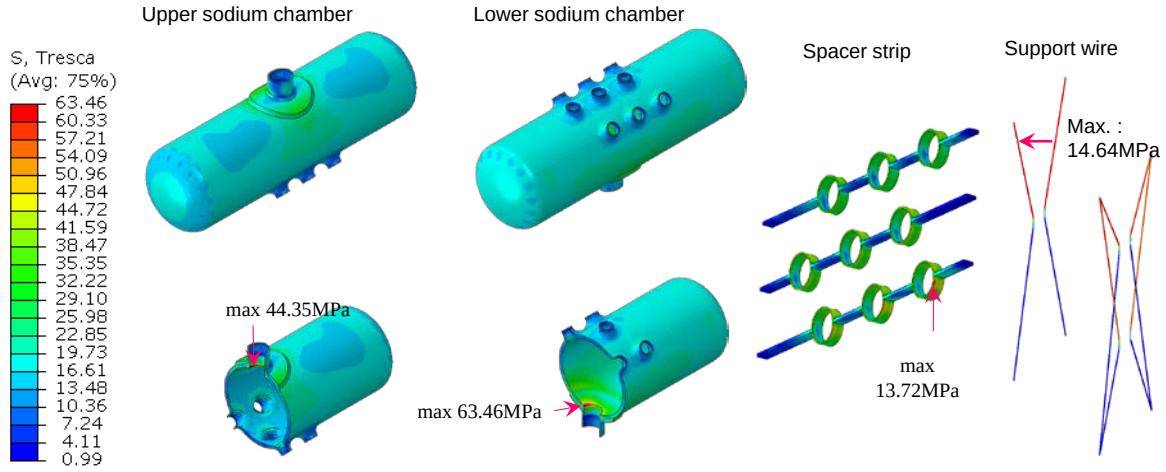

FIG. 10. Local distribution of stress intensity at the end of heat-up under secondary loads

3.3 Evaluation of creep-fatigue damage

The basic concepts of ASME-NH and RCC-MR in determining creep-fatigue damage based on the linear damage summation rule are the same, and the formula is given as follows.

$$\sum_{j=1}^{P}\left(\frac{n}{N_d}\right)_j + \sum_{k=1}^{q}\left(\frac{\Delta t}{T_d}\right)_k \le D\,, \tag{1}$$

where D = total creep-fatigue damage

p = number of different cycle types

$(n)_j$ = number of applied repetitions of cycle type j

$(N_d)_j$ = number of design allowable cycles for cycle type j

q = number of time intervals for the creep damage calculation

$(\Delta t)_k$ = hold time applied for one creep-fatigue load cycle type k

$(T_d)_k$ = allowable time duration determined from the stress-to-rupture curves during the time interval, k

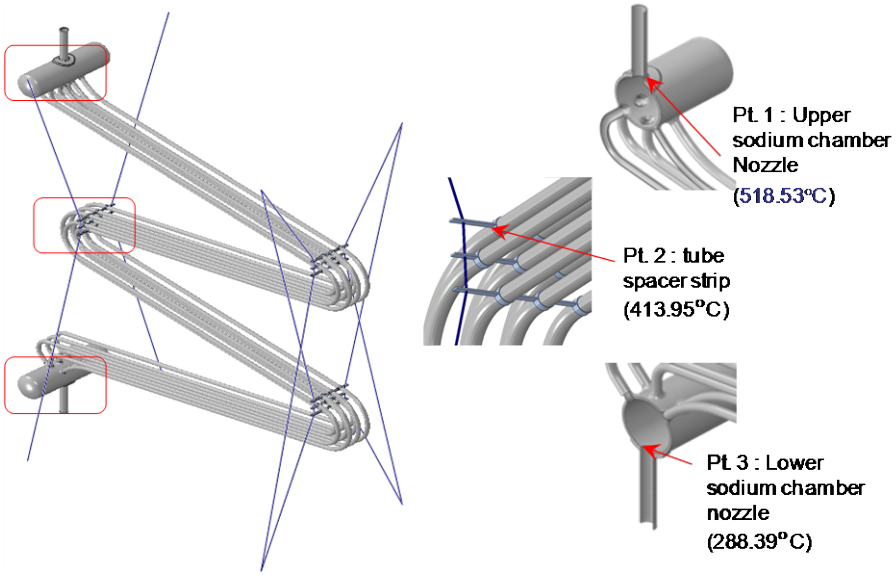

FIG. 11. Three significant locations in design code checking

An evaluation of creep-fatigue damage was conducted for the three points of the stress concentration at the FHX as shown in Fig. 11 according to the recent high temperature design codes of the ASME-NH and RCC-MR code.

3.3.1 Evaluation of damage according to the ASME-NH

The main evaluation procedures of creep-fatigue damage in the ASME-NH are based on simplified inelastic analyses. All strain components for each point, i, in time ($\varepsilon_{xi}, \varepsilon_{yi}, \varepsilon_{zi}, \gamma_{xyi}, \gamma_{yzi}, \gamma_{zxi}$) for the complete load cycle should be determined at a specific point when conditions are extreme for the cycle, either maximum or minimum.

The maximum stress of 63.46 MPa occurred at the end of the heat-up time at the nozzle part of the inner shell to the tubesheet, as shown in Fig. 11. The wall temperature of the maximum stress point was 288.39°C which is below creep range. Therefore, creep-fatigue damage evaluation has been conducted at upper sodium chamber nozzle with the wall temperature of 518.53°C.

The total strain range, ε_t, obtained at bottom sodium chamber nozzle was 0.05% as shown in Eq. (2), which is quite low level in elastic region.

$$\varepsilon_t = 0.05(\%) \tag{2}$$

The corresponding evaluation results of creep-fatigue damage according to the ASME-NH code was calculated as shown in Eq. (3), which means that no damage would be accumulated under the intended load conditions during the life time of 25 years in the FHX mock-up.

$$\frac{n}{>1\times10^{6}} + \frac{\Delta t}{>3\times10^{5}} \le D \tag{3}$$

3.3.2 Evaluation of damage according to the RCC-MRx

An evaluation of creep-fatigue damage according to the French high temperature design code of the RCC-MR was also conducted. The 2010 RCC-MRx (draft) is the merged version of RCC-MR and RCC-MX. RCC-MR is a design and construction code of a sodium cooled fast reactor and high temperature components, while RCC-MX is a design and construction code for research reactors.

The total strain range in RCC-MRx code is determined by summing the elastic-plastic strain range and creep strain range as shown in Eq. (4), and the calculated total strain range was determined as in Eq. (5).

$$\Delta\bar{\varepsilon} = \Delta\bar{\varepsilon}_{el+pl} + \Delta\bar{\varepsilon}_{cr} \tag{4}$$

$$\Delta\bar{\varepsilon} = 0.025 \tag{5}$$

The evaluation results of creep-fatigue damage according to the RCC-MRx code was shown that no damage would occur during the life time of the FHX mock-up. Creep-fatigue damage according to the ASME-NH code was calculated as in Eq. (6). The material property of fatigue strength is available up to 10^8 cycles in RCC-MRx while up to 10^6 cycles in ASME-NH, which makes difference in Eq. (3) and Eq. (6).

$$\frac{n}{>1\times10^{8}} + \frac{\Delta t}{>3\times10^{5}} \le D \tag{6}$$

Therefore, it is shown from the design evaluation according to the ASME-NH and RCC-MRx code that no creep-fatigue damage would occur for FHX mock-up under the intended design transients over the design lifetime.

4. Conclusion

A high temperature design and integrity evaluation of the sodium-to-air heat exchanger, FHX, of the SELFA sodium test loop, has been conducted. The present FHX mock-up is a finned-tube heat exchanger with 9 serpentine tubes and it is for simulating a FHX to be installed in active decay heat removal system of Korean prototype sodium-cooled fast reactor. A flexible wire supporting concept has been adopted in present FHX design to minimize fluid induced vibration of the tubes under severe forced convection condition. The material of the tubes in the FHX are austenitic 316 stainless steel.

Full three-dimensional finite element analyses were conducted for the FHX, and evaluations of creep-fatigue damage at critical location was conducted according to the recent version of ASME-NH and RCC-MRx. The present design of the FHX was shown to be well within acceptable range in terms of creep-fatigue damage according to the two codes. The highest stress intensity (S.I) under secondary loading was calculated to be 63.46MPa at the lower sodium chamber nozzle, which is quite low stress level. The creep-fatigue damage according to the two design codes for the FHX under the specified thermal transient conditions were calculated to be negligible over the design life and the integrity of the FHX mock-up was confirmed in terms of creep-fatigue damage.

ACKNOWLEDGEMENTS

This study was supported by Nuclear Research & Development Program of the National Research Foundation Grant and the International Research & Development Program Foundation funded by the Ministry of Education, Science and Technology in Korea

REFERENCES

[1] Kim, Y.I, Lee, Y.B., Lee, C.B, Hahn, D.H., Sodium colled fast reactor development in Korea, FR-13, 4-7 March, Paris (2013).

[2] Lee, T.H., Eoh, J.H., Lee, H.Y., et. al., "Scientific design of large scale sodium thermo-hydraulic test facility in KAERI," FR 09, Kyoto, December 7-11, Kyoto, Japan (2009).

[3] Lee, T.H. et al., "Preliminary Test Requirements for the Performance Test of Passive Decay Heat Removal System of Sodium-Cooled Fast Reactor," KAERI/TR-3768/2009, Korea Atomic Energy Research Institute (2009).

[4] Lee, T.H., et. al., 2011, Design report of STELLA-1, KAERI/TR-4295/2011.

[5] Eoh, J.H., Lee, T.H., Lee, H.Y., Han, J.W., Lee, Y.B., "Scaled Heat Exchanger Design of the Sodium Thermal-Hydraulic Experimental Facility; STELLA-1," Transactions of the KNS Spring Mtg., Jeju, Korea, October 21-22 (2010).

[6] Lee, H.Y, Kim, J.B, Park, H.Y., "High temperature design and damage evaluation of Mod.9Cr-1Mo steel heat exchanger," Journal of Pressure Vessel Technology, Transactions of ASME, Vol.134, pp. 051101-1~10, Oct. 1 (2012).

[7] Lee, H.Y, Kim, J.B, Park, H.Y., "Creep-Fatigue Damage Evaluation of Sodium to Air Heat Exchanger in Sodium Test Loop Facility," Nuclear engineering and Design, 250, pp.308-315 (2012).

[8] ASME Boiler and Pressure Vessel Code, Section III, Rules for Construction of Nuclear Power Plant Components, Div. 1, Subsection NH, Class 1 Components in Elevated Temperature Service, ASME (2010).

[9] RCC-MRx, Section I Subsection B, 2010, Class 1 N_{1RX} Reactor Components its Auxiliary Systems and Supports, 2010 Edition (Draft), AFCEN.

[10] Chellapandi, P., Srinivasan, R., et. al., 1989, "Structural design of the IHX for PFBR," 10th International Conference on Structural Mechanics in Reactor Technology (SMIRT-10), Anaheim, CA, USA, August 14-18.

[11] Jalaldeen, S., Srinivasan, R., Selvaraj, P., "Chellapandi, P., Comparison of life of two types of decay heat exchangers used in prototype fast breeder reactor," Transactions of the Indian Institute of Metals Volume 63, No. 2-3, 647-651 (2010).

[12] Srinivasan, R., Chellapandi, P., Jebaraj, C., "Structural design approach of steam generator made of modified 9Cr-1Mo for high temperature operation," Transactions of the Indian Institute of Metals Volume 63, No. 2-3, 629-634, 0975-1645 (2010).

[13] Winston,S., Srinivasan, R., Puthiya Vinayagam, P., Chellapandi, P., Chetal, S.C., “Creep-fatigue damage assessment of special type of sodium to air heat exchanger having toroidal shape headers,” Transactions of the Indian Institute of Metals Volume 63, No. 2-3, 611-616 (2010).
[14] ABAQUS Users manual, Version 6.10, Simulia, USA (2010).

Development of a mass transfer model for Sodium purification system in a Fast Breeder Reactor

N. Khatcheressian[a,c,d], **C. Latgé**[b], **X. Joulia**[c,d], **T. Gilardi**[a], **X. Meyer**[c,d]

[a] CEA, DEN, Cadarache DTN/STPA/LIPC, 13108 Saint-Paul Lez Durance, FRANCE

[b] CEA, DEN, Cadarache DTN, 13108 Saint-Paul Lez Durance, FRANCE

[c] Université de Toulouse, INPT-ENSIACET, UPS, Laboratoire de Génie Chimique, 4 Allée Emile Monso, 31030 Toulouse, FRANCE

[d] CNRS, Laboratoire de Génie Chimique, 31030 Toulouse, FRANCE

Abstract. Operating a Sodium Fast Reactor (SFR) in reliable and safe conditions requires to master the quality of the sodium fluid coolant, regarding oxygen and hydrogen impurities contents. A cold trap is a purification unit in SFR, designed for maintaining oxygen and hydrogen contents within acceptable limits. The purification of these impurities is based on crystallization of sodium hydride on cold walls and sodium oxide or hydride on wire mesh packing. Indeed, as oxygen and hydrogen solubilities are nearly nil at temperatures close to the sodium fusion point, i.e. 97.8°C, on line sodium purification can be performed by crystallization of sodium oxide and hydride from liquid sodium flows. However, the management of cold trap performances is necessary to prevent from unforeseen maintenance operations. It is thus essential to understand how a cold trap fills up with impurities crystallization in order to optimize the design of this system and to overcome any problems during nominal operation. This paper deals with the mathematical modeling of crystallization process in a cold trap and predicts the location and the amount of the impurities deposit, on cold walls for sodium hydride and on wire mesh packing for sodium oxide. A modeling of the front propagation by diffuse deposit interface method was developed and parameters sensitivity was evaluated. These first results will enable to understand the consequences of the impurities deposited on the hydrodynamics and heat transfer in a cold trap.

1. Introduction

The development of Sodium Fast Reactor (SFR) is possible thanks to attractive sodium properties. This coolant needs to be purified because of a potential increase of impurities content mostly oxygen and hydrogen. These pollutants can be introduced during the operation of a SFR, continuously (ie hydrogen produced by aqueous corrosion in Steam Generator Unites), periodically during foreseen handling operations or unforeseen events ie sodium-water reaction or air ingress. The main source of impurities in the intermediate sodium loop is due to hydrogen diffusion in steam generators through tube walls.Oxygen ingress from inert cover gas (argon) containing traces of oxygen and air ingress during maintenance can induce a limited pollution of the sodium. Oxygen concentrationin the sodium does not exeed a few ppm and hydrogen a few hundreds of ppB. However, these concentrations are required to be maintained lower than assigned levels. Oxygen level is controled in order to limit generalized corrosion and associated radioactive contamination in primary circuit. Hydrogen concentration is controled at a very low level so that a potential sodium water reaction in a Steam Generator generating hydrogen will be early detected. A higher level would cover small leaks and this might result in propagation into large leak and failure of more tubes. Moreover, these pollutants, at very high contents, could also deposit in the form of sodium hydride and oxide on the cold walls of the circuit, which may lead to the plugging of the narrowed sections or the reduction of heat transfer coefficient in some small heat exchangers, located in ancillary systems, ie purification loops. Thus, by decreasing oxygen and hydrogen content in sodium coolant, a cold trap appears as a key device in a Sodium Fast Reactor. Following the works performed by Latgé [1] and related further in this article, a mathematical model was developed to optimize the design and later on the operation of the sodium

purification systems for future SFRs. The model is based on a coupling between hydrodynamics, mass and heat transfer. Mass transfer involves nucleation and growth kinetics of crystals of sodium oxide and sodium hydride. This paper presents this improved mathematical model for the description of the crystallization phenomena of sodium oxide and hydride in the whole volume of the cold trap.

2. A Sodium purification process based on crystallization

2.1. Sodium purification principle in a cold trap

The solubilities of oxygen and hydrogen in sodium are very low. They reach a value around nil, near the sodium melting temperature i.e. 97.8°C. Noden [2] and Wittingham [3] proposed two correlations to calculate the respective solubilities of oxygen (Equation (1)) and hydrogen (Equation (2)) in sodium as a function of temperature, given in ppm (µg of impurity per kg of Sodium).

$$\log[O(ppm)] = 6.250 - \frac{2444.5}{T(K)} \quad for \quad T(K) = [383;823] \tag{1}$$

$$\log[H(ppm)] = 6.467 - \frac{3023}{T(K)} \; for \; T(K) = [383;673] \tag{2}$$

Thus, crystallization of sodium hydride NaH and sodium oxide Na_2O occurs by decreasing sodium temperature below the saturation temperature. It is performed in a cold trap in which a heat exchange is carried out. The ingoing liquid metal sodium is cooled down, for instance, by an organic fluid, injected at the bottom of the cooling zone, through an extern shell (FIG. 1). Some cold traps can be cooled by other means such as air, Na-K eutectic. To promote heterogeneous crystallization and to trap the sodium oxide and hydride crystals, a support (stainless steel packing) is placed in the cold trap. Purification process by crystallization is achieved by following several steps as shown in FIG. 2.

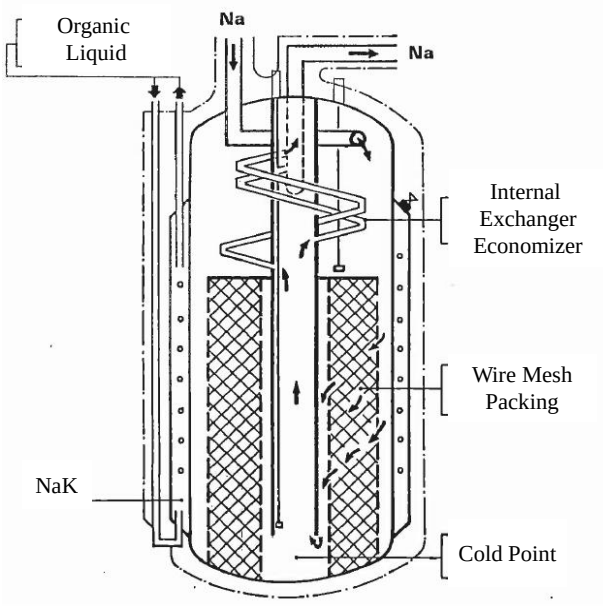

FIG. 1. Cold Trap Scheme

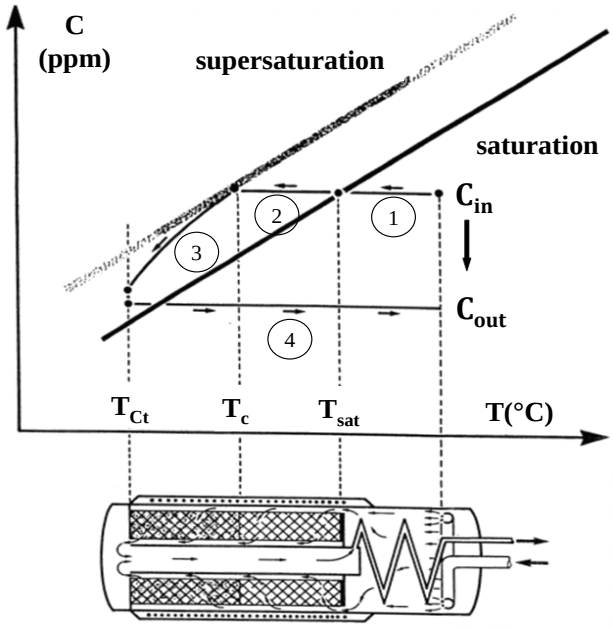

FIG. 2. Evolution of impurity concentration C with temperature T

On FIG.2, the different steps refer to:

1) The sodium is first cooled down in a heat-exchanger-economizer (at the entrance of cold trap) to a temperature close to the saturation temperature T_{sat} of oxygen and/or hydrogen. C_{in} refers to the inlet impurity concentration.

2) The sodium flows through a cooler where it reaches a crystallization temperature Tc below the saturation temperature of oxygen and/or hydrogen. Crystallization of NaH and Na_2O starts by heterogeneous *nucleation* on surfaces and then progresses by *growth,* as described by Feron, Latgé and Saint-Martin [4,5,6].

3) Formed crystals stick to cooled walls (NaH) and/or wire mesh packing (NaH, Na_2O). Thus, oxygen and hydrogen concentrations C in the sodium decrease down to a minimum value (C_{out}) at the bottom of the cold trap (Coldest temperature of the Trap: T_{CT}).

4) Finally, the purified sodium (flowing out through the central tube) is heated up through the heat exchanger-economizer.

2.2. A crystallization process lead by nucleation kinetic

Many improvements of cold traps performance achieved from experimental studies or simulation analysis have been performed over the last decades to understand how a cold trap could fill up with impurities. However, no-one, except Feron and Latgé [4, 5], distinguished nucleation from growth mechanism in crystallization process, but consider only a global mass transfer or growth kinetic within unit order. Although nucleation process does not weight on crystallized impurities quantity, it nevertheless plays a major role on crystallized impurities location, and consequently on the overall process efficiency. Indeed, growth of impurity cannot occur without formed nuclei. Thus, impurities crystallization will only start when a given supersaturation is reached. Experimental studies were carried out in CEA Cadarache, on mock-up ECRIN [4] and EPINAR [6] to understand the basic mechanisms of crystallization of sodium oxide and sodium hydride and to establish their respective nucleation and growth kinetics as described by Latgé [1]. The general form of crystallization kinetics, given for one impurity O or H, in [kg_{Na2O}/s] or [kg_{NaH}/s], is:

$$r_{jX}(T,t) = k_{oX}\ \exp(-\frac{E_X}{RT})\ A_{jX}(t)\left[\frac{(C-C^*)}{1.10^{-6}\ \rho_{Na}}\right]^{n_X} = Ko_X\ A_{jX}(t)\left[\Delta C\right]^{n_X} \quad (3)$$

In this equation, index X refers either to Nucleation (N) or to growth (G) and index j refers the location, on wire mesh packing (p) or cold walls (w). k_0 is the rate constant ($kg/(s.ppm^{nx}.m^2)$), E is the activation energy (J/mol), R is the perfect gas constant (J/(mol.K)), A is the crystallization surface of reference (m^2) (wire or walls for nucleation, nuclei and crystals for growth), n_X is the order of the crystallization process, $C^*(kg/m^3)$ is the saturation concentration for a given temperature calculated by the solubility law, ρ_{Na} is the sodium density in (kg/m^3) and (C-C*) is the supersaturation at temperature T(K).

Nucleation process order for both impurities appears to be much greater than the unit. Table 1 reports the activation energy E and the process order for nucleation and growth kinetics of sodium oxide and sodium hydride.

Table 1. Activation energies and process orders of sodium oxide and sodium hydride [1]

Process	Nucleation (N)		Growth (G)	
Impurity	Na_2O	NaH	Na_2O	NaH
E(kJ/mol)	-60	-450	-45	-43.6
n	5	10	1	2

2.3. Sodium oxide crystallization on wire mesh and Sodium hydride on cold walls

Experiments have unexpectedly revealed that for a cold trap designed with an upper packless cold zone, sodium hydride crystallization occurs preferentially on cold walls of the system (FIG.3) whereas sodium oxide crystallization occurs only on wire mesh packing (FIG.4) as explained by Latgé et al. [1,7]. This can be partly explained by the fact that growth rate of Na_2O is limited by the diffusion of O^{2-} in the boundary layer whereas the growth rate of NaH is limited by the integration step of the H^- ion in the crystal lattice. However, in case of a non-optimized packless cold zone, hydride might as well crystallize on wire mesh packing. Thus, co-crystallization occurs between sodium hydride and sodium oxide. In this case, it is assumed that kinetics parameters for sodium hydride crystallization on cold walls are identical to the one on wire mesh packing.

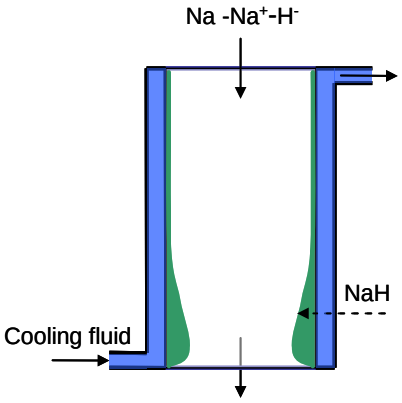

FIG. 3. Trapping scheme of NaH on cold walls

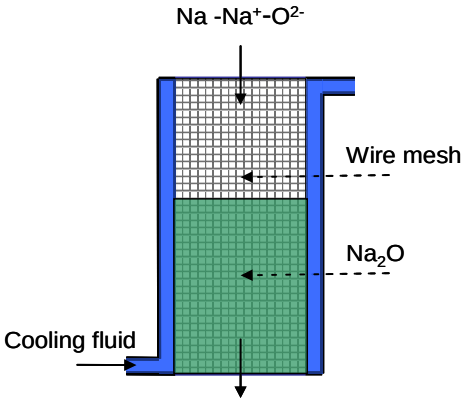

FIG. 4. Trapping scheme of Na_2O on wire mesh

3. Mass transfer modeling for Sodium impurities

Because of these two types of crystallization behaviors, two different modeling approaches have been developed. For both approaches, the system can be considered as a porous media with a porosity ϕ which refers to the void fraction of the liquid phase. This porosity is initially equal to one if the deposit occurs on walls (NaH) and equal to the void fraction of the mesh packing if the deposit occurs on wire mesh (Na_2O). The mixture of crystal and liquid sodium is then treated as a diphasic media in which void fraction changes with time and space, as well as its physical parameters such as permeability, diffusion or thermal conductivity. The fluid is assumed to be incompressible and each infinitesimal volume is assumed isothermal. The model takes into account hydrodynamics in porous media, heat transfer, mass transfer, nucleation and growth kinetics. Both approaches are studied dealing with void fraction evolution on wire mesh packing for oxide and on cold walls for hydride deposit.

3.1. A porous medium in a constant change for sodium oxide crystallization

Crystallization of Na_2O, occurring on wire mesh packing, leads to define a new system. This one is composed of wire mesh, liquid sodium and oxide crystals whose physical properties are mathematical consequences of the compounds properties. Assuming formed oxide crystals remain attached to the wire mesh, velocity of the solid phase is equal to zero. Thus conservative mass on the crystals phase turns to be:

$$\frac{\partial \alpha_{Na2O}}{\partial t} = \frac{\dot{m}_{Na2O}}{\rho_{Na2O}} \tag{4}$$

Where α represents the volume fraction of sodium oxide crystals, ρ [kg_{Na2O}/m^3] its density and $\dot{m}$ its crystallization reaction kinetic per volume in [$kg_{Na2O}/m^3/s$]. The porosity ϕ of the system defined as the volume fraction of the liquid phase, which results thus, from the integration of the following equation:

$$\frac{\partial \phi}{\partial t} = -\frac{\dot{m}_{Na2O}}{\rho_{Na2O}} \tag{5}$$

To define the local source of oxide crystal, the reference surface given in the Equation 3 is defined by the specific area of the wire mesh packing A_P[1/m]. It comes:

$$\dot{m}_{Na2O,X}(T,t) = Ko_{pX}\ A_{pX}(t)\left[\Delta C\right]^{npX} \tag{6}$$

For nucleation process, A_{pN} specific area corresponds to the one offered by the stainless steel packing (Sv in m^2/m^3). However, for growth process, A_{pG} specific area stands for the cumulative oxide surface formed by nuclei and grown crystals.

3.2. A front propagation tracking for sodium hydride crystallization

It has been shown experimentally that the deposit which covers the walls of the system is not just a compact hydride layer but might be composed of solid impurity (crystals) mixed with liquid sodium. The porosity of this deposit layer can be expressed from conservation equations as related above. However, crystal growth on cold walls can be seen as a phenomenon involving a moving interface, with propagation of a deposit front.

3.2.1. Tracking Moving Interface

Ones of the computational techniques for tracking moving interfaces are either the level set method (Sethian and Smereka [8]) or phase field method (Beckermann et al. [9]).They rely on an implicit representation of the interface whose equation of motion is numerically approximated using schemes built from those for hyperbolic conservation laws.

On one hand, the level-set method enables to track a sharp-interface. However, in numerical simulation, an abrupt jump, corresponding to this interface, may cause instabilities. Thus, a smeared out function is used to turn this sharp interface into a diffuse interface.This approach enables to easily handle changes within the interface topology. On an other hand, the phase field method, which is a diffuse interface model, assumes that the interface between the different phases is not a sharp boundary, but has a finite width and is characterized by rapid but smooth transitions in physical quantities. Indeed, the diffuse interface region is viewed as a porous medium where liquid and solid coexist.

To simulate the propagation of the front, the diffuse interface model approach, expressed above, is coupled to the Navier-Stockes equations, as well as heat and mass transfers and sodium hydride crystallization kinetics.

$$\frac{\partial e}{\partial t} + \overrightarrow{v_F}.\nabla e = \gamma \nabla.\left(\varepsilon \nabla e - e(1-e)\frac{\nabla e}{|\nabla e|} \right) \tag{7}$$

In this equation, e is the characteristic function of the deposit: e(r,z)=1 if the point M(r,z) is located inside the deposit, 0 otherwise (FIG.5). v_F corresponds to the velocity of the crystallization front, ε is a parameter controlling interface thickness and γ is a reinitialization parameter. These two last parameters are function of the velocity front.

This equation is similar to a continuity equation for the variable e. The term in Laplacian can be considered as a kind of diffusion term, trying to enlarge the width of the interface. To counteract this diffusion, one has the term with the divergence of the flux. These two terms are in equilibrium in order to control the diffuse interface length.

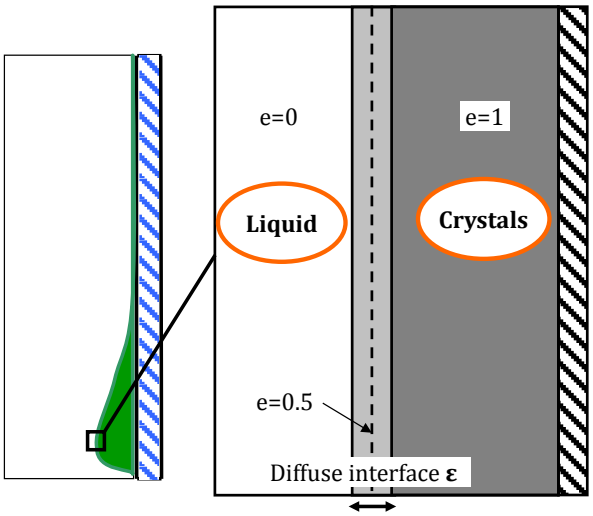

FIG. 5. Surface deposit as a diffuse interface

3.2.2. Velocity Front transporting the interface

The front velocity v_F corresponds to the translation rate of the diffuse interface, such that each elementary volume over the interface keeps the same porosity during its translation. Hence, over the thickness of the diffuse interface, the material derivative of porosity is set to be equal to zero.

$$\frac{D\phi}{Dt} = \frac{\partial \phi}{\partial t} + \vec{v}_F . \nabla \phi = 0 \quad for \quad e \in]0-1[\tag{8}$$

For a given z position in cold trap, radial growth crystallization is assumed. Front velocity field is thus expressed as:

$$v_F(r) = \|\vec{v}_F\| = \frac{\left|\frac{\partial \phi}{\partial t}\right|}{\left|\frac{\partial \phi}{\partial r}\right|} \quad for \ [\partial \phi / \partial r \neq 0] \tag{9}$$

where the porosity ϕ results from mass balance equation on sodium hydride crystal phase as mentioned before with sodium oxide on Equation 5. As growth of impurities occurs on formed nuclei, only the kinetic of nucleation is weighted by the variable e. Hence nucleation kinetics is expressed as:

$$\dot{m}_{NaH,N}(T,t) = e\left[Ko_{wN}\ A_{wN}(t)[\Delta C]^{nwN}\ \right] \ with \quad A_{wN}(0)[1/m] = \frac{1}{\varepsilon} \tag{10}$$

Where ε is the length of the diffuse interface.

4. Coupled transfer models analysis

The numerical model is discretized and then solved by finite element method in Comsol Multiphysics® software. Crystallization on wire mesh has been simulated on ECRIN mock-up (FIG.6) and crystallization on cold walls has been simulated on the upper part of EPINAR mock-up (FIG.7).

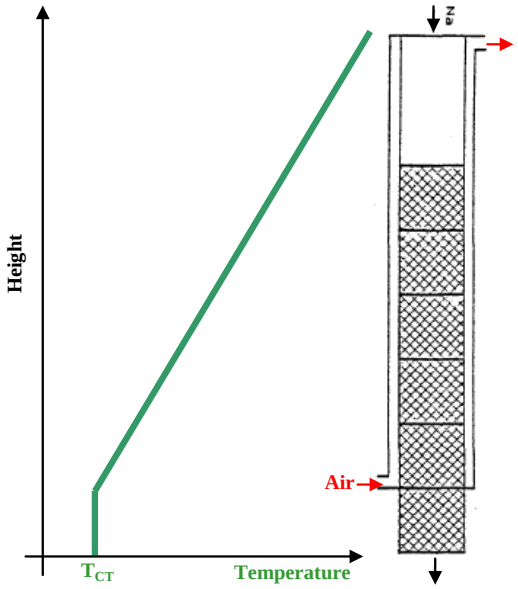

FIG. 6. ECRIN mock-up with an isothermal exit zone in 2D view

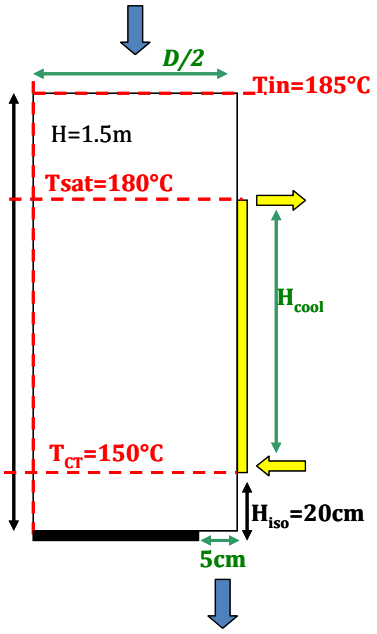

FIG. 7. Upper part of EPINAR mock-up in 2D axisymetrical view

4.1. Sodium Oxide mass profil results

Basic experimental studies on wire mesh packing crystallization, in CEA Cadarache, have been performed on ECRIN mock-up by Latgé [4]. As shown in FIG. 6, ECRIN is a simple cylindrical cold trap with 0.8m height and 0.11m width, cooled by air. An isothermal zone might be added downstream the cooling zone in order to get a longer residence time over the coldest zone (at T_{CT}) with aim to increase the purification efficiency. The geometry of this trap was very simple, in order to establish a plug-flow regime and consequently to identify more easily the kinetics, without any additional difficulties induced by the complexity of the internals.

A concentration of oxygen corresponding to a saturation temperature equal to 180°C (7.2ppm) was set-up during 100 hours. The coldest temperature is set for 150°C. Tests have been performed on ECRIN mock-up to evalutate the impact of wire mesh densities and flow rate on oxide cristallized mass.

4.1.1. Wire mesh packing specific area influence on cristallized mass

Simulated results plotted on FIG.7 and FIG.8 localize oxide crystals finally formed over the packing through ECRIN mock-up for different wire mesh densities, respectively for a fully and isothermal part meshed trap.

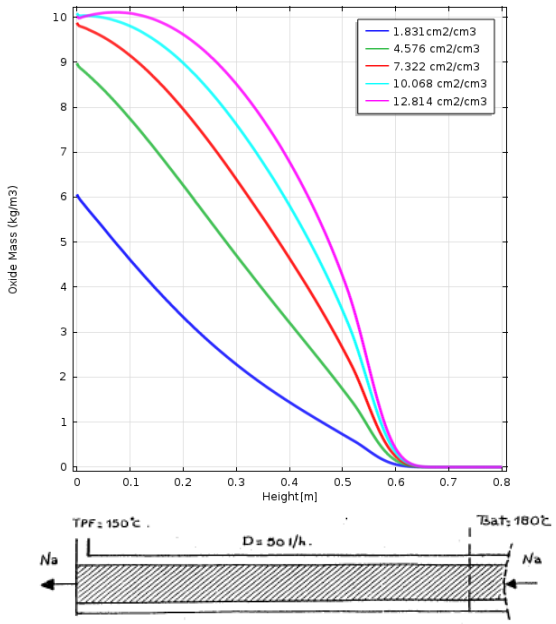

FIG. 8. Oxide Mass profile (kg/m^3) along z for a fully meshed trap

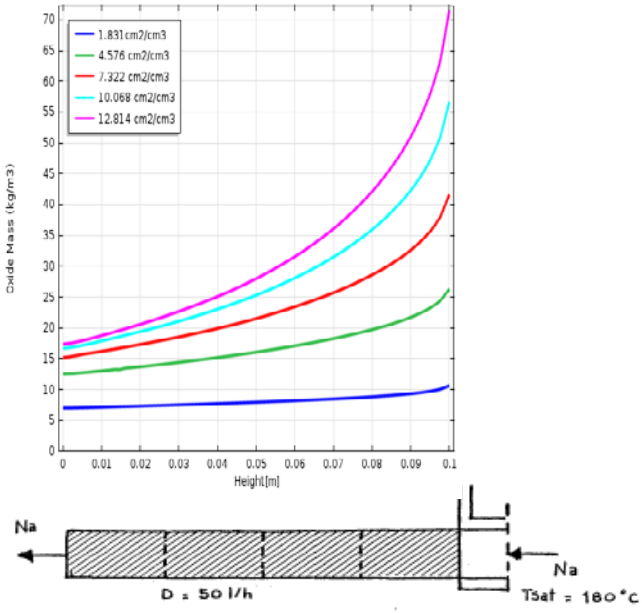

FIG. 9. Oxide Mass profile (kg/m^3) along z for for an isothermal part meshed

According to Equation 6, a higher wire mesh density implies a bigger amount of impurities cristallized by nucleation and obvisously a bigger duration of this latter phase. Although for a given time and elevation, crystal size is smaller, a higher wire mesh density may plug the cold trap, specially for an isothermal meshed trap [4]. Indeed, throught this zone, supersaturation is much more important than for a fully meshed trap. As a result, nucleation gets, in an isothermal zone, a more significant role.

4.1.2. Flow rate influence on cristallized mass

Simulated results plotted on FIG.9 and FIG.10 localize oxide crystals finally formed over the packing through ECRIN mock-up for different flow rates, respectively for a fully and isothermal part meshed trap.

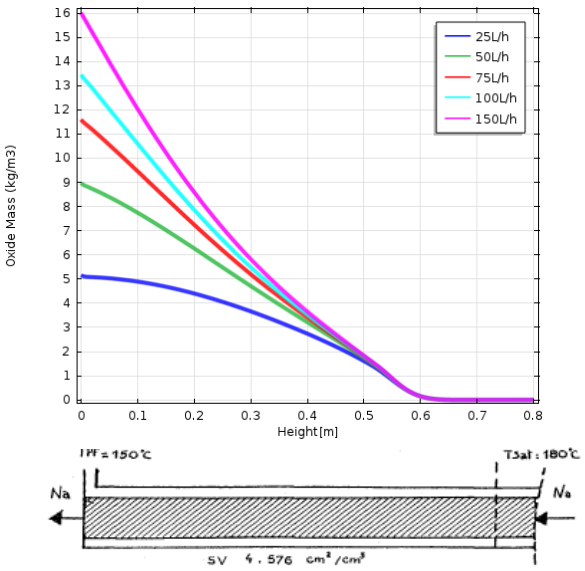

FIG. 10. Oxide Mass profile (kg/m^3) along z for a fully meshed trap

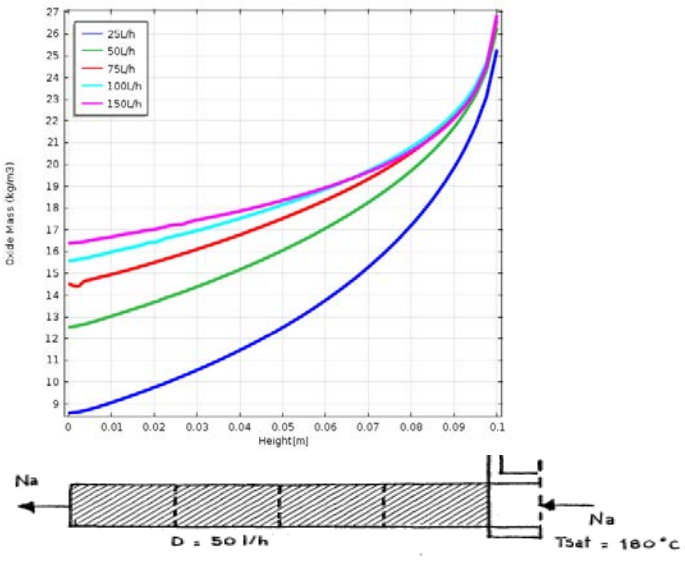

FIG. 11. Oxide Mass profile (kg/m^3) along z for an isothermal meshed trap

Although a higher flow rate brings more impurity through the cold trap, it can prevent from a sufficient cooling which enables an appropriate impurities crystallisation. Thus, increasing the flow rate might lead to crystallize the same amount of sodium oxide mass. It is more obvious for an isothermal meshed trap since boundaries are not cooled down. Thus, increasing the flow rate in order to crystallize more impurities might not be an optimal decision according to purification specifications.

4.2. Sodium Hydride mass profil results

Experimental studies on cold walls crystallization, in CEA Cadarache, have been performed on EPINAR mock-up (FIG.7) by Saint-Martin and Latgé [6]. After performing an endoscopy, it appeared that sodium hydride essentially crystallizes on cold walls, in the upper part of the trap.

4.2.1. Inner Diameter and Flow rate influence on cristallized mass

A concentration of hydrogen corresponding to a saturation temperature equal to 180°C (0.62ppm) was set-up during 2 months. The coldest temperature is set for 150°C. Tests have been performed on EPINAR mock-up to evalutate the impact of the flow velocity, function of the inner diameter and flow rates.Table 2 gathers sodium Hydride mass got for a simulation of 2 months of purification, for a cooling zone height H_{cool}=0.6m.

Table 2. Sodium Hydride Mass (kg) crystallized on cold walls after 2 months of purification

Diameter D [cm] Flow Rate[m^3/h]	**30**	**50**	**70**	**90**
1	1.5	1.3	1.7	2.2
5	3.6	5	6	6.8
10	3.8	6.1	8	11
15	3.7	6.2	8.7	12.7
20	3.6	6.2	8.6	12.1

Simulation results reveal that an optimum exists between diameter and flow rate to get a bigger amount of hydride mass deposit on cold walls.Indeed, as well as shown on FIG. 10 and FIG. 11, a too high flow rate prevents from a good cooling through the trap and does not allow a significant purification. On the opposite, a lower flow rate enables recirculations of the flow due to temperature gradient. The residence time of an impurity through the cooling zone is so larger. However, a too low velocity does not bring enough impurities over these two months of purification to get a sufficient mass deposit and purification specifications may not be respected on the exit of the packless cooling zone. A downstream wire mesh zone is thus critical to bring the purification efficiency on maximum. Moreover, the exit of the cooling zone may be designed and optimized to emphasize fluid recirculations through the walls which would lead to a better purification.

4.2.2. Intern fluid recirculations influence on cristallized mass

In order to evaluate flow recirculations impact on hydride deposit profile, different height of cooling zone have been assigned from 0.4m to 1.2m. Thus, temperature gradient varies from 0.75°C/cm to 0.25°C/cm. Purification is performed over six months. FIG.12 reveals that the higher is the temperature gradient, the more significant are flow recirculations on the bottom part. It comes a denser hydride deposit formed around the coldest point.

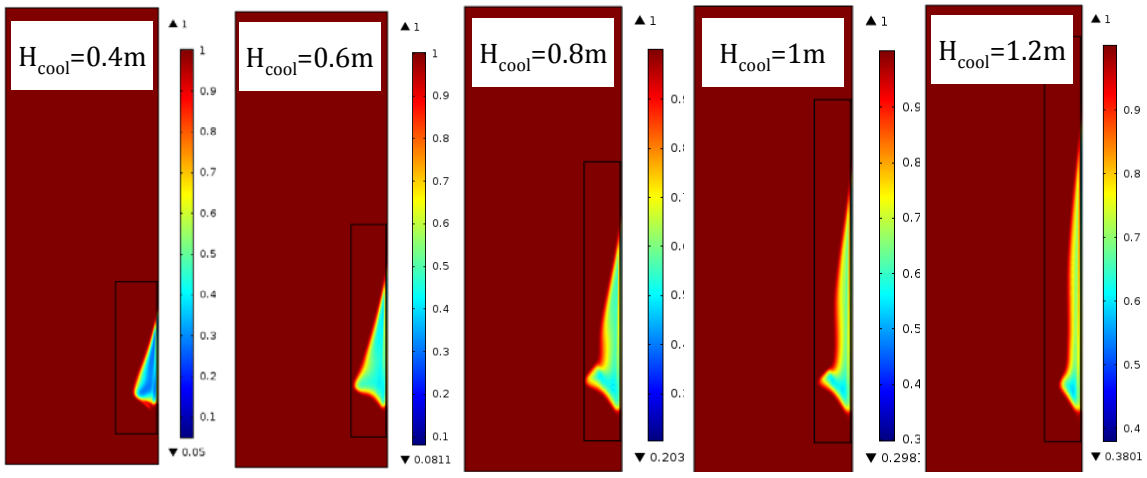

FIG. 12. Porosity profile (-) on non meshed cooling zone after 6 months of purification

5. Conclusion

A model for simulating the sodium purification systems behavior was developed, implementing two kinds of crystallization modeling in cold traps. These first results of simulation enable to apprehend the quantity and location of the cristallized mass according to geometrical and operating parameters. Apprehending the coupling of these physical phenomena should enable to adapt operating conditions in order to optimize purification requirements and to increase cold trap lifetime expectancy.

ACKNOWLEDGEMENTS

This work, developed by CEA and INPT-LGC, is supported by ALSTOM Power Nuclear.

REFERENCES

[1] LATGE, C., “Sodium quality control, In International Conference on Fast reactors”, Kyoto, Japan, (2009).
[2] NODEN, J.N., “A general equation for the Solubility of O_2 in liquid Na”, British Report RB/B/B 2500, (1972).
[3] WITTINGHAM, A., “An equilibrium and kinetic Study of the liquid Sodium Hydrogen Reaction”, Journal of nuclear materials, Vol. 60, (1976), 119
[4] LATGE, C., “Etude de la cristallisation de l'oxyde de sodium en milieu sodium liquide”, Thesis, INPT, Toulouse, France, (1981)
[5] FERON, D., “Etudes des mécanismes de la purification du sodium par les pièges froids” , Thesis, INPT-Toulouse, France, (1979).
[6] SAINT MARTIN, C., and LATGE, C., “Mechanism and kinetics of crystallization of NaH in cold traps”, 4th LIMET Conference 17-21 Octobre, Avignon, France, (1988).
[7] LATGE, C., HULME, G., JONES, D.G., and PERRET, F., “Experimental studies of packless cold traps for validation of the VICSEN code for prediction of cold trap behaviour”, 4th LIMET Conference Avignon, (1988).
[8] SETHIAN , J.A. and SMEREKA , P., “Level Set Methods for Fluid Interfaces”, Department of Mathematiques, universities of California (Berkley) and Michigan (Ann Arbor), course report on http://math.berkeley.edu/
[9] BECKERMANN, C., et al., “Modeling melt convection in phase-field simulations of solidification”, Journal of Computational Physics, 154(1999), pp. 468-496

Activities on Experimental Substantiation of SFR Safety in Accidents with Sodium Boiling

I.M. Ashurko, A.P. Sorokin, V.V. Privezentsev, A.V. Volkov, R.R. Khafizov, E.F. Ivanov

FSUE "SSC RF – Institute for Physics and Power Engineering",
Obninsk, Russian Federation

Abstract. The information about experimental researches of emergency processes accompanied by sodium coolant boiling in the core of a sodium-cooled fast reactor (SFR) which are scheduled to be carried out in the SSC RF-IPPE, is presented in the paper. The description of an upgraded experimental facility AR-1 where tests with modeling of sodium boiling will be carried out is given, and its basic characteristics are presented. The purposes of experimental investigations aimed at acquisition of the experimental data necessary for verification of the computational codes developed for the analysis of severe beyond design basis accidents similar to the ULOF accident are reported, and basic modes that are planned to be studied at the AR-1 are also described: a) a flow mode of two-phase sodium coolant within a sodium plenum located over the SFR core that makes an appreciable influence on dynamics of the ULOF accident, b) modes of sodium boiling within fuel pin bundle under conditions of both forced and natural coolant circulation, c) sodium boiling modes occurring due to events caused by fuel subassembly cross-section blockage, d) modes of sodium boiling in parallel channels under natural primary sodium coolant circulation conditions.

1. Introduction

Within the framework of the Federal Target Program "Nuclear Power Technologies of a New Generation for Period of 2010-2015 and with Outlook to 2020" (FTP) the design of a large-size sodium-cooled fast reactor (SFR) BN-1200 is under development.

The BN-1200 reactor would meet the requirements, including those on safety, imposed to the 4th generation reactor facilities.

One of the key safety requirements imposed to the 4th generation NPPs is assurance of their resistance to any severe accident that may occur during reactor operation in order to eliminate the necessity of evacuation of the inhabitants living in the vicinity of the NPP.

The most unfavorable beyond design basis accident for SFR is that with loss of grid and emergency power supplies and failure of all reactivity control devices (ULOF accident).

In this respect, the following goals are set for the specialists involved in the development and justification of the BN-1200 design:

- development of the new generation computer codes for the analysis and justification of SFR safety under conditions of severe beyond design basis accidents and their verification on the basis of experimental data;
- construction of experimental facilities for obtaining deficient experimental data and carrying out related studies;

- carrying out analytical studies of severe beyond design basis accidents in the BN-1200 by means of the computational codes developed and verified on the basis of the experimental data and evaluation of radioactivity release to the environment;
- development of technical decisions eliminating the possibility of radioactivity propagation outside NPP site in the amount exceeding permissible value for the inhabitants in case of severe beyond design basis accidents, including ULOF accident.

In view of limited amount of experimental data on severe beyond design basis accidents in SFR, the FTP implies updating of the experimental infrastructure of the nuclear power industry for the purpose of obtaining required experimental data.

The paper presents the information on the COREMELT computer code developed for the analysis of the severe beyond design basis accidents which can occur in the SFR. And also information is given on sodium boiling tests that are scheduled to be implemented at the AR-1 test facility located in the State Scientific Center of the Russian Federation – Institute for Physics and Power Engineering (SSC RF–IPPE) and planned to be updated for the purpose of justification of the BN-1200 safety under conditions of the ULOF severe beyond design basis accident and of the design basis accident with fuel subassembly (FSA) cross-section blockage, including acquisition of experimental data required for verification and validation of the COREMELT code regarding sodium boiling modes.

2. Analysis of processes arising in SFR under severe accidents

In order to define the list of experimental data required for verification of computer codes used for analytical studies on severe accidents in the SFR, it is necessary, first of all, to identify physical processes occurring in the course of these accidents.

In this paper the processes of sodium coolant boiling are considered which can arise under the ULOF accident conditions, and also under conditions of the accident with FSA cross-section blockage.

Sodium boiling behavior under the ULOF accident conditions is analyzed with reference to the large-size SFR.

In the large-size SFR usually characterized by positive value of sodium void reactivity effect (SVRE) sodium boiling occurs in the core in case of the ULOF accident that, under certain conditions, may cause melting and displacement of cladding and fuel materials. So, methods of decreasing SVRE value down to the acceptable level are under study. The ultimate goal is to eliminate, by decreasing SVRE, large-scale sodium boiling in the SFR core, that could result in the extensive damage of the core structural elements.

The concept implying sodium plenum located above the core and “flattened” core design (with decreased core height/diameter ratio) was chosen as one of the approaches to decreasing SVRE value in the large-size SFR. The use of such core configuration would allow increasing neutrons leakage in case of sodium boiling onset in the core under ULOF accident conditions. As a rule, coolant boiling appears in the upper core section under the ULOF accident and it may propagate to the central core area in the course of the accident development. With sodium plenum, sodium boiling starts in the upper core section and it first propagates to the sodium plenum volume.

Preliminary calculations have confirmed that upon sodium boiling onset coolant is partially removed from the area at the top of the fuel pins bundle. Since SVRE is negative in this area, reactor power starts to reduce causing decrease of sodium boiling intensity. Finally, the mode of periodical sodium onsets with decreasing amplitude of reactor power, coolant flow rate and reactivity fluctuations is realized on the background of general power decrease. These fluctuations can continue for several dozen seconds. However, the abrupt stability loss may occur in some channels with coolant flow rate decrease down to zero, this being accompanied by the increase of temperature of fuel pin claddings in related channels in the area of DNB appearance. Stable sodium boiling continues in the other channels (no DNB) with the decrease of reactor power.

Apparently, vapor content in sodium plenum has strong effect on the rate of reactor power decrease. In turn, reactor power decrease results in the decrease of fuel pins temperature and, hence, more intensive vapor condensation. Obvious feedback is visible when the mode of two-phase flow in sodium plenum significantly influences the ULOF accident dynamics. Therefore it is important to carry out experimental studies on sodium boiling modes in both fuel pin bundle and FSA sodium plenum, including conditions of sodium natural flow in the parallel channels system.

Nature and scale of sodium boiling process under conditions of blocking of the FSA cross-section will be significantly dependent on the size of the blockage and its location. An accident with total blockage of the FSA cross-section is the most dangerous. It is planned to model the blockage of the FSA cross-section at the AR-1 test facility by means of decrease of coolant flow rate through the test assembly.

3. Description of computational codes applied in SSC RF-IPPE for analyses of severe accidents in SFR

Set of computer codes capable of modeling all types of severe accidents and all their stages was developed at the SSC RF–IPPE for the analysis of severe beyond design basis accidents in the SFR. In particular, the COREMELT computational code is now under development which is designated to model severe accidents in the SFR core. As regards the ULOF accident, COREMELT code permits to model all stages of the accident including coolant boiling, cladding and fuel melting, their relocation and interaction with coolant.

The detailed review of the COREMELT code is given in the separate paper presented at this conference [1], therefore, here only short its description is done.

The COREMELT code is capable of making 3D coupled calculations of neutronic and thermal-hydraulic transients in the SFR. Current COREMELT-2D code version includes neutronic module RADAR and thermal-hydraulic module COREMELT.

A multi-group neutron diffusion equation is solved in R-Z and X-Y geometry in the RADAR module. A TRIGEX code modified for the purpose of the problem solved with a built-in CONSYST code connected to an ABBN-93 nuclear data library is used as a block for the preparation of dynamic neutron data.

A multi-component and multi-phase mathematical model of thermal hydraulics in R-Z geometry in porous body approximation is realized in the COREMELT module. All components are conventionally divided into two groups, namely: moving components and stationary (structural) components. As regards moving components, the complete set of mass, momentum and energy conservation differential equations is solved. Stationary (structural) components simulating various structural elements of the core and reactor vessel, as well as fuel and steel crusts frozen on their surface are described by mass and energy conservation differential equations.

The number of the components may vary depending on complexity of the problem to be solved. All moving components are connected mechanically to each other and to the channel walls (structural components). Heat transfer between all the components is described by the corresponding relationships closing basic set of the differential equations. In the multi-component flow model, there are descriptions of phase transitions, such as evaporation-condensation and melting-freezing.

4. Description of the AR-1 experimental facility

For experimental investigation of sodium boiling that can arise in the SFR under severe accident transient conditions, it is planned to use the AR-1 test facility located in the SSC RF-IPPE (Fig. 1) [2].

FIG. 1. AR-1 test facility

This test facility is applied for investigation of:

- thermal processes in the SFR elements under start-up, operation transient and accident conditions;
- flow stability and heat transfer characteristics under liquid metal coolant boiling modes.

The main characteristics of the AR-1 test facility are presented in Table 1.

Table 1. Main characteristics of the AR-1 test facility

Coolant	Sodium-potassium	Sodium
Pressure, MPa	0.6	1.0
Temperature, °C	900	900
Flowrate, m^3/h	10	10
Electric power, kW	100	100

The AR-1 test facility consists of two loops: test sodium loop and auxiliary loop with sodium-potassium alloy as a coolant.

The closed test loop (Fig. 2) includes an upward leg containing the test fuel subassembly mock-up with electrically heated fuel pin simulators, expansion tank, downward leg and additional electrical heater located at the entrance into the upward leg. Coolant circulation in the test loop can be provided in both forced mode by an electromagnetic pump operation and natural circulation mode due to difference of coolant temperature along the length of the test loop.

Fig. 2 also shows some of measurement instrumentation which is planned to be used for registration of parameters of the two-phase coolant under various boiling modes. The measurement equipment includes:

- thermocouples;
- pressure sensors;
- pressure oscillations sensors;
- pressure gauges;

- ultrasonic sensors;
- potentiometric sensors;
- flow rate meters;
- liquid level meters.

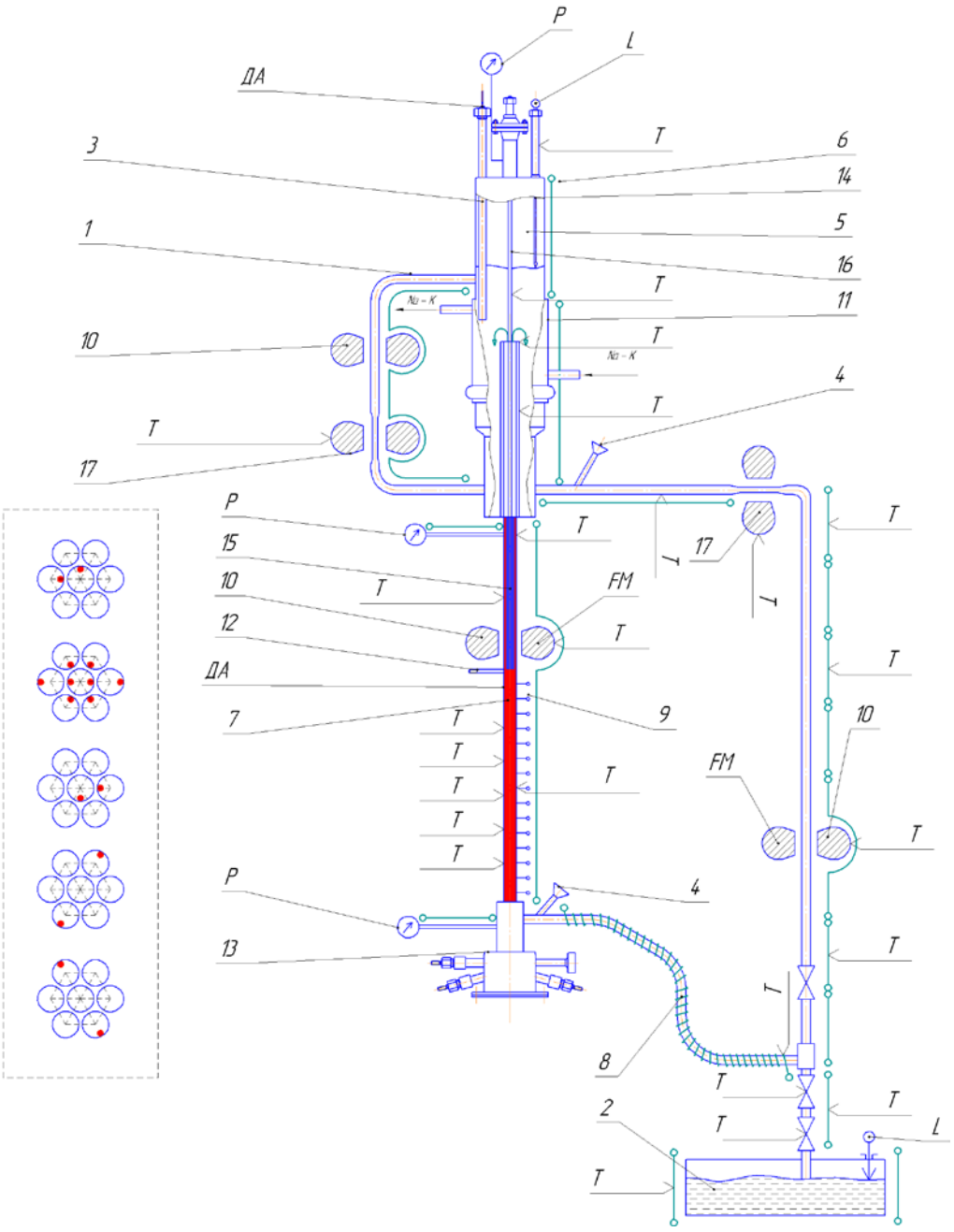

1 – bypass line, 2 – sodium tank, 3 – acoustic sensor, 4 – thermocouple sleeves, 5 – gas cavity, 6 – expansion tank, 7 – subassembly model, 8 – additional heater, 9 – potentiometer sensor taps, 10 – flowmeters 11 – sodium-to-sodium-potassium heat-exchanger, 12 – current lead, 13 – electrical connections unit, 14 – sodium level meter, 15 – restriction area, 16 – restrictors rod, 17 – electromagnetic pumps

FIG. 2. Experimental sodium loop.

The listed devices permit to make measurements of the following parameters during tests:

- electrical power of pin simulators;
- coolant flow rate and its oscillations in the test loop;
- coolant pressure at the inlet and outlet of the test FSA model, pressure oscillations, gas cavity pressure;
- distribution of fuel pin simulator surface temperature along the height of a heating zone;
- coolant temperature in various points of the test loop, including the heated zone;
- registration of the presence of vapor phase along the height of the test FSA model (potentiometric sensors are used for this purpose with electrodes located along all the height of the simulator heating zone, which allow to register a depth of penetration of vapor phase downwards test assembly).

The circulation circuit of the test loop is added by a sodium purification circuit, including a cold trap, a plug indicator and a sampler device.

The auxiliary loop is used for cooling sodium of the test loop. Heat is removed from the test loop through a heat exchanger installed on expansion tank outside wall. Auxiliary loop contains circulating pumps, coolant purification system and air-cooled heat exchanger.

All pipelines and other equipment of the test loop are equipped with electrical heating system that maintains coolant in liquid phase.

The design of the test FSA model having geometry and main elements (active part, sodium plenum, top shielding layer etc.) similar to the FSA of the BN-1200 reactor is under development.

Fuel pin simulators, each of them is a cylindrical cladding with outer diameter of 8 mm and length equal to 1000 mm with refractory coil installed inside it, are collected into bundle of triangular geometry (with pitch to diameter ratio s/d equal to 1.125) located in a hexagonal wrapper made of 3 mm thick heat-resistant sheet steel. Volume between coil and simulator cladding is filled with melted magnesium oxide. Fuel pin simulator cladding consists of two coaxial tubes with outer diameters of 8 mm and 7.2 mm made of heat-resistant stainless steel. Length of a heating zone of simulators is about 600 mm.

A coil made of a molybdenum wire of 1 mm diameter is used as the simulator heating element. Both heater coil diameter and helix pitch distance are equal to 3 mm. One of the heater's ends is attached to a molybdenum current lead of 4 mm diameter connected to the power supply.

Wire of 0.8 mm diameter is used for spacing fuel pin simulators in the FSA model. Wire is wrapped round external surface of the fuel pin simulator with helix pitch distance of 100 mm. Chromel-alumel thermocouple cables are also applied as spacing wires.

The height of the sodium plenum can influence characteristics of the coolant boiling mode. Therefore, for the purpose of investigation of this influence, the design of the FSA model provides possibility of change of the sodium plenum height by means of withdrawal of the displacers simulating absorber elements.

5. Program of the experimental studies at the AR-1 facility

Now updating the AR-1 test facility is underway to provide experimental studies of sodium boiling modes in the SFR fuel subassembly.

The purpose of this modernization of the AR-1 test facility is modeling of coolant boiling processes that can occur in the SFR core under conditions of the ULOF beyond design basis accident and design basis accident with the FSA cross-section blockage. In this respect, the main mode parameters

simulated in the experiments (sodium velocity and temperature in FSA model, heat flux from the fuel pin simulators to the coolant) are chosen from point of view of max degree of approximation to reactor conditions.

At the first stage it is planned to carry out tests related to investigation of sodium vaporization and condensation modes in the area of the core and sodium plenum of a single test subassembly. The program is defined for the first series of tests, which envisages implementation of stationary and non-stationary experiments on study of sodium boiling in the single test FSA, containing 7 fuel pin simulators. The second series of tests is planned to carry out for the test FSA model with 19 fuel pin simulators.

The envisaged measurement instrumentation permits to investigate sodium boiling process both within the bundle of fuel pin simulators and outside of it (in the sodium plenum up to the expansion tank). Indications of detectors are also stipulated to be used for prevention of destroy of the fuel pin simulators by means of switching-off their power supply before exceeding maximum permissible temperature.

In stationary tests the sodium boiling mode is provided by means of step-by-step increase of power of the heaters with the subsequent stabilization of sodium parameters at each power level. Tests are scheduled to be carried out for both sodium forced flow mode through test subassembly and sodium natural circulation mode.

In non-stationary tests it is planned to model conditions characteristic for investigated accidents. So, for modeling of the ULOF transient it is envisaged initially to rich a steady state mode of the AR-1 facility operation, and then to provide reduction of the power released in the fuel pin simulators and decrease of sodium flow rate through the test subassembly in accordance with the preliminary set dependences. Modeling sodium boiling mode caused by the FSA cross-section blockage is stipulated to provide by means of total stop of the coolant flow rate through the test subassembly with the constant power of heaters.

The program of tests envisages investigation of degree and specific features of influence of value of the height of the sodium plenum over the core on accident transient conditions, in particular, on behavior and parameters of sodium boiling mode.

At the next stage it is scheduled an implementation of tests on investigation of stability of sodium boiling in parallel channels under coolant natural circulation mode.

It is expected that the envisaged test program will provide acquisition of all required experimental information for checking the closing relationships used in the two-phase flow models with reference to geometry of the sodium plenum and the fuel pin bundle under various coolant flow modes, for updating flow mode maps used in the COREMELT code, and also for carrying out its additional verification.

6. Conclusion

Within the framework of the BN-1200 design development and substantiation of its safety an implementation of sodium boiling tests at the AR-1 test facility updated for this purpose in the SSC RF-IPPE is planned.

The main objective of scheduled tests consists in acquisition of the experimental data necessary for upgrading and verification of the COREMELT code models used for simulation of the coolant boiling in the SFR core under conditions of severe beyond design basis accidents.

Finally, it will permit to enhance reliability and validity of computational substantiation of the BN-1200 self-protection against severe accidents, such as ULOF beyond design basis accident, accident with blockage of the FSA cross-section.

REFERENCES

[1] ASHURKO, I.M., VOLKOV, A.V., RASKACH, K.F., “Coremelt-2D Code for the Analysis of Severe Accident Processes in Fast Sodium-Cooled Reactor”, Presented at the IAEA FR13 Conference (2013).

[2] ASHURKO, Y.M., et al., “Planning Experimental Studies on Modeling Phenomena Occurring under Severe Accidents in SFR”, International IAEA Workshop on Prevention and Mitigation of Severe Accidents in Sodium-cooled Fast Reactors, Tsuruga, Japan (2012).

Spatial Kinetics in Fast Reactors

Panova, I.S., Belov, A.A., Seleznev, E.F.
Nuclear Safety Institute of the Russian Academy of Sciences (IBRAE RAN),
52, Bolshaya Tulskaya str., 115119 Moscow;
Zhukov, A.M., Matveenko, I.P. and Mikhailov, G.M.
Institute for Physics and Power Engineering (FEI),
1, Bondarenko sq., 249033 Obninsk, Kaluga region
seleznev@ibrae.ac.ru

ABSTRACT

Reactor neutronic calculations designed for calculating of unsteady processes in a real 3D geometry require processing of a large amount of information. They cannot consist of simple models, as they should reflect the processes of variations of all local reactor characteristics. The model complexity and the significant time needed for numerical solution of neutron-transport equations limit the choice of methods that can achieve the required accuracy. Thus there is an urgent need for the development of various methods enabling the solution of unsteady neutron-transport equations and estimates of their errors, spent time and consistency with the experimental data.

1. Introduction

To perform calculations of experiments studying the kinetics of fast reactors, special software (the TIME program) was developed. It uses the diffusion approximation. The use of this approximation is possible at isotropic or linear-isotropic distribution of neutrons, i.e. it is limited by the following two factors:

- the presence of a strong absorber; and
- an abrupt change in the medium properties at distances comparable to the mean free path of a neutron.

Absorption cross-sections in the high-energy area are usually small. Typical neuron mean free paths in fast reactors are much larger than those of thermal reactors. Due to a small size of fuel elements and structural elements, large reactor areas may be considered as homogeneous at distances comparable to the neuron mean free paths. These conditions justify the use of the diffusion theory when calculating unsteady reactor processes [1].

2. Kinetics in Fast Reactors

2.1. Examination algorithms for solving the unsteady neutron-transport equations

The TIME program is designed to solve unsteady neutron-transport equations in 3D hexagonal geometry and in multi-group diffusion approximations taking into account the spectrum of the delayed neutrons and the availability of a source of external neutrons. The program has a modular structure and contains tools responsible for:

- reactor-model generation;
- evaluation of the efficiency of control rods based on a multi-group steady solution;
- calculation of the initial steady state;
- solution of unsteady problem when introducing positive and negative reactivity into the reactor; and
- solution of inverse kinetics equations.

Such a structure gives the user enough possible ways to obtain solutions, whereas the presence of a shell provides a convenient interface.

An unsteady problem is solved in the TIME program through several algorithms:

- via quasi-static approximation using solution of a steady inhomogeneous problem taking into account the spectra of prompt and delayed neutrons for reactivity estimates;
- via quasi-static approximation using solution of a steady homogeneous problem for reactivity estimates taking into account the spectra of prompt and delayed neutrons and the reactor-kinetics parameters (effective fraction of delayed neutrons and the lifetime of prompt neutrons) defined from the start steady state;

- via quasi-static approximation using solution of a steady homogeneous problem for reactivity estimates taking into account the spectra of prompt and delayed neutrons and the reactor-kinetics parameters redefined at each step of the unsteady process;
- via improved quasi-static approximation using solution of a steady homogeneous problem for reactivity estimates taking into account the spectra of prompt and delayed neutrons and with determination of concentrations of delayed-neutron precursors for all calculated cells of the reactor at each step of the unsteady process; and
- via direct solution of unsteady problem with consideration for the availability of an external source of neutrons and the spectra of prompt and delayed neutrons.

The power achieved from the solution of a steady problem and an unsteady problem for undisturbed reactor state should be invariable. For this purpose, an algorithm of searching two conditional normalized parameters is introduced into the program.

Since the effective multiplication factor k_{eff} of the conditionally-critical problem always differs from 1 when calculating real critical states, introducing a correction for "uncriticality" of the critical reactor is necessary in the calculation results. Such a correction reflects the errors of modeling real structures, the use of numerical methods of solution, *etc*.

The reactor power is determined in an iterative process of searching for the second conditionally normalized parameter that considers the fraction of neutrons from the external source in the total number of fission neutrons [2].

The performed calculations have demonstrated that a direct solution of unsteady neutron-transport equations without passing to its simplified shape agrees better with the experimental data. Solutions of problems in quasi-static and improved quasi-static approximations contain errors caused by the use of point-kinetics equations. They include:

1. The assumption introduced on spatial-and-time division of variables resulting in the necessity of solving a conditionally-critical steady problem. The latter is actually observed for a strict steady state at $k_{eff}=1$ and $\rho=0$, i.e. only at constant power. In unsteady processes no calculated eigenvalue of the problem exists experimentally and that limits the possibility of direct parameter measurements [3].
2. The use of integral concepts cannot give an idea of variations of local characteristics measured directly in the reactor. This is due to the fact that at neutron-field deformations its local characteristics change first.
3. Simplifications made when deriving point-kinetics equations lead to consideration of an asymptotic solution of the conditionally-critical problem. Consequently, effective fractions of delayed neutrons, the prompt-neutron generation time and concentrations of delayed-neutron precursors have an invariable representation in time. Variations in their values are due to the difference in nuclear-constant distributions as a consequence of introducing disturbance in the reactor [4].

However, depending on the task, the use of quasi-static and improved quasi- static approximations is possible (note that the latter has proved to be better) to achieve a more rapid estimate.

The rate of propagation of neutron-field disturbances over the reactor depends on the neutron spectrum, and for fast reactors it equals about 10 km/s. Because the fast-reactor dimensions do not exceed 10 m, the asymptotic of transient processes should be expected in 10^{-3} s. This means that the processes which duration is less than the time indicated are non-asymptotic processes.

When conducting experiments, the use of such a small time step is a difficult task. In practice, experimentalists use the channel-width value of ≥ 0.1 s. The solution of spatial-kinetics equations at such a large time step also has an asymptotic nature. Thus, there may be conditions where the accuracy of solution using point-kinetics equations will be sufficient.

Short time for attaining the asymptotics is due to prompt fission neutrons, which lifetime is 10^{-7} s in fast reactors. Fast transients influence concentrations of delayed-neutron precursors, but this impact is not immediate being determined by the half-life of each group of delayed neutrons. Thus the duration of transients in fast reactors is determined by delayed neutrons and can last hundreds of seconds.

In opposition to thermal reactors, where key neutron processes occur in the thermal part of the spectrum and, consequently, the difference between the spectrum of delayed neutrons and that of instant neutrons has no effect on the processes in the thermal area, in case of fast reactors a

consideration of such a difference is rather important. The delayed-neutron spectrum is slightly softer compared to the fission-neutron spectrum though it is still located in the high-energy area.

Concentrations of delayed-neutron precursors depend on the energy of incident neutron and the nucleus of fissile nuclide '*i*'. When solving neutron-transport equations, the precursors of delayed neutrons are usually combined into several groups '*j*', each of them being provided with the total output of neutrons and an average half-life value. In the performed calculations eight groups of delayed neutrons were used.

For reactor kinetics the fraction of delayed neutrons of all neutrons produced during fission is of major importance. It can be defined in different ways. Thus β_j^i - the fraction of '*j*' group of delayed neutrons of '*i*' nuclide – is invariable in time at each point of the reactor and characterizes the very procedure of fission of the given nuclide. $\beta_{m,j}^i(t)$ is the instantaneous fraction of '*j*' group of delayed neutrons of '*i*' nuclide to all neutrons of this nuclide being generated at a time '*t*' integrated over the entire reactor space. Under steady conditions both fractions, β_j^i and $\beta_{m,j}^i(t)$, are equal. In unsteady processes the instantaneous fraction of delayed neutrons varies in the interval [0, 1]. Studying the behavior of the instantaneous fraction of delayed neutrons enables a better understanding of the physics processes.

It is believed that the effects of the shape of delayed-neutron spectrum on the effective fraction of delayed neutrons are minor due to a low dependence on the energy of the neutron value-function. However in accordance with the performed investigations, the spectrum of delayed neutrons can influence not the fraction of such neutrons but the reactivity value.

2.2. Reactor model

To study the fast-reactor kinetics, experiments in BFS-105-2 critical assembly were conducted. The cylindrical assembly core has a height of 40 cm. The core diameter to height ratio equals to 2. MOX-type fuel surrounded by a thick blanket of depleted uranium is used for the critical assembly. Control rods have a composition similar to that of the neutron-absorbing area arranged above the core fuel assemblies. Thus, when moving control rods (except for absorber introduction into the core), a part of the core drops into the breeding blanket. A diagram of the computational model (see Figure 1) shows that control rods are combined into three groups. To measure the kinetic of the reactor core, sensors are being introduced: sensors ## 1 – 3 are located on the periphery of the side blanket, Sensor #4 is at the core center, Sensor #5 is placed in the immediate vicinity of control rods, and Sensor #6 is at the middle of the side blanket. To simulate the movement of control rods, a special algorithm taking into account the movement of the materials and the change in the concentrations of delayed-neutron precursors was used in the TIME code.

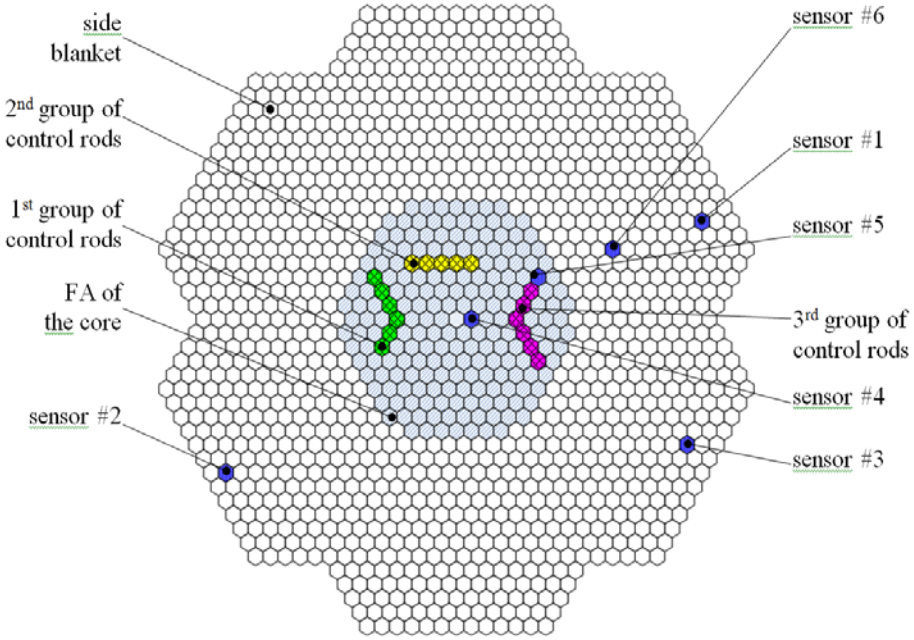

Fig. 1 – Diagram of the calculated reactor model

3. Spatial Kinetics

3.1. Delayed Neutrons

The effects of the reactivity insertion on the concentration of the eight groups of delayed-neutron precursors are the following: if a positive reactivity is inserted, the fraction of neutron groups with short half-life (1 second or less that corresponds to the last three groups) increases, whereas the fraction of the remaining groups decreases. Accordingly, if a negative reactivity is introduced, the behavior of the fraction of short-lived groups has a decreasing character, whereas that of the long-lived groups increases. Thus short-lived groups of delayed neutrons react faster to parameter variations and track the reactor power increase. Plots of variations in the delayed-neutron fraction for each group of the delayed neutrons for a reactivity insertion of $ 0.90 are given in Fig. 2. The same plots for the case where three groups of control rods are inserted over 4 s (from the 3rd s to the 7th s) are presented in Fig. 3.

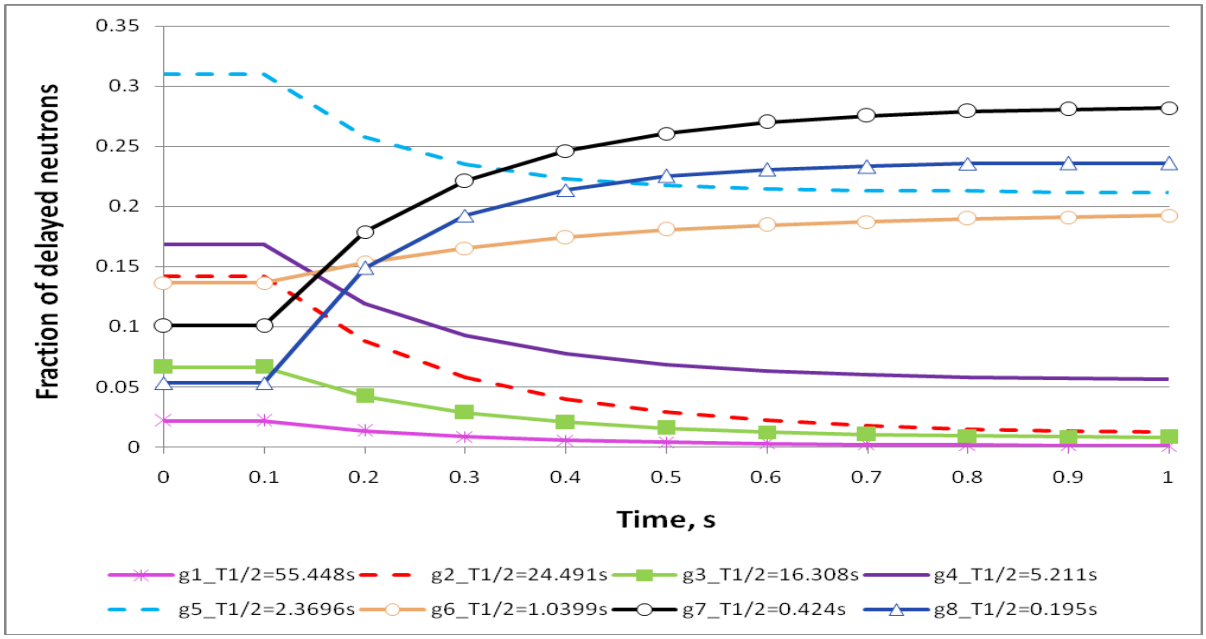

Fig. 2. Plots of variations in the delayed-neutron fraction for each group when introducing a positive reactivity into the reactor

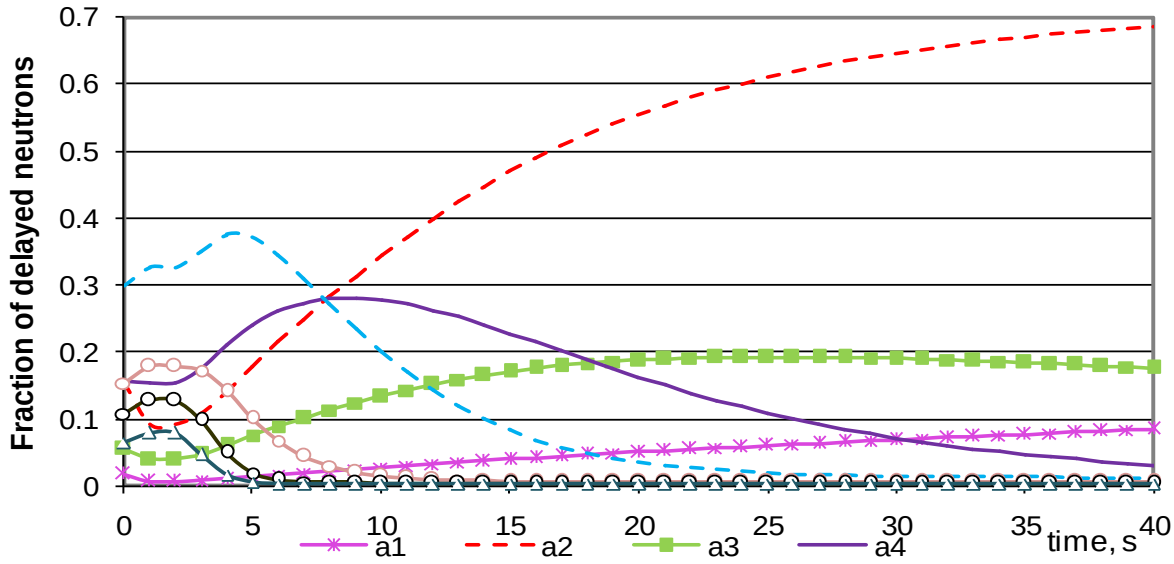

Fig. 3. Plots of variations in the delayed-neutron fraction for each group when introducing a negative reactivity into the reactor

Such a redistribution of concentrations of delayed-neutron precursors leads to the fact that the instantaneous fraction of delayed neutrons decreases significantly when introducing a positive reactivity and increases in case of introducing a negative reactivity. Thus, the reactor-runaway condition may be formulated as follows: if the fraction of delayed neutrons generated by the decay of their precursors tends to zero, the runaway of such a reactor proceeds with prompt neutrons.

Due to changes in the fraction of delayed neutrons when introducing a disturbance into the reactor, the efficiency of control rods depends on both the time of their insertion into the reactor and the conditions preceding this movement.

3.2. Reactivity

To calculate the efficiency of control rods using the rod-dropping method, the TIME program was used.

A plot of reactivity variations following control rod stoppage (the point 0 s) at their different insertion rates (a rapid insertion - 5 s and a slow insertion - 50 s) to the reactor is demonstrated in Fig. 4. The area marked in gray corresponds to the time of the present experiment. It is seen that the faster the rod is introduced into the reactor, the larger is the reactivity by the rod-stoppage instant. With time, the effect of delayed neutrons shows up, and reactivity increases at a slower control-rod introduction rate.

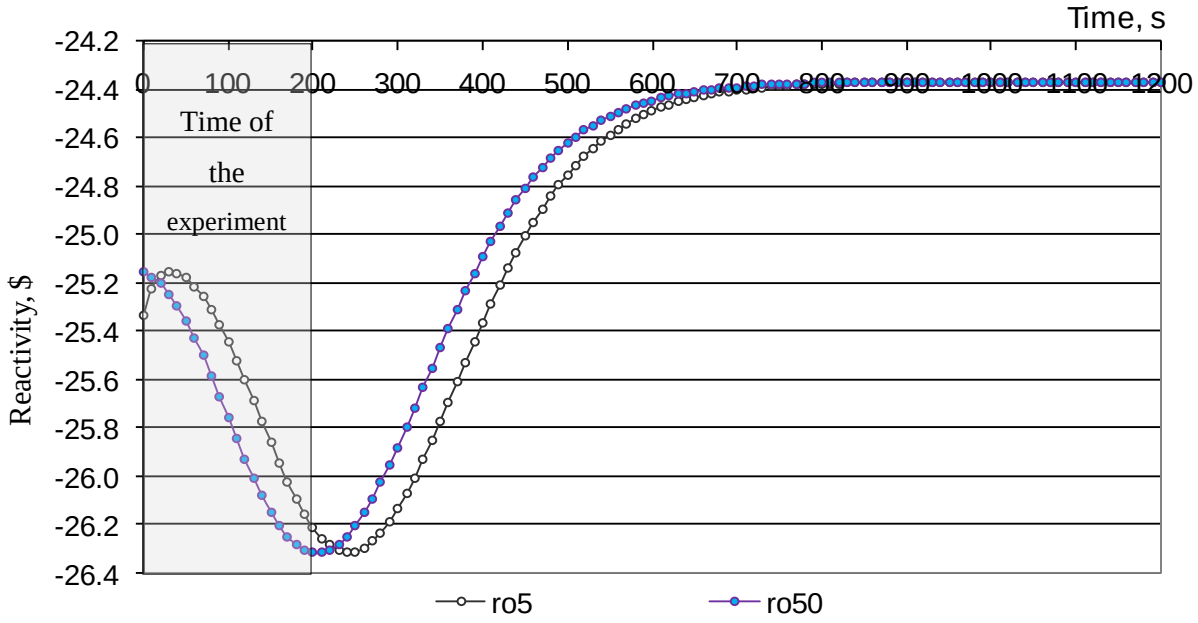

Fig. 4 – Plots of reactivity variations after stopping the motion of three control-rod groups for different insertion rates

Reactivity variations are caused by the following two opposite processes:

1. In case of rapid introduction, the fraction of neutron absorption by the absorber is higher as it gets to a large flux of neutrons. Thus reactivity will be higher at a rapid introduction of control rods into the reactor.
2. However rapid introduction of control rods results in a fast reactor-power decrease, and thus less amounts of delayed-neutron precursors, decaying later, will be accumulated.

A few minutes later reactivity values for both cases become equal. Thus the asymptotics of some unsteady processes in fast reactors is determined by the asymptotics of delayed-neutron processes and equals hundreds of seconds.

Typically, the actuation of scram systems in the reactor occurs not at its steady state but during runaway. The effects of prior input of positive reactivity on the efficiency of control rods were analyzed. A plot of variations in the delayed-neutron fraction when moving control rods during 13 s

(the grey area) and after their stoppage depending on the prior runaway of 13 and 7 cents is demonstrated in Fig 5.

One can see that when a higher value of positive reactivity is introduced, the movement of control rods falls to a smaller fraction of delayed neutrons. Moreover, its lower value remains throughout the experiment. Thus it turns out that positive reactivity preceding the movement of control rods results in a decrease in their efficiency. This important fact explains the need for calculating the reactor behavior during control rod movement not on the reactor steady-state basis, but with consideration for the conditions preceding the movement of control rods.

To study the effects of positive reactivity input, the following two experiments were conducted:

1. The same measured control rod was used to introduce both positive and negative reactivity; and
2. Positive reactivity was introduced by one control rod, whereas negative reactivity was inserted by another control rod.

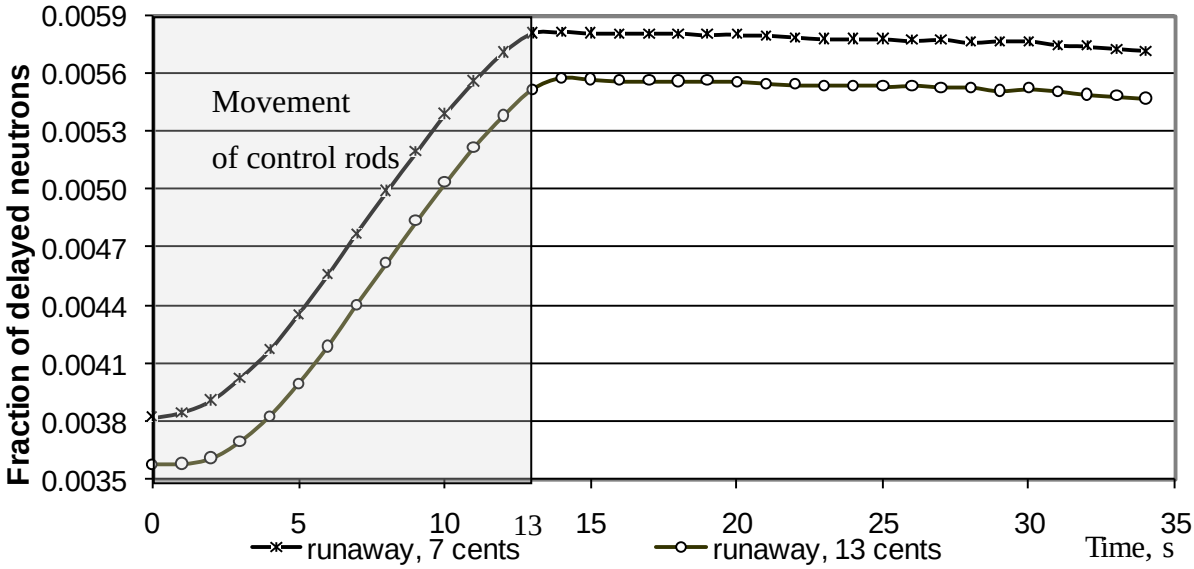

Fig. 5. Variations in the delayed-neutron fraction in case of prior insertion of different positive reactivity

In the performed experiments different end states of the reactor were achieved: in the second calculation the efficiency of control rod was lower. This is evidence of non-observance of commutativity properties with respect to reactivity.

Spatial distributions of medium disturbances in time were considered in the calculations using the readings of six sensors. Plots of reactivity variations at each sensor-location point after control rod stoppage are demonstrated in Fig. 6.

The behavior of these curves gives an indication of heterogeneity of the neutron-field deformation. Thus the efficiency of control rods corresponding to readings of Sensor #5 (located in the vicinity of control rods) has the largest absolute value and an unstable behavior. The sensor located in the central part of the core is characterized by smaller time variations and a more rapid achievement of the asymptotics.

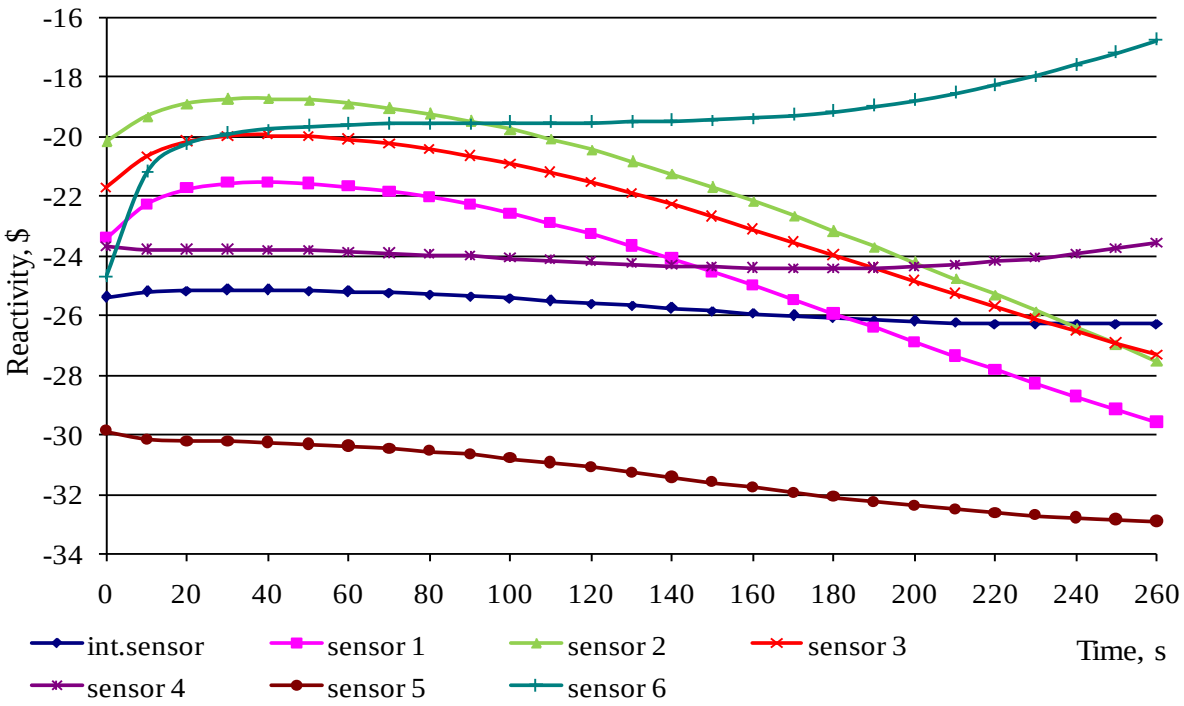

Fig. 6. Plot of reactivity variations based on readings of each sensor after dropping 3 groups of control rods

3.3. First Harmonic

When calculating the efficiency of control rods, special attention should be focused on the coordinates of disturbance introduction into the reactor. Based on the principle of conservatism, the input of reactivity should be modeled at the points having most unstable (i.e. unfavorable) time behavior.

As known from the reactor theory, the solution of unsteady neutron-transport problem has the following shape in the general case:

$$\varphi(r,E,\Omega,t)=\sum_j \varphi_j(r,E,\Omega)\exp(s_j t)\,. \qquad (1)$$

where the set of numbers 's_j' forms the spectrum of eigenvalues of the transport equation. Because 's_0' is the largest real value among all 's_j', all higher harmonics '$\varphi_j(r,E,\Omega)$' of time series expansion (1) attenuate with time (in the asymptotics), and the neutron flux acquires an asymptotic shape of the time-constant "basic" distribution '$\varphi_0(r,E,\Omega)$' varying exponentially only in its amplitude with time:

$$\varphi_{ac}(r,E,\Omega,t)=\varphi_0(r,E,\Omega)\exp(s_0 t) \quad \text{at} \quad t\to\infty\,. \qquad (2)$$

In accordance with a specified value of 's_0', the neutron flux will attenuate ($s_0<0$), grow ($s_0>0$) or remain invariable ($s_0=0$) with time.

The TIME program enables estimating - through the iteration process - the shape of the following harmonics (the first) decaying most slowly of the remaining ones - see Fig. 7.

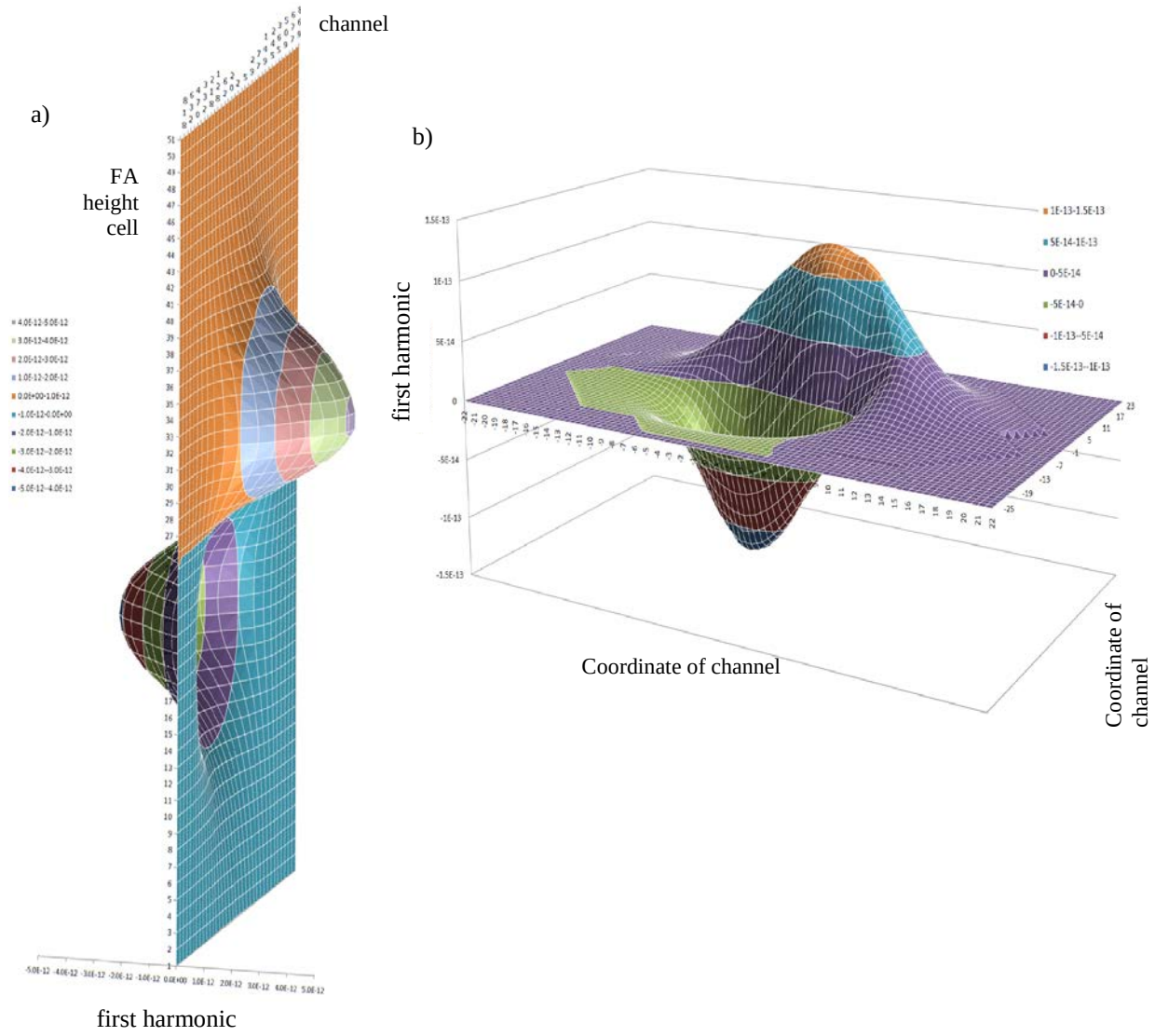

Fig. 7. Distribution of first harmonic
a) throughout the channel height for the central line of FA;
b) normal cross-section for 26 FA height cell.

It can be seen that the first harmonic has alternating signs with a maximum and a minimum in the areas of highest gradients of the zero harmonic inside the core. It is likely that the reactor areas wherein disturbances will provide the longest passing to the asymptotic state can be estimated using the first-harmonic extreme areas.

A similar situation is observed for radial directions.

The search for the second harmonic showed that it has lesser amplitude and disappear very quickly. Partially it is explained for small sizes of our reactor model. Therefore its influence on the reactor kinetic is insignificant.

3.4. Sensor Efficiency

The solution of spatial-kinetics equations allows selecting a location for the ionization chamber where its efficiency in the given experiment would vary in the minimum possible way. The task of finding such points is separated into an axial and a radial component.

The performed investigations of axial sensor location have demonstrated that the best sensor-location place wherein relative efficiency of the sensors is preserved is found in the middle of the channel. When the sensor is moved to the channel edges, its efficiency increases and this affects the accuracy of the measurement, accuracy estimated on the basis of signals issued by the camera. Thus the error in determining the efficiency of control rods will be maximal when placing sensors above or below the reactor core.

The sensor efficiency in the radial direction - being heavily dependent on mutual arrangement of the disturbance-introduction point and the sensor location - should be considered separately for each individual case. In the calculated model, the efficiency of sensors is most stable for the Integral Sensor and the Sensor #4; readings of Sensor #2 and Sensor #5 contain the largest error (see Fig. 1).

Accounting for sensor-efficiency variations is important for the case of inverse solution of the kinetics equation that is widely used in practice to determine the efficiency of control rods as a result of reactivity calculations by use of the signal of the ionization chamber.

3.5. Inverse-Kinetics Equation

The inverse-kinetics equation is solved in the TIME program in the following two ways:

1. Under the assumption of proportionality of the reactor power and the signal strength, i.e. $N(t) = \varepsilon(r_d, t)\int dE'\varphi(r, E, t)\nu_f\Sigma_f$; and
2. Under the assumption of proportionality of the product of sensor efficiency for delayed neutrons of one of the groups and the readings of the sensor integral over the space of delayed neutrons, i.e.
$\varepsilon_j(r_d, t)\langle\Sigma_d(r_d, E)\phi(r_d, E, t)\rangle = \langle\phi^+\chi_{dj}\beta_j\sum_g \nu\Sigma_f\phi\rangle$ [5].

For the first case, the calculated value of the amplitude function is used in the program as a signal. When solving the inverse-kinetics equation, a system of three equations with three unknowns is solved at each time step. As the result, the following parameters are determined: reactivity, efficiency of the sensors and the fraction of external neutron source.

For the second case, a special module is introduced into the program. One of the advantages of this module consists in the possibility of solving the inverse-kinetics equation using both a signal of current from the ionization chamber in a real experiment and the amplitude function determined in the program. Thus the problem reduces to solution of a system of 10 equations with 10 unknowns.

4. Conclusions

Various methods for solving the unsteady reactor-kinetics problems have been investigated in this paper with screening of their advantages and disadvantages. Based on this comparison, key shortcomings of point-kinetics equations are identified, and arguments describing the advantages of a direct solution of the spatial equation are formulated.

A general idea of the tool used, i.e. the TIME program, are given.

As demonstrated, the role of delayed neutrons in the kinetics of fast reactors (as distinct from thermal reactors) is important, and they exert a significant effect on unsteady processes. These effects are manifested as follows:

- effective parameters of reactor kinetics such as the effective fraction of delayed neutrons and the prompt-neutron lifetime are changed;
- the asymptotics of unsteady processes in a fast reactor is determined by that of delayed-neutron processes and can equal hundreds of seconds;
- the efficiency of sensors in unsteady processes changes in both axial and radial directions;
- when using standard methods of control-rod-efficiency measurements (via rod drop), the efficiency of a control rod measured prior to reactor runaway with a positive reactivity generated by another rod will be less than the measured efficiency of the same rod at the measurement start without prior positive-reactivity input. This is due to different end (asymptotic) states of the reactor in such measurements;
- the last-mentioned fact indicates nonobservance of the commutativity property with respect to reactivity. This means that the transition from one state to another characterized by a specified reactivity change may be described by some other reactivity value in the case of inverse process. This suggests a need for:
    - passing to the solution of spatial-kinetics equations in the calculations;
    - calculating directly measured parameters; and -giving up the reactivity concept some day.

REFERENCES

1 Judd, A. (1984) *Fast Breeder Reactors*, Energoatomizdat, Moscow (transl. from English to Russian), pp. 14-19.

2 Seleznev, E.F. (1999) 'Non-criticality' of a critical reactor», *Russian J. "Issues of Nuclear Science and Technology" (VANT), 'Physics of Nuclear Reactors' Series*, #1 (in Russian) , p.9.

3 Feinberg, S.M., Shikhov, S.B. and Troyanskiy, V.B. (1978) The Theory of Nuclear Reactors, Atomizdat, Moscow (in Russian), pp. 43-68.

4 Bell, D. and Glasstone, S. (1974) The Theory of Nuclear Reactors, Atomizdat, Moscow (transl. from English to Russian), pp. 372-377.

5 Kazanskiy, Yu.A. and Matusevich, E.S. (1984) Experimental Methods of Reactor Physics, Energoatomizdat, Moscow (in Russian) , 270p.

Uncertainty Analysis for Fuel Flux Calculations of Fast Reactors with External Fuel Cycle

Seleznev, E.F. [1], Belov, A.A[1], Manturov, G.N. [2], Peregudov, A.A. [2], Semenov, M.Yu. [2], Tsybulya, A.M. [2], Tikhomirov, G.V. [3] and Saldikov, I.S. [3]

[1] Nuclear Safety Institute of the Russian Academy of Sciences (IBRAE RAN) – 52, Bolshaya Tulskaya str., 115119 Moscow;

[2] Institute for Physics and Power Engineering (FEI) – 1, Bondarenko sq., 249033 Obninsk, Kaluga region;

[3] Moscow Engineering and Physics Institute (MEPHI) – 31, Kashirskoye road, 115409 Moscow

Email of the Main Author: seleznev@ibrae.ac.ru

Abstract

The paper focuses on the results of uncertainty analysis when calculating nuclide composition in fuel of fast reactors and on uncertainties of determining nuclide composition in the external fuel cycle. As demonstrated, the main contributions to the uncertainty of nuclide composition are due to:

- uncertainties in operation of the reactor and in the fuel-cycle time;
- uncertainties in nuclide clean-up factors at the Closed Nuclear Fuel Cycle (CNFC) stages when reprocessing spent nuclear fuel;
- uncertainties in isotopic-kinetics cross-sections and and
- uncertainties in nuclide decay data.

Introduction

It is known that long-term development of nuclear power with uranium fuel cycle is only possible on ^{238}U basis [1] that is implemented in two ways: -directly via nuclear fission which probability increases with an increase in mean energy of neutrons in the reactor core; and -through neutron capture with the generation of ^{239}Pu isotope having a much greater probability of fission. The second process plays the key part in the uranium fuel cycle and is most profitable in the high-energy neutron spectrum generated in fast reactors only.

When reprocessing burnt-out fuel, the so-called ‘fresh’ fuel prepared for loading in fuel elements may contain: -a part of fission products contained in fuel extracted from the reactor prior to its reprocessing; and - actinides that can be partly burned in the reactor that allows diminishing the amount of radioactive waste compared to processing with chemical separation of elements of fuel and decreasing the radiation burden on the environment. But at the same time, the presence of any impurities to fissile nuclides in the fuel would deteriorate the fast reactor performance.

As the CNFC enterprises have not collected enough experience of stable operation yet and in many ways are still in search of an optimal reprocessing technology, estimating the requirements to them from the viewpoint of fuel-characteristic optimization is rather important. An estimate of the required clean-up degree of reprocessed fuel from fission products and some actinides would be also appropriate.

In this context, an attempt is made in this paper to evaluate the effects of the degree of fuel clean-up on the performance of reactors and the whole fuel cycle based on uncertainty

analysis of fuel-flux calculations directly in fast reactors and in the external fuel cycle. To solve this problem, the software for solving the BPSD nuclide-kinetics problem [2] was used together with the software that takes into account the effects of uncertainties in operation of external-fuel-cycle enterprises.

1. Solution of the Nuclide-kinetics Problem with Full Nuclide-Transition Matrix

To solve the nuclide-kinetics problem, the BPSD code was used that calculates nuclide concentrations in fuel of the reactor and outside it with uncertainty estimate of the solution.

To identify fuel composition, the following parameters are determined in calculated cells of the reactor model: neutron fluxes; microscopic cross-sections of the processes of capture and fission for all nuclides; fission rates for k nuclide 'λ_f^k'; capture rates 'λ_c^k'; the rate of reactions: (n,2n) – 'λ_{n2n}^k', (n,3n) – 'λ_{n3n}^k', (n,α) – 'λ_α^k'; the rates of nuclide decay and spontaneous fission, *etc*. The rate of 'k' nuclide transition to '*j*' nuclide during the decay process with the half-time '$T_{1/2}^k$' and the probability of channel of this decay as '$\varepsilon_{k\to j}$' is represented as: '$\lambda^{k\to j} = \varepsilon_{k\to j} \ln 2 / T_{1/2}^k$'; the rate of spontaneous fission is represented in the same way; λ_p^k - the summary rates for 'k' nuclide.

Information on nuclide microscopic cross-sections, decay rates and probabilities of the processes is taken from the data library [3].

At each time interval 'Δt' all of the above parameters of the burnup equation are assumed invariable, and at the next time interval they are redefined. The size of the time interval is defined by the user on the basis of physical considerations – mainly to minimize errors in the determination of nuclide concentrations.

Nuclide transformation chains considered in reactor problems may differ depending on specific tasks to be solved. These tasks may be categorized as follows:

- identification of variations in fuel composition within a calculated cell of the reactor model for the case of reactor operation at power and for the reactor-shutdown case to identify changes in the reactor physics; and
- calculation of variations in fuel composition within a calculated cell outside the reactor, *etc*.

The system of nuclide-kinetics equations is an inhomogeneous linear system of equations:

$$\frac{dy^k}{dt} = \sum_{j=1}^{n} a_{kj} y^j + q^k, \left(k = 1, 2, ..., n \right) \qquad (1)$$

with the initial condition: $y^k(0) = y_0^k, \quad (k = 1, 2, ..., n) \qquad (2)$

and the external source: $q^k, \quad (k = 1, 2, ..., n) \qquad (3)$

or in matrix form:

$$\frac{d\vec{y}}{dt} = \hat{A}\vec{y} + \vec{q}, \quad (A \equiv [a_{kj}]) \qquad (4)$$

$$\vec{y}(0) = \vec{y}_0 \qquad (5)$$

with constant coefficients a_{kj} and no external source it has a common analytical solution of the type:

$$y(t) = e^{At} y_0, \quad (t \geq 0), \qquad (6)$$

where: the matrix function 'e^{At}' is the matrix of the '$n \times n$' size.

Series expansion of the function 'e^{At}' necessitates cumbersome matrix multiplications but, if 'A' matrix has '*n*' different eigenvalues, the expansion of 'e^{At}' functions produces the following normal shape of the solution:

$$y = C_1 e^{s_1 t} + C_2 e^{s_2 t} + \ldots + C_n e^{s_n t}, \qquad (7)$$

which parameters are determined by initial conditions or boundary conditions [4].

One of the methods of solving the problem (1-5) was implemented in the ORIGEN code [5]. The main advantage of this code over other burnup codes consists in the ability of representing the whole matrix of isotopic transitions without restrictions on the number of transitional chains that has become possible due to rational use of the matrix exponential method.

To solve the problem in the BPSD system, an iterative process is used. At its first stage, the solution of inhomogeneous equations with an unknown coefficient is determined, namely, via representation of the equation (4) in the following shape:

$$\frac{d\vec{y}}{dt} = \hat{D}\vec{y} + \hat{A}'\vec{y} + \vec{q}, \quad (A \equiv [a_{ik}]) \ , \qquad (8)$$

where: $\hat{D}, \ (D \equiv [a_{ii}])$ is the diagonal part of $\hat{A}$ matrix; and

$\hat{A}' = \hat{A} - \hat{D}$ is the non-diagonal part of $\hat{A}$ matrix;

the diagonal member is responsible for nuclide "consumption" from all reactions, whereas the non-diagonal members are charged with nuclide "generation" from other nuclides.

At the first iterative step the solution of the following system is considered:

$$\frac{d\vec{y}}{dt} = \hat{D}\vec{y} + \vec{q}, \qquad (9)$$

that is solved analytically at the time step 'τ' for the initial (zero) iteration:

$$y_0^k(\tau) = y^k(0)\exp(-\lambda_p^k \tau) + q^k \frac{(1-\exp(-\lambda_p^k \tau))}{\lambda_p^k} \ , \qquad (10)$$

where: -the first term is the remainder of concentration of the nuclide nuclei after accounting for the "decays" from those available at time 0; and -the second term is the "receipt" of nuclide from an external source taking into account its decay in time (0,τ).

Simultaneously we obtain the amount of the same nuclide "decayed" over 'τ' step by the interval end:

$$dy_0^k = y^k(0)(1-\exp(-\lambda_p^k \tau)) + q^k \tau (1 - \frac{(1-\exp(-\lambda_p^k \tau))}{\tau \lambda_p^k}) \qquad (11)$$

This amount transits into other nuclides with a probability proportional to the rates of the corresponding generation processes of other nuclides from this nuclide.

Thus for the 'n' iteration we have:

$$y_n^k(\tau) = y_{n-1}^k(\tau) + \sum_{m \neq k} dy_{n-1}^m \frac{\lambda^{m \to k}}{\lambda_p^m} \frac{1-\exp(-\lambda_p^k \tau)}{\lambda_p^k \tau} \qquad (12)$$

$$dy_n^k = \sum_{m \neq k} dy_{n-1}^m \frac{\lambda^{m \to k}}{\lambda_p^m} [1 - \frac{1-\exp(-\lambda_p^k \tau)}{\lambda_p^k \tau}] \qquad (13)$$

The iteration process is terminated under any law, for example, under the inequality fulfillment law:

$$| y_n^k / y_{n-1}^k - 1 | \leq \varepsilon \ , \text{ for all "k"}, \qquad (14)$$

where: 'ε' is the maximum allowable deviation of nuclide concentrations at two successive iterations.

When analyzing the expression in the brackets (13) we note that for any values of 'λ' the value in the brackets will be always less than 1. Thus we have a tendency to zero formation of "new" nuclei of the required nuclide by the end of the time step that provides the iterative process convergence. The smaller is the size of the time step, the lower is the value of the square bracket in (13), i.e. the faster is the convergence - that is to say that the solution is obtained with fewer iterations.

The solution may be also written in explicit form:

$$y_n^k(\tau) = y_{n-1}^k(\tau) +$$

$$+\sum_{m_n \neq k} \frac{\lambda^{m_n \to k}}{\lambda_p^{m_n}} \frac{1-\exp(-\lambda_p^k \tau)}{\lambda_p^k \tau} \left(1 - \frac{1-\exp(-\lambda_p^k \tau)}{\lambda_p^k \tau}\right)^{n-1} \prod_{j=1}^{n-1} \left(\sum_{m_j \neq k} \frac{\lambda^{m_j \to k}}{\lambda_p^{m_j}}\right) dy_0^{m_1}$$

$$\approx y_0^k(\tau) + \sum_{m \neq k} \{dy_0^m \frac{\lambda^{m \to k}}{\lambda_p^m} \frac{1-\exp(-\lambda_p^k \tau)}{\lambda_p^k \tau} [1 + \left(1 - \frac{1-\exp(-\lambda_p^k \tau)}{\lambda_p^k \tau}\right) \sum_{m \neq k} \frac{\lambda^{m \to k}}{\lambda_p^m} + \quad (15)$$

$$+ \ldots + \left(1 - \frac{1-\exp(-\lambda_p^k \tau)}{\lambda_p^k \tau}\right)^{n-1} \prod_{j=1}^{n-1} \left(\sum_{m_j \neq k} \frac{\lambda^{m_j \to k}}{\lambda_p^{m_j}}\right)]\}$$

from which it follows that at 'n' tending to infinity the last term in the series is actually the product of two factors, each of them being a number raised to (n-1) power, certainly less than 1, and tending to zero that guarantees the convergence. In accordance with Ref. [4], the series (15) may be interpreted as the Neumann series which convergence is proved.

Attention should be paid to the fact that during the iteration process we operate only with non-negative values in equalities (12) and (13). Thus a solution exists and it is positive because there is always at least one nonzero term in the sum (12) (for the initial concentration of at least one nuclide is positive, otherwise the problem makes no sense).

The user of the BPSD system may define independently an optimal ratio between the time-step duration and the speed of solution.

Upper bounds of errors in the solutions may be estimated during the process of iterations but also by the end of the initial iteration defined by criterion (14), by using the following rationale for a function of several parameters: $\delta y(x_1, \cdots, x_q) \equiv \sum_{i=1}^{q} \left|\frac{\partial y}{\partial x_i}\right| \delta x_i$. Thus:

$$\delta y_0^k(\tau) = y_0^k(\tau)(\tau \delta \lambda_p^k + \lambda_p^k \delta \tau) + \delta y^k(0) \exp(-\lambda_p^k \tau) + \delta q^k \frac{(1-\exp(-\lambda_p^k \tau))}{\lambda_p^k}$$

$$+ q^k [\frac{(1-\exp(-\lambda_p^k \tau))}{\lambda_p^k} \frac{\delta \lambda_p^k}{\lambda_p^k} + \frac{2\exp(-\lambda_p^k \tau) - 1}{\lambda_p^k} (\tau \delta \lambda_p^k + \lambda_p^k \delta \tau)] \quad (16)$$

for the first iteration, when solving:

$$y_1^k(\tau) = y^k(0) \exp(-\lambda_p^k \tau) + q^k \frac{(1-\exp(-\lambda_p^k \tau))}{\lambda_p^k} + \sum_{m \neq k} dy_0^m \frac{\lambda^{m \to k}}{\lambda_p^m} \frac{1-\exp(-\lambda_p^k \tau)}{\lambda_p^k \tau} \quad , \quad (17)$$

we obtain the error estimate of:

$$\delta y_1^k(\tau) = \delta y_0^k(\tau) + \sum_{m \neq k} \delta(dy_0^m) \frac{\lambda^{m \to k}}{\lambda_p^m} \frac{1-\exp(-\lambda_p^k \tau)}{\lambda_p^k \tau}$$

$$+ dy_0^m \frac{\lambda^{m \to k}}{\lambda_p^m} \frac{1-\exp(-\lambda_p^k \tau)}{\lambda_p^k \tau} (\frac{\delta \lambda_p^m}{\lambda_p^m} + \frac{\delta \lambda^{m \to k}}{\lambda^{m \to k}}) \quad , (18)$$

$$+ dy_0^m \frac{\lambda^{m \to k}}{\lambda_p^m} \frac{1-\exp(-\lambda_p^k \tau)}{\lambda_p^k \tau} (\frac{\delta \lambda_p^k}{\lambda_p^k} + \frac{\delta \tau}{\tau}) + dy_0^m \frac{\lambda^{m \to k}}{\lambda_p^m} \frac{\exp(-\lambda_p^k \tau)}{\lambda_p^k \tau} (\delta \lambda_p^k \tau + \delta \tau \lambda_p^k)$$

where:

$$\delta dy_0^k = \delta y^k(0)(1-\exp(-\lambda_p^k\tau)) + dy_0^k(0)\exp(-\lambda_p^k\tau)(\lambda_p^k\delta\tau + \tau\delta\lambda_p^k)$$
$$+\left(\delta q^k\tau + q^k\delta\tau\right)\left(1-\frac{(1-\exp(-\lambda_p^k\tau))}{\lambda_p^k\tau}\right) \quad (19)$$
$$+q^k\tau\left(\frac{\delta\lambda_p^k}{\lambda_p^k}+\frac{\delta\tau}{\tau}\right)\left(\exp(-\lambda_p^k\tau)+\frac{(1-\exp(-\lambda_p^k\tau))}{\lambda_p^k\tau}\right)$$

etc.

The information on fission-product releases for fissionable nuclides is taken from files of the ROSFOND Library [3]. The releases of fission products for each of the nuclides may differ in energy of fissioning neutron. There are data for one up to three points by energy in the data libraries; for intermediate energy values a linear data interpolation is provided for that is implemented in the BPSD system.

2. Accounting for the Effects of Errors of CNFC Facilities on Errors of Fuel Nuclide Concentrations

When reprocessing fuel at CNFC facilities, one has to do with chemical compounds of fuel nuclides. In our case we modeled approximately 9 actinides in the actinide list (Th, Pa, U, Np, Pu, Am, Cm, Bk and Cf) and no more than 64 fission products in the fission-product list (H, D, T, He, Li, Be, B, C, N, Ne, Ca, Sc, Ti, V, Cr, Mn, Fe, Co, Ni, Cu, Zn, Ga, Ge, As, Se, Br, Kr, Rb, Sr, Y, Zr, Nb, Mo, Tc, Ru, Rh, Pd, Ag, Cd, In, Sn, Sb, Te, I, Xe, Cs, Ba, La, Ce, Pr, Nd, Pm, Sm, Eu, Gd, Tb, Dy, Ho, Er, Tm, Yb, Lu, Hf, Ta).

The modeled diagram of spent nuclear fuel reprocessing for fast reactor installations is demonstrated in Fig.1. Any addition of “fresh” fuel provides for an addition of depleted uranium with possible takeoff of surplus fissile materials at high Breeding Ratio (BR) of the rector or enriched or MOX fuel at a low BR.

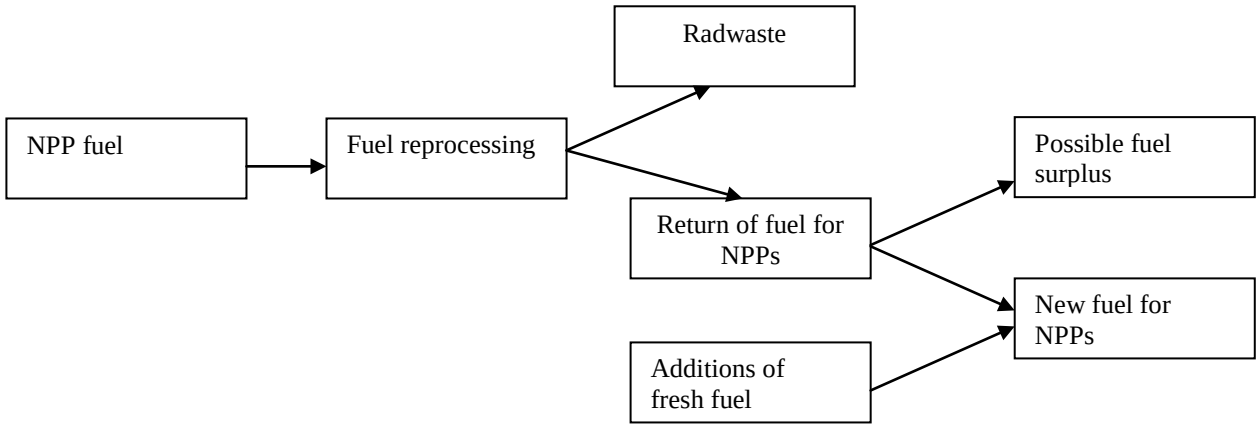

Fig. 1. Diagram of fuel reprocessing at CNFC enterprises

When the decay processes are taken into account and one nuclide transits to another one, the error of decaying nuclide transfers to the error of produced nuclide by the algorithm implemented in BPSD module [1].

It is assumed that the reprocessing procedure is instantaneous during simulation. This assumption is justified by the fact that short-lived nuclides will decay before reprocessing, whereas long-lived nuclides will change only slightly during the reprocessing procedure lasting hardly more than one month. Note that the accuracy of such an assumption can also be estimated.

If several isotopes with their own error estimates constitute one chemical element, then at changes in the mass of this element the error of each its constituent isotope is assumed to be invariable. When estimating mass variations and the relevant errors, the later is assumed to be added to each of the available errors of isotopes.

Thus if we originally have a mass of '*M*' element, irretrievable loss of this mass by '*m*' value will occur during reprocessing with the relevant error estimate '*δm*'; in addition, a part of the considered element will become radwaste being not 'irretrievable loss'. Let us denote their mass '*Mp*'. Then the final mass remaining in the fuel component may be estimated as '*Mn*' with '*δMn*' error that should be added to the error of each nuclide forming the given chemical element.

For chemical elements intended for use in the newly generated fuel the introduction of retention factors '*S*' as the ratio of the element mass in fuel after reprocessing to its mass before reprocessing with the relevant error '*δS*' is proposed. Lists of elements for future fuel composition and elements to be removed from this composition may be varied by the user.

Unlike chemical elements intended for preservation in the fuel, for chemical elements being fission products the introduction of clean-up factors '*G*' as the ratio of the element masses before clean-up to the mass of this element in fuel after clean-up with the relevant error '*δG*' is proposed.

For fuel chemical elements (actinides) let us introduce the loss factor '*P*' with the relevant error '*δP*'. Under the loss factor we understand the fraction of initial mass of actinides irretrievably lost during reprocessing.

Thus let us write the above definitions as:

$$P_i = \frac{m_i}{M_i} \quad , \qquad (20)$$

$$M_{ni} = M_i - m_i - M_{pi} \quad , \qquad (21)$$

$$S_i = \frac{M_{ni}}{M_i} \quad , \qquad (22)$$

$$G_i = \frac{M_i}{M_{ni}} \ . \qquad (23)$$

According to the error definition [4], we have errors for the given parameters: δP_i , δM_{ni}, δS_i and δG_i .

From the equalities (20-23) it follows that when P_i and S_i values are set for actinides and P_i and G_i are set for fission products, we can determine all the required values: m_i, M_{ni} and M_{pi}.

Let us recall that the error of the input element δM_i comprising 'n' nuclides will be determined in our case from the errors of 'k' nuclide of 'i' element at the entry to the reprocessing process obtained from the BPSD module [1] - δM_{ik} .

At the exit from the reprocessing process we have an estimate for the mass of a particular nuclide:

$$M_{n,ik} = M_{ik} \frac{M_{ni}}{M_i}, \qquad (24)$$

with its error estimate $\delta M_{n,ik}$.

Thus, the error of concentration of a nuclide that remained in fuel after reprocessing will always exceed the error of concentrations of the same nuclide before fuel reprocessing. However if "fresh" fuel with ' $M_{s,ik}$ ' mass and the presence of tracked nuclide and its error in this fuel ' $\delta M_{s,ik}$ ' will be added to the new fuel, this new fuel will have the following mass of the tracked nuclide:

$$M_{t,ik} = M_{n,ik} + M_{s,ik}, \qquad (25)$$

with '$\delta M_{t,ik}$' error estimate that can be less than 'δM_{ik}'.

Ref. [5] presents several characteristics of the reprocessing process and demonstrates that losses may reach 0.5% (0.5% uranium and 0.5% neptunium with americium of their initial amount). As shown in Ref. [5], the results of experiments allowed obtaining the coefficients of fuel clean-up from fission products as the ratio of specific components of fission products in fuel before and after reprocessing (see: G_i (23)): Ru(Rh)–13, Sb–120, Cs–3000, Ce(Pr)–19, ^{155}Eu – 33.

Technologies with plutonium separation from uranium during reprocessing allows generating fuel of any enrichment needed for fast reactors and adding plutonium from reprocessed fuel of the blanket to fuel of the core that is necessary to achieve the reactor operation time of the established duration (at the core breeding ratio (CBR) <1).

To estimate the effect of different nuclides on the criticality, calculations on evaluation of the sensitivity coefficient '$\partial K_{эф}^{a}/\partial\rho_a$' were carried out, where '*a*' is the nuclide. The calculation provided for adding the studied nuclide in the amount of 1% of '*x*' fission products to the available materials. The same amount of studied material was added to all fuel assemblies of the core. The calculation results are presented in Table 1 as the ratio: $\frac{\partial K_{eff}^{a}/\partial\rho_a}{|\partial K_{eff}^{^{238}U}/\partial\rho_{^{238}U}|}$, i.e. nuclide sensitivity coefficients are presented relative to ^{238}U which amplitude ratio becomes equal to one.

Table 1. Relative sensitivity coefficients for some nuclides in the core of fast reactor

Element	Sensitivity coefficient	Element	Sensitivity coefficient	Element	Sensitivity coefficient
^{10}B	-35.3	Ru	-1.9	^{235}U	50.4
^{11}B	2.4	Rh	-6.6	^{238}Pu	40.3
O	2.5	Pd	-2.2	^{239}Pu	66.8
Na	2.6	Ag	-6.5	^{240}Pu	9.8
Mn	1.3	Sb	-2.4	^{241}Pu	97.3
Fe	2.5	Cs	-4.4	^{242}Pu	6.4
Mo	0.5	Sm	-32.2	^{241}Am	-8.1
Cr	2.5	Eu	-42.2	^{242}Cm	29.7
Ni	2.1	Gd	-9.4	^{244}Cm	14.9

Knowledge of the reactivity sensitivity coefficients to isotopes of fission products and the content of these isotopes enables optimization of the fuel hold-up time before reprocessing to minimize the effects of fission products in "fresh" fuel on reactivity. The coefficients calculated as the product of the fission-product sensitivity coefficient by its concentration in % (let us call them the 'noxious factors') are demonstrated in Table 2. The data of Table 2 indicate the needed degree of fuel clean-up from specific elements.

Table 2. 'Noxious factors' for some nuclides in the core of fast reactor

Element	The fuel hold-up time		
	24 hours	1 year	5 years
Sm	-60	-120	-120
Ru	-56	-40	-35
Cs	-25	-42	-40
Pd	-20	-30	-35
Eu	-15	-23	-20
Ag	-10,5	-11	-11
Rh	-9	-12	-12
Sb	-2	-0,6	-0,5
Gd	-0,4	-1,4	-2

To estimate the effects of the initial-data error on the results of solving the nuclide-kinetics problem using the BPSD module, a test is selected wherein changes in errors of determining nuclide concentrations for two types of fuel - uranium and plutonium (MOX) – are compared. The test involves calculation of changes in the nuclide composition with burnup of fuel in a fast reactor with several (three) micro-operation times and three shutdowns for fuel reloading with achievement of ~8% of burnup depth of fissioning nuclei. Thus the calculation comprises 6 following steps: each odd step means operation at full power, and each even step means nuclide transitions without power generation.

Five options for solution of the burnup problem with different errors in the initial data were considered for the burnup problem: 0 – only the decay-data error is taken into account; 1 – 0.1% initial-concentration error is added to decay-data errors; 2 – 1% initial-concentration error is added to decay-data errors; 3 - 1% error of one-group cross-sections is added to decay-data errors and to 1% initial-concentration error; 4 - 2% error of one-group cross-sections is added to decay-data errors and to 1% initial-concentration error; 5 - 2% error of initial concentrations and one-group cross-sections is added to decay-data errors;

The results of variations in the resulting errors by the end of the reactor-operation time, when solving the considered problems using BPSD module for plutonium and uranium cores, are demonstrated in Table 3 and Table 4.

Table 3. Resulting errors of some actinides for plutonium core, %

Nuclide	Option					
	0	1	2	3	4	5
^{235}U	0.03449	0.1345	1.035	1.036	1.038	2.038
^{236}U	0.5609	0.6609	1.561	2.564	3.568	4.568
^{237}U	0.3426	0.4426	1.343	2.381	3.420	4.420
^{238}U	0.002213	0.1022	1.002	1.002	1.002	2.002
^{236}Pu	11.1	11.20	12.10	16.10	20.1	21.1
^{238}Pu	0.08527	0.1854	1.087	1.206	1.326	2.328
^{239}Pu	0.1396	0.2493	1.236	1.527	1.818	2.915
^{240}Pu	0.2039	0.3057	1.222	1.643	2.064	3.081
^{241}Pu	0.1859	0.2863	1.189	1.712	2.235	3.238
^{242}Pu	0.09834	0.1983	1.098	1.160	1.222	2.222
^{241}Am	0,4789	0,579	1,480	2,784	4,088	5,089
^{242g}Am	6,944	7,044	7,944	11,10	13,3	15,3
^{242m}Am	3,734	3,834	4,734	6,928	9,122	10,1
^{243}Am	2,234	2,334	3,234	4,262	5,290	6,290
^{242}Cm	1,641	1,740	2,635	5,828	9,021	10,0
^{243}Cm	2,554	2,654	3,548	7,689	11,8	12,8
^{244}Cm	4,422	4,522	5,422	7,440	9,457	10,5
^{245}Cm	7,954	8,054	8,954	12,0	15,0	16,0
^{246}Cm	12,0	12,10	13,0	17,0	21,0	22,0
^{247}Cm	20,2	20,30	21,2	26,2	31,2	32,2
^{248}Cm	30,0	30,10	31,0	37,0	43,0	44,0

Table 4. Resulting errors of some actinides for uranium core, %

Nuclide	Option					
	0	1	2	3	4	5
^{232}U	12.5	12.60	13.5	18.70	23.8	24.80
^{233}U	0.6149	0.7149	1.615	2.564	3.693	4.693
^{234}U	0.8148	0.9148	1.815	2.825	3.835	4.835
^{235}U	0.04372	0.1437	1.044	1.044	1.044	2.044
^{236}U	0.5658	0.6658	1.566	2.566	3.566	4.566
^{237}U	0.8306	0.9306	1.831	3.582	5.334	6.334
^{238}U	0.002822	0.1028	1.003	1.003	1.003	2.002
^{236}Pu	11.4	11.50	12.40	16.90	21.50	22.4
^{238}Pu	2.630	2.733	3.662	8.161	12.7	13.7
^{239}Pu	1.174	1.374	3.173	6.171	9.170	11.2
^{240}Pu	1.566	1.758	3.486	7.300	11.1	13.0
^{241}Pu	1.839	2.028	3.731	8.478	13.2	15.1
^{242}Pu	2.977	3.163	4.839	10.5	16.2	18.1
^{241}Am	2,185	2,372	4,055	9,753	15,5	17,3
^{242g}Am	8,615	8,799	10.4	18,1	25,70	27,5
^{242m}Am	5,406	5,589	7,240	13,9	20,5	22,3
^{243}Am	5,131	5,315	6,968	13,6	20,2	22,1
^{242}Cm	3,327	3,510	5,153	12,7	20,3	22,1
^{243}Cm	4,236	4,417	6,040	14,6	23,1	24,9
^{244}Cm	7,303	7,484	9.115	16,7	24,3	26,1
^{245}Cm	10,8	11,0	12.6	21,1	29,6	31,4
^{246}Cm	14,8	15,0	16,60	26,0	35,5	37,3
^{247}Cm	23,0	23,20	24,70	35,2	45,6	47,3
^{248}Cm	32,8	33,00	34,50	45,9	57,3	59,0

Let us pay attention to error excess in plutonium concentrations for uranium option of the core compared to the plutonium one that is due to low concentrations of plutonium isotopes for uranium loading of the core. However plutonium-isotope errors by the end of reactor operation time for the plutonium core also appear significant and for all isotopes they exceed the errors of their initial concentration. When placing such a plutonium composition back to the reactor after fuel reprocessing, the errors of isotopes will continue to increase. Thus the designer will have to compensate this increase - turning into an error of determining its multiplication factor, ultimately, the reactivity margin - by introducing additional control rods.

The results of calculating a fast reactor (of BN-600 type with breeding blankets) with such fuel demonstrate the following: obtaining BR up to 1.2 is possible in such a reactor; standard arrangement of fuel gives no way of achieving core breeding ratio (CBR) ≈ 1, the expected maximum being ~ 0.8; a considerable fraction of new fuel – up to 40% - is generated in the side blanket and in the axial blanket.

The reactivity loss in the presence of fission products in “fresh” fuel is 0.3% per 1%, whereas in case of burnup during a micro-operation time it is at a level of 1.2% per 1% of burnup. This means that the presence of fission products in “fresh” fuel has a significantly weakened effect on the reactivity loss compared to fission products generated during the reactor operation. The difference in fission products from burnup and presence in “fresh” fuel is due to their distribution over the core. In the first case a maximum is observed in the core center, whereas in the second case one has a uniform distribution throughout the core.

Due to a low CBR (<1) the reactivity loss over a micro-operation time is considerable that indicates the necessity of having a large reactivity margin at its start. Reactivity margin in the form of rods compensating the burnup is also an excess neutron absorber. Instead of boron rods, fuel assemblies of the side blanket may be placed to the reactor that may compensate reactivity excess at the micro-operation start.

Thus the amount of fuel for regeneration and the BR are linked in between and may be optimized by any criteria, e.g. by economic criteria.

Results of calculations nuclide concentrations with uncertainties in nuclide clean-up factors at the CNFC and fuel-cycle time for plutonium core (option 0 from table 3) give in table 5.

Table 5. Resulting errors of some actinides for plutonium core (option 0 from table 3) after reprocessing - δy(rep), %

Nuclide	δy(rep)	Nuclide	δy(rep)	Nuclide	δy(rep)	Nuclide	δy(rep)
^{230}Th	2.09	^{235}U	0.15	^{240}Pu	1.57	^{242}Cm	3.33
^{231}Th	0.47	^{236}U	0.58	^{241}Pu	1.84	^{243}Cm	4.24
^{232}Th	1.68	^{237}U	0.84	^{242}Pu	2.98	^{244}Cm	7.30
^{234}Pa	2.98	^{238}U	0.14	^{241}Am	2.19	^{245}Cm	10.80
^{232}U	12.5	^{236}Pu	11.40	^{242g}Am	8.62	^{246}Cm	14.80
^{233}U	0.63	^{238}Pu	2.63	^{242m}Am	5.41	^{247}Cm	23.00
^{234}U	0.83	^{239}Pu	1.18	^{243}Am	5.13	^{248}Cm	32.80

In the closed fuel cycle, compared to the open fuel cycle, the value of neutrons relative to the accumulation of fissionable nuclei increases, and thus only a due consideration of neutrons will enable the BR maximization. Thus the design of such a reactor should provide a minimum neutron leakage and a minimum neutron absorption in the absorber, coolant, structural materials and fission products. In this connection, any decrease in the amount of fission products in “fresh” fuel would reduce the plutonium fraction in fuel and, consequently, would increase the BR.

Burning of Np, Am and Cm in the considered reactor is also possible.

Conclusions

The paper focuses on the results of estimating the effects of initial-data errors on the results of solving isotopic-kinetics problems using the BPSD nuclide kinetics calculating module.

The originality of this solution is related to the solution of the burnup problem for actinides and fission products with a full nuclide transition matrix and determination of the error in the achieved solution based on initial-data errors.

As demonstrated, the errors in plutonium concentrations for the uranium core exceed those for the plutonium core that is due to low concentrations of plutonium isotopes in the case of uranium core.

Errors for plutonium isotopes by the end of reactor operation time appear significant even for the plutonium core and for all isotopes they exceed the errors of their initial concentration. When placing such a plutonium composition back to the reactor after fuel reprocessing in the CNFC, the errors of isotopes will continue to increase, and the designer will have to compensate this increase - turning into an error of determining its multiplication factor , ultimately, the reactivity margin - by introducing additional control rods.

Taking into account non-uniformity of the power-density field in fuel elements of FAs in the reactor being at a level of 1.05, the error of determining actinide concentrations will considerably exceed the presented values.

REFERENCES

1. Abagyan, A.A., Seleznev, E.F. and Ivanov, V.B. (2004) The possibility of long-term nuclear power development on the basis of modern technologies, *Russian J. Atomnaya Energiya (Nuclear Energy)*, 97(4), pp. 252-260 (in Russian).

2. Seleznev, E.F., Astaryan, D.S., Belov, A.A., *et al*. (2012) Neutronic codes, *Proceedings of the International Scientific Conference 'Innovative Projects and Nuclear Energy Technologies'*, Moscow, November 27-29, 2012, pp.396-407 (in Russian).
3. Zabrodskaya, S.V., Ignatiyk, A.V., Koshcheev, V.N. *et al*. (2007) The Russian national library of evaluated neutron data – ROSFOND, *VANT, 'Nuclear Constants" Series*, #**1-2**, pp.3-21 (in Russian).
4. Korn, G and Korn, T. (1977) *Handbook of Mathematics*, 'Nauka" Publishers, Moscow, 832p. (in Russian).
5. ORIGEN-S: SCALE system module to calculate fuel depletion, actinide transmutation, fission product buildup and decay, and Association source terms (1995) NUREG/CR-0200, Revision 4, Vol.2, Section F7.

CFD computation of thermal stratification in the upper plenum of Monju reactor

Hiroki Yao[a], Jean Riberaud[b], Hiroyasu Mochizuki[c]

[a] Graduate School of Engineering, University of Fukui
1-2-4 Kanawa-cho, Tsuruga, 914-0055, Japan

[b] Genie Atomique, INSTN
Cadarache Nuclear Research Center, 13108, Saint Paul lez Durance, France

[c] Research Institute of Nuclear Engineering (RINE), University of Fukui
1-2-4 Kanawa-cho, Tsuruga, 914-0055, Japan

Abstract. The thermal stratification in the upper plenum of the "Monju" is a benchmark problem organized by IAEA. Although this problem contained the mismatch of energy balance in boundary conditions, the problem was solved by the re-calculation of the boundary conditions using a system code. The calculated temperature by the CFD code in the upper plenum coincided with the simultaneous mixing temperature given by the boundary conditions. This problem is computed using the FLUENT code with a couple of flow-hole configurations. It has been clarified that the height of the thermal stratification interface is very much dependent on the flow-hole configuration. This is because the discharge flow rate from the flow-holes is dependent on the inlet configuration of the flow-hole and the height of the thermal stratification inter face is governed by the flow rate. The discharged flow rate increases due to low local loss coefficient when the flow-hole has a rounded edge. Therefore, there is an obvious difference in the position of the thermal stratification interface between the straight edge and the round edge. Since the more accurate flow-hole configuration was informed recently, we created a new computation scheme to simulate the single round edge of the flow-hole as smooth as possible. Computation was conducted for a 120-degree and also 360-degree sectors. Good agreement is obtained between the measured temperature distribution in the upper plenum and the calculated result. There are not many differences between two models. This is because the thermal stratification interface is very stationary and flow pattern in the upper plenum looks like two-dimensional.

1. Introduction

The analysis of the occurrence of thermal stratification in the upper plenum of the "Monju" reactor is a subject of the IAEA Coordinated Research Programs (CRP). Temperature distributions in the upper plenum of the reactor vessel were measured at "Monju" when the plant was scrammed from a partial load condition during a turbine trip test at 40% of nominal electrical output (45% of nominal thermal output). The primary heat transport system (HTS) and the secondary HTS were cooled by the forced circulation after the reactor trip with small capacity motors, so called pony motors. Flow rates in the three primary and secondary HTSs were decreased to approximately 1/10 of the full power conditions. This test and its results are summarized in the report by Yoshikawa and Minami (2008) as a document of the IAEA CRP. Many organizations which are developing Fast Reactors such as Commissariat à l'Énergie Atomique (CEA, France), Argonne National Laboratory (ANL, USA), Institute of Physics and Power Engineering (IPPE, Russia), Indira Gandhi Centre for Atomic Research (IGCAR, India), Korean Atomic Energy Research Institute (KAERI, Korea) and China Institute of Atomic Energy (CIAE, China) have participated in the benchmark analysis. The same problem is computed by the present authors

in order to develop a coupled computation method between the thermal-hydraulics and structure. The movement velocity of the thermal stratification interface effects on the stress. Therefore, the accurate simulation of the thermal stratification behavior is one of the important issues in the analysis.

Ohira et al.[1] calculated the steady state of the test. Bieder et al.[2], Nishi et al.[3], and Sofu and Thomas[4] calculated the benchmark problem using different CFD codes. Two problems are recognized through their calculations. One of them is underestimation of the temperature near the sodium surface. The other problem is that the calculation overestimates the temperature distribution in the upper plenum as time elapse. All calculated results except the results by Mochizuki et al.[5] overestimate the measured temperature to a large extent. Mochizuki et al. assumed that the flow hole has round edge on both sides. Therefore, this discrepancy may be caused by the low discharge flow rate from the flow-holes provided on the inner shroud. Sofu[6] re-calculated the same problem with the same flow hole configuration as Mochizuki's assumption, and obtained the accurate result up to 15 minutes.

The authors prepared very precise computation models of the upper plenum including (1) the asymmetric configuration in the upper plenum with almost all internals, (2) heat transfer between outer sodium and inner sodium via the inner shroud with flow-holes, and (3) full modeling of the upper core structure and the upper instrumental structure (UIS). The meshing around the flow-holes is made with special attention.

2. General description of the benchmark test

2.1. Description of the upper plenum of "Monju"

The upper plenum of the "Monju" reactor is illustrated in Fig. 1. It consists of the reactor vessel of 7.060 m inner diameter and 50 mm in thickness, an upper core structure (UCS) with flow guide tubes, a fuel handling machine, a plug for thermocouples (TC-plug), and an inner barrel of 6.600 m in outer diameter and 40 mm in thickness with two stages of flow-holes. The outer diameter of the TC-plug is 200 mm. Since there are three loops for the primary HTS, three outlet nozzles are welded on the reactor vessel at an elevation of 27.750 m. The driver region of the core is located beneath the UCS. The outer diameter of the upper instrumental structure (UIS) is 1.997 m. The elevations of the upper support plate, the core top surface and the liquid sodium are 26.120 m, 27.050 m and 33.050 m, respectively. All elevations are measured in absolute terms from the ground. The most part of the sodium flow from the core is guided by the flow guide tubes and the remaining part collides on the honey comb structure which holds the flow guide tubes and control rod guide tubes. These data are written in the report by Yoshikawa and Minami[7].

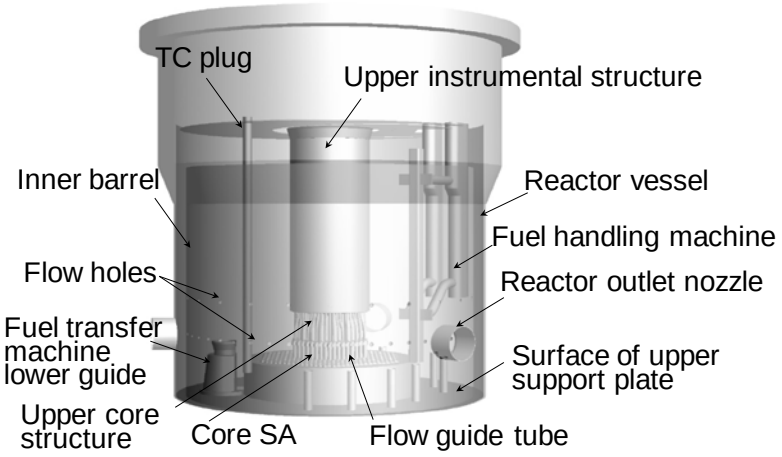

FIG. 1. Structures inside the upper plenum of Monju

A computer aided design (CAD) model above the core is shown in Fig. 2. A part of the sodium flows through the flow-holes into the annulus between the reactor vessel and the inner barrel. Otherwise, sodium

traveling upward in the upper plenum will overflow the inner barrel and end up in the same annular space between the reactor vessel and the inner barrel. The number of flow-holes provided of the lower stage is 48, and their diameter is 92 mm. These are provided at elevation of 27.750 m, where is 5.3m below the liquid sodium surface. The number of flow-holes of the upper stage is 24; they also have a diameter of 92 mm. These flow-holes are located at an elevation of 28.670 m, where is 4.38m below the liquid sodium surface.

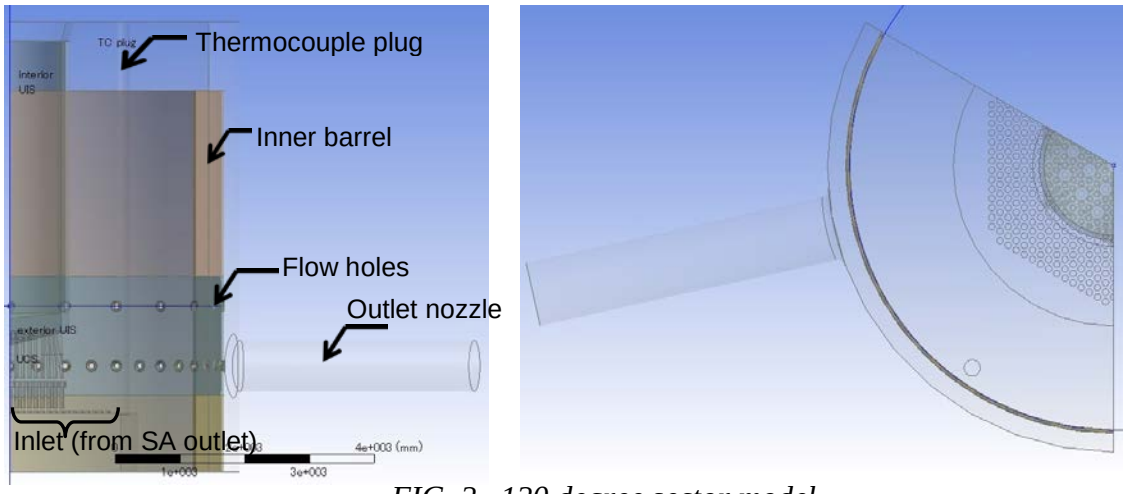

FIG. 2. 120 degree sector model

The vertical positions of thermocouples on the TC-plug are reported by Yoshikawa and Minami[7], and radial position is mentioned by Doi et al.[8]. Three thermocouples are provided on the same height. One is facing the core, i.e., 0 degree, and the other two are installed at locations rotated 60 degrees in clockwise and counter-clockwise direction, respectively. Averaged temperatures on the same height were plotted as a representative temperature in the above reference, and these temperatures in a figure were converted into digital values in the present study.

2.2. General description of the turbine trip test

TABLE 1 Initial major parameters at turbine trip test at "Monju"

Items	Measured
Thermal power (MW/loop)	106
Primary coolant flow rate (kg/s/loop)	702.8
Primary hot leg temperature (^{o}C)	485
Primary cold leg temperature (^{o}C)	362
Secondary coolant flow rate for B (kg/s/loop)	394.4
Secondary hot leg temperature for A&B (^{o}C)	485
Secondary cold leg temperature for A&B (^{o}C)	285
Temperatures at exit of subassemblies for channel 1 to 8	512-513, 509-511, 510-515, 500-513, 499-511, 483-509, 483-509, 427

A turbine trip test at 45% thermal power of "Monju" was conducted in December of 1995 to investigate the overall functions of the plant and the capability of the air cooling system (ACS) in an actual situation. Table 1 shows the relevant parameters of the plant before the transient. In this test, an abnormal situation of the turbine was assumed. The

reactor was scrammed by the signal of turbine trip, and then the pumps in the primary and secondary loops were tripped. Pony motors are started just after the scram and forced circulation is taken over by pumps driven by pony motors before the flow rates in the primary and secondary loops were approximately 10% and 8%, respectively. This means that the flow rates in the HTSs are kept at 10 % and 8 % of the rated ones during the transient except at the very beginning of the transient. During this test, thermal stratification appeared and moved upward in the upper plenum.

3. Analysis

3.1. Analytical model

The code FLUENT-12.0 by ANSYS Inc. is used to calculate the 3D thermal-hydraulics. In the analysis, the standard k-ε model, standard wall function and SIMPLEC (Semi-Implicit Method for Pressure-Linked Equations - Consistent) method are applied to solve the compressible fluid momentum equation coupled with the equation of continuity. It is shown by Shibahara et al.[10] that the turbulence model has only a small effect on the temperature distribution except very early stage of the transient. The accuracy of the turbulence in energy equation is 2nd order upwind.

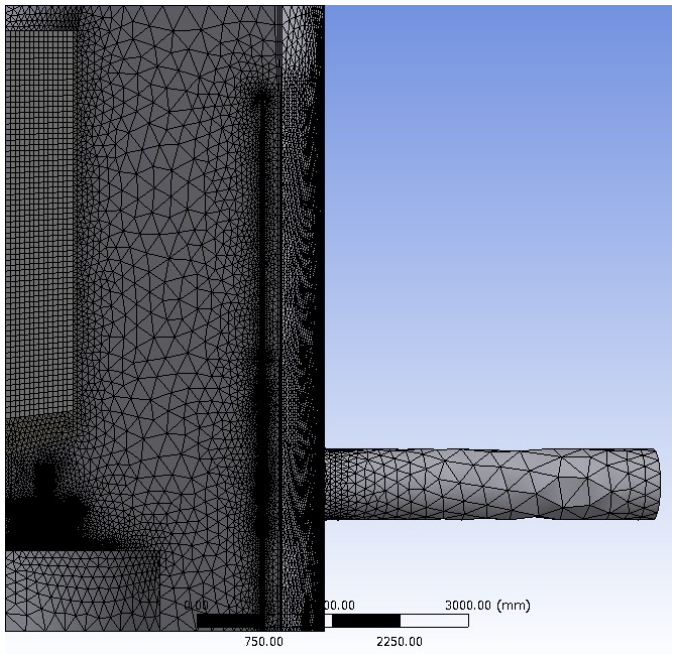

FIG. 3. Overall mesh configuration with mixtures of tetrahedral and hexahedral meshes of 15,000,000

The full-sector of the upper plenum with the internals mentioned before was modeled using a CAD software named “Design Modeler” by ANSYS Inc., and a 1/3 sector calculation model with approximately 15 million hexahedral and tetrahedral meshes was created using meshing software ”Meshing” by ANSYS Inc. Figure 3 shows the overall mesh configuration of the upper plenum, in a cross section plane going through the center of the core and the center of the TC-plug. The hexahedral meshes are used for the layers of the structure. The UIS located in the center of the upper plenum is treated as a solid body with a heat capacity corresponding to steel and sodium. In the heat transfer calculation, no sodium flow is assumed inside the UIS, and heat is transferred by conduction from the center to the surface; and then transferred to the sodium of

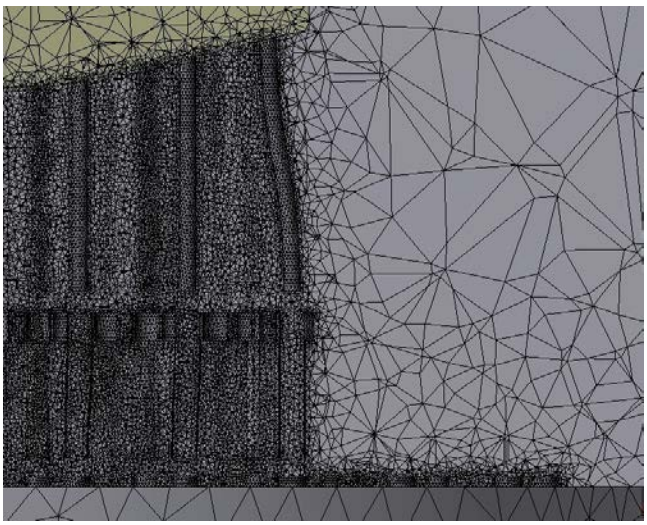

FIG. 4. Mesh configuration above the core

the upper plenum by convection. The TC-plug is situated on the right hand side of the figure. Since three temperatures were measured at one axial elevation, the locations of the thermocouples are modeled exactly in order to accurately calculate the temperature response of each thermocouple. The inner barrel is modeled taking into account the heat transfer between the sodium inside the inner barrel and sodium outside the inner barrel.

Figure 4 shows the mesh configuration above the core. Since the flow guide tubes above the core seem to be important to rectify the flow, their configurations are considered explicitly in the present analysis. The grid plate in this region is deemed to affect the flow pattern. Therefore, holes of the grid plate and flow guide tubes provided beneath the grid plate are modeled with equivalent diameter holes. Fingers above the grid plate are also modeled as shown in Fig. 4.

Figure 5 illustrates the meshes around the flow-hole. The inner barrel is illustrated at the center of the right figure, and the reactor vessel is situated on the right hand side. As one can see from the figure, the flow-hole has a round edge of 20 mm radius. Since there are many flow-holes to be analyzed in our model, the relatively small mesh sizes have been chosen for the computation mesh system, so the shape of the mesh is as smooth as possible. However, it has to be admitted that the local friction factor of the round edge meshing may have a larger value than the reality. Although the real radius is unknown, this radius can represent the flow-hole with a small round radius based on experiences of hydraulics.

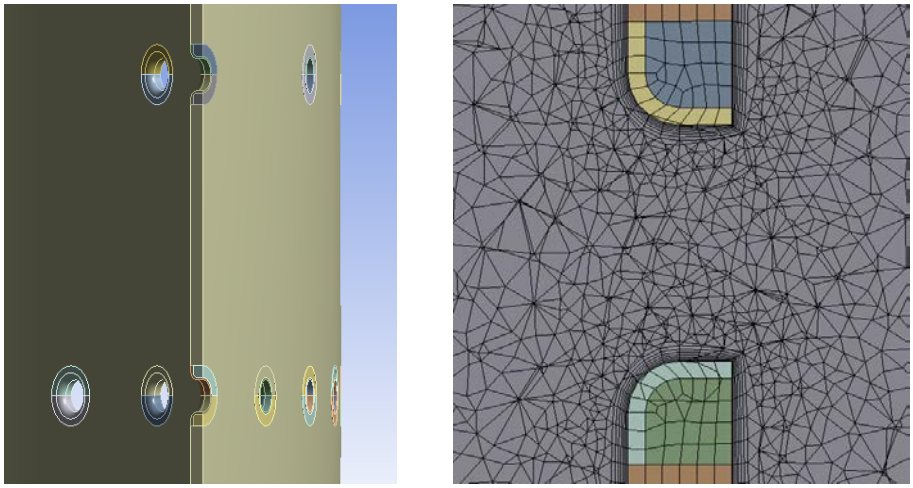

FIG. 5. Mesh configuration for flow-holes with boundary layers

3.2. Boundary conditions

The outlet temperatures flow rates of the subassemblies are given by Yoshikawa and Minami[7]. If simultaneous mixing of sodium is assumed between all fuel subassemblies based on the boundary conditions shown in the IAEA benchmark problem, temperature becomes approximately 482 ºC. Since measured temperature near the liquid sodium surface was approximately 490 ºC, it is clear that the amount of energy into the upper plenum is insufficient. This causes the lower initial equilibrium temperature in the upper plenum. The outlet temperatures were measured using thermocouples at the upper part of the subassemblies. Therefore, these values are reliable within the measurement error. Flow rates from the subassemblies were calculated results using the system code developed in JAEA. The other boundary condition is provided at the outlet of the nozzle. Atmospheric pressure is set at the outlet.

In order to maintain the consistency of the energy transported into the upper plenum, a 1D analysis has been conducted using the NETFLOW++ code (Mochizuki[9]). It is confirmed that the mixing temperature from the subassemblies coincide with the measured temperature.

3.3. Analytical results

After the initial steady state computation, the transient computation is conducted based on the newly deduced boundary conditions. Figure 6 shows the comparison between the measured result and computed result from the initial steady state to 20 min. The computed result traces the measured result with good accuracy. This temperature distribution at 600 seconds is improved to a large extent computed to the results presented from member countries. The height of the thermal stratification interface at 450 ºC in the present computation is approximately 0.4m higher than the measured result although the most results of member countries are approximately 1.4 m higher than the measured result. The major reason of this difference is caused by the difference of the flow-hole configuration, i.e., round edge and straight edge. When the round edge is considered, the number of meshes increases extraordinary. However, it is concluded that the thermal stratification issue cannot be computed without the round edge configuration.

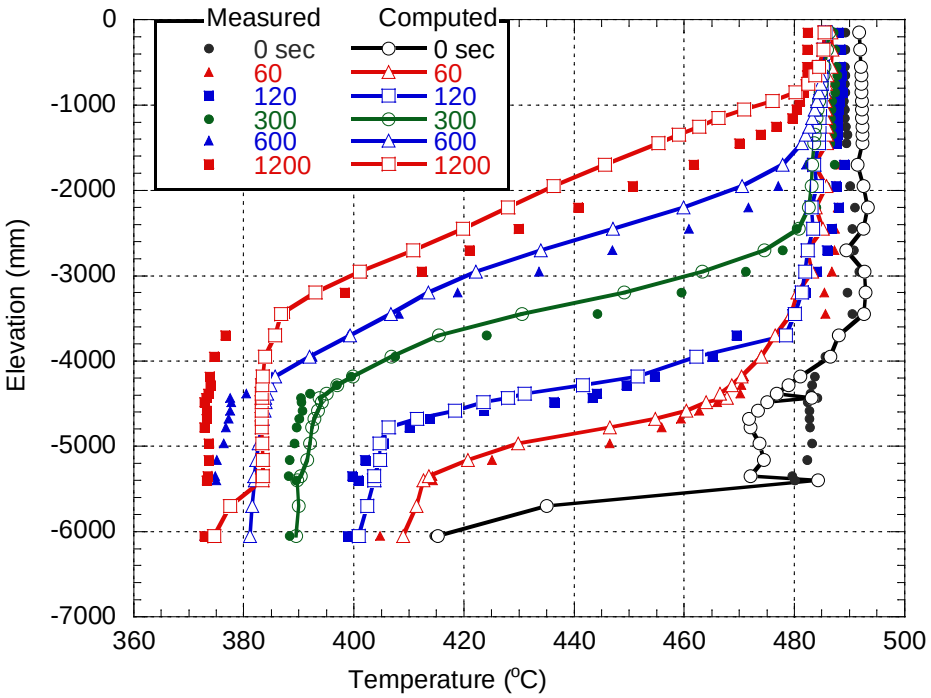

FIG. 6. Comparison between measured and computed result

4. Discussion

4.1. Effect of calculation model

In the present study, an effect of the calculation model is investigated. Up to now, a full sector model[5] with internals and flow-holes with double rond edges has been created as shown in Fig. 7. The same transient with the same boundary conditions is computed under the smaller convergence errors. This result coincides with the above mentioned computation result. Shibahara et al.[11] also computed the same problem using a full sector model and a 1/3 sector model. Since they mentioned that a 1/3 sector model could provide the result with the similar accuracy as the full sector model, a 1/3 sector model is also made in the present study

and used to calculated the transient in order to confirm the sensitivity of the model. The computed results are almost the same between the full sector model and 1/3 sector model. The member organizations except our laboratory in the IAEA CRP used a 1/6 sector model. All results were almost the same when the same boundary conditions were used. Therefore, the internals such as fuel handling machine can be eliminated from the computation model, i.e., the thermal stratification phenomenon of Monju is almost two dimensional.

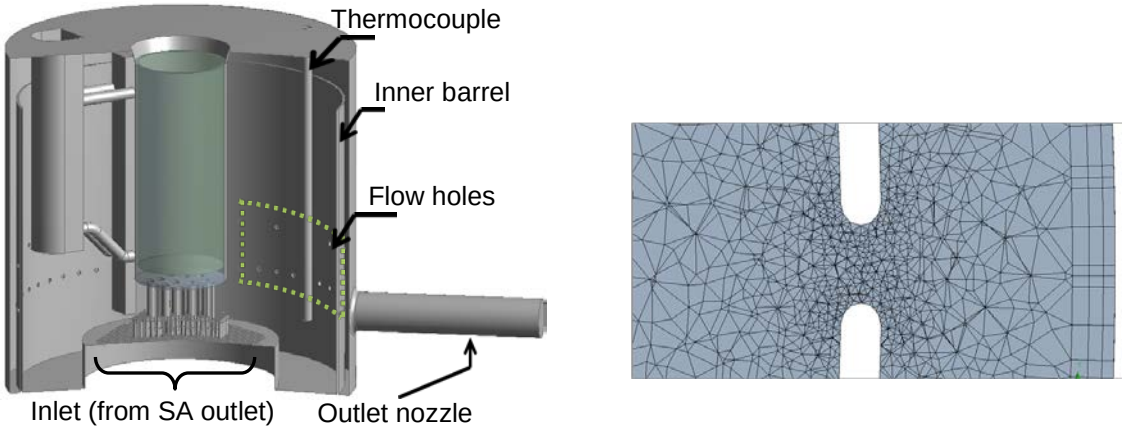

FIG. 7. Full sector computation model with double round edges

4.2. Contour maps during the transient

Figure 8 illustrates the evolution of velocity contours in the upper plenum from initial stage to 1200 sec. The maximum velocity above the core and inside the hot leg at the initial steady state condition is approximately 2.3 and 1.8 m/s, respectively. Therefore, these regions are indicated in red color. The flow from the subassemblies at the initial flows toward the upward and the major flow overflows the inner barrel. However, the flow by the pony motor level moves to the downward once around time 300 sec and moves to upward again. The flow from the flow-hole keeps nearly constant during the transient.

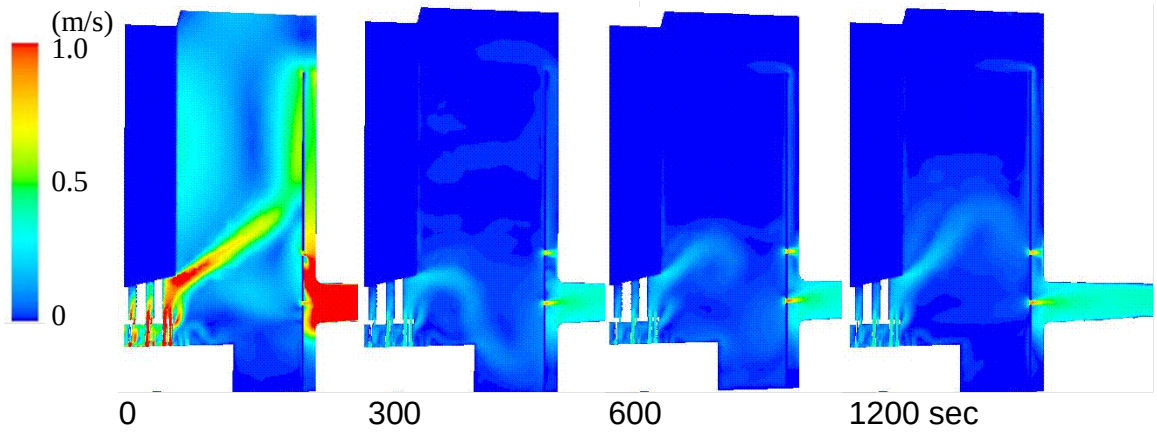

FIG. 8. Evolution of velocity distribution in the upper plenum

Figure 9 illustrates the evolution of the temperature in the upper plenum. There is a thermal stratification interface in the bottom region of the upper plenum at the initial steady state condition. The interface move to the upward after the reactor is scrammed. The thermal stratification in the hot leg is also computed. Since the heat capacity of the upper instrumental

structure is taken into account in the present computation, it can be seen that this part is cooled gradually.

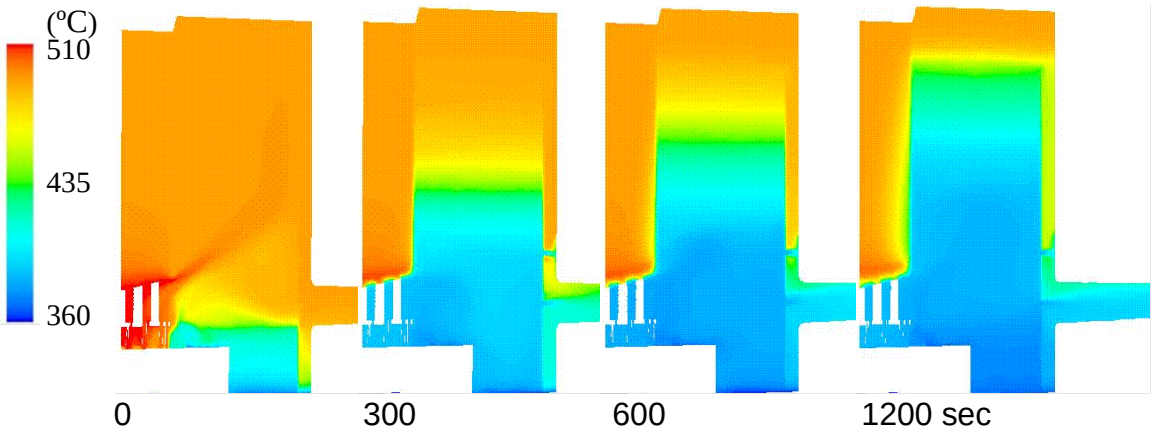

FIG. 9. Evolution of temperature distribution in the upper plenum

Figure 10 illustrates the evolution of the velocity vectors from the flow-hole at the upper level. The right end shows the position of the reactor vessel. The discharged flow at time 0 is skewed downward by the downward flow in the annulus. However, the discharged flow becomes straight as time elapses because of the decrease of the over flow in the annulus. It seems that the discharged flow rate is strongest around 600 sec. The flow pattern for the flow-holes at the lower stage is almost same as that of the upper stage.

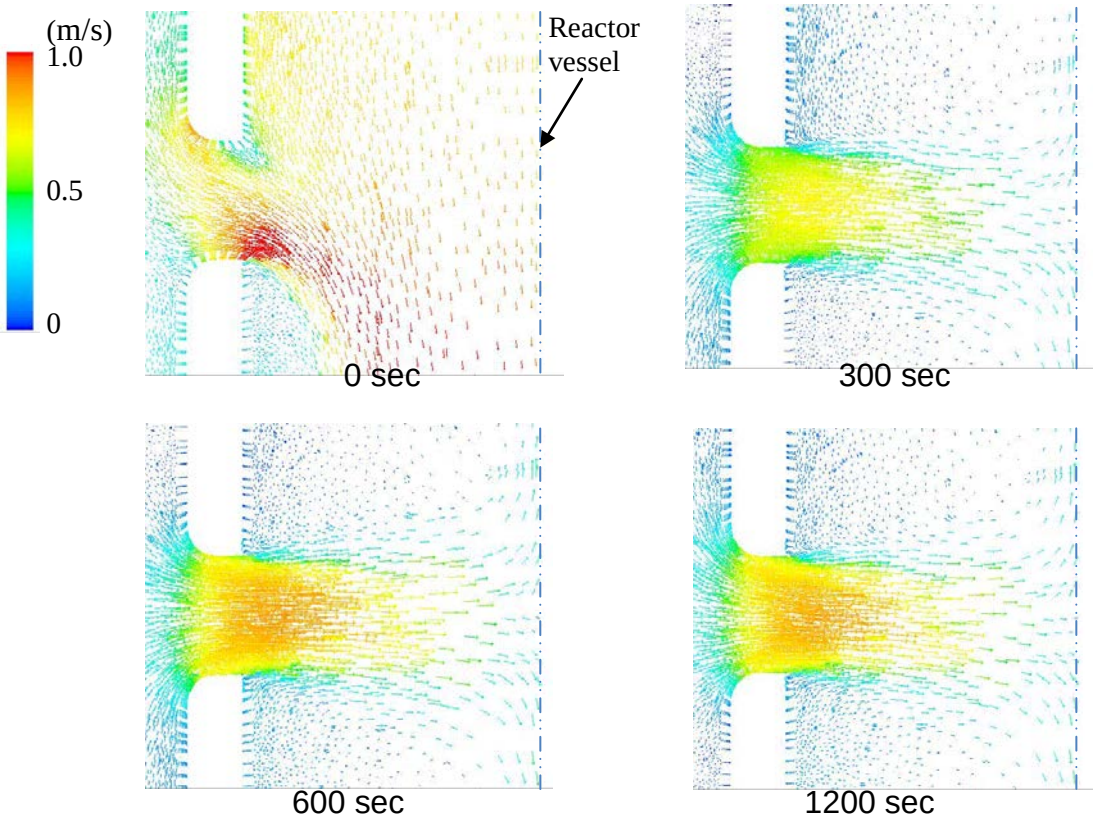

FIG. 10. Evolution of velocity vectors from the flow-hole at the upper level

5. Conclusions

The thermal stratification phenomenon in the upper plenum of the "Monju" reactor was analyzed under the conditions given by the IAEA benchmark problem except flow rates and temperatures from the subassemblies. The following conclusions are obtained from the present study:

(1) The total energy transferred into the upper plenum is not sufficient when the boundary conditions specified in the IAEA benchmark are used and therefore the temperature distribution near the sodium surface was underestimated.

(2) When the boundary conditions are re-calculated with the 1D system code taking into account the bypass flow rate and exact reactor power at the test, the computed temperature near the sodium surface coincides with the measured temperature.

(3) The temperature distributions during the turbine trip transient are predicted with good accuracy using the 1/3 sector and the full sector models. The major factors that influence the thermal stratification are the configuration of the flow-hole, specifically the round edge of the flow-hole.

(4) The similar computation results can be obtained when the computatin model is simplified to 1/3 or 1/6.

REFERENCES

[1] Ohira, H., et al., 2011. Numerical Simulation of Upper Plenum Thermalhydraulics of Monju Reactor Vessel using High Resolution Mesh Models, Proceedings of the 14th international Meeting on Nuclear Thermalhydraulics, Toronto, Canada, NURETH14-28.

[2] Bieder, U., et al., 2011. Trio_U Analysis of Natural Convection in the Upper Plenum of the MONJU Reactor, Proceedings of the 14th international Meeting on Nuclear thermalhydraulics, Toronto, Canada, NURETH14-562.

[3] Nishi, Y., et al., , Benchmark Analyses of Sodium Convection in Upper Plenum of the MONJU Reactor Vessel – Comparison between Plant System Analysis Code CERES and CFD Code, Proceedings of the 14th international Meeting on Nuclear Thermalhydraulics (NURETH-14), Toronto, Canada, NURETH14-361.

[4] Sofu, T. and Thomas, J., 2011. Analysis of Thermal Stratification in the Upper Plenum of the "Monju" Reactor Vessel, Proceedings of the 14th international Meeting on Nuclear Thermalhydraulics, Toronto, Canada, NURETH14-510.

[5] Mochizuki, H., et al., 2011. Analysis of Thermal Stratification in the Upper Plenum of the "Monju" Reactor Vessel – Effect of Chamfer of Flow-Hole on Thermal Stratification-, Proceedings of the 14th international Meeting on Nuclear Thermalhydraulics, Toronto, Canada, NURETH14-432.

[6] Sofu, T., 2011. Parametric Analysis of Thermal Stratification during the Monju Turbine Trip Test, Proceedings of ICAPP'12, Chicago, USA, Paper 12259.

[7] Yoshikawa, S. and Minami, M., 2008.Data Description for Coordinated Research Project on Benchmark Analyses of Sodium Natural Convection in the Upper Plenum of the MONJU Reactor Vessel under Supervisory of Technical Working Group on Fast Reactors, International Atomic Energy Agency, JAEA-Data/Code 2008-024.

[8] Doi, Y., et al., 1996. Thermal Stratification Tests in Monju Upper Plenum - Temperature distribution under normal and scram conditions with 40% power operation-, PNC TN9410 96-117, (in Japanese: http://jolissrch-inter.tokai-sc.jaea.go.jp/pdfdata/PNC-TN9410-96-117.pdf).

[9] Mochizuki, H., 2010. Development of the plant dynamics analysis code NETFLOW++, Nuclear Engineering and Design, 240, pp. 577-587.

[10] Shibahara, M., et al., 2011. Numerical Simulation of Dynamic Flow Structure and Thermal Stratification Phenomena in LMFBR, the 19th International Conference on Nuclear Engineering (ICONE19), Chiba, Japan, ICONE19-43534.

[11] Shibahara, M., et al., 2011. Numerical Analysis of Thermal Stratification in the Reactor Upper Plenum of MONJU with 1/3 Sector and Full Sector Models, Proceedings of the 14th international Meeting on Nuclear Thermalhydraulics, Toronto, Canada, NURETH14-578.

Benchmark Analyses of the Shutdown Heat Removal Tests Performed in the EBR-II Reactor

L.Briggs[s], C. Choi[n], W. Hu[b], L. Maas[e], W. Maschek[g], B. Merk[f], K. Mikityuk[r], H. Mochizuki[l], S. Monti[a], K. Morita[m], A. Del Nevo[i], H. Ohira[k], A. Petruzzi[h], U. Partha Sarathy[j], A. Shin[o], I. Shvetsov[q], M. Stempniewicz[p], G. Su[d], D. Sui[c], B. Truong[t]

[a] International Atomic Energy Agency, Vienna, Austria

[b] China Institute of Atomic Energy, China National Nuclear Corp., Beijing, China

[c] North China Electric Power University, Beijing, China

[d] Xi'an Jiatong University, Xi'an, Shaanxi, China

[e] Institute for Radiological Protection and Nuclear Safety, Fontenay-aux-Roses, France

[f] Helmholtz Centre Dresden-Rossendorf, Dresden, Germany

[g] Karlsruhe Institute of Technology, Eggenstein-Leopoldshafen, Germany

[h] San Piero a Grado Nuclear Research Group, San Piero, Italy

[i] Italian National Agency for New Technologies, Energy and Sustainable Economic Development, Brasimone, Italy

[j] Indira Gandhi Centre for Atomic Research, Dept. of Atomic Energy, Kalpakkam, Tamil Nadu, India

[k] FBR Plant Engineering Centre, Japan Atomic Energy Agency, Tsuruga, Japan

[l] Research Institute of Nuclear Engineering, University of Fukui, Fukui, Japan

[m] Institutie of Environmental Systems, Kyushu University, Fukuoka, Japan

[n] Korea Atomic Energy Research Institute, Daejeon, Republic of Korea

[o] Korea Institute of Nuclear Safety, Daejeon, Republic of Korea

[p] Nuclear Research and Consultancy Group, Petten, Netherlands

[q] Institute for Physics and Power Engineering, Obninsk, Russian Federation

[r] Paul Scherrer Institute, Villigen PSI, Switzerland

[s] Argonne National Laboratory, Argonne, Illinois, USA

[t] TerraPower LLC, Bellevue, Washington, USA

Abstract. The International Atomic Energy Agency (IAEA) established in 2012 a coordinated research project (CRP) on EBR-II Shutdown Heat Removal Tests (SHRT). The CRP aims to improve design and simulation capabilities in fast reactor neutronics, thermal hydraulics, plant dynamics and safety analyses through benchmark analysis of a protected and an unprotected loss-of-flow test from the EBR-II SHRT program. Activities will include core physics studies and thermal-hydraulics/safety assessments. Benchmark specifications provided by Argonne National Laboratory will be used by the CRP participants to develop a neutronic model of the EBR-II core to assess reactor power distribution, decay heat parameters, and reactivity feedback coefficients for subsequent transient scenario safety analysis. Investigations of thermal hydraulics characteristics and plant behaviour will focus on predicting natural convection cooling accurately by evaluating the reactor core flow and temperatures in comparison to experimental data. The ultimate evaluation will be in the prediction of the fission power history during an Anticipated Transient Without Scram (ATWS) by the coupled neutronic/thermal-hydraulic/structural models. This paper outlines the CRP and discusses the SHRT tests and the benchmark specifications.

1. Introduction

Under the auspices of the International Atomic Energy Agency, a Coordinated Research Project (CRP), "Benchmark Analyses of an EBR-II Shutdown Heat Removal Test" has been established to support validation of simulation tools and models for the safety analysis of Sodium-Cooled Fast Reactors (SFR). Validated tools and models are needed both to evaluate SFR passive safety phenomena and to assess reactor designs incorporating passive features into the system response to accident initiators.

Passive safety response in SFR's is the result of reactor design features that will shut down the reactor, remove residual heat, and keep the core cooled during accidents. In addition to the Doppler effect, negative reactivity feedback mechanisms based on thermal expansion and contraction of structural materials, which affect neutron leakage in the fast spectrum core, can be used to passively shut down the fission process. Radial and axial core expansion, subassembly bowing, and control rod driveline expansion are examples of these passive reactivity feedbacks. To keep the core cooled when forced circulation is lost, coolant density changes in sodium can be utilized in the design to produce natural circulation flow. Passive heat removal can be accomplished through use of natural convection, conduction and vessel wall radiation.

The potential for a sodium-cooled fast reactor to survive severe accident initiators with no core damage was extensively demonstrated during landmark shutdown heat removal tests in Experimental Breeder Reactor-II (EBR-II).[1] Two of these tests, identified as the SHRT-17 and SHRT-45R tests, were chosen to be included in this CRP because of the availability of extensive thermocouple and flow rate data at various elevations in two instrumented subassemblies in row 5 of the core (one a fuel subassembly and one representing a blanket subassembly), plus the range of conditions encountered in both tests. They simulated a total loss of pumping power (normal and emergency) to the plant operating at full power and flow.[2]

Argonne National Laboratory has prepared a detailed benchmark specification for the analysis of the SHRT-17 protected loss of flow and SHRT-45R unprotected loss of flow tests. In addition, a neutronics benchmark specification has been prepared for the SHRT-45R test. These specifications provide the necessary benchmark data for collaborative modeling and simulation benchmarking efforts within the international partnerships established through the CRP. A total of nineteen institutions from eleven member states are currently participating in the CRP.

2. Establishment of the Coordinated Research Project

The CRP was initiated in June 2012. It is a four-year project that is being coordinated by the IAEA, with Argonne National Laboratory being the lead technical organization and also a participant in the

benchmark exercises. During the four years of the CRP, Argonne will serve as a technical resource and organize the information exchange for the initial and refined simulation studies, and also parametric sensitivity analyses, among the benchmark participants.

The project aims for validation of state-of-the-art computer software to improve participants' analytical capabilities in fast reactor design and analysis through comparisons of analytical predictions with test data from the EBR-II SHRT-17 and SHRT-45R experiments. The project also aims for training of the next generation of analysts and designers through international benchmark exercises. The project will specifically contribute toward extending the validation and verification base of sodium-cooled fast reactor safety analysis codes to accurately simulate the primary coolant system behaviour during loss of flow transients and the fission power history during unprotected transients. Particular focus will be on predicting the natural convective cooling and reactivity feedback mechanisms accurately.

The results of this research will lead to:

- Improved understanding of fast reactor neutronics, thermal-hydraulics, and system analysis
- Improved understanding of the methodology employed to simulate fast reactor transient behaviour
- Improved verification, validation, and qualification status of this methodology
- Reduced uncertainty in liquid metal fast reactor safety codes, contributing also to the long-term goal of reducing the costs of building liquid metal-cooled fast reactors
- Enhanced reliability of the safety behaviour predictions for new advanced reactor designs.

To date, the following nineteen institutions are participating in the CRP:

- Argonne National Laboratory (USA)
- China Institute of Atomic Energy, China National Nuclear Corp. (China)
- North China Electric Power University (China)
- Xi'an Jiatong University (China)
- Institute for Radiological Protection and Nuclear Safety (France)
- Helmholtz Centre Dresden-Rossendorf e.V. (Germany)
- Karlsruhe Institute of Technology (Germany)
- San Piero a Grado Nuclear Research Group (Italy)
- Italian National Agency for New Technologies, Energy and Sustainable Economic Development, Brasimone Research Centre (Italy)
- Indira Gandhi Centre for Atomic Research, Dept. of Atomic Energy (India)
- FBR Plant Engineering Centre, Japan Atomic Energy Agency (Japan)
- Research Institute of Nuclear Engineering, University of Fukui (Japan)
- Kyushu University (Japan)
- Korea Atomic Energy Research Institute (Republic of Korea)
- Korea Institute of Nuclear Safety (Republic of Korea)
- Nuclear Research and Consultancy Group (Netherlands)
- Institute for Physics and Power Engineering (Russian Federation)
- Paul Scherrer Institute (Switzerland)
- TerraPower LLC (USA)

The CRP schedule is as follows:

2012: Completion of benchmark specifications by Argonne, initiation of CRP through the first research coordination meeting, beginning of model development and blind simulations by participants.

2013: Continuation of model development and blind simulations by participants, preliminary assessment of simulation results, exchange of results and discussion of modeling issues at the second research coordination meeting.

2014: Refinement of simulations, uncertainty analysis, discussion of results at third research coordination meeting.

2015: Draft of final report and identification of future research and development and experimental needs to resolve open issues, final research coordination meeting

2016: Final evaluation and publication of final report.

3. EBR-II Passive Safety Demonstration Tests

The EBR-II plant was a uranium metal-alloy-fuelled liquid-metal-cooled fast reactor designed and operated by Argonne National Laboratory for the U.S. Department of Energy at the Argonne-West site (now the Materials and Fuels Complex at the current Idaho National Laboratory). Operation began in 1964 and continued until 1994. EBR-II was rated for a thermal power of 62.5 MW with an electric output of approximately 20 MW.

The EBR-II reactor accommodated 637 hexagonal subassemblies. The SHRT-17 core was made up of eight main subassembly types: driver, stainless steel, stainless steel reflector, blanket, control rod, safety rod, instrumented subassemblies, and experimental subassemblies. The SHRT-45R core differed somewhat from that for SHRT-17; it contained two types of driver subassemblies, as well as all the other seven subassembly types (but a different set of experimental subassemblies) .

The primary tank in EBR-II is illustrated in Figure 1. All major primary system components were submerged in the primary tank, which contained approximately 340 m^3 of liquid sodium at 371°C. Two primary pumps drew sodium from this pool and provided sodium to the two inlet plena for the core. Subassemblies in the inner core and extended core regions received sodium from the high-pressure inlet plenum, accounting for approximately 85% of the total primary flow. The blanket and reflector subassemblies in the outer blanket region received sodium from the low-pressure inlet plenum.

Hot sodium exited the subassemblies into a common upper plenum where it mixed before passing through the outlet pipe into the intermediate heat exchanger (IHX). Sodium then exited the IHX back into the primary sodium tank before entering the primary sodium pumps again.

Sodium in the intermediate loop traveled from the IHX to the steam generator, where its heat was transferred to the balance-of-plant (BOP). The colder sodium in the intermediate loop then traveled through a similar length of piping back to the IHX. The steam generator consisted of two parallel superheaters and seven parallel evaporators.

EBR-II was operated initially to demonstrate the feasibility of a closed fuel cycle that required the addition of only U^{238} to fuel the breeding process and allow for sustained operation. To achieve the intended fuel utilization, the initial EBR-II operating period was closely tied to research into pyrometallurgical reprocessing for irradiated nuclear fuel. This period lasted five years. Following the fuel cycle demonstration phase, the focus of EBR-II shifted for much of the next ten years towards irradiation experiments of advanced binary and ternary metal fuels and also advanced oxide fuels. During the last fifteen years of operation, EBR-II was used for experiments designed to demonstrate the importance of passive safety in liquid metal reactors (LMR).

The Shutdown Heat Removal Test (SHRT) program was carried out in EBR-II between 1984 and 1986. The objectives of this program were to support U.S. LMR plant design; provide test data for validation of computer codes for design, licensing and operation of LMRs; and demonstrate passive reactor shutdown and decay heat removal in response to protected and unprotected transients. The protected and unprotected transients tested include loss of flow in the primary and/or intermediate sodium loops as well as a loss of heat sink from the balance of plant. Additional tests were performed to examine the response of the system to balance of plant changes, and others were performed to characterize reactivity feedbacks.

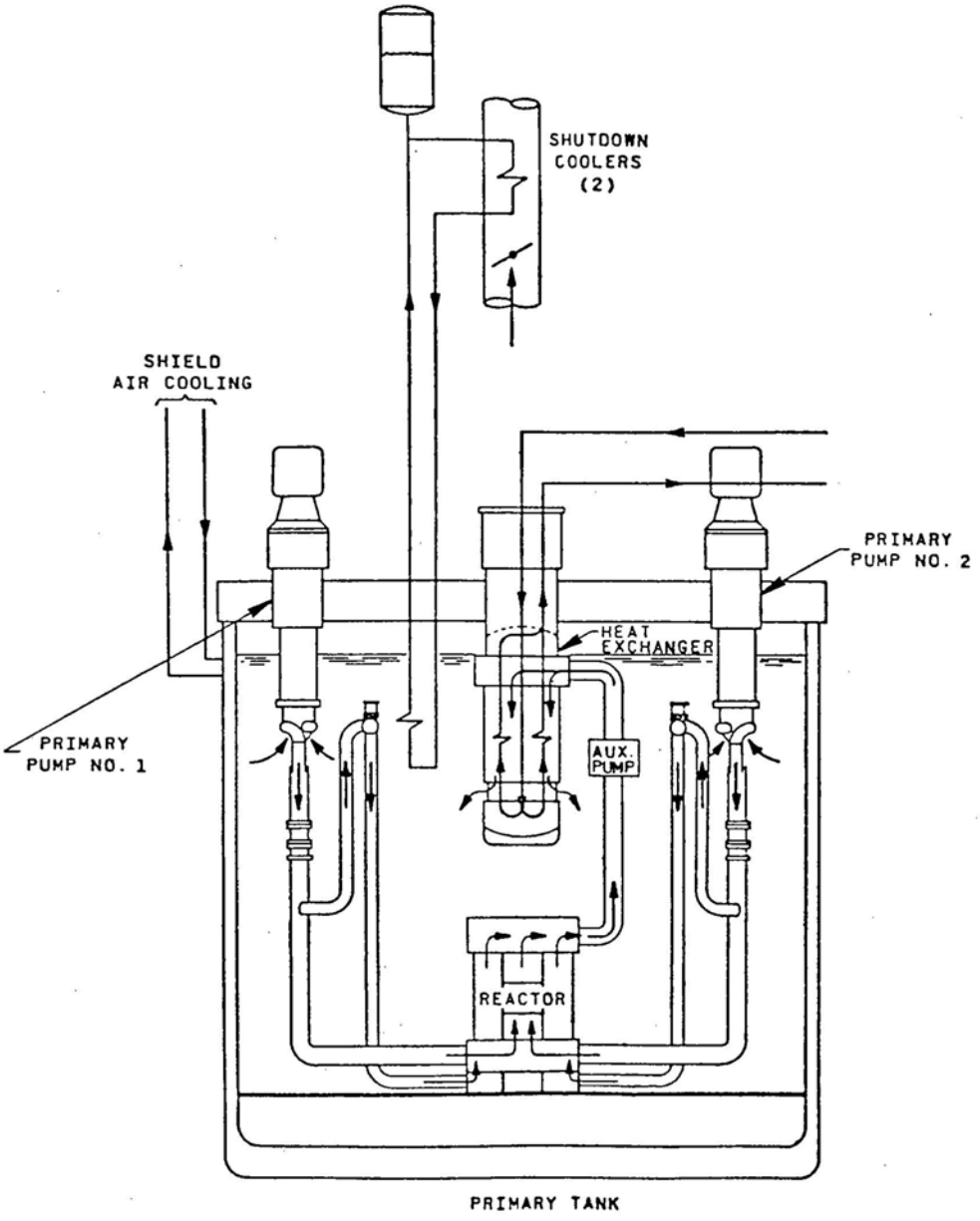

FIG. 1. EBR-II Primary System Components and Sodium Flow Paths

On June 20, 1984, the SHRT-17 loss of flow test was conducted. In this test, a loss of electrical power to all the plant sodium coolant pumps was used to demonstrate the effectiveness of natural circulation cooling characteristics. Starting from full power and flow, both the primary loop and intermediate loop

coolant pumps were simultaneously tripped and the reactor was scrammed to simulate a protected loss-of-flow accident. In addition, the primary system auxiliary coolant pump that normally had an emergency battery power supply was turned off. Temperatures in the reactor quickly rose to high, but acceptable levels as the natural circulation characteristics cooled the reactor down safely at decay heat power levels. SHRT-17 demonstrated that natural phenomena such as thermal expansion of the sodium coolant and thermal inertia of the primary pool sodium, as opposed to electromechanical systems such as electrically driven pumps, can be effective in protecting the reactor against potentially adverse consequences from protected loss-of-flow and loss-of-heat-sink accidents.

On April 3, 1986, the SHRT-45R unprotected loss of flow test was conducted to demonstrate the effectiveness of EBR-II's passive feedbacks. During the test, the plant protection system was disabled to prevented initiation of a scram. Starting from full power and flow, both the primary and intermediate-loop coolant pumps were simultaneously tripped to simulate an unprotected loss-of-flow accident. Temperatures in the reactor quickly rose to high, but acceptable levels as the inherent reactivity feedbacks terminated the fission process. SHRT-45R demonstrated that natural phenomena such as thermal expansion of reactor materials can be effective in protecting the reactor against potentially adverse consequences from unprotected loss-of-flow and loss-of-heat-sink accidents.

EBR-II was heavily instrumented to measure mass flow rates, temperatures and pressures throughout the system. In addition, two special instrumented subassemblies (one a fuel subassembly and one representing a blanket subassembly) were loaded into row 5 of the EBR-II core for both the SHRT-17 and SHRT-45R tests. Both subassemblies were instrumented with flowmeters and a variety of thermocouples designed to provide in-core temperature measurements at various radial and axial positions for characterizing flow redistribution and temperature profiles during transients. The total data recorded were comprehensive enough to accurately characterize the passive safety response of EBR-II during both tests and thus provide an excellent means of validating the EBR-II simulation models being developed by participants in the CRP. Some of the test results for SHRT-45R are presented in [3].

4. Benchmark Specifications

The first Research Coordination Meeting of the CRP was held in June 2012 at Argonne. At that time, registered CRP participants were issued documents containing the benchmark specification and data requirements for both shutdown heat removal tests, plus the neutronic benchmark specifications for the SHRT45R test. The documents provide comprehensive details on the following aspects of the tests:

- Detailed descriptions of both tests, including initial and transient benchmark boundary conditions,
- Detailed reactor core description, with subassembly dimensions for all the types of subassemblies that were in the reactor during the tests,
- Detailed description of the instrumented subassemblies,
- Detailed primary cooling system description with component dimensions,
- Material properties,
- Necessary data for the calculation of reactivity feedback coefficients,
- Detailed decay heat parameters,
- Isotopic compositions of core and blanket subassemblies, and
- Essential measurements for benchmark forcing functions and unique plant-specific component characteristics
- Detailed descriptions of the instrumentation used to measure the data.

Some discussion of the plant-specific behaviour of EBR-II during operation (e.g., specifics about the effect of structural thermal expansion, sodium leakage flow paths, etc.) is also presented.

The benchmark model of the primary sodium circuit is illustrated in Figure 2. This schematic shows the locations and dimensions of the major components and depicts the simplified geometry used for these components in the benchmark model.

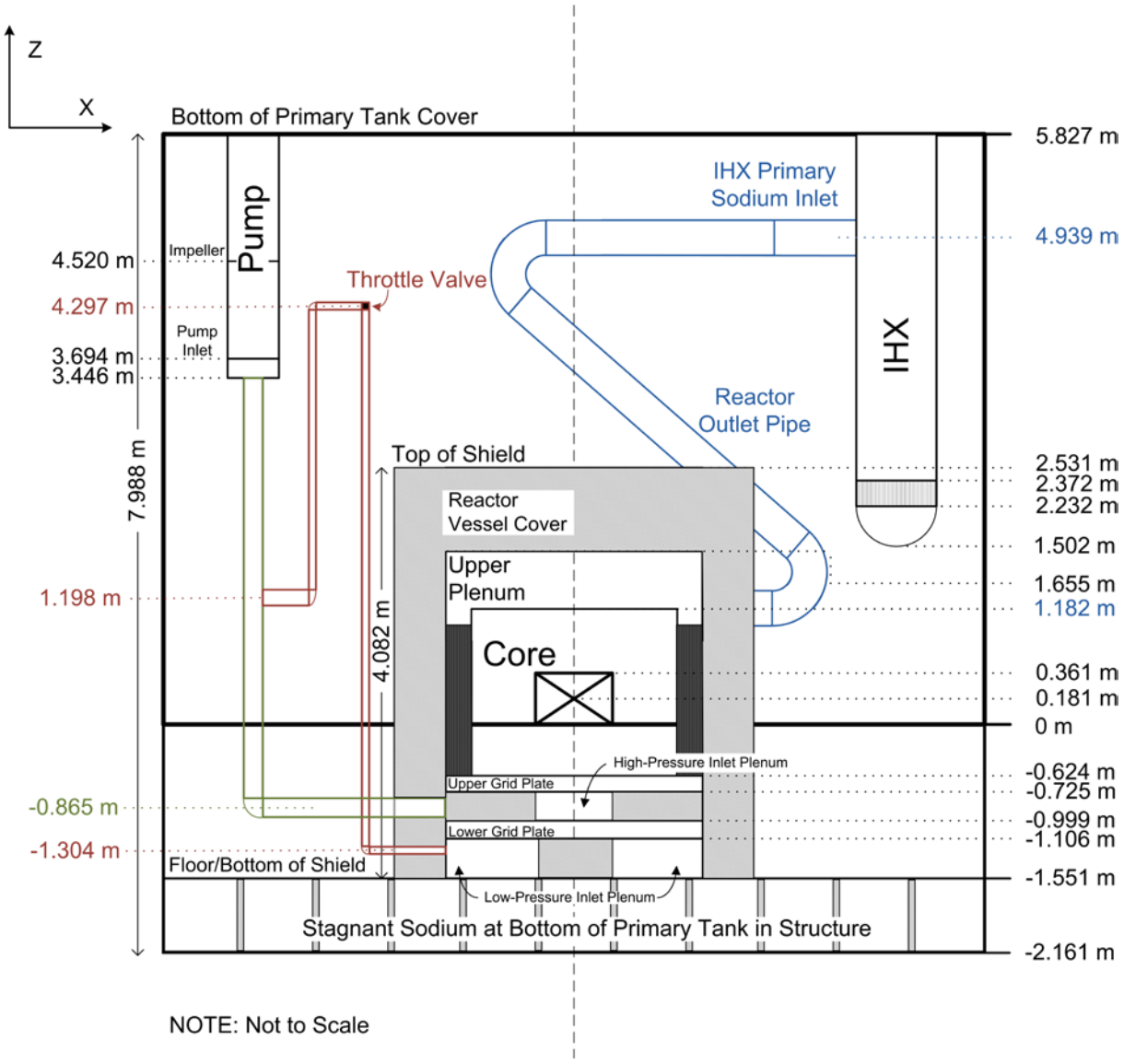

FIG. 2. Benchmark Model of EBR-II Primary Vessel Components

Included with the specifications is a list of the pressures, temperatures, and mass flow rates for which benchmark participants should provide results for both tests. For SHRT-45R, participants need also to compute net reactivity, fission power, and total power. Most of these parameters can be compared not only between codes but also against measured data; in a few cases, the specification asks for computational results for parameters that were not measured during the tests but that are useful for cross-code comparisons.

The complete benchmark specifications can be obtained through a request to the IAEA for formal participation in this activity.

5. Conclusions

Argonne National Laboratory is hosting an IAEA Coordinated Research Project on benchmark analyses of two sodium-cooled fast reactor passive safety tests performed at the Experimental Breeder Reactor-II (EBR-II) within the framework of the US Integral Fast Reactor demonstration program.

The landmark EBR-II passive safety tests showed that, with safety principles of defense-in-depth with multiple redundant systems and barriers to release of radioactivity and the added inherent safety phenomena to prevent severe consequences from unprotected accidents, SFRs are capable of inherent self-protection. Through favorable reactivity feedback and natural circulation cooling, and considering only mechanistic, physically-realizable accident conditions to be relevant for safety (guided by probabilistic risk assessments), it may be possible to virtually eliminate accident-related large radioactive releases from an SFR design.

The extensive data recorded for these tests provide an excellent basis for code and model verification, validation, and qualification, best performed within the framework of international benchmark simulations. The benchmark specifications prepared to support this international collaboration describe the reactor geometry and EBR-II plant components; provide recommended material properties; and identify the initial conditions, power production conditions, and transient boundary conditions needed for the simulation of the tests.

The overall objective is to improve the participants' analytical capabilities in the field of fast reactor simulation and design for verification of passive safety response during loss-of-flow accidents. Particular focus will be on predicting natural convective cooling accurately by evaluating the reactor core flow and temperatures, particularly in comparison to the measurements obtained from the instrumented subassemblies for core axial distributions. The ultimate assessment will be in the prediction of the fission power history during an ATWS by the coupled neutronic/thermal-hydraulic/structural models. Evaluation of uncertainties for prediction of flow rates, fuel, cladding, coolant, and structure temperatures, transition to natural circulation, and fission power history will also be within the scope of the project.

REFERENCES

[1] G. H. Golden, H. P. Planchon, J. I. Sackett and R. M. Singer, "Evolution of Thermal-Hydraulics Testing in EBR-II," *Nuclear Engineering and Design*, **101**, 3-12 (1987).

[2] D. Mohr, L. K. Chang, E. E. Feldman, P. R. Betten and H. P. Planchon, "Loss-Of-Primary-Flow-Without-Scram Tests: Pretest Predictions and Preliminary Results," *Nuclear Engineering and Design*, **101**, 45-46 (1987).

[3] T. Sofu and L. L. Briggs, "Benchmark Specifications for EBR-II Sutdown Heat Removal Tests," *Proceedings, ICAPP'12*, Chicago (2012).

Evaluation of the prompt neutron reproduction time in ELECTRA

E. Suvdantsetseg, S. Bortot, J. Wallenius

Royal Institute of Technology (KTH), Stockholm, Sweden

Abstract. In this paper, an attempt to provide an accurate assessment of the prompt neutron reproduction time in the European Lead Cooled Training Reactor (ELECTRA) and to evaluate its impact on the system transient behaviour has been pursued. ELECTRA is a 0.5 MWth pool-type natural-circulation reactor currently under development at the Royal Institute of Technology (KTH). Due to the small size of the active core, it belongs to the class of reflector-dominant fast systems, which may not be satisfactorily treated by employing standard kinetic models, since the neutron lifetime in the fast core region is orders of magnitude less than the neutron lifetime in the reflector region. Hence, the need for a reliable method to calculate the prompt neutron reproduction time in ELECTRA has been recognized, as it plays a major role in determining the time-dependent behaviour of the system, thus resulting considerably important for both operation and safety. To adequately handle the problem, the Serpent code has been chosen as the preferred calculation tool, since Monte Carlo allows the treatment of complex geometries and nuclear data practically without any approximation. Anyway, as it has been shown that the rigorous way to calculate the prompt neutron reproduction time involves weighting over the adjoint flux, an evaluation of this parameter has been performed also by means of the deterministic code ERANOS. In addition, explicit time-dependent Monte Carlo calculations with MCNP using the time cut-off technique were performed as well for comparison. Results have been compared and the impact of uncertainties on the system dynamic behaviour has been finally investigated by simulating a typical reactivity transient scenario with the use of SAS4A/SASSYS-1.

1. INTRODUCTION

The prompt neutron reproduction time [1] is one of the most important reactor dynamic parameters, as it plays a major role in determining the time-dependent behaviour of a nuclear system, thus resulting considerably important for both operation and safety.

It is acknowledged that the current Monte Carlo codes do not provide the prompt neutron reproduction time in a straightforward way, since a rigorous calculation typically involves weighting over the adjoint flux [2][3]. Nevertheless, the parameter may possibly be evaluated by repeated Monte Carlo simulations using the 1/v poisoning method [4].

Alternatively, deterministic codes can be used for this purpose as they allow to employ either *direct integration* or *iterated fission probability* or *eigenvalue perturbation* methods [4], the latter being based on the same principle as the poisoning method.

However, the prompt neutron reproduction time appears to be quite sensitive to the core geometrical arrangement, resulting particularly tricky to be evaluated in reflector-dominant fast critical systems [4][5][6], where the neutron lifetime in the fast core region can be even orders of magnitude less than the one in the reflector region. In some cases a two-prompt-neutron-group approximation should be applied instead of the more widely used one-prompt-neutron-group approach for reactivity transient simulations in order to properly address the kinetic and dynamic behaviour of such systems [5][6].

Noting that a realistic evaluation is crucial for design basis transient analyses of innovative fast reactor concepts, both a validation and an uncertainty evaluation of the methodologies available to evaluate this parameter are necessary.

This work is dedicated to evaluate the prompt neutron reproduction time in the European Lead Cooled Training Reactor (ELECTRA), which belongs to the class of low-power reflector-dominant fast systems. Calculations have been performed by employing both the Monte Carlo code Serpent [7] and the deterministic code ERANOS [8].

Since the Serpent code is chosen as the main modelling and design tool for ELECTRA, an attempt to validate the methodology employed to evaluate the prompt neutron lifetime against deterministic methods has been pursued. However, due to geometry description limitations in ERANOS, it was not possible to model the cylindrical absorber drums accurately. Hence, a completely different approach has been followed: explicit time dependent Monte Carlo calculations have been carried out with MCNP using the time cut-off technique [9].

2. CALCULATION APPROACHES

2.1. Serpent Monte Carlo calculations

2.1.1. Geometry model

The Monte Carlo code Serpent version 1.1.16 has been used with the JEFF3.1.1 nuclear data library [10]. The reference ELECTRA model implemented in Serpent is presented in Fig. 1.

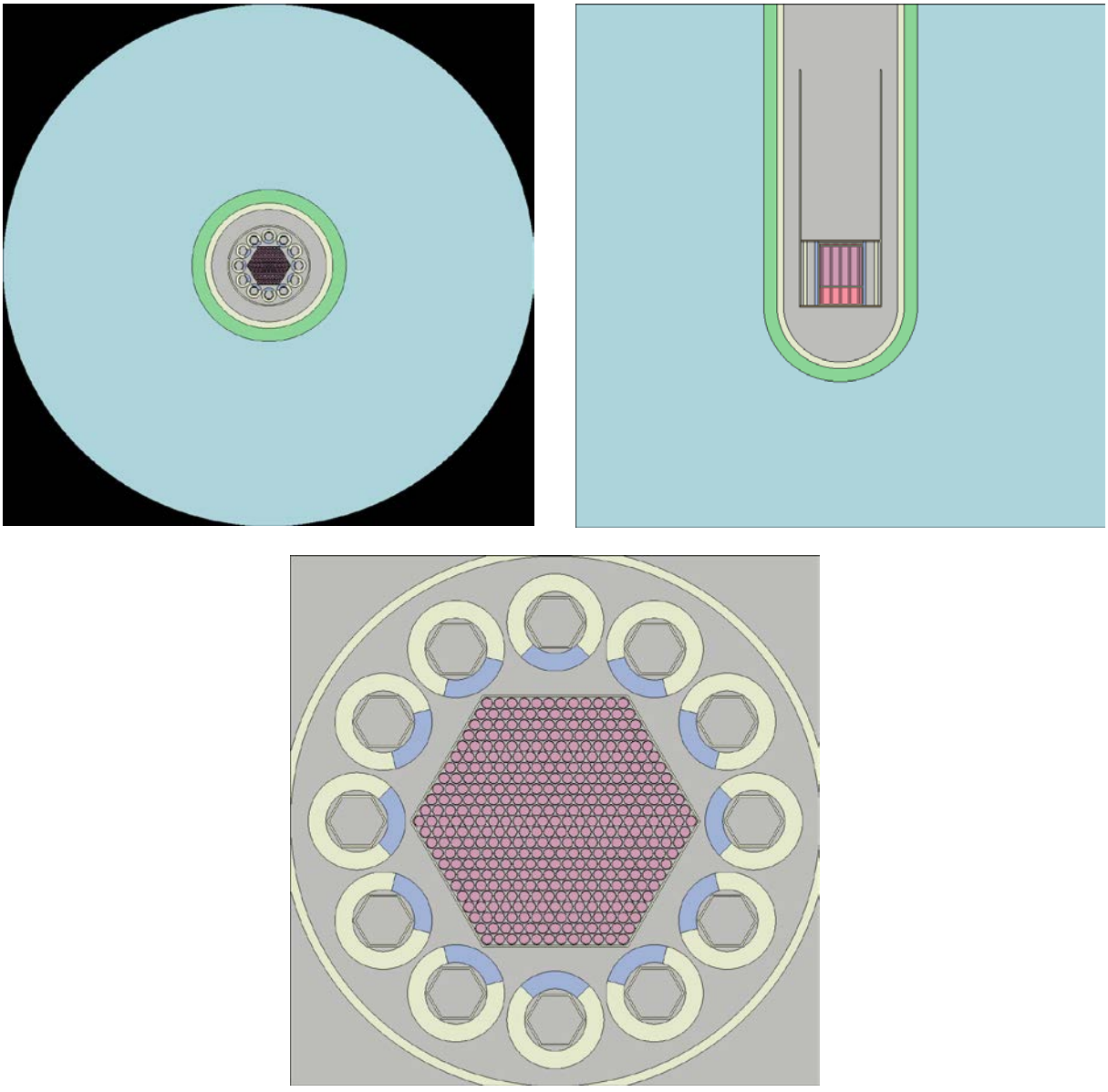

FIG. 1. Cross sections of the reference ELECTRA model implemented in Serpent.

The model includes detailed specifications of core assembly (active core height is 30 cm and the hexagon side length approximately is 16.3 cm), control drums (inner/outer radius 3.5/5.5 cm), lead coolant/reflector (radius ~50 cm), core barrel, vessel and concrete shielding (outer radius ~200 cm) around the vessel. The supporting steel structure around the core is modelled in a simplified fashion. Full details on the referred reactor description can be found in [11,13].

2.1.2. Method

Serpent simulations were run repeatedly in order to apply the poisoning method, as described in the following section.
According to the first-order perturbation theory, if a small concentration of poison is homogeneously added to the system, which has an artificially prepared absorption cross section with $\sigma \sim 1/v$ dependency, the prompt neutron reproduction time Λ_p of the system would be given by:

$$\Lambda_p = \left(\frac{\partial \rho}{\partial N \cdot \sigma \cdot v} \right)_{N=0} = \lim_{N \to 0} \left(\frac{\rho_{poisoned} - \rho}{N \cdot \sigma \cdot v} \right) \quad (1)$$

where ρ - reactivity, N - poison concentration [atoms cm^{-3}], σ – artificial microscopic absorption cross section [b], and v– neutron speed [cm s^{-1}]. Note that $\sigma \cdot v = const$, since the cross section is inversely proportional to the neutron speed.

2.2. ERANOS deterministic calculations

2.2.1. Geometry model

The ERANOS version 2.1 model of ELECTRA has been attempted to be implemented as similar as possible to the Serpent one. At a cell definition level, the fuel assembly has been modelled heterogeneously so as to match perfectly the Serpent geometry. As far as the subcritical cells outside the core region are concerned (e.g., absorbers, lead reflector, core barrel and reactor vessel, etc.), they have been modelled homogeneously. Cell calculations have been performed by means of the ECCO cell code [12], in which the fine group (1968 energy groups) cross sections have been finally condensed into a non-standard 49-energy-groups structure in order to properly account for the very hard neutron spectrum [13]. At a whole core calculation level, it has been necessary to opt for a two-dimensional *R-Z* geometry description due to the limitations of the code (Fig. 2).

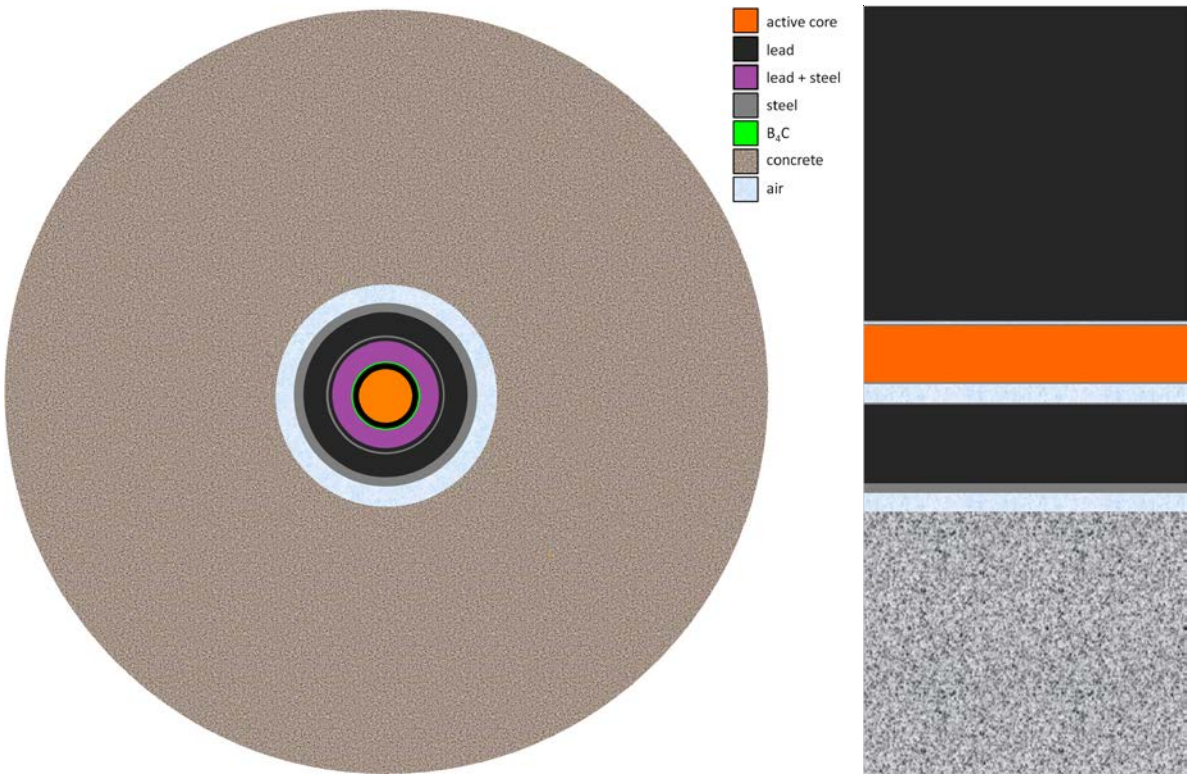

FIG. 2.Cross sections of the reference ELECTRA model implemented in ERANOS: overall radial description in shut-down state (left) and zoom-in of the axial model corresponding to the first radial zone (right).

Therefore, the active core as well as the axially corresponding subcritical media have been modelled as equivalent homogenized cylinders. Moreover, control drums have been necessarily treated in a simplified way: in order to minimize the error in self-shielding effects evaluation, the active segments of the drums have been modelled as a single equivalent cylinder composed by enriched boron carbide surrounding the core at two equivalent distances corresponding to the so-callded shut-down state (i.e., drums facing the core) and supercritical configuration (i.e., drums rotated away from the core). Concerning the remaining part of the drums, structure and coolant volume fractions have been preserved and treated as one homogeneous cylindrical medium, either surrounding or surrounded by the absorbers depending on the situation (subcritical or supercritical). Finally, lead coolant and reflector, steel barrel and vessel, air gap, and concrete have been modelled exaclty as in Serpent.

2.2.2. Method

The prompt neutron reproduction time has been computed by adopting the ERANOS procedure *BETA_EFFECTIVE_CALCULATION* [8], requiring both the direct (Φ) and adjoint (Φ^+) scalar (or angular) neutron fluxes, which have been previously calculated in S_4 (P_1 expansion) transport.
The procedure calculates the parameter in object according to the following formulation:

$$\Lambda_p = \frac{\left\langle \Phi^+, \frac{1}{v}\Phi \right\rangle}{\left\langle \Phi^+, \mathbf{F}\Phi \right\rangle} = \frac{\sum_{g=1}^{G} \int \frac{1}{v_g} \Phi_g \Phi_g^+ d^3r}{\int \left(\sum_{g=1}^{G} \chi_g \Phi_g^+ \right) \left(\sum_{g=1}^{G} v_g \Sigma_{fg} \Phi_g \right) d^3r} \tag{2}$$

where the group velocity $v_g \approx 9.8 \cdot 10^8 \sqrt{E_g^{\sup} + E_g^{\inf}}$ [cm s^{-1}].

2.3. MCNP Monte Carlo calculations

2.3.1. Geometry model

In the MCNP5 model of ELECTRA the fuel assembly, control drums, coolant and reflector have been modelled exactly as in Serpent (see Paragraph 2.1.1). Only a slight simplification has been applied, as the supporting steel structures have been omitted.

2.3.2. Method

If the alpha-eigenvalue is known, the prompt neutron reproduction time can be estimated by:

$$\Lambda_p = \frac{k_p - 1}{\alpha} \tag{3}$$

where k_p is the prompt multiplication factor, and α is the prompt neutron decay constant or the alpha-eigenvalue. Furthermore, by definition, α can be estimated by the *tallies* of the asymptotic neutron population increase over time as:

$$\alpha = \frac{\ln N_1 - \ln N_2}{t_1 - t_2} \tag{4}$$

where N_1 and N_2 are the neutron populations at the asymptotic times t_1 and t_2, respectively. Hence, using the "cut:n" card of MCNP, the alpha-eigenvalue can be estimated by the asymptotic slope of the time derivation of the power rise, which is recorded in the "loss to fission" output for the source mode calculation.

3. RESULTS AND DISCUSSION

3.1. Prompt neutron reproduction times

The estimated values of the prompt neutron reproduction time obtained by employing the different methods described above are shown in Tab. 1. The parameter has been evaluated for the cases of all drums absorbers are facing the core (subcritical state) and absorbers are rotated away at the maximal distance from the core as well the case of no absorber in the system.
The default output value of the Serpent code, which is an unweighted value of the parameter, is shown for purpose of comparison (first row).

Table 1. Evaluated prompt neutron reproduction time Λ_p [10^{-8} s] for ELECTRA.

Method	Subcritical state	Supercritical state	No absorbers
Default Serpent output	6469	7095	10609
1/*v* absorber poisoning method	4.9±0.3	8.1±0.2	17.9±0.2
MCNP time cut-off method	1.7±0.4	6.3±0.8	7.2±0.5
ERANOS	6.3	10.2	26.1

As displayed in the table, the value of Λ_p varies between 17 and 102 ns depending on the absorber position and the chosen methodology. Observing the numerical trend, it can be concluded that the

parameter is strongly dependent on the distance of the absorbers from the core. In addition, it appears to be extremely sensitive to both the chosen methodology and the geometry description.
A systematic trend of discrepancy between the models is clearly seen. The reasons of the discrepancy could be, to some extent, the non-consistent modelling fashion. Differences of up to a factor of 3 between ERANOS and MCNP time cut-off methods indicate inherent issues of the methodologies applied, which must be understood for the future work. However, the results remain similar within an order of magnitude, being in particular the good agreement between ERANOS and the Serpent 1/*v* absorber poisoning method quite encouraging.

3.2. Impact on ELECTRA transient behaviour

As a further step, the influence of the uncertainties affecting the prompt neutron reproduction time on the ELECTRA transient response has been investigated. In particular, an unprotected overpower transient (UTOP) analysis has been performed by means of SAS4A/SASSYS-1 [14].
In Fig. 2, the relative power evolution following a 1 $ reactivity insertion within 1 s is depicted for various prompt neutron lifetimes derived from the respective reproduction times [1].

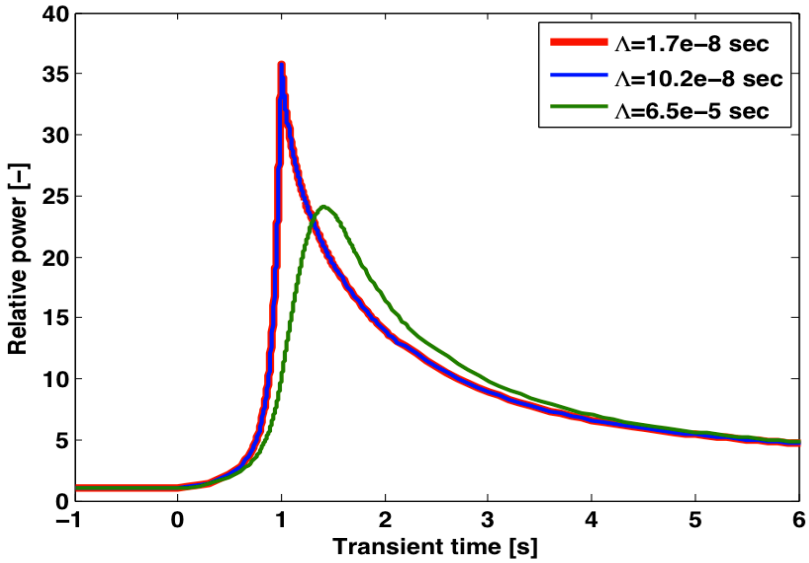

FIG. 3. Relative power as a function of time following 1 $ reactivity insertion.

The transient results show that differences in the relative power evolution are less than 0.1 % for neutron reproduction times varying between 17 and 102 ns, indicating that the important discrepancies from the static neutronics point of view mentioned above do not have repercussions on dynamics, resulting in a definitely negligible effect.
However, it is pointed out that a significantly different transient response is observed when the default Serpent output (shown in the first row of the Table 1.) is mistakenly used for transient calculations (see Fig 3, green curve), as the relative power can be severely under-estimated (by 33 % for the transient simulated here).

4. CONCLUSIONS

In this paper three different methodologies to calculate the prompt neutron reproduction time have been applied in order to evaluate such fundamental safety parameter in ELECTRA, which belongs to the class of reflector-dominant fast neutron systems.
The results have turned out to be quite sensitive to both modelling approaches and methods: in particular, the direct time-dependent calculation appears to predict the lowest figures. Moreover, a general tendency of the parameter to depend on the absorbers location has been observed.
Even though values with discrepancies up to a factor of 3 were obtained for the prompt neutron reproduction time, the reactivity insertion transient analysis has showed that, when the parameter is

below 10 shakes, the reactor power prompt overshoot is mainly a function of both the reactivity feedback mechanisms speed and the reactivity insertion rate, rather than of the neutron reproduction time, thus indicating that even important uncertainties affecting its value result in a negligible impact on the system dynamic response.
Nevertheless, it is also noted that the neutron reproduction time directly obtained from the output of Serpent appears to be based on an incorrect estimator, and can bring to severe under-estimations of the power peak during UTOP accidents.

ACKNOWLEDGEMENTS

The authors are very grateful to Dr. Vincenzo Peluso (ENEA) and Dr. Gerardo Aliberti (ANL) for their valuable support and guidance in the use of ERANOS.

REFERENCES

[1] LEWIS, J., Renaming the Generation Time the Reproduction Time, Ann. Nucl. Energ. 33 (2006) 1071.
[2] HOOGENBOOM, J. E., Methodology of Continuous-energy Adjoint Monte Carlo for neutron, photon, and coupled neutron-photon transport, Nucl. Sci. Eng. 143 (2003) 99-123.
[3] LEPPÄNEN, J., Serpent User Group Meeting Note, Madrid, 2012.
[4] VERBOOMEN, B., et al., Monte Carlo Calculation of the Effective Neutron Generation Time, Ann. Nucl. Energ. 33 (2006) 911-916.
[5] SPRIGGS, G. D., et al., Two-Region Kinetic Model for Reflected Reactors, Ann. Nucl. Energ., 24 (1997) 205-250.
[6] DULIN, V. A., et al., Temporal Distribution of Prompt Neutrons in a Fast Reactor with Hydrogen-Containing Blocks in the Blanket, Atom. Energ. 82 (1997) 166-173.
[7] LEPPÄNEN, J., Development of a New Monte Carlo Reactor Physics Code. PhD thesis, Univ. of Helsinki, Helsinki (2007).
[8] Rimpault, G., et al., The ERANOS Code and Data System for Fast Reactor Neutronic Analyses, Proceedings of the International Conference on the PHYSics Of Reactors (PHYSOR), Seoul (2002).
[9] MCNP X-5 MONTE CARLO TEAM, MCNP – A General N-Particle Transport Code, Version 5, LA-UR-03-1987 and LA-CP-03-0245, Los Alamos National Laboratory (2003).
[10] Jeff Joint Evaluated File (JEF) project, The JEFF-3.1 Nuclear Data Library, Technical Report JEFF Report 21, OECD/NEA (2006).
[11] SUVDANTSETSEG E., et al., Optimization of the reactivity control drum system of ELECTRA, Nucl. Eng. Des. 252 (2012) 209-214.
[12] RIMPAULT, G., Physics Documentation of ERANOS: The Ecco Cell Code, Technical Report DER-SPRC-LEPh-97-001, CEA (1997).
[13] WALLENIUS, J., et al., ELECTRA: European Lead-Cooled Training Reactor, Nucl. Technol. 177 (2012) 303-313.
[14] T. H. FANNING, The SAS4A/SASSYS-1 Safety Analysis Code System, Argonne National Laboratory (2012).

A mathematical model for ELECTRA transient and stability analyses

S. Bortot[a], A. Della Bona[b], E. Suvdantsetseg[a], J. Wallenius[a]

[a] Royal Institute of Technology (KTH)

[b] Politecnico di Milano

Abstract. A mathematical model of the European Lead Cooled Training Reactor (ELECTRA) was developed specifically meant for the present early phase of the system conceptual design. An effort was undertaken to provide a very flexible and straightforward, though accurate, fast-running tool allowing to perform transient design-basis and stability analyses, which play a fundamental role when refining or even finalizing the reactor configuration. A simplified approach was adopted to model the whole primary system, consisting in a lumped-parameter treatment of the main parts constituting the flow region (namely, active core, bypass channel, hot coolant plenum, heat exchanger, cold leg and cold pool). For each subsystem, coupled equations based on point-kinetics for neutronics, and on mass, energy and momentum balances for thermal-hydraulics were developed and implemented in MATLAB/SIMULINK®. Three typical transients were then simulated to illustrate the wide application of the model developed: Unprotected Transient OverPower (UTOP), Unprotected Loss of Heat Sink (ULOHS), and Unprotected coolant flow Blockage Accident (UBA).

1. INTRODUCTION

The European Lead Cooled Training Reactor (ELECTRA) is currently under development at the Royal Institute of Technology (KTH) in Sweden, and consists in a low-power (0.5 MW_{th}) fast reactor operating under natural circulation of the lead coolant, mainly intended for demonstration and educational purposes [1] [2].

One of the most important issues for ELECTRA and, in general, natural circulation systems, is the preservation of stable flow. In fact, the good natural convection capability of metal coolants can be made ineffective by an unstable-regime flow behaviour due to perturbations inducing oscillations of the lead free surfaces in the reactor. Under such circumstances the mass flow rate through the core may oscillate and decrease to the limit of flow reversal, causing fuel and cladding temperatures to transiently increase to significantly high values. In addition, a system like ELECTRA is more tightly coupled than a forced convection reactor both at a physics level (i.e., neutronics, thermal-hydraulics) and at a component level (i.e., core, heat exchanger, primary system layout), since neutronics and thermal-hydraulics undergo strong mutual feedbacks, as well as the core behaviour is influenced by the heat exchange conditions in the Steam Generator (SG). Therefore, the study of stability is to be extended to the overall coupled system, and not limited to the thermal-hydraulics area, as the feedbacks due to any non-nominal power generation within the core cannot be disregarded.

In order to deeply understand these phenomena and to perform design-oriented dynamics analyses, a reliable modelling and simulation tool *ad hoc* developed has been recognized to be necessary. In particular, a plant dynamics simulator expressly meant for this early phase of the reactor conceptual design - in which all the system specifications are still considered open design parameters and thus may be subject to frequent modifications - was to be sought. Therefore, a very flexible, straightforward and efficient mathematic model of ELECTRA has been specifically developed for predicting the reactor response to typical transient initiators as a function of different design provisions, and evaluating how the system stability is affected by the latter, such analyses being directed to both refining (or even finalizing) the reactor design and laying the foundations for establishing viable control strategies.

2. ELECTRA REFERENCE CONFIGURATION

ELECTRA is a 0.5 MW_{th} pool-type reactor in which the power produced in the (Pu0.4, Zr0.6)N fuelled core is transferred to eight SGs by natural circulation of the coolant. In particular, the lead flow enters the core through a bottom plate to be collected in a plenum and then delivered to the SGs, where it is cooled before entering the cold pool through the cold leg (located in the annular space between the reactor vessel and the cylindrical inner vessel) and returning finally to the core. All the primary components are installed inside the reactor vessel, which is shaped as a cylinder with elliptical bottom head and flat roof. Full details concerning the referred reactor configuration can be found in [1] and [2].

3. MATHEMATICAL MODEL

A modular approach has been adopted to model the whole primary system of ELECTRA, consisting in a non-linear, lumped-parameter treatment of the main parts constituting the flow region: active core, bypass channel, hot coolant plenum, heat exchanger, cold leg and cold pool (Fig. 1). For each subsystem, coupled equations based on point-kinetics for neutronics, and on mass, energy and momentum balances for thermal-hydraulics[1] have been developed and implemented in MATLAB/SIMULINK® [3].

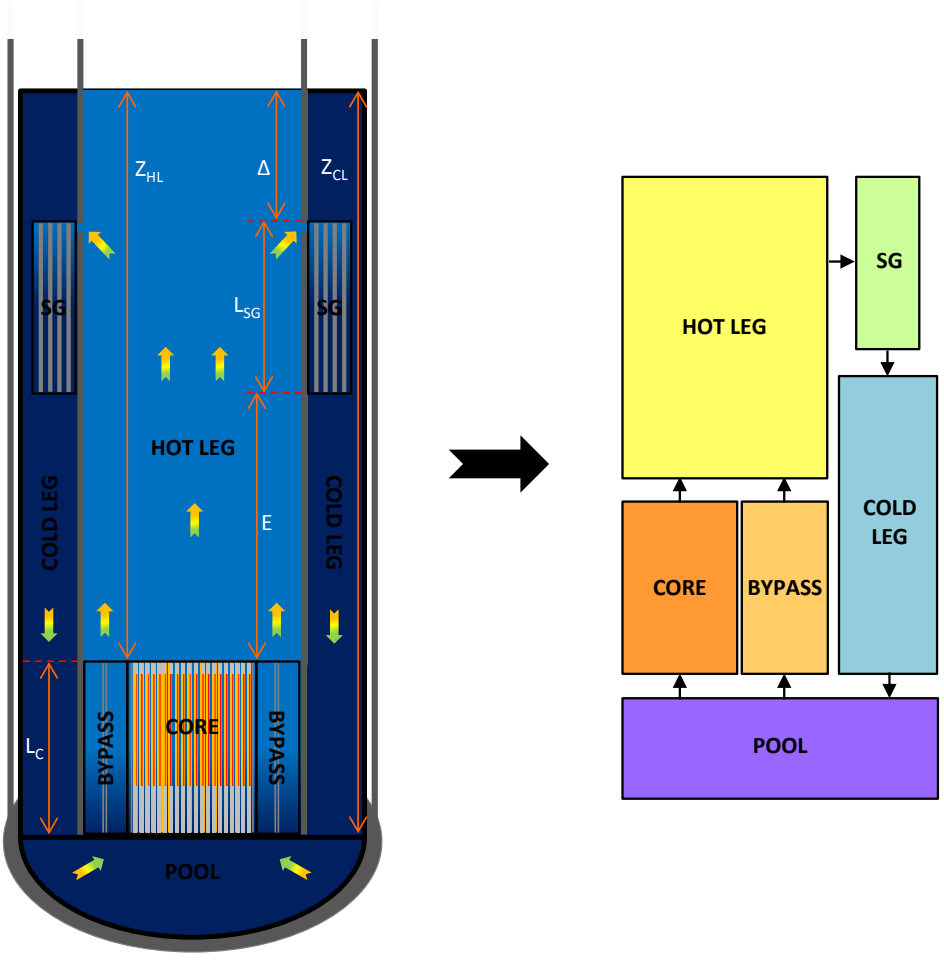

FIG. 1. ELECTRA primary system layout (left) and corresponding modelling block scheme (right).

[1] As far as the coolant-related equations are concerned, both a central and an upstream formulation have been developed.

3.1. Core

3.1.1. Neutronics

The core power *q(t)* is assumed to be a fraction (97 %) of the total reactor power, the remaining 3 % being deposited in the bypass, and is considered as generated only by fission events, the contribution of decay heat being neglected. It is derived from the normalized neutron flux, which is in turn calculated by employing a point-wise kinetics model with six groups of delayed neutron precursors:

$$\frac{dn(t)}{dt} = \frac{\rho(t)-\beta}{\Lambda} n(t) + \sum_{i=1}^{6} \lambda_i c_i(t) \tag{1}$$

$$\frac{dc_i(t)}{dt} = \frac{\beta_i}{\Lambda} n(t) - \lambda_i c_i(t) \qquad i = 1, \dots 6 \tag{2}$$

3.1.2. Reactivity

Consistently with the lumped parameter modelling employed, the reactivity feedback is expressed as a function of the average values of fuel and coolant temperatures, while externally introduced reactivity associated with the rotational angle of a representative control drum is handled as an input parameter. A linear relation for core expansions (axial and radial) and coolant density reactivity effects is adopted, leading to the following expression incorporating constant coefficients:

$$\rho(t) = k_D \left(ln \frac{{T_f}^{eff}(t)}{{T_{f,0}}^{eff}} \right) + \alpha_Z \left({T_f}^{mid}(t) - {T_{f,0}}^{mid} \right) + (\alpha_R + \alpha_L)\left(T_l(t) - T_{l,0} \right) + \rho_{drum}(t) \tag{3}$$

As far as the Doppler effect determination is concerned, an effective average fuel temperature accounting of resonances broadening is adopted.

3.1.3. Thermal-hydraulics

A single-node heat transfer model accounting of four distinct temperature regions corresponding to fuel, helium gap, cladding and coolant has been implemented. In this way the reactivity feedback is enabled to include all the major contributions as well as the margins against technological limits to be monitored. In line with the point model concept, the latter temperatures are assumed to be functions separable in space and time:

$$M_f C_f \frac{d{T_f}^{centr}(t)}{dt} = q(t) - k_f \left({T_f}^{centr} - {T_f}^{surf}(t) \right) \text{ where } \frac{n(t)}{n_0} = \frac{q(t)}{q_0} \tag{4}$$

$$M_g C_g \frac{d{T_f}^{surf}(t)}{dt} = k_f \left({T_f}^{centr} - {T_f}^{surf}(t) \right) - k_g \left({T_f}^{surf} - {T_c}^{int}(t) \right) \tag{5}$$

$$M_c C_c \frac{d{T_c}^{int}(t)}{dt} = k_g \left({T_f}^{surf}(t) - {T_c}^{int}(t) \right) - k_c \left({T_c}^{int}(t) - {T_c}^{surf}(t) \right) \tag{6}$$

$$M_c C_c \frac{d{T_c}^{surf}(t)}{dt} = k_c \left({T_c}^{int}(t) - {T_c}^{surf}(t) \right) - h_{cl} \left({T_c}^{surf}(t) - T_l(t) \right) \tag{7}$$

$$M_{l_{core}} C_l \frac{dT_{l_{core}}(t)}{dt} = h_{cl} \left({T_c}^{surf}(t) - T_{l_{core}}(t) \right) - \Gamma_{core}(t) C_l \left(T_{l_{core}}^{out}(t) - T_{l_{core}}^{in}(t) \right) \tag{8}$$

This separate, multi-zone pin model accounting of the temperature distribution from the fuel centerline to the coolant bulk disregards axial thermal diffusion. Moreover, the resulting nominal average temperatures are employed to calculate physical properties and thermal resistances, which are then assumed constant with temperature and time.

Natural circulation of the coolant is treated by applying the integral momentum balance over the core as follows:

$$\frac{L_{core}}{A_{core}}\frac{d\Gamma_{\text{core}}\,(t)}{dt} + P_{out\ core} - P_{in\ core} + \overline{d_{core}}\,g L_{core} + \Delta P_{loss\ core} + \Delta P_{acc\ core} = 0 \tag{9}$$

Accelerative pressure losses ($\Delta P_{acc\ core}$) have been decided to be disregarded, assuming coolant inlet and outlet velocities constant since lead is single phase. Friction and form losses are expressed by the following relationship:

$$\Delta P_{loss\ core} = \frac{\Gamma_{core}\,(t)|\Gamma_{core}\,(t)|}{2\overline{d_{core}}\,A_{core}{}^{2}} K_{core}\,(t) \tag{10}$$

in which the total pressure loss coefficient (K_{core}) is calculated by combining Rehme's model for the friction factor in wire-wrapped fuel bundles and two correlations for the friction coefficients of the inlet and outlet regions [5].
In order to consider the variation of K_{core} during transients, a correlation has been employed to express the coefficient as a function of mass flow rate:

$$K_{core} = a \cdot \Gamma_{core}^{b} \tag{11}$$

(with a and b being two suitable constants) so as to exploit the steady-state condition:

$$K_{core\,0}\Gamma_{core\,0}^{-b} = K_{core}\,\Gamma_{core}^{-b} \tag{12}$$

and to rewrite Eq. (9) as follows:

$$\frac{d\Gamma_{core}\,(t)}{dt} = -\frac{A_{core}}{L_{core}}\left\{P_{out\ core} - P_{in\ core} + \overline{d_{core}}\,g L_{core} + \frac{\Gamma_{core}\,(t)|\Gamma_{core}\,(t)|^{1+b}\,|\Gamma_{core\,0}|^{-b} K_{core\,0}}{2A_{core}^{2}\,\overline{d_{core}}}\right\} \tag{13}$$

where core inlet and outlet pressures are expressed by using Bernoulli's equation, in which the levels of the hot (Z_{hot}) and cold (Z_{cold}) pools vary as a funciton of time, as well as the average coolant density.

3.2. Bypass

The bypass, defined as the flow region between the core wrapper and the internal vessel, is modelled as an equivalent channel where the coolant rises while being uniformly heated by the fraction f of the reactor total power assumed to be produced within the control drums.
Since the bypass was shown to to play a key role concerning the system thermal-hydraulic stability [1], both an energy balance and a momentum balance have been taken so as to enable to follow the time evolution of coolant temperatures and mass flow rate:

$$M_{l_{BP}} C_l \frac{dT_{l_{BP}}\,(t)}{dt} = q(t)\frac{f}{1-f} - \Gamma_{BP}(t) C_l \left(T_{l_{BP}}^{out}\,(t) - T_{l_{BP}}^{in}\,(t)\right) \tag{14}$$

$$\frac{d\Gamma_{BP}\,(t)}{dt} = -\frac{A_{BP}}{L_{BP}}\left\{P_{out\ BP} - P_{in\ BP} + \overline{d_{BP}}\,g L_{BP} + \frac{\Gamma_{BP}\,(t)|\Gamma_{BP}\,(t)|^{1+BL}\,|\Gamma_{BP\,0}|^{-BL} K_{BP\,0}}{2A_{BP}^{2}\,\overline{d_{BP}}}\right\} \tag{15}$$

Equation (15) is derived under the same hypotheses as Equation (13), but the Blasius relation is here employed for calculating the total pressure loss coefficient (K_{BP}):

$$K_{BP} = c \cdot \Gamma_{BP}^{BL} \quad BL = -0.25 \tag{16}$$

3.3. Hot and cold legs

Modelling the hot and cold leg dynamics is essential not only to properly consider the time delays due to both thermal inertia and transport phenomena, which determine the characteristic time constants of the system free dynamics, but also to enable to reproduce the lead free surfaces oscillations, which directly affect the pressure balances in the reactor and, consequently, the flow regime. Therefore, the hot and cold legs have been described as two free-surface lead tanks on which lumped-parameter mass and energy balances are taken, assuming that no heat transfer occurs except through the inlet and outlet boundaries:

$$M_{l_{HL}} C_l \frac{dT_{l_{HL}}(t)}{dt} = \Gamma_{core}(t) C_l T_{l_{core}}^{out}(t) + \Gamma_{BP}(t) C_l T_{l_{BP}}^{out}(t) - \Gamma_{SG}(t) C_l T_{l_{HL}}(t) \tag{17}$$

$$\frac{dM_{l_{HL}}(t)}{dt} = \Gamma_{core}(t) + \Gamma_{BP}(t) - \Gamma_{SG}(t) \tag{18}$$

$$M_{l_{CL}} C_l \frac{dT_{l_{CL}}(t)}{dt} = \Gamma_{SG}(t) C_l T_{l_{SG}}^{out}(t) - \Gamma_{core}(t) C_l T_{l_{CL}}(t) + \Gamma_{BP}(t) C_l T_{l_{CL}}(t) \tag{19}$$

$$\frac{dM_{l_{CL}}(t)}{dt} = \Gamma_{SG}(t) - \Gamma_{core}(t) - \Gamma_{BP}(t) \tag{20}$$

3.4. Steam generator

Being a detailed design of the SG not available at the current status of development of ELECTRA, a simplified approach has been followed to model this component: a single-node energy balance has been taken by considering the heat transferred to the secondary side ($Q(t)$) as either an input (user-determined) parameter ($\Psi(t)$) or a function of the temperature difference between the primary and the secondary coolant (two-phase water kept at an average constant temperature T_w = 100 °C):

$$M_{l_{SG}} C_l \frac{dT_{l_{SG}}(t)}{dt} = -Q(t) - \Gamma_{SG}(t) C_l \left(T_{l_{SG}}^{out}(t) - T_{l_{SG}}^{in}(t) \right) \tag{21}$$

where:

$$Q(t) = \begin{cases} \Psi(t) \\ K_{SG\ global} \left(T_{l_{SG}}(t) - T_w \right) \end{cases} \tag{22}$$

As far as the coolant mass flow rate dynamics is concerned, the integral momentum balance has been applied coherently with the assumptions made for both core and bypass:

$$\frac{d\Gamma_{SG}(t)}{dt} = -\frac{A_{SG}}{L_{SG}} \left\{ P_{out\ SG} - P_{in\ SG} - \overline{d_{BP}} g L_{SG} + \frac{\Gamma_{SG}(t) |\Gamma_{SG}(t)|^{1+B} |\Gamma_{SG\,0}|^{-B} K_{SG\,0}}{2 A_{SG}^2 \overline{d_{SG}}} \right\} \tag{23}$$

where K_{SG} is calculated by combining the Blasius model for the friction factor and two experimental correlations for the inlet and outlet regions contribution [5], leading to:

$$K_{SG} = A \cdot \Gamma_{SG}^B \tag{23}$$

with A and B being two suitable constants.

3.5. Cold pool

The cold pool model has been developed in order to take into account the additional time delay due to the coolant mixing occurring within the lower plenum, which, depending on the lead mass contained

there (ensuing in turn from the vessel design specifications), might be responsible for a non-negligible thermal inertia with consequent impact on the system dynamic response; such an effect is taken into account by implementing the following energy balance:

$$M_{l_{pool}}\, C_l \frac{dT_{l_{pool}}(t)}{dt} = C_l\left(\Gamma_{core}(t) + \Gamma_{BP}(t)\right)\left(T_{l_{CL}}(t) - T_{l_{pool}}(t)\right) \tag{24}$$

4. TRANSIENT SIMULATIONS

In order to illustrate the potentialities of the model developed and the kind of typical outputs and insights on the system dynamics and stability carachteristics that it allows to draw, some design-basis transient scenarios have been simulated. In particular, perturbations of the nominal state initiated by a control drum partial rotation, by a reduction of the power transferred to the secondary cooling system, and by an accidental increase of core pressure drop are displayed in the following sections.

4.1. Unprotected Transient OverPower (UTOP)

As a first transient, a control drum partial rotation has been reproduced by a positive step-wise[2] 50 pcm reactivity insertion at time t = 1000 s.

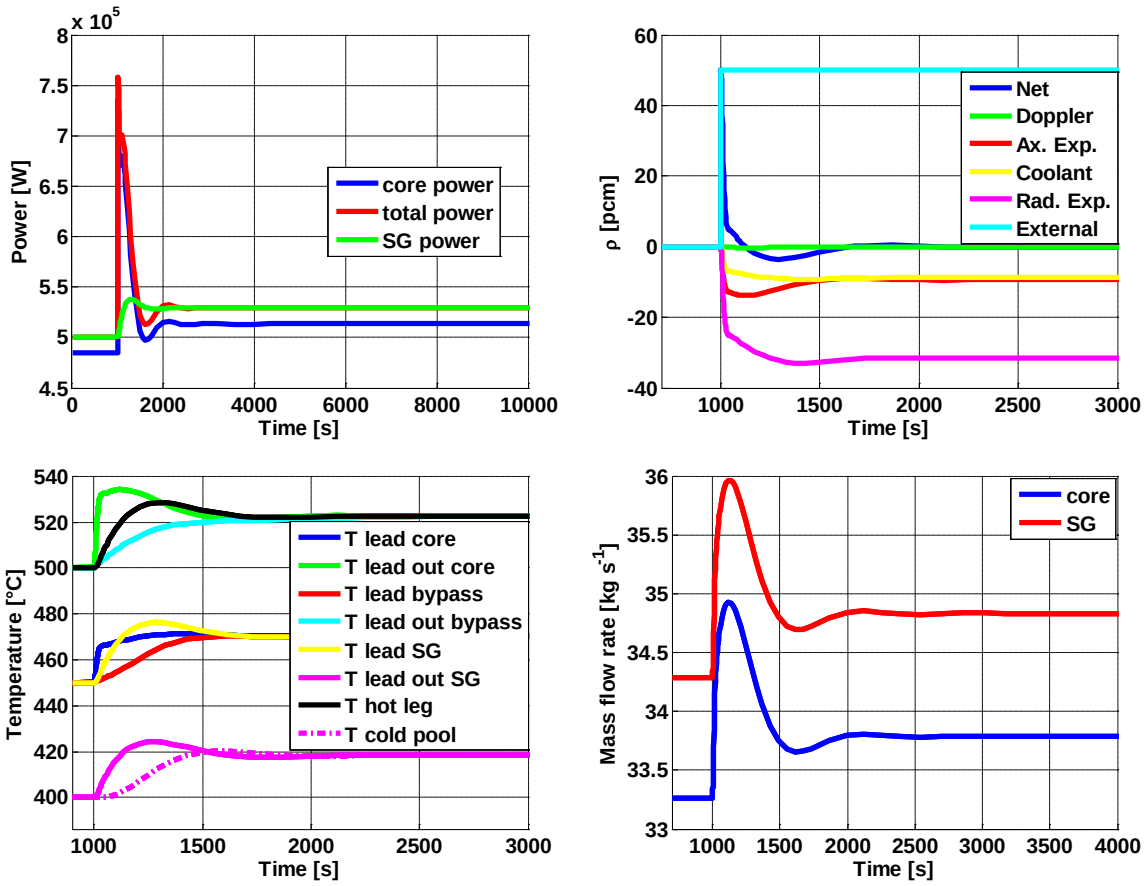

FIG. 2. Transient evolution of power, reactivity, temperatures and mass flow rates following a 50 pcm step-wise reactivity insertion.

[2] Besides step-wise perturbations, several other functions (e.g., ramp, sinusoid, etc.) are available for the user to select, including an option to define customized ones.

In Fig. 2 the time evolution of the main variables of interest, namely power, reactivity, temperatures, and natural circulation[3] mass flow rates, is depicted.

4.2. Unprotected Loss Of Heat Sink (ULOHS)

A change of heat exchange conditions occurring on the SG side and causing a reduction by 50 % of the power transferred to the secondary coolant has been simulated as a second transient scenario. In Fig. 3 the transient behaviour of power, temperatures, and lead free levels is shown.

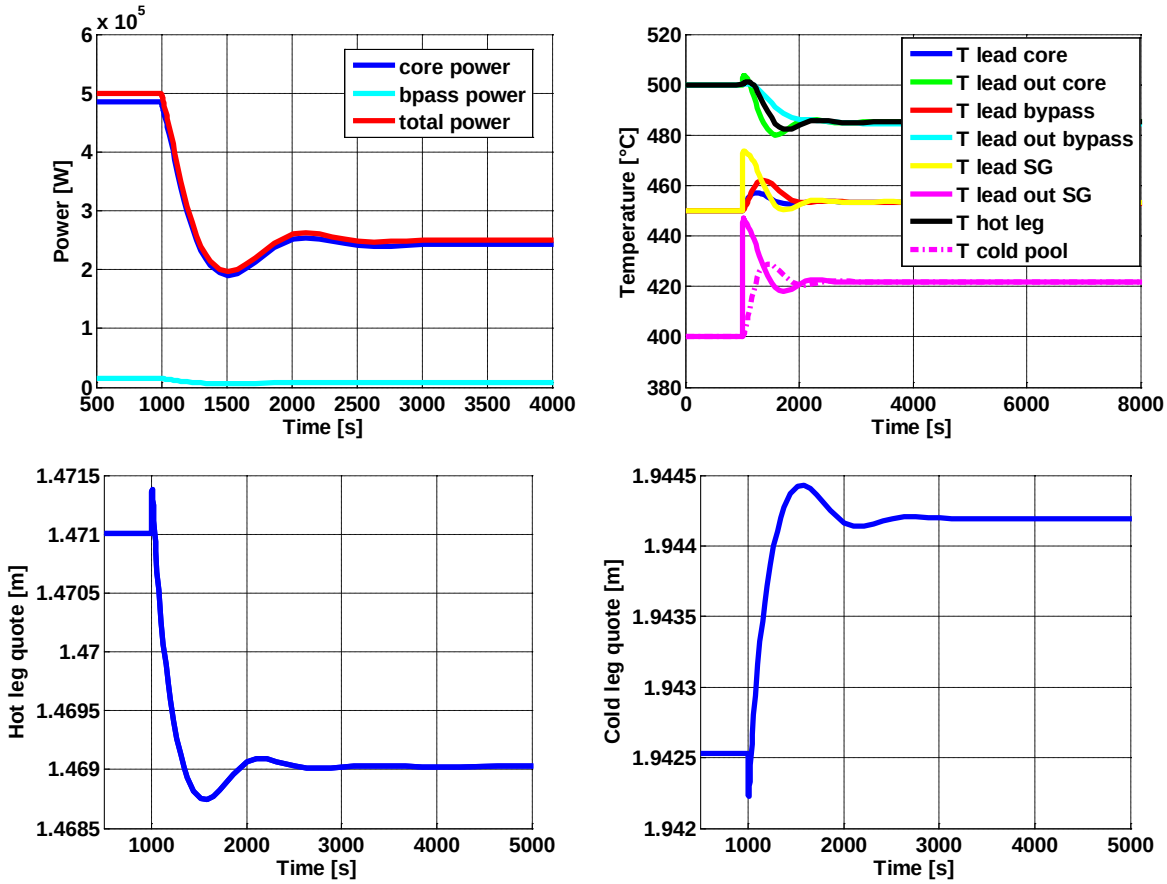

FIG. 3. Transient evolution of power, temperatures, and lead free levels following a 50 % step-wise reduction of the power transferred to the secondary side.

4.3. Unprotected coolant flow Blockage Accident (UBA)

The last transient presented here has been initiated by acting on the core total pressure loss coefficient[4], so as to simulate an accidental enhancement of pressure drop, with consequent undesired variation of lead mass flow rate. K_{core0} has been step-increased by approximately 70 %, leading to a significant reduction of the coolant flow in the core. In Fig. 4 the time evolution of some of the most relevant variables is presented.

[3] A forced convection version of the simuator has been developed in parallel so as to enable the comparative evaluation of the advantages and drawbacks brought by the respective design solutions.
[4] The possibility of performing a UBA simulation is foreseen also for the bypass and the SG channels.

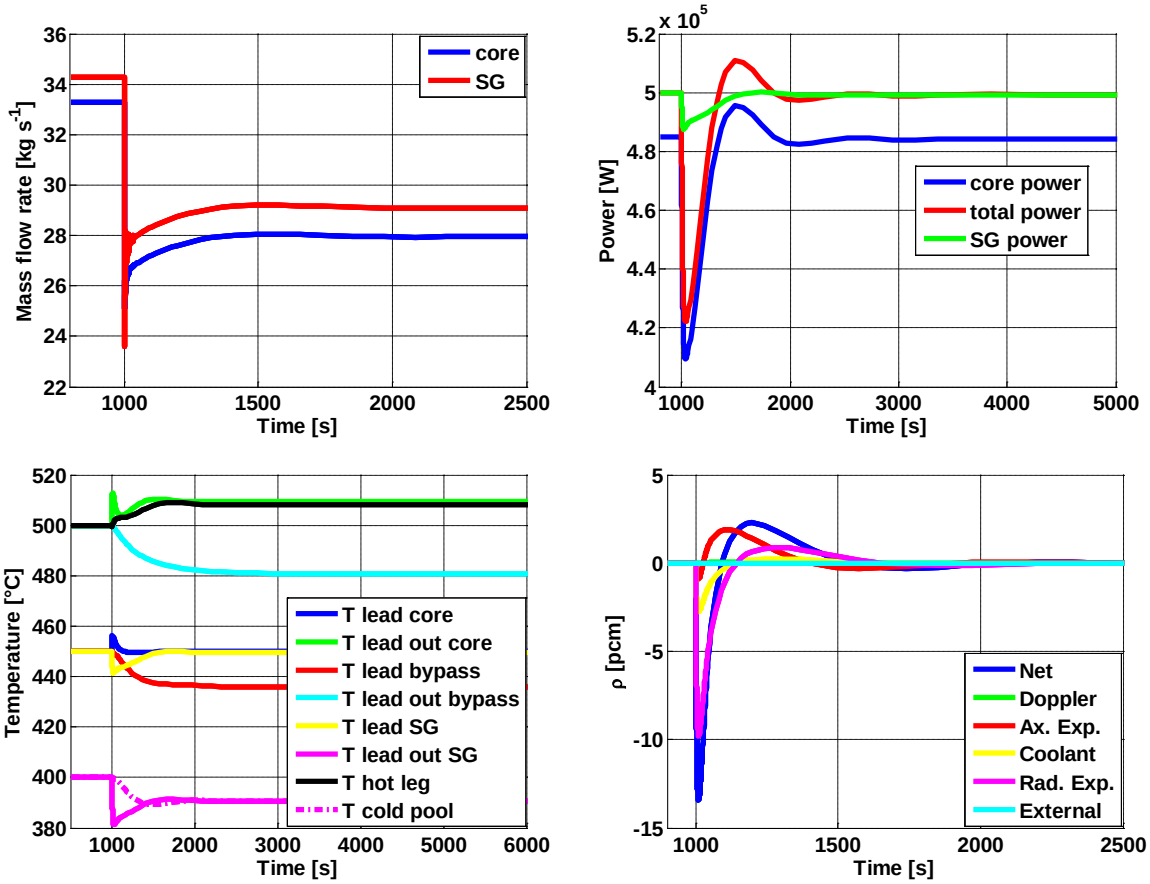

FIG. 4. Transient evolution of mass flow rates, power, temperatures, and reactivity following a 70 % step-wise enhancement of the core total pressure loss coefficient.

5. CONCLUSIONS

In this paper the development of a design-oriented dynamics simulator for ELECTRA has been presented. The system overall model has been conceived to be very flexible, simple and fast running: these features have been required for the main purpose of performing dynamics and stability analyses directed to the finalization of the reactor conceptual design.

The governing equations and modelling assumptions for all the components within the primary system have been discussed, and some typical transient scenarios have been simulated in order to display the capabilities of such a tool.

As a general outcome of the dynamics analyses, the expected strong coupling between different physical subsystems (i.e., neutronics, thermal-hydraulics) and components (i.e., core, SG, etc.) characterizing a natural circulation reactor has been confirmed.

The simulator has shown to suitably catch the dynamics of the main variables of interest (i.e., transient behaviour and new equilibrium values following any perturbation), providing also the characteristic time constants of the various components responses. It allows to track the time evolution of both the power produced within the core, and the heat transferred to the secondary system. Moreover, fuel, cladding and coolant temperatures can be monitored, enabling to verify that the respective technological constraints are not overcome. Finally, the lead free levels oscillations in the hot and the cold leg are clearly reproduced, as well as the resulting effects on the coolant mass flow rates in the core, bypass and SG. In this way it is possible to study the stability characteristics ensuing from

different design solutions concerning for instance both the general reactor layout and components specifications, and the choice of a natural *vs* forced circulation cooling system.
Consequently, it may be concluded that this reliable tool can be employed as a basis for a model-based design optimization (including potential investigation and development of a suitable control system) of ELECTRA and similar innovative small-size LFR systems.

REFERENCES

[1] WALLENIUS, J., et al., ELECTRA-FCC: A Swedish R&D centre for Generation IV systems, Proc. of International Conference on Fast Reactors and Related Fuel Cycles: Safe Technologies and Sustainable Scenarios (FR13), 41987 (T1-CN-199), Paris, France (2013) (CD-ROM).

[2] WALLENIUS, J., et al., ELECTRA: European Lead-Cooled Training Reactor, Nucl. Technol. 177 (2012) 303-313.

[3] SUVDANTSETSEG E., et al., Optimization of the reactivity control drum system of ELECTRA, Nucl. Eng. Des. 252 (2012) 209-214.

[4] The MathWorks, Inc. (2007).

[5] BUBELIS, E., SCHIKORR, M., Review and Proposal for Best-fit of Wire-wrapped Fuel Bundle Friction Factor and Pressure Drop Predictions Using Various Existing Correlations, Technical Report FZKA 7446 (2008).

NOMENCLATURE

A	Coolant area [m^2]
C	Average specific isobaric heat [J kg^{-1} K^{-1}]
c_i	i^{th} precursor density [cm^{-3}]
d	Density [kg m^{-3}]
E	Elevation of the SGs bottom with respect to the core outlet [m]
f	Power fraction produced within the bypass [-]
g	Gravitational acceleration [m s^{-2}]
h_{cl}	Clad-coolant global heat transfer coefficient [W K^{-1}]
k_c	Cladding thermal conductivity [W m^{-1} K^{-1}]
K	Total pressure loss coefficient [-]
K_{total}	Global heat transfer coefficient [W K^{-1}]
k_D	Doppler constant [pcm]
k_f	Fuel thermal conductivity [W m^{-1} K^{-1}]
k_g	Helium gap thermal conductivity [W m^{-1} K^{-1}]
L	Length [m]
M	Mass [kg]
n	Neutron density [cm^{-3}]
P	Pressure [Pa]
q	Core thermal power [MW]
Q	Reactor total power [MW]
t	Time [s]
T	Temperature [°C]
Z	Coolant quote [m]
α_L	Coolant density reactivity coefficient [pcm K^{-1}]
α_R	Radial expansion reactivity coefficient [pcm K^{-1}]
α_Z	Axial expansion reactivity coefficient [pcm K^{-1}]
β	Total delayed neutron fraction [pcm]
β_i	i^{th} precursor group delayed-neutron fraction [pcm]
Γ	Coolant mass flow rate [kg s^{-1}]
δ	Isobaric thermal expansion coefficient [K^{-1}]
Δ	Distance between the lead free level in the cold leg and the SGs top [m]
Λ	Invariant neutron lifetime [s]

λ_i	i^{th} precursor decay constant [s^{-1}]
ρ	Reactivity [pcm]
Ψ	User-defined SG power [MW]

Superscripts and subscripts

0	Steady-state
acc	Accelerative
BP	Bypass
c	Cladding
centr	Centerline
CL	Cold leg
core	Core region
drum	Control drum
eff	Effective
f	Fuel
HL	Hot leg
in	Inlet
int	Internal
l	Lead coolant
loss	Losses
mid	Middle
out	Outlet
pool	Lower plenum
SG	Steam generator
surf	Surface
w	Water

Investigation of fuel elements simulators clads disruption in static sodium at transient heat loads*
Preliminary result

Yu.I. Zagorulko, A.A. Kamaev, Yu.M. Ashurko, M.V. Kascheev, N.S. Ganichev, V.G. Zhmurin

State Scientific Center of the Russian Federation – Institute for Physics and Power Engineering, Obninsk, Russian Federation

Abstract. Adequacy of physical description and modelling of the ULOF-type accidents at sodium cooled fast reactors could be achieved only on the basis of detailed study of such accidents phenomenology including mechanisms of fuel subassembly degradation, materials movement and relocation. Analysis of the ULOF experimental investigation, published in [1] and those discussed in the report (where the pressure effects have been deliberately eliminated) demonstrates, that initial stage of fuel elements degradation and its further development, followed by materials movement and relocation are determined by three dominant processes: 1) thermal attack of fuel melt onto cladding material; 2) development of temperature stresses in the claddings; 3) corium/sodium thermal interaction (TI). Intensity and relative input of the above mentioned processes into resulted post accident subassembly state, on the other hand, are dependent on the thermohydraulic regimes as inside of fuel elements (fuel melt flow regimes), so inside of subassembly hexcan (sodium flow with account for sodium phase transformations at the interfaces with claddings and hexcan surfaces and at the boundary with "cold" sodium. The experiments presented in the report are essentially a part of the ULOF investigation programme, which is carried out at the rig PLUTON and some other installations.

Introduction

Evolution of severe fast reactors accidents of ULOF type is dependent on the behavior of fuel elements claddings (time history and modes of their failure and subsequent materials relocation inside of Fuel Subassembly). It is not quite clear up to date the dominant mechanisms responsible for fuel pins cladings disrupture in the course of ULOF accident to meet its adequate description in the relevant computer physical models/ As well, its is not there is no enough information on the possible input of fuel/sodium thermal interaction (FCI) into the total scenario of the ULOF accident.

The principal objectives of an experimental program, which is carried out at the rig PLUTON on the ULOF investigation, consist in getting on of more detailed information on the modes of fuel elements claddings failure and mechanisms, involved, including here FCI phenomena. Result of the experiments, presented in the report, are reffered to only the first stage of the program. An intension of the authors to make these results to be available to a broad andience was caused by essential difference in FCI energy release, observed in the experiments, performed with fuel pins simulators bundles without hexcan and in the experiment with bundle inside of hexcan, as the energy release was much higher in the last case.

1. Methodology of the experiments

Description of the rig PLUTON experimental part design, its equipment and measurement devices have been reported in details elsewhere [2][3].

The experiments 6-9 have been carried out using 7-rods bundles (grid pitch of 16 and 11.3 mm). Bundle assembly was mounted inside of interaction chamber, containing 3.5-3.6 kg of sodium at temperature 823 K. The energy release was provided due to thermite reaction

* Work partially supported by the State Atomic Energy Corporation ROSATOM

$3Zr+2Fe_2O_3 \rightarrow 3ZrO_2+4Fe$ (temperature of the melt ZrO_2+Fe ~3100 K; thermal effect of the thermite reaction ~ 1.8 MJ/kg) , initiated by a system of electric igniters, assembled inside of the individual fuel element simulators.

Parameters registered in the experiments included: pressure in the gas plenums of the experimental part; geometry and topography of the fuel element simulators claddings defects; residual bend deformations of the claddings, particle size distribution of corium debris, selected in the filter (metal ceramic, porosity of 20 μm). Characteristics of the fuel pins simulators are listed in the table 1.

Table 1. Fuel elements characteristics in the experiments with 7–rods bundles (without hexcan)

№№ of the experiment	Material and geometry of the simulators claddings	Mass of the thermite charge, kg	Thermal energy of the thermite charge, kJ
6	Steel 12H18N10T 14×0.45 mm	0.165	297
7	Steel 12H18N10T 14×0.45 mm	0.488	878
8	Steel 12H12M1BFR 9.3×0.6 mm	0.276	497
9	Steel 12H12M1BFR 9.3×0.6 mm	0.278	500

The experiment 10 has been performed using mock-up rods assembly (MRA) made in geometry of 7-rods bundle (grid pitch of 11.3 mm), mounted inside of a hexcan and fixed by means of bottom and upper spacers. Design of the MRA made it possible to perform its filling-up by sodium as well as sodium dreinage through the orifices in MRA's upper position (overal area 125.6 mm) and lower one (overal area 706.5 mm^2). The assembly hexcan and fuel element simulators could be dismounted for their inspection after experiment. General view of MRA is given in figure 1.

Fuel element simulators were manyfactured from the tubes (9.3×0.6 mm st.12H18N10T) with the height of 475 mm. Thermite charge was fixed inside the tubes by means of end plugs. Energy release was provided due thermite reaction $Al+Fe_2O_3 \rightarrow Al_2O_3$ (T≈2900 K, ΔH=1.4 MJ/kg). Reaction front propagation speed, as it has been estimated in preliminary experiments, equals 0.2 m/s. Fuel element simulators had different density of the thermite charge along their height. The length of the upper part made ~145mm, as for the lower one ~290mm. Principal characteristics of the MRA are listed in the table 2.

Table 2 Characteristics of the MRA's fuel element simulators

№ of the simulator	1	2	3	4	5	6	7
Thermite charge density in the upper part, g/cm^3	0.93	1.09	0.93	0.78	0.93	0.78	0.93
Thermite charge density in the lower part, g/cm^3	1.54	1.60	1.47	1.67	1.74	1.60	1.54
Thermite charge mass, g	29	31	28	30	32	29	29
Thermal energy of the thermite charge, kJ	40.6	43.4	39.2	42.0	44.8	40.6	40.6

On the exterior side of the MRA's hexcan in its upper and lower points were fitted thermocouples. Above sodium mirror (~65mm) in the reaction chamber the assembly of calibrated plate elements was arranged to measure their residual bend deformations due to axial movement of sodium column outside of the MRA volume. Methods for estimation of the sodium column kinematic and induced dynamic loads have been published in [2].

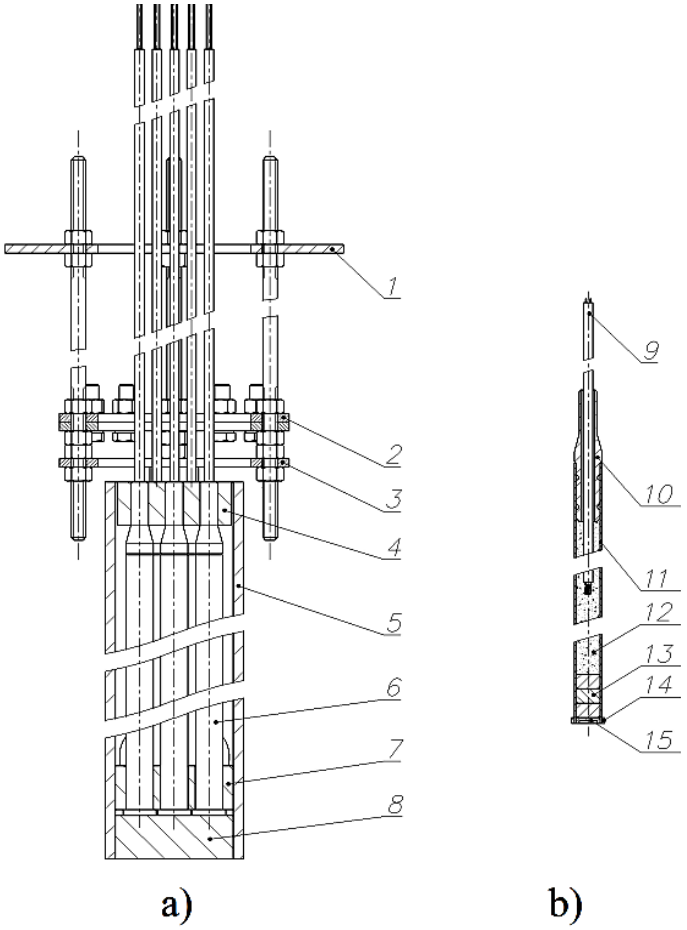

FIG. 1. Mocking-up rods assembly (a) and fuel element simulator (b)

1-supporting plate; 2-assembly of calibrated plate elements; 3-spacer plate; 4-upper spacer; 5-hexcan; 6-fuel pin simulator; 7-lower spacer; 8-plug; 9-electric igniter; 10-end cap; 11-cladding; 12-thermite charge; 13-plug; 14, 15-end plug

2. Experimental results and their discussion

2.1.Experiments №6-№9

General feature observed in topography of claddings damage in the experiments №6-№9 consists in preferable destruction of the rods assembly central simulators as well as claddings defects concentration in the middle area of the bundle (see figures 2-3). In the experiment №6 (not illustrated here) specific area of the damaged peripheral simulators varies from 1 to 18%. The central simulator damaged area was about 61%. One of the defect (cladding local melting) of the simulator №11 was located ~80mm higher of the thermite charge initial boundary, that indicates on the melt axial movement inside of the fuel pin simulator. The most damaged area was observed for №15, №10 and №13 simulators at the distance of 250-350mm below sodium mirror. In the experiment №7 (with the biggest mass of the thermite charge) the total damaged area of the simulators was estimated to be of ~160cm^2. The central simulator cladding was dissected totally in the regions of 60-180 mm and 230-

340mm in reference to sodium mirror. The peripheral elements were also severely damaged. Thermite charges in the simulators №6 and №12 in the experiment №7 were extended on purpose to study the effect of such displacement on the neighbour simulators claddings in the region of their bottom caps. No claddings damage was observed.

In the experiments №6-№7 averaged damage area is approximately proportional to thermite charge mass. In the experiments №8 and №9 carried out with practically equal thermite charge masses the cladding damage total area made 4.53 and 3.98% with central simulator being most severely damaged.

The most pronounced claddings bend deformations were registered in the experiment №7 and much lower ones in the experiments №8 and №9. Claddings deflections were directed outwards from the central simulator to the peripheral ones, having reached the values of 4-8mm. This observation, supposing corium/sodium TI to be responsible for claddings deformations, suggests its occurrence in central region of the bundle.

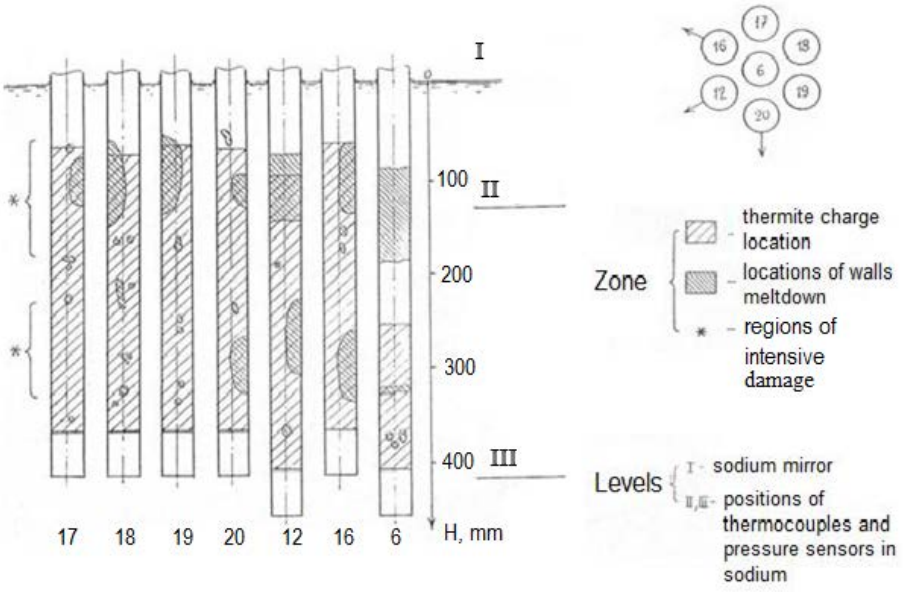

FIG. 2. Positions of the thermite charges in the fuel elements simulators and character of theirs walls disruption in the experiment №7

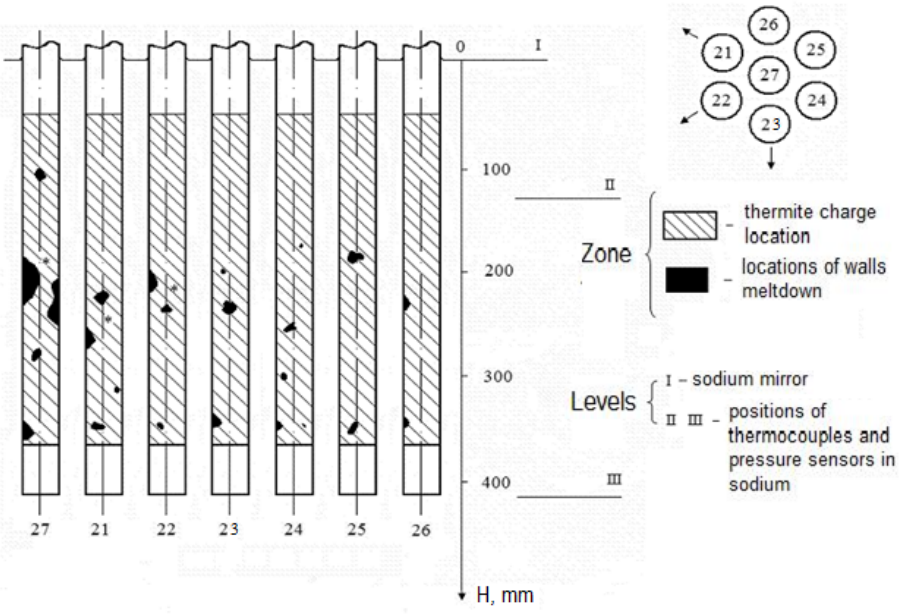

FIG. 3. Positions of the thermite charges in the fuel elements simulators and character of theirs walls disruption in the experiment №8

Considerable distinction in the extent of simulators claddings degradation in the experiments №6-№7 and №8-№9 are most likely explained due to difference in cladding materials composition and rods assembly geometry. Conversion ratio values were estimated by pressure increase in the reaction chamber gas plenum (Ar), assuming adiabatic approximation (see table 3)

Table 1. Corium/sodium TI energetic effects and simulators claddings damage in the experiments №6-№9

№№ of the experiments	Maximum increase of gas pressure in gas plenum, Pa	Conversion ratio η_t, %	Total area of simulators cladding damage, cm^2
6	3.30×10^{3}	2.8×10^{-2}	44.7
7	3.08×10^{4}	8.8×10^{-2}	158.9
8	2.26×10^{4}	7.6×10^{-2}	24.2
9	2.64×10^{4}	7.9×10^{-2}	21.3

In all experiments gas plenum volume equals ~$1.5\times10^{-3}m^3$ and argon initial pressure ~2×10^{4}Pa. Kinetic energy of sodium column was neglected and argon assumed to be perfect gas. With these assumptions

$$\eta_t,\% = \frac{V\cdot\Delta P\cdot 100}{(\gamma-1)Q_m}, \qquad (1)$$

where Q_m – initial thermal energy of corium.

Sieve fractional analysis of the corium debris particles (Fe and ZrO_2), selected in the filter unit, has shown that their mass distribution median size was of 0.234-0.243-mm in the experiment №6 and 0.239mm in the experiment №7 with standard deviations 0.344-0.354 and 0.348mm, correspondingly.

Close to above mentioned particles median size values (0.22 and 0.25mm with standard deviation of 4.6 and 4.3) were estimated for the experiments №8 and №9. Average size of debris particles was approximately one order of magnitude smaller as compared to particles of thermite powder.

2.2.The experiment with MRA

Temperature signals registered by thermocouples fitted on the hexcan exterior surface and argon pressure history in the reaction chamber gas plenum are presented in figures 4, 5.

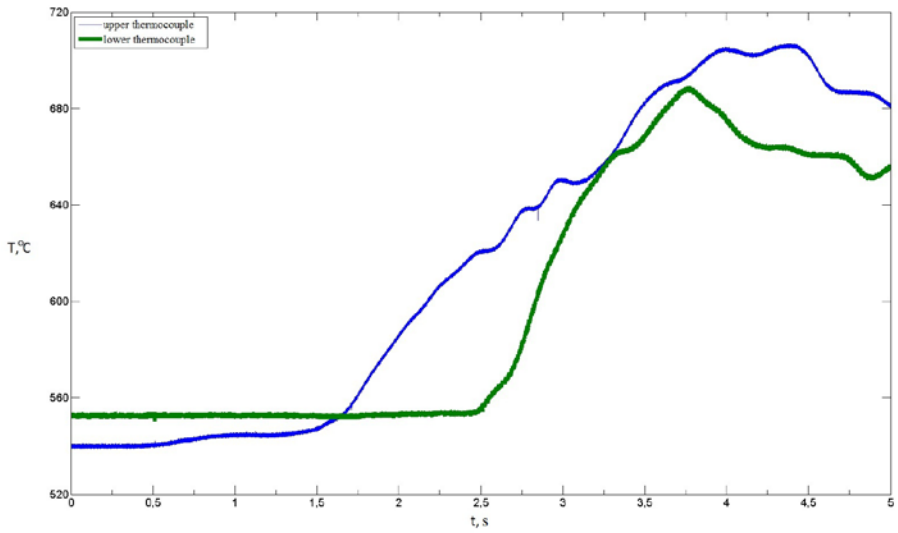

FIG. 4. Temperature measurements at MRA's hexcan wall external side

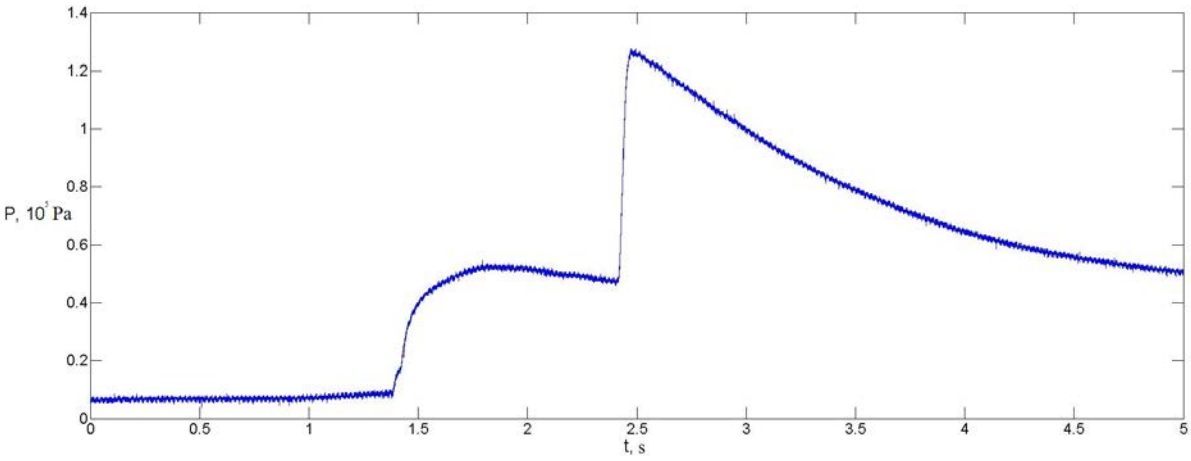

FIG. 5. Argon pressure history in the gas plenum of the interaction chamber

An analysis of these measurements together with experimental data and observations, made after MRA post-experimental preparation, allows assuming a qualitative scenario of physical phenomena taken place in the course of the experiment. Starting point of the events time history can be conditionally referred to the moment of thermite reaction ignition (τ=0.45s). In the time interval 0.43-1.38s reaction front practically had passed the upper part of the thermite charge and a half of the lower part. Sodium boiling and partial drying-up of MRA's region, embraced by thermite reaction, have been developing during this time interval. Pins simulators claddings degradation, corium/sodium TI and continuous flowing-out of sodium through the MRA's orifices took place in the time interval 1.38-1.82s. First TI event, having pressure peak value ~5.36×10^4Pa is characterized during its initial stage by pressure rise rate of 8×10^5Pa·s^{-1}. The second TI event with a pressure peak of 1.3×10^5Pa had the pressure rise rate of ~1.6×10^6Pa·s^{-1}, characteristic for high-energy thermal interactions. The total conversion ratio value, estimated according to relation (1), made ~1%.

A view of partially dismantled MRA after its remove out of reaction chamber and washing in water-ethanol solution is shown in figure 6.

FIG. 6. MRA's view after experiment (partially dismantled and washed-out)

Inlet and outlet MRA's orifices were completely blocked-up by solidified material. At that, blockages were notably denser as compared with material located in the middle region of the MRA. Estimations of materials alkalinity inside of MRA, made after its dismantling suggested that sodium was practically completely expelled out of hexcan during second TI. Relative fractions of damaged claddings area for individual simulators covered the range of ~48-73%. One of the peripheral pin simulators due to its large bending deformation contacted the hexcan interior surface. Relative area fraction of its cladding damage is estimated of ~24%. There were not detected any signs of cladding frontal melting. Only small local defects having a melting-through character have been discovered. Analysis of the damaged claddings parts indicates on their wastage, due to their material contact with melt, similar to ablation process. The principal part of claddings debris retained their initial thickness for exception of thin surface layer (predominantly composed of iron) having a porous structure, easily removed mechanically. The latter observation suggests that embrittlement mechanism of claddings destruction due to temperature stresses development could be involved.

There were not detected any signs of material melting on the interior surface of the hexcan. Among material remnants selected inside of the MRA were detected concretions, having morphology of partially destructed hollow ellipsoids. Their chemical composition is mostly iron.

Sieve fractional analysis of the corium debris was carried out separately for the materials selected in filter unit, within the upper and lower blockages. Averaged sizes of the particles equal 0.257; 0.218 and 0.318mm, relatively. Averaged dynamic loads, caused by sodium column movement in the reaction chamber and calculated by their residual bend deformations of the plate elements, made $\sim 7\times10^4$Pa.

3. Calculation estimations of fuel pins simulators claddings degradation due to different mechanisms

From the experimental observations it follows that material melting and temperature stresses, developing in the claddings, could be considered as contributors to their failure. Comparison of some parameters, critical for the above mentioned mechanisms, was made in the following calculation, assuming idealized (axisymmetry, absence of melt slag lining formation, etc.) development of the relevant processes.

Schematic presentation of materials phases' distribution over fuel pin cross-section is given in figure 7.

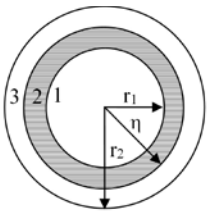

FIG. 7. Materials distribution at fuel element simulator cladding melting: 1-thermite melt-corium simulator; 2-liquid steel; 3-solid steel

Temperature in the region 1

$$T_1 = f(r, z, \tau), \quad 0 < r < r_1, \quad \tau > 0 \ .$$

Thermal conductivity equations

$$\frac{\partial T_2}{\partial \tau} = a_2 \left(\frac{\partial^2 T_2}{\partial r^2} + \frac{1}{r} \frac{\partial T_2}{\partial r} \right), \qquad r_1 < r < \eta, \qquad \tau > 0,$$

$$\frac{\partial T_3}{\partial \tau} = a_3 \left(\frac{\partial^2 T_3}{\partial r^2} + \frac{1}{r} \frac{\partial T_3}{\partial r} \right), \qquad \eta < r < r_2, \qquad \tau > 0.$$

Initial conditions

$$T_1(r,0) = f_1(r), \qquad 0 < r < r_1 ,$$

$$T_{2,3}(r,0) = f_2(r), \qquad r_1 < r < r_2 .$$

Boundary conditions

$$T_1(r_1, \tau) = T_2(r_1, \tau), \quad \tau > 0,$$

$$T_2(\eta, \tau) = T_3(\eta, \tau) = T_{pl} = \text{const},$$

$$-\lambda_2 \frac{\partial T_2(\eta, \tau)}{\partial r} + \lambda_3 \frac{\partial T_3(\eta, \tau)}{\partial r} = \rho_3 L \frac{\partial \eta}{\partial \tau},$$

$$\lambda_3 \frac{\partial T_3(r_2, \tau)}{\partial r} + \alpha \left(T_3(r_2, \tau) - T_C \right) = 0.$$

In the solution of the problem Lebenson's method [4] has been applied, thereby the following solution was obtained:

$$\vartheta_1(Z, \theta) = \overline{F}(Z, \theta), \qquad 0 < R < 1, \tag{2}$$

$$\vartheta_2(R, Z, \theta) = 1 + \frac{T_{pl} - F(Z, \theta)}{(T_{pl} - T_c) \ln H} \ln \frac{R}{H}, \qquad 1 < R < H, \tag{3}$$

$$\vartheta_3(R,\theta) = 1 + \frac{Bi}{\frac{1}{R_2} + Bi \ln\frac{R_2}{H}} \ln\frac{H}{R}, \qquad H < R < R_2. \tag{4}$$

Expression for dimensionless time of clad melting is obtained as follows

$$\theta_{pl} = -Ko \int_1^{R_2} \frac{HdH}{\frac{1-\vartheta_1}{\ln H} + \frac{K_\lambda Bi}{\frac{1}{R_2} + Bi \ln\frac{R_2}{H}}}, \tag{5}$$

In the formulas (2)-(5) $\vartheta = \frac{T - T_c}{T_{pl} - T_c}$ -dimensionless temperature, $R = \frac{r}{r_1}$ -dimensionless radial coordinate, $Z = \frac{z}{r_1}$ -dimensionless longitudinal coordinate, $\theta = \frac{a_2 \tau}{r_1^2}$ -dimensionless time, $a_2 = \frac{\lambda_2}{c_2 \rho_2}$ -thermal diffusivity of liquid steel, $Ko = \frac{\rho_3 L}{C_2 \rho_2 (T_{pl} - T_c)}$ -Kossovitch number, $R_2 = \frac{r_2}{r_1}$ -dimensionless radius (see figure 7), $\vartheta_1 = \frac{F - T_c}{T_{pl} - T_c}$ -dimensionless temperature of the melt, F-melt temperature, T_{pl}-melt point of the steel, T_c-environmental temperature, η - coordinate of melt front, $H = \frac{\eta}{r_1}$ -dimensionless coordinate of melt front, $K_\lambda = \frac{\lambda_3}{\lambda_2}$ -relative thermal conductivity, $Bi = \frac{\alpha r_1}{\lambda_3}$ -Bio number, α-heat-transfer coefficient.

Numerical results, obtained for geometry of fuel elements simulators, used in the experiment give the time of cladding local melting of about 20ms.

Calculations of thermal stress, developed in the cladding, have been carried out according to [5]. The relative thermal stresses can be expressed, as follows

Error! Objects cannot be created from editing field codes.,

$$\frac{\sigma_\theta}{E} = \frac{\beta T_M}{4(1-\nu)R^2}\left(\frac{R^2+H^2}{R_2^2-H^2}\left(\left(R_2^2-H^2\right)(2+C)+2CR_2^2\ln\frac{H}{R_2}\right)+(R^2-H^2)(2+C)+2CR^2\ln\frac{H}{R}-4\left(1+C\ln\frac{H}{R}\right)R^2\right)$$

$$\frac{\sigma_z}{E} = \frac{\beta T_M}{4(1-\nu)R^2}\left(\frac{2R^2}{R_2^2-H^2}\left(\left(R_2^2-H^2\right)(2+C)+2CR_2^2\ln\frac{H}{R_2}\right)-4\left(1+C\ln\frac{H}{R}\right)R^2\right)$$

where $C = \frac{Bi}{\frac{1}{R_2} + Bi \ln\frac{R_2}{H}}$, β-linear elongation coefficient, E-elasticity modulus, ν-Poisson's coefficient, $T_M = T_{pl} - T_c$.

To obtain equivalent stresses the energetic strength theory was applied. The solution obtained is given in figure 8.

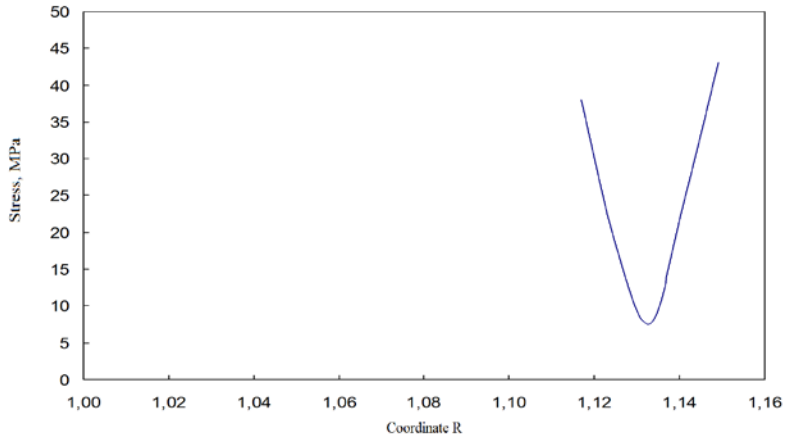

FIG. 8. The equivalent stress dependence on the coordinate R at time of 9,5ms

In the calculation the fourth energetic strength theory was used, where strength criteria is determined by relation $\sigma_{eq} \leq [\sigma]$, with $\sigma_{eq}=[(\sigma_1-\sigma_2)^2+(\sigma_2-\sigma_3)^2+(\sigma_3-\sigma_1)^2]^{0.5}$ and $[\sigma]$ – allowed strength. The strength limit for austenitic steel was selected as $[\sigma]$.

4. Conclusion

Comparison of the extent of fuel elements simulators claddings degradation in static sodium, observed experimentally for 7-rods bundles in free channels and assembled inside of hexcan, demonstrated more severe claddings damage in the case of the bundle in the hexcan. .

The character of fuel elements claddings destruction, observed experimentally, suggests that temperature stresses inside of claddings could play a significant part. It was demonstrated experimentally a possibility of high-energy corium/sodium thermal interaction inside of subassembly mock up. The phenomenon could be explained by encapsulation of some mass of sodium during its dynamic contact with the melt pool.

REFERENCES

[1] Kaiser, A., Peppler, W., Will, H. SIMBATH 1976-1992, Seventeen years of experimental investigation of key issues concerned with severe reactor accidents. In: IAEA Technical Committee meeting on “Evaluation of Material Coolant Interaction and Material Movement and Relocation in Liquid Metal Fast Reactors” O-arai Engineering Center, Iboraki, Japan, 6-9 June 1994. IWGFR 189, p. 167.

[2] Zagorulko, Yu.I., Zhmurin, V.G., Volov, A.N. et al. Energy transformations in the processes of reactor core materials melt/sodium thermal interaction. Atomnaya energiya. Vol. 96. (2004) 367-373 (in Russian).

[3] Zagorulko, Yu.I., Kozlov, F.A., Masagutov, R.F. Experimental Investigations of MFCI in Russia. In: IAEA Technical Committee meeting on “Evaluation of Material Coolant Interaction and Material Movement and Relocation in Liquid Metal Fast Reactors” O-arai Engineering Center, Iboraki, Japan, 6-9 June 1994. IWGFR 189, p. 199/

[4] Lebenson, L.S., Petrolium industry mechanics guidlines. M.-L. ONTI. NKTG SSSZ. 1934 (in Russian).

[5] Timoshenko, S.P., Gulier, J. The theory of elasticity.Principal publishing office on phisical and mathematical literature. Ed. Science. Moscow. 2nd edition. (1979) 600 (in Russian).

STAR-CD / CATHARE coupling methodology for thermal-hydraulic calculations on primary loop and heat exchangers in sodium-cooled fast reactor

B. Farges, T. Sageaux, N. Goreaud

AREVA NP,
Lyon, France

Abstract. The purpose of this paper is to describe a coupling methodology between two codes in order to describe primary thermal-hydraulics inside a sodium-cooled fast reactor (ASTRID prototype). A CFD code (STAR-CD) is used for the modelling of hot and cold plena, while a system code (CATHARE) is used for the modeling of pipes and pumps. Both codes interact through their common boundary conditions at interfaces. The coupling methodology is also used for the simulation of thermal transfer between primary and secondary fluids inside sodium-sodium heat exchanger and sodium-water steam generator. The simulation uses a detailed mesh of the tube bundle: the primary side is modelled by STAR-CD, while the secondary side is modelled by CATHARE. Both codes interact through common wall boundaries placed on the secondary side of the tubes. The main advantage of this method is the computation of the whole primary loop while representing accurately complex 3D phenomena.

1. Introduction

In the context of Generation IV reactors deployment, a 600MWe sodium-cooled fast reactor prototype called ASTRID (Advanced Sodium Technological Reactor for Industrial Demonstration) is currently under preliminary development. This prototype is envisaged as a pool-type sodium reactor, and will be designed to reduce the probability and consequences of severe accidents.

Like other constructed sodium fast reactors (Phenix, SuperPhenix), passive behaviour of the reactor in case of long-term loss of power situation is an important safety feature. The thermal properties of sodium make generalised natural convection possible, provided the reactor design encourages it. Completely passive decay heat removal by natural convection would allow the reactor to overcome severe accident initiators.

The modelling of such transients is a challenge, since it requires consequent calculation domains over important time scales. Indeed, discretisation by CFD at whole-plant scale is still beyond current computing capabilities for industrial purposes. On the other hand, system codes can give fast and useful results but lack the necessary precision for describing local thermal hydraulic behaviour inside large pools, especially for decay heat removal situations where buoyancy forces and recirculation effects make the prediction of the flow paths complicated.

The solution described in this paper consists in a coupling methodology between a system code and a CFD code in order to perform reactor scale loss of power transient calculations. The CFD (STAR-CD) code is used for the modelling of hot and cold plena, while the system code (CATHARE) is used for the modelling of the core, pipes and pumps.

Two situations are investigated as illustrations of the coupling methodology features:

- a detailed study of sodium reactor steam generator thermal hydraulic behaviour. The CFD (STAR-CD) code is used for the modelling the secondary sodium side, while the system code (CATHARE) is used for the modelling of the tertiary (water/steam) side,
- a loss of power transient in the context of ASTRID geometry, the whole reactor is modelled, including inter-wrapper space. The CFD (STAR-CD) code is used for the modelling of hot and cold plena, while the system code (CATHARE) is used for the modelling of the core, pipes and pumps.

First results are encouraging and coherent with former calculations. Nevertheless, the need for validation using experimental data is underlined.

2. First implementation of coupling methodology: steam-generator thermal hydraulic modelling

Computing the detailed velocity fields inside heat exchangers through CFD can provide significant insight. Indeed, such detailed computations enable access to :

- the flow repartition inside the exchanger,
- the pressure drop,
- the possible velocity and temperature heterogeneities.

Hence, CFD computation of the flow inside a heat exchanger provides numerical prediction of its performances and can be used as an optimization tool. Nevertheless, in the case of steam generator, the CFD computation is numerically expensive, due to the phase change of the tertiary side of the exchanger (in the case of fast reactors). On the other hand, system codes as CATHARE have been designed to handle this kind of flows, encountered in the primary sides of PWRs in accidental situations. One option for the energy conversion system of the ASTRID reactor being a water/steam Hirn cycle, the determination and optimization of the steam generators is a top priority. For this reason, a coupling of CFD code and system code through the walls of the tubes has been developed.

2.1. Modelling features

In the approach chosen, STAR-CD is used to compute the secondary side of the steam generator. The modelling domain is shown on figure below.

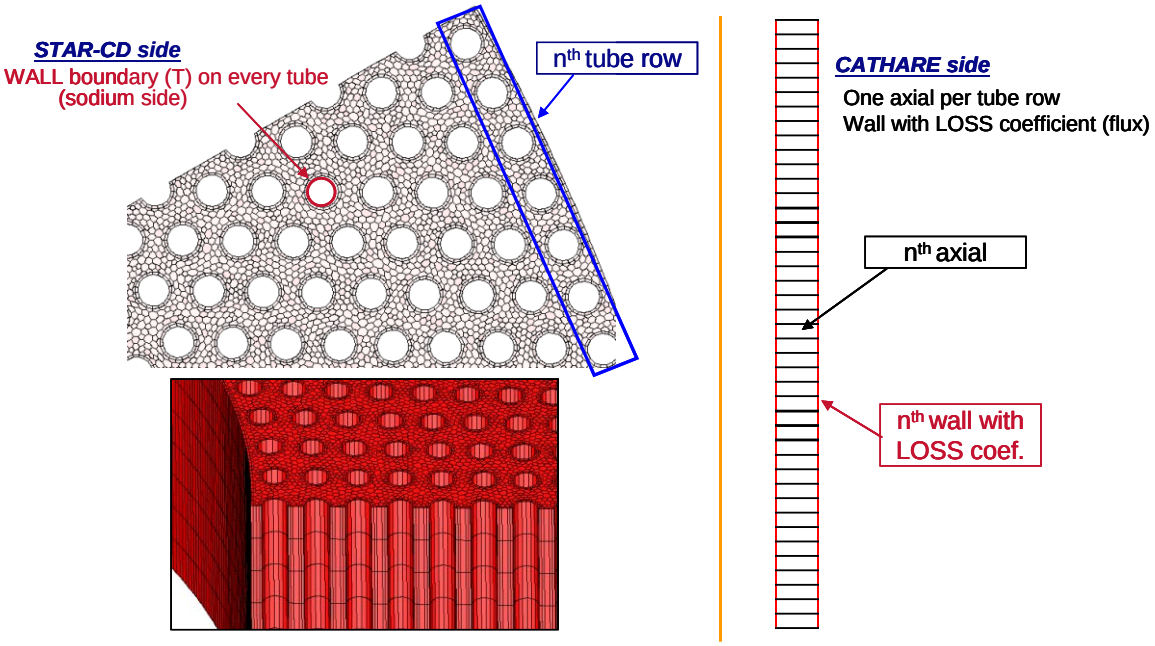

FIG. 1. : Star-CD and CATHARE calculation domain for steam generator modelling.

This modelling domain is made of an inlet and an outlet volume. These volumes can account for any flow heterogeneity induced by local conditions surrounding the component. The model also provides a detailed representation tube bundle. The key features of this part are :

- an explicit representation of each tube. Thus, any radial or azimuthal heterogeneity induced by the design can be taken into account,
- the various grids maintaining the bundle of tubes are taken into account through the pressure drops they induced. A 2D modelling approach through “baffle cells” has been chosen. Though this simplification does not allow for very local effects near the grids, their effect in the global flow is correctly accounted for.

The global CFD model is made of approximately 4 million cells for a 60° sector. Thus, transient computation can be achieved within a reasonable time frame with limited resources. The method being general, the model can be easily extended to 360° if needed.

It is important to notice at this stage that the CFD model does not include any solid cell representing the thickness of the tubes. The choice has been made to include the tube thickness representation in the system code for numerical stability reasons.

The CATHARE modelling is made of 1D elements called “AXIAL”. In this example the choice has been made to model only one tube per row, as CATHARE can affect a “weight” to each 1D element corresponding to the number of tubes of the row. This choice simplifies and accelerates the computation. Should the flow be not symmetrical enough for this simplification, the modelling procedure can be refined so as to model one CATHARE element per tube. In addition, the CATHARE model includes boundary conditions of flow in and out on each row. This flow can be known precisely as the pressure drop on the tertiary side is high enough to guaranty a flat flow distribution inside the tubes. Finally, the CATHARE model includes cells modelling the thickness of the tubes. The exchange boundary condition with STAR-CD is applied on the external face of this wall.

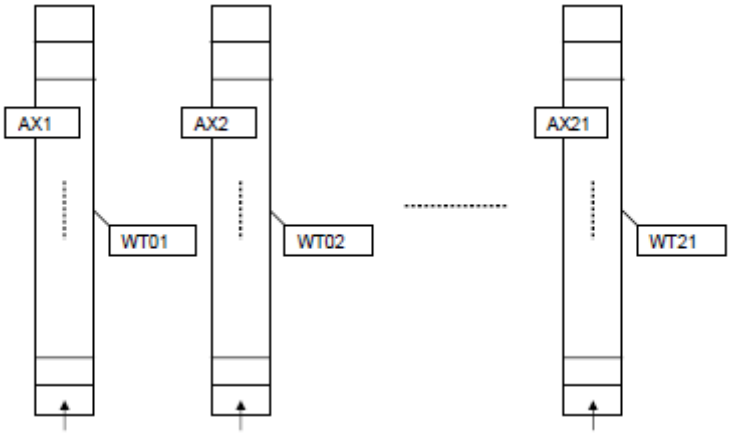

FIG. 2. : CATHARE modelling of the steam generator tube rows.

2.2. Coupling procedure

Consistency between the altitudes of the STAR-CD and CATHARE meshes has been ensured cell by cell. Thus, a correspondence can be made between the boundary conditions of the codes based on their altitude (although this precaution is not compulsory). This consistency between the meshes spares the coding of an interpolating procedure, with the associated risk of error and approximation. At each time step the following operations are performed :

- CATHARE prescribes at the external side of its walls the thermal flux computed by STAR-CD,
- STAR-CD prescribes a temperature computed by CATHARE inside the wall and a thermal resistance corresponding to the thickness of wall at the CATHARE post processing location.

This exchange is achieved through the reading and writing of ASCII files by each code.

The results obtained with this method have been compared former 2D code calculation results used in the frame of the EFR project on an experimental configuration. Results are very similar both for integral data (performance of the steam generator) and for detailed data (temperature profile at the outlet of the tubes), validating this first approach. Some results are shown on the following figures. Integral results corresponding to two-phase flows (altitude of DNB for each row, temperature profile inside the tubes…) and very detailed temperature profiles at the secondary side can be obtained at low cost thanks to this coupling methodology.

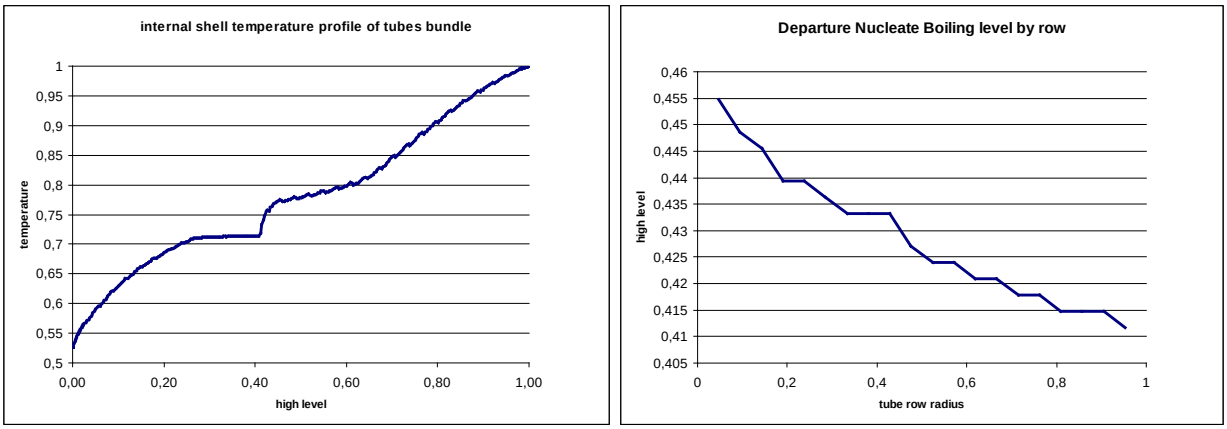

FIG. 3. : Non-dimensional results for steam generator coupled calculations: temperature (left) and location of DNB by row (right).

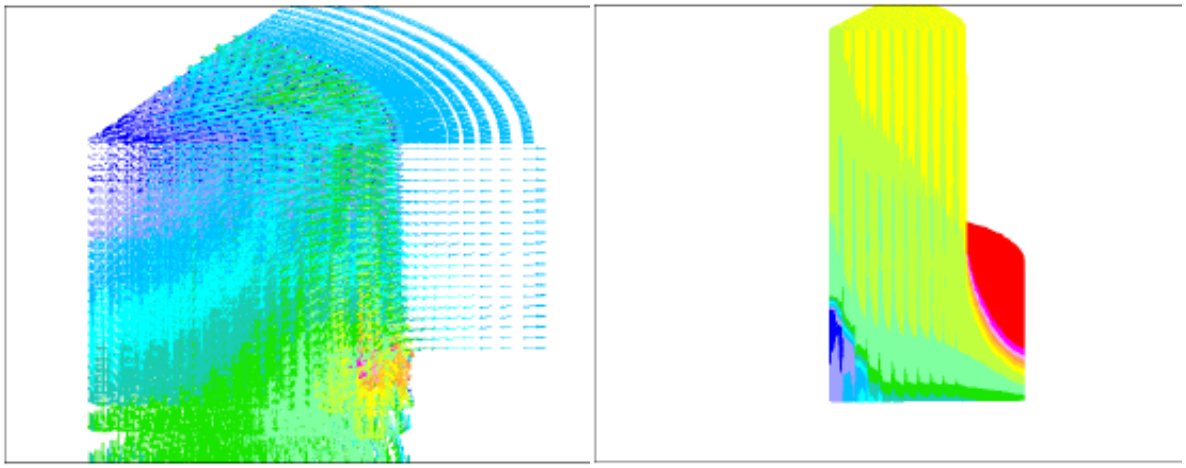

FIG. 4. : Results for steam generator coupled calculations : inlet velocity field (left) and outlet temperature field (right).

3. Implementation of the coupling methodology at whole-reactor level

Thermal hydraulic analysis of hot and cold plena during natural convection cases is a key item to assess the capacity of the reactor to overcome severe transients, such as loss of power. The goal is here to use both a system code and a CFD code to model the whole reactor. In this case, STAR-CD only models cold (lower) and hot (upper) plena (including inter-wrapper flow), while CATHARE models the rest of the reactor. Both codes exchange information at common boundary conditions and calculation domains do not overlap.

3.1. Main ASTRID features and repartition of the calculation domains

Many features of the ASTRID prototype presented in this paper are still being discussed and improved. The geometry of the primary circuit described in this paper consists in a main primary reactor vessel, four sodium secondary circuits exchanging heat with a water-steam energy conversion system. The nature of the tertiary coolant is still an open question; a water-steam circuit is used in the present calculations because of its consequent feedback as regards former conceptions. Decay Heat Removal (DHR) is carried out by sodium-sodium heat exchangers. The decay heat removal systems

modelling consists in a secondary sodium loop linked with a air heat sink. The calculation does not include any kind of specific DHR system through the primary vessel wall. The repartition of calculation domains between the two codes is as follows :

— STAR-CD modelled items :
- the hot (upper) plenum including :
  - the core outlet region,
  - the upper core structure,
  - the inter-wrapper space,
  - the sodium volume enclosed between the following surfaces : the sodium surface, the "redan" (separation between the pools), the core wrapper tubes, the heat exchanger admission,
- the cold (lower) plenum, from the heat exchanger exit to the pump admission.

— CATHARE modelled items :
- the heat exchanger primary side,
- the whole sodium secondary loop,
- the steam generator water-steam tertiary side; boundary conditions represent the rest of the energy conversion system,
- primary pumps, modelled by 1D pipe and pump characteristics,
- the pipe between the pump exit and the diagrid,
- the diagrid (represented by a 0D volume),
- the core, modelled with seven parallel 1D pipes, with accurate representation of the friction processes in the fuel pin zones,
- The whole secondary loop regarding the decay heat removal systems immerged in the sodium hot plenum. Tertiary loop is limited to a 1D pipe representing the air side of the sodium-air heat exchanger,
- The reactor vessel cooling system (modelled by an assembly of 1D pipes and 0D volumes).

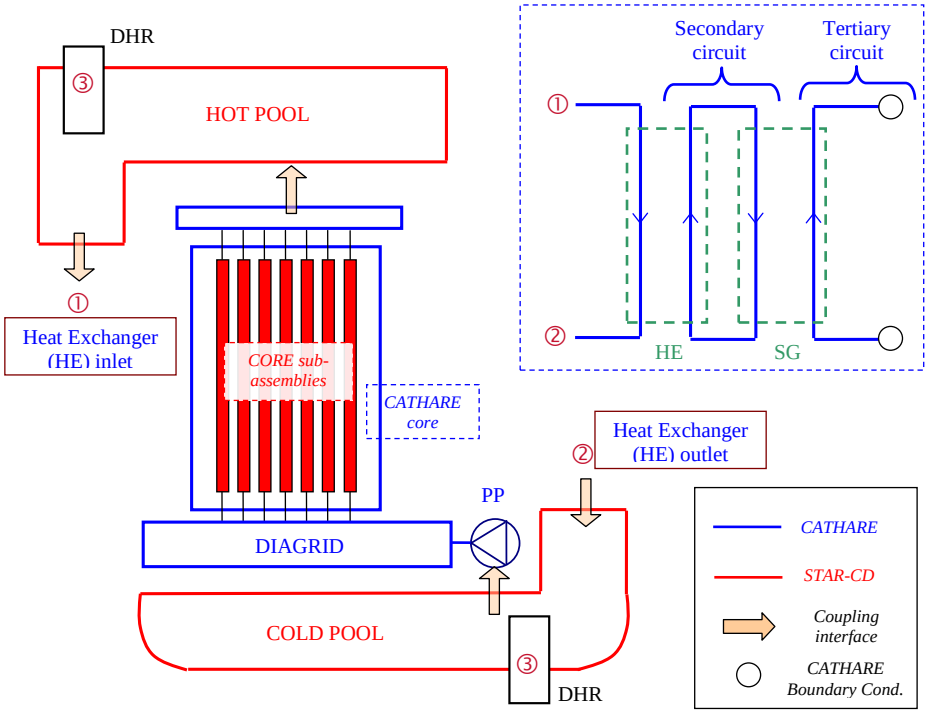

FIG. 5. : Distribution of calculation domains between the two codes.

3.2. CATHARE modelling

The CATHARE system code has been developed in collaboration between CEA, EDF, IRSN and AREVA-NP. CATHARE is the reference code in France for the Pressurized Water Reactor (PWR) safety analysis. It has also been used for others light water reactor concepts (BWR, VVER) and for experimental reactors. In the frame of Generation IV deployment, many developments regarding sodium thermodynamics, heat transfer correlations, transport properties of sodium phases, pressure drop correlations for fuel pin regions and updates of the neutronics point kinetic model were added. In the present case the methodology starts from a complete CATHARE data deck, from which the hot and cold pools have been removed.

3.3. STAR-CD modelling

The modelling of the primary plena consists in a single calculation domain: the steel separation between the plena (the redan) is modelled so as to take into account the thermal communication between the pools. The mesh of the core exit zone, as well as the surroundings of the core itself (modelled in CATHARE), has been refined so as to take into account probable recirculation effects in and around the core.

The inter-wrapper space is directly connected to the rest of the STAR-CD hot plenum domain on its upper side, and to CATHARE diagrid on its lower side. As it consists in a very narrow sodium space between hexagonal wrapper tubes, mesh size is significantly smaller than in the rest of the CFD domain. Hexahedral cells have been used for the meshing of this specific zone, whereas polyhedral cells have been used for the rest of the mesh.

The present study uses a standard high-Reynolds k-epsilon model. The value of non-dimensional parameter y^+ has been checked, especially in the inter-wrapper space zone. For standard non-equilibrium wall functions, the centre of the cell adjacent to the wall should be within the log-law layer which means $30<y^+<300$. The rest of the walls of the STAR-CD domain have been considered adiabatic (which means no radiative transfer outside the vessel is considered).

The mesh consists in over 2 million polyhedral and hexahedral cells (including 800 000 cells for the modelling of interwrapper space).

3.4. Information exchanged through boundary conditions

As seen previously, the two codes calculation domains do not overlap. The only common surfaces they share are their boundary condition at interfaces. The status of these boundaries is symmetrical as regards the code they refer to: an inlet boundary in STAR-CD will correspond to an outlet boundary in CATHARE and vice-versa. The interfacing boundary conditions between the two codes are the following :

- CATHARE inlet / STAR-CD outlet :
  - heat exchanger admission,
  - pump admission,
  - reactor vessel cooling system admission,
- CATHARE outlet / STAR-CD inlet :
  - core exit,
  - heat exchanger exit,
  - reactor vessel cooling system exit (at the top of the cold pool),
- Thermal-only boundary interface :
  - wrapper tube walls (exchange with the inter-wrapper flow).

During the coupled calculation, both codes exchange thermal hydraulic information at each time step. For each code, this information exchange consists in reading data from the other code, using this information during its calculation iteration, and writing data towards the other code at the end of its iteration. For convenience purposes all inlet boundaries are velocity inlets. Outlet boundaries are pressure outlet, since the conservation of the pressure values all around the primary loop is crucial in order for the coupled calculation to model buoyancy-driven flows.

The nature of the information exchanged between the two codes at a given interface depends on the nature of the boundary condition itself. For example, at an interface STAR-CD inlet / CATHARE outlet :

— CATHARE gives to STAR-CD :
- the boundary temperature,
- the boundary mass flow rate which will be later converted into a velocity,

— STAR-CD gives to CATHARE :
- the boundary-averaged temperature value,
- the boundary-averaged piezometric pressure.

One point to keep in mind is that there is an inevitable loss of information while transferring 3D information to a 1D system code. On a CFD boundary condition, the thermal hydraulic values can vary along the surface, while only one single value is necessary for a system code boundary. That is why boundary averaging is performed when transferring data from STAR-CD to CATHARE. This operation does not affect numerical convergence. Concerning exchange through thermal wall boundaries (wrapper tubes), the process is similar as the one described previously in the case of steam generator modelling.

3.5. Transient calculation and results

Based on this methodology, a loss of power transient is simulated. The initial state is the nominal steady state. The transient begins with a reactor trip, a global coast down of all pumps, and a loss of feed water supply at steam generators inlet. The decay heat removal systems are immediately started and function entirely passively. On STAR-CD side, the transient is calculated with the SIMPLE algorithm, both codes alternate computation with a time step ratio, as a CATHARE iteration is significantly faster than a STAR-CD one.

Simulation of loss of power transients can provide a significant insight as regards the natural convection simulation capacity of a given code (as underlined in ref. [2] and [3]). Indeed, natural convection inside a sodium-cooled fast reactor is a key feature as regards the passive behaviour of the reactor. In case of a loss of flow (with reactor scram), residual heat can be conveyed out of the reactor core thanks to natural circulation of the sodium between hot and cold pools. This phenomenon has been observed in reactor Phenix end-of-life tests (ref. [4]).

ASTRID results show the decrease of the primary mass flow rate, along with the pump coast down. Primary mass flow even reaches a negative value, which implies a reverse circulation, for a few minutes before oscillating towards an equilibrium positive value around 1% of the nominal mass flow.

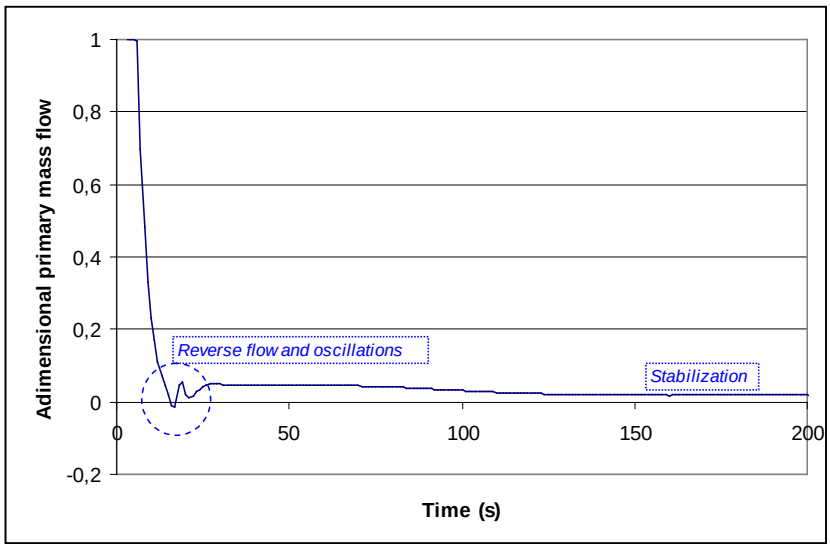

FIG. 6. : Transient calculation : evolution of ASTRID primary mass flow.

The mean core exit temperature predictably falls as a reaction to the reactor trip, the rises as a reaction to the loss of flow. A first peak is reached with a reasonable value (below clad failure criteria). Oscillations then occur, most of them due to the competition between core residual power, evacuation performed by the decay heat removal system and the secondary system. The latter quickly decreases in performance due to the loss of secondary flow. Mean core inlet temperature finally also rises, due to the global increase of sodium temperature, but a strong temperature difference between core inlet and exit subsists, due to thermal stratification.

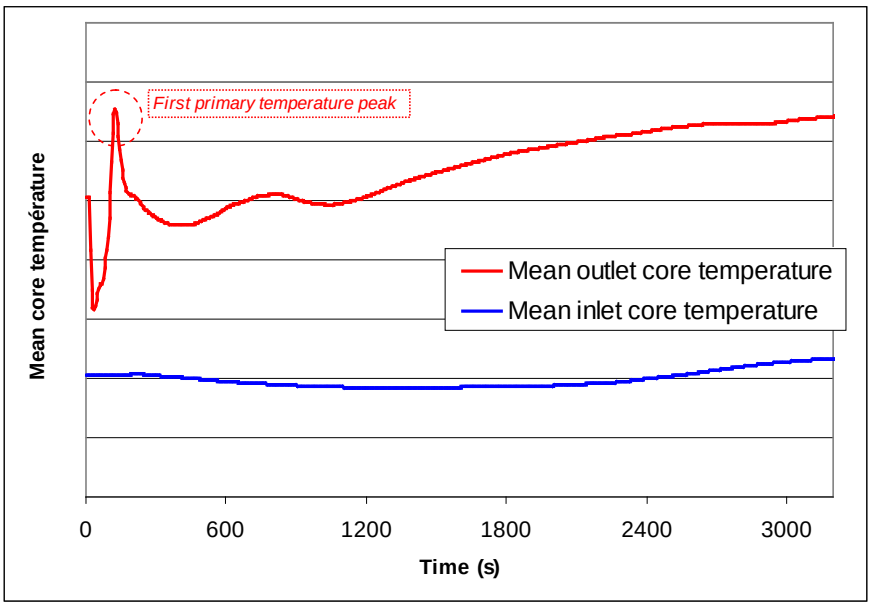

FIG. 7. : Transient calculation: evolution of mean inlet and outlet core temperature.

An interesting interaction mechanism occurs between the interwrapper space and the decay heat exchanger located in the hot pool. Indeed, hot sodium is being cooled by the exchanger and therefore falls at the bottom of the hot pool. It then flows inside the interwrapper space where it receives core

decay heat and conveys it upwards, initiating a local natural convection loop. This interaction can be seen with the post-processing of streamlines, and can provide a significant, fully-passive contribution to the decay heat removal process.

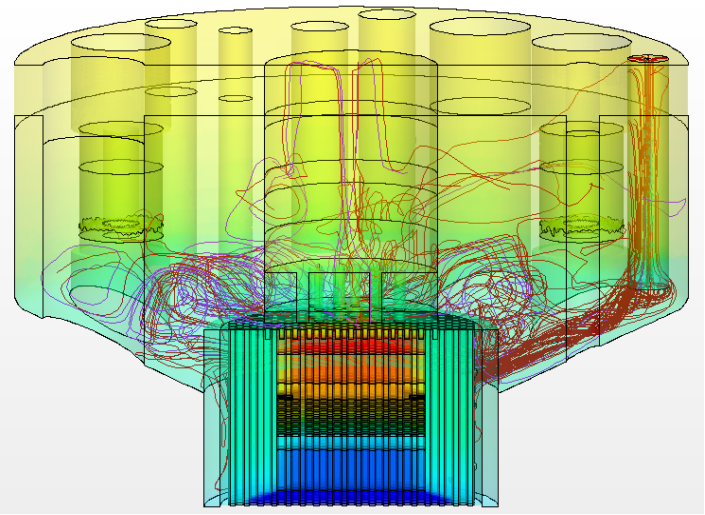

FIG. 8. : Transient calculation : streamlines in the hot pool between the Decay Heat Removal exchanger and the interwrapper space.

4. Conclusion

Two types of coupling methodologies have been developed between a CFD code (STAR-CD) and a system code (CATHARE) :

- thermal coupling through wall boundary conditions,
- thermal-hydraulic coupling through inlet / pressure boundary conditions.

Both have been implemented for calculations in the frame of ASTRID prototype development.

The methodology is functional, and provides consistent results compared with former calculations on previous sodium fast reactor designs. As regards the modelling of a loss of station power transient, natural convection at reactor scale is observed, as well as the favourable effect of interwrapper flow as regards the extraction of residual power out of the reactor core. The coupling methodology can help perform calculations with significant space and time scales within an acceptable range of CPU time, for industrial purposes.

Further validation is required and will be performed in the frame of ASTRID development. More complete developments have to be achieved, such as the optimization of the calculation speed and the interfacing of the codes, allowing the methodology to be more efficient and fully adapted to fast and precise industrial calculations.

REFERENCES

[1] TENCHINE, D., et al., “Status of TRIO-U code for sodium cooled fast reactors”, Nuclear Engineering and Design 242 (2012) 307-315

[2] FANNING, T.H., et al., “Modelling of Thermal Stratification in Sodium Fast Reactor Outlet Plenums During Loss of Flow Transients”, International Conference on Fast Reactors and Related Fuel Cycles (FR09), Kyoto, Japan, December 6 – 11, 2009

[3] HUNG, T.C., et al., “CFD modelling and thermal-hydraulic analysis for the passive decay heat removal of a sodium-cooled fast reactor”, Nuclear Engineering and Design 241 (2011) 421-432

[4] PIALLA, D., et al., “Natural convection test in Phenix reactor and associated CATHARE calculation”, 14th International Topical Meeting on Nuclear Reactor Thermal-hydraulics, NURETH-14, Toronto, Ontario, Canada, September 25-30, 2011

Development and validation of CONV-3D code for calculation of thermal and hydrodynamics of Fast Reactor at the Supercomputer

V.V. Chudanov[1]

[1]*Nuclear Safety Institute, RAS, Moscow 115191, 52 B.Tulskaya, Russia*

Abstract

In IBRAE 3D CFD modules (CONV code) for safety analysis of the operated Nuclear Power Plants (NPPs) are developed. These modules are based on the developed algorithms with small scheme diffusion, for which the discrete approximations are constructed with use of finite-volume methods and fully staggered grids. For solving of convection problem the regularized nonlinear monotonic operator-splitting scheme is developed. The Richardson iterative method with iterative Fast Fourier Transformation (FFT) solver for Laplace's operator as preconditioner is applied for solving pressure equation. Such approach for solving of the elliptical equations with variable coefficients gives multiple acceleration in a comparison with a usual method of conjugate gradients. For modeling of 3D turbulent single-phase flows Quasi DNS approach is used. The CONV code is fully parallelized and highly effective at the high performance computers such as "Chebyshev", "Lomonosov" (Moscow State University).

The developed modules were validated on a series of the well known tests in a wide range of Rayleigh numbers from a range 10^6-10^{16} and Reynolds numbers from a range 10^3-10^5. The software has been applied to the analysis results of test LIVE-L1 (L1 is aimed at investigating the melt pool and crust behaviour during the stages of air circulation at the outer RPV surface with subsequent flooding of the lower head) and joint analyses on transient molten pool thermal hydraulics in the LIVE facility in the framework of ISTC project. Moreover CONV was validated successfully on a series of the experimental tests as: the blind test on simulation of flows in T-junction (OECD/NEA), ERCOFTAC experiment (world database on turbulent flows) natural convection in the closures under extremely high Rayleigh numbers. In all cases the good coincidence of numerical predictions with experimental data was reached, that specifies a possibility of application of the developed approach for a prediction of CFD flows for designing and operating NPPs.

In this paper the examples of use of the developed software for modeling of a fuel assembly, namely, for the analysis of turbulent intermixing in horizontal subchannels of the fuel assembly at normal pressure and temperature are demonstrated (benchmark test Matis-H (OECD/NEA)).

1. INTRODUCTION

During some years in IBRAE, a 3D unified numerical thermalhydraulic technique for safety analysis of the operating NPPs is developing, which includes: 1) methods, algorithms and software for automatic generation of computing grids with local refinement near body borders, 2) methods and algorithms for solving the heat and mass transfer in compressible/incompressible problems for research of 3D thermalhydraulic phenomena, 3) approaches for modeling of turbulence. Briefly we shall stop on details of the developed approach.

For the grid construction in IBRAE, an automatic technology using CAD systems for designing of calculated domain is developed. A generation of structured orthogonal/cartesian grids with a local refinement near boundaries is incorporated into a specially developed program, which is supplied by a friendly interface and can be utilized on parallel computers (Chudanov, 1999).

A computing technique is based on developed algorithms with small scheme diffusion, for which the discrete approximations are constructed with the use of finite-volume methods and fully staggered grids.

For the modeling of 3D turbulent single-phase flows, an LES approach (commutative filters) and also a quasi direct numerical simulation (QDNS) approach are used. For the simulation of 3D turbulent two-phase flows by means of DNS, detailed enough grids and effective numerical methods developed in IBRAE for solving CFD problems are applied. For observation of an interface of two-phase flow, the modified level set (LS) methods and multidimensional advection/convection schemas

of total variation diminishing (TVD) type with small scheme diffusion with use of sub-grid simulation (with local resolution) are used.

A developed numerical technique was used for the construction of the 3D CFD CONV code (set of numerical modules) for safety analysis of the operated Nuclear Power Plants (NPPs). Therefore further, without loss of generality, we shall speak about singularities validation and verification of a numerical technique, i.e. developed modules. The developed modules were validated on a series of well known tests (Chudanov, 1998) in a wide range of Rayleigh numbers (10^6-10^{16}) and Reynolds numbers (10^3-10^5). There are numerical predictions of the blind test on simulation of flows in T-junction (OECD/NEA), ERCOFTAC experiment (world database on turbulent flows) natural convection in the closures under extremely high Rayleigh numbers.

In this paper the examples of use of the developed software for modeling of a fuel assembly, namely, for the analysis of turbulent intermixing in horizontal subchannels of the fuel assembly at normal pressure and temperature are demonstrated (benchmark test Matis-H (OECD/NEA)).

2. CFD NUMERICAL TECHNIQUES

This section deals with the new methods and algorithms for describing of 3D thermalhydraulic processes at NPPs. Among them we consider numerical algorithms for solving of incompressible fluid dynamics, the monotone multi-dimensional schemes of TVD-type for solving of advection equation and the effective algorithm for solving of the elliptical equation for pressure correction.

To simulate thermalhydraulic in incompressible media, the time-dependent incompressible Navier-Stokes equations in the primitive variables [3] coupled with the energy equation are used:

$$\begin{cases} \dfrac{d\rho\vec{\mathrm{v}}}{dt} = -\mathrm{grad}\,P + \mathrm{div}\,\nu\,\mathrm{grad}\,\vec{\mathrm{v}} + \rho g + \mathrm{CSF}, \\ \mathrm{div}\,\vec{\mathrm{v}} = 0 \end{cases} \tag{1}$$

$$\frac{\partial(\rho h)}{\partial t} + \mathrm{div}(\rho\vec{v}h) = \mathrm{div}(k\,\mathrm{grad}\,T); \quad h = \int_0^T c(\xi)d\xi\,. \tag{2}$$

Here the following notifications are used: ρ is the density, $\vec{\mathrm{v}}$ is the velocity vector, P is the pressure, ν is the kinematic viscosity, g - is the gravity acceleration, CSF - source, h is the enthalpy, k is the thermal conductivity, T is the temperature.

Basic features of developed numerical algorithm (Chudanov, 2003, 2008) incorporated in the present approach are the following:

Numerical implementation of operator-splitting scheme for the Navier-Stokes equations is performed as the predictor-corrector procedure with correction for the pressure:

$$\rho\frac{\mathrm{v}^{n+1.2} - \mathrm{v}^n}{\tau} + (C(\nu) - \mathrm{div}\,\nu\,\mathrm{grad})\mathrm{v}^{n+1/2} + \mathrm{grad}\,p^n - \mathrm{CSF}^n = 0,$$

$$\mathrm{div}_h\left(\frac{1}{\rho}\mathrm{grad}_h\,\delta p\right) = \frac{1}{\tau}\mathrm{div}_h\,\mathrm{v}^{n+1/2}, \qquad \mathrm{v}^{n+1} = \mathrm{v}^{n+1/2} - \frac{\tau}{\rho}\mathrm{grad}_h\,\delta p\,. \tag{3}$$

To construct time-integration scheme for the energy equation, its operators are decomposed into two parts associated with the enthalpy and temperature respectively, that results in the following two-step procedure:

$$\frac{h^{n+1/2} - h^n}{\tau} + \tilde{C}\left(\mathrm{u}^n\right)h^{n+1/2} = 0, \quad \frac{h^{n+1} - h^{n+1/2}}{\tau} - \tilde{N}\,T^{n+1} = 0. \tag{4}$$

In the momentum equation, operators are also splitted into two parts. The first part is associated with the velocity transport by convection/diffusion written in the linearized form as $A_1 = C\left(\mathrm{u}^n\right) + N$, where $N = \mathrm{div}\left(\dfrac{\mu}{\rho}\mathrm{grad}\,\mathrm{v}\right)$. The second part deals with pressure gradient $A_2 = \mathrm{grad}$. It should be noted that the gradient and divergence operators are adjoint of each other, i.e. $A_2^* = -\mathrm{div}$.

The analyzed additive scheme of splitting looks like:

$$\frac{\mathrm{v}^{n+1/2}-\mathrm{v}^{n}}{\tau}+A_1\mathrm{v}^{n+1/2}+A_2 p^{n}=f^{n},\ \frac{\mathrm{v}^{n+1}-\mathrm{v}^{n}}{\tau}+A_1\mathrm{v}^{n+1/2}+A_2 p^{n+1}=f^{n},\ A_2^{*}\mathrm{v}^{n+1}=0. \qquad (5)$$

Numerical implementation of this scheme is performed as the predictor-corrector procedure, i.e. introducing the pressure correction $\delta p = p^{n+1} - p^{n}$ in two last equations (5) allows receiving the well-known Poisson equation and equation for velocity correction in form:

$$\mathrm{div}_h \mathrm{grad}_h \delta p = \frac{1}{\tau}\mathrm{div}_h \mathrm{v}^{n+1/2},\quad \mathrm{v}^{n+1} = \mathrm{v}^{n+1/2} - \tau \mathrm{grad}_h \delta p\ .$$

The Fast Fourier Transformation is applied for solving of the selfadjoint and self-consistent grid elliptic problem for pressure that allows achieving high speed of computing algorithm in comparison with the standard approaches.

In computational mathematics there are recognized two variants of fictitious domain methods with continuation of coefficients at lower-order derivatives and with continuation of coefficients at the highest-order derivatives. Both approaches are in common use for prediction of fluid dynamics with phase change processes.

Here the first variant is employed which in physical sense can be considered as inclusion into the momentum equations of model of a porous medium:

$$\frac{\partial \mathrm{v}_\varepsilon}{\partial \tau} + C(\mathrm{v}_\varepsilon)\mathrm{v}_\varepsilon - \mathrm{div}\left(\frac{\mu}{\rho}\,\mathrm{grad}\,\mathrm{v}_\varepsilon\right) + \mathrm{grad}\ p + c_\varepsilon \mathrm{v}_\varepsilon = \mathrm{f}_\varepsilon,$$

$$\mathrm{div}\ \mathrm{v}_\varepsilon = 0 \qquad (6)$$

where p - pressure, normalized on the density. Various formulae of c_ε can be employed for the flow resistance term in the above equations. For equation (6) the modified predictor-corrector procedure with taking into account of fictitious domain method looks like this:

$$\frac{\mathrm{v}_\varepsilon^{n+1/2}-\mathrm{v}_\varepsilon^{n}}{\tau} + A_1\mathrm{v}_\varepsilon^{n+1/2} + A_2 p_\varepsilon^{n} + c_\varepsilon \mathrm{v}_\varepsilon^{n+1/2} = \mathrm{f}^{n},$$

$$\mathrm{divgrad}\ \delta \mathrm{p}^{s+1} = \mathrm{div}_h\left(\frac{\tau c_\varepsilon}{1+\tau c_\varepsilon}\mathrm{grad}_h\ \delta p^{s}\right) + \frac{1}{\tau}\mathrm{div}_h\ \mathrm{v}_\varepsilon^{n+1/2},$$

$$\mathrm{v}_\varepsilon^{n+1} = \mathrm{v}_\varepsilon^{n+1/2} - \frac{1}{1+\tau c_\varepsilon}\mathrm{grad}_h\ \delta p_\varepsilon.$$

For solving of convection problem the regularized nonlinear monotonic operator-splitting scheme was developed (Chudanov, 2001). The special approximation of convection terms $C(\mathrm{v})$ are employed in order to derive the discrete convective operator, which is skew-symmetrical and does not give any contribution to the kinetic energy (i.e. energetically neutral (Chudanov, 2001)).

So, this scheme provides the second order in space and the first one in time. The algorithm is stable at a large enough integration step by time. Details of the presented approach are reported in (Chudanov, 2008).

3. VALIDATION ASPECTS

The developed technique was validated (Chudanov, 2005: 2007; 2008; 2011; Obabko 2011) at the known numerical tests (such as heat transfer through the boundary layer, Benard convection, 2D convection in a lid-driven cavity flow; full turbulent flow of water in a round pipe; backwards facing step flow in 2D channel) in a wide range of Rayleigh numbers from a range 10^6-10^{16} and Reynolds numbers from a range 10^3-10^5. In present paper numerical predictions were compared with experimental results of such processes as: T-junction thermal mixing flow, ERCOFTAC experiment (world database on turbulent flows) natural convection in the closures under extremely high Rayleigh numbers. QDNS calculations were carried out on enough fine grid, i.e. the characteristic grid size was defined by Kolmogorov's scale $h \sim \mathrm{Re}^{-3/4}$. For example, Wilcox (1993) is offered for this purpose to use the following formula $N_{DNS} \sim 0.088\mathrm{Re}^{9/4}$.

3.1 ERCOFTAC experiment

The essence of experiment consists in the following. In the isolated closed domain in the shape of a parallelepiped there is air at pressure and temperature, close to normal. Two opposite walls of domain are supported at a stationary value to temperature, thus temperature of one of walls differs from temperature another. Thus, between walls there is difference of the temperatures, at the expense of which inside of domain there is a continuous circulation of air. Difference of temperatures and the geometrical parameters of domain are selected in such a manner that the airflow passes in a turbulent, non-stationary regime of flux. The rotational structures, air thermal jets arise and hence pulsation of temperature and velocity of a flux in various points of considered domain take place.

During experiment the integrated characteristics of a heat transfer between walls and air inside were measured, and also are measured a fluctuation of temperature originating near to walls and at centre of domain. The given experiment was carried out initially in 1996, but later, in 2000, in view of the urgency this experiment was iterated anew on the modernized facility, that has allowed considerably improving the obtained results. Experiment and the data of measuring are disposed in basis of knowledge of the European community ERCOFTAC and are accessible to its terms. The measurement data are available in the ERCOFTAC database: Case 79.

At calculation of the given experiment the finite-volumetric method on the completely staggered grids - "CONV3D" was applied. The method has a very small scheme diffusion and second order of accuracy on space and time. The method belongs to group quasi-DNS (Direct Numerical Simulation) methods, which at rough grid do not lose the majority of performances of simulated flows (short-wave harmonics of energy specters, for example), and last decade actively develops in IBRAE RAN as universal highly effective algorithm of a numerical solution of set of equations of computational fluid dynamics.

In particular, the given procedure is successfully applied for simulation of a thermal convection of an incompressible fluid in the closed two-dimensional and three-dimensional domains. The numerical predictions were carried out on a Cartesian calculated grid with 513x2049x129 of cells. The results of numerical simulation of experiment ERCOFTAC have a discrepancy with experiment no more than 5% for spectral, Rms and average characteristics of a velocity and temperature. In all figures Rayleigh number is equal 8.6×10^5. In figure 1 the preliminary numerical predictions of a spectrum of temperature in comparison with experimental data from the thermoelectric couple located near to a cold and hot wall, in middle of domain are shown.

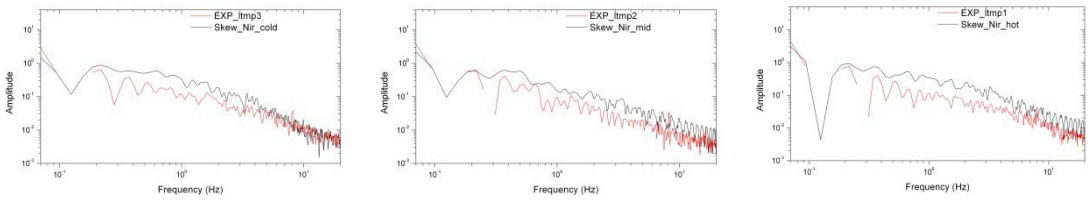

a) cold wall b) middle c) hot wall

Figure 1: Comparison of a temperature spectrum: numerical predictions CONV3D - black solid line, experiment ERCOFTAC - red line.

In figures 2-3 the averaged values of a vertical velocity (mean V) are shown at different values of parameter z. Here and below results are submitted at z=0 and z=130. In figures 4-5 are shown Rms of a vertical velocity at different values of parameter z. In figures 6-7 the averaged values of temperature are shown at different values of parameter z. In figures 8-9 are shown Rms of a temperature at different values of parameter z.

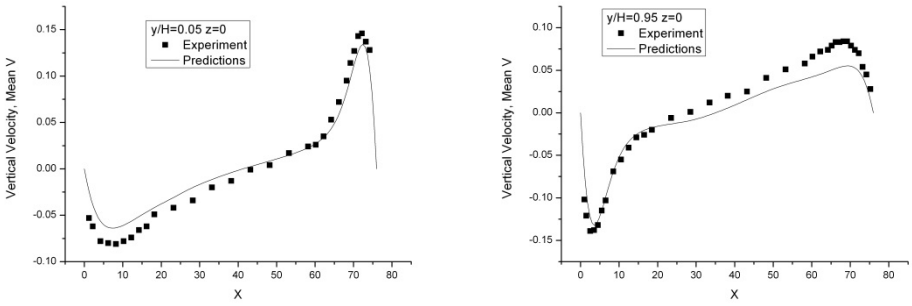

a) **b)**

Figure 2: Vertical velocity, mean V versus X. a) y/H=0.05 and z=0; b) y/H=0.95 and z=0.

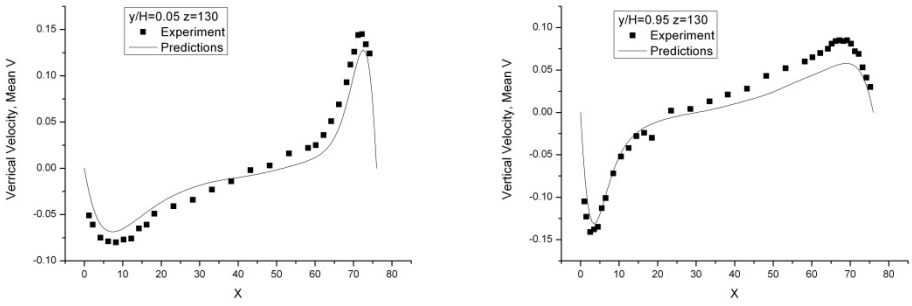

a) **b)**

Figure 3: Vertical velocity, mean V versus X. a) y/H=0.05 and z=130; b) y/H=0.95 and z=130.

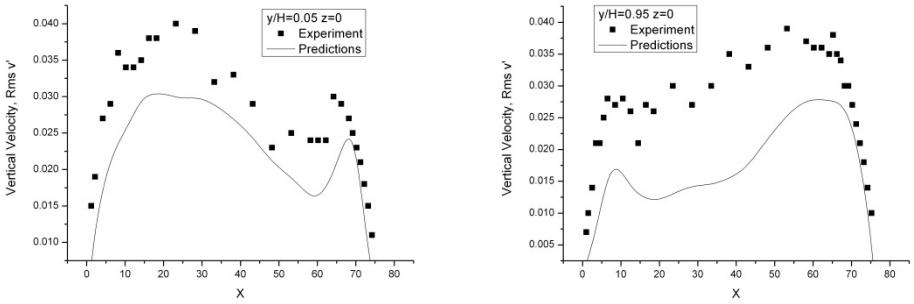

a) **b)**

Figure 4: Vertical velocity, Rms V' versus X. a) y/H=0.05 and z=0; b) y/H=0.95 and z=0.

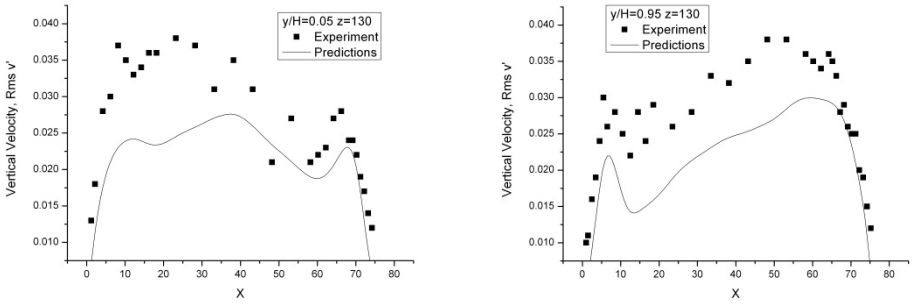

a) **b)**

Figure 5: Vertical velocity, Rms V' versus X. a) y/H=0.05 and z=130; b) y/H=0.95 and z=130.

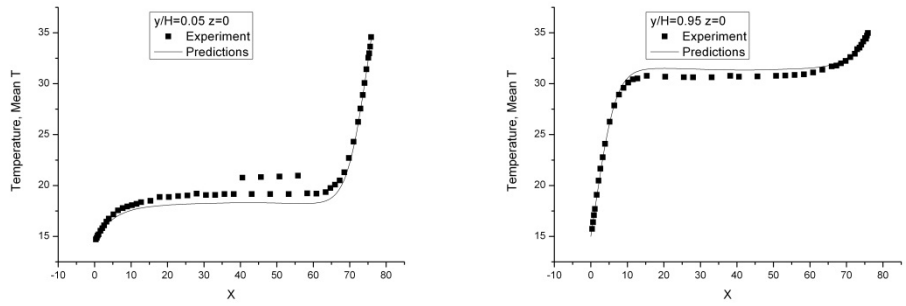

a) **b)**

Figure 6: Temperature, Mean T versus X. a) y/H=0.05 and z=0; b) y/H=0.95 and z=0.

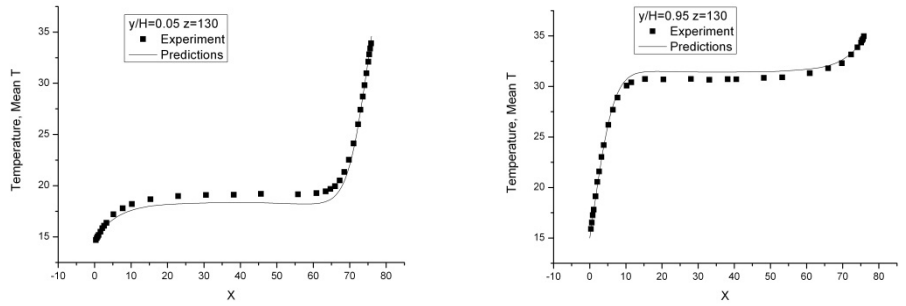

a) **b)**

Figure 7: Temperature, Mean T versus X. a) y/H=0.05 and z=130; b) y/H=0.95 and z=130.

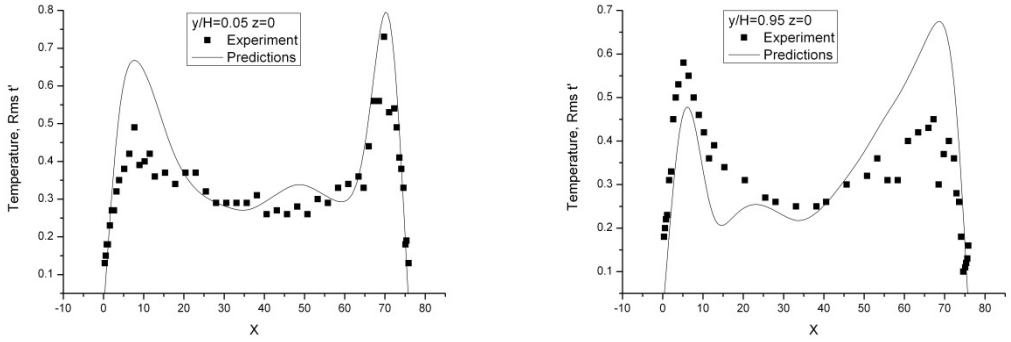

a) **b)**

Figure 8: Temperature, Rms t' versus X. a) y/H=0.05 and z=0; b) y/H=0.95 and z=0.

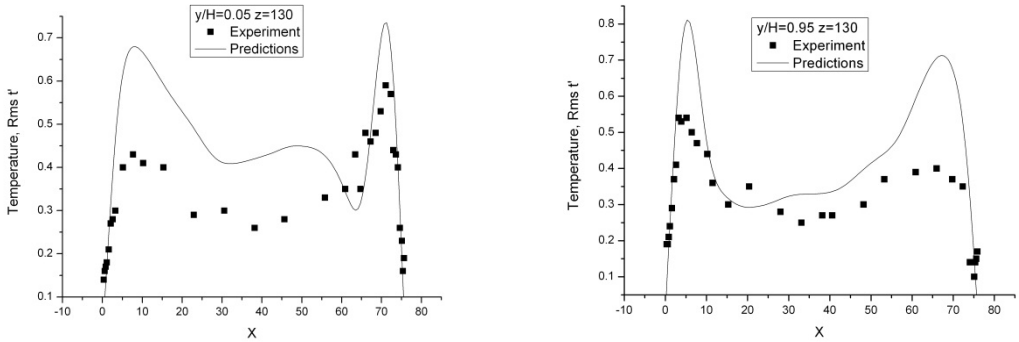

a) **b)**

Figure 9: Temperature, Rms t' versus X. a) y/H=0.05 and z=130; b) y/H=0.95 and z=130.

The velocity is measured in mm/s and temperature is measured in ^{0}C. A good agreement of numerical prediction with experiment is observed, as it is possible to see from all figures. That indicates on good perspectives of use of the given approach in the further study of thermal convection.

3.2 T-junction thermal mixing flow

In this section the results of numerical simulation of thermalhydraulics at T-junction thermal mixing are submitted. A test's singularity is that the hot flux from a vertical pipe is poured into a horizontal pipe with a cold flux.

The Vatenfall experiment [9] is based on water flow in a main pipe of diameter D=140 mm with a side branch of diameter DH=100 mm adjoining the main at a 90 degree angle. The pipes and the T-junction, which is made from a plexiglass block, are transparent so that the velocity can be measured with laser Doppler anemometry (LDA). Velocity data was taken under isothermal conditions with both flows entering in tube. In order to measure thermal striping, time dependent temperature data was collected from thermocouples downstream of the T-junction with flow at 19 ^{0}C entering the main branch and flow at 36 ^{0}C entering the side branch.

The flow enters the cold branch from a stagnation chamber located 80 D upstream of the T-junction and is assumed to be fully developed turbulent flow by the time it reaches the T-junction. The hot branch flow enters at $20D_H$ upstream and is not quite fully developed as it enters the T-junction. The inlet flow rates are 9 and 6 l/s (liters per second), respectively in the cold and hot branches, which corresponds to a Reynolds number of Re 79410 and 107500, respectively. The measurement data are available in (Mahaffy, 2010).

The IBRAE numerical predictions (Obabko, 2011) and results (Mahaffy, 2010) were compared (see figures 10-12). In first case IBRAE predictions are obtained at grid with 12 million nodes and marked by a dashed line (12M). In second case IBRAE predictions are obtained at grid with 40 million nodes and marked by a solid line (40M). Mahaffy predictions (2010) were obtained at grid with 7 million nodes and marked by stars (7M). Experimental data are marked by circles.

In figure 10 the mean velocity U versus y/R (left) and versus z/R (right) at x/D=1.6 sections is shown.

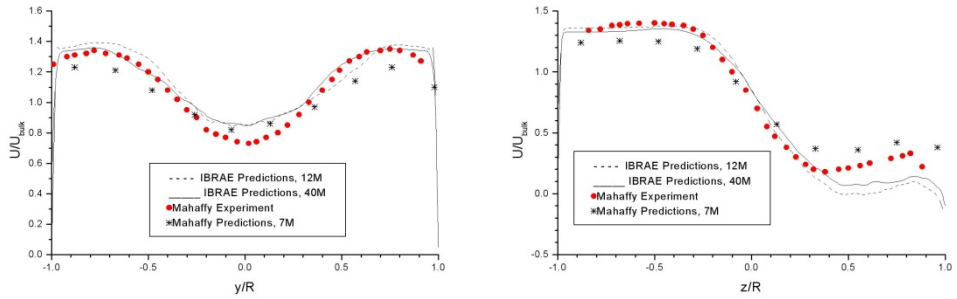

Figure 10: The mean velocity U versus y/R (left) and versus z/R (right) at x/D=1.6 section.

The Rms profiles of the x component (left) and z component (right) of velocity fluctuation versus z/R at x/D=1.6 section shown in figure 11.

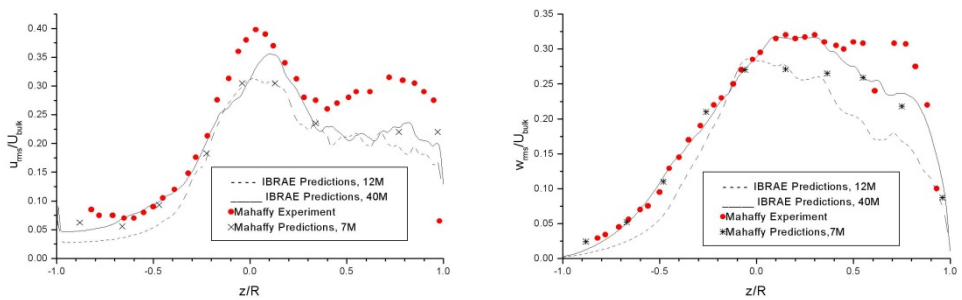

Figure 11: Rms of the x component (left) and z component (right) of velocity fluctuations versus z/R at x/D=1.6 sections.

In figure 12 the Fourier transformation graphs for the temperature are shown. The numerical predictions of CONV3D on a grid with 40 millions nodes are shown by a red line with a marker (▪) and marked as (40M). The CONV3D numerical predictions on a grid with 12 millions nodes are shown by a solid line and marked as (12M). The Mahaffy's experimental data are shown by a solid line with markers (●). The Mahaffy's predictions on a grid in 34 million nodes are shown by a green dashed line with a marker (▲) and marked as (34M). The Mahaffy's predictions on a grid in 70 million nodes are shown by a red dashed line with a marker (▪) and marked as (70M).

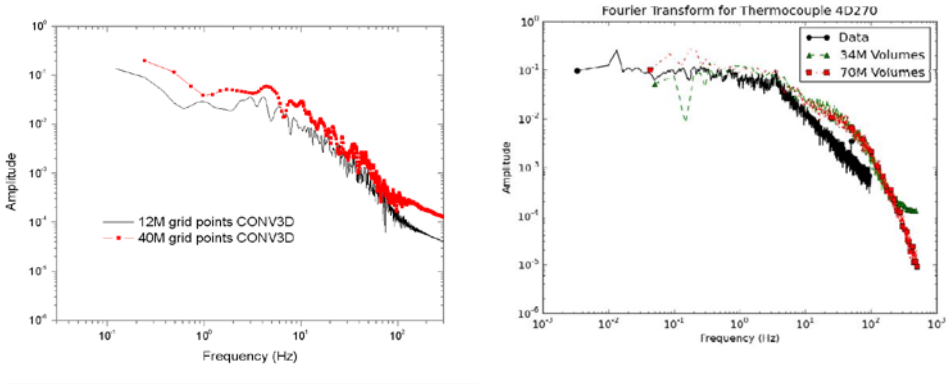

a) b)

Figure 12: – Fourier transformation for the temperature: a) – CONV3D numerical predictions; b) – Mahaffy's data

In figure 13 the Fourier transformation for w velocity on distance 3.6D from T-junction are shown. The numerical predictions of CONV3D and the Mahaffy's data are marked as in figure 12.

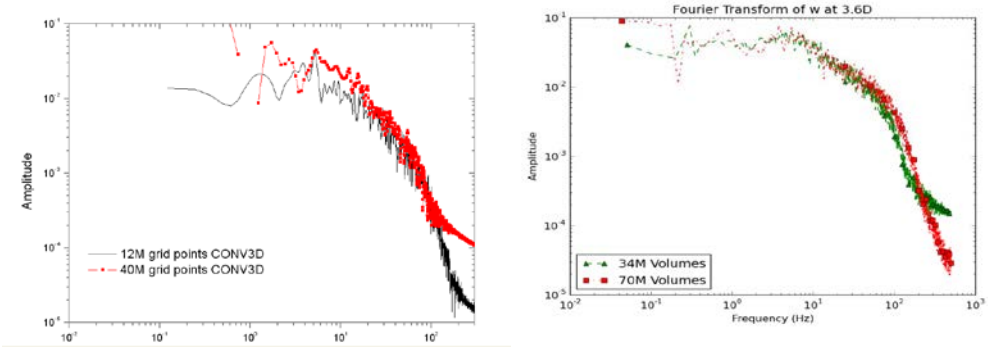

a) b)

Figure 13: – Fourier transformation for the w velocity at 3.6D: a) – numerical predictions CONV3D; b) – Mahaffy's data

A coincidence of numerical predictions and experiment is satisfactory. Failure to take account of some effects and usage of a rough grid are responsible for the observed small discrepancy. That indicates on good perspectives of use of the given approach in the further study of such test as MATIS.

4. MODELING OF THE MATIS-H EXPERIMENT

The spacer grids that support the fuel rods in a nuclear reactor core also act as turbulence-enhancing devices to improve the heat transfer from the hot surfaces of the rods to the surrounding coolant stream. The design of the spacer grids is therefore an important optimization parameter for reactor vendors. Traditional approach to spacer design by experiments is now being supplemented by Computational Fluid Dynamics (CFD). In March 2011, a cold rod 5x5 bundle test is being performed in the MATIS-H facility of the Korea Atomic Energy Research Institute (KAERI) in Daejeon, S. Korea (http://pbadupws.nrc.gov/docs/ML1113/ML111320229.pdf). Data from this test have been reserved specifically for this CFD benchmark exercise, and will be kept secret for its duration. Both

split-type and swirl-type spacer designs will be featured in this benchmark. To aid mesh construction, CAD files of the spacer designs will be made available. Following numerical simulation, participants will supply to the organizers results in the form of lateral (cross-stream) and axial velocity components, and turbulence intensity profiles at specified locations downstream of the spacer. The experiment is conducted in a water circulation loop at ambient pressure and temperature. The test section comprises a square Plexiglas sub-channel of inner dimensions 170 x 170 mm containing a 5x5 rod bundle array over part of its length. To enable good visualization of the lateral flow structure between the rods, the test section is fabricated 2.6 times larger than the prototypic size of PWR fuel bundles. The total channel length is 4900 mm and the section containing the rod bundle arrangement 1700 mm. A 2-D LDA system is positioned end-on to measure the lateral velocities in the bundle at every point in the flow sub-channel. The axial velocity component is measured by changing the location of the LDA probe to the side of the test section. The rods are arranged in a square lattice: the rod diameter is 25.4 mm, the pitch is 33.12 mm, and the wall pitch 18.76 mm. The measuring points were closely distributed with a resolution of 0.75 mm. Flow is maintained by a water storage tank and circulation pump. The tank contains a heater and a cooler to maintain constant temperature conditions during operation of the loop. The water flow rate is controlled by changing the pump speed: maximum discharge 2 m^3/min.

- This cold loop test facility, with the acronym MATiS-H (Measurement and Analysis of Turbulent Mixing in Subchannels – Horizontal), is used to perform hydraulic tests in a rod bundle array at normal pressure and temperature conditions. The rig consists of a water storage tank (*e*), a circulation pump (*f*) and a test section (*a*). The volume of the water storage tank and the maximum flow rate of the circulation pump are 0.9 m3 and 2 m3/min., respectively. The flow rate in the loop during operation is controlled by adjusting the rotational speed of the pump, and the loop coolant temperature is also accurately maintained within a range of ± 0.5°C by controlling the heater (*i*) and the cooler (*h*) in the water storage tank. For monitoring and controlling the loop parameters (flow rate, pressure and temperature), a mass flowmeter (*m*), a gauge pressure transmitter (*o*) and a thermocouple (*n*) are installed at the inlet to the test section.

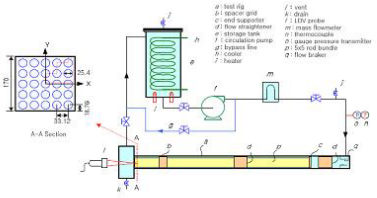

Schematic of MATiS-H test facility

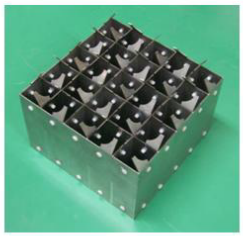

Split-type spacer grid

Figure 14: OECD/NEA MATIS-H benchmark.

The preliminary results of numerical simulation of experiment MATIS-H with the help CONV3D code (figure 15) are submitted below.

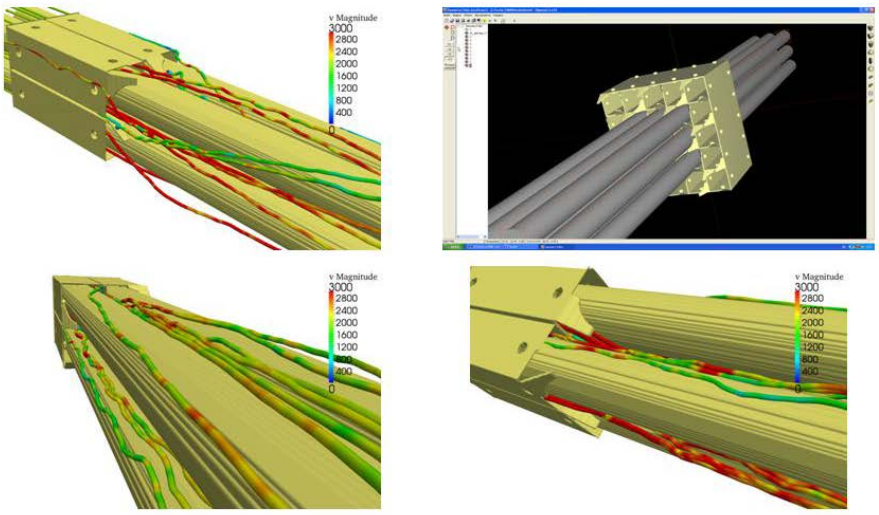

Figure 15: Numerical simulation of MATIS-H experiment.

The calculations were carried out for two spacer grids. The geometries of spacer grids were taken from e-mail of KAERI, and rods are constructed manually with the help GeometryEditor (IBRAE). The calculations were carried out on the supercomputer Lomonosov (MSU, Moscow). For calculations the grid by size 10000000 nodes was chosen. The velocity fields of U, V, W velocity at different removal from split spacer grid are shown in figure 16.

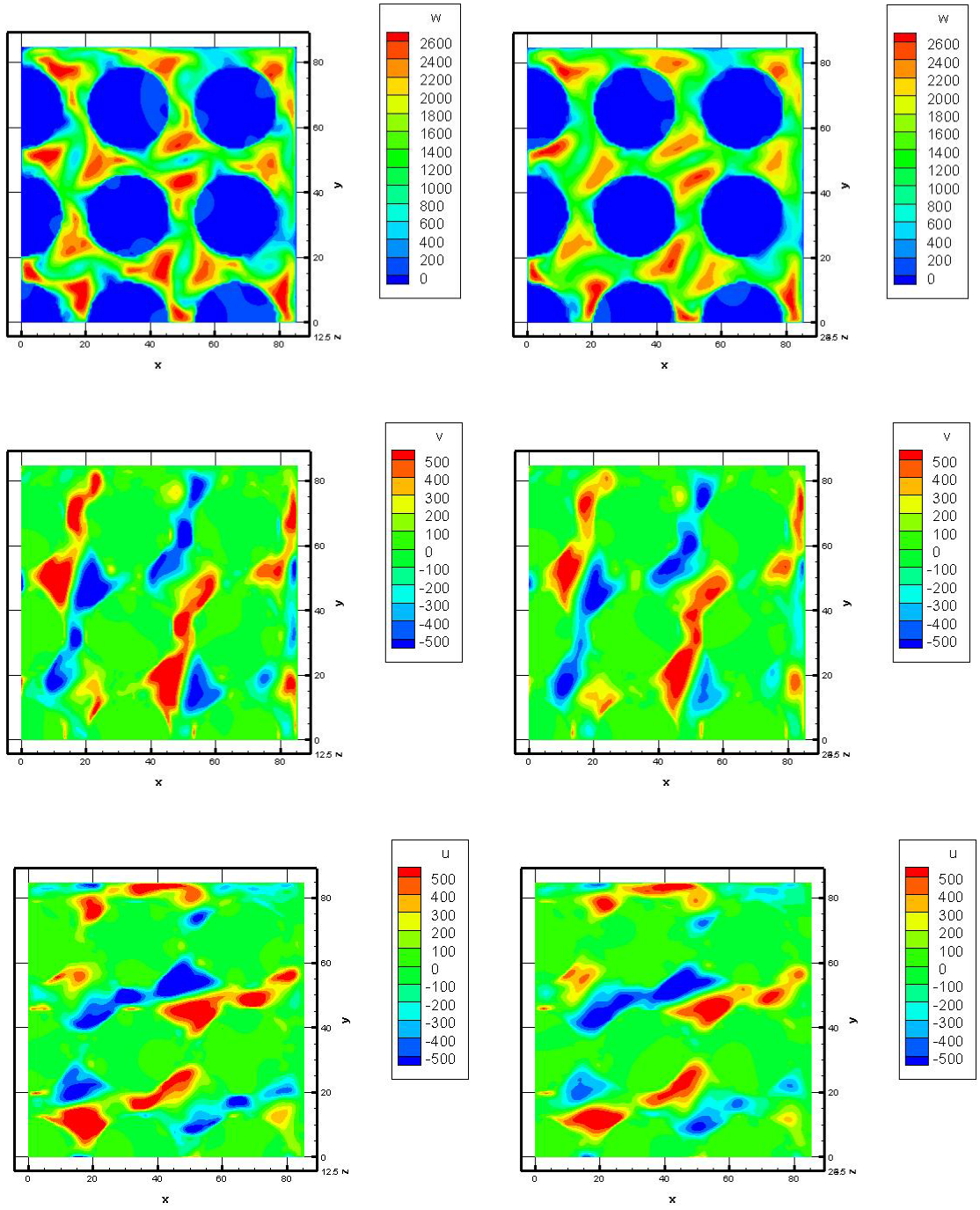

a) Distance of removal =12.5 mm b) Distance of removal =23.5 mm

Figure 16: The velocity fields of W, V, U velocity (top from bottom) at different removal from split spacer grid a) 12.5 mm; b) 23.5 mm

The velocity is measured in mm/s and coordinate is measured mm. The velocity fields of W, V, U velocity at different removal from swirl spacer grid are shown at figure 17. There are preliminary results. Comparison numerical predictions and experimental data will be prolonged with occurrence of the new data.

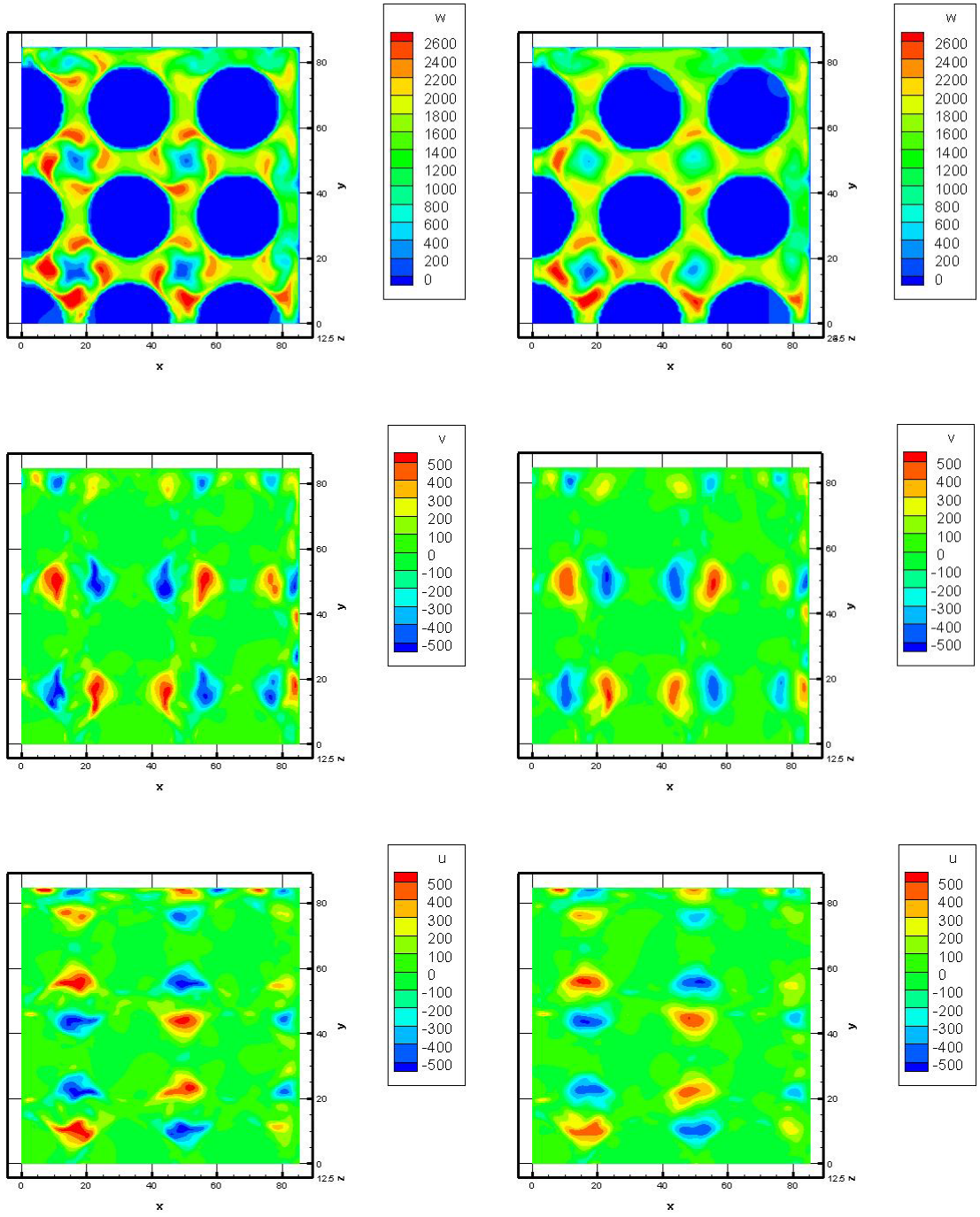

a) Distance of removal =12.5 mm b) Distance of removal =23.5 mm

Figure 17: The velocity fields of W, V, U velocity (top from bottom) at different removal from swirl spacer grid a) 12.5 mm; b) 23.5 mm.

CONCLUSIONS

For 3D simulation of various thermalhydraulic processes on NPP in a wide range of parameters (Ra < 10^{16} and Re=10^3-10^4) the 3D unified numerical thermalhydraulic technique and 3D CFD code for safety analysis of the operated NPPs were developed.

The developed technique was tested in area of turbulent flows, for which the good qualitative and quantitative coincidence with numerical QDNS predictions was obtained. All numerical predictions were obtained without any turbulence model. The numerical simulation results of two test problems and the analysis of turbulent intermixing in horizontal subchannels of the fuel assembly at normal pressure and temperature (Matis-H test) allow speaking of perspective simulation by means of QDNS of thermalhydraulic in fuel assembly with the help of the developed numerical approach.

REFERENCES

1. V.V. Chudanov, et al., "Current status and validation of CONV2D\&3D code", *Proc. OECD/CSNI Workshop on in vessel core debris retention and coolability*, Garching near Munich, Germany, March 3-6. 1998. Nuclear Safety NEA/CSNI/R(98) 18, pp. 223-234 (1998).
2. V.V. Chudanov, et al., "A multi-block orthogonal grid generation using CAD system", *Proc. 8th International Meshing Roundtable*, South Lake Tahoe, California, October 10-13. 199. USA, Sandia Report, SAND 99-2288, pp. 179-186 (1999).
3. V.V. Chudanov, et al. *J. of computing mathematics and of mathematical physics*, Vol.40, № 6, 900-907 (2001).
4. V.V. Chudanov, A.E. Aksenova, V.A. Pervichko, "3D unified CFD approach to thermalhydraulic problems in safety analysis", *Proc. of IAEA Technical Meeting on Use of Computational Fluid Dynamics (CFD) Codes for Safety Analysis of Nuclear Reactor Systems, Including Containment*, University of Pisa, Italy, 11-14 November, 2002. (CD-disk (Session 7). Summary reports IAEA-TECDOC-1379. p.14 (2003).
5. V.V. Chudanov, A.E. Aksenova, V.A. Pervichko, "Methods of direct numerical simulation of turbulence in thermalhydraulic's problems of fuel assembly". *Izvestiya Rossiiskoi Akademii Nauk. Seriya Energetica*, №6, 47-57 (2007).
6. V.V. Chudanov, A.E. Aksenova, V.A. Pervichko, et al. Methods of computational hydrodynamics for the safety analysis of TEK's objects [in Russian] Proceedings of Nuclear Safety Insitute RAS (IBRAE RAS) / ed/ by corresponding member of RAS L.A. Bolshov. – Iss.3. – Moscow: Nauka, 2008. -207 p.: ill.
7. A.V. Obabko, P.F. Fischer, and T.J. Tautges (ANL, USA), S. Karabasov (Cambridge University, UK) V.M. Goloviznin and M.A. Zaytsev, V.V. Chudanov, V.A. Pervichko, and A.E. Aksenova (IBRAE, Russia). CFD Validation in OECD/NEA T-Junction Benchmark. IBRAE/ANL report №ANL/NE-11/25. 2011
8. Chudanov V., Aksenova A., Pervichko V., "CFD Based Numerical Modules for Safety Analysis at NPPs Validation and Verification", Journal of Materials Science and Engineering, 1(3) (August, 2011), ISSN 2161-6221.
9. J. Westin, P. Veber, L. Andersson, C. Mannetje, U. Andersson, J. Eriksson, M. Henriksson, F.Alavyoon, C. Andersson, "High-cycle thermal fatigue in mixing Tees. Large-eddy simulations compared to a new validation experiment". *Proc. 16th International Conference on Nuclear Engineering*. Orlando, USA, May 11–15, 2008. ICONE16-48731 (2008).
10. D.C. Wilcox, *Turbulence modelling for CFD*, DCW Industries, USA, Glendale California. ISBN 0-9636051-0-0 (1993).
11. John Mahaffy and Brian Smith, Synthesis of Benchmark Results, OECD/NEA T-JUNCTION BENCHMARK, 2010.

Verification calculations as per CFD FLOWVISION code for sodium-cooled reactor plants

S.A. Rogozhkin, S.L. Osipov, S.F. Shepelev,[a], A.A. Aksenov, M.L. Sazonova, V.V. Shmelev[b]

[a] JSC "OKBM Afrikantov", Nizhny Novgorod, Russia

[b] "TESIS Ltd.", Moscow, Russia

Abstract. The paper studies the experience in application of CFD FlowVision software for analytical validation of sodium-cooled fast reactor structure components and the results of performed verification, namely:

- development and implementation of new model of turbulent heat transfer in liquid sodium (LMS) in FlowVision software and model verification based on thermohydraulic characteristics studied by experiment at TEFLU test facility;
- simulation of flowing and mixing of coolant with different temperatures in the upper mixing chamber of fast neutron reactor through the example of BN-600 (comparison with the results obtained at the operating reactor).

Based on the analysis of the results obtained, the efficiency of CFD codes application for the considered problems is shown, and the proposals for CFD codes verification development as applied to the advanced sodium-cooled fast reactor designs are stated.

1. Introduction

JSC "OKBM Afrikantov" has been involved in development of sodium-cooled fast reactors for more than 50 years. The reactor plants that have been sequentially developed are BN-350, BN-600 (in operation), BN-800 (under construction). Currently, development of BN-1200, Generation IV reactor, is in progress. Over these years, substantial research has been done to validate thermal-hydraulic characteristics of developed reactor plants – this is mainly analytical and experimental work. Over the last years, CFD methods (CFD codes) that are based upon state-of-the-art computer technologies have been more frequently employed to validate designs.

Use of CFD codes in the nuclear power industry makes it possible to:

- substantially enhance the phenomena analyzing capabilities;
- analyze complex processes in reactor plant equipment and systems; refine their characteristics;
- abandon experimental studies or substantially simplify and reduce their scope for a number of design solutions.

The analysis of the world's scientific literature has shown that the issue with applicability of CFD software packages for analytical studies of liquid metal flows is being actively discussed by specialists in the nuclear field [1]. Validating the possibility of using CFD codes for designing, parameter optimization and safety analysis of the BN reactor plants is a topical challenge.

The main distinctive feature of CFD code application for the BN reactors is the need to take account of:

- heat transfer mechanism in liquid metals;
- integral layout of equipment in the reactor.

2. Turbulent heat transfer in liquid metals

Heat transfer in liquid metals that are characterized by low molecular Prandtl numbers [2] has a range of special features. Fig. 1 shows the effect of the molecular Prandtl number upon the ratio between the thicknesses of the dynamic and thermal boundary layers. In the turbulent thermal flow, the heat transfer is determined by both molecular and turbulent heat conduction coefficients. In conventional media, like air and water, the molecular heat conduction is important only near the wall in the viscous sub-layer. In liquid metals, the coefficient of molecular heat conduction is of the same order of magnitude as the turbulent heat conduction coefficient for the entire flow. Thus, the heat transfer mechanism in liquid metals is far different from the heat transfer mechanism in air and water.

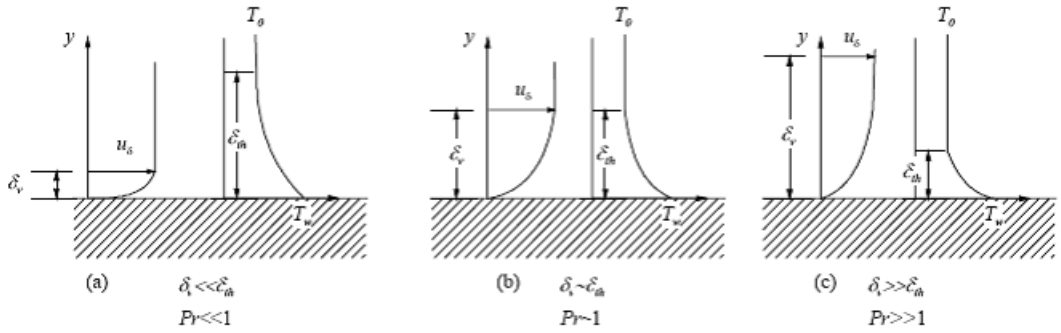

FIG. 1. Effect of the molecular Prandtl number upon the relative thickness of the thermal boundary layer.

3. Developing and testing the LMS turbulent heat transfer model

The turbulent heat conduction is frequently modeled in CFD codes as part of the Reynolds analogy that enables obtaining good results with gas and water used as coolants. For gas and water, the Prandtl number is taken constant and equal to ~ 1. However, because heat conduction in liquid metals is high and viscosity is low, the properties of velocity fields and temperature fields are considerably different. In this connection, the turbulent Prandtl number is not constant. The variable turbulent Prandtl number, when calculated, enables refining the contribution of turbulence to the effective (full) heat conduction coefficient.

The LMS (Liquid Metals Sodium) model [3] was developed based upon the analysis of the existing models of turbulent heat transfer. Turbulent heat conductivity λ_t in model is determined by the following relationship:

$$\frac{\lambda_t}{\rho C_p} \equiv \frac{\nu_t}{Pr_t} \equiv \alpha_t = C_\lambda f_\lambda \frac{k^2}{\varepsilon} \sqrt{\frac{2\sqrt{R\,Pr}}{0.5+R}}.$$

Correspondingly, the correlation for the turbulent Prandtl number Pr_t is

$$Pr_t = \frac{C_\mu f_\mu}{C_\lambda f_\lambda} \sqrt{\frac{0.5+R}{2\sqrt{R\,Pr}}}$$

Here $R = \frac{k_\theta / \varepsilon_\theta}{k/\varepsilon}$ - time scale ratio. Function f_μ is determined by the used k-ε turbulence model for turbulent kinetic energy and its dissipation rate.

Equations for variables k_θ and ε_θ:

$$\frac{\partial(\rho k_\theta)}{\partial t} + \vec{\nabla}(\rho \mathbf{V} k_\theta) = \vec{\nabla}\left(\rho\left(\alpha + \frac{\alpha_t}{\sigma_{k\theta}} \right)\nabla k_\theta \right) + \rho\alpha_t (\vec{\nabla} T)^2 - \rho\varepsilon_\theta$$

$$\frac{\partial(\rho \varepsilon_\theta)}{\partial t} + \vec{\nabla}(\rho \mathbf{V} \varepsilon_\theta) = \vec{\nabla}\left(\rho\left(\alpha + \frac{\alpha_t}{\sigma_{\varepsilon\theta}} \right)\nabla \varepsilon_\theta \right) + C_{P1} \frac{\varepsilon_\theta}{2k_\theta} \rho\alpha_t (\nabla T)^2 + C_{P2} \frac{\varepsilon_\theta}{k} \mu_t P_k -$$

$$- \rho C_{D1} \frac{\varepsilon_\theta^{\,2}}{2k_\theta} - \rho C_{D2} \frac{\varepsilon\varepsilon_\theta}{k} + \rho\xi_{\varepsilon\theta}$$

$$P_k = \nu_t \left(\frac{\partial V_i}{\partial x_j} + \frac{\partial V_j}{\partial x_i} \right) \frac{\partial V_j}{\partial x_i}, \; \nu_t = C_\mu f_\mu \frac{k^2}{\varepsilon}$$

Correction function (for low-Reynolds regimes):

$$\xi_{\varepsilon\theta} = f_{w,\varepsilon\theta} \left[(C_{D1} - 4) \frac{\varepsilon_\theta^2}{2k_\theta} + C_{D2} \frac{\varepsilon\varepsilon_\theta}{k} - \frac{(\varepsilon_\theta - \alpha 2k_\theta / y^2)^2}{2k_\theta} + (2 - C_{P1}) \frac{\varepsilon_\theta}{2k_\theta} \alpha_t (\nabla_x T)^2 \right]$$

Damping functions:

$$f_\lambda = f_{w,\varepsilon\theta} \frac{C_{1\lambda}}{Re_t^{\,1/4}} + \left[1 - \exp\left(\frac{y^+}{A^+} \right) \right]^2, \; f_{w,\varepsilon\theta} = \exp\left[-\left(\frac{Re_t}{80} \right)^2 \right]$$

Turbulent Reynolds number:

$$Re_t = \frac{k^2}{\nu\varepsilon}$$

Dimensionless distance to the nearest wall:

$$y^+ = \frac{C_\mu^{1/4} k^{1/2} y}{\nu}$$

Constants:

$C_\lambda = 0.11 \quad \sigma_{k\theta} = 1.227 \quad \sigma_{\varepsilon\theta} = 1.227$

$C_{P1} = 1.8 \quad C_{P2} = 0.72 \quad C_{D1} = 2.2 \quad C_{D2} = 0.8$

$C_{1\lambda} = 0.1 \quad A^+ = 30.$

The model is implemented in the Russian software package FlowVision [4], [5]. FlowVision simulates complex 3D laminar and turbulent gas and liquid flows inside/around different natural and technical objects. It has a wide spectrum of modeling capabilities implemented in different models and modules: conjugate heat transfer, combustion, radiation, moving bodies, free-surface flows. FlowVision is based on the finite-volume method and rectangular adaptive mesh with local refinement. Grid generation is fully automated. FlowVision uses a subgrid geometry resolution to approximate the curvilinear shape of a computational domain with high accuracy. The efficient parallel algebraic solver provides highly scalable calculations essentially speeding up the most complex simulations.

The LMS model is verified by simulation of mixing processes with two sodium coolant flows having different temperatures. The said processes have been experimentally studied in the TEFLU facility [6].

The TEFLU sodium facility (Fig. 2) consists of a vertical tube 110 mm ID and an axially moving grid. The main flow of cold sodium circulating in the tube, while passing through the grid, is mixed with a jet of hot sodium that is coming from the central hole. In the course of the experiment, three flow modes were investigated, namely, forced convection mode, transient mode and free convection mode. The temperature and velocity of sodium were measured in the radial and axial directions.

In the analysis performed by FlowVision, the input velocity and temperature of the hot jet and main flow were assigned constant according to the conditions of the experiment.

Results obtained by FlowVision with the classic k-ε model at Pr_t=1 and with the developed LMS model are compared in Fig. 3 to experimental data for the forced convection mode.

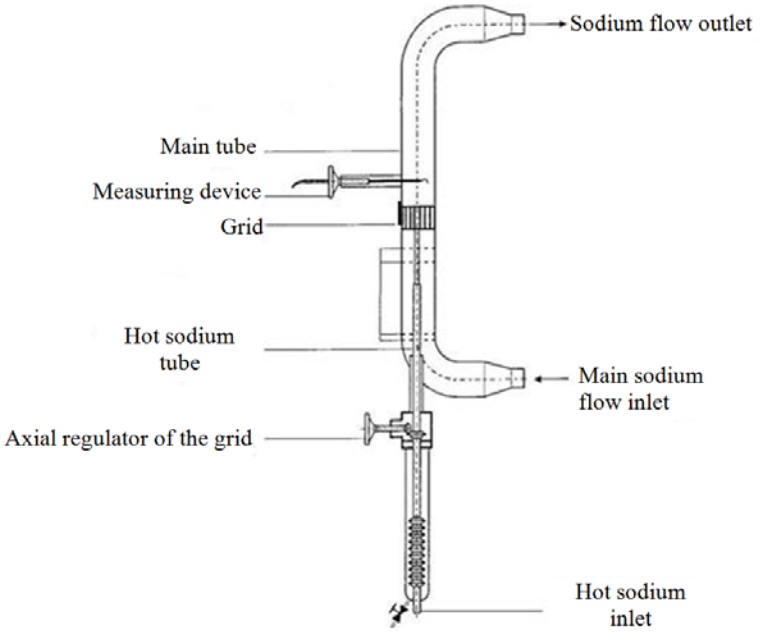

FIG. 2. Test facility model design.

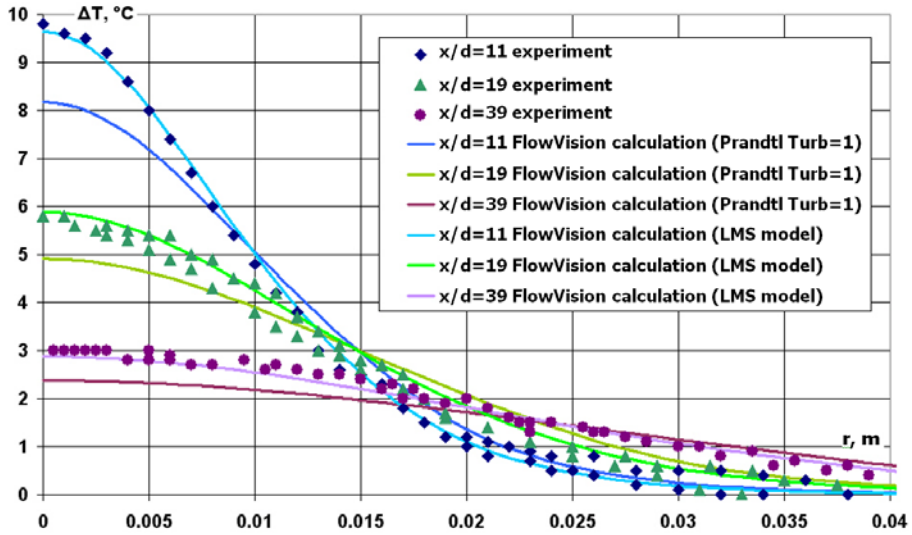

FIG. 3. Radial profiles of temperature; forced convection mode

x – coordinate of the calculational cross section; d – hot sodium tube diameter.

The LMS model testing showed very good convergence of calculated results and experimental data. At the same time, the maximum error in the temperature calculation for the free and forced convection modes does not exceed 2%; for the transient mode, 6%.

4. Modeling the flowing and mixing processes for coolant flows with different temperatures at the upper mixing chamber in the BN-600 reactor

One of the distinctive features of using CFD codes with the BN reactors is the integral layout of equipment, which means that all the primary equipment is placed inside the reactor vessel.

In order to verify the methodical approach employed to model physical processes in the reactor with the integral layout of equipment and to validate the new LMS model of turbulent heat transfer in the sodium coolant, the streaming and mixing of coolant flows with different temperatures was numerically modeled in the BN-600 reactor upper mixing chamber. FlowVision was verified through comparing the calculated temperatures with the temperatures measured by tank thermocouples and IHX inlet thermocouples.

The computer model of the reactor upper mixing chamber took account of the FA nozzles in the core, in-vessel protection tubes, elevator wall and intermediate heat exchanger (IHX) support (Fig. 4, 5). A porous body model was used to simulate the heat exchanger.

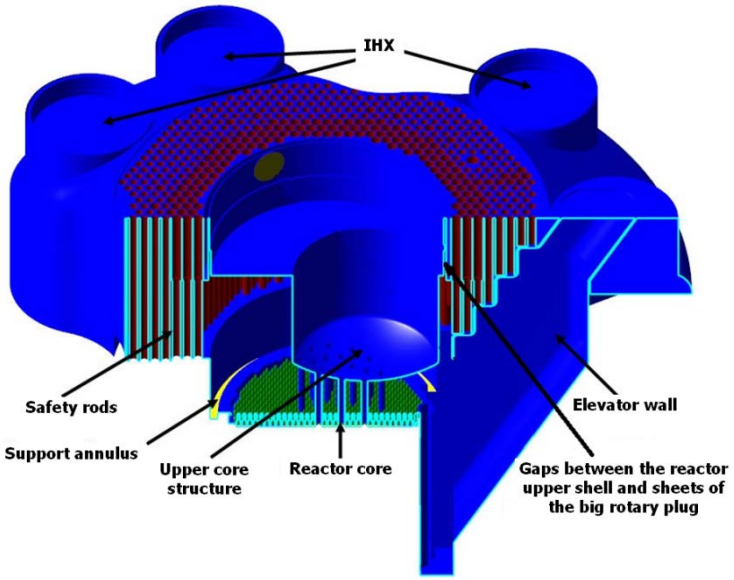

FIG. 4. Computer model of the BN-600 reactor upper mixing chamber.

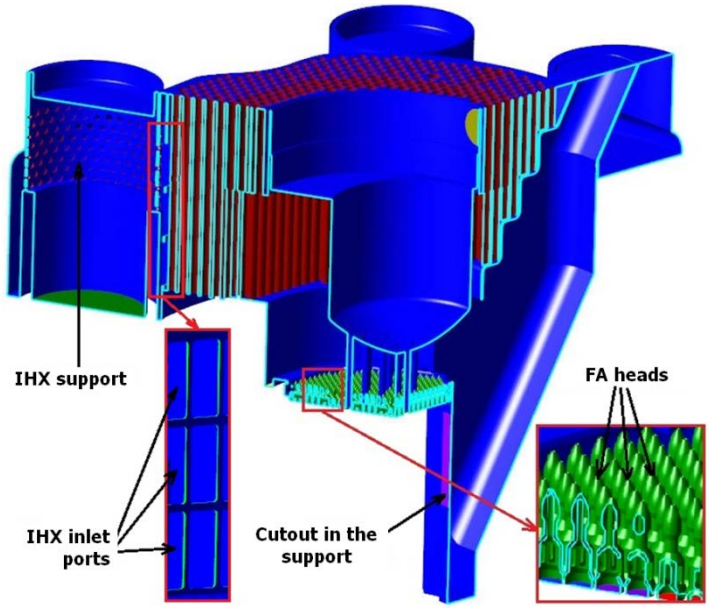

FIG. 5. Fragment of the computer model of the BN-600 reactor upper mixing chamber.

In order to correctly simulate the coolant flow in the reactor upper mixing chamber, all main design elements had to be taken into account, in particular, FA nozzles in the core and in-vessel protection tubes. The characteristic dimensions of these elements are far less than the main part of the construction. Hence, the resolution of flows in the respective channels required lessening the

dimension of calculational cells (the dimensions of the calculational cells in the model are from 0.3 to 5 cm). It resulted in that the calculational mesh was substantially increased and the need arose to use high-performance computers. Fragments of the calculational mesh are shown in Fig. 6. The number of calculational cells in the solved task is 53 million.

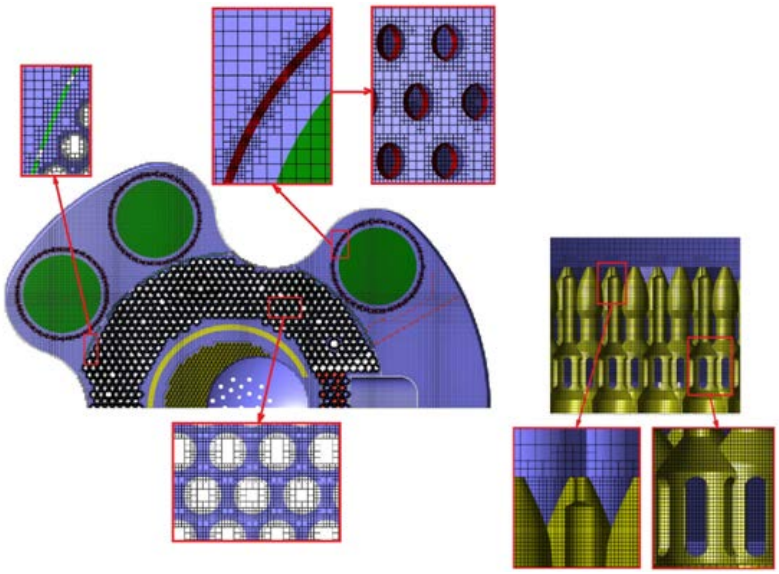

FIG. 6. Fragment of the calculational mesh.

Sodium coolant flow velocity, sodium temperature, flow turbulization ratio and turbulence scale were assigned as the input boundary conditions at the ends of all FAs. The same conditions were determined at the boundaries corresponding to the cross-flow ports in the rotary plug, support annulus, cutout in the support and bypass flow meter outlet (Fig. 7).

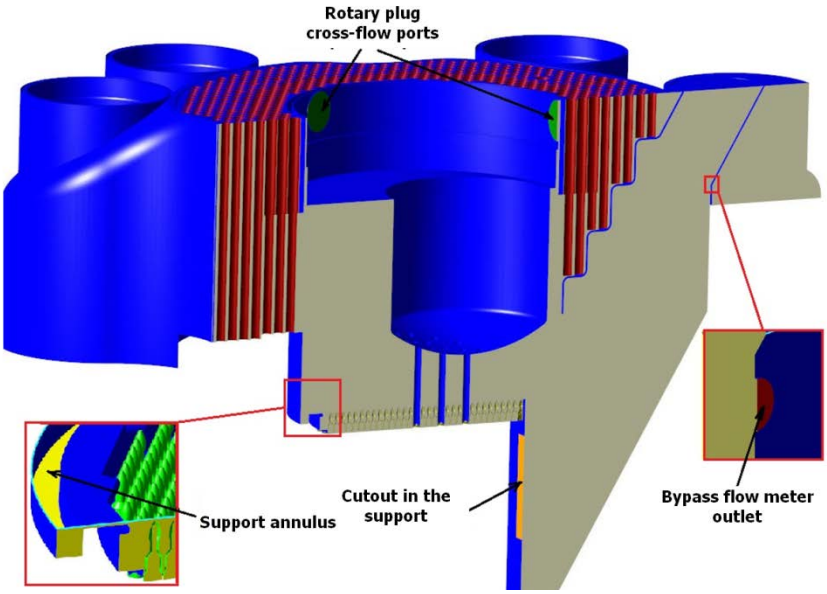

FIG. 7. Boundary conditions.

The streaming and mixing of coolant flows with different temperatures in the BN-600 reactor upper chamber were numerically modeled with the use of 128 processors with 4 cores per processor. In FlowVision, all calculational steps are parallelized, namely, calculational domain decomposition, discretization, iterative solving of algebraic equations, as well as processing and visualization of calculated results. The calculational time was ~ 3 weeks.

As a result of modeling, coolant velocity fields and temperature fields were obtained on the flow path of the reactor upper mixing chamber (Fig. 8).

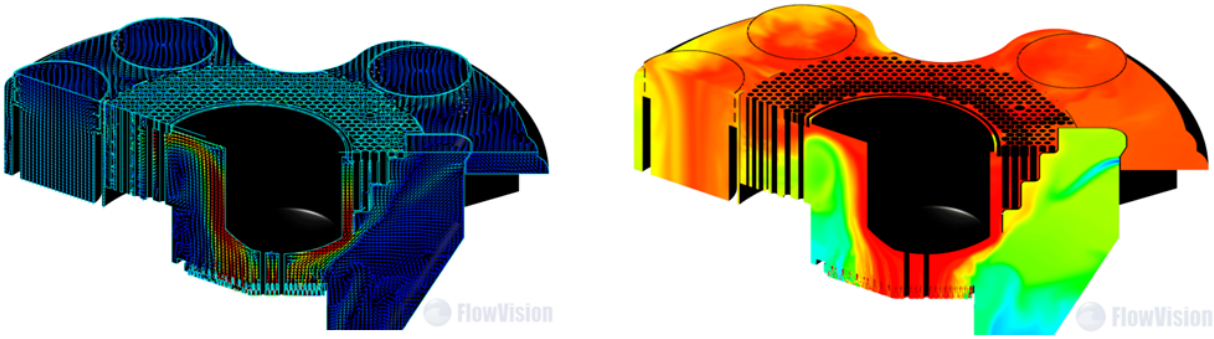

a) Velocity distribution *b) Temperature distribution*

FIG. 8. Numerical modeling results.

The error of the numerically modeled results compared to the results measured in the operating BN-600 reactor does not exceed 11% (Fig. 9, 10).

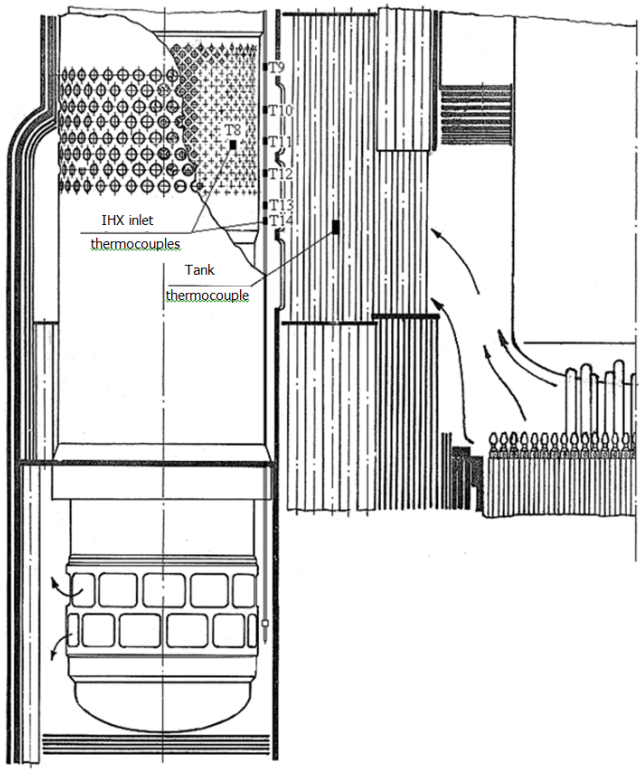

FIG. 9. Thermocouple location diagram.

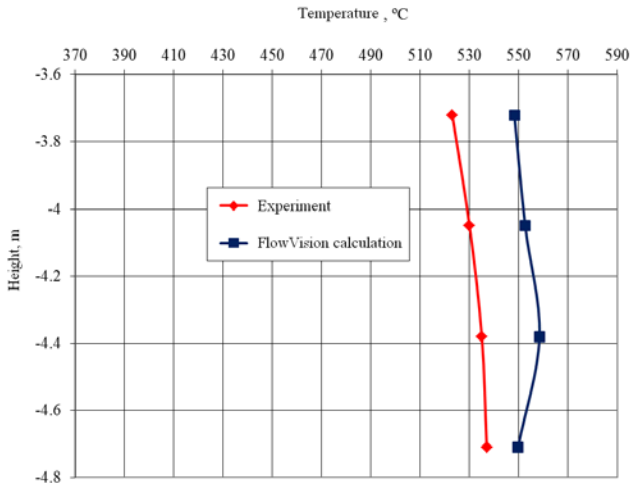

FIG. 10. Numerically modelled results compared to the results measured in the operating BN-600

5. Numerical modeling used for validation of design solutions on BN-1200 central rotary column

The performed verification enabled using FlowVision to model coolant flow in the BN-1200 reactor upper mixing chamber in order to select the shape of the bottom part in the upper core structure (spherical or flat bottom). The shape of the bottom part in the upper core structure determines mixing efficiency of coolant flows with different temperatures and a possibility of gas entrainment at the argon-sodium interface.

In addition to the physical model from the previous task, the numerical modeling of coolant flow in the BN-1200 reactor upper mixing chamber utilized the free surface/interface transfer model VOF (Volume Of Fluid). It is used to model the motion of the sodium layer in the reactor tank. Fig. 10 shows geometrical models used in the calculations.

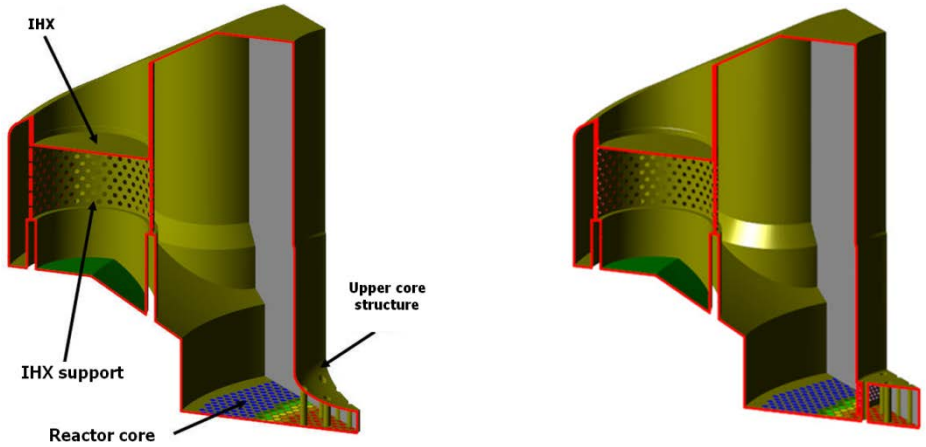

a) Upper core structure with the spherical bottom *b) Upper core structure with the flat bottom*

FIG. 11. Computer models of the BN-1200 reactor upper mixing chamber.

Results shown in Fig. 11a that are calculated for the upper core structure option with the spherical bottom illustrate sodium streaming when it flows from the upper core plane. One can see that the main flow is concentrated near the walls of the upper core structure . A vortex zone is formed near the IHX, as well as waves are formed at the sodium-argon interface, which may result in a gas entrainment and transport in the circulation circuit.

The streaming pattern in the upper core structure with the flat bottom (Fig. 11b) is very much different from that in the upper core structure option with the spherical bottom. The main flow goes from the foundation of the upper core structure to the IHX. The flow is streaming along the heat exchanger walls. In the area upstream of the IHX, a vortex zone is formed but the vortex rotation direction is opposite to that in the option with the spherical bottom. No waves are on the sodium surface and eventually there is no argon entrainment. This testifies to the advantage of this design.

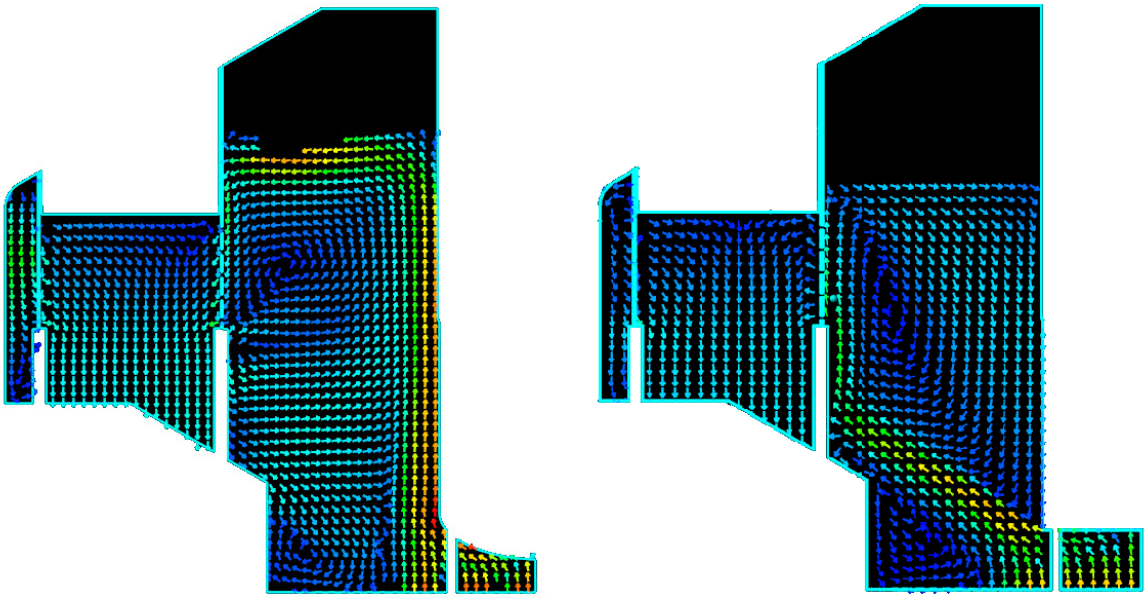

a) Velocity distribution; upper core structure with the spherical bottom

b) Velocity distribution; upper core structure with the flat bottom

FIG. 12. Computer models of the BN-1200 reactor upper mixing chamber.

Based on the comparative analysis of results calculated for two options of the upper core structure design to be used in the BN-1200 reactor upper mixing chamber, recommendations were prepared to optimize the design in order to enhance the mixing efficiency of coolant flows with different temperatures and to prevent the gas entrainment at the sodium-argon interface.

6. Suggestions for verifying CFD codes with respect to the BN reactors

In the course of developing the CFD code verification plan with respect to the BN reactors, the existing Russian and non-Russian experimental data were analyzed that had been obtained in in-pile and out-of-pile experimental facilities. The following can be concluded based on the performed analysis:

- In most available experimental data, there is no comprehensive (in terms of CFD code verification) information about the model geometry and errors of used measurement equipment.
- Given the specificity of heat transfer in the sodium coolant, correct experimental data should be obtained in sodium test facilities. Experimental results from the water test facilities can be used to verify fluid dynamics tasks and the methodical approach employed in CFD codes for solving.
- In-pile studies are the main source of data for the integrated verification of CFD codes.

Currently, available and trustworthy experimental data for verification of CFD codes have been obtained in the BN-600, Monju and Phénix reactors and in the TEFLU sodium facility. In the future, data will be used that are planned to be obtained at the sodium facilities in SCC RF Institute of Physics and Power Engineering and RAS UB Institute of Continuous Media Mechanics as part of work on the BN-1200 reactor plant and preoperational adjustment work on the BN-800 reactor.

It is planned to complete CFD verification work with respect to the BN reactors in 2016.

7. Conclusion

The experience of CFD FlowVision code application using LMS model of turbulent heat transfer in the sodium coolant and specially developed methodical approach aimed at analysing reactors with equipment integral layout shows efficient numerical modeling of thermal-hydraulic processes in BN reactor upper mixing chamber.

REFERENCES

[1] GRÖTZBACH, G., "Anisotropy and buoyancy in nuclear turbulent heat transfer – critical assessment and needs for modeling", FZKA 7363, Forschungszentrum Karlsruhe GmbH, Karlsruhe, 2007.

[2] Handbook on Lead-bismuth Eutectic Alloy and Lead Properties, Materials Compatibility, Thermal-hydraulics and Technology, Chapter 10 [Text] // OECD/NEA Nuclear Science Committee, ISBN 978-92-64-99002-9, 2007.

[3] OSIPOV, S.L., ROGOZHKIN, S.A., FADEEV, I.D. et al., Developing and testing the LMS model to take account of the turbulent heat transfer in the sodium coolant // International Forum "Engineering Systems-2012": Paper Abstract, Moscow, April 10-11, 2012.

[4] AKSENOV, A., DYADKIN, A., POKHILKO, V. Overcoming of Barrier between CAD and CFD by Modified Finite Volume Method // Proc 1998 ASME Pressure Vessels and Piping Division Conference, San Diego. ASME PVP. 1998. V. 377. No. 1.

[5] AKSENOV, A.A., KHARCHENKO, S.A., KONSHIN, V.N., POKHILKO, V.I. FlowVision software: numerical simulation of industrial CFD applications on parallel computer systems // Parallel CFD 2003 Conference. Book of Abstracts. Moscow, 2003. 280-284.

[6] KNEBEL, J., KREBS, L., MULLER, U., AXCELL, B., Experimental investigation of a confined heated sodium jet in a co-flow, J. Fluid Mech, 1998.

FR13, Paris, 4-7 March 2013 T1-CN-199, Paper No 378

DEVELOPMENT AND VERIFICATION OF THE COMPUTER CODES FOR THE FAST REACTORS NUCLEAR SAFETY JUSTIFICATION

A.E. Kisselev, N.A. Mosunova, V.F. Strizhov

Nuclear Safety Institute of the Russian Academy of Sciences

Abstract. The information on the status of the work on development of the system of the nuclear safety codes for fast liquid metal reactors is presented in paper. The purpose of the work is to create an instrument for NPP neutronic, thermohydraulic and strength justification including human and environment radiation safety. The main task that is to be solved by the system of codes developed is the analysis of the broad spectrum of phenomena taking place on the NPP (including reactor itself, NPP components, containment rooms, industrial site and surrounding area) and analysis of the impact of the regular and accidental releases on the environment.

The code system is oriented on the ability of fully integrated modeling of the NPP behavior in the coupled definition accounting for the wide range of significant phenomena taking place on the NPP under normal and accident conditions. It is based on the models that meet the state-of-the-art knowledge level. The codes incorporate advanced numerical methods and modern programming technologies oriented on the high-performance computing systems.

The information on the status of the work on verification of the separate codes of the system of codes is also presented.

1. Introduction

At the present time the integrated system of codes are widely used for the nuclear safety justification of the NPPs with pressurized and boiling water reactors. The integrated system of codes allows modeling the sequence of the NPP accidental conditions from initial event up to fission products release from containment to environment and their subsequent transport.

For the light water reactors safety justifications are performed using MELCOR (USA), ASTEC (EU) and SOCRAT (RF) codes. For the fast reactors the following integrated codes are known: SAS4A (USA) which is a computer code designed to perform deterministic analysis of severe accidents in Liquid Metal cooled Fast Breeder Reactors (LMFBR) and SIMMER (CEA (France) and JAEA (Japan)) for LMFBR disrupted core analysis.

But in whole, the experience in the code development, verification and application is much more extensive for light water reactors than for fast reactors.

So for the fast reactors there is the critical task to develop and introduce into practice the system of modern codes allowing to estimate the safety margins and radioactivity release, if necessary.

The importance and role of the computer codes increases all the time. Codes allow improvement of the engineering design that leads to increase in the reactor installation and fuel cycle productivity; replacement of high-cost experiments with numerical simulations preserving high safety standards, ecological and public safety.

Thought the new generation liquid metal NPP designs have increased safety features it is nevertheless necessary to have an instrument for detailed analysis of the broad spectrum of phenomena taking place on the NPP, including accidents like:

- Transient - OverPower (TOP);
- Loss-Of-Flow (LOF);
- Loss-Of-Heat-Sink (LOHS);
- OverCooling-of-the-primary-loop (OVC)
- Worst-case-Scenario (WS).

Those general positions allow to formulate the requirements to the system of codes for fast reactors nuclear safety justification.

2. Common requirements

The system of codes for fast reactors safety analysis has to meet the following requirements:

- First principles modeling and accounting for the design features;
- Coupled simulation of regimes for normal operation, deviations from normal operation and accidents;
- Flexible topology of themohydraulic circuits, schemes and equipment;
- Modern and effective computational algorithms and numeric schemes compatible with high performance computation systems.

The contemporary systems of codes should contain the set of subsidiary codes and databases:

- Material properties database, including properties of liquid metals, in vessel structural materials etc.;
- Codes for uncertainty and sensitivity analysis;
- Converters from three-dimensional CAD systems to the computer codes formats;
- Graphic user interfaces.

Based on the list of phenomena critically important for NPP safety and list of phenomena taking place during NPP operation under normal and accident conditions, the integrated system of codes has to include the following coupled modules:

- Thermal hydraulic;
- Neutron;
- Transport of gamma radiations, radiative heat generation in the structures;
- Thermomechanics including models for fuel rod claddings, core and its surrounding structures;
- Fuel rod behavior module, release and transport of fission products in the fuel;
- Materials activation module;
- Transport module of activity, fission and corrosion products in the coolant circulation loops and in the NPP compartments;
- Module of impact on the environment and population.

Code adequacy should be confirmed by the experimental data including data available from national and international experimental programs.

As an example of realization of general requirements for the safety assessments of fast reactors below the status of development and verification of codes EUCLID and SOCRAT-BN is discussed.

3. Status and perspectives of the new generation EUCLID code development

Development of the integrated system of codes EUCLID takes the central place in the work program for the codes under the Russian Federal Target Program "A new generation of nuclear power technologies up to 2010-2015 and in perspective up to 2020". The main advantage of the EUCLID code is its flexibility in relation to the type of simulated coolants, fuels, and the geometry of the reactor core, and the ability to perform computer simulations with various levels of accuracy.

Complex software architecture of the EUCLID code is based on the common standards for the development of computer codes and a common format of input data for different modules. The coupling of different models and modules in the EUCLID code is done through specially developed interfaces by modern programming techniques based on object-oriented generalized data structures and methods of their processing.

The EUCLID code applications should cover the following areas:

- Safety analysis and justification of new generation of nuclear power plants under normal and accidental conditions;
- Comparison of alternative projects of NPP;
- Comparison of alternative sites for the NPP;
- Analysis and justifications of SAMG and emergency plans.

Below we consider the basic requirements to the components of the EUCLID code and components included in its first version EUCLID/V1.

Neutron-physical module. Neutron-physical processes in the EUCLID code are simulated on the basis of diffusion (the first version of the code EUCLID/V1) and kinetic (the second version of the code EUCLID/V2) approximations.

Code GUITAR.A is used as the diffusion neutron-physical module in the first version of the code EUCLID. As the basis for development of the GUITAR.A code, Russian well-known certified GEFEST code was taken [1]. The simulation of the reactor neutron field using code GUITAR.A can be done in various approximations using the model of a homogeneous presentation of the assembly (certain fuel assembly corresponds to one computational point on the plan). The GUITAR.A code considers design features of the LFR BREST control rods (rods located in the central area of the fuel assembly). In case of calculations in the approximation of complex diffusion GUITAR.A takes into account the heterogeneity of FA / CR design by using of two methods:

- First, the 3D problem for seven fuel assemblies is solved in the fuel rod approximation – a control rod surrounded by six fuel assemblies, and on the base of calculated neutron field the convolution of constants is made for control rods.
- Second, analysis for the same problem is performed in three directions in the plane using S_n-method and the diffusion approximation.

Based on comparison of these two approaches the so-called factors of discontinuity are obtained at the cell boundaries. Obtained constants and discontinuity factors in turn are used in the reactor calculation.

Thermohydraulic module. Thermohydraulic module of the code EUCLID should allow simulating of non-stationary processes in reactor loops with different types of coolant: liquid sodium, molten lead, eutectic lead-bismuth, etc., as well as different combinations of the coolant and the working medium. Thermohydraulic module in first version of the code EUCLID/V1 should simulate processes using the channel approximation (so-called system thermohydraulic codes), in the second version – using sub-channel and porous medium approximations.

In the first version of the code EUCLID code an improved best estimate HYDRA-IBRAE/LM code is used as thermohydraulic module. The code is intended for simulation of the thermohydraulic phenomena in the reactor loops with lead-bismuth, lead and sodium coolants and with option to simulate water loops. Distinctive features of the code are universality towards the type of fluid, application of up-to-date databases with the properties of coolants and closing relations, high computing speed and verification on the available experimental data base. In the code it is possible to calculate non-condensable gases using various approximations. For extending the code functionality it is provided with a set of specialized software modules, which allow simulating dynamics of individual items of equipment and various processes. Code is designed using object-oriented programming language C++, using a hierarchical approach, encapsulation, and inheritance.

The Fuel Rod Module is used to model processes taking place in a fast reactor fuel rod with different types of nuclear fuel and simulates the following physical processes:

- Heat exchange between the cladding and the coolant taking into account the temperature distribution in the fuel pellet, gas gap and cladding, and their properties dependence on the temperature, relative density and burn-up;
- Stress-strain state and degradation of the cladding with the open and closed gas gap;
- Fuel pellet resizing due to the thermal expansion and swelling caused by the accumulation of gaseous fission products;
- Cladding material properties modification due to the accumulation of radiation damage.

The advanced fuel rod module, which is to be included in EUCLID/V2, will allow to simulate microstructural changes in the fuel and the release of fission products under the cladding using a mechanistic approach based on modern physical models (instead simplified correlations or parametric models) developed and verified on a wide range of experiments (both small scale and large scale experiments, including pile experiments).

The work plan stipulates a step-by-step development and integration of the following models:

- Accumulation and migration of fission products in the fuel matrix, subject to the conditions of irradiation;
- Swelling of the fuel pellet and cladding under irradiation;
- Release of fission gas and hydrogen from the fuel matrix under the cladding used for the calculation of the pressure under the cladding and thermal conductivity of the gas gap between the fuel and the cladding;
- Formation of the columnar grains zone (accounting for enhanced swelling of such a zone) and growth of the fuel pellet central hole;
- Thermochemical state of the fuel, including a representative set of fission products and interactions between individual components;
- Formation of solid deposits on the surface of the oxide fuel core caused by migration of Cs (so-called JOG-structures), leading to changes in the thermal conductivity of the gas gap, Te release under the cladding to take into account its corrosive effects on the cladding.

The Mass Transfer Module, the module of transfer of fission products, activation products and corrosion products should include:

- Formation and evolution of a protective oxide film on the surface of constructional materials;
- Release of constructional materials components into the coolant in the form of metal or oxide compounds in solution or in the form of dispersed particles;
- Generation of activation products and their impurities in the reactor core;
- Release of fission products and actinides into the coolant after the cladding depressurization, their chemical interactions with the coolant and with structural materials;

- Flow of hydrogen, water and impurities into the coolant in the case of inter-loop leaks, chemical interactions of hydrogen-containing reagents with the coolant and its impurities, structural materials and sediments;
- Inflow of air to the coolant after the primary loop depressurization, chemical interaction of air with coolant and its impurities, structural materials and sediments;
- Tritium generation, transfer along the loop and removal, chemical interaction of tritium with the coolant and its impurities, structural materials and sediments.

Currently some physical models and stand-alone programs, which will be implemented in the EUCLID code, are being developed.

The Module of transport of radioactive and chemically hazardous substances in the environment including migration of radionuclides in the atmosphere and water, should include the following components:

- Calculation of release and discharge characteristics based on the results of the integral reactor code predictions;
- Input of meteorological information;
- Radioactive substances transport module in the atmosphere (atmospheric transport) and their deposition on the surface;
- Simulation of radionuclides transport in water reservoirs located nearby NPP, as well as in sea water of the foreshore;
- Analysis of radiation doses from clouds, contaminated surfaces and internal irradiation caused by the inhalation;
- Evaluation unit of internal radiation doses of people due to the intake of radionuclides in the human body through the food chain;
- Health risk assessment of the population living in the placement of NPP by emissions and discharges of radioactive substances into the environment during normal operation of NPP and in the case of accidents;
- Relative risk estimation of operating NPP in the future, or its change to the traditional sources of energy on fossil fuels;
- Assessment of economic consequences of NPP operating in the region of its location.

At present, the first version of the EUCLID code has been developed, it consists of the thermohydraulic, neutron-physical and fuel rod modules. Engineering calculations of reactors with lead and sodium coolants, including cross-verification calculations against certified codes used by designers of SFR and LFR NPPs have been started. Step-by-step integration of individual software modules and their verification as a part of a system is in progress.

4. Current status of SOCRAT-BN code for sodium fast reactors severe accident analyses

This time, a number of modules and models for the EUCLID code are designed and tested in a frame of SOCRAT-BN code [2] which was developed for simulation of sodium fast reactor behavior under severe accident conditions.

SOCRAT-BN code is based on a SOCRAT/V1 code, certified for light water reactors severe accident analyses.

The general structure of SOCRAT-BN code is presented in Fig.1.

There are two main computational blocks in a code structure. First – for a steady-state calculations, second – for analyses of transients.

Steady-state block is developed for assessment of reactor state before the accident. The main goal is to model a realistic initial and boundary conditions. There are three modules in this block:

1. Neutron-physics module:

— 3D neutron field simulation accounting for the behavior of fuel nuclide composition depending on time and fuel campaign;
— Neutron fluency simulation.

2. Thermal hydraulic module: Coupled thermal hydraulic and neutron-physical steady-state simulation in a fuel campaign time scale approach.
3. Steady-state fuel rod module for a LMFBR fuel simulation.

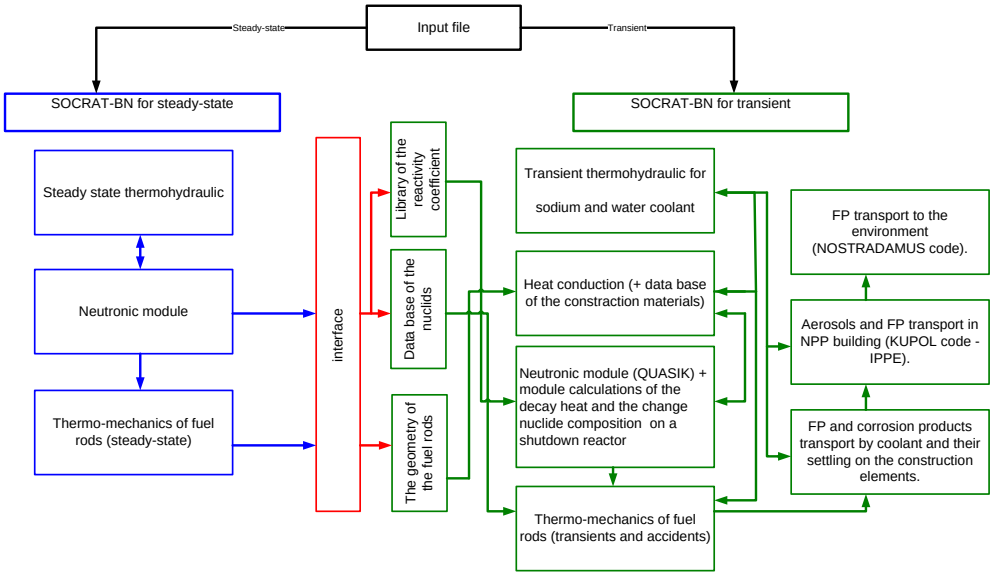

FIG. 1. General structure of the integral code SOCRAT-BN

Transient block includes a range of models and modules for a coupled simulation of accidents in a LMFBR – from the initial event up to the fission products release into atmosphere and consequent FP transport.

SOCRAT-BN code validation matrix consists of two main parts: in-pile experiments and out-of-pile experiments.

Out-of-pile experiments are mainly used for code verification against separate effect test data. These experiments devoted for a specific phenomena investigation allow us to simulate a wider range of processes, which is impossible to investigate on real reactor In-pile experiments devoted for an assessment of integral effects.

The most important phenomena from SOCRAT-BN whole list is heat exchange and hydrodynamic of coolant in similar-to-reactor conditions. Below an example of two-phase sodium flow simulation is presented for a pipe with inner diameter 6 mm. These experiments were performed in 1980-1982, Italy (ISPRA) [3]. We use these tests for validation of closure correlations – wall friction for a single-phase and two-phase sodium flow.

Basic parameters of the experiments are presented in the table 1. Test-section scheme is presented in the Fig.2.

Table 1. Experimental conditions

№	Volume flow, 10^{-6} m^3/s	Outer pressure, bar	Inlet temperature, K	Power, kW
1	75÷230	1,0	838	26,6
2	30÷120	1,0	843	26,319

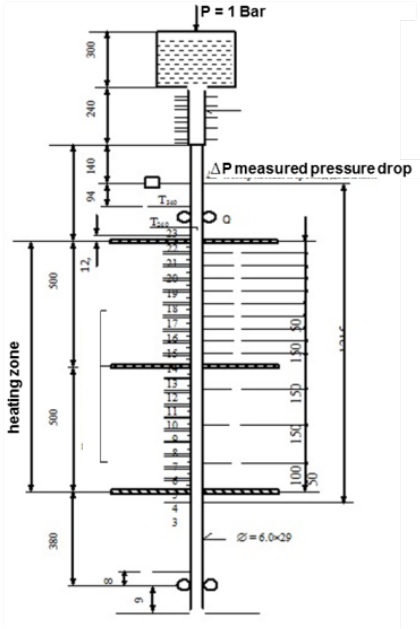

FIG. 2. Test-section nodalization

Results of SOCRAT-BN calculation data comparison against experimental data are presented in the Fig.3.

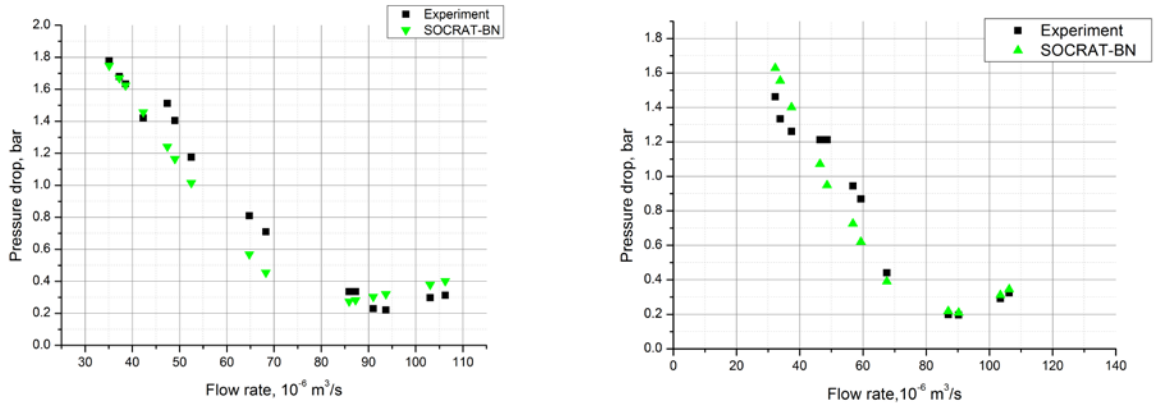

a) b)

FIG. 3. Pressure drop dependence from a sodium volume flow a) – q=1.38 MW/m^2, b) – q=1.27 MW/m^2

These experiments include the two-phase sodium flow regime (minimum observed at the experimental curve corresponds to transition from single-phase to two-phase sodium flow) with a mass void fraction X in a range from 1.9 to 15 %, which corresponds to the volume void fraction range α from 79 % to 95 % [3]. From Fig 3 one can conclude that there is a reasonable agreement of SOCRAT-BN results with experimental data.

In-pile experiments simulation allows us to validate a coupled work of the set of different thermal-hydraulic models which are implemented in SOCRAT-BN code. As an example some results of the transient regime for BN-600 simulation are described below. Nodalization scheme of the BN-600 reactor [4] is presented in the Fig.4. The main feature of this scheme is the detailed description of the reactor vessel with the core channels, intermediate heat exchangers, secondary side loops and steam generators. The third loop is simulated as boundary condition.

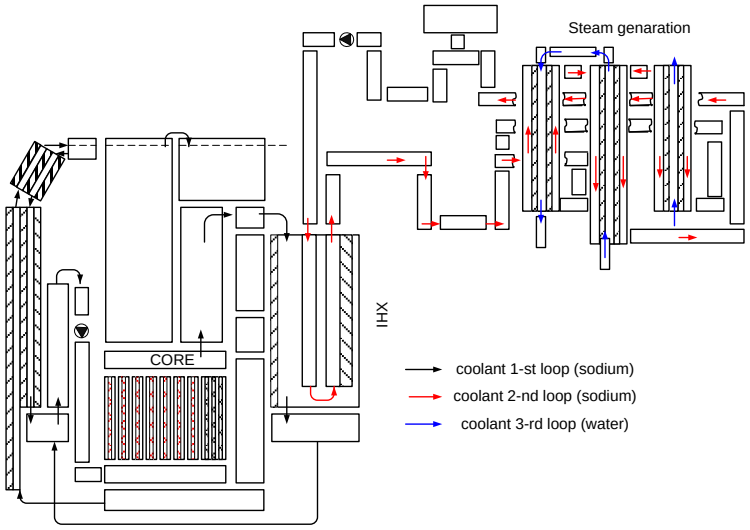

FIG. 4. Nodalization scheme of the BN-600 reactor

In the test presented below the reactor scram at 35% power level was analyzed which led to the automatic reduction of coolant flow rates through the primary and secondary circuits [4]. In the Fig.5 there is a time dependence of the core outlet temperature, inlet and outlet temperature of the heat-exchanger (primary and secondary sides) for this regime.

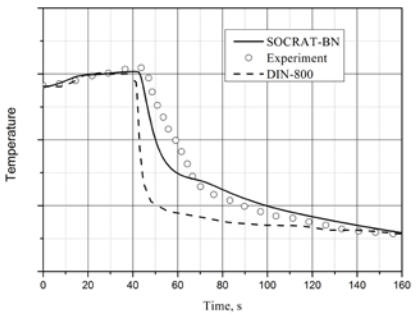

a)

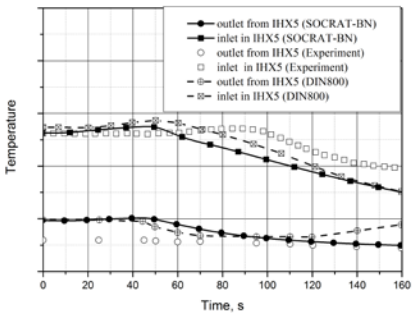

b)

FIG. 5.Time dependence of the core outlet temperature: a) – inlet core sodium temperature; b) – inlet and outlet IHX sodium temperature

From Fig. 5 one can conclude that SCORAT-BN results are in the good agreement with the measured data (relative error about 5%).

5. Summary

In the paper some results achieved on the development of the system of codes for the safety analysis of fast reactors and justification are presented.

It is shown that universal new generation EUCLID code after the initial phase of development allows to simulate neutronic, thermohydraulic and thermo-mechanic processes in a core of the liquid metal reactor in a coupled manner. It is assumed that the work on the development, verification and validation of the code will be completed accordingly to the program of work. Computer code of new generation based on the modern physical and mathematical models will be distributed to design institutions to be used for safety justification of LMR.

Specialized integral computer code SOCRAT-BN for sodium reactors is being validated and used for test applications. The first phase of development will be completed in 2014. Validated models and modules from SOCRAT-BN will be implemented in the EUCLID code.

REFERENCES

[1] Seleznev E.F., Belov A.A. Computational support of BN-600 operation // Atomnaya Energia, V. 108, No. 4, PP. 256-259.

[2] Rtishchev N.A., Chaly R.V., Tarasov A.E., Semenov V.N., Butov A.A., Vozhakov I.S., Zhigach S.A., Kudashov I.G., Usov E.V., Probaturin N.A., Osipov S.L., Gorbunov V.S., Anfimov A.M. «Development of SOCRAT-BN Code». Proceedings of the «International Scientific and Technical Conference - 2012», Moscow, ENTEC, 2012, PP. 348-359.

[3] H.M. Kottowski and C. Savatteri. «Two phase flow liquid metal boiling characteristics». 10.1615/ICHMT.1982.AdvCourHeatTransfNucReactSaf.120, pages 259–286

[4] Bogdanov E.V., Klochkova O.B., Gorbunov V.S., Sobolev V.A. «Improvement of engineering codes for analyzes of dynamics of BN reactors». Thermal Physics conference 2005. Plenary presentation.

[5] Anfimov A.M. et al. "Development of integral codes for analysis of BN reactors severe accidents". Development of integral codes for analysis of BN reactors severe accidents". In proceeding: «Fast sodium reactor technology development» (FR-2011). – N. Novgorod: «OKBM Africantov». – 2011. – p. 97-98.

THERMAL-HYDRAULIC ASSESSMENT OF HLM-COOLED PIN BUNDLE IN CIRCE POOL FACILITY

M. TARANTINO*[1], I. DI PIAZZA[1], P. AGOSTINI[1], P. GAGGINI[2], D. MARTELLI[3], N. FORGIONE[3]

1. Italian National Agency for New Technologies, Energy and Sustainable Economic Development, C.R. ENEA Brasimone, Italy
2. Italian National Agency for New Technologies, Energy and Sustainable Economic Development, C.R. ENEA Bologna, Italy
3. University of Pisa, Department of Civil and Industrial Engineering (DICI) Largo Lazzarino, Pisa, Italy

*Corresponding Author: mariano.tarantino@enea.it (tel. +39 0534 801 262, fax +39 0534 801 250)

Abstract

Since the Lead-cooled Fast Reactor (LFR) has been conceptualized in the frame of GEN IV International Forum (GIF), ENEA is strongly involved on the HLM technology development.
Currently ENEA has implemented large competencies and capabilities in the field of HLM thermal-hydraulic, coolant technology, material for high temperature applications, corrosion and material protection, heat transfer and removal, component development and testing, remote maintenance, procedure definition and coolant handling. In this frame the CIRCE pool facility has been refurbished to host a suitable test section able to thermal-hydraulically simulate the primary system of a HLM cooled pool reactor. In particular a fuel pin bundle simulator (FPS) has been installed in the CIRCE pool. It has been conceived with a thermal power of about 1 MW and a linear power up to 25 kW/m, relevant values for a LMFR. It consist of 37 fuel pins (electrically simulated) placed on a hexagonal lattice with a pitch to diameter ratio of 1.8. The pins have a diameter of 8.2 mm and an active length of 1 m. Along the FPS, three spacer grid properly designed by ENEA have been installed. The FPS has been deeply instrumented by several thermocouples. In particular three sections of the FPS have been instrumented to monitor the heat transfer coefficient along the bundle as well as the cladding temperature in different rank of sub-channels. A first set of experiments were run to investigate the thermal-hydraulic behavior of the fuel pin bundle both under forced (by gas lift) and buoyancy driven circulation into the pool. The paper reports the experimental data carried out as well as a preliminary analysis and discussion, also in comparison with CFD calculations performed by CFX code.

1. INTRODUCTION

With the growing lack of fossil fuels, their increasing costs and the problem of CO2 emissions, energy is one of the critical problems to be faced by our society. Nuclear fission can be a part of a sustainable energy mix, although safety and waste issues have to be considered and managed carefully.
Presently, the European Union produces 35% of its electricity via nuclear fission in so-called second and third generation light water reactors (LWR). In this process about 2500 tons of spent fuel is generated. It contains 25 tons of Pu, 3.5 tons of minor actinides (MA, like Np, Am, and Cm) and 3 tons of long-lived fission products (LLFP).
Nuclear waste must be managed with in an appropriate way. The current adapted approach is geological disposal, possibly preceded by used fuel reprocessing. This latter depends on fuel cycle choices and waste management policies of individual country. In any case, the time scale involved in geological disposal exceeds that of the history of accumulated technological knowledge. As a result geological disposal of nuclear waste does suffer from public acceptance problems.
In various studies, partitioning and transmutation (P&T) in critical and/or sub-critical fast spectrum transmuters has been identified as a way to reduce the volume and the decay time of nuclear waste. This reduces the required monitoring period to technologically feasible and manageable time scales. Also in the framework of the GEN IV initiative this approach has been put forward.
At European level a collaborative effort supported by the European Commission (EC) and European research institutes and industries was started to bring advanced fuel cycles and the P&T strategy together in order to investigate its economic and technical feasibility. The exploratory research done in the field and the launch of the Sustainable Nuclear Energy Technology Platform (SNE-TP) in 2007 lead to a joined effort from the European nuclear fission research community to issue a Strategic Research Agenda (SRA) that describes the roadmap towards sustainable nuclear fission energy.
SNE-TP community identifies the sodium fast reactor technology as the reference but also highlights the need for the development of an alternative track with lead or gas cooling. In addition, the need for R&D activities in

support of accelerator driven systems (ADS) was stressed to allow the demonstration of ADS technology by the construction of the first ADS Demo facility (MYRRHA).
With regard to alternative fast reactor technologies as described in the SRA, lead cooled fast reactor (LFR) systems are very promising in meeting the Gen IV requirements in terms of sustainability, economics, safety and reliability and proliferation resistance & physical protection [1]. This assessment is based on inherent properties of the reactor coolant and on basic design choices.
In the European Strategic Nuclear Infrastructure Initiative (ESNII) Implementation plan, the roadmap for the development, design construction and operation of a lead cooled fast reactor is put out. The conceptual design of a LFR Demonstrator (ALFRED - Advanced Lead Fast Reactor European Demonstrator) is foreseen for 2013.

2. The CIRCE Experiment

In the frame of the National Program (ENEA – Minister of Economic Development Program Agreement) on Gen. IV Reactors Development, ENEA assumed the commitment to design, implement and carry out a large scale integral test named CIRCE experiment. The main objective of CIRCE experiment is to investigate the thermal-hydraulic behaviour of a LFR primary system both under nominal condition and transient scenario.
To achieve these goals the CIRCE large scale facility, already representative of a HLM pool-type reactor, has been fitted with a DHR heat exchanger and suitable instrumentations. The defined experiment will be performed on the CIRCE large scale facility at the ENEA Brasimone Research Centre, where an appropriate test section was erected in the frame of the EUROTRANS project [4] [5], and properly up-graded to match the above depicted requirements.

2.1. The CIRCE Facility and ICE Test Section

CIRCE basically consists of a cylindrical vessel (Main Vessel S100) filled with about 70 tons of molten Lead-Bismuth Eutectic (LBE) with argon cover gas and recirculation system, LBE heating and cooling systems, several test sections welded to and hung from bolted vessel heads for separate-effect and integral testing, and auxiliary equipment for eutectic circulation [5]. The facility is complete of a LBE storage tank (S200), of a small LBE transfer tank (S300) and of the data acquisition system. The main vessel S100 consists of a vertical vessel 8500 mm height, connected by gates to the other systems, from both the LBE and gas sides. It is equipped with electrical heating cables, installed on its bottom and lateral surface. This heating system allows operating in a temperature range of 200 ÷ 400°C. The main vessel is also equipped by a skimming line and a passive pressure safety system, in order to guarantee the LBE top level and to prevent accidental overpressures.
The ICE test section has been designed to reproduce, as better as possible, the thermal-hydraulic behaviour of the XT-ADS and EFIT primary system [6] [7]. The ICE test section, to be placed in the CIRCE main vessel (S100), consists of the following main components, as depicted in Figure 1.

- Downcomer : it is the volume between the test section and the main vessel which allows the hydrodynamic connection between the outlet section of the Heat Exchanger (HX) with the inlet section of the feeding conduit.
- Flow Meter: it is a Venturi-Boccaglio flow meter. Bubble tubes [8] are adopted to measure the pressure gradient along the throat of the Venturi pipe.
- Fuel Pin Simulator (FPS): it is a mechanical structure needed to take on the Heat Source (HS). It is connected in the lower section to the flow meter, and in the upper section is hydraulically linked to the riser, ensuring the continuity of the main flow path.
- Riser: it is a pipe connecting the fitting volume with the separator. In the lower section, a nozzle is installed to allow the argon injection.
- Separator: it is a volume needed to connect the riser with the HX. It allows the separation of the LBE flowing downward into the HX from the Argon flowing in the test section cover gas through the free surface. Moreover, the separator assures that the overall LBE flow rate flows directly into the HX (shell – side) before falling down in the downcomer.
- Heat Exchanger [8]: it corresponds to the heat sink of the system at full power. It consist of double-wall bayonet tubes (with helium gap) feed by low pressure boiling water. It has a thermal duty of 800 kW.
- Decay Heat Removal: it corresponds to the heat sink of the system in the case of DHR scenario. It is hydraulically de-coupled by the primary system being placed into the downcomer. The decay heat removal heat exchanger has been designed to have a thermal duty of 40 kW, which represents the 5% of the ICE nominal power (800 kW).It is feed by low pressure air.

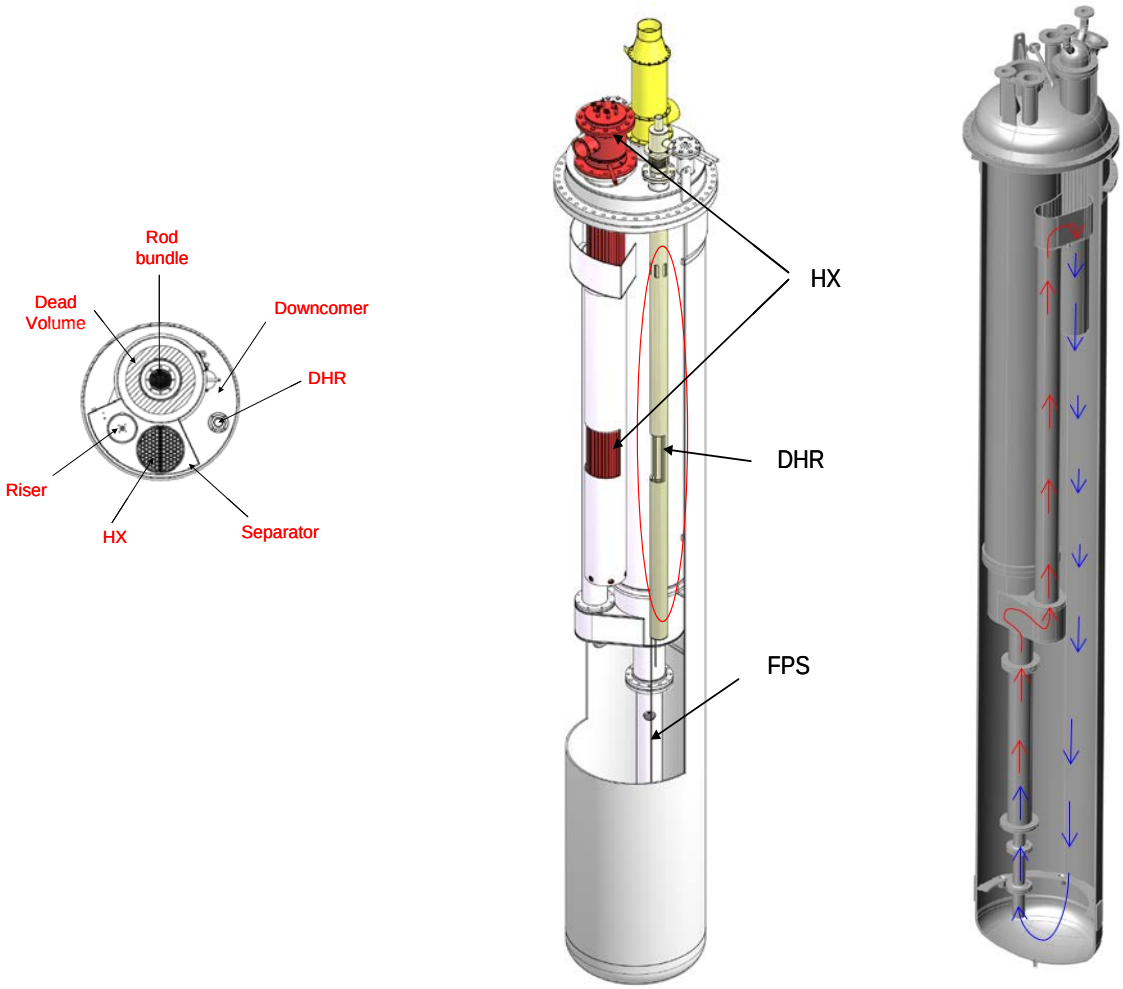

Figure 1 ICE Test Section Overview

2.1. Fuel Pin Simulator

The ICE heat source consists of a pin bundle made by electrical heaters with a nominal thermal power of 800 kW; it has been designed to achieve a pin power density of 500 W/cm^3 and an average liquid metal velocity of 1 m/s, in accordance with the reference values adopted for LMFR cooled by lead. The ICE heat source consists of 37 pins placed in a wrapped hexagonal lattice with a pitch to diameter ratio of 1.8 (see Figure 2). Each pin has an outer diameter of 8.2 mm, a power about 25 kW and a wall heat flux of 1 MW/m^2. The foreseen active length is 1000 mm and the adopted cladding material is AISI 316L. To get an average LBE velocity of 1 m/s, a flow rate of 55.2 kg/s is needed through the HS. To promote the circulation along the ICE test section, the gas lift pumping system has been adopted. The gas lift technique was successfully tested and qualified during the previous experimental campaigns performed in CIRCE [8] and a pressure head of 40 kPa is available to promote the LBE circulation along the flow path. The fuel rods inside the heat source are simulated by electrical pins.

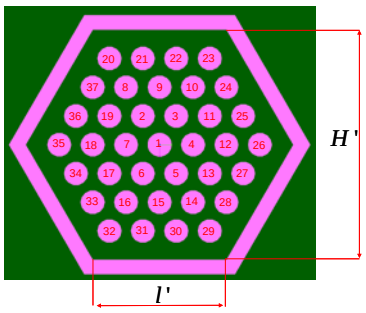

Figure 2. Cross section of the ICE Heat Source (l'=55.4 mm, H'=96 mm)

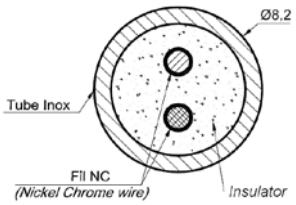

Figure 3. Cross section of the pin bifilar type (active part)

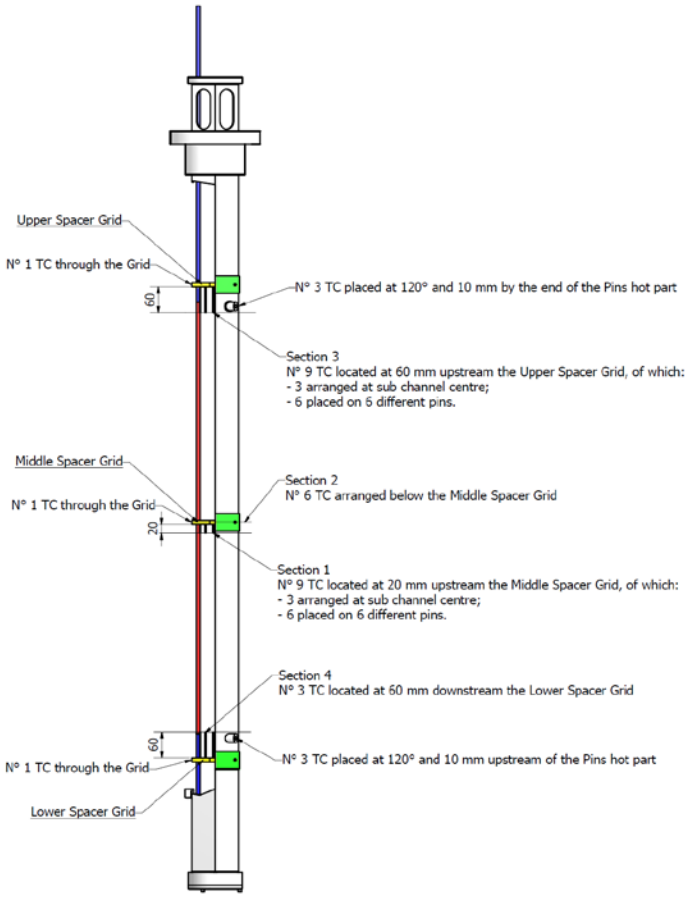

Figure 4. Fuel Pin Simulator sketch and measurement sections

The electrical pin adopts a double wire solution geometry for the pin manufacturing, as reported in Figure 3. Due to the internal geometry adopted for the Bifilar-type pins, the thermal flux around the pins is not uniform. Inside the Heat Source, the relative position between the pin bundle and the wrapper is assured by three appropriate grid assemblies (see Figure 4) placed along the axis of the component and fixed to the wrapper. The upper and lower spacer grids are placed at the interface between the active and non-active length of the pins to enclose the mixing zones. The middle spacer grid is placed in the middle section of the bundle active length. From the hydraulic point of view, the FPS assures that the overall LBE flow rate runs along the HS, without any by-pass. Moreover, the FPS allows to couple the HS with the test section.

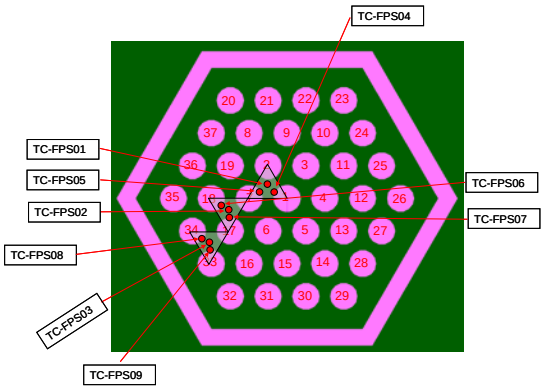

Figure 5. View of the section 1 dedicated to the HTC measurement. In red the TCs installed, 20 mm below the middle spacer grid.

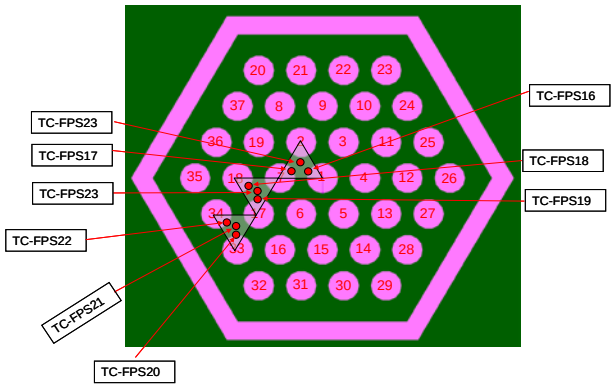

Figure 6. View of the section 3 dedicated to the HTC measurement. In red the TCs installed, 60 mm below the upper grid.

The active zone of the fuel pin simulator was instrumented by several thermocouples and three different section have been defined.

Section 1: 20 mm upstream the middle spacer grid. In this section three different sub-channels have been identified for the HTC measurement at the middle height of the bundle (see Figure 5). In each sub-channels both

pin cladding and LBE bulk temperature are measured by TCs (9)
Section 2: on the matching surface between the middle spacer grid and the fuel pins. In this section the same sub-channels have been identified as in the section 1, aiming for the hot spot factor evaluation due to the installation of the spacer grid itself. In this case only the pin cladding temperature is monitored by TCs (6).
Section 3: 60 mm upstream the upper spacer grid. In this section the same sub-channels have been identified as in the section 1 and 2 for the HTC measurement at the upper height of the bundle (Figure 6). In each sub-channels both pin cladding and LBE bulk temperature are measured by TCs (9).

3. Experiment Description and Results

The first experimental run performed in the frame of the CIRCE Experiment is a protected loss of flow (PLOF) and protected loss of heat sink (PLOH). The test aiming to simulate the loss of the main heat exchanger (HX), the consequent scram of the core, and activation of the DHR system to remove the decay heat power (5% of the nominal value) in a HLM nuclear system. During the transition the gas lift will be stopped to simulate the pure transition from the forced to the natural circulation under the decay heat removal regime. The test will be performed starting from the nominal conditions, and performing the PLOH+LOF transition. The following main parameter will be adopted:

Nominal Steady State

- thermal power in the HS:700-800 kW
- HLM flow rate: 55 kg/s (by gas lift)
- ΔT along the HS: 100°C
- average velocity into the HS:1m/s
- average temperature along the main flow path: 350°C
- vessel heating system: not-active
- HX flow rate: 0.5 kg/s
- DHR: not active
- duration of the test: 3-5 hour of steady state

PLOH+LOF transient

- Isolation of the main HX (isolating the feed water)
- Core "scram" at 20-50 kW (decay power)
- start-up of the DHR-system (air flow rate of 0.3 kg/s)
- "Main pump" turn-off (the gas injection is interrupted)
- vessel heating system: not-active
- duration of the test: 36-72 hours

3.1. Experimental Results

Figure 7 shows the power transient during the run of the experiment. The experiment starts with a nominal power of 730 kW, and after 7 hours the transition to 50 kW takes place.
During the full power run, the gas is injected into the riser to promote the main circulation along the primary system, with an argon flow rate of 1.8 Nl/s. The primary flow rate, which quickly reaches its nominal value, is around 55-58 kg/s. That is the same flow rate which flows through the FPS, being no bypass. In the first stage the LBE flow rate shows strong oscillations (Figure 7) that are related to use of volumetric blowers to inject the gas into the pool. After few hours a check valve has been put in service to dump such oscillations.
After the transition from the full power to the decay power, the blowers are shut down to simulate the station black-out and the transition from the forced to the natural circulation into the pool takes place. The main flow rate under natural circulation is close around 8 kg/s, which is the 14% of the nominal flow rate. During the full power run the HX is fed by water with a flow rate of 0.65 kg/s and the water pressure at the inlet of the bayonet tubes (upward the manifold) is close around 2 bar. After the station black-out simulation the feedwater is closed and the water into the HX falls down, as the thermal power removed by the HX.
As can be noted, during the full power run the power removed by the HX is close around 620-650 kW. It is less than the power supplied by the FPS of about 100 kW. Such discrepancy is strongly related to the power losses through the vessel (the heating cable are switched off during the test, thus the losses are not replaced) and the technique used to measure the removed power through the HX. Indeed, being not available a direct measurement on the water side (the steam is directly discharged in atmosphere and a measurement of the steam quality is not available), the thermal duty of the HX is calculated by an energy balance on the LBE side by the measurement of LBE temperature at the inlet and outlet section. Such measurements, although accurate at the inlet section, are not so accurate at the outlet section, where the thermocouples installed (9 TCs) are not able to weight the power exchanged in each subchannels of the HX. As consequence the average temperature at the outlet section of the HX is estimated with a certain uncertainty, which affects the estimation of the whole power exchange by the HX. Anyway, clearly appear by the temperature trends into the pool and into the FPS (Figure 8) that a steady state condition is achieved under the forced circulation at full power after 4-5 hours of transients.
Figure 8 shows the average inlet and outlet temperature through the FPS, and as can be noted a thermal difference of about 80°C is achieved during the full power steady state condition, being the average inlet temperature of 285°C, and the average outlet temperature of 365°C.
The transition from the forced to natural circulation is then simulated at an average temperature through the FPS of 325°C. At the time on which the station black-out is simulated, as the feedwater and gas injection are stopped,

the power into the FPS drops to 50 kW, and the DHR-HX is started. In the experiment here reported the air flow rate through the DHR is 0.22 kg/s, and the removed power (calculated by an energy balance on the air side) is equal to 22 kW.

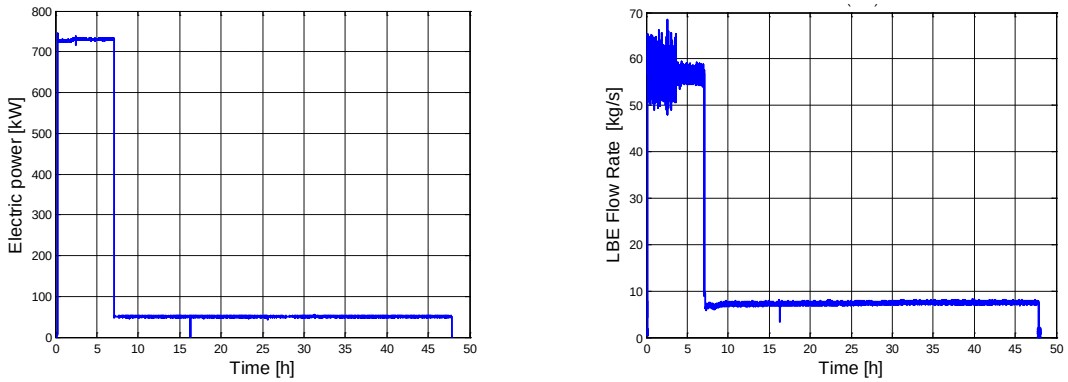

Figure 7. Electrical power supplied to the FPS (left) and LBE flow rate through the primary system measured by the Venturi flow meter (left).

As can be noted (Figure 8), after the transition from the forced to natural circulation the removed power from the DHR-HX and heat losses from the system are not large enough to compensate the decay power into the FPS. After a transient of 40 hours the average temperature into the pool still increases, till to reach 385°C at the outlet section of the FPS. Under the natural circulation flow regime, the thermal difference along the FPS falls down to around 35°C.

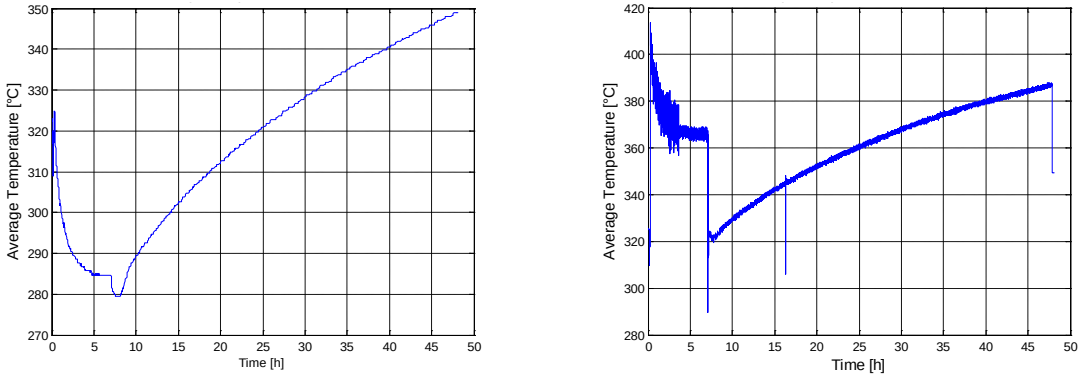

Figure 8. Inlet (left) and outlet (right) average temperature through the FPS.

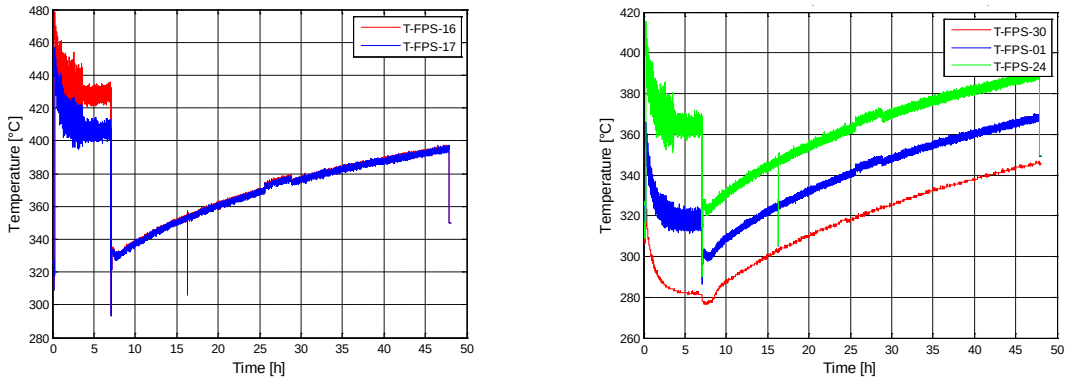

Figure 9. Cladding temperature (right) on the pin 1 and pin 7 of the FPS measured in section 3. LBE temperature (left) measure in the central sub-channel along the active length of the FPS.

Figure 9 reports the cladding temperature trends on the pin 1 and 7 in section 3, which corresponds with the highest cladding temperature in the central sub-channel.
As can be noted, during the full power steady state conditions the maximum temperature is well below 450°C. Between pin 1 (T-FPS-16) and pin 7 (T-FPS-17) there is a difference of about 20-30 °C, which is strongly related to the not-uniformity of the power generation into the electrical heater simulating the fuel pins. After the transitions from the forced to natural circulation the cladding temperatures fall down at 330°C, ad later start to increase continuously with an inertia driven by the thermal inertia of the pool. As can be noted the difference

between the cladding temperature on the pin 1 and 7 are dumped being the wall heat flux strongly reduced during the natural circulation scenario.

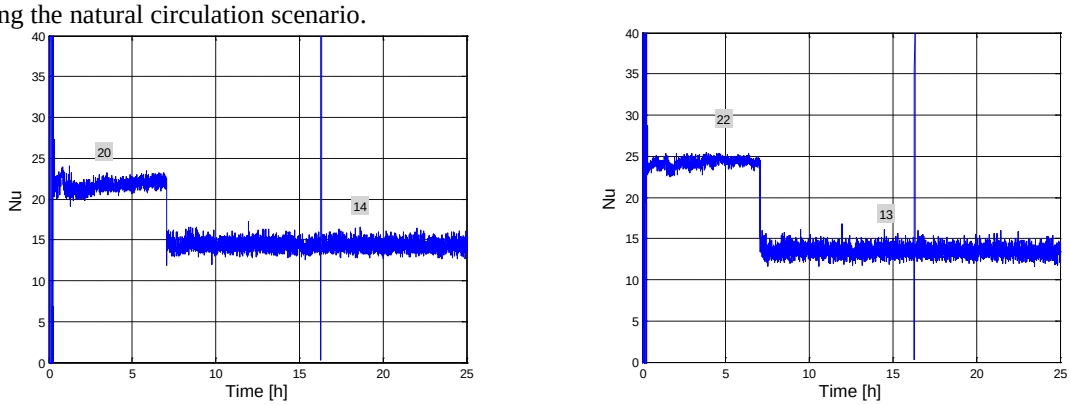

Figure 10. Nu in Section 1 (left) and in Section 3 (right) evaluated into the central sub-channel averaging the cladding temperatures.

In Figure 9 (right) is also reported the LBE bulk temperature measured along the central sub-channel, respectively into the Section 1 (T-FPS-01), Section 3 (T-FPS-024) and Section 4 (T-FPS-030). From the available measurements, clearly appear that the temperature profile into the central sub-channel has a linear trend, as expected for a constant heat flux.
For what concern the heat exchange into the central sub-channel, the Nusselt number has been calculated on the Section 1 and Section 3 assuming as cladding temperature the average temperature between the pin 1 and pin 7 (. As can be noted, the Nusselt number into the Section 1 and 3 matches well, as expected for a fully developed flow, both under forced and natural circulation, going from 20-22 under forced circulation to 13-14 under natural circulation. Moreover, the Nusselt number during the transients reaches soon an asymptotic condition, although the average temperature of the system rise due to the global thermal unbalance (see Figure 10).

4. Comparison with CFD computations

A CFD model of the ICE bundle has been developed and computations have been carried out to compare experimental results with computational results and to have a detailed overview of the local phenomena occurring in the wrapped bundle and in the spacer grid region.
The computational grid has been designed to be accurate for the higher Reynolds number actually encountered during the ICE experiment (with w_0~1 m/s, the sub-channel Reynolds number based on the hydraulic diameter is Re_{sc}~$1.31 \cdot 10^5$). The spatial resolution chosen implies y+~1 in the first node close to the wall in the whole domain; therefore the mechanical viscous sublayer is described by 8-10 grid points. The total number of nodes of the model is about $1.24 \cdot 10^7$. The resolution of the thermal boundary layer is automatically guaranteed, being the Prandtl number of the fluid Pr~0.019. The model is fully structured, includes the conjugate heat transfer in the three spacer grids and the entry non-active zone. The fully grid-independence has been assessed in [10].
The SST (Shear Stress Transport) k-ω model by Menter [12] is extensively used in this work. A second order closure RSM-ω model [11] has been also used; this latter model has separate equations for the various Reynolds Stresses and thus it allows capturing the anisotropy of the turbulence transport.

4.1. Computational Results

Figure 11 shows the streamwise velocity distribution, with the SST turbulence model, in the unperturbed section G0 20 mm upstream of the middle spacer grid, corresponding to one of the measurement section (section 1) of the ICE bundle. From the hydrodynamic point of view, the influence of the wall is limited to the external rank of pins; moreover, the internal side of the external pins appears to be not influenced by the wall boundary layer and the flow features are similar to the internal sub-channels. For the present average streamwise velocity w_0~1 m/s, the velocity maximum in the internal sub-channels is w_{max}~1.25 m/s. For the influence of the wall, in the corner sub-channel the bulk velocity reaches ~0.75 m/s while in the side sub-channels is around ~0.9 m/s.
Figure 12 shows the temperature distribution in the section G0. The most relevant feature is the presence of a cold region (named ‘zone CCC’) in the bulk of the fluid close to the side wrap wall, while the corner sub-channel bulk temperature (zone CCP) is relatively similar to the internal central sub-channel bulk temperature (zone CCI). It is confirmed that the transversal temperature drop between the ‘cold’ region (zone CCC) and the internal central channel bulk (zone CCI) is around 25-30 °C, and it is not negligible if compared with the bulk-wall temperature drop around 50-60 °C.

The reason for the presence of the cold region (zone CCC) in the transversal section is the relatively low power received per unity mass flow rate in that region. In fact, with respect to the internal central sub-channel (zone CCI), there are adiabatic conditions on the wrap wall and the fluid does not receive heat from one side.
Figure 13 shows the vertical lines (generatrix) defined along the corner pin wall to evaluate heat transfer along z in the different regions.
Figure 14 shows the temperature profiles versus z along the three lines defined above in the corner pin. The difference between Line c and Line 1 represents practically the azimuthal temperature difference in the corner pin along z. This temperature drop is ~20-30 °C in the fully developed region with the higher values in the corner region. In the spacer grid zone, due to the grid shape, there is flow acceleration in the corner gap with a sharp minimum along Line 3, and the recirculation region with a local maximum downstream along Line 1; practically there is an azimuthal temperature inversion in the spacer grid region. A relevant feature is that the maximum clad temperature in the most critical pin (corner pin in the corner region, Line c, at the end of the active zone) is always less than 500 °C.

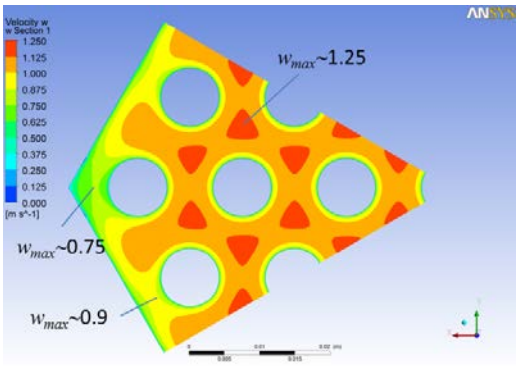

Figure 11. Streamwise velocity distribution in a transversal section 20 m upstream the middle spacer grid (section G0).

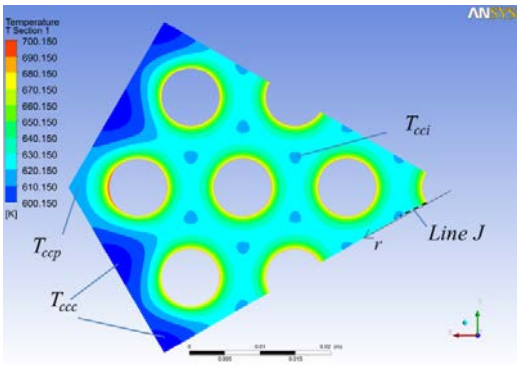

Figure 12. Temperature distribution in a transversal section 20 mm upstream the middle spacer grid (section G0).

This situation is reflected also in the Nusselt number curves represented in Figure 15, according to the 'bulk' Nu_1 definition, with a value much lower (~20) for Line c with respect to Line 1 (~25-28) in the fully developed region.
Regarding the overall Nusselt numbers, two different Nusselt numbers have been defined, namely Nu_1 based on the bulk temperature and Nu_2 based on the central channel temperature and coherent to the experimental HTC measurements. Figure 16 shows the overall Nusselt number Nu_1 versus the sub-channel Reynolds number Re_{sc}, for all the bundles modelled. All the CFD results refer to the STT *k-ω* model. In black dashed line and red pointed line, the Mikityuk and the Ushakov correlations [13] for heat transfer in liquid metal rod bundles are reported respectively. Both correlations are applicable in the present Reynolds number range and for *p/d*=1.8 of the ICE bundle. Results for sub-channel, 37-pin, 19-pin practically coincide, while for the 7-pin bundle Nu_1 is ~10% higher. There is a good agreement with the experimental correlations both in values and in Reynolds-slope in the whole turbulent range.
Figure 17 shows the Nusselt number Nu_2 based on the central channel temperature, versus the sub-channel Reynolds number. The red square symbols represent the preliminary experimental data obtained for the ICE bundle in the CIRCE facility. There is a good agreement between numerical and experimental results with a under-estimation around 15% at the higher Reynolds numbers. It is remarkable that both SST and RSM models provide similar results for the overall heat transfer, and these results are consistent with known correlations and experimental data.
A practical indication of the CFD computations is the maximum clad temperature in the pin bundle.
Figure 18 shows the maximum clad temperature T_{max} in the bundle against the sub-channel Reynolds number under LOFA (q″~50 kW/m^2) and nominal power (q″~1 MW/m^2) versus the sub-channel Reynolds number Re_{sc}; the limiting safety temperature of 550 °C is also indicated.
In LOFA conditions, the temperature is below 400 °C for Reynolds numbers ~10^4; therefore a protected loss of flow does not appear a critical condition if a minimum flow (w_0~0.05-0.1 m/s) can be maintained by natural circulation by means of a DHR. For the nominal wall heat flux q″~1 MW/m^2, the maximum clad temperature reaches 550 °C for Re_{sc}~10^5 and 1000°C for Re_{sc}~2-3·10^4 (w_0~0.2 m/s). Several others sensitivity analysis are reported in [10], for example the study of the influence of the anisotropy of the pin wall heat flux in the ICE bundle.

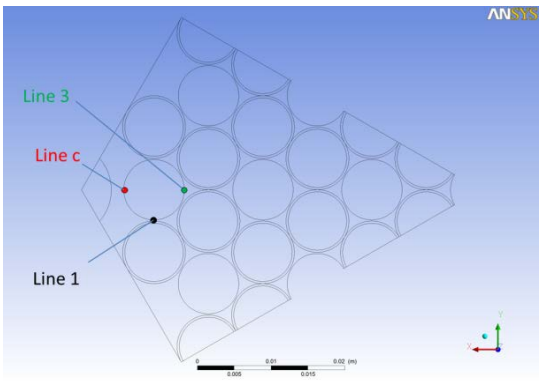

Figure 13. Vertical lines defined in the side pin of the 37-pin model to study the temperature behavior along z.

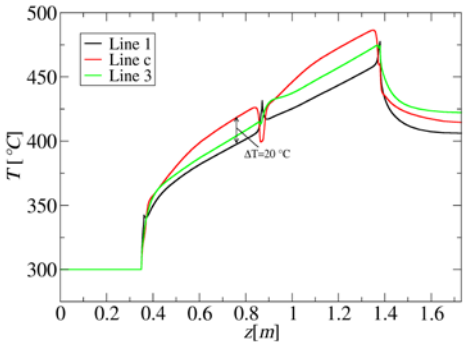

Figure 14. Temperature versus z along the three different vertical lines defined above for the 37-pin model.

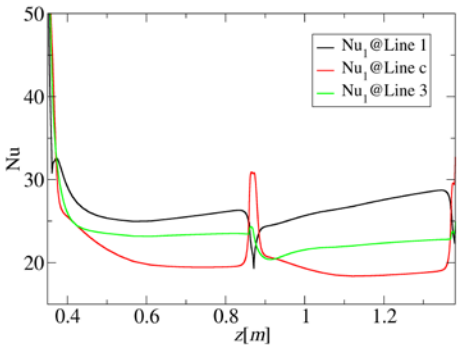

Figure 15. Nusselt number Nu1 versus z along the three different vertical lines defined above for the 37-pin model.

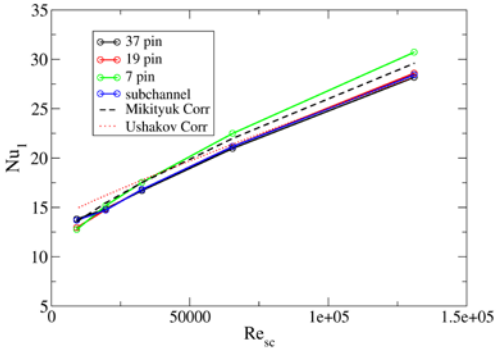

Figure 16. Nusselt number Nu_1 for all the geometries modeled against the sub-channel Reynolds number.

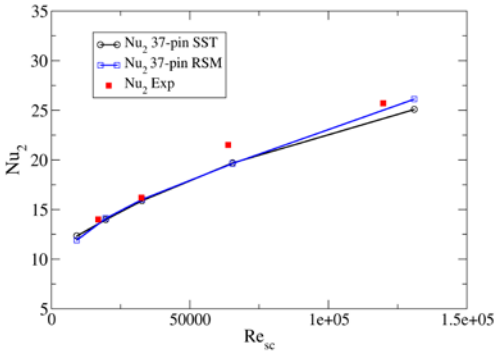

Figure 17. Nusselt number Nu2 against sub-channel Reynolds number: comparison between the CFD–SST numerical model and the preliminary experimental results for the ICE bundle.

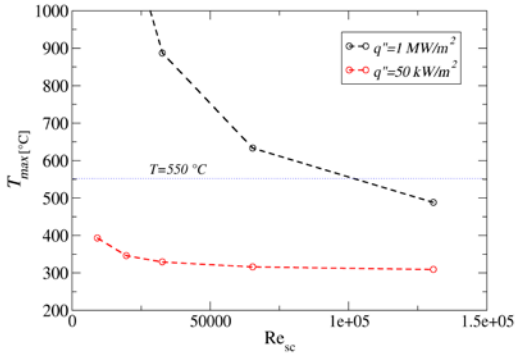

Figure 18. Maximum clad temperature in the bundle against the sub-channel Reynolds number under LOFA and nominal conditions.

5. CONCLUSIONS

The Integral Circulation Experiment, ICE, has been designed and carried out to reproduce the thermal–hydraulic behaviour of primary system pool-type nuclear reactor, cooled by HLM, in a relevant scale (1 MW).
The experiment performed on the CIRCE pool facility consisted of a full power steady state run followed by a protected loss of flow and cold sink (PLOF+PLOH). For the run of the experiment the FPS, representative of LFR fuel assembly, has been deeply instrumented aiming to investigate the thermal-hydraulic behaviour of a fuel bundle cooled by LBE, both under forced and natural circulation. The available instrumentation allowed to evaluate the Nusselt number (and thus the HTC) of the fuel pin bundle, under the transient scenario simulated.

As results, the Nusselt number along the FPS is constant and close around 22 under forced circulation (LBE velocity ~ 1m/s) and full power (q" ~ 80 W/cm^2), and it falls down close around 13 under natural circulation (LBE velocity ~ 0.15 m/s) and decay power (q" ~ 5 W/cm^2). Thus, the results carried out have shown as the primary system of LFR nuclear system is technological feasible.
Other tests will be run, and several operational and accidental transients will be simulated (unprotected loss of flow, unprotected loss of heat sink, protected loss of flow), allowing to characterize in depth the thermal–hydraulic behaviour of a HLM pool system.
Finally, the experimental data already collected during the ICE activity will allow to improve and validate physical model (turbulence model for CFD tools) as well as numerical tools (system codes) when employed on HLM pool system.
In particular, in this first step, a CFD computational study has been carried out on fluid flow and heat transfer in the 37-pin HLM-cooled bundle of the ICE test section. The CFX code has been used for the study and k-ω and Reynolds Stress-ω models have been applied. Comparison with experimental results has been performed on the average heat transfer coefficients at various mass flow rates, from nominal to reduced PLOFA condition.
Several interesting points emerged from the overall analysis of the results:

— A good agreement has been obtained in the comparison with experimental results and known heat transfer correlations for HLM cooled bundles. This would indicate that the turbulent Prandtl number approach used in the turbulence modeling is sufficient to capture the overall heat transfer mechanism; moreover, results indicate that Pr_t~1 is indicated for CFD modeling and simulation of HLM cooled bundles.

— The full 37-pin geometry showed particular features on temperature distribution in the generic unperturbed section far from the spacer grids. In particular, it is evident that the side subchannels have a lower bulk temperature than the central subchannels (~30 °C), due to the presence of the wrap and to the reduced power per unit mass received by the fluid in the side subchannels. The corner pin evidenced an azimuthal temperature distribution due to the different fluid flow and heat transfer conditions on the corner side and on the internal side. This maximum azimuthal temperature difference is ~20 °C in nominal conditions.

As general conclusion, it has been definitely proved that fine-grid CFD with turbulence models is fully applicable to the study of HLM cooled bundles in a wide range of flow conditions.

Acknowledgements

The work has the financial support of the Italian Minister of Economic Development through the Program Agreement with ENEA, PAR2011.

References

[1] L. Cinotti et al. "Lead-cooled system design and challenges in the frame of Generation IV International Forum", Journal of Nuclear Materials, NUMA45871, 2011.
[2] IAEA, Technical Meeting on Fast Reactor Physics and Technology, Kalpakkam, India, 14 - 18 November 2011Conference ID:41429 (TM-41429)
[3] Handbook on Lead-bismuth Eutectic Alloy and Lead Properties, Materials Compatibility, Thermal-hydraulics and Technologies, OECD-NEA 6195, 2007.
[4] Tarantino M., Scaddozzo G., Report ENEA ET-F-S-001, "Test specifications of the Integral Circulation Experiments" Deliverable D. 4.15, DM4 DEMETRA, IP-EUROTRANS, 2006.
[5] Turroni P., Cinotti L. ,Corsini G., Mansani L, "The CIRCE Facility", AccApp'01&ADTTA'01, Nuclear Application in the new Millennium, Reno (Nevada- USA), November 11-15, 2001.
[6] Artioli C," Specification for the EFIT Core and Fuel Element Design", Deliverable D. 1.6, DM1 DESIGN, IP-EUROTRANS, 2006.
[7] Van den Eynde G.," Specification for the XT-ADS Core and Fuel Element Design", Deliverable D. 1.7, DM1 DESIGN, IP-EUROTRANS, 2007.
[8] Benamati G., Foletti C., Forgione N., Oriolo F., Scaddozzo G., Tarantino M., "Experimental study on gas-injection enhanced circulation performed with the CIRCE facility", Nuclear Engineering and Design, vol. 237, pp. 768-777, Iss. 7, 2007.
[9] Di Piazza, M. Scarpa, M. Tarantino, A pre-test CFD analysis of HLM fuel pin bundle, Proceedings of the 20th International Conference on Nuclear Engineering ICONE20, July 30-August 3, 2012, Anaheim, California, USA.
[10] M. Scarpa, ICE bundle 'CFD thermal-hydraulic analysis of HLM cooled rod bundles' Master Thesis, University of Pisa, 2013.
[11] ANSYS CFX Release 13 User Manual
[12] F. R. Menter, Two-equation eddy-viscosity turbulence models for engineering applications, AIAA J, 32, pp.269-289, 1994.
[13] K. Mikityuk, Heat transfer to liquid metal: Review of data and correlations for tube bundles, Nuclear Engineering and Design, vol. 239, 680–687, 2009.

Sensitivity analyses by Generalized Perturbation Theory (GPT) methods applied to GUINEVERE and MYRRHA lead fast reactors.

M. Carta[a], A. Gandini[c], V. Fabrizio[c], V. Peluso[b], G. Bianchini[a], L. Ricci[c]

[a] ENEA C.R. Casaccia, via Anguillarese, 301 - 00123 S. M. di Galeria (Roma) – Italy

[b] ENEA C.R. Bologna, Via Martiri di Monte Sole, 4 - 40129 Bologna – Italy

[c] Univ. of Rome "La Sapienza", Corso Vittorio Emanuele II 224, 00186 Roma – Italy

Abstract. The GUINEVERE experiment (Generation of Uninterrupted Intense NEutrons at the lead VEnus REactor) is an experimental program in support of ADS (Accelerator Driven Systems) and Lead Fast Reactor technologies presently carried out at SCK in Mol (Belgium). GUINEVERE is presently part of the 7th EURATOM FP project FREYA (Fast Reactor Experiments for hYbrid Applications) which started on March 2011. The program aims at supporting experimentally the MYRRHA project, which should start by 2023. The present paper is focused on the analysis, by numerical simulations, of the transferability to the MYRRHA reference system, of the behaviour of selected spectral indexes measured in GUINEVERE following a localized or global perturbation in the core. The analysis, carried out by means of GPT (Generalized Perturbation Theory) methodologies implemented in the ERANOS European neutronic code, consisted in the calculation of the different sensitivity coefficients required for determining the correlation coefficients among analogous integral quantities in GUINEVERE and MYRRHA. To obtain such correlation coefficients the dispersion matrix BOLNA, at 15 energy groups, has been used. The results, which include a discussion on the different calculated sensitivity profiles, show a very good correlation for all the spectral indexes taken into account, especially for the high energy spectral indexes.

INTRODUCTION

Several experiments have been so far performed to provide support to Accelerator Driven Systems (ADS) technology, like MUSE [1] and KUKA [2], and in general to lead cooled subcritical systems. In particular, under this point of view an important role is played by the GUINEVERE (Generation of Uninterrupted Intense NEutrons at the lead VEnus REactor) experimental program [3], launched in 2007 as European project included in the Integrated Project (IP) EUROTRANS of the Sixth EU Framework Programme, and presently part of the FREYA (Fast Reactor Experiments for hYbrid Applications) project [4], started on March 2011, of the Seventh EU Framework Programme. The GUINEVERE program has been conceived and structured to provide a full support to the MYRRHA (Multipurpose hYbrid Research Reactor for Hig-tech Applications) [4] project. The experience, performed by using a modified lay-out of the Venus critical facility located at the Belgium SCK•CEN Mol site, is devoted to perform both critical and subcritical analyses in a lead matrix core. The GUINEVERE subcritical experiments are performed by coupling the subcritical core, having different degrees of subcriticality, to a modified GENEPI accelerator, GENEPI-C [5] (GEnérateur de NEutrons Pulsé Intense-Continue), built by the CNRS in Grenoble, working in current mode and delivering 14 MeV neutrons by bombardment of deuterons on a tritium-target.

An important (and obvious) issue concerning the measurements already performed and to be performed in GUINEVERE is the representativity of such measurements with respect to the reference system MYRRHA, representativity which has to embrace (as much as possible) the most important

neutron properties characterizing this last system, under the point of view of both the normal operation and the safety aspects. The subcritical normal operation includes, for example, the on-line reactivity monitoring of the system, and a large effort is presently done at international level to provide reliable and accurate measurement techniques to face this challenge (far from criticality and in presence of an external source it is not obvious which kind of techniques are best adequate to answer the need). Besides the different kinetics parameters estimation at stake, it is of fundamental importance a reliable characterization of the energy spectrum of the neutron field pertinent to the two facilities GUINEVERE and MYRRHA. In this frame the problem of the transferability to the MYRRHA situation, of selected experimental spectral indexes measured in GUINEVERE is crucial, especially taking into account the MOX+lead+bismuth neutron field present in MYRRHA.
As a preliminary contribution to this general problem, the present paper is focusing on the analysis, by numerical simulations, of the representativity, with respect to analogous quantities relevant to the MYRRHA reference system, of the behaviour of some integral quantities to be measured in the GUINEVERE facility following a localized or global perturbation in the core. The analysis has been carried out by means of different GPT (Generalized Perturbation Theory) calculation routes implemented into the ERANOS European neutronic code [6]. In particular, the analysis has been focused on the behaviour of the spectral indexes Pu-239 fissions/ U-235 fissions, U-238 fissions/ U-235 fissions and Np-237 fissions/ U-235 fissions following a localized (core shell) or global (whole active core) lead (GUINEVERE) or lead-bismuth (MYRRHA) 20% density reduction. The calculations have been performed by modelling the two systems by cylindrical 2D geometries (the only geometries currently allowing a full use, in the ERANOS code, of the GPT potential). To obtain the correlation coefficients the dispersion matrix BOLNA [7], at 15 energy groups, has been used.

GUINEVERE AND MYRRHA FACILITIES

The GUINEVERE critical layout nominally consists of 97 fuel assemblies (91 fuel assemblies + 6 safety rods with fuel followers), on about 60 cm active length (Fig. 1, left). The fuel is metallic uranium 30% enriched in U^{235}. The square core has a side of about 1 meter, and contains 12×12 elements, either fuel or lead. The core is surrounded by a cylindrical lead reflector, about 30 cm thickness in radial direction and about 40 cm height for the upper and lower part.

A schematic layout of the core of the MYRRHA facility (operating in critical mode) is shown in Fig. 1, on the right. Basic features of MYRRHA are a proton accelerator of 600 MeV, a spallation target and a multiplying core with MOX fuel. The spallation target and the coolant are liquid lead-bismuth. The coolant core inlet temperature is 300 °C (assumed in the calculations in this work).

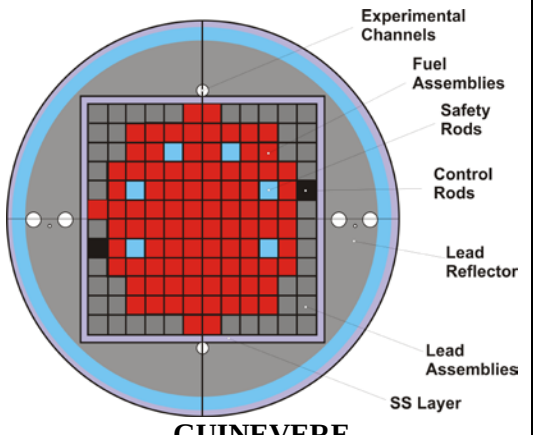

GUINEVERE

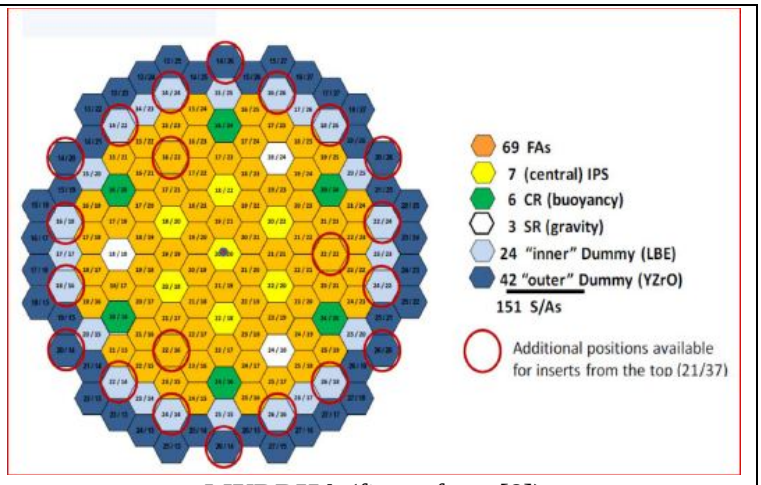

MYRRHA (figure from [8])

***Figure 1** – GUINEVERE and MYRRHA facilities schematic layouts.*

THE THEORETICAL APPROACH

The theoretical approach, shortly recalled here in a very simplified way, is based on the pioneering works on the subject performed by A. Gandini [9]. Let us consider ℓ (ℓ=1,2,...L) calculated integral quantities (reaction rates, spectral indexes) $Q^{cal}_{A,\ell}$ relevant to an experimental facility A (GUINEVERE for example). Such integral quantities depend on some parameters p_j (i.e. evaluated cross sections) relevant to the physical system, and then $Q^{cal}_{A,\ell} = Q^{cal}_{A,\ell}(p_1, p_2, ..., p_J)$. If we assume the first order approximation we can write:

$$Q^{cal}_{A,\ell} = Q^{ex}_{A,\ell}(p^{ex}_1, p^{ex}_2, ..., p^{ex}_J) + \sum_{j=1}^{J} \frac{\partial Q^{cal}_{A,\ell}}{\partial p_j}(p_j - p^{ex}_J)$$

where $Q^{ex}_{A,\ell}(p^{ex}_1, p^{ex}_2, ..., p^{ex}_J)$ are measured integral quantities depending on the experimental parameters p^{ex}_j, with associated variance-covariance dispersion matrix. Afterwards we can define a vector $\mathbf{y_A}$ whose components are the relative deviations $(p^{ex}_J - p_j)/p_j$ and $(Q^{ex}_\ell - Q^{cal}_\ell)/Q^{cal}_\ell$. This vector, with the appropriate constraints, can be minimized via the Lagrange multipliers method assuming as likelihood function of vector $\mathbf{y_A}$ a multivariate Gaussian distribution. This leads to a new estimate random vector $\tilde{\mathbf{y}}_\mathbf{A} = \tilde{\mathbf{y}}_\mathbf{A}(\mathbf{S_A}, \mathbf{D})$ (where $\mathbf{S_A}$ is the sensitivity coefficients matrix for the system A and **D** is the dispersion matrix) whose components are the "best" adjustments obtainable on the basis of the experimental information available from the system A.

The transposition of the information to the reference system B (MYRRHA for example) is then obtained by the relationship:

$$\tilde{\mathbf{y}}_B = \mathbf{S}_B \tilde{\mathbf{y}}_A(\mathbf{S_A}, \mathbf{D})$$

where $\mathbf{S_B}$ is the sensitivity coefficients matrix for the system B. Finally the correlation matrix can be defined as:

$$\mathbf{R_{BA}} = \frac{\mathbf{S_B^T D S_A}}{\sqrt{\mathbf{S_B^T D S_B}}\sqrt{\mathbf{S_A^T D S_A}}}$$

The sensitivity coefficients are calculated by Generalized Perturbation Theory (GPT) methods [10].

CALCULATION DETAILS

All the calculations have been performed by the ERANOS code [6] which allows several types of perturbation analysis (classical and generalized - uncertainties and correlations analyses are performed into the code by a dedicated module). All flux calculations have been performed at 49 energy groups [11]. In particular, GUINEVERE and MYRRHA have been modelled in cylindrical RZ geometries (Fig. 2), and for the geometries shown in Fig. 2 a 20% reduction on the lead density for GUINEVERE and of the lead-bismuth for MYRRHA (hereafter lead for GUINEVERE and lead-bismuth for MYRRHA will be denoted as "coolant") has been assumed as perturbation. Two cases have been considered: 1) a 20% coolant reduction localized in an annulus (about 10 cm), distant from the center R=9 cm for MYRRHA and R=4 cm for FREYA, and axially extended all along the core active length (about 60 cm for both systems); 2) a 20% coolant density reduction distributed over all the active cores.
The behaviour of three different spectral indexes, following the two types of perturbation, has been taken into account: Pu-239 fissions/ U-235 fissions (in the following denoted as F9/F5); U-238 fissions/ U-235 fissions (F8/F5); Np-237 fissions/ U-235 fissions (F7/F5). The sensitivities coefficients have been evaluated firstly at 49 energy groups [11] and then, after a condensation procedure, these coefficients have been reduced at 15 energy groups to be coupled with the covariance matrix BOLNA [7] (the BOLNA energy structure is shown in the results). The flow chart of the calculations is the following:

- direct and adjoint flux calculation for the reference state, in RZ geometry;
- importance source creation for each different index analysed;
- adjoint flux calculation with external adjoint source for the reference state, where the external source is the source created by the step above;
- sensitivity analysis due to the difference between reference and perturbed cross-sections;
- energy condensation of the sensitivities coefficients from 49 energy groups to 15 energy groups;
- uncertainty and correlation analysis for the systems.

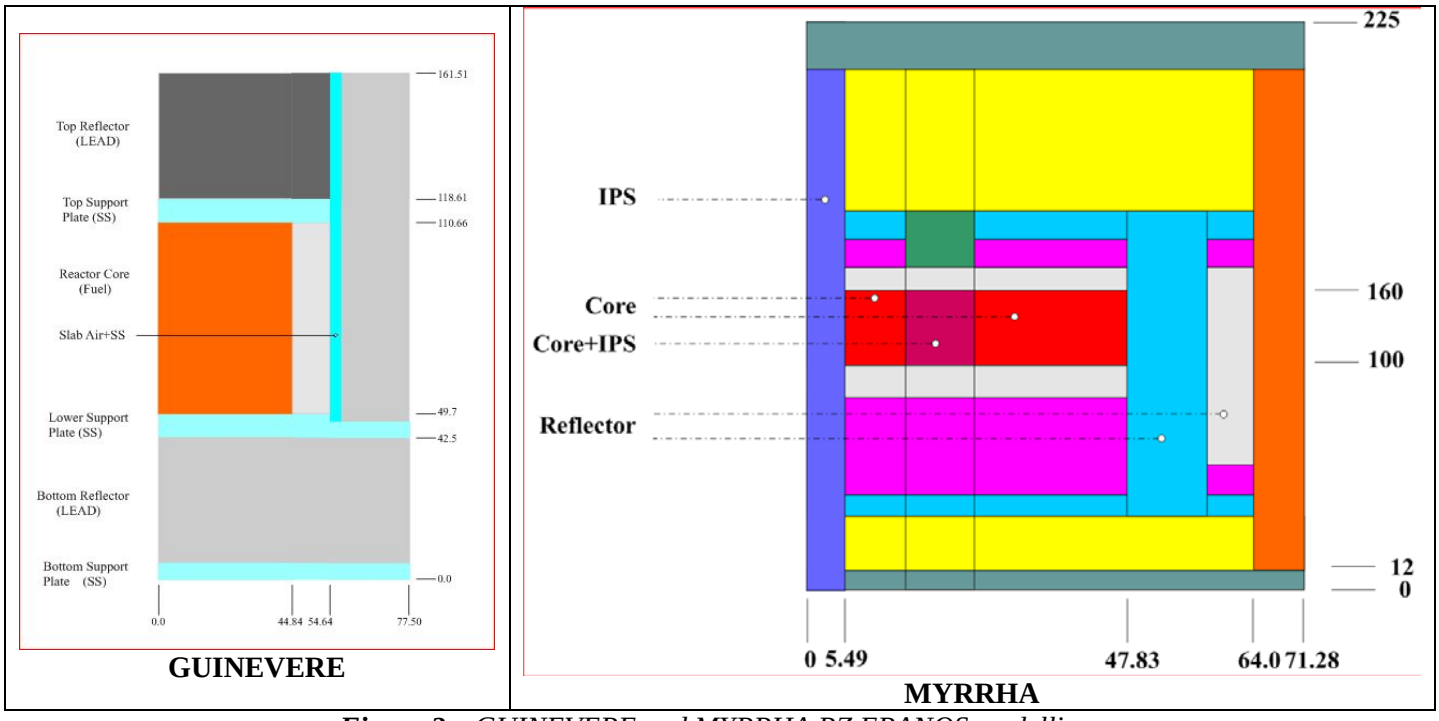

Figure 2 *– GUINEVERE and MYRRHA RZ ERANOS modelling.*

RESULTS

In Fig. 3 are shown the GUINEVERE and MYRRHA reference and perturbed (-20% coolant density over the whole core) spectra.

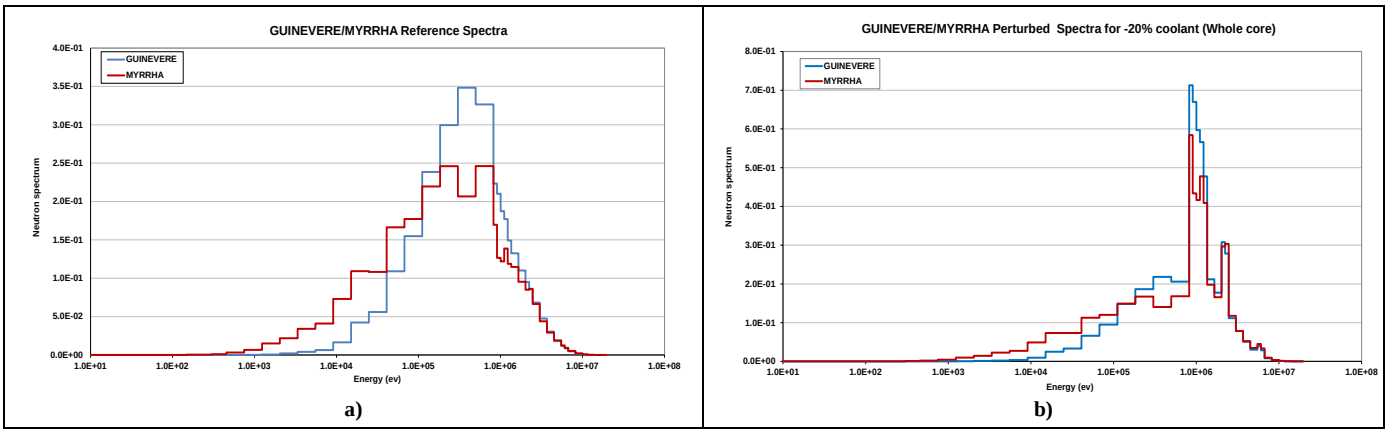

Figure 3 *– GUINEVERE and MYRRHA reference and perturbed spectra.*

The following reactivity values were obtained when going from the reference situation to the perturbed one: $\Delta k/k \approx -900$ pcm for GUINEVERE and $\Delta k/k \approx -550$ pcm for MYRRHA. For the reference situation (Fig. 3a) the GUINEVERE spectrum (in the energy region 100kev ÷ 1MeV) is harder than the MYRRHA one because the oxygen presence in the core for the MYRRHA case (it can be noticed that in MYRRHA the effect of the O-16 large elastic scattering resonance is located around 430keV). With a 20% (weight) decrease of coolant over the whole core, the spectra become harder in both systems (Fig. 3b). In particular, in Fig. 3b it can be recognized the hardening effect on the flux deriving by the U-238 fast fission rate enhancement together with the (less pronounced) partial removal of the lead (and also bismuth for MYRRHA) inelastic scattering effect at energies around 2MeV.

In Fig. 4 are shown the sensitivity profiles for the different spectral indexes taken into account for the case of partial coolant voiding in the core (-20% density in a core shell). For both GUINEVERE and MYRRHA the reactivity values, obtained when going from the reference situation to the perturbed one, were $\Delta k/k \approx -20 \div -30$ pcm. It can be noticed that 1) the MYRRHA sensitivity profiles are larger than the GUINEVERE ones; 2) the "leading" reactions affecting the sensitivity profiles are the lead (+bismuth for MYRRHA) inelastic and elastic (large resonances in the keV energy region) scattering reactions; 3) the sensitivity profiles in GUINEVERE and MYRRHA show, more or less depending on the response considered, similar behaviours. For F9/F5 (Figs. 4a-4b) it can be noticed the reverse sign for the elastic scattering contributions above 1MeV (where the Pu-239 fission cross section is higher than the U-235 fission cross section). For the MYRRHA case the positive elastic scattering contribution is extended to lower energies than GUINEVERE because of the different spectrum profiles in the perturbed situation (see Fig. 3b). The F8/F5 spectral index (Figs. 4c-4d) is mainly affected by the high energy inelastic removal mitigation following the lead (or lead/bismuth) decrease (leading of course to positive contributions). The F7/F5 spectral index (Figs. 4e-4f) sensitivity profile shows a sort of middle course between the F9/F5 and F8/F5 behaviours.

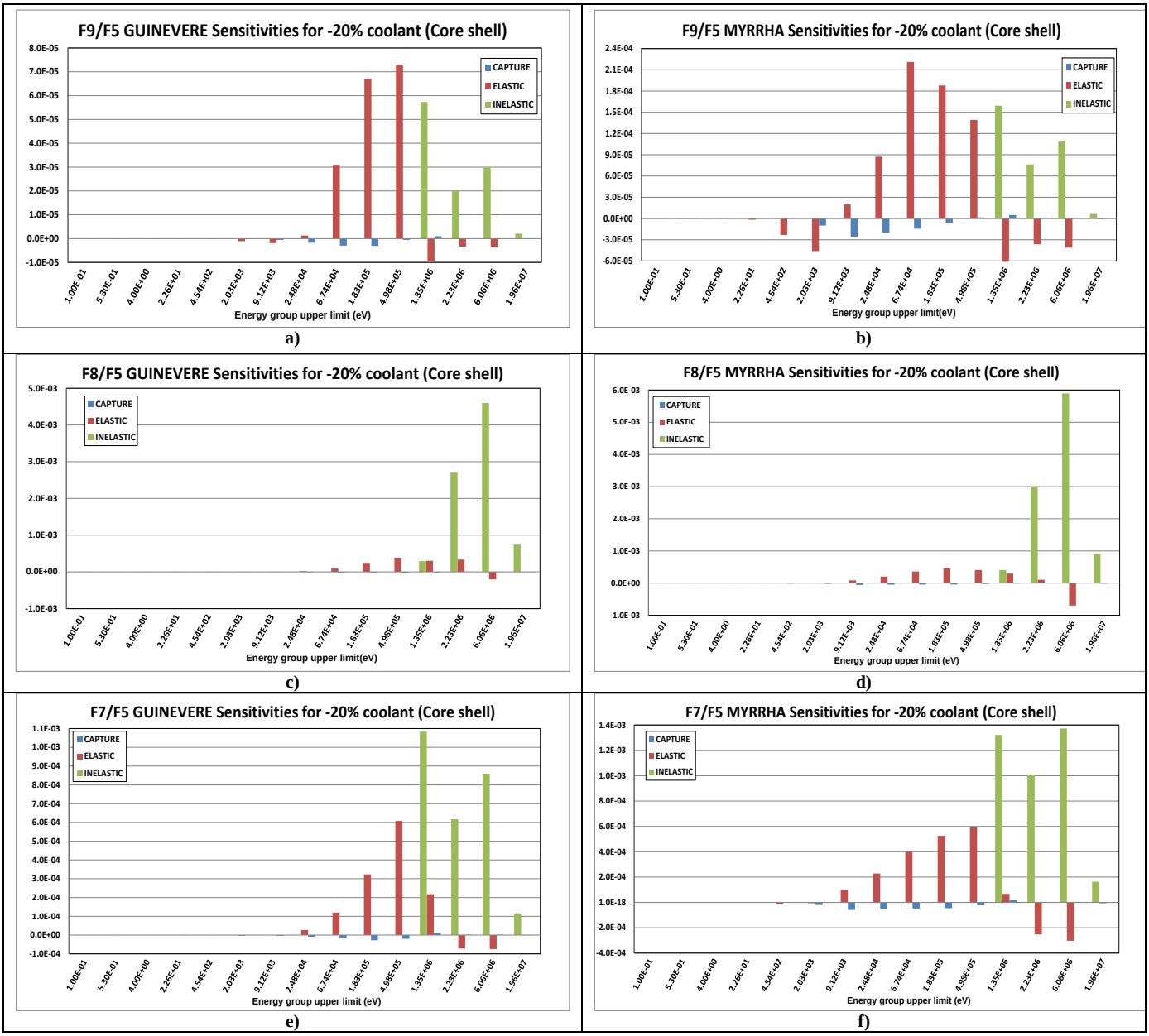

Figure 4 *– GUINEVERE and MYRRHA sensitivity profiles for different spectral indexes. Case of partial (-20%) coolant density reduction in a core shell.*

In Fig. 5 are shown the sensitivity profiles for the different spectral indexes taken into account for the case of partial (-20%) coolant density reduction over the whole core.

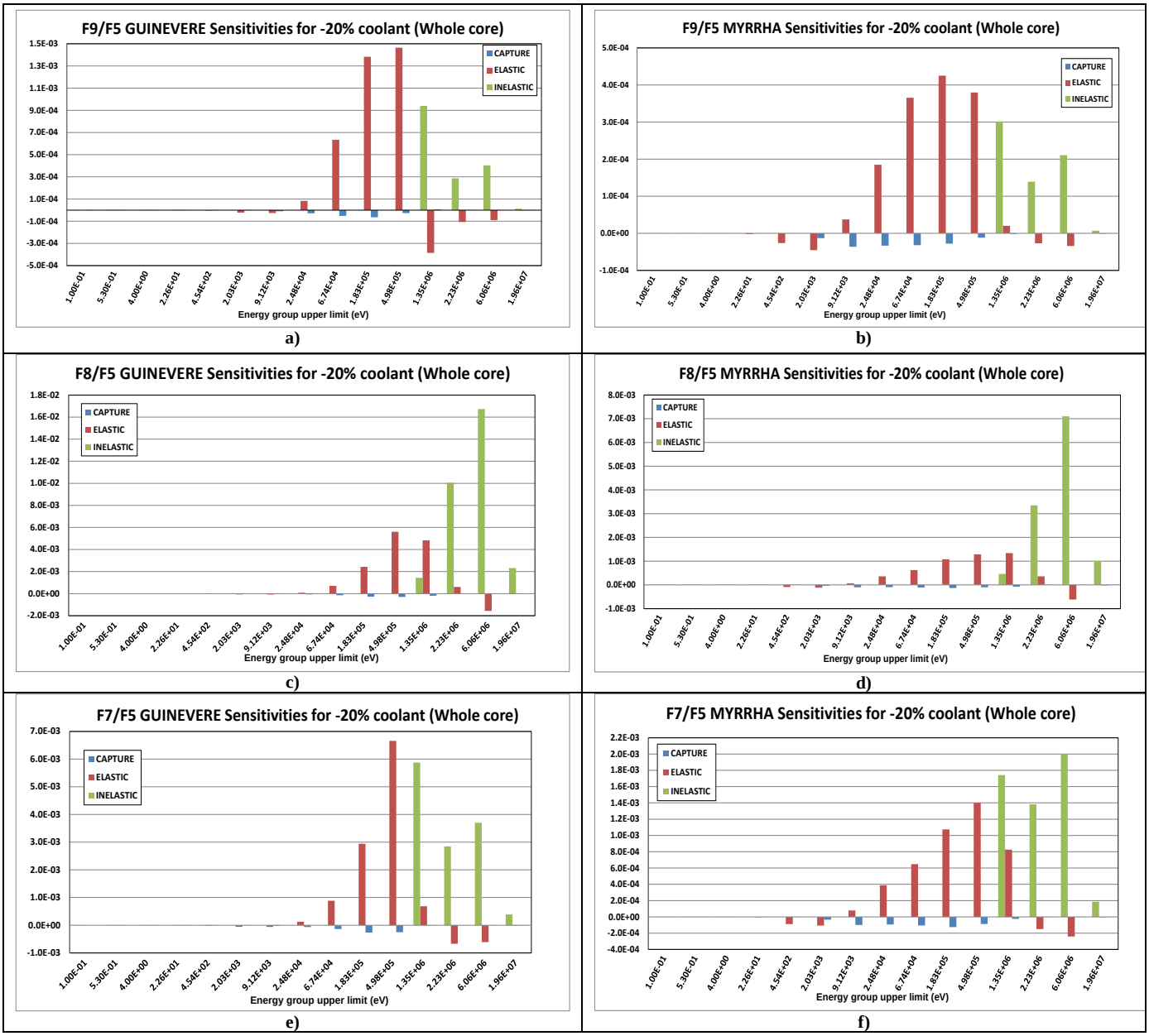

Figure 5 *– GUINEVERE and MYRRHA sensitivity profiles for different spectral indexes. Case of partial (-20%) coolant density reduction over the whole core.*

Of course all the contributions are larger for the whole core than the case of partial coolant voiding (only in a core shell). For the GUINEVERE F9/F5 spectral index the relative behaviour (Fig. 5a) is similar to the core shell voiding case (Fig. 4a), whereas for the MYRRHA F9/F5 spectral index (Fig. 5b) a relative increase of the elastic scattering contribution in the energy region 20÷70keV can be noticed compared to the case in Fig. 4b. For the F8/F5 index (Figs. 5c-5d) the behaviours for both GUINEVERE and MYRRHA are similar than those in Figs. 4c-4d. For the GUINEVERE F7/F5 index (Fig. 5e) a relative increase of the elastic scattering contribution in the energy region 20÷70keV (as for MYRRHA F9/F5) can be noticed than the case in Fig. 4e.
In Fig. 6 are shown the total sensitivity profiles for the different two hypothesis (core shell or over the whole core) about coolant voiding.

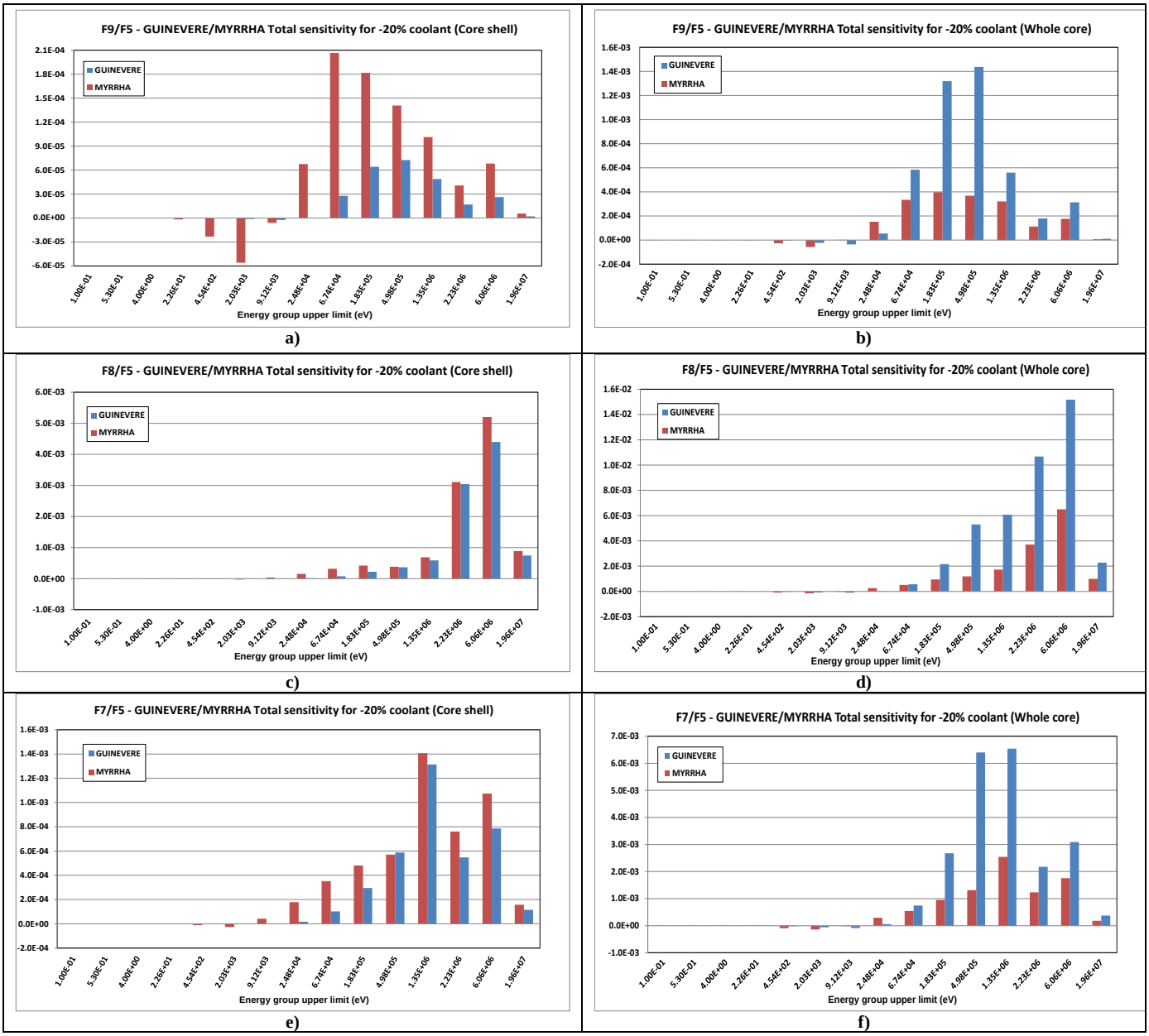

Figure 6 *– GUINEVERE and MYRRHA total sensitivity profiles for different spectral indexes.*

It can be noticed that the spectral indexes sensitivity energy components in the GUINEVERE case are similar (except for the F9/F5 spectral index) than those for MYRRHA in the case of the core shell partial voiding (similar Δk/k), whereas evident largest GUINEVERE sensitivity profiles than MYRRHA are observed in the case of partial voiding of the whole core.
In Tab. 1 are shown the correlation coefficients obtained from the analysis.

Table 1. GUINEVERE/MYRRHA correlation coefficients

	-20% coolant in core shell	**-20% coolant over the whole core**
F9/F5	8.89E-01	9.16E-01
F8/F5	9.95E-01	9.90E-01
F7/F5	9.81E-01	9.48E-01

As anticipated by the sensitivity profiles behaviour, a very good (and encouraging) correlation is found for all the spectral indexes taken into account, especially for the high energy F8/F5 and F7/F5 spectral indexes.

CONCLUSIONS

The present work has been focused on the analysis, by numerical simulations, of the transferability to the MYRRHA situation assumed as reference system, of the behaviour in GUINEVERE of the spectral indexes Pu-239 fissions/ U-235 fissions, U-238 fissions/ U-235 fissions and Np-237 fissions/ U-235 fissions following a localized (core shell) or global (whole active core) lead (GUINEVERE) or lead-bismuth (MYRRHA) 20% density reduction.
The analysis, carried out by means of GPT (Generalized Perturbation Theory) methodologies implemented into the ERANOS European neutronic code, and using the dispersion matrix BOLNA, provided encouraging results suggesting a very good correlation for all the spectral indexes taken into account, especially for the high energy spectral indexes.

ACKNOWLEDGEMENTS

Heartfelt thanks from all of us to Pino (Giuseppe) Palmiotti (Idaho National Laboratory, USA) for his indispensable support in wandering through the GPT uncertainty calculation meanders.
The GUINEVERE and FREYA projects are performed, respectively, within the 6th and 7th EURATOM Framework Programmes under the Contracts FI6W-CT2005-516520 and FP7-2010-269665, with the financial support of the European Commission, SCK•CEN, CNRS and CEA.

REFERENCES

[1] M. Salvatores et al., "MUSE-1: A First Experiment at MASURCA to Validate the Physics of Sub-Critical Multiplying Systems Relevant to ADS", Proc 2nd Int Conf on Accelerator-Driven Transmutation Technologies and Applications, Kalmar, Sweden, Vol 1, p 513, 1996.
[2] C. H. Pyeon, et al., “Experimental Analyses for Accelerator Driven Subcritical Reactor in Kyoto University Critical Assembly by using Foil Activation Method,” Proc. Int. Topl. Mtg. on Mathematics and Computation, Supercomputing, Reactor Physics and Nucl. Biological Applications (M&C2005), Avignon, France, Sep. 12-15, on CD-ROM, (2005). American Nuclear Society.
[3] P. Baeten et al., ‘The GUINEVERE project at the VENUS facility”, Proc. PHYSOR 2008, Interlaken, Switzerland, September 14–19, 2008.
[4] http://freya.sckcen.be/.
[5] J.M De Conto et al., "GENEPI-3C, a versatile neutron generator for the GUINEVERE ADS feasibility studies", PAC09 - Proceedings of the 23rd Particle Accelerator Conference, Vancouver, British Columbia, Canada (2009).
[6] G. Rimpault et al., “The ERANOS code and data system for fast reactor neutronic analyses”, Proc. PHYSOR 2002, Seoul, Korea, October 7-10, 2002.
[7] NEA WPEC Subgroup 26, International Evaluation Co-operation, “Uncertainty and target accuracy assessment for innovative system using recent covariance data evaluations”, Volume 26, 2008, ISBN 978-92-99053-1.
[8] H. A. Abderrahim, "ADS, What’s that? and what for? MYRRHA: an International Large Research Infrastructure and a unique worldwide Irradiation Facility and P&T tool", NOMAGE 4, Nordic Nuclear Materials Forum for Generation IV Reactors, Halden, Norway, 2011.
[9] A. Gandini, "Uncertainty Analysis and Experimental Data Transposition Methods Based on Perturbation Theory" in *Handbook of Uncertainty Analysis*, Y. Ronen Ed., CRC Press, Boca Raton, Florida, 1988.
[10] A. Gandini, “Generalized Perturbation Theory (GPT) Methods. A Heuristic Approach”, Advances Nucl.Sci.Techn., Vol 19, Plenum Press, 1987
[11] G. Bianchini et al., “Set-Up of a Deterministic Model for the Analysis of the GUINEVERE Experience”, PHYSOR 2010, Pittsburgh, Pennsylvania, US, (2010).

Keynote Address

Interaction of advanced oxide fuels with sodium in operating conditions for Sodium-cooled Fast Reactors

A.L. Smith[1,4], D. Bykov[1], P.E. Raison[1], R.J.M. Konings[1], J.Y. Colle[1], G. Wallez[2], O. Benes[1], C. Apostolidis[1], A. Kovacs[1], E. Suard[3], A.K.C. Cheetham[4]

[1] European Commission, JRC-Institute for Transuranium elements, Postfach 2340, Germany

[2] Laboratoire de Chimie de la matière condensée – UPMC- Chimie ParisTech, Paris, France

[3] Institut Laue Langevin, Rue Jules Horowitz, BP 156, 38042, Grenoble cedex 9, France

[4] University of Cambridge, Department of Materials Science & Metallurgy, Cambridge CB2 3QZ, UK

Presented by A. Smith and P. Raison

Abstract. The present work reports studies of the phases forming in the Na-U-O, Na-Pu-O and Na-Np-O systems. In the event of a clad breach in Sodium-cooled Fast Reactors the metallic sodium coolant will enter the pin and react with the (U, Pu, Np, Am)O_2 fuel. The structural, thermomechanical and thermodynamic investigations of the phases forming in the ternary phase diagrams Na-M-O (M = U, Pu, Np, Am) are hence of primary importance for the safety assessment and thermodynamic modelling of the system in such conditions. As part of our program of research at the Institute for Transuranium Elements, we have evidenced numerous compounds, and have characterized them using room temperature and high temperature X-Ray diffraction, Infrared and Raman spectroscopy, Knudsen effusion cell mass spectrometry.

The structure of the β-Na_3UO_4 compound, subject of controversy in the literature, was solved. Its coefficients of thermal expansion were also estimated using high temperature X-Ray diffraction. We have determined the structure of the high temperature form of Cs_2MoO_4, a phase that forms in between fuel and cladding.

The Na-Np-O ternary phase diagram, previously investigated in the 1960s was also re-examined. We report the following hexavalent and heptavalent compounds: α-Na_2NpO_4, β-Na_2NpO_4, γ-Na_2NpO_4, $Na_2Np_2O_7$, β-Na_4NpO_5 and Na_5NpO_6.

A revision of the Na-Pu-O system was carried out. Sodium plutonates Na_2PuO_3, Na_5PuO_5, Na_4PuO_5 and Na_5PuO_6 were obtained in Ar (plutonium oxidation states 4+ and 5+) and O_2 atmospheres (plutonium oxidation states 6+ and 7+). Crystal structures of these compounds were refined by the Rietveld method from conventional X-ray powder diffraction measurements.

In terms of thermodynamic characterization, we report the Knudsen effusion cell mass spectrometric study of α-Na_2NpO_4 and the calculation of its enthalpy of formation at 298.15 K (-1761.0 ± 7.7) $kJ.mol^{-1}$, in good agreement with the value reported in the literature from solution calorimetry (-1763.9 ± 7) $kJ.mol^{-1}$.

1 Introduction

Various types of nuclear reactors can be envisaged for the production of energy. The current worldwide fleet is mainly composed of Pressurized Water-cooled Reactors (PWR) but other options

are envisaged for the next generation of reactors (i.e. liquid metal cooled reactors, molten salt reactors, gas cooled rectors, etc.) [1]. In that regard we are interested in the safety aspects of Sodium-cooled Fast Reactors (SFR) and more specifically in the potential interaction of the sodium coolant with the fuel. Though various types of fuels, e.g. nitrides, carbides, metals, are potential candidates, $(U,Pu)O_2$ mixed oxide fuels are currently considered as reference for SFRs for which substantial experience has already been accumulated in terms of fabrication, reactor operation, reprocessing and risk assessment. However, $(U,Pu)O_2$ mixed oxides have also various drawbacks: for instance, in case of a clad breach, though extremely rare during normal operating conditions, sodium will enter the fuel pin and react with the fuel. Studies carried out in the past in equilibrium conditions have revealed the formation of an urano-plutonate of sodium of general formula Na_3MO_4 with $M = U_{1-x}Pu_x$ [2]. The compound thus formed is of lower density and has a lower thermal conductivity than the fuel leading to local swelling and development of hot spots that could damage further the cladding up to a pin failure, restrain the flow of coolant within a sub-assembly of fuel pins, or result in a contamination of the primary coolant with plutonium, minor actinides or highly radioactive fission products.

One main goal of the International Generation IV program is moreover to recycle the minor actinides (Np, Am, Acm) generated during the irradiation process in conventional nuclear reactors, and re-use them for energy generation. One solution to reduce the waste's radiotoxicity is indeed to recover the longlived isotopes from the spent fuel and re-irradiate them in a fast reactor to transmute them in less radioactive elements with shorter half-lives [3, 4]. The introduction of neptunium and americium to mixed oxide fuel will introduce a much more complex chemistry, for which many data are still missing.

Our program of research includes the structural investigation of the following ternary systems: Na-U-O, Na-Np-O, Na-Pu-O and Na-Am-O. In each ternary phase diagram investigated, numerous compounds have been identified and characterized by X-ray diffraction. In the Na-U-O system for instance, not less than ten sodium-uranate compounds are known to form (e.g. $NaUO_3$, $Na_2U_2O_7$, Na_4UO_5 Na_3UO_4, etc) (Table 1). But a number of uncertainties remain about the structure and chemical composition of some of these phases, especially for the sodium neptunates and plutonates investigated in the 1960's with the Debye Scherrer method.
Using X-Ray diffraction coupled to neutron diffraction, we have firstly solved the structure of β-Na_3UO_4 the product of interaction between sodium and hyperstoichiometric urania. Our first results on the Na-Np-O system have been recently published [15]. We also report herein the first Knudsen effusion cell mass spectrometry measurements carried out on α-Na_2NpO_4 [16]. Our work on the Na-Pu-O system is ongoing. Finally, we have solved the structure of the high temperature phase of Cs_2MoO_4, a compound that forms inbetween fuel and cladding.

Table 1 : Summary of the structural parameters of the phases forming in the Na-U-O system.

Compound	**α-Na_2UO_4**	**β-Na_2UO_4**	**$Na_2U_2O_7$**	**α-Na_4UO_5**	**β-Na_4UO_5**	**$NaUO_3$**
Symmetry	orthorhombic	orthorhombic	rhombohedric	cubic	tetragonal	orthorhombic
Space group	Pbam (55)	Pbca (61)	R-3m (166)	Fd3m(227)	I4/mmm (87)	Pbnm (62)
a (nm)	0.97623(3)	0.58079(3)	0.3911(2)	0.4766(5)	0.751720(10)	0.57739(2)
b (nm)	0.57287(2)	0.59753(3)	0.3911(2)	0.4766(5)	0.751720(10)	0.59051(29
c (nm)	0.34956(1)	1.17179(6)	1.7857(5)	0.4766(5)	0.4632582)	0.82784(2)
Cell volume V(nm^3)	0.19549	0.40666	0.31392(1)	0.10826	0.26177	0.28226
Reference	[5]	[5]	[6]	[7]	[8]	[9]
Compound	**α-$Na_{5.33}UO_5$**	**β-$Na_{5.33}UO_5$**	**α-Na_3UO_4**	**γ-Na_3UO_4**	**$Na_{11}U_5O_{16}$**	**Na_4UO_4**
Symmetry	tetragonal	tetragonal	cubic	cubic	cubic	cubic
Space group	?	?	Fm-3m (225)	Fd-3m (227)	P4232 (208)	Fm-3m (225)
a (nm)	0.526(1)	0.586	0.4766(5)	0.956(4)	0.9543(2)	0.478(1)
b (nm)	0.526(1)	0.586	0.4766(5)	0.956(4)	0.9543(2)	0.478(1)

c (nm)	1257(1)	0.549	0.4766(5)	0.956(4)	0.9543(2)	0.478(1)
Cell volume V(nm^3)	0.34778	0.1882	0.10853	0.87372	0.86907	0.10922
Reference	[10]	[10]	[11]	[12]	[13]	[14]

2 Experimental methods

2.1 Raw materials and solid state synthesis

Compounds were prepared from depleted uranium oxide (^{238}UO2 from JRC-ITU stocks) or neptunium oxide (^{237}NpO2 from ORNL, Oak Ridge) with sodium oxide (Na_2O 80% + Na_2O_2 20%, Alfa Aesar) or sodium carbonate (Na_2CO_3 99.95%, Sigma). Plutonium in PuO_2 was presented mainly by the isotopes ^{239}Pu (85.5%) and ^{240}Pu (13.2%). The sodium oxide and sodium carbonate were stored in an argon filled dry box because of their hygroscopy. The mixtures were heated under oxygen or argon flow in a tubular furnace, and regrinded in between each thermal treatment to enhance the crystallinity.

2.1 X-Ray diffraction

The crystal structures of the phases in the Na-U-O, Na-Pu-O and Na-Np-O systems were determined at room temperature by X-ray diffraction (XRD) using a Bruker D8 X-ray diffractometer mounted in a Bragg-Brentano configuration with a curved Ge monochromator (111) and a ceramic copper tube (40 kV, 40mA) equipped with a LinxEye position sensitive detector. The data was collected by step scanning in the angle range $10° < 2\theta < 120°$. The sample preparation for XRD analysis consisted in dispersing the powder on the surface of a silicon wafer with 2 or 3 drops of isopropanol. Structural analysis was performed by the Rietveld method with the Fullprof2k suite [17].
The thermal stability of certain of these phases was also assessed by high temperature X-ray diffraction using a Bruker D8 X-ray diffractometer equipped with an Anton Paar HTK 2000 chamber. Measurements were conducted in helium up to 1273 K. From these data, some reactions of decomposition were characterized and the material's coefficients of thermal expansion calculated.

2.3 Knudsen effusion cell mass spectrometry

Knudsen effusion cell mass spectrometric measurements were performed on the α-Na_2NpO_4 compound. The sample's purity was confirmed by ICP-MS analysis, which yielded a sodium to neptunium ratio of 2.01 ± 0.04.
The experimental set up consists of a Knudsen effusion cell coupled to a quadrupole mass spectrometer QMG422 (Pfeiffer Vacuum GmbH), equipped with a cross beam electron bombardment ion source, an axial faraday cup, and a 90° Second Electron Multiplier detector connected to an electrometer. The mass spectrometer covers the range of 1 to 512 amu. The Knudsen cell is placed in a high temperature furnace heated by tungsten-coil heating elements. The system in its whole is placed in an high vacuum chamber (10^{-7}-10^{-8} mbar). The apparatus, specifically designed to study radioactive materials, is placed in a 5 cm thick lead shielded glove box. The measurements were made at 40 eV ionization electron energy.

3. Results and discussion

3.1 Investigation of the fuel sodium reaction product

Na_3MO_4 (M = U, Pu, $U_{1-x}Pu_x$) was reported to form following the interaction between fuel and sodium under the oxygen potential conditions of the reactor [18]. However, the crystal structure of Na_3UO_4 remains a subject of controversy, which we have tried to resolve.
Scholder and Gläser [11] first reported in 1964 a face centered cubic (f.c.c.) phase with cell parameter 4.77 Å, the sodium and uranium atoms being randomly distributed throughout the cationic sites (α phase). In 1970, Bartram and Fryxell [13] obtained at 973 K, a new phase which had many additional reflections compared to the f.c.c. phase of Scholder and Gläser [11]. They assigned it a cubic symmetry with cell parameter 9.54 Å (β phase) and chemical composition $Na_5U_{11}O_{16}$. Around the same period, in 1972, Marcon et al. [12] also evidenced the formation of a high temperature (>1273 K) partially ordered phase of Na_3UO_4 which was f.c.c. with the space group Fd-3m and cell parameter

9.56 Å (γ-form). In 1985, Lorenzelli et al. [19] confirmed the existence of two phases of Na_3UO_4, the high temperature phase corresponding to the one reported by Marcon et al., but mentionned that the low temperature could not be $Na_{11}U_5O_{16}$ as reported by Bartram and Fryxell [13], but rather Na_3UO_4 with an unresolved structure. They tried an indexation in the tetragonal and orthorhombic systems without any success. The authors nevertheless evidenced a reversible phase transition between the α and β forms around (1348 ± 25) K.
The β-Na_3UO_4 compound was synthesized in the present work in a stainless steel container at 1273 K. An ab initio structure determination using the program EXPO2009 [20] on the X-ray diffraction data acquired at the ITU, and the neutron data collected at the Institut Laue Langevin, revealed a monoclinic symmetry and allowed us to determine the atomic positions. High temperature X-ray diffraction data provided the thermal expansion of the material (*to be published*).

3.2 Structural investigation of the Na-Np-O phase diagram

Keller and his coworkers appear as the pioneers of the studies on the interaction of minor actinides (Np, Am) with alkali metals [21, 22]. The authors described the thermal, hydrolytic and structural properties of ternary oxides containing hexavalent and pentavalent transuranium elements and compared them to the corresponding uranates. They found that neptunates and uranates were very often isostructural. However, a number of uncertainties remained about these phases, explored at that time with the Debye-Scherrer method. Morrs pointed out in 1982 [23] and 1994 [24] a need for re-examination of the sodium neptunates in terms of structural and thermodynamic characterization.
We started re-visiting this system as part of our program of research [15]. The following compounds in which neptunium has the oxidation state VI and VII were reported: α-Na_2NpO_4, β-Na_2NpO_4, γ-Na_2NpO_4, $Na_2Np_2O_7$, α-Na_4NpO_5 and Na_5NpO_6. The corresponding structural parameters are summarized in Table 2.

Table 2 (taken from [15]): Summary of the structural parameters of the phases froming in the Na-Np-O system.

Compound	**α-Na_2NpO_4**	**β-Na_2NpO_4**	**γ-Na_2NpO_4**	**$Na_2Np_2O_7$**	**β-Na_4NpO_5**	**Na_5NpO_6**
Temperature	RT	RT (after heating at 1273K)	1273 K	RT	RT	RT
Symmetry	orthorhombic	orthorhombic	Tetragonal	monoclinic	tetragonal	monoclinic
Z	2	4	4	2	2	2
Space group	Pbam (55)	Pbca (61)	?	$P2_1$ (4)	I4/mmm (87)	C2/m (12)
a (nm)	0.9715(3)	0.5782(5)	0.6018(5)	0.6830(3)	0.7530(5)	0.581(5)
b (nm)	0.5732(3)	0.5930(5)	0.6018(5)	0.7809(3)	0.7530(5)	0.998(5)
c (nm)	0.3459(3)	1.1649(5)	1.1980(5)	0.6317(3)	0.4619(5)	0.574(5)
α	90	90	90	90	90	90
β	90	90	90	111.28(1)	90	110.66(5)
γ	90	90	90	90	90	90
Cell volume V(nm^3)	0.19259(1)	0.3994(1)	0.4339(1)	0.31392(1)	0.2619(1)	0.311(1)

A preliminary sketch of the ternary Na-Np-O phase diagram was suggested from the aforementioned studies between 673 to 1273 K, that covers a large range of oxidation potentials [15].

3.3 Knudsen effusion cell studies

We report here the first Knudsen effusion cell high temperature mass spectrometric measurements on α-Na_2NpO_4 [16]. The experiments, carried out under vacuum in a tungsten and alumina cell, have revealed the vaporization behaviour of α-Na_2NpO_4 when heated up to 2700 K.

3.3.1 Enthalpy of formation at 298.15 K

α-Na_2NpO_4 was found to decompose to NpO_2, Na_2O and O_2 in the interval 1030 to 1206 K.

$$Na_2NpO_4(cr) = NpO_2(cr) + Na_2O(s) + O_2(g) \quad \text{(Eq. 1)}$$

The gaseous phase is in equilibrium condition with the condensed phase under Knudsen condition. The enthalpy of formation of α-Na_2NpO_4 at 298.15 K was subsequently estimated at 298.15 K at (-1761.0 ± 7.7) kJ.mol^{-1} using an enthalpy increment method on the interval 1030 to 1115 K. This value is in good agreement with the value reported by Goudiakas *et al.* [25] (-1763.9 ± 7) kJ.mol^{-1} who used solution calorimetry.

Sodium oxide formed by decomposition of α-Na_2NpO_4 was found to vaporize congruently in the interval 1115 to 1206 K. The sodium oxide vaporization is still a subject of controversy. Hildenbrand and Lau [26] reported a vaporization into the Na(g) and O_2(g) vapour species (Eq. 2), while Steinberg and Schofield [27] suggested the formation of the sodium superoxide molecule NaO_2(g) (Eq. 3).

$$Na_2O(cr) = 2\,Na(g) + ½\,O_2(g) \quad \text{(Eq. 2)}$$

$$2\,Na_2O(cr) = 3\,Na(g) + NaO_2(g) \quad \text{(Eq. 3)}$$

The Na+ and O_2^+ species detected in large concentrations between 1115 and 1206 K were hence attributed to the equilibrium decomposition reactions (Eq. 4) and (Eq. 5), when considering the sodium oxide vaporization mechanisms of Hildenbrand and Lau, and Steinberg and Schofield respectively.

$$Na_2NpO_4(cr) = NpO_2(cr) + 2Na(g) + O_2(g) \quad \text{(Eq. 4)}$$

$$Na_2NpO_4(cr) = NpO_2(cr) + 3/2\,Na(g) + ½\,NaO_2(g) + 1/2\,O_2(g) \quad \text{(Eq. 5)}$$

Using an enthalpy increment method, the enthalpy of formation of α-Na_2NpO_4 at 298.15 K was estimated at (-1761.9 ± 20.4) kJ.mol-1 and (-1758.8 ± 22.3) kJ.mol^{-1} with the hypotheses of Hildenbrand and Lau [26] and Steinberg and Schofield [27] for the vaporization of Na_2O respectively. Both these values are in good agreement with the value reported by Goudiakas *et al.* [24] (-1763.9 ± 7) kJ.mol^{-1} who used solution calorimetry. The uncertainty limits are larger than for the previous calculation in the interval 1030 to 1115 K. This is due to a larger uncertainty in the determination of the enthalpies of reaction by linear regression for the mechanisms (Eq. 4) and (Eq. 5), when compared to the mechanism (Eq. 1). The value (-1761.0 ± 7.7) kJ.mol^{-1}, was hence selected over the other two in the present work. Nevertheless, the results gathered in the interval 1115 to 1206 K are satisfying for both hypotheses (Eq. 4) and (Eq. 5), meaning the controversy between Hildenbrand and Lau, and Steinberg and Schofield could not be resolved. This suggest the vaporization of Na_2O(cr) is a complex process that involves all species Na, O_2, NaO, Na_2O, and NaO_2.

3.3.2 Sublimation of Na_2NpO_4

Both masses 253 and 292 were recorded between 1360 and 1620 K. The mass 253 corresponds to the signal of NpO^+, whereas the mass 292 corresponds either to $Na_2WO_4^+$ or $NaNpO_2^+$. As they were recorded in both tungsten and alumina cells, we suggest a sublimation of Na_2NpO_4(cr) in the temperature range 1360 to 1620 K, in parallel with the decomposition to neptunium oxide, sodium oxide and oxygen. The possible dissociation reactions (Eq. 6), (Eq. 7) and (Eq. 8) are proposed to explain the occurrence of the NpO^+, $NaNpO_2^+$, and Na^+ signals in this region.

$$Na_2NpO_4 + e^- = NpO^+ + 2\,Na + 3/2\,O_2 + 2e^- \quad \text{(Eq. 6)}$$

$Na_2NpO_4 + e^- = NaNpO_2^+ + NaO_2 + 2e^-$ (Eq. 7)

$Na_2NpO_4 + e^- = Na^+ + NaNpO_4 + 2e^-$ (Eq. 8)

Our high temperature diffraction measurements carried out on α-Na_2NpO_4 revealed a phase transition to a high temperature tetragonal phase between 1173 and 1273 K, and the formation of the β phase of the compound, orthorhombic, space group *Pbca*, upon cooling to room temperature [15]. It is hence furthermore suggested that the phase in simultaneous decomposition and sublimation between 1360 and 1620 K is the tetragonal phase, and no longer the α form.

3.4 Structural investigation of the Na-Pu-O phase diagram

Our results on the Na-Pu-O system show a certain disagreement with the data reported in the literature with respect to the symmetry of the known phases [28]: Na_2PuO_3, Na_5PuO_5, Na_4PuO_5 and Na_5PuO_6. $Na_2Pu_2O_7$ was observed as a decomposition product of Na_5PuO_6 and Na_4PuO_5 and to our knowledge was never reported before. At the same time, the existence of some reported compounds can be questioned. For example, $Na_4Pu_2O_5$, Na_6PuO_5, Na_2PuO_4 and Na_6PuO_6 could not be obtained in the present studies. The data on the Na-Pu-O system will be published shortly.

3.5 Structural investigation of Cs_2MoO_4

Cesium and molybdenum, as some of the most common fission products, also need to be taken into account in the safety assessment. Their oxides (basic Cs_2O and acidic MoO_3) readily react with each other to yield a series of cesium molybdates with formula $Cs_2Mo_nO_{3n+1}$ (n = 1-5, 7) [29], of which Cs_2MoO_4, as the most thermally stable, had been predicted to exist in oxide fuels [30]. At high burn-up, it was shown that Cs_2MoO_4 forms between the fuel and the clad a layer circa 150-200 μm thick [31], that would be in direct contact with sodium coolant in case of a clad breach.

Former studies have established the crystal structure at room temperature (α form, orthorhombic *Pnma*, a = 11.608 Å; b = 6.562 Å; c = 8.510 Å) [32] and reported a phase transition to an unknown β form around 841 K [33, 34]. Mean linear thermal expansion was measured at $\alpha_l = 44\ 10^{-6}\ K^{-1}$ in the 300-773 K range [35]. As little is known about the behavior of Cs_2MoO_4 at actual fuel's temperature, our study aimed at characterizing the structure of β form by high temperature XRD. β-Cs_2MoO_4 ($P6_3/mmc$, a = 6.844 Å; c = 8.982 Å at 948 K) exhibits a disordering of the MoO_4 tetrahedra array at transition point, which results in an increase of the unit cell volume. The mean thermal expansion ($\alpha_l = 48\ 10^{-6}\ K^{-1}$) remains similar to that of the α form, so still higher than that of the fuel itself ($10\ 10^{-6}\ °K^{-1}$ around 773 K) [36]. Furthermore, the expansion becomes much more anisotropic ($\alpha_{max} - \alpha_{min} = 74\ 10^{-6}\ K^{-1}$) than for the α form ($22\ 10^{-6}\ K^{-1}$). Besides, even tough the interaction with liquid sodium has already been considered by several authors, we have investigated the stability of possible $(Cs_{1-x}Na_x)_2MoO_4$ ($x \leq 0.2$) solid solutions by solid-state synthesis. According to XRD, the cell parameters of the compound remains unchanged, as well as the electron density on the Cs site, accounting for a too faint solubility of sodium to be observed. So, in agreement with the former studies, interactions between sodium coolant and cesium molybdate seem to be negligible [37].

4 Conclusions

Different chemical aspects related to the failure of a pin cladding are being investigated. To evaluate the potential quantity of radioactive materials released in the primary circuit in case of a clad breach, also called source term, a complete understanding of the different systems M-Na-O (M = U, Pu, Np, Am, Cm) and Fission-Products-Na must be achieved. The first results obtained in the present work already allowed to lift some important controversies such as the cristallographic structure of the main products of reaction, Na_3UO_4 and the high temperature form of Cs_2MoO_4. This work is ongoing and future results on phase diagrams, thermomechanical and thermodynamic properties of the materials will be reported in scientific journals. At last the data obtained will also be used in the ASTEC-Na simulation code developped under the frame of the European-funded project JASMIN [38].

ACKNOWLEDGEMENTS

The main author would like to acknowledge the European Commission for its financial support for grantholders and the support of European Actinet-i3 program.

REFERENCES

[1] GEN-IV international program
[2] M.A. Mignanelli, P. E. Potter, *J. Nucl. Mat.* 130 (1985) 289-297
[3] L. Koch, J. Less-Common Met. 122 (1986) 371-382
[4] C.T. Walker and G. Nicolaou, J. Nucl. Mater. 218 (1995) 129-138
[5] E.H.P.Cordfunke and D.J.W. IJdo, J. Solid State Chem. 115 (1995) 299-304
[6] M. Gasperin, J. Less-Common Met. 119 (1986) 83-90
[7] C. Keller, L. Koch, and K.H. Walter, J. Inorg. Nucl. Chem. 27 (1965) 1205-1233
[8] I.P. Roof, M.D. Smith, and H.-C. zur Loye, J. Cryst. Growth 312 (2010) 1240-1243
[9] S. Van den Berghe, A. Leenaers, and C. Ritter, J. Solid State Chem. 177 (2004) 2231-2236
[10] S. Pillon, Etude des diagrammes de phases U-O-Na, Pu-O-Na et U,Pu-O-Na. PhD thesis, Univ. Du Languedoc, (1989)
[11] R. Scholder and H. Gläser, Z. Anorg. Allg. Chem. 327 (1964) 15-27
[12] J.-P. Marcon, O. Pesme, and M . Franco, Rev. Int. Hautes Temper. et Refract. 9 (1972) 193-196
[13] S.F. Bartram and R.E. Fryxell, J. Inorg. Nucl. Chem. (1970) 3701-3706
[14] S. Pillon, F. Ingold, P. Fischer, G. Andre, F. Botta, and R.W. Stratton, J. Nucl. Mater. 206 (1993) 50-56
[15] A.L. Smith, P.E. Raison, and R.J.M Konings, J. Nucl. Mater. 413 (2011) 114-121
[16] A.L. Smith, J.Y Colle, O. Benes, A. Kovacs, P.E. Raison, R.J.M Konings, J. Chem. Thermodyn., in press, DOI 10.1016/j.jct.2012.11.034
[17] J. Rodriguez-carvajal, Physica B 192 (1993) 55-69
[18] M.A. Mignanelli and P.E. Potter, Thermochim. Acta 129 (1988) 143-160
[19] R. Lorenzelli, T. Athanassiadis, and R. Pascard, J. Nucl. Mater. 130 (1985) 298-315
[20] A. Altomare, M. Camali, C. Cuocci, C. Giacovazzo, A. Moliterni, and R. Rizzi, J. Appl. Cryst. 42 (2009) 1197-1202
[21] C. Keller, L. Koch, and K.H. Walter, J. Inorg. Nucl. Chem. 27 (1965) 1205-1223
[22] C. Keller, L. Koch, and K.H. Walter, J. Inorg. Nucl. Chem. 27 (1965) 1225-1232
[23] L.R. Morss, Actinides-1981. Pergamon, Oxford, Edelstein edition, (1982)
[24] L.R. Morss, E.H. Appelman, R.R. Gerz, and D. Martin-Rovet, J. Alloy. Compd. 203 (1994) 289-295
[25] J. Goudiakas, X. Jemine, and J. Fuger, J. Chem. Thermodyn. 23 (1991) 513-520
[26] D.L. Hildenbrand and K.H. Lau, J. Chem. Phys. 98 (1993) 4076-4081
[27] M. Steinberg and K. Schofield, J. Chem. Phys. 94 (1991) 3901
[28] Bykov D., Raison Ph., Konings R., Smith A., Eloirdi R., 2012 MRS

Spring Meeting, Symposium Y, San Francisco, USA, April 10-13, 2012, Y.10.2

[29] H. R. Hoekstra, Inorg. Nucl. Chem. Lett. 9 (1973) 1291-1301

[30] K. Minato. T. Ogawa. K. Fukuda. M. Shimizu. Y. Tayama, I. Takahashi, J. Nucl. Mater. 208 (1994) 266-281

[31] M. Tourasse, M. Boidron, B. Pasquet, J. Nucl. Mat. 188(1992)49-57

[32] W. Gonschorek, T. Hahn, Z. Kristallogr. Kristallgeom. Kristallphys. Kristallchem. 138 (1973) 167-176

[33] D. Bodo, H. Kessler, C. R. Séances Acad. Sci. Ser. C 282 (1976) 839

[34] R. J. M. Konings, E. H. P. Cordfunke, Thermochim. Acta 124 (1988) 157-162

[35] K. Minato, M. Takano, K. Fukuda, S. Sato, H. Ohashi, J. Alloys Compd. 255 (1997) 18-23

[36] D. G. Martin, J. Nucl. Mater. 152 (1988) 94-101

[37] La réaction Cs_2MoO_4/Na: Application à l'interaction combustible/sodium lors de la rupture de gaine à fort taux de combustion dans un RNR
Thèse de Doctorat, , Université de Provence (Aix-Marseille I)

[38] Joint Advanced Severe accidents Modelling and Integration for Na-cooled fast neutron reactors JASMIN FP7 European research program

Sensitivity and Uncertainty Analyses Applied to Neutronics Calculations for Safety Assessment at IRSN

Evgeny Ivanov [*], Tatiana Ivanova, Sophie Pignet

Institut de Radioprotection et de Sûreté Nucléaire (IRSN), France

ABSTRACT

The requirements to the fuel cycles and advanced reactor systems have increased role of robust sensitivity and uncertainty (S/U) techniques for safety assessment. Providing technical support for French nuclear safety authority, IRSN has been working in this area to meet the safety requirements, i.e., to be able to assess safety margins for the fuel cycles and future fast reactors in France. The paper provides IRSN's mission and vision relevant to this topic and overview the ongoing work illustrated by some examples, including contributions to the OECD/NEA Expert Groups.

1. INTRODUCTION

Proper consideration of uncertainties is an essential part of the safety assessment. This is particularly important for innovative systems where the state of knowledge is not as advanced as for existing plants. Currently, reactor simulation and modelling involve multi-physics processes (neutronics, thermal-hydraulic, structural mechanics, and fuel behaviour) with feedback effects. Nevertheless, their qualification (Verification and Validation) procedure must include the qualification of separate physics models and codes [1]. The validation of stand-alone neutronics codes is one of the major elements of the multi-physics calculations on support of the reactor safety assessment. Importance of this validation increases role of reliable and robust approaches for sensitivity and uncertainty (S/U) analyses. Providing technical support for French nuclear safety authority, IRSN has been working in this area to meet the safety requirements, i.e., to be able to establish reliable safety margins for the fuel cycles and future fast reactors in France. The present paper provides IRSN's mission and vision relevant to this topic. The principle stages of the work in this area are shown in Figure 1 as well as all sources of uncertainty to be addressed while S/U analyses. The work includes (1) identification of the most representative safety scenarios; (2) implication of S/U analyses to establish modeling uncertainties for the target systems; and (3) propagation of the modeling uncertainties to the safety margins.

The identification of the most representative safety-related configurations is a basic element of reactor safety assessment. Section 2 develops this subject.

Presently, the efforts are directed on conducting the neutronics calculations for safety studies by high-accurate codes with minimal approximations. The three-dimensional (3-D) Monte Carlo codes are commonly used for fuel cycle criticality safety assessment, providing the best-estimate k_{eff} values. In the reactor physics, there is also a tendency to perform safety studies by the best estimate-codes. The follow up paper [2] presets the results of the study in the view of more general perspective to implement those codes/methods for reactor simulations.

Section 3.1 describes the technique that establish best-estimate modelling bias and bias uncertainties for both fuel cycle and fast reactors by the combined use of integral experiments data and uncertainties in nuclear data. The elements of this technique, such as data of integral experiments on measurements of safety-related parameters, sensitivity coefficient of these parameters to neutron cross sections, are discussed in Section 3.2 and 3.3, respectively.

The major needs and challenges, while applying sensitivity and uncertainty analysis to neutronics calculations for safety assessment are discussed in Section 4.

[*] Corresponding author, email: evgeny.ivanov@irsn.fr

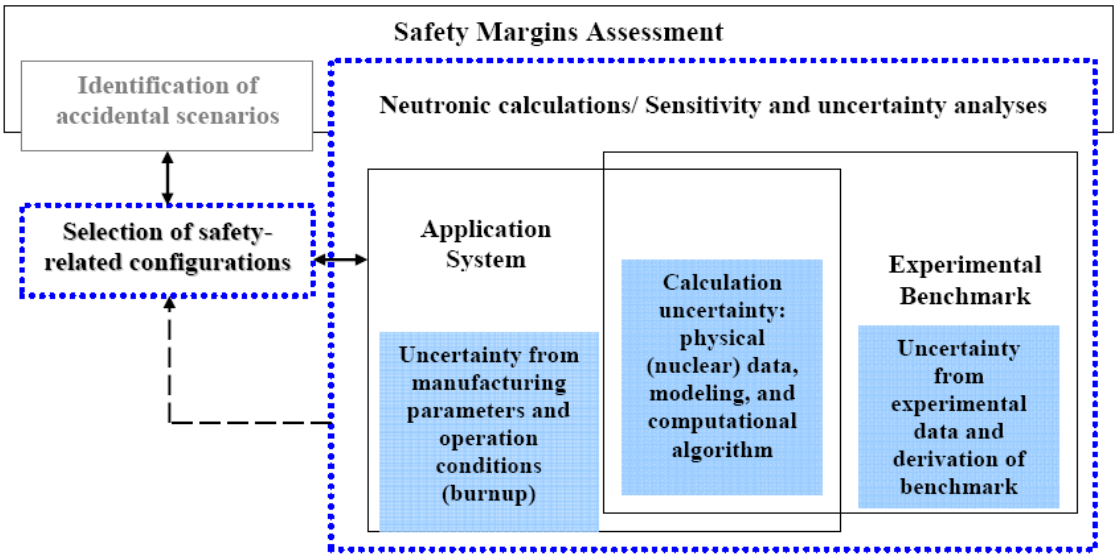

Figure 1. Sensitivity and uncertainty analyses applied to neutronics calculations for safety assessment

The overview of the ongoing work is illustrated by some examples, including contributions to the OECD/NEA Expert Groups on Uncertainty Analyses for Criticality Safety Assessment (UACSA) [3], Uncertainty Analyses for Modeling (UAM) [1], and "Adjustment" Sub-group 33 of WPEC [4].

2. DEVELOPMENT OF SAFETY-RELATED CONFIGURATIONS

The first very important step of the S/U analysis for reactor and fuel cycle safety assessment is identification of safety-related configurations, i.e., selection of the most representative configurations from the subsequent stages of an accidental process. Plausible accidental scenarios should be considered in order to understand physics and the dominant parameters impacting the accidental processes. Then the configurations applicable for neutronics calculations should be identified. Currently, this identification is mostly based on the expert judgment, retained to design and size the safety architecture provisions must be as exhaustive as possible. The lack in the exhaustiveness of the configurations should be covered by the notion of envelope situations.

An example of such envelope consideration is discussed in [5] for SFR application. In the past, designers used to demonstrate the safety of the core computing a total void effect. It means that they quantified the difference of reactivity between the core with sodium and the same core without sodium, in spite of a spatial trend of reactivity is well known. This is due to the fact that the reactivity of sodium voiding is determined by the competition of several physical processes (leakages, decrease of absorptions, decrease of fissions at low energy, etc.). For this reason, the study of local effects and the definition of the area of sodium void effect integration are important. It might be the volume of the core active part, the total volume of the core or only the volume where void effect is positive. In the last case, concepts could be compared against the maximum of reactivity that corresponds to the conservative way of safety level evaluation.

This example shows that the identification of the most representative configurations from the subsequent stages of an accidental process is not trivial and requires a careful analysis of the multi-physical processes, in order to select the most representative configurations for further sensitivity and uncertainty analysis. Unfortunately, the scenarios considered are not always comprehensive and plausible, reflecting, on the one hand, a lack of the multi-physics experiments, and on the other hand, difficulties in clear understanding the coupling processes. This makes the identification of the safety-related configurations even more complex and requires collaboration of reactor's designers and safety assessors.

3. SENSITIVITY-BASED UNCERTAINTY ANALYSES

3.1. Method for uncertainty assessment

The safety approach requires validation of analytical methods and data used in neutronics simulations for nuclear criticality and reactor safety assessment in order to quantify a computational bias and the bias uncertainty. Uncertainty originates from errors in physical data, manufacturing uncertainties, and modeling and computational algorithms.

The continuous improvement to the computational algorithms and tools coupled to the increase of computing capabilities, suggest that the major source of the modelling uncertainty is found in the nuclear cross-section data. To account for these uncertainties, a validation tool based on generalized linear least-squares methodology (GLLSM) is being developed and tested at IRSN. The method sometimes referred to as "data adjustment". However, the function of the tool is not to obtain an adjusted library of nuclear data, but rather to establish the high-confidence bias for the calculation parameter and the bias uncertainty while validating the computations. The functions of the tool are to compute uncertainties in calculated integral parameters due to uncertainties in the input nuclear data and to make variation of the nuclear data to provide correct calculated results. The equations of the GLLSM are presented in [6]. Presently, the code is limited to operations with k_{eff} [7, 8] but being extended to the reactor-type parameters.

The NEA Working Party on International Nuclear Data Evaluation Co-operation (WPEC) Subgroup 33 was established to study issues of the adjustment method [4]. IRSN has recently been involved into the group's work and has contributed the results of the adjustment procedure for two different application cases - models of fast reactors.

3.2. Integral experiments data

The key to validation of neutronics simulations for criticality safety and reactor physics is the generation of a database of benchmark experiments that covers a broad range of systems that are similar to the particular applications of interest.

An extensive database of integral experiment has been created at IRSN for criticality safety needs. It comprises calculated k_{eff} values and computed neutronics characteristics for more than 2200 benchmark configurations. The benchmarks are mostly selected from the Handbook of the International Criticality Safety Benchmark Experiments Project (ICSBEP Handbook) [9]. For the reactors, the set of the integral data includes the k_{eff} measurements collected for criticality safety in addition to reactivity coefficients, β_{eff}, Λ_{eff}, reaction rates, power distribution and other reactor parameters for dozens of configurations from the Handbook of the International Reactor Physics Experiment Evaluation Project (IRPhEP Handbook) [10].

Given that the integral data plays key role in the validation procedure it is also important to ensure that the uncertainties for the benchmark experiments are well evaluated and that correlations between the uncertainties are well established. Previous studies [11; 12] demonstrate that the experimental correlations may not be negligible when assessing the biases and uncertainties. The correlations between the experimental uncertainties (also called "experiment correlations" hereafter) arise from the use of the same fuel and structural materials, the same container tank or cladding, and common methods for measurements and instrumentation. Unfortunately, only a limited amount of experiment correlation data is published in the ICSBEP Handbook and no correlation data is available in the IRPhEP Handbook.

The work is going on at IRSN to identify, quantify and document correlations in the experimental uncertainties for the set of the selected benchmarks. To establish the experimental correlation the method presented in [11] is used. Some correlation matrices for the experimental uncertainties were created for a set of integral experiments selected for fast reactor studies. For example, correlations have been established for a set of Mixed Plutonium-Uranium Oxide (MOX) fuelled configurations used for fast reactor applications. The selected set of the benchmarks, shown in Table 1, covers a range of plutonium enrichments, ^{240}Pu contents, core sizes, and diluents. To be noted that the experimental uncertainties for all ZEBRA k_{eff} values are being revised for further use in the validation

studies. The correlations in benchmark k_{eff} uncertainties established for the above discussed configurations are demonstrated in Figure 2. The major correlations appeared due to use of same fuel in experiments performed at the same facility [13].

Table 1. Characteristics of selected benchmarks [14]

Assembly	V, litres	Pu, at%	Benchmark k_{eff} uncertainty, %
ZEBRA22	2261.3	18	0.08
ZEBRA23	2373.7	18	0.13
ZEBRA24	2434.2	18	0.08
ZEBRA25	2552.3	18	0.13
MZA	2256.0	18	0.16
MZB	7110.4	18	0.10
ZPR-6/7-12	12478.7	19	0.23
ZPR-6/7-99	11678.8	11	0.22
SNEAK7A	453.6	8	0.29
SNEAK7B	1260.6	8	0.35

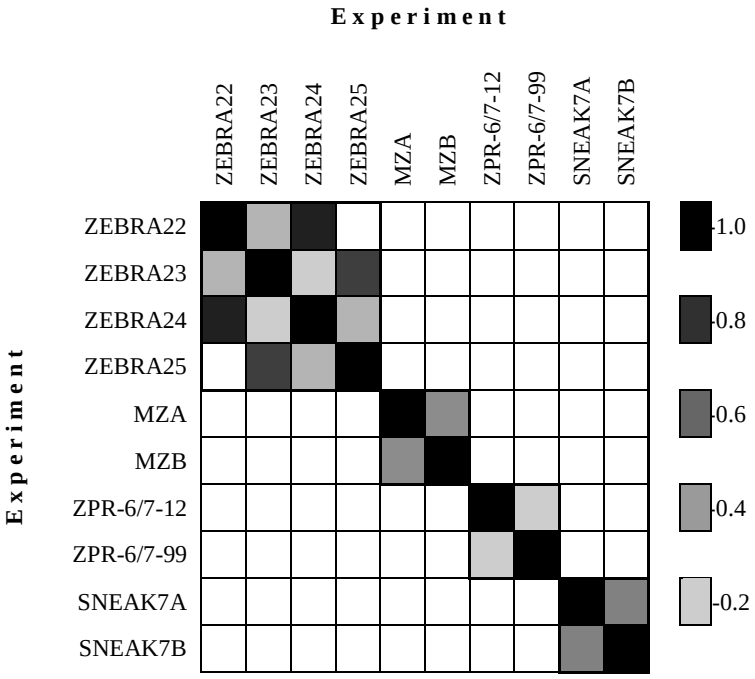

Figure 2. Correlations in benchmark k_{eff} uncertainties for the set of selected benchmarks [13]

The SNEAK7 [10] experiments provide a unique set of experimental data on delayed neutrons effective fraction. Based on these configurations, a methodology was proposed how to evaluate the uncertainty in β_{eff} and select experimental value for benchmark [15]. In addition, a benchmark was created to analyze components of the β_{eff} uncertainty [16].

3.3. Sensitivity Computations

For criticality safety assessment (CSA), use of the sensitivities have recently become more common and is continuously growing together with development of best-estimate methods for criticality codes validation. For CSA, it is necessary to actually generate group-wise sensitivity coefficients for multiple reaction types for every nuclide in each system included in the analysis for systems with variable (often complex) geometries, ranging from soft spectra to hard spectra. This is a situation which explains why Monte Carlo techniques have become used to compute sensitivities, supplanting one- (1-D) or two-dimensional (2-D) deterministic tools.

The EG UACSA was established to address issues related to Sensitivity/Uncertainty (S/U) studies for CSA. The Expert Group has focused recently proposed a benchmark (UACSA Phase III) to test the sensitivity calculation methods and tools. The benchmark problems were selected to investigate methods/codes performance associated with the sensitivity computations for typical CSA applications [17].

The benchmark exercises were aimed to test several aspects of the sensitivity computation. If only 1-D and 2-D sensitivity tools are available for sensitivity computations, it necessitates the conversion of many of the 3-D inputs used for criticality computation to 1-D or 2-D models. The impact of the revised models on the sensitivities is expected to be small. Several configurations were proposed for the benchmark study to demonstrate this effect.

To provide an accurate estimation of the sensitivity coefficients for systems, in which resonance self-shielding is important, the sensitivity coefficients require additional terms to account for the first-order implicit effect of perturbations in the material number densities or nuclear data upon the shielded

group-wise macroscopic cross-section data [18]. Several configurations were also proposed in the framework of EG UACSA benchmark to study whether and how this portion of sensitivity is important.

IRSN participated in this benchmark, using several Monte Carlo techniques for sensitivity calculations. Results of the calculations are documented and discussed in details in [19]. The sensitivity results were generated with the computational tools available or developed at IRSN. The adjoint-based first-order-linear perturbation theory sensitivity coefficients were calculated using the well-known SCALE/TSUNAMI-3D Monte Carlo code, SCALE/TSUNAMI-1D deterministic code and a new module of DRAGON4 called SENS. Coupling between the APOLLO2 deterministic code and the MORET 5 multi-group Monte Carlo code generated sensitivities through direct perturbation technique. One more approach for sensitivity computation is under development now in MORET 5 code, which uses the differential operator sampling method to compute k_{eff} derivatives to macroscopic cross sections.

In general, the study demonstrates a good agreement in the codes performance. Nevertheless, further enhancements are required to improve the codes being developed. The implicit terms corresponding to parameters that perturb self-shielded multi-group cross sections are currently neglected in eigenvalue sensitivity techniques implemented in the APOLLO2-MORET 5 and DRAGON4/SENS codes, although this term contributes notably to the complete sensitivity for some configurations. The major areas for improvement are also scattering sensitivities for low-absorption materials and for ^{238}U. The next development step in SENS is to implement a higher Legendre polynomial order for the scattering cross sections, using flux moments. In TSUNAMI-3D computations for the simplified models, cell weighted cross sections are not currently fully accounted while generating cell-waited cross sections.

Lessons learnt from this benchmark are a step forward to further sensitivity codes development not only for criticality safety but also for reactor physics [20]. This work shows that the detailed 3-D and simplified models provide similar sensitivity results if the homogenization is performed correctly and that the sensitivity generated for pin-cell models should be extended to finite systems for further uncertainty study only with caution.

Implicit portion of sensitivity, originating from cross-section shielding effect, impacts resonant isotopes and cannot be neglected in the sensitivity computations for some moderated systems of fuel cycle. But this effect can be neglected for configurations that cover the whole range of systems of interest for fast reactor design and safety assessment. There are several ways to provide accurate sensitivity estimation for systems, in which resonance self-shielding is important: (1) to apply an algorithm in the sensitivity tool, (2) to run calculations using hyper-fine energy group structure, or (3) to use subgroup representation for neutron cross sections. The comparison of these methods indicates that the different approaches produce comparable results (see Figure 3). This conclusion is useful for further implementation of sensitivity capabilities to the MORET 5 code [21], which will implement options 1 and 3 for the sensitivity computations. The implementation is being performed in collaboration with the Institute for Physics and Power Engineering (IPPE) [22].

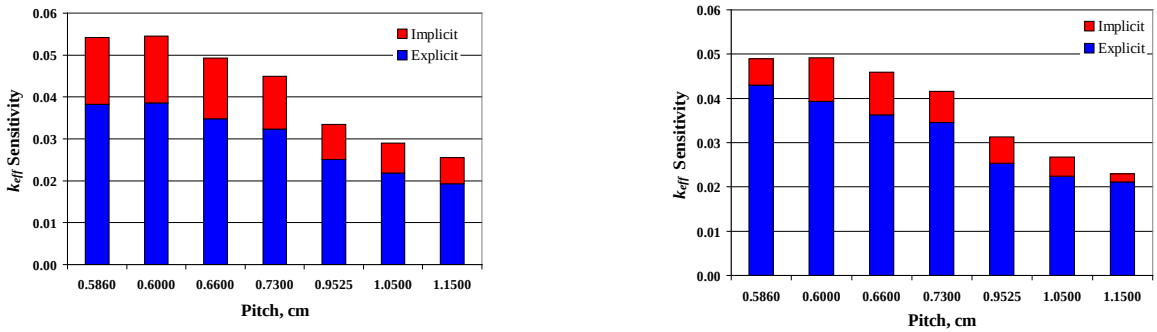

a) TSUNAMI-3D results (algorithmic calculation of 'implicit' sensitivity)

b) MMKKENO results provided by IPPE (subgroup calculation)

Figure 3. Integrated 'explicit' and 'implicit' sensitivities for ^{238}U scattering as a function of pitch variation for infinite square array of MOX pin-cells model (one of the UACSA Phase III models)

Sensitivities of k_{eff} and reactor parameters to neutron cross sections are commonly used for the reactor design studies. Typically, the sensitivity capabilities are integrated into 1-D, 2-D or 3-D deterministic design oriented codes, which apply adjoint-based first-order-linear perturbation theory and generalized perturbation theory [23]. Several sensitivity codes are used at IRSN for the reactor studies, depending on the application: ERANOS [24], APOLLO 2 [25], and SCALE/TSUNAMI-1D and -3D codes [26].

4. NEEDS AND CHALLENGES

The identification of the most representative configurations from the subsequent stages of an accidental process is a basic element for the reactor safety assessment. The scenarios considered are not always comprehensive and plausible, reflecting, on the one hand, a lack of the multi-physics experiments, and on the other hand, difficulties in clear understanding the coupling processes. All these will require a careful analysis of the multi-physical processes to select the most representative and most uniform configurations for further sensitivity and uncertainty analysis. This selection is challenging and requires in-depth understanding of all the processes in reactor.

The current S/U analysis used at IRSN relies on first-order or generalized perturbation theories method to obtain sensitivity coefficients. The utility of this approach is limited by treatment of nonlinearity, and computer execution time when considering large number of computing parameters and weakly connected systems (large cores). Other approaches are derivative based stochastic sampling method, which has been developing world over, or direct perturbation, being implemented to APOLLO2-MORET 5 sequence [19]. The drawback of these methods is that computer execution time limits their use to small input data set. In addition, these approaches do not allow combination of the integral data with the differential (covariance) data in order to obtain best-estimate uncertainty values, while sensitivity data assimilation for further uncertainty analysis. Since all these limitations, in future work, it will be desirable to develop the two approaches and to combine them for best-estimate uncertainty prediction.

The integral experiments available in the IRPhEP Handbook and other open sources are oriented on the reactor mock-up with regular geometries which are not relevant to accidental states where the regularity is perturbed. This clearly demonstrates an experimental need and may require international efforts to address it. The experiments performed on the BFS facility at IPPE have a great potential to contribute to this safety studies.

The uncertainties that originate from the error in kinetic parameters are among the major contributors to the overall modeling uncertainty for the reactivity values, which are extremely important safety relevant parameters. Evaluating the experimental values for the β_{eff}, for example, to derive accurate uncertainties, is therefore an important but not trivial task. A specific methodology is needed, which is different from the methodology used for k_{eff} evaluation. The method has been recently proposed and implemented for several experiments of β_{eff} measurements performed on fast assemblies [15]. To refine the method, its justification should be extended to other accurate and reliable experimental data that can be obtained on the BFS facility.

5. CONCLUSIONS

The current tendencies in the safety requirements and the code developments are towards implementation of best estimate techniques to safety assessment for fuel cycle [27] and reactor concepts. The work sequence defined to address these needs at IRSN. It is based on the previous experience and extended to best estimate approaches for sensitivity and uncertainty analysis. The work will integrate the expertise in reactor physics, uncertainty and sensitivity analysis, and will contribute to the development and assessment of advanced/ optimized uncertainty methods for use in reactor safety assessment.

The major effort is focused on the identification of the safety-related configurations for the reactor applications. For innovative systems where the state of knowledge is not as advanced as for existing

power plants, this is particularly challenging and will require in-depth understanding of all the multi-physics processes in reactor in order to select the most representative and most uniform configurations for further sensitivity and uncertainty analysis.

The application of Monte Carlo codes with explicit geometry description for reactor simulation will be continuously growing. Even though implication of Monte Carlo codes is limited by accuracy while calculating small reactivity effects, in general, they provide best-estimate calculations for reactor safety analysis. The Monte Carlo MORET code, developed at IRSN for the criticality calculations, is continuously being adopted for reactor calculations by introducing reactor-oriented capabilities, such as kinetic parameters computation [28].

The best-estimate technique based on GLLSM method is used to quantify the uncertainty originated from the neutron cross-sections. The tool assessing technological uncertainties is under development. The activity of the OECD/NEA EG UACSA assists in testing the utility of these approaches and software tools for safety assessment.

Given that the integral data plays key role in the S/U analysis, the efforts have been focused on extending the database of the integral experiments with the new configurations available in the ICSBEP and IRPhEP Handbooks and on analysis of the experimental data from the sodium fast reactors. One of the major paths of the work is to identify, quantify and document the correlations in the experimental uncertainties for the selected benchmarks. The effort has been undertaken to evaluate the experimental uncertainties of kinetic parameters, such as β_{eff} [13, 15].

The sensitivity capabilities are being implemented into the codes developed at IRSN. Performance of these codes has been recently demonstrated on one of the benchmarks proposed by the OECD/NEA EG UACSA [19, 20].

Sensitivity and uncertainty analysis capabilities must be further developed and tested for uncertainty propagation through neutronics calculations on comprehensive benchmark frameworks in order to be used for the safety assessment.

REFERENCES

1. M. Avramova, K. Ivanov, “Verification, validation and uncertainty quantification in multi-physics modelling for nuclear reactor design and safety analysis”, Progress in Nuclear Energy, 52 (2010), pp. 601-614.
2. E. Ivanov et al., “Computation of BFS Experiments with Monte Carlo Codes”, Proc. of International conference BFS-50 years, Obninsk, Russia, February 27-March 1, 2012.
3. T. Ivanova et al., **“**OECD/NEA Expert group on Uncertainty Analysis for Criticality Safety Assessment: Current Activities”, Proc. of PHYSOR 2010, Pittsburgh, Pennsylvania, May 9-14, 2010, USA, on CD-ROM, American Nuclear Society, LaGrange Park, IL (2010).
4. C. de Saint-Jean et al. “Assessment of Existing Nuclear Data Adjustment Methodologies”, NEA/WPEC-33, NEA/NSC/WPEC/DOC(2010)429.
5. V. Tiberi, E. Ivanov, S. Pignet, “An Approach of SFR Safety Study through the Most Penalizing Sodium Void Reactivity”, Proc. of PHYSOR 2010, Pittsburgh, USA, May 9-14, 2010, USA, on CD-ROM, American Nuclear Society, LaGrange Park, IL (2010).
6. T. Ivanova et al., “Use of International Criticality Safety Benchmark Evaluation Project Data for Validation of the ABBN Cross-Section Library with the MMK-KENO Code”, *Nucl. Sci. Eng*, **145**(2), October 2003, pp. 247-255.
7. T. Ivanova, N. Leclaire, E. Letang, J-F. Thro, “Use of Fission Product Experiments for Burnup Credit Validation”, Proc. of ANS Nuclear Criticality Safety Division Topical Meeting (NCSD 2009), US, Richland, Washington, September 13-17, 2009.
8. T. Ivanova, E. Létang, I. Duhamel, “Impact of Cross-Section-Covariance Data on Results of High-Confidence Criticality Validation”, *Journal of Korean Physical Society*, **59** (23), pp. 1170 - 1173, 2011.
9. International Handbook of Evaluated Criticality Safety Benchmark Experiments, NEA/NSC/DOC(95)03, NEA-OECD (2010).

10. International Handbook of Evaluated Physics Benchmark Experiments, NEA/NSC/DOC (2006)1, NEA-OECD (2010).
11. T. Ivanova et al., "Influence of the Correlations of Experimental Uncertainties on Criticality Prediction", *Nucl. Sci. Eng*., **145**(1), September 2003, pp. 97-104.
12. M. Ishikawa, "How to Determine Error Matrix of Integral Data" input for OECD/NEA WPEC Sub-group 33, available on the EG web-site.
13. E. Ivanov, "Step toward innovative systems, role of experimental correlations for validation of neutron cross-sections libraries", Participants to the JEFF Project In Memory of John Rowlands, JEFF/DOC-1400, OECD/NEA, November 2011, p. 14.
14. J.L. Rowlands, "Accuracy of criticality calculations made using current nuclear data libraries for MOX fuelled fast critical assemblies", *Annals of Nuclear Energy*, **37**, Issue 12, December 2010.
15. Evgeny Ivanov, Sophie Pignet, "Specificity of Experimental β_{eff} Evaluation for Reactor Physics Benchmarks", Transactions of the ANS, **105,** 2011, ISSN: 0003-018X, p. 286.
16. Summary Record of OECD Benchmark for Uncertainty Analysis in Best-Estimate Modeling (UAM) for Design, Operation and Safety Analysis of LWRs, Expert Group on Uncertainty Analysis Fourth Workshop (UAM-4), NEA/NSC/DOC(2010)?, Pisa, Italy, April 14 – 16, 2010.
17. T. Ivanova, "Benchmark Phase III for the Expert Group on Uncertainty Analysis for Criticality Safety Assessment: Computation of k_{eff} Sensitivity Coefficients to Neutron Data", http://www.oecd-nea.org/science/wpncs/UACSA/.
18. M. L. Williams, B. L. Broadhead, C. V. Parks, "Eigenvalue Sensitivity Theory for Resonance-Shielded Cross Sections," *Nucl. Sci. Eng*., **138**, 177–191 (2001).
19. C. Laville, et al, "Sensitivity Calculations for UACSA Benchmark Phase III by IRSN", Proc. of International Conference on Nuclear Criticality (ICNC2011), September 19 – 22, 2011.
20. T. Ivanova et al, "OECD/NEA Expert group on Uncertainty Analysis for Criticality Safety Assessment: Results of Benchmark on Sensitivity Calculation (Phase III)", submitted to PHYSOR 2012 –Advances in Reactor Physics – Linking Research, Industry, and Education Knoxville, Tennessee, USA, April 15-20, 2012, on CD-ROM, American Nuclear Society, LaGrange Park, IL (2012).
21. L. Heulers et al, "MORET 5 – Overview of the new capabilities implemented in the multigroup/continuous-energy version", Proc. of International Conference on Nuclear Criticality (ICNC2011), September 19 - 22, 2011.
22. K.F. Raskach, A.A. Blyskavka, "An Experience of Applying Iterated Fission Probability Method to Calculation of Effective Kinetics Parameters and k_{eff} Sensitivities with Monte Carlo", Proc. of PHYSOR 2010, Pennsylvania, USA, May 9-14, 2010, on CD-ROM, American Nuclear Society, LaGrange Park, IL (2010).
23. M. L.Williams, "Generalized Contribution Response Theory," *Nucl. Sci. Eng*., **108**, 355–383 (1991).
24. G. Rimpault et al., "The ERANOS Code and Data System for Fast Reactor Neutronics Analyses" *Proc. of PHYSOR 2002*, Seoul, Korea (2002).
25. R. Sanchez et al., *Apollo2 Year 2010*, Nuclear Engineering and Technology, Vol.42 N°5 (2010).
26. SCALE: A Modular Code System for Performing Standardized Computer Analyses for Licensing Evaluation, ORNL/TM-2005/39, Version 6, Vols. I-III, Oak Ridge National Laboratory (2009), RSICC/ORNL CCC-750.
27. F. Fernex, Y. Richet, Y. Deville, "MACSENS: a Software Workbench for Criticality Calculation Validation, Proc. of International Conference on Nuclear Criticality (ICNC2011), September 19 - 22, 2011.
28. A. Jinaphanh et al., "Calculating the kinetic parameters in the continuous energy Monte Carlo code MORET", Proc. of PHYSOR 2010, Pennsylvania, USA, May 9-14, 2010, on CD-ROM, American Nuclear Society, LaGrange Park, IL (2010).

Experimental and calculating substantiation of reactivity balance and energy-release distribution in BN-600 core

A.V. Moiseev, Yu.S. Khomyakov, S.V. Surov

State Scientific Center of the Russian Federation – Institute for Physics and Power Engineering named after A.I. Leypunsky, Obninsk, Kaluga region, Russia

Abstract. This paper summarizes the results of a series of experimental and theoretical studies carried out in 2003-2010 on the substantiation of neutron-physical characteristics of BN-600 core. This work caused BN-600 transition to the new core 01M2 with high burnup 11.2% h.a., need for analysis and comprehension of the BN-600 experience in anticipation of the end of BN-600 design life cycle and extending it to 10-15 years, development and introduction of new methods of analysis, in particular, the beginning of use for BN-600 core calculation precision method of Monte Carlo, free from most of the limitations of traditional diffusion codes. In the experiments was a change of equipment and measurement techniques. By the beginning of this work cycle energy-release of BN-600 had not been measured for about 10 years. As a result of experimental and calculating studies was created the coordinated and consistent database of neutron-physical characteristics for the fast sodium reactor of medium power. With the account of long-term operating experience of the BN-600 were finally brought and tested measurement methods of reactivity characteristics based on the new reactimeter methodology and gamma scanning of fuel assemblies. The development and application of new programs for neutronic calculations (new version of GEFEST and JARFR codes based on ABBN-93 constant system, the ModExSys system and MMKKENO code based on the Monte Carlo method) has allowed at a new level to understand and evaluate the methodological features of calculation of basic parameters of the BN-600 core. Substantiated values of the basic neutron-physical characteristics of the BN-600 core with high level of accuracy.

1. INTRODUCTION

This paper presents the results of experimental and theoretical work done in 2003-2010 years on substantiation of neutron-physical characteristics of the BN-600 core. Why after a long period of BN-600 operation was necessary in such serious enough research? The work was stimulated by several factors.

First – transition to the new core 01M2 with high burnup 11.2% h.a. This is the fourth upgrade of the BN-600 core. Its key feature is that the transfer was made without changing the constructive of the core almost by reducing conservatism of design decisions. Justification reduced design margins, conforming to the rules of nuclear safety, has been the subject of serious discussion, including the licensing of the core.

Second – need for analysis and comprehension of the BN-600 experience in anticipation of the end of BN-600 design life cycle and extending it to 10-15 years. The BN-600 is a unique power plant which has no analogues in the world and it was necessary to understand whether it is possible to bring the level of operational measurements to international benchmarks. In this case, the situation with the experience of the BN-350 will not be repeated, which in the neutron-physical part was only qualitative. Currently there is almost no way to analyze data on the characteristics of the BN-350 core for verification studies and accounting measurements in the BN-350 in new projects.

Third – development and introduction of new methods of analysis. In particular, the beginning of use for BN-600 core calculation precision method of Monte Carlo, free from most of the limitations of traditional diffusion codes.

Fourth – in the experiments was a change of equipment and measurement techniques. And by the beginning of this work cycle energy-release of BN-600 had not been measured for about 10 years.

2. ANALYSIS AND SUBSTANTIATION OF REACTIVITY BALANCE FOR BN-600

2.1. State of problem and the tasks

Reactivity balance is the ratio between potential reactivity of a core in different states with regard to the relevant effects of reactivity and worth of the reactor control system, it determines nuclear safety of a reactor. Taking into account high standard of the conservative approach to the justification of nuclear safety, prediction accuracy of reactivity balance is the determining value for selecting the design and operating margins, as well as the development of requirements for nuclear fuel.
To date design value of the error for BN-600 core: maximum excess reactivity adopted 0,4 % Δk/k, shim rods worth 7 %, safety rods worth 8 %, subcriticality error after setting safety rods ~ 0,8% Δk/k.
It should be noted several facts that cause, with a formal approach, doubts about the declared value for the above parameters:

- direct calculation of the BN-600 core criticality by programs like GEFEST (TRIGEX, JARFR), based on the diffusion approximation is different from the true value to ~ 1,0 % Δk/k;
- as showed the further analysis only the neglect in these codes of the heterogeneous structure of control rods system may lead to errors ~ 7-15% in the calculation of their worth;
- moreover, the estimates show that the constant error in the calculation of criticality fast reactor core remains at ~ 1,5 % Δk/k, and after accounting macro experiment on critical facility is reduced to ~ 0,5% Δk / k. On the calculation of criticality have a major impact the level of technological errors ~ 0,5 % Δk/k.

The correct evaluation of design values so much depends on the methods that experts use for correcting calculated results.
As a result, justification of design values accuracy and a way of subcriticality error estimation were the subject of discussion at the beginning of this work. This discussion was not only scientific and technical, but also include the issues of licensing design documents for 01M2 core. And also for justification of nuclear safety of the BN-600 reactor core ongoing work on the tests in the BN-600 fuel assemblies with MOX fuel.
To solve the problem was decided:

- to work out a precise model of BN-600 core, on the basis of which to carry out cross-verification of codes GEFEST, TRIGEX JARFR in order to clarify the causes of discrepancies between the results of related codes;
- to analyze the methodical errors of codes, based on the diffusion approximation, by the method of Monte Carlo;
- to conduct experiments using a new reactimeter of Beloyarsk NPP, conduct (re)evaluation of the experimental data;
- perform a joint calculation analysis of all the codes involved and complete their coordinated verification applied to the uranium core of the BN-600.

As the main target was taken Beloyarsk NPP requirement of halving the reserve for the error of core subcriticality, as the most critical bottleneck in the justification of balance reactivity.

2.2. Calculation and methodical base for substantiation of the reactivity balance

Currently, justification of nuclear safety of the BN-600 reactor core is based on the results of calculations made using three-dimensional neutronics codes, namely: TRIGEX [1], JARFR [2] and GEFEST [3] (Table 1). These codes have quite similar methodological basis. In particular, they use 26-group diffusion approximation of transport equation, but different methods of mesh errors minimization. MMKKENO code is used for precise 299-group calculations by Monte-Carlo method [4]. These codes with embedded ABBN-93 nuclear data library [5] form integrated system used in the Russian fast reactor designs.

Coordinated use of the codes based on different methodological basis, is provided by the ModExSys information system [6]. The database of the system contains information on the states of BN-600 reactor, calculation models, measurements, experimental and calculated data.
For analyzing methodical accuracy of the calculation ModExSys provides calculation models consistent on mass balance and geometry with different degrees of detail in the description of the core components, and models for the different codes: TRIGEX and MMKKENO.

Table 1. The Russian system of calculation codes for BN reactors

Code	TRIGEX	JARFR	GEFEST	MMKKENO
Method of calculation	Diffusion approximation	Diffusion approximation	Diffusion approximation	Monte-Carlo method
Nuclear data libraries	ABBN-93	ABBN-93/78	ABBN-93/78	ABBN-93
Number of groups	299/26	299/26	299/26	299
Group constant module	CONSYST	CONSYST/ MIM	CONSYST ARAMAKO	CONSYST
Main assignment	Research estimates for BN reactors, analysis of experiments	Design calculation of BN reactors	Core following and design calculation of BN-600 type reactor	Research estimates for BN reactors, analysis of experiments
Organization - Users	IPPE, RIAR, OKBM	KI, OKBM, RIAR	BNPP, IBRAE, VNIIAES	IPPE

2.3. Experimental methods

Experimental methods for controlling reactivity characteristics of the BN-600 core is based on the use of digital reactimeter with algorithms that take into account the presence of spatial effects [7].
Experiments on measuring control rod worth are the regular operations for the BN-600 and conducted before the beginning of reactor run after refueling, at the end of reactor run – before reloading. Measurements are performed at temperatures corresponding to the reloading state of cold reactor: T_{Na}~230˚C.
The worth of a single rod is carried out by "dropping a rod". It determined by the difference between the reactor reactivity at the time of start the rod movement and reactor reactivity after 180 seconds from the time of arrival the rod to the lower state.
To reduce the measurement error of large negative reactivity control rod system worth is determined using data on the worth of single rods and the interference factor:

$$\rho_{system} = K_{\text{int.}} \cdot \sum_{i=1,}^{N} \rho_i \qquad (1)$$

where: K_{int} - interference factor, ρ_i - worth of a single rod, ρ_{system} - worth of control rod system, N - amount of control rods in the system.
On the basis of control rod worth measurements developed methods for measuring of other characteristics of the reactivity balance: max excess reactivity, reactivity change rate, total temperature and power reactivity effect.

2.4. Analysis of control rods worth

In this work were assessed 1073 measurements of control rods worth from 39th to 56th reactor run.
Here it is not possible to provide a detailed description of the study because of its volume. Therefore are given only integral results and conclusions:

- adoption of new reactimeter with new software led to a relatively small shift of the measured values for the worth of a single control rod in the range of 2-3 %;
- use of modern constants of delayed neutrons ABBN-93 in reactimeter instead of obsolete, received during first criticality of the BN-600, led to a systematic reduction of the experimental data by about 5-7%;
- identified the need to adjust the coefficients of interference for shim rods system and safety rods system, which reduced the worth of shim rods system by 3 % at the beginning of reactor run and 9 % at the end of reactor run; for safety rods system reduction was 20 %;
- all changes are reflected in the new edition of the measurement technique of neutron-physical characteristics of BN-600;
- worth calculations for control rods of BN-600 proved to be very sensitive to the mesh errors, that allows to select a mesh that best describes the worth for each group of control rods;
- in particular, the worth calculations for shim rods in the diffusion approximation (GEFEST, TRIGEX, JARFR) may well coincide with the precision Monte Carlo calculations due to the mutual compensation of mesh and transport errors;
- worth calculations for safety rods with coarse mesh (1 point on fuel assembly) give values closer to a more accurate calculation of the Monte-Carlo;
- homogenization in the calculation of control rods leads to an overestimation of worth: by ~ 7% for shim rods and ~ 18% for safety rods.

The results of this work led to a better understanding of the real values of the control rods worth and the level of calculated description (Fig. 1). By results of this work recommendations issued on the control rods worth for 01M2 core of the BN-600 and refined their design values (Fig. 2).

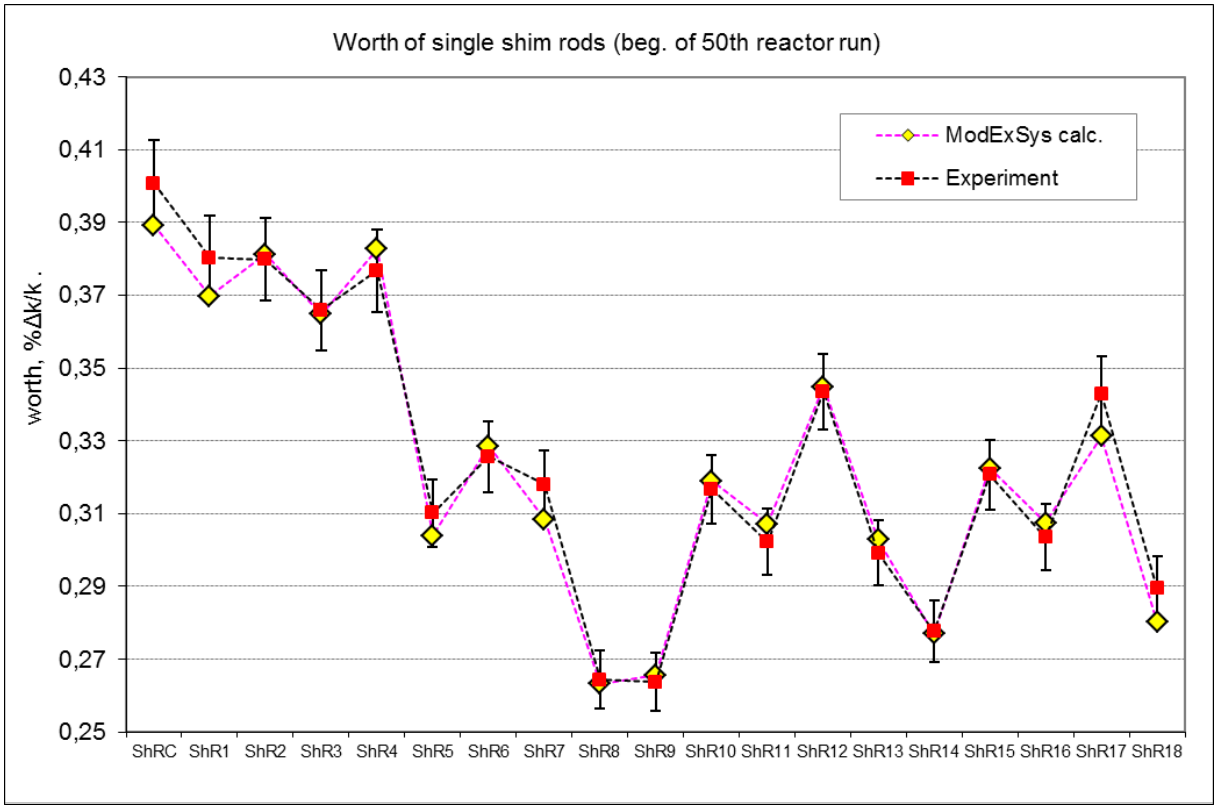

FIG. 1. Quality of the description of ShR worth values using advanced calculation methods

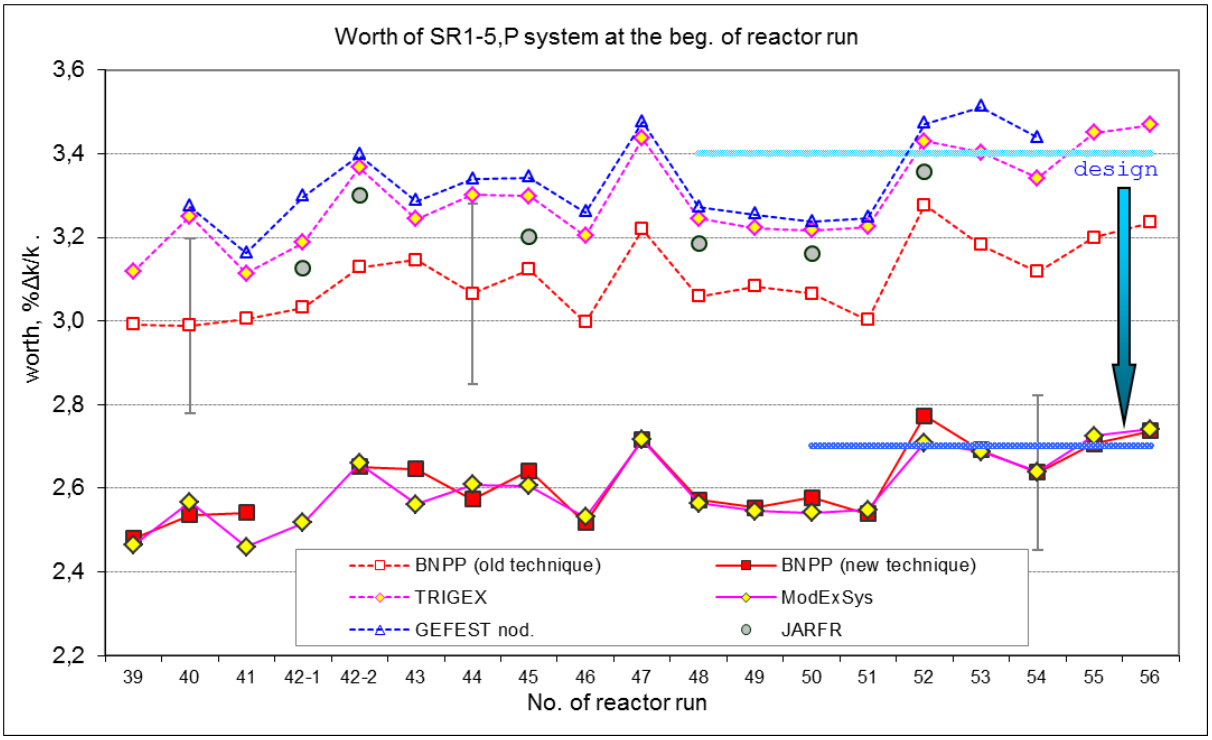

FIG. 2. Calculated (TRIGEX, GEFEST, JARFR, ModExSys) and experimental (BNPP) values of safety rods system worth

2.5. Analysis of max excess reactivity

Max excess reactivity is physical characteristic determining upper boundary of positive reactivity, which can be released implicitly in the core. For the purpose of assurance of reactor nuclear safety this value should be compensated by reactivity control system, i.e. reactor control rods taking into account core neutronics. Since it is impossible to simulate experimentally reactor with max excess reactivity, this reactivity is determined on the basis of indirect combined measurements of criticality, worth of shim rods system and "integral curve" of shim rods system.

Of course, direct analytical simulation of BN-600 reactor condition with max excess reactivity is possible. However, in view of that computer codes have various methodological errors (in particular, diffusion approximation error), excess reactivity is often evaluated using also analysis of critical conditions facilitating minimization of these errors.

To account systematics for discrepancies and reduce the influence of the technological component of the criticality forecast error proposed special method for adjustment predictions using results of current measurements [6]. This method proved very effective. It has been shown that it is appropriate take into account the dependence of heterogeneous error from depth compensation system.

$$k_{eff} = k_d \cdot \delta_k \cdot \left(1 + \varepsilon_k \cdot \left(\frac{1}{k_d} - \frac{1}{k_d^{ULS}}\right)\right) \qquad (2)$$

where: k_d - $k_{eff.}$ values calculated by diffusion code for the state being of interest to us and the state characterized by control rods position on the upper limit switches (ULS); ε_k – correction factor taking into account methodological component of error of immersed shim rods system worth evaluated by Monte Carlo method using MMKKENO code.

δ_k – the total correction to $k_{eff.}$ taking into account the systematic component of the errors of calculation by the standard model of the BN-600 core with use of a diffusion code and actually measured criticality of core previous states with the implementation of various technological errors.

In view of (2) excess reactivity is defined as:

$$\rho_{XR} = \left(1 - \frac{1}{k_d^{ULS} \cdot \delta_k}\right) \cdot 100 \qquad (3)$$

Were evaluated and analyzed the results of 37 measurements of the excess reactivity at the beginning and end of reactor run from 39th to 56th. Final results comparing excess reactivity calculations and the experimental data shown in Fig. 3. Based on the data we can state the possibility of prediction excess reactivity up: 0,2 % Δk/k at the beginning of reactor run and 0,3 % Δk/k – in the burned-out state at the end of reactor run. However, it should be noted that these results can be achieved only on the basis of the analysis and consideration of previously measured critical states of the BN-600.

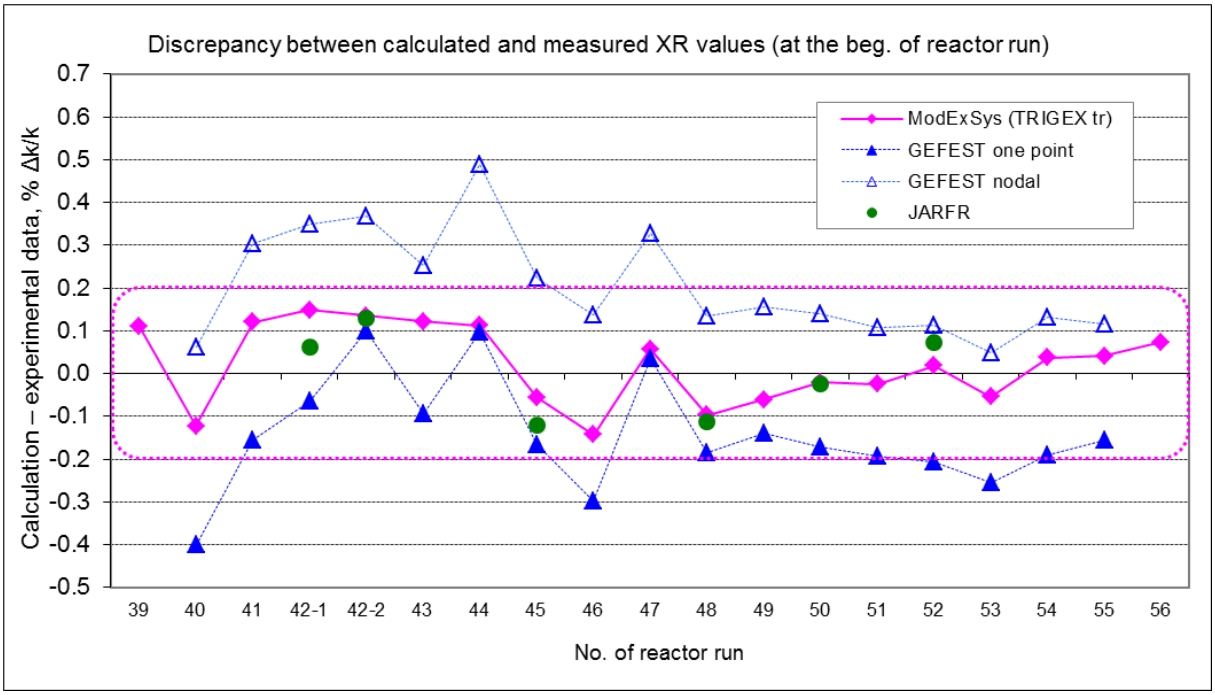

FIG. 3. Results of analysis of experimental determination of max excess reactivity

2.6. Analysis of reactor subcriticality after safety rod setting in MXR state

Fig. 4 illustrates the assessment of the level of subcriticality, which according to the requirements of nuclear safety should not be lower than 1 %. In the design documents the value itself and its accuracy is determined based on the difference between max excess reactivity and control rods worth. However, in the experiment and in the calculation, adjusted for the measured criticality, between MXR and control rods worth arises correlation error, which is difficult to assess.

Therefore the level of subcriticality better to define by direct calculation, but considering the influence of control rods heterogeneity according to the expression:

$$\rho_{subcrit}^{ModExSys} = \frac{1}{k_{eff}^{ModExSys}} - 1 = \frac{1}{k_{TRIGEX}^{LLS} \cdot \delta_k \left(1 + \varepsilon_k \cdot \left(\frac{1}{k_{TRIGEX}^{LLS}} - \frac{1}{k_{TRIGEX}^{ULS}}\right)\right)} - 1 \qquad (4)$$

Results of the comparison with the experiment show that for this approach the level of ~ 0,4% Δk/k is a sufficient margin to compensate the uncertainty of the forecast calculation for BN-600 subcriticality after safety rods setting.

2.7. Alalysis of reactivity change rate

Experimental assessment of reactivity change rate in fuel burn is determined by the dependence of the excess reactivity of effective operating days. And neptunium effect of reactivity is eliminated: the

dependence based starting from operating time of at least 10 effective days. Also excludes periods of reactor operation at power levels less than the nominal.

On Fig. 5 compared the measured values and calculated values of reactivity change rate, resulting from the difference of excess reactivity at the beginning and end of reactor run. It also shows the behavior of the rate, if the calculation method take into account burn of boron-10 in the control rods.

As can be seen from the data, the reactivity change rate calculation agrees with experiment within 6%.

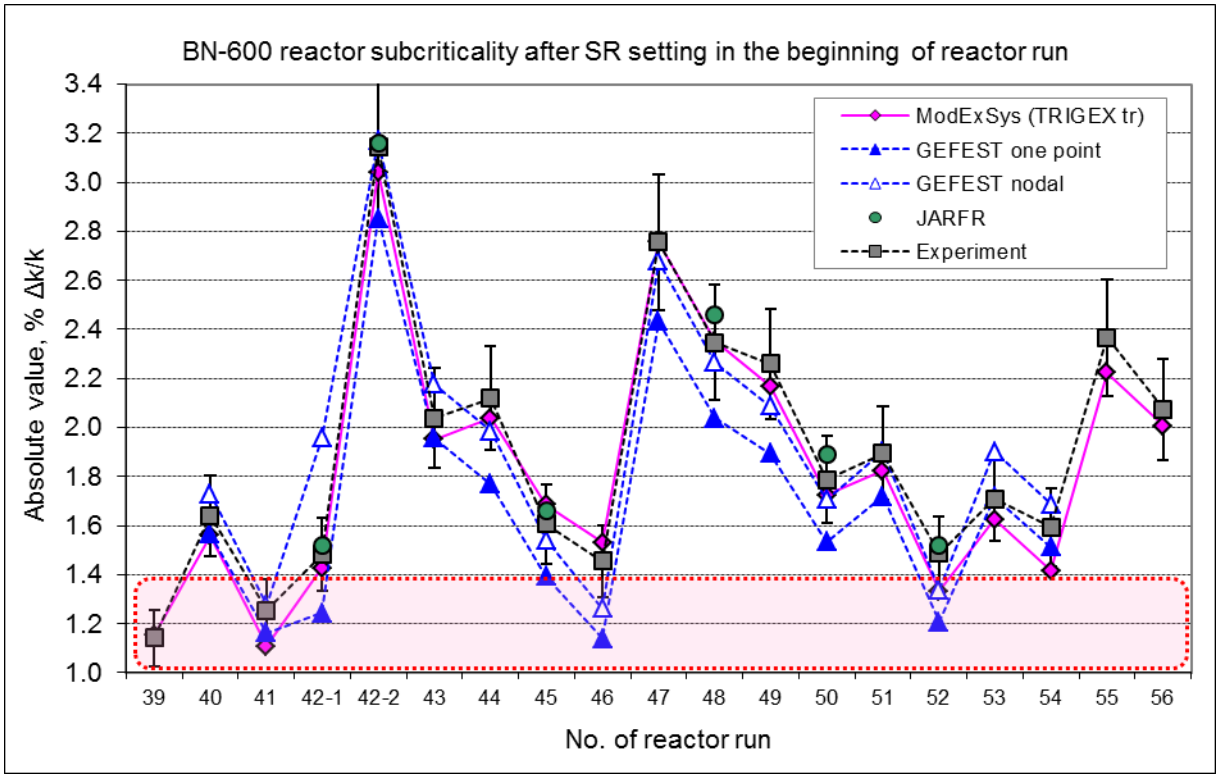

FIG. 4. Analysis of BN-600 reactor subcriticality after safety rod setting in MXR state

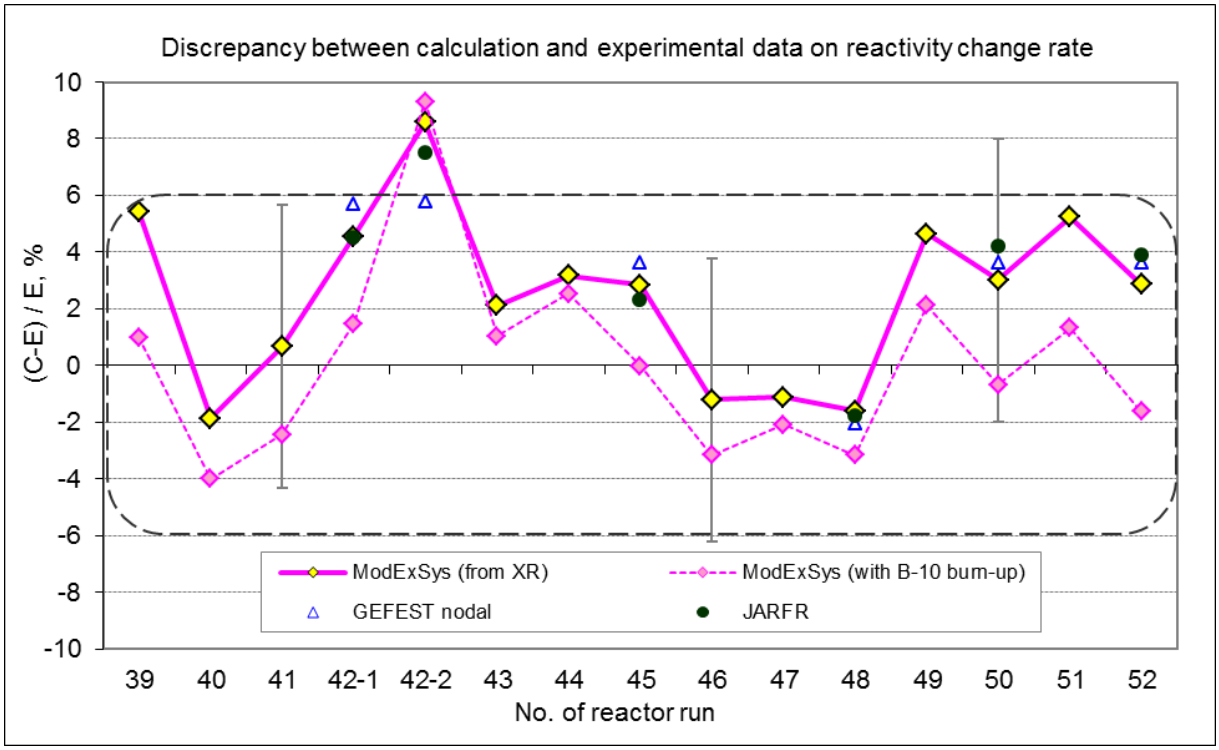

FIG. 5. Discrepancy between analytical and experimental data on reactivity change rate

3. ANALYSIS OF POWER DISTRIBUTION IN THE BN-600

3.1. γ-scanning technique to measure the distribution of energy in the BN-600 core

In the BN-600 there is no means for automated control of fuel assembly (FA) energy release and power. Experimental work on the analysis of BN-600 energy profile conducted at the time of first criticality and then periodically at stages of modernization of its core.

Technique includes two main steps. At the first step of measurements the reactor operates at a low power level ~0.5 % N_{nom} on which there is FA activation. At the second step by means of scanning installation is measured flux of gamma quanta from decay of the collected fission product La^{140}. The scheme of the measurement described in detail in [8]. A series of experiments was carried out: after 44, 48 and 50 refueling.

3.2. Analysis of the energy release distribution in the BN-600 core

Calculation of the neutron field distribution for BN-600 is the main method of forecasting and monitoring of the local characteristics: energy release in pins, FA power, radiation doze on constructional materials, burning out of fuel. For BN-600 it is carried out using the same code system: TRIGEX, JARFR, GEFEST and MMKKENO.

The analysis of measurement results made in the transition to the core 01M2 of BN-600 showed the adequacy of numerical simulation [9]. Within the core the maximum error does not exceed 5.5% for diffusion codes GEFEST, JARFR and TRIGEX with ABBN-93 constants (Fig. 6). Blanket and IVS characterized by systematic discrepancy between calculation and experiment with increasing distance from the core boundary. For these external cells calculation systematically underestimates the energy release and the neutron flux by 20-25%. In this case, the real level of discrepancy depends strongly on the choice of methods and algorithms to reduce the mesh error.

For fuel assemblies on the border of core and blanket discrepancies completely eliminated by taking into account the methodological errors of the diffusion approximation. For fuel assemblies at the periphery such accounting also significantly improves the agreement between calculation and experiment, but not completely eliminate the discrepancy. We associate the remaining discrepancies with the constant and model errors. And further improvements of agreement between calculation and experiment in this area is of great interest. From a practical point of view, demonstrated level of discrepancy does not represent significant challenges for BN-600. Since the energy release level is low in the peripheral areas.

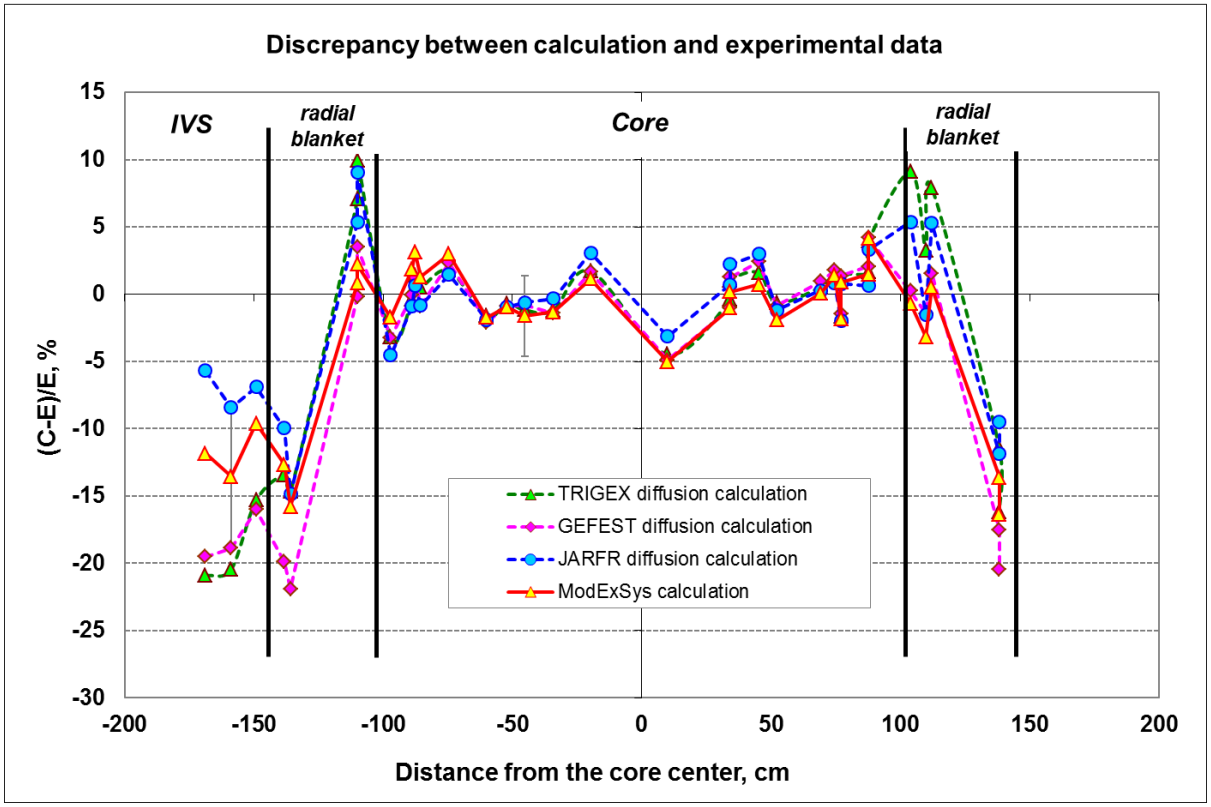

FIG. 6. Deviation calculation of the experiment for energy release in 48-th reloading

4. CONCLUSION

Based on years of BN-600 operating experience were finally brought and tested measurement techniques of reactivity characteristics based on the new reactimeter and techniques for γ-scanning assemblies. Issued a new version of measurement techniques of neutron-physical characteristics of the BN-600 core. As a result was revalued previously performed measurements and clarified some of the design parameters of the core, obtained with the use of measurements.

The development and application of new programs for neutronic calculations (new version of GEFEST and JARFR codes based on ABBN-93 constant system, the ModExSys system and MMKKENO code based on the Monte Carlo method) has allowed at a new level to understand and evaluate the methodological features of calculation of basic parameters of the BN-600 core. Cross verification of codes led to the coherence of the results obtained by different codes using the same mesh options.

As a result of experimental and calculating studies was created the coordinated and consistent database of neutron-physical characteristics for the fast sodium reactor of medium power. Completed verification of code system TRIGEX, JARFR, GEFEST and substantiated improved values of the basic neutron-physical characteristics of the BN-600 core with high accuracy. In general, were additionally confirmed the design parameters of the core, and the assessment of their uncertainties has been further substantiated.

Accounting of the experimental data and codes verification improved the forecast precision of the maximum excess reactivity to 0.2 % Δk/k. Forecast of BN-600 core subcriticality can be made with an accuracy 0.2-0.4 % Δk/k. Based on this analysis the forecast accuracy for shim rods worth 7%, safety rods worth 8 %.

Calculation of energy release distribution by BN-600 assemblies describes the experimental data in the core with an accuracy better than 5%. For blanket and IVS computational and experimental discrepancies increase to an amount not exceeding 20-30 %.

ACKNOWLEDGEMENTS

The authors thank B.A. Vasilyev, M.R. Farakshin, V.A. Zheltyshev, V.V. Maltsev, V.F. Roslyakov, A.A. Belov, E.F. Seleznev, M.Yu. Semenov for discussion of the topics and the materials provided to summarize in this paper.

REFERENCES

[1] A.S. Seregin, T.S. Kislitsina, Abstract of TRIGEX.04. Preprint FEI-2846, Obninsk, 2000.
[2] L.N. Yaroslavtseva, JAR code package for nuclear recator neutronics analysis. VANT, Series: «Physics and Technology of Nuclear Reactors», 1983, Edition 8 (37), pp.41-43.
[3] E.F. Seleznev, Development and use of operating codes for reactor neutronics analysis. Dissertation, VNIIAES, Moscow, 2000.
[4] A.A. Blyskavka, G.N. Manturov, M.N. Nikolaev, A.M. Tsiboulia, CONSYST/MMKKENO code package for analytical studies on nuclear reactors by Monte Carlo method in multi-group approximation with scattering indicatriss in P_n-approximation. Preprint FEI-2887, Obninsk, 2001.
[5] G.N. Manturov, M.N. Nikolaev, A.M. Tsiboulia, 1995. Group constants system ABBN-93. – Verification report. Interdepartmental Commission on Certification of Reference Data in the Various Subject Areas of Nuclear Science, Engineering and Technology, TSNIIAI, Moscow.
[6] A.V. Moiseev, System for modeling and computational analysis of neutron-physical experiments at fast power reactors. Dissertation, IPPE, Obninsk, 2010.
[7] I.P. Matveenko, V.A. Lititsky and A.G. Shokod'ko. Taking into account spatial effects for reactivity measurements. VANT, Series: «Physics and Technology of Nuclear Reactors», 2008, Edition 2, pp.41-47.
[8] Yu.S. Khomyakov, A.L. Kochetkov, V.V. Izotov et al., Control over the distribution of energy in the BN-600 by γ-scanning assemblies. Nuclear energy, 2008, vol.105, issue 6, pp. 339-344.
[9] A.V. Moiseev, Yu.S. Khomyakov, E.F. Seleznev, M.R. Farakshin et al., Analysis of accuracy for calculation of power profile in the BN-600 reactor. Nuclear energy, 2010, vol.108, issue 2, pp.63-70.

Turbulence and Coherent Structures in a Tight 19 Pin Rod Bundle Separated by a Grid Spacer

Elia Merzari, Paul Fischer, W. David Pointer

Argonne National Laboratory

Presented by W. David Pointer

Abstract. The flow in tight pin bundles (pitch to diameter ratio below 1.1) has been the object of several investigations. The large difference in velocity within the cross section induced by the tight pitch creates the possibility of a Kelvin-Helmholtz instability and the generation of a vortex street in the gap. Recently, it has been proven that the presence of a grid spacer of the type usually encountered in SFRs (Sodium Fast Reactors) does not prevent this instability. Such SFR spacers (e.g. the PFR spacers) are usually comprised of a honeycomb array with dimples attached to surface to insure separation. Most investigations of this phenomenon conducted so far have been limited to single pins or wedges of real bundles. Grid spacers are usually ignored. In the present work the first large scale Large Eddy Simulation (LES) of the flow in a realistic 19 pin bundle has been conducted. The code used is the spectral element CFD code Nek5000. The focus will be in particular in analyzing in the interaction of coherent structures generating in different gap regions and the characterization of the vortex network in a realistic rod bundle.

INTRODUCTION

The accurate prediction of the flow in rod bundles is crucial for both the design and the safe operation of nuclear reactor systems. However the geometry complexity and the non-uniformity of the flow introduce peculiar features that can be reproduced only with three-dimensional CFD. In fact, even in bare rod bundles, i.e., bundles that do not contain any spacing device, the structure of the flow is inherently complex.

It is now a well established fact that the flow in rod-bundles, especially when tightly packed, differ substantially from the flow in pipes and channels [1]. Part of this complexity is due to the presence of turbulence driven secondary flows. However, the most astounding feature of rod-bundle flow is the presence of large scale coherent structures that develop in the streamwise direction in the region of the narrow gap. This gap vortex street is due to a large scale instability and dominates turbulent mixing.

In a real fuel assembly hundreds of sub-channels and narrow gaps are present , causing the gap vortex streets in different gaps to interact, forming a gap vortex network. While the flow dynamics of the gap vortex street has been examined in detail, the dynamic of the gap vortex network has historically been subject to less scrutiny.

The gap vortex network can be the main source of turbulent mixing in tight lattice rod bundles. Since, accurate prediction of mixing coefficients is essential to evaluate the performance of reactor cores (both at operation and during accident conditions), the current limited knowledge of the phenomenon has hindered the use of the tight lattice concept, which is looked upon to design long-life reactor cores. The present paper represents one step toward gaining a better understanding of turbulent mixing in the presence of the gap vortex network.

A comprehensive historical review on the subject of the gap vortex street is provided by Meyer [2], who guides the reader through the experimental discovery, the controversy and the recognition of these patterns as the driver of turbulent mixing. The simulation of these coherent patterns has recently been achieved through CFD techniques. The first example is due to the pioneering work of Chang and Tavoularis [3], which employs Unsteady Reynolds Averaged Navier-Stokes (URANS). Several other works followed [4, 5, 6] applying the same methodology, with different codes and turbulence models, to different geometries. Recently these structures have also been simulated through LES [7].

Most of the studies conducted so far, however, rely on some form of geometric simplification. Even the most complete geometry studied [6], which consists of a significant portion of a CANDU rod bundle, does not include the spacing devices used in actual reactors. On the other hand the simulations performed by Merzari et al. [7], which included the same spacer design used in this paper, considered a single pin.

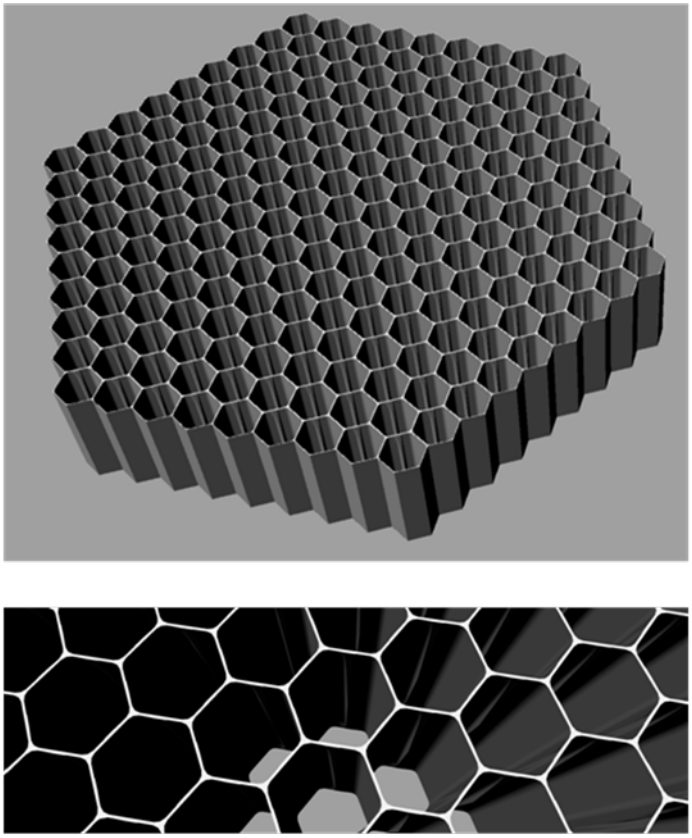

FIG. 1. Spacer grid design

The present paper represents the first attempt to simulate and capture these coherent structures in a realistic assembly. The simulations have been performed using the spectral element LES code Nek5000 (see “Methodology” section).

The geometry investigated is a triangular lattice SFR bundle with pitch to diameter ratio equal to 1.08. This value is consistent with values that are looked upon for long-life reactor cores. Typically SFR bundles are spaced using wire-wrappers. However a minority of these reactors (among which the PFR) are spaced through grid-spacers. A three-dimensional representation of the spacers used here can be found in Fig. 1.

The present paper is somewhat intentionally limited in scope. The analysis is limited to a 19 pin bundle, which is significantly smaller than bundles commonly found in SFR cores (although they are usually found in the blanket) but sufficient to examine the physics of the gap vortex network. The

features of the flow in an infinite lattice are first recalled, then the results related to the 19 pin bundle are presented with a particular focus on the characterization of the coherent structures. Fig. 2 presents a snapshot of the turbulent flow field in the 19 pin calculation.

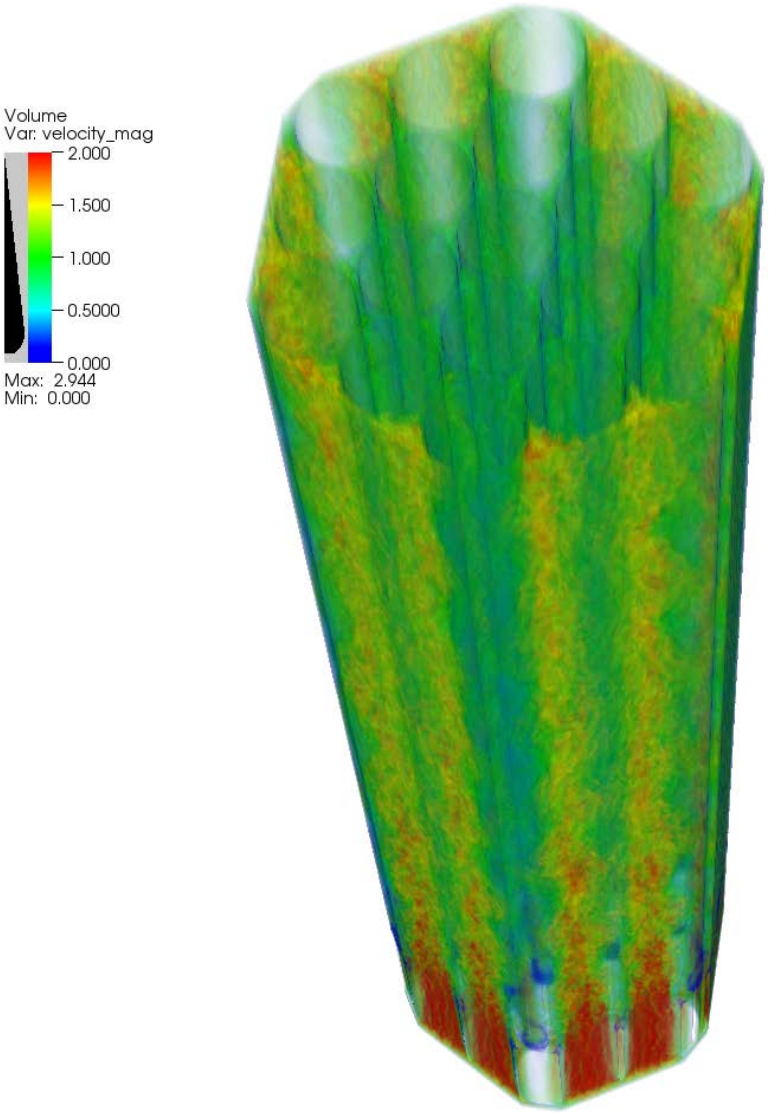

FIG. 2. Volume rendering of the Velocity Magnitude in the 19 pin bundle. The values have been normalized by the bulk velocity.

METHODOLOGY

The present paper focuses on the simulation of an infinite lattice rod-bundle array and a 19 pin rod bundle, both characterized by a honeycomb spacer grid. The spacers are 25 pin diameters apart: this implies that the minimum computational domain required is fairly large. Periodic boundary conditions in the streamwise direction are used to limit the domain to one span, thus reducing the computational cost.

The Reynolds number considered in this paper is 15,000, consistent with current designs proposed for small, modular, long-life SFR cores [8]. The rod bundle investigated has a triangular lattice with pitch to diameter ratio equal to 1.08.

The spacer grids considered in the present work are shown in Fig. 1. They consist of honeycomb grids 3.125 pin diameters in length, in contact with each pin through a cosine shaped dimple. In the present case the grids are separated by 25 pin diameters. In the cross section the blockage ratio reaches 40 % of the flow area in the region of the spacers.

Moreover, while considering an infinite triangular pitch lattice a single pin with lateral periodic boundary conditions has been simulated. It is consistent with the methodology used in Merzari et al. [4], which has already demonstrated the capability to reproduce the gap vortex street in bare rod bundles for a tighter lattice (P/D=1.06). For coding simplicity the domain has been rearranged in a hexagonal domain with 3 periodic sets of boundary conditions in the cross section. The equivalence between the two domains was discussed in Ninokata et al. [9].

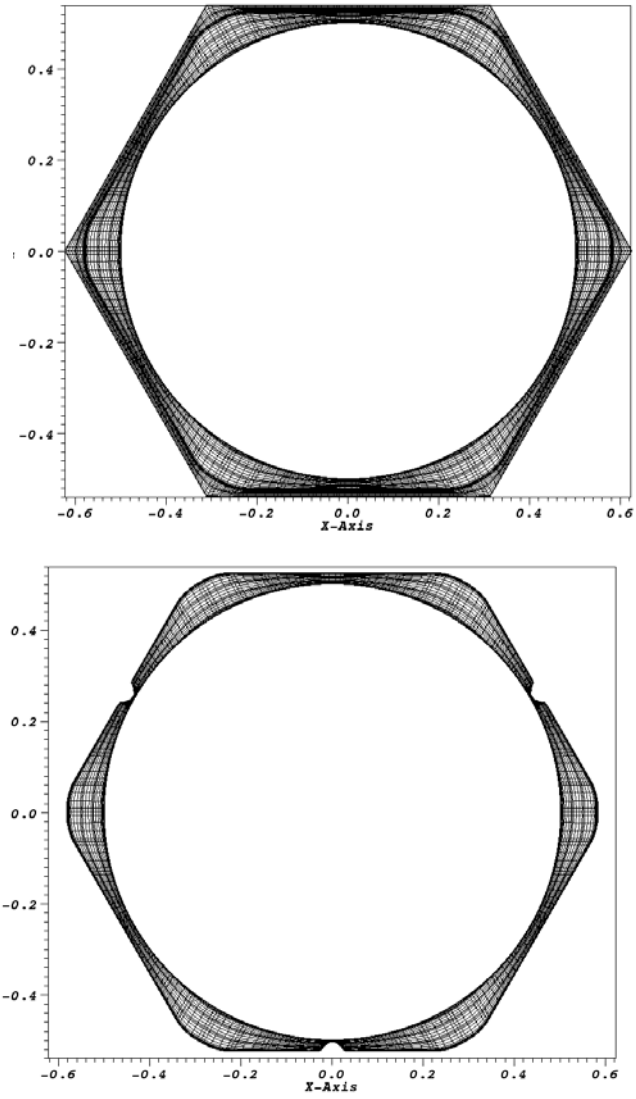

FIG. 3. Mesh for the single pin case. (Top) cross section in the bare bundle region. (Bottom) cross section in the spacer region.

The CFD spectral element code Nek5000 [10] has been used to perform all the calculations discussed here. Spectral elements methods are a class of higher-order methods in space. Polynomial functions of up to the 7^{th} degree have been used to discretize the velocity field in each element. In the generalized weighted residual framework, the present spectral element method can be classified as a Galerkin method where the test functions and the basis functions for each element are Lagrange polynomials evaluated on Gauss-Lobatto-Legendre collocations points (for the velocity).

The approach used to simulate turbulence in the present work is LES. In LES, large-scale turbulence is simulated while smaller scales are modeled. Since smaller scales have a nearly universal behaviour, LES is a more reliable methodology than is Reynolds-averaged Navier-Stokes (RANS), in the sense that it generally depends less on the model details. It is also preferable to use in place of direct numerical simulation because it can be performed at a reasonable computational cost. The contribution of the smaller scales to the energy cascade is in the present case modeled through a local, element-based explicit cut-off filter in wave-number space. The energy is removed from the smallest simulated scales (high wave-numbers), thus mimicking the effect of smaller eddies [11]. This procedure allows for a coarser grid and therefore lower computational cost. Time advancement has been carried out through the characteristics method [12], which allows for higher Courant numbers to be reached. The Nek5000 code has been extensively validated and is massively parallel.

Examples of the grids used are shown in Fig. 3 (single pin case) and Fig. 4 (19 pin case) for streamwise-normal cross sections. The figures depict the elements and the actual collocation points for the coarse mesh. The discretization is designed to allow for at least one point near the wall at $y^+<1$ and five points within $y^+<10$. The corner channels have been removed in the 19 pin mesh to avoid excessive bypass flow.

The simulations were carried out by using the spectral element code Nek5000 [10] on the Argonne computer system Intrepid (an IBM Blue Gene/P system with 40,960 quad-core compute nodes)—with up to 200,000,000 collocation points for the 19 pin bundle. The computations was performed on up to 16384 processors and required approximately 10 million CPU-hours to complete.

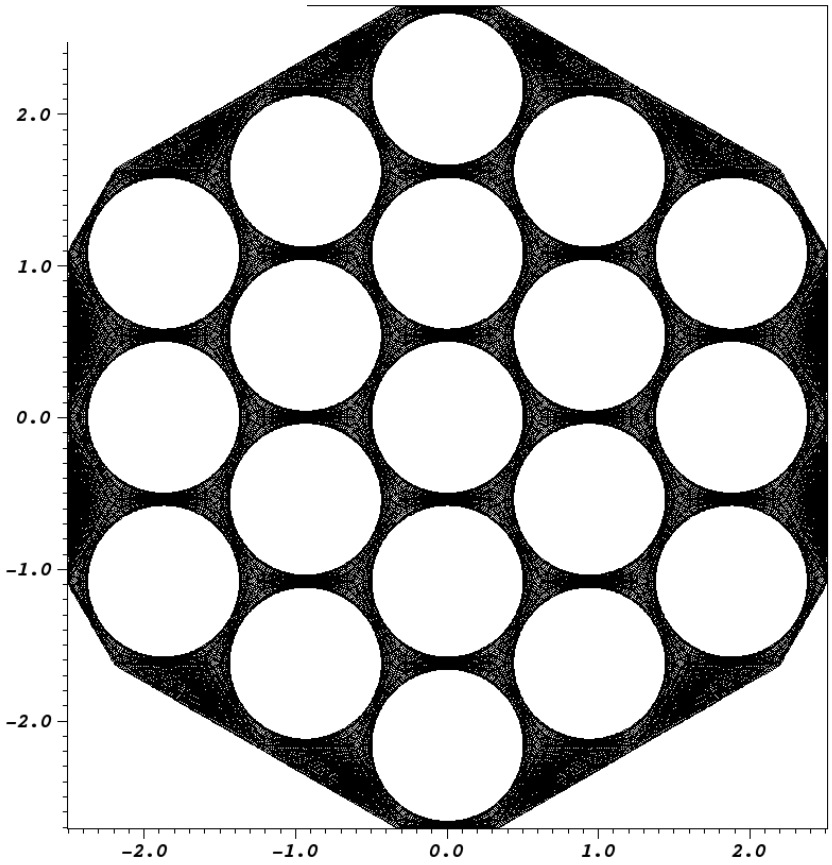

FIG. 4. Mesh for the 19 pin bundle.

One of the key methods to identify the gap vortex street is Proper Orthogonal Decomposition (POD) [13]. It allows for the recognition of the most energetic modes of turbulence by performing an eigenvalue decomposition of the covariance matrix. Such a matrix is computed according to Sirovich

et al. [14]. A set of *M* snapshots of the flow field is collected and the following eigenvalue-eigenvector problem is solved to obtain the POD eigenmodes:

$$C_{mn} a_{n,i} = \lambda_i a_{n,i}\,, \tag{1}$$

where $a_{n,i}$ are the real coefficients that define the eigenmodes, λ_i are eigenvalues and no summation is performed over i. The matrix *C* (size MxM) is defined as:

$$C_{mn} = \frac{1}{M}\left(\overrightarrow{u_m}, \overrightarrow{u_n}\right), \tag{2}$$

where u_m, u_n are snapshots of the velocity field. Each eigenmode $\overrightarrow{\sigma_i}(\vec{x})$ can be then computed using equation:

$$\overrightarrow{\sigma_i}\left(\vec{x}\right) \cong \sum_n a_{n,i} \vec{u}_n\left(\vec{x}\right), \tag{3}$$

RESULTS

In the first part of this section a summary of the feature of a single pin flow will be presented. Figure 5 shows a snapshot of the flow field (velocity magnitude), it is possible to notice a quasi-sinusoidal path in all similar to what was observed in a rod bundle and other simplified geometry [4]. The values are normalized by the bulk velocity. Apparently the spacing device only perturbs the gap vortex street, but the latter recovers quickly (in 8 pin diameters).

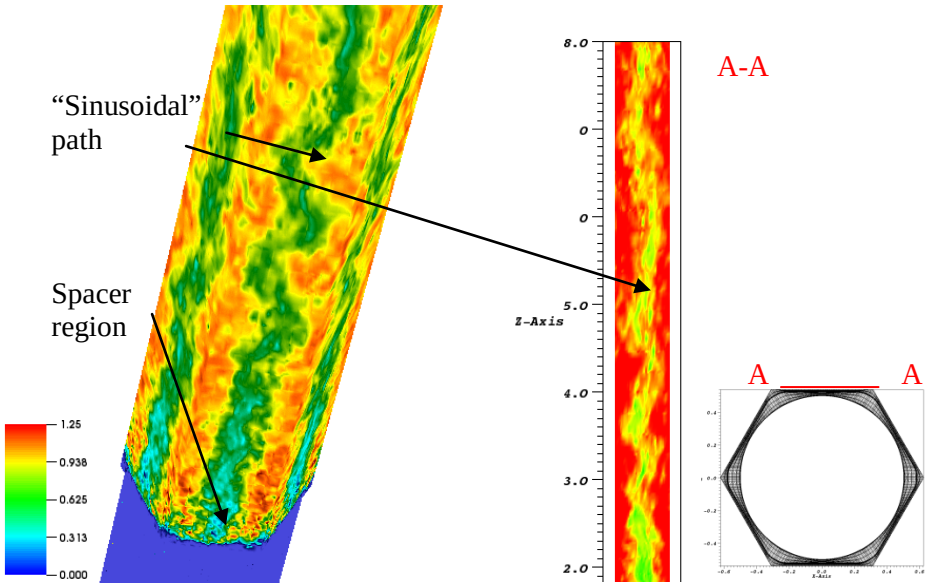

FIG. 5. Velocity magnitude in the wake of the spacers. The arrows indicate respectively the spacer region and the sinusoidal path. (Left) 3D view, (Right) and narrow gap section

Merzari et al. [15] identified the POD modes of turbulence responsible for the gap vortex street in a bare bundle and a simplified geometry. Modes of the same type were found in the present simulation. Figure 6 shows the most energetic mode of turbulence obtained by decomposing a covariance matrix

constructed from 2,000 snapshots collected at intervals of 0.0004 TOT (turn-over times). It is possible to notice the alternating pattern of the cross velocity in the narrow gap.

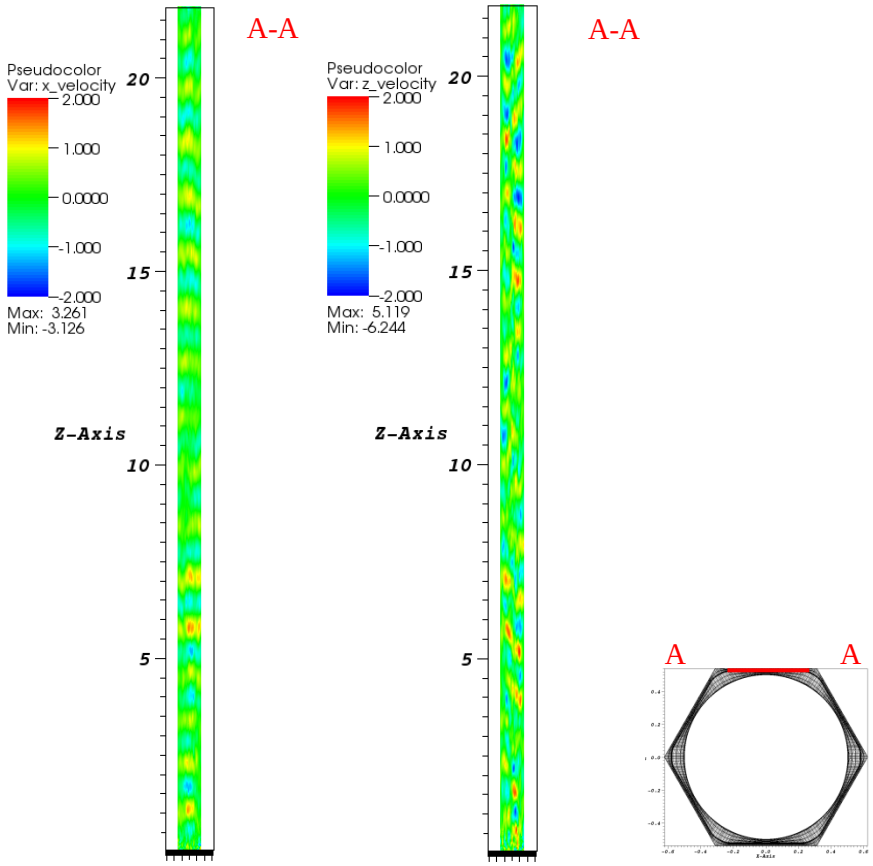

FIG. 6. Most energetic eigenmode: section contour plots: (left) cross velocity on the upper boundary, (right) streamwise velocity on the upper boundary

The flow in the 19 pin rod bundle is considerably more complicated. The presence of edge-sub-channels with a much lower blockage ratio leads to a edge sub-channel dominated flow. In fact, the velocity is much higher in the lateral sub-channels (Fig. 7), particularly at the exit of the spacer but it remains true throughout the domain. In both Fig. 7 and Fig. 8 the velocity is normalized by the bulk velocity.

In such a bundle, the effect of the gap vortex network is therefore hidden by the dominant dynamics. An interesting effect is that POD in the proper form cannot be applied to investigate the interior of the domain, since the most energetic modes of turbulence are related to the edge-channels. We have developed a way to overcome this limitation, by limiting POD to some parts of the domain. Before the covariance matrix is assembled, the velocity field is clipped out but in the region of interest which in this case is the centre of the domain.

Throughout the following the z direction represents the streamwise direction.

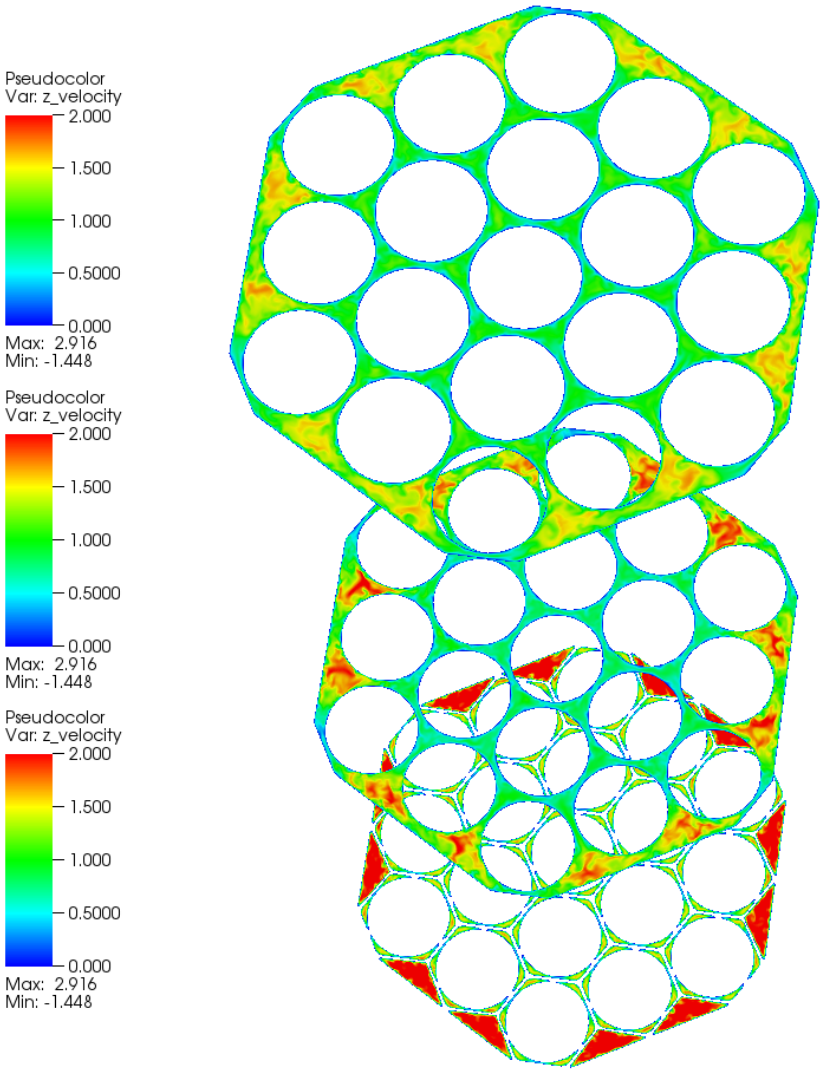

FIG. 7. Streamwise cross section plots of the streamwise velocity (z/D=-1, z/D=4, z/D=12).

The gap vortex network is indeed present in the interior of the domain as can be observed in Fig. 8. A quasi-sinusoidal path develops in the streamwise direction along with a pulsating cross velocity.

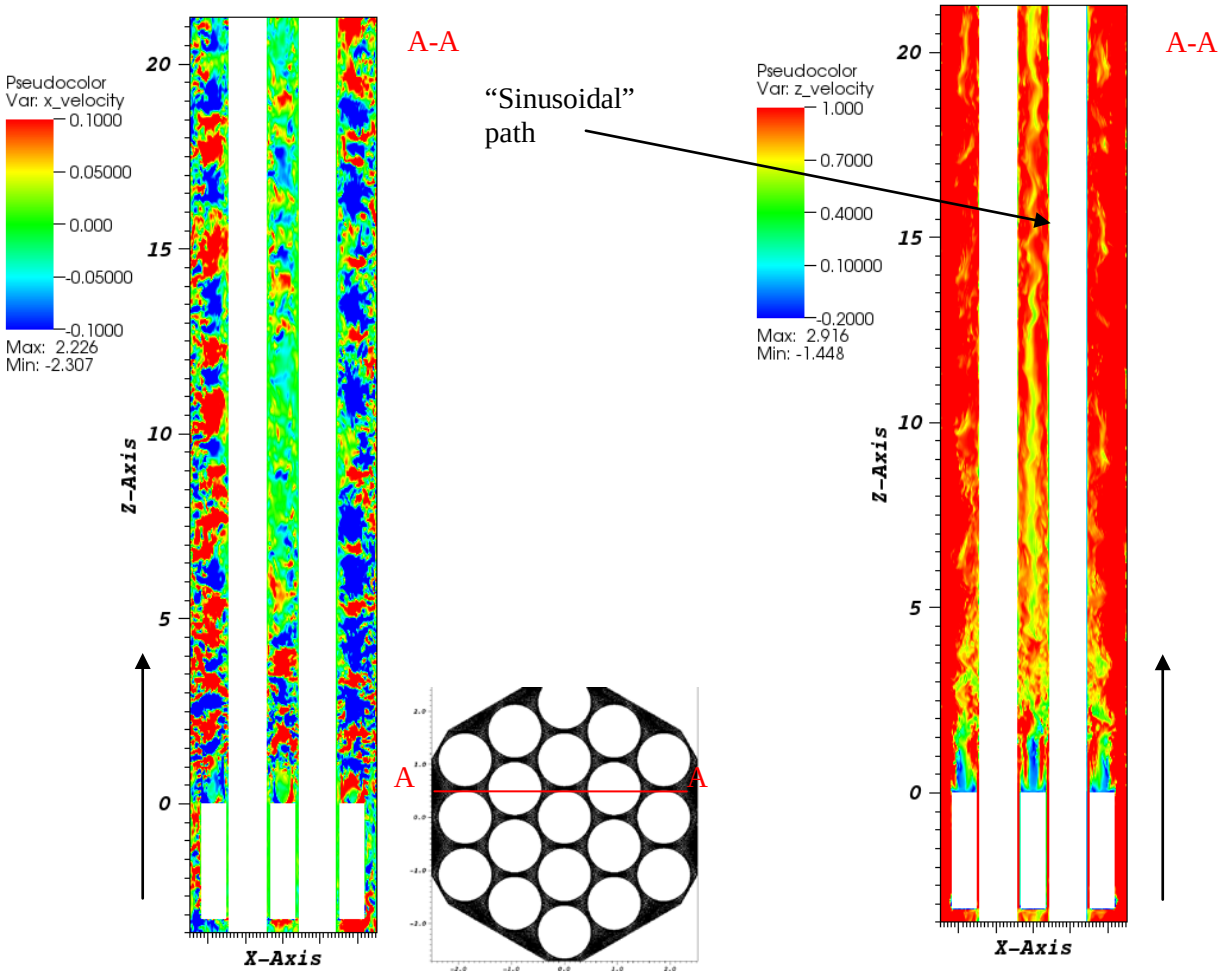

FIG. 8. (Left) Cross Velocity on plane. (Right) Streamwise velocity on plane. Arrows represent the streamwise direction.

A more detailed understanding can be achieved using correlation analysis. We recorded the time signal at 700 locations: 7 cross section location (Fig. 9) x 100 axial locations (equally spaced in the wake of the grid spacer). Autocorrelation as a function of time as well as two-point space correlation were computed. The autocorrelation $R(\tau)$ for a function $f(t)$ is defined as:

$$R(\tau) = \frac{1}{T}\int_0^T f(t) f(t+\tau) dt \tag{4}$$

where T is the a sufficiently large integration time.

The cross velocity signal is considerably stronger in the immediate wake of the spacer (Fig. 10), it is also however much more incoherent (Fig. 11) both across gaps and axially. As the effect of the spacers dies out the typical properties of the gap vortex street emerge within each individual channel, and these include:

- A strongly anisotropic, non-gaussian behaviour (Fig. 12), with the fluctuating component of the cross velocity dominating the wall-normal component. In isotropic turbulence phase plots lead to the formation of circles, indicating equivalent preponderance for both velocity components.
- High time autocorrelation even at relatively large time lags (Fig. 13), suggesting the presence of a coherent temporal signal.
- High spatial coherence in the streamwise direction (Fig. 14 – top). The two-point correlation peak after a given lag, corresponding to the time it took for the coherent part of the signal to travel across the streamwise distance separating the two points.

For all of these effects it is possible to notice a trend toward a stronger gap vortex street as the observer moves in the streamwise direction.

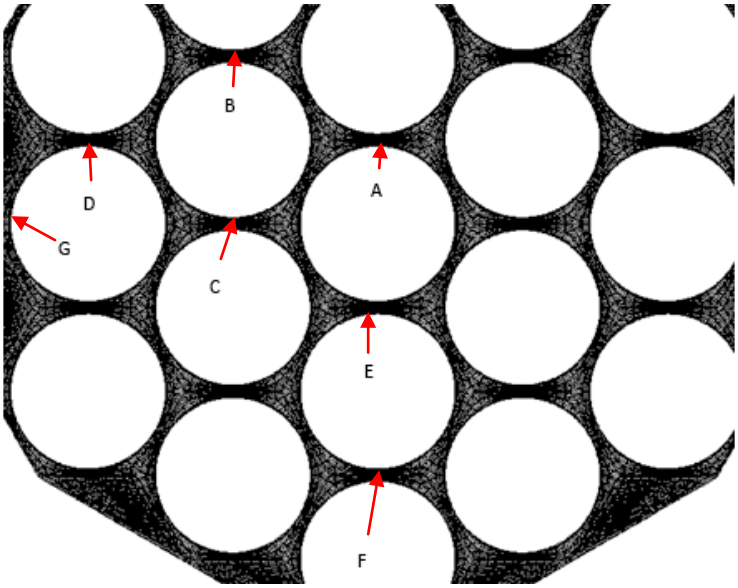

FIG. 9. Location of Monitoring Points on the Cross Section Plane

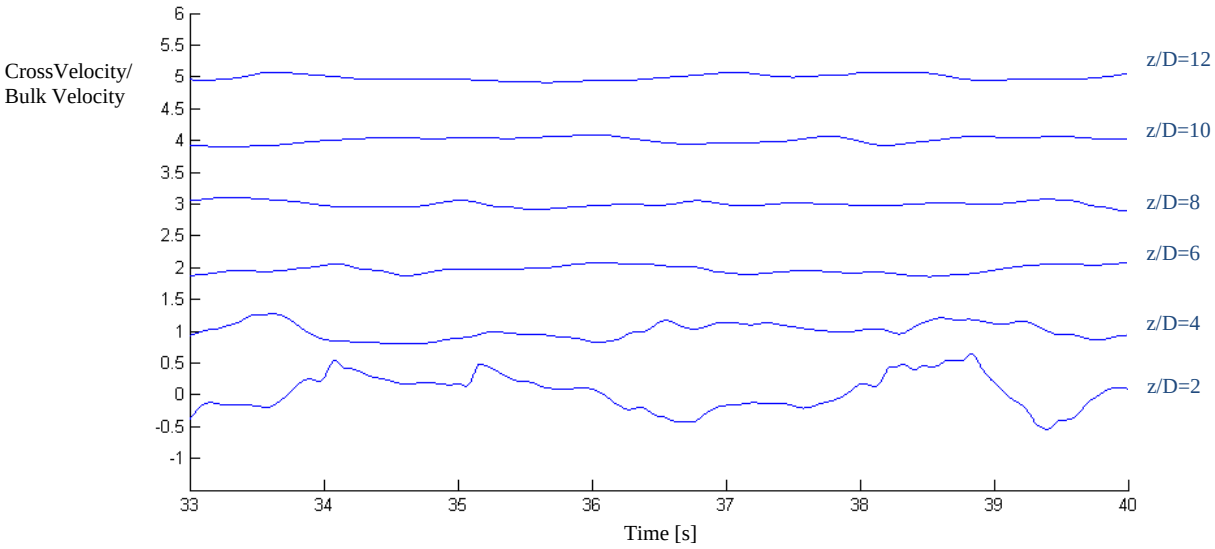

FIG. 10. Temporal signal of cross velocity on monitoring point A at 6 axial locations. The velocity signals are offset by 1.

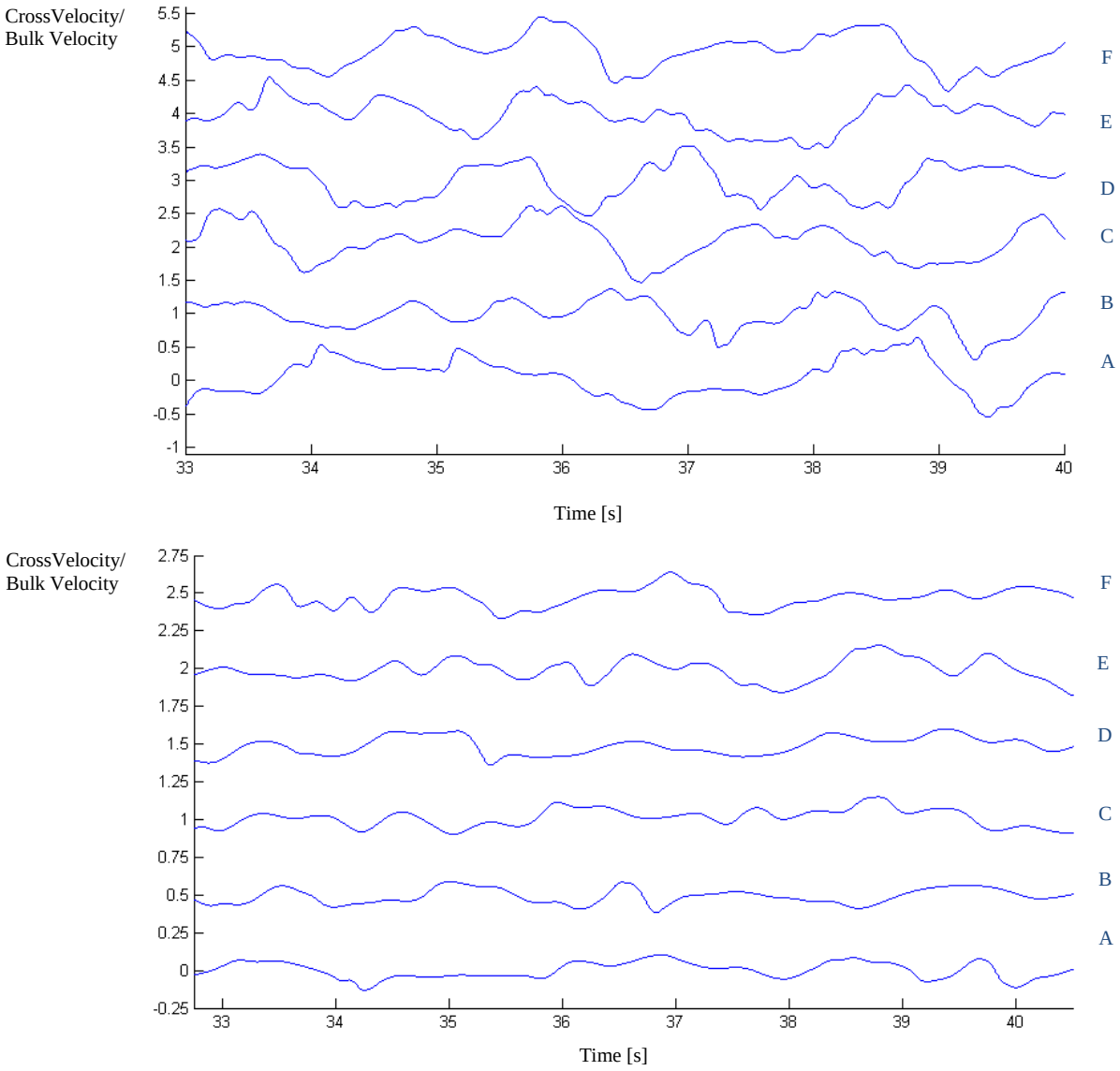

FIG. 11. Comparison of Time signal in different gaps. (top) Streamwise location z/D=2, (bottom)Streamwise location z/D=12.

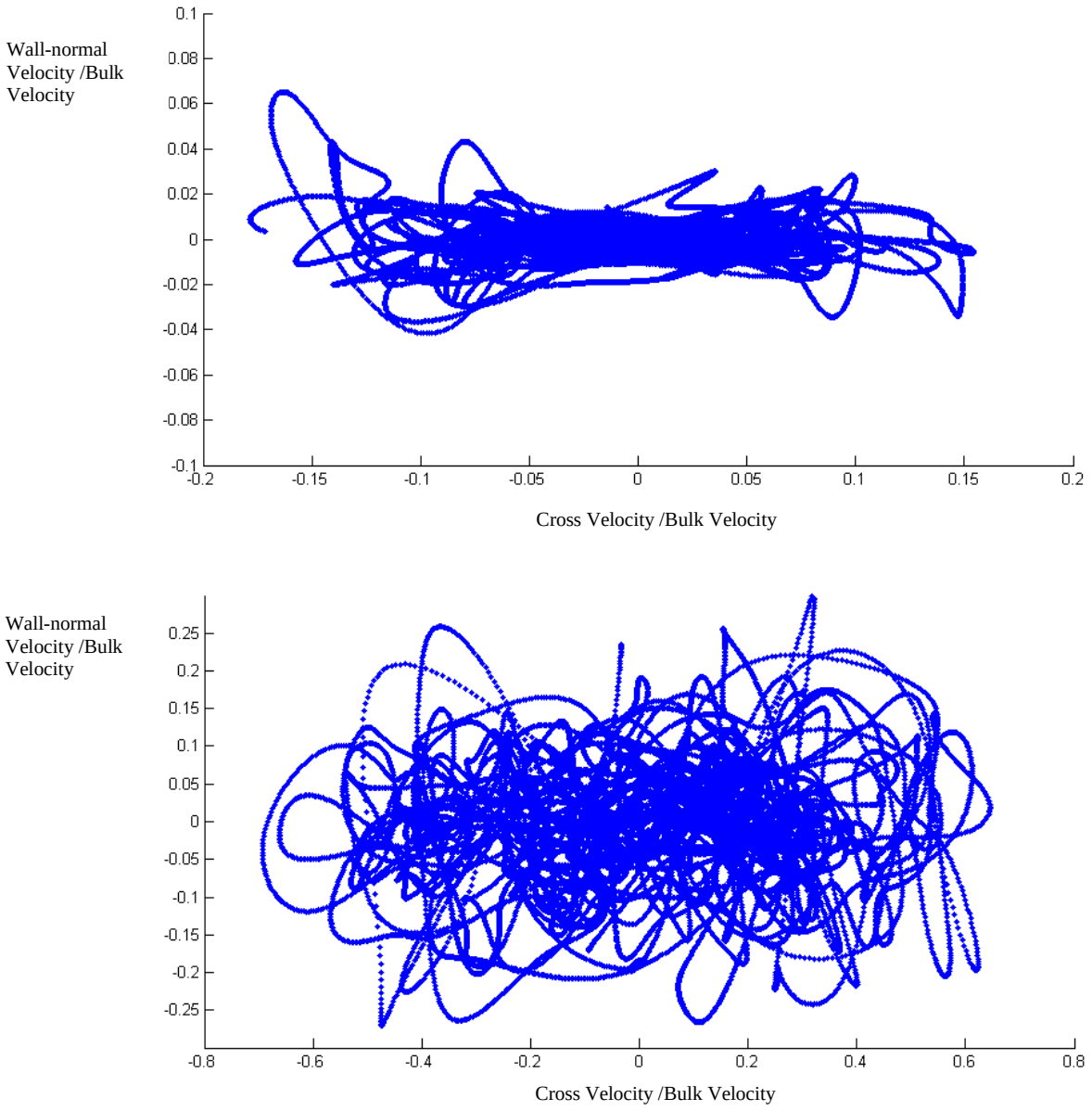

FIG. 12. Phase space comparison for all gaps. (Top) z/D=16, (Bottom) z/D=2

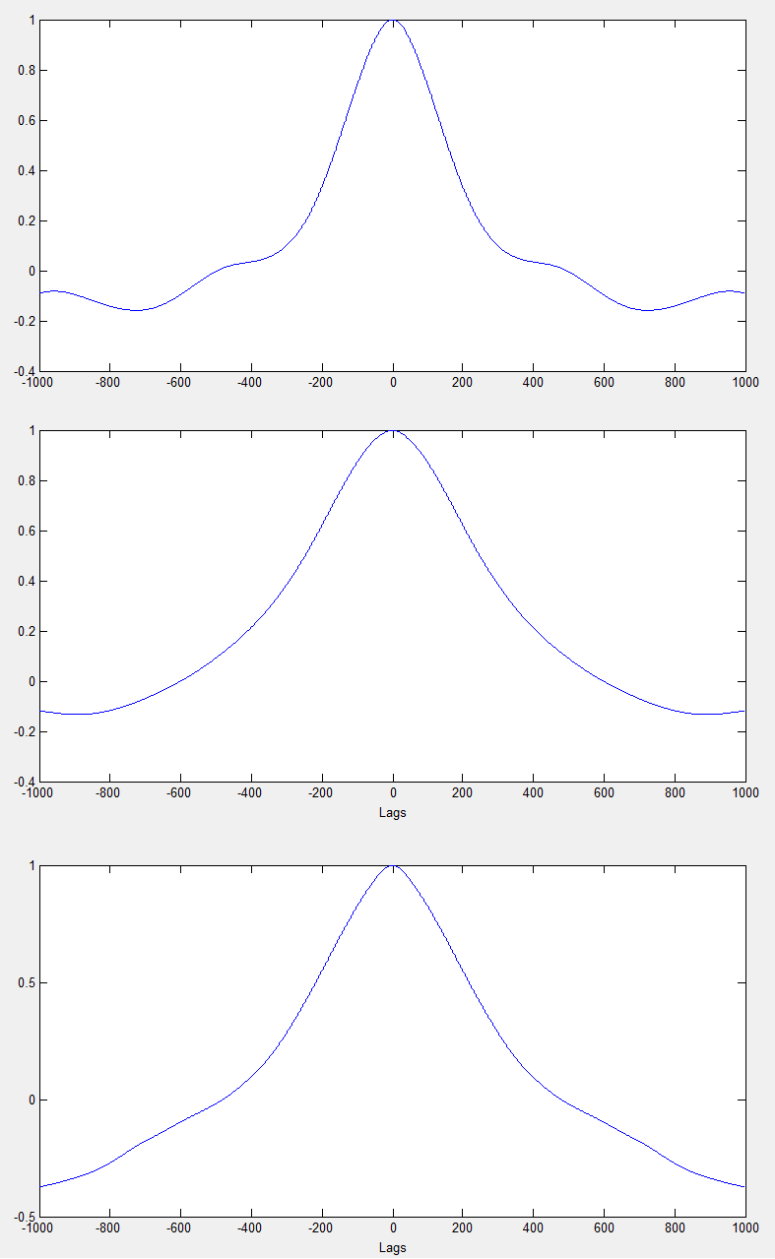

FIG. 13. Autocorrelation for the time signal of the cross velocity .Each time lag represents 1 ms. (Top) z/D=2. (Centre) z/D=8. (Bottom) z/D=16

Figure 14 shows how that the signals at different locations are correlated across gap. High values of correlation are typically observed , as indicated in previous work [7]. Based on this observation, it appears that the grid spacer disrupts but does not remove the gap vortex network. The gap vortex street recovers starts recovering its properties 12 D downstream the spacer. This distance is somewhat longer than what observed for the single pin calculation (8 D).

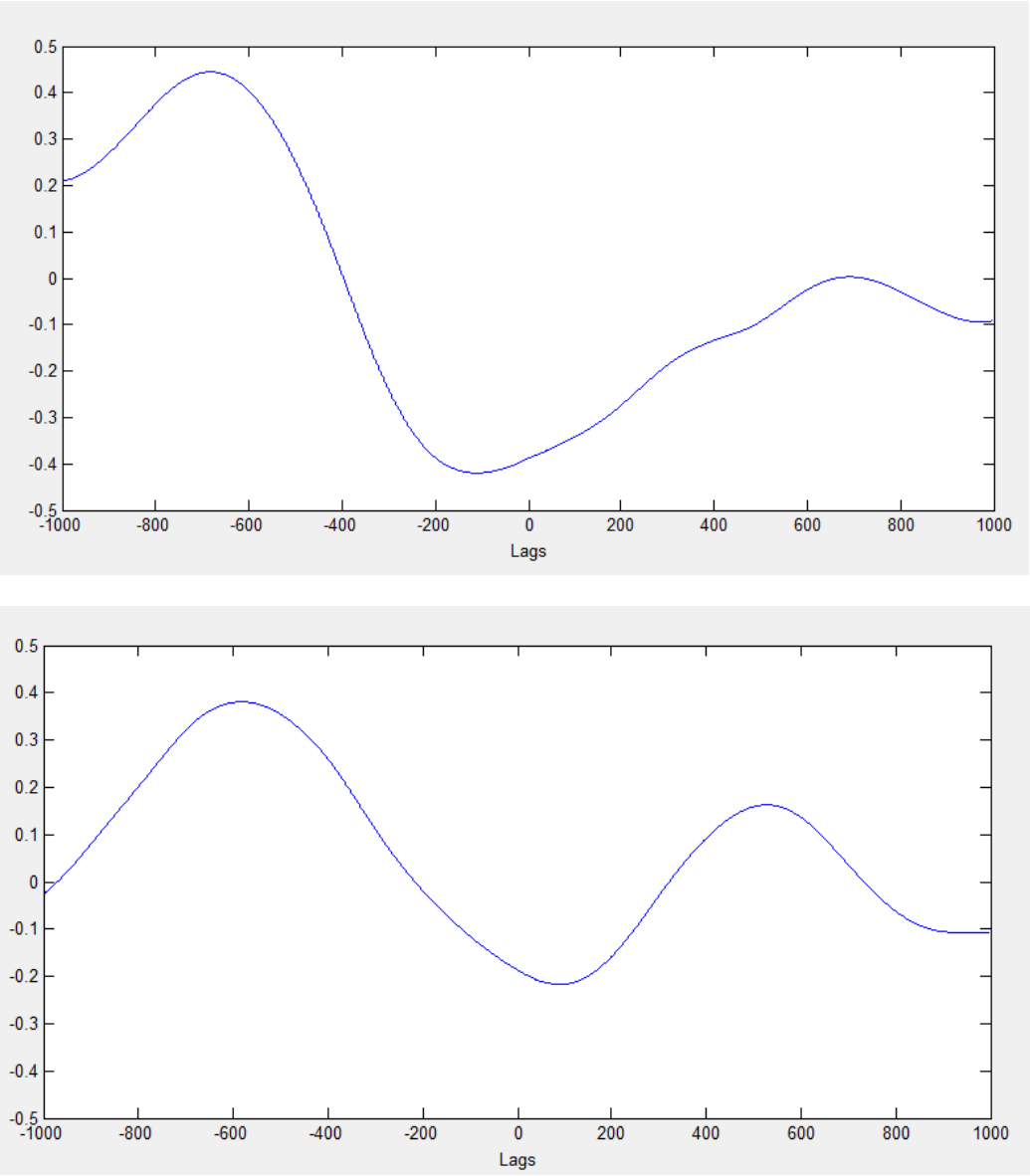

FIG. 14. Cross Correlation for the time signal of the cross velocity. Each time lag represent 1 ms. (Top) Monitoring point A(z/D=12) vs. Monitoring Point A (z/D=16). (Bottom) Monitoring point B (z/D=12) vs. Monitoring Point A (z/D=16).

The most energetic POD mode obtained by processing approximately 1,000 snapshots (separated by 0.0004 TOT each) is shown in Fig. 15. Regional clipping has been applied and the focus is the region around the central pin. The mode presents a strong similarity with the principal mode for the single pin analysis (Fig. 6). It appears to be however less regular. This can be attributed to a combination of the effect of regional clipping and the additional complexity brought by the gap vortex network.

Additional POD, focused on larger or different regions of the domain, will need to be performed to examine in more detail the dynamics of the vortex network.

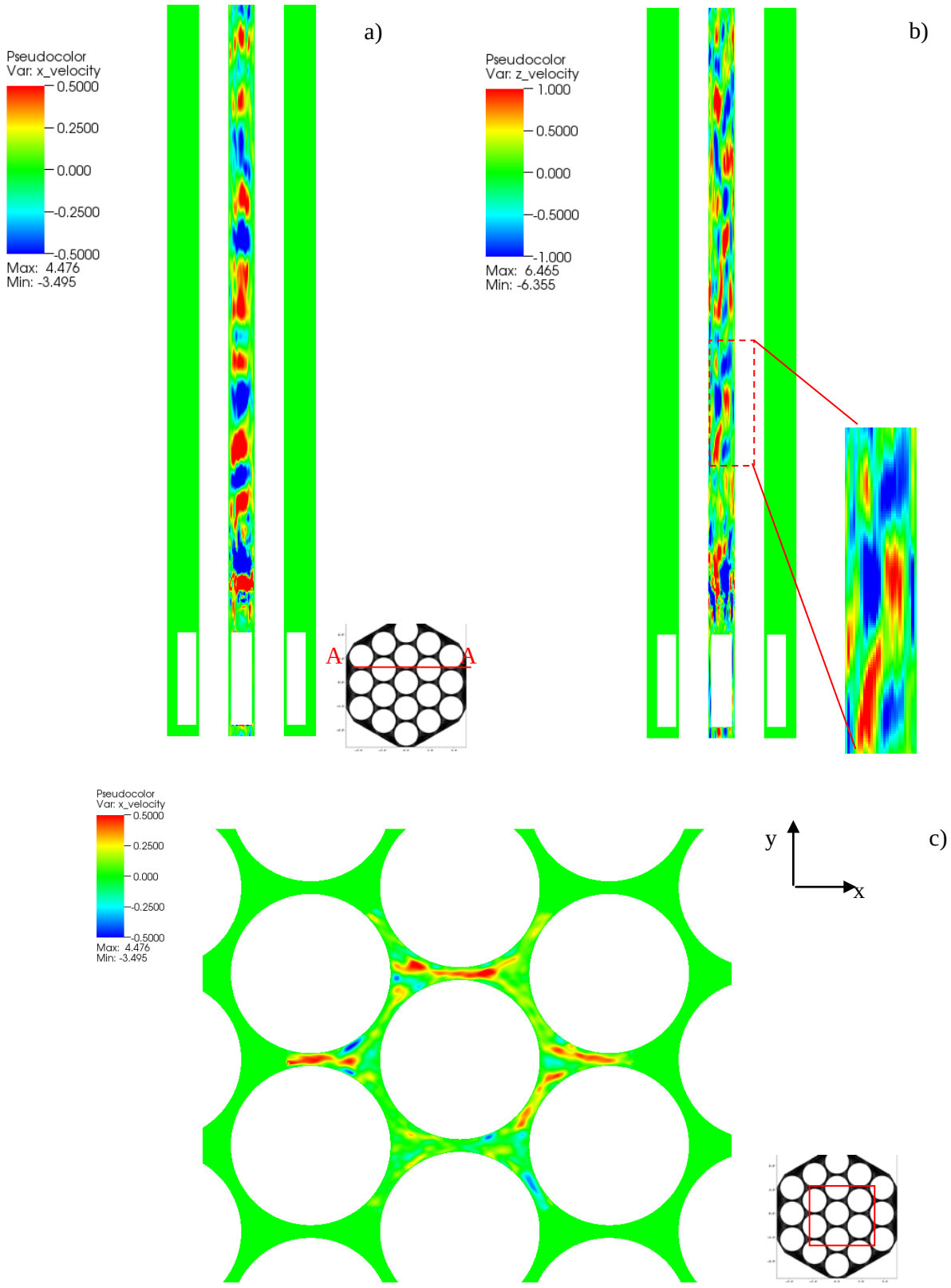

FIG. 15. Principal POD mode. a) Cross velocity, b) Streamwise velocity with detail c) Velocity in direction x, in the cross plane for z/D=12

CONCLUSIONS

A Large Eddy Simulation of the flow in a very tight 19 pin rod bundle was conducted using the spectral element code Nek5000. The flow is clearly edge-channel dominated.

A gap vortex network has been, for the first time, observed in a realistic rod bundle with no geometrical simplifications and/or infinite approximations. However, the vortex street is not as dominant as in the single channel calculation due to the presence of the dominant edge-channels. An important consequence is that traditional POD did not lead to useful results for the present simulation. A revised version with regional clipping has been developed. The results confirm the presence of the gap vortex street.

Time series analysis leads to confirmation of the presence of the gap vortex network. Its properties, far from the spacer grid, are overall not dissimilar from what observed in bare bundles. As observed for the single pin case [7] the effect of the spacers dies out rather quickly, within approximately 12 D

ACKNOWLEDGEMENTS

This work was completed under the auspices of the U.S. Department of Energy Office of Nuclear Energy as part of the NEAMS Program. The submitted manuscript has been created by the University of Chicago as Operator of Argonne National Laboratory ("Argonne") under contract No. DE-AC02-06CH11357 with the U.S. Department of Energy.

REFERENCES

[1] K. Rehme, The structure of turbulence in rod bundles and the implications on natural mixing between the subchannels, *Int. J. Heat Mass Transfer* **35** (1992), p. 567

[2] L. Meyer "From discovery to recognition of periodic large scale vortices in rod bundles as source of natural mixing between subchannels—A review", *Nuclear Engineering and Design*, **240**, pp. 1575-1588 (2010)

[3] D. Chang and S. Tavoularis, Unsteady numerical simulations of turbulence and coherent structures in axial flow near a narrow gap, *Trans. ASME* **127** (2005), pp. 458–466.

[4] E. Merzari, H. Ninokata, "Proper Orthogonal Decomposition of the flow in a tight-lattice rod-bundle", *Nuclear Engineering and Design*, **241**, 4621-4632 (2011)

[5] D. Chang and S. Tavoularis, Convective heat transfer in turbulent flow near a gap, *J. Heat Transfer* **128** (2006), pp. 701–708.

[6] D. Chang and S. Tavoularis, Numerical simulation of turbulent flow in a 37-rod bundle, *Nucl. Eng. Des.* **237** (2007), pp. 575–590.

[7] E. Merzari, W.D. Pointer, P. Fischer and H. Ninokata, "Numerical Simulation of the flow in a Tight-Lattice SFR Rod-Bundle with Grid Spacers", *Proceedings of NURETH-14*, Toronto (CANADA), September 2011.

[8] N. Ueda, I. Kinoshita, A. Minato, S. Kasai, T. Yokoyama and S. Maruyama, "Sodium cooled small fast long-life reactor "4S"", *Progress in Nuclear Energy*, **47**, pp. 222-230 (2005).

[9] H. Ninokata, E. Merzari and A. Khakim, “Analysis of Low Reynolds Number Turbulent Flow Phenomena in Nuclear Fuel Pin Subassemblies of Tight Lattice Configuration”, *Nuclear Engineering and Design*, **239**, 855-866 (2009)

[10] Fischer P.F., Lottes J., Pointer W.D., and Siegel A., “Petascale algorithms for reactor hydrodynamics,” *J. Phys. Conf. Series* (2008)

[11] J.S. Mullen and P.F. Fischer, "Filter-Based Stabilization of Spectral Element Methods" *Comptes Rendus de l'Académie des sciences Paris, **332**, Série I - Analyse numérique*, 265-270 (2001)

[12] Maday Y., Patera A and Ronquist E.. “An operator-integration-factor splitting method for time dependent problems: Application to incompressible fluid flow”, *Journal of Scientific Computing*, pp. 263-292 (1990)

[13] G. Berkooz, P. Holmes, J.L., Lumley, The proper orthogonal decomposition in the analisys of turbulent flow, *Annual Reviews of Fluid Mechanics*, **25**, 539-575 (1993)

[14] L. Sirovich, Turbulence and the dynamics of coherent structures, Part I: Coherent structures, *Quarterly of Applied mathematics*, **XLV**, 561-571 (1987)

[15] E. Merzari, H. Ninokata, A. Mahmood, M. Rohde, “Proper Orthogonal Decomposition of the flow in geometries containing a narrow gap”, *Theroretical and Computational Fluid Dynamics*, **23**, 333-351 (2009b)

ADVANCED MULTIPHYSICS MODELING OF FAST REACTOR FUEL BEHAVIOR

D. Yun, A. M. Yacout

Argonne National Laboratory,
9700 S. Cass Avenue,
Argonne, IL, 60439, USA.

J. Cheon

Korean Atomic Energy Research Institute,
1045 Daedeok-daero, Yuseong,
Daejeon 305-353, Republic of Korea

Abstract. Evaluation of fast reactor fuel thermo-mechanical performance using fuel performance codes is a key aspect of advanced fast reactors designs. Those fuel performance codes capture the multiphysics nature of fuel behavior during irradiation where different, mostly interdependent, phenomena are taking place. Existing fuel performance codes do not fully capture those interdependencies and present the different phenomena through de-coupled models. Recent developments in multiphysics simulation capabilities and availability of advanced computing platforms led to advancements in simulation of nuclear fuel behavior. This paper presents current experiences in applying different multiphysics simulation platforms to evaluation of fast reactors metallic fuel behavior. Full 3D finite element simulation platforms that include capabilities to fully couple key fuel behavior models are discussed. Issues associated with coupling metallic fuels phenomena, such as fission gas models and constituent distribution models, with thermo-mechanical finite element platforms, as well as different coupling schemes are also discussed.

1. Introduction

Fuel performance modeling and evaluation is an important area of activities associated with the development and licensing of advanced nuclear reactors [1]. It needs to capture the multiphysics nature of fuel behavior during irradiation where different, mostly interdependent, phenomena are taking place. Various fast reactors fuel performance codes have been developed in the past 40 years, where some are specifically designed for metallic fuel applications such as LIFE-METAL code [2] (other codes were developed for oxide fuel). However, most existing fuel performance codes do not fully capture those inter-dependencies and typically present the different phenomena through de-coupled models.

Recent developments in multiphysics simulation capabilities and availability of advanced computing platforms led to advancements in simulation of nuclear fuel behavior. Many of these platforms involve finite-element analyses (FE) as the basis for development. Although some of the

existing fuel performance codes utilize FE analysis, they do not contain full coupling between the different fuel behavior phenomena. An example is the ALFUS code [3] that has been developed for analysis of U-Pu-Zr ternary metallic fuel pins at steady-state conditions (its mechanical analysis model is based on axisymmetric 2-D (r-z) finite-element method, which is also similar to the approach used in FEMAXI-III, the light water reactor oxide fuel performance code [4]). This paper presents current experiences in applying different multiphysics simulation platforms to metallic fuel behavior evaluation in fast reactor. Two multiphysics platforms are considered for modeling the fuel thermo-mechanical behaviors. A computational model of U-Pu-Zr metallic fuel was developed using COMSOL platform, that is, the finite element multi-physics simulation platform COMSOL™ (version 4.2a) [5]. The simulations include calculations of the temperature distribution within the modeled fuel element, fission gas and fission product induced fuel swelling, fuel cladding mechanical interaction (FCMI), etc. The other platform under consideration is the MOOSE multi-physics platform which was used at the US Idaho National Laboratory to develop the BISON fuel behavior code [6-8]. In this case, coupling sophisticated fission gas behaviors models was explored. While the experience associated with the BISON code, so far, are mostly associated with modeling of oxide fuel behaviors, it is ideal to simulations of fast reactor metallic fuels as well as demonstrated in this paper The fission gas model that is coupled here [9] with the BISON code has shown its capabilities on capturing key physics and phenomena in irradiated metallic U-Pu-Zr fuels. The approach demonstrated and discussed in this paper has other useful implications on the future coupling of other important constitutive models for metallic fuels such as the constituent redistribution model [10, 11] and models for the effects of porosity and sodium infiltration on the thermo-mechanical properties, as well as, anisotropic fuel growth in metallic fuel [12].

2. Simulation Tool

The model developed specifically for metallic fuel performance evaluation in this work utilizes computational modules available within the COMSOL multi-physics package, version 4.2a. These modules include a heat transfer module and a (plane strain) structure mechanics module. The mathematics module suite in COMSOL was also used extensively to implement the fission-gas-induced swelling correlation and the thermally- and irradiation-induced creep models.

The computational setup consists of a 2-D axisymmetric geometry representation of a cylindrical nuclear fuel element. While 3-D models are readily available within this COMSOL framework and have been used for other fuels modeling applications, 2-D axisymmetric model was used for the purpose of demonstrating a general fuel modeling capability. Fuel and cladding materials were defined in the model by assigning property values to the corresponding domains in the geometry. In this simulation, HT-9 was used as the cladding material, consistent with Experimental Breeder Reactor – II (EBR-II) experiments of interest.

Materials properties such as thermal conductivities, thermal expansion coefficients, elastic modulus, etc., are key components of the overall multi-physics model in this study. The details of these properties are not presented in this paper as they are very well defined and presented in the literature [13-17]. The thermal conductivity input does take into account the initial as-manufactured fuel porosity and the porosity induced by irradiation through a factor, P, and sodium infiltration as well. In the multi-physics model, porosity factor, P, is constantly updated using the current calculated fission gas bubble density and size. All properties are temperature dependent and are therefore fully coupled with the thermal model.

The computational model includes a time-dependent fission-gas/fission-products swelling model for the U-Pu-Zr fuel that is based on correlation of fuel swelling to fuel temperature and burnup [18]. The following is an example of the models coupling, where fission gas release and fuel swelling

behavior models coupled with the hydrostatic stress calculated by the structural mechanics module. With given bubble number density and ratio of fission gas in solution in the fuel matrix, and retained gas calculated by the fission gas correlation [18], the local gas bubble radius can be calculated through the typical Van der Waals gas equation of state:

$$P(V - NB) = NRT$$

where N is the number of gas atoms in the bubble, B is the Van der Waals constant, 8.5×10^{-23} cm^3/atom, and P is the pressure which is derived from the capillarity equation:

$$P = (\frac{2\gamma}{r_b} + P_h)$$

where r_b is the bubble equilibrium radius, γ is the surface energy and P_h is the hydrostatic stress. The Van der Waals equation of state, however, is applicable for gas at the state close to the ideal gas, i.e., for bubbles of relatively large size. For gas bubble with size smaller than 0.5μm radius, a hard sphere approximation by Harrison was applied [19]. These considerations to couple the fuel hydrostatic stress with fission gas release and fuel swelling correlations have not been taken in the earlier work.

Other physics models involved in the overall multi-physics model include fuel and cladding creep. The cladding creep model has two components, an irradiation creep component and a thermal creep component [20, 21], and both are coupled with the stress and temperature calculations models. Currently, work to couple a more sophisticated fission gas model, FASTGRASS [22], into the COMSOL thermo-mechanical model is underway. This is a challenging activity as it involves a large number of differential equations to be solved on a densely distributed computational mesh, magnified by the limited accessibility to COMSOL's source code.

Another fission gas model, GRSIS, that was developed for metallic fuels is also under consideration [23], where the logics of the original GRSIS model are preserved while accommodating the model using the IDA method [24]. This method resolves the computational issues with large number of stiff equations where the GRSIS model is modified and corrected by making further simplification, derivative correction, and conservation correction. The model is also being improved to take into account the effect of negative hydrostatic pressure on the number of gas atoms in a bubble, and to extend a capability of describing the fission gas kinetics in α phase region.

$$\frac{dC_{s0}}{dt} = Y \cdot \dot{F} - \sum_{i=1}^{6} J_m(i) - J_n$$

$$\frac{dN_{b1}}{dt} = \frac{1}{\rho_1}\left(J_n + J_m(1) - \sum_{i=1}^{6} J_g(1,i) - \sum_{i=2}^{3} J_g(i,1) - N_{b1}\frac{d\rho_1}{dt} \right)$$

$$\vdots$$

$$\frac{dN_{b6}}{dt} = \frac{1}{\rho_3}\left(\sum_{i=1}^{3} J_g(i,6) + J_m(6) - N_{b6}\frac{d\rho_3}{dt} \right)$$

where $C_{si} = \rho_i N_{bi}$, C_{si} gas concentration, ρ_i the number of gas atoms in a bubble, and N_{bi} bubble concentrations. ρ_i is given by a function of temperature and hydrostatic pressure.

The situation with the BISON code is ideal for such coupling implementations due to the accessibility to the source code combined with code architecture that is designed with coupling such models in mind. While the details of the BISON code and the associated MOOSE multiphysics

platform can be found in [6, 8], the approach with which the FASTGRASS model was coupled to the BISON code and discussion of the implications of such approach on the other constitutive models for metallic fuels are discussed in a later section.

3. Validation Problem and Results by COMSOL Simulations

In order to validate the multi-physics model and demonstrate its applicability to modeling metallic fuel performance, a pin from EBR-II irradiation experiment (pin T470 of experiment X425) was simulated and simulation results were compared to post-irradiation examination (PIE) data from this experiment. Table 1 presents the fuel fabrication data and irradiation conditions at peak burnup of 16.55 at.% for this irradiation experiment. Detailed axial distribution of estimated fast fluence, mid-wall cladding temperature, local burnup and linear heat rate are available and have been incorporated in the model. Swelling is not observed for HT9 cladding before a high fast-neutron damage is reached (200 dpa at 400 ^{0}C). For EBR-II conditions the corresponding burnup value is of the order of 20 at %, which is beyond the burnup the fuel has reached in this experiment.

Fig. 1 compares the axial distribution of cladding diametral strain simulated by our model and measured strain for pin T470 of experiment X425 at its peak burnup of 16.55 at.%. The axial location is characterized by L/L_0 (fraction of fuel length). The axial location of $L/L_0=0$ is the bottom of the fuel slug and the axial location of $L/L_0=1$ is the top of the fuel slug. The PIE data and LIFE-METAL prediction are directly reproduced from reference [25]. It was found that, at this burnup level, our model reproduced the shape of the axial cladding diametral strain distribution well while overestimating the magnitude of the cladding strains. Compared with the LIFE-METAL predictions, the COMSOL model provided more reasonable estimates for the top axial portion of the fuel but over-predicted cladding strain at axial locations near the center and upper bottom portion of the fuel. As the thermally-induced creep strain contribution to the cladding diametral strain was shown to be significantly smaller than the irradiation-induced creep strain contribution, the seemingly consistent trend of difference between the simulation results and PIE data at axial locations other than the top and bottom portions indicates the possibility the fuel cladding mechanical interaction (FCMI) forces were overestimated. The cladding diametral strains measured from the experiments, however, should be considered very accurate (relative errors from measurements should be less than 1%).

Table 1 Fuel fabrication data and irradiation condition for X425 at peak burnup of 16.55 at.%.

Parameter	**Value**
Fuel alloy nominal composition	U-19Pu-10Zr
Fuel slug radius (mm)	2.16
Cladding thickness (mm)	0.38
Cladding outer radius (mm)	2.92
Peak linear heat rate (kW/m)	35.27
Peak mid-wall cladding temperature (˚C)	548
Peak fast fluence (n/cm^2) (E > 0.1 MeV)	1.64×10^{23}
Peak burnup (at.%)	16.55

Further validation analyses were also performed by comparing simulation results obtained by COMSOL with PIE measured cladding diametral strain at two other burnup levels: at peak burnups of 11.1 at.% (Fig. 2) and 19.9 at.% (Fig. 3). At both burnup levels COMSOL simulations over-predicted cladding diametral strain. The comparison shown in Fig. 3 demonstrated a trend similar to that shown in Fig. 1 where it over-predicted the cladding diametral strain in the center portion of the fuel.

Figure 1 Comparison of simulated and PIE measured cladding diametral strain for pin T470 at peak burnup of 16.55 at.%.

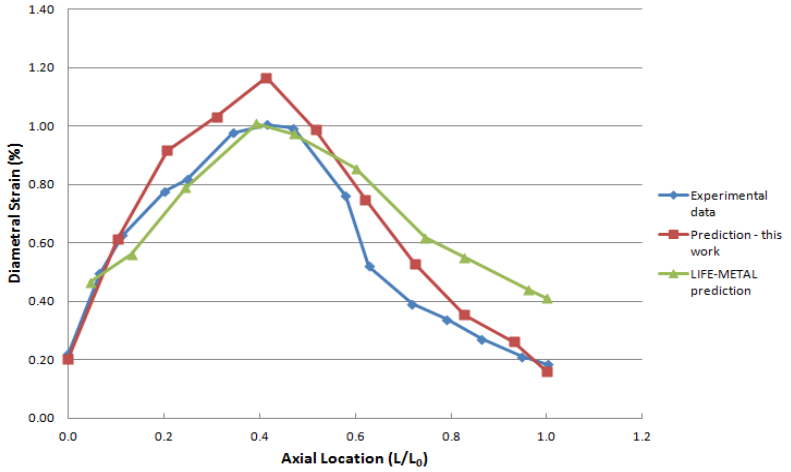

Figure 2 Comparison of simulated and PIE measured cladding diametral strain for pin T470 at peak burnup of 11.1 at.%.

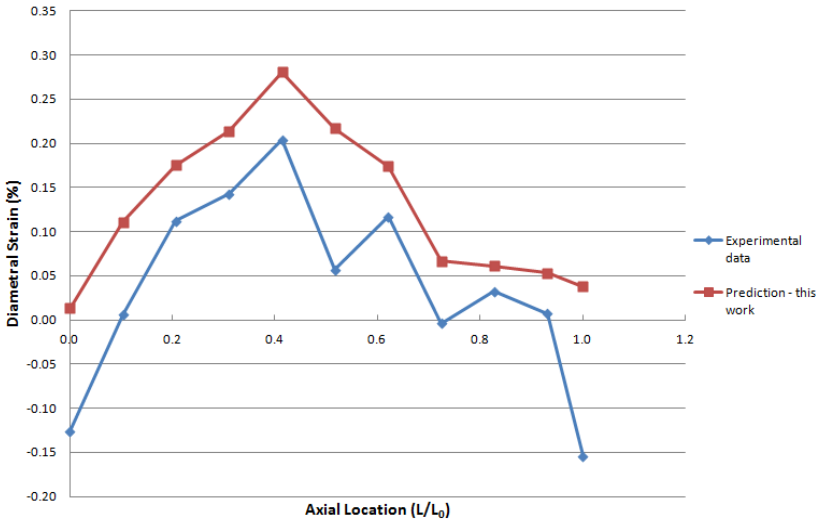

At peak burnup of 11.1 at.% the discrepancies are noticed at both ends of the fuel. At 11.1 at.% peak burnup, the local burnup levels at the bottom and the top of the fuel slug are about 9 at.% and 7 at.%, respectively. Consequently, the fuel slug should have swelled enough to contact the cladding, suggesting possible relation between the discrepancies and FCMI. The negative values at both extremes of the cladding are reflections of the surface roughness encountered during the measurements. They also reflect, to some degrees, the uncertainty associated with the experimentally measured cladding diametral strains.

As comparisons at three different burnup levels all showed over-predictions around the center portion of the fuel, it is necessary to investigate the physical reasons behind these over-predictions and possible relation to FCMI. The main possible source of discrepancies is likely to be the fission gas release. If the released gas was under-predicted, the forces caused by gas bubble swelling would be

greater, leading to increased FCMI and higher cladding diametral strains. The fission gas release prediction by the COMSOL model is compared to pertinent experimental data in Fig. 4.

Figure 3 Comparison of simulated and PIE measured cladding diametral strain for pin T470 at peak burnup of 19.9 at.%.

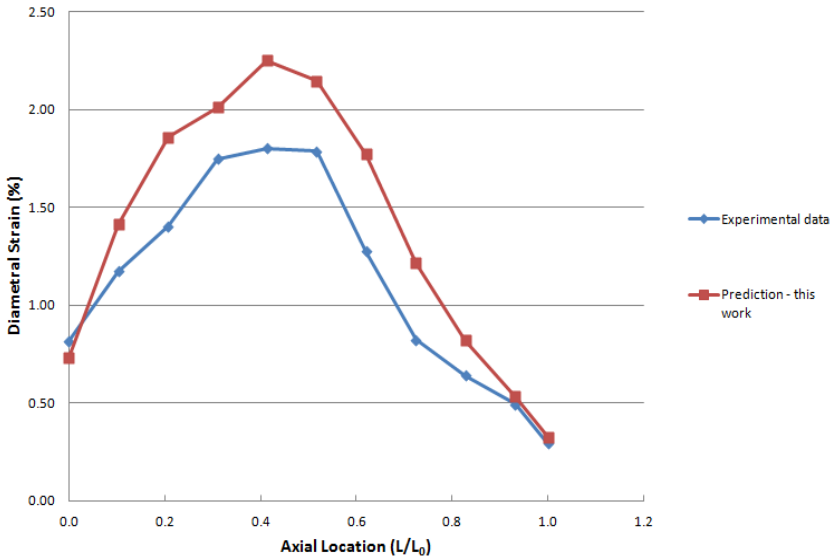

Figure 4 Comparison of simulated fission gas release and experimentally measured fission gas release of generic U-Pu-Zr fuel.

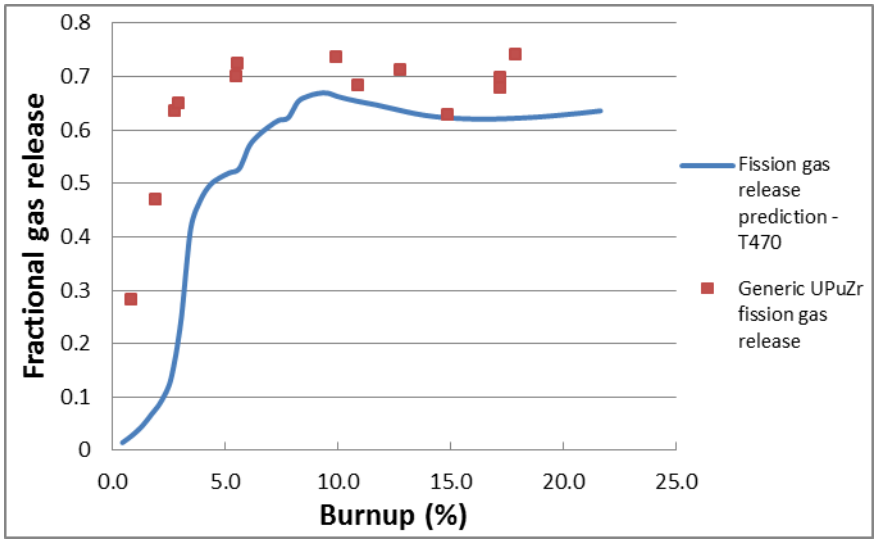

As there were no fission gas release measurements specifically from pin T470 of experiment X425, generic fission gas release data for U-19Pu-10Zr fuel has been used in this comparison [26]. Those generic fission gas release data, however, are considered to be a realistic reflection of this experiment. Fig. 4 shows that the COMSOL model consistently under-predicts the gas release. This under-prediction, when factored into the prediction of cladding diametral strains by COMSOL

simulation, could explain the over-predictions of the cladding diametral strains where under-predicted fission gas release can lead to under-prediction of FCMI.

4. Experience with the BISON Code

In this section, details of the experience with the BISON code are provided to demonstrate a methodology to couple multi-physics models to this general fuel performance platform. Fig. 5 shows a schematic diagram of the implementation of fission gas behavior model into the BISON code at a conceptual level. This serves as a high level roadmap for the implementation work conducted. At the beginning of each time step, BISON passes key variables to the fission gas model (FASTGRASS module) such as the temperature distribution and the distribution of hydrostatic stress. In order for the FASTGRASS module to deal with the information, the variables need to be processed as domain averages. The domains referred to here are computational volumes (or in 2-D axisymmetric geometry, areas) of the constituting elements of the FASTGRASS module. The FASTGRASS module then calculates the fission gas release and volumetric swelling strains for each of its elements. The calculated values of released gas and swelling are then de-convoluted and passed back to BISON in order to move the BISON simulation forward on to the next time step. It should be noted that at the conceptual level the coupling of fission gas model and the BISON code may seem straight forward. However, the technical implementation of this coupling is complex as the fission gas model possesses certain attributes that are not entirely compatible with the BISON framework.

Figure 5 Visual illustration of the current coupling strategy between BISON and fission gas model, and the needs for future improvements on the coupling implementation

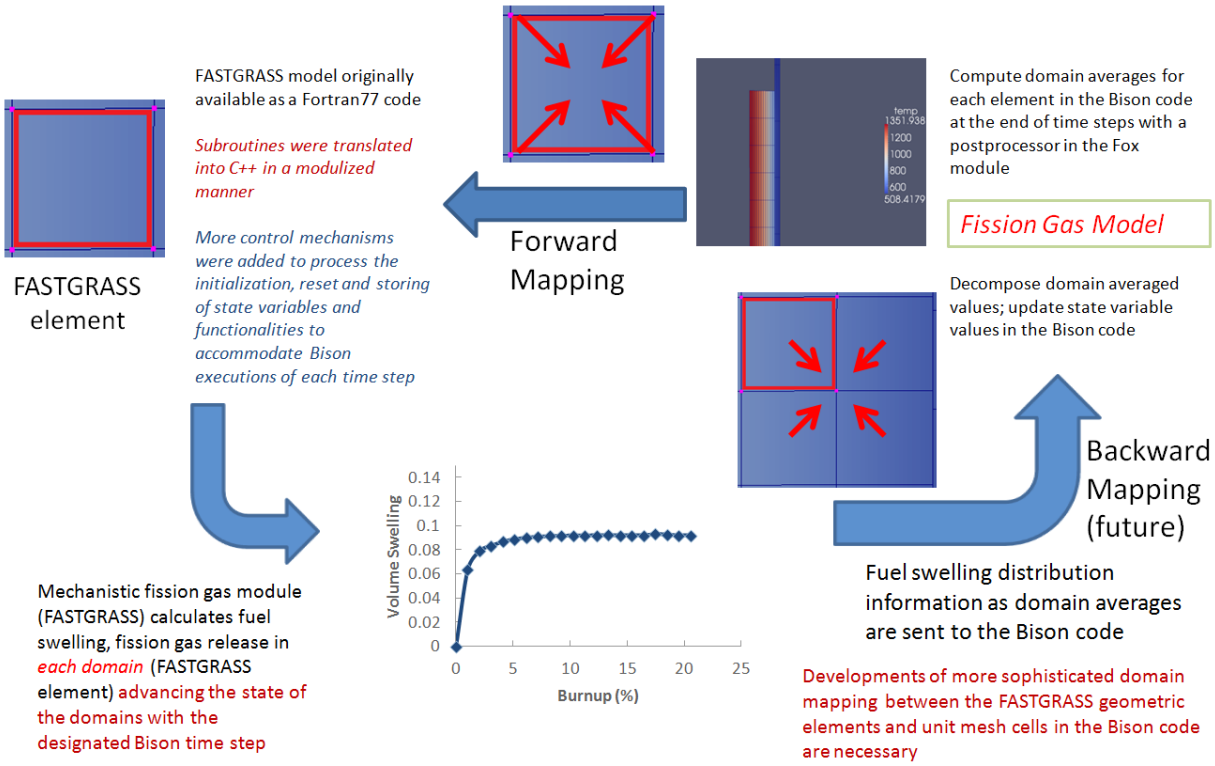

It needs to be stressed that approximations are made in the current implementation of the FASTGRASS module in the BISON code. These approximation stems from the fact that separate simulation by the FASTGRASS module is performed on each geometric element of the module. To

account for the long range migration of fission gas along the temperature and stress gradients, a single FASTGRASS run with a geometry representation that matches the finite element meshing scheme must be executed.

To demonstrate the successful realization of the above shown set of mechanisms, it is necessary to compare a simple BISON simulation that includes the FASTGRASS module to that calculated using FASTGRASS stand alone simulations. Fig. 6 shows the simulated fractional fission gas release calculated by the BISON code with the FASTGRASS module (the red curve) together with that calculated by the FASTGRASS standalone code (blue curve). The simulation case used here is the current example problem in the BISON repository at the Idaho National Laboratory (as of Sept. 2012). Although this specific problem simulates oxide fuel behavior, it is used here for demonstration purposes of the coupling between modules which applies to metallic fuels as well. The purpose is to use a simple simulation to demonstrate the outcome of the current implementation of the FASTGRASS module. As the same approach has been adopted to simulate fission gas behaviors in metallic fuels [27], this demonstration shows the feasibility of incorporating a mechanistic fission gas model for metallic fuels into the BISON code.

It should be noted that the change in state variables such as temperature and hydrostatic stress were calculated from the BISON code and are passed to FASTGRASS standalone code as input parameters. A coarse spatial and temporal discretization was used for the FASTGRASS standalone simulation. It was also observed that the values of the total fission gas generated by these calculations are consistent as they are pure reflection of the power density (or fission density) and the yield of fission gas species.

Figure 6 Comparison between fractional gas release calculated by the BISON code with the FASTGRASS module and the fractional gas release calculated by the standalone FASTGRASS code

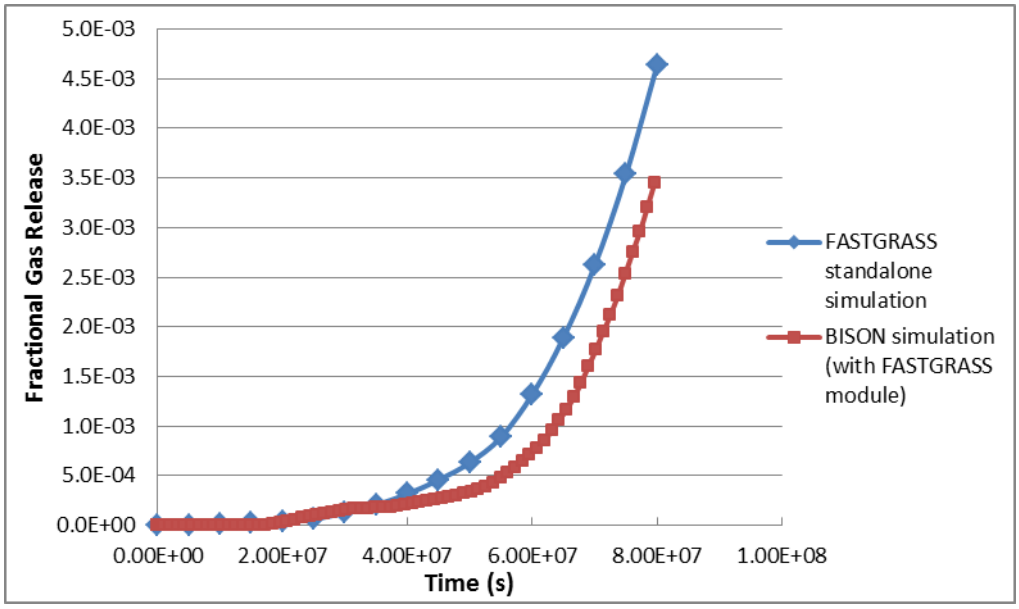

It is worth mentioning here that the difference between the BISON calculated fractional fission gas release and that calculated by the FASTGRASS standalone code reflects, to some extent, the effect of long range fission gas transport between mesh elements. In the presence of a large temperature

gradient, fission gas and constituent migration in the radial direction become significant, influencing the gas bubble size distribution and thereby the fission gas swelling and release.

The above demonstrated approach for the coupling between FASTGRASS fission gas model and the BISON code can be useful for future implementations of other constitutive models such as the constituent redistribution model. Similar approach and technical considerations may be taken. Moreover, there is a need to develop constitutive equations for porous fuel. Fuel swelling and contraction is governed by the variation of the radius of isolated gas bubble on which mechanical force balance equation is imposed. The increased porosity is taken into account as a correction factor in material properties [12, 13]. When porosity increases due to the bubble coalescence, however, other mechanisms for the contraction such as creep are needed to accommodate the deformation of fuel matrix into pores as in the sintering theory. Fuel deformation due to porosity depends on stress, temperature, porosity fraction, and material properties of dense solid.

5. Summary

This paper presents experiences in applying different multiphysics simulation platforms to metallic fuel behavior evaluation in fast reactor. Finite element simulation platforms that include capabilities to fully couple key fuel behavior models are discussed. Issues associated with coupling metallic fuels phenomena, such as fission gas models and constituent distribution models, with thermo-mechanical finite element platforms, as well as different coupling schemes are also discussed. Here, a multi-physics thermo-mechanical computaional model was developed to evaluate performance of U-Pu-Zr metallic fuel under steady-state operation conditions. COMSOL based simulated cladding diametral strain for an EBRII irradiation experiment was compared to PIE measurement data. The comparison shows reasonable agreement while overestimating the cladding strain due to inadequate account for fission gas release and associated over-prediction of FCMI.

A high level roadmap for the implementation of fission gas behavior model in the BISON code is provided in this paper as well. Preliminary verifications showed that the approximation by the current implementation, ignoring the long range transport of fission gas along temperature and stress gradient, has resulted in lower predicted gas release than that predicted by the standalone FASTGRASS simulation. The coupling scheme or approach has useful implications towards future implementations of other constitutive models such as the constituent redistribution model and model to account for porosity effects.

Acknowledgments

This work was supported by the U.S. Department of Energy under Contract number DE-AC02-06CH11357.

References

[1] S. S. Hecker et al., “Properties of plutonium and its alloys for use as fast reactor fuels,” Journal of Nuclear Materials, Vol. 383, pp.112-118, (2008).

[2] M. C. Billone, et al., “Status of the Fuel Element Modeling Codes for Metallic Fuels,” Proc. Int. Conf. Reliable Fuels for Liquid Metal Reactors, American Nuclear Society, Tucson, Arizona, pp.77-92, (1986).

[3] T. Ogata et al., “Development and Validation of ALFUS: An irradiation Behavior Analysis Code for Metallic Fast Reactor Fuels,” Nuclear Technology, Vol. 128, pp. 113-123, (1999).

[4] T. Nakajima et al., "FEMAXI-III: A computer Code for the Analysis of Thermal and Mechanical Behavior of Fuel Rods," JAERI-1298, Japan Atomic Energy Research Institute, (1985).
[5] COMSOL Multiphysics User's Guide manual, COMSOL Inc., www.comsol.com.
[6] R. Williamson, et al, "Multidimensional multiphysics simulation of nuclear fuel behavior," Journal of Nuclear Materials, vol. 423, pp. 149-163, (2012).
[7] BISON training workshop materials, INL BISON and BISON User Group distribution, (2012).
[8] MOOSE training workshop materials, INL MOOSE and MOOSE User Group distribution, (2012).
[9] D. Yun, J. Rest, G. L. Hofman, A. M. Yacout, "An initial assessment of a mechanistic model, GRASS-SST, in U-Pu-Zr metallic alloy fuel fission-gas behavior simulations," Journal of Nuclear Materials, accepted manuscript, 2013.
[10] Y. S. Kim, G. L. Hofman, S. L. Hayes, Y. H. Sohn, "Constituent redistribution in U-Pu-Zr fuel during irradiation," Journal of Nuclear Materials, vol. 327, pp. 27-36, (2004).
[11] Y. S. Kim, S. L. Hayes, G. L. Hofman, A. M. Yacout, "Modeling of constituent redistribution in U-Pu-Zr metallic fuel," Journal of Nuclear Materials, vol. 359, pp. 17-28, (2006).
[12] A. M. Yacout, D. Yun, M. Stan, "Finite Element Simulations of Zr Based Metallic Fuels: Thermo-mechanical Model Validations and Predictions," to be presented at *ICAPP 2013*, April, 2013
[13] T. H. Bauer, et al., "In-pile Measurement of the Thermal Conductivity of Irradiated Metallic Fuel," Nuclear Technology, Vol. 110, (1995).
[14] T. Kobayashi, et al., "Development of the SESAME Metallic Fuel Performance Code," Nuclear Technology, Vol. 89, pp. 183-193, (1990).
[15] A. Karahan, Ph. D. Thesis, "Modeling of Thermo-mechanical and Irradiation Behavior of Metallic and Oxide Fuels for Sodium Fast Reactors", Massachusetts Institute of Technology, June, 2009.
[16] L. Leibowitz, et al. "Thermal Conductivity and Thermal Expansion of Stainless Steels D9 and HT9," Vol. 9, pp. 873-883, International Journal of Thermophysics, (1988).
[17] N. Yamanouchi, et al., "Accumulation of Engineering Data for Practical Use of Reduced Activation Ferritic Steel: 8 % Cr-2%W-0.2%V-0.04%Ta-Fe," Journal of Nuclear Materials, Vol. 191, pp. 822-826, (1992).
[18] M. C. Billone, et al., "Status of the Fuel Element Modeling Codes for Metallic Fuels," Proc. Int. Conf. Reliable Fuels for Liquid Metal Reactors, American Nuclear Society Tucson, Arizona, pp.77-92, (1986).
[19] J. W. Harrison, J. Nucl Mater. Vol.31, pp.99, (1969).
[20] M. B. Toloczko et al., "Variability of irradiation creep and swelling of HT9 Irradiated to High Neutron Fluence at 400 – 600 ^{0}C," Effect of Radiation on Materials 18th Symposium ASTM-1325, (1999).
[21] H. J. Ryu et al., "Review of HT9 Cladding Creep Correlations for Advanced Liquid Metal Fast Reactors," Transactions of the American Nuclear Society, vol. 94, pp. 797-798, Transactions of the American Nuclear Society 2006 Annual Meeting and Embedded Topical Meeting - Nuclear Fuels and Structural Materials for the Next Generation Nuclear Reactors, (2006).
[22] J. Rest, "FASTGRASS: A Mechanistic Model for the Prediction of Xe, I, Cs, Te, Ba, and Sr Release from Nuclear Fuel under Normal and Severe-Accident Condition," NUREG/CR-5840 ANL-92/3, 1992.
[23] C. B. Lee, D. H. Kim, and Y. H. Jung, "Fission gas release and swelling model of metallic fast reactor fuel," Journal of Nuclear Materials, vol. 288, no. 1, pp. 29–42, Jan. 2001.
[24] A. C. Hindmarsh, P. N. Brown, K. E. Grant, S. L. Lee, R. Serban, D. E. Shumaker, and C. S.

Woodward, “SUNDIALS: Suite of nonlinear and differential/algebraic equation solvers,” ACM Trans. Math. Softw., vol. 31, no. 3, pp. 363–396, Sep. 2005.

[25] T. Ogata et al., “Chapter 75, Metal fuel modeling and simulation,” in: Comprehensive Nuclear Materials, Elsevier, (2011).

[26] Pahl, R. G.; et al. In Proceedings of International Fast Reactor Safety Meeting, Snowbird, UT, 1990, American Nuclear Society: La Grange Park, IL, Vol. IV.

[27] Di Yun, Marquis A. Kirk, Peter Baldo, Jeffery Rest, Abdellatif M. Yacout, Zinetula Z. Insepov, “In Situ TEM Investigation of Xe Ion Irradiation Induced Defects and Bubbles in Pure Molybdenum Single Crystal,” Journal of Nuclear Materials, Volume 437, Issues 1-3, June 2013, Pages 240-249

Current Status of the LIFE Fast Reactors Fuel Performance Codes

A. M. Yacout and M. C. Billone

Argonne National Laboratory,
9700 South Cass Avenue,
Argonne, IL 60439,
U.S.A.

Abstract. The LIFE series of fuel performance codes have been developed in the US to evaluate the thermo-mechanical behavior of fuel elements in a fast-reactor environment. The oxide version of the code (LIFE-4) remains to be the national reference for modeling the thermal, mechanical, and materials performance of fast-reactor oxide fuel and blanket pins during both normal and transient operations. The metallic fuel version of the code (LIFE-METAL) was under development up to the termination of the US Integral Fast Reactor (IFR) program in the early 1990's, where it was calibrated and validated using large database from metallic fuel irradiated at both EBR-II and FFTF. Recent institutional and industry interest in the development of advanced sodium cooled fast reactors renewed interest in those fuel performance codes, for design and licensing activities as well as its use for verification and validation of other newly developed fuel performance codes. This paper presents the current status of both oxide and metallic versions of the LIFE code, recent applications, and ranges for its calibration and validation databases as well as current and future activities developments.

1. Introduction

There is a continued interest in the deployment of advanced fast reactors in order to meet requirements for future nuclear energy systems such as waste minimization, resource sustainability, non-proliferation, as well as economics challenges. Closed fuel cycle fast reactor systems that are based on either metallic or oxide fuels are expected to be compatible with those requirements. While most of the experiences with past deployments of fast reactors were limited to experimental and demonstration/prototype reactors, there is current interest in the commercial deployment of such reactor systems. Commercial fast reactor designs such as those proposed by Toshiba [1], General Electric [2], and TerraPower [3] are dependent on past experience with metallic fuels use in fast reactors. Meanwhile, other proposed commercial reactors, e.g. in Russia and France [4, 5] consider mixed oxide $(Pu,U)O_2$ as the fuel of choice. Fuel performance codes that predict the behavior of those fast reactors fuels are important in relation to reactor design, licensing and operations. The codes are complex and consider large number of interdependent chemical, thermal, mechanical, and irradiation phenomena. Examples of those codes include LIFE-METAL [6,7], ALFUS [7,8], MACSIS [9], PUMA [10], and FEAST [11] for metallic fuel, and LIFE-4 Rev 1 [12,13], SIEX-3 [14], CEDAR [15], for oxide fuel. Reference 16 provides a summary of the early developments of fast reactor fuel performance code.

Given current interest in fast reactors utilizing both types of fuel and associated need for fuel performance assessment, this paper provides an overview of the status of the LIFE series of codes developed in the US for both oxide and metallic fast reactors fuels. A comprehensive calibration and validation using data generated within the US fast reactors program are associated with both metallic

(LIFE-METAL) and oxide (LIFE-4 Rev 1) versions of the code. The following sections provide summary descriptions of the codes, their calibration and validation, recent applications and possible future plans.

2. History of Code Development

The original LIFE code, LIFE-I [17] was developed at Argonne National Laboratory to predict the in-pile behavior of fast reactors fuel elements during the early 1970's. An improved version of the code, LIFE-II [18] was selected by the division of the US Atomic Energy Commission responsible for the fast reactors program as several fuel performance codes from different organizations were under consideration. This decision focused the fuel-element code development activities on the LIFE code under the guidance of national groups that included experts from industry and national laboratories. This led to the subsequent versions of the code, LIFE-III and LIFE-4 [19, 20], including version for carbide and nitride fuels (LIFE4-CN [21]) and a version for gas cooled fast reactors [22]. The latest versions are the mixed oxide version LIFE-4 Rev. 1, and the version associated with the Integral Fast Reactors (IFR) program for metallic fuel, that is, LIFE-METAL. Both versions represent the closest to official US calibrated and validated oxide and metallic liquid metal fast reactors fuel performance codes. Throughout the development of the different versions of the code, experimental data from EBR-II, FFTF, and TREAT reactors, as well as out of pile experiments were used to calibrate and validate the codes and guide the codes model development.

3. LIFE-4 Rev. 1

The LIFE-4 Rev. 1 is the latest revision of the original LIFE code developed to calculate the thermal and mechanical behavior of oxide fuel elements in a fast-reactor environment. The code is the national reference for the thermal, mechanical and materials performance of fast-reactor oxide fuel and blanket pins during normal operation and during transients up to cladding breach. It integrates a broad material and fuel-pin irradiation database into a consistent framework for use and extrapolation of the database to reactor design conditions.

The code has a one-dimensional generalized-plane-strain mechanical analysis procedure for fuel ($(U,Pu)O_2$ and UO_2) and cladding (several types, including different types of 316 stainless steel, HT9, and D9). It has a steady-state and transient thermal analysis system for fuel and cladding. Thermal and mechanical behaviors, including thermal expansion, fuel restructuring, cladding deformation, and cladding breach, are calculated from many phenomenological models. The thermal analysis included establishing fuel and cladding temperatures, and calculating stress-strain-independent, but temperature-dependent, diffusion phenomena. Those diffusional phenomena include pore migration, grain growth, oxygen migration, plutonium migration, and fission gas release. The mechanical analysis is a stress-strain calculation in the fuel and cladding and it includes elastic creep (irradiation and thermal creep), plastic flow, swelling, and thermal-expansion strains. In addition, the code includes a wastage model (fuel-cladding chemical interaction and sodium corrosion of outer cladding surface), and it takes into account the fuel cladding mechanical interaction (FCMI) in calculating the cladding diametral strains.

Fuel properties considered in the code include thermo-physical, physical, and mechanical properties. Thermo-physical properties include liquidus and solidus temperatures, thermal conductivity, fuel heat capacity, heat of fusion, thermal expansion, expansion on melting, and oxygen redistribution. Physical properties include hot pressing and densification, and fuel creep. Fuel mechanical properties include, shear modulus, Poisson's ratio, bulk modulus, fracture stress, crack healing, yield stress, ductility, Young's modulus, and fatigue. Cladding properties include thermo-physical and mechanical properties. Thermo-physical properties include cladding thermal expansion, specific heat, and cladding (and other stainless steel components such as TREAT capsule) thermal conductivity. Mechanical properties include cladding density, cladding (and other stainless steel components such as TREAT capsule) density, cladding shear modulus, cladding Poisson's ratio, cladding interaction with coolant, yield stress, ductility, Young's modulus, and fatigue

For analysis, the fuel element is divided axially into a maximum of 9 fueled sections and 1 plenum section. Each axial section is divided radially into a maximum of 20 cylindrical rings for mechanical analysis (this number of rings was found to be adequate for preventing code instabilities and accurate simulations). Each axial node is mechanically independent of all other axial nodes. Axial "lock-up" effects or similar axial coupling effects are not modeled. Thus, if a given pin section was run as part of a one-node or five-node problem, the computed temperatures, stresses, etc., would be the same, except for the following calculated parameters. Those parameters are plenum pressure, which will be different because of differences in the total amounts of fission gas released, gap conductance and axial vapor-phase transport. Because of this axial independence, each axial node can be solved separately. Finally, the code has a special option for blanket fuel pins that are characterized by larger diameters.

3.1. Code Calibration and Validation

The LIFE-4 (Rev 1) calibration used integral pin test measurement data including fuel central hole radius, fuel columnar zone radius, fuel equiaxed zone radius, melt radii, fuel column axial strain, fuel cladding wastage, post-irradiation fuel-cladding gap and fission gas release from fuel column to plenum. The code calibration was done by adjusting the less-well-defined parameters in the fuel models and properties within physically realistic limits or measurement uncertainties to minimize the deviations between code results and fuel pin post-irradiation examination (PIE) data. Code calibration included both thermal and mechanical calibration. The beginning-of-life thermal calibration was performed by adjusting the high-temperature end of the fuel thermal conductivity equation, the accommodation coefficient in the gap conductance model, and constants in the pore velocity expression. For the later-in-life thermal calibration, changes were made to the dependence of fuel thermal conductivity on burn-up (due to accumulation of fission products). The steady state thermal calibration used data from 95 sections from 52 pins. The primary parameters used for the mechanical calibration were constants in the fission gas release expressions and the fuel swelling model. The key fuel pin data used were fission gas release and cladding mechanical strains. During the mechanical calibration, the measured and calculated cladding swelling were adjusted to be equivalent in order to make the calibration independent of cladding swelling and dependent only on cladding in-reactor creep correlations [23]. Data from 90 sections from 23 fuel pins were used in the mechanical calibration. Also, several other fuel constants were changed during the course of calibration to achieve improvements in code predictions that cannot be obtained by varying the parameters described above. The transient thermal calibration used data from four TREAT tests with irradiated fuel and three tests on un-irradiated pins. The transient mechanical calibration involved six fuel pins (one un-irradiated pin) including the five pins used in thermal calibration. Tables 1 and 2 show parameter ranges for both fabrication and operating conditions.

Table 1. The Calibration Range for the Steady State LIFE-4 Code Fabrication Parameters

Pin Parameters	**Fuel**	**Blanket**
Fuel material	$(U,Pu)O_2$	UO_2
Cladding material	CW316, D9, HT9	same as fuel
Pin diameter (mm)	5.8-7.0	10.3-12.9
Fuel density (% TD)	85 – 95	90-95
Smear density (% TD)	80 – 90	85-92
Oxgyen:Metal ratio	1.93-2.0	1.98-2.0
Pu weight fraction	0.15-0.25	0.0-0.02

Table 2 The Calibration Range for the Steady State LIFE-4 Code Operating Parameters

Operating Parameter	**Fuel**	**Blanket**
Peak power (kW m^{-1})	16 – 50	6 – 50

Peak fast flux ($n.cm^{-2}\ s^{-1}$)	$1.5 - 5.0x10^{15}$	$0.5-5.0x10^{15}$
Cladding temperature, ^oC	360-700	360-700
Peak burnup (at%)	0 – 13	0 – 3
Peak fast fluence ($n.cm^{-2}$)	$0 - 1.5x10^{23}$	$0 - 1.5x10^{23}$

The code validation was performed considering code predictions for fuel pins, which were not used in the calibration of the code and used to uncover uncertainties not revealed by the calibration results. No adjustments were made to code calibration constants for analysis of the validation pins. In addition, benchmark problems that have known analytical solutions were used to verify the code's mathematics.

Finally, a summary of the uncertainties associated with the code predictions at steady state and transient conditions are shown in Table 3.

Table 3 Summary of Uncertainties in LIFE-4 Predictions (Calibration and Validation Results Combined)

Parameter	No. Observations	Avg. Deviation	RMS Deviation
Power-to-Melt, kW/m			
Fuel	33	0.25	2.18
Blanket	8	-0.08	1.36
Max. Fuel Temp. (^oC)			
Fuel	29	-2.6	32
Blanket	8	2.75	17.8
$\Delta D/D_o$ Mechanical (% $\Delta D/D_o$)	130	-0.03	0.25
Fission Gas Release (% Release)	49	2.5	8.8
Central Void (mm)	129	0.03	0.1
Columnar Zone (mm)	124	-0.02	0.18
Equiaxed Zone (mm)	91	0.02	0.26
PIE Radial Gap (mm)	56	-0.02	0.04
FCCI (mm)	30	0.002	0.0086
Fuel Column $\Delta L/L_o$ (%)	10	0.7	1.36

3.2. Code Limitations

Numerous limitations exist on the ability of LIFE-4 to predict various features of the actual behavior of fuel pins, which are caused by errors in, or lack of, models of fuel and cladding behavior. The following are examples of important code shortfalls, which are mainly related to limitations that were imposed on the code developers in the past, mostly to reduce the computation time.

As mentioned before, the axial mechanical analysis in the code is a simple one, which assumes that no axial section of fuel is affected by the condition or behavior of any other axial section, that is, axial lock-up effects are not taken into account. This limitation leads to mechanical diametral strains near the bottom of the fuel column that tend to be somewhat under-predicted. The same strains near the top of the fuel column tend to be over-predicted.

Another consequence of the simplicity of the code's mechanical analysis is that the thermal and mechanical analyses in the code are primarily coupled through the gap-conductance model. Both analyses are not solved simultaneously; instead, the thermal analysis uses the fuel-cladding gap or

contact pressure from the mechanical analysis of the previous time step. Consequently, the code has a tendency to become somewhat unstable and produce oscillating solutions under certain conditions.

3.3. Recent Applications

The LIFE-4 Rev. 1 code development has been frozen since the early 1990's after being used in different US and international programs (mainly activities related to the Japanese fast reactor program). More recent applications include assessments related to plutonium disposition program, where mixed uranium-plutonium oxide (MOX) fuel performance analysis were evaluated for applications to irradiation of surplus weapons plutonium in the Russian BN-600 nuclear reactor [24]. Another application was related to assessment of fuel for sodium- or NaK cooled fast reactors for fission surface power systems and reached the conclusion on the choice of fuel for this application [25]. The most recent application of the code was in support of activities related to sensitivity analysis associated with fast reactor fuel performance codes and identification of important macroscopic parameters of interest to the US fuel modeling and simulation activities [26,27].

3.4. Future Activities

As part of recent applications of the code, calculations were performed for some of the validation and calibration pins data and output data from the code were verified with the code manual data. Full re-validation and re-calibration effort to bring the code up to date is expected in the future. This is especially important as international collaborations between the US and other countries interested in the code are established (more data generated in international programs can be added to the code database). In addition, key phenomena models will need to be revisited in light of new developments over the past 20 years in relation to mixed oxide fuel (e.g., inclusion of mechanistic fission gas release models). New types of fuels, such as transmutation fuels will need to be considered as additional options to the code (where minor actinides addition to fuel and possible He gas release will need to be taken into account.

4. LIFE-METAL

4.1. Code Description

As mentioned before, the LIFE-METAL fuel performance code is one of the variations of the LIFE-4 code that was developed during the Integral Fast Reactor program (IFR) to predict the behavior of metallic fuel rods in sodium cooled fast reactors environment. The code structure and thermo-mechanical models are similar to the LIFE-4 code, while fuel properties and phenomena that are specific to metallic fuel (e.g., constituent redistribution, and gap sodium infiltration into fuel) are among the differences between the two codes. The LIFE-4CN code [16, 21] was used as the basis for the LIFE-METAL code development. The code was used for pre-test data packages and post-test interpretation of experimental irradiations and as the main fuel-element design tool in the USA for the PRISM concept during the IFR program. While transient capabilities are present in LIFE-METAL, high temperature phenomena (e.g., fuel melting, fuel/cladding eutectic formation) encountered under accident conditions are not yet modeled. These transient calculations arc performed using FPIN code [28] which uses LIFE-METAL steady-state predictions to establish initial conditions for the transient.

Physical, thermal, mechanical, and irradiation property correlations for test and design cladding materials (e.g., austenitic 316, D9, and ferritic HT9) are included in the code. Some work has been done during LIFE-METAL development to improve the correlations (e.g., D9 creep and swelling) in order to get a better fit to the data base within the operating range of interest for metallic fuels. Wastage correlations for sodium/cladding interaction and time and strain-failure correlations are also included. Models were developed for Ni depletion from D9 cladding and carbon depletion from HT9 cladding due to the fuel/sodium/cladding chemical interaction (FCCI). Empirical eutectic penetration correlations, based upon fuel behavior test apparatus (FBTA) [29] and whole-pin-furnace (WPF) [30] test data are also incorporated.

Code predictions that are of interest to nuclear design are changes in fuel length and fissile content due to burnup and breeding. Thermal predictions of fuel temperature, design margins to fuel melting, and design margins to low-melting-temperature alloy (e.g., U-Fe) formation are also of interest. Mechanical predictions useful to designers are fuel-cladding mechanical interaction (FCMI) and fuel-cladding chemical interaction (FCCI), cladding deformation and design margin to significant coolant flow area reduction, and cladding damage and design margin to cladding failure due to fuel and fission-gas-pressure loading.

The code has been extensively used for planning of steady state and transient experiments at EBR-II to provide initial conditions for transient fuel performance codes such as FPIN code and for performance evaluation of new fuel designs and out of pile experiments [29,30]. For example, the code was used to evaluate the expected performance of EBR-II Mk-V fuel design [31-33] and check the performance against pre-specified design criteria (e.g., cumulative damage function – CDF and thermal strain limits).

4.2. LIFE-METAL Calibration/Validation

The calibration effort has been extensive using post irradiation examination (PIE) data that are available from a large number of metallic fuel-pin irradiations at EBR-II and FFTF [34]. PIE data include fission gas release, fuel volumetric change, cladding diametral change, cladding wastage and fuel axial growth. Axial profiles are available for fuel radial growth at low burnup (prior to and including initial fuel-cladding contact) and for cladding radial growth for a wide range of burnups and fast fluences. Some data available on a more limited basis are radial and axial variations in U, Pu, Zr concentrations, fission gas porosity, axial variations in fraction of porosity filled (logged) with Na, and depth of C-depleted and Ni-depleted zones in HT9 and D9, respectively. Fairly complete sets of data are available for 80 fuel-pin irradiations (111 pins in total were used in the validation). Limited PIE data (e.g., fuel length change, cladding diameter change) are available for hundreds of irradiated fuel pins. Tables 4 and 5 show the fabrication and operating parameter ranges associated with the code calibration, respectively.

Table 4. The Calibration Range for the Steady State LIFE-METAL Code Fabrication Parameters

Pin Parameters	**Fuel**
Fuel material	U-xZr-xPu
Zr weight fraction	0.06-0.14
Cladding material	CW316, D9, HT9
Pin diameter (mm)	5.8-7.0
Smear density (% TD)	75 – 85
Pu weight fraction	0 – 0.26

Table 5. The Calibration Range for the Steady State LIFE-METAL Code Operating Parameters

Operating Parameter	**Fuel**
Peak power (kW m^{-1})	33 -54
Peak fast flux (n.cm^{-2} s^{-1})	1.7 - 2.48x10^{15}
Cladding temperature, ^{o}C	499-649
Peak burnup (at%)	0.5 - 19.5

The calibration/validation database includes data from the 111 fuel element irradiations. This data base includes three cladding types (cold-worked, austenitic D9 and 316 stainless steels and HT9 ferritic/martensitic steel) and eight fuel compositions (U-10Zr, U-3Pu-10Zr, U-8Pu-10Zr, U-19Pu-6Zr, U-19Pu-10Zr, U-19Pu-14Zr, U-22Pu-10Zr and U-26Pu-10Zr, where the numbers represent weight percents). The data from the 111 irradiations fall into one or more of the following categories: fission gas release (FGR), fuel axial strain ($\Delta L/L_o$), fuel diametral strain $(\Delta D/D_o)_f$, cladding diametral strain $(\Delta D/D_o)_c$ and penetration depth (wastage) at the cladding inner diameter (ID) due to ingress of fission products (FP) and egress of cladding constituents. For the last three categories, axial profiles are often available. This implies a large number of data points per fuel element irradiation. Also, in the case of fuel axial expansion and peak cladding strain, which are routinely measured for all elements within a subassembly, the number of data points is much larger than the number of validation cases. Table 6 summarizes the number of fuel/cladding combinations for the calibration/validation data set, as well as the number of data points for each category. The "+" superscript next to a number indicates that more data are available from sibling elements within a subassembly than used directly in the calibration/validation effort.

Table 6. Summary of Fabrication, Operating Conditions, and PIE Data for LIFE–METAL Validation. (PICT is peak inner cladding temperature, FGR is fission gas release, $(\Delta L/L_O)_f$ is fuel axial strain, and $(\Delta D/D_O)_c$ is cladding diametral strain)

				Number of PIE Data Points				
Fuel Type	Cladding Type	Burnup Range, at.%	PICT, °C				(ΔD/Do)c	
				FGR	Wastage	(ΔL/Lo)f	Peak	Profile
U–10Zr	D9	0.8 – 18.0	535–620	10	14	13+	6+	5+
	316SS	0.5 – 5.0	500	3	–	4+	1+	0+
	HT9	2.8 – 18.5	530–660	4	30	19+	19+	7+
U–3Pu–10Zr	316SS	0.5 – 5.0	500	4	–	4+	1+	0+
U–8Pu–10Zr	D9	0.8 – 18.0	535–565	10	–	11+	5+	5+
	316SS	0.5 – 5.0	500	4	–	4+	0+	0+
	HT9	2.8 – 16.0	530	1	–	3+	1+	1+
U–19Pu–10Zr	D9	0.8 – 18.0	535–590	12	21	14+	9+	9+
	316SS	0.5 – 5.0	500	4	6	4+	2+	0+
	HT9	2.8 – 19.5	530–590	8	9	9+	17+	10+
U–19Pu–6 Zr	HT9	5.0 – 10.0	575	2	–	1+	2+	1+
U–19Pu–14Zr	HT9	6.0 – 13.0	590	2	–	2+	2+	1+
U–22Pu–10Zr	316SS	0.5 – 5.0	500	4	–	4+	1+	0+
U–26Pu–10Zr	316SS	0.5 – 5.0	500	3	–	4+	1+	0+
	HT9	2.2	534	1	–	0+	–	–
DATA TOTAL				72	80	92+	68+	51+

4.3. Recent Applications

The LIFE-METAL code remains as a design tool in support of the advanced fast reactors program in the US, given the comprehensive data base used in its calibration/validation. A recent fuel design evaluation utilized the code to evaluate a metallic fuel option for fission surface power for space reactor design [25]. Another application was related to Toshiba Corporation and Central Research Institute of Electric Power Industry (CRIEPI) initiation of the pre-application review of its Super Safe Small and Simple (4S) fast reactor in the US, through informing the United States Nuclear Regulatory Commission (NRC) on the reactor's systems and fuel design [1]. The LIFE-METAL code has been used in this activity where evaluation of 4S reactor fuel design was performed. In addition, recent fuel design activities associated with fast reactor programs outside the US have brought back interest in the code as an option for design evaluation studies. This interest motivates a future activity for improving the code models to accommodate possible advanced designs that include minor actinides (MA) and high burnups designs.

4.4. Future Activities

The latest calibration of the LIFE-METAL code has been performed just before the termination of the IFR project in 1994. Sets of data test problems that correspond to data from different EBR-II experiments (9 experiments) are available and have been recently used to verify the code calculations. Currently, those data sets are being revised to re-calibrate the database and produce more pins data to be used in the code validation. The revised data sets will be based on a more detailed operating parameters generated through a consistent and enhanced methodology that tracks the detailed operating history of each pin [35].

As for future plans for improving the code, modeling effort will be required to re-evaluate the effect of constituent redistribution, fission product migration, and fission gas release through updated mechanistic models for those phenomena. Those code improvements can provide better predictions of fuel swelling and fuel thermal behavior. Other planned additions to code models are related to expanding the type of transmutation fuel that contains minor actinide elements as relevant experimental data become available.

5. Summary

Although the LIFE series of codes have been developed decades ago, they remain to be the most up to date fast-reactor fuel performance codes for oxide and metallic fuels in the US. Recent US efforts to develop comprehensive 3D fuel performance codes, such as BISON code [36], are being applied to fast reactor fuel simulation. However, the full implementation of the different phenomena affecting fast reactors fuel behavior and comprehensive calibration and validation efforts are still in progress. Meanwhile, the recent interest in using the LIFE codes in different applications motivates efforts to undergo re-assessment and improvements of the codes as described in this paper.

ACKNOWLEDGEMENTS

This work was performed at Argonne National Laboratory and was supported by the Toshiba Corporation under interagency agreement, through the U.S. Department of Energy contract DE-AC02-06CH11357.

REFERENCES

[1] Yasushi Tsuboi, Kazuo Arie, Nobuyuki Ueda, Tony Grenci, A. M. Yacout, “Design of the 4S Reactor,” Nuclear Technology, Volume 178 , Number 2, May 2012 , Pages 201-217.
[2] Pre-application Safety Evaluation Report for the Power Reactor Innovative Small Module (PRISM) Liquid-Metal Reactor, Final Report, NUREG-1368, February 1994.
[3] Tyler Ellis, et al, “Traveling-Wave Reactors: A Truly Sustainable and Full-Scale Resource for Global Energy Needs," Proc. of ICAPP10, San Diego, CA, June 13-17, 2010. 4S

Reactor," Nuclear Technology, Volume 178 , Number 2, May 2012 , Pages 201-217.
[4] O. M. Saraev, et al, " BN-800 design validation and construction status," Atomic Energy, August 2010, Volume 108, Issue 4, pp 248-253.
[5] J. ROUAULT, J.P. SERPANTIÉ, D. VERWAERDE, "French R&D programme on the SFR and the ASTRID prototype (Summary)," Proceedings of International ConferenceF on Fast Reactors and Related Fuel Cycles: FR09, Kyoto, Japan, 7–11 December 2009.
[6] M. C. Billone, Y. Y. Liu, E. E. Gruber, T. H. Hughes, and J. M. Kramer, "Status of Fuel Element Modeling Codes for Metallic Fuels", Proc. ANS Int. Conf. on Reliable Fuels for Liquid Metal Reactors, September 7-11, 1986, p. 5.
[7] T. Ogata, Yeon Soo Kim, A.M. Yacout, "Metal Fuel Performance Modeling and Simulation," Book Chapter, Comprehensive Nuclear Materials, Vol 3, 2012, Pages 713-753.
[8] Ogata, T. and Yokoo, T. (1999) Nucl. Technol. 128, 113.
[9] W. Hwang et al., "MACSIS: A Metallic Fuel Performance Analysis Code for Simulating In-Reactor Behavior under Steady-State Conditions," Nuclear Technology, Vol. 123, pp. 130-141, (1998).
[10] Jin Sik Cheon, Byoung Oon Lee, Chan Bock Lee, "Status of Development of Metal Fuel Performance Code," PUMA, (KAERI–Korea), Proc of Nuclear Fuels and Structural Materials for the Next Generation Nuclear Reactors (NFSM), Embedded topical meeting of 2012 ANS Annual Meeting, Chicago, IL, June 24-28, 2012.
[21] Karahan, A. and Buongiorno, J. (2010) J. Nucl. Mater., 396, 283-293.
[32] A. Biancheria, A. Boltax, B. E. Sundquist, Int. Conf. Reliable Fuels for Liquid MetalReactors, Tucson, 1986. Hinsdale, IL: American Nuclear Society, pp. 3-75 – 3-91.
[43] A Boltax, "Mixed Oxide Fuel Pin Performance," in Materials Science and Technology: A Comprehensive Treatment, Ed. R. W. Cahn, P. Haasen, E. J. Kramer, Volume 10B, 1994.
[54] R. B. Baker and D. R. Wilson, "SIEX3 — A Correlated Computer Code for the Prediction of Fast Reactor Mixed-Oxide Fuel and Blanket Pin Performance," International conference on reliable fuels for liquid metal reactors, Tucson, AZ, USA, 7 Sep 1986.
[65] T. Mizuno and S. Shikakura, "Development of the fast reactor fuel performance code CEDAR," PNC Technical Review, no. 76, pp. 37–44, 1990.
[76] M.C. Billone, R.O. Montgomery, Y.R. Rashid and J. L. Head, "Advancements in the behavioral modeling of fuel elements and related structures," Nuclear Engineering and Design 134 (1992) 23-36.
[87] V. Z. Jankus and R. W. Weeks, LIFE-I, a FORTRAN-IV Computer Code for the Prediction of Fast-Reactor Fuel-element Behavior, USAEC Report ANL-7736 (November 11970).
[98] V. Z. Jankus and R. W. Weeks, "LIFE-II A Computer Analysis of Fast-reactor Fuel-element Behavior as a Function of Reactor Operating History," Nuclear Engineering and Design 18 (1972)83-96.
[109] J. D. Stephen, A. Biancheria, M. C. Billone, Proc. Advanced LMFBR Fuels, Tucson, 1977. Hinsdale, IL: American Nuclear Society, pp. 562-581.
[20] B. L. Harbourne, et.al, Int. Conf. Fast Breeder Reactor Fuel Performance, Monterey, 1979. Hinsdale, IL: American Nuclear Society, pp. 619-641.
[21] Y. Y. Liu, S. Zawadzki, M.C. Billone, U.P. Nayak and T. Roth, "DEVELOPMENT OF LIFE4-CN: A COMBINED CODE FOR STEADY-STATE AND TRANSIENT ANALYSES OF ADVANCED LMFBR FUELS," Second International Seminar on Mathematical/Mechanical Modeling of Reactor Fuel Elements, Berlin, Germany, August 20-21, 1979.
[22] T-C. S. HSIEH and M.C. BILLONE, " LIFE-GCFR: A COMPUTER CODE FOR PREDICTING GAS-COOLED FAST-REACTOR FUEL PERFORMANCE," Nuclear Engineering and Design 68 (1981) 31 - 51.
[23] Boltax, A.; et al., 1990. In International Fast Reactor Safety Meeting, Snowbird, UT, 1990; American Nuclear Society: Hinsdale, IL, 1990; Vol. II, pp 427–436.
[24] A. M. Yacout, Private Communications, Argonne National Laboratory, October 30, 2007.
[25] Fission Surface Power Team, "Fission Surface Power System Initial Concept Definition," National Aeronautics and Space Administration and Department of Energy, NASA/TM—2010-216772, August, 2010.
[26] Yacout AM, Williams BJ, Unal C., "Sensitivity Analysis Using LIFE-4 Fuel Performance

Code," Technical Report LA-UR-10-06575. Los Alamos National Laboratory; 2010.
[27] Williams BJ, Yacout A, Unal C. Application of VU capabilities to LIFEIV fuel performance code. Technical Report LA-UR-11-05765. Los Alamos National Laboratory; 2011.
[28] Hughes, T. H., and J. M. Kramer, "The FPIN2 Code – An Application of the Finite Element Method to the Analysis of the Transient Response of Oxide and Metal Fuel Elements," Proc. Conf. Sci. & Tech. Fast Reactor Safety, 427, Guernsey, UK (May 1986).
[29] A. B. Cohen, H. Tsai and L. A. Neimark," Fuel/cladding compatibility in U-19Pu-l0Zr/HT9-clad fuel at elevated temperatures," J. of Nucl. Materials 204 (1993) 244-251
[30] Kramer, J. M., Y. Y. Liu, M. C. Billone, and H. C. Tsai, "Modeling the Behavior of Metallic Fast Reactor Fuels During Extended Transients," J. Nucl. Mater., 204 (1993) 203.
[31] Liu, Y. Y., H. Tsai, M. C. Billone, J. W. Holland, and J. M. Kramer, "Behavior of EBR-II Mk-V-Type Fuel Elements in Simulated Loss-of-Flow Tests," J. Nucl. Mater., 204 (1993) 194.
[32] ANL-IFR-169, Integral Fast Reactor Program Annual Progress Report FY 1991, June 1992.
[33] ANL-IFR-246, Integral Fast Reactor Program Annual Progress Report FY 1994, Dec 1994.
[34] Crawford, D. C., D. L. Porter, and S. L. Hayes, "Fuels for sodium-cooled fast reactors: US perspective," J. Nucl. Mater., 371 (2007) 202.
[35] A. M. Yacout, S. Salvatores, and Y. Orechwa, "Degradation Analysis Estimates of the Time-to-Failure Distribution of Irradiated Fuel Elements," Nuclear Technolow, 113:(2), pp. 177-189, Feb. 1996.
[36] R. L. Williamson S. R. Novascone, "Application of the BISON Fuel Performance Code to the FUMEX-III Coordinated Research Project," INL/EXT-12-25530, April 2012.

Thermohydraulic model experimental studies for codes verification of fast reactors

N. Pribaturin[a], O. Kashinsky[b], V. Berdnikov[b], S. Lezhnin[a]

[a] Nuclear Safety Institute of the Russian Academy of Sciences, Novosibirsk Division, Novosibirsk, Russia

[b] Institute of Thermophysics, Siberian Branch of the Russian Academy of Sciences, Novosibirsk, Russia

Abstract. The aim of the experimental research was the completion of the database with new experiments to obtain detailed data on the three-dimensional structure and heat transfer of the liquid flow and creation of the new benchmark. The comprehensive experimental study of the structure free convective boundary layer and laminar-turbulent transition under high Rayleigh number at the vertical heating surface was carry out. We investigated the correlation between heat transfer and fluid dynamics qualitatively different stages of the flow also. The data on the local fields of temperature and speed, three-dimensional data on the secondary flow in the zones of the laminar-turbulent transition and the turbulent boundary layer were obtained. Also on the model liquids were carried out studies on the mixing of liquid layers having different temperatures in the regime of mixed convection. The overall structure of the flow, spatial distributions of the temperature on the wall of the channel and the channel cross section were investigated. The dates on three-dimensional structure of the temperature and velocity fields were obtained.

Introduction

The development of computer codes for the analysis of safety of reactor assemblies with liquid metal coolants should be constructed on the basis of application of not only numerical and instrumental methods of supercomputing but also on the basis of fundamental results in experimental hydrodynamics and heat transfer involving both single-phase and two-phase flows of liquid metal coolants. For a whole class of situations even when a mechanism of a physical phenomenon is clear and this phenomenon may be included into the matrix of verification of a computer code its adequate simulation and correct calculation may not be achieved due to a presence of uncertainty in the choise of a proper closure relation. An important problem is a limiting size of the data base on the thermophysical phenomena for the flow of coolants with low Prantl number, three-dimensional convective flows, development of turbulence and mixing of liquid metal coolants [1]. Data on laminar – turbulent transition are especially important for practical applications because local heat transfer coefficient changes drastically in this case. In particular, studies of boundary layer development on vertical heated surfaces and those on the mixing of liquids with different temperatures have a direct relation to the understanding of processes of convective heat transfer in fuel rod assemblies. The study of such phenomena should proceed by understanding of their physical mechanisms with a gradual increasing the complexity of the study objects. In this connection the physical modeling of relatively simple geometrically but complex on their structure non isothermal flows becomes especially

important. This modeling can be used as tests for the development of adequate numerical models and methods of calculations.

The foundation of the possibility of simulation of liquid metal media convection by other liquids shows that the equivalent contribution of the convection in integral heat transfer takes place at significantly higher values of Grashoff number than for non-metallic liquids [3]. The spatial forms of flows are in this case practically similar. Therefore, using experimental data obtained for non-metallic liquids it is possible to move significantly into the region of high Grashoff numbers for liquid metals. The performing of experiments on transparent liquids with moderate and high Prandtl numbers will allow to reduce the amount of experiments with liquid metal coolants and to make less elaborate measurements of temperature and velocity fields.

Main results of an experimental study of evolution of local characteristics of free convection boundary layers at the walls of a flat vertical liquid layer heated to different temperatures are presented in this report along with the studies of the flow structure at the flow of two jets of liquid having different temperatures in a vertical pipe in the regime of mixed convection. The vertical liquid layer between two parallel walls of different temperatures is a canonical object in the studies boundary layer stability and laminar-turbulent transition at thermo gravitational convection.

Free convection in vertical liquid layer

The development of free convection layer in liquid bounded by a vertical channel of rectangular cross section whose opposite walls were heated up to different temperatures is studied. The scheme of experimental set-up is shown in Fig. 1. Inner dimensions of the channel are: height H = 660 mm; width (equal to the distance between hot and cold walls) L = 58 mm, chanel depth W = 165 mm. Two heat exchangers (1, 2) are placed on the sides of the test volume, they keep side walls of the channel at different temperatures. The heated heat exchanger (1) is transparent, liquid flow visualization is performed through it. The cooled heat exchanger (2) is made of two brass plates. Top and bottom ends of the test section have thermal insulation (3, 4). To keep the condition of constant wall temperatures inner volumes of heat exchangers (1, 2) were connected to liquid thermostats. The accuracy of temperature stabilization in thermostats was 0.025 °C. All measurements were performed at stationary boundary conditions, for this the test section was kept thermally stabilized continuously for 4 hours.

During experiments temperature profiles were measured at the walls of the test section and in the liquid over the whole cross section and over its height. Temperature measurements were performed by micro thermocouple probes with the diameter of 0.03 mm. Flow visualization and liquid velocity profiles were made using PIV technique.

During the experiments the height of the liquid layer was varied in the limits of 90 to 660 mm, also the temperature difference between hot and cold walls was varied. The use of the present geometry and ethil alcohol as the test liquid allowed to study the liquid flow up to Rayley number $Ra_x = (\beta g/a\nu)\cdot\Delta T_m \cdot x^3$ of 1012. Here, $\Delta T_m = (T_1 - T_m)$; T_m is temperature in the middle section y = L/2 at the level x over the layer height., β is volumetric dilatation coefficient, g is gravity acceleration, a thermal diffusivity coefficient, ν is kinematic viscosity coefficient, x is longitudinal coordinate.

The development and stability of boundary layer, evolution of temperature and velocity of free convection boundary layer over the longitudinal coordinate, there correlation with the spatial shape of secondary flows at the walls heated to different temperatures, effect of free convection on the flow pattern were investigated in the experiments performed. Fig. 2 shows the picture of the development of thermo gravitational flow at the hot wall over the layer height. The following zones may be selected for the boundary layer flow: laminar, with Rayley number based on current distance $Ra_x < 6\times10^8$;

zone of developed two-dimensional secondary flow $Ra_x < 2{,}3\times10^9$ with the threshold of its generation $Ra_x = 6\times10^8$; zone of significantly three-dimensional flow where the Rayley number $Ra_x > 2{,}3\times10^9$. The process of formation of a two-dimensional vortex in the boundary layer has a periodical in time character. Therefore the border of the laminar boundary layer is not strictly determined but is in the periodical motion. In the layers restricted by height a core with stable liquid stratification is formed. The longitudinal temperature gradient in the core center depends on relative dimensions of the layer H/L and temperature difference between the walls. With increasing $Ra_x \geq 2{,}1\times10^{10}$ the core turbulization and unsteady sporadical transfers of hot liquid to cold wall and back are observed. After averaging the velocity field at long time interval the formation of hierarhy of large scale vortices can be observed.

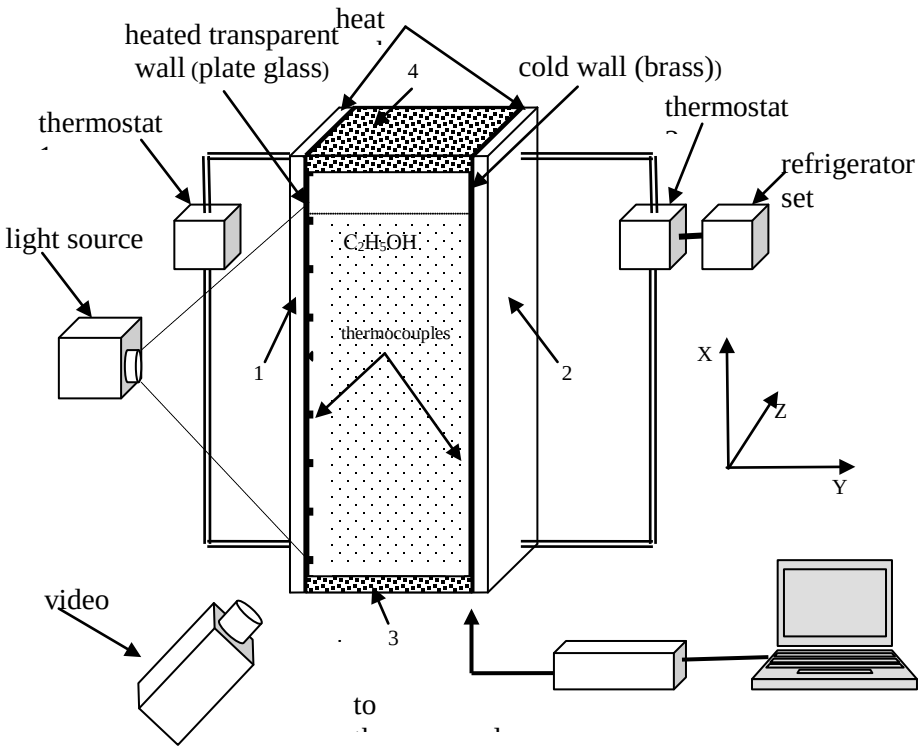

FIG. 1. Experimental setup for investigation of natural convection

Joint processing of temperature measurements and flow visualization show the quantitative relation between hydrodynamics, characteristics of secondary flows and local heat transfer. Data of this processing are shown in Fig. 3. A lag of thermal transition with respect to hydrodynamic transition exists. The height distributions of time averaged heat flux and local heat transfer coefficient have three characteristic regions (see Fig. 4): laminar ($Ra_x < 2{,}3\times10^9$) where local heat transfer decreases monotonously with height; zone of thermal transition ($2{,}3\times10^9 < Ra_x < 5\times10^9$) where local heat transfer increases with height, turbulent zone ($Ra_x > 5\times10^9$) where local heat transfer decreases with height. Temperature and velocity fluctuations appear in the upper part of laminar region. The lack of stability of laminar boundary layer and appearance of two-dimensional periodic flows does not result yet to the deviation of heat transfer correlation typical for laminar flow. Only the generation of developed three dimensional flow corresponds to the transition boundary from laminar heat transfer to turbulent one. Therefore, the regions of hydrodynamic and thermal laminar – turbulent transitions are not the same.

Intensity of local heat transfer fluctuations reaches the highest values in the middle of the thermal transition region. Frequency spectra of local haet transfer fluctuations for upper part of laminar region and down part of thermal transition region at Rayley number based on the height of the liquid layer $Ra_H = 7{,}9\times10^{10}$ contain a peak at the constant frequency equal to 0.44 Hz. The RMS deviation of local heat flux from its time-averaged value reaches 30 %.

Experiments performed in a wide range of vertical layer height and temperature difference between walls show practically unchanged scenarium of flow development at hot wall. The scenario of laminar – turbulent transitions in boundary layers at hot and cold walls do not depend on the type of the boundary at the upper cut of the layer. If the upper boundary is free a stationary vortex structure is formed in a near-surface layer due to thermocapillary effect. This structure remains practically unchanged at high when an unsteady vortex flow is formed in the boundary layer.

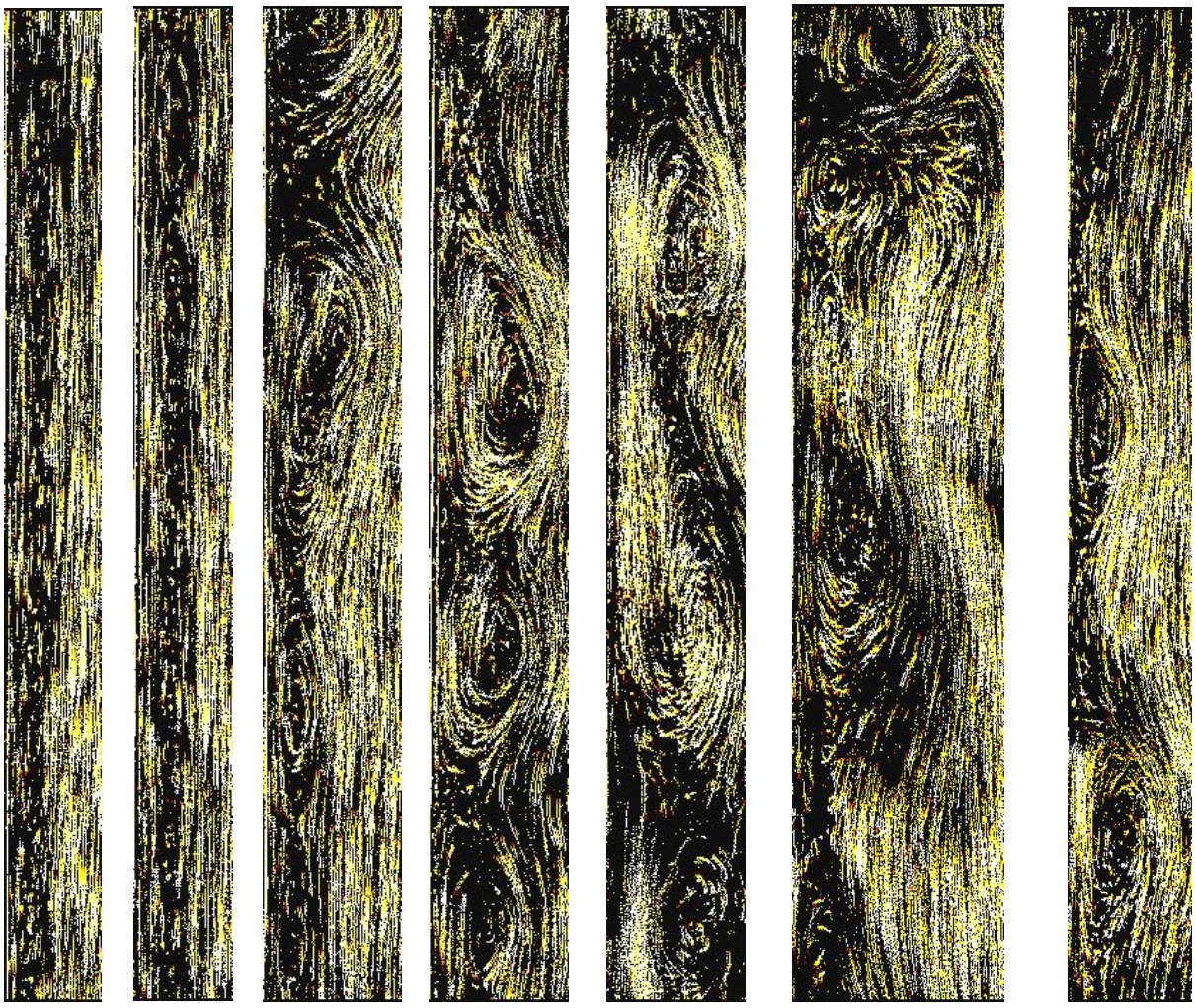

FIG. 2. Structure of thermo gravitational flow near hot surface.
Cold wall temperature – 16ºC , hot wall 20ºC. Rayley number $Ra_H = 7{,}9x10^{10}$

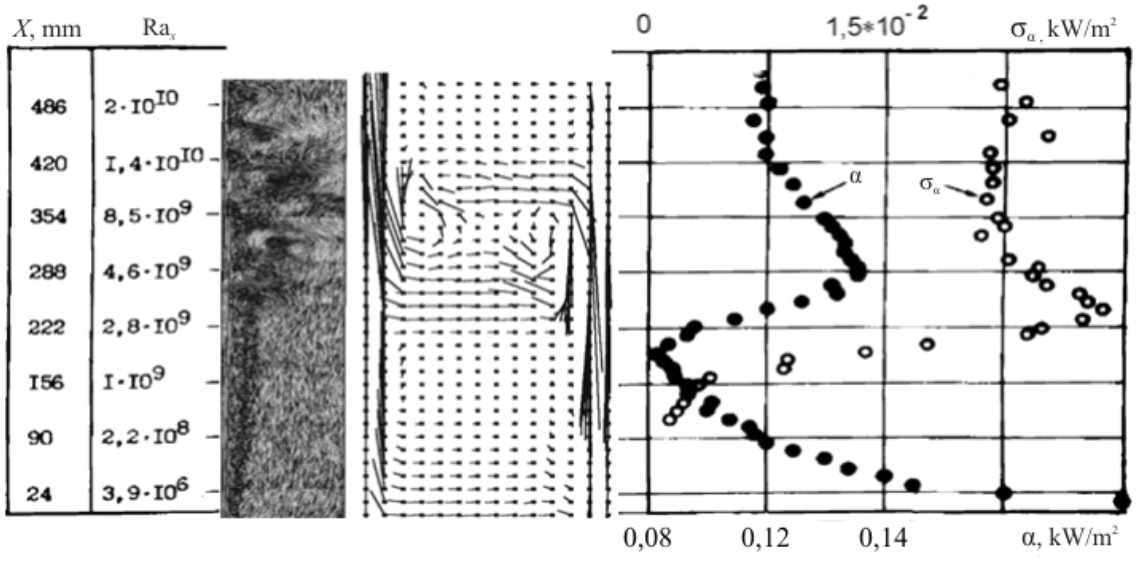

FIG. 3. Spatial form of flow in a plane of hot wall, instantaneous field of trajectories, Distribution of heat transfer coefficient and heat transfer density.
Cold wall temperature -16ºC; hot wall + 20ºC

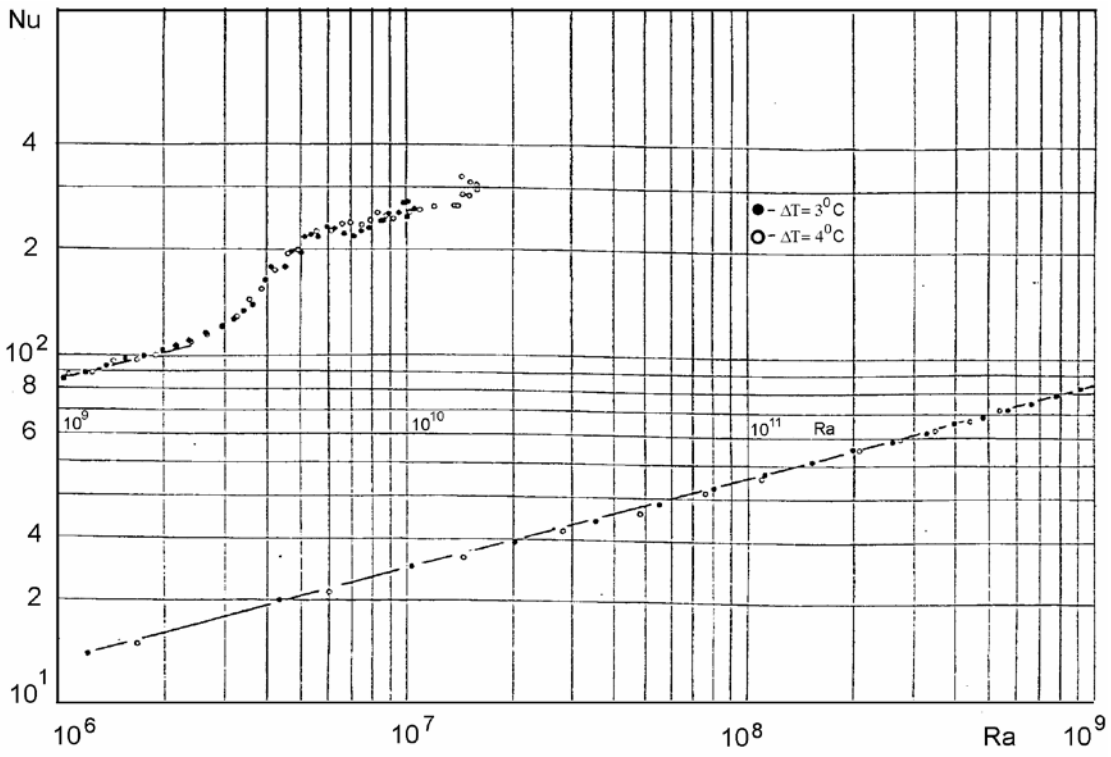

FIG. 4. Dependence of Nu number on Rayley number based on longitudinal distance x for free convection flow in a vertical layer with walls of different temperatures

Mixed convection of two liquid jets

The following problem was considered at the experimental study of convective mixing of liquid jets with different temperatures. Cold liquid flows upward with low velocity in a vertical pipe. At some distance downstream a jet of liquid of higher temperature is injected to it. Mixing zone, temperature profile, pipe wall temperature are the quantities to be determined.

Experiments were performed in a vertical pipe 42 mm i.d. 2.2 m long. Cold liquid (water) with the temperature of 30 ºC was pumped through it. A jet of hot water with the temperature of 60 °C was supplied near the inner wall of the main tube through a nozzle 15 mm diameter. Experiments were performed at constant flow rates of cold and hot liquids. Superficial liquid velocities were 0.224 m/s for cold water and 0.046 m/s for hot water. The total average liquid velocity was 0.27 m/s. The Reynolds number based on inner tube diameter and cold liquid viscosity was $Re = 1.42x10^4$. According to [3] such flow conditions correspond to the regime of mixed convection.

The temperature distribution on the pipe wall was measured using infrared system. The liquid temperature profiles inside the tube were obtained by micro thermocouples using automatic traversing system. Experimental results obtained show a complicated three dimensional structure of temperature field depending on the distance from the point of injection and circumferential angle.

Three-dimensional distribution of time-averaged wall temperature are shown in Fig. 5. A strong non uniformity in the temperature is observed. In the region corresponding to the position of the nozzle injecting hot liquid (α = 50 – 90 deg) higher wall tempewrature was detected. In an opposite part of the pipe ((α = -90 deg) the wall temperature corresponds to that of cold liquid. The angle α = 90 deg corresponds to the position at which hot liquid is injected. A rapid temperature drop in the first region and intensive temperature rise in t5he second one is observed depending on the distance from the injection point due to intensive liquid mixing. A gradual temperature increase with increasing distance from the injection point is observed in the central part of the pipe. At negative α values a liner rise of the wall temperature is detected. At positive α values the wall temperature decreases more intensively at small Z. Measurements of instantaneous temperature at the pipe wall at various distances from the mixing point showed that regions with strong ang weak wall temperature fluctuations exist. The region of high fluctuations merges the line of interaction of hot and cold jets.

Radial temperature profiles obtained with microthermocouple are shown in Fig. 6 for Z = 50, 250 and 450 mm. The bottom plane shows the cold liquid temperature. The strongest non uniformity in temperature profiles is observed at Z = 50 mm. The flow can be conditionally separated on “cold” and “hot” parts. A weak temperature rise is observed in the first part during motion to the pipe axis. The temperature rise is observed in the second part during motion from the axis to the pipe wall. With increasing Z a wall temperature rise in the first region and its decrease in the second region is observed. This results in the temperature equalization over the pipe cross section.

A study of temperature fluctuations and time-averaged liquid temperature depending on the circumferential angle and the distance from the injection point was performed. The measurements showed that the growth of temperature fluctuations takes part during transition from the regions of low temperature to those of high temperature where intensive liquid mixing takes place. The thermal striping was studied in paers [4 – 6]. According to the data of different authors, the temperature oscillations have the frequency in the range of 1 to 10 Hz.[7]. With increasing Z the temperature fluctuations in the “cold” region grow, while in the “hot” region they decrease.

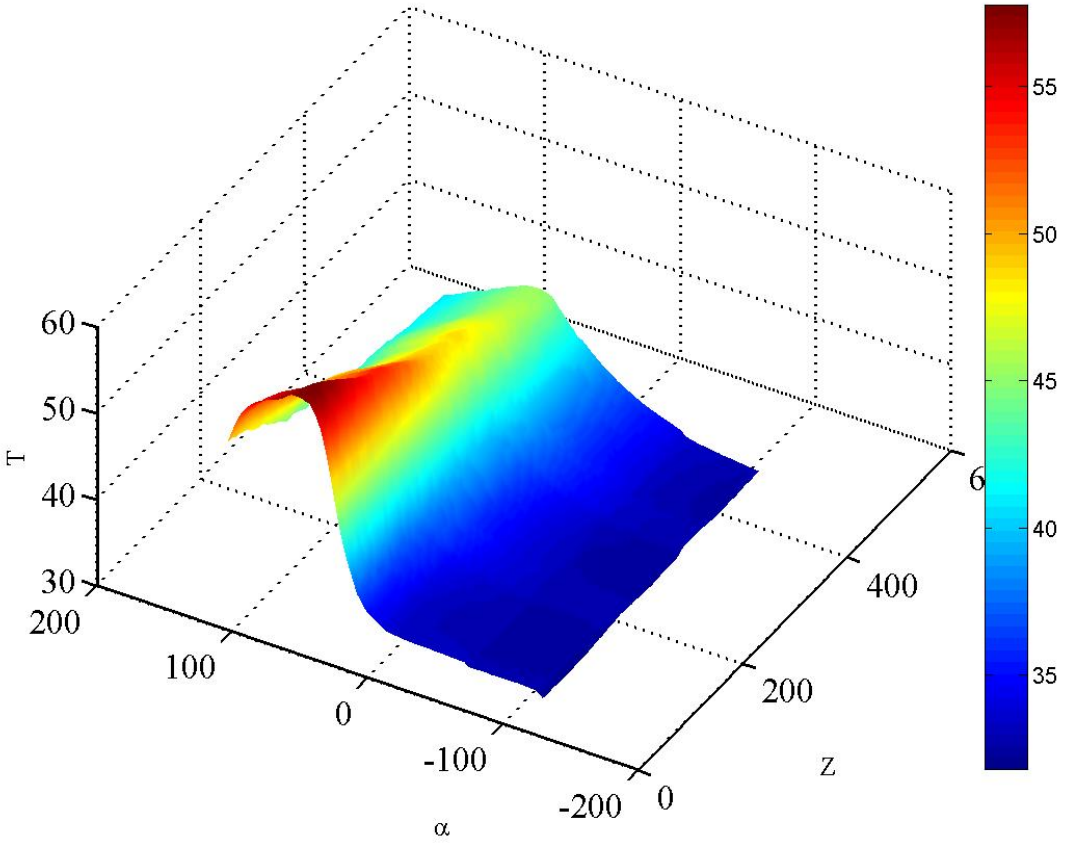

FIG. 5. Pipe wall temperature distribution (pipe segment is restricted to axial angles +90 and -90 deg). The temperature scale is shown on colored vertical diagram

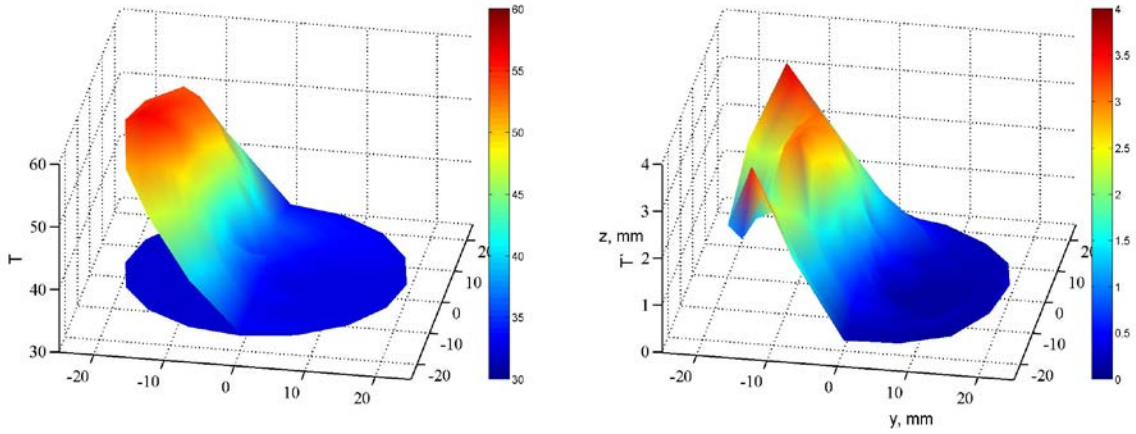

z= 50 mm

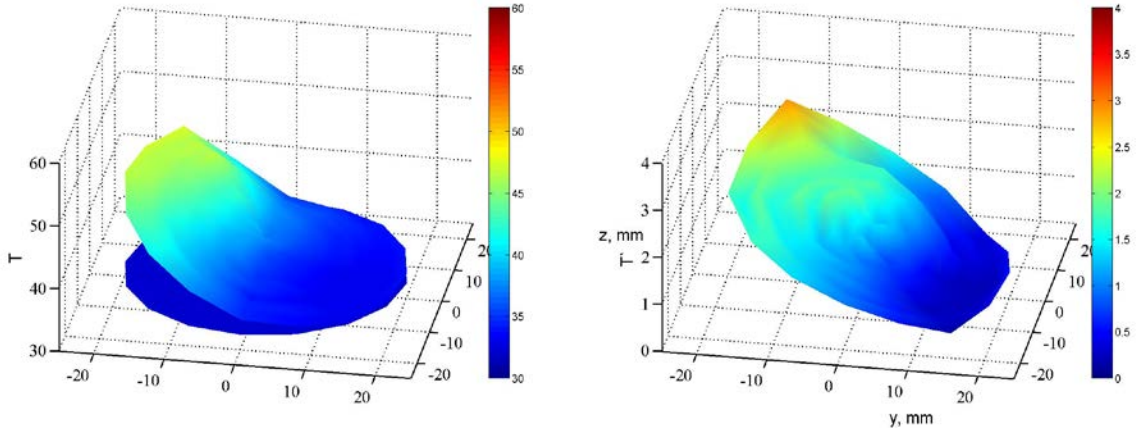

z= 250 mm

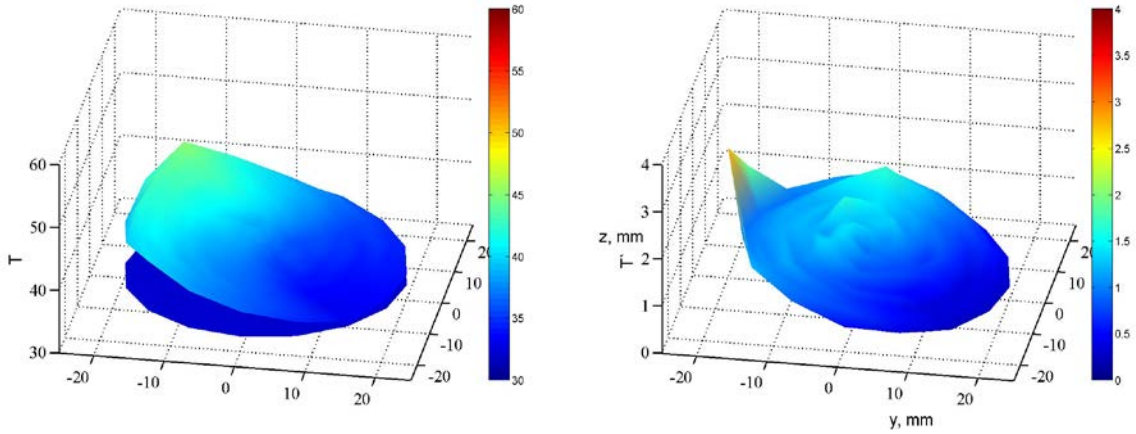

z= 450 mm

FIG. 6. Distribution of averaged temperature (left) and temperature fluctuations (right) in pipe cross section in the mixing zone at distances 50, 250 and 450 mm from the point of hot liquid injection

Conclusions

A complex experimental study of the structure of free convection boundary layer near a vertical heat transfer surface in the regime of laminar-turbulent transition is performed. The correlation between heat transfer and flow hydrodynamics is studied for qualitatively different stages of the flow. The data on local temperature and velocity fields, three dimensional data on secondary flows in the region of laminar-turbulent transition and in turbulent boundary layer.

The studies of mixture of layers of different temperatures in the regime of mixed convection were performed. The general flow structure was investigated, spatial temperature distributions on the test pipe wall and over the channel cross section were obtained. A three dimensional structure of the temperature field during mixing of liquids of different temperatures was constructed from the measurements.

REFERENCES

[1] Yadigaroglu G., Andreani M., Dreier J., Coddington P. Trends and needs in experimentation and numerical simulation for LWR safety // Nuclear Engineering and Design 221 (2003) 205–223

[2] Praser H. Novel experimental measuring techniques required to provide data for CFD verification // Engineering and Design 238 (2008) 744–770

[3] Kutateladze S.S., Berdnikov V.S. Structure of thermogravitational convection in flat variously oriented layers of liquid and on a vertical wall // Int. J. Heat Mass Transfer. 1984. Vol.27. N9. P. 1595-1611

[4] Lin-Wen Hu *, Mujid S. Kazimi LES benchmark study of high cycle temperature fluctuations caused by thermal striping in a mixing tee // International Journal of Heat and Fluid Flow. 2006. V. 27. P. 54–64

[5] T. Lu, P.X. Jiang, Z.J. Guo, Y.W. Zhang, H. Li. Large-eddy simulations (LES) of temperature fluctuations in a mixing tee with/without a porous medium // International Journal of Heat and Mass Transfer 53 (2010) 4458–4466

[6] Jeong Ik Lee, Lin-wen Hu∗, Pradip Saha, Mujid S. Kazimi. Numerical analysis of thermal striping induced high cycle thermal fatigue in a mixing tee // Nuclear Engineering and Design 239 (2009) 833–839

[7] V.S. Naik-Nimbalkar, A.W. Patwardhan, I. Banerjee, G. Padmakumar, G. Vaidyanathan. Thermal mixing in T-junctions // Chemical Engineering Science. 2010 V. 65. P. 5901-5911

Experimental Potentialities of the MBIR Reactor

Yu. Dragunov, A. Lopatkin, I. Lukasevich, N. Romanova, I. Tretiyakov
Joint Stock Company "N.A. Dollezhal Research and Development Institute of Power Engineering" (NIKIET)
M. Svyatkin
Joint Stock Company "State Scientific Center – Research Institute of Atomic Reactors" (RIAR)
L. Kochetkov
Federal State Unitary Enterprise "State Scientific Center of the Russian Federation – A.I. Leypunskiy Institute of Physics and Power Engineering" (IPPE)

The prospects of nuclear power are closely linked with the evolution of fast-neutron reactors and a closed nuclear fuel cycle. Therefore the Federal Special Program entitled "Nuclear Energy Technologies of New Generation for the Period up to 2015 and for Long-Term Outlook up to 2020" envisions the creation of a multi-purpose research fast reactor MBIR.

The MBIR reactor is expected to be constructed and put into operation by 2020 at the RIAR site in Dimitrovgrad and to be a modern facility for the international center of joint use.

The MBIR is a nuclear research facility based on a liquid-metal-cooled fast-neutron reactor of the thermal power 150 MW. The experimental potential of the facility is defined by a set of in-vessel and ex-vessel devices to be used for a broad spectrum of research activities.

The report presents data on the general design of the reactor and a brief description of the experimental capabilities as envisioned by the reactor design.

Introduction

The development of Russian innovative reactor technology projects dictates the need for building a fast research reactor with expanded experimental capabilities to replace the BOR-60 reactor after its service life is expired.

First of all, this is necessitated by the requirement to achieve a higher in-core neutron flux and study the fuel and materials for the feasibility evaluation of reactor technologies with different coolant types in a range from gas to liquid metals. This can be implemented in the experimental loop reactor internals representing special loop channels installed directly inside the reactor core, the heat from which is removed by independent ex-vessel cooling circuits.

The creation and construction of the MBIR research reactor is one of the tasks to be implemented under the Federal Special Program (FSP) "Nuclear Energy Technologies of New Generation for the Period up to 2015 and for Long-Term Outlook up to 2020", which is intended to ensure the evolution of innovative nuclear power technologies.

The MBIR project is developed on a cooperative basis by a number of leading organizations in the Russian nuclear industry. It is planned that the reactor will be deployed at the RIAR site in Dimitrovgrad, the Ulyanovsk Region.

Major objectives

The MBIR reactor will ensure conducting the following research:

1. Studies into advanced types of nuclear fuel and absorber, including tests of fuel elements, fuel assemblies, absorber elements and other core elements developed based on new design and technological approaches.
2. Tests of fuel elements and fuel assemblies in transient, cyclic and emergency modes of

operation.

3. In-pile tests of and studies into problems of the closed nuclear fuel cycle, disposal of actinides and burning of long-lived fission products.
4. Radiation tests of advanced structural materials.
5. Study of new and modified liquid-metal coolants and respective their monitoring instrumentation and quality control tools.
6. Physical, materials testing, thermal-hydraulic and other in-pile experiments for the purpose of code verification.
7. Tests and field approval of new equipment types for different process systems, innovative instruments as well as control, monitoring and diagnosis systems.
8. Production of radioisotopes for different applications, generation of modified materials.
9. Applied research using neutron beams (neutron radiography and tomography of different materials and products).
10. Medicinal use of neutron beams (neutron therapy).

MBIR concept

The MBIR concept places priority on research and experimental tasks for evaluating the feasibility of the existing and advanced innovative designs of power reactor facilities rather than on production ones, though production of isotopes and applied activities on extracted neutron beams, as well as electricity generation will improve the efficiency of the reactor utilization.

The MBIR is viewed as the base fast research reactor intended to cover the needs of Rosatom State Corporation in experimental research in fast-neutron fields with ultrahigh flux levels in different heat-carrying media. So the MBIR reactor concept envisages the achievement of a neutron flux of not less than $5.0 \cdot 10^{15}$ $cm^{-2} \cdot s^{-1}$ and the existence of up to three experimental loop facilities containing different working fluids.

To ensure reliable and safe operation of the MBIR reactor, reference approaches (proven in analog facilities) and structural materials with well-studied physical and strength properties to be used as extensively as possible.

No creation of a new fuel type is envisioned for the MBIR reactor with the fuel supplies cost to be minimized through using the fuel matrix and the fuel element design proven in the BOR-60 and BN-600 reactors.

To secure informational and technological advantages, as well as to improve the efficiency of the MBIR reactor utilization and develop international cooperation in research on innovative reactor technologies, efforts are made for the international collaboration at as early stage as the design development and generation of the future research program. One of the underlying conceptual provisions is the implementation of the task to establish an international user center based on the MBIR reactor.

Basic parameters and characteristics of the reactor

The MBIR is a nuclear research facility with a multi-purpose liquid-metal-cooled fast-neutron reactor of the thermal power 150 MW to include in-vessel and ex-vessel facilities and devices for carrying out a broad spectrum of research activities. Table 1 gives the basic technical data of the MBIR research facility adopted on the basis of the conceptual design results.

Table 1 - Main technical characteristics of the MBIR reactor

Description	**Value**
Reactor thermal power, MW	150
Design layout of the heat removal systems	Loop-type
Number of cooling loops	2
Number of cooling circuits in the reactor facility	3
Primary and secondary coolants	Sodium
Tertiary coolant	Water/steam
Ultimate heat sink in the emergency heat removal system (EHRS)	Air
Principle of heat removal from the core	Forced circulation at reactor power operation Cooldown by natural circulation at shut down reactor
Reactor coolant temperature (inlet/outlet), $^{\circ}$C	354/547
Primary circuit pressure, MPa, not more than	0.6
Maximum neutron fluence, $cm^{-2} \cdot s^{-1}$	$\sim 5.5 \cdot 10^{15}$
Fuel type	Mixed uranium-plutonium oxide fuel
Outer fuel element diameter, mm	6.0
Number of CPS members	8
CPS member absorber	B_4C
In-pile SFA storage	35 to 50 cells
Design service life, year	50
Reactor utilization factor	0.65
Design life, year	50

A 3-D representation of the MBIR reactor is given in Figure 1.

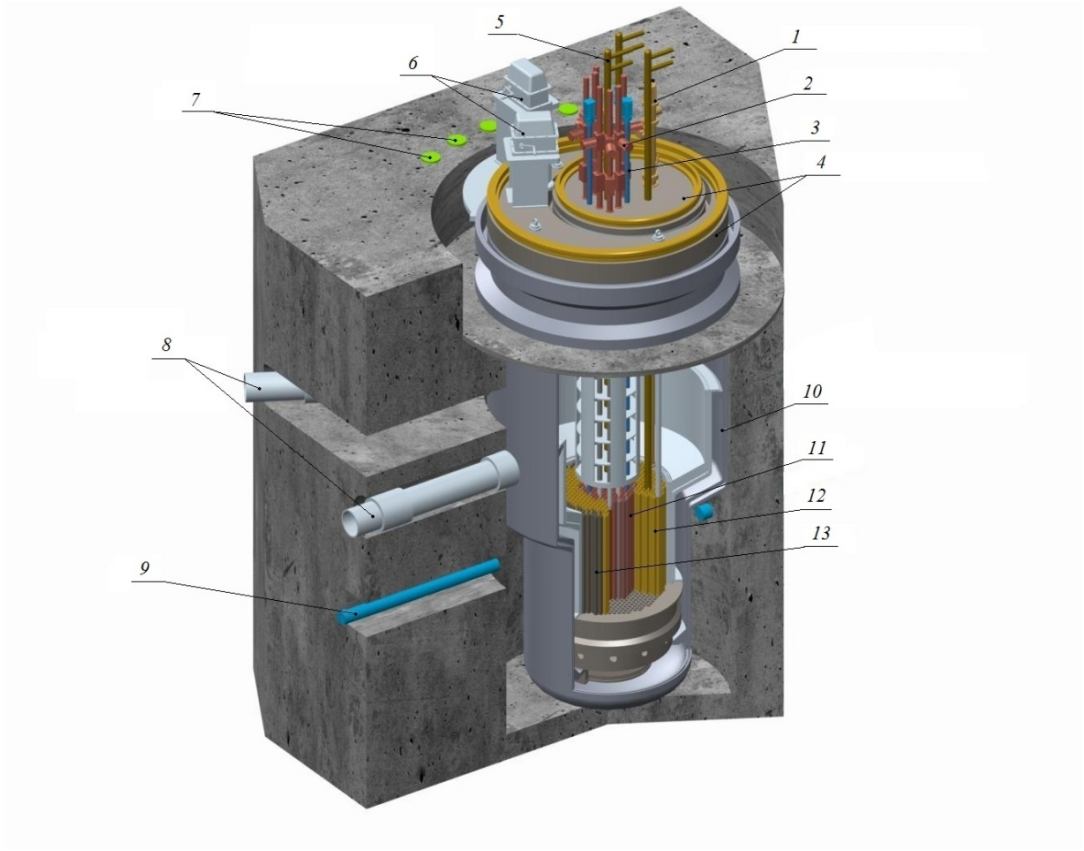

Figure 1. Reactor MBIR:

1 – refueling mechanism, 2 – CPS actuator drives; 3 - EC, 4 – rotary plugs; 5 – LC; 6 – rotary plug rotators; 7 - VEC; 8 – Primary circuit pipelines; 9 – HEC; 10 – vessel and safeguard shroud; 11 – FA; 12 – side reflector; 13 - IRS

The MBIR will include the following experimental equipment installed inside the reactor vessel:

- loop channels (LC) for modeling the conditions of operation of nuclear power plant (NPP) cores with different coolants;

- facilities of the channel-loop type with different coolants;

- instrumented material test assemblies for testing fuel, absorber and structural materials;

- non-instrumented material test assemblies;

- non-instrumented isotope production assemblies.

The arrangement of the experimental volumes inside the reactor core is shown in Figure 2, and the neutronic characteristics are given in Table 2.

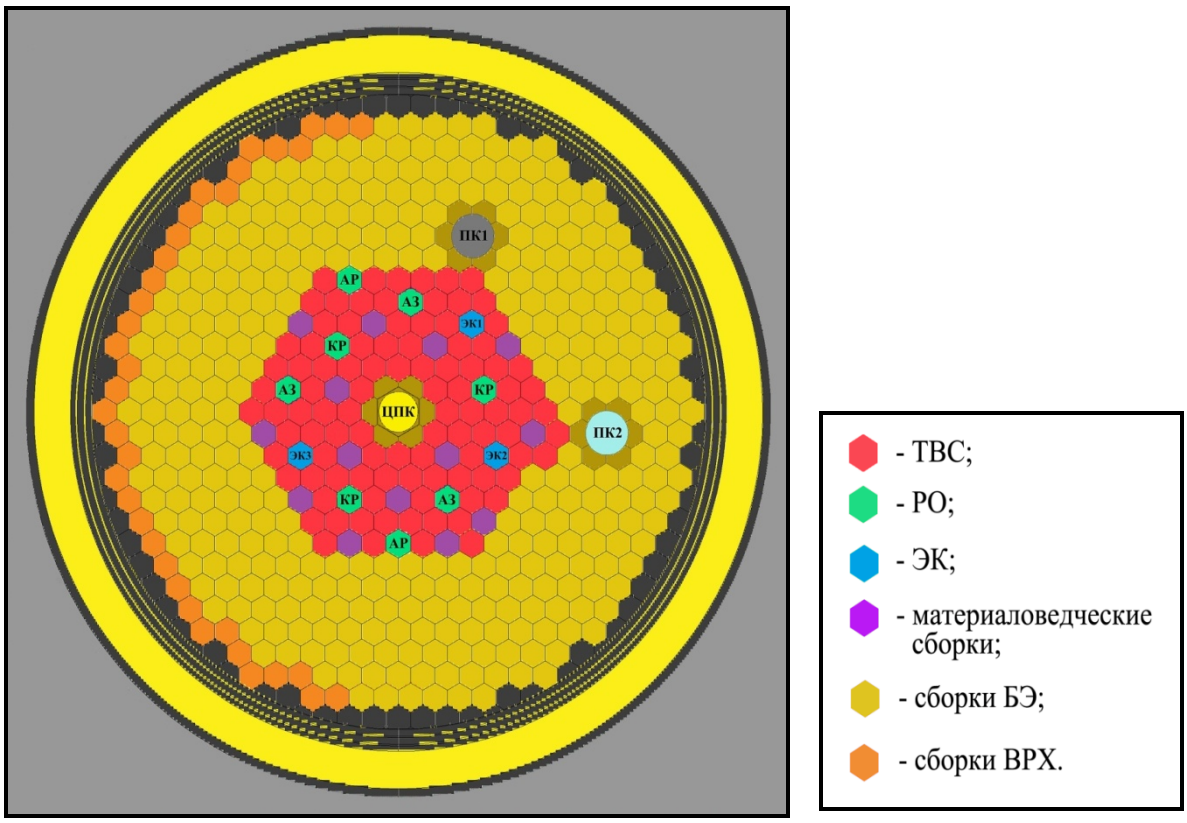

Figure 2. In-core arrangement of the experimental volumes

ТВС – FA; РО – CM; ЭК – EC; Материаловедческие сборки – Material Test Assemblies; Сборки БЭ – Side Reflector Assemblies; Сборки ВРХ – IRS Assemblies

Table 2 – Neutronic characteristics of the MBIR core

Characteristic	**Value**
Number of FAs	97
Effective reactor core diameter, cm	88.3
Fuel height, cm	55
Share of PuO_2 in fresh fuel, %	34.3
Duration of cycle between refuelings, day	92
Max./aver. burn-up of discharged FAs, % h.a.	~ 9.0
Reactivity decrease per cycle between refuelings, %	2.6
Average FA power, MW	1.41
Maximum linear rating of fuel element, W/cm	470
Maximum/average in-core neutron flux, $cm^{-2} \cdot s^{-1}$	$5.49 \cdot 10^{15}$ / $3.5 \cdot 10^{15}$
Share of fast (E_n>0.1 MeV) neutrons in the reactor core	0.7

The MBIR building design includes five compartments for the equipment of the loop facilities with five different types of coolant (sodium, lead, lead-bismuth, gas, salt melts), to each of which one of the LCs in the reactor can be connected. Meanwhile, there are three LC locations inside the reactor core: one in the core center and the two other on the periphery.

The channel-loop facility is an independent channel of the size not exceeding that of a regular cell, in which there are maintained and monitored the preset thermodynamic parameters of the fluid (coolant) and the fuel element cooling by natural or forced circulation organized within the channel, with the measuring cables and service lines led to beyond the reactor vessel.

Instrumented assemblies are experimental devices of the dimensions not exceeding those of a regular cell, which contain test samples fitted with measuring sensors, from which they can be led to beyond the irradiation zone up to 50 service lines (measuring and/or power lines, gas lines of the sample loading system and so on).

Non-instrumented assemblies are experimental devices with samples not fitted with measuring and monitoring devices.

Heat is removed from the instrumented and non-instrumented assemblies by the reactor primary coolant.

Table 3 presents characteristics of the experimental volumes inside the reactor vessel.

Table 3 – Characterization of the in-vessel experimental volumes

Experimental device	**Location**	**Number**	**Size at the core level, mm**	**NF* in cell, $cm^{-2} \cdot s^{-1}$**
Positions for non-instrumented material test assemblies and isotope production assemblies	Core	Up to 14	One core cell Width across flats - 72	Max – $4.9 \cdot 10^{15}$ Core average – $3.6 \cdot 10^{15}$
Positions for non-instrumented material test assemblies and isotope production assemblies	SR	Not limited	One core cell Width across flats – 72	
Experimental channels for instrumented irradiation devices and and/or channel-loop facilities	Core	Up to 3	One core cell Width across flats - 72	$(3.7\text{-}4.0) \cdot 10^{15}$
LC locations	Core center SR	1 Up to 2	In place of seven core cells Ø 100	$5.04 \cdot 10^{15}$ $(1.1\text{-}1.6) \cdot 10^{15}$

- NF – neutron flux

The MBIR layout suggests that there is an in-reactor storage (IRS) of spent FAs (SFAs) in the side reflector (SR) zone. This makes it possible to reduce considerably the reactor cooling time after the shutdown pending the refueling operations, and increase the reactor utilization factor.

The reactor facility will have ex-vessel horizontal and vertical experimental channels (Table 4).

Table 4 – Ex-vessel experimental channels

Experimental devices	Diameter, mm	Number
Horizontal experimental channels (HEC)	200	3
Vertical experimental channels (VEC)	~ 350 ~ 50	Up to 9 2

The core heat is removed over two loops (Figure 3). Heat is transferred from the core to the ultimate heat sink (turbine) over three circuits. The primary and secondary coolants is sodium, and the tertiary circuit fluid is water-steam. The whole of the reactor facility's primary circuit is enclosed in a safeguard shroud.

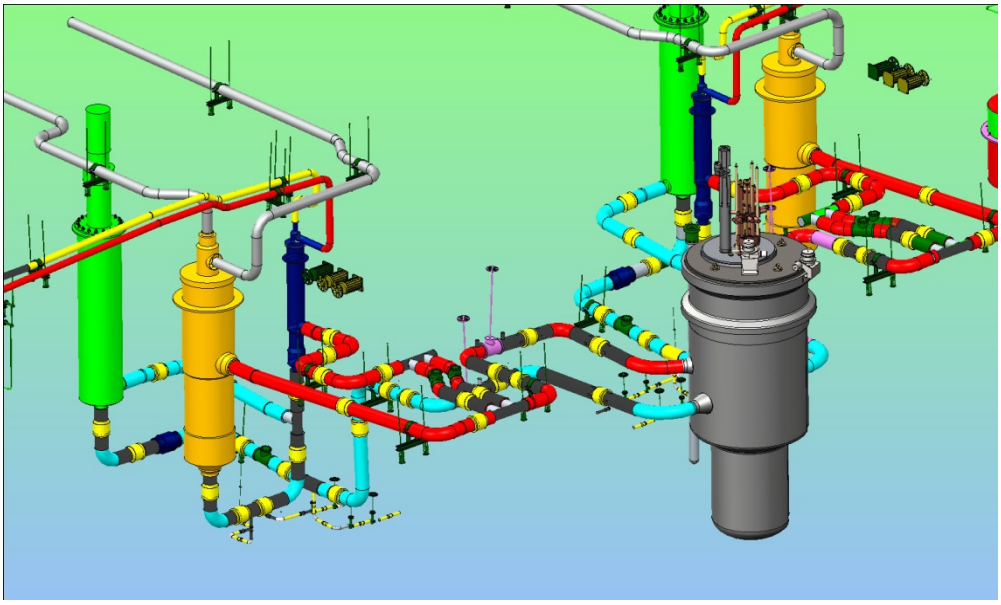

Figure 3 – A fragment of the 3D-geometry MBIR reactor heat removal system loop

The emergency heat removal system (EHRS, Figure 4) is a two-circuit system with transfer of heat to the ultimate sink (the atmospheric air in the air heat exchanger).

The EHRS primary and secondary coolant is sodium. The movement of the sodium inside both circuits and of the air inside the heat exchanger is provided by natural circulation.

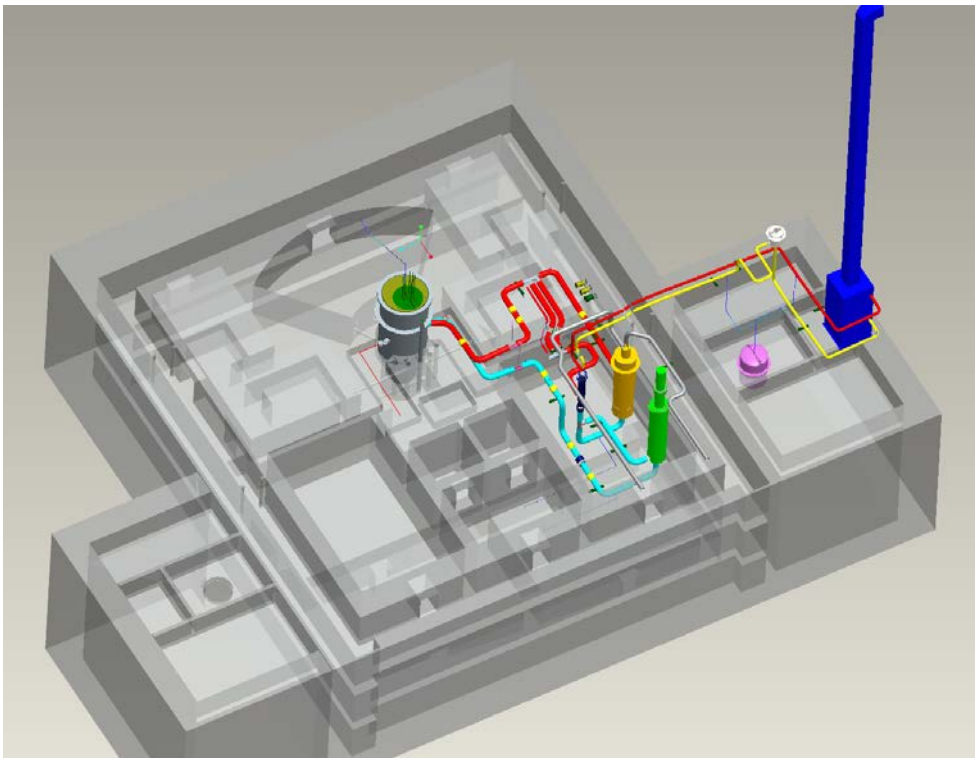

Figure 4 Layout of the heat removal circuit inside the reactor building

Since the end of 2011, the development of the detailed design and design documentation has been under way. The near-term plans include the completion in 2013 of the MBIR detailed design.

The implementation of the MBIR project to be commissioned, as scheduled, in 2019 will make it possible to provide the industry with the research resources required to evaluate the feasibility of and support innovative and evolutionary reactor technology projects, and may form the basis for international cooperation.

Conclusion

The MBIR project developed within the frameworks of the FSP should be implemented in as short time as possible, so much attention is given at the initial phase to the development of the project implementation schedules with fixed key stages. At present time, the zero-level MBIR project implementation schedule has been approved, which defines the major project development stages, such as the dates for the development of the engineering and design documentation, for the commencement of the construction and for the fabrication of major components, as well as for the commencement of the assembly and commissioning activities, and highlights the licensing issues.

In 2010, as defined by the approved plan, the specifications (the technical assignment to develop) for the MBIR reactor facility were developed and approved, and work was begun on the conceptual design. The MBIR conceptual design was completed in 2011.

Since 2011, the development of the detailed design has been underway and, in parallel, the development of design documentation has been begun. The near-term plans include the completion of the design development and the licensing of the design.

EFFECT OF HETEROGENEITY OF JSFR FUEL ASSEMBLIES TO POWER DISTRIBUTION

Toshikazu Takeda, Yoichiro Shimazu, Koki Hibi and Koji Fujimura

Research Institute of Nuclear Engineering, University of Fukui
1-2-4Kanawa-cho, Tsuruga-shi, Fukui 914-0055, Japan

Abstract. The Japanese sodium-cooled fast reactor JSFR is an oxide fueled system rated at 1,500 MWe. The core is composed of large fuel assemblies with an inner duct for each assembly. Thus, the assembly heterogeneity is rather strong. The purpose of the present paper is to make clear the effect of the heterogeneity to assembly and core characteristics, especially to power distribution. The inner duct is located at one corner of a hexagonal assembly, and the effect of the location has been investigated. We have compared the power distribution when the inner duct is always located near the core center and/or far from the core center. The power at the core center increased and decreased by ~10%, respectively compared to the case when the inner duct is randomly located. Thus, the location has important effect to power distribution.

1. Introduction

Many scenarios of possible energy futures foresee an important role for nuclear power. Acceptance of nuclear power with large-scale contributions to the world's energy mix depends on satisfaction of key drivers to enhance sustainability in terms of economy, safety, adequacy of natural resources, waste reduction, and nonproliferation. Fast reactors with recycle significantly enhance the sustainability indices. Therefore, due to their flexibility to produce new fissile material and/or to reduce the amount of waste and its impact on the environment, fast reactors are needed to make nuclear power a truly long term option.

Japan has a long track record of maintaining a commitment to fast reactor technology. Considerable efforts have been focused on innovative design approaches to achieve optimal safety, waste minimization, enhanced proliferation resistance, and economical competiveness. Studies carried out over the past decade [1, 2] have concluded that these objectives could be achieved. All types of fast reactor designs were considered, including advanced loop and pool configurations, various fuel types and coolants, and complete costs over the entire life cycle. The system chosen in Japan for detailed design is a sodium-cooled fast reactor known as the Japan Sodium-cooled Fast Reactor (JSFR), a two-loop, oxide-fueled system rated at an electrical output of 1,500 MW [3–5]. In Figure 1 shows a 3D view of the plant arrangement. In this JSFR, technical innovations such as a large fuel assembly using large-diameter fuel pins stacked with annular pellets, an inner duct to discharge molten fuel during a hypothetical core destructive accident, and a tall steam generator using straight, double-wall heat transfer tubes are adopted [6].

Technological innovation in the fields of safety and reliability is the key for commercialization of fast reactor for sustainable development. It is pursued in a wide range of scientific and technical area, including nuclear data, reactor physics, engineering design, and methods of validation and qualification.

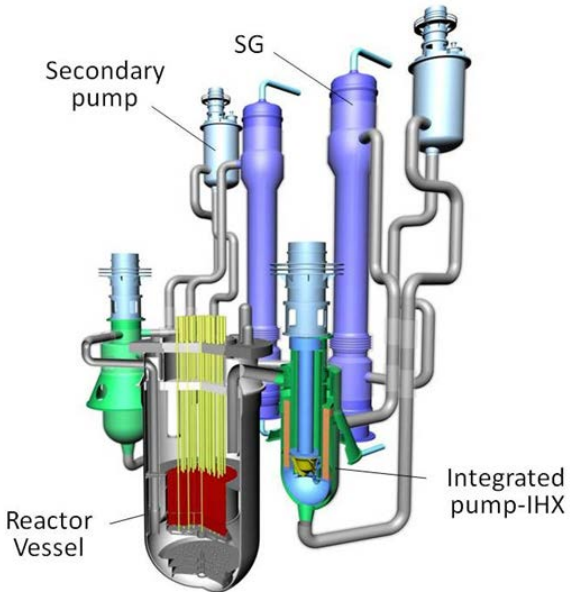

Fig.1 Schematic of JSFR-1500, showing the 2-loop arrangement with straight-tube heat exchangers, and with the primary pumps integrated into the Intermediate Heart Exchanger (IHX) (reproduced from [7])

To design the FBRs of the future, it is a requirement that one is able to calculate the physical characteristics accurately, that is, without the need of mock-up experiments. This requires advanced modeling tools. High-priority issues are the modeling of neutronics, fuel and structural materials, and thermal-hydraulics. In the present paper, the neutronics field is illustrated with emphasis of the heterogeneity effect of fuel assemblies to power distribution.

2. NEUTRONICS CALCULATION METHODS

The calculation methods for JSFR have been developed based on deterministic methods. As a nuclear data set we have selected the JENDL-4.0 [8] nuclear data set since the core performance parameters of various fast reactor cores and critical assemblies calculated with JENDL-4.0 are closer to the measured data than the results of JENDL-3.3. Figure 2 shows the ratio of calculation to measurement (C/E ratio) of k_{eff} of several fast systems, comparing JENDL-3.3 and JENDL-4.0. In particular, JENDL-4.0 improves the underestimation of k_{eff} for uranium-fueled cores compared to JENDL-3.3 (results of the BFS facility in Figure 2).

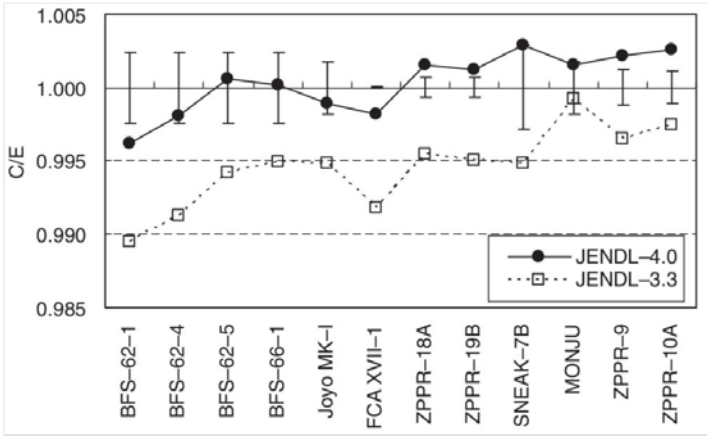

Fig. 2 Comparison of the C/E ratio for k_{eff} , using JENDL-3.3 and JENDL-4.0 for several fast systems (reproduced from [8])

To obtain effective groupwise cross sections, the SLAROM-UF [9, 10] code has been selected. Traditionally in Japan, effective cross-sections are calculated in 70 energy groups with the SLAROM and SRAC codes [11], using equivalence theory with a Dancoff factor. In this kind of calculations, the problem-specific composition and geometry can only be taken into account partially, because the group cross-sections are calculated with a fixed neutron energy spectrum rather than a full problem-dependent neutron energy spectrum.

The SLAROM-UF code has been developed by JAERI to treat ultrafine energy groups, using up to a hundred thousand groups below 50 keV. The use of ultrafine energy groups leads to an improvement for the criticality calculations.

JSFR is a 1,500MWe fast reactor with a core of 6.77m diameter and 1.5m height, as shown in Figures 3 and 4. In the case of a severe accident in a traditionally designed core the molten fuel may accumulate in some part of the core, and cause a recriticality. To prevent the occurrence of recriticality, there is an inner duct installed in each fuel assembly. In case of accidents, the molten fuel flows upward through the inner duct, and a recriticality is prevented.

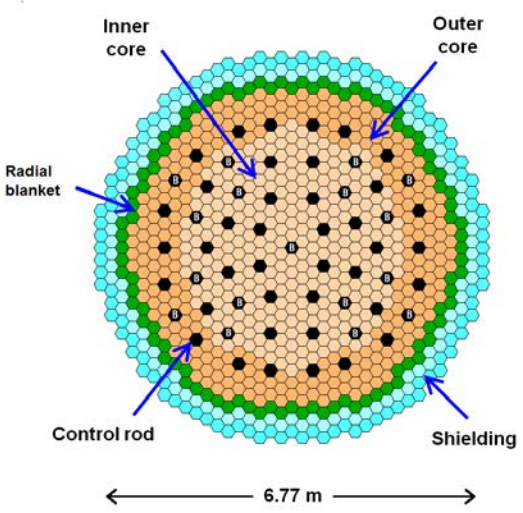

Fig. 3 Core map of JSFR-1500

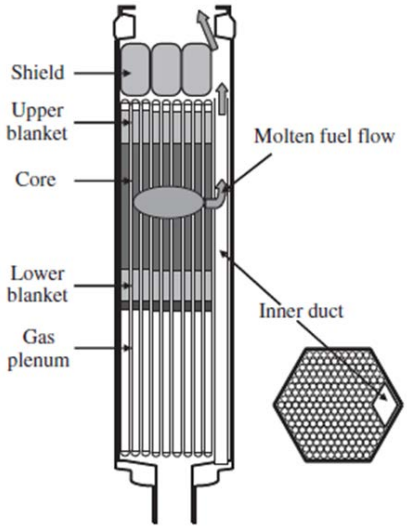

Fig. 4 JSFR fuel assembly with inner duct (so-called modified FAIDUS conceptt Structure)[6]

Thus the JSFR fuel assembly has a complicated form, and the accurate description of the assembly should be taken into account when calculating assembly averaged cross-sections. To calculate the homogenized cross-sections, the Method of Characteristics (MOC) has been used because the complex geometry can be taken into account accurately. The effects of heterogeneities on the assembly-averaged cross-sections are taken into account by the MOC calculation. For ultrafine group calculations, the modeling options in SLAROM-UF are limited to one spatial dimension (1D): the presence of the inner duct cannot be treated. For this reason, it was chosen to incorporate the BACH code [12], a 2D MOC code for hexagonal geometry. Thus, SLAROM-UF acts as a cross-section production module, producing effective cross-sections in a 70-group structure, while BACH is used to determine an accurate flux distribution and cross sections to be used in the core calculations.

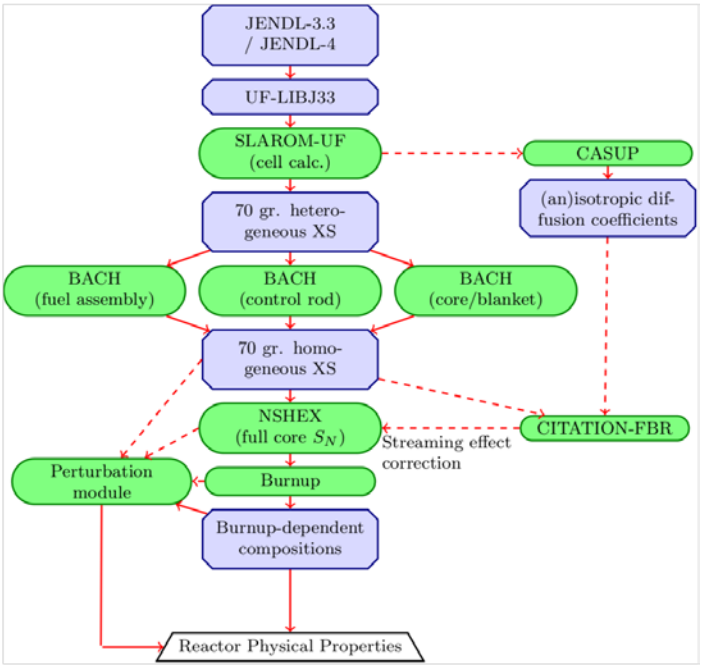

Fig. 5 Flow chart of a reactor physics calculation

Assembly averaged cross sections are calculated assuming an infinite lattice of repeating assemblies. For special assemblies, such as control rod assemblies, color set calculations are used.

After the preparation of homogenized cross sections, core calculations are performed with diffusion or transport theory. The code NSHEX is a nodal Sn transport code, described in more detail in [13]. It is capable of treating Hexagonal-Z geometry with several options for the nodal expansion order and Sn quadrature sets. The diffusion code CITATION-FBR also can be used. (An improved version for FBR applications of the traditional diffusion code CITATION [14]; CITATION-FBR is developed by JAEA). This code is used in triangular-Z geometry. CITATION-FBR is capable of using anisotropic diffusion coefficients. This allows one to take into account effects of anisotropy in the case of a voided lattice, and so forth. The overall neutronics calculation flow system is shown in Fig. 5.

3. NUMERICAL RESULTS

In order to verify the accuracy of the BACH code, we have compared the k_∞ values and the intra-assembly reaction rate distributions. Table 1 compares the k_∞ values of the JSFR fuel assemblies with and without an inner duct. The references are given by the continuous energy Monte-Carlo code MVP [15]. The BACH results are in good agreement with the reference and the difference is within 0.1% dk. Figure 6 compares the U-238 capture rate distributions, calculated by the BACH code and the reference continuous-energy Monte-Carlo code MVP, in a JSFR assembly. Good agreement is found, which shows the accuracy of the BACH code.

Table 1 Comparison of assembly k_∞ values of JSFR fuel assemblies with and without an inner duct

Case	MVP	BACH
Without inner duct	1.28438±0.0048%	1.28385 (-0.05% Δk)*
With inner duct	1.27232±0.0040%	1.27174 (-0.06% Δk)*

* Difference from reference

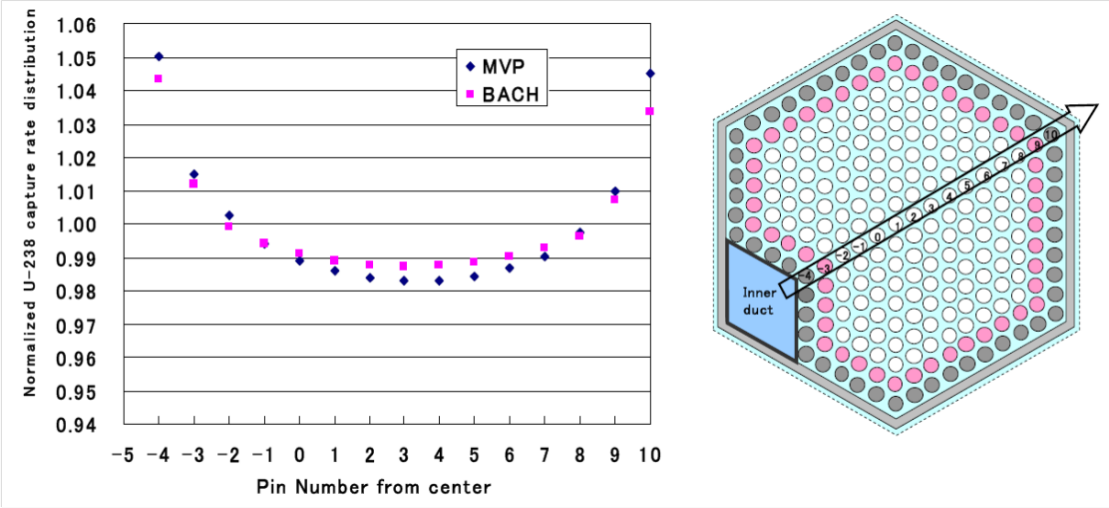

Fig.6 U-238 Capture Rate Distribution in a JSFR fuel assembly. Fuel assemblies are grouped into three groups to take into account the influence of the wrapper tube and sodium channels on the self-shielding

Next, let us consider a multi-assembly model as shown in Fig.7. The model consists of 2 core assemblies, 3 radial blanket assemblies and 2 shielding assemblies. The boundary condition (b. c.) is reflective b. c.

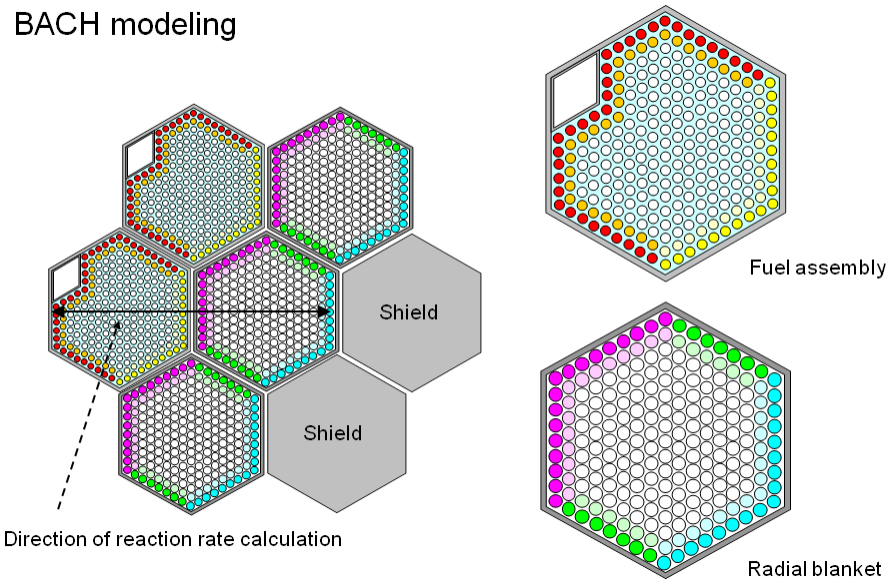

Fig. 7 Seven assemblies model consisting of fuel assemblies, blanket assemblies and shielding assemblies

We considered the effect of the presence of adjacent different assemblies to effective cross sections of individual pins. Two cases are considered. In Case 1, an infinite assembly model (cylindrical model in SLAROM-UF) was used to calculate the effective cross sections. In Case 2, the one dimensional slab model consisting of 2 core assemblies, one blanket assemblies and two shielding assemblies was used. Pin by pin calculations in the seven assemblies were performed in 70-energy groups using BACH. The k_{eff} values for Cases 1 and 2 are 0.7876 and 0.7880, respectively. The difference is very small. Therefore, the use of the infinite assembly model in calculating effective cross sections is satisfactory.

This is also confirmed by the comparison of various reaction rate distributions for Cases 1 and 2. Figure 8 shows the U-238 capture rate distribution in the core fuel assembly and the adjacent blanket assembly. The agreement is within 1% except a blanket pin just adjacent the shielding assembly.

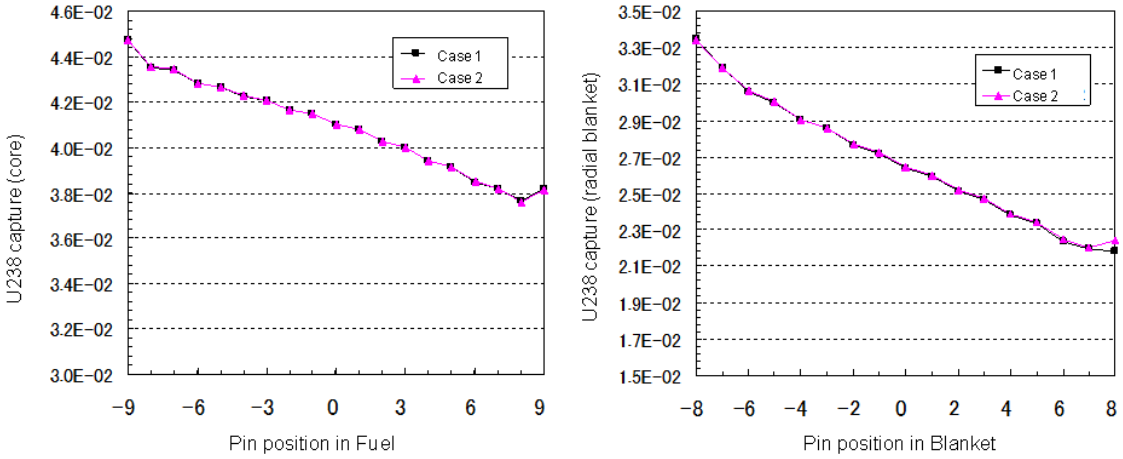

Fig. 8 U-238 capture rate distribution in the 7 assembly model for Case 1 and 2

The effect of the inner duct to core characteristics has been investigated by performing 3-D core calculations with the diffusion code CITATION. The calculations were performed in 70 energy groups with 24 triangular meshes in an assembly. The 4th cycle was simulated. Figure 9 shows the XY cross section of the core model used, and the position of the inner duct. The inward and outward models simulate the core when the inner duct are located near the core center and apart from the core center, respectively.

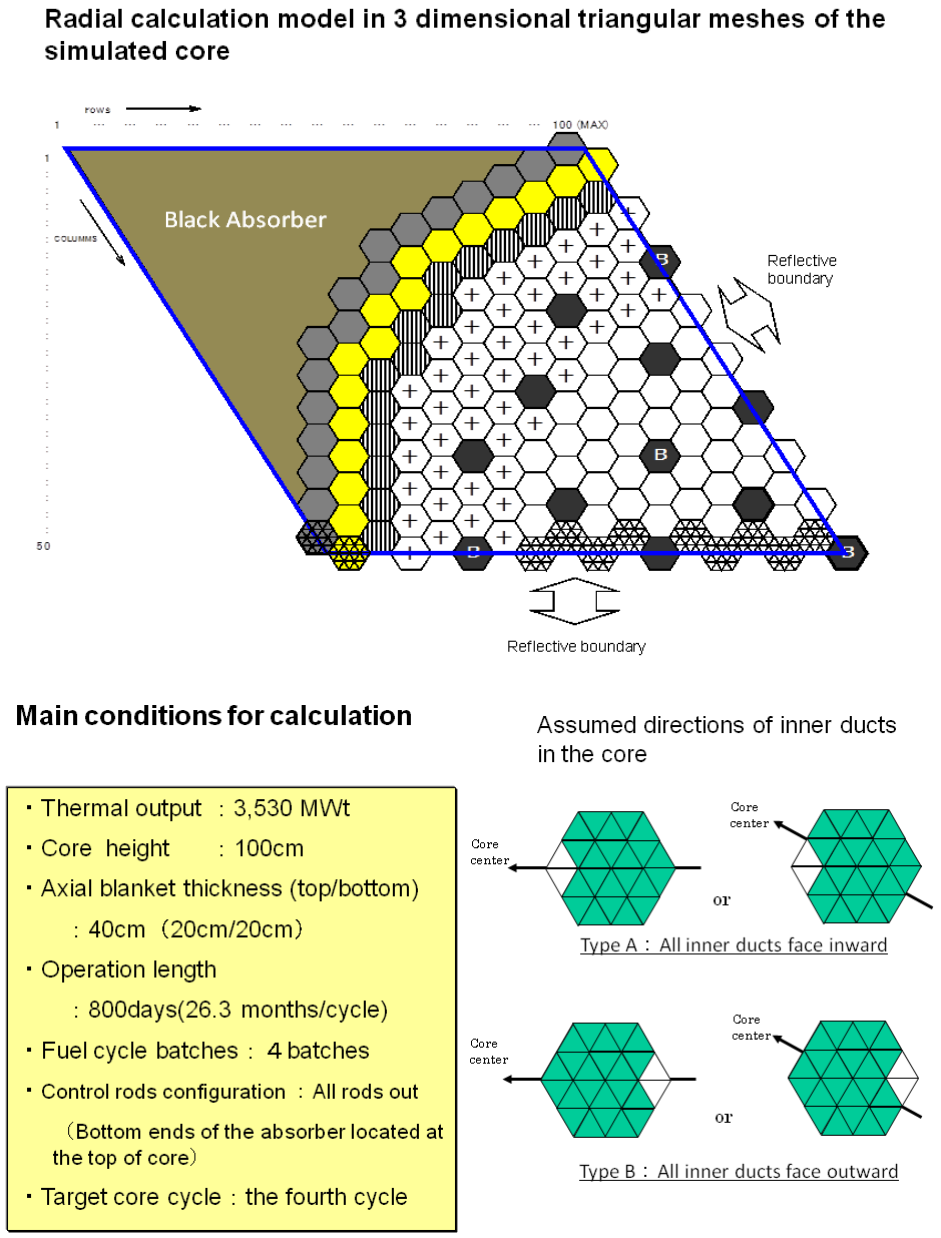

Fig. 9 XY cross section of the core model used, and the position of the inner duct

Table 2 shows the k_{eff} values at BOC (beginning of cycle), MOC (middle of cycle) and EOC (end of cycle) calculated by the inward and outward models, and the homogeneous model. In the homogeneous model, an assembly is homogenized. The difference between the inward and outward models is about 0.3% Δk. In the outward model, there is much fuel near the core center, and k_{eff} becomes larger compared to the inward model. The homogeneous model gives us about the average values of the inward and outward models. The burnup reactivity loss during one cycle calculated by the 3 models is almost the same.

Table 2 k_{eff} values of the 3D diffusion calculations for the inward and outward models of the inner duct

Cycle	k_{eff} values		
	Inward model	Outward model	Homogeneous model
BOC	1.0129	1.0162	1.0142
MOC	1.0044	1.0075	1.0055
EOC	0.9949	0.9977	0.9958
Burn up reactivity (% $\Delta k/k$)	1.79	1.82	1.82

Figure 10 compares the neutron flux distribution for the 3 models; the inward model, outward model and the homogeneous model at BOC and EOC of an equilibrium cycle. In the outward model, the flux at the core center is 30% larger than the inward model.

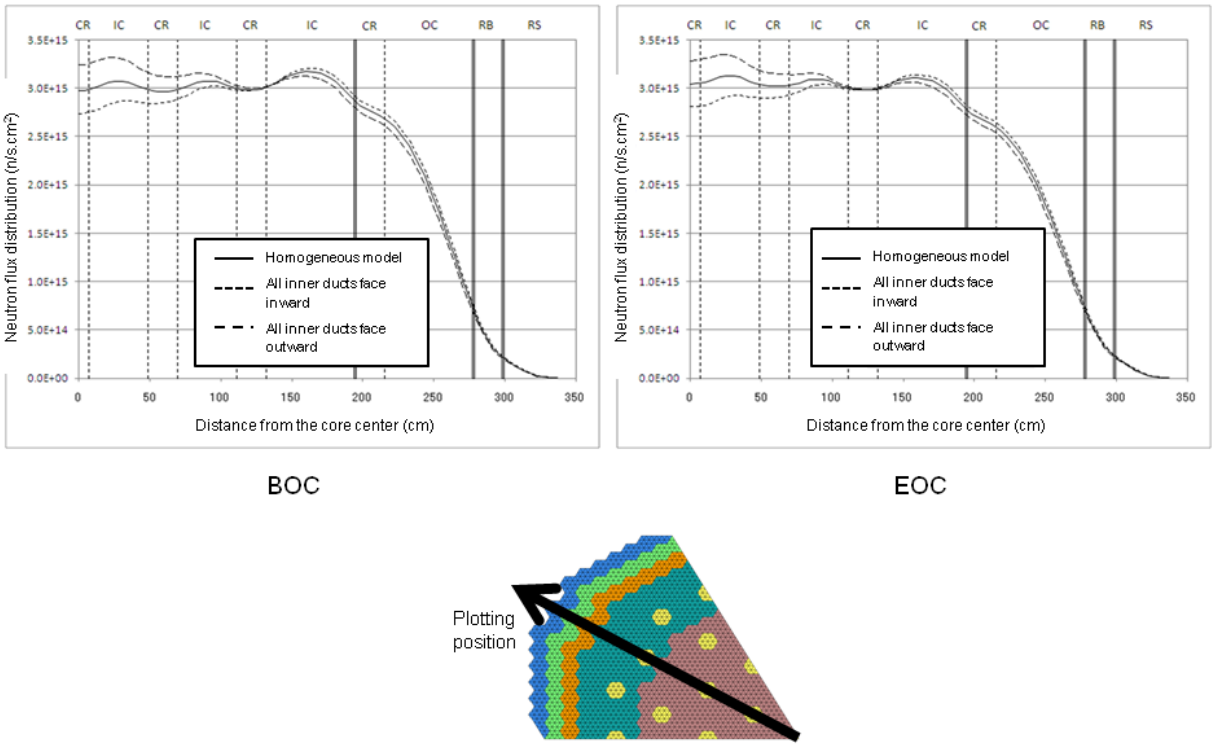

Fig. 10 Comparison of flux distributions for the 3 models

Figure 11 compares the power distributions for the 3 models at BOC and EOC. The similar trend is seen for the power distributions.

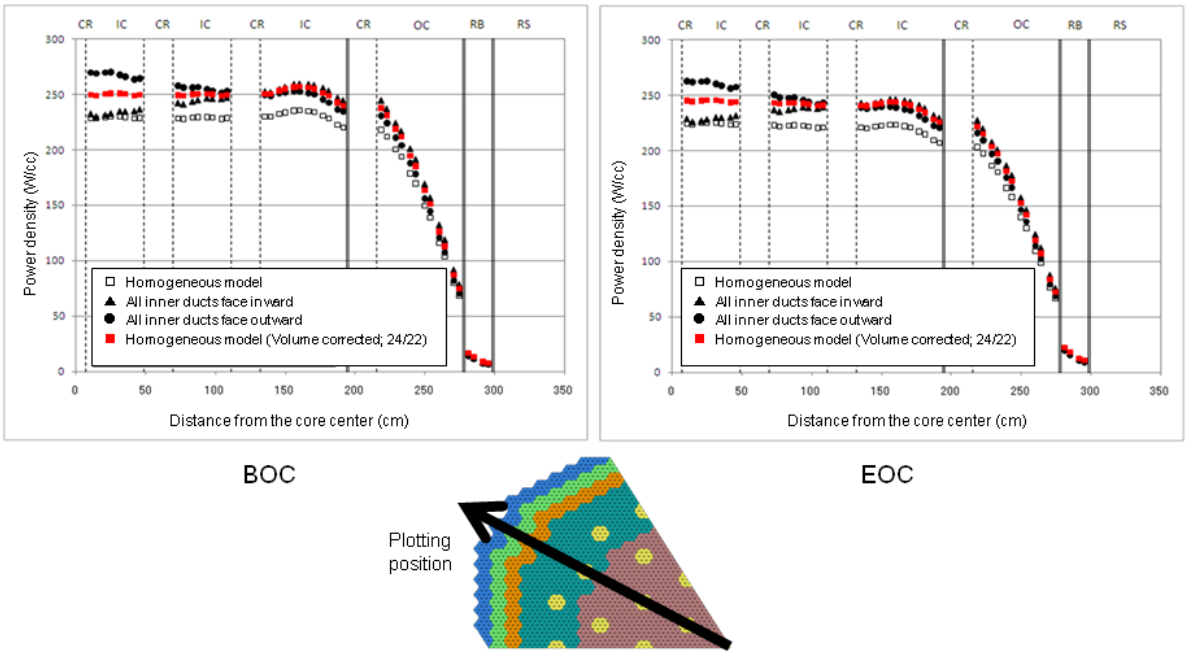

Fig. 11 Comparison of power distributions for the 3 models

4. CONCLUSIONS

The Japanese sodium-cooled fast reactor JSFR is an oxide fueled system rated at 1,500 MWe and the core is composed of large fuel assemblies with an inner duct. Thus, the assembly heterogeneity is rather strong. The effect of the heterogeneity to assembly and core characteristics has been investigated using the BACH code.

The verification test of the BACH code was performed in an infinite assembly model by comparing the k_∞ values and the reaction rate distribution calculated by BACH and the reference Monte-Carlo method. Good agreement showed the accuracy of BACH. The effect of the presence of different assemblies to effective cross sections was investigated using the seven assembly model consisting of fuel assemblies, blanket assemblies and shielding assemblies. It was found that the infinite assembly model suffices to calculate effective cross sections in 70 energy groups.

The effect of the inner duct to core characteristics was investigated by performing 3-D diffusion calculations. We used 3 models; the inward model and outward model in which the inner duct is located near the core center and apart from the core center, respectively, and the homogeneous model. The k_{eff} difference between the inward and outward models was 0.3% Δk. This difference is not negligible. Furthermore, there was a remarkable effect to flux and power distributions. Therefore, we have to pay attention in the inner duct location in fuel loading of JSFR.

ACKNOWLEDGEMENTS

Present study is the result of “Core R&D program for commercialization of the fast breeder reactor by utilizing Monju” entrusted to University of Fukui by the Ministry of Education, Culture, Sports, Science and Technology of Japan (MEXT).

REFERENCES

[1] K. Aizawa, "R&D for Fast Reactor Fuel Cycle Technologies in JNC", Proc of GLOBAL2001, No. 050, Paris, France, September (2001).

[2] K. Ito and T. Yanagisawa, "Last Twenty years Experiences with Fast Reactor in Japan", Proc. of the International Conference on Fast Reactors and Related Fuel Cycles, IAEA-CN-176-INV-07, Kyoto, Japan, December (2009).

[3] Y. Chikazawa, S. Kotake, and S. Sawada, "Comparison of Pool/Loop Configurations in the JAEA feasibility study 1999-2006", Proc. of the International Conference on Fast Reactors and Related Fuel Cycles, IAEA-CN-176-08-08, Kyoto, Japan, December (2009).

[4] Y. Sagayama, "Launch of Fast Reactor Cycle Technology Development Project in Japan", Proc. of Global 2007, Boise, USA, September (2007).

[5] H. Niwa, "Current Status and Perspective of Advanced Loop Type Fast Reactor in Fast Reactor Cycle Technology Development Project", Proc. of GLOBAL2007, Boise, USA, September (2007).

[6] Kazumi Aoto, Yoshitaka Chikazawa, Shoji Kotake, Takaya Ito, "Status of JSFR development in phase I FaCT project", In Proc. Int. Conf. GLOBAL 2011, Paper nr. 471611, December 11 – 16 2011, Makuhari, Japan (2011)

[7] Alan E. Waltar, Donald R. Todd, Pavel V. Tsvetkov, "Fast Spectrum Reactors", Springer (2011). Appendix C.

[8] G. Chiba, K. Okumura, K. Sugino, Y. Nagaya, K. Yokoyama, T. Kugo, M. Ishikawa and S. Okajima, "JENDL-4.0 Benchmarking for Fission Reactor Applications", Journal of Nuclear Science and Technology, 48-2, pp. 172-187 (2011).

[9] T. Hazama, G. Chiba, W. Sato, K. Numata, "SLAROM-UF: Ultra Fine Group Cell Calculation Code for Fast Reactor – Version 20090113", JAEA-Review 2009-003 (2009).

[10] T. Hazama, G. Chiba, K. Sugino, "Development of a Fine and Ultra-Fine Group Cell Calculation Code SLAROM-UF for Fast Reactor Analyses", Journal of Nuclear Science and Technology, 8, pp. 908 – 918 (2006).

[11] K. Tsuchihashi et.al., JAERI-1302 (1986).

[12] T. Takeda, H. Imai, T. Kitada, H. Nishi, J. Ishibashi and A. Kitano, "Development of 3-D Detailed FBR Core Calculation Method Based on Method of Characteristics", Mathematics and Computation, Supercomputing, reactor Physics and Nuclear and Biological Applications, Palais des Papes, Avignon, France, September 12-15, on CD-ROM, American Nuclear Society, LaGrange Park, IL (2005).

[13] H. Ikeda and T. Takeda, "A New Nodal Sn Transport Method for Three-Dimensional Hexagonal Geometry", Journal of Nuclear Science and Technology, Vol.31, No.6, pp.467-509 (2006).

[14] T.B. Fowler and D.R. Vondy, "CITATION," ORNL-TM-2496, Oak Rodge National laboratory(1967)

[15] H. Nakagaw, etal., Proc., Int. Top. Mtg. Advances in Reactor Physics, Mathematics and Computation, Paris, 281, (1987)

A Study on Applicability of TRACE Code for Sodium-cooled Fast Reactor

Yong-Won Choi*, Andong Shin, Moo-Hoon BAE, Namduk SUH

Korea Institute of Nuclear Safety, P.O. Box 114 Yusong, Daejeon, ROK
*Corresponding author: k722cyw@kins.re.kr

Abstract.

Since 2002, Korea Atomic Energy Research Institute (KAERI) has been developing Korean Sodium-cooled Fast Reactor. KAERI is targeting to apply the licensing of the prototype SFR by 2017. To prepare the licensing of the prototype SFR, Korea Institute of Nuclear Safety (KINS) has also started regulatory research program. For the audit calculation of sodium cooled fast reactor (SFR), TRACE code is under consideration as a tool for SFR safety analysis. Sodium related properties and models are already implemented in TRACE code. However, it is needed to evaluate applicability of TRACE code for SFR before real audit calculation. In this study, to evaluate the applicability of TRACE code, the wall to liquid metal heat transfer correlation is reviewed and its effects on the wall and fluid temperatures are studied using TRACE code and sodium properties calculated by TRACE code are compared with ANL's data.

1. Introduction

In order to prepare the licensing of a Korean prototype sodium-cooled fast reactor (SFR), regulatory audit technologies of SFR must be secured. Major characteristics of SFR being developed by KAERI are the usage of metal fuel, sodium coolant, fast reactor concept, passive system, pool type reactor and high operating temperature. Fig. 1 shows the development status of Korean SFR. [6]

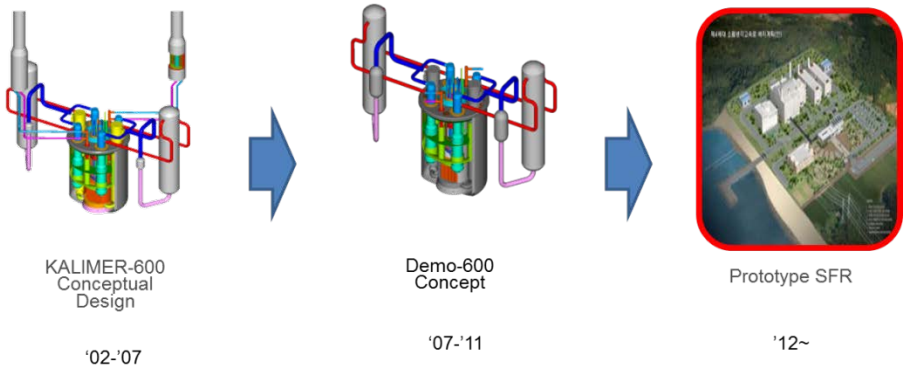

FIG. 1. The development status of Korean SFR

Because of these SFR characteristics, unique design methodology is expected to be used for licensing application instead of conventional methodologies that were used for light water reactors. Hence, the regulatory audit technology for system safety of SFR is under development in KINS since 2012 and TRACE code is under consideration as a regulatory code for SFR. However, for this, the evaluation of the applicability of TRACE for the design basis accident analysis of a sodium-cooled fast reactor is required. Therefore, in this study, a basic applicability of TRACE for SFR is evaluated. This study is composed of two parts: confirmation of correlation relating the heat transfer to liquid metal and confirmation of sodium properties of TRACE code. The heat transfer to liquid metals significantly

differs from the heat transfer to water. The main reason of this difference is that liquid metals have a very low Prandtl number. Hence, a proper selection of the correlation for heat transfer to liquid metal flow is important. Therefore, the researches for heat transfer to liquid metal were reviewed and the sensitivity analysis of the wall-to-fluid temperature difference depending on the heat transfer correlation is performed to evaluate the applicability of TRACE. Moreover, the applicability of TRACE for changes of sodium properties and equation of state are evaluated. Use of different sodium properties and equation of state can lead to different results of heat transfer calculation. Hence, the utilization of proper properties and equation of state is important. So, in this study, the evaluation of applicability on TRACE to the change of sodium properties and equation of state are performed. The results are presented in this study.

2. Evaluation of Applicablity of TRACE Code to SFR

For evaluation of applicability of TRACE code, the heat transfer correlation for SFR and fluid property evaluation mainly were analyzed. At first, the heat transfer from the surface of the fuel rod cladding to the coolant is generally governed by the heat transfer correlations. And the heat transfer to liquid metals significantly differs from the heat transfer to water due to lower Pr number in liquid metal. So, in this study, the wall to liquid metal heat transfer correlation is reviewed from previous researches. And its effects on the wall and fluid temperatures are studied using TRACE code. Secondly, we have evaluated sodium properties for single phase in TRACE code. The accuracy of the thermodynamic properties used by the TRACE code for sodium was evaluated. For this, the sodium properties evaluated by TRACE code are compared with ANL's data [4] for single phase.

2.1. Heat transfer correlation for Liquid Metal

The main reason for the difference of heat transfer between liquid metals and water is that liquid metals have a very low Prandtl number (Pr). In other words, the contribution to the total heat transfer from the thermal conductivity (compared to the contribution from the convection) is much higher for liquid metal compared to water. Hence, a proper selection of the correlation for heat transfer to liquid metal flowing is important.

2.1.1. Review of Previous Researches

In this chapter, the previous researches and thesis [1],[2],[3] for heat transfer to liquid metal were reviewed.

2.1.1.1. Heat transfer to liquid metal: Review of data and correlation for tube bundles (Konstantin Mikityuk, 2009) [1]

In Mikityuk's thesis, he reviewed various heat transfer correlation for liquid metal and proposed new correlation. The correlations reviewed by Mikityuk are as following.

- Correlations by Dwyer and Tu (1960), Friedland and Bonilla (1961)

$$Nu = 0.93 + 10.81x - 2.01x^2 + 0.0252x^{0.273}(\psi Pe)^{0.8} \quad \text{[Eq. 1]}$$

$$Nu = 7.0 + 3.8x^{1.52} + 0.027x^{0.27}(\psi Pe)^{0.8} \quad \text{[Eq. 2]}$$

- Correlation by Mareska and Dwyer (1964)

$$Nu = 0.93 + 10.81x - 2.01x^2 + 0.0252x^{0.273}(\psi Pe)^{0.8} \quad \text{[Eq. 3]}$$

- Correlation by Subbotin et al (1965)

$$Nu = 0.58\left(\frac{2\sqrt{3}}{\pi}x^2 - 1\right)^{0.55} Pe^{0.45} \quad \text{[Eq. 4]}$$

- Correlation by Ushakos et al. (1977)

$$Nu = 7.55x - \left(\frac{20}{x^{18}}\right) + \left(\frac{0.041}{x^2}\right) Pe^{0.56+0.19x} \quad \text{[Eq. 5]}$$

- Correlation by Borishanski et al. (1969)

$$Nu = 24.15\log(-8.12 + 12.76x - 3.65x^2) + 0.0174\left(1 - e^{-6(x-1)}\right)B, \quad \text{[Eq. 6]}$$

$$\text{where } B = \begin{cases} 0, & Pe < 200 \\ (Pe - 200)^{0.9}, & Pe > 200 \end{cases}$$

- Correlation by Graber and Rieger (1972)

$$Nu = 0.25 + 6.2x + (0.032x - 0.007)\,Pe^{0.8 - 0.024x} \quad \text{[Eq. 7]}$$

- Correlation by Zhukov et al. (2002)

$$Nu = 7.55x - 14x^{-5} + 0.007\,Pe^{0.64 + 0.246x} \quad \text{[Eq. 8]}$$

Where, Pe is Peclet number, x is pitch to diameter ratio and ψ means ratio of eddy diffusivity of heat to eddy diffusivity of momentum. And new correlation was suggested by Mikityuk. This correlation has been derived as a best fit to the data analyzed. Eq.9 shows new correlation suggested by Mikityuk.

- New correlation by Militiyuk (2009)

$$Nu = 0.047(1 - e^{-3.8(x-1)})(Pe^{0.77} + 250) \quad \text{[Eq. 9]}$$

For Pe number : 30-5000, pitch to diameter ratios : 1.1-1.95

And he carried out a sensitivity study of the wall-to-fluid temperature difference depending on the heat transfer correlation. To compare the predictions of different correlation in terms of the wall-to-fluid temperature drop under specific lead-cooled reactor conditions, all nine correlations were added to the TRACE code. And the clad-to-coolant temperature differences calculated by the different correlations were reviewed under the normal operation. Fig.2 shows the result of sensitivity study by Mikityuk.

FIG. 2. the result of sensitivity study by Mikityuk [1]

The interesting point is that all three correlations with the lowest RMS error, thus, Ushakov et al.(1977) and Graber and Rieger (1972) and the one derived as a part of this study; results to very similar predictions under the considered conditions.

2.1.1.2. Development of MARS/LMR and Calculation of Steady State for KALIMER-600 (KAERI, 2007) [2]

In this study, the correlations used by MARS/LMR were investigated. For this, KAERI's report [2] was reviewed. According to this report, MARS/LMR used Subbotin correlation in laminar region and modified Schad correlation in turbulent region. Specially, as dependent variable, the pitch to diameter ratio with Re, Pr number for heat transfer of liquid metal reactors in turbulent region was added to the Schad correlation. Eq.10 and Eq.11 show Subbotin and modified Schad correlations used by MARS/LMR.

- Subbotin correlation (Laminar region)

$$Nu = 5.0 + 0.025Pe^{0.8} \quad \text{[Eq. 10]}$$

- Modified Schad correlation (Turbulent region)

$$Nu = [-16.15 + 24.96\left(\frac{P}{D}\right) - 8.55(\frac{P}{D})^2\,]Pe^{0.3} \quad \text{[Eq. 11]}$$

2.1.1.3. Applicability of RELAP5-3D for Thermal-Hydraulic Analyses of a Sodium-Cooled Actinide Burner Test Reactor (INL, 2006) [3]

Lastly, we have reviewed INL's report[3]. This report reviewed heat transfer correlation used by RELAP5-3D and recommended another correlation for accuracy. At first, the default correlation for single phase heat transfer to liquid metals of RELAP5-3D is Bird correlation (Eq.12). Also this correlation is for constant wall temperature.

- Correlation by Bird et al. (1960, for constant wall temperture)

$$Nu = 5.0 + 0.025Pe^{0.8} \quad \text{[Eq. 12]}$$

By the way, Bird et al. also presented a corresponding equation for constant heat flux. The correlation is Eq.13.

- Correlation by Bird et al (1960, for constant heat flux)

$$Nu = 7.0 + 0.025Pe^{0.8} \quad \text{[Eq. 13]}$$

According to INL's report, Eq.13 is probably more applicable for the ABTR core than Eq.12 because fast reactors tend to have relatively flat power profiles. And RELAP5-3D also has an optional heat transfer correlation (Eq.14) that was developed by Westinghouse for rod bundles with liquid metals.

- Correlation by Westinghouse (Todreas and Kazimi, 1990, for 1.1<P/D<1.4 and 10≤Pe≤5000)

$$Nu = 4.0 + 0.33(\frac{P}{D})^{3.8}(\frac{Pe}{100})^{0.86} + 0.16(\frac{P}{D})^{5.0} \quad \text{[Eq. 14]}$$

However, Todreas and Kazimi who developed Westinghouse correlation showed that it agreed well with experimental data at P/D=1.15, but underestimated the Nusselt number at P/D=1.30. Also they showed that the correlation of Borishanskii et al. (1969) more accurately reflected the experimental data, particularly at larger values of P/D.

- Correlation by Borishanskii et al. (1969)

$$Nu = 24.15\log\{-8.12 + 12.76\left(\frac{P}{D}\right) - 3.65\left(\frac{P}{D}\right)^2\} \quad \text{[Eq. 15]}$$

For 1.1<P/D<1.5 and Pe≤200

$$Nu = 24.15log\{-8.12 + 12.76\left(\frac{P}{D}\right) - 3.65\left(\frac{P}{D}\right)^2\}+0.0174(1-e^{(6-\frac{6P}{D})})\{Pe - 200\}^{0.9}$$

For 200≤Pe≤2000 [Eq. 16]

2.1.2. Implementation of Heat transfer correaltion to TRACE code and Sensitivity study

The effects on the wall and fluid temperatures with change of liquid metal heat transfer correlation were studied through implementaion of each correlation to TRACE code.

In this study, 7 correlations for heat transfer of liquid metal reactors were selected from previous researches with low Root Mean Square (RMS) error and based on following reasons. Table1 shows the selected correlations and reasons for selecting.

Table 1. The selected correlations and reason for selecting

Correlation	Reason for selecting
Correlation of Mikityuk [Eq.9]	***from ref [1], Low RMS error***
Correlation of Ushakos et al [Eq.5]	***from ref [1], Low RMS error***
Correlation of Graber and Rieger [Eq.7]	***from ref [1], Low RMS error***
Correlation used by KAERI (Bird et al. 1960) [Eq.12]	***from ref [2], Used by MARS-LMR***
Correlation of Bird et al. for constant heat flux [Eq.13]	***from ref [3], Recommendation by INL***
Correlation of Westinghouse [Eq.14]	***from ref [3], Used by RELAP5-3D***
Correlation of Borishanskii et al. [Eq.15]	***from ref [3], Recommendation by INL***

And to compare the predictions of different correlation, all seven correlations were implemented to the TRACE code using TRACE Patch 3 source [5]. Fig. 3 shows TRACE code source for implementation of heat transfer correlations.

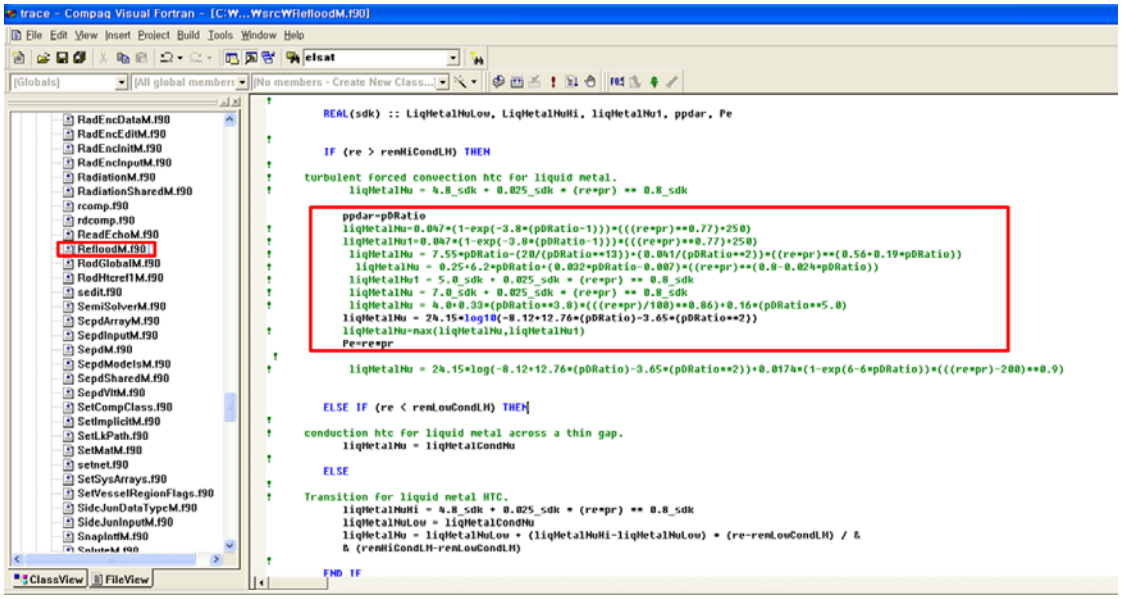

FIG. 3. TRACE code source for implementation of heat transfer correlations.

Also to evaluate the effects on the wall and fluid temperature difference depending on the heat transfer correlation, sensitivity analysis was performed using TRACE code. Fig. 4 shows node composition for sensitivity analysis. The node was composed by 1 pipe of 13cells , 1 heat structure, 1 fill, and 1 break. And as coolant, sodium was used. Also this node composion is for outer core part of DEMO 600 [6], this reactor is proven type reactor developed by KAERI. The initial conditions are as follows.

- 1 Pipe of 13 cells, 1 Heat structure, 1 fill, 1 Break
- Coolant : Na
- Initial Conditions
  - Mass flow rate (inlet) : 3466.6 kg/s (637.14K, 3.82e5Pa)
  - Outlet (Break) Condition : 693.34K, 3.82e5Pa
  - Power : 7.39693e^{8} W
  - Pe number=116.5

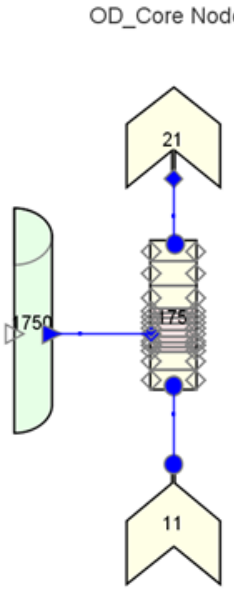

FIG. 4. Node Composition for sensitivity analysis

Fig. 5 is the result of sensitivity study. This graph shows the wall to fluid temperature difference depending on the heat transfer correlation. As shown in this graph, the Westinghouse correlation has the highest values of clad to coolant temperature difference. Also we re-arranged the results according to Nusslet number with Fig. 6. As shown in Fig. 6, depending on increase of Nusselt number, the clad to coolant temperature drops are decreased. Therefore, based on this result, implementation of the correlations into TRACE has been successfully achieved can be confirmed.

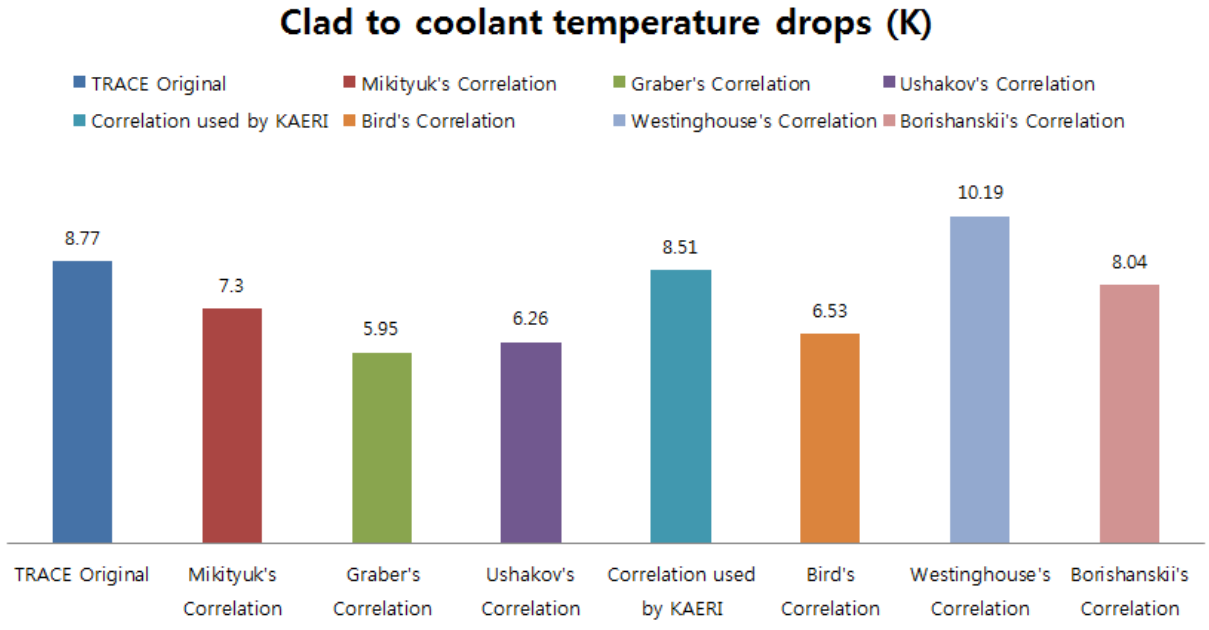

FIG. 5. Result of sensitivity study

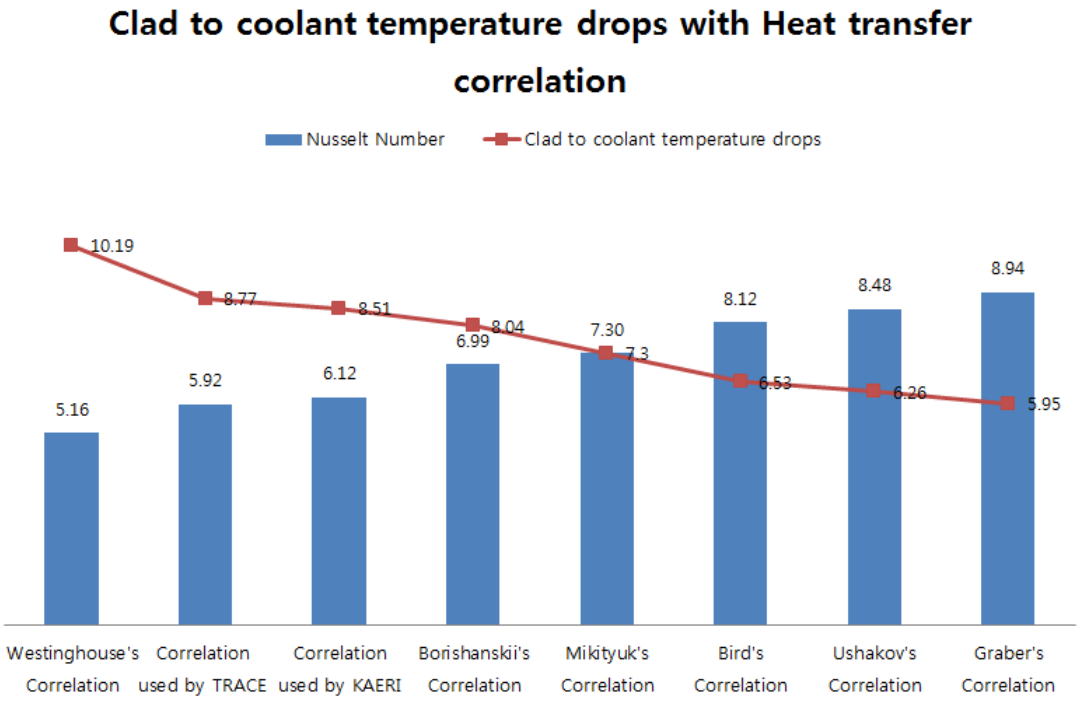

FIG. 6. Result of sensitivity study (Re-arrangement)

2.2. Fluid Property Evaluation for Single Phase

For evaluation of applicability of TRACE code to SFR, it is required to evaluate the accuracy of the thermodynamic properties used by the TRACE code for sodium For this, the sodium properties evaluated by TRACE code are compared with ANL's data [4] for single phase. Table 2 is summary of fluid property comparisons. Fluid properties with respect to these seven parameters have been evaluated. From the summary, the RMS error of each fluid property in TRACE code is very low. For example, RMS error of the liquid specific heat capacity at constant pressure is only 0.0056.

Table 2. Summary of fluid property comparisons

Parameter	N(data point)	RMS error
Enthalpy	9	**0.0603**
Liquid specific volume	9	**0.0029**
Liquid coefficient of thermal expansion	9	**0.0359**
Liquid specific heat capacity at constant pressure	10	**0.0056**
Liquid thermal conductivity	10	**0.0483**
Liquid dynamic viscosity	10	**0.0244**
Sound speed	9	**0.0305**

Fig 7. and Fig. 8 show each sodium property with temperature. Specially, Fig. 7 is the change of enthalpy of saturated liquid with temperature. From this graph, we can see that the calculated enthalpy of the liquid shows a reasonable agreement with the values reported by ANL [4]. However, in this graph we can find discrepancies that values predicted by TRACE code were lower than the values reported by ANL with about 10%. The reason is that the TRACE code uses a constant value for the

specific heat capacity at constant volume. So, the specific heat capacity at constant volume in TRACE code will be changed from constant value to value calculated by correlation are recommended.

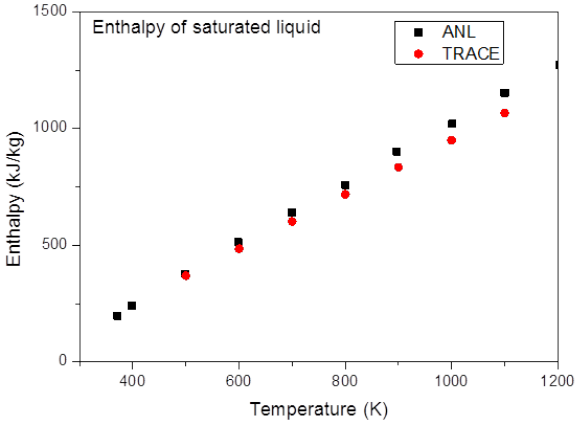

FIG. 7. Sodium property evaluation of TRACE code with ANL's data I (Enthalpy of saturated temperature)

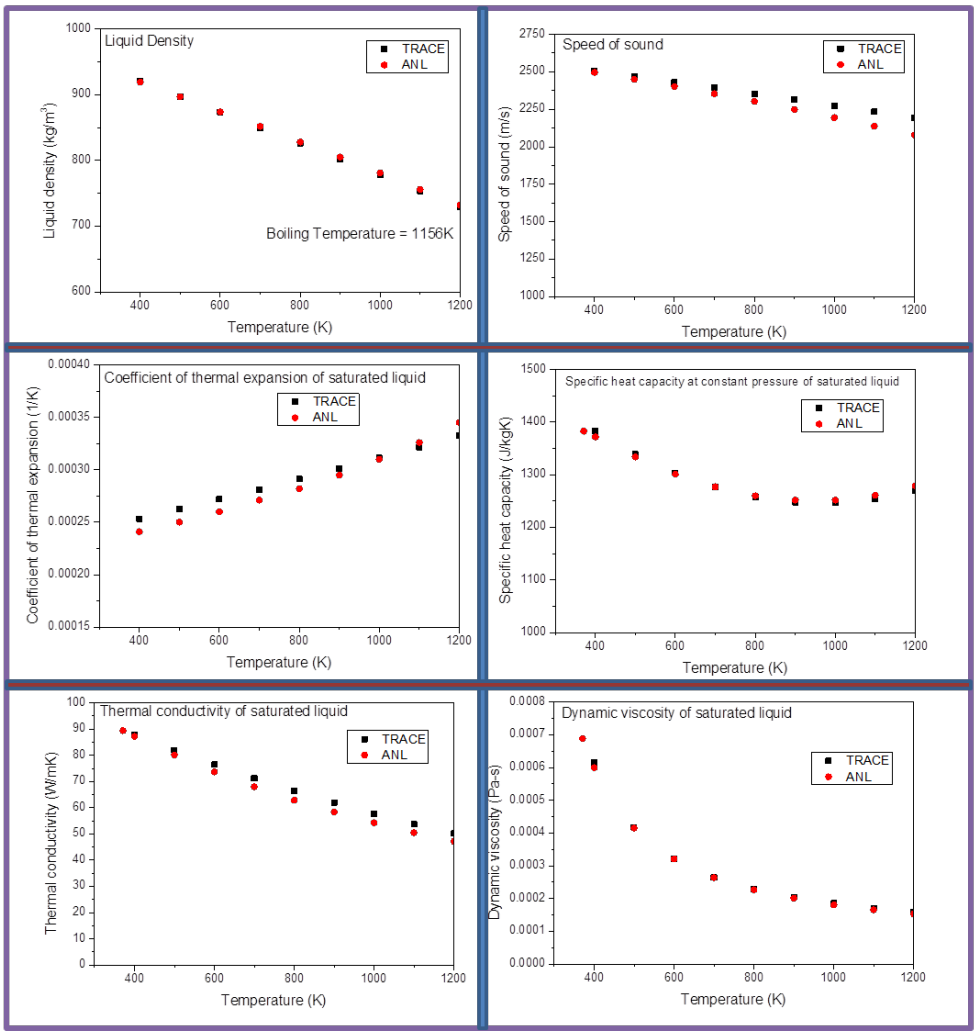

FIG. 8. Sodium property evaluation of TRACE code with ANL's data II

And Fig. 8 is the result of evaluation for liquid density, sound speed, coefficient of thermal expansion, specific heat capacity at constant pressure, thermal conductivity and dynamic viscosity. These graphs show that the results calculated by TRACE code are in reasonable agreement with the values reported by ANL. Synthetically, the sodium properties calculated by TRACE code for single phase shows a reasonable agreement with the values reported by ANL. However, a little modification for the specific heat capacity at constant volume is required. And the implementation requires only minor changes to the coding.

3. Conclusion

With development of Korean SFR, a regulatory code for SFR is required. TRACE code is proper for safety analysis of SFR, considering the efforts of NRC for development of TRACE code and excellence of TRACE. However, it is also needed to evaluate applicability of TRACE code for SFR before real audit calculation. So, in this study, liquid sodium heat transfer correlation was reviewed and implemented to TRACE code for further investigation. We checked that the heat transfer correlations for sodium coolant are implemented to TRACE code properly. Also, general sodium properties for single phase were compared with ANL's data and shows reasonable agreement. However, a little modification for the specific heat capacity at constant volume is required. Because the enthalpy predicted by TRACE code is lower than the value reported by ANL with about 10% due to use of a constant value for the specific heat capacity at constant volume in TRACE code.

REFERENCES

[1] Konstantin Mikityuk, "Heat Transfer to liquid metal: Review of data and correlations for tube bundles", Nuclear Engineering and Design, Dec. 2008.
[2] G. S. Ha, et al., "Development of MARS-LMR and Steady-State Calculation for KALIMER-600", KAERI/TR-3418/2007, May 2007.
[3] C. B. Davis, "Applicability of RELAP5-3D for Thermal-Hydraulic Analyses of a Sodium-Cooled Actinide Burner Test Reactor", INL, July 2006.
[4] J. K. Fink and L. Leibowitz, "Thermodynamic and Transport Properties of Sodium Liquid and Vapor", ANL/RE-95/2, Jan. 1995.
[5] TRACE V5.0 Theory Manuel, USNRC, 2010.
[6] G. S. Ha, et al., "Safety Evaluation for Transients of Demonstration SFR", KAERI/TR-4288/2011/, Feb. 2011.

The UNICO Multi-Physics Code to Analyze Transients in Sodium Fast Reactor

Iu. Shvetsov, Iu.M. Ashurko, I.R. Suslov, K.F. Raskach, L.M. Zabudko, E.E. Marinenko

State Scientific Center of the Russian Federation, Institute for Physics and Power Engineering named after A.I. Leypunsky, Obninsk, Russia

Abstract. The Russian multi-physics code UNICO is designed to analyze in detail the temperature and velocity fields in a fast reactor core, under transient conditions. The code is meant to make 3D coupled computation of neutronic, thermal-hydraulic and thermal-mechanic characteristics to the accuracy of each separate core fuel assembly (FA). A core thermal hydraulic model is a set of fuel assemblies installed into an inter-wrapper space. Sodium thermal hydraulics in the core inter-wrapper space is calculated in 3D approximation and the relevant equation system is solved in the triangular difference mesh. Sodium velocity and temperature distributions are taken into account inside each fuel assembly. A 3D FA model is used to calculate the temperature of fuel and steel cladding. Based on the information about the temperature of fuel, fuel element cladding and FA wrappers the core deformation behaviour is analyzed and then the respective changes in neutronic characteristics are calculated. The results of test calculations are given; they confirm the fact that insufficiently correct consideration of spatial distribution of thermal hydraulic parameters in the reactor core can cause appreciable errors (uncertainties).

1. Introduction

One of the current tendencies to improve the nuclear reactor design process consists in improving the accuracy of reactor neutronic and thermal hydraulic characteristics calculation within the framework of justification of the reactor performance and safe operation. First of all, calculation refinement allows the degree of conservatism to be decreased in the course of designing, thus, resulting in reducing unit costs of energy production.

In the conventional engineering codes commonly used in the practice of transient calculations the core is at most represented in the form of a set of a few channels (the number of fuel assemblies that form the core of a typical fast power reactor usually runs to about a few hundreds). At the same time, a point neutron kinetics model is used to calculate neutronic characteristics, in which relatively simple algebraic relations are used to estimate reactivity temperature effects. The coefficients in these relations are determined in advance and without any consideration of the real spatial structure of temperature fields in the elements of the core which varies in the course of a transient.

The “multi-physics” approach to transients modeling is considered more advanced, when there is a joint solution of a transient neutron transport equation and a set of thermal hydraulics equations. There are a number of applied problems as applied to which the multi-physics approach has its obvious advantages, for instance:

- transients that cause asymmetrical operation of heat-exchanging loops and thus, a significant azimuth asymmetry of the temperature field in the core;
- transients that cause a significant variation of coolant heating in the core, when the core thermal-mechanical distortion has a more significant effect on the reactivity;
- accidents related to the ingress of foreign substances (oil, gas) into the core;

— finally, a significant improvement of calculation accuracy can be expected for local temperature values close to the control rods and in the periphery of the core due to a more precise consideration of spatial power density distribution.

The Russian multi-physics code UNICO is meant to analyze in detail the velocity and temperature fields in the fast reactor core during transients. The code comprises 3D coupled calculation of neutronic, thermal hydraulic and thermal-mechanic characteristics with the accuracy to each separate core FA.

2. General Structure of the UNICO Code and Characteristics of its Main Modules

The code structure is given in Figure 1.

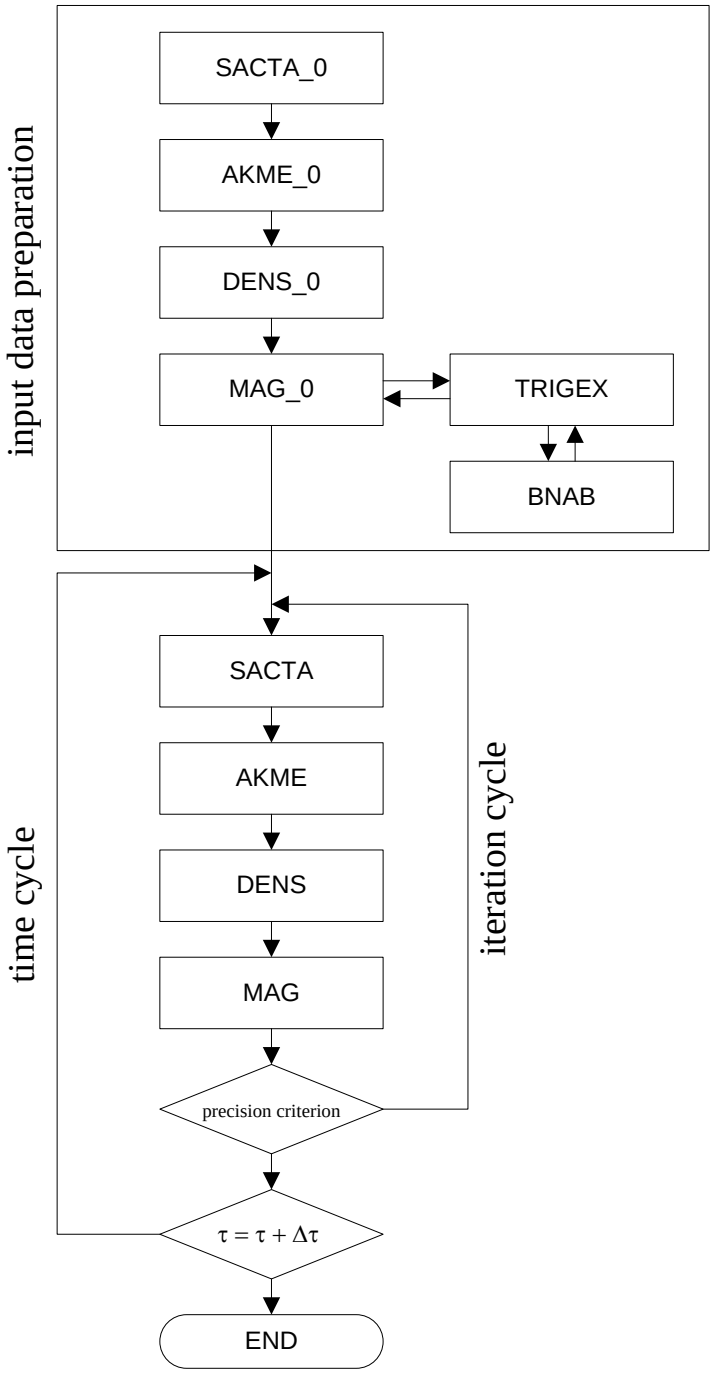

FIG. 1. UNICO general structure

The code consists of four main modules. Their functions are the following:

- «SACTA» - to calculate the coolant temperature inside the core fuel assemblies (FA) and in its inter-wrapper space (IWS), fuel temperatures and temperatures of steel elements of the structure (FA wrappers, fuel element cladding, etc.);
- «AKME» - to calculate FA wrapper bending deformation;
- «DENS» - to calculate variations in substance concentrations in the core volume due to temperature changes in components density and bending deformation of FA wrappers;
- «MAG» - to calculate spatial power density distribution for each core FA.

The calculation starts with preparation of input data and constants required for each module. At each time step, internal iterations are conducted till the preset precision criterion has been achieved; for instance, reduction of the one-iteration temperature variation, maximum in the region, to the preset limit.

2.1. SACTA Module

The SACTA module is based on the code of the same name developed earlier [1], [2]. Its principal objective consists in a rather detailed estimation of temperature distributions in the core FA wrappers and in the steel and boron shielding assemblies. It is these temperatures that finally determine their bending in steady-state and transient conditions and the corresponding changes in reactivity. Temperature distributions depend, on the one hand, on the spatial power density distribution, and, on the other hand, on the spatial sodium flow pattern both in the inter-wrapper space (IWS) and inside fuel assemblies. From outside the FA wrapper is flown about by sodium from the IWS. Its movement in the IWS is determined by the forced and natural convection and has a 3D pattern. In the SACTA module the core model is represented as a set of assemblies installed into the IWS sodium and actually the coupled problem of heat transfer between the sodium flow inside a FA and the flow in the IWS is solved. The SACTA module consists of two main parts:

- a set 3D thermal hydraulic models of assemblies (FAs, control rod assemblies, shield assemblies);
- 3D-thermal hydraulic model of inter-assembly space.

The thermal hydraulic model includes:

- quasi – 3D model of a FA wrapper;
- a simplified 3D thermal hydraulics model to calculate sodium temperature fields inside the FA;
- a thermal conductivity model of a cylindrical multi-layer element flown about by the coolant (a fuel element, a shielding element, a control rod assembly element).

The following simplifying assumptions were used for the assembly model:

- the wrapper thermal conductivity is neglected in the angular and axial directions;
- the flow inside the assembly is assumed flat-parallel and the velocity field profile in the assembly cross-section is calculated by means of a specialized “channel-by-channel” HYDRON code and is preset as input data.

2.1.1. The core assembly thermal hydraulic model

In the azimuthal direction all the assemblies are divided into 6 sectors, in the radial direction the channel division may be different for different assemblies. Figure 2 shows a 1/6 part of the computational region of fuel assembly as an example, that covers its cross-section. As it is shown in the figure, a varied pitch is used for FAs with the mesh refinement towards the periphery. This mesh is

used to determine the temperature field inside the FA via the solution of heat transfer equation and the solution of thermal conductivity equation for the wrapper. Since in the rod bundles with wire-wrapped spacers additional heat exchange related to winding can have a significant effect, as it is known from the experiments, special correlations [3] developed for this case at the IPPE are used to calculate the effective heat transfer coefficient between the channels.

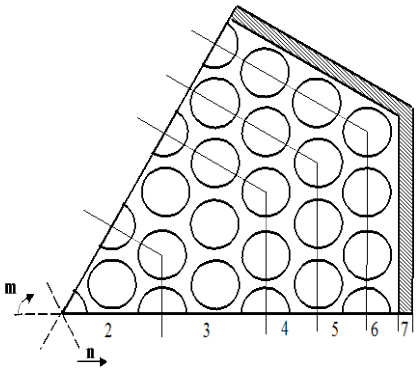

FIG. 2. 1/6 part of the computational region that models FA thermal hydraulic properties.

2.1.2. IWS thermal hydraulic model.

A hexagonal structure of the core inter-wrapper space is an important specific feature of the problem under consideration. It is practical to use approximations of initial differential set of heat – and mass - transfer equations in the triangular mesh to describe the processes in the similar structures. The triangular mesh pitch is chosen equal to half a FA pitch. Figure 3 shows a difference mesh and elementary volumes for which the difference analogues of the corresponding equations are written. The set of equations is defined within the scope of the "porous body" model, due to which it becomes possible to consider local changes in the IWS clear opening caused by thermal expansion and, thus, bending. The coolant is assumed incondensable, but its properties are temperature-dependent.

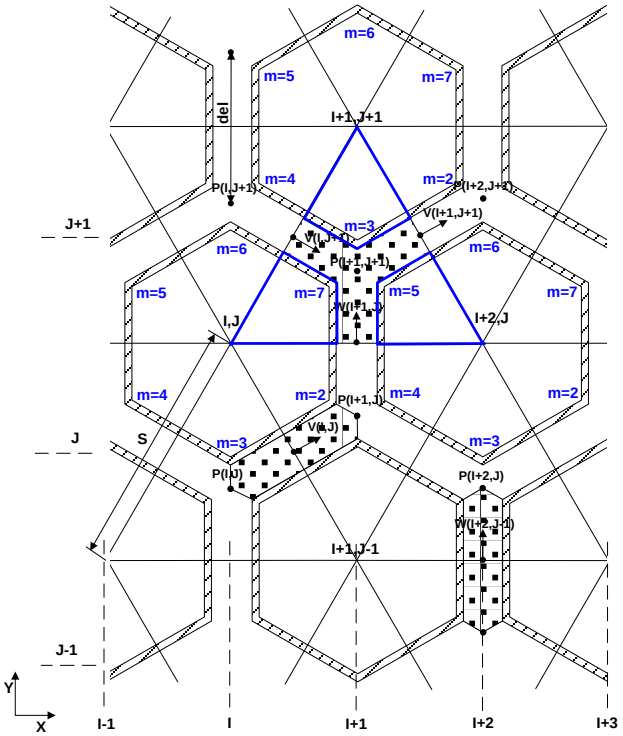

FIG. 3. Difference mesh with approximation of the set of IWS thermal hydraulics equations.

2.2. ACME Module

The ACME module [4], [5] is a 3D model of equilibrium mechanical state of fast reactor assemblies (FA, shielding and blanket assemblies, control rod assemblies) in view of the impact of non-uniform temperature and neutron fields under the conditions of non-uniform swelling and irradiation creep. The ACME code calculates FAs bowing, dilations, interactions and withdrawal forces.

The model is based on the following assumptions:

- FAs wrapper is treated as a beam hinged in the top and bottom plates of the pressure header;
- a step-by-step method is used to consider transient load conditions;
- the energy method is used to solve the model set of equations. The equilibrium position of the core assembly system is determined in compliance with the Lagrange variational principle.

The model takes into account the following effects:

- thermal and swelling dilation and bowing
- creep bulging and bowing,
- wrapper size reduction caused by creep under contact forces.

Restraints in the applicability of the model arise from the accepted simplifying assumptions. In particular, the model does not take into account:

- thermal creep of the wrapper material;
- friction forces between the assemblies and torsion;

The following values are calculated: displacement of bent axes of the core elements under transients, caused by non-uniform temperature and neutron fields; wrapper size increase due to swelling and creep under internal coolant pressure and wrapper size decrease under contact forces; contact forces that impact the core components in the course of reactor operation in steady-state and transient conditions.

In Figure 4 an illustration of calculated bent FA axes in the sodium fast reactor core of medium power at rated and rated-and-a-half coolant heating is given. As it might be expected, FA bending deformations are maximum in the core periphery, as it is the place where the maximum temperature non-uniformity is observed along the FA wrapper perimeter.

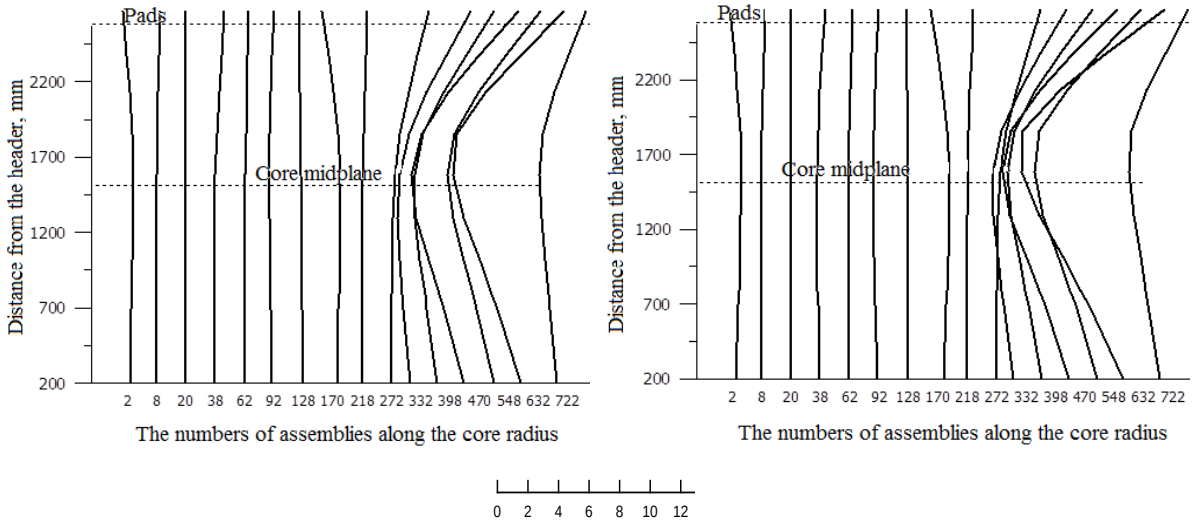

Displacement scale, mm

a) rated heating *b) rated-and-a-half heating*

FIG. 4. FA axes bending.

2.3. DENS Module

Variation of the core components temperature results in their expansion and relative displacement. The DENS module calculates the relevant changes in substance concentrations in the core volume. At the same time, the following effects are taken into account:

- changes in the bulk concentration of fuel in the cell due to temperature variations;
- changes in the bulk concentration of steel in the cell due to temperature variations (with consideration of assembly wrapper steel and cladding steel of fuel rods, absorbers and shielding elements);
- sodium displacement from the cell caused by changes in the bulk concentrations of fuel and steel in it;
- impact of the core distortion, caused by the bending deformations of FA wrappers, on reactivity.

2.4. MAG Module

The neutronic module MAG solves steady-state and time-dependent diffusion equations in HEX-Z and Δ-Z geometry. The module is based on the stand-alone code with the same name [6], [7], [8].

At preliminary step (before the dynamics calculation) a parameterized few group cross-sections library is generated with the TRIGEX package. The following algorithm is implemented. Firstly, for the given reactor model cross-sections corresponded to a reference values of parameters are calculated. The set of parameters includes fuel temperature, sodium density (separately in the core and in the sodium plenum, if it is present in the designed model) and steel temperature. Then cross-sections for maximal and minimal values of parameters are generated with extra TRIGEX runs. The TRIGEX calculation is based on the 26-group BNAB system.

When the library of parametrized cross-sections is used, the correct modeling of reactivity effects directly determined by the prepared few-group cross sections library and approximation algorithms becomes very important. In order to analyze these effects a specialized MAG_CFLIB code is used. It allows to run a sets of steady-state calculations with variation of approximation parameters and to determine the reactivity effects.

The MAG_CFLIB provides some other possibilities, in particular, to perform effective fitting of cross-sections to fit the values of reactivity effects known from the experiments or from high-precision calculations. The dynamics cross-sections are prepared directly by the CONST subroutine in the MAG module using spatial distribution of all parameters (fuel temperature, sodium density, steel temperature) in each axial layer of each FA (or in each calculation cell).

3. UNICO Code Testing Results

The UNICO code was tested under the task of calculation of the core parameters dynamics at the postulated coolant temperature variation at the core inlet. A high power sodium fast reactor was chosen as an object to be analyzed.

Two different scenarios were considered. In the first one a symmetrical (independent of the angular coordinate) change in the core inlet temperature was postulated. In particular, it was assumed that at the time moment t = 2 s the core inlet sodium temperature jumps upwards or downwards by $\delta T = 100$ °C. In figures 5 and 6 the calculated transient results are given for the case when all the components of the reactivity effect are taken into account. The observed variations of the assembly results from the “cold” sodium wave moving along the core height. In general, the tested FA power increased by 6%, when the inlet temperature went down by 100 °C.

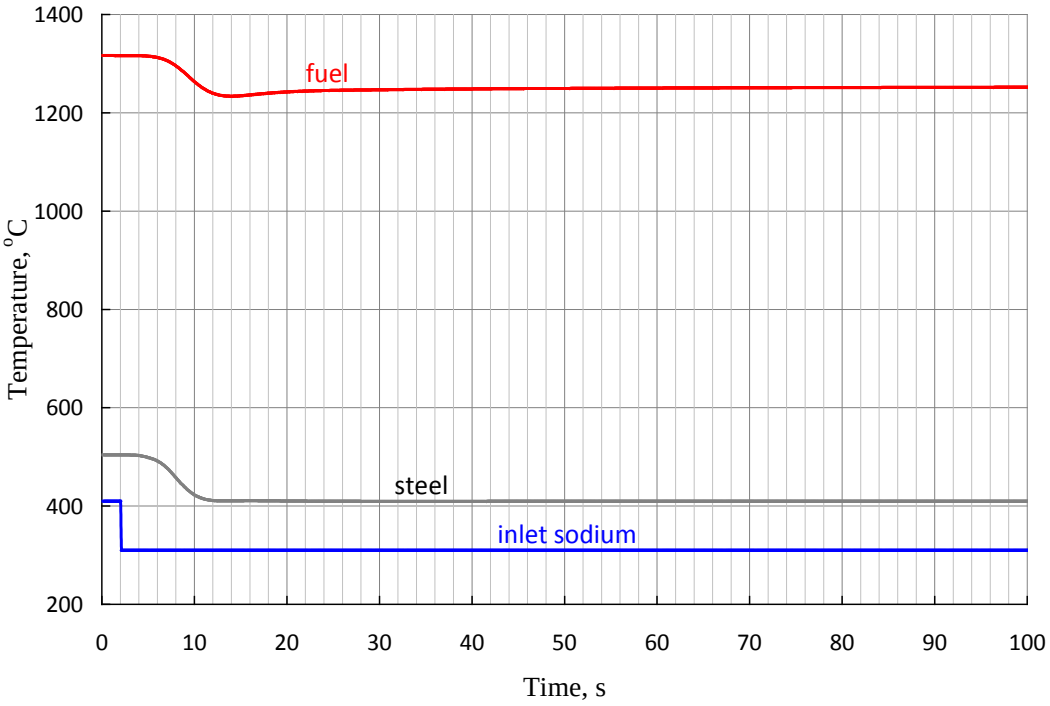

FIG. 5. Fuel, cladding, and sodium temperatures dynamics in the tested assembly.

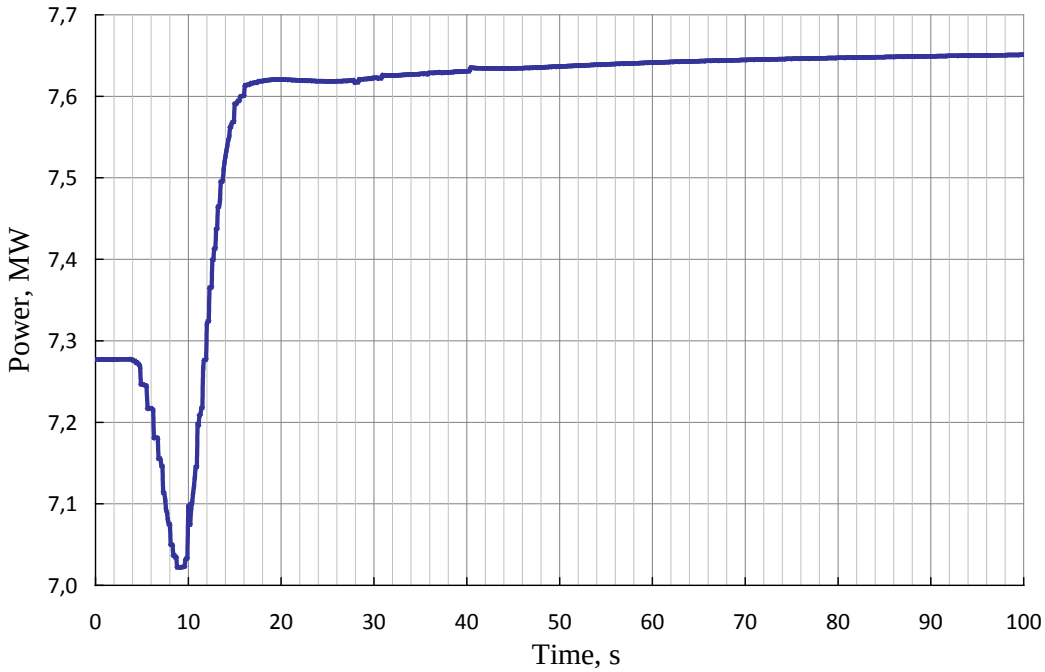

FIG. 6. Relative power dynamics in the tested assembly.

In the second scenario an angular-asymmetrical perturbation of core inlet sodium temperature was postulate. In particular, it was assumed that at the time moment t =2 s the inlet sodium temperature jumps 100 °C upwards or downwards only in a ¼ part of the core inlet cross-section, i.e. in sector X<0, Y>0. In the rest part of the inlet cross-section the sodium temperature increases in such a way

that the bulk temperature remains equal to the inlet temperature before perturbation. It is done with the purpose to only single out the effect of azimuthal non-uniformity. As the calculation has shown, the integral power increase is not high, of about 1%, at this initial perturbation. However, the local power density variations are higher and after the transient are equal to plus-minus 3% depending on the temperature perturbation sign in the sector chosen (Fig. 7).

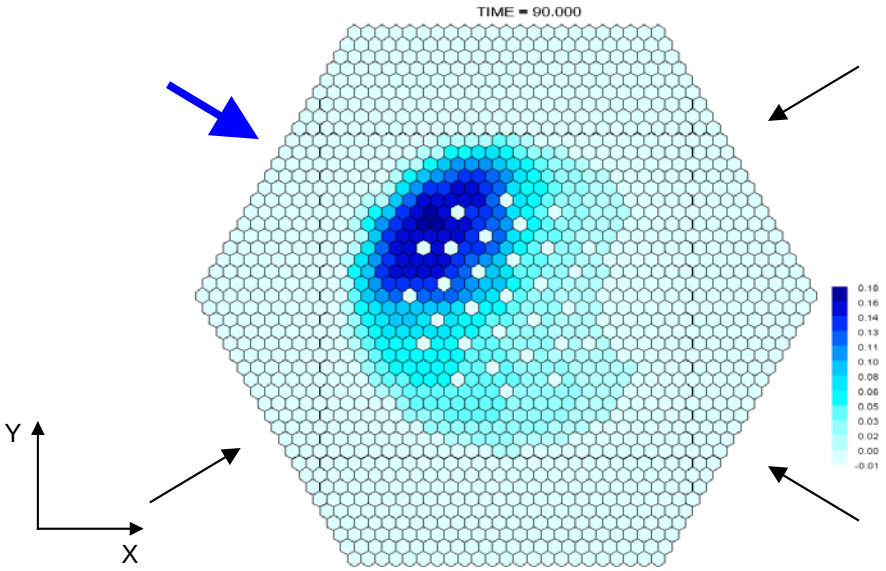

a) δT= - 100 °C

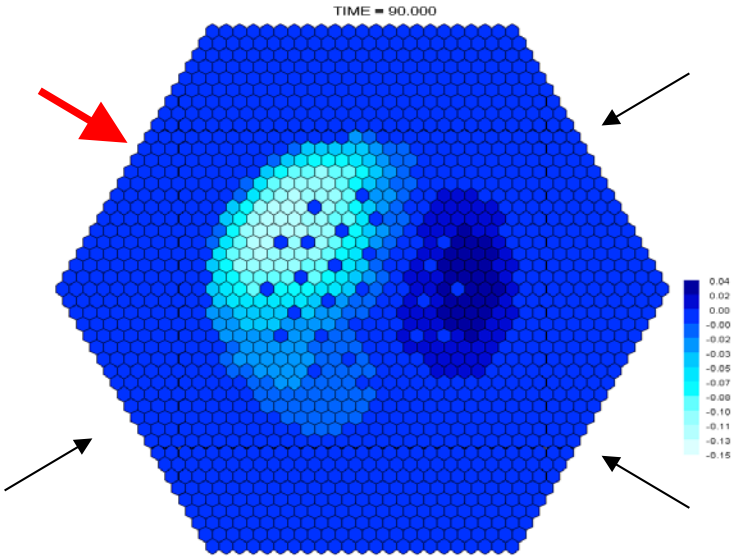

b) δT= + 100 °C

FIG. 7. Relative variation of assembly power at the core inlet temperature perturbation in section X<0, Y>0

Thus, the computational results of the test problems confirm the code operability. Further efforts are assumed to be directed to the code verification based on experimental data.

REFERENCES

[1] Yu.E. Shvetsov. The Thermal Hydraulic Code SACTA-3D for Assembly-by-Assembly Analysis of Core Temperature Conditions. Interagency Workshop: “Thermal Hydraulic Safety Aspects of Cores Cooled by Water and Liquid Metals”. Abstracts, p. 134-136, SSC RF-IPPE, Obninsk, Russia (2008).

[2] I.A. Kuznetsov, Yu.E. Shvetsov. Calculation of thermal-hydraulic parameters of fast neutron with account of inter-fuel-assembly space influence. Book of extended synopses. International meeting FR09, 7-11 of December, 2009, p.483. Kyoto, Japan. IAEA, CN-176, 2009.

[3] Analysis of thermal and hydraulic characteristics of SA of liquid metal cooled fast reactors. Edited by A.V. Zhukov. Moscow, Energoatomizdat, 1985.

[4] L.M. Zabudko, Yu.I. Likhachev, A.A. Proshkin. Performance of fast reactors fuel subassemblies, M, Enegroatomizdat, 1988.(book)

[5] Verification and validation of LMFBR static core mechanics codes. Part I. Final report of co-ordinated research program on intercomparison of LMFBR core mechanics codes. IAEA, Vienna. 1990, IWGFR/75.

[6] I.R.Suslov,D.M.Babanakov MAG – The Code for Fine Mesh VVER Calculations. Proc. of 6-th Symposium AER, 1996.

[7] I.R.Suslov A preliminary result of calculation of exrapolated-to-zero-mesh-size solution (EZMSS) of the second AER kinetic benchmark by finite-difference code MAG. Proceedings of the tenth Symposium of AER. Moscow, 2000, P.449-454.

[8] I.R.Suslov. The System of Computation Benchmarks for VVER Neutronic Calculations. Yadernaya Energetika. Izvestiya Vysshih Uchebnyh Zavedeniy №2, 2008 h. 80-89.